Ibrahim Dincer
Can Ozgur Colpan
Mehmet Akif Ezan   *Editors*

Environmentally-Benign Energy Solutions

Springer

Green Energy and Technology

Climate change, environmental impact and the limited natural resources urge scientific research and novel technical solutions. The monograph series Green Energy and Technology serves as a publishing platform for scientific and technological approaches to "green"—i.e. environmentally friendly and sustainable—technologies. While a focus lies on energy and power supply, it also covers "green" solutions in industrial engineering and engineering design. Green Energy and Technology addresses researchers, advanced students, technical consultants as well as decision makers in industries and politics. Hence, the level of presentation spans from instructional to highly technical.

Indexed in Scopus.

More information about this series at http://www.springer.com/series/8059

Ibrahim Dincer · Can Ozgur Colpan ·
Mehmet Akif Ezan

Editors

Environmentally-Benign Energy Solutions

Editors
Ibrahim Dincer
Faculty of Engineering and Applied Science
University of Ontario Institute
of Technology
Oshawa, ON, Canada

Can Ozgur Colpan
Dokuz Eylul University
Buca, Izmir, Turkey

Mehmet Akif Ezan
Faculty of Engineering, Department
of Mechanical Engineering
Dokuz Eylul University
Buca, Izmir, Turkey

Preface

Environmental problems, including air, water, and soil pollution as well as climate change, have become major concerns to many in achieving a sustainable future. Such problems need to be overcome both locally and globally through joint efforts in all sectors, including government, industry, and academia. Several abatement methods and solutions have been proposed during the past decade to reduce the negative impacts of these environmental problems and utilize energy resources more effectively. Researchers, engineers, and scientists from different disciplines have proposed new materials, designs, and modeling approaches for improving the performance of the renewable and alternative energy technologies and reducing the emissions from the conventional energy technologies in this regard.

This book consists of four key sections on *environmental issues and strategies*, *renewables and waste management*, *system analysis, modeling, and simulation*, and *alternative materials and designs* which are based on numerous invited conference papers which were selected from the 7th Global Conference on Global Warming (GCGW-2018), which was held in Izmir, Turkey, between June 24–28, 2018. This conference aimed to provide a forum for the exchange of technical information, dissemination of high-quality research results, presentation of the new policy and scientific developments, and promotion of future priorities for more sustainable development and energy security. Participants from all disciplines related to global warming (e.g., ecology, economics, education, engineering, information technology, management, natural sciences, physical sciences, and social sciences) contributed to this unique event. The recent research findings in several topics linked to global warming included sustainable transportation, hydrogen energy and fuel cells, energy storage systems, bioenergy, wastewater management, sustainable buildings, refrigeration systems, solar energy, wind energy, geothermal energy, computational fluid dynamics, energy conversion and storage, and environmental policies and strategies.

This edited book covers a number of major topics linked to global warming, including material, design, analysis, assessment, evaluation, improvement, modeling, and optimization. We hope that this edited book will provide a unique source of impact and solutions to global warming. The editors of this unique edited book

would like to warmly thank the editorial team of Springer and all contributing authors for their efforts that have made this book a true and unique source of information.

Oshawa, Canada   Dr. Ibrahim Dincer
Izmir, Turkey   Dr. Can Ozgur Colpan
Izmir, Turkey   Dr. Mehmet Akif Ezan

Contents

System Analysis, Modeling and Simulation

Environmental Issues and Strategies

Environmental Problems and Solution Proposals from the Perspective of Secondary School Students

Ebru Güller, Ayça Tokuç, Gülden Köktürk and Kutluğ Savaşır

Abstract The problems we face today such as climate change are a product of the society's current outlook on the environment. Therefore, finding and implementing a solution requires a different outlook. One approach can be a systematic change in schooling children on these concepts. This paper presents the preliminary results of a project that focuses on creating awareness on the concepts of natural and built environment and their interaction with each other. The project involved 130 students, who have different socio-economic backgrounds, academic and art achievements, from six secondary schools. One part of the project involved the determination of the most important natural and built environmental problems and solution proposals according to participants in groups consisting of four–five participants in a group setting. During this study, they discussed their problems and proposals within a wider setting including other participants and supervising academicians. This chapter groups and discusses these problems and solution proposals. The results indicate that most of the children are aware of many problems such as environmental pollution, which was the most discussed topic. Yet, some important problems were not mentioned, and energy management was the least detailed and understood issue in the discussions.

Keywords Children and architecture · Nature · Environmental awareness · Environmental perception · Natural environment · Built environment

1 Introduction

Sustainable development and climate change are interrelated topics that define complex systems with lots of variables. Research shows these problems to be mostly human induced [1, 2]. These problems are the product of the society's current outlook on the environment as a source that can be utilized as necessary. Since the

E. Güller (✉) · A. Tokuç · K. Savaşır
Department of Archtecture, Dokuz Eylul University, Izmir, Turkey
e-mail: ebru.guller@deu.edu.tr

G. Köktürk
Department of Electrics and Electronics Engineering, Dokuz Eylul University, Izmir, Turkey

3

efficiency of any system involving humans depends on human behaviour, the solution also requires a different outlook. It is vital to create collective action in society to spread a sustainable lifestyle. Studies to better understand the pro-environmental behaviours of humans are numerous, yet the factors that predict engagement with nature are not universal. Personal factors include childhood experience, knowledge and education, personality and self-construal, sense of control, values, political views and worldviews, goals, felt responsibility, cognitive biases, place attachment, age, gender and chosen activities [3]. Social factors include religion, urban versus rural residence, norms, social class, proximity to problem sites and cultural and ethnic variations [3].

A number of theories and policies to change the interaction of humans with their environment were proposed [4, 5]. In this context, one of the ways to create individual engagement with energy issues is communication through messages and education. Scannel and Gifford [6] interviewed 324 residents living in three regions of British Columbia to learn their perceptions on climate change problem, the strength of their attachment to their local area and their personal engagement with the issue. They found place attachment, receiving the local message and gender (female) as significant predictors of engagement. Bertolotti and Catellani [7] researched the framing of climate-related policies by policy-makers and the media, either in terms of achievement of potential gains or in terms of avoidance of potential losses. They carried out two studies on university students and found that a message is more persuasive when its outcome and the regulatory concerns underlying the policy "fit". More specifically, while a message on "growing" of renewable energy resources was more persuasive when the content emphasized positive "growing", conversely a message on "avoiding" greenhouse gas emissions was more persuasive when it was framed in terms of "avoiding" negative environmental consequences. They also found that the focus of the participant played an important role in persuasiveness. While these studies focus on intentions and self-reported behaviour, Kormos and Gifford [8] did a meta-analysis and found that the correlation between intentions and actual behaviour was 0.45, which corresponded to about 20% of overlap between them. Psychology-based interventions on how to use a building can modify behaviour and cause high reductions in energy consumption, for instance Matthies et al. calculated there can be decreases of 43% electricity and 10% heating energy consumption after such interventions [9].

Education is an effective way to increase pro-environmental human behaviour. The positive interventions can be supported and sustained [10], or critical thinking on climate change issues can be assimilated into the education environment [11] in a structured setting such as a school. Stanford University studied the effects of environmental education on school children all the way from infant school to high school. After researching more than a hundred scientific studies published on the subject from 1994 to 2013 by other institutions, they concluded that 83% of school children improved their ecological behaviour and 98% scored better in other subjects such as maths and science [12]. However, when we look at Turkey's conditions, neither the living environment nor the present education system encourages more ecological behaviour [13, 14]. Since an educational environment that will enable children

to experience sustainability is lacking in Turkey, it can be said that the education programme is also insufficient in environmental education [15]. Knowledge transfer, which is restricted to science courses, does not question the relationship between the natural and the built environment. Although the courses on environmental education, which are included in the current primary education programme as an elective course, provide a certain amount of knowledge in this field, unfortunately, they do not fully realize their goals in an education model mainly based on memorization. Therefore, there is a need for interactive, practical studies based on active education to raise environmental awareness amongst children [14, 16]. Many actors including Children Universities, the Chambers of Architects, and people studying this field, carry out independent studies in order to establish the relationship between children and the environment. For example, TMMOB Chamber of Architects of Ankara Branch started Child and Architecture studies in 2002. Numerous professional volunteers (architects and volunteers from other professions) have been searching for what can be done in order to instil environmental awareness in various primary and secondary schools through focused workshops [17]. The Scientific and Technological Research Council of Turkey (TUBITAK) supports the projects to be organized in order to raise awareness on nature, science and technology within the 4004 Education in Nature and Science Schools Program since 2007 [18].

Creating awareness by gaining an environmentally sensitive mindset via education would be more efficient beginning from children's age, when a person learns values and behaviours. Knowledge of nature, examination of the interaction between natural and built environment and obtaining environmental consciousness from a young age are significant in terms of internalizing sustainability as a lifestyle [19, 20]. For this purpose, the perception of natural and built environment of secondary school students in terms of environmental education and awareness is the topic of this chapter. Research shows that the individual's current attitudes and knowledge play an important role in framing the message [3]; therefore, this study proposes and presents the results of this project that aims to increase environmental consciousness, gain knowledge about nature and love of nature. "The Nature and Architecture for Little Designers Project" is designed with this consciousness and consists of various activities that complement each other. It is mainly set up as nine activities: "First Meeting", "Pre-test", "Environmental Awareness", "We are Inspired by Nature", "What Kind of a Creature?", "Nature and Architecture", "What Kind of a Nest?", "Presentations of the Groups" and "Post-test". Six workshops realized in 2017–2018 on the relationship between nature and architecture by experimenting with differing design themes in secondary schools. The education took place from 9:00 to 17:00, and the students talked, thought and gained knowledge about the environment; they worked in groups and designed their own living beings and home for these beings during the workshops. The project was supported and continued for the next year, and its results are being evaluated, when this chapter is being written. The context of this chapter is the results of the "Environmental Awareness" activity of the project held in 2017–2018. It details and discusses the results from 130 participants.

2 Environmental Awareness

The environmental awareness activity aimed to create awareness on the concepts of natural and built environment and their interaction with each other in a school setting. It was designed to detect current environmental problems through the eyes of secondary school students and to increase environmental awareness and sensitivity to the environment while developing solution proposals for these problems.

The participants were students in the 5th, 6th and 7th grades of secondary schools, which corresponds to 10–12 years old, within the Konak Municipality of Izmir. In line with the decision of the project team, the six schools in the project were determined by the İzmir Konak District National Education Directorate, three of them in the socio-economically disadvantaged regions and the other three in the advantageous regions. So, the students would be selected from different socio-economic backgrounds. There were seven students from each grade with a balance between genders. The students took permission from their parents to participate in the project. In this context, children with high academic achievements, strong artistic aspects, ability in different fields, cognitive and creative aspects were included in the study. In addition, children, who were dominant or silent or noncompliant in the classroom, who had concentration problems, etc., were also included in the project. The research involved 130 students in total from six secondary schools.

Environmental awareness activity of the Nature and Architecture for Little Designers project is designed as an interactive, participatory and productive programme. The activity was carried out in six schools on different days. In each school, students formed groups of 4–5 people around one desk. The groups consisted of at least one student from each grade with a balance between genders. The activity was done in an interactive workshop format and took about an hour. The students talked, thought and gained knowledge about the environment, and they worked in groups during the activity.

Firstly, the topics of the natural environment, built environment, architecture and sustainability were conversed with the students through questions and answers. Students evaluated the current environmental problems and their solutions in groups. They discussed amongst their groups to identify the most significant five environmental issues and solutions and wrote these issues on coloured post-its—pink for problems and green for solution proposals. The questions discussed included how to ensure harmony and balance between nature and architecture. The comments and suggestions of the children, the main problems that the children decided on as a group and their suggestions for solutions are collected in the panel by means of post-its. Later, the groups talked about the issues they identified and why they thought these were significant in an interactive question–answer session (Fig. 1). Meanwhile, the keywords of the groups were aggregated on the board.

Fig. 1 Pink and green post-its (left); a group discussing their post-its with the other participants (right)

3   Results

Within the scope of this study, perception of natural environment and existing environmental problems were determined from the viewpoint of the students via group studies and conversations. An interactive environment has been created, where the keywords for natural and built environment are discussed by the group. Headings and solutions are combined when sharing between groups. Mutual information sharing is provided.

In the environmental awareness activity, the groups discussed and listed the most significant problems they perceived in the balance between the built and the natural environment and generated solutions for these problems. These problems and solutions are given and grouped in Tables 1, 2, 3, 4, 5, 6, 7, 8 and 9. According to the group discussions, nine main headings of problems are determined. These are environmental pollution, failure to protect the natural environment, harming animals, global warming, energy management, insufficient recycling, problems of built environment, traffic problems and negative effects of technology. There were 43 subheadings of problems in total. A total of 155 solutions were proposed and aggregated into 111 solutions.

Table 1 Problems determined by students: environmental pollution

Problems		Solution proposals	Kazım Karabekir MS.	Misak-ı Milli MS.	Necati Bey MS.	Rıdvan Nafiz Edgüer MS.	Güzelyalı MS.	26 Ağustos MS.
Environmental pollution	Throwing trash to the environment	Surveys should generate awareness				☐		
		People and community should gain awareness	☐				☐	☐
		Children should be made conscious; they should study about environment pollution at school		☐				☐
		Recycling consciousness should be created			☐			
		More garbage containers should be put on the streets	☐				☐	

(continued)

Table 1 (continued)

Problems	Solution proposals	Kazım Karabekir MS.	Misak-ı Milli MS.	Necati Bey MS.	Rıdvan Nafiz Edgüer MS.	Güzelyalı MS.	26 Ağustos MS.
	Increasing recycling containers	☐					
	Waste substances should not be thrown to the nature						☐
	Garbage refinement factories	☐					
	Not leaving trash in picnic areas, putting waste bins in forests to raise consciousness		☐	☐	☐		☐
Polluted air from factories and waste harm the nature	Mandatory factory audits. This audit aims to make sure that factory waste is not disposed of in nature					☐	

Table 1 (continued)

Problems	Solution proposals	Kazım Karabekir MS.	Misak-ı Millî MS.	Necati Bey MS.	Rıdvan Nafiz Edgüer MS.	Güzelyalı MS.	26 Ağustos MS.
	Giving special education to factories				☐		
	Installing filters on factory chimneys	☐	☐	☐	☐		
Water pollution	Not spilling oil from ships and factories to pollute water					☐	
	Installing filters to sinks					☐	
	Water treatment plants	☐					
	Dirty water should not flow to lakes and rivers from sewer pipes		☐				☐

Table 1 (continued)

Problems	Solution proposals	Kazım Karabekir MS.	Misak-ı Millî MS.	Necati Bey MS.	Rıdvan Nafiz Edgüer MS.	Güzelyalı MS.	26 Ağustos MS.
Air pollution, ozone layer depletion	Installing filters in factory pipes and building chimneys		☐	☐	☐	☐	☐
	Usage of public transit vehicles instead of cars			☐	☐		
	Hybrid cars			☐			
	Planting trees			☐			
	Using natural gas instead of coal		☐		☐		
	Decreasing the use of stoves		☐				

Table 1 (continued)

Problems	Solution proposals	Kazım Karabekir MS.	Misak-ı Millî MS.	Necati Bey MS.	Rıdvan Nafiz Edgüer MS.	Güzelyalı MS.	26 Ağustos MS.
	To inform factory directorships and to work for prevention of smoke damage to the environment						☐
Sea pollution	Making people conscious about sea pollution				☐		
	Waste reduction; not disposing of waste into the sea			☐	☐		☐
	Waste recycling instead of throwing waste into the sea	☐		☐			

(continued)

Table 1 (continued)

Problems	Solution proposals	Kazım Karabekir MS.	Misak-ı Millî MS.	Necati Bey MS.	Rıdvan Nafiz Edgüer MS.	Güzelyalı MS.	26 Ağustos MS.
People being unconscious and insensitive against the environment and nature, polluting nature	We must not pour oil into sinks			□			
	Placing waste bins in shores	□		□			
	Raising awareness to not pour factory wastes into the sea		□				
	Installing filters to factory chimneys			□			
	Increasing the use of public transport			□			
	Recycling instead of burying batteries to ground			□			

Table 1 (continued)

Problems	Solution proposals	Kazım Karabekir MS.	Misak-ı Millî MS.	Necati Bey MS.	Rıdvan Nafiz Edgüer MS.	Güzelyalı MS.	26 Ağustos MS.
	Giving conferences in various places					□	
	Establishing nature education schools to increase awareness in people				□		
	Being sensitive to nature and not polluting environment	□					
	Not building homes on forests, not cutting trees, not eliminating oxygen	□					

(continued)

Table 1 (continued)

Problems	Solution proposals	Kazım Karabekir MS.	Misak-ı Millî MS.	Necati Bey MS.	Rıdvan Nafiz Edgüer MS.	Güzelyalı MS.	26 Ağustos MS.
Cause fires due to glasses thrown on the floor	Writing articles, preparing posters to educate people				□		
	We can write survey questions on trash cans so that people can throw into the waste bins according to directions		□				

Table 2 Problems determined by students: failure to protect the natural environment

Problems		Solution proposals	Kazım Karabekir MS.	Misak-ı Millî MS.	Necati Bey MS.	Rıdvan Nafiz Edgüer MS.	Güzelyalı MS.	26 Ağustos MS.
Failure to protect the natural environment	Lack of adequate forests	Projects to increase forests should be made attractive					☐	
	Trees are inadequate, plants and trees to be insufficient	Trees should be planted instead of buildings that are not in use by anyone or unfinished					☐	
		Plant and tree planting can solve both the air pollution and the lack of greenery					☐	

(continued)

Table 2 (continued)

Problems	Solution proposals	Kazım Karabekir MS.	Misak-ı Milli MS.	Necati Bey MS.	Rıdvan Nafiz Edgüer MS.	Güzelyalı MS.	26 Ağustos MS.
	Project like tree planting in schools at October should be done				☐	☐	
	Two trees should be planted for each new building. There should be more green space instead of buildings						☐
Unconscious tree cutting	To raise awareness of people to prevent the cutting of trees, especially young trees		☐		☐		

(continued)

Table 2 (continued)

Problems	Solution proposals	Kazım Karabekir MS.	Misak-ı Milli MS.	Necati Bey MS.	Rıdvan Nafiz Edgüer MS.	Güzelyalı MS.	26 Ağustos MS.
	To warn people, to plant seedlings	☐					
	We need to do less damage to natural structures in our environment			☐			
	People should understand the importance of trees, should not either cut or allow others to cut trees			☐			☐
	Plant more trees in place of cut ones	☐	☐	☐	☐		☐
	We should recycle paper or similar materials		☐				

(continued)

Table 2 (continued)

Problems	Solution proposals	Kazım Karabekir MS.	Misak-ı Milli MS.	Necati Bey MS.	Rıdvan Nafiz Edgüer MS.	Güzelyalı MS.	26 Ağustos MS.
	Should prevent the use of natural gas		□				
	Should use the pens and papers economically, prohibit cutting trees for pleasure and punish persons who cut trees arbitrarily						□
Destroying trees cause oxygen deficiency, decreasing of trees and oxygen	Should work on planting trees	□	□				
	Renewable energy sources should be increased		□				

Table 2 (continued)

Problems	Solution proposals	Kazım Karabekir MS.	Misak-ı Millî MS.	Necati Bey MS.	Rıdvan Nafiz Edgüer MS.	Güzelyalı MS.	26 Ağustos MS.
Failure to protect the green areas	Teach people to ensure that they do not harm green areas						□
Failure to protect the seas	Should not spill bunker fuel to sea, and rescue of marine animals from garbage			□			
Disrespect for natural beauty	Organize congresses in the name of nature and to raise awareness		□				
Forest fires	Should teach people in a cautious way				□		

(continued)

Table 2 (continued)

Problems	Solution proposals	Kazım Karabekir MS.	Misak-ı Millî MS.	Necati Bey MS.	Rıdvan Nafiz Edgüer MS.	Güzelyalı MS.	26 Ağustos MS.
	People on picnics should make sure to extinguish the fires they kindle				☐		
	Picnic areas should be limited		☐				
	Robots should protect forests, people should not throw combustible materials to the nature						☐
	Should punish people who leave braziers burning						☐

Table 2 (continued)

Problems	Solution proposals	Kazım Karabekir MS.	Misak-ı Millî MS.	Necati Bey MS.	Rıdvan Nafiz Edgüer MS.	Güzelyalı MS.	26 Ağustos MS.
	Not leaving glass bottles in the forest, we should not throw cigarette butts on the ground, we should not throw brazier ashes into the forest						□
	Warning signs should be present in picnic areas, etc.						□
Natural disasters	Plant trees on mountains and steep slopes against landslides						□

Table 3 Problems determined by students: harming animals

Problems		Solution proposals	Kazım Karabekir MS.	Misak-ı Milli MS.	Necati Bey MS.	Rıdvan Nafiz Edgüer MS.	Güzelyalı MS.	26 Ağustos MS.
Harming animals	Unconsciousness, poaching, hunting of animals in danger of extinction	Increasing animal shelters and animal-related associations					☐	
		Protecting animals in danger of extinction		☐	☐	☐		☐
		Giving regulatory fines of high amounts				☐		
		Installing cameras in forests and forming security units				☐		
		Prohibiting hunting				☐		

Table 3 (continued)

Problems	Solution proposals	Kazım Karabekir MS.	Misak-ı Millî MS.	Necati Bey MS.	Rıdvan Nafiz Edgüer MS.	Güzelyalı MS.	26 Ağustos MS.
	Not hunting of animals in danger of extinction and paying attention to hunting bans			□			
	Not going to circuses			□			
Violence to animals, harming animals	Special shelters can be created for animals				□		
	To give punishments				□	□	□
Not caring for animals adequately	Increasing people's awareness of animals					□	
Not protecting animals adequately	To open additional animal shelters				□		
	Closing zoos		□				

Table 4 Problems determined by students: global warming

Problems		Solution proposals	Kazım Karabekir MS.	Misak-ı Milli MS.	Necati Bey MS.	Rıdvan Nafiz Edgüer MS.	Güzelyalı MS.	26 Ağustos MS.
Global warming	Global warming	Should use the electrical vehicles				□		
		Should use less non-renewable energy resources			□			
	Melting of glaciers	Discontinue excessive use of natural and human resources					□	
	Ozone layer puncture due to aerosol used in deodorants	Use of public transportation instead of cars, filter installation to factories					□	
		We need to reduce the usage of deodorants and perfumes			□		□	

Table 5 Problems determined by students: energy management

Problems		Solution proposals	Kazım Karabekir MS.	Misak-ı Millî MS.	Necati Bey MS.	Rıdvan Nafiz Edgüer MS.	Güzelyalı MS.	26 Ağustos MS.
Energy management	Not using renewable energy	To use renewable energy resources such as solar panels and wind turbines	☐		☐		☐	
	Unnecessary consumption of fossil fuels	Usage of renewable energy resources				☐		

Table 6 Problems determined by students: insufficient recycling

Problems	Solution proposals	Kazım Karabekir MS.	Misak-ı Milli MS.	Necati Bey MS.	Rıdvan Nafiz Edgüer MS.	Güzelyalı MS.	26 Ağustos MS.
Insufficient recycling	We need to increase recycling bins, they should be established in central places					□	
	Should be made the things with recycling	□		□			
Spread of waste that can be recycled into nature	Usage of recycling bins	□					
Throwing spent batteries to garbage	Batteries must be disposed of in the recycle bin instead of garbage			□		□	
Waste of paper and using paper unconsciously	We can dispose of used paper in recycling bins					□	
	Let's plant many trees						□

Table 7 Problems determined by students: problems of built environment

Problems		Solution proposals	Kazım Karabekir MS.	Misak-ı Millî MS.	Necati Bey MS.	Rıdvan Nafiz Edgüer MS.	Güzelyalı MS.	26 Ağustos MS.
Problems of built environment	Distorted and irregular urbanization	Restricting population		☐				
		Constructing buildings in a nature-friendly way					☐	
		Doing architectural drawing according to a configuration			☐			
		Urban transformation					☐	

Table 7 (continued)

Problems	Solution proposals	Kazım Karabekir MS.	Misak-ı Milli MS.	Necati Bey MS.	Rıdvan Nafiz Edgüer MS.	Güzelyalı MS.	26 Ağustos MS.
	Man-made buildings and concrete should remain at a certain level, should not destroy forests to build, the government should not let building a house in the forest	☐		☐			
	Building with nature (It's more sensible to plant trees instead of cutting trees)			☐			

(continued)

Table 7 (continued)

Problems		Solution proposals	Kazım Karabekir MS.	Misak-ı Millî MS.	Necati Bey MS.	Rıdvan Nafiz Edgüer MS.	Güzelyalı MS.	26 Ağustos MS.
		Not make more buildings than the population		☐				
	Increasing immigration	Limiting and decreasing immigration					☐	
	Too many detached houses destroy nature	In order to prevent excessive urbanization, higher buildings (two-, three-floor apartment buildings) can be built instead of detached houses			☐		☐	

(continued)

Table 7 (continued)

Problems	Solution proposals	Kazım Karabekir MS.	Misak-ı Milli MS.	Necati Bey MS.	Rıdvan Nafiz Edgüer MS.	Güzelyalı MS.	26 Ağustos MS.
Increasing natural elements in buildings instead of creating concrete jungles	Deconstruction and greening of some lands, building detached houses with gardens	□	□				
Skyscrapers are unsuitable to human nature	More detached houses	□					
Factory	Being environmentally friendly factories				□		
Noise pollution	Coating houses with styrofoam insulation	□					
Non-earthquake-resistant areas	To make houses and buildings earthquake resistant, not building houses on earthquake fault lines						□

Table 8 Problems determined by students: traffic problems

Problems		Solution proposals	Kazım Karabekir MS.	Misak-ı Milli MS.	Necati Bey MS.	Rıdvan Nafiz Edgüer MS.	Güzelyalı MS.	26 Ağustos MS.
Traffic problems	Excessive use of cars	Public transportation instead of individual cars can be used to limit excessive use of cars	☐					
	Exhaust gas, fossil fuels using in cars are polluting nature	Electrical cars can be used		☐				
		To use public transportation	☐		☐			

Table 9 Problems determined by students: negative effects of technology

Problems		Solution proposals	Kazım Karabekir MS.	Misak-ı Milli MS.	Necati Bey MS.	Rıdvan Nafiz Edgüer MS.	Güzelyalı MS.	26 Ağustos MS.
Negative effects of technology	Environmental damage from technology	Making technology less harmful					□	
	Release of radioactive materials to nature	Reducing the usage of technological tools and working to reduce their damages					□	
	Nuclear wastes	Not making nuclear weapons, most people in Chernobyl died	□					
	Base stations, radiation emitted from base stations	Removing base stations	□					
		Base stations spread electromagnetic signals, transmitting signals with Bluetooth instead of base stations		□				

4 Discussion

Environmental education starts at home and relates to the near environment, and the behaviour and attitude towards the environment are shaped by this education [21]. Improving the perception of the environment and gaining sensitivity can only be possible with a participatory, holistic, questioning, and nature-centred education [22]. Although the information is being transferred via common education methods in our schools, the observation, research, inquiry, co-thinking and designing and the experience parts are still missing. Therefore, it is recommended that an interactive course method should be considered in environmental education. Although many social responsibility projects, extracurricular activities and conferences are being held in this area, reviewing the current course method is a priority. The way it is taught in the classroom should be adapted to the age and the nature of children and should also be practical, entertaining and funny besides theory. The lessons in school instruction can also be combined with outdoor experiential learning [23]. There are plenty of activities that can be done in the school garden or in a playground or nearby park. While observing plants, trees and birds, they can also find out environmental problems such as pollution, gas emissions and recycling.

In the following table (Table 10), under how many subheadings that the nine questions which came forward in the environmental awareness study are detailed and the total number of solution proposals produced by the students for the relevant topics are seen. As it is clear in the table, in the children's environmental awareness study, while identifying problems and solution suggestions in the titles of environmental pollution, protection of the natural environment, harming animals and issues with the built environment have reached a certain level; in the titles of global warming,

Table 10 Preliminary results of the environmental awareness activity [24]

Main headings	Subheadings	Number of solutions for subheadings
Environmental pollution	7	38
Protection of the natural environment	9	26
Harming animals	4	12
Global warming	3	5
Energy management	2	2
Not enough recycling	4	6
Issues with the built environment	8	14
Traffic issues	2	3
Negative effects of technology	4	5
Total	43	111

energy management, recycling, traffic and negative effects of technology, with a limited knowledge, creative solutions have been found to remain limited. Problems such as light pollution and user requirements have never been mentioned. This is may be due to both the lack of knowledge and the awareness level of the families which are the reflection of the society, not being enough mature. Students being affected by the environment they live in have been manifested in problem determinations; for example, the students living in the landslide area have developed creative solutions to this problem. Especially in two schools in the socio-economically disadvantaged region, the issues of energy management, recycling and negative effects of technology have never even been on the agenda. It has been observed that these children have limited access to technology. In addition, recycling is not done in their homes and schools. The fact that individuals do not have sufficient knowledge about environmental problems means that the negative attitudes and behaviours that cause these problems will persist. With this awareness, it is necessary to systematize environmental education, which is inevitable in today's world, from pre-school to university process. Especially in the process of primary education, it must be considered with a holistic approach integrated in each course, and in order to achieve this, first of all, the level of the awareness of teachers should be increased. In this way, environmental problems can be overcome by developing the appropriate attitude and behaviour for a sustainable life.

5   Conclusion

The "Nature and Architecture for Little Designers Project" proposed and evaluated a new interactive education model. The aims of the project included educating children on protection of natural resources, being respectful to all living beings, living with nature, avoiding unnecessary consumption, creating behaviour patterns in harmony with nature, having a critical outlook to nature and its problems and gaining positive behaviours inductive to nature. In the environmental awareness activity, the environmental problems are seen from children's point of view, and they tried to create their own solutions in groups. During the group presentations, all the solutions were discussed with the other groups and the trainers. This active education improved the knowledge and awareness of the students in the subject. The effect of this activity can be seen in the following activities, in which they incorporated their knowledge and awareness, so that living being and nest designs were affected. For instance, one group that proposed the reduction of carbon dioxide content in the air as a solution for climate change designed a living being that breathes in carbon dioxide and breathes out oxygen.

According to the analysis results of the environmental awareness activity, it was found that children are in fact aware of many problems. For instance, environmental pollution issue was discussed in detail. Yet, some important problems regarding the built environment were not mentioned including if the environment is suitable for children, handicapped or elderly people. Although the current system does good job

of teaching the students love of nature, there is a discrepancy between thought and action so it is worthwhile to research how and when children start to lose their love of nature or start to behave irresponsibly. Therefore, it is important to follow and evaluate the effectiveness of the awareness training given as well as the continuing such trainings. Having good role models or being role models themselves would be the focus in the future studies.

Consequently, the Nature and Architecture for Little Designers Project was a process, in which students noticed their responsibilities towards nature, while having fun in various activities that brought them together with nature. In this process, the participants observed and interpreted nature, explored their own creativity with individual and group work, and developed their two- and three-dimensional expression skills. Environmental awareness was one of the important preparatory activities which provided a base to reach these aims. When we evaluate these kind of studies, in particular for Turkey, this study is valuable especially as a practice that will support current education system. It is also important for children to meet with scientists and professionals in this field as individuals, to establish a relationship between university and child, and important for children to explore their own skills and perhaps their interests. Taking children's ideas into account, discussing with them and making decisions will increase the sense of self-confidence and value in children, and provide environmental awareness and responsibility to the adults of the future.

References

1. Marten GG (2010) Human ecology: basic concepts for sustainable development. Routledge
2. Intergovernmental Panel on Climate Change (IPCC) (2014) Climate change 2013: the physical science basis. In: Stocker TF et al. (eds) Contribution of working group I to the fifth assessment report of the intergovernmental panel on climate change. Cambridge University Press, Cambridge, UK
3. Gifford R, Nilsson A (2014) Personal and social factors that influence pro-environmental concern and behaviour: a review. Int J Psychol 49(3):141–157
4. Swim JK, Stern PC, Doherty T, Clayton S, Reser JP, Weber EU, Howard GS (2011) Psychology's contributions to understanding and addressing global climate change mitigation and adaptation. Am Psychol 66:241–250
5. Larrosa C, Carrasco LR, Milner-Gulland EJ (2016) Unintended feedbacks: challenges and opportunities for improving conservation effectiveness. Conserv Lett 9(5):316–326
6. Scannell L, Gifford R (2013) Personally relevant climate change: the role of place attachment and local versus global message framing in engagement. Environ Behav 45(1):60–85
7. Bertolotti M, Catellani P (2014) Effects of message framing in policy communication on climate change. Euro J Soc Psychol 44(5):474–486
8. Kormos C, Gifford R (2014) The validity of self-report measures of proenvironmental behavior: a meta-analytic review. J Environ Psychol 40:359–371

9. Matthies E, Kastner I, Klesse A, Wagner HJ (2011) High reduction potentials for energy user behavior in public buildings: how much can psychology-based interventions achieve? J Environ Stud Sci 1(3):241
10. Coffey JH, Horner RH (2012) The sustainability of school wide positive behavior interventions and supports. Except Child 78(4):407–422
11. Wals AE, Jickling B (2002) Sustainability in higher education: from doublethink and newspeak to critical thinking and meaningful learning. Int J Sustain High Educ 3(3):221–232
12. Iberdrola SA (2019) Environmental education for kids. Benefits of environmental education in kids. https://www.iberdrola.com/top-stories/environment/enviromental-education-for-kids. Site accessed 15 May 2019
13. Köse Ç, Barkul Ö (2012) A Study on the problems of the implementation of project type primary structures. Megaron 7(2):94–102
14. Kılınç A (2010) Can project-based learning close the gap? Turkish student teachers and proenviromental behaviours. Int J Environ ve Sci Educ 5(4):495–509
15. Yoleri S (2012) Children and the environment: creating environmental awareness among preschool children. J Buca Fac Educ 34:100–111
16. Genç M (2015) The project-based learning approach in environmental education. Int Res Geographical Environ Educ 24(2):105–117. https://doi.org/10.1080/10382046.2014.993169
17. TMMOB Chamber of Architects Ankara Branch (2009) Çocuk ve mimarlık toplumsal eğitim modeli. TMMOB, Ankara
18. The Scientific and Technological Research Council of Turkey (2019) http://tubitak.gov.tr/en/announcements/4004-education-in-nature-and-science-schools-program-call-results. Site accessed 15 May 2019
19. Tokuç A, Güller E (2009) A Bridge to the future with sustainable toy design. International Congress Architecture & Children Papers, 26–33
20. De Leeuw A, Valois P, Ajzen I, Schmidt P (2015) Using the theory of planned behavior to identify key beliefs underlying pro-environmental behavior in high-school students: implications for educational interventions. J Environ Psychol 42:128–138
21. Çabuk B, Karacaolu ÖC (2003) Üniversite öğrencilerinin çevre duyarlılıklarının incelenmesi. Ankara University J Fac Educ Sci 36(1–2):189–198
22. Ozaner S (2004) Çevre sorunlarına çağdaş yaklaşımlar, 1. Baskı, Beta Basım Yayım Dağıtım, İstanbul
23. Cole LB, Hamilton EM (2019) Can a green school building teach? A pre- and post-occupancy evaluation of a teaching green school building. Environ Behavior. https://doi.org/10.1177/0013916518825283
24. Guller E, Tokuç A, Kokturk G, Savaşır K (2018) The nature and architecture for little designers project. Project Report

Biochar Application for Greenhouse Gases Mitigation

Özlem Demir

Abstract Agricultural applications significantly increase the atmospheric emissions of non-CO_2 greenhouse gases, nitrogen oxides and methane. Therefore, studies on new strategies to reduce greenhouse gases are become more important. Biochar produced from different organic materials as a by-product of slow pyrolysis and/or rapid pyrolysis, gasification or combustion processes can be used for carbon sequestration, greenhouse gases mitigation, soil improvement, waste management and wastewater treatment. Biochar application is promising technology as a climate change mitigation tool to reduce carbon emissions from soils. The agricultural implementation of biochar may have an important effect on global warming reduction by greenhouse gas emission mitigation and carbon sequestration. Besides, biochar can support the improvement of soil structure and productivity and increase the yields in agriculture. In this study, biochar application and especially the potential for reducing greenhouse gas emissions are reviewed. Further research is necessary to realize the effective mechanisms in biochar application to reduce greenhouse gas emissions.

Keywords Biochar · Greenhouse gases mitigation · Carbon sequestration · Soil amendment

1   Introduction

Sludge management aims to eliminate waste in an environmentally friendly manner. However, it includes system management based on many environmental factors considering secondary pollutants such as greenhouse gas (GHG) emissions and heavy metal contamination. Available sludge disposal methods have some challenges. High GHG emissions generated by landfill contribute to global warming significantly [1–3]. Landfill causes emissions such as leachate transfer water, air and soil, while land application leads to heavy metals [4] and permanent organics contamination [5]. In the sludge management, composting is an applicable technology in terms of cost

Ö. Demir (✉)
Engineering Faculty, Environmental Engineering Department,
Harran University, Şanlıurfa, Turkey
e-mail: odemir@harran.edu.tr

and economy, providing organic fertilizers via recycling of organic nutrients [1–3]. However, the nitrogen loss and GHG emissions are the drawbacks of the composting [2, 6–8]. Therefore, the composting with other agents such as sawdust, agricultural wastes and alkaline mineral amendments has been investigated in order to reduce the GHG emissions [2, 9–11]. Wastewater treatment sludge is a renewable energy source because it is produced in a very high quantity and has high energy content. Many technologies, such as anaerobic digestion and incineration, can convert wastewater sludge into the usable energy [5]. As an alternative of fossil fuel, biogas produces during the anaerobic digestion of sludge to produce heat and electricity; however, heating and mixing require additional energy for the digestion. Besides, the anaerobic digestion can convert only approximately 40–50% of the organic matter into biogas with conventional digesters [5]. In the incineration process, sludge volume can be reduced and energy recovery in the form of heat and electricity is possible. The requirement for expensive technologies to reduce emissions from incineration plants is one of the drawbacks of incineration process [12]. Therefore, alternative technologies are required for energy recovery from sludge [5].

According to the International Panel on Climate Change (IPCC), greenhouse gases (GHGs) that are responsible for climate change and have a higher global warming effect than carbon dioxide (CO_2) emissions [13] are methane (CH_4) and nitrogen oxide (N_2O) [2]. Biochar amendment has been proposed as an efficient technology for adsorption of GHGs, ammonia and extractable ammonia [11, 13, 14] increasing the organic matter degradation [15, 16]. It offers some advantages such as low cost, environmentally friendly, high stability and porosity and easy operation [1, 2, 14]. The characteristics of biochar vary according to the operating parameters of the raw material and pyrolysis [17, 18]. Pyrolysis is widely used method in order to convert the sludge to energy by a thermo-chemical process. The degradation of organic material considering high temperature and an oxygen-free condition is occurred in the pyrolysis. Bio-oil, gas and biochar are produced with pyrolysis of sewage sludge [5, 19, 20]. Under oxygen-limited conditions, biomass is transformed into biochar, syngas and bio-oil as a result of thermo-chemical reactions [18]. Biochar yields are tightly based on the temperature of pyrolysis, heating rate, characteristics of raw material used biochar production, particle size and operating conditions. Biochar with high efficiency can be obtained by slow pyrolysis. Agricultural implementation of biochar has an important impact in reducing GHG emissions and global warming by atmospheric carbon through sequestering to soil [21]. Biochar can be used for carbon sequestration with the retention of carbon fraction in a stabilized form. Soil amendment in order to improve soil quality is another application field of biochar with less environmental and health risks. So, the crop yield also increases [22]. Additionally, it can be used as an adsorbent for water purification or GHGs mitigation [5].

In this study, the application fields of biochar are mentioned, and especially, the applications of biochar for GHGs mitigation are evaluated.

2 Biochar

Biochar is a product of pyrolysis with a carbon-rich content (65–90%), numerous pores and oxygen functional groups and large surface area [21] and produces as results of the thermochemical conversion of a biomass in oxygen-limited conditions [18] within a closed system with high carbon contents [23]. Biochar can be produced with several production techniques especially pyrolysis. Organic matters are pyrolyzed at low temperatures (<700 °C) and under the absence or scarce of O_2 and then carbonaceous part named as biochar is remained [24, 25]. The operated condition of pyrolysis categorizes it as fast and slow pyrolysis. In the slow pyrolysis, it can be said that the retention time varies from minutes to hours at temperature <450 °C, while the fast pyrolysis occurs with a few seconds at higher temperature 500 °C [26]. These operating conditions also affect the characterization of biochar [27]. The other factors affected to the biochar are heating rate, pressure, pyrolysis reactor type and inert carrier gas [17]. The co-products of biochar production are bio-oil and gases that are used to generate energy [26]. The influence of feedstock biomass should be considered as an important parameter affected the physical and chemical characteristics of biochar [28].

Biochar can be used for soil improvement, waste management, reduction in greenhouse gases and energy production in a cost-effective and environmentally friendly manner [29]. Some advantages such as GHG emissions mitigation, improvement of soil fertility and increment in crop production for agricultural purposes have drawn an increasing attention day by day [24, 30–32].

2.1 Biochar Production

Biochar as by-products of slow pyrolysis product and/or rapid pyrolysis, gasification or combustion has become an attractive issue in the sludge management due to the variety of biomass used in the pyrolysis [21]. The production methods of biochar are evaluated in the following section.

2.1.1 Pyrolysis

The thermal decomposition of organic matters under oxygen-limited conditions at 300–900 °C is pyrolysis process. The cellulose, hemicellulose and lignin are degraded to solid, liquid and gaseous products. The solid products are called as char, while liquid products are as bio-oil. Syngas is the gaseous mixture of carbon monoxide (CO), carbon dioxide (CO_2), hydrogen (H_2) and C_1-C_2 hydrocarbons [29].

2.1.2   Gasification

Air, steam, oxygen, CO or gas mixtures play an important role as an agent for the conversion of biomass in the gasification process. The products of gasification as a thermochemical partial oxidation process are gaseous liquid and solid products [29].

2.1.3   Hydrothermal Carbonization

Pyrolysis and gasification processes are operated efficiently with high yields if the biomass has low moisture content. However, when the biomass has high moisture contents, in order to obtain high yield product, a drying stage is required. Therefore, pyrolysis and gasification processes are insufficient when the high moisture content of biomass is concerned. Hydrothermal processes are the promising technology to present a technology to operate with high moisture content biomass. In the hydrothermal carbonization process, in order to characterize the products, temperature, pressure, retention time and the water/biomass ratio should be considered [29]. Hydrothermal process is conducted in a heated reactor contained biomass and water mixture for the stabilization. In hydrothermal carbonization, the mixture of biomass and water is poured into the closed reactor, and then, the pressure and temperature are increased. Biochar, bio-oil and biogas are obtained in the hydrothermal process below 250 °C, 50–400 °C and above 400 °C, respectively [29].

2.1.4   Other Technologies

The other technologies used for the thermochemical conversion of biomass are flash carbonization [33–35] and torrefaction [36–38]. Flash carbonization is a process which can convert the biomass to gas-state and solid-state products at high pressure (1–2 MPa). Temperature of 300–600 °C and a reaction time of 30 min were used for this process [29]. The other technology is a thermal pretreatment application of biomass under slow heating rate. It can be referred to as mild pyrolysis. Removal of moisture, carbon dioxide and oxygen in biomass can be achieved at 200–300 °C by torrefaction. Through different decomposition reactions of torrefaction, biochar with higher calorific and heating values can be obtained [39].

2.2   *Biochar Characteristics*

The heating rate, the maximum process temperature pressure and the reaction time are the most important factors of the pyrolysis process [40]. Other parameters affecting biochar characteristics and properties are reaction vessel design, inert carrier gas flow rate and the treatment of post-pyrolysis [28].

2.2.1 Sludge-Derived Biochar Characteristics

Biochars can be obtained through different processes considering the type of biomass and pyrolysis operational conditions. Nevertheless, sludge-derived biochar has drawn more attention in recent years. Even though most applications of sludge-derived biochar are still in infancy, biochar has already been applied for soil amendment, catalysis and water purification [41]. Some studies related to the sludge-derived biochar are summarized in Table 1.

Sludge contains nitrogen, phosphorus, organic matter and valuable nutrients that can improve the physical characteristics of the soil and increase the yield of the product. However, heavy metals and other toxic and hazardous materials can change soil-plant systems and affect human health. Pyrolysis of wastewater sludge has been reported to be beneficial in conventional incineration processes. Studies on fuel, nutrient recovery and control of heavy metal emissions are generally involved, but the effects of biochar obtained from sludge are rarely investigated [53].

Zielinska et al. [54] evaluated the characteristics of biochar from different wastewater sludge at different temperatures. The sludge samples were pyrolyzed in a laboratory furnace at 500, 600 and 700 °C in an oxygen-limited environment. According to the results, it can be concluded that a reduction in biochar yield due to volatilization of some organic fractions was observed with increasing pyrolysis temperature. The pH of the biochar produced at low temperatures is generally neutral but depends on the pH of the sludge. High pyrolysis temperatures (≥ 550 °C) support the formation of biochar with alkaline pH. At the neutral pH, the biochar produced from sludge at high temperatures (up to 700 °C) was characterized by pH ranging from 12.0 to 13.0 [54].

According to the studies in the literature, there is a significant effect of sludge pyrolysis on carbon percentage changes, but there is a decrease compared to the original raw material. Carbon losses are due to increased volatility of carbon during pyrolysis [41]. In addition, the increases in pyrolysis temperature result in an increase in ash content compared to feedstock. This increase is an expected condition for sewage sludge biochar since the non-volatile minerals form the ash and removal of volatile organic decomposition products occur. As a result of the complexity of sewage sludge, mineral fractions of both sludge and sludge-derived biochar are higher than other feedstocks. The estimation of ash content in biochar is very difficult. Additionally, the content of ash in biochar will be higher than in the feedstock, regardless of the temperature. It can be said that an increase in temperature will bring an increase in the percentage of ash in case of sewage sludge pyrolysis [55]. When the sludge is pyrolyzed at temperatures above 600 °C, the phosphorus content of sewage sludge become more concentrated. Since phosphorus content of the sludge is related to the inorganic fraction of the sludge. On the other hand, the volatilization of nitrogen during pyrolysis through the loss of the NH_4–N and NO_3–N fractions result in decrease of sludge nitrogen content when process temperature is increased. As a result of sludge pyrolysis, surface area of sludge was developed varying between 6 to almost 40 times compared to the raw sludge. Temperature up to 600 °C increases as the surface area decreases at higher temperatures [54].

Table 1 Some studies related to the sludge-derived biochar

Biochar production method	Aim of the study	Results of the study	References
Pyrolysis at 500 °C	Carbon mineralization of soil amended	Reduction in organic matter content in soil with biochar	[42]
Pyrolysis at 300–700 °C	Investigate N, P, K contents of sludge biochar	High-temperature sludge contains less N and more P and K	[43]
Pyrolysis at 400 °C	Optimization of pyrolysis to enhance sludge dewaterability	Optimal temperature: 400 °C Optimal biochar dose: 70% dry sludge	[44]
	Determination of physicochemical characteristics and toxicity of soil with biochar	Reduction of leaching of nutrients from the soil and toxicity	[45]
Prepared from dry sewage sludge	To assess sludge-derived biochar performance for soil improvement with other amendment	Sewage sludge-derived biochar can be a potential alternative for reusing wastes	[46]
Pyrolysis at 500 °C	Investigation of the effect of sludge biochar on growth yield and metal bioaccumulation of cherry tomato	No difference in growth of tomato with/without biochar	[47]
	To evaluate different rates of application of biochars on the growth and morphological traits of eucalyptus seedlings	Improvement of the growth and the morphological traits of the eucalyptus seedlings	[48]
Pyrolysis at 400 °C	To investigate the effect of sludge biochar on adsorption of Cr, Mn, Cu and Zn	Adsorption mechanism: Surface precipitation Reduction in the mobility of heavy metal in co-contaminated soil	[49]
Pyrolysis at 500 °C, 600 °C, 700 °C	To evaluate the effect of sewage sludge pyrolysis on freely dissolved (C-free) polycyclic aromatic hydrocarbon (PAH) contents in biochar	Sewage sludge-derived biochar have from 2.3- to 3.4-times lower C-free PAH contents compared to the control	[54]

Table 1 (continued)

Biochar production method	Aim of the study	Results of the study	References
Pyrolysis at 300 °C	Comparison of sludge-derived biochar: To investigate the effects of biochar on the soil characteristics, ecotoxicity and plant yield	Reduction in the soil toxicity after biochar compared with the control soil. A significant increase in Poa pratensis L. biomass in soils with 1 and 2% additions of each of the biochar. The addition of biochar impacts the content of mobile forms of Cu, Pb and Cd than the 0.5% dose compared with the control	[50]
Different pyrolysis temperature	Investigation of the surface properties of sludge-derived biochar using three feedstocks of wastewater sludge	400 °C demonstrates more uniform surface charge distribution of biochar. 300 °C achieved most reduction in DTPA-extractable metals of SDBCs	[51]
Different pyrolysis temperature	To investigate the effect of pyrolysis temperature, retention time and biomass chemical impregnation on biochar production	Highest yield at a temperature of 300 °C. Increased in biochar surface area with increasing pyrolysis. Removal of 70% of Cr(III) and only 30% of As(V) adsorption	[52]

3 Application of Biochar

3.1 Wastewater Treatment—Adsorption

3.1.1 Adsorption of Wastewater Pollutant

Biochar has recently characterized by adsorption properties and compared with activated carbon. However, it was previously known as a soil supplement [23]. The use of biochar to remove organic and heavy metal contaminants in water and wastewater treatment offers a new promising technology [56]. Biochar is produced at the end of the pyrolysis of biomass and can be used as an effective bio-sorbent [23].

The removal efficiency by adsorption using biochar is affected by the type and concentration of the surface functional groups [57]. The properties of biochar such as coordinating top electrons, surface adsorption, precipitation as insoluble substances, metal exchange with cations, surface functional groups and electrostatic interactions and heavy metals affect the adsorption of heavy metals [58].

Biochar is highly effective in the removal of organic and inorganic contaminants both soil and water. Biochar is different from activated carbon, with its final physicochemical properties [21]. Many researchers suggest that biochar is more advantageous than activated carbon in Pb removal because of the low feedstock costs of biochar [59, 60]. Biochars are cost-effective adsorbents for the adsorption of organic pollutants and heavy metals [21, 33–36, 59]. It was reported that the digested sludge-derived biochars are effective in adsorbing several contaminants [37] such as Pb, Cr and As [38, 61] and organic materials from wastewater [62–65]. Such as the type of raw material, the other parameters of particle size, surface area, pH, dosage of contaminant adsorbate and reaction time should be also considered to determine the adsorption capacity of biochar. It can be said that the biochar has removal capacity of materials in cost-effective manner compared to the other adsorbents. Alhashimi et al. [23] reported that biochar has lower effect than activated carbon in terms of environmental effects.

Tang et al. [66] tried to determine the chemical properties of biochar obtained in their study and found that the biochar production efficiency decreased with increasing pyrolysis temperature and biochar produced at 450 °C achieved the highest ammonium removal efficiency due to the higher surface area and functional group density. The results showed that biochar produced from digested sludge can be used as an adsorbent for the ammonium removal. Chen et al. [58] investigated the effects of biochar derived from sludge on the mechanism of cadmium adsorption. It was concluded increase in dosage results in decreases in adsorption capacity. The optimal dose was 0.2%. pH had a significant impact on the removal capacity of biochar, while temperature had a poor effect on the adsorption. When the pH of the solution is less than 2 of pH, the adsorption capacity of biochar was less than 20 mg/g and higher than 40 mg/g when the pH is higher than 3.

3.2   Soil Improvement

The physical structure of the soil is significantly affected by the existence of biochar. Furthermore, since the depth of penetration of water and air into the root is defined by the physical composition of the soil horizons. Biochar impacts the physical properties of the soil, which can directly affect plant growth. In addition to the reaction to the capacity to capture of the cations and the reaction to environmental-temperature changes, the reaction of soil to water, its ability to collect, soil preparation ability and permeability are affected by the presence of biochar [67].

Biochar alters the physical structure of the soil in a way that improves the structure and aeration of the soil, resulting in an increase in soil-specific surface area [68, 69].

The properties of soil such as surface area, water holding capacity, residence to penetration and bulk density can be affected by biochar application for soil improvement [70]. Cation and anion exchange capacities of soil can be increased by biochar [68, 69] increasing the pH. Increase in total nitrogen and phosphorus encourages the root growth and reduces existing aluminum [71, 72]. Furthermore, the effects of drought can be minimized using biochar. The increase in moisture of the soil as a result of biochar application can reduce nutrient leakage and soil erosion. [73]. The surface of the biochar may include the active groups which can adsorb the toxic chemicals in acidic soils and heavy metals in the contaminated soils [74, 75]. Biochar as a soil conditioner promotes plant growth improving the soil characteristics such as soil and water retention capacity. There is a great interest in the implementation of biochar to the soil due to its benefits [76, 77]. It is known that soil structure and pH can be improved, usage of fertilizer can be increased and aluminum toxicity can be reduced and soil habitat for worm populations can be enhanced as a result of biochar application [69, 78–80].

The biochar application as a soil amendment requires further investigations to provide a knowledge considering global warming and food production [81]. The evaluation of the literature review about the biochar impacts on GHG emissions and crop product may help to provide suggestions for further research [82]. In the biochar application, global warming and food safety must be evaluated together considering GHG emissions and crop product. To identify the correlation between agricultural production and GHG emissions and intensity as a term of global warming potential has been used [32, 83, 84]. The environmental factors such as soil properties, temperature and moisture play an important role to determine the effects of the biochar on GHG emissions [85]. The studies related to the biochar usage as soil amendment proved that the biochar addition to soil encourages the plant growth compared to the soil without biochar [86, 87].

3.3 Waste Management

Surface and groundwater are faced with a serious problem due to contamination of agricultural and animal waste [88]. The use of feedstock for this waste as well as for pyrolysis bioenergy [89] requires good environmental management. Economic opportunities for energy recovery have been created, in particular by producing a reliable source of raw materials [88]. This reduces the energy requirement and minimizes the CH_4 emissions that will occur if landfilling is used [83]. Hossain et al. [90] also emphasized that converting the waste sludge into biochar with pyrolysis can improve waste management, reducing transportation costs and production volume. A significant quantity of CH_4 and N_2O can be released with landfilling and anaerobic digestion. Therefore, biochar productions with these wastes can an effective waste management technology reducing the waste disposal cost and GHG emissions [21].

3.4 Carbon Sequestration

In the process called carbon sequestration, carbon is retained and stored, and thus, releasing of carbon to the atmosphere is prevented. [58]. It is important to transfer the carbon to a carbon pond to reduce emissions of C into the atmosphere. Atmospheric CO_2 concentrations can be affected by the transformation of the carbon circulation between atmosphere and plants to a biochar cycle. Based on its structure, it can be said that the biochar is more stable than carbon as biologically and chemically. The sequestered carbon is difficult to release as CO_2 [59]. Nearly 10% of existing anthropogenic carbon emissions can be reduced by adding 1% of the annual net carbon consumption of plants to biochar [22, 60]. Biochar with its ability to retain carbon can be used for carbon sequestration. The soil quality can also be improved using biochar as a soil amendment, and an increase in crop production [22] can be achieved with an environmentally friendly manner and less health risk compared to the sludge [5, 91].

3.5 Climate Change Mitigation

Agriculture contributes to global warming with methane (CH_4) and nitrous oxide (N_2O) emissions by 52% and 84%, respectively [92]. The "biochar" phenomena for GHGs mitigation was not discussed before 2005 [93], and agricultural applications considering GHGs mitigation become important day by day [32]. According to the IPCC [94], GHG emissions increased despite the awareness of climate change represented by a number of policies. The GHG emission must be decreased to the level of temperature to 2 °C [94]. CO_2 is one of the GHGs which can be captured by adsorption using some adsorbents like activated carbon. Novel adsorbents from biochar have been investigated by several studies [29, 95]. The negative emission technologies which can remove CO_2 from the atmosphere which can prevent the increasing in climate change [21]. Biochar production for soil amendment is promising technology to mitigate climate change, reducing soil GHG emissions and sequestrating carbon in soil [18]. Some researchers suggested that in case of the biochar application to soil, the carbon can be sequestered in the soil more than 1000 years [96, 97]. Thus, the degradation of CO_2 released from the biomass is prevented. The carbon sequestration is a method that can be applied to reduce the effects of agriculture on climate change [98].

4   Biochar for GHGs Mitigation

In the nature of the biomass degradation, carbon is released as CO_2, however, in the biochar usage blocks this degradation by carbon sequestration [98]. Carbon stability of biochar is high when its O/C_{org} and H/C_{org} ratios are lower than 0.2 and 0.7, respectively, and carbon content of biochar will be sequestered in soils for > 1000 years [28]. Thus, the global impact of agriculture can be reduced with biochar application [98]. The production of biochar and its amendment to soil was proposed as a negative emission technology [99] with potential emission of 0.7 Gt Ceq/yr [18, 100]. In terms of GHG emissions, biochar has negative emissions of -0.9 kg CO_2 eq./kg owing to carbon sequestration while activated carbon has higher GHG emissions of 6.6 kg CO_2 eq./kg [23]. Microorganisms responsible for photosynthesis fix the atmospheric CO_2 and then convert to biomass when they die in the carbon cycle. The mineralization and microbial respiration lead to the return of CO_2 to the atmosphere. Recalcitrant biochar holds the CO_2 in the soil for a long time, thus GHG emissions are reduced [21, 101].

According to the study by Woolf [102], biochar in the soil application can be effective in the reduction of the anthropogenic CO_2 emissions by 12%. Decreased [82] or a suppressed [103] GHG emissions using biochar as a soil amendment were revealed. The researchers also reported that biochar could also decrease indirect GHG emissions by reducing the usage of nitrogen fertilizer [104].

Brassard et al. [28] reported that a biochar impacts on soil GHG emissions, positively or negatively. This situation is depended on the temperature, surface area, C/N ratio feedstock, production process and soil application rates. Some studies demonstrated that since biochar has high biochemical stability could stay in soils during a long period [105, 106]. Thus, biochar may have also permanent effects on soil properties [30, 32]. Some researchers have conducted studies to evaluate the effects of operational conditions of the biochar production on the adsorption capacity. In the pyrolysis, temperature increases the carbon content, surface area and biochar porosity and decreases the density of surface oxygen functional groups of the char [29].

According to Bracmort [107], one of the main agricultural sources of N_2O emissions is the lands of the cultivated land and the pasture lands. Biochar can reduce greenhouse gas emissions by significantly reducing N_2O release when applied to soil. Rondon et al. [108] reported a 50% reduction in N_2O emissions in soybean lands in the East Colombia Plain. In addition, CH_4 emissions from biocaryl acid soils have decreased significantly. According to Yanai et al. [109], a reduction in N_2O emissions of 85% was observed in soils containing 10% biochar [78].

4.1   Effects of Biochar on Soil CO_2 Emissions

The source of soil CO_2 emissions are native soil organic matter, the mineralization of added carbon compounds, mineralization of dead roots and the direct respiration from plant roots [110, 111]. Soil temperature, moisture and the substrate utilization determine CO_2 emissions from soils [112]. Biochar amendment can impact the soil CO_2 emissions. According to some researchers, a biochar amendment is responsible for a reduction in soil CO_2 emissions [24]. There is a confliction about the effect of biochar on CO_2 emissions. An increase [113] and decrease [114] in CO_2 emissions in case of biochar implementation can be referred. There is uncertainty related to the reason for the biochar amendment impacts on.CO_2 emissions of the soil.

CO_2 emissions increase with increasing soil temperature until ~40 °C [111, 115, 116]. Decrease in soil albedo with biochar amendment may indirectly increase soil temperature in the field; thus, an increase in CO_2 efflux can be observed [117, 118].

Biochar shows a lower bulk density and higher water holding capacity compared to the soil. The addition of biochar to soil may increase soil aeration [30, 119]. Reactivation of soil nutrients, soil microbes and increasing O_2 availability may increase CO_2 emissions [120]. The addition of liable to change carbon compounds to the soil increases CO_2 emissions [121].

Biochar addition may lead to decrease or increase soil carbon mineralization in a long period. [24, 122, 123]. If the addition of biochar has long been proven to be suitable for the mineralization of natural soil carbon, the addition of biochar may greatly reduce CO_2 emissions [102]. The microbial biomass of the soil can be increased by increasing the use of the system carbon following the accumulation of organic carbon of the soil, microbes and nutrients to the surface of the biochar with biochar amendment [24]. Biochar amendment reduces the activity of enzymes which has the ability to mineralize the carbon thus soil CO_2 emissions are reduced [124] although this has not been proven [125].

4.2   Effects of Biochar on N_2O Emissions

In addition to CO_2, CH_4 and N_2O are also known to have an effect on climate change [21]. CH_4 and N_2O have 30 and 210 times higher global warming effect than CO_2 emission, respectively, and were reported as major GHG by IPCC [2, 126]. One of the wide application areas of biochar is the reduction in N_2O and CH_4, due to the carbon sequestering ability of biochar [21]. The presence of a lower amount of nitrogen for denitrification and nitrification is indicative of reduced N_2O emissions.

Reduction of N_2O emissions using biochar application rates of 1–2% by weight is confirmed through the meta-analyses [82, 127]. However, in some studies emphasize that there is no difference between biochar and control system in terms of emission reduction [128, 129]. Some others indicated that an increase in N_2O emissions is observed in the soil biochar amended [130–132].

4.2.1 Processes Related to N$_2$O Emissions Affected by Biochar

N$_2$O produced by microorganisms in the soil during nitrification and denitrification is 300 times more effective in the absorption of thermal radiation [21]. Nitrification, denitrification and nitrate ammonification are the main factors affected to N$_2$O emissions from soil [133]. Nitrification and denitrification are responsible for nearly 70% of global N$_2$O emission from soil [134] and can be reduced using biochar as soil amendment [135]. The production of N$_2$O is associated with moisture in the soil. The high moisture content (>70%) provides a low moisture content (<50%) nitrification environment while promoting anaerobic conditions for denitrification. In the high moisture content (80%) conditions, approximately 8–23 times more N$_2$O is produced compared to the low moisture content (40%) [135]. N$_2$O is released in soils by nitrification and denitrification [136], and many researches demonstrated that after soil biochar amendment, decrease in N$_2$O emissions is occurred as a result of a variety of soil microbial population [18, 24, 135, 137, 138].

4.2.2 Buffering Capacity of Biochar

The biochar's pH of 8.6 means that biochar has acid buffering capacity for reducing N$_2$O emissions. Increases in pH of soil increase N$_2$O released by denitrification due to the encouragement of activity of N$_2$O reductase enzymes [109]. Biochar changes pH, and N$_2$O ratio alters during denitrification.

4.2.3 Effects of Biochar on Microorganisms

The changes in microbial abundances can be responsible for the reduction in N$_2$O emissions in soil amendment application [24]. Biochar application achieves the reduction in N$_2$O emission in the presence of N$_2$O-producing earthworms [139, 140]. Liu et al. [141] suggested that decreasing of the ammonia-oxidizing and nitrite-oxidizing bacteria population in soil with biochar can reduce N$_2$O emission. Sun et al. [142] reported that biochar reduced the transfer of electrons to soil denitrifying microorganisms to reduce N$_2$O to N$_2$.

4.2.4 Adsorption of NH$_4^+$ or NO$_3^-$

Increases in the adsorption of NH$_4^+$ or NO$_3^-$ while aeration is increased lead to decrease in denitrification rates [24, 30]. Nitrate (NO$_3^-$) adsorption of the biochar results in the reduction in N$_2$O emissions. Biochar is effective in adsorption of dissolved ammonium [143], nitrate [144], phosphate [90] and other ionic solvents [145] in soil and water. Felber et al. [146] suggested that biochar obtained from green waste limits the presence of nitrogen in the soil by adsorption of NO$_3$ or NH$_4$. Sarkhot et al. [147] identified extractable NH$_4$ and NO$_3$ in a biochared soil. They suggested that

the soil amendment with biochar leads to a reduction in inorganic NH_4 and NO_3, which can be extracted with KCl. NH_4 and NO_3 can be retained by biochar with its adsorption capacity [132]. Adsorption of either NH_4 and NO_3 reduced N_2O/N_2 ratio according to the study by Kamman et al. [86]. Amendment with biochar of slurry, manure or chemical fertilizer provided remarkable mitigation of N_2O emissions due to the sorption feature of the biochar [148].

4.2.5 Increased Soil Aeration

Soil aeration due to the addition of biochar causes a reduction in N_2O emissions [139, 149]. Mukherjee et al. [70] reported that GHG emissions of biochar derived from slow pyrolysis of oak at 650 °C were reduced by 92%. Sludge-derived biochar can be obtained heating the digested sludge at high temperatures resulting in high porosity ion exchange capacity, as well as various surface functional groups [66, 150]. It can be concluded from the study that the characteristics of biochar determine the increase or decrease in soil GHG emissions and soil properties also affect the results [18].

4.2.6 Soil and Environmental Condition

Biochar N_2O mitigation depends not only on the features of the biochar but also on the soil type and environmental conditions [151–153]. While a biochar application led to increase in emissions in one soil, a decrease in emissions can be observed in the other soil with the same biochar [154]. This can be attributed to N_2O formation mechanisms occurring in different soils contained biochar differently affected. Understanding the relationship between biochar and microbial activity is crucial to choose and apply mitigation option balancing N_2O formation and consumption in soil [155]. Up to date, specific environmental conditions were applied to the N_2O formation mechanisms for most N_2O-biochar studies. For example, studies at high water-filled pore space asserted that the main N_2O formation mechanism is heterotrophic denitrification. However, this explanation has not been always supported as a correct interpretation. Many factors, not just water-filled pore space, manage the mechanism of N_2O production [134]. Thus, the requirement of novel studies that investigate N_2O produced through different biochar application is become more important [155].

4.2.7 Biochar Characteristics

Biochars increase N_2O emissions after the biochar application as a soil amendment [155]. Yanai et al. [109] revealed that high soil moisture content of 73–83% supports the production of N_2O and this is not observed in the low moisture content. The application of 10% biochar to the soil achieved N_2O emission reduction by 89%.

Renner [156] identified the nitrogen-based fertilizer as the main source of N_2O emissions. Biochar modified soil showed a reduction in N_2O emissions of up to 80% in Columbia. Jia et al. [157] conducted a study to determine the effects of biochar on vegetable production in pots and revealed that biochar modification could reduce N_2O emissions by 77–82%. The amount of biochar applied affects biochar-induced reductions in N_2O. In another study, there was no decrease in N_2O emissions after 4% biochar was added to soil [131]. Biochar which has high C_{total}/N_{total} ratio (>30) serves as a contributor to reduce soil N_2O emissions according to the several researches [28, 158]. It is reported that the biochar impacts on soil GHG emissions [82] and is an effective method for both sequestration of carbon and present potential to decrease non-CO_2 GHG emissions [155]. Biochar soil amendment has an impact on soil N cycle that reduces N_2O emissions [159]. Biochar assists the biological N fixation because of low N contents and high C/N ratios. Biochar can remove NH_3 from the soil, reducing the potential of ammonia from agricultural land [160, 161].

4.3   Effect of Biochar on CH_4

CH_4, has 25 of global warming potential, is one of the important GHGs [126]. Approximately, 50% of the global anthropogenic emissions of CH_4 is based on the agricultural sector with rice production [162]. Soil microorganisms produce CH_4 under anaerobic conditions by methanogenesis. CH_4 has absorbed thermal radiation capacity with 20 times stronger than CO_2 retained in the troposphere and supports global warming [163, 164]. Anaerobic methanogenic archaea (methanogens) and CH_4 consumption by methanotrophic bacteria determine the net CH_4 production between soils/ecosystems and the atmosphere [40]. CH_4 production by methanogens and CH_4 intake by methanotrophs are responsible for CH_4 flow measured in the soil–atmosphere interface. Both methanogens and methanotrophs can be present everywhere. CH_4 produces in soil under anaerobic conditions. Acetate, formate, CO_2 and H_2 are produced during anaerobic decomposition of organic matter in soil. O_2, the main limiting factor for the oxidation of CH_4, is required for Methanotrophs in the soil [165].

With biochar applications, soil conditions will be more suitable for methanotrophs and disadvantageous for methanogens increasing the CH_4 sink capacity of soil [40]. Biochar application to the soil also helps to reduce non-carbon dioxide GHG emissions [163, 164]. Biochar is kept nearly 50% of the carbon content in the feedstock during the pyrolysis process and remains stable in the soil for many years [143]. The soil type and microorganisms, water and fertilizer and the physical and chemical characteristics of the biochar are the factors affecting the amount of CH_4 released. [163, 164]. The biochar can remain stable in soils up to 4000 years due to its refractory structure to microbial degradation [166]. Biochar application to soil for atmospheric CO_2 was then recommended as a new approach [167]. NH_4^+ produced in soil or added as fertilizers can restrict CH_4 oxidation since some methanotrophs can use NH_4^+ as an energy source instead of CH_4. Biochar application could arrange the

maintenance of NH_4^+–N in soil for usage by methanotrophs [40]. However, there was no effect of NH_4^+–N on CH_4 consumption [168, 169]. At the same time, the diffusion of atmospheric CH_4 into soil with improved aeration may be increased by biochar application [40].

The reduction in GHGs can be achieved through the biochar application reducing N-fertilizer and labile-C inputs. Qian et al. [170] concluded that the use of four different biochar-compound fertilizers as biochar and bentonite, increased the biochar-compound fertilizer grain yields by 10–31% and reduced CH_4 emissions by 25–50% and N_2O emissions by 17–39%. Feng et al. [88] investigated the soil amendment performance of biochar of corn stalk produced by the slow pyrolysis at 300 and 500 °C, and it was concluded that CH_4 emission was remarkably decreased compared to control run without biochar. Thus, they discussed that after biochar amendment; soil content in terms of dissolved organic carbon was increased and presented more carbon sources promoting the growth of methanogenes and increasing in CH_4 emissions. Increasing in CH_4 uptake in soil and CH_4 diffusion through the soil attributed to improved soil aeration with biochar amendment were reported by Karhu [119].

Laird et al. [89] reported that the potential reduction obtained from biochar has been predicted between 0.7 and 2.6 Gt C/year by 2050. According to Woolf et al. [102], C sequestration using biochar can reduce fossil fuel emissions led to global warming. Biochar can be classified as a recalcitrant; however, it can be slowly mineralized [27]. The properties of biochar have effects on the stability of biochar. Some authors reported that the retention time of biochars can be lasted many decades. Singh et al. [97] revealed that the mean retention time of biochar was affected by pyrolysis temperature and it is varied from 90 to 1600 years for clay-rich soil. Major et al. [113] produced biochar from old mango at 400 and 600 °C for 48 h. Two years after the biochar application to a savanna Oxisol, they observed that less than 3% of applied biochar had been respired. According to another study, after the biochar application, total indirect CO_2 emissions were reduced, while paddy CH_4 emissions from soil were increased [84]. Liu et al. [32] investigated the effects of biochar application on GHG emissions and crop product in terms of yield-scaled greenhouse gas intensity (GHGI). A reduction of 29% in yield-scaled GHGI was observed. Biochar amendment in drylands may offer environmental advantages than that in paddy fields.

The biochar application studies related to the GHGs mitigation are summarized in Table 2.

5   Conclusions

Biochar is a co-product of thermochemical conversion of biomass in an oxygen-limited environment. From the literature, it was concluded that there are some biochar production techniques such as pyrolysis, gasification or hydrothermal carbonization. The quantities and qualities of biochar are affected by different pyrolysis conditions and feedstock. The raw materials used for the production of biochar and the feature

Table 2 Biochar application studies related to the carbon sequestration and GHGs mitigation

Raw material for biochar	Biochar production method	Aim of the study	Results of the study	References
Sugarcane bagasse, hickory wood	Pyrolysis	CO_2 Adsorption	Adsorption capacity 73.55 mg/G at 25 °C	[171]
Rice straw	Microwave Pyrolysis	CO_2 Adsorption	Higher CO_2 adsorption capacity of biochar using microwave Adsorption capacity 80 mg/G at 20 °C Optimal temperature for pyrolysis: 550 °C	[172]
Wood switchgrass and pig manure	Pyrolysis	To reduce N_2O emission without increasing CO_2 emission	Determination of the biochar characterization with the increase or decrease in soil GHG emissions	[18]
Cattle slurry and Hen manure	Slow	Composting with barley straw with/without biochar	Most reduction in NH_3 and NH_4 losses at low flow aeration rates in case of biochar addition to composting	[16]
Eucalyptus grandis	Slow Pyrolysis	Composting of poultry manure	Reduction losses of nitrogen in the mature compost with biochar	[15]
Charcola or biomass-derived black carbon ©	Pyrolysis	To establish significant long term sink for atmospheric CO_2	50% of initial C sequestration Landuse change can be offset annually in soil by C emission	[143]
Wood and poultry manure		Evaluation of biochar effect on emission and leaching from an Alfisol and Vertisol	Decreases in N_2O emisions by 14–73% from the Alfisol and by 23–52% from the Vertisol	[173]

Table 2 (continued)

Raw material for biochar	Biochar production method	Aim of the study	Results of the study	References
Bamboo (BC) chips and rice straw (SC)		Biochar effect on CH_4 and CO_2 emissions in soil	Increases CH_4 and CO_2 emissions from the paddy soil by adding rice straw Reduction in CH_4 emissions from soil amended with BC and SC by 51.1 and 81.2% respectively	[174]
Crop straw		Measure of mitigation of climate change	Gradually increase in the reduction of the overall C intensity of rice production for the cycles Significant reduction of N_2O emission in a single crop cycle with biochar	[60]
Charcoal	Pyrolysis	N_2O reduction	Improvement microbial N_2O reduction and increases in the abundance of microorganisms cable of N_2 fixation	[137]
Rice husk	Pyrolysis	Biochar and nitrogen fertilizer (NH_4NO_3) were employed to remediate OPP-contaminated soil and the greenhouse gas (GHG) emission was investigated	The addition of biochar slightly increased the emission rate of GHGs from the soil without thermal treatment, but significantly increased the emission rate of GHGs from the soil after thermal treatment	[175]

Table 2 (continued)

Raw material for biochar	Biochar production method	Aim of the study	Results of the study	References
Rice straw		Effect of rice straw biochar application on nitrification	Significantly reduction in the N_2O emissions up to 37.6% in oxisol-derived granite and 46.4% in RTU oxisol-derived tertiary red stones with biochar	[138]
	Fast Pyrolysis	To assess carbon sequestration and GHG reduction.	Increases in N_2O emissions only biochar application Decrease in N_2O emissions by 47% with anaerobic digested sludge	[135]
Bamboo leaf biochar	Fast Pyrolysis	To measure GHG emissions from soil	Increases in soil GHG emissions with increasing biochar application rates Decreases in also NH_4-N, NO_3-N concentration of soil with biochar	[176]
Oilseed rape straw	Prolysis at 400–800 °C	Analyze winter oilseed rape scenarios in terms of their global warming impact using life-cycle approach	Reduction in GHG emissions by 73–83% in two biochar scenarios as compared to the reference mainly due to the increased C sequestration	[177]
Wood	Gasification	Determine the effect of biochar on CO_2 and N_2O emissions	Reduced N_2O emissions in the laboratory and in the continuous corn cropping system in the field No effect on cumulative CO_2 emission in the field	[178]

of the production affect the biochar properties. The proper production techniques applied and chosen raw material should be considered as significant parameters to optimize the biochar application. According to the information obtained from the literature, the pyrolysis process parameters (temperature, retention time, heating rate, feedstock particle size) affect the quality and quantity of the biochar produced and thus the environmental effects. Sludge-derived biochar through pyrolysis may be an important resource for reuse of sludge in agricultural and many other environmental applications, considering the advantages among the final disposal strategy for sludge. Recently, biochar application gradually draws more attention as an efficient and promising technology to adsorb GHGs due to its advantages like low cost, environment-friendly, excellent stability, high porosity, easy preparation and operation. Biochar production for soil amendment was promising technology to mitigate climate change, reducing soil GHG emissions and sequestrating carbon in soil. The carbon sequestration is promising method to reduce the effects of agriculture on climate change. Agriculture can be improved by using sludge-derived biochar, and additional income sources are provided to farmers. Depending on the carbon sequestration, crop yield and productivity may increase, improving sustainable land use in agriculture. In addition, greenhouse gas emissions can be reduced. Due to the adsorption capacity, biochar can be used for treatment of wastewater with high concentration of heavy metals, pesticides and other organic contaminants. Biochar with its ability to retain carbon can be used for carbon sequestration. The soil quality can also be improved using biochar as a soil amendment, and an increase in crop production can be achieved with an environmentally friendly manner and less health risk compared to the sludge. The properties of soil such as surface area, water holding capacity, residence to penetration and bulk density can be affected by biochar application for soil improvement.

It has been concluded that the use of biochar provides a unique opportunity to reduce non-CO_2 GHG, but future research is needed to maximize its benefits and assess the environmental and economic sustainability of the biochar production.

References

1. Zhang J, Lü F, Shao L, He P (2014) The use of biochar-amended composting to improve the humification and degradation of sewage sludge. Bioresour Technol 168:252–258. https://doi.org/10.1016/j.biortech.2014.02.080
2. Awasthi MK, Wang Q, Ren X, Zhao J, Huang H, Awasthi SK et al (2016) Role of biochar amendment in mitigation of nitrogen loss and greenhouse gas emission during sewage sludge composting. Bioresour Technol 219:270–280. https://doi.org/10.1016/j.biortech.2016.07.128
3. Awasthi MK, Wang Q, Huang H, Ren X, Lahori AH, Mahar A et al (2016) Influence of zeolite and lime as additives on greenhouse gas emissions and maturity evolution during sewage sludge composting. Bioresour Technol 216:172–181. https://doi.org/10.1016/j.biortech.2016.05.065
4. Zapusek U, Lestan D (2009) Fractionation, mobility and bio-accessibility of Cu, Zn, Cd, Pb and Ni in aged artificial soil mixtures. Geoderma 154:164–169. https://doi.org/10.1016/j.geoderma.2009.10.012

5. Cao Y, Pawłowski A (2013) Life cycle assessment of two emerging sewage sludge-to-energy systems: evaluating energy and greenhouse gas emissions implications. Bioresour Technol 127:81–91. https://doi.org/10.1016/j.biortech.2012.09.135
6. Sánchez-Monedero MA, Serramiá N, Civantos CGO, Fernández-Hernández A, Roig A (2010) Greenhouse gas emissions during composting of two-phase olive mill wastes with different agroindustrial by-products. Chemosphere 81:18–25. https://doi.org/10.1016/j.chemosphere.2010.07.022
7. Liu D, Zhang R, Wu H, Xu D, Tang Z, Yu G et al (2011) Changes in biochemical and microbiological parameters during the period of rapid composting of dairy manure with rice chaff. Bioresour Technol 102:9040–9049. https://doi.org/10.1016/j.biortech.2011.07.052
8. Ermolaev E, Sundberg C, Pell M, Jönsson H (2014) Greenhouse gas emissions from home composting in practice. Bioresour Technol 151:174–182. https://doi.org/10.1016/j.biortech.2013.10.049
9. Szanto GL, Hamelers HVM, Rulkens WH, Veeken AHM (2007) NH_3, N_2O and CH_4 emissions during passively aerated composting of straw-rich pig manure. Bioresour Technol 98:2659–2670. https://doi.org/10.1016/j.biortech.2006.09.021
10. Li R, Wang JJ, Zhang Z, Shen F, Zhang G, Qin R et al (2012) Nutrient transformations during composting of pig manure with bentonite. Bioresour Technol 121:362–368. https://doi.org/10.1016/j.biortech.2012.06.065
11. Awasthi MK, Pandey AK, Bundela PS, Wong JWC, Li R, Zhang Z (2015) Co-composting of gelatin industry sludge combined with organic fraction of municipal solid waste and poultry waste employing zeolite mixed with enriched nitrifying bacterial consortium. Bioresour Technol 213:181–189. https://doi.org/10.1016/j.biortech.2016.02.026
12. Rulkens W (2008) Sewage sludge as a biomass resource for the production of energy: overview and assessment of the various options. Energy Fuels 22:9–15. https://doi.org/10.1021/ef700267m
13. Malińska K, Zabochnicka-Świątek M, Dach J (2014) Effects of biochar amendment on ammonia emission during composting of sewage sludge. Ecol Eng 71:474–478. https://doi.org/10.1016/j.ecoleng.2014.07.012
14. Jiang T, Ma X, Tang Q, Yang J, Li G, Schuchardt F (2016) Combined use of nitrification inhibitor and struvite crystallization to reduce the NH_3 and N_2O emissions during composting. Bioresour Technol 217:210–218. https://doi.org/10.1016/j.biortech.2016.01.089
15. Dias BO, Silva CA, Higashikawa FS, Roig A, Sánchez-Monedero MA (2010) Use of biochar as bulking agent for the composting of poultry manure: effect on organic matter degradation and humification. Bioresour Technol 101:1239–1246. https://doi.org/10.1016/j.biortech.2009.09.024
16. Chowdhury MA, de Neergaard A, Jensen LS (2014) Potential of aeration flow rate and biochar addition to reduce greenhouse gas and ammonia emissions during manure composting. Chemosphere 97:16–25. https://doi.org/10.1016/j.chemosphere.2013.10.030
17. Novak JM, Busscher WJ (2013) Selection and use of designer biochars to improve characteristics of southeastern USA coastal plain degraded soils. Adv Biofuels Bioprod 69–96. https://doi.org/10.1007/978-1-4614-3348-4_7
18. Brassard P, Godbout S, Palacios JH, Jeanne T, Hogue R, Dubé P et al (2018) Effect of six engineered biochars on GHG emissions from two agricultural soils: a short-term incubation study. Geoderma 327:73–84. https://doi.org/10.1016/j.geoderma.2018.04.022
19. Kim Y, Parker W (2008) A technical and economic evaluation of the pyrolysis of sewage sludge for the production of bio-oil. Bioresour Technol 99:1409–1416. https://doi.org/10.1016/j.biortech.2007.01.056
20. Pokorna E, Postelmans N, Jenicek P, Schreurs S, Carleer R, Yperman J (2009) Study of bio-oils and solids from flash pyrolysis of sewage sludges. Fuel 88:1344–1350. https://doi.org/10.1016/j.fuel.2009.02.020
21. Qambrani NA, Rahman MM, Won S, Shim S, Ra C (2017) Biochar properties and eco-friendly applications for climate change mitigation, waste management, and wastewater treatment: a review. Renew Sustain Energy Rev 79:255–273. https://doi.org/10.1016/j.rser.2017.05.057

22. Hossain MK, Strezov V, Yin Chan K, Nelson PF (2010) Agronomic properties of wastewater sludge biochar and bioavailability of metals in production of cherry tomato (*Lycopersicon esculentum*), Chemosphere. 78:1167–1171. https://doi.org/10.1016/j.chemosphere.2010.01.009

23. Alhashimi HA, Aktas CB (2017) Life cycle environmental and economic performance of biochar compared with activated carbon: a meta-analysis. Resour Conserv Recycl 118:13–26. https://doi.org/10.1016/j.resconrec.2016.11.016

24. Lehmann J, Rillig MC, Thies J, Masiello CA, Hockaday WC, Crowley D (2011) Biochar effects on soil biota—a review. Soil Biol Biochem 43:1812–1836. https://doi.org/10.1016/j.soilbio.2011.04.022

25. Nguyen TTN, Xu CY, Tahmasbian I, Che R, Xu Z, Zhou X et al (2017) Effects of biochar on soil available inorganic nitrogen: a review and meta-analysis. Geoderma 288:79–96. https://doi.org/10.1016/j.geoderma.2016.11.004

26. Bridgwater AV (2012) Review of fast pyrolysis of biomass and product upgrading. Biomass Bioenerg 38:68–94. https://doi.org/10.1016/j.biombioe.2011.01.048

27. Enders A, Hanley K, Whitman T, Joseph S, Lehmann J (2012) Characterization of biochars to evaluate recalcitrance and agronomic performance. Bioresour Technol 114:644–653. https://doi.org/10.1016/j.biortech.2012.03.022

28. Brassard P, Godbout S, Raghavan V (2016) Soil biochar amendment as a climate change mitigation tool: key parameters and mechanisms involved. J Environ Manage 181:484–497. https://doi.org/10.1016/j.jenvman.2016.06.063

29. Cha JS, Park SH, Jung SC, Ryu C, Jeon JK, Shin MC et al (2016) Production and utilization of biochar: a review. J Ind Eng Chem 40:1–15. https://doi.org/10.1016/j.jiec.2016.06.002

30. Sohi SP, Krull E, Lopez-Capel E, Bol R (2010) A review of biochar and its use and function in soil. Adv Agron 47–82. https://doi.org/10.1016/s0065-2113(10)05002-9

31. Cornelissen G, Nurida NL, Hale SE, Martinsen V, Silvani L, Mulder J (2018) Fading positive effect of biochar on crop yield and soil acidity during five growth seasons in an Indonesian Ultisol. Sci Total Environ 634:561–568. https://doi.org/10.1016/j.scitotenv.2018.03.380

32. Liu X, Mao P, Li L, Ma J (2019) Impact of biochar application on yield-scaled greenhouse gas intensity: a meta-analysis. Sci Total Environ 656:969–976. https://doi.org/10.1016/j.scitotenv.2018.11.396

33. Kou Xu R, Cheng Xiao S, Hua Yuan J, Zhen Zhao A (2011) Adsorption of methyl violet from aqueous solutions by the biochars derived from crop residues. Bioresour Technol 102:10293–10298. https://doi.org/10.1016/j.biortech.2011.08.089

34. Qiu Y, Cheng H, Xu C, Sheng GD (2008) Surface characteristics of crop-residue-derived black carbon and lead(II) adsorption. Water Res 42:567–574. https://doi.org/10.1016/j.watres.2007.07.051

35. Mohan D, Pittman CU, Bricka M, Smith F, Yancey B, Mohammad J et al (2007) Sorption of arsenic, cadmium, and lead by chars produced from fast pyrolysis of wood and bark during bio-oil production. J Colloid Interface Sci 310:57–73. https://doi.org/10.1016/j.jcis.2007.01.020

36. Wang X, Xing B (2007) Sorption of organic contaminants by biopolymer-derived chars. Environ Sci Technol 41:8342–8348. https://doi.org/10.1021/es071290n

37. Paz-Ferreiro J, Nieto A, Méndez A, Askeland MPJ, Gascó G (2018) Biochar from biosolids pyrolysis: a review. Int J Environ Res Public Health 15. https://doi.org/10.3390/ijerph15050956

38. Jin H, Capareda S, Chang Z, Gao J, Xu Y, Zhang J (2014) Biochar pyrolytically produced from municipal solid wastes for aqueous As(V) removal: adsorption property and its improvement with KOH activation. Bioresour Technol 169:622–629. https://doi.org/10.1016/j.biortech.2014.06.103

39. Zhang Z, Zhu Z, Shen B, Liu L (2019) Insights into biochar and hydrochar production and applications: a review. Energy. 171:581–598. https://doi.org/10.1016/j.energy.2019.01.035

40. Lehmann J (2009) Biochar for environmental management : an introduction. Biochar Environ Manag Sci Technol 1–12. https://doi.org/10.1016/j.forpol.2009.07.001

41. Capodaglio AG, Callegari A, Dondi D (2017) Properties and beneficial uses of biochar from sewage sludge pyrolysis. In: 5th International conference on sustainable solid waste management 16

42. Gascó G, Paz-Ferreiro J, Méndez A (2012) Thermal analysis of soil amended with sewage sludge and biochar from sewage sludge pyrolysis. J Therm Anal Calorim 769–775. https://doi.org/10.1007/s10973-011-2116-2

43. Yuan H, Lu T, Wang Y, Chen Y, Lei T (2016) Sewage sludge biochar: nutrient composition and its effect on the leaching of soil nutrients. Geoderma 267:17–23. https://doi.org/10.1016/j.geoderma.2015.12.020

44. Wu Y, Zhang P, Zeng G, Ye J, Zhang H, Fang W et al (2016) Enhancing sewage sludge dewaterability by a skeleton builder: biochar produced from sludge cake conditioned with rice husk flour and $FeCl_3$. ACS Sustain Chem Eng 4:5711–5717. https://doi.org/10.1021/acssuschemeng.6b01654

45. Kończak M, Oleszczuk P (2018) Application of biochar to sewage sludge reduces toxicity and improve organisms growth in sewage sludge-amended soil in long term field experiment. Sci Total Environ 625:8–15. https://doi.org/10.1016/j.scitotenv.2017.12.118

46. Penido ES, Martins GC, Mendes TBM, Melo LCA, do Rosário Guimarães I, Guilherme LRG (2019) Combining biochar and sewage sludge for immobilization of heavy metals in mining soils. Ecotoxicol Environ Saf 172:326–333. https://doi.org/10.1016/j.ecoenv.2019.01.110

47. Hossain MK, Strezov V, Nelson PF (2015) Comparative assessment of the effect of wastewater sludge biochar on growth. Yield and metal bioaccumulation of cherry tomato. Pedosphere 25:680–685. https://doi.org/10.1016/S1002-0160(15)30048-5

48. Gonzaga MIS, Mackowiak C, de Almeida AQ, de C. Júnior JIT (2018) Sewage sludge derived biochar and its effect on the growth and morphological traits of eucalyptus grandis W.Hill ex maiden seedlings. Cienc Florest 28:687–695. https://doi.org/10.5902/1980509832067

49. Zhou D, Liu D, Gao F, Li M, Luo X (2017) Effects of biochar-derived sewage sludge on heavy metal adsorption and immobilization in soils. Int J Environ Res Public Health 14. https://doi.org/10.3390/ijerph14070681

50. Mierzwa-Hersztek M, Gondek K, Klimkowicz-Pawlas A, Baran A, Bajda T (2018) Sewage sludge biochars management—ecotoxicity, mobility of heavy metals, and soil microbial biomass. Environ Toxicol Chem 37:1197–1207. https://doi.org/10.1002/etc.4045

51. Lu H, Zhang W, Wang S, Zhuang L, Yang Y, Qiu R (2013) Characterization of sewage sludge-derived biochars from different feedstocks and pyrolysis temperatures. J Anal Appl Pyrolysis 102:137–143. https://doi.org/10.1016/j.jaap.2013.03.004

52. Agrafioti E, Diamadopoulos E (2012) A strategic plan for reuse of treated municipal wastewater for crop irrigation on the Island of Crete. Agric Water Manag 105:57–64. https://doi.org/10.1016/j.agwat.2012.01.002

53. Liu T, Liu B, Zhang W (2014) Nutrients and heavy metals in biochar produced by sewage sludge pyrolysis: its application in soil amendment. Polish J Environ Stud 23:271–275

54. Zielińska A, Oleszczuk P, Charmas B, Skubiszewska-Zięba J, Pasieczna-Patkowska S (2015) Effect of sewage sludge properties on the biochar characteristic. J Anal Appl Pyrolysis 112:201–213. https://doi.org/10.1016/j.jaap.2015.01.025

55. Novak J, Lima I, Xing B, Gaskin JW, Steiner C, Das KC et al (2009) Characterization of designer biochar produced at different temperatures and their effects on a loamy sand. Ann Environ Sci 3:195–206. https://repository.library.northeastern.edu/cgi/viewcontent.cgi?article=1028&context=aes

56. Inyang M, Gao B, Ding W, Pullammanappallil P, Zimmerman AR, Cao X (2011) Enhanced lead sorption by biochar derived from anaerobically digested sugarcane bagasse. Sep Sci Technol 46:1950–1956. https://doi.org/10.1080/01496395.2011.584604

57. Yenisoy-Karakaş S, Aygün A, Güneş M, Tahtasakal E (2004) Physical and chemical characteristics of polymer-based spherical activated carbon and its ability to adsorb organics. Carbon N Y 42:477–484. https://doi.org/10.1016/j.carbon.2003.11.019

58. Chen T, Zhou Z, Han R, Meng R, Wang H, Lu W (2015) Adsorption of cadmium by biochar derived from municipal sewage sludge: impact factors and adsorption mechanism. Chemosphere 134:286–293. https://doi.org/10.1016/j.chemosphere.2015.04.052

59. Cao X, Ma L, Gao B, Harris W (2009) Dairy-manure derived biochar effectively sorbs lead and atrazine. Environ Sci Technol 43:3285–3291. https://doi.org/10.1021/es803092k

60. Lu H, Zhang W, Yang Y, Huang X, Wang S, Qiu R (2012) Relative distribution of Pb2+ sorption mechanisms by sludge-derived biochar. Water Res 46:854–862. https://doi.org/10.1016/j.watres.2011.11.058

61. Zhou F, Wang H, Fang S, Zhang W, Qiu R (2015) Pb(II), Cr(VI) and atrazine sorption behavior on sludge-derived biochar: role of humic acids. Environ Sci Pollut Res 22:16031–16039. https://doi.org/10.1007/s11356-015-4818-7

62. Kacan E (2016) Optimum BET surface areas for activated carbon produced from textile sewage sludges and its application as dye removal. J Environ Manage 166:116–123. https://doi.org/10.1016/j.jenvman.2015.09.044

63. Shi L, Zhang G, Wei D, Yan T, Xue X, Shi S et al (2014) Preparation and utilization of anaerobic granular sludge-based biochar for the adsorption of methylene blue from aqueous solutions. J Mol Liq 198:334–340. https://doi.org/10.1016/j.molliq.2014.07.023

64. Silva TL, Ronix A, Pezoti O, Souza LS, Leandro PKT, Bedin KC et al (2016) Mesoporous activated carbon from industrial laundry sewage sludge: adsorption studies of reactive dye Remazol Brilliant Blue R. Chem Eng J 303:467–476. https://doi.org/10.1016/j.cej.2016.06.009

65. Yao H, Lu J, Wu J, Lu Z, Wilson PC, Shen Y (2013) Adsorption of fluoroquinolone antibiotics by wastewater sludge biochar: role of the sludge source. Water Air Soil Pollut 224. https://doi.org/10.1007/s11270-012-1370-7

66. Tang Y, Alam MS, Konhauser KO, Alessi DS, Xu S, Tian WJ et al (2019) Influence of pyrolysis temperature on production of digested sludge biochar and its application for ammonium removal from municipal wastewater. J Clean Prod 209:927–936. https://doi.org/10.1016/j.jclepro.2018.10.268

67. Weil NC, Brady RR (2016) The nature and properties of soils, 15th Edition. Soil Sci Soc Am J 80:1428. https://doi.org/10.2136/sssaj2016.0005br

68. Singh B, Singh BP, Cowie AL (2010) Characterisation and evaluation of biochars for their application as a soil amendment. Aust J Soil Res 516–525. https://doi.org/10.1071/sr10058

69. Liang B, Lehmann J, Solomon D, Kinyangi J, Grossman J, O'Neill B et al (2006) Black carbon increases cation exchange capacity in soils. Soil Sci Soc Am J 70:1719. https://doi.org/10.2136/sssaj2005.0383

70. Mukherjee A, Lal R, Zimmerman AR (2014) Effects of biochar and other amendments on the physical properties and greenhouse gas emissions of an artificially degraded soil. Sci Total Environ 487:26–36. https://doi.org/10.1016/j.scitotenv.2014.03.141

71. Chan KY, Van Zwieten L, Meszaros I, Downie A, Joseph S (2008) Using poultry litter biochars as soil amendments. Aust J Soil Res 46:437–444. https://doi.org/10.1071/SR08036

72. Cheng CH, Lehmann J, Thies JE, Burton SD, Engelhard MH (2006) Oxidation of black carbon by biotic and abiotic processes. Org Geochem 37:1477–1488. https://doi.org/10.1016/j.orggeochem.2006.06.022

73. Lorenz K, Lal R, Preston CM, Nierop KGJ (2007) Strengthening the soil organic carbon pool by increasing contributions from recalcitrant aliphatic bio(macro)molecules. Geoderma 142:1–10. https://doi.org/10.1016/j.geoderma.2007.07.013

74. Berek AK, Hue N, Ahmad A (2011) Beneficial use of biochar to correct soil acidity. Food Provid 3–5

75. Uchimiya M, Lima IM, Thomas Klasson K, Chang S, Wartelle LH, Rodgers JE (2010) Immobilization of heavy metal ions (Cu [II], Cd [II], Ni [II], and Pb [II]) by broiler litter-derived biochars in water and soil. J Agric Food Chem 58:5538–5544. https://doi.org/10.1021/jf9044217

76. Quayle WC (2010) Biochar potential for soil improvement & soil fertility. Water 49:22–24. https://doi.org/10.2307/2329135

77. De Gryze S, Cullen M, Durschinger L, Lehmann J, Bluhm D, Six J (2010) Evaluation of the opportunities for generating carbon offsets from soil sequestration of biochar. An Issues Pap Comm Clim Action Reserv Final Version 1–99. https://doi.org/10.1017/cbo9781107415324.004

78. Duku MH, Gu S, Ben Hagan E, Biochar production potential in Ghana—a review. Renew Sustain Energy Rev 15:3539–3551. https://doi.org/10.1016/j.rser.2011.05.010
79. Schmidt MWI, Noack AG (2000) Black carbon in soils and sediments: analysis, distribution, implications, and current challenges. Global Biogeochem Cycles 14:777–793. https://doi.org/10.1029/1999GB001208
80. Lehmann J, Pereira J, Silva D, Steiner C, Nehls T, Zech W et al (2003) Nutrient availability and leaching in an archaeological Anthrosol and a Ferralsol of the Central Amazon basin: fertilizer, manure and charcoal amendments. Plant Soil 249:343–357
81. Jeffery S, Verheijen FGA, van der Velde M, Bastos AC (2011) A quantitative review of the effects of biochar application to soils on crop productivity using meta-analysis. Agric Ecosyst Environ 144:175–187. https://doi.org/10.1016/j.agee.2011.08.015
82. Cayuela ML, van Zwieten L, Singh BP, Jeffery S, Roig A, Sánchez-Monedero MA (2014) Biochar's role in mitigating soil nitrous oxide emissions: a review and meta-analysis. Agric Ecosyst Environ 191:5–16. https://doi.org/10.1016/j.agee.2013.10.009
83. Mosier AR, Halvorson AD, Reule CA, Liu XJ (2006) Net global warming potential and greenhouse gas intensity in irrigated cropping systems in Northeastern Colorado. J Environ Qual 35:1584. https://doi.org/10.2134/jeq2005.0232
84. Zhang A, Bian R, Pan G, Cui L, Hussain Q, Li L et al (2012) Effects of biochar amendment on soil quality, crop yield and greenhouse gas emission in a Chinese rice paddy: a field study of 2 consecutive rice growing cycles. F Crop Res 127:153–160. https://doi.org/10.1016/j.fcr.2011.11.020
85. Bai M, Wilske B, Buegger F, Bruun EW, Bach M, Frede HG et al (2014) Biodegradation measurements confirm the predictive value of the O: C-ratio for biochar recalcitrance. J Plant Nutr Soil Sci 177:633–637. https://doi.org/10.1002/jpln.201300412
86. Kammann C, Ratering S, Eckhard C, Müller C (2012) Biochar and hydrochar effects on greenhouse gas (carbon dioxide, nitrous oxide, and methane) fluxes from soils. J Environ Qual 41:1052. https://doi.org/10.2134/jeq2011.0132
87. Tang J, Zhu W, Kookana R, Katayama A (2013) Characteristics of biochar and its application in remediation of contaminated soil. J Biosci Bioeng 116:653–659. https://doi.org/10.1016/j.jbiosc.2013.05.035
88. Feng Y, Xu Y, Yu Y, Xie Z, Lin X (2012) Mechanisms of biochar decreasing methane emission from Chinese paddy soils. Soil Biol Biochem 46:80–88. https://doi.org/10.1016/j.soilbio.2011.11.016
89. Laird DA, Brown RC, Amonette JE, Lehmann J (2009) Review of the pyrolysis platform for coproducing bio-oil and biochar. Biofuels, Bioprod. Biorefining 3(5):547–562. https://doi.org/10.1002/bbb.169
90. Hossain MK, Strezov Vladimir V, Chan KY, Ziolkowski A, Nelson PF (2011) Influence of pyrolysis temperature on production and nutrient properties of wastewater sludge biochar. J Environ Manage 92:223–228. https://doi.org/10.1016/j.jenvman.2010.09.008
91. Kistler RC, Brunner PH, Widmer F (1987) Behavior of chromium, nickel, copper, zinc, cadmium, mercury, and lead during the pyrolysis of sewage sludge. Environ Sci Technol 21:704–708. https://doi.org/10.1021/es00161a012
92. Smith P, Martino D, Cai Z, Gwary D, Janzen H, Kumar P et al (2008) Greenhouse gas mitigation in agriculture. Philos Trans R Soc B Biol Sci 363:789–813. https://doi.org/10.1098/rstb.2007.2184
93. Verma M, Godbout S, Brar SK, Solomatnikova O, Lemay SP, Larouche JP (2012) Biofuels production from biomass by thermochemical conversion technologies. Int J Chem Eng 2012:1–18. https://doi.org/10.1155/2012/542426
94. Climate, Climate Change 2014: mitigation of climate change. Summary for Policymakers and Technical Summary, 2014. https://doi.org/10.1017/cbo9781107415416.005
95. Samanta A, Zhao A, Shimizu GKH, Sarkar P, Gupta R (2012) Post-combustion CO_2 capture using solid sorbents: a review. Ind Eng Chem Res 51:1438–1463. https://doi.org/10.1021/ie200686q

96. Haefele SM, Konboon Y, Wongboon W, Amarante S, Maarifat AA, Pfeiffer EM et al (2011) Effects and fate of biochar from rice residues in rice-based systems. F Crop Res 121:430–440. https://doi.org/10.1016/j.fcr.2011.01.014

97. Singh BP, Cowie AL, Smernik RJ (2012) Biochar carbon stability in a clayey soil as a function of feedstock and pyrolysis temperature. Environ Sci Technol 46:11770–11778. https://doi.org/10.1021/es302545b

98. Wang Z, Zheng H, Luo Y, Deng X, Herbert S, Xing B (2013) Characterization and influence of biochars on nitrous oxide emission from agricultural soil. Environ Pollut 174:289–296. https://doi.org/10.1016/j.envpol.2012.12.003

99. UNEP (2016) The Emissions Gap Report 2016. ISBN 978-92-807-3617-5

100. Smith P (2016) Soil carbon sequestration and biochar as negative emission technologies. Glob Chang Biol 22:1315–1324. https://doi.org/10.1111/gcb.13178

101. Yang Q, Han F, Chen Y, Yang H, Chen H (2016) Greenhouse gas emissions of a biomass-based pyrolysis plant in China. Renew Sustain Energy Rev 53:1580–1590. https://doi.org/10.1016/j.rser.2015.09.049

102. Woolf D, Amonette JE, Street-Perrott FA, Lehmann J, Joseph S (2010) Sustainable biochar to mitigate global climate change. Nat Commun 1. https://doi.org/10.1038/ncomms1053

103. Wu F, Jia Z, Wang S, Chang SX, Startsev A (2013) Contrasting effects of wheat straw and its biochar on greenhouse gas emissions and enzyme activities in a Chernozemic soil. Biol Fertil Soils 49:555–565. https://doi.org/10.1007/s00374-012-0745-7

104. Zhang A, Cui L, Pan G, Li L, Hussain Q, Zhang X et al (2010) Effect of biochar amendment on yield and methane and nitrous oxide emissions from a rice paddy from Tai Lake plain, China. Agric Ecosyst Environ 139:469–475. https://doi.org/10.1016/j.agee.2010.09.003

105. Atkinson CJ, Fitzgerald JD, Hipps NA (2010) Potential mechanisms for achieving agricultural benefits from biochar application to temperate soils: a review. Plant Soil 337:1–18. https://doi.org/10.1007/s11104-010-0464-5

106. Wang J, Xiong Z, Kuzyakov Y (2016) Biochar stability in soil: Meta-analysis of decomposition and priming effects. GCB Bioenergy 8:512–523. https://doi.org/10.1111/gcbb.12266

107. Bracmort K (2010) Biochar: examination of an emerging concept to mitigate climate change. Congr Res Serv 11

108. Rondon M, Ramirez JA (2005) Greenhouse gas emissions decrease with charcoal additions to tropical soils. In: 3rd USDA symposium greenhouse gases carbon sequestration in agriculture and forestry 208

109. Yanai Y, Toyota K, Okazaki M (2007) Effects of charcoal addition on N_2O emissions from soil resulting from rewetting air-dried soil in short-term laboratory experiments: original article. Soil Sci Plant Nutr 53:181–188. https://doi.org/10.1111/j.1747-0765.2007.00123.x

110. Hanson PJ, Edwards NT, Garten CT, Andrews JA (2000) Separating root and soil microbial contributions to soil respiration: a review of methods and observations. Biogeochemistry 48:115–146. https://doi.org/10.1023/a:1006244819642

111. Luo Y, Zhou X (2006) Soil respiration and the environment. https://doi.org/10.1016/b978-0-12-088782-8.x5000-1

112. Raich JW, Tufekcioglu A (2000) Vegetation and soil respiration: correlations and controls. Biogeochemistry 48:71–90. https://doi.org/10.1023/A:1006112000616

113. Major J, Lehmann J, Rondon M, Goodale C (2010) Fate of soil-applied black carbon: downward migration, leaching and soil respiration. Glob Chang Biol 16:1366–1379. https://doi.org/10.1111/j.1365-2486.2009.02044.x

114. Kuzyakov Y, Subbotina I, Chen H, Bogomolova I, Xu X (2009) Black carbon decomposition and incorporation into soil microbial biomass estimated by 14C labeling. Soil Biol Biochem 41:210–219. https://doi.org/10.1016/j.soilbio.2008.10.016

115. Fang C, Moncrieff JB (2001) The dependence of soil CO_2 efflux on temperature. Soil Biol Biochem 33:155–165. https://doi.org/10.1016/S0038-0717(00)00125-5

116. Richardson J, Chatterjee A, Darrel Jenerette G (2012) Optimum temperatures for soil respiration along a semi-arid elevation gradient in southern California. Soil Biol Biochem 46:89–95. https://doi.org/10.1016/j.soilbio.2011.11.008

117. Genesio L, Miglietta F, Lugato E, Baronti S, Pieri M, Vaccari FP (2012) Surface albedo following biochar application in durum wheat. Environ Res Lett 7. https://doi.org/10.1088/1748-9326/7/1/014025

118. Meyer S, Bright RM, Fischer D, Schulz H, Glaser B (2012) Albedo impact on the suitability of biochar systems to mitigate global warming. Environ Sci Technol 46:12726–12734. https://doi.org/10.1021/es302302g

119. Karhu K, Mattila T, Bergström I, Regina K (2011) Biochar addition to agricultural soil increased CH4 uptake and water holding capacity—results from a short-term pilot field study. Agric Ecosyst Environ 140:309–313. https://doi.org/10.1016/j.agee.2010.12.005

120. Reicosky DC (1997) Tillage-induced CO_2 emission from soil Tillage-induced CO_2 emission from soil. Nutr Cycl Agroecosystems 49:273–285. https://doi.org/10.1023/A:1009766510274

121. Kuzyakov Y (2010) Priming effects: interactions between living and dead organic matter. Soil Biol Biochem 42:1363–1371. https://doi.org/10.1016/j.soilbio.2010.04.003

122. Wardle DA, Nilsson MC, Zackrisson O (2008) Fire-derived charcoal causes loss of forest humus. Science 320 (80):629. https://doi.org/10.1126/science.1154960

123. Spokas KA (2012) Impact of biochar field aging on laboratory greenhouse gas production potentials. GCB Bioenergy 5:165–176. https://doi.org/10.1111/gcbb.12005

124. Jin H (1989) Thesis: Characterization of Microbial Life Colonizing Biochar and Biochar-Amended Soils. J Chem Inf Model 53:160. https://doi.org/10.1017/CBO9781107415324.004

125. Bailey VL, Fansler SJ, Smith JL, Bolton H (2011) Reconciling apparent variability in effects of biochar amendment on soil enzyme activities by assay optimization. Soil Biol Biochem 43:296–301. https://doi.org/10.1016/j.soilbio.2010.10.014

126. IPCC (2007) Summary for policymakers. In: Solomon S et al (eds) Climate change 2007: the physical sciences basis. Working Group I Contribution to the Fourth Assessment Report of the IPCC. https://books.google.com.co/books?id=8-m8nXB8GB4C

127. Van Zwieten L, Kammen C, Cayuela ML, Singh BP, Joseph S, Kimber S et al (2015) Biochar effects on nitrous oxide and methane emissions from soil. Biochar Environ Manag Sci Technol Implement 976. https://books.google.com/books?id=gWDABgAAQBAJ&pgis=1

128. Scheer C, Grace PR, Rowlings DW, Kimber S, van Zwieten L (2011) Effect of biochar amendment on the soil-atmosphere exchange of greenhouse gases from an intensive subtropical pasture in northern New South Wales Australia. Plant Soil. 345:47–58. https://doi.org/10.1007/s11104-011-0759-1

129. Sánchez-García M, Sánchez-Monedero MA, Roig A, López-Cano I, Moreno B, Benitez E et al (2016) Compost versus biochar amendment: a two-year field study evaluating soil C build-up and N dynamics in an organically managed olive crop Plant Soil 408. https://doi.org/10.1007/s11104-016-2794-4

130. Spokas KA, Reicosky DC (2009) Impacts of sixteen different biochars on greenhouse gas production. Ann Environ Sci 3:179–193

131. Clough TJ, Bertram JE, Ray JL, Condron LM, O'Callaghan M, Sherlock RR et al (2010) Unweathered wood biochar impact on nitrous oxide emissions from a bovine-urine-amended pasture soil. Soil Sci Soc Am J 74:852. https://doi.org/10.2136/sssaj2009.0185

132. Saarnio S, Heimonen K, Kettunen R (2013) Biochar addition indirectly affects N_2O emissions via soil moisture and plant N uptake. Soil Biol Biochem 58:99–106. https://doi.org/10.1016/j.soilbio.2012.10.035

133. Baggs EM (2011) Soil microbial sources of nitrous oxide: recent advances in knowledge, emerging challenges and future direction. Curr Opin Environ Sustain 3:321–327. https://doi.org/10.1016/j.cosust.2011.08.011

134. Butterbach-Bahl K, Baggs EM, Dannenmann M, Kiese S, Zechmeister-Boltenstern S (2013) Nitrous oxide emissions from soils: how well do we understand the processes and their controls? Philos Trans R Soc B Biol Sci 368. https://doi.org/10.1098/rstb.2013.0122

135. Bruun EW, Müller-Stöver D, Ambus P, Hauggaard-Nielsen H (2011) Application of biochar to soil and N_2O emissions: potential effects of blending fast-pyrolysis biochar with anaerobically digested slurry. Eur J Soil Sci 62:581–589. https://doi.org/10.1111/j.1365-2389.2011.01377.x

136. Oertel C, Matschullat J, Zurba K, Zimmermann F, Erasmi S (2016) Article in press G Model Greenhouse gas emissions from soils—A review. Chem Erde. https://doi.org/10.1016/j.chemer.2016.04.002

137. Harter J, Krause HM, Schuettler S, Ruser R, Fromme M, Scholten T et al (2014) Linking N2O emissions from biochar-amended soil to the structure and function of the N-cycling microbial community. ISME J 8:660–674. https://doi.org/10.1038/ismej.2013.160

138. He L, Zhao X, Wang S, Xing G (2016) The effects of rice-straw biochar addition on nitrification activity and nitrous oxide emissions in two Oxisols. Soil Tillage Res 164:52–62. https://doi.org/10.1016/j.still.2016.05.006

139. Augustenborg CA, Hepp S, Kammann C, Hagan D, Schmidt O, Müller C (2012) Biochar and earthworm effects on soil nitrous oxide and carbon dioxide emissions. J Environ Qual 41:1203. https://doi.org/10.2134/jeq2011.0119

140. Bamminger C, Marschner B, Jüschke E (2014) An incubation study on the stability and biological effects of pyrogenic and hydrothermal biochar in two soils. Eur J Soil Sci 65:72–82. https://doi.org/10.1111/ejss.12074

141. Liu L, Shen G, Sun M, Cao X, Shang G, Chen P (2014) Effect of biochar on nitrous oxide emission and its potential mechanisms. J Air Waste Manag Assoc 64:894–902. https://doi.org/10.1080/10962247.2014.899937

142. Sun L, Li L, Chen Z, Wang J, Xiong Z (2014) Combined effects of nitrogen deposition and biochar application on emissions of N_2O, CO_2 and NH_3 from agricultural and forest soils. Soil Sci Plant Nutr 60:254–265. https://doi.org/10.1080/00380768.2014.885386

143. Lehmann J, Gaunt J, Rondon M (2006) Bio-char sequestration in terrestrial ecosystems—a review. Mitig Adapt Strateg Glob Chang 11:403–427. https://doi.org/10.1007/s11027-005-9006-5

144. Mizuta K, Matsumoto T, Hatate Y, Nishihara K, Nakanishi T (2004) Removal of nitrate-nitrogen from drinking water using bamboo powder charcoal. Bioresour Technol 95:255–257. https://doi.org/10.1016/j.biortech.2004.02.015

145. Radovic LR, Moreno-Castilla C, Rivera-Utrilla J (2001) Carbon materials as adsorbents in aqueous solutions. Chem Phys Carbon 227–405

146. Felber R, Leifeld J, Horák J, Neftel A (2014) Nitrous oxide emission reduction with greenwaste biochar: comparison of laboratory and field experiments. Eur J Soil Sci 65:128–138. https://doi.org/10.1111/ejss.12093

147. Sarkhot DV, Berhe AA, Ghezzehei TA (2012) Impact of biochar enriched with dairy manure effluent on carbon and nitrogen dynamics. J Environ Qual 41:1107. https://doi.org/10.2134/jeq2011.0123

148. Angst TE, Patterson CJ, Reay DS, Anderson P, Peshkur TA, Sohi SP (2013) Biochar diminishes nitrous oxide and nitrate leaching from diverse nutrient sources. J Environ Qual 42:672. https://doi.org/10.2134/jeq2012.0341

149. Rogovska N, Laird D, Cruse R, Fleming P, Parkin T, Meek D (2011) Impact of biochar on manure carbon stabilization and greenhouse gas emissions. Soil Sci Soc Am J 75:871. https://doi.org/10.2136/sssaj2010.0270

150. Chen X, Jeyaseelan S, Graham N (2002) Physical and chemical properties study of the activated carbon made from sewage sludge. Waste Manag 22:755–760. https://doi.org/10.1016/S0956-053X(02)00057-0

151. Cayuela ML, Sánchez-Monedero MA, Roig A, Hanley K, Enders A, Lehmann J (2013) Biochar and denitrification in soils: When, how much and why does biochar reduce N_2O emissions? Sci Rep 3. https://doi.org/10.1038/srep01732

152. Malghani S, Gleixner G, Trumbore SE (2013) Chars produced by slow pyrolysis and hydrothermal carbonization vary in carbon sequestration potential and greenhouse gases emissions. Soil Biol Biochem 62:137–146. https://doi.org/10.1016/j.soilbio.2013.03.013

153. Nelissen V, Saha BK, Ruysschaert G, Boeckx P (2014) Effect of different biochar and fertilizer types on N_2O and NO emissions. Soil Biol Biochem 70:244–255. https://doi.org/10.1016/j.soilbio.2013.12.026

154. Sánchez-García MA, Roig M, Sanchez-Monedero A, Cayuela ML (2014) Biochar increases soil N_2O emissions produced by nitrification-mediated pathways. Front Environ Sci 2. https://doi.org/10.3389/fenvs.2014.00025

155. Kammann C, Funke A (2017) Hydrothermal carbonization of biomass residuals: a comparative review of the chemistry, processes and applications of wet and dry pyrolysis. Biofuels 2:71–106. https://doi.org/10.4155/bfs.10.81

156. Renner R (2007) Rethinking biochar. Environ Sci Technol 41:5932–5933. https://doi.org/10.1021/es0726097

157. Jia J, Li B, Chen Z, Xie Z, Xiong Z (2012) Effects of biochar application on vegetable production and emissions of N_2O and ch4. Soil Sci. Plant Nutr. 58:503–509. https://doi.org/10.1080/00380768.2012.686436

158. Hanley K, Enders A, Cayuela ML, Sa MA, Lehmann J, Sánchez-Monedero MA et al (2013) Biochar and denitrification in soils: when, how much and why does biochar reduce $N_{(2)}O$ emissions? Sci Rep 3:1–7. https://doi.org/10.1038/srep01732

159. Zheng W, Guo M, Chow T, Bennett DN, Rajagopalan N (2010) Sorption properties of greenwaste biochar for two triazine pesticides. J Hazard Mater 181:121–126. https://doi.org/10.1016/j.jhazmat.2010.04.103

160. Oya A, Iu WG (2002) Deodorization performance of charcoal particles loaded with orthophosphoric acid against ammonia and trimethylamine. Carbon N Y 40:1391–1399. https://doi.org/10.1016/S0008-6223(01)00273-1

161. Tsutomu I, Takashi A, Kuniaki K, Kikuo O (2004) Comparison of removal efficiencies for ammonia and amine gases between woody charcoal and activated carbon. J Heal Sci 50:148–153. https://doi.org/10.1248/jhs.50.148

162. Brevik EC (2012) Soils and climate change: gas fluxes and soil processes. Soil Horizons 53:12. https://doi.org/10.2136/sh12-04-0012

163. Cai Z, Xing G, Yan X, Xu H, Tsuruta H, Yagi K et al (1997) Methane and nitrous oxide emissions from rice paddy fields as affected by nitrogen fertilisers and water management. Plant Soil 196:7–14. https://doi.org/10.1023/A:1004263405020

164. Xiong Z-Q, Xing G-X, Zhu Z-L (2007) Nitrous oxide and methane emissions as affected by water. Soil Nitrogen Pedosphere 17:146–155. https://doi.org/10.1016/s1002-0160(07)60020-4

165. Dalal RC, Allen DE, Livesley SJ, Richards G (2008) Magnitude and biophysical regulators of methane emission and consumption in the Australian agricultural, forest, and submerged landscapes: a review. Plant Soil 309:43–76. https://doi.org/10.1007/s11104-007-9446-7

166. Baldock JA, Smernik RJ (2002) Chemical composition and bioavailability of thermally altered *Pinus resinosa* (Red pine) wood. Org Geochem 33:1093–1109. https://doi.org/10.1016/S0146-6380(02)00062-1

167. Jha P, Biswas AK, Lakaria BL, Subba Rao A (2010) Biochar in agriculture—prospects and related implications. Curr Sci 99:1218–1225

168. Tate KR, Ross DJ, Scott NA, Rodda NJ, Townsend JA, Arnold GC (2006) Post-harvest patterns of carbon dioxide production, methane uptake and nitrous oxide production in a *Pinus* radiata D. Don plantation. For Ecol Manage 228:40–50. https://doi.org/10.1016/j.foreco.2006.02.023

169. Jacinthe PA, Lal R (2006) Methane oxidation potential of reclaimed grassland soils as affected by management. Soil Sci 171:772–783. https://doi.org/10.1097/01.ss.0000209357.53536.43

170. Qian L, Chen L, Joseph S, Pan G, Li L, Zheng J et al (2014) Biochar compound fertilizer as an option to reach high productivity but low carbon intensity in rice agriculture of China. Carbon Manag. 5:145–154. https://doi.org/10.1080/17583004.2014.912866

171. Creamer AE, Gao B, Zhang M (2014) Carbon dioxide capture using biochar produced from sugarcane bagasse and hickory wood. Chem Eng J 249:174–179. https://doi.org/10.1016/j.cej.2014.03.105

172. Huang YF, Te Chiueh P, Shih CH, Lo SL, Sun L, Zhong Y et al (2015) Microwave pyrolysis of rice straw to produce biochar as an adsorbent for CO_2 capture. Energy. 84:75–82. https://doi.org/10.1016/j.energy.2015.02.026

173. Singh BP, Hatton BJ, Singh B, Cowie AL, Kathuria A (2010) Influence of biochars on nitrous oxide emission and nitrogen leaching from two contrasting soils. J Environ Qual 39:1224. https://doi.org/10.2134/jeq2009.0138

174. Liu Y, Yang M, Wu Y, Wang H, Chen Y, Wu W (2011) Reducing CH_4 and CO_2 emissions from waterlogged paddy soil with biochar. J Soils Sediments 11:930–939. https://doi.org/10.1007/s11368-011-0376-x

175. Zhen M, Song B, Liu X, Chandankere R, Tang J (2018) Biochar-mediated regulation of greenhouse gas emission and toxicity reduction in bioremediation of organophosphorus pesticide-contaminated soils. Chinese J Chem Eng 26:2592–2600. https://doi.org/10.1016/j.cjche.2018.01.028

176. Lu X, Li Y, Wang H, Singh BP, Hu S, Luo Y et al (2019) Responses of soil greenhouse gas emissions to different application rates of biochar in a subtropical Chinese chestnut plantation. Agric For Meteorol 271:168–179. https://doi.org/10.1016/j.agrformet.2019.03.001

177. Thers H, Djomo S, Elsgaard L, Knudsen MT (2019) Biochar potentially mitigates greenhouse gas emissions from cultivation of oilseed rape for biodiesel. Elsevier. 671:180–188. https://doi.org/10.1016/j.scitotenv.2019.03.257

178. Fidel R, Laird D, Parkin T (2019) Effect of biochar on soil greenhouse gas emissions at the laboratory and field scales. Soil Syst 3:8. https://doi.org/10.3390/soilsystems3010008

Assessment of Enterprise Emission Inventory Considering Entropy Production for a Cement Production Line

M. Ziya Sogut, Kateryna Synylo and T. Hikmet Karakoc

Abstract The cement sector, which has a high energy consumption in the industrial sector, has significant environmental pollutant potential and besides high energy costs. In the sectoral evaluations, in addition to the efficient and efficient use of energy, alternative studies have become a necessity to eliminate such threats. The energy consumption behavior of this sector, especially fossil source, can be considered as an important environmental impact due to low system efficiency. In this context, irreversibility, which can be seen as the production of entropy in the thermodynamic process, will directly affect the emission potential with thermal effect. In this study, entropy production of the cement production line was examined with exergy analysis, and the losses due to irreversibility were evaluated. The potential of the enterprise emission inventory is then investigated for this potential, which is generally considered to be thermal irreversibility. According to the analysis, the analysis of the process was found at 56.92%. Along with the fossil fuel consumption estimates, CO_2 emission potentials represent 0.40% of the cumulative total. At the end of the study, some suggestions were made to improve the environmental and economic effects of reducing the potentials reached according to the analysis.

Keywords Cement · Efficiency · Irreversibility · Emission · Sustainability

M. Z. Sogut (✉)
Maritime Faculty, Piri Reis University, Tuzla, Istanbul, Turkey
e-mail: mzsogut@gmail.com

K. Synylo
Institute of Ecological Safety, National Aviation University, Kiev, Ukraine

T. H. Karakoc
Department of Airframe and Powerplant Maintenance, Faculty of Aeronautics and Astronautics, Eskişehir Technical University, 26470 Eskisehir, Turkey

Nomenclature

$\dot{E}$	Energy rate (MW)
$\dot{E}x$	Exergy rate (MW)
$\dot{Q}$	Heat rate (MW)
$\dot{W}$	Work rate (MW)
$\dot{m}$	Mass flow rate (kg s^{-1})
h	Specific enthalpy (kJ kg^{-1})
P	Pressure (kPa)
T	Temperature (K)
ex	Specific exergy (MJ kg^{-1})
ke	Specific kinetic energy (kJ kg^{-1})
pe	Specific potential energy (kJ kg^{-1})
s	Specific entropy (kJ kg^{-1} K^{-1})

Greek Letters

η_{II}	Exergy efficiency

Subscripts

0	Ambient conditions
dest	Destruction
in	Inlet
mass	Mass transfer related
out	Outlet
work	Work related
ch	Chemical
ke	Kinetic
pot	Potential
ph	Physical
th	Thermal

1 Introduction

National or international organizations around the world are making great efforts to combat global climate change, which is mainly caused by many reasons, such as greenhouse gas emissions, which are important players in global climate change, are an impact of direct or indirect fossil fuel consumption. Generally, fossil fuel consuming thermal systems increase this effect with low system efficiency. Increasing competition conditions, especially in the industrial sector, is affected not only by the environment but also by costs. Especially in production processes, continuity, quality, and low cost of energy inputs have become an important target for many enterprises or sectoral structures. Among these sectors, the cement sector is an energy-intensive sector where multilateral studies are carried out in terms of energy consumption potential and costs.

The cement sector is the main sector for many countries, which has an average annual increase of 6–8% and consumes 3.6 GJ/ ton of energy per ton on average. This sector, which consumes about 98% of energy consumption in production processes, mainly uses fossil fuel resources. Cement production, in terms of production costs, with an energy input per product of 45–55%, is defined in two ways as dry or wet systems in production processes, and these production systems have high energy consumption at every stage of the production line. This sector, which is aware of the intensity of energy consumption also carries out intensive studies to reduce energy consumption and costs. In this context, while the environmental quality in production is ensured with ISO 9001 and ISO 14000, ISO 50001 energy management system has also developed sensitivity to energy management in enterprises. However, mostly based on fossil fuel consumption in cement production, inefficiencies caused by production processes have an important environmental impact based on not only economic losses but also pollutants and emissions.

As with all thermal systems, the environmental impacts caused by the systems are directly the result of losses or irreversibility of the system. In this context, these effects of the systems are examined based on the first and second law of thermodynamics. In fact, the first law directly defines a quantitative potential, while the second law defines the irreversibility of the system with reference to the dead-state conditions. In this context, the value of entropy produced by the systems is shaped according to exergy destruction in the system. While energy does not consume in a system, the ability of the system, defined as exergy, is consumed depending on irreversibility. For this reason, the actual dimensions of irreversibility are defined in the systems.

In cement production having intense fossil fuel consumption, the process inefficiencies and losses due to irreversibility are high in systems where the production lines. Therefore, cement production releases a significant amount of CO_2 both directly and indirectly. The direct emissions are produced by the calcination process, and the contribution of CO_2 obtains nearly 50%. Indirect emissions are produced by the burning of fossil fuels, and the contribution of additional CO_2 emissions obtains 40%. According to global evaluation, [1] emissions from cement production contribute 4.5% of global CO_2 releases from fossil-fuel burning and cement production.

The cement sector is a multi-faceted sector with scientific or sectoral evaluations. Actual studies can be classified as sectoral reporting [2, 3], performance analysis [4–6], production based on energy and exergy analysis, [7–9], process improvements, and emission analysis [10, 11]. However, the studies based on the assessment of enterprise emission inventory with especially in the exergetic approach like in this study can be seen that have quite limited. Accordingly, this chapter first assessed thermal process efficiencies according to actual production and energy consumption data of a cement plant. In this study, the corporate emissions inventory approach has been presented, and then, emissions associated with thermal irreversibility, which is a significant effect of this, have also been assessed. Possible emission savings were also questioned by assessing the improvement potentials in the study.

2 Background

2.1 Cement Sector

The cement sector, which develops as the leading sector all over the world, is very limited in terms of international criteria despite the increasing trade load. In this sector that mostly serves domestic markets, the potential of international trade is 7%. The cement sector, which is densely populated locally, has direct or indirect intensive energy consumption. Considering the processing properties of production processes, although it has a capital intensive business structure, it is considered as one of the most polluting industries in terms of environmental criteria. Considering the sectoral potential, it has a share of approximately 5% of the total load on greenhouse gas emissions only [12].

While the cement sector has developed the national competition, it has made development a priority issue in all components of production, infrastructure development, studies based on increasing of production, sustainable business models, and technology searches to improve the quality of production comes first. However, the basic issue in this sector is the reduction of threats caused from emissions for a sustainable environment that develops as social pressure. For this purpose, the development of business strategies, particularly sustainable carbon management, has been the main approach with the internationally recognized climate agreements. Despite the global crisis, production in the cement sector has shown an upward trend. When taken reference from 2010 to 2014, the sector had an average growth trend of 4–5% per year in the world. In this sector, China, which reached a production potential of approximately 4.2 billion tons compared to the data of 2014, is the first country with a big difference. India, the EU, the USA, Brazil, and Turkey have followed this country, respectively [13, 14]. Economic growth and increasing demand for urbanization increase the production demands of the direct or indirect production sector. As a matter of fact, when the sectoral demand is taken as reference in 1990, it is estimated that it will reach at least five times [15].

Cement production is the sector in which energy cost effects are followed closely. Sectoral players, in particular, make many studies based on reducing energy cost effects. However, the effective use of energy, which is the basic input in this process, is a priority issue. Generally, in sectoral assessments, energy use performance is simply assessed on the principle of conservation of energy. This environment-independent process will not directly reflect the actual conditions as a performance criterion. Especially in such a high-intensity energy-consuming production process, environmental parameters have a significant impact. In this respect, the second law of thermodynamics, exergy approach is prominent. For a thermal system, exergy is defined as the maximum work that can be achieved in the system for dead-state conditions. This definition refers to the size of direct or indirect real irreversibility in the systems, and the potential for loss and the capacity of the entropy generated. The environmental scope of the loss effect resulting from this aspect will increase the direct and indirect emission impact. This study also investigated the emission potential due to exergetic efficiency.

According to global evaluation, emissions from cement production contribute 4.5% of global CO_2 releases from fossil-fuel burning and cement production. In the sectoral analysis, the CO_2 emission potential for the production of cement per tonne is 0.89 ton CO_2 [1]. In this respect, the CO_2 emission load that will be released against world cement production will exceed the EU's total CO_2 emission potential when 2030 scenarios are evaluated [16]. For this context, the total and individual contributors of CO_2 at a global level are given in Fig. 1.
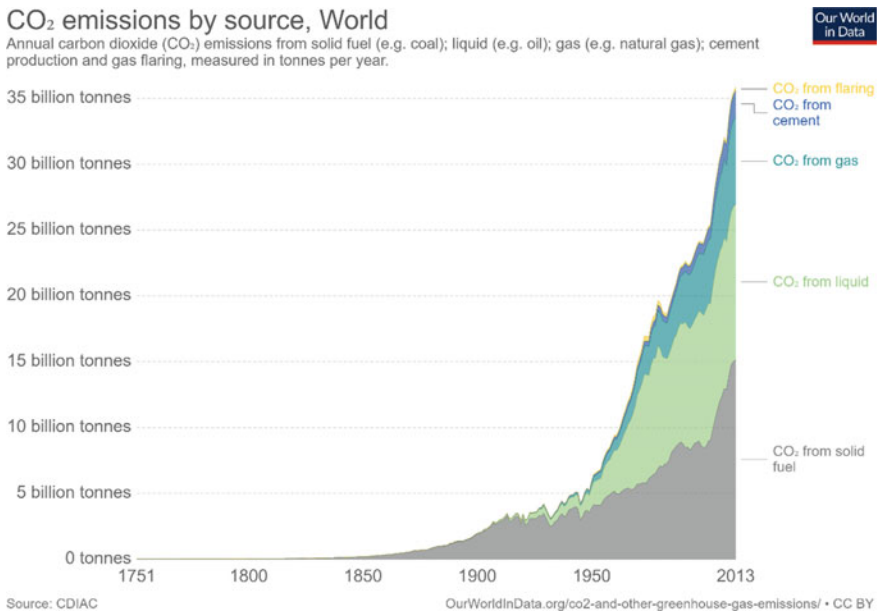
Fig. 1 The total and individual contributors of CO_2 at a global level [17]

Cement production is a process that produces significant CO_2 emissions. This basis is evaluated in two contexts. The first one is the production of cement based on raw material. In the cement or manufacturing process, carbonates (mostly $CaCO_3$-limestone) oxidized by heat contact. In this process, CO_2 decomposes, and this is a chemical reaction process defined directly in clinker production. The stoichiometric curve defines the directly generated CaO curve, and in these recent studies, it has been reported that it contributes 5% to the total CO_2 potential, regardless of land [18]. Another source is fossil fuels used for combustion processes in production. The fossil fuels consumed for the product temperature which is directly or indirectly more than 1000 °C in the production process have direct or indirect emission effect as a result of combustion. This provides a potential increase of about 60%, including the electricity purchased in the entire production process [19].

Cement production usually has a distinct production process. There are two models in production processes, wet and dry. However, the dry system is the common production process all of the world in cement sector. Information about the dry production system is given briefly as below.

3 Dry System Cement Production

Dry system cement production is a process that is managed and monitored from raw material processing to packaging. The basic components or units are raw material preparation, farina mill, rotary kiln process, and cement processes, respectively. In addition, moisture control is an important parameter in every stage of production. A cement production flow process was given in Fig. 2.

Depending on the production plan, the farina, which is produced from natural raw materials by passing through the farina mill, is stored at 50–60 °C [3]. The obtained farina enters the preheater cyclones at a temperature of 50–60 °C depending on the cement product to be produced and heated to 1000–1100 °C by the calcining process until the rotary kiln process. In this section, the product from rotary kiln about 2.5 rpm rapidly is defined as clinker with between 1300 and 1500 °C. At this point, the product converted into clinker is subjected to the sintering process. Then, clinker cooled to 100–120 °C with a high capacity fan group in the cooling process is sent to cement mills for cementing together with cement additives.

In the dry system cement production, coal and its derivatives, petroleum-derived fuels and natural gas together with electricity are used as an energy source. In this production process, energy is a very important production cost. Figure 3 shows the share of energy and other items in unit cost.

The share of energy cost in the cement sector is about 50–60% of the unit product cost. It is seen that the share of fuel costs is between 35 and 40%, while the share of electricity costs is 20–25%. The high energy cost of sector based on energy intensive in countries like Turkey is one of the most important factors that cause the competition
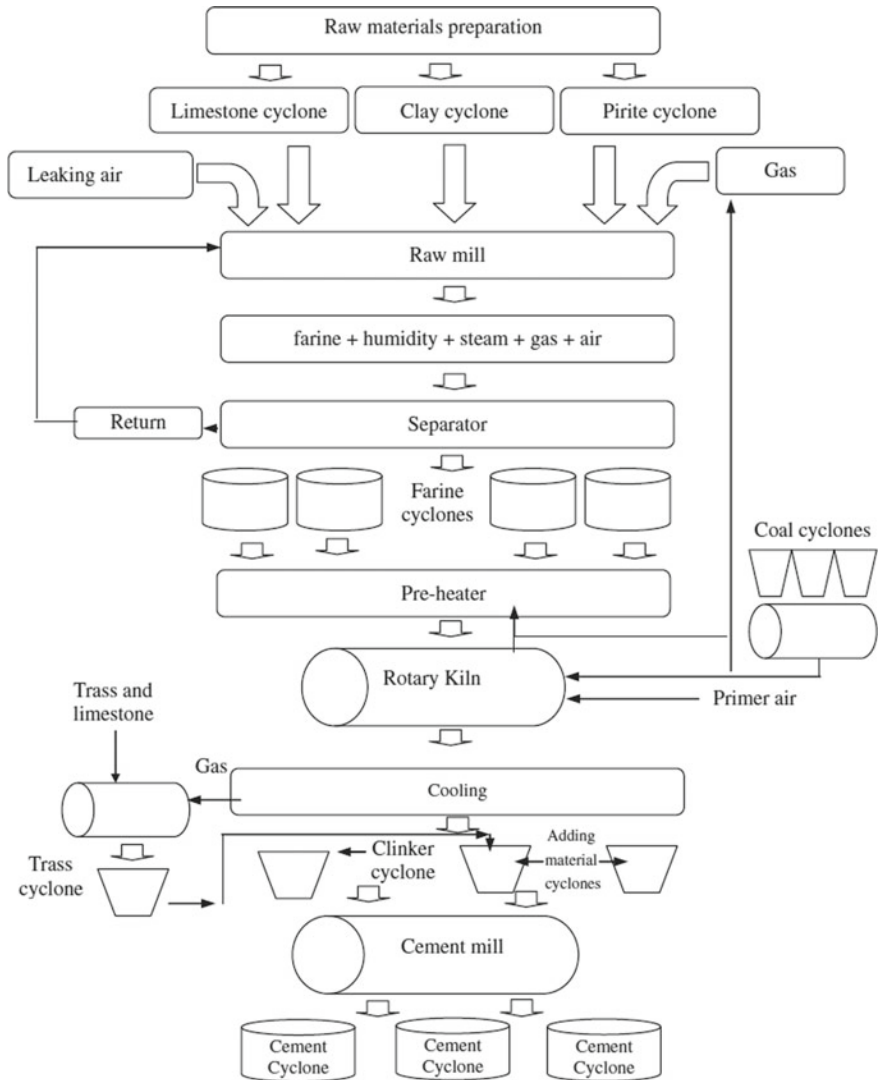
Fig. 2 Flow diagram of a dry system cement plant process [8]

power of the sector to fall. The preferred fuel in the cement sector is petroleum coke and coal and its derivatives. In particular, the use of petroleum coke accounts for about 70% of total fuel consumption.

Fig. 3 Cost components in cement production [Modifed from Ref. 13]

COST COMPONENTS IN THE CEMENT INDUSTRY
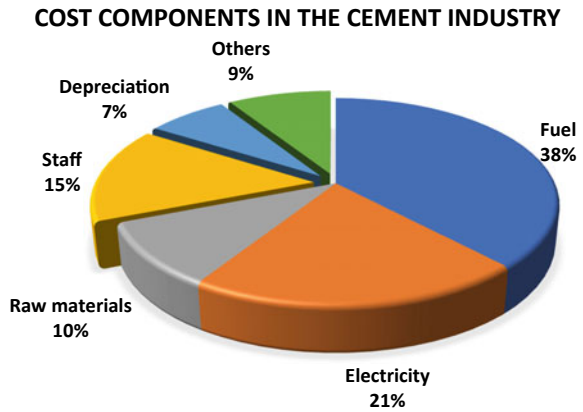
4 Emission Inventory

Today, environmental management has become the most important issue in sustainable development strategies. In this context, global carbon estimates are made for each year, and the process is taken under control. In the cement sector, CO_2 emissions from fossil fuel consumption are monitored not only in the environmental direction but also as part of the global carbon budget [20].

As a matter of fact, the databases formed within this scope include all of the cement-derived emissions defined directly and indirectly in the IPCC. According to IPPC evaluations; at least the cement production affects the surrounding vegetation negatively. This is especially effective for areas with limestone quarries and raw carbonate minerals. In production, CO_2 emits as a by-product, while fossil fuel consumption and high CO_2 emissions occur. However, for CO_2 emission estimates in cement production, clinker values, which are intermediate products instead of cement data, are taken as a basis. It is important that the clinker is an intermediate product that uses the energy most intensively in cement production and that it is the basic input in the formation of cement. In this context, emission estimation should be seen as a holistic structure.

Due to the impact of the emission burden on cement, all nations conduct studies on forecasts and expectations in this regard. In this respect, clinker production data and emission factor, which are mostly defined by IPCC, have become a preference for institutional structures. According to the reference year conditions, the values formed in the estimations are recorded and developed with global shares. Clinker ratio in cement production is a criterion on which the sector is based. In fact, the 0.95 value defined by the IPPC in 1970 is defined by the linear interpolation of the emission factor for the reference year in each country [15].

In institutional structures, the environmental impact created by losses in thermal processes is often dealt with in a structure defined by the CO_2 emission factor. However, in institutional inventory studies, the institutional impact must be addressed
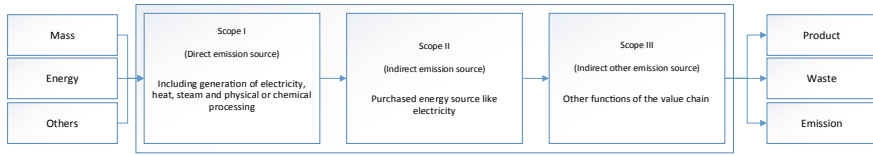
Fig. 4 Enterprise emission inventory

holistically on the basis of the carbon footprint. The corporate emissions inventory approach for an emission inventory that can be defined in a unified manner is defined in Fig. 4 [21].

5 Theoretical Analysis

5.1 Energy Terms

Energy-consuming processes are evaluated according to the principle of conservation of energy in thermal load distributions. In this context, it is primarily examined with the mass balance in processes with the flow process. The mass balance, which is independent of time for continuous flow processes, is defined by the balance between the incoming and outgoing substance (s). Mass balance with a dry flow capability in cement manufacturing processes:

$$\sum \dot{m}_{\text{in}} = \sum \dot{m}_{\text{out}} \tag{1}$$

The energy flow considering the energy conservation concept refers to an energy balance in essentially flow processes. Independent energy balance for the processing time in the form of a continuous flow can be stated as

$$\sum \dot{E}_{\text{in}} = \sum \dot{E}_{\text{out}} \tag{2}$$

General energy balance due to each flow component can be written as given below:

$$\sum \dot{m}_{\text{in}}(h + \text{ke} + \text{pe})_{\text{in}} - \sum \dot{m}_{\text{out}}(h + \text{ke} + \text{pe})_{\text{out}} + \sum \dot{Q} - \dot{W} = 0 \tag{3}$$

Here, h, ke, pe, $\dot{Q}$, and $\dot{W}$ state the specific enthalpy, kinetic energy, potential energy, and net heat transfer rate passed from the control volume boundaries with net work rate defined on the control volume, respectively [22, 23]. Besides, in many energy analysis including steady-state condition, kinetic and potential energy change have a very low effect, and for this analysis, process is assumed as adiabatic phase. Thus, the energy rate of the flow or energy analyses in control volume is expressed

by the enthalpy change, in cases where kinetic and potential effects are neglected. Accordingly, the enthalpy of any material is defined by

$$dh = c_p dT \tag{4}$$

where dh states enthalpy change of the material, while dT is the temperature change for inlet and output of material, and c_p is specific heat capacity of material under constant pressure.

5.2 Exergy Terms

Actual systems are affected by climatic conditions. Their environmental conditions are an important parameter for the irreversibility of systems including the dead state. The maximum work potential of the systems in energy flow conditions is defined by the concept of exergy in thermodynamic processes. Exergy systems are the maximum job potential to be produced as the dead-state conditions. Exergy flow rate for any point of the system in the flow process, as defined below, as a form of physical, chemical, kinetic, and potential exergises [24–26]

$$\dot{E}x = \dot{E}x^{\mathrm{KE}} + \dot{E}x^{\mathrm{PE}} + \dot{E}x^{\mathrm{PH}} + \dot{E}x^{\mathrm{CH}} \tag{5}$$

As in energy system analysis, kinetic and potential exergies can be ignored depending on the load effects. In this case, the total exergy of the thermal system is the sum of the physical and chemical exergies as follows:

$$\dot{E}x^{\mathrm{TH}} = \dot{E}x^{\mathrm{PH}} + \dot{E}x^{\mathrm{CH}} \tag{6}$$

The overall exergy balance for the flow process of a system with boundaries depends on the flow potential of the total incoming and outgoing materials. This balance for continuous flow form:

$$\sum \dot{E}x_{\mathrm{in}} - \sum \dot{E}x_{\mathrm{out}} = \sum \dot{E}x_{\mathrm{dest}} \tag{7}$$

Exergy balance, on the other hand, is related to exergy flow in a holistic form, connected to the exergy rates of the mass flow rate, net heat, and net work with for flowing and exiting materials. Equations related to this are

$$\dot{E}x_{\mathrm{heat}} - \dot{E}x_{\mathrm{work}} + \dot{E}x_{\mathrm{mass,in}} - \dot{E}x_{\mathrm{mass,out}} = \dot{E}x_{\mathrm{dest}} \tag{8}$$

$$\dot{E}x_{\mathrm{heat}} = \sum (1 - (T_0/T)) \dot{Q} \tag{9}$$

$$\dot{E}x_{\mathrm{work}} = \dot{W} \tag{10}$$

$$\dot{E}x_{\text{mass}} = \sum \dot{m} \cdot \text{ex} \tag{11}$$

For any point of a system, physical or matrix flow exergy due to unit mass flow for conditions where there is no reaction relationship:

$$\text{ex} = (h - h_0) - T_0(s - s_0) \tag{12}$$

In energy and exergy analyses, the performance of the system is defined in the simplest form depending on the efficiency. This form is defined as the ratio of the output obtained in the system to the energy potential given to the system. This is also defined by the exergy flow in the system under similar conditions [24–26]:

$$\varepsilon = \dot{E}x_{\text{out}} / \dot{E}x_{\text{in}} \tag{13}$$

5.3 CO₂ Emission Terms

In emission analyses, the emission calculation method that has been developed together with the concept of exergy in recent years is the method of carbon emission metric. This method shows that a thermal structure actually has three separate carbon-emission centers. In this case, the total equivalent CO_2 emissions of the system

$$\sum CO_2 = CO_{2i} + \Delta CO_{2j} = \frac{\omega_{CO_{2i}} \sum \dot{Q}_{W_i}}{\eta_{Ii}} + \frac{\omega_{CO_{2j}} \sum \dot{Q}_{BW_j}}{\eta_{Ij}} (1 - \psi_{Ri}) \tag{14}$$

where ω_{CO_2} is unit energy CO_2 emission factor, $\sum \dot{Q}_W$ is waste energy, $\sum \dot{Q}_{BW}$ is equivalent to boiler energy consumption, and ψ is rational exergy efficiency [27].

6 Case Study

In this study, an evaluation study was conducted in Turkey in order to create an inventory of emissions within the corporate structure of the cement industry. Cement production in Turkey is completely dry cement production. In this study, a general performance evaluation was made based on the reference exergy analysis. In this respect, sectoral efficiency evaluations were made. The clinker and cement production distribution according to sectoral potentials can be seen in Fig. 5.

According to the evaluations, the capacity utilization rate in clinker was 88.24%, while this rate was 62.07% in cement. In particular, the intermediate clinker can be
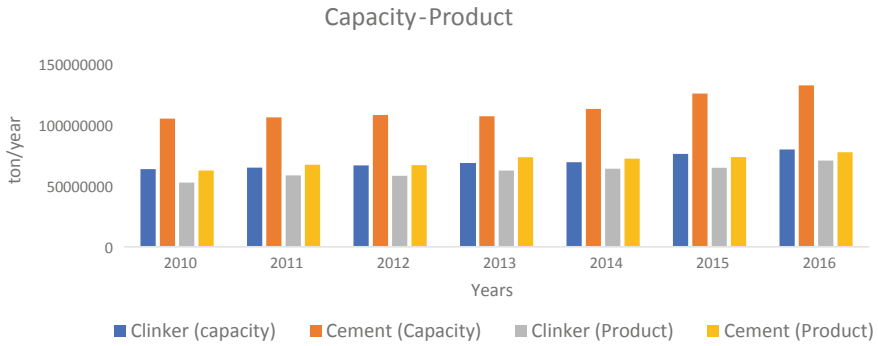
Fig. 5 Capacity and product distrubition

found directly at the market, which may differ from cement. Energy use distributions based on years are examined on the basis of productions, and consumption distributions related to years are given in Fig. 6.

When proportionalized with clinker increase in demand based on 2010, while the change in clinker was 5.31%, this value was 3.17% in energy consumption. When a similar evaluation is taken into consideration for cement, this value is 3.71% in cement, while the energy consumption in cement is 4.22%. All these consumption distributions have an increasing effect on both product aspects. While the change in energy consumption of the sector shows differences in coal consumption, and 2010–2016 fossil fuel consumption distributions have been realized as in Fig. 7.

The cement sector mostly consumes coal derivatives as the main source. Although their distribution rates vary depending on the years, in petrochemicals, this value varies between 35 and 55%, 31–43% of imported coal and 9–22% of domestic coal. In all these distributions, the basic criterion should be seen economically. It can be
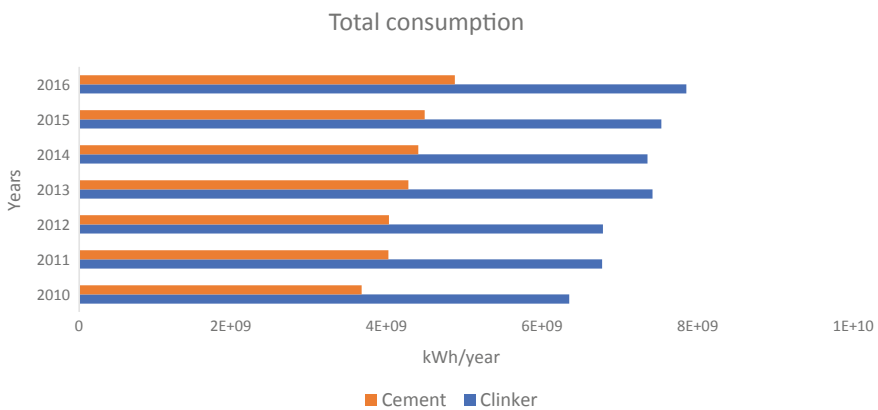
Fig. 6 Total energy consumption
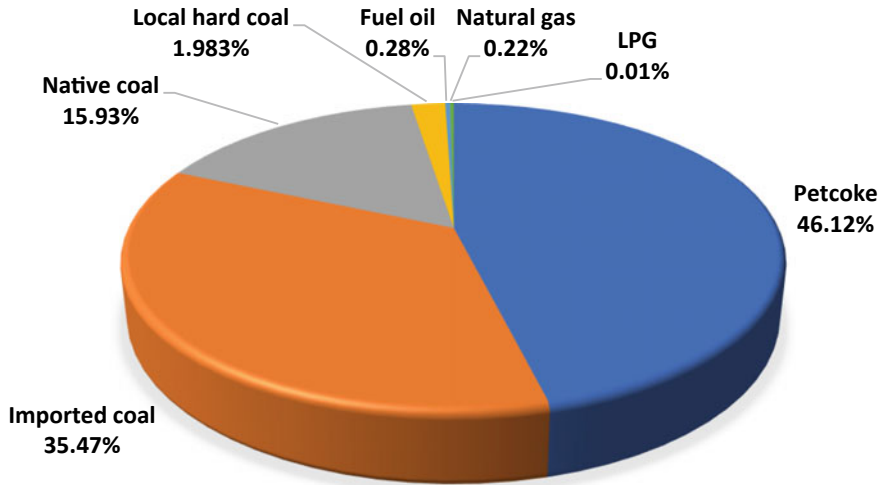
Fig. 7 Fuel consumption rate between 2010 and 2016

seen as the most important variable in meeting the coal demand of enterprises. In this context, an emission definition has been developed by evaluating the share of fossil fuels in total energy for each year. First of all, a fuel-based evaluation was made by considering the system performances consumed in production. Impact performances affecting the system directly or indirectly, especially in fuel-based performances were evaluated. Results are given in Fig. 8.

There is no significant difference in fuel performance in years. In particular, fuel differences have low fluctuations over the years due to the low exergy factor. However, the impact of coal-driven consumption on this performance directly affects system performance. In the study, while the energy efficiency of the years was 56.92%,
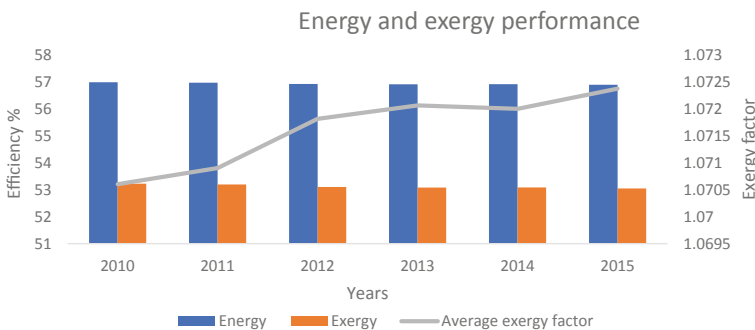
Fig. 8 Energy performance of the fuel used in cement production

the exergy performance was 53.12%. All this distribution is important for emission load analysis, based on unit consumption, for years of exergy losses in clinker and cement production. Accordingly, the yearly exergy breakdown distributions are given in Fig. 9.

Electricity, local lignite, petro-coke can be seen as the main energy source in the cement sector of Turkey which has a dry process production process. But in recent years, natural gas has become one of the sources that started to use this sector. In addition, the waste energy sources used as alternative energy sources by this sector are also important. In the average consumption of the sector, electricity is distributed in average 17–23%, coke consumption 20–27%, and local lignite consumption 50–55%. In particular, the secondary fuel used as an alternative has a total fuel ratio of 3–4%. In this study, a sectoral analysis was made with reference to 2010–2015 years. Within this scope, the consumption energy distributions of the sector were found 46.12% petroleum coke, 35.47% imported coal, 15.93% domestic coal, 1.98% domestic coal,
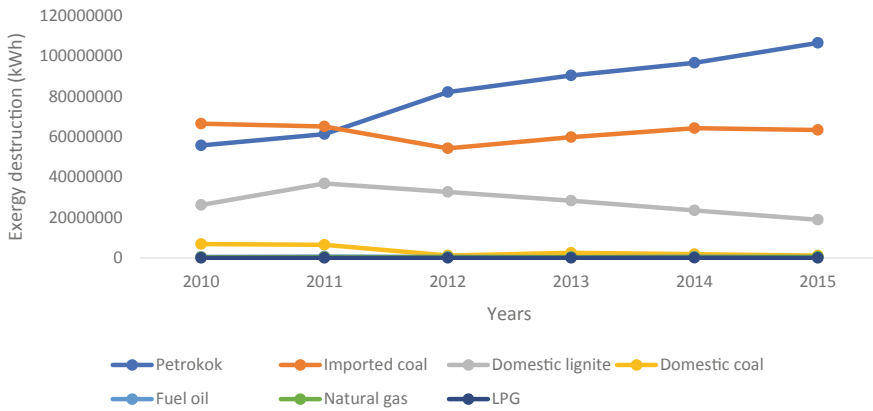
(a) Clinker production
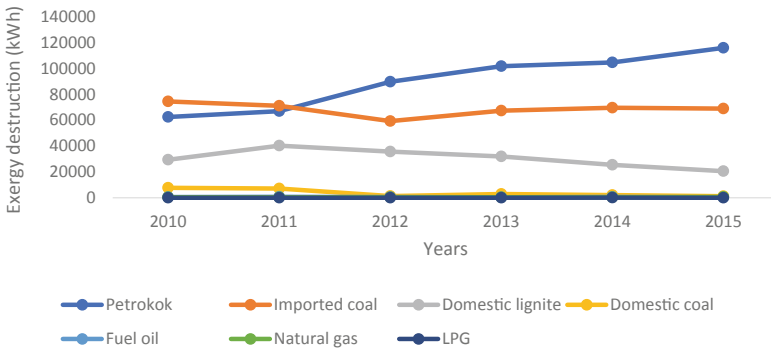
(b) Cement production

Fig. 9 Exergy destruction of clinker and cement
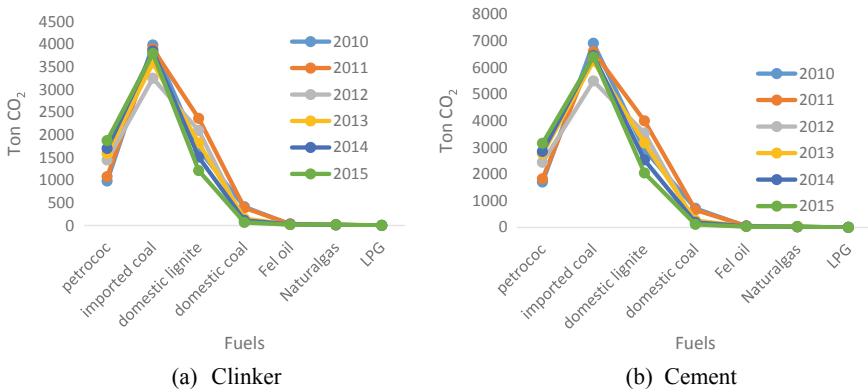
Fig. 10 CO_2 emission potential of clinker and cement production

0.28% fuel oil, 0.22% natural gas, and 0.001% LPG consumption, respectively. Energy consumptions related to fuel consumption and emission evaluations related to these consumed systems were examined separately. According to these, the fossil-derived emission potentials of the clinker and cement production in the production process were calculated separately, and the results were given in Fig. 10.

The average CO_2 emission potential of clinker production in 2010–2015 was found 7193.91 tons of CO_2, and the average production of cement was found 11780.21 tons of CO_2. Compared to this national emission inventory, total emission risk corresponds to approximately 1.88% considering clinker production, and cement production corresponds to 3.07% of total emission potential.

7   Conclusions

This work presents an improved approach to assessing the national emission potential of the cement industry, together with the improved emission inventory. In this analysis, according to the second law analysis of production, the exergy efficiency of the process was found 56.92%. Along with the fossil fuel consumption analyses made, CO_2 emission potentials represent a potential of 0.4% of the cumulative total. Improvements to be made especially during the production process and actions to reduce consumption will also reduce direct emissions. In this respect, energy management practices should be developed for each process.

References

1. Marland G, Boden T (2015) Global, regional and national fossil-fuel CO_2 emissions. Carbon Dioxide Information Analysis Center, Oak Ridge National Laboratory Oak Ridge, TN, USA
2. Worrell E, Galitsky C (2004, January) Energy efficiency improvement opportunities for cement making. Environmental Energy Technologies Division, the U.S. Environmental Protection Agency
3. Schumacher K, Sathaye J (1999, July) India's Cement Industry: productivity, energy efficiency and carbon emissions and environmental energy technologies division. The Environmental Science Division, Office Of Biological And Environmental Research, Office Of Energy Research, U.S. Department Of Energy
4. Meng Y, Ling TC, Mo KH, Tian W (2019, June 25) Enhancement of high temperature performance of cement blocks via CO_2 curing, Sci Total Environ 671:827–837. Elsevier
5. Ahdaya M, Imqam A (2019, May) Investigating geopolymer cement performance in presence of water based drilling fluid, J Pet Science Eng 176:934–942
6. Hoffmann B, Häfele S, Karl U (2013) Analysis of performance losses of thermal power plants in Germany—a system dynamics model approach using data from regional climate modelling. Energy 49:193–203. Elsevier
7. Karakus AA, Boyar S, Akdeniz RC, Hepbasli A (2002) An exergy analysis in a mixed feed industry: evaluation of an extruder pellet line. In: EE&AE'2002—International scientific conference, Rousse, Bulgaria, 04–06.04.2002
8. Sogut Z (2012) A research on exergy consumption and potential of total CO_2 emission in the Turkish cement sector. Energy Conv Manag 56:37–45
9. Sogut Z, Oktay Z(2008) Energy and exergy analyses in a thermal process of a production line for a cement factory and applications. Int J Exergy 5:218–240
10. Sheinbaum C, Ozawa L (1998) Energy use and CO_2 emissions for Mexico's cement industry. Energy 23(9):725–732
11. Zaim KK (1996) Emissions due to fossil-fuel consumption and cement production in Turkey (1970–1991). Energy 21:325–331
12. Loreti Group (2008) Greenhouse gas emission reductions from blended cement production. Retrieved on November 10, 2009 from https://www.climateactionreserve.org/wp-content/uploads/2009/03/future-protocol-development_blended-cement.pdf
13. Çevik B (2016, May) Cement sector, Türkiye İş Bank., Department of Economic Research. https://ekonomi.isbank.com.tr/UserFiles/pdf/sr201604_CimentoSektoru.pdf
14. Yusuf K (2015) TR63 section cement sector report, Eastern Mediterranean Development Agency, Hatay. http://www.dogaka.gov.tr/Icerik/Dosya/www.dogaka.gov.tr_626_KN2F58CG_cimento-Sektor-Raporu-2015.pdf
15. Robbie M (2018) Andrew Global CO_2 emissions from cement production. Earth Syst. Sci. 10:195–217. https://www.earth-syst-sci-data.net/10/195/2018/essd-10-195-2018.pdf
16. ECA (2007) Activity report 2006. The European Cement Association. retrieved from the Cembureau website http://www.cembureau.be/Documents/Publications/ActivityReport2006.pdf
17. Ritchie H, Roser M (2019) CO_2 and other greenhouse gas emissions. Published online at OurWorldInData.org. Retrieved from:'https://ourworldindata.org/co2-and-other-greenhouse-gas-emissions. (Online Resource)
18. Boden TA, Andres RJ, Marland G (2017) Global, Regional, and National Fossil-Fuel CO_2 Emissions, Carbon Dioxide Information Analysis Center, Oak Ridge National Laboratory, US Department of Energy, Oak Ridge, Tenn., USA, last Access: 28 June 2017, available at: http://cdiac.ess-dive.lbl.gov/trends/emis/meth_reg.html
19. IEA: energy technology perspectives 2016: towards sustainable urban energy systems,.International Energy Agency, Paris, ISBN 978-92-64-25233-2, (last access: 8 September 2014), 2016, available at: www.iea.org/etp2016
20. Le Quéré C, Andrew RM, Friedlingstein P, Sitch S, Pongratz J, Manning AC, Korsbakken JI, Peters GP, Canadell JG, Jackson RB, Boden TA, Tans PP, Andrews OD, Arora VK, Bakker

DCE, Barbero L, Becker M, Betts RA, Bopp L, Chevallier F, Chini LP, Ciais P, Cosca CE, Cross J, Currie K, Gasser T, Harris I, Hauck J, Haverd V, Houghton RA, Hunt CW, Hurtt G, Ilyina T, Jain AK, Kato E, Kautz M, Keeling RF, Klein Goldewijk K, Körtzinger A, Landschützer P, Lefèvre N, Lenton A, Lienert S, Lima I, Lombardozzi D, Metzl N, Millero F, Monteiro PMS, Munro DR, Nabel JEMS, Nakaoka S-I, Nojiri Y, Padìn XA, Peregon A, Pfeil B, Pierrot D, Poulter B, Rehder G, Reimer J, Rödenbeck C, Schwinger J, Séférian R, Skjelvan I, Stocker BD, Tian H, Tilbrook B, van der LaanLuijkx IT, van der Werf GR, van Heuven S, Viovy N, Vuichard N, Walker AP, Watson AJ, Wiltshire AJ, Zaehle S, Zhu D (2017) Global Carbon Budget 2017. Earth Syst Sci Data Discuss https://doi.org/10.5194/essd-2017-123. In review

21. Beverage Group (2010) Beverage Industry Sector Guidance for Greenhouse Gas Emissions Reporting. Beverage Industry Environmental Roundtable January 2010, UK. https://www.fcrn.org.uk/sites/default/files/Beverage_Industry_Sector_Guidance_for_GHG_Emissions_Reporting_v2.0.pdf

22. Cengel AY, Boles MA (2005) Thermodynamics: an engineering approach. McGraw-Hill Science

23. Cornelissen RL (1997) Thermodynamics and sustainable development: the use of exergy analysis and the reduction of irreversibility. Ph.D. thesis, University of Twente, The Netherlands

24. Kotas TJ (1985) The exergy method of thermal plant analysis, Tiptree. Anchor Brendon Ltd., Essex

25. Wall G (2003) Exergy tools. In: Proceedings of the institution of mechanical engineers. Wilson Applied Science &Technology Abstracts Plus Text, 125–136

26. Rosen MA, Dincer I (2004) Exergy as a driver achieving sustainability. Int J Green Energy 1(1):1–19

27. Kilkis SA (2009) A rational exergy management model for sustainable buildings to reduce compound CO_2 emissions. In: Proceedings of 40th congress on HVAC&R e KGH, 2009, pp 391–412

Retrofitting of R-22 Air-Conditioning System with R1234ze(E)

Atilla G. Devecioğlu and Vedat Oruç

Abstract In this study, the effect on energy parameters and total equivalent warming impact (TEWI) using R1234ze(E) as a substitute for R22 in an air-conditioning device was investigated. The R22 system was retrofitted with R1234ze(E) changing compressor oil. The experimental data was obtained for three different ambient temperatures (30, 35 and 40 °C). It was seen that the power consumption of R1234ze(E) was smaller than that of R22 about by 41%. Although the cooling capacity of R1234ze(E) was 50% lower, its coefficient of performance (COP) was reduced only by 5% compared to R22. Furthermore, refrigerant charging amount of R1234ze(E) was smaller by 16% than R22. The results indicated that TEWI value of R1234ze(E) was lower than that of R22 by 65% due to small GWP (global warming potential) value and proper COP of the alternative refrigerant tested in the study. Hence, it can be expressed that R1234ze(E) can be used in air-conditioners of small capacity as an alternative to R22.

Keywords GWP · TEWI · Retrofitting · R22 · R1234ze(E)

1 Introduction

According to Regulation (EU) No 517/2014, the refrigerants with GWP > 750 will be prohibited to use in air-conditioning systems including 3 kg or less refrigerant after January 1, 2025 [1]. Currently, R410A having a GWP of 2088 is widely used in split type air-conditioners [2]. In recent years, R32 with GWP of 675 is becoming widespread in the market for split type air-conditioners of low capacity. Almost all synthetic refrigerants with low GWP have a characteristic of flammability. Thus, there is a limit for the amount of gas charge into the systems.

The phase-out process of R22 is still continuing in developing countries. At the same time, the available devices operating with R22 are currently utilized by changing

A. G. Devecioğlu (✉) · V. Oruç
Department of Mechanical Engineering, Dicle University, Diyarbakır, Turkey
e-mail: atillad@dicle.edu.tr

V. Oruç
e-mail: voruc@dicle.edu.tr

their refrigerants with alternative ones. The global warming potential (GWP) value of almost all HFC gases that can be used as alternatives to R22 is close to that of R22. The studies related to the application of refrigerants with low GWP are currently conducted. One of the suitable synthetic refrigerants is HFO-based R1234ze(E).

Many previous investigations focused on using R1234yf or R1234ze(E) as a substitute for R134a usually in refrigeration systems [3–7]. Moreover, the cooling capacity of R1234yf was seen to be slightly smaller than that of R134a for varied compressor rotational speed in automotive air-conditioners [8, 9]. In order to be a guiding reference for experimental investigations, some theoretical studies were also conducted comparing the thermodynamic performance of these new generation refrigerants in different refrigeration systems [10–12]. Some review papers have been published considering R1234ze(E) and R1234yf [13, 14].

R134a was compared with R1234yf and R1234ze(E) refrigerants considering vending machines at different ambient temperatures [15]. They determined that COP of R1234ze(E) and R134a was almost the same, but that of R1234yf was smaller about by 5% in comparison with the other two refrigerants. In addition, the suction pressure of R1234ze(E) was smaller than that of R134a and R1234yf. The literature survey points out that the energetic performance of R22 is better than that of HFC-based refrigerants with zero ODP value used as alternatives to R22 [16–20].

Similarly, R22, R1234yf and R1234ze(E) were compared for air-conditioning systems in a [21]. COP values of R1234ze(E) were determined higher about by 5–9% compared to R1234yf. The cooling capacity of R1234ze(E) was found to be low, but power consumption was seen to be decreased as well depending on reduced compressor discharge temperature. It was pointed out that R1234ze(E) may be a suitable candidate refrigerant for air-conditioners. In the experimental investigation by Devecioğlu and Oruç [22], R1234ze(E) was used as a substitute for R134a in a refrigeration system and energy performance of the system was improved utilizing a plate-type heat exchanger in order to reduce the cooling capacity loss.

In this study, R22 split type air-conditioner of small capacity was retrofitted with R1234ze(E). The energy parameters of the system such as cooling capacity and COP of R1234ze(E) were compared with those of R22. TEWI analysis was also performed to analyze environmental impacts. Thus, some suggestions were remarked on the suitability of using R1234ze(E) as a substitute for R22 in available air-conditioning systems. Utilization of HFOs and especially R1234ze(E) in air-conditioning systems operating with R22 is not seen in the literature. In this respect, the present investigation is different from previous comparisons of R22 and HFC-based refrigerants.

2   Experimental Setup

A split type air-conditioner having a cooling capacity of 2.05 kW and originally constructed to work with R22 was used as an experimental setup to study energetic parameters. The detailed information on utilized experimental setup can be found

in the previous study by Oruç et al. [20]. The experimental setup is schematically demonstrated in Fig. 1.

The specifications of measuring instruments utilized in experiments are presented in Table 1. The thermodynamic properties of investigated refrigerants are determined through REFPROP software [23].
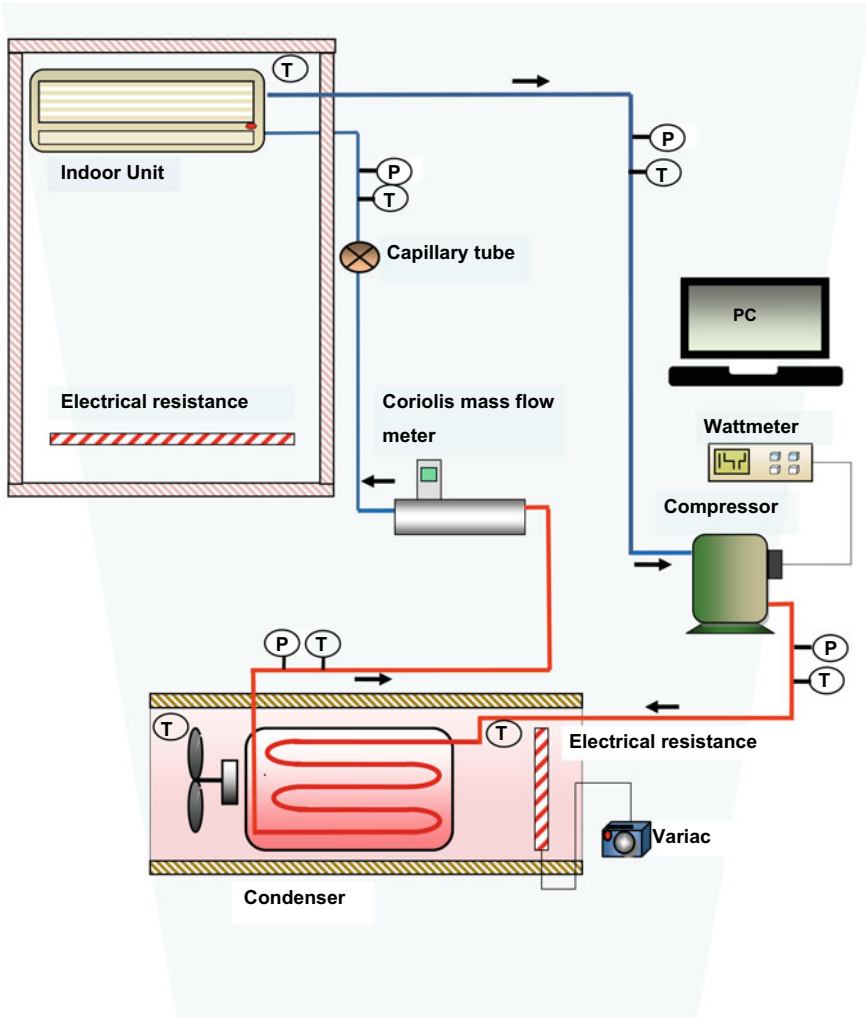
Fig. 1 Sketch for representation of experimental setup

Table 1 Specifications of measuring devices

	Measurement range		Accuracy
Pressure gauges	0–40	Bar	±1% FSO
Thermocouples K-type	−50/150	°C	±0.5 °C
PT100	−100/500	°C	±0.5 °C
Coriolis mass flow meter	0–250	kgh⁻¹	±0.1%
Wattmeter	0–6000	W	±1.5%

2.1 Tested Refrigerants

HFOs are unsaturated organic compounds and consisted of hydrogen, fluorine and carbon. They are synthetic refrigerants including carbon–carbon double bond. R1234ze(E) is suitable for middle temperature applications of air- and water cooled chillers, refrigerators and heat pump systems [14]. Chemical formulation is in the form of 1,3,3,3-tetrafluoropropene (Trans, CHF=CHCF$_3$). R1234ze(E) used in the study is an HFO-based refrigerant with a GWP of 6. Both investigated refrigerants are pure substances. Therefore, their temperature glide values are zero. Retrofitting of the system was achieved by changing the compressor oil such that mineral oil (MO) and polyol ester oil (POE) types were used for the cases of R22 and R1234ze(E), respectively. In the experimental study, 800 g of R22 was charged into the system, while this amount was 670 g for investigating the case of R1234ze(E). The refrigerant of R22 is neither flammable nor toxic. R1234ze(E) is also non-toxic, but is classified by ASHRAE as slightly flammable so that high amounts of this refrigerant should not be charged into indoor systems. Some thermodynamic and physical properties of the tested refrigerants are given in Table 2 [23–25].

Table 2 Properties of studied refrigerants

	R22	R1234ze(E)
ODP	0.055	0
GWP	1810	6
Flammability	A1	A2L
T_{cr} (°C)	96.1	109.4
P_{cr} (kPa)	4990	3630
T_{bo} (°C) (1 atm)	−40.8	−18.9
Lubricant	MO	POE
ρ_{liq} (kg/m^3)	1281.5	1240.1
ρ_{vap} (kg/m^3)	21.2	11.7
q_{latent} (kJ/kg)	205	184.3
k_{liq} (W/mK)	94.7×10^{-3}	83.1×10^{-3}
k_{vap} (W/mK)	9.4×10^{-3}	11.6×10^{-3}
Properties are valid for 0 °C		
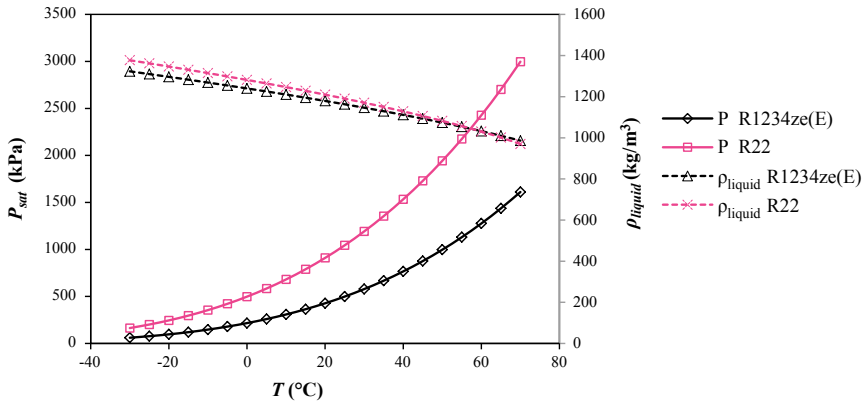
Fig. 2 Variation of vapor pressure and liquid density with temperature

q_{latent} is latent heat of evaporation, ρ is density and k is thermal conductivity coefficient. Subscripts of liq, vap, bo, cr refer to liquid, vapor, boiling and critic, respectively.

It is seen in Fig. 2 that the vapor pressure of R1234ze(E) is considerably lower than that of R22. Generally, the system can be safely operated at lower pressures. Liquid density of R1234ze(E) is smaller compared to R22. Hence, the required amount of refrigerant charging into the system will be decreased in the case of using R1234ze(E).

2.2 Evaluation of Experimental Data

The cooling capacity, Q_e, of the system is calculated as

$$Q_e = \dot{m}\left(h_{o,e} - h_{i,e}\right) \tag{1}$$

where $\dot{m}$ is the mass flow rate, while $h_{o,e}$ and $h_{i,e}$ are the enthalpy values at outlet and inlet of evaporator, respectively. Then, the coefficient of performance (COP) of the system can be determined as

$$COP = \frac{Q_e}{W_{comp}} \tag{2}$$

where W_{comp} is power consumption of the compressor. When the temperature of the air flowing over condenser was reached a specified value, then the system was attained steady-state regime.

Total equivalent warming impact (TEWI) is a parameter indicating the global warming impact of refrigeration and air-conditioning systems [26]. TEWI develops from the direct contribution of used refrigerant to greenhouse gas and indirect contribution of CO_2 emission because of energy consumption of the system during its working period. TEWI is expressed as the emission of kg CO_2. TEWI can be calculated as follows [27]

$$\text{TEWI} = (\text{GWP} \times m \times L \times N) + \text{GWP} \times m \times (1 - \alpha_r) + (E_{\text{annual}} \times \beta \times N) \tag{3}$$

where m is the amount of refrigerant charged into the system in kg and α_r is the recovery efficiency. The refrigerant leakage into the atmosphere directly contributes to greenhouse gas formation. Annual refrigerant leakage, $L,$ is defined as percentage of total refrigerant amount. N is the operation period of system in years. For computing indirect contribution, annual power consumption of system, E_{annual}, is found in kWh/year. The system has been assumed to operate different periods for each month. β is the indirect emission factor in $kgCO_2$/kWh which represents amount of CO_2 emission for generating 1 kWh energy, and it changes depending on the method of electric energy generation [26]. The numerical values of mentioned parameters in Eq. (3) are given in Table 3. Some parameters are obtained from experimental data, and the other ones are taken by assumptions for TEWI calculations. The mass of refrigerant charged into air-conditioner, $m,$ and E_{annual} are obtained from experimental study.

Only the case of cooling mode was considered for air-conditioner in the investigation. The cooling is needed from May to September in most regions of Turkey. The assumed average operating hours for each month are presented in Table 4. For the daily working period, air-conditioner worked on an on-off basis and full consumption of energy was assumed to take place only half of 8–12 h period.

Table 3 Parameter values for TEWI calculations

Parameter	L	β	N	α_r	m_{R22}	$m_{\text{R1234ze(E)}}$
Value	7%	0.48	10	70%	800 g	670 g

Table 4 Information for operation period of the system

Months	May	June	July	August	September
Days	31	30	31	31	30
Operating hours	4	5	6	6	4

3   Results and Discussions

The distribution of cooling capacity, Q_e, with ambient temperature, T_a, is given in Fig. 3 for tested refrigerants. Generally, Q_e is reduced as a result of increasing T_a. It can be noted that Q_e of R22 is higher about by 95% compared to R1234ze(E). Hence, this alternative refrigerant may not compensate the amount of Q_e computed for peak loads. Therefore, the basic components should be selected larger for the air-conditioner which will be operated using R1234ze(E) to deliver the same amount Q_e in R22 case.

The dependence of power consumption of compressor, W_{comp}, on T_a is demonstrated in Fig. 4. W_{comp} increases at higher T_a values for both refrigerants. Evidently, W_{comp} of R1234ze(E) is seen to be lower than that of R22 about by 50%. This result occurs due to reduced pressure values at the suction and discharge of the compressor.

Figure 5 indicates COP distribution for the refrigerants. It is clear that COP is reduced as T_a increases for both refrigerants. Moreover, the highest COP can be obtained in R22 which has grater COP about by 5% in comparison with R1234ze(E).

The values of TEWI, which indicates direct contribution of refrigerant emission to the atmosphere and indirect contribution of CO_2 (originated due to required energy of an air-conditioner during its operation life) on global warming impact, are shown in Table 5. Obviously, while the direct contribution of R1234ze(E) is 4, that of R22 is 1448 CO_2-eq. Similarly, the indirect contribution of R1234ze(E) is smaller about by 40% compared to R22. As a result, TEWI of R1234ze(E) is computed to be lower nearly by 65% than TEWI of R22.

Fig. 3 Variation of cooling capacity with ambient temperature
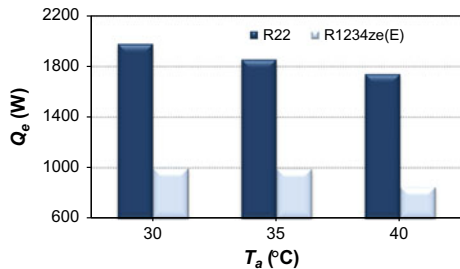
Fig. 4 Variation of compressor power consumption with ambient temperature
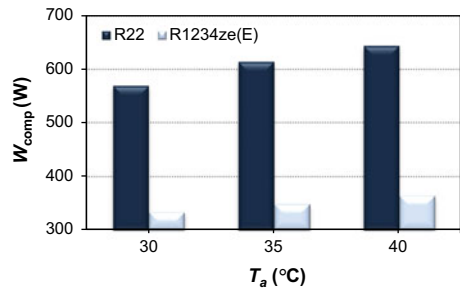
Fig. 5 Variation of COP
with ambient temperature for
the refrigerants
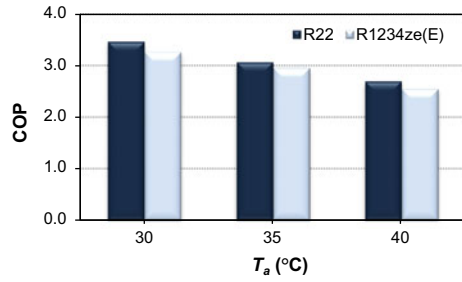
Table 5 Results on TEWI computations

Parameter	R22			R1234ze(E)		
T_a (°C)	30	35	40	30	35	40
Direct impact (CO_2-eq)	1448	1448	1448	4	4	4
Indirect impact (CO_2-eq)	2096	2261	2372	1228	1287	1342
TEWI (CO_2-eq)	3544	3709	3820	1232	1291	1346

4   Conclusion

The general finding from the present experimental study can be summarized as
follows:

- R1234ze(E) can be suitably used in air-conditioners with small capacity; however,
  some basic components of the system such as evaporator and condenser should be
  larger in this case.
- Reduced amount of W_{comp} for R1234ze(E) is a significant result. Since COP of
  R1234ze(E) is lower only by 5% COP of R22, the tested alternative refrigerant is
  suggested to be utilized in air-conditioners.
- Considering flammability risk, refrigerant should not be preferred for larger sys-
  tems requiring a higher amount of refrigerant charge. Fortunately, the required
  mass is reduced when R1234ze(E) is utilized.
- Since evaporation pressure and compressor discharge pressures of R1234ze(E)
  were determined to be lower, it can be safely used in the air-conditioners designed
  to operate with R22.
- Compared to R22, TEWI of R1234ze(E) was calculated to be lower about by
  65%, and therefore, the alternative refrigerant has a substantial reduced impact on
  global warming. Hence, R1234ze(E) may be utilized in air-conditioners for the
  long term.

References

1. Regulation (EU) No 517/2014 of the European Parliament and the Council of 16 April 2014 on fluorinated greenhouse gases and repealing Regulation (EC) No 842/2006. Official Journal of the European Union. http://eur-lex.europa.eu/legal-content/EN/TXT/PDF/?uri=CELEX: 32014R0517&from=EN. Accessed 19 Dec 2017
2. Devecioğlu AG (2017) Seasonal performance assessment of refrigerants with low GWP as substitutes for R410A in heat pump air conditioning devices. Appl Therm Eng 125:401–411
3. Fukuda S, Kondou C, Takata N, Koyama S (2014) Low GWP refrigerants R1234ze(E) and R1234ze(Z) for high temperature heat pumps. Int J Refrig 40:161–173
4. Navarro-Esbri J, Mendoza-Miranda JM, Mota-Babiloni A, Barragan-Cervera A, Belman-Flores JM (2013) Experimental analysis of R1234yf as a drop-in replacement for R134a in a vapor compression system. Int J Refrig 36:870–880
5. Navarro-Esbri J, Moles F, Barragan-Cervera A (2013) Experimental analysis of the internal heat exchanger influence on a vapour compression system performance working with R1234yf as a drop-in replacement for R134a. Appl Therm Eng 59:153–161
6. Mota-Babiloni A, Navarro-Esbri J, Barragan-Cervera A, Moles F, Peris B (2014) Drop-in energy performance evaluation of R1234yf and R1234ze(E) in a vapor compression system as R134a replacements. Appl Therm Eng 71:259–265
7. Jankovic Z, Atienza JS, Suarez JAM (2015) Thermodynamic and heat transfer analyses for R1234yf and R1234ze(E) as drop-in replacements for R134a in a small power refrigerating system. Appl Therm Eng 80:42–54
8. Zilio C, Brown JS, Schiochet G, Cavallini A (2011) The refrigerant R1234yf in air conditioning systems. Energy 36:6110–6120
9. Cho H, Lee H, Park C (2013) Performance characteristics of an automobile air conditioning system with internal heat exchanger using refrigerant R1234yf. Appl Therm Eng 61:563–569
10. Navarro-Esbri J, Moles F, Peris B, Barragan-Cervera A, Mendoza-Miranda JM, Mota-Babiloni A, Belman JM (2014) Shell-and-tube evaporator model performance with different two-phase flow heat transfer correlations. Experimental analysis using R134a and R1234yf. Appl Therm Eng 62:80–89
11. Llopis R, Sánchez D, Sanz-Kock C, Cabello R, Torrella E (2015) Energy and environmental comparison of two-stage solutions for commercial refrigeration at low temperature: fluids and systems. Appl Energy 138:133–142
12. Zheng N, Zhao L (2015) The feasibility of using vapor expander to recover the expansion work in two-stage heat pumps with a large temperature lift. Int J Refrig 56:15–27
13. Wang CC (2014) System performance of R-1234yf refrigerant in air-conditioning and heat pump system e an overview of current status. Appl Therm Eng 73:1412–1420
14. Mota-Babiloni A, Navarro-Esbri J, Moles F, Barragan-Cervera A, Peris B, Verdu G (2016) A review of refrigerant R1234ze(E) recent investigations. Appl Therm Eng 95:211–222
15. Sethi A, Vera Becerra E, Yana Motta S (2016) Low GWP R134a replacements for small refrigeration (plug-in) applications. Int J Refrig 66:64–72
16. Torella E, Cabello R, Sanchez D, Larumbe JA, Llopis R (2010) On-site study of HCFC-22 substitution for HFC non-azeotropic blends (R417A, R422D) on a water chiller of a centralized HVAC system. Energy Build 42:1561–1566
17. Llopis R, Torrella E, Cabello R, Sanchez D (2012) HCFC-22 replacement with drop-in and retrofit HFC refrigerants in a two-stage refrigeration plant for low temperature. Int J Refrig 35:810–816
18. Yang Z, Wu X (2013) Retrofits and options for the alternatives to HCFC-22. Energy 59:1–21
19. Aprea C, Maiorino A, Mastrullo R (2014) Exergy analysis of a cooling system: experimental investigation on the consequences of the retrofit of R22 with R422D. Int J Low-Carbon Technol 9:71–79
20. Oruç V, Devecioğlu AG, Berk U, Vural İ (2016) Experimental comparison of the energy parameters of HFCs used as alternatives to HCFC-22 in split type air conditioners. Int J Refrig 63:125–132

21. Oruç V, Devecioğlu AG (2018) Retrofitting an air-conditioning device to utilize R1234yf and R1234ze(E) refrigerants as alternatives to R22. J Brazilian Soc Mech Sci Eng 40(226):1–9
22. Devecioğlu AG, Oruç V (2018) Improvement on the energy performance of a refrigeration system adapting a plate-type heat exchanger and low-GWP refrigerants as alternatives to R134a. Energy 155:105–116
23. Lemmon EW, Huber ML, McLinden MO (2013) NIST Standard Reference Database 23: Reference Fluid Thermodynamic and Transport Properties-REFPROP, Version 9.1, National Institute of Standards and Technology, Standard Reference Data Program, Gaithersburg
24. DuPont (2015) Thermodynamic properties of DuPont™ Freon® 22 (R22) Refrigerant. Technical Information. https://www.chemours.com/Refrigerants/en_US/assets/downloads/k05736_Freon22_thermo_prop.pdf. Accessed 27 Nov 2015
25. Honeywell (2014) Solstice® ze Refrigerant (HFO-1234ze), http://www.honeywell-refrigerants.com/europe/wp-content/uploads/2014/10/Solstice-ze-brochure-Fourth-Generation-LR-140925.pdf. Accessed 25 Jan 2015
26. Devecioğlu AG, Oruç V (2017) The influence of plate-type heat exchanger on energy efficiency and environmental effects of the air-conditioners using R453A as a substitute for R22. Appl Therm Eng 112:1364–1372
27. Belman-Flores JM, Rodríguez-Muñoz AP, Gutiérrez Pérez-Reguera C, Mota-Babiloni A (2017) Experimental study of R1234yf as a drop-in replacement for R134a in a domestic refrigerator. Int J Refrig 81:1–11

Bioactive Façade System Symbiosis as a Key for Eco-Beneficial Building Element

Suphi S. Oncel and Deniz Şenyay Öncel

Abstract The problems in today's built environment have a strong interrelation with key factors like pollution, global warming, energy and limited natural resources. When thinking of an ideal city the management of all these factors plays an important role in sustainability. Searching a magical solution to all these problems in this dynamic structure is not realistic, but some novel approaches like using the greenery (plants and microalgae) as bioactive elements adapted throughout the urban environment especially in the form of living façades on the buildings is getting more attention with regards to their eco-friendly potential. Bioactive façades can create a positive impact on managing some important parameters like thermal comfort, energy efficiency, wastewater recycle, CO_2 capture and real estate price increase in microscale focusing on a single building as well as global warming, pollution control, urban heat islands, social wealth and sustainable future in macroscale focusing on a big city. The aim of this review will be the key parameters for an efficient bioactive façade with regards to pros and cons, challenges and future. The review will cover the background of using plants as living walls or green walls and then will focus on the microalgae and photobioreactor adapted buildings.

Keywords Global warming · Building · Bioactive · Façade · Green wall · Microalgae

1 Introduction

Civilization idea for a well-organized life triggered the act of urbanization. Starting with the first constructions of ancient cities, people are moving to the cities for higher living standards due to increased opportunities in education, social life, economic activities and health. Today, nearly 50% of the world's population is concentrated

S. S. Oncel (✉)
Department of Bioengineering, Ege University, Izmir, Turkey
e-mail: suphi.oncel@ege.edu.tr

D. Şenyay Öncel
Department of Biomechanics, Dokuz Eylül University, Izmir, Turkey
e-mail: deniz.oncel@deu.edu.tr

in the cities, and this trend will tend to continue with an acceding character [1–3]. Regards to UN estimations over 4 billion global urban dwellers, including more than 863 million informal ones, are currently a part of the cities. The urban population will pass 6 billion keeping in mind the projections of world population increase nearly to 10 billion with a rate of 100 thousand dwellers adding each day. This estimation will result in a ratio of 66% regards to the urban population density by 2050. This fast flow to the cities come to a point where planning and management become a key for sustainability [1, 4].

Sustainability for urbanization will encompass the ability to meet present needs without violating the borders for the future generations to meet their own needs, in other words keeping the scale pans in equilibrium. The dense population flow puts an immense shade on all the attraction points of cities leading pollution, contamination, crowd, heavy traffic, crime and poverty all together resulted in an unsustainable and environment threatening chaotic nodes. A striking statistics shared by UN which states as of 2016 90% of urban population has been exposed to polluted air, resulting in 4.2 million deaths and more than half of the global urban population were exposed to air pollution levels at least 2.5 times higher than the safety standard shows how serious is the situation and the need to take an action is a must [5]. Related to the energy and goods transfer as well as the social state, a sustainable city should highlight a major issue that is its ecologic footprint comprising climate change, biodiversity loss, ecologic cycles or waste generation [6, 7].

Today, cities are acting like deep sinks with an average area of 2% of the global land but consuming all the sources around its living zone which is higher compared to its original area [7]. In other words, cities are directly affecting their backyards, most of the times negatively. Having a share of 20% for residential activities and 35% for transport, cities total energy load in the global consumption will exceed 80% by 2040 [8]. Actually, the critical point of this example is not just the consumption ratio but the risk lies in the product of this activity: greenhouse gases which are the main reason for global warming and climate change. Having an approximate impact of 55% on global warming, CO_2, the major contributor 75%, is coming from the cities [7, 9]. This ratio will act as a boomerang on the cities leading a global rise of about 2 °C in the temperature and 3.8 m (can be higher according to different scenarios) in the sea levels destroying the highest populated coastal megacities, keeping in mind 90% of the urban areas are on the coastal zones, under flood and even affecting near areas by saltwater intrusions to water reservoirs [4, 9, 10].

Cities will continue to be the major cites of socioeconomic activities, but for preventing future problems, an integrated approach should be built regards to urban built environment comprising environment and sustainability. The first step can be taken with increasing green areas in the cities. Keeping in mind the already built environment is vertical, and occupying a wide surface area, the novel solutions can be the use of the vertical faces in other words setting greenery on the building façades. In this way, green infrastructure will be better connected to the living network of the city elements providing a healthier functionality encompassing ecological and social benefits [11]. Today, the standards like LEED or BREEAM which are encouraging

the society to shift to green solutions to decrease the footprint of the urbanization on the environment can be a good catalyst to have more greenery applications in the cities.

2   Bioactive Green Solutions

Using greenery as an urban element can be a strong green solution for novel city design but without underestimating the limitations of traditional buildings regards to the additional costs on management and construction. Even if this green solution is targeting an eco-friendly future, aesthetic look integrated with functionality is the main challenge in the success of this symbiosis approach [12].

Creative thinking on the design process catalyzes the interaction between biology and construction engineering to have an innovative use of greenery. From this point of view, biological specification of the greenery, both plants and algae, to be used will play the key role for a successful adaptation. Well-integrated greenery will elevate the urban character of a building to a sustainable and environment-friendly level. From the engineering point of view, the building envelope which is the actual border between the inside and outside can be the strategic site for the self-sufficiency focusing on energy, gas emissions, contamination and waste treatment.

Greenery-related bioactive solutions can transform the cities and heal the destruction of the urban environment especially after the industrial revolution that replaces the vegetation and soil with waste and concrete [13, 14]. Considering the conventional applications, two main classes for greenery integration to buildings can be made, first is the use of plants with green wall technology and the second is the use of microalgae with photobioreactor technology, with specific emphasis on the key points of attention for a successful application (Table 1).

The benefits of the green façades are actually related to the nature of the living elements, plants and microalgae, that is their ability regards to mass and heat transfer. The green layer added to the building plays a key role in the heat transfer between the indoor and outdoor as being a sustainable thermal resistance element that will result in progress in the thermal performance and overall building energy consumption (Fig. 1). Technically speaking, the thermal interaction of the building envelope and outside environment which is affecting indoors is related with emitted, absorbed, reflected or transmitted radiation (coming shortwave solar radiation including direct, scattered and reflected and exchanging long-wave thermal radiation from surfaces around), convection (natural and forced convection regards to evapotranspiration and wind) and conduction (through the wall, plant layer, PBR vessel, etc.) [12, 14].

On the other hand, the mass transfer based on the photosynthetic nature of both the plants and microalgae makes them to be an effective bio-filter. With the help of the photosynthesis, green façades can use CO_2 and solar energy to produce O_2 and still survive on their own produced food (Fig. 2). Keeping in mind the importance of respiration at night (CO_2 production, O_2 and sugar consumption) that can result

Table 1 Key points of attention to be considered regards to plant and microalgae in green wall systems

Green Façade	Plant	Microalgae
Application	Using cost-effective and light materials to resist in changes in outdoor environment (rain, snow, wind, sun)	Using cost-effective and light materials to resist in changes of outdoor environment (rain, snow, wind, sun) and the specifications of the bioprocess (sterilization temperatures, pH changes)
Maintenance	Expertise in plant biology considering the growth needs, pruning and weeding and technical capacity to maintain the selected green wall system	Expertise in microalgae biology considering the growth needs and technical capacity to maintain the selected photobioreactor system including process steps from inoculation to harvesting
Sustainability	Over-watering, poor drainage, heterogeneous canopy formation, orientation, environmental changes or infections	Nutrient deficiencies, contamination risks, leakage risk, poor mixing/aeration, sterilization, orientation, dynamic outdoor conditions with temperature and light fluctuations
Water use	Effective irrigation, preventing evaporation loss, effective water recycle, alternative sources (rain, wastewater)	Preventing evaporation loss, effective water recycle, alternative sources (rain, wastewater)
Art and aesthetics	Plant loss, color fading, infected plants, heterogeneous canopy and plant layer	Diluted culture, flocculated cells, biofilm formation, color fading
Benefits and function	Active/passive system, thermal comfort, humidity regulation, insulation, air purification, bio-filter, bio-curtain, health, acoustics, heat island, nursery for wildlife, use of wastewater, without forgetting the environmental friendship and carbon footprint	Active/passive system, thermal comfort, humidity regulation, insulation, air purification, bio-filter, bio-curtain, health, acoustics, heat island, use of wastewater, biochemicals and biomass like value-added products for various industries without forgetting the environmental friendship and carbon footprint

(continued)

Table 1 (continued)

Green Façade	Plant	Microalgae
Economy	Cost-benefit analysis to see the feasibility for investment and long-term maintenance with regards to labor, green wall system construction and energy need-saving relation	Cost-benefit analysis to see the feasibility for investment and long-term maintenance with regards to labor, photobioreactor system (including inoculation, production, control, monitoring and harvesting systems) construction and energy need-saving relation
Terminology	Light, photosynthesis, respiration, leaf area index, stomatal behavior, evapotranspiration, radiation, canopy, foliage, shoot density, longevity, wind speed, fertilization, growth and covering rate, irrigation, carbon sequestration	Light, photosynthesis, respiration, cloud effect, night loss, shear stress, mass and heat transfer, doubling time, mixing time, aeration, kLa, degassing, dissolved gas concentration, productivity regards to biomass and biochemicals, carbon sequestration
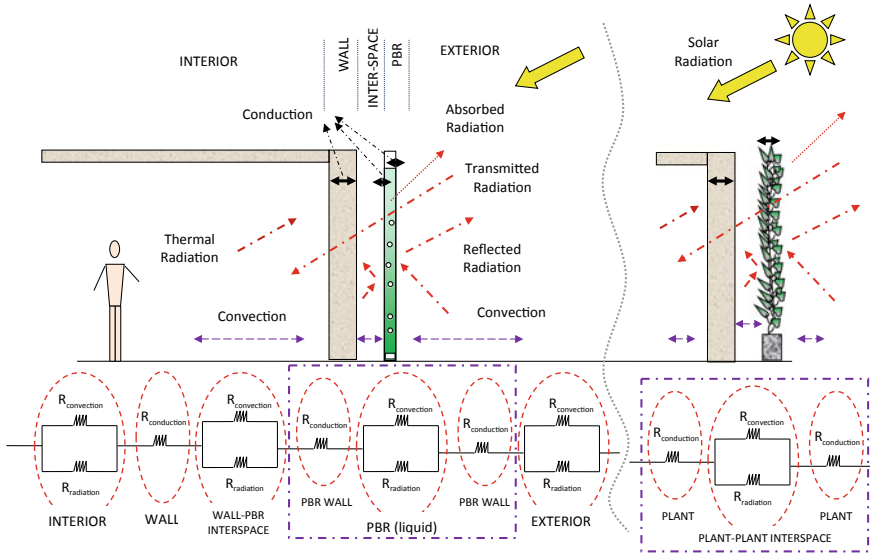
Fig. 1 Generalized heat transfer through a photobioreactor (PBR)-based and plant-based green façade systems and the related thermal resistance networks (main difference between PBR and plant is highlighted by purple borders)
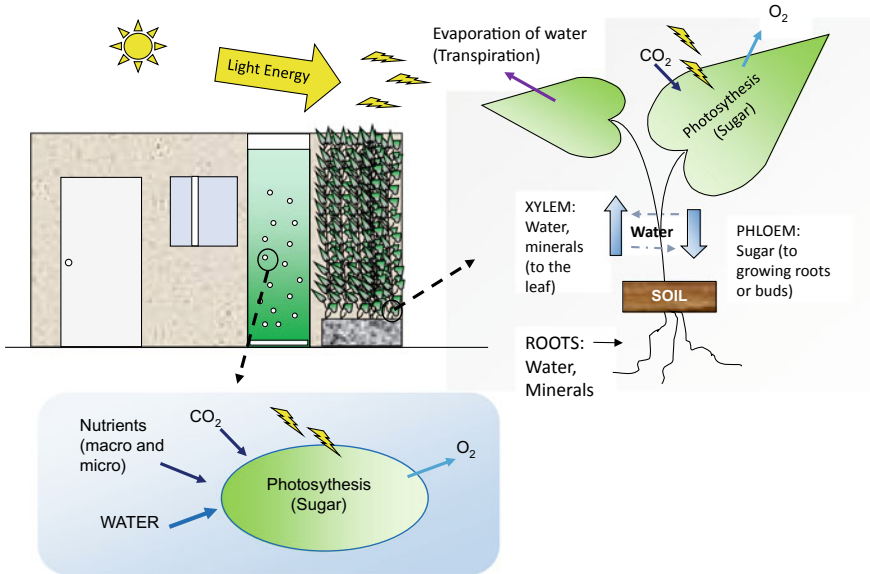
Fig. 2 Mass transfer through plant- and microalgae-based green wall system regards to photosynthesis period

in air quality problems, a well-adapted green façade can capture dust particles and sequester flue gas that increases their potential as a building component [12, 15].

2.1 Green Walls

Today, green wall technology is an effective approach to integrate the plants to urban environment without putting pressure on the land. It is improving urban scenery and transforming vegetation to a sustainable building element for practical purposes. Green wall is the technical terminology comprising all forms of vegetated wall surfaces that can be classified into two basic types, green façades and living walls.

The green façades are simply the use of plants over the building's vertical face. These systems can be subdivided into two classes as direct (a more traditional approach where the plants that have climbing skills by their claw-like extensions creep over the wall face) or indirect (where simple frames or wires that prevent plant collapsing and supply a guided route aiming an overall covering of the building envelope that they are attached).

Compared to the green façade systems, living walls are newer systems that can be used with a wider variety of plant species other than the specific climbers. A uniform growth over the building façade is possible with the living walls due to the special frames incorporated with trays, flexible bags, geotextile felts or planter boxes [16–18]. Living walls are separated from the building surface by the planted frame interface. They can be classified according to the planter box types (trellis, modular panel and felt layer systems) or according to the plantation character (continuous in which plants individually cultivated in the lightweight and permeable screens supply a uniform foliage all over the building wall or modular in which the plantation is done in a puzzle-like planter boxes that can easily be rearranged or changed without disturbing the overall vegetation) [16, 17, 19].

The plant species used in green wall systems are usually conventional herb–shrub or climber types, which have a successful background in gardening and agriculture, like *Hereda helix*, *Parthenocissus tricuspidata*, *Ophiopogon japonicus*, etc. But with a special emphasis on their real-life applications in green wall systems, the use of these species is quite limited to the moderate climate zones. Targeting a progress to reach a worldwide application, studies should focus on other potential species also regards to the integration with the building considering the dynamic interaction with the outdoor environment [18].

Green wall technology targets certain environmental benefits such as increasing air quality acting as a bio-filter for toxic chemicals, heavy metals, CO_2 and dust particles; increasing interior comfort by affecting acoustic, temperature and humidity; increasing energy performance acting as an additional thermal layer; increasing biodiversity and habitat; increasing building's market value giving an aesthetic scenery; and decreasing the urban heat island effect. On the other hand, green walls have the potential to act as a passive bio-curtain which can enhance the protection of the building envelope from the dynamic outdoor environment (sun, wind, rain) and their

results like overheating and degradation of the coating materials [3, 15–17]. Considering the studies about the plant use as green façade elements, the scientific literature focuses on these key benefits under three basic approaches, case study focusing on real-life experiments, computational analysis validated by case studies or just computational analysis to view the potential under various scenarios (Table 2). The key

Table 2 Detailed summary quoted from the studies regards to the benefits of plant-incorporated green wall systems

Objective	Key findings	References
Case study		
Study of the thermal performance and dynamic characteristics of two building floors with greenery and not, during cooling period in Greece	• Green façade improves the thermal behavior of the building • The temperature decrease in the east wall, due vegetation vary from 1.9 to 8.3 °C • In average, vegetation lowered the exterior surface temperature by about 5.7 °C	[20]
Study of the effect of vegetation on the thermal performance, regards to the interrelation with solar heat capture, watering regime, moisture distribution, of a turf-based vertical planting module comprised vertical greening system	• Green wall decreased indoor temperatures and solar heat, which reduced power consumption in air-conditioning compared to bare wall (the rooms were at 25.7 ± 1.72 °C for bare wall and 26.1 ± 1.60 °C for green panels by air-conditioners) • Green wall support the thermal comfort with a temperature difference of over 2 °C was maintained even late at night • The temperature range of the exterior surface is limited to 27.9–29.5 °C with green wall systems • Moisture distribution of the growth medium along the green façade is important	[21]
Measurement of the key parameters such as external solar radiation, solar radiations behind leaf layers, number of leaf layers and their area coverage on the canopy, that are selected by a developed thermal model, to establish the bio-shading coefficients that represent the shading performance with a special focus on the vertical deciduous climbing plant Virginia Creeper in a building, Brighton, UK	• Single climbing plant can reach a height of 5–6 m with a spread of 1.5 min in two summer seasons • The average transmissivity values are 0.45, 0.31, 0.27, 0.22 and 0.12 corresponding to one to five leaf layers • The maximum shading at the lowest point of the bio-shading coefficient curve is 0.45 at around Day 225 • Bio-shading coefficient function can be used in the dynamic thermal analysis • The methodology can be applied for the study of shading performance of different plants in different climates	[22]
Focusing on a technique for particle adsorption on vegetation using living walls located near traffic road and woodland and to classify the total amount of particles by counting of particles on ESEM photographs	• Particle amount was different for leaf sides (for road location 7000 particles for the upper side and 3200 particles for the underside per $1275 \times 950 \ \mu m$) • Difference in particle amount was found between the two different locations (around 7000 particles for the upper side of the leaf at the road location and roughly 3300 for the woodland location)	[23]

(continued)

Table 2 (continued)

Study of the effect of eight different vertical greenery systems (Hort Park, Singapore) on the acoustics impacts and on the sound absorption coefficient	• Green façade has acoustics benefits in the tropical environment • Not all vertical greenery systems have a good noise reduction • Sound absorption coefficient increases with higher greenery coverage • Stronger attenuation at low to middle frequencies due to the absorbing effect of substrate while a smaller attenuation is observed at high frequencies due to scattering from greenery • A reduction of 5–10 dB for low to middle-frequency range • In the high frequencies, some greenery systems are better (highest insertion loss of 8.8 dB) compared to the others (insertion loss 2–3.9 dB)	[24]
Comparison of the growth, shading and interaction of four different climbing plants as a green façade element	• Green façades reduce the heat on the wall by producing shade • Microclimate between the building and the vegetation results in lower temperatures and higher relative humidity • Greenery acts as a wind barrier and shows the evapotranspiration effect • The light transmission factor was from 0.04 in July to 0.37 in April, with the developed foliage, and was between 0.38 and 0.88 in the period without leaves for the south west orientation • Building wall surface temperature without shade was 5.5 °C higher than partially covered section reaching maximum values of 15.2 °C on the southwest side in September • Relative humidity of the interspace was higher than the outside (7% higher in July) and lower in the period without leaves (8% lower in December) during the period with leaves • During the period without leaves, the values of the temperature in the interspace were higher than the outside temperature, while in the period with leaves, the inside temperature was slightly lower than the outside • In the southwest orientation, the interspace reached 3.8 °C higher temperatures in winter and 1.4 °C lower in summer	[25]
Investigation of the effects of different green vertical systems on the energy savings of the test unit in dry Mediterranean continental with regards to shadow produced, insulation provided, evaporative cooling by evapotranspiration and the barrier effect to the wind	• During spring and summer, green façade covered 62% of the surface of the façade • Differences between outside and intermediate illuminance range from 15,000 lux in April, to 80,000 lux in August • The surface temperature in sunny areas was ~5.5 °C higher than in shaded areas • Temperature difference was higher in August and September, reaching maximum values of 17.62 °C on the northwest side in September	[26]

Table 2 (continued)

Investigation of the effects of green vertical systems (direct, indirect and living wall, buildings in Delft, Rotterdam and Benthuizen) on the thermal behavior and airflow compared to a bare wall	• No difference was found in the air temperature and wind profiles starting from 1 m in front of the façades till inside the foliage • Green façades are effective as natural sunscreens, due to a reduction of the surface temperatures behind the green layer compared to the bare • Wind velocity found inside the air cavity of 20 cm thickness of the indirect greening system was higher • An optimal air cavity thickness for greening systems can be around 40–60 mm • With reduced wind velocity (<0.2 m/s) the exterior surface resistance is equalized to the interior surface resistance resulting in energy savings	[27]
Evaluation of the shading effect and thermal performance of green walls for naturally ventilated west facing building	• Blue trumpet vine (*Thunbergia grandiflora*) was selected due to its specifications like fast growth, giving a consistent density and full leave coverage through minimum pruning compared to the others, Ivy gourd (*Coccinia grandis*) and Mexican creeper (*Antigonon leptopus*) • Green façade performance increased when room air velocity was high • The room temperature was reduced from outside ambient air temperature to the maximum of 9.93 °C, with an average of 3.63 °C during daytime • With low air velocity, the temperature difference had maximum of 6.72 °C (~0.91 °C lower than normal room) • Green façade had higher air temperature compared to normal room and outside at night • Leaves of the selected climbers did not obstruct wind when cross ventilation was provided and inside air velocity with green façade was higher than room without especially in the daytime • Relative humidity increase is not significant (maximum of 6.8%) only occurred in daytime, while outside relative humidity is the lowest with minor effect to thermal comfort • At night while relative humidity of outdoor is the highest, the normal room had higher relative humidity than test room with leaves	[28]

(continued)

Table 2 (continued)

Study of microclimate effect of a living wall system on the thermal performance in a hot and humid climate (Wuhan, China) regards to the ventilation and different wall–vegetation distances	• Living wall system has a cooling effect (maximum temperature reduction of exterior wall surface is 20.8 °C, interior wall surface is 7.7 °C, interior space is 1.1 °C) compared to the bare wall • Cool air between the wall and greenery has an identical mean relative humidity as the ambient • Exterior wall surface is losing heat to the interspace by radiative heat exchange • Sealed interspace air layer performs better in cooling the wall surface than with a naturally ventilated air layer • Smaller wall–vegetation distance tested (30, 200, 400 and 600 mm) has better cooling effect but higher relative humidity	[29]
Investigation of the potential effects of the energy behavior on building envelopes by using living wall in a Mediterranean climate (Northern and Central Italy)	• Temperature difference on the external surface of the bare wall and the covered wall is 12–20 °C during sunny days • Temperature differences reduce to 1–2 °C during cloudy days • Incoming heat flux through the bare wall was higher compared to the living wall • Outgoing heat flux through the living wall was higher (-87 W/m^2 against the incoming heat flux of 30 W/m^2 of the corresponding bare wall) • Total outgoing heat flux of living wall is -37 W/m^2 compared to the outgoing heat flux of -23 W/m^2 of bare wall	[30]
Investigation the effects of green façades on the interspace and surface temperatures	• Plants reduced air and surface temperatures compared to bare walls and non-transpiring plant sections • Plant physiology and leaf area/morphology are important for cooling • Temperature differences are higher during mid-late afternoon when green wall is 3 °C cooler than bare • *Prunus* provided wall cooling in controlled environment studies, but weaker for surface cooling capacity (6.3 °C) compared to *Stachys* and *Hedera* (>7.0 °C) • *Fuchsia* enhanced evapotranspiration cooling, whereas *Jasminum* and *Lonicera* was better in shade cooling	[31]
Contribution of green façades to the energy savings of a building during summer and winter period in Mediterranean climate	• During summer 50% covering (south façade) reduce outside wall surface temperature up to 14 °C • For a set point of 24 °C in July (maximum outside temperatures 37–39 °C), the green façade results in a daily energy consumption reduction of 1% • During the first days of September shading by the greenery reduced the indoor temperature by ~1 °C	[32]

<div align="right">(continued)</div>

Table 2 (continued)

Evaluation of the effects of green façades on the outdoor thermal comfort regards to mean radiant temperature	• Green façades changed the diurnal mean radiant temperature profile and reduce mean radiant temperature both during the day and at night • Maximum mean radiant temperature was at 15:00 h, but when one wall was removed, then it was at 17:00 h (10.9–12.9 °C higher at 0.5 m distance) • Removing green wall can lead to an increase in surface temperature of 6.7 °C	[33]
Evaluation of the effects of ivy covered green walls with various orientations, on the exterior surface temperatures, heat flux through the walls, localized outdoor air temperatures, relative humidity, absolute humidity, air infiltration and air velocity immediately adjacent to the façades on a building (Chicago, IL) during summer	• Ivy layers reduced exterior surface temperatures by 0.7 °C across all façades (12.6 °C hourly maximum), depending on orientation and time • The ivy layers yield 10% reduction in heat flux through the walls depending on orientation and time • Plant layers reduced outdoor interspace temperatures by 0.8–2.1 °C, varying with façade orientation • Relative humidity was higher, but absolute humidity was not affected inside the plant layers • The plant layers reduced wind speeds near the façades (0–43%) that resulted in an average reduction in air infiltration rates (4–12%)	[34]
Finding the contribution of vertical greenery systems to noise reduction	• Green wall showed a similar or better acoustic absorption coefficient compared to common building materials, and its effects on low frequencies were better than those of some current sound-absorbent materials at low frequencies • A sound reduction index of 15 dB and a weighted sound absorption coefficient of 0.40 is reached • Green wall reduces the reverberation time from 4.2 to 5.9 highlighting and quantifying the sound absorption capacity of this construction system	[35]
Study of heat loss and insulation properties to monitor the energy use of plant cover over a brick cubical constructed around a test unit filled with water at 16 °C through two winter periods	• Temperature differences were affected by weather parameters, aspect, diurnal time and canopy density • Largest savings in energy were at more extreme weather (cold temperatures, strong wind or rain) • Covering with ivy (*Hedera helix*) reduced mean energy consumption by 21% compared to bare cuboids during the first winter (means of 4.3 and 5.4 kWh per week) • During the second winter, when foliage was more extensive a 37% mean saving was achieved (3.7 compared to 5.9 kWh per week) • Green façades could increase energy efficiency by 40–50% and enhance wall surface temperatures by 3 °C	[36]

Table 2 (continued)

Investigation of the cooling, transpiration and shading effects of green façade systems (covered with *Parthenocissus tricuspidata, Hedera helix and Fallopia baldschuanica* compared to bare walls) for the buildings and the street canyon in Berlin, Germany, through the outdoor studies regards to the transpiration rates, surface temperatures, air temperature, relative humidity and incoming shortwave radiation during summer period	• No cooling effect was detectable for the street canyon • Exterior wall surface temperatures (15.5 °C) were lower than those of the bare, while it was up to 1.7 °C for the interior wall (during nighttime) • Cooling effects mainly depended on shading, and a lower proportion was due to transpiration • Insulation of the direct greenings reduced radiation during nighttime • Green walls mitigate indoor heat stress as long as the plants are sufficiently irrigated with up to 2.5 L m^{-2}d^{-1} per wall area	[37]
Investigation of an active living wall system as a potential element for cooling, bio-filtration and humidification to reduce installed in University of Seville (Spain)	• Active living wall system lead to a drop in temperature between 0.8 and 4.8 °C at different distances from the system • The cooling process was more efficient when the initial conditions of the room were drier and warmer	[38]
Quantification of the thermal external behavior of a green façade building (Madrid, Spain) compared to a bare one and evaluate the impacts of both walls on the variation of the urban temperature range at the microclimate scale in accordance with environmental physical data at different seasons and times	• Maximum air temperature reduction measured in situ is between 2.5 and 2.9 °C during summer period • Maximum air temperature reduction measured in situ is around 1.5 °C during autumn period	[13]
Evaluation of the thermal performance of green façades with projection for mitigating the climate change impact in London by quantifying the cooling potential, thermal comfort levels and microclimate modification during summer	• Green façade reduces the exterior surface temperature by up to 12 °C • Green façade reduces the ambient air temperature between 0.5 and 4.1 °C compared to a distance of 2 m away • Green façade adjacent wind speed can be decreased up to 0.7 ms^{-1}	[39]
Investigation of the effects of green façades (one with evergreen plants (*Pandorea jasminoides* and the other with *Rhyncospermum jasminoides*) and on a bare wall in Mediterranean climate (Bari, Italy)	• Daytime temperatures for green walls during warm days were lower compared to bare wall up to 9.0 °C • Nighttime temperatures during the cold days for the green walls were higher compared to bare wall up to 3.5 °C • The highest cooling effect reached with a wind speed of 3–4 ms^{-1}, an air relative humidity within the range 30–60% and a solar radiation higher than 800 Wm^{-2} • The long-term investigation showed both *Pandorea jasminoides* and *Rhyncospermum jasminoides* are suitable for green façades for Mediterranean climate	[40]
Analysis of the surface temperatures for green walls (felt layer wall, planter boxes wall, direct climbing plants wall, indirect climbing plants wall) compared to a bare wall	• All four types of green façades were able to maintain lower temperatures than the bare wall • Felt layer and planter boxes wall had lower temperatures • Daily average (1.9–4.8 °C) and maximum surface temperatures (7.1–13.4 °C) behind the felt layer wall were lower than the bare wall • Higher solar radiation and ambient temperatures increase the cooling potential of the felt layer and the planter boxes	[41]

Table 2 (continued)

Investigation and comparison of the capacities of a potted plant, passive green wall and an active green wall placed rooms including *Epipremnum aureum, Nephrolepis exaltata, Peperomia obtusifolia, Schefflera arboricola* and *Spathiphyllum wallisii*, to remove particulate matter and total volatile organic compounds (residential room, Sydney, and classroom, Beijing)	• Active green walls resulted in higher reductions in particulate matter and total volatile organic compounds concentrations • Passive walls showed a lesser reduction in particulate matter concentration • In the residential room, the active green wall, compared to potted plants and the passive green wall, maintained total volatile organic compounds at lower (72.5%) concentrations • In the classroom, the active green wall reduced the average total volatile organic compounds concentration by ~28% over a 20 min testing period compared to levels with no green wall and a filtered HVAC system in operation • In the classroom with the HVAC system operating, the active green wall reduced the particulate matter concentration by 42.6%	[42]
Evaluation of the effects of a modular living wall system (using *Buxus sempervirens* L.) on the particulate matter removal capacity regards to plant planting designs and their topographical dynamics	• The planting design with heterogeneous topography resulted in higher particulate matter densities (PM10, PM2.5 and PM1) on leaf surfaces compared to homogenous • Since there was no variability in PM accumulation on the plants with different heights within the random design, the use of plants of slightly different heights (i.e., 10–20 cm and 30–40 cm in this study) is unlikely to negatively affect the PM capture ability of each other by shielding • The cluster design, the absence of any variability in PM capture between short and tall plant clusters, suggests the importance of overall topography in PM accumulation rather than plant height per se • As living walls typically comprise a diverse collection of species, interspersing plants that are morphologically different may also increase topographical heterogeneity of the planting area resulting in higher PM capture levels	[43]

Case study and computational analysis

Definition of the thermal performance of the double-skin green façade system by developing a simulation model and validation by experiments in a test facility	• For the same solar radiation, the temperature increase of the plant was about twice lower than for the blinds • Temperature of the greenery never exceeded the temperature of 35 °C, when blinds could exceed 55 °C • Green double-skin façade resulted in a cooling capacity decrease by 20% • Energy consumption of the cooling system is lower in green façade • Green double-skin façade for the naturally ventilated buildings reduces the operation time of ventilation in the warm period and increases the operation time in the cold period	[44]

(continued)

Table 2 (continued)

Analysis of the influence of the orientation and plant covering percentage of wall sections on the thermal behavior of buildings during summer (Greece) by using a thermal network model	• Green façade reduced the temperature differences between the exterior and interior surfaces relative to bare • Green wall resulted in higher thermal comfort conditions • Increased foliage covering percentage increased their positive effect • Green wall surface is more effective for east or west orientation • Placing insulation on the exterior surface resulted in lower temperature variations • The cooling effect on the exterior and interior surfaces of a green wall is more profound • The use of vegetation on poorly orientated walls can compensate their poor passive design or reduce efficiently the need for cooling loads • Well-adapted green wall enhance energy conservation and regulates the microclimate around the built environment	[45]
Evaluation of the thermodynamic transmission process of the vertical greenery system (using evergreen plant, *Euphorbia x lomi*) by monitoring solar radiation and weather conditions and develop a thermodynamic transmission model to simulate heat flux and temperature variations to optimize the design to contribute to an eco-friendly urban environment	• Green wall radiation transmission is related with canopy transmittance and reflectance • Thermal shielding effectiveness varies with orientation (south wall with a higher coefficient (0.31) than the north) • South wall has lower heat flux absorbance and heat flux loss than the north wall • Due to more intensive canopy, evapotranspiration effect south wall can transfer more heat flux • Green walls reduce heat flux and temperature more effectively than control walls (when global solar radiation and temperature of the south control wall reaches maximum values of 1168 Wm^{-2}, 48.48 °C), the south green walls have lower values (586.89 Wm^{-2}, 39.65 °C) • The differences between back and front sides of the green wall demonstrate clear shading effects (the hourly global average solar radiation reduced by 31.54 Wm^{-2} in the south and 11.36 Wm^{-2} in the north)	[46]
Evaluation of the substrate materials (polyester, polyurethane and polyamide polypropylene) used in living walls regards to the analysis of water volume retained, pressure drop, saturation efficiency and water consumption	• The water retained increases with higher water flow • The pressure drop increases with greenery and high air speed and water flow • Cooling efficiency is enhanced with vegetation and low air speed • Water consumption is increased at higher air speeds. Therefore, low air (between 0.25 and 0.5 ms^{-1}) and water flows are better for homogeneous wetting • Polyamide polypropylene has the greatest pressure drop and the best saturation efficiency • Polyurethane has the lowest resistance to air flow, with an intermediate efficiency level and high water consumption and water retention capacity • Polyester presents the lowest saturation efficiency, a medium level of pressure drop and high water consumption	[47]

Table 2 (continued)

Development of a mathematical model of a green façade with climbing vegetation to evaluate the thermal effects of plants on heat transfer through building façades (in Chicago, IL, during the summer) regards to the plant physiological parameters such as leaf area index, average leaf dimension, and leaf absorptivity addition to the weather conditions, climate zones, wall assembly types and façade orientation	• Green façade improves effective thermal resistance by 0.0–0.7 m^2K/W, depending on wall parameters, climate zones and plant characteristics (particularly leaf area index) • Improvements are more efficient in warm climates with high solar radiation and low wind speeds • On hot sunny days, green façade can reduce exterior surface temperature by 0.7–13.1 °C, reduce the heat flux through the exterior wall by 2–33 W/m^2, and provide an effective R-value of 0.0–0.71 m^2K/W, depending on wall orientation, leaf area index, and radiation attenuation coefficient	[48]
Development of a heat and moisture transfer model (incorporating evapotranspiration, shading effect and additional thermal resistance) for green façade in a transient building simulation program in order to investigate its dynamic performances coupled with a multi-zone building code with a specific focus on the coupled heat and mass transfers and the model accuracy to assess the vegetation impacts together with building design	• The thermal benefits are higher for the west walls in summer and winter • Green wall impact is more for hot climates due to decreased cooling and heating loads • Shading reduces the surface temperature variation and the evapotranspiration ensures the passive cooling when the water is enough • The numerical simulation is in agreement with experimental data, and the average bias of the simulation through one summer month is only 0.22 °C for the green façade with a mean-root-square error of 1.42 °C	[49]
Investigation of the effects of green façades and rooftops in terms of acoustic level and sound-decay time indicators at low-frequency third octave bands by numerical simulations in the time domain of sound propagation in a canyon street of infinite length for various scenarios regards to green coverage ratio and the location of vegetation	• Numerical predictions show a more significant effect in the upper part and outside the street, depending on the location of the plant surfaces, frequency bands and number of reflections on the treated materials • Vegetation on sound levels leads to gain of 5 dB • Green façade is insignificant at street level, with maximum deviations in terms of sound attenuation and decay time being less than 3 dB and 0.5 s • Greening the façades and rooftops of buildings yields a gain of between −16 and −24 dB depending on the third octave	[50]
Investigation of Darcy–Forchheimer equation applicability to describe airflow through vegetation and to evaluate the differences in the aerodynamic parameters between plant species with a special emphasis on their morphology	• Darcy–Forchheimer model described airflow through vegetation regardless of its morphology • Studying aerodynamic properties of vegetation in relation to their morphology provides opportunities to model the interaction between vegetation with its environment	[51]

<div align="right">(continued)</div>

Table 2 (continued)

Study of the radiation properties of and thermal properties of the windowed building envelope equipped with a climber installed (*Lonicera japonica*) green wall in humid-subtropical region, Hong Kong	• Northeast oriented green wall with 0.24 leaf area index radiation properties and shading-induced energy savings in summer • An innovative radiation apportionment model was developed to determine the shortwave transmissivity, reflectivity and absorptivity of the climber canopy which were, respectively, 0.382, 0.074 and 0.543 in sunny weather and 0.449, 0.098 and 0.454 in cloudy weather • According to model, shading alone could shield against insolation up to 497 W/m^2 behind the canopy and 356 W/m^2 indoors • Average daily energy savings at 0.226 kWh/m^2 resulted a USD 0.03 and 0.062 kg CO_2, respectively, decrease according to the local costs • According to the model, the extrapolated seasonal savings from a total of six green walls installed at the experimental site could reach USD 75.8 and 157.9 kg CO_2	[52]
Investigating the effect of vertical greenery on thermal comfort and air cooling through its effect on ambient façade surface energy fluxes and air temperature in Hong Kong and providing a parametric study from validated models to find the quantity and location of façade greening required for potential air cooling and thermal comfort improvement of a neighborhood of varying densities	• Model validation showed acceptable modeling of façade surface temperature, air temperature, relative humidity and wall-emitted long-wave fluxes • Parametric study showed that 30–50% of façades in the high-density urban setting of Hong Kong must be greened to reach ~1 °C reduction in both daytime and nighttime air temperature and to improve daytime pedestrian thermal comfort by at least one thermal class • Higher greened façade ratio will be required to obtain similar thermal benefits in low and medium density urban settings • Benefits for pedestrians can be improved by placing the vertical greening facilities along with podium than tower heights	[53]

Computational analysis

Simulation of the effects of vertical greenery systems on the temperature and energy consumption of buildings	• 100% greenery coverage from vertical greenery systems is effective in lowering the mean radiant temperature of a glass façade building • Low shading coefficient of plant usage can lower the energy cooling load significantly • 50% greenery coverage from vertical greenery systems and a shading coefficient of 0.041 reduce the envelope thermal transfer value of a glass façade building by 40.68%	[54]
Introduction of a novel inverse modeling approach for modeling the thermal response of vertical green systems	• Predicted temperature of greenery deviates by less than ± 1.3 °C compared to the measured values • Heat flux on the inner side of the building envelope deviates by less than ± 0.3 W/m^2 compared to the measured values	[55]

findings of these studies are the main driving force for future research in the field.

Specific data on temperature effect which is actually the key incentive for the public interest due to its energy-related advantages showed that green walls creating insulation related with the stagnant air layer can reduce the energy consumption due to air-conditioning up to 30–60% [15, 27]. This energy advantage is related with the fact that a green façade will block and absorb solar radiation by shading the building envelope. Also, the supportive specifications like supplying evapotranspirative cooling, increasing albedo, providing thermal insulation due to the stagnant air zone and increasing convective shielding are important factors to mention in favor of thermal interactions [27, 56].

The thermal stagnant zone can provide a significant thermal resistance of 0.31 and 0.68 m^2 K/W between covered and bare parts of the building façades depending on the foliar density, greening system, season, orientation and location [3, 57]. This insulation effect can reduce maximum income heat flux by 75% and maximum outgoing heat flux by 60% [16].

The effect of the green walls can be even higher if the systems are transformed into active bio-filters rather than traditional passive ones. In other words, if the indoor air is forced to pass through the green walls to increase the evaporative cooling potential as well as the capacity of air purification and humidification drops in temperature can reach 4.8 °C [13, 58]. The surface temperature values of green wall applied façades can even reach up to 11.6 °C difference compared to a bare wall which can result in an energy saving as high as 90% [16]. The success of these targets is strongly related with specific design features such as the types and character of the used plants, type of the green wall system and the construction materials, building specifications and orientation and also local climate [18, 59].

3 Microalgae and Production Systems

Microalgae, having more than 40,000 known species, are the oldest resident of this planet that has the key role in building our atmosphere. Even if they have a share of just 0.5% in total plant biomass they are producing more than 75% of the needed oxygen and can sequester up to 2 kg CO_2 in each kg of their biomass [60, 61]. From the industrial standpoint, keeping the biological terminology in mind due to their subcellular structure and composition (eucaryotic or procaryotic), microalgae term comprises the plant like photosynthetic microorganisms found in water and soil which can be colonial or free living with a simple reproductive systems giving them the rapid growing capability compared to terrestrial plants [61]. They have strong scientific attention due to their unique abilities to produce a wide variety of chemicals that can be used in key industries like food, feed, pharmaceuticals, waste treatment and even energy. Giving some key numbers like their oil content reaching more than 50% of their dry biomass and coupled with their rapid growth rate and photosynthetic yield of tenfold, microalgae can produce up to 100 times more oil than terrestrial oilseed plants which theoretically may reach a production amount of

70–420 t/hectare per year of biomass and about 15,000–60,500 L of algae oil/hectare per year or the prices of chemicals like astaxanthin reaching thousands of dollars in biotechnology market can explain the reason of this attention [62–64].

Microalgae culturing techniques rooted in the ancient observations of wild animals feeding on algal biomass in the lakes or lagoons. With the progress in biotechnology potential application areas of microalgae-based products forced to have reliable production methods comprising all the steps from upstream to downstream. First attempts on microalgae cultivation other than direct harvesting of the biomass from natural waters are the use of simple production systems. These systems are artificial water pools, that are in contact with the outdoor environment, usually used for the production of outdoor resistant species like *Spirulina*, *Dunaliella* or *Chlorella* and classified according to their shapes (rectangular or circular ponds) or mixing strategy (mixed or unmixed) [60, 63]. Unmixed ponds can be defined as small-scaled natural ponds where the aeration or mixing is done by the help of wind or manpower without specific mixing or aeration systems [60, 63].

Compared to unmixed systems, mixed open systems are technically more sophisticated reaching a surface-to-volume ratio usually up to 10 m^{-1}. Their basic designs are raceway ponds, circular ponds and cascade systems. Among these designs, raceways are the most conventionally recognized systems which are shallow, around 30–40 cm, rectangular ponds having a defined flow route with the help of the separator wall constructed inside the pond, are mixed by large horizontal impellers. Earthrise Farms, which owns world-leading large raceway ponds, have a production facility constructed on an area around 440 decares [62, 63, 65]. Circular ponds are mixed by center pinned impellers that can reach a diameter of 50 m and can cover an area of 50,000 m^2. These types of ponds are widespread in Japan, Taiwan and Indonesia. On the other hand, cascade systems, which are also known as thin-layer cascade or inclined ponds, have a more sophisticated design compared to other open systems. They can provide effective light utilization, aeration and mixing simultaneously, and this way they can even be used in low illumination and temperature climates. These designs have two major compartments keeping in mind the needs for efficient production, one is for the mixing, aeration and illumination and the other is for the storage and process control. The solar stage that is in the form of cascades allows the culture to flow freely in a thin layer enhancing light harvesting. This design also leads to swirl formation during the flow leading a turbulent regime that establishes better aeration and mixing. The storage tank integrated to the solar stage is the site for control especially for temperature and pH. Cascade systems constructed in Trebon (Czech Republic) in 1960s are good examples for the success of this design that have an enhanced surface-area-to-volume ratios of 100 m^{-1} resulting denser cultures of 35 g L^{-1} [60, 65].

Photobioreactors (PBRs) are closed systems which are uniquely separated from the open systems by their strict separation of the surrounding environment from the microalgae culture by the help of the reactor vessel. Even if they can be built outdoors to utilize the opportunity of the free energy from the sun for heat exchange and light harvesting, the importance of the culture isolation from the outdoor atmosphere is the key to prevent the contamination risk and ease of process control.

Compared to open ponds, this controlled environment gave the possibility to produce a wide variety of species without the limitation of just resistant ones like *Spirulina* or *Dunaliella*. PBRs have various designs that can be used for heterotrophic, mixotrophic or photoautotrophic cultivations with various process types like continuous, batch or semi-continuous to focus on more efficient production regards to different process parameters [60, 64, 65]. Basically, the designs have two compartments: the solar receiver and the culture tank. Solar receiver is the site for light harvesting which can be illuminated naturally or artificially. This compartment is important for the success of the design considering the optimum illumination, light saturation levels and photoinhibition risks. On the other side, culture tank that usually has a lower volume compared to the solar stage, houses the vital production systems like control, circulation, degassing and mixing. Changing with the design type and process specifications these compartments can be separated or integrated. PBRs can be classified as panel, tubular and fermenter (tanks and columns) types according to the basic design geometries [60, 64, 65].

Panel PBRs, or sometimes named as flat plates or flat panels, are conventionally well-known vertical designs that have a single vessel acting as a unified solar stage and culture reservoir. They have an increased surface-to-volume ratio targeting efficient illumination. These systems are suitable for outdoor applications due to their compact and modular design. Panel systems can be modified with simple frames and joints to be oriented according to the sun and also with mixing systems to be hydraulically, pneumatically or mechanically mixed. These systems can also have baffles to increase the mixing efficiency. Usually, their height and width dimensions are around 1.5 m × 2.5 m with an optical path of 0.1 m for enhanced light utilization as well as the decreased weight [62, 65].

Fermenter-type PBRs are also important for microalgae production which can be divided into stirred tanks and aerated columns due to mixing process and geometry. The design actually routed to the concept of conventional bioreactors, well known from industrial applications, but with the modifications for effective illumination to fulfill the needs of microalgae. Stirred tank PBRs are mechanically mixed cylindrical glass or steel vessels, having a height-to-diameter ratio usually around 3, aerated by sparger or nozzle systems. These systems are mostly used in laboratory applications rather than for the outdoor industrial applications due to the construction limitations related to the geometry. The design concept targets the enhancement of the illumination and mixing interrelation with a special emphasis on the optimal process parameters of the produced microalgae. In other words, internal or external illumination strategies with different light sources (cool white, daylight, LED, optical fibers, etc.) are in consideration for better production. Considering airlift and bubble columns which are cylindrical vessels having higher height–to-diameter ratios compared to stirred tank PBRs, the ability to reach mass transfer coefficients of $0.006 \, \text{s}^{-1}$ by aeration rates of 0.25 vvm is an important point to highlight about the potential of the design. These systems can have a working capacity up to 500 L and are usually hydraulically or pneumatically mixed systems without a need of a mechanical mixer (unless modified with internal mixers) and supply these mass transfer coefficients with lower energy consumption. Regards to the airlift or bubble column, existence

of the draft tube is giving their main characteristics. In other words, if a PBR has a draft tube, it is called an airlift and if not a bubble column. The draft tubes separate the gas enrichment site (riser) from the less turbulent site of gravity (downcomer) resulting in an efficient light harvesting and gas transfer at the same time. Internal loop, external loop or separated columns are the subtypes of airlift systems regards to the position of the draft tube which leads unique specifications to each design. As mentioned, the lack of the draft tube is the key distinguishing character of the bubble column from an airlift. The lack of the draft tube resulted in a more chaotic flow regime compared to an airlift PBR having a well-defined route of flow between the riser and downcomer zones [14, 60, 65].

Tubular PBRs are also common designs known in industry, having different geometries like helical, vertical or conical. These PBRs are simply the stack of transparent tubes (diameter around 0.1 m) connected by U-bends or manifolds oriented in horizontal or vertical bundles. Compared to the other designs, due to the limitation by the narrow tubes, they usually have a separate culture reservoir in order to provide degassing and to mount the monitoring probes of the control systems. The mixing is done by the circulation of the culture inside the tubes with the use of pumps or airlifts integrated in the system. Similar to the panel PBRs; they have an increased surface-to-volume ratios up to 80 m^{-1} (some very high ratios up to 2000 m^{-1} also reported). The main attention has to be paid on the tube length in order to prevent the O_2 accumulation which can lead to productivity loss or high pumping power consumption which can result in cost increase [62, 64, 65].

3.1 Potential Role of Photobioreactors in Building Façades

Using photobioreactors as a potential tool for urban environment through the integration of the building façades is a novel approach compared to the green walls. Considering their key superiority that is the rapid growth, microalgae can reach high densities in a short period and cover the façade easily in the well-defined and controlled volume of the PBR system. On the other hand, microalgae can be cultivated all year long without the stress of the management and extra care spend to grow the plants. Similar to the green walls a well-adapted system should focus on to enhance, thermal comfort, air quality, light, acoustics and resistance to building aging. PBR systems are not in contact with the environment like green walls which supports diversity of urban wildlife as feed and nest, but this disadvantage can be preferred especially by the residents who may complain from the unwanted animals or their wastes.

PBR integration will give active responsibility due to the controlled connection and circulation between the outdoor and indoor. Circulation of indoor air through the PBR will help the gas and heat exchange other than catching dust particles. Especially, anthropogenic CO_2 will be sequestered by microalgae for photosynthesis and produced O_2 will be flowed back to the indoors for fresh air. Focusing on a PBR façade integrated building a simulation study showed a 13% decrease in the CO_2

level when compared to a standard building with 200 residents [66]. Other than the gas exchange circulation, considering the culture volume will also affect the thermal comfort by acting as a bio-heat exchanger in which excess thermal energy can be controlled by shifting the PBRs' orientation or even pumping the culture to different building faces (for example, shaded face in the summer) depending on the outdoor temperature and irradiation. Temperature control will also be supported by the shading effect of the dense cultures that are acting like bio-curtains. Keeping in mind the possible transfer of the cultures between the faces of the building will also help to control the illumination of the culture. As a result of better temperature control, PBR façades can decrease the building energy consumption by more than 33% considering fuel usage and 10% considering electricity usage [12, 14].

High light intensities also have a crucial effect on the temperature of the façades especially in hot seasons triggering the heat load of the building, but compared to green walls, the mounted PBRs can be constructed as moving units which will help orientation adjustment and sweeping away the accumulated heat especially between the PBRs and building wall by increasing the airflow in the interface. Also, the easy replacement or dilution of the culture just by the help of the pumping systems will serve as an advantage over the green walls where the bio-curtain density can be adjusted according to the temperature or illumination dynamics. The compact design of the PBRs also makes it possible to be used as real curtains over the windows of the building where the active density changes or orientation will provide an effective illumination inside the building [12, 60, 67]. Considering the acoustic quality an extra barrier of PBR vessel leads to sound insulation and enhances the indoor comfort of the building. According to some studies mentioned in the literature using green walls showed a beneficial effect on the sound frequencies related to parameters like thickness of the foliage and construction materials. The sound absorption reaching up to 60 dB and reverberation time reduction up to 5.9 by the plant-based green façades are also encouraging for the PBR façade concept [24, 35, 50].

With a special emphasis on the energy consumption and lifelong management costs energy saving, built area and integration with the environment considering the mutual relation between the microalgae and the building needs will specify the sustainability and the success of the application [68–70]. Regards to the economy simulations on green walls with an assumption of 50 years of building service life, the success of a PBR system will be directly connected to the cost and payoff balance to get a chance for application [15, 27, 65]. Other than this basic bottleneck, PBRs should also have an integrated design approach to serve as an effective building element. Keeping in mind the average building service life to have a realization in the building sector, PBRs should have a durable nature enough to resist the outdoor conditions comprising lightweight materials with feasible costs. For example, they need to be: cleaned easily for a better scenery and contamination prevention, modular and mountable with an ability of adjustable orientation to harvest light or decrease heat load effectively, well-constructed leakage resistant system to serve the optimized environment for the microalgae culture with a special emphasis on the control systems under the dynamic nature of the outdoor environment, easily adapted to older buildings because the potential market for the building will be great for renovations.

In addition to these technical points of interest, the investment encouraging topics like self-sufficient buildings using recycled waste or rain waters to produce a value-added product like microalgae to be used in various industries (some of which are having very high value addition like biochemicals) will help to support the sustainability and environment-friendly approach of the applications.

Other than various concepts like Marina City Tower (USA), Process Zero Building (USA), FSMA Tower (UK), Le CONEX (France) and In Vivo (France) introduced at the design stage only few real-life proofs considering full scale like the Algae House for International Building Exhibition, Hamburg, Germany, by ARUP or the pilot-scale PBR façade at CSTB Headquarters, Champs-sur-Marne, France, by XTU architects [12, 14] shows the reality that the technology is still at the starting stage. But the advantages regards to key benefits from microalgae will be the driving force for the future.

4 Conclusion

Focusing on the environment and the carbon footprint the green wall and PBR systems as alternative element in the urban environment will have high potential if will be supported by new legislations and subsidies by the governments to motivate the ordinary people about the benefits. With a simple brainstorming more the real-life applications more the influence on the people and if the market will see the spark in the economic and environmental advantages more the demand which will serve as the real catalyst for the developing market.

References

1. Addanki SC, Venkataraman H (2017) Greening the economy: a review of urban sustainability measures for developing new cities. Sustain Cities Soc 32:1–8
2. Yang H, Xu Z, Fan M, Gupta R, Slimane RB, Bland AE, Wright I (2008) Progress in carbon dioxide separation and capture: a review. J Environ Sci 20:14–27
3. Tudiwer D, Korjenic A (2017) The effect of living wall systems on the thermal resistance of the façade. Energy Build 135:10–19
4. Elmqvist T, Andersson E, Frantzeskaki N, McPhearson T, Olsson P, Gaffney O, Takeuchi K, Folke C (2019) Sustainability and resilience for transformation in the urban century. Nat Sustain 2:267–273
5. Sustainable development goals, UN database, https://www.un.org/sustainabledevelopment/cities/. Accessed 29 April 2019
6. Phillis Y, Kouikogloua VS, Verdugo C (2017) Urban sustainability assessment and ranking of cities. Comput Environ Urban Syst 64:254–265
7. Koop SHA, Van Leeuwen CJ (2017) The challenges of water, waste and climate change in cities. Environ Dev Sustain 19:385–418
8. International Energy Agency (2017) Key world energy statistics
9. Mondal MK, BalsoraH K, Varshney P (2012) Progress and trends in CO_2 capture/separation technologies: a review. Energy 46:431–441

10. Creutziga F, Baiocchic G, Bierkandtd R, Pichlerd PP, Seto C (2015) Global typology of urban energy use and potentials for an urbanization mitigation wedge. PNAS 112(20):6283–6288

11. Koc CB, Osmond P, Peters A (2017) Towards a comprehensive green infrastructure typology: a systematic review of approaches, methods and typologies. Urban Ecosystems 20:15–35

12. Öncel SŞ, Köse A, Öncel DŞ (2016) Façade integrated photobioreactors for building energy efficiency. In: Pacheco-Torgal F, Rasmussen ES, Granqvist CG, Ivanov V, Kaklauskas HA, Makonin S (eds) Start-up creation the smart eco-efficient built environment. Woodhead Publishing

13. Paschoalino de Jesus MD, Lourenco JM, Arce RM, Macias M (2017) Green façades and in situ measurements of outdoor building thermal behavior. Build Environ 119:11–19

14. Elrayies GM (2018) Microalgae: prospects for greener future buildings. Renew Sustain Energy Rev 81:1175–1191

15. Perini K, Rosasco P (2016) Is greening the building envelope economically sustainable? An analysis to evaluate the advantages of economy of scope of vertical greening systems and green roofs. Urban Forestry Urban Greening 20:328–337

16. Feng H, Kasun H (2014) Lifecycle assessment of living walls: air purification and energy performance. J Clean Prod 69:91–99

17. Manso M, Castro Gomes JP (2016) Thermal analysis of a new modular system for green walls. J Building Eng 7:53–62

18. Oncel SS, Köse A (2016) Photobioreactors for sustainable buildings. Dokuz Eylül Üniversitesi Fen ve Mühendislik Dergisi 52:77–88

19. Charoenkit S, Yiemwattana S (2016) Living walls and their contribution to improved thermal comfort and carbon emission reduction: a review. Build Environ 105:82–94

20. Eumorfopoulou EA, Kontoleo KJ (2009) Experimental approach to the contribution of plant-covered walls to the thermal behaviour of building envelopes. Build Environ 44:1024–1038

21. Cheng CY, Cheung Ken KS, Chu LM (2010) Thermal performance of a vegetated cladding system on façade walls. Build Environ 45:1779–1787

22. Kenneth I, Marta L, Andrew M (2010) Shading performance of a vertical deciduous climbing plant canopy. Build Environ 45:81–88

23. Ottele M, van Bohemen HD, Fraaij ALA (2010) Quantifying the deposition of particulate matter on climber vegetation on living walls. Ecol Eng 36:154–162

24. Wong NH, Tan AYK, Tan PY, Chiang N, Wong C (2010) Acoustics evaluation of vertical greenery systems for building walls. Build Environ 45:411–420

25. Pérez G, Rincón L, Vila A, González JM, Cabeza LF (2011) a). Behaviour of green façades in Mediterranean Continental climate. Energy Convers Manag 52:1861–1867

26. Pérez G, Rincón L, Vila A, González JM, Cabeza LF (2011) b). Green vertical systems for buildings as passive systems for energy savings. Appl Energy 88:4854–4859

27. Perini K, Ottelé M, Fraaij ALA, Haas EM, Rossana R (2011) Vertical greening systems and the effect on air flow and temperature on the building envelope. Build Environ 46:2287–2294

28. Sunakorn P, Yimprayoon C (2011) Thermal performance of biofaçade with natural ventilation in the tropical climate. Procedia Engineering 21:34–41

29. Chen Q, Baofeng L, Xiaohu L (2013) An experimental evaluation of the living wall system in hot and humid climate. Energy Build 61:298–307

30. Mazzali U, Peron F, Romagnoni P, Pulselli RM, Bastianoni S (2013) Experimental investigation on the energy performance of living walls in a temperate climate. Build Environ 64:57–66

31. Cameron RWF, Taylor JE, Emmett MR (2014) What's 'cool' in the world of green façades? How plant choice influences the cooling properties of green walls. Build Environ 73:198–207

32. Coma J, Perez G, Sole C, Castell A, Cabeza LF (2014) New green façades as passive systems for energy savings on buildings. Energy Procedia 57:1851–1859

33. Liang TC, Hien WN, Jusuf SK (2014) Effects of vertical greenery on mean radiant temperature in the tropical urban environment. Landscape Urban Planning 127:52–64

34. Susorova I, Azimi P, Stephens B (2014) The effects of climbing vegetation on the local micro-climate, thermal performance, and air infiltration of four building façade orientations. Build Environ 76:113–124

35. Azkorra Z, Perez G, Coma J, Cabeza LF, Bures S, Alvaro JE, Erkoreka A, Urrestarazu M (2015) Evaluation of green walls as a passive acoustic insulation system for buildings. Appl Acoust 89:46–56
36. Cameron RWF, Taylor JE, Emmett MR (2015) A Hedera green façade e Energy performance and saving under different maritime-temperate, winter weather conditions. Build Environ 92:111–121
37. Hoelscher MT, Nehls T, Jänicke B, Wessolek G (2016) Quantifying cooling effects of façade greening: shading, transpiration and insulation. Energy Build 114:283–290
38. Urrestarazu P, Fernández-Canero R, Franco A, Egea G (2016) Influence of an active living wall on indoor temperature and humidity conditions. Ecol Eng 90:120–124
39. Jimenez MS (2018) Green walls: a sustainable approach to climate change, a case study of London. Architectural Sci Rev 61(1–2):48–57
40. Vox G, Blanco I, Schettini E (2018) Green façades to control wall surface temperature in buildings. Build Environ 129:154–166
41. Kokogiannakis G, Darkwa J, Badeka S, Li Y (2019) Experimental comparison of green façades with outdoor test cells during a hot humid season. Energy Build 185:196–209
42. Pettit T, Irgaz PJ, Torpy FR (2019) The in-situ pilot-scale phytoremediation of airborne VOCs and particulate matter with an active green wall. Air Qual Atmos Health 12:33–44
43. Weerakkody U, Dover JW, Mitchell P, Reiling K (2019) Topographical structures in planting design of living walls affect their ability to immobilise traffic-based particulate matter. Sci Total Environ 660:644–649
44. Stec WJ, van Paassen AHC, Maziarz A (2005) Modelling the double skin façade with plants. Energy Build 37:419–427
45. Kontoleon KJ, Eumorfopoulou EA (2010) The effect of the orientation and proportion of a plant-covered wall layer on the thermal performance of a building zone. Build Environ 45:1287–1303
46. Jim CY, He H (2011) Estimating heat flux transmission of vertical greenery ecosystem. Ecol Eng 37:1112–1122
47. Franco A, Fernández-Cañero R, Pérez-Urrestarazu L, Valera DL (2012) Wind tunnel analysis of artificial substrates used in active living walls for indoor environment conditioning in Mediterranean buildings. Build Environ 51:370–378
48. Susorova I, Angulo M, Bahrami P, Stephens B (2013) A model of vegetated exterior façades for evaluation of wall thermal performance. Build Environ 67:1–13
49. Djedjig R, Bozonnet E, Belarbi R (2015) Analysis of thermal effects of vegetated envelopes: integration of a validated model in a building energy simulation program. Energy Build 86:93–103
50. Guillaume G, Gauvreau B, L'Hermite P (2015) Numerical study of the impact of vegetation coverings on sound levels and time decays in a canyon street model. Sci Total Environ 502:22–30
51. Koch K, Samson R, Denys S (2019) Aerodynamic characterisation of green wall vegetation based on plant morphology: an experimental and computational fluid dynamics approach. Biosys Eng 178:34–51
52. Lee LSH, Jim CY (2019) Energy benefits of green-wall shading based on novel-accurate apportionment of short-wave radiation components. Appl Energy 238:1506–1518
53. Morakinyo TE, Lai A, Lau KKL, Ng E (2019) Thermal benefits of vertical greening in a high-density city: case study of Hong Kong. Urban Forestry Urban Greening 37:42–55
54. Wong NH, Tan KAY, Tan PY, Wong NC (2009) Energy simulation of vertical greenery systems. Energy Build 41:1401–1408
55. Šuklje T, Hamdy M, Arkar C, Hensen JLM, Medved S (2019) An inverse modeling approach for the thermal response modeling of green Façades. Appl Energy 235:1447–1456
56. Hunter AM, Williams NSG, Rayner JP, Aye L, He D, Livesley SJ (2014) Quantifying the thermal performance of green façades: a critical review. Ecol Eng 63:102–113
57. Pérez G, Coma J, Sol S, Cabeza LF (2017) Green façade for energy savings in buildings: the influence of leaf area index and façade orientation on the shadow effect. Appl Energy 187:424–437

58. Chena N, Tsayb Y, Chiub W (2017) Influence of vertical greening design of building opening on indoor cooling and ventilation. Int J Green Energy 14(1):24–32
59. Riley B (2017) The state of the art of living walls: lessons learned. Build Environ 114:219–232
60. Oncel SS, Kose A, Vardar F, Torzillo G (2015) From the ancient tribes to modern societies, microalgae evolution from a simple food to an alternative fuel source. In: Kim SK (ed) Handbook of marine microalgae. Biotechnology advances. Academic Press
61. Sayre R (2010) Microalgae: the potential for carbon capture. Bioscience 60:722–727
62. Oncel S (2013) Microalgae for a macro energy world. Renew Sustain Energy Rev 26:241–264
63. Kose A, Oncel SS (2017) Algae as a promising resource for biofuel industry: facts and challenges. Int J Energy Res 41:924–951
64. Randrianarison G, Ashraf MA (2017) Microalgae: a potential plant for energy production. Geol Ecol Landscapes 1(2):104–120
65. Oncel SS (2015). Biohydrogen from microalgae, uniting energy, life, and green future. In: kim SK (ed) Handbook of marine microalgae Biotechnology advances. Academic Press, pp 159–196
66. Ryong T et al (2014) Analysis for energy efficiency of the algae façade-focused on closed bioreactor system. KIEAE J 14(6):15–21
67. Perini K, Rosasco P (2013) Cost-benefit analysis for green façades and living wall. Build Environ 70:110–121
68. Araji MT, Shahid I (2018) Symbiosis optimization of building envelopes and micro-algae Photobioreactors. J Build Eng 18:58–65
69. Pruvost J, Le Gouic B, Lepine O, Legrand J, Le Borgne F (2016) Microalgae culture in building-integrated photobioreactors: biomass production modeling and energetic analysis. Chem Eng J 284:850–861
70. Tae Ryong K, Seung Hoon H (2014) Analysis for energy efficiency of the algae façade, focused on closed bioreactor system. KIEAE J 14:15–21

Life Cycle Cost Analysis of the Buildings in Turkey Related to Energy Consumption Due to External Wall Insulation

Okan Kon and İsmail Caner

Abstract For five different climate zones which specified on Turkey building thermal insulation standard (TS 825) depending on the different thermal insulation materials, minimum insulation thickness, life cycle saving (LCS), life cycle total cost (LCT), energy saving (ES), and payback period of energy consumption for ten years are found. Then the life cycle saving (LCS), life cycle total cost (LCT), energy saving (ES), and payback period of the energy consumption are investigated according to optimum insulation thickness for the degree-day values base on the heating system efficiency and the cooling performance coefficient value (COP). Minimum insulation thickness and optimum insulation thickness are compared for life cycle saving (LCS) and life cycle total cost (LCT) depending on energy consumption and energy saving (ES). Extruded polystyrene (XPS), expanded polystyrene (EPS), glass wool, rock wool, and polyurethane are used as a thermal insulation material and electricity is used as an energy source.

Keywords Life cycle saving · Life cycle total cost · TS 825 · Optimum insulation thickness · Energy saving

Symbols

HDD	Heating degree-day
CDD	Cooling degree-day
DD	Degree-day
x	Insulation thickness (m)
k	Insulation material heat conduction coefficient (W/m·K)
η	Heating system efficiency
C	Cost ($)
COP	Cooling performance coefficient

O. Kon · İ. Caner (✉)
Department of Mechanical Engineering, Engineering Faculty,
Balikesir University, Cagis Campus, 10145 Balikesir, Turkey
e-mail: ismail@balikesir.edu.tr

ES   Energy saving ($/m^2)
LCS   Life cycle saving ($/m^2)
LCT   Life cycle total cost ($/m^2)
PWF   Present worth factor
i Interest rate
g Inflation rate
R Thermal resistance (m^2·K/W)
U Heat transfer coefficient (W/m^2·K)
N Life (year)
E Annual energy load (kWh/m^2)
r Interest rate
$C_{noH\text{-}C}$ Uninsulated buildings' heating and cooling cost
$C_{H\text{-}C}$ Insulated buildings' heating and cooling cost

Index

opt   Optimum
e   Electricity
ins   Insulation
C   Cool
H   Heat
wm   Wall
ip   Internal plaster
op   External plaster
i   Internal
o   External

1   Introduction

Energy is a measure of the quality of human life and also an indicator of socioeconomic growth. Determining the energy consumption characteristics and energy types of buildings is necessary for planning the future energy demand and investments. It is difficult to estimate future energy consumption values due to lack of measurement-based information and statistical data such as consumption per person and per square meter [1]. Generally, there are three main parameters that affect the energy requirement for heating in a building; meteorology, architectural design, and materials [2].

As the heat loss and heat bridges increase from the external envelope of the houses, the energy performance is negatively affected. In the case of thermal insulation, the external envelope of the structure will be protected against atmospheric conditions

and physical changes such as expansion and contraction which may occur in different climatic conditions will be prevented. Safer and long-lasting buildings will be obtained by preventing internal stresses and cracks in the wall [3].

A correctly selected thermal insulation material provides fuel and energy savings. The economic improvement occurred by savings and the reduction of air pollution creates a healthy environment and a comfortable living space in the building [3].

The purpose of the study is to compare the minimum and optimum insulation thickness which specified on Turkey building insulation standard (TS 825) for five different climate zones, according to life cycle saving, life cycle total cost and energy saving for ten years. As an energy source electricity are used and as an insulation material, extruded polystyrene (XPS), expanded polystyrene (EPS), glass wool, rock wool, polyurethane are used.

2 Materials and Methods

2.1 Degree-Day Calculation

Table 1 shows that heating and cooling degree-day values. Cooling degree-day values are not found for third, fourth and fifth zones because of the average air temperatures for all months are below 22 °C. Degree-day values calculations are as follows [4–6];

$$\text{If } (T_o \leq T_i) \quad \text{HDD} = 30 \sum_{1}^{12} (T_i - T_o) \tag{1}$$

$$\text{if } (T_o > T_i) \quad \text{HDD} = 0 \tag{2}$$

$$\text{if } (T_o > T_i) \quad \text{CDD} = 30 \sum_{1}^{12} (T_o - T_i) \tag{3}$$

$$\text{if } (T_o \leq T_i) \quad \text{CDD} = 0 \tag{4}$$

Table 1 Heating and cooling degree-days [7]

Zone	Heating Degree-Day (HDD)	Cooling Degree-Day (CDD)
Zone 1	1415	555
Zone 2	2395	176
Zone 3	3179	–
Zone 4	3947	–
Zone 5	5027	–

2.2 Heat Transfer, Energy Consumption, and Optimum Insulation Thickness Equations

Overall heat transfer coefficient, U, for a wall,

$$U = \frac{1}{R_i + R_{ip} + R_{wm} + R_{ins} + R_{op} + R_o} \tag{5}$$

where R_i and R_o are the internal and external film thermal resistance. R_{ip} and R_{op} are the internal plaster and external plaster thermal resistance. R_{wm} is thermal resistance of the wall material and R_{ins} is thermal resistance of insulating materials [5, 8, 9].

Annual heating load equation is [9, 10];

$$E_H = \frac{0.024 \cdot U \cdot HDD}{\eta} \tag{6}$$

Annual cooling load equation is [9, 10];

$$E_C = \frac{0.024 \cdot U \cdot CDD}{COP} \tag{7}$$

Calculation of degree-day [9, 10];

$$DD = \frac{CDD}{COP} + \frac{HDD}{\eta} \tag{8}$$

where CDD is cooling degree-day, HDD is heating degree-day, COP is cooling performance coefficient, and η is heating system efficiency. Optimum insulation thickness equation is [10];

$$x_{opt} = \left(\frac{0.024 \cdot C_e \cdot PWF \cdot k \cdot DD}{C_{ins}} \right)^{\frac{1}{2}} - k \cdot R_{wt} \tag{9}$$

where C_e is the cost of electricity, PWF is present value factor, k is heat thermal conductivity of insulation material, C_i cost of insulation material, and R_{wt} thermal resistance of the uninsulated wall. Energy saving (ES) and life cycle total cost (LCT) and life cycle saving (LCS) energy consumption equations are [9, 10];

$$LCS = C_e \left(\begin{array}{c} (E_H(noins) - E_H(withins)) + \\ (E_C(noins) - E_C(withins)) \end{array} \right) PWF - x \cdot C_{ins} \tag{10}$$

$$ES = C_e \left(\begin{array}{c} (E_H(noins) - E_H(withins)) + \\ (E_C(noins) - E_C(withins)) \end{array} \right) \tag{11}$$

$$LCT = C_e(E_H + E_C)PWF + x \cdot C_{ins} \tag{12}$$

If $i < g$ real interest rate is [11];

$$r = \frac{g - i}{1 + i} \tag{13}$$

If $g < i$ real interest rate is [11];

$$r = \frac{i - g}{1 + g} \tag{14}$$

Then

$$\text{PWF} = \frac{(1 + r)^N - 1}{r(1 + r)^N} \tag{15}$$

where i is interest rate and g are inflation rate. N is lifetime (10 years).

Payback period is [12];

$$\text{Payback period} = \frac{C_{\text{ins}}}{(C_{\text{noH}-\text{C}}) + (C_{\text{H}-\text{C}})} \tag{16}$$

2.3 Parameters Used in Calculations

Electricity price is taken as 0.108 \$/kWh [13]. Electricity is used as an energy source for the cooling season and the cooling performance coefficient is taken as 2.5 [14]. For electricity consumption, the heating system efficiency is 99% [11]. The interest rate and the inflation rate are taken 4% and 5%, respectively [15]. Lifetime was taken 10 years. Accordingly, PWF is found at 9.49. Table 1 shows heating and cooling degree-days. The properties of insulating materials are given in Table 3 and maximum wall heat transfer coefficient values which recommended in TS 825 are given in Table 2. Table 4 gives the external wall structural components and properties.

Table 2 Maximum wall heat transfer coefficient (U_{w}) values recommended in TS 825 [7]

Zone	U_{w} (W/m²·K)
Zone 1	0.66
Zone 2	0.57
Zone 3	0.48
Zone 4	0.38
Zone 5	0.36

Table 3 Properties of insulation materials [16]

Insulation materials	Thermal conductivity (W/m·K)	Price C_{ins} ($/m³)
Extruded polystyrene	0.031	180
Expanded polystyrene	0.039	120
Glass wool	0.040	75
Rock wool	0.040	80
Polyurethane	0.024	260

Table 4 External wall structural components and properties [7, 17]

Structural components	Thickness (m)	Thermal conductivity (W/m·K)
Internal plastering with cement and lime	0.020	1.000
Horizontal perforated brick	0.085	0.330
Air gap	0.050	0.278
Horizontal perforated brick	0.135	0.330
External plastering with cement	0.030	1.600

3   Results and Discussion

In five climatic zones for five different insulation materials, the highest insulation thickness is obtained between 0.018 and 0.069 m for glass wool and rock wool and the lowest insulation thickness is obtained between 0.011 and 0.041 m for polyurethane depending on the heat transfer coefficients recommended in TS 825. The thermal conductivity coefficients of glass wool and rock wool are highest with 0.04 W/m·K value. Polyurethane has the lowest with 0.024 W/m·K value. The highest life cycle saving (LCS) value was found between 10.277 and 68.144 $/m² for glass wool insulation material and the lowest for polyurethane insulation material between 8.797 and 62.659 $/m². The maximum payback period is between 1.38 and 2.33 years for polyurethane insulation and the lowest in glass wool insulation material between 0.67 and 1.12 years. The payback period changes depending on the price of the insulation materials and heating and cooling costs. The highest value for life cycle total cost (LCT) was found for polyurethane between 29.667 and 55.625 $/m² and the lowest value was for glass wool between 28.187 and 50.140 $/m². Life cycle saving (LCS) and Life cycle total cost (LCT) values depend on kWh electricity price, interest and inflation rates, insulation thickness, insulating material unit volume price, heating

and cooling system efficiency. Polyurethane has the highest unit volume price with 260 \$/m^3 and glass wool has the lowest unit volume price of 75 \$/m^3. The highest energy saving (ES) was calculated in the fifth region with 7.726 \$/m^2. TS 825 has the single heat transfer coefficient value (U) for each climate zone for external wall. Therefore, a single energy saving (ES) value is calculated for each zone instead of the energy saving (ES) value for each insulation material. While an energy saving (ES) value is obtained at the optimum insulation thickness, a separate heat transfer coefficient (U) is calculated depending on each insulation material, heat conductivity, and insulation thickness. Thus, different energy saving (ES) value obtains for each climate zone and insulation material. These calculations have been shown in Figure 1: (a) Minimum insulation thickness chart, (b) life cycle saving chart (LCS) depends on the insulation materials, (c) life cycle total cost chart (LCT) depends on the insulation materials, and (d) energy saving chart (ES) depends on zones. In Table 5, payback periods based on insulation materials are given at minimum insulation thickness.

The highest optimum insulation thickness in five climatic zones for five different insulation materials was obtained between 0.105 and 0.216 m for glass wool and the lowest insulation thickness in 0.09–0.082 m for polyurethane. The optimum insulation thickness depends on the electricity price, interest, and inflation rates,

Fig. 1 **a** Minimum insulation thickness chart, **b** life cycle saving chart (LCS) depends on the insulation materials, **c** life cycle total cost chart (LCT) depends on the insulation materials, and **d** energy saving chart (ES) depends on zones

Table 5 Payback period based on insulation materials at minimum insulation thickness

Insulation materials	Payback period (year)				
Extruded polystyrene (XPS)	2.05	1.63	1.48	1.51	1.23
Expanded polystyrene (EPS)	1.76	1.33	1.23	1.25	1.04
Glass wool	1.12	0.86	0.79	0.81	0.67
Rock wool	1.20	0.92	0.84	0.86	0.71
Polyurethane	2.33	1.82	1.67	1.69	1.38

the unit volume price of the insulation material, the heating and cooling degree-day values, and the thermal conductivity of the insulation material. Glass wools' heat transfer coefficient is 0.04 W/m·K and unit price is 75 $/m^3, for polyurethane, the heat conduction coefficient is 0.024 W/m·K, and the unit volume price is 260 $/m^3. The highest life cycle saving (LCS) value was found between 19.544 and 82.098 $/m^2 for glass wool and the lowest for polyurethane between 13.225 and 68.985 $/m^2. The highest payback period was calculated between 2.24 and 3.93 years and the lowest was between 1.56 and 2.73 years. The highest value for life cycle total cost (LCT) was between 25.241 and 49.298 $/m^2 for polyurethane and the lowest value was between 18.923 and 36.185 $/m^2 for glass wool. The highest value for energy saving (ES) was glass wool between 2.889 and 10.358 $/m^2 and the lowest value was for polyurethane between 2.380 and 9.516 $/m^2. Polyurethane has the highest unit volume price of 260 $/m^3 and glass wool has the lowest unit volume price of 75 $/m^3. There are different (U) values of the wall for each climate zone, depending on each insulation material and optimum insulation thickness for energy saving at optimum insulation thickness. The energy saving (ES) value depends on the kWh price of the electricity, the heating and cooling system efficiency, the heating and cooling degree-day values, and the insulation thickness. In addition, the energy saving (ES) at the optimum insulation thickness depends on insulation price. These calculations have been shown in Figure 2: (a) Optimum insulation thickness chart, (b) life cycle saving chart (LCS) depends on the insulation materials, (c) life cycle total cost chart (LCT) depends on the insulation materials, and (d) energy saving chart (ES) depends on the insulation materials. Table 6 shows that the payback period depending on the insulation materials at the optimum insulation thickness.

For the five different insulation materials, optimum insulation thickness calculated between 0.036 and 0.105 m in the first zone, 0.060–0.163 m in the third zone, and 0.082–0.216 m in the fifth zone. Life cycle saving (LCS) values were found between 13.225 and 19.544 $/m^2 in the first zone, between 37.005 and 46.779 $/m^2 in the third zone, and between 68.985 and 82.098 $/m^2 in the fifth zone. Life cycle total cost (LCT) was found between 18.923 and 25.241 $/m^2 in the first zone, between 28.022 and 37.796 $/m^2 in the third zone, and between 36.185 and 49.298 $/m^2 in the fifth zone. Energy saving (ES) was calculated as 2.380–2.889 $/m^2 in the first zone, 5.543–6.217 $/m^2 in the third zone, and 9.516–10.358 $/m^2 in the fifth zone.

These calculations have been shown in figures: Figure 3—in the case of different insulating materials for the first zone, (a) the life cycle saving chart (LCS), (b) life
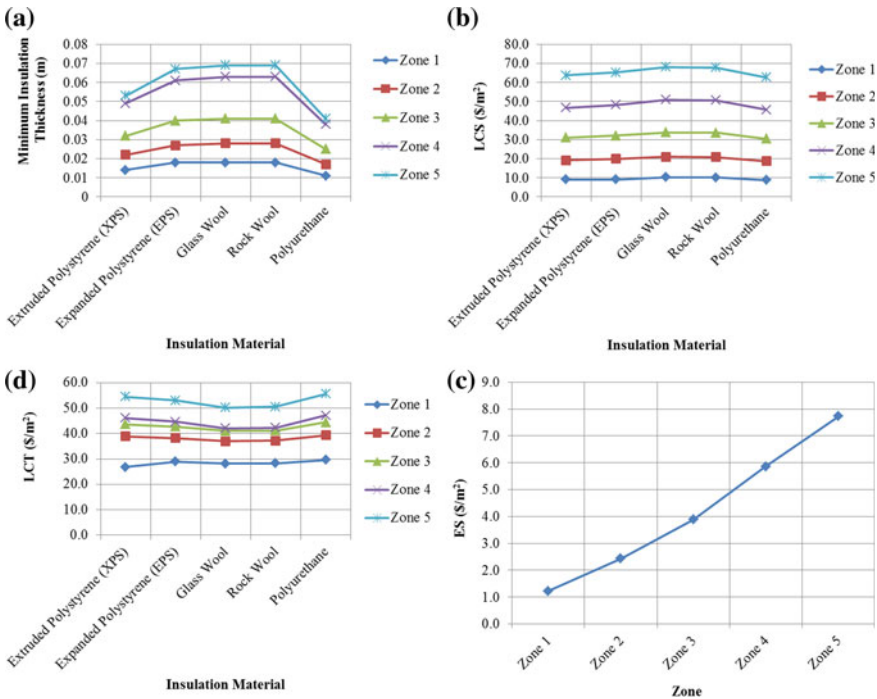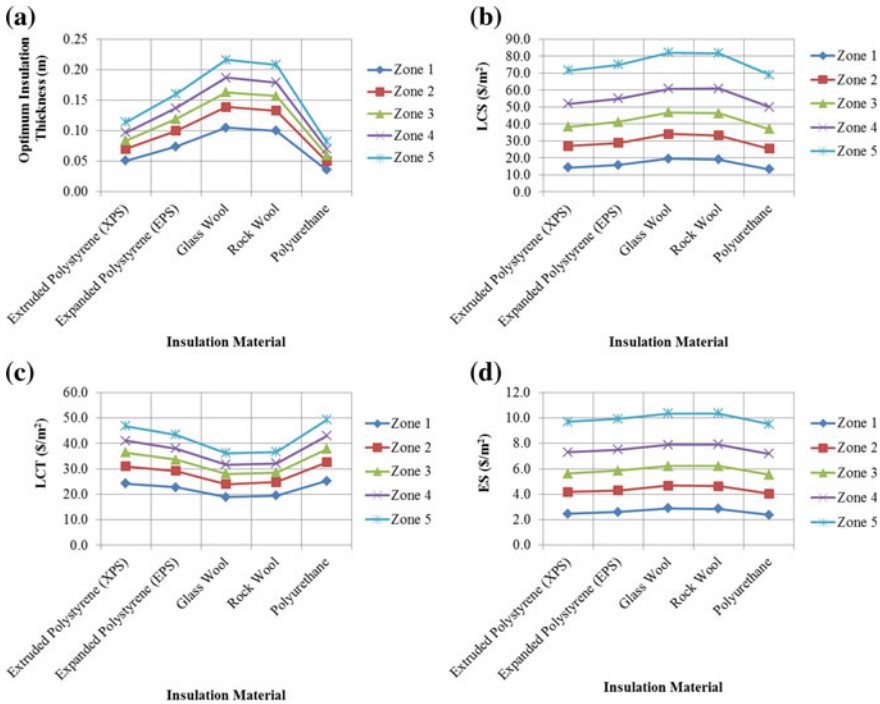
Fig. 2 a Optimum insulation thickness chart, **b** life cycle saving chart (LCS) depends on the insulation materials, **c** life cycle total cost chart (LCT) depends on the insulation materials, and **d** energy saving chart (ES) depends on the insulation materials

Table 6 Payback period depending on the insulation materials at the optimum insulation thickness

Insulation materials	Payback period (year)				
Extruded polystyrene (XPS)	3.72	3.00	2.68	2.39	2.12
Expanded polystyrene (EPS)	3.42	2.79	2.44	2.19	1.94
Glass wool	2.73	2.23	1.97	1.78	1.56
Rock wool	2.81	2.30	2.02	1.81	1.61
Polyurethane	3.93	3.21	2.81	2.53	2.24

cycle total cost chart (LCT), and (c) energy saving chart (ES) depending on the insulation thickness; Figure 4—in the case of different insulating materials for the third zone, (a) Life cycle saving chart (LCS), (b) life cycle total cost chart (LCT), and (c) energy saving chart (ES) depending on the insulation thickness; and Figure 5—for different insulating materials for the fifth zone, (a) life cycle saving chart (LCS) (b) life cycle chart (LCT), and (c) energy saving chart (ES) due to insulation thickness. According to optimum insulation thickness and thermal conductivity of insulation materials, heat transfer coefficient (U) values calculated as; extruded polystyrene
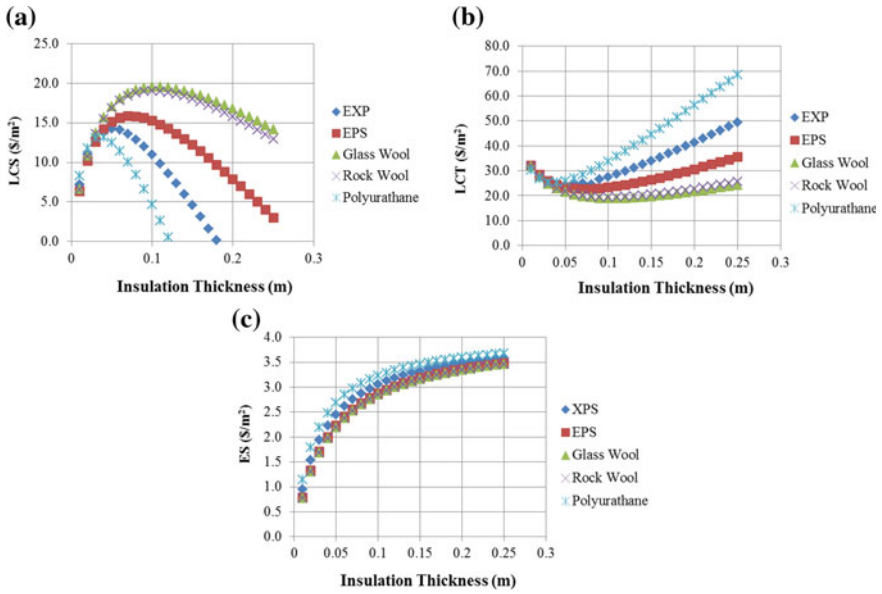
Fig. 3 At different insulating materials for the first zone. **a** the life cycle saving chart (LCS), **b** life cycle total cost chart (LCT), and **c** energy saving chart (ES) depending on the insulation thickness
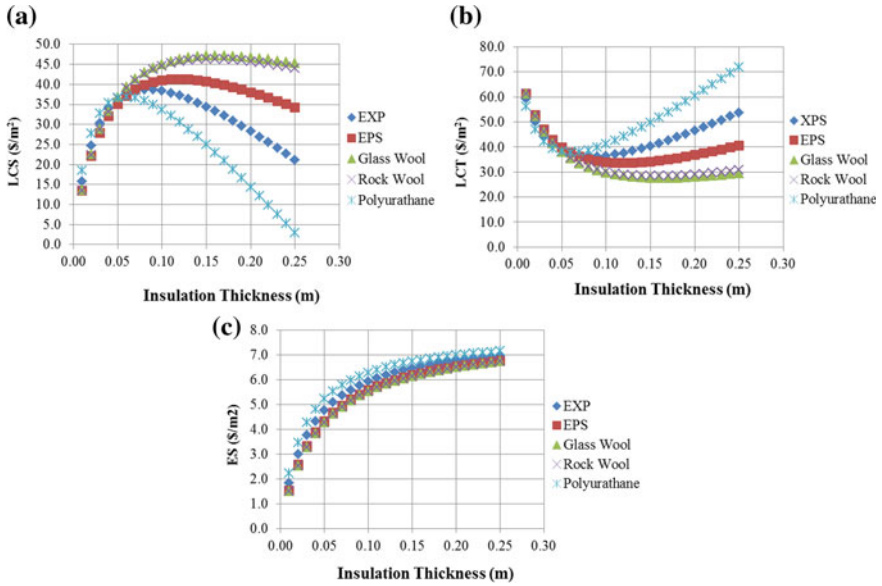
Fig. 4 At different insulating materials for the third zone. **a** Life cycle saving chart (LCS), **b** life cycle total cost chart (LCT), and **c** energy saving chart (ES) depending on the insulation thickness
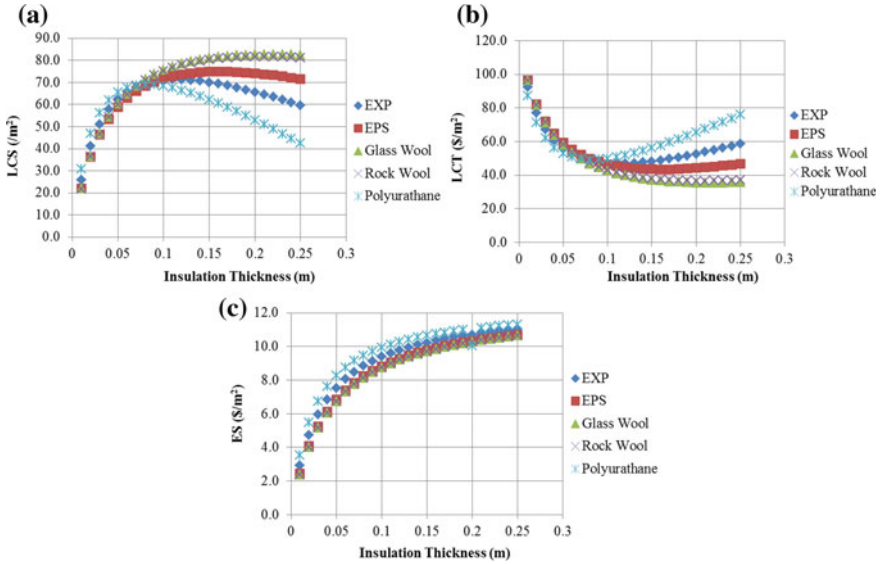
Fig. 5 At different insulating materials for the fifth zone. **a** Life cycle saving chart (LCS), **b** life cycle total cost chart (LCT), and **c** energy saving chart (ES) due to insulation thickness

(XPS) 0.21–0.37 W/m^2·K, expanded polystyrene (EPS) 0.19–0.34 W/m^2·K, for glass wool 0.16–0.27 W/m^2·K, rock wool 0.16–0.28 W/m^2·K, Polyurethane is calculated between 0.22 and 0.39 W/m^2·K. As the insulation thickness increases, the life cycle saving (LCS) value initially increases then decreases. Life cycle total cost (LCT) value initially decreases and then increases. The optimum insulation thickness is the value that maximizes the life cycle saving (LCS) value and minimizes the life cycle total cost (LCT). Energy saving (ES) value increases as the insulation thickness increases. This increase is less in high insulation thicknesses.

4 Conclusions

When we examined the results, glass wool has the highest insulation thickness and life cycle saving (LCS) in both insulation thickness and the lowest is Polyurethane. The highest life cycle total cost (LCT) value is for polyurethane and lowest for glass wool. Polyurethane has the highest payback period at minimum and optimum insulation thickness and the lowest is glass wool. At the optimum insulation thickness, the highest energy saving (ES) is for glass wool and the lowest is polyurethane. The highest energy saving (ES) value at minimum insulation thickness was found in the fifth zone.

According to TS 825, the minimum insulation thickness for five climatic zones which depends on the different insulation materials, minimum insulation thickness, life cycle saving (LCS) of energy consumption, life cycle total cost (LCT) of energy consumption, and payback period are calculated between 0.011 and 0.069 m, 8.797–68.144 $/m^2, 28.187–55.625 $/m^2, 0.67–2.33 years, respectively. Energy saving (ES) is calculated as 1.228–7.726 $/m^2 between the first and fifth zones. The optimum insulation thickness for different degree-day values and depending on different insulation materials is calculated between 0.036 and 0.216 m. Life cycle saving (LCS) of energy consumption, life cycle total cost (LCT) of energy consumption, energy saving (ES), and payback period are calculated between 13.225 and 82.098 $/m^2, 18.923–49.298 $/m^2, 2.380–10.358 $/m^2, 1.56–3.93 years, respectively. Life cycle saving (LCS) and energy saving (ES), which are the important parameters for energy saving, reach higher values at optimum insulation thickness that recommended in TS 825. The life cycle total cost (LCT) value is lower than the minimum insulation thickness at the optimum insulation thickness recommended for TS 825. Depending on these results, it is necessary to increase the minimum insulation thickness values for external walls which specified in TS 825.

References

1. Öz MEU (2006) Determination of residential energy consumption chatacteristics and comparison fuel cells with alternative energy systems for the houses in Bursa. Ph.D. Thesis, Uludağ Universty, Institute of Science, Department of Mechanical Engineering, Bursa (in Turkish)
2. Durmayaz A, Kadıoğlu M (2003) Heating energy requirements and fuel consumptions in the biggest city centers of Turkey. Energy Convers Manag 44(7):1177–1192
3. Bektaş V (2018) Comparison of the thermal insulation materials in the buildings. MA Thesis, Anadolu University and Bilecik Seyh Edebali University, Institute of Science, Graduate School of Sciences Department of Civil Engineering, Bilecik (in Turkish)
4. Ulaş A (2010) Basen on TS 825 directive, analysis of heat loss, fuel consumption, carbondioxide emission and cost for buildings. M.Sc. Thesis, Gazi University, Institute of Science, Department of Mechanical Engineering, Ankara (in Turkish)
5. Kon O (2014) Determining theoretically and practically the optimum insulation thickness of buildings used for different purposes according to heating and cooling loads. Ph.D. Thesis, Balikesir Universty, Institute of Science, Department of Mechanical Engineering, Balikesir (in Turkish)
6. Gültekin ML, Kadıoğlu M (1996) Marmara bölgesinde ısıtma soğutma derece-günlerinin dağılımı. Tesisat Mühendisliği Dergisi, 31 (in Turkish)
7. Turkish Standard, TS 825 Thermal insulation requirements for buildings, December 2013
8. Uygunoğlu T, Keçebaş A (2011) LCC analysis for energy-saving in residential buildings with different types of construction masonry blocks. Energy Build 43(9):2077–2085
9. Jraida K, Farchi A, Mounir B, Mounir İ (2017) A study on the optimum insulation thickness of building walls respect to different zones in Morocco. Int J Ambient Energy 38(6):550–555
10. Alghoul SK, Gwesha AO, Naas AM (2016) The effect of electricity price on saving energy transmitted from external building walls. Energy Res J 7(1):1–9
11. Dombaycı ÖA, Gölcü M, Pancar Y (2006) Optimization of insulation thickness for external walls using different energy-sources. Appl Energy 83(9):921–928
12. Tolun M (2010) Investigation of insulation problem for zones of different degree-days. M.Sc. Thesis, Istanbul Technical University, Institute of Energy (in Turkish)

13. Data from Uludağ Electricity Distribution Corporation (2017 datas)
14. Kaynakli Ö (2011) Parametric investigation of optimum thermal insulation thickness for external walls. Energies 4(6):913–927
15. Arslanoglu N, Yigit A (2017) Investigation of efficient parameters on optimum ınsulation thickness based on theoretical-taguchi combined method. Environ Prog Sustain Energy 36(6):1824–1831
16. Kurekçi NA (2016) Determination of optimum insulation thickness for building walls by using heating and cooling degree-day values of all Turkey's provincial centers. Energy Build 118:197–213
17. Turgutlu brick and tile industrialists association. http://www.turgutlutuglasi.org/. Accessed 27 Nov 2017

Investigation of Fuel Preference Effects for Integrated Buildings Considering Low-Carbon Approach: A Case Study

M. Ziya Sogut, Hamit Mutlu and T. Hikmet Karakoc

Abstract In the building groups considered as campuses or integrated structures, the energy demand based on the heat source is observed to be mostly made with regional integrated solutions. In carbon management of such structures, control and reduction of potential, reduction of energy-related threats are considered as priority strategies. In this study, first, the energy performance of the integrated buildings in which low carbon technologies evaluated instead of a fossil-based solution was evaluated. Next, the CO_2 emission potentials related to the thermal systems compared different fossil and the environmental effect was examined separately. In the process analysis, the resource preferences together with the energy preferences, the effects of different types of resources, and energy consumption performance were analyzed separately. It was observed that the technology applied was 45.38% more effective than standard natural gas systems, 71.07% fuel consumption of fuel oil 4 and 63.28% more effective use of LNG.

Keywords Integrated buildings · Low carbon · Technologies · Energy efficiency · Carbon management

Nomenclature

$\dot{E}x$	Exergy (kJ/h)
LHV	Lower thermal value of fuel (kJ/h)
M_{fuel}	Fuel (kg)
T_0	Environment temperature (°C)

M. Z. Sogut (✉)
Piri Reis University, Maritime Faculty, Tuzla, Istanbul, Turkey
e-mail: mzsogut@gmail.com

H. Mutlu
Mechanic Project Company, Bursa, Turkey

T. H. Karakoc
Department of Airframe and Powerplant Maintenance, Faculty of Aeronautics and Astronautics, Eskişehir Technical University, 26470 Eskisehir, Turkey

T Resource and interior temperature (°C)
$\dot{Q}_\text{h}$ Total thermal load of the building (kJ/h)
$\sum \dot{Q}_\text{W}$ Total energy (kJ/h)
$\sum \dot{Q}_\text{BW}$ Boiler energy consumption (kJ/h)

Greek letters

η_device Thermal efficiency of the device
γ Exergy factor
γ_fuel Fuel-based exergy factor
η_I Energy efficiency
ψ Exergy efficiency

1 Introduction

In recent years, the development of low carbon technologies, the introduction of low carbon or zero carbon standards in building standards, the vitality of independent evaluation and certification programs such as LEED energy star in energy efficiency have changed the energy system design and implementation criteria for essentially integrated structures. In particular, the effects of energy costs along with the advantages of technology, management systems that can be put under control can support a system design work that is energy efficient and applicable to all structures, especially mechanical systems. Approximately, 65% of the building energy consumption defines the demand for heating, and in such system solutions, low-carbon technologies are seen as a solution that is prominent for reducing the effect of fossil resources.

Developments in building technologies have positively affected the energy needs of buildings in the building sector. However, the energy use rate in the building sector, which has reached 40% of fossil resource consumption, has a tendency to fall with the development of low-carbon technologies. Especially low carbon technologies, especially heat pump technologies and renewable energy sources, stand out in sectoral preferences.

The most important reason for the sectoral preferences is the reduction of the fossil source emission threat. Low-carbon technologies in this regard will have a catalyst effect. The most important reason for the sectoral preferences is the reduction of the fossil source emission threat. In fact, according to the World Energy Agency's assessment, the sectoral prevalence of low carbon technologies will develop and this impact is predicted to be an improvement to CO_2 emissions by approximately 2050 [1].

In sectoral evaluations, energy analyses based on the first law of thermodynamics are applied in the performance analysis based on energy efficiency. Although such

analyses are primarily based on a performance evaluation, the potential of the fossil source threat is primarily related to the environment in which the system is located.

This effect due to irreversibility has an emission threat depending primarily on the losses they cause. In this respect, the exergy analysis, which is based on the qualitative conditions of irreversibility, comes to the fore. In the building sector, the irreversibility potential caused by thermal processes, together with multiple analyses, also describes the burden of useful usable energy [2, 3].

Exergy is expressed as the highest attainable work that can be achieved for all energy-borne processes in the environment. In this way, it is seen as the minimum energy demand based on the comfort conditions for the environmental parameters for which the structure is primarily based. This definition also refers to the minimum energy consumption of the building and the minimum environmental threat in a beneficial work condition [4, 5].

In this respect, this study is an infrastructure study showing the effectiveness of low-carbon technologies for mechanical project processes. The study of the manageable energy system for an integrated structure in the study has been examined with different fuels. In this context, the mechanical system design and analysis using the water source VRV/VRF system are presented. This study is primarily planned to define as the concept of integrated structure, the concept of exergy, analyses of the integrated buildings, and evaluations of the results.

2 Integrated Buildings

Moving along with the industrial sector in energy consumption, the building sector has approximately 40% of its final energy consumption. It has 50% of the global emission potential in energy consumption. In this respect, the energy consumption of building sector plays a leading role in the consumption of fossil resources and has approximately 65% of the energy consumption from heating applications. The building sector, which is an important parameter in social strategies, should be seen as the main application area in energy management policies.

The integrated buildings, which are used for multipurpose buildings except for residential type buildings, are used in many properties such as military, housing, commercial, and education. These types of structures, which are constructed according to different requirements, consist of structures with different intended uses. Comprehensive structure differences should be seen not only from the point of view of the energy systems but also from the manufacturing process as integral structures that should be evaluated in terms of their structural features.

Mechanical design in integrated structures, just as in architecture, brings an energy-efficient solution together with all its components and actors. In this context, the design process should be studied with minimum labor and time loss. The integrated design is briefly referred to as the integrated design of all components, such as architectural, static, mechanical, and electrical installation. In this context, in mechanical systems, it is aimed to keep the heat demands at a very low level due

to comfort conditions, to increase the share of renewable energy, and to establish a holistic structure that can approach the targets of net-zero energy. Although this approach has been described in recent years by many evaluation certification programs such as LEED, many types can be seen including green building concept, low-carbon, and zero-carbon buildings. However, the integrated building concept has been developed as a building model contributed by all the actors in the building process. In this respect, the building groups with the properties of the settlement are also integrated into the manufacturing process [6].

Campuses are the ones that provide the energy needs and especially the heat energy demand with steam, boiling water, or hot water systems in a central structure. Generally, together with the preference of fossil fuel, classical boiler or fluid bed technology is the most common. The design infrastructure for an integrated structure is shaped not only by architectural foundations but also by many disciplines and approaches. Energy has an 83% effect on life cycle costs. However, nowadays, energy preferences in houses have a rather diffuse structure. Figure 1 shows these distributions.

Energy consumption behaviors in buildings should not be evaluated only on housing types. Energy consumption habits of these houses should be examined in terms of the system activities used. The system efficiencies used in this context also have very low values. All these evaluations have made low or zero-carbon approaches valuable in building system preferences.

However, today, low-carbon technologies are applied as energy-efficient solutions instead of conventional system preferences. In low-carbon technologies, different heat pump preferences, organic Rankine cycles, and geothermal energy applications can be seen as energy-efficient solutions according to regional situations. In this study, the effectiveness of the applied heat pump application was investigated as a comparison with different fuel preferences in an integrated structure.
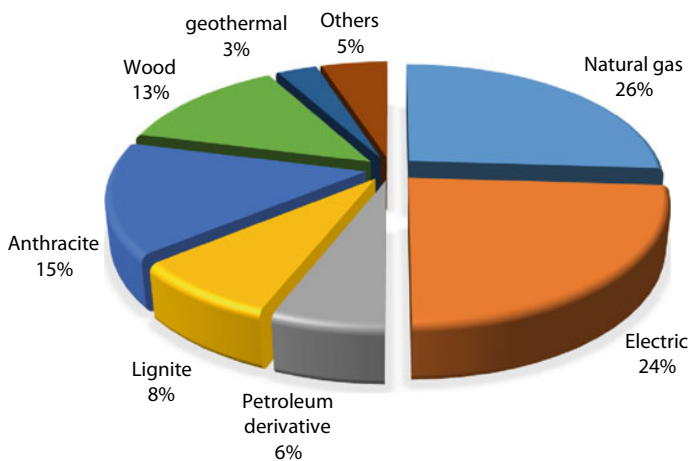
Fig. 1 General energy consumption behavior of houses [7]

3 Low-Carbon Approach

The fight against global climate change has become an important issue in the social strategies for all nations since the late 1990s. In recent years, low-carbon approaches have been developed as processes evaluating all elements based on the reduction of greenhouse gas emissions. This approach, which is mainly to increase the consumption of the fossil fuel, has highlighted the new applications defined as low-carbon technologies instead of classical technologies. These processes can basically be divided into five disciplines. These are given in Fig. 2.

The standards, in which the energy requirements of buildings are defined, differ in many ways for countries. However, although national standards provide standardization, sometimes, they are below expectations, depending on local circumstances. In this respect, low-carbon standards developed in the world are considered as a sectoral target for applications. In particular, while it has reduced the consumption of fossil fuel from the building, it has contributed in terms of sustainable energy management to the reduction of the costs. Another approach to carbon strategies is zero-carbon technologies. The zero-carbon approach has developed solutions where technologies with a direct zero emission effect are applied. For example, these solutions can be expressed as the approaches that demand hydro or biomass energy sources that use energy recycling technologies for some applications, which do not have any waste properties instead of fossil fuels and maximizes the use of renewable energy instead of fossil fuels [8].

In recent years, low and zero-carbon approaches, which are used as standard for many countries, have encouraged and extended new and existing buildings considering energy management. In these buildings, applications of the low and zero-carbon or PT like low-temperature heating system are countable. However, in such preferences, how energy is used, efficiency and sustainability are important issues. The advantages of low carbon technologies are, in particular, the continuation of new buildings with integrated design, production, and installation-based energy management. In this context, such approaches are shaped by strategy and standards in process management. Low-carbon technologies in buildings, especially passive systems, are
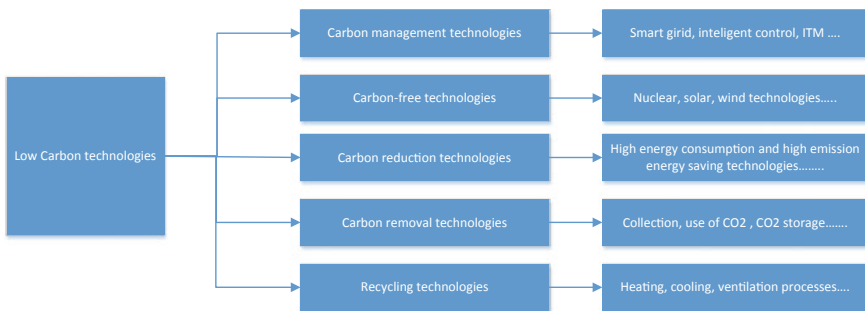
Fig. 2 Low-carbon technologies

technologies that need to be evaluated in many ways. These structures, which are defined as parameters and zero energy buildings in Fig. 3, define the energy demand of the building and management tools.

All these technologies or approaches have shown the requirement for new standards for applications of the buildings. For example, from 2006, the EU has done very important studies about the building sector. The building energy performance directive is one of them and it is quite to provide energy efficiency and performance analysis for the member countries. According to this, UK and Scotland have published first standards as leading countries and aimed to reduce greenhouse gas emissions by 80% with these standards.

Accordingly, by the implementation that came into force in 2008, all new buildings until 2019 are covered in this standard. In this scope, this standard includes some processes like smart and recovery structure, improvement of the systems or buildings. These applications are a healthy application in the life cycle of buildings for building structures. Considering the reduction of the emissions threat, the construction materials of the buildings related to LCS can be expressed having the reduction of the emission by 80% between 1000 and 1500 kg CO_2/m^2 (only about 500 kg CO_2/m^2 for construction). With all environmental transformations, a typical building, waste management, and the transfer, as well as recovery, are considered in this context. The standard has found a field of application in this respect and includes the improvement

Fig. 3 Concept map in zero and low-carbon approaches [9]

of materials preference in buildings, the preference of materials having low emission factor and the recovery technologies.

According to the usage characteristics and structure of the buildings, the emission potential varies between 0 and 100 kg CO^2/m_2 as yearly. For buildings, LCSs have been defined to reduce the emission loads under 10 $kgCO_2/m^2$ for each year. In this context, together with the issues described above, reducing energy consumption, significant gains in development the alternative energy systems application like renewable and recovery are achieved. The energy demands of buildings supplied based on existing systems are related to climatically and geographically values, classic or incorrect analysis. In this context, the LCS can be evaluated as a step or phase considering zero-carbon concepts [10].

There are three basic stages in creating a zero- or low-carbon standard in a structure. These are in turn; is primarily the reduction of energy demand. In this context, measures to minimize energy need based on building components are developed together with passive applications, and the minimum rule is defined. In this context; for example, for a house of 75 m^2 energy efficiency in terms of a minimum of 46 kWh/m^2. The second basic approach is to determine the carbon compliance limit. In this context, the carbon equivalent defined above should be considered as a limit, and action should be taken for the energy points that cause it. In the third stage, the effect direction should be defined in the remaining CO_2 emission loads and the reasons should be questioned. In particular, action processes such as how energy should be managed with the types of energy purchased and the reduction of demand are developed. As can be seen in Table 1, low and zero-carbon buildings can be seen in this context with many applications and different standard approaches [11].

Today energy demand calculations are handled by national rules. These rules are defined under local circumstances and apply to approximate calculations based on limit conditions. These approaches have a low impact on direct or indirect sustainable energy management. The building sector has been developed as an important solution for low-carbon approaches in social strategies with an emission effect of 40%. In this

Table 1 Zero or low carbon building applications [12]

Country	Building type	Criteria	Energy	Performance criteria kWh/m^2 . yıl	Renewable energy rate %	Standard
Belgium	House	Energy	Heating Hot water	45	–	Code of Belgium air conditioning and energy
Cyprus	House	Energy	Network	180	25	Action plan of zero energy Building
France	House	Energy	Network	50	–	RT2012
Denmark	House	Energy	Network	20	51–56	BR10
Latvia	House	Energy	Network	95 kWh/m^2 . year	–	Housing regulations No 383 09/07/2013

respect, sustainable energy management is the main approach, and the reduction of fossil fuel consumption with low or zero-carbon approach has come to the forefront. Zero-carbon approaches aim to reduce the threat of direct or indirect emissions. In the building sector, renewable, recyclable, passive, or zero-energy approaches to fossil resources are such approaches. Today, the technologies applied to these approaches are mainly absorbed systems in heat flows, mainly in electrical systems [10].

Nowadays, the use of these technologies within the scope of combating greenhouse gas has become important policies for many countries. Important strategies for the preferences of these technologies were defined and system examples were developed [13]. As a matter of fact, energy demands in buildings have also been improved in this context. In this respect, all requirements, especially building designs, have been developed with versatile engineering studies. High insulation materials, passive building solutions have been the key players. For this purpose, in many countries, low and zero energy concept in the buildings (new or existing) is evaluated as the strategic value with its technologies like, PT and low temperature heating system. As a matter of fact, energy demands in buildings have also been improved in this context. In this respect, all requirements, especially building designs, have been developed with versatile engineering studies. High insulation materials, passive building solutions have been the key players. Although not a generally accepted standard, some countries have developed their own standards. These standards provide solutions covering many methods and applications. These structures and applications, which have the many parameters, directly concern energy consumption behavior in buildings. These parameters of the structures given in Fig. 4 and also defined as zero-energy buildings should be considered as integrated components at the energy demand for building and management tools and in this context, they should be evaluated as holistic in capacity analyses [11].

The conditions in which the building sector is in place highlight the need for such a standard. As a matter of fact, it has developed works to improve the energy
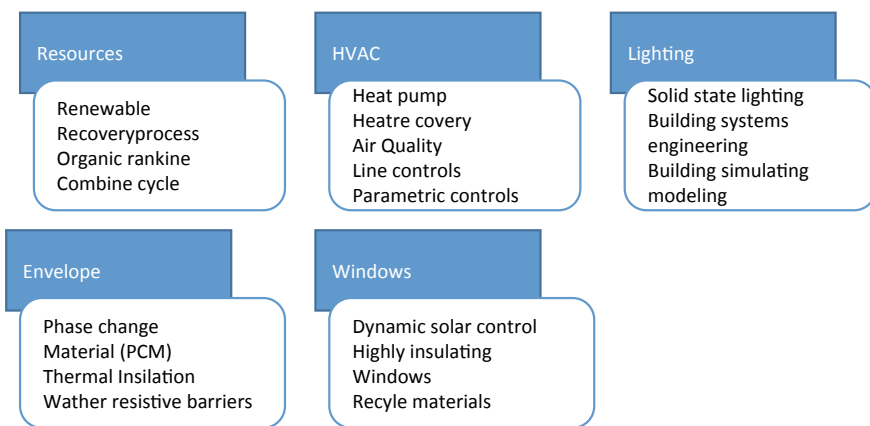
Fig. 4 Parameters of zero-carbon buildings

performance of buildings, especially in the European Union. He has also carried out certification works for the member countries on this subject. It also developed its low-carbon standard in 2008, aimed at reducing its standard work to 80% in the UK, and Scotland's fight against emission. The standard was defined especially for new buildings and in this context 2019 was selected as the target year. This standard approach provides guidance for many criteria, from structural components in buildings to energy usage behavior and technology preferences. The most important target is defined as reducing 80% in the 1000–1500 kg CO_2/m^2 in the scope of the fight against emission (around 500 kgCO_2e/m^2 for construction only). The standard is provided for all processes on the basis of the developed standard. In this respect, it develops a re-approach for all elements in buildings. It contains many components which are suitable for recycling which should be considered together with the building components.

When existing building stock is evaluated, it has a high emission potential. This value reaches up to 100 g CO_2/m^2 per m^2. However, it is aimed to have a low-carbon approach and 10 kg CO_2/m^2 per year for the buildings. This defined the target process, the development of directly or indirectly effective energy solutions is prioritized. In addition, energy demand analyses, in which instant climate data are valued, are evaluated within the scope of the standard. In fact, the low-carbon approach should be seen as a transitional step [10].

4 Low-Carbon Technologies

The key player in tackling global climate change is the reduction of CO_2 emission-equivalent greenhouse gas emissions that contribute to the formation of this impact. In this context, technological solutions of all the stakeholders that can be considered within the scope of responsibility can be considered as the priority point of influence. As can be seen in Fig. 5, system and technology solutions based on sectoral solutions can be seen as focal points in innovation and implementation periods.

In 2020, the emissions reduction target of 20% of the European Union had a positive impact also on developments in low-carbon technologies. This has been particularly important in heating and insulation systems and applications in the building industry. Approaches to improve energy efficiency in air-conditioning systems, energy performance product development, application in mini and medium capacities in power generation technologies, and system automation applications can be evaluated as developments. In addition, different certification programs developed in standards (LEED, Breams, ISO50001, etc.), together with sectoral diversity, have made low-carbon technologies important in technological changes.

Today, the adoption and implementation of low-carbon technologies, together with many factors, are quite low due to their financial impact. These approaches, which have a counterpart in developed countries, are defined by many mechanisms in terms of control, production, distribution, and use. However, the application procedures of such systems are prioritized in terms of multidirectional system requirements. This
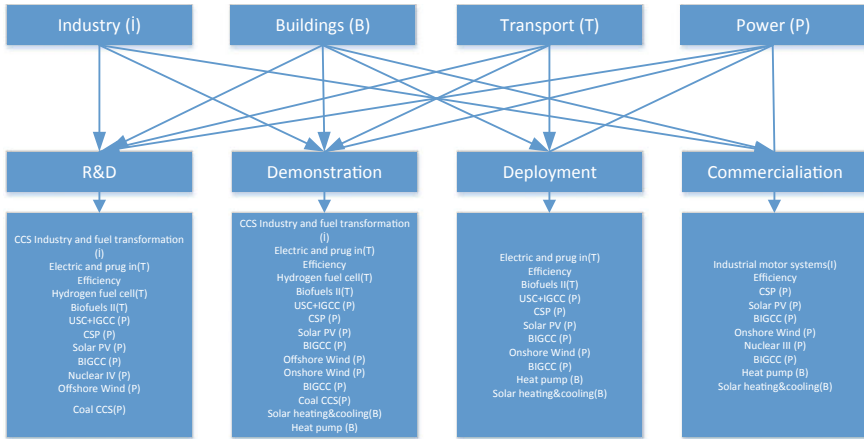
Fig. 5 Key technology development priorities for sectors (modifed from Ref. [14])

approach, which is defined as demand management in terms of needs, is a structure that should be managed by taking into account the risks, preferences, geographical, and regional constraints in the preferences of low-carbon technologies.

5 Exergy Theory

The most important productivity criteria of the mechanical system in energy efficiency-based project processes are fuel choice and system choice. As a matter of fact, in this project, energy and cost analysis related to loading calculations were made separately for four different sources. For process heating data, the outside air temperature is $-12\ ^\circ C$, indoor temperature $22\ ^\circ C$, system water temperature $10\ ^\circ C$, and system water temperature $45\ ^\circ C$. Considering the total heat load requirements, the fuel and cost relationship of the system can be evaluated. In this context, total fuel consumption;

$$M_{\text{fuel}} = \frac{\dot{Q}_{\text{heat}}}{\text{LHV}_{\text{fuel}} \cdot \eta_{\text{boiler}}} \tag{1}$$

where LHV is low-heat value, η_{boiler} is thermal efficiency [15]. In thermal processes, actual consumption depends on ambient temperatures. The exergy concept defined according to the second law of thermodynamics is often dealt with in terms of chemical where combustion reactions occur, thermal dependent on temperature and mechanical exergy concept related to differential pressure [4]. In this context, heating and cooling systems and applications of structures are defined directly by thermal exergy. Heat sources in buildings can be considered as a heat machine and

can be seen as a heat transfer structure between heat sources. In addition to heat loads in particular, the exergy factor defines the total load with the Carnot equation of the total heat load and expresses the building's exergy demand. Particularly in heat loads, the exergy factor defines the total load with the Carnot equation of the total heat load and expresses the building's exergy demand [16]. This factor is expressed as a ratio between the exergy and energy load of the system. The obtained factor defines a proportionally correlation for demanded between loads of the exergy and heat for the system [3, 4]. Accordingly, the exergy factor is:

$$\gamma = \frac{\dot{E}_x}{\dot{Q}_h} = \left(1 - \frac{T_0}{T}\right) \tag{2}$$

The building's minimum energy demand is based on the minimum exergy requirement defined directly between the dead-state temperature and the comfort temperature. This structural feature relates to the value defined in the comfort conditions of the building [16]. Accordingly, exergy demand is:

$$\dot{E}_x = \dot{Q}_h \cdot \left(1 - \frac{T_0}{T}\right) \tag{3}$$

Here, Q_h is the heat demand of buildings based on the construction materials, T_0 is the surrounding temperature of the building, T is the source temperature of the heating system. Heat demand is directly related to fuel consumption. The relationship of fuel with exergy is directly dependent on the conditions of the dead state. In this context, demand energy consumption can be considered as limit value. Unlike the energy limit value, the exergy efficiency of the building is defined directly by the rational exergy. It is also expressed as the ratio of the exergy demand to the fuel potential in buildings [3, 5].

$$\psi = \frac{\dot{E}_{x,heat}}{\dot{E}_{x,fuel}} \tag{4}$$

Irreversibility-related losses of systems are the basis of entropy production. In particular, the inversities within the boundaries of the system directly affect the efficiency. A holistic approach to exergy efficiency is also calculated based on the first law efficiency. For a process, exergy efficiency refers to the relationship between energy efficiency and exergy factor. In this context, the exergy efficiency of the process is [2]:

$$\psi = \frac{\eta_l}{\gamma_{fuel}} \tag{5}$$

Here, γ_{fuel} is the heat-based exergy factor. It is 1.06 for the natural gas in the study and 1.08 for coal.

5.1 CO₂ Emission Terms

In emission analyses, the emission calculation method that has been developed together with the concept of exergy in recent years is the method of carbon emission metric. This method shows that a thermal structure actually has three separate carbon emission centers. Carbon emission metric is a result of negativity based on thermal efficiency and rational exergy. In this case the total equivalent CO_2 emissions of the system

$$\sum CO_2 = CO_{2i} + \Delta CO_{2j} = \left(\frac{\omega_{CO_2 i} \sum \dot{Q}_{W_i}}{\eta_{Ii}} \right) + \left(\frac{\omega_{CO_2 j} \sum \dot{Q}_{BW_j}}{\eta_{Ij}} \right) (1 - \psi_{Ri})$$

(6)

where ω_{CO_2} is unit energy CO_2 emission factor, $\sum \dot{Q}_W$ is waste energy, $\sum \dot{Q}_{BW}$ is equivalent to boiler energy consumption, ψ is rational exergy efficiency [17].

6 Results and Discussion

In the study, first, the energy demand of the campus is defined for four alternative fuel types depending on the dead-state temperature change. Considering the performance, the exergy efficiency of the system to be applied for each type of fuel has been examined and the exergy destruction based on the irreversibility has been found. In the integrated structure, CO_2 emissions potential for each type of fuel was defined and as alternative solution, the effectiveness of the water-source heat pump, which will be preferred instead of existing system with fosil fuel source, has been assessed. The integrated structure referred in this study has a total heating capacity of 918,316 kWh/year with a closed area of 12,000 m² directly. The exergy input values requested by the system considering the dead-state conditions are examined and their distributions are given in Fig. 6.

When the exergy demands of fuel preferences are evaluated, LNG has the highest value with 1.18%, based on average demand. However, natural gas preference has a load of 0.59%. In this respect, it can be said that natural gas preference expresses the lowest energy demand. Exergy demand is calculated directly dependent on taken reference to adiabatic flame temperature and load requested by the system. This refers to the demand for exergy required by the system as a result of direct fuel consumption. These data were evaluated with the combustion chamber temperatures and system losses were investigated separately. Accordingly, combustion losses due to the fuel type of the system were calculated and the results are given in Fig. 7.

In boiler technology, combustion chambers transfer energy to fluid depending on the construction they have. Considering the combustion chamber temperatures with reference to the combustion chamber temperatures, thermal losses were found to be 10.51% for the natural gas, 8.07% for the fuel oil, 11.67% for the LNG, and 11.40%
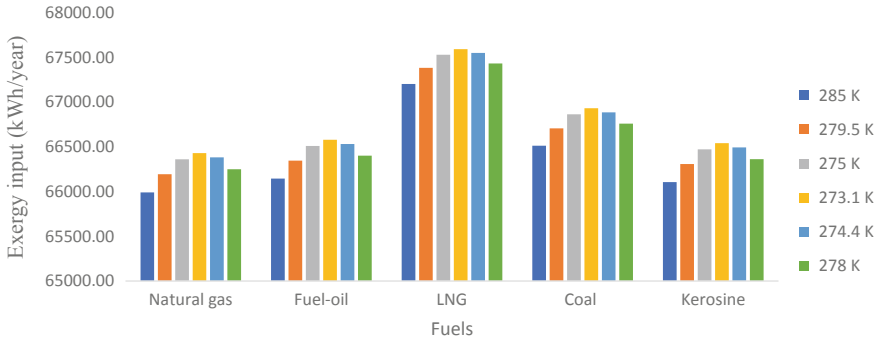
Fig. 6 Exergy input based on fuel demand
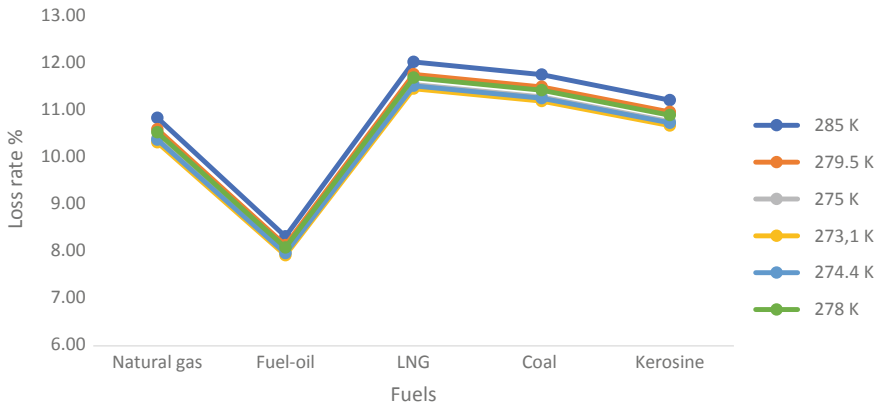
Fig. 7 Heat losses based on fuels in the combustion room

for the coal in consideration of the adiabatic flame temperature and the combustion chamber temperatures. Depending on the fuel type examined, the chimney losses of the systems were also evaluated and the energy and exergy efficiency were examined and the results based on dead-state changes were given in Figs. 8 and 9.

Natural gas has the highest value with 89.62% if exergy factors related to fuel sources are taken into consideration. However, when boilers and thermal systems are evaluated, the exergy efficiency of the natural gas system was found as 51.56%. According to these performances, the losses due to the irreversibilities of the systems were investigated and the entropy loads generated of the system are defined separately. Accordingly, the total entropy production and improvement potential of the system is given in Fig. 10.

According to the analyses made, the exergy destruction of the system was found 8.5% in average natural gas, whereas this value is 65.7% in coal. However, distributions of the exergy destruction show difference significantly considering the dead-state temperature. As a matter of fact, when the distributions are analyzed, this
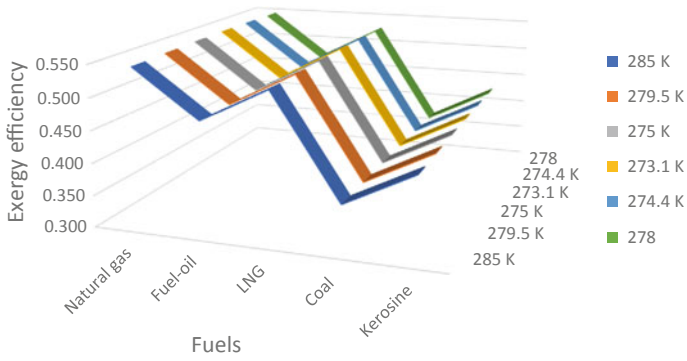
Fig. 8 Exergy efficiency of domestic boiler systems
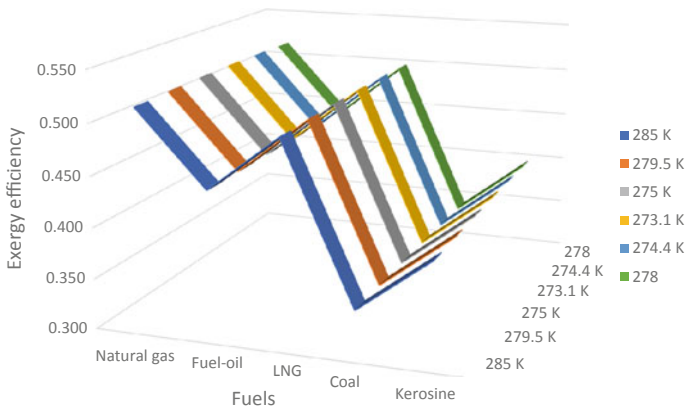
Fig. 9 Exergy efficiency of fuels for domestic boiler
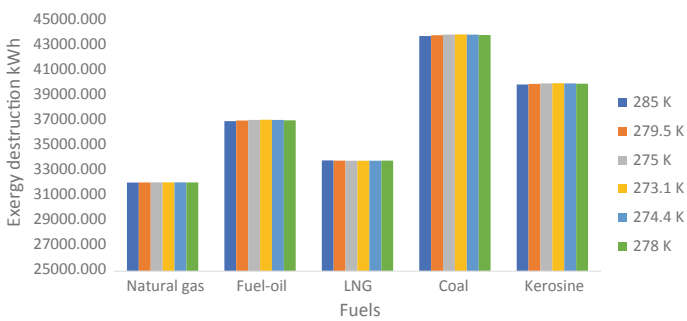
Fig. 10 Exergy destruction based on fuels
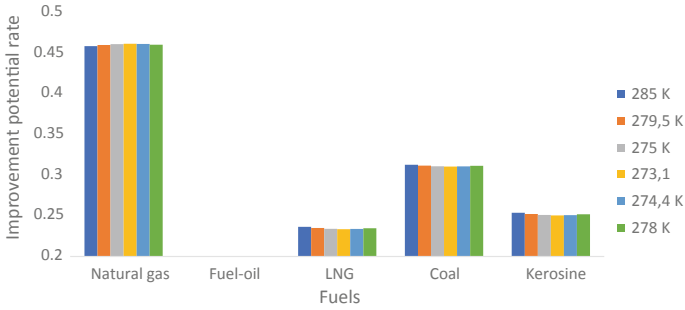
Fig. 11 Improvement potential rate based on fuels

change in natural gas is 45.89% and this value is 46.16% in coal. Exergy analyses provide an important opportunity for process improvements. In this respect, system improvements to reduce exergy consumption are defined with improvement potential. The distribution of these development potentials depending on fuel types can be seen in Fig. 11.

The improvement of potential change was found to be 45.67%, which, when evaluated together with the dead-state temperature change, varies according to the fuels. The improvement is based on the total energy of 23.47% for natural gas. However, considering the fuel distribution, a potential of about 32% can be mentioned. Based on these distributions, important exergy consumption potentials for all fossil fuels, including natural gas, are noteworthy. Based on all these distributions, CO_2 emission potential (ton CO_2) related to exergy destruction is given in Table 2.

Fuel consumption from fossil fuels continues its pioneering impact on all processes. However, preferring low-carbon technologies in structures integrated with heating processes will provide significant savings in consumption. As a matter of fact, VRV/VRF or heat pump preferences were evaluated in terms of fuel preference for integrated structures and low-carbon technologies, and their thermoeconomic results are given in Table 3.

Table 2 CO_2 emission potential of fuels

Dead state temperature	285 K	279.5 K	275 K	273.1 K	274.4 K	278 K
Fuels	Emission potantial (ton CO_2)					
Natural gas	3135.97	3127.64	3120.85	3118.00	3119.95	3125.37
Fuel-oil	5708.13	5707.20	5706.47	5706.17	5706.37	5706.96
LNG	3427.18	3416.10	3407.08	3403.29	3405.89	3413.09
Coal	10304.36	10302.71	10301.40	10300.86	10301.23	10302.27
Kerosene	6209.29	6205.23	6201.94	6200.56	6201.50	6204.13

Table 3 Thermo-economic evaluation of low carbon preference for integrated Building

	Natural gas (m^3)	Fuel-oil (4) (kg)	LNG (m^3)	Coal (kg)	Heat pump (kWh)	VRV/VRF (kWh)
Heating demand (kWh)	475456	475456	475456	475456	475456	475456
Fuel consumption	52171.262	51758.5	53293.7	208991.6	76686.5	118864
Unit cost of fuel ($)	0.63	1.17	0.9	0.45	0.255	0.255
Total cost ($)	32867.895	60557.5	47964.4	94046.2	19555.1	30310.3

While heat pump preference for natural gas systems provides a saving of 40.5%, the rate of VRV was found to be 7.78%. These values were taken as reference for coal, 79.2% in the heat pump and 67.8% in VRV. These values should also be evaluated in terms of emission savings.

7 Conclusions

This study examines firstly the manageable energy system for the campus defined as integrated building considering different fuels. In this context, the mechanical system design and performance analysis based on the water-based VRV/VRF system was made. The study also examined the emission load effects for different types of fuels. In this scope;

– All conventional fuel preferences have been shown to have a high CO_2 emission potential.
– When fossil fuel consumption was evaluated, the use of natural gas seen that increase the emission threat by 46% compared to coal.
– In heat pump preference, financial savings of about 41% in costs was found, despite the consumption of natural gas provides.
– In VRV preferences, this effect has an advantage of 8%.

The integrated structures prefer low-carbon technologies in their multifaceted energy preferences, indicating a structure where economic gains are ensured as well as energy and environmental impacts. In these preferences, first of all, it is necessary to make a need optimization by considering demand management. In this study, reference is made to the evaluation of low-carbon approaches such as heat pump with structural analysis. In addition, the exergy analysis and exergo-economic and exergo-environmental analysis of the intelligent building management together with the cost analysis will also contribute to these processes.

References

1. Soner T, Söğüt Z (2012) Building sector energy efficiency and environmental performance evaluation projection in Turkey. Turkish Society of Plumbing Engineers, Issue 82, November–December 2012
2. Xydis G, Koroneos C (2009) Polyzakis A. Energy and exergy analysis of the Greek hotel sector: an application energy and buildings 41:402–406
3. Hepbasli A (2012) Low exergy (LowEx) heating and cooling systems for sustainable buildings and societies. Renew Sustain Energy Rev 16:73–104
4. Annex 49. Energy conservation in buildings and community system slow exergy systems for high performance buildings and communities (1 Dec 13)
5. Cornelissen RL (1997) Thermodynamics and sustainable development: the use of exergy analysis and the reduction of irreversibility. Ph.D. thesis, University of Twente, The Netherlands
6. Soner Y (2012) Integrated Design in Buildings, TMMOB Chamber of Machine Engineers Adana branch, Adana. http://www.mmo.org.tr/resimler/dosya_ekler/e5eb703282528c4_ek.pdf?tipi=68&turu=X&sube=1
7. Keskin T (2010) Development of turkey's national climate change action plan project current situation in the energy sector assessment report, Ankara (TR). http://iklim.cob.gov.tr/iklim/Files/Enerji_Sektoru_Mevcut_Durum_Degerlendirmesi_Raporu.pdf
8. Bevan W, Lu S (2012) A multidisciplinary literature review of low and zero carbon technologies into new housing. In: Smith SD (ed) Proceedings of the 28th Annual ARCOM Conference, 3–5 September 2012, Edinburgh, UK, Association of Researchers in Construction Management, pp 1435–1444
9. Ziya MZ, Mutlu H, Karakoc TH (2018) Effects of low carbon technologies in carbon management of intagreted buildings: a case study. In: 7th Global Conference on Global Warming (GCGW-2018), June 24–28, 2018, Izmir, Turkey
10. RIBA (2009) Climate Change Toolkit, 04 Low Carbon Standards and Assessment Methods, Royal Institute of British Architects 66 Porland Place, London W1B 1AD T 020 7580 5533-175, 1834. www.architecture.com
11. Sogut MZ, Yalcın E, Karakoç TH (2019) Carbon technologies and energy management in integrated structures. 14th National Installation Engineering Congress—17–20 April 2019/Izmir
12. UK (2008) Zero carbon homes and nearly zero energy buildings UK building regulations and EU directives zero Carbon Hub, Layden House, 76-86 Turnmill Street, London EC1M 5LG. http://www.zerocarbonhub.org/sites/default/files/resources/reports/ZCHomes_Nearly_Zero_Energy_Buildings.pdf
13. Rawlson O'Neil King (2014) Market potential of net-zero energy commercial buildings in North America and Worldwide Adoption, CABA, non-profit trade organization promotes home and building automation, 1173 cyrville road, suite 210, Ottawa, ON K1J 7S6. www.caba.org
14. TSE Thermal insulation rules in building (TS-825), Turkish Standards Institute Necatibey Street No. 112 Ministries, Ankara, Turkey (2008)
15. IEA (2008) Energy technology perspectives: scenarios and strategies to 2050. OECD/IEA, International Energy Agency, Paris
16. Wall G (2009) Exergetics, Bucaramanga. http://www.exergy.se/ftp/timetoturn.pdf. 1 Dec 13
17. Kilkis B (2004) An exergy aware optimization and control algorithm for sustainable buildings. Int J Green Energy 1(1): 65–77. https://doi.org/10.1081/ge-120027884

Electricity Market Structure and Forecasting Market Clearing Prices

Kürşad Derinkuyu and Mehmet Güray Güler

Abstract Electricity markets are evolving into a complex competitive business environment with an increasing role of the private sector in production, consumption, and retailing of electricity. Even transmission and distribution activities have private share in many countries. Technology is also rapidly adding new concepts such as smart grids, batteries, and prosumers (participants that are both on the production and consumption side). This study first gives a brief history on the liberalization of electricity markets, specifically concentrates on the Turkish markets. Other European markets also had similar historical developments. Secondly, we provide the market participants and their roles as well as briefly introduce the problems they need to solve. Then the paper discusses the market types such as day-ahead market, intraday market and balancing power market. Furthermore, we explain the auction mechanism to determine prices in these markets. Finally, we give an illustration for predicting the electricity prices of next days using a forecasting methodology called ARIMA. We use a real data set from Turkish market and provide a step-by-step procedure for calculating the prices using an open-source statistical software R.

Keywords Electricity markets · Day-ahead market · Market-clearing prices · Price forecasting · ARIMA

1 Introduction

Liberalization policies around the world also affected the electricity markets. Discussions on unbundling and desire to establish a new form between public and private sector first started in Chile, England, and Norway and then spread to other markets in the 1990s. Since electricity has special characteristics due to its non-storability

K. Derinkuyu
Department of Industrial Engineering, TOBB University of Economics and Technology, Ankara, Turkey
e-mail: kderinkuyu@etu.edu.tr

M. G. Güler (✉)
Department of Industrial Engineering, Yildiz Technical University, Istanbul, Turkey
e-mail: mgguler@yildiz.edu.tr

and real-time balancing requirement, the electricity markets need central authorities for regulation, physical, and financial operations. The policy makers and market participants face many interesting problems to manage this unique commodity.

From the regulation side, pricing, tariff, and incentive mechanisms are important decisions for efficiently working markets. Also, problems arising during the physical transaction of electricity are another dimension of this management problem. Long-term planning is needed for transmission line investments, whereas real-time balancing problem has to be managed both physically and financially. Both producers and consumers use portfolio optimization and forecasting techniques to secure their assets. This complex structure of the market participants causes most of the time conflicting objectives, and each participant tries to highlight its own objective.

To draw the big portray, we first focus on the alternative market designs and market participants. Then we provide information about the historical development of Turkish electricity markets. The other electricity markets also passed through similar historical developments. Then we will provide detailed information about day-ahead, intraday, and balancing power markets from the regulatory perspective. Finally, we turn our interest to a very common problem of predicting future market prices of electricity. We illustrate the problem by modeling it with a statistical method called ARIMA and employ an open-source statistical program (R) to forecast prices using this statistical model.

2   Market Designs

Power systems deal with electricity both as a service and a commodity. Under a vertically integrated monopoly design, all of the activities are provided by a single authority and this may cause inefficiency in the system. That is why power system can be divided into functionally independent parts: generation, transmission, distribution, and trading (retail and wholesale). Transmission and distribution parts deal with providing better electricity services, whereas generation, wholesale, and retail parts threat electricity as a commodity. Figure 1 shows the layers of the power system.

Boisseleau [1] explains the electricity market designs by dividing the structure into three main stages. In the first stage, the vertical unbundling degree is chosen [2]. There are four categories in vertical unbundling [3]:

- **Vertically Bundled Monopoly**: The generation, transmission, distribution, and trading activities are united and under the control of one company. This was the main model before liberalization policies.

Fig. 1 Layers of a typical power system

- **Single Buyer Model**: Single buyer is responsible for the transmission, distribution, wholesaling, and retailing activities. However, there are multiple generation companies for competition.
- **Wholesale Level Competition**: In addition to the generation companies, there are wholesale companies that could buy electricity directly from generation companies.
- **Retail Level Competition**: Final consumers are eligible to choose their electricity providers at the retail level. There is a consumption limit in Turkey to become eligible. As of 2018, 2000 kWh yearly consumption (or approximately 68 TL/month electricity bill) is required. (In most of the European countries, there is no limit.)

In most of the developed countries, vertical unbundling is on the last phase. Eligible consumers are now having chance to choose their own provider. At the end of 2017, in Turkey, over 800 generation companies, 155 wholesale companies, and 21 distribution and regulated retailer companies are active. Other European countries also have similar figures depend on their market size and age. Figure 2 shows physical and financial trade in Turkey.

After the chosen of unbundling level, the second-stage problem is how to design the wholesale markets and pricing regimes on these markets [4]. There are two main models and both of them could be available in the same region:
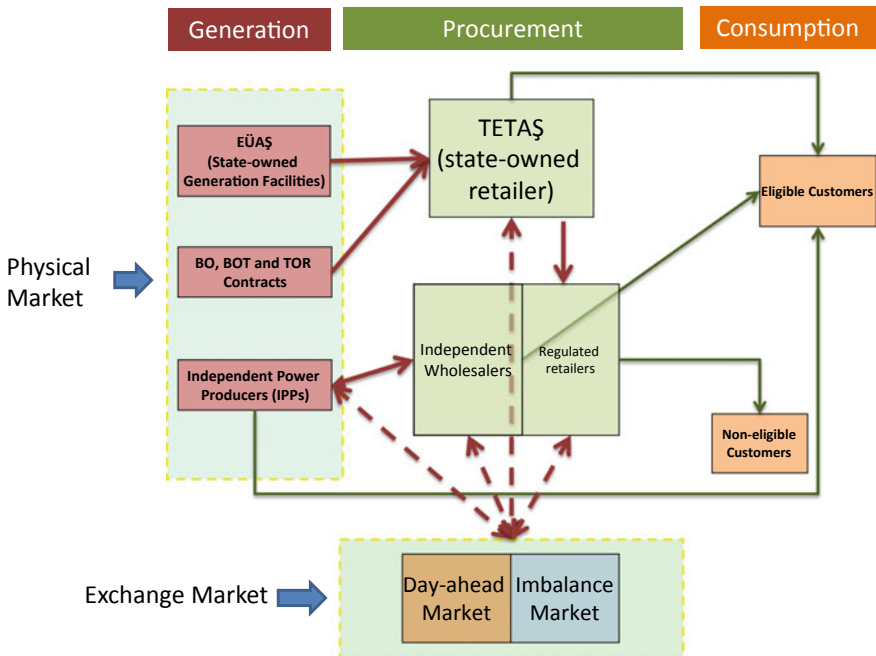
Fig. 2 Physical and financial trade in Turkey (*Source* Turkish Energy Foundation)

- **Bilateral Agreement Model**: In this model, the companies make bilateral trade agreements with each other without providing any information about the market prices. Since there is no reference price construction mechanism, this is an inefficient system for all parties. Nowadays, this system is used for the long-term contracts and the prices usually refer to the prices set in the organized markets.
- **Organized Market Model**: To be able to establish reference prices for the market participants, organized markets are preferable. These markets have two main types: Exchange and Pool Models. In pool models, usually, there is no demand-side participation and demand is predicted a priori. Electricity generating companies submit their cost functions of generating units. Unit commitment and economic dispatch problems are solved to determine prices and schedule of generating units [5]. On the other hand, exchange models both the buyers and sellers of electricity submit portfolio-based bids [6].

The third stage of the market design is about financial rules such as contract intervals, auction types, and pricing mechanisms. For long-term contracts, there are futures and options to buy and sell electricity. The experience for the different countries shows that these derivatives are functional if they are connected to the physical delivery of electricity [7]. For the short-term transactions, two spot markets are available:

- **Day-Ahead Market**: This is the major market before real-time delivery to arrange the net positions of the market participants. Electricity prices of the next day are determined with an interval of fifteen minutes, half-hourly, or hourly basis. The prices established in this market are used as reference prices to the other markets.
- **Intraday Market**: After the closure of day-ahead market, trading option is available until a few hours (1.5 h for Turkish market) before the physical delivery of the electricity. This market enables the participants to revise their positions. This kind of adjustments is necessary due to changes in the demand forecast or generation amount of renewable energy.

Although there are sophisticated forecasting techniques, they are not 100% accurate. Up to this point, all the market agreements are based on the expectations but not on real production and consumption. In real time, system operator is responsible for the stability of the power system by considering transmission line constraints and it needs additional activities. To finance these actions, there are two options available:

- **Balancing Power Market**: This is a real-time market to balance the load on the electricity network. If the predefined ancillary services are not enough to secure supply–demand balance under transmission constraints, system operator could give additional orders to market participants. The cost of these extra orders is reflected the ones that cause imbalance on the system.
- **Ancillary Services**: There are also additional services for system protection. Reactive power control can be used for voltage drops. Frequency (primary and secondary) control is an automatic system that insures the grid frequency stays within a specific range. Operating reserve and demand management are other methods

to provide sufficient energy generation or decrease consumption on energy-scarce days.

Figure 3 shows wholesale markets in Turkey. Similar markets are available in most of the developed countries.

Another decision on the market design is auction types. These auctions could be one-sided or two-sided auctions. Under the one-sided auction mechanism, demand is estimated and only the supplier side gives price bids. This mechanism is usually preferred in pool models. Two-sided auctions accept bids from both demand and supply sides and preferred in exchange models.

Lastly, market price construction is an important step for wholesale markets. There are two main mechanisms used in the markets:

- **Pay-As-Bid Pricing Model**: In this model, all the accepted bids are receiving the price they ask for. Although it looks reasonable, some studies claim that the model causes price inflation due to asymmetric information between market participants [4].
- **Market-Clearing Price Model**: All the market participants are getting the same price which corresponds to intersection of supply and demand curves.

In addition to these market choices, transparency and market monitoring activities should also be well established to be able to construct well-functioning markets.
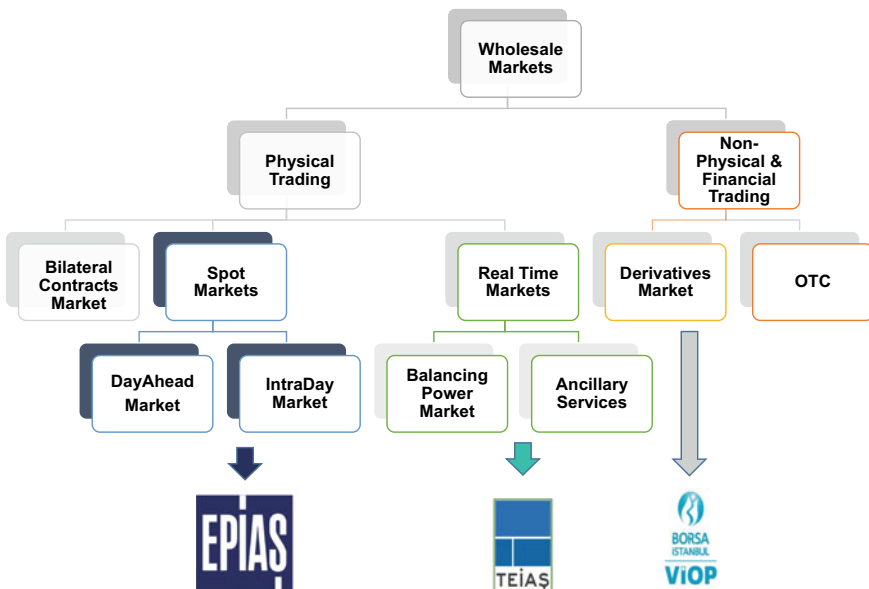
Fig. 3 Wholesale markets in Turkey (*Source* Energy Exchange Istanbul)

3   Development of Electricity Markets in Turkey

Electricity generation was started with the help of foreign investments during the early years. Each province, such as Istanbul, Izmir, Ankara, and Antakya, built their own generation plants. The first one was built in Istanbul in 1913. In the 1930s, nationalization policies were applied all over the country and Ministry of Energy and Natural Resources was established in 1963. The historical cornerstones of Turkish electricity market could be seen as follows:

- 1913: First electricity generation plant in Istanbul.
- 1963: Establishment of Ministry of Energy and Natural Resources.
- 1970: Turkish Electricity Authority (TEK) was formed as a vertically integrated monopoly and controlled generation, transmission, distribution, and trade.
- 1984: Law No. 3096 gave permission to the private sector to invest in the electricity sector.
- 1994: Built–operate–transfer (BOT) implementations were begun.
- 1994: TEK was divided into two companies: TEAS responsible for generation, transmission, and trade and TEDAS responsible for distribution.
- 1997: Law No. 4283 is allowing build–operate (BO) implementations.
- 2001: Electricity Market Law No. 4628 changed the whole system dramatically. Eligible consumers, market operator, and system operator definitions were introduced.
- 2001: Energy Markets Regulatory Authority was established.
- 2001: TEAS was divided into three companies. TEIAS responsible for transmission, EUAS responsible for generation, and TETAS is responsible for trade.
- 2006: Balancing and settlement applications have been started. Imbalances based on marginal prices were settled for a monthly and three-time period.
- 2009: Day-ahead planning was introduced. Balancing and settlement activities are done on hourly basis.
- 2011: Day-ahead market has been launched (December 1st). Demand side could give their own bids. Collateral mechanism became operational.
- 2011: Feed-in tariff mechanism and different incentive prices for different renewable energy technologies were introduced.
- 2013: Electricity Market Law No. 6446 defined the independent market operator.
- 2015: Independent market operator, Energy Exchange Istanbul (EXIST) has been established.
- 2015: Intraday market has been launched (July 1st).
- 2016: Transparency platform was opened for public usage.
- 2016: Built-in open code day-ahead market software was started to operate (June 1st). Social welfare as an objective function and paradoxically accepted bids were defined.

The restructuring of the Turkish electricity market has started in 2003 and gone through four main stages [8]:

Premarket Age (March 2003–August 2006): Organized market was not established yet. TEIAS operates the grid by giving orders to state-owned generation company EUAS.

Triple Pricing Age (August 2006–December 2009): A day was divided into three intervals: daytime, night, and peak hours. Since there are no well-defined reference prices, the participants heavily used the balancing market.

Day-Ahead Planning (December 2009–December 2011): Hourly price regime was introduced for only supply-side bids.

Day-Ahead Market (December 2011–now): Both the supply and demand sides are allowed to place bids for the determination of the day-ahead prices.

As of January 2018, there are 817 generation companies, 154 wholesale companies, 21 distribution companies, and additional 21 retail companies for last resort. There are five layers in the electricity system and their current position is as follows:

- **Generation**: There is a 20% market limitation on generation and the state-owned EUAS is controlling around 15% of the total installed power.
- **Transmission**: TEIAS is transmission system operator and natural monopoly. It also operates balancing market and ancillary services. System operator is the part of TEİAS and called National Load Dispatch Center.
- **Wholesale**: TETAS is state-owned wholesale company and making take-or-pay contracts with BO/BOT/TOR plants. It also manages the purchase guarantees with domestic coal plants and nuclear plants. It mostly sells those energies to 21 retail companies used for last resort. There is again 20% market limitation in this sector.
- **Distribution**: TEDAS is divided into 21 non-overlapped regions. All of these regional distribution companies are privatized.
- **Retail**: As of 2018, eligible consumer limit is 2000 kWh per year and around 5 million consumers are eligible. Those consumers could get their electricity from any wholesale company. The limit is expected to drop zero within two years.

At the end of 2017, Turkey has 85,200 MW installed power which includes 26,637 MW natural gas power plants, 19,776 MW hydropower plants with big reservoir, 8794 MW imported coal and 9773 MW lignite-based power plants. On the renewable side, 7497 MW river and other hydropower plants, 6516 MW wind, 3421 MW solar, and 2636 MW other (such as biomass and geothermal) power plants are installed.

4 Day-Ahead Market

Market operators in US and European electricity markets determine the reference electricity prices for next day by organizing blind auctions either using pool or exchange methodology. Social welfare maximization is used as an objective function. This function represents the additional benefit of each participant if the corresponding order is accepted. Pool model solves the unit commitment and economic dispatch

problems to determine prices. Additional payment is allowed above the market price if the solution with this additional payment improves social welfare. Lagrangean relaxation is heavily used to solve this type of problems [9–11]. In European exchange models, participation is optional and demand side is flexible. Market participants give their orders by using a portfolio-based approach. No side payment (except Turkish market) is allowed [6, 12].

For the congestion management of transmission lines, there are implicit or explicit auctions are used. Under explicit auction mechanism, capacity and energy traded separately, through regular capacity auctions such as for the lines between Turkey and Bulgaria. In the implicit auction, capacity and energy effectively traded together as in Norway and Italy. For the implicit auction, either volume coupling or price coupling rule is used. Volume coupling first determines interconnector flows using a single algorithm and then separate algorithms are used for the prices of each region. European Market Coupling Company has used this methodology to couple Nordic and Central Western European markets until 2014. Under the price coupling, single algorithm simultaneously determines volumes, interconnector flows, and prices in all of the regions. Price Coupling of Regions (PCR) developed the algorithm, named EUPHEMIA, to apply this methodology in most of the European countries.

In Turkey, Energy Exchange Istanbul is responsible for day-ahead market auctions. Settlement and collateral mechanisms are also managed by the exchange. Table 1 shows the daily operations in Turkish day-ahead market.

There are several order types available in the exchanges. Three major order types are single orders, block orders, and flexible orders.

- **Single orders** are effective only one period (which could be 15 min, half an hour, or hour). Either a stepwise or piecewise linear function is used to represent relationship between volume and price. Accepted volume corresponds to the market-clearing price on the given order function.
- **Block orders** are either accepted or rejected fully. They are usually given for consecutive time periods. Volume and price are constant during these time periods. If volume is changeable, then it is called profile block.

Table 1 Daily operations in Turkish day-ahead market (*Source* Energy Exchange Istanbul)

Time slot	Operation
00:00–16:00	Bilateral agreements for the next day are entered into the system by market participants
00:00–12:30	DAM participants submit their bids for the upcoming day
12:30–13:00	Collateral payments are checked and bids are validated. If there is an unusual bid submission, the market operator has the right to call the participant for confirmation
13:00–13:10	MCPs are determined by the optimization tool
13:10–13:30	Results are published and objections to the bid matchings are received
13:30–14:00	Objections are evaluated and resolved
14:00	Finalized MCPs are publicly announced
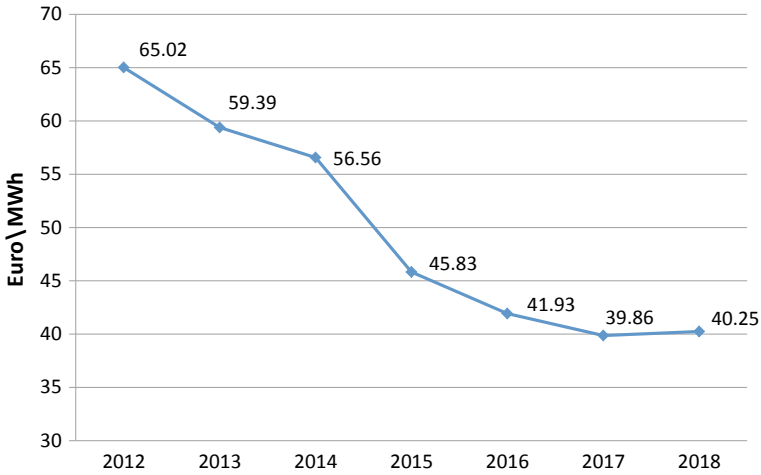
Fig. 4 Average market-clearing prices in Turkey (€/MWh)

- **Flexible orders** do not have any period information. As long as price is in the acceptable range, the algorithm places this order on any period.

There are also other order types that are active in Spain and Italy. These special order types focus on ramp-up/down limitations and price equality in all regions.

In recent years, market-clearing prices in all over the world are decreasing due to renewable energy and incentive policies on this energy. Since there is no fuel cost, marginal production cost is near zero on these energy types. This causes a problem on classical power units such as coal or natural gas. Figure 4 shows the average market-clearing prices in Turkey between 2012 and 2016.

5 Intraday Market

Intraday market is another opportunity for market participants before real-time delivery. After the closure of day-ahead market, there is up to 36 h available before delivery and in the meantime, some factors could change. After all, all the order decisions are based on forecasting of production and consumption. If the weather temperature is higher or lower than expectation, this could change the consumption behavior. Also, we cannot be sure about exact production level of renewable energy.

In Turkey, intraday market opens at 18.00 for the following day based on continuous market principle and the transactions can be done 1 h and 30 min prior to the physical delivery. This time is even shorter in some European exchanges. There are two different types of orders: Hourly and Block orders.

- **Hourly orders** can be matched partially. There are four types of hourly orders: Active order, Hourly Order with Expiration Time, Immediate or Cancel (IoC), Fill or Kill (FoK).

  – Active Order: Default order type and waits in the list to be matched. If it is matched partially, remaining part continues to wait.
  – Hourly Order with Expiration Time: Order is available only for a given time period.
  – Immediate or Cancel (IoC): It does not wait in the list. It matches with all the appropriate orders in the list and remaining part will be cancelled.
  – Fill or Kill (FoK): It does not wait in the list. This order should be either match fully or cancelled out immediately.

- **Block orders** are not divisible and they are placed for a minimum of one and a maximum of 24 h. They will be matched if there is exactly equal opposite side block available. There are two types of block orders: Active Order or Block Order with Expiration Time.

  – Active Order: Default order type, and waits in the list to be matched. It should be matched fully.
  – Hourly Order with Expiration Time: Order is available only for a given time period.

Matching orders quickly is the main focus of the intraday market, especially, for the multiple regions. Cross-Border Intraday Market Project (XBID) is working on this problem.

6 Balancing Power Market and Ancillary Services

Transmission system operator is responsible for the real-time balance of the electricity grid. System operator manages balancing power market and ancillary services to insure sufficient supply and good quality of electricity energy to consumers with low cost in a continuous manner. Real-time balancing activities are necessary for the system security and system operator performs these activities by minimizing the balancing cost. There are several control mechanisms available such as primary frequency control, secondary frequency control, and tertiary control reserve capacities. In addition, demand control is also popular in recent years. Because of the characteristics of electricity energy, system operator also arranges reactive power services.

System operator evaluates the eligibility of generators to be able to use them in balancing activities. Eligible generators should have some specific properties such as size and speed of adjustment for frequency changes on the grid. The part of the operational reserve used as primary frequency control capacity to stabilize the system frequency through automatic increase or decrease of unit active power output. The plants should have at least 50 MW installed power and react within 30 s. Secondary

frequency control capacity is chosen to release the primary control reserve. This will bring the frequency back to its nominal value. Unlike the mandatory rules for primary frequency reserve capacities, the market participants are free to serve as secondary frequency reserve capacities.

Tertiary control reserve capacity is manually chosen after the secondary frequency control reserve was put into the service. These balancing entities should react within 15 min to release the secondary frequency control reserve in case of another frequency deviation risk.

On the balancing power market, system marginal prices are equal to the maximum accepted hourly offer price for the energy deficit and the minimum accepted bid price applied for the energy surplus in the system. All of these balancing activities are causing imbalance cost and this cost is applied to the market participants that deviate from their balance responsibilities. Since extra production is sold cheaper and extra consumption is bought higher prices in balancing power market than day-ahead market, the market participants try to the balance their portfolio as accurate as possible before the real time.

7 Electricity Price Prediction

Predicting electricity prices in a liberated market as significant added values for all of the players in the market. An electricity producer can decide to produce itself or buy from a subcontractor to supply the electricity that it committed to. Similarly, a consumer can choose to make a bilateral contract or purchase from a pool. A factory, for example, can move its production to cheaper hours [13]. Such decisions depend on the price levels; therefore, there is an increasing importance attached to predicting them in advance [14]. Although it is traded in market places like commodities, it has a special structure: it is not storable and must be consumed instantly. The average fluctuation in treasury bonds is below 0.5%, about 1.5% in stocks and less than 4% in commodities like petroleum or natural gas, it can be up to 50% in market-clearing prices [15]. Therefore, it is not an easy task.

Horizon for electricity price forecasting can be divided into three ranges: short, medium, and long-term. Short-term generally involves forecasts from a few minutes up to a few days ahead and is of prime importance in day-to-day market operations [16]. A wide range of analysis can be found in the literature. Different categories proposed by several researchers; however, a recent review by Weron states that the prediction efforts can be grouped under five categories: Multi-agent, Fundamental, Reduced form, Statistical, and Computer Intelligence [16]. In this chapter, we focus on one of the statistical methods: ARIMA models. ARIMA models are widely used in time series analysis and provide successful results in forecasting future electricity prices [17–21]. In the subsequent parts, we give a definition and structural properties of ARIMA models. Then we illustrate the usage of them through a real-life example.

7.1 ARIMA Models

A time series is a collection of observations of some economic or physical phenomenon drawn at discrete points in time. Sampling from adjacent points usually restricts the usage of conventional statistical methods which mainly assumes that the observations are independent and identically distributed. Time series analysis tackles this issue and infers information from the past data to forecast future values of the series [22, p. 2]. The ARIMA models (also known as the Box–Jenkins models) exploit the autocorrelation structure in the data and are one of the widely used models for analysis time series. ARIMA is an acronym for autoregressive integrated moving average and depends on three different concepts which we will analyze in the sequel.

Autoregressive Models: In this model, the current value of the process is expressed as a finite, linear aggregate of previous values of the process and a random shock [22, p. 78, 23]. Let y_t denote the value of a process observed at time t and let $t, t-1, t-2, \ldots, t-p$ be equally spaced time intervals. Then:

$$y_t = \phi_0 + \phi_1 y_{t-1} + \phi_2 y_{t-2} + \cdots + \phi_p y_{t-p} + \epsilon_t \tag{1}$$

is an autoregressive (AR) process of order p and denoted by AR(p). Here, ϕ_i are the coefficients of observations y_i, a is a constant, and ϵ_i is a random shock and it is normally distributed with mean zero ($E[\epsilon_i] = 0$) and variance σ^2 ($\text{Var}(\epsilon_i) = \sigma^2$). It is also called a *white noise*. The name *auto-regressive* stems from the celebrated linear regression model where a dependent variable, say y, is explained with a linear combination of independent group of variables, say $x_1, x_2, \ldots, x_p$, through a linear model that can be written as follows:

$$y = \beta_0 + \beta_1 x_1 + \beta_2 x_2 + \cdots + \beta_n x_n + \epsilon$$

Here, the variable y is said to be regressed over the variables $x_1, x_2, \ldots x_n$. In (1), the variable y_t is regressed over its own past p-values; hence, the model is an *auto*regressive model. The parameters ϕ_i can be estimated from the data and their derivation is beyond the scope of this text. We would rather focus on the application of these models on real data sets.

Moving Average: In a moving average model, an observation at time t can be written as a linear combination of the previous error terms as follows:

$$y_t = \theta_0 + \theta_1 \epsilon_{t-1} + \theta_2 \epsilon_{t-2} + \cdots + \theta_p \epsilon_{t-q} + \epsilon_t \tag{2}$$

The equation in (2) is called a moving average of order q and denoted by MA(q). By substituting the values of $y_{t-1}, y_{t-2}, \ldots$, one can show that the AR(1) process can be written as:

$$y_t = \phi_0 \sum_{i=0}^{\infty} \phi_i^i + a_1 \epsilon_1 + a_2 \epsilon_2 + \cdots + \epsilon_t \tag{3}$$

which is a MA(∞) process. Hence, the AR models and MA models are related.

ARIMA Models: Any model that contains both AR and MA terms is called an autoregressive moving average (ARMA) model. An ARMA(p, q) model contains p autoregressive terms and q moving average terms and can be written as:

$$y_t = c + \phi_0 + \phi_1 y_{t-1} + \cdots + \phi_p y_{t-p} + \theta_1 \epsilon_{t-1} + \cdots + \theta_p \epsilon_{t-q} + \epsilon_t \quad (4)$$

An ARMA model needs the assumption that the times series should be (weakly) stationary. A stationary time series has two properties [22, p. 28]. Their mean does not depend on time and the autocovariance between any two observations y_t and y_{t+d} depends only on d, but not t. Covariance of two random variables, say x and y, shows the extent to which the variables behave similarly. Autocovariance is the covariance of the same variable with itself at different time points. Time series with trends, or with seasonality, is not stationary—the trend and seasonality will affect the value of the time series at different times [24]. Please note that stationarity does not imply independence, i.e., data can be dependent but still stationary. However, many real-life problems are nonstationary: they either have trends or seasonality. There is a very simple way to circumvent the problem of nonstationary data. Let y_t be a times series with a linear trend and define d_t as follows:

$$d_t = y_t - y_{t-1} \quad (5)$$

The new process d_t is a stationary process whenever y_t has a linear trend. Hence, taking the *difference* between two consecutive data points in a time series with linear trend transforms the series into a stationary process. Similarly, taking the second difference (i.e., the difference of the differences) will transform a times series with a quadratic trend into a stationary process. Taking the difference is the discrete analog of a derivative. Hence, converting the process d_t to the original process is called integration. An ARMA model used for a differenced time series data is called an ARIMA(p, d, q) (autoregressive *integrated* moving average) model. Here, d shows the level of differencing. For example, an ARIMA(1, 1, 1) model can be written as:

$$d_t = c + \phi_1 d_{t-1} + \theta \epsilon_{t-1} + \epsilon_t \quad (6)$$

Here, d_t is the transformed variable by taking the difference as defined in (5). The notation of ARIMA models is generally enhanced with the backshift operator B. It represents differencing, i.e., $BD_t = D_{t-1}$. For example, the model in (6) can be rewritten using B as follows:

$$(1 - B)(1 + a_1 B)y_t = c + (1 - b_1 B)\epsilon_1$$

Writing the model in (6) to explicitly find y_t in terms of the other values results in the following:

$$y_t = c + (1 + \phi_1)y_{t-1} - \phi_{t-2} + \epsilon_t - b_1 \epsilon_{t-1} \quad (7)$$

In order to forecast the value of y_t, the parameters c, ϕ_1 and b_1 must be estimated. The estimation procedure employs maximum likelihood estimation or least squares methods and we would not give the details in this chapter. We refer the readers to the celebrated book of G. E. P. Box and G. M. Jenkins for the estimation algorithms [23].

ARIMA models can also handle seasonality. A seasonal ARIMA model is denoted by ARIMA$(p, d, q)(P, D, Q)_m$ where m is the number of observations per season and P, D, and Q are the seasonal counterparts of an ARIMA model, i.e., the AR order, the differencing order, and the MA order, respectively.

Forecasting the future process can be performed through the following steps:

1. **Specify the model**: An ARIMA model is specified by three parameters: p, d, and q. First step is to identify these parameters, i.e., to determine stationarity of the data, order of AR, order of MA. If there is a trend in the data, one should take a difference and check the stationarity. A second difference (difference of the difference) can be taken if the stationarity is not satisfied. Although visual inspection provides valuable insights, autocorrelation plots like autocorrelation function (ACF) or partial autocorrelation function (PACF) are basic instruments necessary to identify ARIMA models in stationary series. Plotting the ACF of the data will give the MA order. If the ACF vanished after some lag, that number is the order of MA. Partial autocorrelation (PACF), on the other hand, gives the AR order. Similar to ACF, if the PACF vanishes after some lags, the AR order is that number. The seasonal part of AR or MA model can be observed in the seasonal lags of the PACF and ACF. For example, an ARIMA$(0, 0, 0)(0, 0, 1)_{12}$ model will show a spike only at lag 12 in the ACF and an exponential decay in the seasonal lags of PACF. An ARIMA$(0, 0, 0)(1, 0, 0)_{12}$ will have a single spike at lag 12 in the PACF but an exponential decay in the seasonal lags of the ACF [24].

2. **Estimating the coefficients**: Once the model is chosen, the next step is to estimate the parameters. Most of the computer packages use either maximum likelihood estimators or least square estimation. There can be several alternative models. The models can be chosen with respect to their Akaike information criterion (AIC) or Bayesian information criterion (BIC) scores. Both depend on the likelihood value and provide a unique performance indicator to choose a model.

3. **Verify the model**: The ARIMA models are built using several assumptions like the normality of residuals. These assumptions should be checked to verify the validity of the assumptions.

4. **Calculate Forecasts and Quality of Prediction**: The future values can be calculated once the model is verified. There are several ways to calculate the quality of prediction. Let e_t denote the error of forecast at time t. The error is defined as the difference between the real value and the forecasted value. The mean absolute percentage error (MAPE), the mean absolute error (MAE), and root mean square error (RMSE) are given as

$$\text{MAPE} = \frac{1}{n} \frac{\sum |e_t|}{y_t} \quad \text{MAE} = \frac{1}{n} \sum |e_t| \quad \text{RMSE} = \left(\frac{1}{n} \sum e_t^2 \right)^{\frac{1}{2}}$$

There are several computer programs or languages (MATLAB, Python, R, etc.) and several libraries which can aid a decision maker to perform the steps above. In the following section, we will illustrate how to use such a program to make forecasts for future prices. In particular, we will use R language which is used as open-source statistical software that has many libraries developed by practitioners and academicians. We will provide a real-life example using R.

7.2 An Illustration from Turkish Electricity Market

In this section, we will model hourly prices of Turkish market using an ARIMA model and forecast the future values using this model. We obtained hourly prices of four weeks from 05.11.2018 to 02.12.2018 from website of EPİAŞ. The plot of MCP is given in Fig. 5.

We will use R-Studio (Version 1.1.383) to perform our analysis. It can be downloaded from www.rstudio.com. We will use `forecast` package to fit an ARIMA model for the prices given in Fig. 5 and then forecast MCPs of next day. Any R package can be installed from *Tools* ➜ *Install Packages* menu. The following code will read the data from the text file and write it as a time series with frequency 24 to a variable called `dataMCP`:
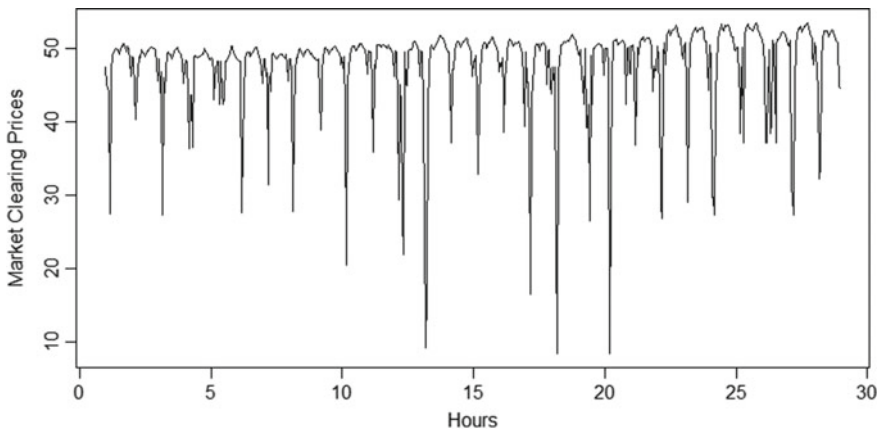
Fig. 5 Hourly market-clearing prices

```
> dataMCP = read.table(file = "MCPData.txt",header =
FALSE)
> dataMCP = ts(dataMCP$V1,start = c(1,1),frequency = 24)
```

The MCP data has some extreme values and general application procedure is to remove the extreme values [25] and replace them with the boundaries. The extreme values can be defined as the values that are away from the mean by at least three standard deviations. To give an intuition, less than 0.3% of a normal random variable is three standard deviations or more away from the mean. Hence, this conversion does not affect more than 99.7% of the data. The following code assigns the boundary values to the extremes:

```
> UpperBoundary = mean(dataMCP) + 3*var(dataMCP)^0.5
> LowerBoundary = mean(dataMCP) – 3*var(dataMCP)^0.5
> dataMCPTruncated = dataMCP
> dataMCPTruncated[dataMCP<LowerBoundary]          =
LowerBoundary
> dataMCPTruncated[dataMCP>UpperBoundary]          =
UpperBoundary
```

Finding the best ARIMA parameters is a tedious task. One should make differencing if necessary and then check the PACF and ACF values. Figure 5 shows that there is no obvious trend in the data; hence, differencing is not needed. The PACF values in Fig. 6 show that the MCP values are affected by the previous hour and the prices of the same hour of the previous day, the day before, and two days before, as one might expect due to the seasonality. The ACF values in Fig. 7 show that the prices are correlated with the previous price but there is an exponential decay which shows that the model is not a pure AR or not a MA model, but a mixture of both. Hence, one should try several different ARIMA models to find the optimal representation.

The forecast package has a function called auto.arima that handles the model identification in a systematic manner. It takes differences to maintain stationarity if necessary and fits different AR and MA orders to the model. Then it picks the model with the greatest AIC score. It also reports estimated values of all parameters.

8   Results and Discussion

The following code calls the forecast package which has auto.arima function in it and then invokes auto.arima function and prints out the results.
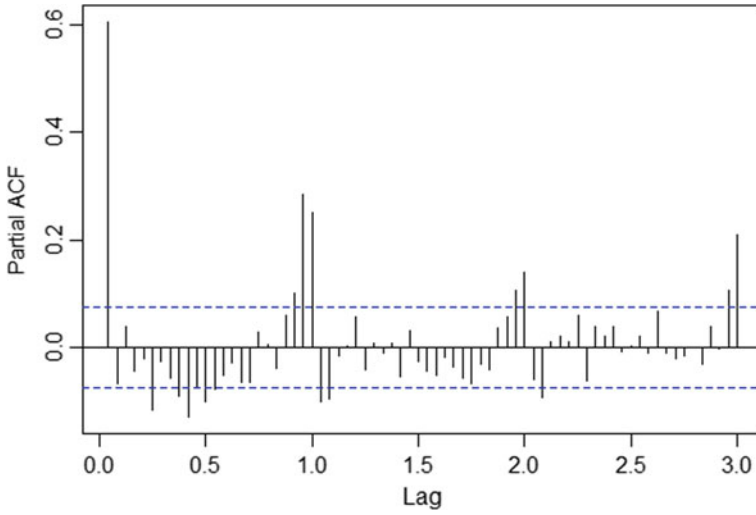
Fig. 6 Market-clearing prices—PACF
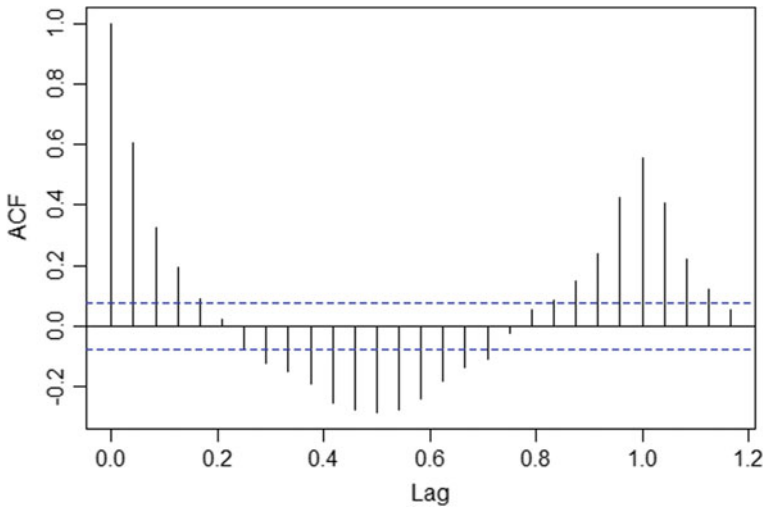
Fig. 7 Market-clearing prices—ACF

```
> require(forecast)
> ARIMAfit = auto.arima(MCPData, approximation=FALSE,
trace=FALSE)
> summary(ARIMAfit)
```

The code runs for a few minutes and the output is given in Table 2. It turns out that the model has AR(1) and MA(1) components with values 0.6451 and -0.2739. The seasonal part, on the other hand, has an integration of order 1 and AR of order 2 with values -0.7063 and -0.3811. The value of error measures (like MAE, MAPE, etc.) is also reported in the output.

The `auto.arima()` function handles the model selection part; however, the assumption of the ARIMA modeling should also be checked. The following code makes a normality test on the residuals and plots the histogram of the residuals.

```
> checkresiduals(ARIMAfit)
    Ljung-Box test
data: Residuals from ARIMA(1, 0, 1)(2, 1, 0)[24]
Q* = 77.038, df = 44, p-value = 0.001515
Model df: 4.  Total lags used: 48
```

The Ljung–Box test is a statistical hypothesis test which tests the normality of the error terms. The null hypothesis is "the error terms are normal." It turns out that the p-value is too small and hence, the normality assumption is violated. However, this violation does not hinder the forecast values but the confidence interval estimation should be reported carefully since the calculation of the confidence intervals depends on the normality assumption of the errors.

The final step is to predict future prices. The following code first reads the real values of the next week from a text file and then converts variable to a time series which starts at week 29 (recall that we have used four-weeks data to fit an ARIMA

Table 2 Auto.arima output

```
Series: MCPData
ARIMA(1,0,1)(2,1,0)[24]

Coefficients:
        ar1      ma1     sar1     sar2
      0.6451  -0.2739  -0.7063  -0.3811
s.e.  0.0683   0.0865   0.0373   0.0378

sigma^2 estimated as 9.761:  log likelihood=-1663.17
AIC=3336.34   AICc=3336.43   BIC=3358.71

Training set error measures:
              ME     RMSE    MAE    MPE      MAPE    MASE      ACF1
Training set 0.04219 3.0584 1.669 -0.36145 3.95689 0.768796 0.0040845
```

model) and then generates `n.ahead` many forecasts using an ARIMA model fitted above.

```
> realvalues = read.table(file = "realvalues.txt",header = FALSE)
> realvalues = ts(realvalues$V1,start = c(29, 1),frequency = 24)
> pred = predict(ARIMAfit.2, n.ahead = 24*3)
```

In Fig. 8, we plot the real prices of one month, i.e., the prices between 05.11.2018 and 04.12.2018. The days to be forecasted (02.12.2018–04.12.2018) are plotted with red.

In Fig. 9, we plot the data after day 25 and then add the predicted values with blue and the real values with red. We do not plot the first 24 days to enhance the readability of the plot. Figure 9 is generated using the following code:

```
> plot(MCPData,type='l',xlim=c(25, 31),ylim=c(25, 55), xlab = 'Days',ylab
= 'Market Clearing Prices')
> lines((pred$pred),col='blue')
> lines((realvalues),col='red')
```

It turns out that forecasts of first two days almost coincide the real values; however, there is a downward trend starting at the third day. The MAPE value for three days is 6.5% which shows that for the next 72 h, the average absolute percentage error is fairly small.
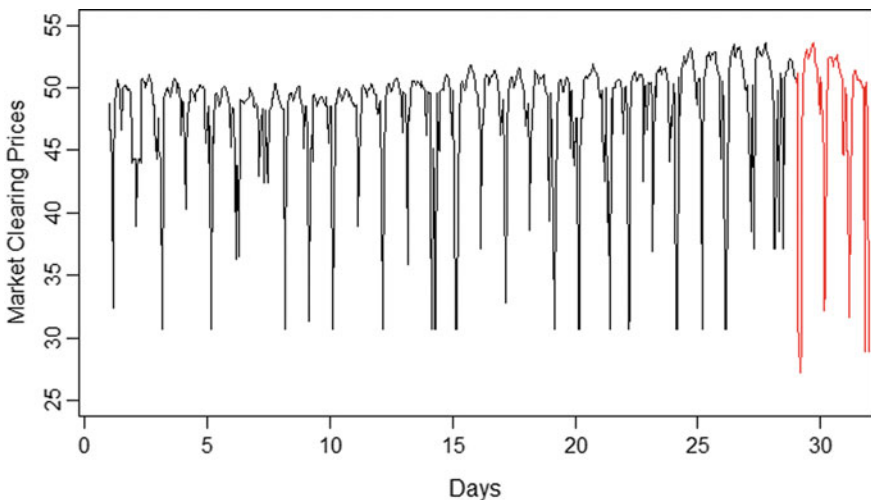
Fig. 8 The MCP data between 05.11.2018 and 09.12.2018
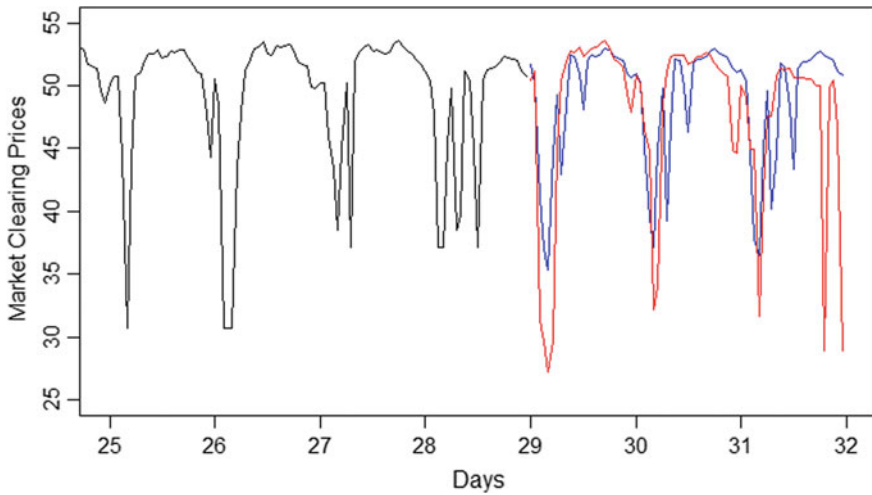
Fig. 9 Forecasted and real values for the next week

9 Conclusion

Market clearing prices are publicly available. A producer or a consumer can optimize their revenues with good next-day price forecasts. There are several forecasting methods proposed in the literature and ARIMA models are one of the statistical forecasting tools that have been used to forecast market-clearing prices. Although estimating their parameters and finding the right model turns out to be a bit tedious, it can be easily applied with the emerging open-source statistical tools like R. Its power is due to its large community which supports R with many different packages. Moreover, several packages of R are developed by people who have academic background. These built-in packages make R very easy to use for complicated tasks even for inexperienced users. In this work, we used a package called forecast in R to develop an ARIMA model in order to forecast future market-clearing prices in Turkish electricity market. The auto.arima() function in the package automates many tasks and provides an easy forecasting process. The same tool can be used for similar prediction problems.

References

1. Boisseleau F (2004) The role of power exchanges for the creation of a single European electricity market: market design and market regulation
2. Kütaruk K (2013) Day ahead markets. Master thesis, Middle East Technical University, School of Natural and Applied Sciences
3. Hunt S (2002) Making competition work in electricity, vol 146. Wiley

4. Maria NS (2010) Day-ahead electricity market: proposals to adapt complex conditions in OMEL. Master thesis, Universidad Pontificia Comillas, Madrid, Spain
5. Van Vyve M (2011) Linear prices for non-convex electricity markets: models and algorithms. In: CORE Discussion Paper 2011/50
6. Derinkuyu K (2015) On the determination of European day ahead electricity prices: the Turkish case. Eur J Oper Res 244(3):980–989
7. Korkulu Z (2008) Serbestleştirilmiş Elektrik Piyasalarında Türev Araçların Kullanılması, Vadeli İşlem ve Opsiyon Piyasaları. Proficieny thesis, EMRA
8. Derinkuyu K, Tanrisever F, Baytugan F, Sezgin M (2015) Combinatorial auctions in Turkish day ahead electricity market. In: Industrial engineering applications in emerging countries, p 51
9. Araoz V, Jörnsten K (2011) Semi-Lagrangean approach for price discovery in markets with non-convexities. Eur J Oper Res 214(2):411–417
10. Li T, Shahidehpour M (2005) Price-based unit commitment: a case of Lagrangian relaxation versus mixed integer programming. IEEE Trans Power Syst 20(4):2015–2025
11. Phan DT (2012) Lagrangian duality and branch-and-bound algorithms for optimal power flow. Oper Res 60(2):275–285
12. Martin A, Müller JC, Pokutta S (2014) Strict linear prices in non-convex European day-ahead electricity markets. Optim Meth Softw 29(1):189–221
13. Emir T, Güler MG (2018) Production planning using day-ahead prices in a cement plant. In: Exergetic, energetic and environmental dimensions. Elsevier, pp 149–166
14. Kölmek F (2016) Türkiye Elekrik Piyasasında Fiyat Oluşumunun Analizi ve Fiyat Tahmin Modelleri. Doktora Tezi, Hacettepe Üniversitesi, Ankara
15. Weron R (2006) Modeling and forecasting electricity loads and prices: a statistical approach. Wiley, p 403
16. Weron R (2014) Electricity price forecasting: a review of the state-of-the-art with a look into the future. Int J Forecast 30(4):1030–1081
17. Contreras J, Espinola R, Nogales FJ, Conejo AJ (2003) ARIMA models to predict next-day electricity prices. IEEE Trans Power Syst 18(3):1014–1020
18. Cuaresma JC, Hlouskova J, Kossmeier S, Obersteiner M (2004) Forecasting electricity spot-prices using linear univariate time-series models. Appl Energy 77(1):87–106
19. Lagarto J, de Sousa J, Martins A, Ferrao P (2012) Price forecasting in the day-ahead Iberian electricity market using a conjectural variations ARIMA model. In: 2012 9th International Conference on the European Energy Market, pp 1–7
20. Shafie-Khah M, Moghaddam MP, Sheikh-El-Eslami MK (2011) Price forecasting of day-ahead electricity markets using a hybrid forecast method. Energy Convers Manage 52(5):2165–2169
21. Weron R, Misiorek A (2005) Forecasting spot electricity prices with time series models. In: Proceedings of the European electricity market EEM-05 conference, pp 133–141
22. Shumway RH, Stoffer DS (2017) Time series analysis and its applications: with R examples. Springer
23. Box GE, Jenkins GM, Reinsel GC, Ljung GM (2015) Time series analysis: forecasting and control. Wiley
24. Hyndman RJ, Athanasopoulos G (2018) Forecasting: principles and practice. OTexts
25. Weron R, Misiorek A (2008) Forecasting spot electricity prices: a comparison of parametric and semiparametric time series models. Int J Forecast 24(4):744–763

Energy, Environment and Education

Yunus Emre Yuksel

Abstract Renewable energy sources have more advantages than fossil fuels to generate power, especially to save environment. However, like every new emerging technology, they need to be publicized in a suitable way. Education plays a crucial role to increase awareness on energy and environment and develop positive attitudes toward renewable energy sources and environment. In this study, elementary science course books from fifth to eighth grade have been analyzed in terms of sufficiency for energy and environment education. Also, a survey has been conducted to a total of 191 pre-service teachers of which 62.3% was from elementary science department and 37.7% from primary education department. Analysis results show that mean values obtained from renewable energy sources attitude scale of pre-service teachers from both departments are above average. There is a statistically significant difference in favor of elementary science education pre-service teachers in the results of independent *t* test.

Keywords Energy · Fossil fuel · Renewable energy · Environment · Education

1 Introduction

As daily life standards improve, consumption of fuels, materials and croplands increase as well. In order to meet the daily life needs, people demand more and more energy each passing day. There are many disadvantages of increasing energy consumption such as degradation of energy sources, air pollution because of hazardous emissions, acid rains, global warming, etc. The earth is waiting patiently and tries to fix those environmental problems with its own effort; however, unless any precaution is taken, earth will be insufficient to save itself and also creatures on it. The main problem is that many people think that energy and environment problems are virtual things and those problems are far from us. Even in universities, some students are not aware of those complications. Therefore, energy and environmental

Y. E. Yuksel (✉)
Mathematics and Science Education Department, Education Faculty, Afyon Kocatepe University, Afyonkarahisar, Turkey
e-mail: yeyuksel@aku.edu.tr

education should be a compulsory part of the current curricula of education systems in each education level from primary school to university.

After the first oil crisis in mid-1970s, countries tried to take some precautions because oil is not infinite, and it has some disadvantages. Progress to transition to renewable energy systems (RES) such as wind, solar and biomass has speeded up due to advantages of RES [1–5]. However, this transition was not enough when compared to hydropower systems. Still hydropower systems have the biggest share among renewables [6, 7].

There are many new technological developments and methods in renewable energy area, and those novel technologies can be integrated with current energy infrastructure by means of competent and well-trained people [8, 9]. According to Jennings [10], the price of renewables will be decreased due to increasing investments in them, and fossil fuel prices will go up. Also, Jennings addressed that lack of education about RES of demanding people or professional suppliers causes bad reputation about RES. In another study, Gelegenis and Harris [11] have compared Greek and British courses in terms of energy education. According to this study, many energy engineering courses given in UK are accredited by national professional institutes and organizations. The main goal of energy engineering courses is to provide knowledge of fossil fuel and renewable energy sources and sustainable use of energy sources. Acikgoz [12] has outlined the current status of renewable energy education in Turkey. In that study, he or she has also claimed that energy education consisting renewable energy education should address entire population as audience. Generally, the objectives of energy education are making students aware of nature and the reasons of energy crisis, making them aware of renewable and nonrenewable energy sources, potential sources of energy and current technologies of energy generation systems.

When it comes to the appropriate level for energy education, Kandpal and Broman [8] have mentioned that basic principles of energy conversion may be introduced in primary school and also operation of simple energy devices may be explained in the secondary school level. Table 1 indicates age groups and relevant types of energy education program.

Çoker et al. [13] have mentioned that renewable energy sources topic is not only for the scientific research but also a topic for daily life. In their study, they have investigated Turkish primary and secondary students' knowledge on renewable energy sources. Open-ended questions were used for data collection. According to the results, it was concluded that students knew main energy sources (75.7% of students mentioned sun as an energy source), and however, they mentioned electricity as an electricity source not an energy carrier. This misconception was found to be higher in lower grades (4–5 grade).

In another study conducted to determine the views of ten elementary science preservice teachers on hydrogen as energy carrier, pre-service teachers defined energy sources as solar with 90%, hydropower and wind with 70%, petroleum and coal with 50%, natural gas 40% and nuclear with 30%. Only two pre-service teachers defined geothermal as an energy source. Interestingly, none of them was aware that hydrogen

Table 1 Age group and relevant RE education programs

Age group	Types of program
5–10	Simple concepts about environmental studies and other relevant subjects
10–13	Relevant concepts and experiments in science curriculum
13–16	Relevant concepts and experiments in science curriculum Pre-vocational courses for renewable energy
15–18	Relevant concepts, technologies, demonstrations and experiments Vocational course for renewable energy technologies area
>17	Certificate and diploma programs for technicians and mechanics Undergraduate and postgraduate degree level programs Practicing for updating knowledge and skills
>25	Mid-career courses, In service trainings for technicians and other professionals
Any age	Awareness programs for national, regional and local government officers, policy makers, administrators and other general public

Adopted from [8]

is an energy carrier [14]. This study also revealed the importance of energy education in education faculties.

Keramitsoglou [15] focused on the knowledge, perceptions and attitudes toward renewable energy sources of 234 high school students. Analysis results revealed that high school curriculum should be developed to improve the four main strategic directions which are equity, flexibility, enhancement of the participatory approach and creativity.

The purpose of the study is to determine the attitudes of elementary science and primary education pre-service teachers toward renewable energy sources. Participants are 191 pre-service teachers studying in Afyon Kocatepe University in Afyonkarahisar, Turkey. Moreover, the difference of attitudes toward renewable energy sources between these two department pre-service teachers has been analyzed by using independent *t* test.

1.1 Objectives of Energy Education

After including energy education in the current education curriculum, following objectives should be targeted:

- To achieve to use energy in an effective way,
- To motivate and direct people to save energy,
- To differentiate the energy sources as renewable and non-renewable,
- To be aware of the environmental effects of non-renewable energy sources,
- To be aware of the benefits of renewable energy sources,
- To be aware of new developing technologies about energy systems,
- To be aware of the energy related problems of the world,

• To define "sustainability" concept and apply this concept as a part of daily life.

People educated properly about energy will be able to define energy related problems, analyze, synthesize and find a solution for the problem, and hence, they will be energy literate [16].

2   Environmental Effects of Fossil Fuel Usage

When human being first discovered the fire, civilization began. Then people burned wood and started to make tools by using metals or cook some meats. After burning wood, consequently carbon dioxide (CO_2) was emitted to the air [17]. Awareness of people on the damage of CO_2 started centuries later than the fire was discovered. In 1996, Hoel and Kverndokk [18] mentioned that CO_2 was main greenhouse gas and 70–75% of all CO_2 emissions was because of fossil fuels. Nowadays, in order to produce electricity, we use mainly coal, oil and natural gas.

Figure 1 shows the share of energy sources of the World between 1990 and 2016 [19]. There are many environmental damages of coal usage to the environment such as atmospheric pollution, impact on global warming and impact on water quality where mining is performed. In this frame, atmospheric pollution affects human health, crops, forests, freshwater fisheries and unmanaged ecosystem [20]. Table 2 indicates the effects of power generation from coal fuel cycle on human health, atmosphere, lands, etc.
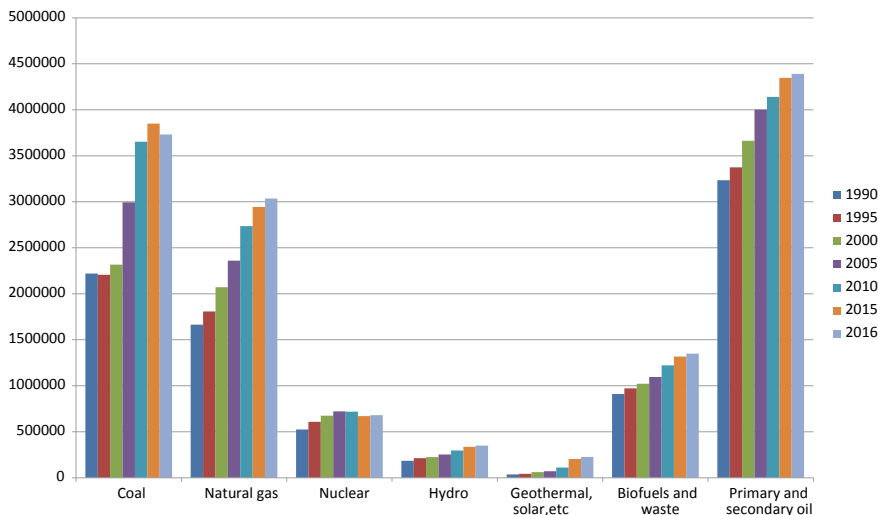
Fig. 1   Total primary energy supply by source for world between 1990 and 2016 [19]

Table 2 Effects of power generation from coal fuel cycle

Burden	Receptor	Impact	Priority
Occupational health			
Accidents	Workers	Minor injuries	Medium
		Major injuries	High
Noise	Workers	Hearing loss	Medium
Physical stress	Workers	Musculoskeletal injury	No data
Atmospheric emissions			
Particulates, SO_2, NO_x, precursors of O_3	General public	Acute mortality (PM_{10})	High
		Acute mortality (SO_2)	High
		Sore throat	Low
		Chest discomfort	Medium
		Phlegm	Medium
		Cough	Medium
		Chronic cough	High
		Chronic bronchitis	High
		Asthma	High
		Emergency room visits	High
		Eye irritation	Medium
	Pre-school children	Croup	High
	Air quality	Visibility	Low
CO_2 and climate change	General public	Health effects	High
		Employment	High
	Low lying areas	Loss of homes/land	High
Lead	Children	Intelligence	Negligible
	Babies	Neo-natal mortality	Negligible
	Adults	Hypertension	Negligible
Mercury	General public	Toxicity	Negligible
Other heavy metals	General public	Toxicity	Negligible
Other burdens			
Noise	General public	Public nuisance	Low
Physical presence	General public	Visual intrusion	Low

Adopted from [20]
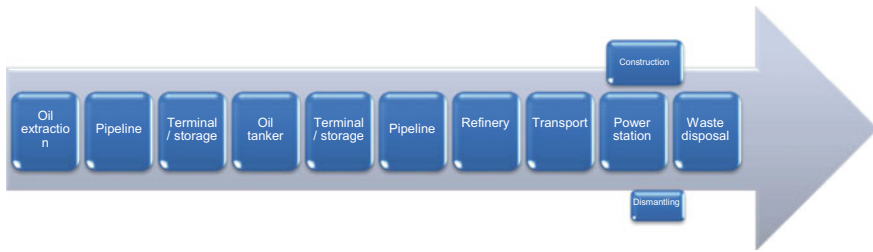
Fig. 2 Process steps for oil-to-electricity cycle [20]

Crude oil is treated to produce petroleum products which are necessary for transportation, heating buildings, medicines and also plastics. Streams, lakes, seas and even rocks and soils can be affected by spilt oil.

Figure 2 demonstrates the process steps for production of electricity from oil [20]. It should be noticed that each step has some potential for environment, health and other damages. Main damages of oil-to-electricity cycle are acute mortality and morbidity, chronic morbidity, ozone depletion, occupational health problems, damages to agriculture, forests and marine ecosystems and global warming [21].

In spite of being the cleanest fossil fuel, natural gas has also environmental impacts. Coal or petroleum have higher carbon content which leads to emitting CO_2. Natural gas, however, has lower carbon content, also emits less CO_2 when burned. For example, for 1000 kcal of energy, coal, petroleum and natural gas emit 407, 273 and 203 g CO_2, respectively [22]. In a case study, the effects of replacing coal with natural gas to drive electricity production plants were calculated. In that study, the replacement of coal by gas has helped to decrease projected global temperature after 25 years [23].

3   The Importance of Renewable Energy Education

Education should not be limited with dissemination of information. It should cover integration of knowledge to daily life, cultural values development and physical, emotional, mental and moral development of individuals and society. Hence, it can be said that education plays crucial role in any aspect of life. As new technologies arise, special education and information programs will be necessary both to train professionals and to increase the awareness of public. Developing countries are faced with many difficulties in developing scientific education. Also, those countries may not have enough equipment or laboratory materials. Therefore, they have difficulty in producing local products [24]. Following paragraphs list, some studies found in the literature showing the lack of renewable energy education in current curriculum.

Guven and Sulun [25] conducted a survey study in order to explore the awareness and knowledge of pre-service teachers on renewable energy. Renewable energy awareness scale and renewable energy knowledge level test were administered to

196 pre-service teachers as participants in Turkey. In conclusion, results of the study indicate that there is lack of education regarding renewable energy and pre-service teachers are not well-informed about the renewable energy subject.

Ntona et al. [26] have investigated students' views and attitudes toward energy and its usage in terms of environment. A total of 249 secondary school students in Greece participated in the study. As a result of paper, the authors claimed that a radical change in patterns of human behavior toward to sustainable environmental education process was needed.

Zografakis et al. [27] shared results of their study conducted to determine attitudes of 321 students and their parents' routine energy-related behavior in Crete-Greece. Students are from different grades of school, from secondary to senior high school. In order to increase the rate of energy literacy and to improve behaviors of pupils and their parents regarding to energy use, energy education should be one of the most urgent subjects which will be promoted.

4   Case Study 1: Analysis of Elementary Science Books Used in Turkey in Terms of Energy and Environment

In this part of the study, elementary science books used in secondary schools in Turkish Republic [28–31] have been analyzed in terms of energy and environment concepts.

4.1   Analysis of the Fifth-Grade Book

Energy and environment concepts are found in the sixth unit named "Human and Environment" of the elementary science books. The name of the chapter is "The relationship between human and environment." Recommended instruction hour for this subject is 10 h. The concepts used in this unit are environment pollution, preserving the environment, interaction of human and environment and local and global environmental problems.

The learning outcomes of this subject are as follows:

- To define the importance of the interaction between human and environment,
- To present suggestions for the local or national environmental problems,
- To make an inference toward possible future environmental problems,
- To exemplify benefits and damages of human and environment interactions.

Also, biodiversity concept is presented in this unit as "numerical richness of eidos and diversity of plant and animal in an environment." The other concept presented in the unit is natural life which is exemplified with forests, deserts, seas, lakes and lowlands. Moreover, habitat is defined as "the place that living beings live naturally." Factors that cause the degradation of biodiversity in Turkey forest ecosystems are

listed. Plants and animals which are either becoming extinct or having possibility to become extinct are mentioned. There are some activities for students to find solutions for environmental problems.

4.2 Analysis of the Sixth-Grade Book

The fourth unit of the sixth-grade elementary science book is "substance and heat." The third chapter of the unit consists of heat conductivity, heat insulation and heat insulation materials. There are four learning outcomes for this subject as follows:

- To categorize materials in terms of heat conductivity,
- To determine the selection criteria of heat insulation materials used in buildings,
- To develop alternative heat insulation materials,
- To discuss the importance of heat insulation in buildings and effective use of source for family and country economy.

The fourth chapter of the fourth unit of the book is "fuels." Concepts included in this chapter are solid fuels, liquid fuels, gas fuels, renewable and non-renewable energy sources. There are three learning outcomes of this subject:

- To classify fuels as solid, liquid and gas and exemplify those fuels.
- To define fossil fuels as non-renewable energy sources and to emphasize the importance of renewable energy sources.
- To discuss the effects of different types of fuels on human and environment.
- To investigate and report precautions that should be taken for poisoning caused by stove gases.

Fuels are described as "materials giving heat when they are burned." The examples of solid, liquid and gas fuels are given. In the same subject of the unit, renewable and non-renewable energy sources are described and exemplified.

4.3 Analysis of the Seventh-Grade Book

The first unit of the seventh-grade book is "Solar system and beyond." In this unit, there is a chapter named "Space researches and space pollution." In this chapter, to define the reason of the space pollution and to guess possible outcomes of that pollution are given as learning outcomes. In the fourth unit of the book, there is a chapter on "domestic wastes and recycling." There are five learning outcomes which are as follows:

- To differentiate domestic wastes as recyclable and non-recyclable,
- To prepare a project for recycling domestic wastes,
- To investigate recycling in terms of effective use of sources, to emphasize the economic benefits of recycling,

- To make recycling and waste management a part of daily life,
- To make a project for recycling unused stuff.

In this chapter, recycling is defined, and the benefits of recycling are listed with examples.

The solar collectors and their working principles are simply defined in the first chapter of the fifth unit of the book named "absorption of the light."

4.4   Analysis of the Eighth-Grade Book

In the second unit which is "DNA and genetic code" of the eighth-grade book, the effects and damages of environmental pollution is mentioned in the chapter of "mutation and modification." Also, in order to prevent the environment, it is stated that biotechnology is used.

Semimetals are mentioned as materials for solar panels in the periodic system chapter. The cause of acid rains and their effects are mentioned in the fourth chapter of the fourth unit.

The sixth unit of the eighth-grade book is "energy conversions and environmental science/living beings and life." In energy conversions part, photosynthesis, respiration and fermentation are defined. The third chapter named "substance cycles and environmental problems" covers global climate change, greenhouse effect, environmental problems and ecological footprint subjects. The fourth chapter is about sustainable development. Learning outcomes of this chapter are as follows:

- To save and use sources efficiently,
- To prepare a project for efficient use of sources,
- To define the importance of decomposing solid wastes for recycling,
- To suggest a solution for recycling benefits on national economy,
- To suggest a solution for possible future problems regarding saving energy.

5   Case Study 2: Pre-service Teachers' Awareness on Renewable Energy

The purpose of this case study is to investigate the attitudes of pre-service teachers toward renewable energy concept in terms of their department.

5.1 *Methodology*

In this study, which targets identifying and comparing the attitudes of pre-service teachers in elementary science education and primary education departments toward renewable energy, survey model was employed.

5.2 *Participants*

The total population of the study is comprised of 191 students in Afyon Kocatepe University Education faculty elementary science education and primary education departments in Afyonkarahisar, Turkey. The reason for selecting these two departments is that energy and environment topics are available mainly in science lessons instructed by elementary science and primary teachers in schools. All the population participated in the study. The demographic information of pre-service teachers in the population of the study is given in Table 3.

As presented in Table 3, 68.1% of pre-service teachers attending this study is female, while 31.9% of the population is male. When the departments of the participants are analyzed, it is seen that 62.3% of the population is from elementary science education department and 37.7% is from primary education department. The grade level of sample group consists of 1.6% from second grade level, 41.9% from third grade level and 56.5% from fourth grade level. Last demographic information is related to whether pre-service teachers attending this study have taken a lecture regarding environment or not. 50.8% of the participants have taken a course on environment before; however, 49.2% have not taken any course on environment.

Table 3 Demographic information of the population

Variable	Level	Frequency (f)	Percentage (%)
Sex	Male	61	31.9
	Female	130	68.1
Department	Elementary science education	119	62.3
	Primary education	72	37.7
Grade level	2	3	1.6
	3	80	41.9
	4	108	56.5
Prior course for environmental education	Attended	97	50.8
	Not attended	94	49.2

5.3 Data Collection Tool

As data collection tool, attitude scale for renewable energy sources developed by Gunes et al. [32] is used. This attitude scale which is comprised of 26 items is a five-point Likert scale (totally disagree, disagree, neutral, agree and totally agree). The renewable energy attitude scale used in this study consists of four sub-factors which are "willingness to apply," "importance of education," "national interests" and "environmental awareness and investments." The importance of education sub-factor with total scale is preferred in this study because of convenience of the study. For the reliability of the scale, the Cronbach alpha reliability coefficient is 0.87 which is highly reliable. For importance of education sub-factor, the Cronbach alpha reliability coefficient is 0.80. Cronbach alpha reliability coefficient for total score of this study has been found 0.87, and for importance of education, sub-factor has been found as 0.70.

5.4 Data Analysis

For data analysis, Statistical Package for the Social Sciences (SPSS) has been used [33]. For data analysis, SPSS (Statistical Package for the Social Sciences) software was used. Frequency and percentage values regarding demographic information of participants were presented. Reliability statistics were carried out for each sub-factor and whole scale. Independent *t* test was used to determine the difference regarding attitudes toward renewable energy sources between elementary science education and primary education departments. Also, independent samples *t* test was carried out in order to determine the difference between the departments regarding "importance of education."

5.5 Findings

In this study, the aim is to investigate total scores obtained from renewable energy sources attitude scale of elementary science education and primary education department pre-service teachers. Another aim is to analyze significant differences between these two departments. Besides, total scores and scores of the importance of education sub-factor are calculated.

Table 4 shows number of pre-service teachers from each department and their mean scores and standard deviations obtained from RES attitude scales.

According to the table, the mean value of 119 elementary science education pre-service teachers is 92.2, while mean value of primary education department pre-service teachers is 87.3. The scale consists of 26 items, and the highest point for each item is 5. Hence, the highest score which can be obtained from the scale is 130.

Table 4 Mean and standard deviations of total points obtained from RES attitude scale

Department		N	Mean	Std. deviation
Total points	Elementary science education	119	92.22	15.56
	Primary education	72	87.25	15.98

As seen from the mean values in table, the scores of elementary science education pre-service teachers are higher than primary education pre-service teachers. Also, it can be said that both mean values are above average.

Table 5 indicates that there is a statistically significant difference in favor of elementary science education department pre-service teachers when scores obtained from renewable energy attitude scale are compared according to the results of independent t test.

Independent samples t test result shows the scores of elementary science education pre-service teachers are higher than primary education pre-service teachers, correspondingly Table 6 demonstrates that there is a statistically significant difference in favor of elementary science education department pre-service teachers when scores obtained from the importance of education sub-factor are compared according to the results of independent samples t test. The reason of higher scores of pre-service teachers in elementary science education than those in primary education may be that there are some chapters and subjects in physics, chemistry and biology courses related to the renewable energy and environment which are absent or in lower detail in primary education courses.

Table 5 Independent t test results of elementary science education and primary education pre-service teachers for renewable energy attitude scale

	Department	n	$\overline{X}$	SD	t	p
Renewable energy attitude scale	Elementary science education	119	92.23	15.56	2.12	0.035
	Primary education	72	87.25	15.99		

Table 6 Independent t test results of the importance of education sub-factor

	Department	n	$\overline{X}$	SD	t	P
The importance of education sub-factor	Elementary science education	119	24.92	5.18	2.57	0.011
	Primary education	72	22.90	5.41		

6 Conclusion

In this study, the aim was to determine the difference between elementary science and primary education pre-service teachers' attitudes toward renewable energy. Also, with a brief introduction and literature review, elementary science books used as course books in Turkish secondary schools have been analyzed in terms of which and how much renewable energy and environment subjects are covered. As a result of book analyzes, it can be said that there are enough subjects related to renewable energy and environmental topics although they can be improved as well. Lack of experts in renewable energy education or lack of well-trained teachers may result in students having misconceptions. Moreover, integration of knowledge about renewable energy and environment to daily life should be increased by increasing number of experiments and applications in school life. Survey analysis conducted to 191 pre-service teachers reveal that there is a statistically significant difference in attitude toward renewable energy sources in favor of elementary science education pre-service teachers. These results can be interpreted as the result of elementary science education curriculum's having more topics relevant to renewable energy, environment and sustainability, elementary science teachers are equipped than primary education teachers.

References

1. Jefferson M (1996) Global prospects for renewable energy. Renew Energy 8:1–5
2. Arent DJ, Wise A, Gelman R (2011) The status and prospects of renewable energy for combating global warming. Energy Econ 33:584–593
3. Manzano-Agugliaro F, Alcayde A, Montoya FG, Zapata-Sierra A, Gil C (2013) Scientific production of renewable energies worldwide: an overview. Renew Sustain Energy Rev 18:134–143
4. Gross R, Leach M, Bauen A (2003) Progress in renewable energy. Environ Int 29:105–122
5. International Energy Agency (2012) World Energy Outlook 2012 (WEO-2012). https://www.iea.org/newsroom/news/2012/november/world-energy-outlook-2012.html. Accessed 22 Apr 2019
6. De Vries BJM, Van Vuuren DP, Hoogwijk MM (2007) Renewable energy sources: their global potential for the first-half of the 21st century at a global level: An integrated approach. Energy Policy 35(4):2590–2610
7. Deng YY, Blok K, van der Leun K (2012) Transition to a fully sustainable global energy system. Energy Strategy Rev 1(2):109–121
8. Kandpal TC, Broman L (2014) Renewable energy education: a global status review. Renew Sustain Energy Rev 34:300–324
9. Gupta CL (2003) Role of renewable energy technologies in generating sustainable livelihoods. Renew Sustain Energy Rev 7(2):155–174
10. Jennings P (2009) New directions in renewable energy education. Renew Energy 34:435–439
11. Gelegenis JJ, Harris DJ (2014) Undergraduate studies in energy education—a comparative study of Greek and British courses. Renew Energy 62:349–352
12. Caglayan A (2011) Renewable energy education in Turkey. Renew Energy 36:608–611
13. Bünyamin Ç, Hakan Ç, Osman B (2010) Conceptions of students about renewable energy sources: a need to teach based on contextual approaches. Procedia Soc Behav Sci 2:1488–1492

14. Yuksel YE (2019) Elementary science teacher candidates' views on hydrogen as future energy carrier. Int J Hydrogen Energy 44(20):9817–9822
15. Keramitsoglou KM (2016) Exploring adolescents' knowledge, perceptions and attitudes towards renewable energy sources: a colour choice approach. Renew Sustain Energy Rev 59:1159–1169
16. DeWaters JE, Powers SE (2011) Energy literacy of secondary students in New York State (USA): a measure of knowledge, affect, and behavior. Energy Policy 39(3):1699–1710
17. Dincer I, Rosen MA (1999) Energy, environment and sustainable development. Appl Energy 64(1–4):427–440
18. Hoel M, Kverndokk S (1996) Depletion of fossil fuels and the impacts of global warming. Resour Energy Econ 18(2):115–136
19. International Energy Agency. International Energy Agency Statistics (2018). https://www.iea.org/statistics/?country=WORLD&year=2016&category=Energy%20supply&indicator=TPESbySource&mode=chart&dataTable=BALANCES. Accessed 27 Apr 2019
20. ExternE (Externalities of Energy) (1995) Vol 4: oil and gas EUR 16523 EN. The European Commission, Luxembourg
21. Perman R, Ma Y, McGilvray J, Common M (2003) Natural resource and environmental economics. Pearson Education
22. Stefano DP, Aldo F, Tommaso L (2001) Natural gas, cars and the environment. A (relatively) 'clean' and cheap fuel looking for users. Ecol Econ 38(2):179–189
23. Hayhoe K, Kheshgi HS, Jain AK, Wuebbles DJ (2002) Substitution of natural gas for coal: climatic effects of utility sector emissions. Clim Change 54(1–2):107–139
24. Benchikh O (2004) UNESCO's global renewable energy education and training programme (GREET programme). In: Science Forum
25. Guven G, Sulun Y (2017) Pre-service teachers' knowledge and awareness about renewable energy. Renew Sustain Energy Rev 80:663–668
26. Ntona E, Arabatzis G, Kyriakopoulos GL (2015) Energy saving: views and attitudes of students in secondary education. Renew Sustain Energy Rev 46:1–15
27. Zografakis N, Menegaki AN, Tsagarakis KP (2008) Effective education for energy efficiency. Energy Policy 36(8):3226–3232
28. Özkan İ, Mısırlıoğlu Z (2018) Elementary science course book 5th grade. Ada, Ankara
29. Çiğdem Ç, Minoğlu Balçık G, Karaca Ö (2018) Elementary science course book 6th grade. Sevgi, Ankara
30. Gezer İ (2018) Elementary science course book 7. Aydın, Ankara
31. Aytaç A, Türker S, Bozkaya T, Üçüncü Z (2018) Elementary science course book 8th grade. Tutku, Ankara
32. Güneş T, Kazım A, Gözüm AİC (2013) Renewable energy sources attitude scale for science teachers: validity and reliability study. J Educ Sci Res 3(2):269–289
33. IBM. Spss (2016) Statistics for Windows, Version 24. 0 [Computer Software]. IBM Corp., Armonk, NY

Plastic: Reduce, Recycle, and Environment

Nasreen Bano, Tanzila Younas, Fabiha Shoaib, Dania Rashid and Naqi Jaffri

Abstract Plastic is a general term utilized for a wide scope of high subatomic weight natural polymers obtained for the most part from the different hydrocarbon and oil subsidiaries. Plastic is non-biodegradable, as it does not break down to a natural, environmentally safe condition after some time by natural procedure. Global world is attempting to recycle more plastic. Plastics that are disposed off in daily routine are becoming noticeable execration for environment; more than half of the world is facing these problems. Underdeveloped countries constitute more than half of the world and have heaps or gyre of plastics and other wastes. The time rate of wastage of plastic is increasing which can be observed by seeing oceans. It is hard now to clean them up at this stage. It is a nature of a plastic that when it reveals to the heat or sunlight, it starts to discharge harmful poisonous chemicals. It takes approximately thousand years to degrade, so dumping them in ocean or in landfill does not mean they will be gone, but they will be here after centuries. This paper focuses on the effects of reduction and recycling of plastics on environment.

Keywords Gyre · Recycling · Discarded · Biodegradable · Plastic · Waste

N. Bano · T. Younas · F. Shoaib · D. Rashid · N. Jaffri (✉)
100 Clifton, Karachi, Pakistan
e-mail: naqijafri10@gmail.com

N. Bano
e-mail: nasreen.bano@szabist.edu.pk

T. Younas
e-mail: Tanzila@szabist.edu.pk

F. Shoaib
e-mail: fabihashoaib@gmail.com

D. Rashid
e-mail: daniarashid118@gmail.com

1 Introduction

Polymers are one of the man-made inventions; Bakelite is the first polymer manufactured by Yonkers back in 1970. There was a dying need of replacement of shellac in electrical wiring which leads to the invention of polymers. Due to high adaptability, performance, and low cost, polymers, i.e., plastics and rubbers, gained rapid growth. These are utilized in vast applications such as packaging, automobiles, and electrical appliances. 1930 is known as an era of transition, as majority of the common thermoplastics were developed in this era.

Ethylene is the derivative of vinyl plastics; these were used in waterproofing of the fabrics. But with the invention of polyethylene, the production of vinyl resin was stopped. These are used in high ratio worldwide. Low-density polyethylene captured industry for two decades. But with the development of high-density polyethylene, its production discontinued. Low-density copolymer of ethylene (LDPE) replaced HDPE, due to its versatile properties. This process of development in polymers was at its peak in the nineteenth century and leads to the invention of many useful polymers such as polymethyl methacrylate, polystyrene, nylons, and thermoplastics.

Plastic is most accepted and favored material among all other materials. For environment, it is being cursed [1], which is destroying environment by evolving day by day. Most of the plastics are usually produced from non-renewable resources [2, 3] like natural gases, fossil fuel, petro-based polymers, etc., processed with the help of concentrated energy techniques that in response demolishes unsustainable environment. Plastics could also be produced from renewable resources [4–7]. Bioplastics are plastics derived from inexhaustible biomass sources, for example, vegetable fats and oils, corn starch, straw, woodchips, and sustenance squander.

By research, on the wastage of plastic, it shows up that half of the discarded plastic that proceeds in oceans comes from five developing countries: China, Indonesia, Sri Lanka, Vietnam, and Philippines, and by observing the record of top 20 countries that wastes a lot, USA comes in the record at number 20 which is the most developed country [8].

1.1 Plastic Waste

By calculating the rate waste of plastics, that are discarded in the form of bottles, shopping bags, and children toys, it is around 8 million ton, and most of the part of this wastage is turn out to be in the oceans. Quite a bit ends up in landfill, and rest of it results in plastic pollution making its way into our waterways [9].

1.2 Plastic Usage

The use of plastics in customer products is moderately more in the developed countries as compared to underdeveloped countries. In opulent countries such as Japan and western part of Europe, the usage of plastic is higher. Figure 1 shows per capita consumption of plastic materials worldwide in 2015 by region (in kilograms), the NAFTA countries had the world's highest per capita consumption of plastic materials, at some 139 kilograms, and while in year 2016, the production of plastic worldwide amounted to some 335 million metric tons [10]. The future consumption of plastics is probably going to build the quickest in developing countries, especially in China, India, and a few nations in Latin America [11] in different autonomous and non-autonomous products [12–16].

Let us take example of China; the percentage rate of waste of plastic that flows into oceans is 28% of world that is 2.4 million tons of plastic which is discarded into oceans. In last 10 years, more amount of plastic was manufactured than in whole century which shows the use of plastic, which is increasing day by day. By this fact, wastage of plastic is predictable, because more than 50% plastics are used only once and then disposed off. This disposed off plastic floats in oceans, floating plastics amount is 46%, and it takes several years to get deep down into the ocean and be a part of heap or ocean gyre.
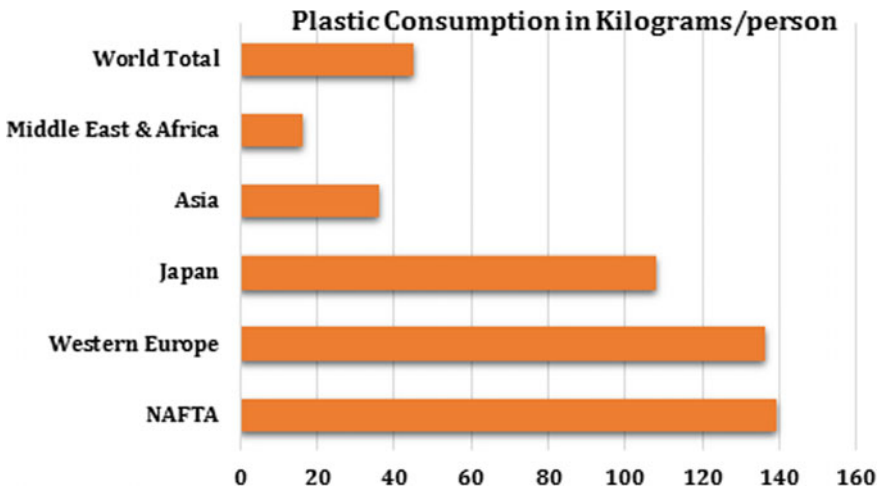
Fig. 1 Consumption of plastic materials. Modified from https://www.statista.com/statistics/270312/consumption-of-plastic-materials-per-capita-since-1980/

1.3   Plastic Degradation

Plastics take a lot of time to degrade, which is approximately 500–1,000 years to break down into little pieces, which leak down into the dirt and discharge synthetic concoctions, which in the long run achieve the water supply. Assembling of plastic bag is harmful to the earth in light of the fact that non-renewable assets are utilized (petroleum and natural gas).

Biodegradation [17] is brought by natural action, i.e., enzyme, especially by catalyst activity and prompting changes in the material's chemical structure. The biodegradability of plastics is subject to the synthetic structure of the material. The biodegradation of plastics continues effectively under various soil conditions as indicated by their properties.

Plastics are not biodegradable; it is a disadvantage which could be changed into advantage by recycling these plastics. Plastics are becoming threats and nightmares to municipal organizations. Governments all over the world should do ban on polystyrene shopping bags and increasing level of plastic manufacturing until and unless it should start recycling or nay other solution to it. Plastics were gathered in landfills or dumping area and start polluting environment.

The microscopic particles of plastic that could not be seen from naked eye are broken into little microscopic segments that are present in water, air, and lands; we are breathing it and drinking it, which is also affecting human health. These are the unhygienic reasons that so many new dreadful diseases and viruses have been produced. People are not aware of this severe issue. They do not take it seriously because it is against their convenience.

1.4   Plastic Reduction

Consumers are regularly deficient with regard to the advantage of conceivable logical data; the layman is commonly unfit to completely value the size and the suggestions of even the regular natural issues. However, the overall population is progressively thoughtful toward ecological safeguarding. In some areas, where government is taking action to ban plastic bags, many critics were objected on this ban because it will affect their ease. People need to get aware of this issue and should support government in this matter, as it is for healthy lifestyle and to create a healthy green environment. The alternative solution to this problem could be the replacement of plastic product, e.g., plastic bag to cloth bags or paper bags [18] and so on.

Following lifestyle could help us in plastic reduction:

- Quit utilizing plastic straws, even in cafés. In the event that a straw is an unquestionable requirement, buy a reusable hardened steel or glass straw.
- Utilize a reusable produce pack. A solitary plastic pack can take 1,000 years to corrupt. Buy or make own reusable produce sack and make certain to wash them regularly.

- Surrender gum. Gum is made of synthetic rubber, otherwise known as plastic.
- Purchase cardboard boxes rather than containers. Regular items like clothes cleaning agent may come in cardboard packaging which is more effectively reused than plastic.
- Buy nourishment, similar to grain, pasta, and rice from mass canisters, and fill in a reusable sack or holder.
- Reuse containers for putting away remains or shopping in mass.
- Utilize a reusable container or mug for your drinks.
- Stop purchasing frozen food, in light of the fact that their bundling is for the most part plastic.

1.5   Plastic Recycling

Plastic recycling [19] depends upon the type of plastic. Before recycling, plastics and non-plastics are separated as every type that could be recycled due to constraints with them. By the research, it is confirmed that plastic wastage is becoming a threat to marine life also because 1 million seabirds and 100 thousand marine animals have been killed because of plastic, as it poisons the water by releasing chemicals.

We all are responsible for global warming and other environmental issues. The most common product of plastic that is wasted by the people is shopping bags. It is a crucial origin of disposing pile or dumping piles that can be seen in every streets especially in underdeveloped countries.

Various plastics can be reused. Likewise, the materials recovered can be given a second life. In any case, this strategy is not totally utilized, in view of difficulties with the gathering and orchestrating of plastic waste. Many developing countries (and even some developed countries) have poor waste organization workplaces which every now and again result in plastics (and other waste) being imprudently orchestrated into waterways and waterbodies. Notwithstanding the way that reusing is the best strategy to oversee plastic waste, its ampleness is exceedingly depended upon open care, monetary plausibility, and the execution of open establishments to make reusing progressively capable (reusing compartments and specific waste get-together trucks).

1.6   Plastic Trends

Medical [20], aerospace, automotive [21], packaging, household appliances, and construction industries are using plastics which is replacing conventional materials such as glass, metal, and cloth. The global trend for plastic production is quite clear that plastics industry is continuously prospering around the globe [22–25], it is also depicted from Fig. 2.

2014-2015 U.S medical plastics market size
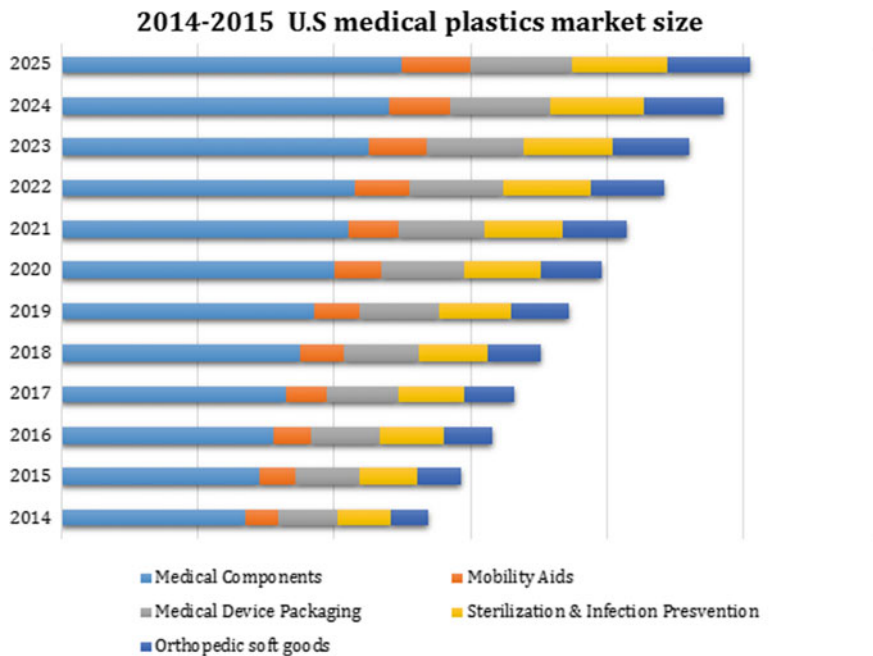
Fig. 2 US medical plastics market size by application, 2014–2025 (USD million). Modified from
https://www.grandviewresearch.com/industry-analysis/medical-plastics-market

It is pivotal for the plastics business of things to come to play a lot bigger, progressively vehement, role in broad daylight training, i.e., public education and scattering of unprejudiced technical information regarding the industry. Natural issues of today are helpfully examined inside two wide classes; worldwide issues and local, i.e., neighborhood issues.

The accompanying talk inspects every one of these natural worries with an end goal to get it, the degree to which the plastics business conceivably adds to it. Genuine ecological issues do not include the polymer business straightforwardly. For example, the loss of biodiversity and the expansion in urban populace thickness are rejected from the present discourse.

2   Global Environmental Issues

The global environmental issues and their effects in relevance to plastic industry are as follows:

1. Consumption of petroleum product vitality and crude material assets which utilizes non-renewable energy sources as a hotspot for vitality just as crude materials. It is adding to future vitality emergency and future deficiency of basic crude

materials. As polymers are blended generally from petroleum product assets, e.g., raw petroleum. Be that as it may, the asset utilization by the business is generally little (not exactly about 4%).

2. A dangerous atmospheric deviation as the arrival of ozone harming substances, e.g., CO_2, methane, NO_x, and CFCs into the environment. They affect direct well-being impacts because of high temperature. As a consequence, ocean level raises and conceivable relocation of population occurs. Flimsy climate conditions, increment in vector-borne and irresistible infections result in loss of rural profitability. All ventures, including the plastics business, discharge some ozone-depleting substances. Polymer industry does not create a lopsided offer of the emanations.

3. Consumption of stratospheric ozone, identified as arrival of ozone exhausting substances (ODS, e.g., CFCs and CHFCs into the environment). Exhaustion of the ozone layer results in more elevated amounts of UV-B radiation achieving the world's surface.

Following outcomes are reported:

- Higher occurrence of skin and eye harm because of expanded UV-B radiation
- Different effects on human well-being
- Changes in horticultural efficiency just as marine and in crisp water biological systems
- Potential changes in the biogeochemical cycles.

Plastics industry in the USA does not utilize any critical dimensions of CFCs. Worldwide, the utilization of HCFCs in plastic froths is additionally being eliminated.

4. Acidification of the earth can be identified as acidic gas (NO_x and SO_x) discharge predominantly from the copying of petroleum products.

Its effects are as following:

- Harm to freshwater environments including inland fisheries.
- Disability of the ripeness of rural soil because of acidic draining.
- Harvest and woods harm by direct fermentation and biotoxicity due to solubilized metals.

Polymer industry utilizes non-renewable energy sources, yet not at an unbalanced dimension. The burning of PVC has been professed to result in the arrival of HCl into nature adding to acidification. However, this is viewed as an irrelevant commitment to acidification.

2.1 Reduce Use of Plastic

Although plastic was introduced under 100 years back, it has rapidly turned into a staple in our regular daily existences—from light changes to vehicles to PCs,

plastics are unavoidable. Lamentably, this blast in plastic items has been wrecking our environment. Synthetic plastics are not biodegradable, which implies that once they are made, they will be with us in our landfills and seas for hundreds of years. There is likewise an entire clothing rundown of poisonous synthetic compounds that spill into our air, water, and soil from the assembling and transfer of plastics. Reusing can help mitigate a portion of these issues. However, the most ideal approach to shield the earth from plastics is to supplant them with more eco-accommodating materials.

Metal, wood, and glass: A standout among the most ideal approaches to dispose of plastic in home or business is to pick items produced using progressively customary materials like metal, wood, or glass. These materials are cleaner to fabricate and simpler to discard. Glass alongside metals like aluminum and steel can be reused uncertainly, which means they do not need to finish up in landfills. Wood is likewise simpler to reuse and discard. These items are normally costly, yet their strength and green lifecycle make them worth the cost. Whenever purchasing wood items endeavor to ensure they are eco-accommodating and originating from economically gathered timberlands. One must search for marks from the Forest Caretaking Council, which affirms that wood items like furnishings, paper, and ground surface are eco-accommodating at each phase of their life from planting to the home. Likewise endeavor to search for items produced using reused and recovered metal and glass.

2.2 Renewable Energy Sources for Plastic Production

Bagasse: Compostable, eco-accommodating bagasse is incredible for supplanting plastic when there is a need of dispensable plates, glasses, or take-out boxes. Bagasse—the mash left over when juice is extricated from sugarcane or beets. It is utilized for an assortment of purposes including as a biofuel. It can likewise be squeezed into a cardboard-like material used to make waterproof sustenance compartments, which is an incredible use for assembling waste that would somehow or another be discarded. Since it is produced using plants, it will biodegrade effectively in a home and mechanical manure heap.

Bioplastics: Once in a while, it is elusive non-plastic rendition of the items you need, so when you need to depend on plastics endeavor to discover eco-accommodating ones. PLA or CPLA is produced using corn rather than oil, while taterware is a comparable material produced using potato starch. Both will biodegrade in mechanical fertilizer destinations, despite the fact that be mindful when buying these items as some are not compostable in home manure canisters. Numerous organizations are likewise now beginning to fabricate jugs and bundling utilizing PLA or different plastics produced using non-oil sources.

Biodegradable plastics: Biodegradable plastics cannot avoid being plastics that separate by the action of living structures. Biodegradable plastics can clarify different waste organization issues, especially for unimportant packaging that cannot be adequately disconnected from common waste. Nevertheless, biodegradable plastics are not without discussion. In spite of the way that biodegradable plastics can be

absolutely used by life frames into carbon dioxide and water, there are claims that oxo-biodegradable plastics may release metals into the earth.

3   Main Causes of Plastic Pollution

Plastic contamination has progressively turning into a noteworthy annoyance and posture critical dangers to the whole condition prompting area, air, and water contamination. Additionally, plastics impact the indigenous habitat and have grave ramifications for people, natural life, and plants. Since they contain various dangerous mixes, the major correspondents to these problems involve are as follows:

- Vast range of plastic trash
- High demand and usage of plastics
- Fishing nets a threat to water life
- Discarding of plastic scrap and garbage.

3.1   Vast Range of Plastic Trash

Plastics are playing very important role in the material nowadays; after using plastics, they are dumped or sank to the water. Because of this behavior, land and water are being polluted. Like many developing countries such as Pakistan and India, other struggling countries have lots and lots of dumping ground or garbage lot. Heaps of trash or garage in every street can be seen, which is very hazardous. It is polluting environment as well as it will give very harmful effect on human health too as shown in Fig. 3.

3.2   High Demand and Usage of Plastics

Plastic is a material which is available everywhere in this world. Its availability is a very unique nature of this material. Any person could afford this because it is very cheap and every time available, that is why its usage is increasing day by day as shown in Fig. 4, which is becoming a threat to our environment.

3.3   Fishing Nets a Threat to Water Life

Fish is a necessity for more than half of the people in this world, and they are being killed by polluting the groundwater. In fishing, nets that are usually used are made

Fig. 3 Side effects of plastics trash
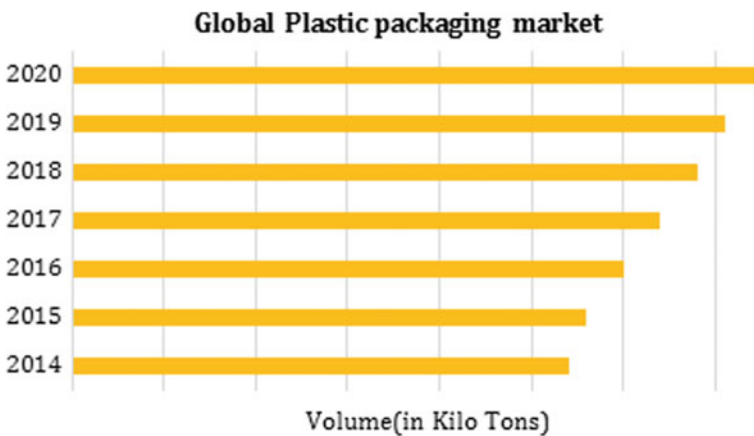
Fig. 4 Consumption of plastics in packaging industry. Modified from web https://www.visiongain. com/Report/1622/Flexible-(Converted)-Plastic-Packaging-Market-Report-2016-2026

up of plastic. These nets do not seem to create any problem and pollution, but this is not the reality as these nets are fully submerging into the water for a very long time. After a long time, these nets start to penetrate by discharging hazardous toxins and poison in the water. These nets also broken down and lost, which remain in water for long period of time. These plastics are threat to marine life [26, 27]. Fishes are being victim of this pollution, and by eating these fishes, humans are getting affected.

Derelict fishing gear could be a problem for navigation; they may cause injury or harm for commercial and recreational divers. It also gets caught on rocky and coral reefs or float on the ocean surface. Derelict gear can degrade marine habitats

by inhibiting access to habitats via multiple layers of gear, suffocating habitat by trapping fine sediments, and contributing to habitat destruction through scouring.

Sea plastic contamination is a worldwide issue with extremely noteworthy negative consequences both inside the sea and outside, i.e., in our world ecosystem. This way of contamination includes majorly disposed of nylon plastic fishing nets. Every year, with an expected 640,000 tons (1.28 billion pounds) of fishing gear is left in the sea.

These abandoned fishing nets are also known as "ghost nets" could stay in the marine biological system for exceptionally significant amount of time as shown in Fig. 5. They incidentally catch marine warm-blooded animals, ocean fowls, and fish in extremely substantial numbers, including whales, dolphins, sharks, seals, and ocean turtles, which can be seriously hurt and may die because of starvation and powerlessness to surface for air. Overall, these nets catch and damage between 30 and 40 marine creatures for each net when left in the sea.

3.4 Discarding Plastic Scrap and Garbage

Plastics hardly decompose; burning is not the solution as it is a threat due to its profoundly noxious. Smoke of the burned plastics can lead to fatal illness, and burned plastics as long as it remain in the landfills it releases deadly toxins [28].

Fig. 5 Silent killer ghost net. Reproduced from web https://m.gettyimagesbank.com/view/discarded-fishing-ghost-nets-in-ocean-environmental-damage/697932870

4 Procedure of Plastic Recycling

Recycling of plastics comprises the following steps. Majority of the recycling facilities follow these steps; however, few steps can be combined or excluded as required.

4.1 Assortment

Collection of the plastic materials for recycling is the first stage in the cycle. This stage is dependent on the accurate disposal of the plastic waste. If it is mixed with the normal waste, then it cannot be recycled. In order to cater this, collection of recycling material system should be enforced by the government in a systematic manner as shown in Fig. 6. Collection points should be nearby and easily accessible to the people for its promotion and efficacy [29].

4.2 Categorization

After collection, sorting of plastics is second step. For this purpose, different machines are arranged in an order according to the final product need. Plastics are sorted into different order according to many different ways such as material type,

Fig. 6 Collection of plastic materials. Reproduced from web https://commons.wikimedia.org/wiki/File:Trash_Recycling_with_Disposal_Containers.jpg

color, size, and shape. Then accordingly, they are recycled. If any incorrect type of plastic is recycled in the process, it can reduce its production rate and at sometimes the whole batch is rejected [29, 30].

4.3 Cleaning

Similar to many other processes, cleaning via washing is carried out in order to remove impurities from the plastics stock. Non-plastic waste like labels, adhesives, and residual materials should be removed. Structural integrity is reduced with the presence of the impurities [30].

4.4 Shredding

Shredding is carried out in order to breakdown large pieces into small particles as shown in Fig. 7. Reshaping, processing, and transportation can be made easy by increasing the plastics surface area. By resizing plastics, we can increase the surface area of the plastics.

4.5 Quality Testing and Identification

For quality testing, plastics are separated on the basis of different parameters. These parameters include density, size, melting point, and color. Density testing is carried

Fig. 7 Shredding of plastic. Reproduced from web https://www.youtube.com/watch?v=ohLYdtIULEU

out by floating tiny plastic particles in large water tank. Dense particles will get settle down and light weight will keep floating.

Sizing is done by air classification. In a small air tunnel, particles are dropped and bigger particles remain lower in the tank; however, smaller pieces will fly high. Similar to this, other testing is also carried out by different tests. This is done by analyzing the collected plastic sample particles [29–31].

4.6 Pellet Formation

This is the last step in the process. In this, plastics are transformed into the reusable materials for future production as shown in Fig. 8. Pellets are formed by crushing and melting the small particles [29]. This is done in various specialized stages.

5 Analysis of Recycling Products

Plastics ought to be reused in view of various reasons as following:

Fig. 8 Pellets of plastic. Reproduced from web https://www.greenbiz.com/newsletters-subscribe

5.1 Raw Material: Sustainable Source

Recycled plastics are one of the goals of sustainable development. Recycled plastics can be redesigned to be used in different appliances. They serve as a raw material to different manufacturing industries.

5.2 Reduction of Environmental Problems

Since plastics are non-biodegradable, they represent a high hazard to the general population and the earth overall. Blockages of drainage and sewer lines may occur due to plastic materials. By recycling plastics, environment can be clean and green.

5.3 Reduction of Landfill Issues

By recycling plastics, the quantity of the plastics sent to the landfill sites can be decreased. As these sites occupy a vast area, decreasing the beauty of the earth, majority countries have allocated areas specifically meant for burying plastics. By doing so, these sites will receive less amount of plastic waste. Rest of the areas can be utilized for various useful purposes, instead of dumping plastics, such as farming, human settlement, or economic activities. As population is increasing at an exponential rate, providing shelter is an issue. The land can be used for such activities instead of dumping garbage.

5.4 Energy Efficient

There is a vast difference in energy utilization when creating the product from scratch or from recycled material. This saved energy can be consumed in other important socio-economic activities between the recycling of materials including plastics which requires less energy as compared to making the plastic from scratch. This saves energy, and that energy can be diverted to other important things in the economy. Billions in the economy can be saved by recycling plastics, so it should be promoted and well implemented.

5.5   *Sustainable Lifestyle and Alternative Income*

It provides an opportunity to the individuals to earn good for their life. By adopting plastic collection and recycling as a business, one can improve his lifestyle and contribute to the economy of the country.

6   Discussion and Result

The exact time of the process of breaking down of plastic cannot be estimated, but through researches in the past years, it is believed that this process takes more than hundred years. The plastic, which decomposes through light that is photodecomposition, produces fragments that contaminate water and pollute soil. The accumulation of plastic has other many harmful effects for the environment. As compared to other materials like glass, paper, or iron, plastics have a low recovery rate. This means that they are less efficient to be processed again and be reused. The recycling processes are much expensive than the raw materials so manufacturing prefer using newer material than using the recycled one. Against the usage of plastic bags and plastic-made food containers, some countries have banned the manufacturing of such products and have enforced fines on using them and not disposing them properly. However, in the end, the main aim is to use lesser plastic products and dispose them in a way that they cause no harm to the environment. New solutions for this problem are also introduced like use of biodegradable plastics and the zero-waste philosophy embraced by the government [32].

7   Conclusion

The world's population is increasing rapidly; each individual is contributing in increasing the pollution on this planet. There is so much of plastic wasted daily that there is no other way but to recycle it. Products like beverages and food containers, plastic cups, utensils, plastic bags, toys, diapers, trash bags, and bottles used for different purposes are made of plastic, not counting the plastic that is used in furniture manufacturing, home appliances, automobiles, and computers.

References

1. Harchekar JS, Kandalgaonkar SR (2018) Ban on plastic! A blessing or a curse
2. Forward G (2019) Plastics & the non-renewable component—greening forward. [online] Greening Forward. Available at: http://greeningforward.org/plastics-the-non-renewable-component/ (Accessed 10 May 2019)

3. Liggins M (2019) Plastic bags are a non-renewable resource. [online] City Times. Available at: https://www.sdcitytimes.com/opinion/2012/12/18/plastic-bags-are-a-non-renewable-resource/ (Accessed 10 May 2019)
4. Dorgan JR, Lehermeier HJ, Palade LI, Cicero J (2001) Polylactides: properties and prospects of an environmentally benign plastic from renewable resources. Macromol symposia 175(1):55–66
5. Reddy RL, Reddy VS, Gupta GA (2013) Study of bio-plastics as green and sustainable alternative to plastics. Int J Emer Technol Adv Eng 3(5):76–81
6. Iwata T (2015) Biodegradable and bio-based polymers: future prospects of eco-friendly plastics. Angew Chem Int Ed 54(11):3210–3215
7. Modi AA, Shahid R, Saeed MU, Younas T (2018) Hemp is the future of plastics. In: E3S Web of conferences, vol 51, p. 03002. EDP Sciences
8. Sustainabledevelopment.un.org (2019) [online] Available at: https://sustainabledevelopment.un.org/content/documents/2843WESS2013.pdf (Accessed 17 October 2017)
9. Mail Online (2017) 8 million tons of plastic dumped into oceans each year. [online] Available at: http://www.dailymail.co.uk/sciencetech/article-2951256/Study-World-dumps-8-8-million-tons-plastics-oceans (Accessed 15 Oct 2017)
10. Statista (2019) Regional consumption of plastic materials per capita 2015 | Statistic. [online] Available at: https://www.statista.com/statistics/270312/consumption-of-plastic-materials-per-capita-since-1980/ (Accessed 5 May 2019)
11. Andrady AL (ed) (2003) Plastics and the environment. Wiley
12. Younas T, Akbar MA, Motan I, Ali Y, Atif M (2017) Design and fabrication of an autonomous multifunctional robot for disabled people. In: 2017 4th IEEE international conference on engineering technologies and applied sciences (ICETAS). IEEE, pp. 1–6
13. Bano N, Aziz M, Ghani U, Taha M, Ahmed H (2018) Automatic Book Scanner. IOP Conf Ser: Mater Sci Eng 417(1):012032
14. Saeed A, Ezzi DM, Niazi ARK, Hans MM, Amin W (2018) Steps towards sustainability: Energy generating swing ride. In: 2018 9th international renewable energy congress (IREC). IEEE, pp 1–5
15. Saeed A, Ahmed U, Anwar MU, Fatima M (2018) Steps toward sustainability: Energy through flywheels. In: 2018 7th international conference on renewable energy research and applications (ICRERA). IEEE, pp. 111–116
16. Younas T, Manzoor M, Kumari J (2017) Non-conventional machining processes as expedient alternatives for conventional machining processes. In: 2017 IEEE 3rd international conference on engineering technologies and social sciences (ICETSS). IEEE, pp. 1–5
17. Zheng Y, Yanful E, Bassi A (2005) A review of plastic waste biodegradation. Crit Rev Biotechnol 25(4):243–250
18. Lifewithoutplastic.com (2019) Life without plastic. [online] Available at: http://www.lifewithoutplastic.com/store/how_plastics_affect_the_environment. Accessed 14 May 2019
19. Anon (2017) [online] Available at: http://www.thoughtco.com/benefits-of-plastic-recycling. Accessed 12 Oct 2017
20. Grandviewresearch.com (2019) Medical plastics market size, share, trend | industry report, 2018–2025. [online] Available at: https://www.grandviewresearch.com/industry-analysis/medical-plastics-market. Accessed 1 May 2019
21. Szeteiová K (2010) Automotive materials plastics in automotive markets today. Institute of Production Technologies, Machine Technologies and Materials, Faculty of Material Science and Technology in Trnava, Slovak University of Technology Bratislava
22. Plastivision 2020 (2019) Top 4 Plastic Industry Trends for 2019. [online] Available at: https://www.plastivision.org/blog/top-4-plastic-industry-trends-for-2019/. Accessed 14 Apr. 2019
23. Grida.no (2019) Global plastic production and future trends | GRID-Arendal. [online] Available at: http://www.grida.no/resources/6923. Accessed 14 Apr. 2019
24. Gourmelon G (2015) Global plastic production rises, recycling lags. New Worldwatch Institute analysis explores trends in global plastic consumption and recycling. Recuperado de http://www.worldwatch.org

25. Thompson RC, Moore CJ, Vom Saal FS, Swan SH (2009) Plastics, the environment and human health: current consensus and future trends. Philos Trans Royal Soc B: Biol Sci 364(1526):2153–2166
26. Moore CJ (2008) Synthetic polymers in the marine environment: a rapidly increasing, long-term threat. Environ Res 108(2):131–139
27. Derraik JG (2002) The pollution of the marine environment by plastic debris: a review. Mar Pollut Bull 44(9):842–852
28. Anon (2019) Causes-effects-solutions-of-plastic-pollution. [online] Available at: http://www.conserve-energy-future.com/causes-effects-solutions-of-plastic-pollution. Accessed 15 Oct 2017
29. PLASgran Ltd. (2019) How is plastic recycled?—Plasgran plastic recycling specialists. [online] Available at: https://www.plasgranltd.co.uk/how-is-plastic-recycled/. Accessed 5 May 2019
30. Company C (2019) Plastic recycling—processes, stages, and benefits. [online] Norcalcompactors.net. Available at: http://www.norcalcompactors.net/processes-stages-benefits-plastic-recycling/. Accessed 7 May 2019
31. Prsi.com (2019) Air classifier | polymer recovery systems. [online] Available at: http://prsi.com/products/air-classifier/. Accessed 5 May 2019
32. Anon (2019) Plastic pollution. [online] Available at: http://www.britannica.com/science/plasticpollution. Accessed 14 Oct 2017

Renewables and Waste Management

Heating and Ventilation Performance of a Solar Chimney Designed in a Low-Cost Ecological Home

Hakan Baş and Ayça Tokuç

Abstract The Mediterranean climate requires both winter and summer performance from a building. Construction costs, the environmental impact of construction, energy demand of the building, occupants' health, and thermal comfort are a few of the issues that need consideration in the design of a low-cost ecological home. A solar chimney is a passive design strategy that can be used both as a passive heating and a natural ventilation device. This study aims to design and investigate the heating and ventilation performance of a solar chimney in winter and its overheating risk in summer in a low-cost ecological home designed on the rural site of Izmir, Turkey. This paper performs a comprehensive two-dimensional, numerical computational fluid dynamics (CFD) analysis of the designed solar chimney. The time-dependent transient analysis conducted in the winter and a hot summer day show that solar irradiation is the major driving force in chimney performance. The contribution of the solar chimney to space heating is significant in winter since the average mean temperature inside the chimney is around 44 °C besides the chimney does not cause overheating in summer. The ecological home and solar chimney are under construction and experimental works will be conducted to further this study.

Keywords Solar chimney · Natural ventilation · Computational fluid dynamics (CFD) · Air movement · Passive system

1 Introduction

The focus of this study is to design a solar chimney and investigate its heating and ventilation performance in a new-designed low-cost ecological home located on the rural site of Turkey. There are many reasons for motivation:

H. Baş (✉)
Department of Architecture, Katip Çelebi University, Izmir, Turkey
e-mail: hakan.bas@ikc.edu.tr

A. Tokuç
Department of Architecture, Dokuz Eylül University, Izmir, Turkey
e-mail: ayca.tokuc@deu.edu.tr

Firstly, it is well-documented that the emission of greenhouse gases particularly CO_2 is the major reason for climate change and buildings and the building construction sector has a pivotal role in the reduction of global carbon emissions. Buildings are responsible for nearly 39% of total direct and indirect CO_2 emissions and 36% of global final energy consumption [1]. More specifically, in Turkey, buildings consume 20% of the nation's overall energy [2] and the domestic target to reduce the energy consumption of Turkey is a 20% decrease on 2011 levels by 2023. To achieve this target, the government encourages energy-efficient building design and construction policies for the new buildings. While energy efficiency is a good policy, energy efficiency measures usually increase the cost of building with payback times spanning multiple years, causing questions about whether it is a good investment and for whom [3]. In this context, it is important to consider the cost-effectiveness of the proposed systems while providing energy efficiency.

Secondly, there is a tendency to minimize ventilation rates of air-conditioned spaces in buildings since ventilation-based heat losses increase the heating and cooling energy cost significantly. However, people spend most of their time indoors and low ventilation rates negatively affect indoor air quality (IAQ), human health, occupant comfort, and productivity. A number of studies show that the ventilation rate below 10 l/s per person results in health problems, also called sick building syndrome (SBS) [4–6]. The main cause of SBS phenomenon is airborne infections and adequate ventilation is necessary to mitigate its effects [7–10].

Ventilation is the exchange between indoor and outdoor air, which enables discharge of polluted air and intake of presumably fresh and clean air [11]. However, the natural exchange of heated indoor air with cold outdoor air is not an energy-efficient way since it causes a loss of heated air. Providing an energy-efficient solution for ventilation and reducing ventilation-based heat losses in buildings, mechanical ventilation with heat recovery system is generally proposed. It is well published that mechanical ventilation with a heat recovery system (MVHR) is more energy efficient than natural ventilation; however, it is claimed that it causes more health-related symptoms. Jaakkola et al. [12] studied an office building with 2150 employees to test the effects of mechanical ventilation on SBS. They found that although the mean ventilation rate was 26 l/s/person, mechanical ventilation caused symptoms typical of the SBS, which are nasal, eye, and mucous membrane symptoms, lethargy, skin symptoms, and headache. Finnegan et al. [13] conducted a doctor-administered questionnaire to inquire into symptoms associated with SBS in naturally and mechanically ventilated office buildings. Significant excesses in the nasal, eye and mucous membrane symptoms with lethargy, dry skin, and headaches were found in mechanically ventilated buildings when compared to naturally ventilated buildings.

Compared with mechanical ventilation with heat recovery (MVHR), the natural ventilation system is not considered an energy-efficient solution but it causes less SBS syndrome. Providing an energy-efficient approach for building ventilation, natural ventilation integrated with passive solar systems is a sustainable alternative system that is widely used to improve both energy efficiency and indoor air quality in buildings. In this regard, a solar chimney is the focus of this study in terms of

achieving energy-efficient space air-conditioning, as well as providing good IAQ to maintain safe and healthy indoor environments, well-being, and sustainability.

The natural ventilation provided by a solar chimney is caused by either buoyancy or wind. To enhance buoyancy, a chimney is placed facing the South (in the northern hemisphere) and its southern wall is a transparent sheet, i.e., glazing, that allows the collection and use of solar irradiation [14]. A solar chimney has many environmental benefits. First, it collects, stores, and transfers energy for heating of the spaces. Second, it acts as a buffer zone reducing infiltration and physical heat losses from the adjacent space and third, it provides the supply of preheated air in ventilating the adjacent space. In operation, at first, the glazing acts as a solar aperture and collects solar energy to heat the air inside, and thus creates a higher temperature difference between the inside and outside, which is sufficient to generate air movement in the upward direction—in reverse to gravity.

The factors that influence the performance of a solar chimney depend on the type of solar chimney, geometrical variables such as chimney height and width, glazing inclination, inlet and outlet opening area, height/gap ratio, and also ambient variables such as properties of the glazing, absorber walls and inside, outside air temperature, solar irradiation, external wind velocity, and humidity [15]. Bassiouny and Koura [16] investigated the effect of chimney width, both analytically and numerically. They found that increasing chimney width by a factor of three improved the air change per hour by almost 25%. Mathur et al. [17] conducted an experimental study on a solar chimney to study the effect of solar radiation and the air gap between absorber and glass cover. They found that the airflow increases with an increase in solar radiation and the gap between absorber and glass cover. In another study, Mathur et al. [18] investigated the effect of inclination of absorber on the airflow rate of roof solar chimney. They found that the optimum inclination varies from 40 to 60 depending upon latitude. They also concluded that the flow rate increases with an increase in the air gap and inlet height [18]. Many passive solar chimneys are designed without the use of any numerical model and calculation. The design generally is done by intuition, imitation, or rules of thumb [19]. However, predicting the calculation performance of the proposed model with numerical study at an early design stage can prevent ineffective design prototypes. Computational fluid dynamics (CFD) technique is used for solar chimney design with the improvement of computer power and technology. With the use of CFD, it is possible to make an initial prediction of temperature and air velocity field in a chimney in relation to outer weather conditions. CFD can help to improve and optimize the performance of the model, depending on the initial predicted performance of the chimney.

This study investigates the design, heating, ventilation performance of a solar chimney. The solar chimney was specifically designed for a low-cost ecological home located on the rural site of Izmir. Its effects on heating and ventilation performance of the building were investigated through transient CFD simulations. First, the model was developed and validated through the published experimental data. Then two scenarios that represent the winter and summer worst cases were simulated. The first case represented the 15th of January and investigated the best possible heating performance of the solar chimney on a winter day when the daily maximum solar

irradiance is at the lowest rates. The second case represented the 15th of July and investigated the worst case in summer (overheating risk) when the daily maximum solar irradiance is at the highest rates.

2 Low-Cost Ecological Home Design with a Solar Chimney

2.1 Climate and Location

The project site is located in the city of Izmir, Turkey which is at 38.23°N latitude and 26.84°E longitude. The climate of Izmir shows the characteristic features of typical Mediterranean climate labeled with Csa in the Köppen climate classification. The city mostly experiences hot-dry summers and wet mild winters. July is the warmest month with an average maximum temperature of 33.2 °C and January is the coldest month with an average minimum temperature of 5.9 °C. According to the heating degree hours data between the years of 2008 and 2018, Izmir is classified as a heating-dominated climate with heating degree hours of 934 and cooling degree hours of 660. Figure 1 shows the daily average maximum and minimum external temperatures and Fig. 2 shows the hourly average solar insolation rate in the city of İzmir according to the meteorological database of Turkish State Meteorological Service between 1990 and 2010 [20].

2.2 Project Description

The low-cost ecological home was designed in eco-village Seferihisar that is located at the open part of the land and is surrounded by large fields in the town of Seferihisar in İzmir. The project site is an ideal location for the design of an ecological home
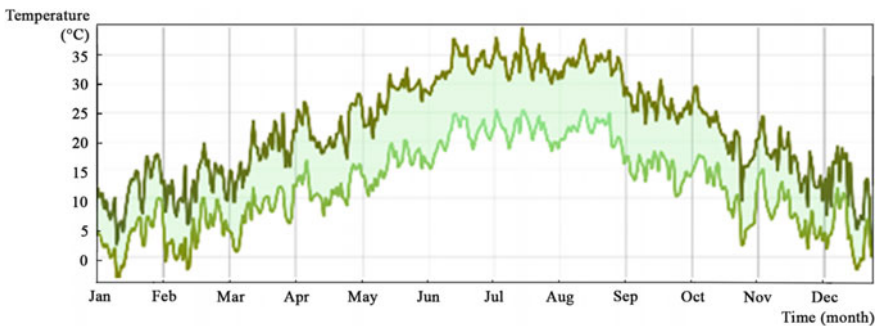
Fig. 1 Daily average maximum and minimum external temperatures (between the years of 1990 and 2010) in İzmir
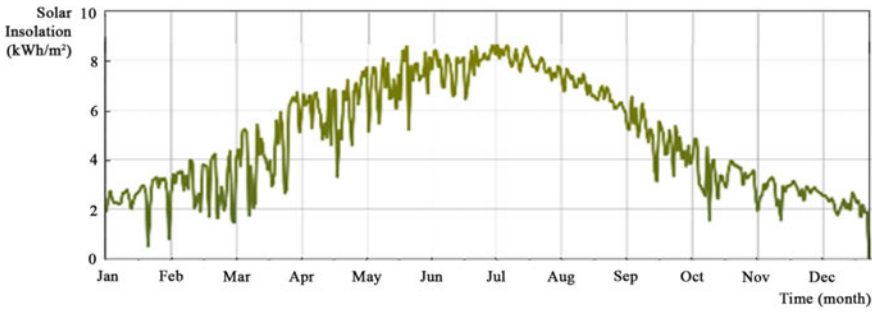
Fig. 2 Hourly average solar insolation (between the years of 1990 and 2010) in İzmir

and a solar chimney since it can take advantage of the sun and wind without any physical obstructions.

From a larger perspective, the project aims to take advantage of local climatic conditions to reduce fossil fuel dependency for space heating, cooling, and ventilation. To achieve this, it focuses on using renewable solar energy in building design. Therefore, an in-depth analysis of climatic conditions has been considered in the initial design process. Due to the limited budget of the project, low-cost passive energy systems for air-conditioning were adopted in place of the high-cost mechanical systems having a high maintenance cost. More specifically, the project aims to provide energy efficiency, good IAQ, and sustainability by means of a solar chimney as mentioned in the literature review. The solar chimney was designed as an integrated solution to reduce both space heating and cooling energy use and to provide energy-efficient ventilation. The solar chimney was attached to the living room, where it is mostly used during the day. It occupies a small indoor space area and a small portion of the South façade in order not to block the impressive lake scenery when looking from the living room.

The project has been designed for a family of four. It has a very simple building program that consists of a living room, a kitchen, and two bedrooms and it was designed as a one-story detached house that is 8 m wide and 8 m deep with the front façade oriented to the South. In the design of a passive solar home, maximum solar façade area is necessary to take advantage of the solar power. However, due to the parcel structure and land restriction in the eco-village, it was not possible to use an elongated building form on the East and West axis, which would maximize the solar façade area on the Southside. Against this problem, the height of the building on South facade was maximized—it changes from 2.60 m at the middle to 3.10 m at the apex of the building (from North to South) to increase the solar façade area. In this way, on the South façade, the height of the solar chimney was determined as 3.10 m. As different from the South façade, the northern facade was kept as small as possible to minimize the heat losses from the building. Figure 3 shows a view from the low-cost ecological home that is under construction.

Fig. 3 A view of the low-cost ecological home

3 Method

The preliminary design of the building and the solar chimney considered conditions of cost, scenery, and space use as well as the desire to make use of solar energy for space heating and ventilation. In this chapter, the designed solar chimney is evaluated in terms of heating, ventilation, and overheating. The chimney was solved in a commercial finite-volume solver, ANSYS-FLUENT v18.1 that is a CFD simulation tool capable of such an analysis. The case was solved as transient to simulate accumulation of heat depending on the variance of solar radiation through the day. The following were assumed to define the model:

(1) The flow is laminar, continuous, incompressible, and two-dimensional.
(2) Frictional forces in reverse to the airflow are neglected.
(3) One-directional heat transfer is assumed in the heat transfer process through the glazing aperture into the absorber wall.
(4) Air temperature and wind force at different points of the inlet grille are equal.
(5) Thermal capacities of glazing and absorber wall are neglected.

The governing equations are as follows:
Two-dimensional, incompressible, transient flow equations are given by

Continuity:

$$\frac{\partial \rho}{\partial t} + \frac{\partial (\rho\, u)}{\partial x} + \frac{\partial (\rho\, v)}{\partial y} = 0 \tag{1}$$

X—Momentum

$$\frac{\partial (\rho u)}{\partial t} + \frac{\partial \left(\rho u^2\right)}{\partial x} + \frac{\partial (\rho u v)}{\partial y} = -\frac{\partial p}{\partial \mathrm{x}} + \frac{1}{\mathrm{Re}_r}\left[\frac{\partial \tau_{xx}}{\partial x} + \frac{\partial \tau_{xy}}{\partial y}\right] \tag{2}$$

Y—Momentum

$$\frac{\partial (\rho v)}{\partial t} + \frac{\partial \left(\rho v^2\right)}{\partial y} + \frac{\partial (\rho u v)}{\partial x} = -\frac{\partial p}{\partial y} + \frac{1}{\mathrm{Re}_r}\left[\frac{\partial \tau_{xy}}{\partial x} + \frac{\partial \tau_{yy}}{\partial y}\right] \tag{3}$$

Energy:

$$\frac{\partial (E_t)}{\partial t} + \frac{\partial (u E_t)}{\partial x} + \frac{\partial (v E_t)}{\partial y} = -\frac{\partial (up)}{\partial x} - \frac{\partial (vp)}{\partial y}$$
$$+ \frac{1}{\mathrm{Re}_r}\left[\frac{\partial}{\partial x}\left(u\tau_{xx} + v\tau_{xy}\right) + \frac{\partial}{\partial y}\left(u\tau_{xy} + v\tau_{yy}\right)\right] - \frac{1}{\mathrm{Re}_r\,\mathrm{Pr}_r}\left[\frac{\partial q_x}{\partial x} + \frac{\partial q_y}{\partial y}\right] \tag{4}$$

where p is the pressure, ρ is the density, t is the time, u and v are the velocity components, τ is the stress, Re is the Reynolds number, E_t is the total energy, q is the heat flux, and Pr is the Prandtl number.

The numerical model is validated in accordance with the results of the natural convection experiment conducted by Bouchair [21] and the study by Gan and Riffat [22] that utilized its results for validation. Time-dependent transient analyses were conducted in a cold winter day and a hot summer day using twenty years average climate data [20]. Time-dependent temperature and velocity magnitude change in the solar chimney data are evaluated after the simulation.

4 Passive Solar Design

Passive solar systems are divided into three. These are direct gain, indirect gain, and isolated gain. Direct gain is the system that collects solar energy by large glazing aperture and distributes it passively as heat. Indirect gain contains the system referred to as the Trombe wall technology that consists of a thick masonry wall behind a glass external layer to passively heat the building. Isolated gain is another passive system which consists of an insulated wall and a glass external layer to collect solar energy in a place that is thermally segregated from the adjacent space. Due to the thermal segregation between two separated spaces, the isolated gain system enables preheating of the air in combination with ventilation. One of the isolated systems is

a solar chimney that is the focus of this study since it provides both passive heating and ventilation.

In this project, the low-cost ecological home was oriented to the South, which provides net solar energy gain and has impressive lake scenery. Therefore, to use an indirect system—a Trombe wall—having a high percentage of blind façade was not a sensible solution since it occupies most of the façade for passive solar heating and therefore blocks the scenery. Another option of the direct gain system with large glazing area on South is an effective solution for space heating but it is insufficient since its use could not be sufficient for building ventilation. Therefore, in place of a Trombe wall and direct gain system, a solar chimney that provides both space heating and ventilation but does not block scenery due to its vertical thin channel geometry was preferred.

4.1 Solar Chimney Design

A wide range of factors such as geometry, function, position, and glazing type should be considered in the design of a solar chimney. Solar chimneys are classified depending on these factors. According to geometry, a solar chimney can have open- or close-ended channel geometry. According to function, it can be used for ventilation, heating, or cooling. According to position, it can be located on either the wall or the roof. According to glazing, a solar chimney can use single or multi-glazing or has vertical or inclined glazing [23].

In this project, the solar chimney consists of two separate but interconnected parts (Fig. 4). The lower part of the chimney has close-ended channel geometry and it was designed for space heating and ventilation function (Fig. 5a). Yet the upper part of the chimney has open-ended channel geometry and it was designed for space cooling and ventilation function (Fig. 5b). The chimney is located on the South façade wall and uses a double glazing window. The operation of the chimney is quite simple. The chimney has three insulated grilles located in different positions, the position of which can be changed seasonally. Depending on the operation mode of the insulated grilles, the chimney can provide ventilation and heating in winter and prevent overheating risk in summer.

This project was designed for a real client; therefore, the cost and the space requirement of the chimney were very important due to the private preferences. In low-cost housing, a number of studies investigate the energy consumption [24, 25] indoor air quality (IAQ) [26, 27] and occupant thermal comfort [28, 29]. In the final stage of this study, while the solar chimney occupies only 11% of the South facade area, it accounts for 1% of the total floor area. On the other hand, the cost of solar chimney accounts for only 3% of the total building cost. Therefore, a compromise between the performance of solar chimney, its cost, its space requirements, and the scenery was achieved.

The geometrical features of the proposed solar chimney are given in Fig. 6a. The solar chimney has a close-ended vertical channel geometry, which is 2.40 m tall and

Fig. 4 The solar chimney system placed on the South facade (the left side of the picture)
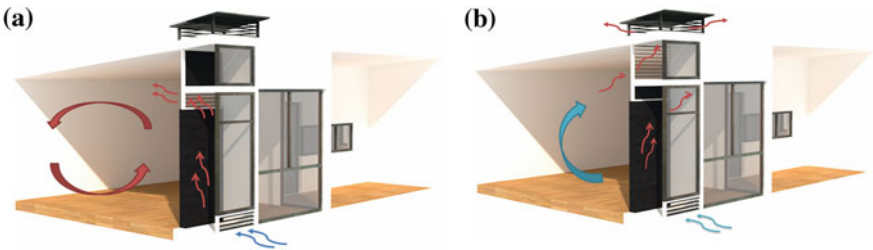
Fig. 5 **a** Winter operation mode of the solar chimney, **b** summer operation mode of the solar chimney

its horizontal cross-section is 0.57 m/0.88 m with the major dimension along the east-west orientation. The dimension of 0.57 m is for service accessibility. It has two insulated grilles, one of them is below the glazing and the other one is between the chimney and the adjacent room. Insulated grilles were designed to be airtight thus to prevent reverse heat flow and to reduce heat losses when the chimney is not in operation. In addition, there is a flap on the upper side of the glazing to prevent overheating risk in summer. The inlet opening is also 0.30 m high and 0.88 m wide. The solar chimney was oriented to the South to provide maximum benefit from the sun and integrated to the main room whose relation is shown in Fig. 6b.
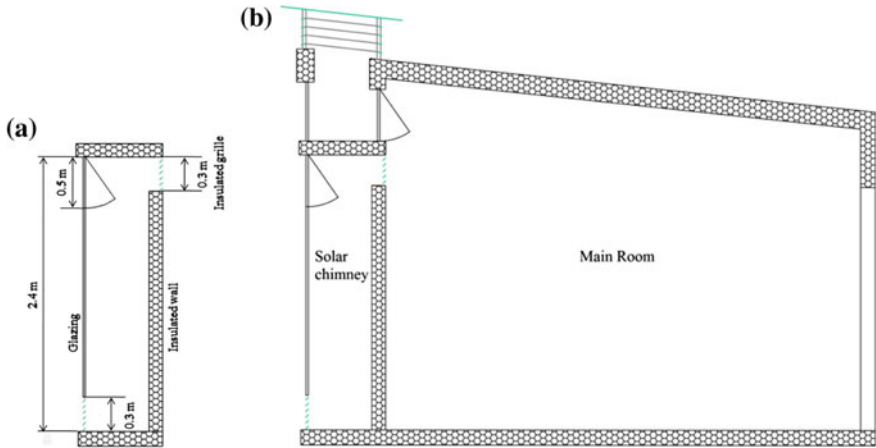
Fig. 6 **a** Section of the solar chimney, **b** section of the solar chimney integrated into the main room

4.2 Validation of the CFD Model

The results of the natural convection experiment conducted by Bouchair [21] and the study by Gan and Riffat [22] that utilized its results for validation have been used to validate the CFD model. The published solar chimney used for validation is 3 m tall, and its horizontal cross-section is 0.20 m high and 1 m wide [22]. Its solar collecting transparent element lied along the east-west orientation. The inlet opening of the chimney also had 0.20 m height and 1 m width. In the validation study, the solar heat gain of the chimney was calculated from the mean total solar irradiance and mean solar gain factor. Double glazing, whose solar gain factor is 0.64 was used. The mean solar irradiance on the vertical South surface was taken to be 438 W/m². The exhaust air entering into the chimney was assumed to be at 20 °C with 50% relative humidity and the outside air temperature was 0 °C. A uniform rectangular mesh structure with a maximum mesh size of 5 mm was used.

The model results show good agreement between the published results given in Table 1, which shows the difference in results between the published study and this model's simulation results. The agreement between airflow patterns is shown in Fig. 7a, b. The variables of the outside temperature, solar irradiance, and glazing type are given in Table 1 and the effects of these variables on the chimney performance

Table 1 Published and simulated performance of the 3 m high solar chimney without wind forces

Glazing type	$T(°C)$	$Q(W/m^2)$	Published T_w (°C)	Simulated T_w (°C)	Published T_g (°C)	Simulated T_g (°C)
Double	10	280	63.2	62.93	20.2	20

Q—wall solar heat gain; T_g—area-weighted mean temperature of the interior surface of the glazing; T_w—area-weighted mean temperature of wall surface facing glazing
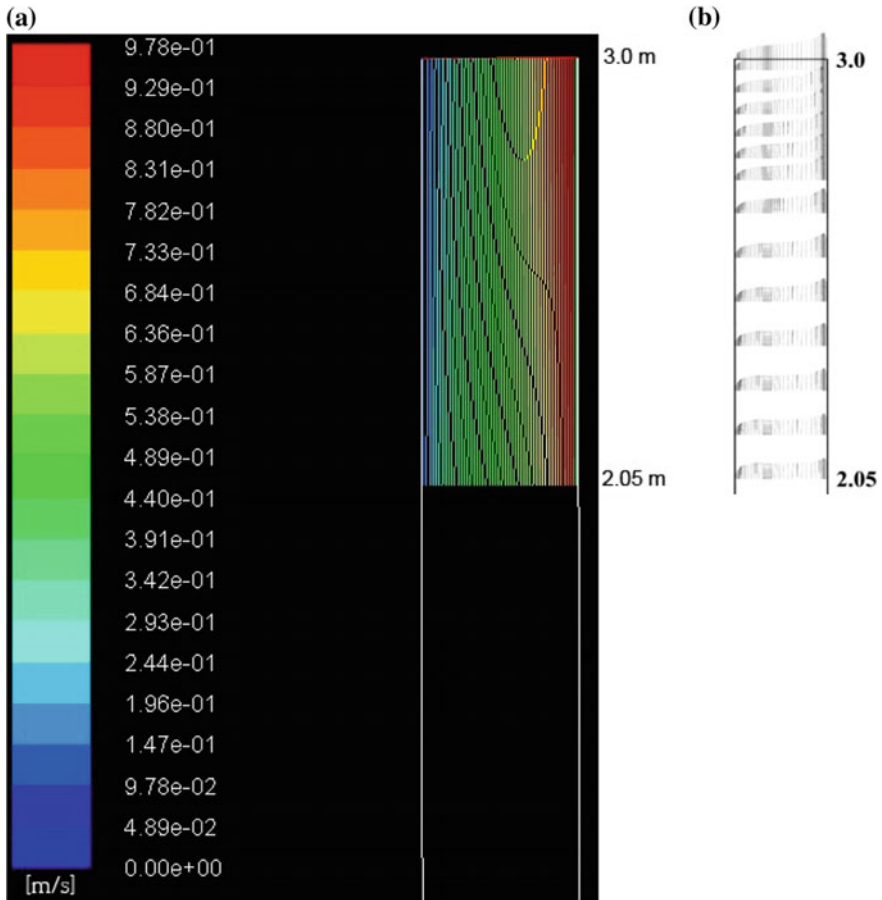
Fig. 7 a Predicted airflow pattern in the model (velocity scale 1 m/s), **b** airflow pattern in the published study

are compared. The deviation from the published result is found to be 0.27 °C which is equal to 0.42% for area-weighted average wall surface temperature and 0.20 °C which equals to 1% for area-weighted average glazing surface temperature. This fit around 1% of natural convection in solar chimneys is enough for the purpose of this study.

4.3 Numerical Study of the Solar Chimney

The validated model was used to conduct a transient analysis to test the effect of time-dependent variations of outside air temperature and global solar radiation on chimney temperature stratification, airflow behavior, and chimney wall and glazing temperature. To achieve this, a user-defined function (UDF) was written in C programming language and linked with the FLUENT solver to assign varying values to boundaries for global solar radiation, outdoor air temperature, and sky temperature data. The study is based on the application of the finite-difference model to the chimney glazing assuming unsteady-state one-dimensional heat transfer. Glazing emits heat toward the wall surface and the chimney is heated.

4.3.1 Simulation Setup Details

The SIMPLE algorithm was used to solve velocity and pressure conservation equations. Second-order and second-order upwind algorithms were used to solve the pressure area and momentum equations, respectively. The first-order upwind algorithm was used for turbulent kinetic energy and turbulent dissipation rate. The convergence criterion for all parameters was assumed to be 10^{-4}. The inlet volumetric flow rate was 100 l/s and external emissivity of the wall was 0.90. As the turbulence model, a widely used, standard k–ε turbulence model was used.

4.3.2 Mesh Structure

The mesh size and mesh arrangement is the major indicator in solving equations. The frequency and the quality of mesh arrangement are vital in providing time-efficiency and accuracy. In this study, a uniform rectangular mesh structure has been selected and the maximum mesh size was defined as 5 mm. In total, the mesh structure consists of 55,200 quadrilateral cells.

5 Results and Discussion

Solar irradiance is the driving force of the chimney; therefore, the effect of time-dependent variations in solar irradiance during the day was calculated with transient simulations. In addition, its transient nature allowed for accurate simulation of temperature and velocity field.

5.1 Winter Case

The simulation was performed in fifteen-minute intervals from 9.00 a.m. to 16.00 p.m. for the 15th of January. Since solar irradiance is one of the driving forces in chimney performance and its intensity fluctuates during the day, the influence of time-dependent variations of solar irradiance on chimney performance was calculated during the day. Figure 8a illustrates the average temperature field in the chimney during the day. The general tendency of the air temperature is increasing in accordance with an increase in height. The area-weighted average wall temperature is around 44 °C and varies from a minimum of 7 °C to a maximum of 52 °C during the simulation time. Figure 8b shows the velocity field when the flaps of the grilles are open. Air velocity varies from 0.0 to 1.21 m/s inside the chimney. While the air velocity is around 0.5 m/s around the inlet grille, it is stagnant on the glazing surface. As long as the air rises, air movement increases and reaches its peak value with 1.21 m/s around the grille between the chimney and the adjacent room.
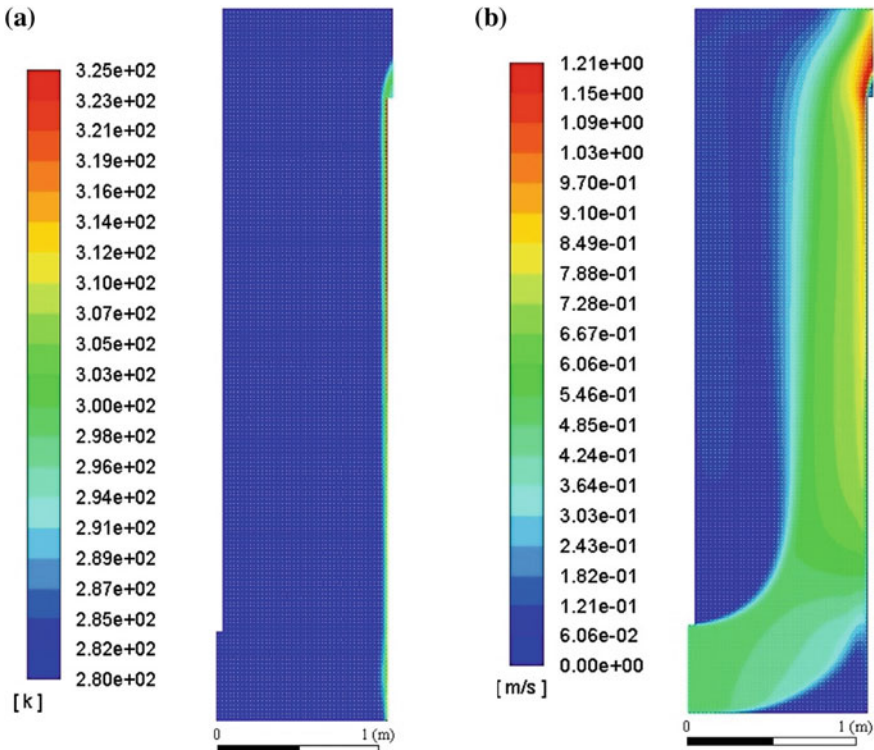
Fig. 8 **a** Contours of static temperature in the chimney for winter, **b** contours of velocity magnitude in the chimney for winter

5.2 Summer Case

The transient simulation was performed for the 15th of July during the day. Figure 9a shows the static temperature variations of wall and interior domain for different heights of the chimney. The general tendency of the air is that its temperature increases with the increase in height. Chimney wall temperature and heat gain are considerably high in summer. The area-weighted average wall temperature is around 80.07 °C and the area-weighted average glazing temperature is around 35.00 °C. Overheating risk is possible even if the chimney is ventilated. Figure 9b shows the velocity field when the flaps of grilles are open. Velocity varies from 0.0 to 0.9 m/s inside the chimney. Air velocity is quite stagnant around the glazing surface, yet it reaches the peak around the upper grille.

This study aims to design a solar chimney and investigate its heating and ventilation performance in a new-designed low-cost ecological home located on the rural site of Izmir, Turkey. The results show that the proposed solar chimney shows good heating and ventilation performance in the climate of Izmir and can be utilized as a passive heating device to reduce heating demand in winter. In addition, it is found that the chimney can be operated without the need for any mechanical devices and electricity use by only using buoyancy force taken from renewable solar energy.

There are similarities between the overall conclusions of this study and previous studies conducted in different climates and cities. Rabani et al. designed a new Trombe wall in the form of a solar chimney that has 3 m height, 1 m length, and
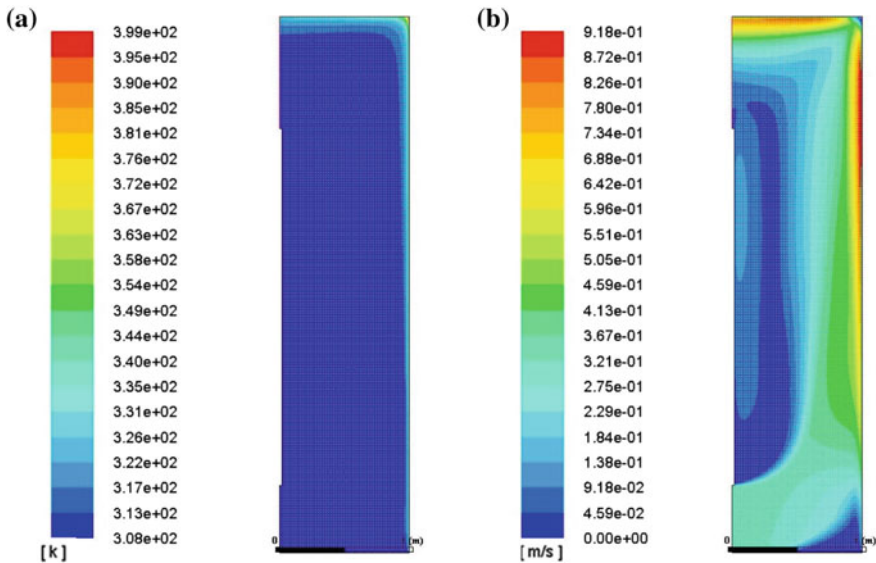
Fig. 9 **a** Contours of static temperature in the chimney for summer, **b** contours of velocity magnitude in the chimney for summer

0.20 m width. Different from the conventional systems, this system receives solar radiation from three directions (East, South, and West). They tested the heating performance of the system during winter operation for Yazd city (Iran) in the desert climate. They found that the average wall temperature (absorber) reaches around 47 °C on the coldest winter days, similar to our findings of 44 °C. When comparing the performance of these solar chimneys, it should be noted that our system has less glazing surface area; therefore, the temperature might be lower. Also, it should be noted that the difference in solar intensity depending on the climate and location changes the results to some extent.

Studies conducted in different climates of cities focus on testing of glazing type, air gap, chimney height, and the tilt angle of the glazing to achieve the high-performance solar chimneys. But, the chimney in this study was designed for a real client and it is, therefore, different from a theoretical and experimental study since providing a compromise between its cost and its space requirement, and scenery problem was very important in design process along with the performance of the chimney. Therefore, the design optimized these special requirements. For example, Mathur [17] found that the airflow increases with an increase in the gap between absorber and glass cover at Jaipur (India). In our study, this gap was taken as 0.57 m that is quite bigger than the gap determined in most of the studies. This gap is very important for the occupant since keeping that space clean is important for providing IAQ. With this preference of large gap, a ventilation rate that is enough to operate the chimney without any additional mechanical types of equipment was achieved.

In the designed solar chimney, in summer operation, the area-weighted average wall temperature was found as 80.07 °C. This means that the absorber wall can cause conductive heat transfer toward the adjacent space even though it is well insulated and there is a ventilation system that exhausts the warm air outside. It should be said that the insulation level of the absorber wall and grille and their airtightness are very important in the solar chimney design.

The designed solar chimney is easy to maintain for the function of heating and ventilation. Using renewable solar energy in the operation of the chimney cannot cause pollution on the environment and CO_2 emission. However, the cost, the space requirement, and the need for expertise in performance evaluation (such as CFD techniques) are three limitations of the solar chimney system. While the cost of the chimney accounts for 3% of the total cost, the space requirement of the chimney accounts for 1% of the total floor area. Therefore, in this study, these limitations have been considered at the early design stage, which led to a satisfactory solution.

6 Conclusion

In this paper, the design process of a solar chimney in a low-cost ecological home was explained and its heating and ventilation performance was tested using a full-scale CFD model. In transient simulations, it is found that temperature distribution

and flow behavior were primarily influenced by the solar irradiation rate. The temperature stratification inside the chimney shows that the air temperature would reach a maximum of 52 °C on a winter day with the least amount of solar irradiation. Therefore, the solar chimney can significantly contribute to space heating in winter. Air movement in the chimney is sufficient to operate the chimney and it varies from 0.5 to 1.21 m/s.

In conclusion, the proposed solar chimney shows good heating and ventilation performance in the climate of Izmir and can be utilized to considerably reduce heating demand. Also, the chimney is operated without the need for any mechanical device and electricity use. However, there is a possibility of overheating risk and shading can be applied to the chimney to prevent this and thus improve its summer performance.

As further research, the effect of various design configurations and different material properties on chimney performance can be tested to make the chimney more energy efficient. In addition, on-site measurements will be carried out when the building is completed.

References

1. IEA (2017) The global status report: towards a zero-emission, efficient, and resilient buildings and construction sector. https://www.iea.org/topics/energyefficiency/buildings/. Accessed 20 April 2019
2. Enerji veTabii Kaynaklar Bakanlığı (2016) Denge Tablosu. http://www.eigm.gov.tr/tr-TR/Denge-Tablolari/Denge-Tablolari. Accessed 25 April 2019
3. Winkler H, Spalding-Fecher R, Tyani L, Matibe K (2002) Cost-benefit analysis of energy efficiency in urban low-cost housing. Dev South Afr 19(5):593–614)
4. Mendell MJ (1993) Non-specific symptoms in office workers: a review and summary of the epidemiologic literature. Indoor Air 3:227–236
5. Godish T, Spengler JD (1996) Relationships between ventilation and indoor air quality: a review. Indoor Air 6:135–145
6. Menzies D, Bourbeau J (1997) Building-related illnesses. New Engl J Med 337:1524–1531
7. Gustafson TL, Lavely GB, Brawner ER Jr, Hutcheson RH Jr, Wright PF, Schaffner W et al (1982) An outbreak of airborne nosocomial varicella Pediatrics 70(4):550–556
8. Bloch AB, Orenstein Walter A, Ewing WM, Spain WH, Mallison GF, Herrmann KL (1985) Hinman A R (1985) Measles outbreak in a pediatric practice: airborne transmission in an office setting. Pediatrics 75(4):676–683
9. Hutton MD, Stead WW, Cauthen GM, Bloch AB, Ewing WM et al (1990) Nosocomial transmission of tuberculosis associated with a draining abscess. J Infect Dis 161(2):286–295
10. Calder RA et al (1991) Mycobacterium tuberculosis transmission in a health clinic. Bull Int Union Against Tuberc Lung Dis 66(2–3):103–106
11. Wargocki P, Sundell J, Bischof W, Brundrett G, Fanger PO, Gyntelberg F, Hanssen SO, Harrison P, Pickering A, Seppanen O, Wouters P (2002) Ventilation and health in non-industrial indoor environments: report from a European multidisciplinary scientific consensus meeting (EUROVEN). Indoor Air 2002(12):113–128
12. Jaakkola JJK, Heinoneon OP, Seppänen O (1991) Mechanical ventilation in office buildings and the sick building syndrome. An experimental and epidemiological study. J Indoor Air 1(2)
13. Finnegan MJ, Pickering CA, Burge PS (1984) The sick building syndrome: prevalence studies. Br Med J 289(8)

14. Sakonidou EP, Karapantsios TD, Balouktsis AI, Chassapis D (2008) Modeling of the optimum tilt of a solar chimney for maximum air flow. Sol Energy 82(2008):80–94
15. Shi L, Zhang G, Yang W, Huang D, Cheng X, Setunge S (2018) Determining the influencing factors on the performance of solar chimney in buildings. Renew Sustain Energy Rev 88:223–238
16. Bassiouny R, Koura Nader SA (2008) An analytical and numerical study of solar chimney use for room natural ventilation. Energy Build 40(2008):865–873
17. Mathur J, Bansal NK, Jain M, Mathur S, Anupma (2005) Experimental investigations on solar chimney for room ventilation. Sol Energy 80(2006):927–935
18. Mathur J, Mathur S, Anupma (2006) Summer-performance of inclined roof solar chimney for natural ventilation. Energy Build 38(2006):1156–1163
19. Balcomb JD (1992) Introduction, passive solar buildings. In: Balcomb JD, Barker G (eds) Hancock. The MIT Press, Cambridge, MA, pp 1–37
20. Turkish State Meteorological Service (2011) Private communication for climate data
21. Bouchair A (1994) Solar chimney for promoting cooling ventilation in southern Algeria. Build Serv Eng Res Technol 15(2):81–93
22. Gan G, Riffat SB (1998) A numerical study of solar chimney for natural ventilation of buildings with heat recovery. Appl Therm Eng 18(1998):1171–1187
23. Tan AYK, Wong NH (2012) Natural ventilation performance of classroom with solar chimney system. Energy Build 53(2012):19–27
24. Georges L, Massart C, Van Moeseke G, De Herde A (2012) Environmental and economic performance of heating systems for energy-efficient dwellings: case of passive and low-energy single-family houses. Energy Policy 40:452–464. Life-cycle energy, costs, and strategies for improving a single family house. J Ind Ecol 4(2), 135–156
25. Morrissey J, Moore T, Horne RE (2011) Affordable passive solar design in a temperate climate: an experiment in residential building orientation. Renew Energy 36(2):568–577
26. Truong H, Garvie AM (2017) Chifley passive house: a case study in energy efficiency and comfort. Energy Procedia 121:214–221
27. Makaka G, Meyer EL, McPherson M (2008) Thermal behaviour and ventilation efficiency of a low-cost passive solar energy efficient house. Renew Energy 33(9):1959–1973. Keoleian GA, Blanchard S, Reppe P (2000)
28. Nguyen AT, Reiter S (2014) Passive designs and strategies for low-cost housing using simulation-based optimization and different thermal comfort criteria. J Build Perform Simul 7(1):68–81
29. Garde F, Adelard L, Boyer H, Rat C (2004) Implementation and experimental survey of passive design specifications used in new low-cost housing under tropical climates. Energy Build 36(4):353–366

Anaerobic Digestion of Aquatic Plants for Biogas Production

Tülay Güngören Madenoğlu, Nasim Jalilnejad Falizi, Habibe Serez, Nalan Kabay, Aslı Güneş, Rajeev Kumar, Taylan Pek and Mithat Yüksel

Abstract Limited reserves of fossil fuel resources and negative environmental impacts increased energy demands toward renewable energy technologies. Bioenergy is one of the solutions, and biogas production from wastes and residues by anaerobic digestion (AD) is a promising technology. Municipal solid wastes, sludge from wastewater treatment plants, agricultural plant wastes, forestry residues and manure are the widely used sources in AD for biogas production. Aquatic plants can be evaluated as a renewable energy source. If waste and residues of these plants are

T. Güngören Madenoğlu (✉) · N. Jalilnejad Falizi · H. Serez · N. Kabay (✉) · R. Kumar · M. Yüksel
Chemical Engineering Department, Faculty of Engineering, Ege University, 35100 Bornova, Izmir, Turkey
e-mail: tulay.madenoglu@ege.edu.tr

N. Kabay
e-mail: nalan.kabay@ege.edu.tr

N. Jalilnejad Falizi
e-mail: nasim.jalilnejad@gmail.com

H. Serez
e-mail: habibesrz@gmail.com

R. Kumar
e-mail: rajeevkumar@gmail.com

M. Yüksel
e-mail: mithat.yuksel@ege.edu.tr

N. Jalilnejad Falizi
Biotechnology Division, Graduate School of Natural and Applied Sciences, Ege University, Izmir, Turkey

A. Güneş
Bayındır Vocational School, Ege University, Izmir, Turkey
e-mail: asligunes@gmail.com

Landscape Architecture Department, Izmir Democracy University, Izmir, Turkey

T. Pek
ITOB-OSB, Tekeli, Menderes, Izmir, Turkey
e-mail: taylanpek77@gmail.com

not utilized in beneficial use, greenhouse gases (GHG) will be emitted through land-filling or direct combustion. Wastes should be converted to biogas with a high yield to decrease the quantity of wastes and biogas with a high-energy content. Substrate to inoculum ratio, temperature regime, C/N ratio, pH, volatile fatty acid and ammonia content are important process parameters for AD. Modified Gompertz, Cone and first-order equations are widely used model equations for kinetic parameters that are used in kinetic models (Monod, modified Andrew, Ratkowsky) for identification of optimum substrate concentration and temperature for each specific feed. This chapter evaluates effective process parameters on AD of aquatic plants for biogas production and application of kinetic analysis for assignment of optimum conditions.

Keywords Anaerobic digestion (AD) · Aquatic plant · Biogas · Kinetic analysis, methane

1 Introduction

Increasing energy demands, decreasing resources of fossil fuels and concern about environmental protection are the main reasons to use renewable and environmentally benign energy sources [1]. Biomass is one of the renewable sources having advantages of wide availability and great energy potential. While the energy potential of biomass in 2016 was about 50 EJ that was 14% of the world's final energy use, its realistic potential was estimated as 150 EJ by 2035 [2]. Most of the biomass potential was originated from agricultural residues and wastes, energy crops, forestry products and residues. Comparing with these agricultural and terrestrial plants, aquatic plants are accepted as prominent renewable energy resource since they are harvested with high yields and significant contributors to future biomass potential [3, 4]. Water lettuce, water hyacinth and salvinia as aquatic plants are very aggressive invader plants that are used in phytoremediation but they can form a layer over the rivers, lakes or ponds and threaten the irrigation, navigation systems and aquatic life. To overcome these negative impacts of aquatic plants, herbicides are used to suppress their vegetation or they are piled and then burned. These applications are not environmentally friendly preferences. Instead, aquatic plants can be evaluated in energy production such as biogas production by AD. Produced biogas can be supplied to a variety of uses including electricity, heat and power generation. AD also provides waste minimization and remaining solid residue after AD can be used as biofertilizer.

Hydrolysis, acidogenesis, acetogenesis and methanogenesis are the main reaction steps in AD. Simple sugars, sucrose, glucose and fructose, are formed by hydrolysis of carbohydrates. Proteins and lipids decay to amino acids and long-chain fatty acids, respectively. Fermentation reactions of acidogenic bacteria convert simple sugars, amino acids and long-chain fatty acids to intermediate compounds (VFAs) such as acetic acid, propionic acid, butyric acid and valeric acid. Intermediate compounds are metabolized into acetic acid, carbon dioxide and hydrogen by acetogenic bacteria. Two varieties of methanogens are active in the final step which is methanogenesis.

One of the groups directs formation of methane by reduction of CO_2 using H_2 as the electron donor, and other group cleaves acetic acid into CH_4 and CO_2 [5].

Composition of the substrate is important for AD as every fraction is not decomposed easily. Lignocellulosic substrate is mainly consisting of cellulose, hemicellulose, lignin, extractives and inorganics. Main fractions of holocellulose (cellulose and hemicellulose) are easily decomposed by microorganisms during AD. But lignin forms a rigid structure inside holocellulose, and it retards decomposition of substrate [6]. High holocellulose content and low lignin content of aquatic plants are advantages for biogas production [7].

Biogas production from aquatic plants such as water lettuce, water hyacinth, cabomba and salvinia was investigated by using AD [3, 8–13]. The pilot-scale digestions resulted in biogas yield (approximately 50% of methane content) as 267 L biogas kg^{-1} VS and 221 L biogas kg^{-1} VS for water hyacinth and cabomba, respectively [8]. Biogas potential of water hyacinth was changing between 200 and 300 L biogas kg^{-1} VS with almost 70% of methane content [9]. Vaidyanathan et al. [10] obtained a higher yield of biogas with water hyacinth as 671 L biogas kg^{-1} VS with 64% of methane content. AD of water lettuce was performed in laboratory-scale digesters with digested cattle manure as inoculum and gas yields were found in the range of 533–707 L kg^{-1} VS with the average methane content of 58–68% at temperatures of 29.5–37.5 °C after thirteen days [11]. Ratios of carbon to nitrogen (C/N) and carbon to phosphorus (C/P), content of hemicellulose, pH and buffering capacity of substrate [12], digestion temperature, concentration of substrate (that is total solid (TS) or volatile solid (VS) content) and inoculum type are the effective parameters for biogas production [14]. Serez [15] investigated AD of water hyacinth (Fig. 1) with waste sludge at laboratory and pilot scales (Fig. 2) by changing substrate concentration and digestion temperature. Elsewhere, a similar study with only lab-scale batch digester was performed by using water lettuce as substrate [7].

Chuang et al. [13] experimented anaerobic digestion of water hyacinth using pig manure as inoculum to produce hydrogen and methane. They selected substrate concentration and incubation temperature as 10–80 g L^{-1} and 25–65 °C, respectively. Optimum substrate concentration and temperature for maximum yields of methane

Fig. 1 Fresh water hyacinth (left) and water lettuce (right)

Fig. 2 Pilot-scale anaerobic digester (left) and control panel (right)

and hydrogen were searched by application of kinetic analysis. Biogas yield increased by increasing substrate concentration but up to 60 g L^{-1}. Excessive organic feed (80 g L^{-1}) showed adverse effect on AD. Optimum temperatures for maximum hydrogen and methane productions were 47.8 and 62.5 °C, respectively. Optimum conditions depend on the types of substrate and inoculum in addition to reactor type used in AD.

Kinetic analysis is used for modeling and scaling up the reactor employed, identifying optimum conditions that should be defined for each specific feed. Before application of kinetic analysis, kinetic parameters should be assigned by model equations such as modified Gompertz, Cone and first-order kinetics [16, 17]. Experimental and predicted values should be compared in terms of correlation coefficient and fitting errors. Kinetic parameters of model equation giving the best fit are used further in kinetic models. The influence of substrate concentration was included in Monod and modified Andrew models while the impact of temperature was investigated in Ratkowsky model [7, 13].

2 Effect of Process Parameters on AD

2.1 Substrate to Inoculum Ratio

Concentration of substrate and inoculum in AD must be in an ideal balance to avoid excessive loading of organic material and to stabilize bacterial activity. Low concentration of substrate causes low methane production, while high concentration results in total inhibition or long lag-phase time for acclimation [18]. The substrate to inoculum ratio is important for methanogenesis, and optimum value is determined by achieving the highest methane production. In the literature, the highest amount of methane production was reached at a substrate to inoculum ratio of 0.5 based on VS (volatile solid) for the fresh human fecal and the digested sewage sludge as inoculum [19]. The use of higher inoculum concentration generated higher methane production rate requiring lower adaptation time in AD of swine wastewater with sewage sludge as inoculum (substrate to inoculum ratio of 1:1 based on VS) [14]. Ratio of substrate to inoculum can be expressed as total solid (TS) or volatile solid (VS).

Serez [15] reported AD of water hyacinth by changing substrate concentration at constant waste sludge concentration and at digestion temperature and then by changing digestion temperature at constant substrate and waste sludge concentrations (Table 1).

In that study, lab-scale batch studies were performed, and variation of cumulative biogas production obtained at different water hyacinth concentrations was shown in Fig. 3a. According to the report, the highest biogas yield was found as 66.1 mL g^{-1} VS at 50 g TS L^{-1} of substrate concentration. Low value of biogas yield is due to the low concentration of inoculum used. Madenoğlu et al. [7] performed further studies with water lettuce and using higher inoculum concentration. They used waste sludge as inoculum and mixed with substrate (water lettuce) with different ratios based on TS concentration. Change in cumulative biogas production (mL g^{-1} VS) with time at varying substrate (30, 40 and 50 g TS L^{-1}) and waste sludge concentrations (3.4 and 6.8 g TS L^{-1}) was investigated at a constant digestion temperature of 35 °C (Fig. 4a,

Table 1 Operating conditions for AD of water hyacinth in lab-scale digester

Digestion temperature (°C)	Water hyacinth (g TS L^{-1})	Waste sludge (g TS L^{-1})	Ratio of WH:WS based on TS (g TS:g TS)	Ratio of WH:WS based on VS (g VS:g VS)
35	40	3.4	20:1.7	16:1.2
35	50	3.4	25:1.7	20:1.2
35	60	3.4	30:1.7	24:1.2
45	50	3.4	25:1.7	20:1.2
55	50	3.4	25:1.7	20:1.2

Remarks WH—water hyacinth, WS—waste sludge, TS—total solid, VS—volatile solid
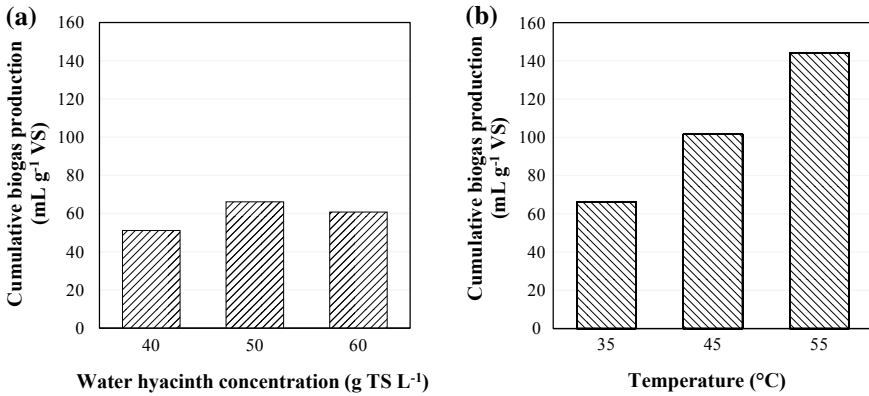
Fig. 3 Variation of cumulative biogas production with **a** water hyacinth concentration (at waste sludge concentration of 3.4 g TS L^{-1} and 35 °C) and **b** digestion temperature (at water hyacinth concentration of 50 g L^{-1} and waste sludge concentration of 3.4 g TS L^{-1}). Adapted from Serez [15]
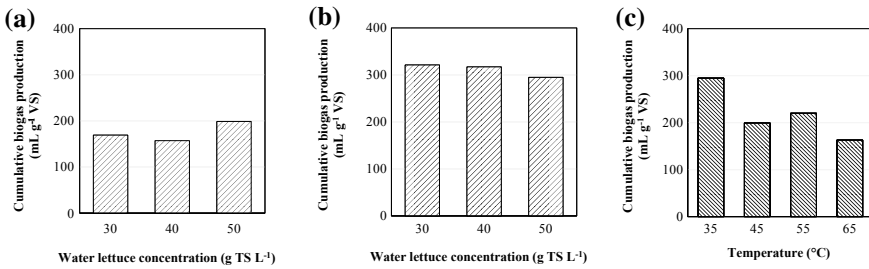
Fig. 4 Variation of cumulative biogas production with **a** water lettuce concentration (at waste sludge concentration of 3.4 g TS L^{-1} and 35 °C), **b** water lettuce concentration (at waste sludge concentration of 6.8 g TS L^{-1} and 35 °C) and **c** digestion temperature (at water lettuce concentration of 50 g L^{-1} and waste sludge concentration of 6.8 g TS L^{-1}). Adapted from Güngören Madenoğlu et al. [7], with permission from John Wiley and Sons

b). Whereas there was a slight change by increasing substrate concentration from 30 to 50 g TS L^{-1}, a remarkable increase was obtained by increasing waste sludge concentration from 3.4 to 6.8 g TS L^{-1}. Biogas production was increased twofold (from 168.8 to 321 mL g^{-1} VS) by increasing waste sludge concentration (from 3.4 to 6.8 g TS L^{-1}) at a constant substrate concentration (30 g TS L^{-1}). In addition, methane content was almost same as 72.5% which corresponds 122.4 mL CH$_4$ g^{-1} VS and 232.7 mL CH$_4$ g^{-1} VS. The reason of sharp increase in biogas yield with a high sludge concentration was due to the fact that an increase in microorganism quantity resulted in better biodegradability.

Comparing the results of water hyacinth and water lettuce at the same operating conditions, both aquatic plants gave the highest biogas yield at a substrate concentration of 50 g L^{-1}, but biogas yield was found to be higher when water lettuce was used as substrate (Figs. 3a and 4a).

2.2 Temperature Regime

Temperature is one of the most important parameters affecting not only bacterial activity but also biodegradation rate and methane yield. AD can be performed at four different temperature regimes that are psychrophilic (15–25 °C), mesophilic (20–40 °C), thermophilic (50–65 °C) and hyperthermophilic (65–75 °C). Thermophilic conditions are more advantageous as reaction rates are higher at a high digestion temperature yielding higher productivity, but biogas yield can be lower because of the tendency of acidification. High-energy input, negative impacts for environmental changes and lower stability, lower methanogenesis are the other disadvantages of thermophilic conditions. Even though mesophilic conditions show better process stability, low biodegradation and low methane content occur in this regime [20]. In psychrophilic regime, organic materials can be digested at ambient temperature. While energy requirement is lower, biodegradation, methane production and stability can be also lower compared to mesophilic condition because of the negative effect of temperature fluctuation in the environment. Wei et al. [21] emphasized that biogas production at thermophilic condition (55 °C) was more than double at psychrophilic (15 °C) condition. In addition, the passive disintegration of solid under thermophilic condition was easier than at psychrophilic condition [22]. In the hyperthermophilic regime, persistent biomaterials, proteins and lipids can be treated, but methane production can stop because of proliferation of acidogenic communities [12]. Lee et al. [23] co-digested waste activated sludge with kitchen garbage at two-phased hyperthermophilic conditions. High-performance treatment was achieved by acidogenesis at 70 °C and by methanogenesis at 55 °C. High protein solubilization of sludge was confirmed by the presence of specific bacteria (*Coprothermobacter* sp.) at 70 °C. Wang et al. [24] described a relation between temperature and C/N ratio. The increase of C/N ratios reduced the ammonia formation, but maximum methane production potential was achieved with C/N ratios of 25:1 and 30:1 at 35 and 55 °C, respectively. Effect of ammonia inhibition can be reduced by increasing the C/N ratio of feed when temperature increased.

Effect of digestion temperature was investigated at constant water hyacinth and waste sludge concentrations as summarized in Table 1 [15]. Change in cumulative biogas production with time at varying digestion temperatures (35, 45, and 55 °C) was shown in Fig. 3b for water hyacinth concentration of 50 g TS L^{-1} and waste sludge concentration of 3.4 g TS L^{-1}. The highest biogas yield as 144.2 mL g^{-1} VS was obtained at 55 °C. Even though methane content reached up to 70% at 55 °C, biogas yield at this temperature was not high enough. Therefore, further studies were carried out with higher inoculum concentration and temperature.

Madenoglu et al. [7] studied on the effect of mesophilic and thermophilic temperatures on biogas yield of water lettuce. Effect of digestion temperatures (35, 45, 55 and 65 °C) on cumulative biogas production (mL g^{-1} VS) was investigated at constant substrate and waste sludge concentrations of 50 g TS L^{-1} and 6.8 g TS L^{-1}, respectively (Fig. 4c). The maximum biogas yield reached was 289 mL g^{-1} VS at 35 °C while the minimum yield at 65 °C as 162 mL g^{-1} VS in which methane content was only 50.4%. Bacterial activity was almost diminished at 65 °C. Although the methane content was satisfactory as 79% at 45 and 55 °C, maximum biogas yields obtained were not as high as at 35 °C.

AD of water hyacinth with waste sludge was investigated using a pilot-scale batch digester [25]. Effect of digestion temperature (35, 45, and 65 °C) was searched at a water hyacinth concentration of 20 g TS L^{-1} and using a waste sludge concentration of 1.7 g TS L^{-1}. Similar to lab-scale studies, the highest biogas and methane yields were obtained at 35 °C as 176.9 and 108.8 mL g^{-1} VS (61.5% of methane), respectively (Figs. 5 and 6). Yields of pilot-scale studies [25] with water hyacinth were found to be lower compared with the lab-scale studies [15] since both concentrations of the substrate and inoculum were lower in pilot-scale studies.
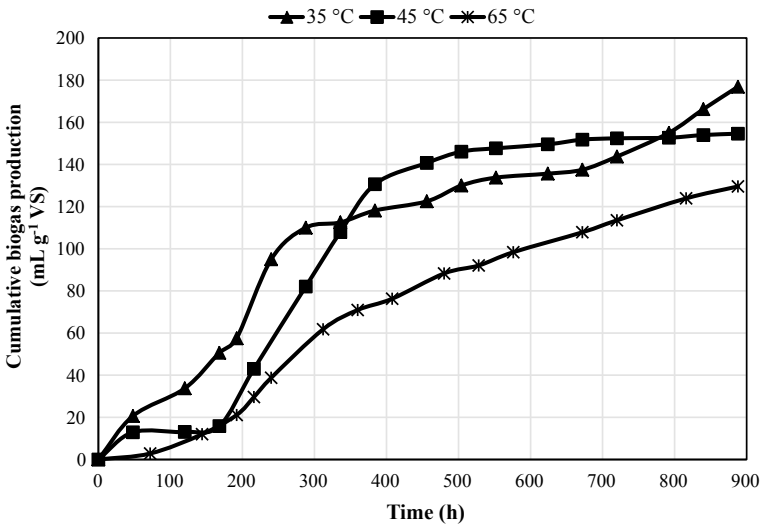
Fig. 5 Variation of cumulative biogas production with time at different digestion temperatures (at water hyacinth concentration of 20 g TS L^{-1} and waste sludge concentration of 1.7 g TS L^{-1})
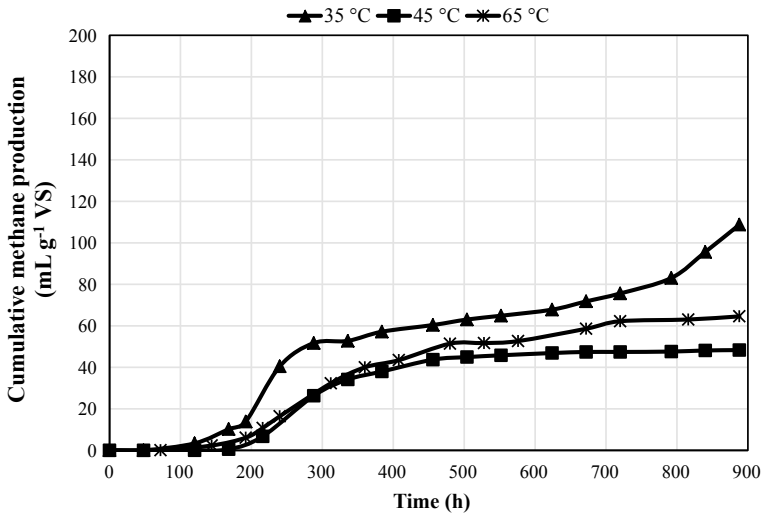
Fig. 6 Variation of cumulative methane production with time at different digestion temperatures (at water hyacinth concentration of 20 g TS L^{-1} and waste sludge concentration of 1.7 g TS L^{-1})

2.3 C/N Ratio

The C/N ratio defines the performance of digestion process as anaerobic bacteria need nutrients to build its cell structure and to growth. High value of C/N ratio shows a low protein solubilization rate and low total ammonium nitrogen (TAN). Insufficient nitrogen to build cell of bacteria leads to failure in microbial activity and lower biogas yield. Substantially, low ratio of C/N in substrate increases the ammonia inhibition effect that is toxic for methanogens and carbon source cannot be evaluated and digested effectively. Ammonia inhibition can be controlled by adjustment of C/N ratio. The optimum C/N ratio for AD was recommended between 20 and 35, and the ratio of 25 was the most commonly used value [26–28].

Wang et al. [29] investigated AD of multi-component substrates, using a mixture of dairy manure, chicken manure and wheat straw to obtain a high methane yield by adjusting C/N ratios. They concluded that C/N ratios of 25:1 and 30:1 had better digestion performances because of stable pH and low concentrations of TAN and free NH$_3$. The optimum C/N ratio was 20 for co-digestion of algae with corn straw [30] while the optimum C/N ratio was 15.8 for co-digestion of food waste with cattle manure [31]. The optimum C/N ratio was 25 for the anaerobic co-digestion of rice straw and *Hydrilla verticillata* that is an aquatic weed [16]. It can be concluded that the optimum C/N ratio for AD depends on both substrate and the inoculum.

2.4 VFA, Ammonia and pH

Volatile fatty acids (VFAs) are formed as intermediates during AD of organics and mainly composed of acetic acid, propionic acid, butyric acid and valeric acid. Meanwhile, protein- or nitrogen-rich compounds are degraded to ammonia that are mainly in the forms of ammonium ion (NH_4^+) and free ammonia (NH_3). The pH of the medium affects the progress of digestion and products. High organic loading causes accumulation of VFAs and results in a certain pH decrease and unsuccessful AD [32–34]. Presence of ammonia with high concentration results in higher pH. Buffering capacity of AD was improved by neutralization of VFAs with ammonia [35, 36]. The optimum pH range of AD process was recommended between 6.8 and 7.4 [37]. Anaerobic bacteria need different pH ranges for their growth. Optimum pH for acidogenesis bacteria is between 5.5 and 6.5 [38] while for methanogenesis bacteria between 6.5 and 8.2 [39]. As bacterial activity depends on pH values, two-stage AD was preferred for hydrolysis/acidification and acetogenesis/methanogenesis processes to increase the yield.

Madenoğlu et al. [7] investigated the effect of substrate (water lettuce) and inoculum (waste sludge) concentrations, and temperature on aqueous phase composition at the end of AD. Biogas formation was directly connected with degradation of compounds in the aqueous phase. Carbohydrate hydrolysis products were analyzed, and only glucose was identified among the products. Its concentration increased by increasing substrate concentration while low glucose concentration was handled by doubling waste sludge concentration from 3.4 to 6.8 g TS L^{-1}. This situation was explained by a high-rate conversion of glucose to methane gas through VFAs with increased waste sludge concentration. Total VFAs concentration was defined as summation of acetic acid, propionic acid, butyric acid and *iso*-butyric acid. Continuous degradation of VFAs produced methane gas. Total VFAs increased by increasing substrate concentration. Parallel to biogas formation, total VFAs decreased by doubling waste sludge concentration from 3.4 to 6.8 g TS L^{-1}. Total VFAs concentration decreased from 115 to 41 mg L^{-1} by doubling waste sludge concentration from 3.4 to 6.8 g TS L^{-1} at constant substrate concentration of 50 g TS L^{-1}. Concentrations of VFAs were not high enough to change pH of the aqueous phase, and final pH was between 8.1 and 8.4 at a digestion temperature of 35 °C. Increase in final pH compared to initial pH of 7.0 was caused by the increase in total ammonia nitrogen (TAN) that was total of ammonium (NH_4-N) and ammonia (NH_3-N) content. At the end of AD, TAN, final NH_4-N and NH_3-N were found as 349–673 mg L^{-1}, 329–635 and 19–65 mg L^{-1}, respectively. Inhibitory effect of TAN concentration was in the range of 1.500 and 10.000 mg L^{-1}, and toxicity level for bacteria was 30 g L^{-1} [40]. As their values were well below the limits, medium of bacteria was comfortable for their activities. Ammonia is prevailing at a pH greater than 9.25 while ammonium ion is at a pH less than 7.0 in the solution [41, 42]. The ratio of NH_4^+: NH_3 was between 89.2:10.8 and 95.0:0.5 at 35 °C [7].

Separately, the effect of digestion temperature on aqueous solution of AD was also examined [7]. A high reaction rate expected at thermophilic conditions was not

confirmed as biogas and methane yields decreased as a result of accelerated growth of acid-forming bacteria and suppressed activity of methanogenic bacteria. The concentrations of VFAs obtained, especially propionic acid, were 209 and 1856 mg L^{-1} at 55 and 65 °C, respectively. In the same temperature range, NH_4^+ concentrations ranged between 595 and 690 mg L^{-1}. The pH of aqueous solution slightly increased from 7.0 to 7.7 during AD in thermophilic conditions due to the parallel increase of both VFAs and TAN. The ratio of NH_4^+: NH_3 was between 90.7:9.3 and 97.7:2.3 at a temperature range of 35–65 °C. When ratio of NH_4^+: NH_3 is high and pH of the medium exceeds 8, the performance of AD starts to decline that leads to a low gas formation [43, 44]. Additionally, high pH causes increase in concentrations of CO_3^{2-} and S^{2-} ions that give rise to elimination of trace metals which is necessary for bacterial activity [45]. Since bacterial activity is mostly inhibited at extremely thermophilic and hyperthermophilic conditions (>65 °C), methanogenic bacteria cannot convert VFAs into methane and excessive accumulation of VFAs cause a sharp drop in pH [13, 37].

3   Model Equations for Kinetic Parameters

Modified Gompertz, Cone and first-order kinetic models [41, 46] can be used to simulate to estimate kinetic parameters for methane production. Modified Gompertz (Eq. 1), Cone (Eq. 2) and first-order (Eq. 3) model equations were fitted to cumulative methane production data and kinetic parameters (y_m, U, λ, k_{hyd}, k and n) were calculated by the following equations:

$$y(t) = y_m \cdot \exp\left\{-\exp\left[\frac{U \cdot e}{y_m}(\lambda - t) + 1\right]\right\}, \ t \geq 0 \tag{1}$$

$$y(t) = \frac{y_m}{1 + \left(k_{hyd} \cdot t\right)^{-n}}, \ t > 0 \tag{2}$$

$$y(t) = y_m \cdot (1 - \exp(-k \cdot t)), \ t \geq 0 \tag{3}$$

The cumulative methane production is $y(t)$ in mL/g VS, the maximum methane production potential is y_m in mL/g VS, the maximum methane production rate is U in (mL/g VS)/h, e is 2.718, the lag-phase time is λ in h, the hydrolysis rate constant is k_{hyd} in 1/h, the shape factor is n, the rate constant is k in 1/h, and the incubation time is t in h. The volumetric overall methane production rate ($R_{overall}$, in mL CH_4/L/h) can be calculated by (Eq. 4) as follows:

$$R_{overall} = \left(\frac{y_m}{(y_m/U)+}\right)\frac{1}{V} \tag{4}$$

The total volume of the digestion mixture is V in mL. This equation includes process performance, rate and retardation in methane production.

All these kinetic models fitted to AD of water lettuce with waste sludge at different substrate concentrations and temperatures [7]. Cumulative methane productions well fitted only to modified Gompertz and Cone models since first-order kinetic models did not give a good fit. Correlation coefficient for both modified Gompertz and Cone models ranged between 0.94 and 0.99. In addition, the correlation coefficient is not satisfactory alone to decide on best fit of experimental and predicted values. Differences between these values were calculated for each condition, and it was emphasized that modified Gompertz model deviated from experimental values up to 32%. Cone model was found to be more flexible in order to fit experimental values as it contains a shape factor of "n".

Kinetic models should be applied to find the best fit for AD of each substrate at different operating conditions as the composition of feed (substrate and inoculum) affects the best model selection. For instance, fish or meat wastes with high protein and fat contents do not give a good fit for the first-order kinetic model as lag-phase time is reasonably long. Kafle et al. [47] experienced that situation with fish wastes and decided that modified Gompertz model was the best model giving low fitting error. Similar results of Kafle et al. [47] were obtained by Zhan et al. [48] in AD of pig manure with dewatered sewage sludge as sludge can contain high nitrogen. Budiyono et al. [49] applied AD of carbohydrate-rich feed of vinasse, and they implied that the first-order kinetic model gave the best fit as the carbohydrates degraded quickly and biogas was produced in a short lag-phase time. Syaichurrozi [50] co-digested an aquatic plant (Salvinia) with rice straw to adjust C/N ratio in an optimum range and application of kinetic analysis which revealed that Cone model gave the lowest fitting error compared to modified Gompertz and first-order kinetic models.

4   Kinetic Models

Rate of substrate degradation and biogas (also methane) formation is interrelated with each other and directly affected by the substrate concentration. Kinetic models of Monod (or Michaelis–Menten) and modified Andrew highlight this relationship [51]. Limiting step was included in Monod model while inhibition effect of substrate concentration was only described by modified Andrew model. That is the reason why modified Andrew model is satisfactory at high concentrations of substrate. These models are not only used in methane production but also in hydrogen production by AD. Identification of digestion kinetics in AD is important for designing of digesters, understanding effect of process parameters and selecting optimum parameters for biogas production with a high yield [52].

4.1 Effect of Substrate Concentration

Monod (Eq. 5) and modified Andrew (Eq. 6) models were used to describe the effect of substrate concentration on methane production rate. Modified Gompertz equation (Eq. 1) was used to calculate methane production rate (R).

$$R = \frac{R_{max} S}{K_s + S} \tag{5}$$

$$R = \frac{R_{max} S}{K_s + S + S^2 / K_i} \tag{6}$$

The methane production rate is R in mmol/L/d, the methane production rate constant is R_{max} in mmol/L/d, the substrate concentration is S in g/L, the saturation constant is K_s in g/L, and the inhibition constant is K_i in g/L. The fitting parameters (R_{max}, K_s and K_i) can be calculated by nonlinear regression method. In Monod model, K_s represents the affinity of the microorganisms to substrate.

Chen et al. [53] applied Monod model for AD of sucrose, food waste and nonfat dry milk (NFDM) with digested sludge and found high correlation coefficients as 0.858, 0.976 and 0.980, respectively. The values K_s of sucrose, food waste and NFDM were given as 1.4, 8.7 and 6.6 g COD L^{-1}, respectively. Since the affinity of the microorganisms to substrate depends on carbohydrate content, the substrate with high carbohydrate content gave a lower K_s value. Madenoğlu et al. [7] fitted both Monod and modified Andrew models for AD of water lettuce with waste sludge and found good fit with high correlation coefficient for both models as 0.996. Chuang et al. [13] also applied these both models to AD of water hyacinth and obtained high correlation coefficient for both models as 0.998. High methane production rate constant (R_{max}), saturation constant (K_s) and low inhibition constant (K_i) are favored for anaerobic digestion. Comparing these two studies, Madenoğlu et al. [7] reached higher R_{max} (47.8 mmol/L/d > 37.3 mmol/L/d) and K_s (234.5 g/L > 24 g/L) but lower K_i (14,650 g/L < 973,087.5 g/L) values.

4.2 Effect of Temperature

The effect of digestion temperature on production of methane was defined by Ratkowsky equation [13]. The effect of temperature on methane production potential and rate was given by Eqs. 7 and 8, respectively. Modified Gompertz equation (Eq. 1) can be used to calculate methane production potential (P) and rate (R) as follows:

$$P = [A_1 (T - T_{min})]^2 \{1 - \exp[B_1 (T - T_{max})]\}^2 \tag{7}$$

$$R = [A_2 (T - T_{min})]^2 \{1 - \exp[B_2 (T - T_{max})]\}^2 \tag{8}$$
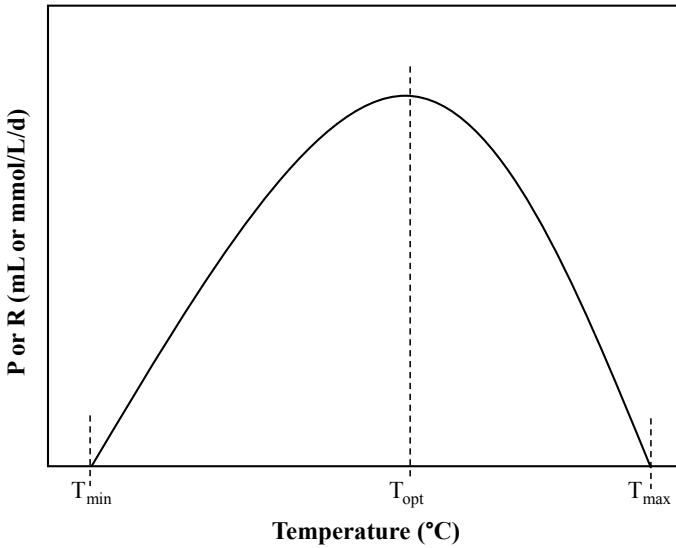
Fig. 7 Representation of Ratkowsky model for minimum (T_{min}), maximum (T_{max}) and optimum (T_{opt}) temperatures

The methane production potential is P in mL, the methane production rate is R in mmol/L/d, A_1 (mL$^{0.5}$/°C), A_2 (mL$^{0.5}$/°C), B_1 (mL/°Cd$^{0.5}$) and B_2 (mL/°Cd$^{0.5}$) are all parameters in Ratkowsky model. The fitting parameters (A, B, T_{min} and T_{max}) can be calculated by nonlinear regression method. Minimum and maximum temperatures, T_{min} (°C) and T_{max} (°C), required for AD process can be determined from curve, and maximum point of the curve represents the optimum operating temperature, T_{opt} (°C) (Fig. 7).

Optimum operating temperatures for AD of water lettuce with waste sludge was determined as almost 45 °C for P and R while minimum and maximum temperatures were 8.8 and 74.8 °C, respectively [7]. Fermentative hydrogen production from digested sludge was performed, and optimum temperatures were found by Ratkowsky model as 39.3 and 34.2 °C for P and R, respectively [54]. Optimum digestion temperature ranges of water hyacinth with pig manure were found as 47.8–57.5 °C and 50.0–62.5 °C for hydrogen and methane productions, respectively [13]. Selection of optimum temperature ranges was based on the values found in Eqs. 7 and 8.

5   Conclusions

Biogas production from agricultural wastes, residues and especially aquatic plants by AD provides a solution for waste minimization and sustainable alternative to fossil fuels. Effective parameters in AD process are substrate to inoculum ratio,

temperature regime, C/N ratio, pH, VFAs and ammonia contents. Optimum C/N depends on digestion temperature. VFA and TAN contents affect pH of medium and activity of microorganisms. Biogas production with high yield and high methane content can be accomplished by selecting optimum conditions with application of kinetic analysis. Optimum parameters depend on each feed employed and should be specified by choosing suitable kinetic models. Effect of substrate concentration and temperature on kinetic models should be examined for identification of inhibition effect of high substrate concentration, minimum–maximum temperature range and optimum temperature for biogas production.

References

1. Liu X, Zhang S, Bae J (2017) The nexus of renewable energy-agriculture-environment in BRICS. Appl Energy 204:489–496
2. IRENA (2014) REmap 2030 global bioenergy supply and demand projections. Available via Google. https://www.worldenergy.org/wp-content/uploads/2016/10/World-Energy-Resources-Full-report-2016.10.03.pdf. Accessed 05 May 2019
3. Mishima D, Kuniki M, Sei K et al (2008) Ethanol production from candidate energy crops: Water hyacinth (*Eichhornia crassipes*) and water lettuce (*Pistia stratiotes L.*). Bioresour Technol 99:2495–2500
4. Wilkie A, Evans J (2010) Aquatic plants: an opportunity feedstock in the age of bioenergy. Biofuels 1:311–321
5. Meegoda JN, Li B, Patel K et al (2018) A review of the processes, parameters, and optimization of anaerobic digestion. Int J Environ Res Public Health 15:E2224
6. Wanwu LX, Khalid H, Zhu Z (2018) Methane production through anaerobic digestion: participation and digestion characteristics of cellulose, hemicellulose and lignin. Appl Energy 226:1219–1228
7. Güngören Madenoğlu T, Jalilnejad Falizi N, Kabay N et al (2019) Kinetic analysis of methane production from anaerobic digestion of water lettuce (*Pistia stratiotes L.*) with waste sludge. J Chem Technol Biotechnol 94:1893–1903
8. O'Sullivan C, Rounsefell B, Grinham A et al (2010) Anaerobic digestion of harvested aquatic weeds: water hyacinth (*Eichhornia crassipes*), cabomba (*Cabomba Caroliniana*) and salvinia (*Salvinia molesta*). Ecol Eng 36:1459–1468
9. Mallik MK, Singh UK, Ahmad N (1990) Batch digester studies on biogas production from *Cannabis sativa*, water hyacinth and crop wastes mixed with dung and poultry litter. Biol Waste 31:315–319
10. Vaidyanathan S, Kavadia KM, Shroff KC et al (1985) Biogas production in batch and semi-continuous digesters using water hyacinth. Biotechnol Bioeng 27:905–908
11. Nipaney PC, Panholzer MB (1987) Influence of temperature on biogas production from Pistia stratiotes. Biol Waste 19:267–274

12. Chunlan M, Yongzhong F, Xiaojiao W et al (2015) Review on research achievements of biogas from anaerobic digestion. Renew Sust Energ Rev 45:540–555
13. Chuang YS, Lay CH, Sen B et al (2011) Biohydrogen and biomethane from water hyacinth (*Eichhornia crassipes*) fermentation: effects of substrate concentration and incubation temperature. Int J Hydrogen Energ 36:14195–14203
14. Córdoba V, Fernández M, Santalla E (2018) The effect of substrate/inoculum ratio on the kinetics of methane production in swine wastewater anaerobic digestion. Environ Sci Pollut Res 25(22):21308–21317
15. Serez H (2016) Wastewater treatment using energy plants at ITOB industrial zone and biogas production by anaerobic fermentation of the energy plants. M.Sc. thesis, Ege University
16. Kainthola J, Kalamdhad AS, Goud VV (2019) Enhanced methane production from anaerobic co-digestion of rice straw and *Hydrilla verticillata* and its kinetic analysis. Biomass Bioenerg 125:8–16
17. Yang D, Deng LW, Zheng D et al (2015) Separation of swine wastewater into solid fraction, concentrated slurry and dilute liquid and its influence on biogas production. Fuel 144:237–243
18. González-Fernández C, García-Encina PA (2009) Impact of substrate to inoculum ratio in anaerobic digestion of swine slurry. Biomass Bioenerg 33:1065–1069
19. Fagbohungbe MO, Herbert BMJ, Li H et al (2015) The effect of substrate to inoculum ratios on the anaerobic digestion of human faecal material. Environ Technol Innov 3:121–129
20. Bowen EJ, Dolfing J, Davenport RJ et al (2014) Low-temperature limitation of bioreactor sludge in anaerobic treatment of domestic waste-water. Water Sci Technol 69:1004–1013
21. Wei RR, Cheng GW, Luo JJ et al (2010) Biogas and bio-energy production from anaerobic digestion of piggery manure at different temperatures. J Agric Mech Res 4:170–174
22. Kaparaju P, Angelidaki I (2008) Effect of temperature and active biogas process on passive separation of digested manure. Bioresour Technol 99:1345–1352
23. Lee M, Hidaka T, Tsuno H (2009) Two-phased hyperthermophilic anaerobic co-digestion of waste activated sludge with kitchen garbage. J Biosci Bioeng 108:408–413
24. Wang X, Lu X, Li F et al (2014) Effects of temperature and carbon-nitrogen (C/N) ratio on the performance of anaerobic co-digestion of dairy manure, chicken manure and rice straw: focusing on ammonia inhibition. PLoS ONE 9:e97265
25. Kabay N (2016) Optimization studies at MBR treatment system of ITOB Organized Industrial Zone and Biogas Production by Cultivating Energy Plants in Wastewater-SAN-TEZ Project Supported by Ministry of Science, Industry and Technology of Turkish Republic (Project No: 0330.STZ.2013-2)
26. Zhang T, Liu L, Song Z et al (2013) Biogas production by co-digestion of goat manure with three crop residues. PLoSOne 8:e66845
27. Punal A, Trevisan M, Rozzi A et al (2000) Influence of C:N ratio on the start-up of up-flow anaerobic filter reactors. Water Res 34:2614–2619
28. Yen HW, Brune DE (2007) Anaerobic co-digestion of algal sludge and wastepaper to produce methane. Bioresour Technol 98:130–134
29. Wang X, Yang G, Feng Y et al (2012) Optimizing feeding composition and carbon–nitrogen ratios for improved methane yield during anaerobic co-digestion of dairy, chicken manure and wheat straw. Bioresour Technol 120:78–83
30. Zhong W, Chi L, Luo Y et al (2013) Enhanced methane production from Taihu Lake blue algae by anaerobic co-digestion with corn straw in continuous feed digesters. Bioresour Technol 134:264–270
31. Zhang C, Xiao G, Peng L et al (2013) The anaerobic co-digestion of food waste and cattle manure. Bioresour Technol 129:170–176
32. Buyukkamaci N, Filibeli A (2004) Volatile fatty acid formation in an anaerobic hybrid reactor. Process Biochem 39:1491–1494
33. Cysneiros D, Banks CJ, Heaven S et al (2012) The effect of pH control and 'hydraulic flush' on hydrolysis and volatile fatty acids (VFA) production and profile in anaerobic leach bed reactors digesting a high solids content substrate. Bioresour Technol 123:263–271

34. Pham TN, Nam WJ, Jeon YJ et al (2012) Volatile fatty acids production from marine macroalgae by anaerobic fermentation. Bioresour Technol 124:500–503
35. Wang Q, Peng L, Su H (2013) The effect of a buffer function on the semi-continuous anaerobic digestion. Bioresour Technol 139:43–49
36. Banks CJ, Humphreys PN (1998) The anaerobic treatment of a lingo-cellulosic substrate offering little natural pH buffering capacity. Water Sci Technol 38:29–35
37. Yokoyama H, Moriya N, Ohmori H et al (2007) Community analysis of hydrogen-producing extreme thermophilic anaerobic microflora enriched from cow manure with five substrates. Appl Microbiol Biotechnol 77:213–222
38. Kim J, Park C, Kim TH et al (2003) Effects of various pretreatments for enhanced anaerobic digestion with waste activated sludge. J Biosci Bioeng 95:271–275
39. Lee DH, Behera SK, Kim JW et al (2009) Methane production potential of leachate generated from Korean food waste recycling facilities: a lab-scale study. Waste Manage 29:876–882
40. Sung S, Liu T (2003) Ammonia inhibition on thermophilic anaerobic digestion. Chemosphere 53:43–52
41. Syaichurrozi I, Budiyono B, Sumardiono S et al (2013) Predicting kinetic model of biogas production and biodegradability organic materials: biogas production from vinasse at variation of COD/N ratio. Bioresour Technol 149:390–397
42. Markou G, Georgakakis D (2011) Cultivation of filamentous cyanobacteria (blue-green algae) in agro-industrial wastes and wastewaters: a review. Appl Energy 88:3389–3401
43. Hansen KH, Angelidaki I, Ahring BK (1998) Anaerobic digestion of swine manure: inhibition by ammonia. Water Res 32:5–12
44. Karlsson A, Ejlertsson J (2012) Addition of HCl as a means to improve biogas production from protein-rich food industry waste. Biochem Eng J 61:43–48
45. Callander IJ, Barford JP (1983) Precipitation, chelation, and the availability of metals as nutrients in anaerobic digestion. II. Applications. Biotechnol Bioeng 25:1959–1972
46. Zhen G, Lu X, Kobayashi T et al (2015) Mesophilic anaerobic co-digestion of waste activated sludge and *Egeria densa*: performance assessment and kinetic analysis. Appl Energy 148:78–86
47. Kafle GK, Kim SH, Sung KI (2012) Ensiling of fish industry waste for biogas production: a lab scale evaluation of biochemical methane potential (BMP) and kinetics. Bioresour Technol 127:326–336
48. Zhang W, Wei Q, Wu S et al (2014) Batch anaerobic co-digestion of pig manure with dewatered sewage sludge under mesophilic conditions. Appl Energy 128:175–183
49. Budiyono B, Syaichurrozi I, Sumardiono S et al (2014) Kinetic model of biogas yield production from vinasse at various initial pH: comparison between modified Gompertz model and first order kinetic model. Res J Appl Sci Eng Technol 7:2798–2805
50. Syaichurrozi I (2018) Biogas production from co-digestion Salvinia molesta and rice straw and kinetics. Renew Energ 115:76–86
51. Wang JL, Wan W (2009) Kinetic models for fermentative hydrogen production: a review. Int J Hydrogen Energy 34:3313–3323
52. Fernandez-Rodriguez MJ, Rincon B, Fermoso FG et al (2014) Assessment of two-phase olive mill solid waste and microalgae co-digestion to improve methane production and process kinetics. Bioresour Technol 157:263–269
53. Chen WH, Chen SY, Khanal SK (2006) Kinetic study of biological hydrogen production by anaerobic fermentation. Int J Hydrogen Energy 31(15):2170–2178
54. Wang JL, Wan W (2008) Effect of temperature on fermentative hydrogen production by mixed cultures. Int J Hydrogen Energy 33:5392–5397

Prediction of Solar Energy Potential with Artificial Neural Networks

Burak Goksu, Murat Bayraktar and Murat Pamik

Abstract The energy requirements have been met from fossil fuels since the early 1800s. Considering the environmental awareness and limited fossil resources, using renewable energy resources are compulsory to meet the increasing energy demand. Solar and wind energy, biofuels, and natural gas are leading ones. Solar energy is an effective and clean energy source compared in terms of sustainability, reliability, and economy. In the maritime sector, eco-friendly and sustainable qualities are sought in all of the efforts to reduce costs. Therefore, in many maritime fields, solar energy is used as an alternative energy source. The purpose of this study is achieving maximum efficiency from solar panels by using optimization technique. The energy estimation was performed by artificial neural networks method on solar panels based on weather changes in Izmir Gulf. The results are compared with the "Renewable Energy General Administration" data of Turkey. As a result, the obtained data will be informative to the researcher who will study solar energy's maritime applications. Besides, this study will be a possible source to make comparisons with similar solar energy studies.

Keywords Neural networks · Emissions · Energy saving · Solar energy

1 Introduction

Solar energy radiation is an important influence on calculations to create solar energy models [1]. Energy requirement increases by about 4–5% every year in the world [2]. Considering the reduction of fossil fuel reserves and emissions to environment,

B. Goksu · M. Bayraktar (✉) · M. Pamik
Department of Marine Engineering, Dokuz Eylul University, Izmir, Turkey
e-mail: murat.bayraktar@deu.edu.tr

B. Goksu
e-mail: burak.goksu@deu.edu.tr

M. Pamik
e-mail: muratpamik@hotmail.com

B. Goksu · M. Bayraktar
Department of Marine Engineering, Bulent Ecevit University, Zonguldak, Turkey

interest in alternative energy sources has increased. In this context, usage of the solar energy can provide solutions to meet this energy need. Solar energy is a real renewable energy that can be used anywhere in the world and will not be consumed as long as the sun exists [3]. Expensive initial investment costs are the biggest concern while the use of solar energy is seen as positive by all [4]. Generating energy from solar panels is quite usable and practical if high installation costs are reduced [5]. However, it is possible to use solar energy in rainy and closed weather, and it is a fact that the energy received is seriously lowered. In addition, storage of the produced energy is also not preferred due to its high cost [6].

Renewable energy accounts for about 3% of the world's energy needs [7]. Along with the developing technology, the cost of using solar energy and other alternative energy resources has been reduced by a certain amount. The potential of renewable energy sources has increased in this respect [8]. The efficiency of solar panels used to generate energy from the sun is low, and power outputs vary according to weather conditions and solar irradiation [9]. There are factors such as latitude, daily variability, climate, and geographic diversity, which are largely responsible for determining the intensity of solar flow throughout the Earth's atmosphere. The amount of energy transferred from the sun to the earth is about 239 W/m^2 when the energy reflected back into the space is removed [10].

This study was carried out by using artificial neural networks method to estimate solar energy potential for Izmir region. Detailed literature review are described in the Table 1 and similar studies have been scrutinized in terms of titles, methods and case areas of the studies.

The estimation of solar radiation is quite important for power plants that use solar energy as renewable energy [17]. In this period, where natural energy resources have become important due to environmental awareness, the use of solar energy comes to significant point and this also puts forward together in making accurate estimates for efficient installation to benefit from solar energy. Using wrapper mutual information methodology (WMIM), Bouzgou and Gueymard [11] make forecasting about solar irradiance. WMIM is very realistic method when the statistical results are evaluated [11]. Using and selection of estimation tools constitute a very important part to create appropriate energy management. In this way, tools give information about the production and consumption of the system to be installed. Extraterrestrial horizontal irradiation, solar declination, and zenith angle are calculated by global horizontal solar irradiation, global tilted solar irradiation, ambient temperature, relative humidity, wind speed, wind direction, precipitation, sunshine duration, and atmospheric pressure data values using artificial neural network methodology. In this article, solar irradiation values are estimated together with this ANN method in Notton et al. [12] studies. Despite the development of new methods about estimation and forecasting, ANN is a very successful and promising method [12].

Solar energy, one of the most used renewable energy sources in the world, directly affects people's lives. The main purpose of Feng et al. [13] that estimates solar radiation values for areas where have difficult to obtain meteorological data and no archive data is available. The neural network model, which is composed of Levenberg–Marquardt (LM) algorithm and backpropagation (BP), has been generated to predict

Table 1 Literature review

Study		Method	Site
[11]	Fast short-term global solar irradiance forecasting with wrapper mutual information	Wrapper mutual information methodology	Tamanrasset, Algeria; Madina, Saudi Arabia
[12]	Some applications of ANN to solar radiation estimation and forecasting for energy applications	Artificial neural network methodology	Bouzareah, Algeria
[13]	An LM-BP neural network approach to estimate monthly mean daily global solar radiation	Levenberg–Marquardt (LM) algorithm and backpropagation (BP) neural network	Jinghe, Xifeng town, Yan'an, China
[14]	Solar radiation forecasting using artificial neural network and random forest methods: application to normal beam, horizontal diffuse, and global components	Smart persistence, artificial neural network and random forest	Odeillo, France
[15]	Modelling the global solar radiation climate of Mauritius using regression techniques	Regression analysis	Mauritius
[16]	An improved algorithm for estimating incident daily solar radiation from measurements of temperature, humidity, and precipitation	Improved algorithm (reformulation of the Bristow–Campbell model)	Albany, NY Albuquerque, NM Bismarck, ND Boise, ID Boston, MA etc. (40 stations)
[17]	A 24-h forecast of solar irradiance using artificial neural network: application for performance prediction of a grid-connected PV plant at Trieste, Italy	Artificial neural network	Trieste, Italy
[18]	Simultaneous estimation of daily solar radiation and humidity from observed temperature and precipitation: an application over complex terrain in Austria	Simultaneous estimation	Austria (Warth, Ranshofen, Aflenz etc.) 24 stations

Table 1 (continued)

Study		Method	Site
[19]	The optimized artificial neural network model with Levenberg–Marquardt algorithm for global solar radiation estimation in Eastern Mediterranean Region of Turkey	Artificial neural network	Eastern Mediterranean Region of Turkey
[20]	Adaptive neuro-fuzzy approach for solar radiation prediction in Nigeria	Adaptive neuro-fuzzy	Nigeria
[21]	Short-term solar irradiation forecasting based on dynamic harmonic regression	Dynamic harmonic regression	Spain

monthly mean daily global solar radiation (M-GSR) values in Shaanxi Province by such parameters as aerosol optical thickness (AOT), cloud fraction (CF), cloud optical thickness (COT), precipitable water vapor (PWV), air temperatures (T), sunshine duration (S0), air pressure (P), vapor pressure (Pw), and relative humidity (RH) values. The data obtained compared against remotely sensed radiation products. Referring to these comparisons, the accuracy of the values reached is quite high and has great stability (correlation coefficient (R) = 0.96, root mean squared error (RMSE) = 1.34 MJ m^{-2}, and mean bias error (MBE) = 0.15 MJ m^{-2}). This LM-BP neural network is the estimation method for people to take full advantage of solar energy [13].

Thornton and Running [16] have forecasted the solar radiation values from 40 different stations with opposite climates using daily temperature, radiation, humidity, and precipitation observations. In the summer season, the smallest errors and deceptions were occurred [16]. The Study done by Benali et al. [14] was carried out for a season. Solar radiation values vary in spring and autumn seasons; therefore, making predictions at these times is more complicated than when daily parameters such as winter and summer are stable. For this reason, Thornton and Running have selected the smart persistence, artificial neural network (multilayer perceptron), and random forest methods in this article. In this study, solar irradiation values have been measured on Odeillo, France, and the forecasted results have been evaluated with the solar data measured in a meteorological association [14].

The study of Doorga et al. [15] has been carried out in Mauritius in which has plenty of sun throughout the year. Sunshine-based, temperature-based, and hybrid-parameter-based are investigated using twenty-nine years meteorological data which contain sunshine hours, temperature, and relative humidity. Using these parameters, solar irradiation values were calculated and forecasting was performed. Hybrid-parameter-based models were more effective than others compared to the data obtained [15].

Independent algorithms have been tested and combined by Thornton et al. [18]. Based on temperature and precipitation data, radiation and moisture estimation algorithm was developed [18]. Çelik et al. [19], have modeled a neural network to estimate global solar irradiation and used input parameters as air temperature, sunshine duration, latitude, altitude, longitude, and month of the year. The main purpose of the study, the variability of the different input parameters in the Eastern Mediterranean Region of Turkey, is to evaluate the suitability of the ANN to predict the global solar irradiation [19]. Olatomiwa et al. [20] have aimed to scrutinize the suitability of neuro-fuzzy method to estimate the solar irradiation at a particular site in Nigeria. Such meteorological data as minimum and maximum temperature and sunshine duration have been used for input parameters. The high availability in many areas and their strong relations with the global solar irradiation, these parameters have been chosen for this study [20]. In another article, Trapero et al. [21] estimated short-term solar irradiation with 24-h data. Global horizontal and normal solar irradiation values were used in the study which uses dynamic harmonic regression model [21].

The literature review relating to the calculation methods of solar irradiation and their applications sites are described in this part. The remainder of this study consists of "Materials and Methods," "Results and Discussion," and "Conclusions" parts, respectively.

2 Materials and Methods

Artificial neural networks (ANN) is the application of learning ability, which is the most basic function of a human brain, by computer systems. Sample data set is used to carry out the learning process of networks. ANN provides the user with the necessary model without the need for prior knowledge and assumptions between input and output variables. It is the fact that ANN is preferred as predicting method for this study [22].

Considering the historical development of ANN, a turning point of 1970 is accepted. It seems that research had been stopped because of a problem that many researches were made before this date and which were not resolved in 1969. Solving the problem of 1969 has an important role for today's popularities. The premises are based on the work of McCulloch and Pitts in 1942 [23].

Apart from other prediction models, ANN has the ability to adapt in different situations. This calculation method, which can work with missing information, can decide under uncertainties and is tolerant to errors, shows successful applications in almost every field of life. At the stage of determining, the structure of the network to be created the choice of network parameters is not a certain standard. Also, problems can be shown only with numerical information, and despite the inability to explain when finish the training, interest in these networks is increasing day by day [24]. The entries that create the ANN are described in Fig. 1.
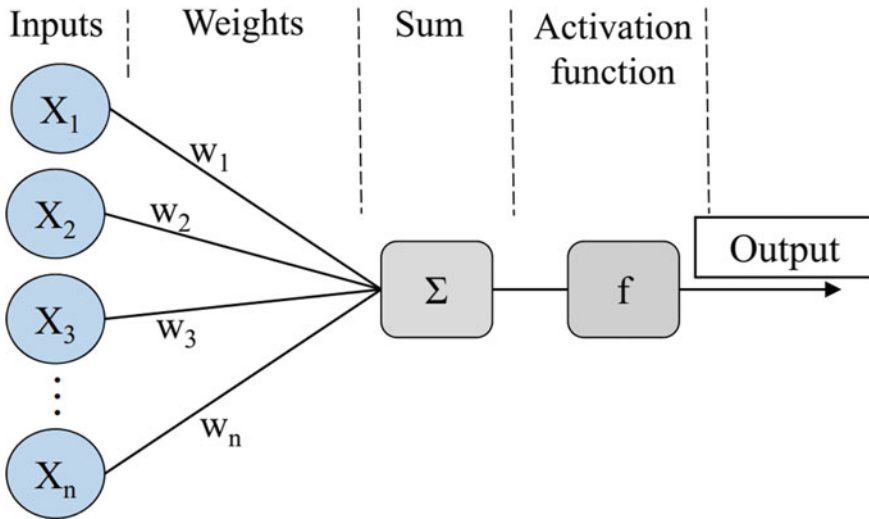
Fig. 1 The model of single-layer artificial neuron [25]

ANN is practiced in various fields such as space, automotive, banking, defense, electronics, entertainment, finance, insurance, manufacturing, medical, oil, robotics, real estate, telecommunication, and transportation [26].

Characteristic features of ANNs are listed below [27]:

- They perform machine learning; the basic function is to be learned by computers. By learning about actual events, they try to make similar decisions about incidents that do not happen.
- They use examples; in order for ANN to be able to learn about the incidents, it is necessary to identify the existing examples. They have the ability to make generalizations using examples. If there are no examples, it is not possible to train ANN.
- They must first be trained and then tested for safe operation, where the topic of training is to show individual instances of any network. Relations between the samples are determined by operating the network's own mechanisms.
- The results of the input data which cannot be found in the sample can be estimated.
- The missing information does not hinder the study; ANNs can work with incomplete information after being trained themselves. New events are given accurate results despite deficient knowledge.
- Have fault tolerance; artificial neural networks are able to tolerate faults thanks to their ability to work with lacking information.
- Deterioration occurs gradually; ANNs are tolerant to faults and provide a degree of impairment.

Besides them; network topology does not depend on precise rule, it requires experience, behavior at learning and testing stage is inexplicable, network training may not

be in one session, and it may be a disadvantage that not all of the results are optimal [26].

Calculation of the Turkey global solar radiation distribution is done by HELIOSAT model. This model is based on the analysis of a radiation transfer equation and simple statistical relationships, and using the hourly data, daily kWh/m^2 data is obtained. In the verification studies, this model estimates with approximately 2% error on solar radiation distribution [28]. In this study, radiation values were described in Fig. 2.

Moreover, annual temperature and humidity values of Izmir province were recorded between 2017 and 2018 [29]. The data obtained throughout the one year for the Izmir region are shown in Fig. 3.

Izmir province has been selected because of the suitability of solar energy usage and many solar energy applications have been found in this region. Furthermore,
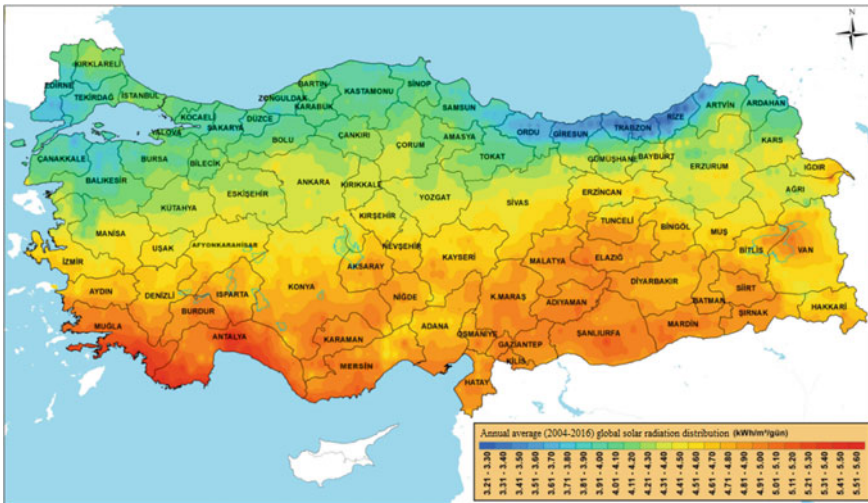
Fig. 2 HELIOSAT model of Turkey global solar radiation average (2004–2016) [28]
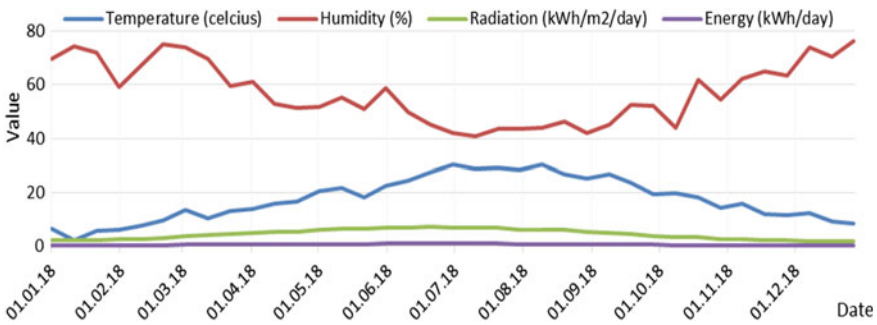
Fig. 3 Temperature, humidity, radiation, and energy values

Table 2 Comparison of performance criteria in different hidden neuron numbers

	5 Hidden neurons 70% Training 15% Validating 15% Testing	10 Hidden neurons 70% Training 15% Validating 15% Testing	20 Hidden neurons 70% Training 15% Validating 15% Testing	30 Hidden neurons 70% Training 15% Validating 15% Testing
MSE	1.62×10^{-8}	2.45×10^{-10}	0.002	0.034
Epoch	3	6	8	6
R value	1	0.999	0.985	0.931

The SP-130 type panel is used; the panel efficiency and panel area values are used as input in artificial neural network analysis.

The determination of the optimal neural network parameters depends on the clarification of the data set. In this study, "Mean Square Error" and "Regression" values are used to measure the performance of the network. Table 2 shows the regression (R) and mean squared error (MSE) parameters of the trained network. The reason for using Levenberg–Marquardt algorithm is quick learning feature [26].

The Levenberg–Marquardt (LM) algorithm is an iterative technique that determines the minimum of a multivariable function expressed as the sum of the squares of nonlinear real-valued functions. It has become a standard technique for nonlinear least square problems commonly adopted in a wide range of disciplines [30].

The regression (R) value indicates the degree of relationship between the outputs and the targets. R represents a close relationship when it approaches "1," and a far relationship when it approaches "0." MSE parameter implies the mean value of the square of difference between calculated outputs and desired output value of relevant inputs. The ideal expected MSE value is "0," and it means zero error [31]. The performance results of the modeled artificial neural networks with different hidden neurons are described in the Table 2. The intended performance parameters are MSE and R values and the second column of the table have the best results to simulate the network for solar energy prediction. For getting high training speed, the second-order algorithms such as Newton and Levenberg–Marquardt (LM) algorithms are chosen. The high accuracy of the second-order algorithms is due to the use of the Hessian matrix. LM algorithm is composed of error backpropagation and Newton algorithm, and it uses for small- and medium-sized patterns as the most efficient training algorithm [32].

3 Results and Discussion

The energy (kWh) obtained from the example panel is used as the output while the temperature, humidity, radiation, panel efficiency, and panel area input values are in the application part of the work. All the data are transferred to the MATLAB package program by dividing one year into 10-day periods. The increase of the information about the input and output values in the data set enables the artificial neural network

to give more accurate results in the prediction part after the learning process. The topology of the ANN is shown in Fig. 4.

The creation of the artificial neural network structure and the estimation of the predicted values were done with the help of the "MATLAB Neural Network Tool." The network was trained using 70% of the sample data, verified with 15%, and tested with the remaining 15%. The regression values for the network are shown in Fig. 5.

The first five columns are the input values for the last column's estimated values and are shown in Table 3. In prediction session, the previously created and trained artificial neural network has been simulated.

Temperature, humidity, and radiation values were randomly selected depending on the data set. Using artificial neural network estimation model on these inputs, energy values were calculated on panel which has 0.623 m^2 area and 0.21 panel
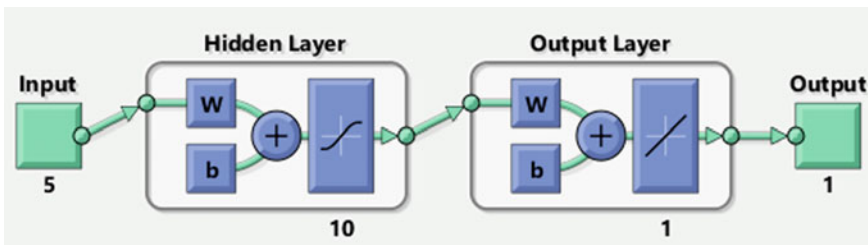
Fig. 4 Artificial neural network topology
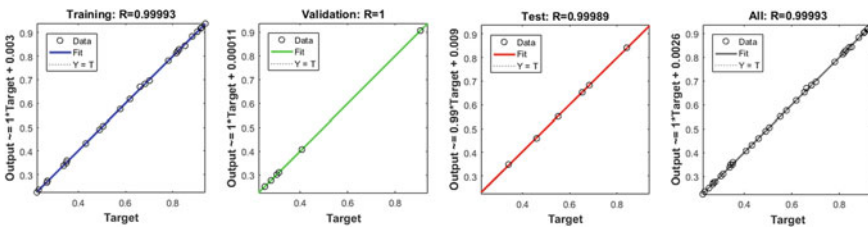
Fig. 5 Artificial neural network regression values

Table 3 Experimental data

Case	Temperature (°C)	Humidity (%)	Radiation (kWh day/m^2)	Panel efficiency	Panel area (m^2)	Energy (kWh day)
1	6	70	2	0.21	0.623	0.263
2	14	61	5	0.21	0.623	0.654
3	22	52	7	0.21	0.623	0.916
4	29	43	7	0.21	0.623	0.916
5	22	50	4	0.21	0.623	0.523
6	12	67	2	0.21	0.623	0.259

efficiency. The obtained energy output (kWh day) values when compared to the existing HELIOSAT data set, very similar results have been achieved and described in Table 3.

4 Conclusions

Proving the sustainability of renewable and environmentally friendly energy resources, demand for fossil fuels can be reduced. Solar energy is a significant alternative renewable energy source in terms of safety, maintainability, and reliability. Considering the geography of Turkey, Izmir is one of the provinces that have the highest radiation and solar fraction values. This study will be useful in decision-making process since there are studies on obtaining energy from this region. In this study, optimized ANN model was developed for Izmir province. Radiation, temperature, humidity, panel area, and efficiency values are utilized for the purpose of obtaining high accurate solar energy estimation. The energy output from the sun has reached its maximum level in summer when the radiation and temperature values increase.

The amount of energy obtained from the sun largely depends on the radiation values compared to other inputs and this is clearly seen in rows of 3 and 4 in Table 3. The effects of temperature and humidity values are less than the radiation for the sake of benefit from solar energy that is clearly visible compared to all cases. Moreover, at low radiation levels, the effect of temperature and humidity are noticeable on energy outputs.

The aim of this study is to give preliminary information about the total amount of energy to be obtained daily in working conditions when it is integrated with solar energy systems. In this way, the solar energy is utilized more efficiently and its usage is enhanced in this region. Consequently, this study will be a significant source for researchers who work on solar energy and panels.

References

1. Şenkal O, Kuleli T (2009) Estimation of solar radiation over Turkey using artificial neural network and satellite data. Appl Energy 86(7–8):1222–1228
2. Karademir A (2015) Transformatör T-bağlantı yapısının çekirdek kayıplarına etkisi
3. Timmons D, Harris JM, Roach B (2014) The economics of renewable energy. Global Development and Environment Institute, Tufts University, 52
4. Imteaz MA, Ahsan A (2018) Solar panels: real efficiencies, potential productions and payback periods for major Australian cities. Sustain Energy Technol Assess 25:119–125
5. Roos CJ (2009) Solar electric system design, operation and installation: an overview for builders in the US Pacific Northwest
6. Report on Solar Energy Storage Methods and Life Cycle Assessment. http://www.energy.ca.gov/2013publications/CEC-500-2013-073/CEC-500-2013-073.pdf. Last accessed 2018/02/02

7. Rahman MM, Islam AS, Salehin S, Al-Matin MA (2016) Development of a model for techno-economic assessment of a stand-alone off-grid solar photovoltaic system in Bangladesh. Int J Renew Energy Res (IJRER) 6(1):140–149

8. Renewable Energy Prospects for the European Union. http://www.irena.org/publications/2018/Feb/Renewable-energy-prospects-for-the-EU. Last accessed 2018/02/02

9. Xu W, Mu C, Tang L (2016) Advanced control techniques for PV maximum power point tracking. In: Advances in solar photovoltaic power plants. Springer, Berlin, Heidelberg, pp 43–78

10. Kabir E, Kumar P, Kumar S, Adelodun AA, Kim KH (2018) Solar energy: potential and future prospects. Renew Sustain Energy Rev 82:894–900

11. Bouzgou H, Gueymard CA (2019) Fast short-term global solar irradiance forecasting with wrapper mutual information. Renew Energy 133:1055–1065

12. Notton G, Voyant C, Fouilloy A, Duchaud JL, Nivet ML (2019) Some applications of ANN to solar radiation estimation and forecasting for energy applications. Appl Sci 9(1):209

13. Feng J, Wang W, Li J (2018) An LM-BP neural network approach to estimate monthly-mean daily global solar radiation using modis atmospheric products. Energies 11(12):3510

14. Benali L, Notton G, Fouilloy A, Voyant C, Dizene R (2019) Solar radiation forecasting using artificial neural network and random forest methods: application to normal beam, horizontal diffuse and global components. Renew Energy 132:871–884

15. Doorga JR, Rughooputh SD, Boojhawon R (2019) Modelling the global solar radiation climate of Mauritius using regression techniques. Renew Energy 131:861–878

16. Thornton PE, Running SW (1999) An improved algorithm for estimating incident daily solar radiation from measurements of temperature, humidity, and precipitation. Agric For Meteorol 93(4):211–228

17. Mellit A, Pavan AM (2010) A 24-h forecast of solar irradiance using artificial neural network: application for performance prediction of a grid-connected PV plant at Trieste, Italy. Solar Energy 84(5):807–821

18. Thornton PE, Hasenauer H, White MA (2000) Simultaneous estimation of daily solar radiation and humidity from observed temperature and precipitation: an application over complex terrain in Austria. Agric For Meteorol 104(4):255–271

19. Çelik Ö, Teke A, Yıldırım HB (2016) The optimized artificial neural network model with Levenberg–Marquardt algorithm for global solar radiation estimation in Eastern Mediterranean Region of Turkey. J Clean Prod 116:1–12

20. Olatomiwa L, Mekhilef S, Shamshirband S, Petković D (2015) Adaptive neuro-fuzzy approach for solar radiation prediction in Nigeria. Renew Sustain Energy Rev 51:1784–1791

21. Trapero JR, Kourentzes N, Martin A (2015) Short-term solar irradiation forecasting based on dynamic harmonic regression. Energy 84:289–295

22. Öztemel E (2012) Yapay sinir ağlari. PapatyaYayincilik, Istanbul

23. Azar AT, Vaidyanathan S (2015) Computational intelligence applications in modeling and control. Springer International Publishing

24. Yegnanarayana B (2009) Artificial neural networks. PHI Learning Pvt. Ltd.

25. Yüksek AG (2007) Hava kirliliği tahmininde çoklu regresyon analizi ve yapay sinir ağları yönteminin karşılaştırılması. Doctoral dissertation, Cumhuriyet Üniversitesi, Sivas

26. Demuth HB, Beale MH, De Jess O, Hagan MT (2014) Neural network design. Martin Hagan

27. Samarasinghe S (2016) Neural networks for applied sciences and engineering: from fundamentals to complex pattern recognition. Auerbach Publications

28. Türkiye Global Güneş Radyasyonu uzun yıllar ortalaması (2004–2016) Heliosat Model Ürünleri, https://www.mgm.gov.tr/kurumici/radyasyon_iller.aspx. Last accessed 2018/02/02

29. İzmir Aylık Hava Durumu. https://weather.com/tr. Last accessed 2018/02/01

30. Lourakis MI (2005) A brief description of the Levenberg-Marquardt algorithm implemented by levmar. Found Res Technol 4(1):1–6

31. Rafiq MY, Bugmann G, Easterbrook DJ (2001) Neural network design for engineering applications. Comput Struct 79(17):1541–1552
32. Wilamowski BM, Yu H (2010) Improved computation for Levenberg–Marquardt training. IEEE Trans Neural Netw 21(6):930–937

Thermodynamic Modeling of a Seawater-Cooled Foldable PV Panel System

Olgun Konur, Suleyman Aykut Korkmaz, Onur Yuksel, Yigit Gulmez, Anil Erdogan, K. Emrah Erginer and Can Ozgur Colpan

Abstract Solar-powered systems can supply clean and sustainable energy for both service requirements and also for the propulsion of marine vessels. However, the restricted available area for photovoltaic panels and high setup costs inhibits the sufficient energy production for satisfying the whole needs of vessels. Due to the limited panel area that can be installed on the vessel, it is necessary to improve the system efficiency in order to obtain more power from the existing solar panel system. In this study, cooling solar panels from the back surface with seawater in an open loop cooling water circuit for a 527-W solar-powered system are investigated. In order to observe the effects of cooling the panels, thermodynamic modeling and analysis of a foldable photovoltaic panel set have been carried out. The result illustrates the potential of these systems as the power output difference of the panel set is more than the consumed power for cooling on above-specific irradiation conditions. The remaining power output, which would be up to 37% of the uncooled system, is high enough to be utilized to speed up the marine vessels or to increase their range.

O. Konur (✉) · S. A. Korkmaz · O. Yuksel
Department of Marine Engineering, Dokuz Eylul University, Izmir, Turkey
e-mail: olgun.konur@deu.edu.tr

S. A. Korkmaz
e-mail: aykut.korkmaz@deu.edu.tr

O. Yuksel
e-mail: onur.yuksel@deu.edu.tr

Y. Gulmez
Department of Marine Engineering, Iskenderun Technical University, Iskenderun, Hatay, Turkey
e-mail: yigitgulmez@gmail.com

A. Erdogan · C. O. Colpan
Department of Mechanical Engineering, Dokuz Eylul University, Izmir, Turkey
e-mail: anilerdogan1992@hotmail.com

C. O. Colpan
e-mail: ozgur.colpan@deu.edu.tr

K. E. Erginer
Department of Maritime Education, Dokuz Eylul University, Izmir, Turkey
e-mail: emrah.erginer@deu.edu.tr

Keywords Solar energy · Seawater-cooling systems · PV panel · Thermodynamic analysis

1 Introduction

The crystalline silicon solar cells, as the biggest shareholder in the photovoltaic (PV) industry, can only reach up to 26.6% cell efficiency values without the use of concentrators [1]. As a result of more comprehensive researches for silicon-based solar cells, the maximum cell efficiency value of 46% [1] has been achieved with the help of nanotechnology and multi-junction products with concentrating PV technology.

Silicon solar cells are specialized semiconductor diodes in which electrical current is being driven by the energy of photons. $I–V$ characteristic of a silicon solar cell can be derived from the diode law for ideal diodes. The diode law is a function of the temperature that shows the negative impact on energy efficiency upon increasing temperatures. The temperature coefficient states the effect of the temperature on cells or solar panels. Lowering the temperature coefficient still lies as a challenge among solar panel manufacturers that could not be lowered to zero because of the natural characteristic of crystalline silicon cells [2]. As can be deduced from the information given above, a cooling system fitted to the solar modules would increase the power output substantially. The heat exchange from the surface of the solar cell/panel can be achieved by a fluid flow like air or water. The land applications of these systems mostly utilize from the water as the cooling medium because of good thermo-physical properties of water. The water is heated up during the cooling process and then utilized as hot water for domestic applications. This system is called the hybrid systems; also known as photovoltaic/thermal (PV/T) systems.

As the environment around marine vessels is water-rich and relatively cool, water would also be an effective source to be used for cooling purpose. PV/T systems stand as an alternative for marine vessels that need hot water, but the requirement for continuous cooling water supply for the PV system and the limited space for the collection tank cause restrictions against utilizing these systems. On the contrary, open loop cooling water systems can meet the continuous cooling water demand of PV cooling systems; only by discharging the collected waste heat out of the system. In the open-cooling water circuits, the water is taken from the environment by a pump; and discharged though the vessel is overboard after the cooling duty is accomplished.

A considerable amount of papers on the cooling systems of PV panels has been published in the literature. Tiwari and Sodha [3] evaluated the performance of PV/thermal water/air heating system with a parametric study. They developed a thermal model of integrated photovoltaic and thermal solar (IPVTS) water/air heating system. Four configurations, (a) unglazed with tedlar (UGT), (b) glazed with tedlar (GT), (c) unglazed without tedlar (UGWT) and (d) glazed without tedlar (GWT), were tried. The results showed that IPVTS system efficiency is about 65% in winter conditions and 77% in summer conditions. Also, IPVTS system with water has higher daily efficiency than with air for all configurations except GWT. Odeh and

Behnia [4] investigated the efficiency enhancement of PV modules using a cooling water system. They developed long-term performance modeling for a solar system with water cooling. To evaluate the model, an experimental setup was developed to validate the PV module with cooling. Results indicated that an increase of about 15% in system output was observed at peak radiation conditions. Du et al. [5] analyzed the performance of water-cooled concentrated photovoltaic (CPV) system. The active water-cooling system was tested with experimental setup and the effect of water flow rate analyzed. The results of the experiment showed that the CPV module's operating temperature decreased under 60 °C and its power output increased. Teo et al. [6] investigated the effects of the active cooling systems on photovoltaic (PV) modules. To achieve the active cooling of the PV cells, they designed a manifold to send the air uniformly to the back of the panel. They practiced simulations and experiments with and without active cooling. According to results, without active cooling, solar cells can achieve an efficiency of 8–9%. When the active cooling was implemented, the efficiency of the solar cells reached to between 12 and 14%. Bahaidarah et al. [7] studied performance analysis of PV model with water cooling for hot climates. They developed a mathematical model, which can predict various parameters affecting the performance, using EES (Engineering Equation Solver) software. The results of the numerical model illustrated that with active cooling module temperature decreased 20% and panel efficiency increased by 9%. Moharram et al. [8] enhanced the performance of the PV panels using water cooling. A mathematical model was developed to determine when to start the cooling process. A water spray cooling system model was proposed to determine the cool down period of PV panels. Based on the results of the models, PV panels had the maximum output energy if cooling of the panels started when the temperature of the PV panels reached a maximum allowable temperature (MAT) of 45 °C. Baloch et al. [9] conducted an experimental and numerical investigation about the converging channel cooling method. Experimental setups for uncooled PV and converging channel cooled PV systems were carried out subjected to the hot climate of Saudi Arabia for June and December. An extensive system model enhanced to numerically evaluate the performance of the PV systems. Temperatures are measured for an uncooled PV showed cell as 71.2 and 48.3 °C for June and December, respectively. With converging cooling, cell temperature was reduced remarkably to 45.1 °C for June and 36.4 °C for December. The power output and the alteration efficiency increased by 35.5 and 36.1%, respectively, when compared to the performance of an uncooled PV system. Popovici et al. [10] studied on the enhancement of the PV panel efficiency using air-cooled heat sinks. They presented a numerical model to reduce the temperature of the panel surface with a high thermal conductivity material. The numerical simulation was carried out using ANSYS-Fluent software to investigate the cooling efficiency. According to results, the temperature decreased at least 10 °C, and the produced maximum power increased from 6.97 to 7.55% comparing to uncooled panels for different angles. Kane et al. [11] conducted a study on optimization of thermoelectric (TEM) cooling technology for active cooling of a photovoltaic panel. The mathematical model of TEM was developed, and the performance enhancement of the PV system with thermoelectric cooling through this model was carried out. Results showed that PV system exposed

to wide spectrum other than visible light. Schiro et al. [12] studied on efficiency enhancement of photovoltaics using water cooling. The steady-state thermal model of photovoltaics was developed to compute the cooling regime. Also, a dynamic model was developed to predict the effect of external parameters. The model was validated with the experimental investigation. The results of the model indicated that water cooling improved overall performance. Bashir et al. [13] investigated the effect of back surface water cooling on the efficiency of PV modules. They experimented with four PV modules. Two of them had back surface water cooling, and the other two PV was used without cooling. The results showed that there was a linear relationship between the module efficiency and temperature. The average temperature of c-Si and p-Si modules without cooling was 13.6 and 7.2% lower, respectively, than the same modules without cooling. Because of the temperature drop, the average module efficiency of c-Si and p-Si was 13 and 6.2% higher, respectively, compared to the modules without cooling. Salem et al. [14] conducted a study about performance improvement of water cooling using Al_2O_3/PCM mixture. The study was carried out experimentally. Results showed that using the compound technique for cooling was more effective than using cooling with 100% water. 25% Al_2O_3/PCM and 75% water mixture ensured the highest PV performance. Ahmed et al. [15] assessed the performance of the combined PV with thermal water-cooling system for hot climate conditions. The experimental results of the study illustrated that the average surface temperature of the PV modules decreased from 44.8 to 30.3 °C on the back surface and from 46.6 to 36.9 °C on the front side with water cooling. PV with thermal cooling had 8% higher efficiency than PV module without cooling.

The studies discussed above outline that the thermal cooling has a remarkable effect on PV panel efficiency and the output temperature of the module. Studies involve mathematical modeling and experimental analyses and generally focus on hot climate conditions. However, these studies lack the consideration of the thermal cooling of a PV panel under different ambient conditions for marine applications. Marine vessels, especially yachts can use solar power, and for the cooling of the PV panel can be carried out easily with seawater. In this study, cooling solar panels with seawater in an open loop cooling water circuit for a 527-W solar-powered system is investigated. In order to observe the effects of cooling the panels, a thermodynamic analysis has been carried out. The thermodynamic model's data set is composed of the previous experimental study shown in Ref. [16]. The data was taken from one solar panel with eight cells on June irradiation conditions at Izmir, and the model is customized for the whole system based on it. In the model, the seawater in the ambient passes through a cooling system on the backside of the panel that is installed with a pump, so that the heat generated on the panel cools down and reduces the panel surface temperature. By taking the mass flow rate of the cooling water into account, the feasibility of cooling the solar panel system is investigated according to the solar irradiation changes by time.

2   Materials and Methods

In this study, a cooler integrated PV system designed for a solar boat race is investigated to predict the optimum power output parameters by building the thermodynamic model of the system via EES (Engineering Equation Solver) software. The model is validated with the data taken from the previous experimental research of Konur and Erginer [16], which was conducted with one solar panel with eight cells on June irradiation conditions of Izmir. The experimental research provides the required data of panel surface temperature, power output, ambient temperature, cooling water inlet/outlet temperatures and pressure, solar irradiation and volumetric flow rate of cooling water for cooled and uncooled conditions. A reference point is picked up from the solar irradiation—power output graphics of the experimented solar panel. The other results are validated using the following formulations shown in Sects. 2.2 and 2.3 for both cooled and uncooled solar panels. As the results are consistent with the experimental results as shown in Fig. 3, the 527-W solar panel system parameters designed for the solar boat race are then used in the same model to get an optimum cooling water volumetric flow rate on specific irradiation conditions.

2.1   Geometrical Properties

Solar panel used in the experiment was made of an FR4 layer at the bottom, a monocrystalline solar cell in the middle, and a Teflon fluoropolymer layer on the top surface as shown in Fig. 1. Water-cooling system is designed as a duct-flow-type heat exchanger that directly interacts with the back surface of the solar panel. The heat exchanger is established with an insulating layer made of Plexiglas and packing in the middle of the Plexiglas and solar panel, which allows the water to flow through
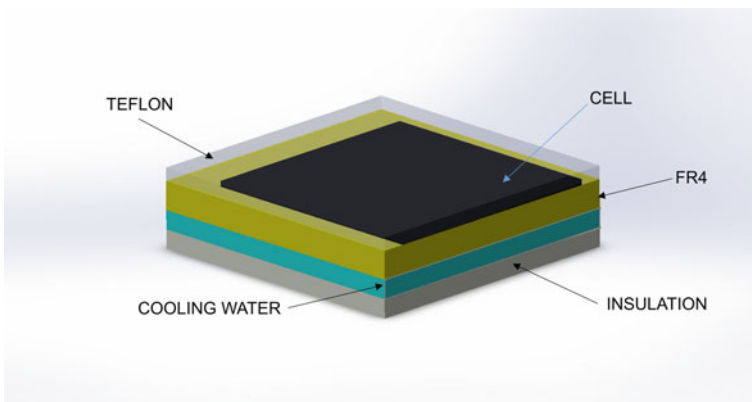
Fig. 1 Cross-sectional view of solar panel for one cell

Table 1 Geometric parameters of experimented and theoretically investigated solar panel systems

Properties	Experimented solar panel system	527 W Solar panel system
L_{teflon} (Teflon thickness)	0.007 m	0.007 m
L_{cell} (cell thickness)	0.003 m	0.003 m
L_{FR4} (FR4 layer thickness)	0.015 m	0.015 m
b_{PV} (solar panel breadth)	0.36 m	0.419 m
l_{PV} (solar panel length)	0.70 m	3.894 m
N_{cell} (number of cells)	8	156
A_{PV} (solar panel area)	0.252 m^2	3.263 m^2
H_{heat_exc} (heat exchanger height)	0.01 m	0.01 m
W_{heat_exc} (heat exchanger width)	0.34 m	0.40 m
L_{heat_exc} (heat exchanger length)	0.68 m	3.874 m
D_{gasket} (dimensions of gasket between panel and cooler; square type)	0.01 m × 0.01 m	0.01 m × 0.01 m
β_{cell} (packing factor of solar panel)	0.7484	0.7470

a duct of 10 mm height. The geometrical properties of the experimented solar panel that is used for validating the model are given in Table 1. The geometric parameters of the 527 W solar-powered system, which is the main focus of this paper, are also shown in the same table.

2.2 Thermal Model

The thermal model of the system has a resemblance to PV/T systems as these systems benefit from the waste heat produced from the PV panel by a heat exchanger. These systems are commonly made of glass, cell, a layer of Tedlar and an integrated heat exchanger at the bottom, which are not viable for solar boats because of their excessive weight. Flexible and light-weighted panels are manufactured for solar boats to endure the rough conditions of water and get better performance. An equivalent thermal resistance diagram of the investigated water-cooled and uncooled flexible solar panel system is shown in Fig. 2.

The assumptions for the developed model are given as follows:

- The system is considered to be in steady-state conditions.
- Contact resistances between each layer are neglected.
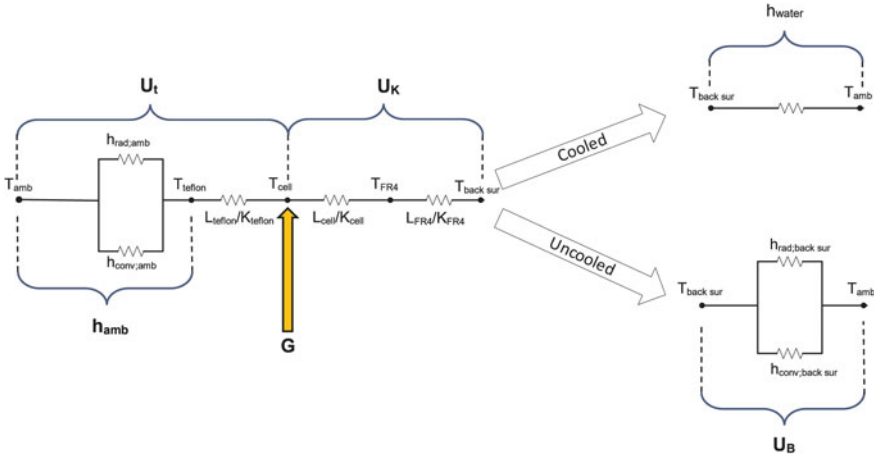
Fig. 2 Equivalent thermal resistance diagram for both cooled and uncooled PV system

- Simultaneous heating and cooling variations of the PV panel through time are considered to be negligible.
- Cooling water flow below the PV panel is assumed as uniform.
- Radiation heat transfer between the insulation and back surface of the PV panel is neglected.

Solar irradiation is directed to the solar cell. Heat is distributed from the cell to two sides; one of which travels through the ambient by passing the Teflon layer, and the other passes the cell and the FR4 layer through the back surface of the panel. U_t describes the overall heat transfer coefficient from the ambient to the cell surface. U_K refers to the overall heat transfer coefficient from the cell surface to the back surface of the FR4 layer. U_{tK} is the combination of U_t and U_K. U_{tf} describes the overall heat transfer coefficient from the top surface ambient to the water flowing through the backside of the panel. The defined U_t, U_K, U_{tK}, and U_{tf} parameters are formulated as shown in Eqs. 1–4.

$$U_t = [(L_{\text{teflon}}/K_{\text{teflon}}) + (1/h_{\text{amb}})]^{-1} \tag{1}$$

$$U_K = [(L_{\text{cell}}/K_{\text{cell}}) + (L_{\text{FR4}}/K_{\text{FR4}})]^{-1} \tag{2}$$

$$U_{tK} = (U_t \cdot U_K)/(U_t + U_K) \tag{3}$$

$$U_{tf} = (U_{tK} \cdot h_{\text{water}})/(U_{tK} + h_{\text{fluid}}) \tag{4}$$

Penalty factor due to the presence of solar cell material, Teflon and FR4 is defined as h_{p1}, which can be found by Eq. 5. h_{p2} is also described in Eq. 6 as the penalty factor due to the interface between FR4 and the cooling water. These factors refer

to the amount of energy divided to the related section and are used in the energy balance to find specific terms such as the panel back surface temperature ($T_{\text{back sur}}$) and the rate of thermal energy transferred to the cooling water ($\dot{Q}_u$) as shown in Eqs. 15 and 24.

$$h_{p1} = (U_t)/(U_t + U_K) \tag{5}$$

$$h_{p2} = (h_{\text{water}})/(U_{tK} + h_{\text{water}}) \tag{6}$$

U_{tB} is described as the overall heat transfer coefficient from FR4 layer to the ambient of back surface to calculate the uncooled process as given in Eq. 7. U_{KB} is defined as the overall heat transfer coefficient from the back surface of the cell to back surface ambient on uncooled condition in Eq. 8. It is also denoted that U_t and U_{tK} should be calculated separately for the uncooled process by Eqs. 9 and 10 because of the radiation heat transfer coefficient variation with the Teflon surface temperature [3, 7, 17].

$$U_{tB} = (L_{\text{FR4}}/K_{\text{FR4}}) + \left(1/\left(h_{\text{conv,back sur}} + h_{\text{rad,back sur}}\right)\right) \tag{7}$$

$$U_{KB} = (L_{\text{FR4}}/K_{\text{FR4}}) + \left(1/\left(h_{\text{conv,back sur}} + h_{\text{rad,back sur,uncooled}}\right)\right) \tag{8}$$

$$U_{t,\text{uncooled}} = \left[(L_{\text{teflon}}/K_{\text{teflon}}) + \left(1/h_{\text{amb,uncooled}}\right)\right]^{-1} \tag{9}$$

$$U_{tK,\text{uncooled}} = \left(U_{t,\text{uncooled}} \cdot U_K\right)/\left(U_{t,\text{uncooled}} + U_K\right) \tag{10}$$

Thermal and physical parameters used in the thermal model for the experimented and new designed 527 W systems are shown in Table 2. While the experimented system references are taken from the measured data, reference panel temperature and efficiency values for the 527-W system are obtained from the catalog of the panel manufacturer [18].

Surface temperatures of each layer (Teflon, cell, FR4) are found by energy balance equations in Eqs. 11–16.

$$T_{\text{teflon}} = [(K_{\text{teflon}} \cdot T_{\text{cell}}) - (U_t \cdot L_{\text{teflon}} \cdot (T_{\text{cell}} - T_{\text{amb}}))]/K_{\text{teflon}} \tag{11}$$

$$T_{\text{teflon,uncooled}} = \left[\left(K_{\text{teflon}} \cdot T_{\text{cell,uncooled}}\right) - \left(U_{t,\text{uncooled}} \cdot L_{\text{teflon}} \cdot (T_{\text{cell,uncooled}} - T_{\text{amb}})\right)\right]/K_{\text{teflon}} \tag{12}$$

$$T_{\text{cell}} = \left[((\alpha\zeta)_{\text{eff}} \cdot G) + (U_t \cdot T_{\text{amb}}) + (U_K \cdot T_{\text{back sur}})\right]/(U_t + U_K) \tag{13}$$

$$T_{\text{cell,uncooled}} = [\zeta_{\text{teflon}} \cdot G \cdot ((\alpha_{\text{cell}} \cdot \beta_{\text{cell}}) + (\alpha_{\text{FR4}} \cdot (1 - \beta_{\text{cell}})))$$
$$+ \left(T_{\text{amb}} \cdot \left(U_{t,\text{uncooled}} + U_{KB}\right)\right)]/(U_t + U_{KB}) \tag{14}$$

$$T_{\text{back sur}} = \left[\left(h_{p1} \cdot (\alpha\zeta)_{\text{eff}} \cdot G\right) + (U_{tK} \cdot T_{\text{amb}}) + \left(h_{\text{water}} \cdot T_{\text{water,average}}\right)\right]/(U_{tK} + h_{\text{water}}) \tag{15}$$

Table 2 Thermal and physical parameters of experimented and theoretically investigated solar panel systems

Properties	Experimented solar panel system	527-W solar panel system
K_{teflon} (Teflon conductivity)	0.195 W/m K [19]	0.195 W/m K
K_{cell} (solar cell conductivity)	148.9 W/m K [20]	148.9 W/m K
K_{FR4} (FR4 conductivity)	0.25 W/m K [21]	0.25 W/m K
T_{amb} (ambient temperature)	305 K [16]	305 K
$T_{\text{water,in}}$ (cooling water inlet temperature)	296 K [16]	296 K
$T_{\text{ref,panel}}$ (reference panel temperature)	295.6 K [16]	293 K (NOCT conditions)
$\eta_{\text{ref,panel}}$ (reference panel efficiency)	0.159 [16]	0.166 [18]
V_{air} (air velocity of ambient)	1 m/s	1 m/s
$\varepsilon_{\text{teflon}}$ (emissivity of Teflon)	0.88 [22]	0.88
ε_{FR4} (emissivity of FR4)	0.90 [23]	0.90
P_{water} (cooling water pressure)	1.5 bar [16]	1.5 bar
α_{cell} (absorptivity of solar cell)	0.85 [22]	0.85
α_{FR4} (absorptivity of FR4)	0.65 [22]	0.65
ζ_{teflon} (transmissivity of Teflon)	0.96 [24]	0.96
G (reference solar irradiation value)	1000 W/m^2	1000 W/m^2

$$T_{\text{back sur,uncooled}} = \left[\left(h_{p1} \cdot (\alpha\zeta)_{\text{eff}} \cdot G \right) + \left(U_{tK,\text{uncooled}} \cdot T_{\text{amb}} \right) \right.$$
$$\left. + \left(h_{\text{amb,uncooled}} \cdot T_{\text{amb}} \right) \right] / \left(U_{tK,\text{uncooled}} + h_{\text{amb,uncooled}} \right) \qquad (16)$$

Convective heat transfer coefficient is a function of wind speed as can be seen in Eq. 17 [25]. Wind speed is assumed as 1 m/s for both upper and bottom surface calculations. It should be noted that the combined heat transfer coefficient to ambient (h_{amb}) is found by combining the radiation heat transfer coefficient ($h_{\text{rad,amb}}$) in Eq. 18 [26] and convective heat transfer coefficient ($h_{\text{conv,amb}}$) to ambient for upper and bottom surfaces on the cooled process as given in Eq. 21. Convective heat transfer coefficient for the uncooled process is calculated by following formulations shown in Eqs. 19, 20, and 22.

$$h_{\text{conv,amb}} = 10.45 - V_{\text{air}} + 10 \cdot (V_{\text{air}})^{1/2} \qquad (17)$$

$$h_{\text{rad,amb}} = \varepsilon_{\text{teflon}} \cdot \sigma \cdot \left[(T_{\text{back sur}})^2 + (T_{\text{amb}})^2 \right] \cdot (T_{\text{back sur}} + T_{\text{amb}}) \qquad (18)$$

$$h_{\text{rad,amb,uncooled}} = \varepsilon_{\text{teflon}} \cdot \sigma \cdot \left[\left(T_{\text{teflon,uncooled}} \right)^2 + \left(T_{\text{amb}} \right)^2 \right] \cdot \left(T_{\text{teflon,uncooled}} + T_{\text{amb}} \right) \tag{19}$$

$$h_{\text{rad,back sur,uncooled}} = \varepsilon_{\text{FR4}} \cdot \sigma \cdot \left[\left(T_{\text{back sur,uncooled}} \right)^2 + \left(T_{\text{amb}} \right)^2 \right]$$
$$\cdot \left(T_{\text{back sur,uncooled}} + T_{\text{amb}} \right) \tag{20}$$

$$h_{\text{amb}} = \left[\left(1/h_{\text{conv,amb}} \right) + \left(1/h_{\text{rad,amb}} \right) \right] / \left[\left(1/h_{\text{conv,amb}} \right) \cdot \left(1/h_{\text{rad,amb}} \right) \right] \tag{21}$$

$$h_{\text{amb,uncooled}} = \left[\left(1/h_{\text{conv,amb}} \right) + \left(1/h_{\text{rad,amb,uncooled}} \right) \right] / \left[\left(1/h_{\text{conv,amb}} \right) \cdot \left(1/h_{\text{rad,amb,uncooled}} \right) \right] \tag{22}$$

Heat removal factor (F_R) is considered for calculating $\dot{Q}_u$ in Eqs. 23 and 24 [27]. F' is the collector efficiency factor and assumed as 1 because the cooling water directly flowing below the FR4 layer. Heat exchanger is designed as duct-flow-type. h_{water} is calculated according to the mass flow rate of water ($\dot{m}_{\text{water}}$) using the EES software.

$$F_R = \left[\dot{m}_{\text{water}} \cdot C_{p,\text{water}} \cdot 1000 \cdot \left(1 - e^{\frac{-A_{\text{PV}} \cdot U_{tf} \cdot F'}{\dot{m}_{\text{water}} \cdot C_{p,\text{water}} \cdot 1000}} \right) \right] / \left(A_{\text{PV}} \cdot U_{tf} \right) \tag{23}$$

$$\dot{Q}_u = \left[\left(h_{p1} \cdot h_{p2} \cdot (\alpha\zeta)_{\text{eff}} \cdot G \right) - \left(U_{tB} \cdot \left(T_{\text{water,in}} - T_{\text{amb}} \right) \right) \right] \cdot A_{\text{PV}} \cdot F_R \tag{24}$$

$T_{\text{water,out}}$ can also be calculated from the well-known energy equation, as $\dot{Q}_u$ is found by Eq. 24. $(\alpha\zeta)_{\text{eff}}$ is defined as the product of effective absorptivity and transmissivity as given in Eq. 25 [3].

$$(\alpha\zeta)_{\text{eff}} = \zeta_{\text{teflon}} \cdot \left[(\alpha_{\text{cell}} \cdot \beta_{\text{cell}}) + (\alpha_{\text{FR4}} \cdot (1 - \beta_{\text{cell}})) - (\eta_{\text{cell}} \cdot \beta_{\text{cell}}) \right] \tag{25}$$

2.3 Electrical Model

The final step of the model is to calculate the power output obtained by the cooling effect. PV efficiency is needed to be determined for different temperatures. Reference cell temperature and panel efficiency at that point are chosen from the experimental data to validate the model. Then, the reference points given by the solar panel manufacturer are used on the model to simulate the new solar panel set efficiency as given in Eqs. 26–28 [27].

$$\eta_{\text{cell}} = \eta_{\text{ref,cell}} \cdot \left[1 - 0.0045 \cdot (T_{\text{cell}} - T_{\text{ref}}) \right] \tag{26}$$

$$\eta_{\text{PV}} = \eta_{\text{cell}} \cdot \zeta_{\text{teflon}} \cdot \beta_{\text{cell}} \tag{27}$$

$$P_{\text{output}} = \eta_{\text{PV}} \cdot A_{\text{PV}} \cdot G \tag{28}$$

3   Results and Discussion

EES software provides a parametric study of the equations given in Sect. 2. The experimental and calculated data sets are defined and shown as a graphic in Fig. 3. The time parameters on the *x*-axis correspond to the solar irradiation data that are measured at that specific time. The irradiation values can be found in the study of Konur and Erginer [16]. The difference is considered to be caused by the measurement errors of the experiment, and also by the assumptions taken from Table 2. Nonetheless, power output difference values validate the model by showing similarity in Fig. 3. The standard deviation value for the difference between calculated and experimented power output differences is calculated as 1.37 W by utilizing the statistical analysis module of SPSS software.

The 527-W system model is built with the parameters shown in Tables 1 and 2 in the next step. The cooling water volumetric flow rate chart is obtained as shown in Fig. 4. 8 L/min pumping capacity is considered to be proper as it would lead to 109-W power output difference under 1000 W/m² solar irradiation condition.

The volumetric flow rate of 8 L/min is then defined as constant in the model. The effect of changing solar irradiation on power output difference with constant ambient temperature is investigated in Fig. 5 to determine the feasibility of the cooling system.

The only power consumption for the cooling system will cause from the cooling water pump. The pump should be selected by considering the ability of self-priming as it would be placed over the sea level. The power consumption of a commercially
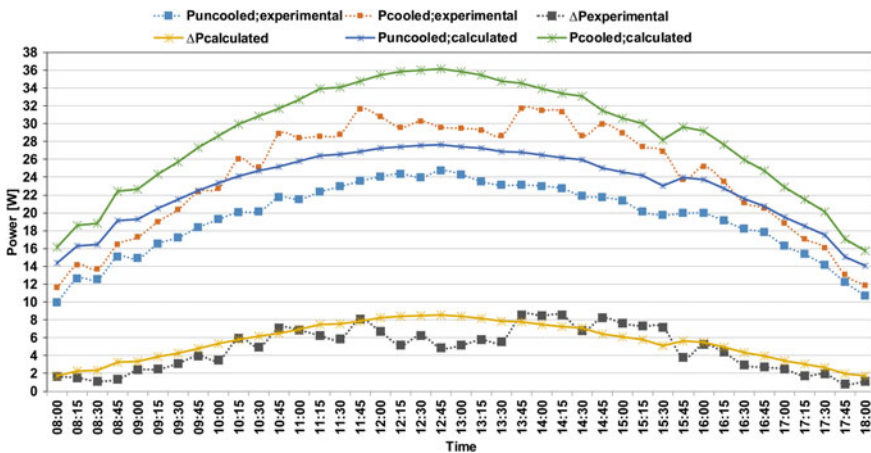
Fig. 3   Validation graphic of experimented and modeled systems by utilizing power outputs
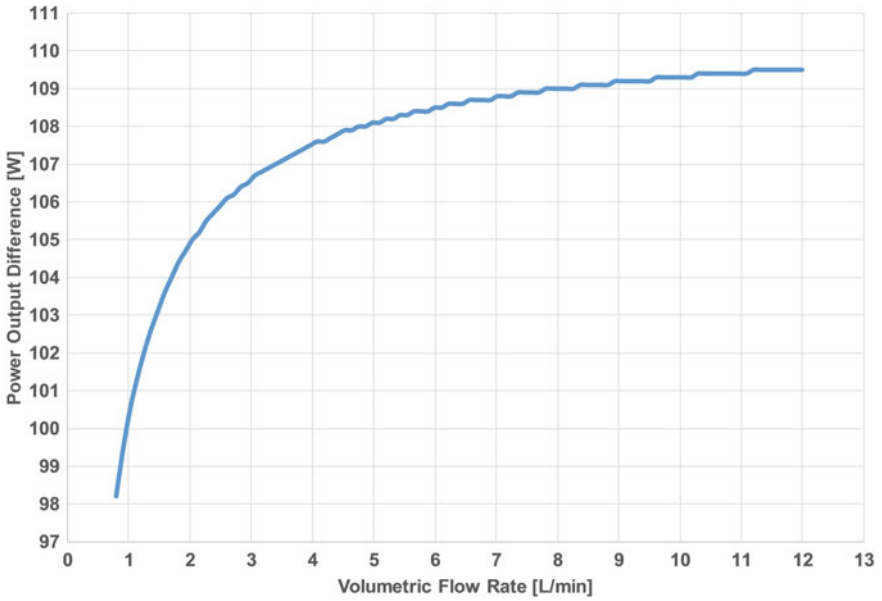
Fig. 4 Obtained power output difference according to changing volumetric flow rate for new panel system
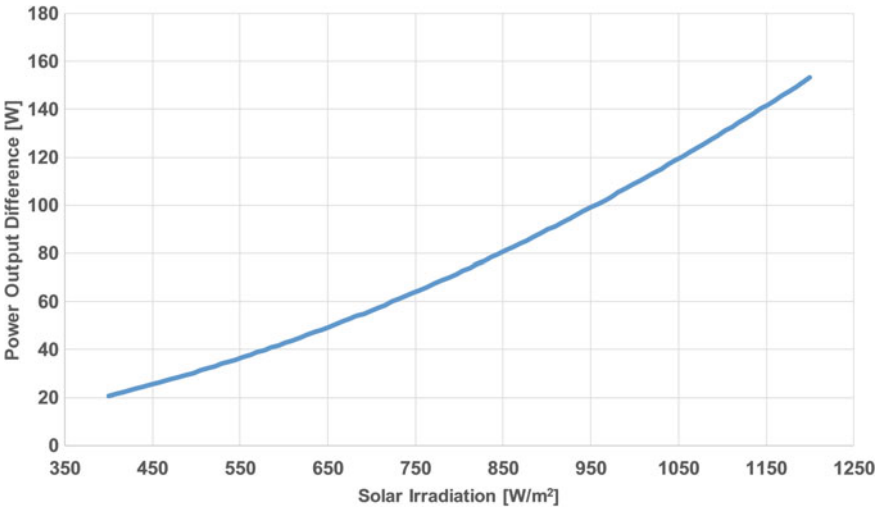
Fig. 5 Effect of solar irradiation on the power output difference

available water pump is given as 38.4 W at 1.5 bar and 8 L/min pumping capacity in Ref. [28]. Thus, the cooling water system would cause power consumption rather than gain for the irradiation values below 600 W/m^2 for the given parameters.

4 Conclusions

PV/T systems are well-known systems, but these systems' main purpose is to provide heat from the solar irradiation and improve the panel efficiency as a consequence. In this study, only the efficiency improvement is considered for foldable solar panels considering feasibility for marine vessels. The thermal energy produced by the solar system is regarded as waste heat, which is removed from the system by an open loop cooling water circuit. The thermal model calculations of the water-cooled solar panel system are validated through the experimental results of the author's referenced study. Based on the results derived from the study, the following conclusions are drawn:

- The simulation results show the potential of these systems as the power output difference of the panel set is more than the consumed power for cooling on above specific irradiation conditions.
- The remaining power output, which would be up to 37% of the uncooled system, is high enough to be utilized to speed up the marine vessels or to increase their range.
- Volumetric flow rate should be carefully selected for the cooling water system as the power output difference may be reduced with the increasing power consumption of the cooling water pump.
- Solar irradiation value of 600 W/m^2 has a critical role in the proposed system design. The cooling water system should be equipped with a shut-off system that prevents power consumptions higher than the power produced with the cooling system.

The experimental study and the current study were carried for the June irradiation conditions of Izmir, Turkey. A more comprehensive study for a year-long period of different locations may be recommended to attract the potential technology developers and end-users utilizing from the solar systems for marine vessels, accordingly.

References

1. NREL (2018) PV research cell record efficiency chart. https://www.nrel.gov/pv/assets/pdfs/pv-efficiency-chart.20181221.pdf. Accessed on 22 Apr 2019
2. Meral ME, Dinçer F (2011) A review of factors affecting operation and efficiency of photovoltaic based electricity generation systems. Renew Sustain Energy Rev 15:2116–2186
3. Tiwari A, Sodha MS (2006) Performance evaluation of hybrid PV/thermal water/air heating system: a parametric study. Renew Energy 31(2006):2460–2474

4. Odeh S, Behnia M (2009) Improving photovoltaic module efficiency using water cooling. Heat Transfer Eng 30(6):499–505
5. Du B, Hu E, Kolhe M (2012) Performance analysis of water cooled concentrated photovoltaic (CPV) system. Renew Sustain Energy Rev 16(9):6732–6736
6. Teo HG, Lee PS, Hawlader MNA (2012) An active cooling system for photovoltaic modules. Appl Energy 90(1):309–315
7. Bahaidarah H, Subhan A, Gandhidasan P, Rehman S (2013) Performance evaluation of a PV (photovoltaic) module by back surface water cooling for hot climatic conditions. Energy 59:445–453
8. Moharram KA, Abd-Elhady MS, Kandil HA, El-Sherif H (2013) Enhancing the performance of photovoltaic panels by water cooling. Ain Shams Eng J 4(4):869–877
9. Baloch AA, Bahaidarah HM, Gandhidasan P, Al-Sulaiman FA (2015) Experimental and numerical performance analysis of a converging channel heat exchanger for PV cooling. Energy Convers Manage 103:14–27
10. Popovici CG, Hudişteanu SV, Mateescu TD, Chereches̗ NC (2016) Efficiency improvement of photovoltaic panels by using air cooled heat sinks. Energy Procedia 85:425–432
11. Kane A, Verma V, Singh B (2017) Optimization of thermoelectric cooling technology for an active cooling of photovoltaic panel. Renew Sustain Energy Rev 75:1295–1305
12. Schiro F, Benato A, Stoppato A, Destro N (2017) Improving photovoltaics efficiency by water cooling: modelling and experimental approach. Energy 137:798–810
13. Bashir MA, Ali HM, Amber KP, Bashir MW, Ali H, Imran S, Kamran MS (2018) Performance investigation of photovoltaic modules by back surface water cooling. Therm Sci 22(6)
14. Salem MR, Elsayed MM, Abd-Elaziz AA, Elshazly KM (2019) Performance enhancement of the photovoltaic cells using Al$_2$O$_3$/PCM mixture and/or water cooling-techniques. Renew Energy 138:876–890
15. Ahmed MS, Mohamed ASA, Maghrabie HM (2019) Performance evaluation of combined photovoltaic thermal water cooling system for hot climate regions. J Sol Energy Eng 141(4):041010
16. Konur O, Erginer E (2016) Effect of sea water cooling systems to the energy efficiency of solar panels on marine vessels. In: GMC 2016 conference proceedings book
17. Enteria N, Akbarzadeh A (2014) Solar energy sciences and engineering applications. CRC Press, Boca Raton
18. Sunpower Corp. (2017) https://us.sunpower.com/sites/sunpower/files/media-library/spec-sheets/sp-sunpower-maxeon-solar-cells-gen3.pdf. Accessed on 8 Feb 2018
19. Chemours (2017) https://www.chemours.com/Teflon_Industrial/en_US/assets/downloads/teflon-fep-film-properties.pdf. Accessed on 5 Feb 2018
20. Haynes W (2013) CRC handbook of chemistry and physics, 94th edn. CRC Press, Boca Raton
21. Klouda P (2004) Thermally conductive printed circuit board materials. www.ewh.ieee.org/soc/cpmt/presentations/cpmt0412b.pdf. Accessed on 5 Feb 2018
22. Redrok Energy (2017) http://www.redrok.com/concept.htm#emissivity. Accessed on 27 Jan 2018
23. Adam J (2002) PCB modelling refresher. http://webparts.mentor.com/flotherm/support/supp/mm/pcb_modelling/. Accessed on 27 Jan 2018
24. Bilgen E (2013) Intersol eighty five: proceedings of the ninth biennial congress of the international solar energy society, vol 1. Elsevier, Amsterdam
25. Khabari A, Zenouzi M, O'Connor T, Rodas A (2014) Natural and forced convective heat transfer analysis of nanostructured surface. In: Proceedings of the world congress on engineering 2014, vol I, London, UK
26. Çengel Y, Ghajar AJ (2015) Heat and mass transfer, 5th edn. McGraw-Hill Education, New York
27. Duffie JA, Beckman WA (2013) Solar engineering of thermal processes, 4th edn. Wiley, London
28. Marinetech (2018) http://www.tekneyataksesuarlari.com/24V-UP2-P-Tatli-ve-Tuzlu-Su-Transfer-Pompasi-Pervaneli,PR-1396.html. Accessed on 20 Feb 2018

Effect of Using Photovoltaic Power Systems in Sustainable Energy Action Plan of a Big County Municipality in Turkey

Mert Biter and Mete Cubukcu

Abstract Integration of solar photovoltaic energy systems to urban planning is one of the key priorities of local authorities who cares the global warming threat. "Covenant of Mayors" (CoM), which is the most extensive association of local governments in the world, has started serious works on fighting against climate change and required the local governments' preparation of sustainable energy action plans (SEAP). Bornova Municipality has calculated its reference greenhouse gas emission inventory as 31,432 t CO_2e (CO_2 equivalent) in the SEAP delivered to the CoM on February 7th, 2013. In accordance with the CoM goal, it has committed to reduce its greenhouse gas emission value by 25% by 2020 and realized the installation of a 300 kWp photovoltaic power system (PVPS) in 2013 as the most important project. The main objective of this study is to use the real-time data of 300 kWp plant and evaluate its contribution to the reduction of greenhouse gas emission. Moreover, usable potential roof surface areas of the service buildings of Bornova Municipality have been calculated and the contribution of the increase of the PVPS capacity to the goal of greenhouse gas emission reduction by 2020 has been studied.

Keywords Sustainable energy action plan · Greenhouse gases · Photovoltaic power systems · Covenant of Mayors

1 Introduction

Industrialized cities and increase of population forced the human beings to consider different energy resources and fossil fuels for their requirements [1]. Nobel prize-awarded Swedish scientist Svante Arrhenius (1859–1927) emphasized the seriousness of this circumstance in his study on the relationship between the carbon dioxide in the atmosphere and the average temperature of the earth in 1896 and entered the literature as the very first person who suggested that that would lead to global warming

M. Biter (✉) · M. Cubukcu
Ege University Solar Energy Institute, Izmir, Turkey
e-mail: mertbiter35@gmail.com

M. Cubukcu
e-mail: mete.cubukcu@ege.edu.tr

almost a century in advance [2]. The global energy use has grown since the industrial revolution in close relation with the increase of welfare [3]. Use of conventional fuels including, without limitation, coal as a source of energy for development for many years by countries significantly increased the impacts of the climate change after 1950. Cities, accounting for more than 3/4 of global final energy consumption, are equipping themselves with governance tools to improve energy efficiency [4]. Transition the global economy from fossil fuels to renewable energy sources has been identified as a key strategy for mitigating climate change [5]. The Paris agreement is a milestone in global climate policy due to its wide international support [6]. Local communities or municipalities are one of these actors, as local action is seen as key to combating climate change [7], and energy and climate planning at the municipal level is a vital part of this decarbonization [8–10]. Green energy plays a significant role in the strategic energy planning process for any country [3].

The role of local authorities in tackling climate change can be traced through the emerging local sustainable energy and climate action plans which commit to voluntary emissions reduction targets [11]. The sustainable energy action plan is the most common and widespread strategy due to its voluntary nature [12].

"CoM" is created under the European Commission and of which basic objective is to reduce the emission of greenhouse gas and to encourage and support the use of renewable energy resources for a world that fights against global warming. Relevant administrations that have signed this commit themselves to reduce their greenhouse gas emission value by 20% as a minimum by 2020 and prepare a SEAP containing their strategies and actions. The number of those that signed the CoM is 7755 all over the world and the number of the local administration that has signed it is 11 in Turkey as of February 21st, 2018 [13].

Bornova is one of the most important metropolitan counties of Izmir with its population of 442.389 inhabitants as of 2017, industrial estates and factories, hospitals and universities within its boundaries. The geographic structure of Bornova looks like a basin or a lowland surrounded by mountains. From the sea level, the altitude changes from 20 to 200 m within the residence area, but it reaches to 600 m in the mountains [14]. A part of Bornova is shown in Fig. 1 [15]. Besides its membership to CoM, it is also a member of such extremely significant non-governmental organizations as "Energy Cities" and "United Nations Global Compact."

Bornova Municipality became a party to CoM on May 5th, 2011, and presented its SEAP on February 7th, 2013. It has targeted to reduce its greenhouse gas emission by 25% by 2020 to comply with the scope of CoM.

2 Overview

Cities are essential players of the world in the efforts of adaptation to climate change and reduction of carbon emission [16, 17]. That is to say, 74% of the population

Fig. 1 A picture of Bornova county

live in cities in Europe; it is for this reason why and how cities will be engaged in the climate policy. This is the main issue in discussions for the time being [18–22]. Therefore, combating climate change is an issue of priority for the European Union and the Union has targeted to achieve reduction rates of 20% by 2020, 40% by 2030, and 80% by 2080 as compared to the levels of the 1990s in the short and long terms [23].

2.1 Covenant of Mayors Initiative

Once the European Union had adopted the climate and energy package, following the perception of the key role of the cities in reducing the impacts of climate change in 2008, the European Commission (EC) activated CoM initiative in order to encourage local authorities to apply sustainable energy policies in their respective regions [24]. A community of municipalities has the largest network of the world, and the *Covenant of Mayors* focused on spreading and supporting the use of clean energy resources for cities that have reduced greenhouse gases and combat the adverse impacts of climate change.

Urban administrations that signed the Covenant of Mayors have committed themselves to reduce their greenhouse gas emission values by 20% as a minimum by 2020 by applying the strategies and actions which they will design and include into SEAP in accordance with the "20-20-20 Climate–Energy Package" [25] which the European Union has approved. Climate and energy package targets:

- To save 20% in energy consumption as compared to the ordinary projection in 2020 (business as usual (BAU));
- To increase the share of renewable energy in energy consumption by 20% in 2020;
- To reduce CO_2 emissions by 20% in 2020 as compared to the value in 2005 [26].

2.2 Sustainable Energy Action Plan

Climate change requires more comprehensive studies to take sustainable development into consideration. Cinocca et al. [26] drew attention to the fact that the sustainable development studies burden the local administrations with more responsibility and to the importance of the principle "Think globally and act locally." Therefore, strengthening of the reduction and adaptation strategies in climate on cities basis has vital importance in terms of sustainable development [17, 27].

2.2.1 Definition and Scope of the Sustainable Energy Action Plan

European Union leads the global combat against climate change and tries to achieve all emission values by reducing the CO_2 rate by 20% and increasing the share of renewable energy by 20% and accomplishing a 20% reduction in energy consumption on 20-20-20 basis in question [28]. Local administrations have a significant role in the achievement of the European Union's goals of energy and climate. CoM consists of urban administrations comprised of the European and non-European countries in the reduction of the greenhouse gas emissions originating from the municipalities' use of energy by 2020 [29].

SEAP is an important document containing the steps planned in order to achieve the 2020 goals by a Covenant signatory. It uses the results of the basic emission inventory (BEI) and identifies the best actions and opportunities so that a local administration could achieve its greenhouse gas reduction goal. A tangible reduction goal is identified for a particular period, and long- and medium-term strategies are turned to actions. Signatories commit themselves to present their sustainable energy action plans during the year in which they declare their commitment.

CoM focuses on those actions as contained in the boundaries of authority of a municipality. SEAP should take into consideration the CO_2 reduction and the energy consumption of the end users. CoM promises cover the whole geographical area of the local administration. Both the public and the private sectors should therefore be included into the plan. A municipality is expected to commence SEAP studies about its own buildings, plants, and vehicle fleet in order to set an example. Main sectors on which the SEAP studies will basically focus are buildings, plants, and transportation. Then, local electricity generation (if applicable), long-term land use planning affecting energy consumption, incentive to the products with higher energy efficiency in the market and public utility purchases within the municipal boundaries
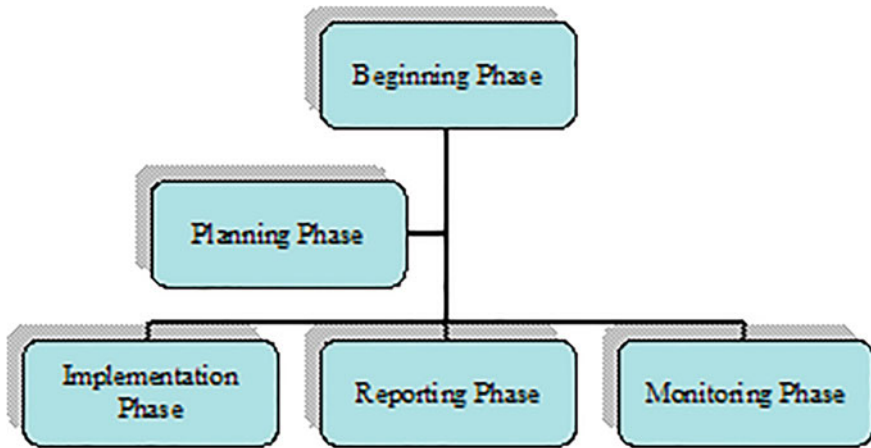
Fig. 2 Preparation phases of SEAP

should also be included into the contents of SEAP. Industry is not one of the key sectors of CoM, and the relevant CoM-signatory municipality may decide whether or not it will carry out any studies on industry. Under normal conditions, factories as contained in the European CO_2 emission trading system (ETS) are excluded from SEAP studies.

Preparatory process of SEAP is comprised of the beginning phase, planning, implementation, reporting, and monitoring steps. This may be represented by a flowchart (Fig. 2).

2.2.2 SEAP Structure

Sustainable energy action plan is dependent upon the results of the basic emission inventory quantifying the energy consumption and greenhouse gas emission quantities in the area remaining within the urban limits for a designated reference year. It further describes the short- and long-term actions to be applied in the priority areas developed in order to achieve the estimated greenhouse gas reduction goal [30]. Local administration that will prepare SEAP may make use of the following list [31]:

- Presentation of a summary containing the views of the mayor who occupies the managerial position in SEAP
- Description of the whole strategy from the beginning to the end

    - Objectives and goals.
    - Description of vision and current due diligence.
    - Coordination and structure of the established organization.
    - Personnel capacity to be assigned.
    - Inclusion of all stakeholders.

    – Budget.
    – Financial resources and supports anticipated for the planned investments.
    – Plans containing follow-up studies.

- Study containing the basic emission inventory (reference GHG inventory) should be included
- SEAP's outlines should be comprised of the methods and actions planned until 2020 (the year 2030 should also be taken into consideration in the long run)

    – Long-term goals and promises should be included.
    – Short- and long-term activities should be clearly described.
    – Description of the study to be carried out.
    – Person or company responsible for the relevant section should be designated.
    – Start and finish times should be identified.
    – Basic turning points should be represented (an important project to leave an impression).
    – Cost of the studies.
    – Estimated energy saving and renewable energy generation amount.
    – Estimated greenhouse gas reduction amount.

2.3 Local Administrations Preparing SEAPs in Turkey

Although cities occupy only 2% of the surface of the earth, their role in the amount of greenhouse gases they produce is clearly known [32]. This awareness has started to gradually increase in our country as well, and our local administrations have become parties to CoM and prepared sustainable energy action plans in order to be able to combat the climate change in the global area. Number of the local administrations preparing SEAPs is 11 as of March 24, 2019 [33] and is shown in Table 1.

Out of these 11 municipalities excluding Bornova, we will review the sustainable energy action plans as prepared by the Eskişehir Tepebası Municipality and Antalya Metropolitan Municipality in so short a manner.

2.3.1 Eskisehir Tepebasi Municipality

Greenhouse gas inventory of Tepebasi City was calculated as 749,119 tCO$_2$e in 2010 (Table 2) and this year is considered as the reference year [34].

Tepebası Municipality prepared the following actions and committed itself to reduce the greenhouse gas emission by 23% by 2020:

- To carry out energy efficiency studies in all residential and non-residential buildings;

Table 1 Local administrations preparing SEAPs in Turkey

Signing municipalities	Year of signing	SEAP presentation year
Çankaya Municipality	2015	2017
Bursa Metropolitan Municipality	2016 (2030-compliant)	2017
Maltepe Municipality	2014	2016
İzmir Metropolitan Municipality	2015	2016
Nilüfer Municipality	2014	2016
Kadıköy Municipality	2012	2016
Eskişehir Tepebaşı Municipality	2013	2014
Seferihisar Municipality	2011	2013
Bornova Municipality	2011	2013
Antalya Metropolitan Municipality	2013	2014
Karşıyaka Municipality	2011	2012

Table 2 Greenhouse gas emission by Tepebasi City

Category	Energy consumption (MWh)	CO_2e (t)
Buildings, equipment, plants, and industry	1,189,151	355,702
Transportation	1,099,072	291,259
Other emissions		102,158
Total	2,288,222	749,119

- To speed up the process of transition to natural gas in the existing residential buildings;
- To support the lighting area and electrical appliances by equipment with higher energy efficiency;
- To plan an urban transformation focusing on energy efficiency and renewable energy;
- To prefer electric vehicles for public transportation and prioritize the streetcar project in public transportation;
- To construct bicycle tracks and support bicycle use;
- To achieve transition to smart system applications in traffic;
- To make use of renewable energy in the municipal buildings and other residential buildings;
- To generate electricity by using biogas at the solid waste plant;
- To organize events on energy efficiency and energy saving.

Table 3 Greenhouse gas emission by Antalya Province

Category	Energy consumption (MWh)	CO_2e (t)
Buildings, equipment, plants, and industry	6,583,799	3,255,971
Transportation	8,556,095	2,054,890
Other emissions	0	529,243
Total	15,139,834	5,840,104

2.3.2 Antalya Metropolitan Municipality

Taking the year 2012 as a reference year, the Antalya Metropolitan Municipality (AMM) has determined its annual greenhouse gas inventory as 5,840,104 t CO_2e. It has been calculated that the relevant emission is consisted of buildings, equipment, and plants with 55.8%, of transport sector with 35.2% and of other sectors with 9% [35] (Table 3).

Antalya Metropolitan Municipality has committed itself to take the following actions and reduce the total emission amount by 23% by 2020:

- To bring energy efficiency to the forefront and prepare a renewable energy-based urban transformation plan;
- To carry out heat insulation studies at existing residential buildings, municipal service buildings, and business enterprises;
- To use fittings with higher energy efficiency in lighting;
- To plan photovoltaic integration works for street lighting;
- To increase the share of bus rapid transit and light rail system;
- To construct the infrastructure necessary for the proliferation of bicycle use;
- To encourage the use of electric or CNG-fueled vehicles;
- To optimize the traffic systems by renewable energy;
- To increase the renewable energy applications at hotels;
- To make use of solar energy in agricultural land;
- To support biomass recovery from forestry and agricultural wastes;
- To generate electricity by making use of solar energy and wind energy;
- To apply the solid waste and wastewater management in an effective manner;
- To establish information points on the matter in the municipality;
- To organize training for economic driving techniques.

2.4 Examples of Local Administrations Preparing SEAPs in Europe

One of the objectives of CoM is to support the efforts of the local administrations in the processes of concretization of their energy and climate change policies [30, 36].

Main focus of CoM is the greenhouse gas emissions exposed as a result of the energy combustion, and the contribution of CO_2 arising from the energy used in residences and tertiary sectors and transportation to the global emissions is 70% [29, 37]. It is for this reason that the formation of CoM has turned the main focal point of the efforts toward the energy sector in order to be able to combat the climate change all over the world. Two European municipalities that prepared a sustainable energy action plan and present good examples are briefly included here below.

2.4.1 Birmingham City Council

It is now a necessity to bring into being large-scale energy programs in order to achieve the carbon reduction goal in a definite and strong manner. Birmingham City Council has determined a pretentious greenhouse gas reduction goal and committed itself to reduce the carbon dioxide percentage per capita by 60% by 2026 and by 32% by 2020 as compared to the 1990 level. Birmingham City Council has identified 2005 as the reference year for the basic emission inventory which is the most important phase of SEAP. All energy consumption and CO_2 mission amount-related thereto in 2005 are given in Table 4.

They are expected to achieve their goals by applying the opportunities and strategies as presented below [38]:

- To carry out energy efficiency studies in all its buildings and enterprises;
- To bring into being such strategies as flexible working models, property management, tracking and management of energy use under the designation "Transformation Program";
- To spend thirty million pounds for energy-related works every year;
- To install smart measuring systems at small- and medium-sized enterprises, thus ensuring energy saving;
- To bolster up the heat pumps used for heating and cooling in commercial and industrial buildings;
- To replace all the vehicle fleet of the city council with either electric or liquefied petroleum gas (LPG) fueled vehicles;
- To make pedestrian walkways healthier, thus ensuring dependence on personal vehicles to be reduced;
- Instead of 15 million l of fossil fuel, to use biofuel of the same amount highway transportation;

Table 4 Greenhouse gas emission by Birmingham City

Category	Energy consumption (MWh)	CO_2 (t)
Buildings, equipment, plants, and industry	18,126,712	5,396,401
Transportation	6,139,625	1,579,150
Total	24,266,337	6,975,551

- To cover the energy requirements of residences, business enterprises, stadiums, etc., by solar energy; 60 new professions are expected to appear in connection with this in the region;
- To generate 300 MWe electric power from non-recoverable waste heaps by 2026;
- To extend the heating and cooling network of the city by the use of the combined heat and power (CHP) system;
- To organize festivals and trainings under the designation "awareness campaigns";
- To introduce national financial resources and grant programs.

2.4.2 Dublin City Council

Dublin City Council joined in CoM on March 2, 2009, and presented the sustainable energy action plan which it had undertaken on December 6, 2010. Dublin City Council aimed at bringing into being a sustainable energy action plan covering the steps which it would take in order to be a smart energy city by 2030. It is anticipated to develop carbon-neutral and low-carbon-generating buildings and low-carbon transport system with the progress in the information technology and to achieve a CO_2 reduction of 50% in the long term. In line with the European Commission and Kyoto Protocol, it aims at reducing the CO_2 emission by 20% by 2020 and has identified 2006 as the reference year for the basic emission inventory. According to the data from 2006, the population of the city of Dublin is 506,211. Energy consumption and consumption-dependent CO_2 emission amount of the city of Dublin is given in Table 5.

Actions and strategies as contained in the sustainable energy action plan have been considered under four main headings as legislation, financial, behavioral, and technology. Actions which will enable the Dublin City administration to achieve its ultimate carbon reduction goal in 2020 are briefly represented here below [39]:

- To ensure that Dublin will be one of the leading cities of Europe in terms of sustainability, equity richness, and dynamism by 2030;
- To support the sustainable space planning for the construction of new buildings and identify high standards in terms of energy efficiency;
- To use the CHP system and try to design much more efficient and zero-carbon buildings;

Table 5 Greenhouse gas emission by Dublin City

Category	Energy consumption (MWh)	CO_2 (t)
Buildings, equipment, plants, and industry	11,294,467	3,936,601
Transportation	4,586,243	1,181,927
Total	15,880,710	5,118,528

- Dublin City Council will establish a sustainability unit under the designation "*minus 3% project*" and monitor the energy service purchase, paper use, waste recycling, water management, and employees' travels and try to improve such processes in terms of sustainability;
- To carry out a feasibility study for the establishment of the Dublin regional heating corporation;
- To build wastewater treatment plants and to improve renewable heat and electric generation infrastructural works;
- To provide free parking places in order to encourage electric vehicles;
- To make use of the national and European Union financial assistance programs;
- To organize various campaigns in order to reduce energy bills.

3   Material and Method

The elaboration and development of a SEAP constitute a decision-making problem [40]. The local authorities have to identify the best fields of actions and opportunities for reaching their long-term CO_2 reduction target [31] (EC-European Commission Covenant of Mayors 2010 Brussels, Belgium). Based on these EU targets, and in order to implement the Renewable Energy Directive [41] and the Energy Efficiency Directive [42], many local authorities established their action plans. The experience of these studies is reported in several scientific articles. For instance, Italian cities' experiences [4] and Sweden's successful implementation [43] are shared. The Municipality of Bornova has also prepared its SEAP with the guidance and instructions of CoM to fight the climate change.

3.1   Current Situation of Bornova Municipality and SEAP

The current situation related to 2011, the year which is defined as the reference year for BEI of Bornova Municipality, is illustrated in Table 6 as corporate inventory.

Table 6 Bornova Municipality energy consumption and amount of greenhouse gas emission

Category	Energy consumption (MWh)	CO_2e (t)
Buildings, equipment, and facilities	3468	1488
Street light and traffic signals	10,809	5448
Vehicle fleet (own)	19,243	4463
Subtotal	33,520	11,453
Public transportation	83,367	19,979
Total	116,887	31,432

As seen from Table 6, the greatest share of corporate emissions of Bornova Municipality belongs to fuel consumptions caused by public transportation with Bornova departure and arrivals. This system is operated by İzmir Metropolitan Municipality. Figure 3 explains this information clearly.

As it is understood in Fig. 3, when emissions caused by public transportation (64%) are taken out of the inventory, the emissions of Bornova Municipality itself will decline from 31,432 ton CO_2e to 11,453 CO_2e.

Main strategies and projects, which Bornova Municipality includes into SEAP prepared in compliance with its 2020 goals, are outlined below [15]:

- Construction of a photovoltaic plant with 300 kWp power;
- Energy efficiency improvements in service buildings;
- Prioritization of renewable energy resources in the urban transformation applications;
- Encouragement of electric vehicles and construction of electric charging stations;
- Utilization of renewable energy in the lighting of public parks and gardens;
- Project of a new service building with a high energy efficiency which contains all departments;
- Awareness raising in the community by creating energy information points in the county.
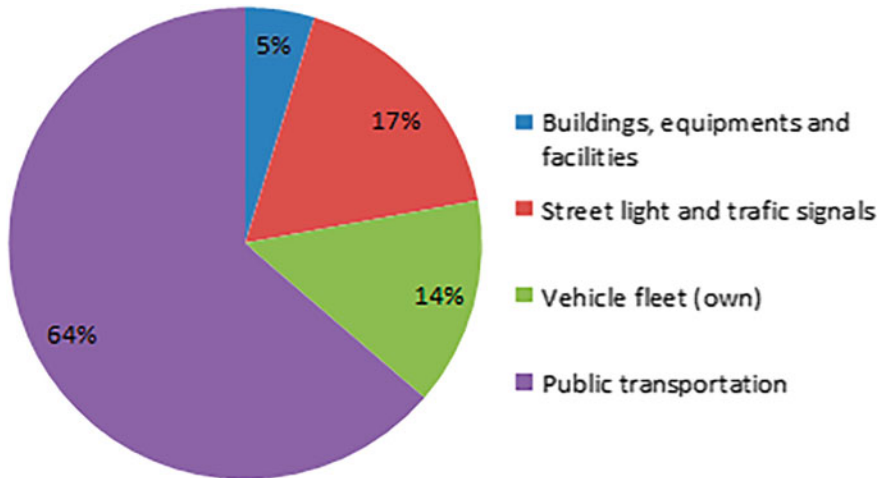
Fig. 3 GHG emission amount of Bornova Municipality

Fig. 4 Planned layout area of the PVPS

3.2 *Example of a 300 kWp PVPS Installation*

Installation of the 300 kWp PVPS is the leading one of the noteworthy projects of Bornova Municipality which is intended to reduce the greenhouse gas emission. PVPS is located in Evka 3-Bornova, Izmir, and its coordinates are 38.463206 N, 27.257028 E.

Its satellite image and planned layout are shown in Fig. 4. Real-time monthly energy generation data and CO_2 reduction amount of the project during 2015–2017 are given in Table 7.

3.3 *PVPS Potential of Service Buildings of Bornova Municipality*

Buildings as owned by the Municipality of are categorized by their activity area as the following: 15 service buildings, 9 community centers, 8 sports facilities, 6 wedding halls, 4 theater halls, 28 lodgings, 7 public marketplaces, and 8 healthcare facilities. Upon examining the technical capacities of these buildings, those that are most suitable for PVPS installation are given in Table 8.

Table 7 Energy generation data of 300 kWp PVPS during 2015–2017

Year	2015 (kWh)	2016 (kWh)	2017 (kWh)
January	22,434.66	22,778.97	22,287.69
February	23,861.58	27,099.06	25,174.65
March	30,268.92	31,984.26	11,890.08
April	40,456.06	41,891.97	41,568.36
May	44,449.82	38,443.35	40,556.13
June	37,786.47	41,206.80	41,019.81
July	38,439.90	44,869.32	41,654.61
August	46,241.73	41,464.17	29,013.12
September	36,581.04	38,187.36	24,294.90
October	34,108.77	34,333.02	27,408.18
November	28,824.75	24,951.78	26,538.78
December	27,513.75	23,784.30	19,440.75
Total	410,967.46	410,994.36	350,847.06
CO_2 reduction (ton)	223	223	190

Table 8 Buildings that are most suitable for PVPS installation

Building name	Usage purpose	Gross area (m^2)	Roof area (m^2)
BELGEM Classroom	Education	2900	1500
Technical Works Site	Municipal services	8153	4790
Muhammed Yıldız Sports Facilities	Sport activities	6555	3590

3.4 Forecast of PVPS Energy Generation and CO_2 Emission at Selected Service Buildings

Buildings suggested for the installation of PVPS are selected because of their location in different districts, frequently usage during the day and suitability in terms of visibility and awareness. Additionally, the sites do not remain in shade in terms of roof surface. The planned layouts are shown in Figs. 5, 6, and 7, respectively.

PVPS parameters and CO_2 reduction quantities are given in Table 9.

4 Results and Discussion

Urban greenhouse gas inventory which is the starting point of the SEAP studies represents the reflection of the physical growth of the town and its economic and commercial life in terms of energy and carbon densities. Evaluations of the urban

Fig. 5 BELGEM Classroom
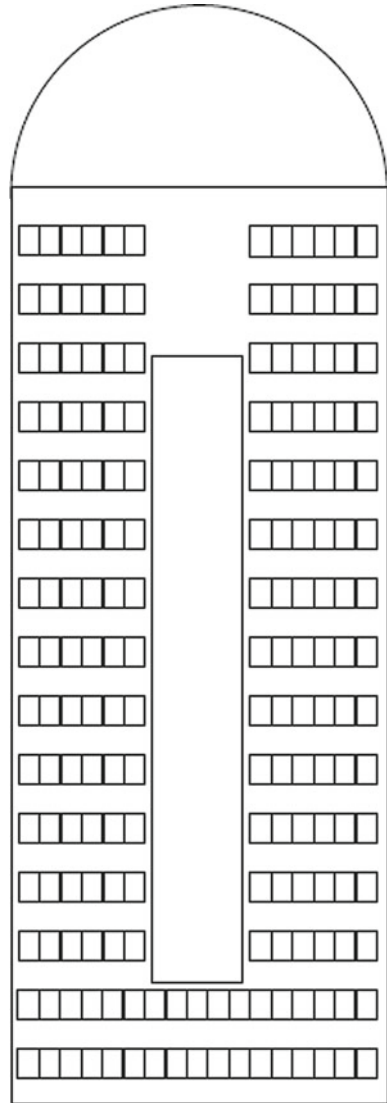
flows of energy and their combination with a sustainability vision are of vital importance for those towns which will face the adverse impacts of the climate changes in the medium and long terms. CoM is an important initiative so that local administrations can benefit from successful practices in European cities and display their best practices later. Besides, provided that one supports CoM and fulfills its commitments, it is possible to get financial support from research and funding programs of European Union.

Fig. 6 Technical Works Site
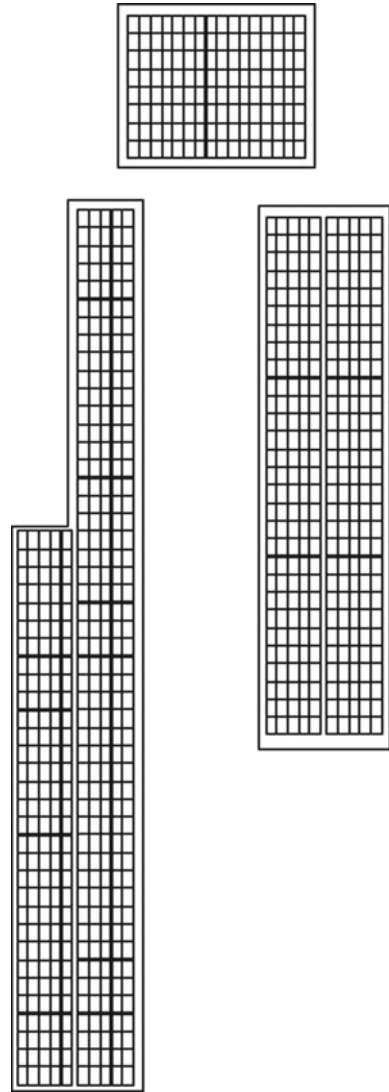
   The membership of Bornova Municipality to CoM is an important step for sustainable urban development. On the other hand, there are still several to-do lists to catch 2020 target. Within this scope, additional PVPS installations will be definitely beneficial. Particularly, the usage of the roofs should be considered. Additionally, Bornova Municipality should form an active strong monitoring system to follow its SEAP activities and update them if required. CoM requires to deliver the monitoring reports biennially. An applicable CoM and its SEAP strategy will also create an ecotourism brand value for Bornova.

Fig. 7 Muhammed Yıldız
Sports Facilities
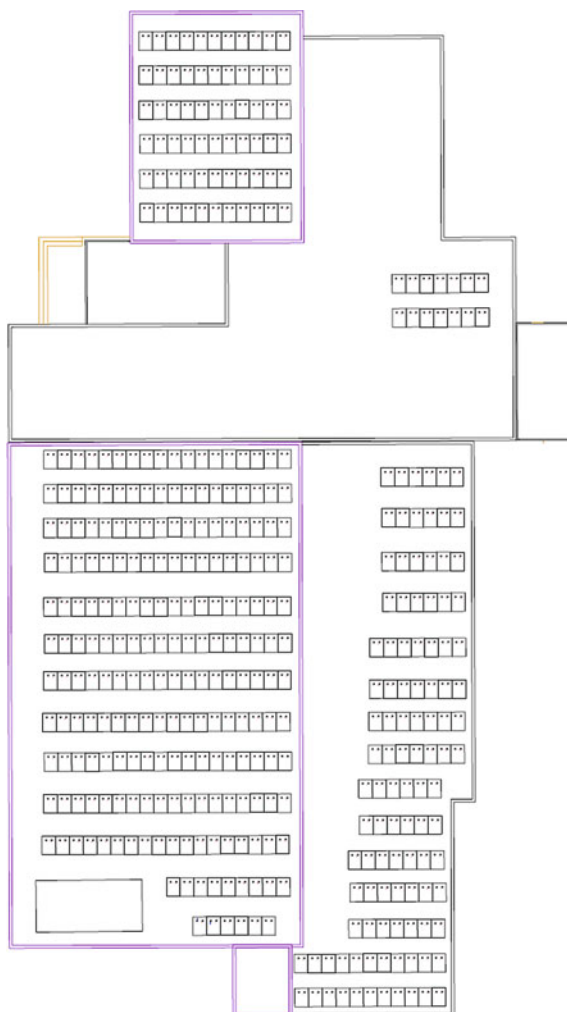
Table 9 PVPS parameters and CO_2 reduction quantities

Building name	Usable area (m^2)	Number of PV modules	PVPS power (kWp)	Energy generation (kWh/year)	CO_2 reduction (t/year)
BELGEM Schoolroom	631	190	51.30	94,170	51
Technical Works Site	1284	818	220.86	405,880	220
Muhammed Yıldız Sports Facilities	1418	400	108	198,195	108
Total				698,245	379

5   Conclusions

With CoM initiative, municipalities are actively involved in a common strategy toward energy and environmental sustainability, and they commit to the energy and climate directives of European Union. Bornova Municipality also realized several actions under its commitment to CoM to reduce greenhouse gas emission value by 25% by 2020. 300 kWp PVPS installation was one of its significant projects under the planned SEAP actions. From the starting day in 2013 for operation to the present, it contributed about 1000 t CO_2 reduction in total. On the other hand, the quality test checks and remediation are required for the existing 300 kWp PVPS according to the real-time operation results listed in Table 7. Moreover, this study has analyzed the potential of photovoltaic solar energy production of three buildings as 698,245 kWh/year and their total CO_2 reduction contribution as 379 t CO_2 per year.

References

1. Işıldar GY (2012) Avrupa Yeşil Başkenti Hamburg: Eko-Kent Kriterleri ve Performans Göstergeleri Açısından İncelenmesi. SÜ İİBF Sosyal ve Ekonomik Araştırmalar Dergisi 23:241–262
2. Maslin M (2004) Global warming, a very shot introduction. Oxford University Press, Oxford
3. Bhowmik C, Bhowmik S, Ray A, Pandey MK (2017) Optimal green energy planning for sustainable development: a review. Renew Sustain Energy Rev 71:796–813
4. Nastasi B, Matteo DU (2016) Solar energy technologies in sustainable energy action plans of three Italian big cities. Energy Procedia 101:1064–1071
5. Tocchi L (2016) Sustainable energy: strategic planning and economic programs in Lazio region. Procedia Soc Behav Sci 223:879–883
6. Fragkos P, Tasios N, Paroussos L, Capros P, Tsani S (2017) Energy system impacts and policy implications of the European intended nationally determined contribution and low-carbon pathway to 2050. Energy Policy 100:216–226
7. UN (1992) Earth Summit Agenda 21 – The United Nations Programme of Action from Rio. United Nations Publication no. E.93.I.11, United Nations Department of Public Information, New York
8. Damso T, Kjaer T, Christensen TB (2016) Local climate action plans in climate change mitigation-examining the case of Denmark. Energy Policy 89:74–83
9. Pasimeni MR, Petrosillo I, Aretano R, Semeraro T, De Marco A, Zaccarelli N, Zurlini G (2014) Scales, strategies and actions for effective energy planning: a review. Energy Policy 65:165–174
10. Van Staden M, Musco F (2010) Local governments and climate change: sustainable energy planning and implementation in small and medium sized communities. Advances in global change research. Springer, Dordrecht, The Netherlands
11. Pablo-Romero MP, Pozo-Barajas R, Sanchez-Braza A (2016) Analyzing the effects of energy action plans on electricity consumption in Covenant of Mayors signatory municipalities in Andalusia. Energy Policy 99:12–26

12. Berghi S (2016) Energy planning for metropolitan context: potential and perspectives of sustainable energy action plans (SEAP) of three Italian big cities. Energy Procedia 101:1072–1078
13. Covenant of Mayors (2018) https://www.covenantofmayors.eu/about/covenant-community/signatories/action-plan.html?scity_id=4235. Accessed on 03 Feb 2018
14. Bornova Sub-governorship (2019) http://www.bornova.gov.tr. Accessed on 4 May 2019
15. Bornova Municipality (2019) https://www.covenantofmayors.eu/about/covenant-community/signatories/action-plan.html?scity_id=4235. Bornova Municipality Sustainable Energy Action Plan. Accessed on 22 Mar 2019
16. Kousky C, Schneider SH (2003) Global climate policy: will cities lead the way? Clim Policy 3(4):359–372
17. Rosenzweig C, Solecki W, Hammer SA, Mehrotra S (2010) Cities lead the way in climate-change action. Nature 467(7318):909–911
18. Castan Brato V (2017) Urban governance and politics of climate change. World Dev 93:1–15
19. De Gregorio Hurtado S, Olazabal M, Salvia M, Pietrapertosa F, Olazabal E, Geneletti D, D'Alonzo V, Feliú E, Di Leo S, Reckien D (2014) Implications of governance structures on urban climate action: evidence from Italy and Spain. BC3 working paper series. Basque Centre for Climate Change, Bilbao, pp 1–47
20. Heidrich O, Reckien D, Olazabal M, Foley A, Salvia M, De Gregorio Hurtado S, Orru H, Flacke J, Geneletti D, Pietrapertosa F, Hamann JJP, Tiwary A, Feliu E, Dawson RJ (2016) National climate policies across Europe and their impacts on cities strategies. J Environ Manage 168:36–45
21. Olazabal M, De Gregorio Hurtado S, Olazabal E, Pietrapertosa F, Salvia M, Geneletti D, D'Alonzo V, Feliú E, Di Leo S, Reckien D (2014) How are Italian and Spanish cities tackling climate change? A local comparative study. BC3 working paper series. Basque Centre for Climate Change, Bilbao, pp 1–27
22. Reckien D, Flacke J, Olazabal M, Heidrich O (2015) The influence of drivers and barriers on urban adaptation and mitigation plans-an empirical analysis of European cities. PLoS ONE 10(8):21
23. European Commission (2011) A roadmap for moving to a competitive low carbon economy in 2050. European Commission, Brussels
24. Monforti-Ferrario F, Kona A, Peduzzi E, Pernigotti D, Pisoni E (2018) The impact on air quality of energy saving measures in the major cities signatories of the Covenant of Mayors initiative. Environ Int 118:222–234
25. Directive 2009/29/EC of the European Parliament and of the Council of 23 Apr 2009
26. Cinocca A, Santini F, Cipollone R (2018) Monitoring methodologies and tools for the sustainable energy action plans to support the Public Administration. Energy Procedia 148:758–765
27. Van Staden M, Musco F (2010) Local governments and climate change: sustainable energy planning and implementation in small and medium sized communities, Berlin
28. Famoso F, Lanzafame R, Monforte P, Scandura PF (2015) Analysis of the Covenant of Mayors initiative in Sicily. Energy Procedia 81:482–492
29. Lombardi M, Pazienza P, Rana R (2016) The EU environmental-energy policy for urban areas: the Covenant of Mayors, the ELENA program and the role of ESCos. Energy Policy 93:33–40
30. Delponte I, Pittaluga I, Schenone C (2017) Monitoring and evaluation of sustainable energy action plan: practice and perspective. Energy Policy 100:9–17
31. EC-European Commission (2010) How to develop a sustainable energy action plan (SEAP)—guidebook. Covenant of Mayors, Brussels, Belgium
32. Oliver-Sola J, Armero M, Martinez de Foix B, Rieradevall J (2013) Energy and environmental evaluation of municipal facilities: case study in the province of Barcelona. Energy Policy 61:920–930
33. Plans and Actions (2019) https://www.covenantofmayors.eu/plans-and-actions/action-plans.html. Accessed on 24 Mar 2019
34. Eskişehir Tepebası Municipality Sustainable Energy Action Plan. https://www.covenantofmayors.eu/about/covenant-community/signatories/action-plan.html?scity_id=6730. Accessed on 27 Mar 2019

35. Antalya Büyüksehir Municipality Sustainable Energy Action Plan. https://www.covenantofmayors.eu/about/covenant-community/signatories/action-plan.html?scity_id=6521. Accessed on 22 Mar 2019
36. Derissen S, Quaas MF, Baumgärtner S (2011) The relationship between resilience and sustainable development of ecological-economic systems. Ecol Econ 70:1121–1128
37. Duren RM, Miller CE (2012) Measuring the carbon emissions of megacities. Nat Clim Change 2(8):560–562
38. Birmingham Municipality Sustainable Energy Action Plan. https://www.covenantofmayors.eu/about/covenant-community/signatories/action-plan.html?scity_id=1902. Accessed on 1 Apr 2019
39. Dublin Municipality Sustainable Energy Action Plan. https://www.covenantofmayors.eu/about/covenant-community/signatories/action-plan.html?scity_id=1817. Accessed on 5 Apr 2019
40. Marinakis V, Papadopoulou A, Siskos J, Psarras J (2012) Sustainable energy communities: a methodological framework for the support of local and regional stakeholders. In: Proceedings of the 23rd national conference of the Hellenic operational research society (HELORS), Athens, Greece. ISBN:978-960-87277-8-6
41. EU Directive 2009/28/EC (2009) Directive 2009/28/EC of the European Parliament and of the Council of 23 April 2009 on the promotion of the use of energy from renewable sources and amending and subsequently repealing Directives 2001/77/EC and 2003/30/EC. OJ L 140, pp 16–62
42. EU Directive 2012/27/EU (2012) Directive 2012/27/EU of the European Parliament and of the Council of 25 October 2012 on energy efficiency, amending Directives 2009/125/EC and 2010/30/EU and repealing Directives 2004/8/EC and 2006/32/EC. OJ L 315, pp 1–56
43. Wretling V, Gunnarsson-Östling U, Hörnberg C, Balfors B (2018) Strategic municipal energy planning in Sweden—examining current energy planning practice and its influence on comprehensive planning. Energy Policy 113:688–700

Hybrid Cooling Tower for a Solar Adsorption Cooling System: Comparative Study Between Dry and Wet Modes in Hot Working Conditions

Mohamed-Abdelbassit Kheireddine, Amar Rouag, Adel Benchabane, Nora Boutif and Adnane Labed

Abstract This study investigates the applicability of a hybrid cooling tower (HCT) of solar adsorption air-conditioning system in the hot working conditions of the region of Biskra, Algeria. A calculation method is presented to size the cooling tower and to define the main characteristics of the sprayed water. In addition, the effect of the ambient and humid temperatures on the heat transfer coefficients and the total heat transfer area were determined for both dry and wet modes. Results were compared with experimental measurement obtained from the literature, and good agreement was found. It has been concluded that the wet mode presents an effective solution for the region of Biskra. The ambient operating temperature limits of the cooling tower can be increased from 33 to 51 °C, respectively, for the dry and wet modes. Besides, it was found that the maximum mass flow rate of sprayed water is about 0.036 kg s^{-1} which is sufficient to operate the cooling tower and consequently the solar adsorption system.

M.-A. Kheireddine (✉) · A. Rouag · A. Benchabane · N. Boutif
Laboratoire de Génie Energétique et Matériaux (LGEM), Faculté des Sciences et de la Technologie, Université Mohamed Khider Biskra, BP 145, 07000 Biskra, Algeria
e-mail: mkheireddine6@gmail.com

A. Rouag
e-mail: rouagamar@yahoo.com

A. Benchabane
e-mail: adel.benchabane@gmail.com

N. Boutif
e-mail: bw_nora@yahoo.fr

A. Rouag
Laboratoire de Développement des Energies Nouvelles et Renouvelables dans les Zones Arides et Sahariennes (LENREZA), Université Kasdi Merbah Ouargla, BP 511, 30000 Ouargla, Algeria

A. Labed
Laboratoire de Génie Mécanique (LGM), Faculté des Sciences et de la Technologie, Université Mohamed Khider Biskra, BP 145, 07000 Biskra, Algeria
e-mail: adnanelabed@yahoo.fr

Nomenclature

A	Total heat transfer area, m^2
C_f	Factor of friction
Cp	Heat capacity, J/kg K
D	Diameter, m
F	Correction factor
g	Gravity, m/s^2
h	Convective heat transfer coefficient, W/m^2 K
H	Enthalpy, kJ/kg
j	Colburn factor
l	Depth of the finned coil, m
L	Height of the finned coil, m
L	Latent heat, kJ
L_t	Length of the tube, m
$\dot{m}$	Mass flow rate, kg/s
N	Number of rows
Nu	Nusselt number
P_l	Longitudinal pitch, m
Pr	Prandtl number
P_t	Transverse pitch, m
$\Re$	Thermal resistance, W/K
Re	Reynolds number
R_{ext}	Radius, m
S	Surface per meter of length, m^2/m
U	Overall heat transfer coefficient, W/m^2 K
V	Velocity, m/s
w	Humidity, kg of water/kg dry air

Greek Symbols

ν	Cinematic viscosity, m^2/s
ϕ	Heat flux, W
λ	Themal conductivity, k s
μ	Dynamic viscosity, Pa s
η	Efficiency
ρ	Density, kg/m^3

Subscripts

a   Air
pf   Process fluid
f   Fin
ai   Air inlet
ao   Air outlet
pfi   Process fluid inlet
pfo   Process fluid outlet
e   External
h   Hydraulic
i   Internal
g   Global

1 Introduction

In Algeria, the most part of the electric power consumed in summer is used in the field of cooling of domestic and commercial buildings. Indeed, the rising demand for efficient energy use and the higher comfort standards have gained an increasing interest during latest years [1].

Renewable energies are increasingly used and developed because it allows saving energy and contributing to sustainable development. Solar energy in hot countries is a non-neglected source because its exploitation can become an important factor of its development. These advantages could be profitable, especially in air-conditioning applications where energy consumption is very important.

Solar air conditioning can be accomplished by three classes of systems: sorption cycles, desiccant cycles and solar mechanical processes [2]. Recently, several works in the field of air conditioning by solar adsorption were performed [3–7]. The authors of the manuscript can give the example of the ACS08 machine marketed by SorTech solar adsorption cooling system [3]. The ACS08 air-conditioning machine, with a nominal cooling capacity of 8 kW, serves to cool domestic and commercial buildings. Also, a novel solar silica gel-water adsorption air conditioning with cooling capacity of 3.6 and 5.7 kW to reach to 15 °C of chilled water was developed and tested in China, by Lu et al. [4, 5]. This cooling installation (Fig. 1) includes a set of thermal systems such as refrigeration machine (chiller), solar heating system and air cooling system (air cooling tower).

The main problem of these air-conditioning machines, particularly in hot climate, is how to provide effectively a cooling fluid to cool the adsorbent of the chiller [8]. As a solution, hybrid cooling towers, HCT, are used to operate in dry and wet modes. At low ambient temperatures, the cooling tower is operating in dry mode. In this case, ambient air is used directly to cool the cooling fluid at low ambient temperatures. During peak temperatures, the cooling tower operates in a wet mode when a spray
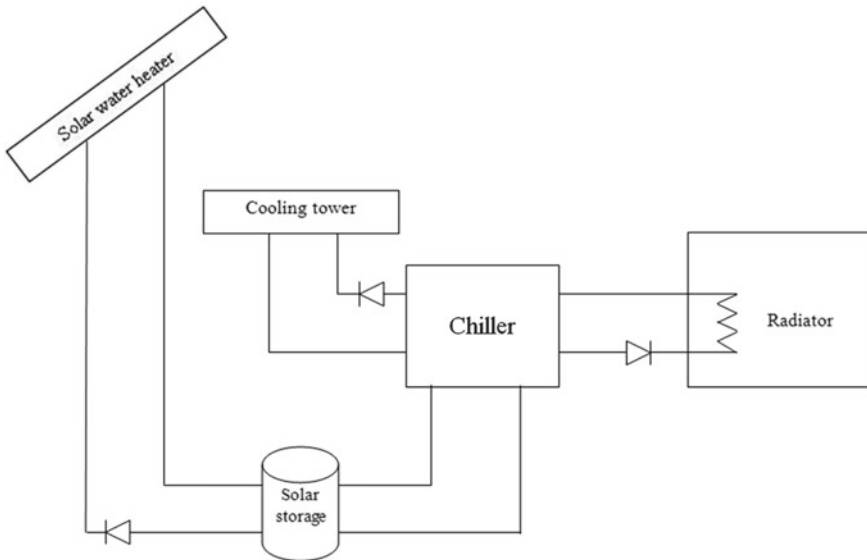
Fig. 1 Scheme of a solar adsorption cooling machine studied by Lu et al. [4]

water system is activated to cool the ambient air [3–6]. Indeed, spraying water is often used as a technological solution in hot regions, especially during peak temperatures [9–12]. Alkhedhair et al. [9] presented an experimental study of air pre-cooling with water sprays to enhance the performance of natural draft dry cooling tower, DCT, during high ambient temperature at different droplet sizes and air velocities. Dehaghani and Ahmadikia [10] studied the retrofit of a wet cooling tower, WCT, in order to reduce water and fan power consumption using a wet/dry approach. Ghafoor and Munir [11] studied available and actually installed solar thermal-driven technologies used for cooling or air-conditioning purposes. A review analysis has been performed taking into account research on experimental and simulated solar cooling systems in terms of COP. Always in order to decrease the inlet air temperature, Ounis et al. [12] proposed to use the condensed water, coming from the evaporator, to humidify a grid positioned behind the condenser of an air-conditioning system. In all of these cases, the goal was to reduce the air temperature at the cooling tower inlet by humidifying the ambient air to ensure the continued operation of the system in hot regions, especially during hot times.

The present paper interests to the applicability of the solar adsorption air-conditioning systems in the hot regions by studying the performances of a HCT. The objective is to study and design the cooling tower by estimating the heat transfer area and the main characteristics of the sprayed water appropriate to the region of Biskra in order to prevent the malfunction in hottest summer days ($T > 33$ °C).

2 System Description

The studied system is a HCT, which is a combination of a DCT and a sprayed water system. The air heat exchanger of the DCT is a finned tube heat exchanger with same geometrical and thermo-physical parameters of the DCT of Citherlet et al. [3] (Table 1).

2.1 Dry Mode

The process fluid to be cooled is the ethylene glycol 34 vol.% which flows in the tubes of the DCT heat exchanger. Process fluid is cooled by a cross-flow of ambient air moved by fans and passing through the heat exchanger (Fig. 2a).

2.2 Wet Mode

A simple installation called spray water system is added as shown in Fig. 2b. In this case, the dry system can become a wet system when the ambient temperature or process fluid temperature increases. The adiabatic cooling allows enhancing the thermal performance of coolers by reducing the temperature of the inlet air. This temperature reduction is obtained by water misting at the air inlet through series of ramps of misting placed in front of the finned tubes heat exchanger. The adiabatic transformation is realized by the evaporation of the misted water against or with the inlet airflow.
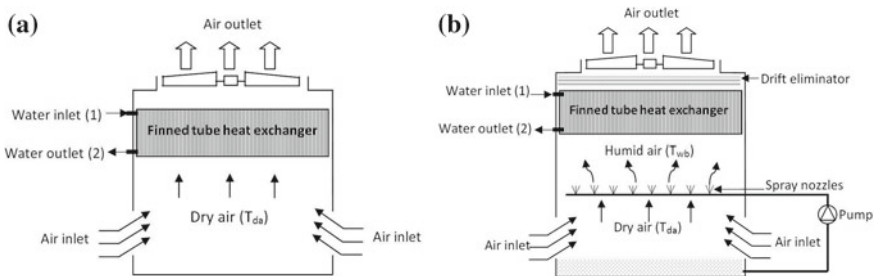
Fig. 2 Hybrid cooling tower, HCT: **a** dry mode and **b** wet mode

3 Sizing and Calculation Method

The studied heat exchanger is a finned tubes heat exchanger with a number of rows. The tubes are arranged in staggered rows to ensure several passes by row. The total number of tubes is the same in each row.

The studied flow is a cross-flow where the external fluid is the air which arrives with maximum air mass flow rate of 4.3 kg s^{-1} on the tube wall by forced convection. In the tubes, the process fluid flows with a mass flow rate of 3.19 m^3 h^{-1}.

The LMTD method [13] is used to calculate the required heat transfer area of the finned tubes heat exchanger by using the following assumptions: (i) The studied system is an open steady-state system for both air and sprayed water; (ii) Overall heat transfer coefficient is constant [14]; (iii) Mass flow rates for both air and process fluid are constants and (iv) Airflow is considered as a counter-flow to simplify the sizing calculation.

3.1 Dry Cooling Tower DCT (Dry Mode)

At the air side, the external heat transfer coefficient can be calculated by using the Wang et al. [15] correlation:

$$h_e = j\rho_a Cp_a V_a Pr_a^{-2/3} \tag{1}$$

For $N \geq 2$ and $200 < Re < 1000$

$$j = 0.086 Re_{Dc}^{j3} N^{j4} \left(\frac{S_a}{D_e}\right)^{j5} \left(\frac{S_a}{D_h}\right)^{j6} \left(\frac{S_a}{P_t}\right)^{-0.93} \tag{2}$$

The Reynolds number Re_{Dc} is calculated from the external diameter of the tubes D_e

$$Re_{Dc} = \frac{V_a D_e \rho_a}{\mu_a} \tag{3}$$

Where $j_3 = -0.361 - \frac{0.042N}{\log(Re_{Dc})} + 0.158\log\left[N\left(\frac{S_a}{D_c}\right)^{0.41}\right]$ \qquad (4)

$$j_4 = -1.224 - \frac{0.076\left(\frac{P_L}{D_h}\right)^{1.42}}{\log(Re_{Dc})} \tag{5}$$

$$j_5 = -0.083 + \frac{0.076N}{\log(Re_{Dc})} \tag{6}$$

$$j_6 = -5.735 + 1.21 \log\left(\frac{\mathrm{Re}_{\mathrm{Dc}}}{N}\right) \tag{7}$$

The internal heat transfer is calculated as:

$$h_i = \frac{\mathrm{Nu}\lambda_w}{d_i} \tag{8}$$

Nusselt number for water flow inside a pipe is given by the correlation proposed by Gnielinski [16] in Eqs. (9) and (10) for $0.6 < \mathrm{Pr} < 1.5$

$$\mathrm{Nu} = 0.0214\left(\mathrm{Re}^{0.8} - 100\right)\mathrm{Pr}_{\mathrm{pf}}^{0.4}\left[1 + \left(\frac{d_i}{L_t}\right)^{\frac{2}{3}}\right] \tag{9}$$

For $1.5 < \mathrm{Pr} < 500$

$$\mathrm{Nu} = 0.012\left(\mathrm{Re}^{0.87} - 280\right)\mathrm{Pr}_{\mathrm{pf}}^{0.4}\left[1 + (d_i/L_t)^{\frac{2}{3}}\right] \tag{10}$$

This correlation is applied for $0.06 < \mathrm{Pr} < 2000$, $2300 < \mathrm{Re} < 106$, $0 < d_i/L_t < 1$.
Overall heat transfer coefficient of the heat exchanger is calculated by the Eq. (11) [14]:

$$U = \left[\left(\frac{1}{h_i} + \mathfrak{R}_i\right)\frac{S_e}{S_i} + \frac{S_e}{2\pi\lambda_t}\mathrm{Ln}\frac{d_e}{d_i} + \frac{1}{\eta_g h_e} + \mathfrak{R}_e\right]^{-1} \tag{11}$$

The overall efficiency η_g of the finned tube surface is given by:

$$\eta_g = 1 - (1 - \eta_f)\frac{S_{\mathrm{f\text{-}m}}}{S_{\mathrm{f\text{-}m}}} \tag{12}$$

where $S_{\mathrm{f\text{-}m}}$ and $S_{\mathrm{tot\text{-}m}}$ are the net and the total heat transfer areas of the finned tubes per meter of length, respectively.

$$S_{\mathrm{f\text{-}m}} = 2N_{\mathrm{f\text{-}m}}\left(P_t P_l - \frac{\pi d_e^2}{4}\right)$$

$$\text{And } S_{\mathrm{tot\text{-}m}} = S_{\mathrm{net\text{-}m}} + S_{\mathrm{f\text{-}m}} \tag{13}$$

The logarithmic mean temperature difference (LMTD) of the finned tubes heat exchanger is defined by the following relation:

$$\Delta T_{\mathrm{ML}} = \frac{\left(T_{\mathrm{ai}} - T_{\mathrm{pfo}}\right) - \left(T_{\mathrm{ao}} - T_{\mathrm{pfi}}\right)}{\log\frac{(T_{\mathrm{ai}}-T_{\mathrm{pfo}})}{(T_{\mathrm{ao}}-T_{\mathrm{pfi}})}} \tag{14}$$

Table 1 Input parameters of the DCT studied by Citherlet et al. [3]

Process fluid	Ethylene glycol 34 vol.%
Fins material	Aluminum
Tubes material	Copper
Maximum inlet air temperature (°C)	33
Process fluid inlet temperature (°C)	41
Process fluid outlet temperature (°C)	34
Air volumetric flow rate (m³/h)	12,900
Fluid volumetric flow rate (m³/h)	3.19
Heat power exchanged (kW)	24
Spacing between fins (mm)	2.40
Number of rows	10

The total heat transfer area of the finned tubes heat exchanger needed to cool the fluid to the desired temperature can be calculated using the Eq. (15):

$$A = \frac{\phi}{U \, \Delta T_{\mathrm{ML}}} \tag{15}$$

with

$$\phi = \dot{m}_{\mathrm{pf}} \mathrm{Cp}_{\mathrm{pf}} \left(T_{\mathrm{pfi}} - T_{\mathrm{pfo}} \right) \tag{16}$$

The same geometrical and thermo-physical parameters of the DCT of Citherlet et al. [3] are used as input parameters for the dry mode calculation (Table 1).

3.2 Wet Cooling Tower WCT (Wet Mode)

In this part, the same heat transfer area of Citherlet et al. [3], $A = 271.43 \ \mathrm{m}^2$, is considered. The spray humidification system is presented in Fig. 3. This system is integrated in the front of the heat exchanger to improve the operating limits of the cooling tower when the ambient air temperature exceeds 33 °C. For that, the following assumptions are considered in the humid air calculations: (i) The humid air is considered as a mixture of ideal gases; (ii) Dalton's law is used which postulates that the pressure, internal energy, enthalpy and entropy of a mixture of ideal gases at temperature T and pressure P are, respectively, the sum of the partial pressures, partial internal energies, partial enthalpies and partial entropies of gas constituents [17]; (iii) During its passage through the water nozzles, the air is humidified until the partial pressure of water vapor becomes equal to the saturated vapor pressure of water at the liquid temperature. This humidification of the air is accompanied by an air temperature variation which will be calculated.
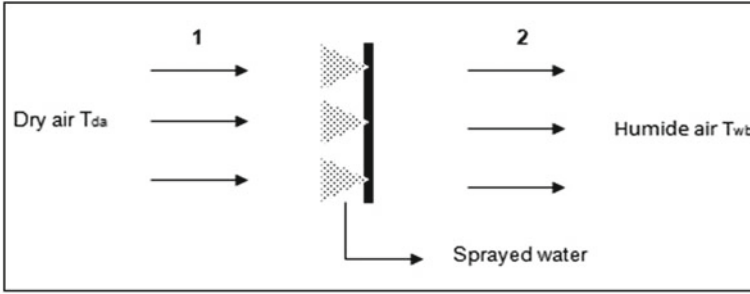
Fig. 3 Schematic diagram of inlet air cooled by sprayed water

3.2.1 Mass Conservation of Dry Air

$$\dot{m}_{da}^1 - \dot{m}_{da}^2 = 0 \tag{17}$$

Sprayed water mass conservation is written as:

$$\dot{m}_{da}^1 \omega_1 + \dot{m}_{liq} - \dot{m}_{da}^2 \omega_{sat}^h = 0 \tag{18}$$

$$\delta\omega = \delta\omega_{sat}^h - \omega_1$$

$\delta\omega$ is introduced to allow writing the liquid mass flow rate as:

$$\dot{m}_{liq} = \dot{m}_{da}^1 \delta\omega \tag{19}$$

3.2.2 Energy Conservation

Applying the first principle for an open system in steady state and permanent flow for n inlet and p outlet:

$$0 = \dot{Q} + \dot{W} + \sum_{i,o} \dot{m}_{i,o}\left(h + \frac{1}{2}v^2 + gz\right)_{i,o} \tag{20}$$

With neglecting the kinetic energy variations and potential energy, the Eq. (20) becomes

$$0 = \dot{Q} + \dot{W} + \sum_{i,o} \dot{m}_{i,o}(h)_{i,o} \tag{21}$$

Considering that the system does not exchange heat or mechanical work with the outside, the Eq. (21) simplified as the Eq. (22):

$$0 = \sum_{i,o} \dot{m}_{i,o}(h)_{i,o} \tag{22}$$

Energy conservation reduced to enthalpy conservation, enthalpy flux is constituted: (i) in the inlet: air enthalpy flux and water enthalpy flux; (ii) in the outlet: enthalpy flux of the saturated air.

$$\dot{m}_{1da} = \dot{m}_{2da} \tag{23}$$

According to above equations

$$\dot{m}_{1da}\big[(Cp_{da} + \omega_1 Cp_v)T_1 + \omega_1 L\big] + \dot{m}_{1da}\delta\omega\, Cp_{liq}T_1$$
$$- \dot{m}_{1da}[(Cp_{da} + \omega_{sat}^h Cp_v)T_{wb} + \omega_{sat}^h L = 0 \tag{24}$$

where T_{wb} is the wet-bulb temperature of the humid air.

On the basis of the fact that $\dot{m}_{1da} = \dot{m}_{2da}$, Eq. (24) can be divided by $\dot{m}_{1da}$

$$(Cp_{da} + \omega_{sat}^h Cp_v)T_{wb} = (Cp_{da} + \omega_1 Cp_v + \delta\omega Cp_{liq})T_1 + (\omega_1 - \omega_{sat}^h)L \tag{25}$$

But $(\omega_1 + \omega_{sat}^h) = -\delta\omega$

$$(Cp_{da} + \omega_{sat}^h Cp_v)T_{wb} = \big[Cp_{da} + \omega_{sat}^h Cp_v + \delta\omega(Cp_{liq} - Cp_v)\big]T_1 - \delta\omega L \tag{26}$$

The wet-bulb temperature can be calculated as:

$$T_{wb} = \frac{\big[Cp_{da} + \omega_{sat}^h Cp_v + \delta\omega(Cp_{liq} - Cp_v)\big]T_1 - \delta\omega L}{(Cp_{da} + \omega_{sat}^h Cp_v)} \tag{27}$$

Then:

$$T_{wb} = T_1 + \frac{\delta\omega\big[(Cp_{liq} + Cp_v)T_1 - L\big]}{(Cp_{da} + \omega_{sat}^h Cp_v)} \tag{28}$$

Generally, the term $Cp_{liq}(Cp_{liq} + Cp_v)T$ is very small than L, Eq. (28) can be simplified to:

$$T_{wb} \approx T_1 - \frac{L(\omega_{sat}^h + \omega)}{(Cp_{da} + \omega_{sat}^h Cp_v)} \tag{29}$$

4 Algorithm Validation

In order to validate the dry mode calculation method, the obtained results are compared with those of the experimental study of Citherlet et al. [3] by using the same geometrical and thermo-physical parameters of the DCT of Table 1. Results show that there is a good agreement between the experimental results of Citherlet et al. [3] and the calculated values (Table 2).

To validate the wet mode calculation method, Fig. 4 shows a comparison between the numerical results of the developed calculation method and the experimental results of Boulet et al. [18]. In this case, the variation of wet-bulb temperature versus the ambient air temperature for different flow rates of sprayed water is presented. For the same mass flow rate (1.12 l/h), the average relative error between the compared results in Fig. 4 is 3.87%.

Table 2 Validation results with Citherlet et al. [3] in the DCT case

	Citherlet et al. [3]	Present paper
Heat transfer area A (m^2)	270.6	271.43
Overall transfer coefficient U (W/m^2 K)	28.6	34.65
Tubes volumes (l)	37	36.67
Finned tubes heat exchanger length (m)	2	2
Finned tubes heat exchanger width (m)	1.16	1.009
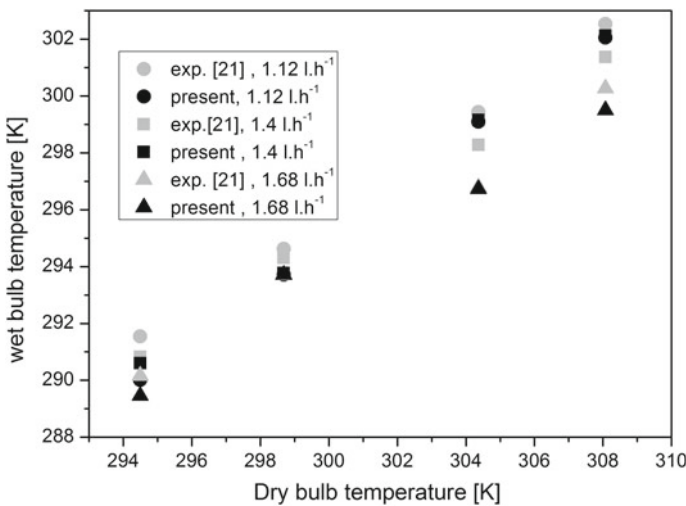
Fig. 4 Validation of the present calculation method with the experimental measurement of Boulet et al. [18] for three volumetric flow rates

5 Results and Discussion

As shown in Fig. 5, when the ambient air temperature exceeds 33 °C the required heat transfer area increases enormously, this makes the DCT unable to reduce the fluid temperature to the desired temperature (34 °C). However, the ambient temperature in the region of Biskra exceeds this value during summer [19]. These ambient conditions cause the malfunction of the cooling tower and thus air-conditioning system. A supplementary sprayed water system is integrated to the DCT to reduce the air inlet temperature before entering to the finned tubes heat exchanger. This latter operates when the ambient temperature exceeds 33 °C. Thus, the cooling tower operates at wet mode.

Figure 6 shows the variation of the heat transfer area required to cool the process fluid to the desired temperature (34 °C). With the inlet air temperature equal to the wet-bulb temperature calculated above, the heat transfer area increases with the increasing of the inlet air temperature. For the same heat transfer area of the DCT ($A = 271.43$ m^2), the operating limits of the cooling tower can be increased to 51 °C of ambient temperature.

Figure 7 shows the variation of mass flow rate of the sprayed water versus the ambient inlet air temperature. According to Fig. 7, it is clear that the increasing of the ambient air temperature induces the increasing mass flow rate of sprayed water to reach 0.036 kg/s when the ambient air temperature reaches 51 °C. This value of mass flow rate is acceptable in comparison with the gain obtained from this solution.

It must be noted that one of the disadvantages of the wet mode, in semiarid and Saharan regions, is the phenomenon of the fouling of the cooling tower due to the sandstorms which can reduce its performance over the time [20, 21]. This
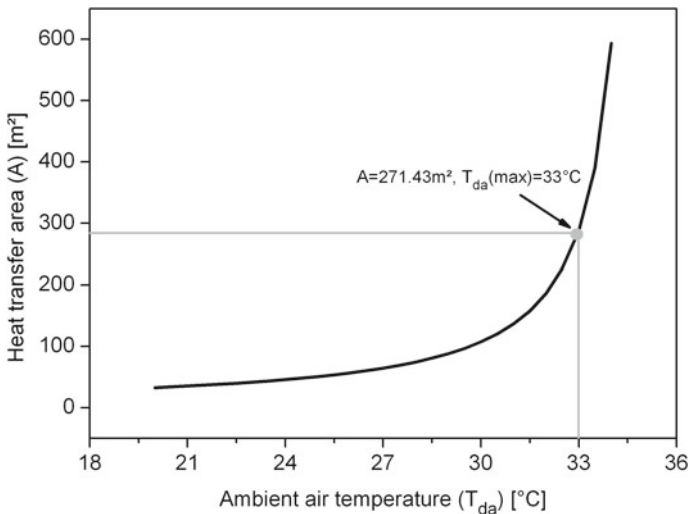
Fig. 5 Effect of ambient air temperature on the heat transfer area of the heat exchanger
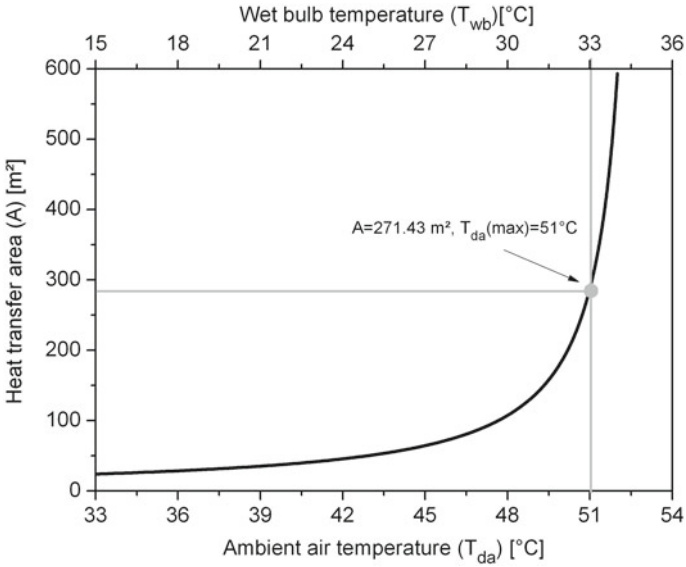
Fig. 6 Effect of inlet air temperature on the heat transfer area in wet mode
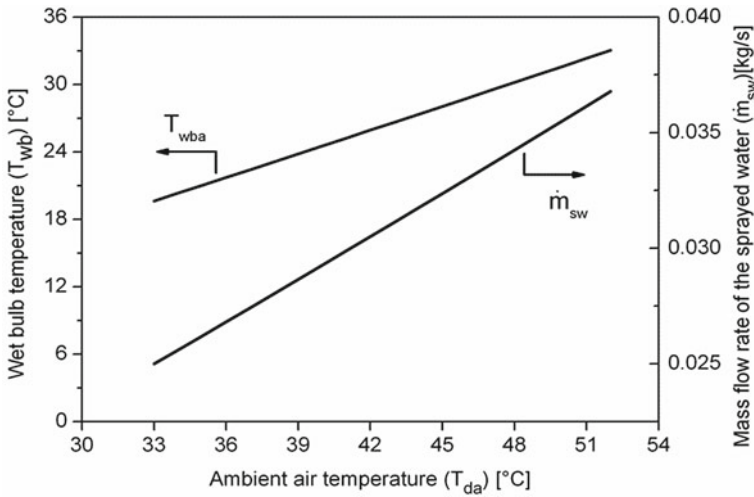
Fig. 7 Wet-bulb temperature and mass flow rate of sprayed water versus ambient air temperature
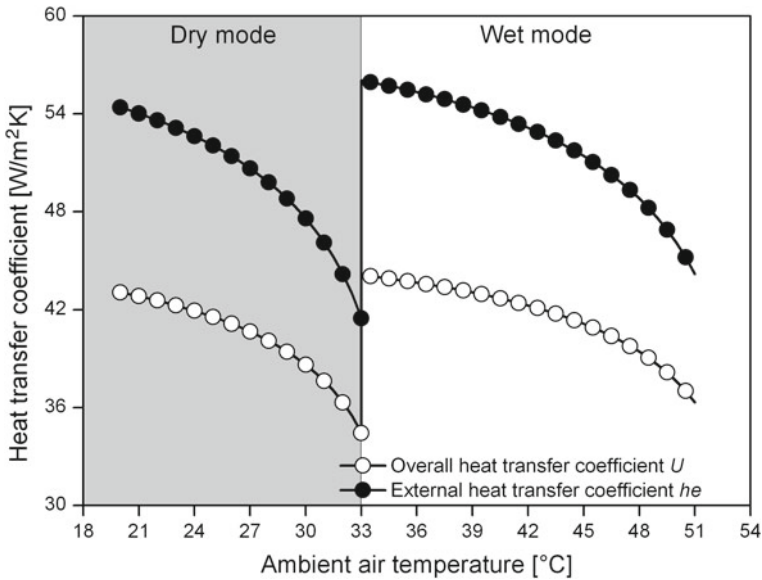
Fig. 8 Variation of the heat transfer coefficients versus the inlet air temperature for dry and wet modes

phenomenon is not considered in the present study, and extended studies are needed in the future.

Figure 8 illustrates the variation of the overall and the external heat transfer coefficients versus the inlet air temperature for both dry and wet modes of the HCT. Overall and external heat transfer coefficients decrease with the increasing of the inlet air temperature and reach their lowest values at 33 °C in the dry mode. After running the spray humidification system (wet mode), the heat transfer coefficients increase significantly due to the decrease of the inlet air temperature, and it then decreases with the increasing of the ambient temperature.

6   Conclusion

The present paper interests to the applicability of hybrid cooling tower, HCT, of a solar adsorption cooling system in the hot arid Saharan regions. The aim of this work is to design the cooling tower by estimating its heat transfer area and to define the main characteristics of the sprayed water system of wet cooling tower (WCT) appropriate to the region of Biskra.

In the case of dry mode, the LMTD method is used to size the finned tube heat exchanger of the DCT. Numerical results are compared with experimental DCT, obtained from the literature. It has been concluded that the required heat transfer area of the finned tubes heat exchanger increases enormously when the ambient air

temperature exceeds 33 °C. That is what prevents the DCT to decrease the process fluid temperature to the desired temperature. As a solution, this study proposes to study a HCT by coupling a spray humidification system to the same heat transfer area of the sized DCT.

In the case of wet mode, the spray system of the HCT works only when the ambient air temperature exceeds 33 °C, in order to keep the inlet air temperature lower than this value and to cool the process fluid. The proposed calculation method allowed defining the main characteristics of the sprayed water. Results showed that the hybrid solution can increase the operating limits of the system to 51 °C, with 0.036 kg/s of maximum mass flow rate of sprayed water. The parametric study showed that the sprayed water improves the heat transfer by improving the external and the overall heat transfer coefficients.

References

1. Labed A, Rouag A, Benchabane A, Moummi N, Zerouali M (2015) Applicability of solar desiccant cooling systems in Algerian Sahara: experimental investigation of flat plate collectors. J Appl Eng Sci Technol 1(02):61–69
2. Duffie JA, Beckman WA (2013) Solar engineering of thermal processes, 4th edn. Wiley, New York
3. Citherlet S, Hildbrand C, Bony J, Kleijer A, Bunea M, Eicher S (2011) Analyse des performances de la climatisation solaire par adsorption et potentiel pour la Suisse. Rapport final, Projet SOLCOOL HEIG-VD, Office fédérale de l'énergie OFEN, 25 Janvier 2011
4. Lu Z, Wang R, Xia Z, Wu Q, Sun Y, Chen Z (2011) An analysis of the performance of a novel solar silica gel–water adsorption air conditioning. Appl Therm Eng 31(17–18):3636–3642
5. Lu ZS, Wang RZ, Xia ZZ, Lu XR, Yang CB, Ma YC, Ma GB (2013) Study of a novel solar adsorption cooling system and a solar absorption cooling system with new CPC collectors. Renew Energy 50:299–306
6. Liu YL, Wang RZ, Xia ZZ (2005) Experimental study on a continuous adsorption water chiller with novel design. Int J Refrig 28(2):218–230
7. Jakob U, Mittelbach W (2008) Development and investigation of a compact silica gel/water adsorption chiller integrated in solar cooling systems. Presented at VII Minsk international seminar "heat pipes, heat pumps, refrigerators, power sources", Minsk, Belarus, 8–11 Sept 2008
8. Rouag A, Benchabane A, Labed A, Belhadj K, Boultif N (2016) Applicability of a solar adsorption cooling machine in semiarid regions: proposal of supplementary cooler using earth-water heat exchanger. Int J Heat Technol 34(2):281–286
9. Alkhedhair A, Gurgenci H, Jahn I, Guan Z, He S (2013) Numerical simulation of water spray for pre-cooling of inlet air in natural draft dry cooling towers. Appl Therm Eng 61(2):416–424
10. Dehaghani ST, Ahmadikia H (2017) Retrofit of a wet cooling tower in order to reduce water and fan power consumption using a wet/dry approach. Appl Therm Eng 125:1002–1014
11. Ghafoor A, Munir A (2015) Worldwide overview of solar thermal cooling technologies. Renew Sustain Energy Rev 43:763–774

12. Ounis H, Benchabane A, Rouag A (2016) Accessoire à grille humidifiée pour l'amélioration de l'éfficacité des échangeurs à air: proposition d'un mécanisme pour les aéro-refroidisseurs et les condenseurs., 160057, 01/02/2016, Algeria
13. Rapin PJ, Jacquard P (1992) Installations frigorifiques: technologie, 6th edn. Ed. Pyc
14. Kern DQ (1951) Process heat transfer. McGraw-Hill, New York
15. Wang C-C, Chi K-Y, Chang C-J (2000) Heat transfer and friction characteristics of plain fin-and-tube heat exchangers, part II: correlation. Int J Heat Mass Transfer 43(15):2693–2700
16. Gnielinski V (1976) New equations for heat and mass transfer in turbulent pipe and channel flow. Int Chem Eng 16(2):359–368
17. Wylie EB (1984) Simulation of vaporous and gaseous cavitation. J Fluids Eng 106(3):307–311
18. Boulet P, Tissot J, Trinquet F, Fournaison L (2013) Enhancement of heat exchanges on a condenser using an air flow containing water droplets. Appl Therm Eng 50(1):1164–1173
19. INFO-CLIMAT (2019) www.infoclimat.fr/climatologie/annee/2014/biskra/valeurs/60525.html. Acceded 21 Apr 2019
20. Khan J-U-R, Qureshi BA, Zubair SM (2004) A comprehensive design and performance evaluation study of counter flow wet cooling towers. Int J Refrig 27(8):914–923
21. Qureshi BA, Zubair SM (2006) A complete model of wet cooling towers with fouling in fills. Appl Therm Eng 26(16):1982–1989

Experimental Investigation on Heat Transfer Coefficient and Thermal Efficiency of Solar Air Heaters Having Different Baffles

Charaf-Eddine Bensaci, Abdelhafid Moummi and Adnane Labed

Abstract The courant research presents the heat transfer and thermal efficiency in an experimental investigation of solar air collector system for several configurations in Biskra Region (Algeria). Experiments were performed for forced convection airflow in the air duct of SAH to define the performance. A conventional solar air heater considered for the comparison purpose was working under similar conditions for all the configurations. The effect of baffles configurations and arrangement on the convective heat transfer coefficient and thermal efficiency were compared. The results showed that the thermal performance is proportional to the solar intensity at the Type I and a specific mass flow rate.

Keywords Heat transfer · Thermal efficiency · Baffles · Mass flow rates

Nomenclature

A	Absorber plate surface area, m^2
Φ	Heat flux, $W\,m^{-2}$
h	Convective heat transfer coefficient, $W\,m^{-2}\,K^{-1}$
$h(x)$	Local convective heat transfer coefficient, $W\,m^{-2}\,K^{-1}$
Q_u	Useful heat gain, $W\,m^{-2}$
T_{ab}	Absorber temperature, K

C.-E. Bensaci (✉) · A. Moummi · A. Labed
Laboratoire de Génie Mécanique (LGM), Université Mohamed Khider Biskra, BP 145, 07000 Biskra, Algeria
e-mail: faf_3@yahoo.fr

A. Moummi
e-mail: moummi.abdelhafid@gmail.com

A. Labed
e-mail: adnanelabed@yahoo.fr

C.-E. Bensaci · A. Moummi
Laboratoire de Génie Civil, Hydraulique, Developpement Durable et Environnement
(LAR-GHYDE), Université Mohamed Khider, BP 145, 07000 Biskra, Algeria

T_f Fluid temperature, K
ΔT Temperature difference, K
$\dot{m}$ Mass flow rate, kg s^{-1}
Q_v Volume flow rate m^3 h^{-1}
U Velocity, m s^{-1}
η Thermal efficiency
I_G Incident solar radiation, W m^{-2}

Greek Symbols

C_p Specific heat J kg^{-1} K^{-1}
ρ Fluid density, kg m^{-3}
α_abs Absorptivity of absorber plate

Subscripts

i   Inlet
o   Outlet
SAH   Solar air heater

1 Introduction

The energy can be exploited by using devices called solar air heater collectors. There are many applications of solar air heaters as crop drying [1, 2], building heating [3], marine products. The studied systems absorb the solar radiation, transform it into thermal energy and then transfer this thermal energy to the air flowing under the absorber plate. Many of the research on heat transfer in roughened and smooth plates have been noted in the literature. One of the oldest studies investigated the effect of the geometric parameters (p/e), (e/D)) on the thermo-hydraulic performance (friction factor and heat transfer) [4]. Improved heat transfer by placing obstacles with single window cut on the two opposite heated surfaces was obtained by Habib et al. [5]; they also observed that by increasing the baffles conductivity, the baffles spacing, the Reynolds number, and the heat flux had approximately same effect on the convective heat transfer coefficient. The ideas were developed at the beginning of the twenty-first century; Ahmed-Zaïd et al. [6] studied and compared the results obtained from tested configurations using obstacles, barriers and without them on the flat plate solar air collector system. Ay et al. [7] achieved a study by the infrared thermography technique inside heat exchangers for computing the heat transfer coefficient over the

plate-fin based on the finite difference method. Moummi et al. [8] have created a turbulent flow for decreasing dead zones by the use of baffles perpendicular to the air duct. Ho et al. [9] presented a mathematical formulation for double-pass SAH with recycling. The results presented that the double-pass collector type with recycling was the thermo-hydraulic parameters better than the model without recycling. Hans et al. [10] reviewed the performance of solar air heaters by use different roughness geometries, and twenty-three configurations have been considered to determine from thermo-hydraulic viewpoint to the best performing roughness geometry. Labed et al. [11] studied an experimental and theoretical study to optimize the performance of solar air heater by proposing a novel roughness case, and the solar air collector was the studied system for single pass. In the same year, Gupta and Kaushik [12] investigated many roughness elements types under the absorber plate of the system duct. Akpinar and Koçyiğit [13] presented the performance of a novel SAH with roughness and without it by an experimental investigation. It was found that the ideal efficiency value was specified by the SAH for all operating conditions, and it was significantly better than that without roughness. They defined the energy and exergy of SAHs, and comparisons were made among them at various air mass flow rates. El-Khawajah et al. [14] are examined the arranging of the simple fins and the transverse fins for increase in the heat transfer between wire mesh layers flowing air, and the highest value of SAH thermal performance was found when they used six transverse fins. Chabane et al. [15] presented a heat transfer study for new solar air collector's design. Experimental and theoretical investigations on single-pass solar air heater were carried out to simulate the heat transfer by Aissaoui et al. [16]. Bensaci et al. [17] presented a numerical study on natural convection heat transfer inside the air gap between the absorber plate and the glass cover; in the application on a flat plate SAH, the Navier–Stokes and energy equations were solved using the finite volume method to estimate the thermal performance. Menasria et al. [18] presented numerical investigation on the bottom wall of the solar air heater duct with continuous rectangular baffles having an inclined upper part for obtaining the thermo-hydraulic of the fully developed turbulent flow characteristics. Ghritlahre and Prasad [19] implicated the ANN technique on the solar air heaters to predict the performances for versus models. Baissi et al. [20] carried out an experimental study to improve thermal performance of the SAH.

In the current work, a single-pass SAH system was presented to determine the convective heat transfer coefficient, thermal efficiency, and enlarged exchange area. This research aimed to test several configurations (transversal obstacles with and without baffles, smooth plate) and their effects, environmental conditions, solar radiation, inlet temperature, and air mass flow rate on the thermal performances.

2 Experimental

2.1 *Thermal Analysis*

In the present study, the steady-state heat transfer rate was supposed to equal the heat loss in the air channel [21]:

$$Q_\mathrm{u} = Q_\mathrm{conv} \tag{1}$$

where

$$Q_\mathrm{u} = \dot{m} C_\mathrm{p} (T_\mathrm{o} - T_\mathrm{i}) \tag{2}$$

the mass flow rate ($\dot{m}$) is

$$\dot{m} = \rho Q_\mathrm{v} \tag{3}$$

The convection heat transfer of the air duct can be given by:

$$Q_\mathrm{conv} = h A (T_\mathrm{s} - T_\mathrm{b}) \tag{4}$$

where

$$T_\mathrm{b} = (T_\mathrm{o} + T_\mathrm{i})/2 \tag{5}$$

$$T_\mathrm{s} = \sum T_\mathrm{ab}/4 \tag{6}$$

A measure of the system performance defined as the useful heat gain ratio on the solar radiation, and the absorbing area we presented that as follows:

$$\eta = Q_\mathrm{u}/I_\mathrm{G} A \tag{7}$$

We compensated Eq. (2) in Eq. (7), and the thermal efficiency can be given as:

$$\eta = \dot{m} C_\mathrm{p} (T_\mathrm{o} - T_\mathrm{i})/I_\mathrm{G} A \tag{8}$$

The local convective heat transfer coefficient $h(x)$ described the heat transfer phenomena between the fluid (air) and the absorber.

The convective heat flux from the absorber to the fluid (air) is written as:

$$\Phi = h_{(x)} (T_\mathrm{ab} - T_\mathrm{f}) \tag{9}$$

where T_{ab} is the superficial absorber temperature in X-point, given as an average along the absorber width L.

The local heat transfer coefficients are defined in each position (X) for versus air mass flow rates by Moummi et al. [8]:

$$h(x) = \frac{eU\rho_f C_p \frac{\partial T_f(x)}{\partial x}}{T_{ab}(x) - T_f(x)} \qquad (10)$$

2.2 Experimental Setup

An experimental system was a solar air heater (SAH), which was constructed and tested in the Mohamed Khider University—Biskra (latitude 34° 48′N, longitude 5° 44′E, altitude 85 m above sea level), Algeria. The SAH component sizes were thickness of the glass cover is 5 mm, the air gap between the absorber plate and the glass cover height is 30 mm, the air duct height is 25 mm, the absorber sizes are 1.5 m × 0.75 m with the thickness of 0.5 mm and the rear insulation (polystyrene) thickness is 40 mm. The galvanized steel is the type of absorber with a black coating ($\alpha_{abs} = 0.95$). The SAH was positioned in inclined support having an inclination angle of 34° and was oriented to the south to receive the maximum solar radiation during all the experiments. The heated air flowed between the absorber inner surface and the backplate (air duct) with or without baffles. A front view sight of the experimental setup and schematic diagram of the constructed system was shown in Figs. 1 and 2, respectively.

Fig. 1 Experimental setup model (SAH)
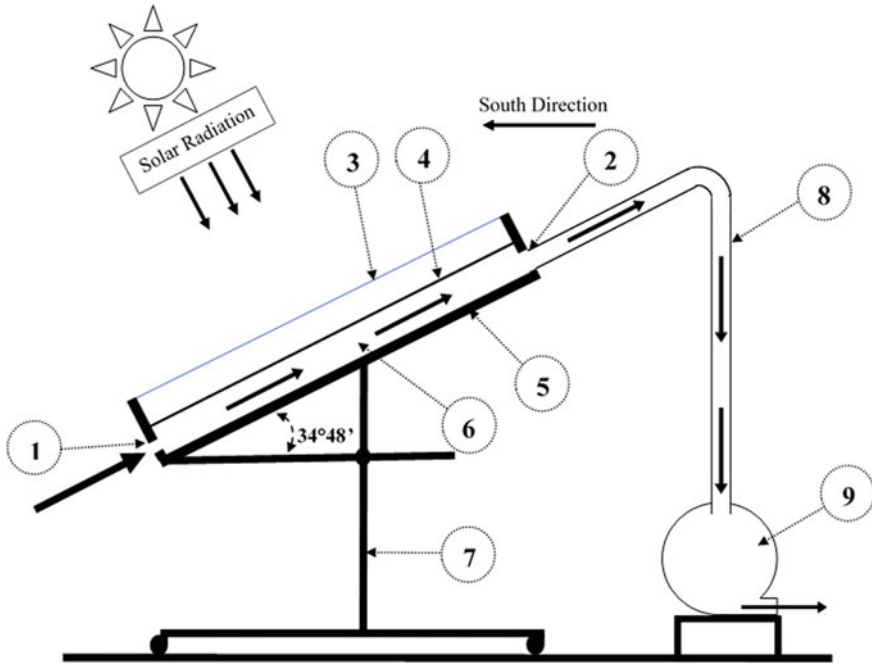
Fig. 2 Schematic diagram of experimental setup (SAH). Inlet port (1), outlet port (2), glass cover (3), absorber plate (4), insulating material (polystyrene) (5), air duct (6), metal support (7), insulated tube (8), blower (9)

In this study, we used three configurations with roughness (Type I and Type II) and without roughness or smooth plate (Type III); photographic views of different configurations are shown in Fig. 3, and these configurations are mentioned as follows:

- Type I: using transverse obstacles in the dynamic air vein.
- Type II: using transverse obstacles and baffles in the dynamic air vein.
- Type III: no baffles in the dynamic air vein (smooth plate).

Thermocouples were positioned evenly on the bottom and absorber plate's locations on the air duct.

The recorded test data of SAHs were measured at the time range of 30 min, the tests from 9 a.m. to 3 p.m. The measured parameters in the experiments were inlet temperature, outlet temperature, the temperatures of an absorber, and bottom plates in each X distance, air velocity, wind velocity, and solar radiation. The temperature measured by PT 100 type to 04 wires thermocouples with an accuracy 0.1 °C, pressure transducer (Kimo CP301) with an accuracy ± 0.1 Pa and 0.5% of reading, Kimo-type (VT300) anemometer an accuracy $\pm 1\%$ and reading ± 0.1 m/s of velocity, the pyranometer with 1% accuracy were used.

| Type I | Type II | Type III |
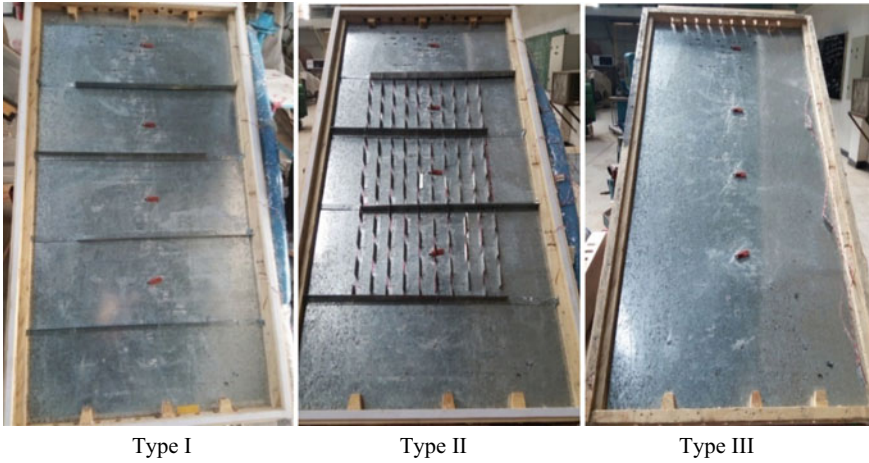
Fig. 3 Photographs of different tested SAHs configurations

3 Results and Discussion

In this part, we present the experimental test results of the experiments performed from May to June 2017. The comparison between three configurations and the experiments were performed under climatic conditions of Biskra, Algeria. Figures 4,
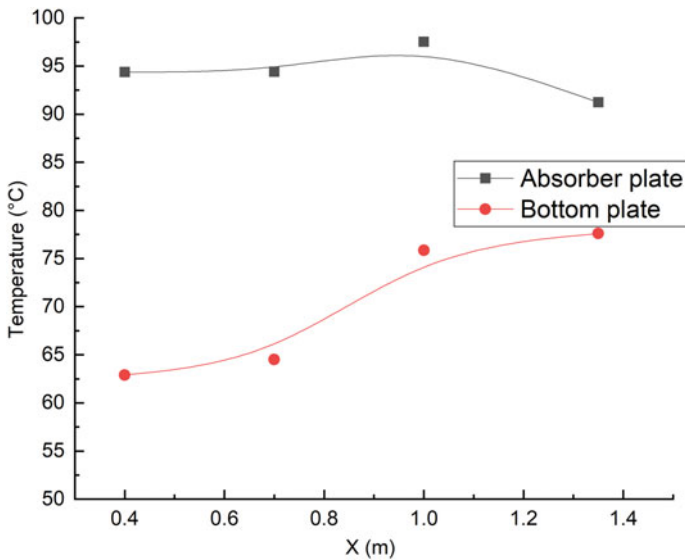
Fig. 4 Temperature of the absorber and bottom plates of Type I versus the SAH length ($\dot{m} = 0.035$ kg/s)
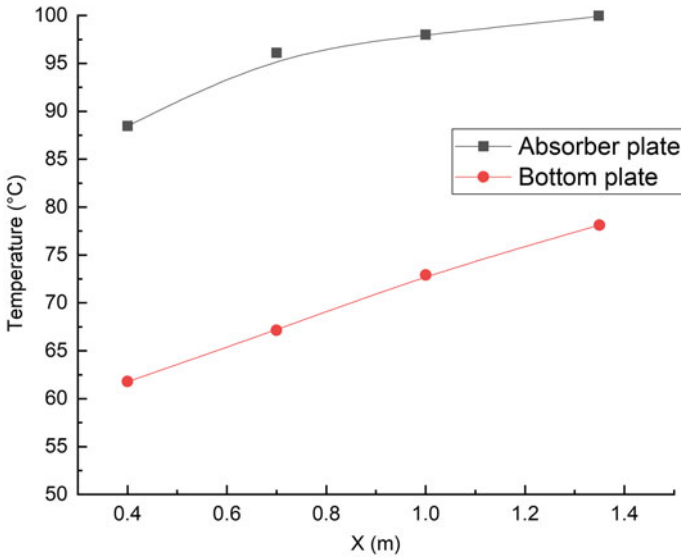
Fig. 5 Temperature of the absorber and bottom plates of Type II versus the SAH length ($\dot{m} = 0.035$ kg/s)

5, and 6 show the temperature of the absorber and bottom plates versus the SAH length, and the values of the temperatures were measured along the air duct from the inlet cross section to the outlet after the test section at distance of 15 cm, corresponding to the types I, II, and III, respectively, at $\dot{m} = 0.035$ kg/s. The curves evolution of the temperature take a similar behavior, where the absorber plate temperature increases in the flow direction and the bottom plate temperature increases in the flow direction at the same time, for example in the Type II "$T_{bp} = 62.44$ °C, $T_{ab} = 88.83$ °C" and "$T_{bp} = 67.22$ °C, $T_{ab} = 95.10$ °C" at $X = 0.4$ m and $X = 0.7$ m (Fig. 5). The temperature difference is important with the smooth plate of the order of 72 °C at $X = 0.4$ and 85 °C at $X = 0.7$ in the absorber plate, that corresponds to poor heat exchange between the fluid (air) and the absorber (Fig. 6). In the presence of transverse obstacles, the exchange is effective in along the air duct. The transverse obstacles clearly play a very important role where results in acceptable heat exchange in the presence of the fins, because it offers a minimum passage section in front of the fluid, narrowing and sudden enlargement, to lengthen the air trajectory, the stay extension, and to create a turbulent flow within the dynamic air for reducing the dead zones. The temperature difference $\Delta T = (T_o + T_i)$ versus the daily time at $\dot{m} = 0.017$ kg/s increased with the solar intensity from the sunrise, the maximum value in the midday from 12:00 to 1:00 p.m., as shown in Fig. 7, then afternoon decreased. The maximum ΔT values for all different configurations (Type I, Type II, Type III) were 27.5 °C, 28 °C, and 23 °C, respectively.

In order to present the relationship between the fluid and the absorber plate, the local convective coefficient versus the length of the SAH is shown in Fig. 8, for $\dot{m}$
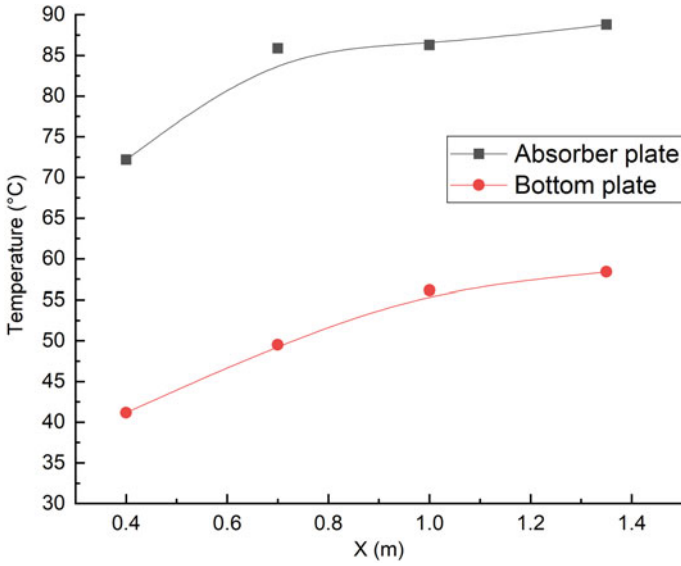
Fig. 6 Temperature of the absorber and bottom plates in a smooth plate (Type III) versus the SAH length ($\dot{m} = 0.035$ kg/s)
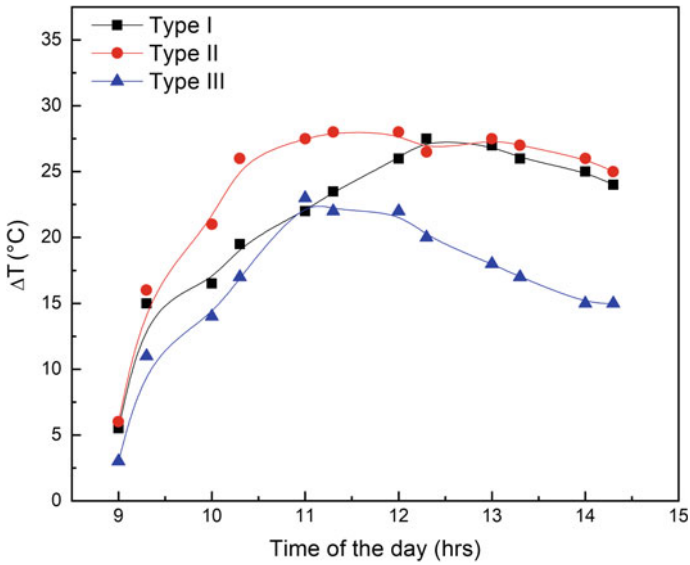
Fig. 7 Temperature difference versus time of the day for three configurations ($\dot{m} = 0.017$ kg/s)
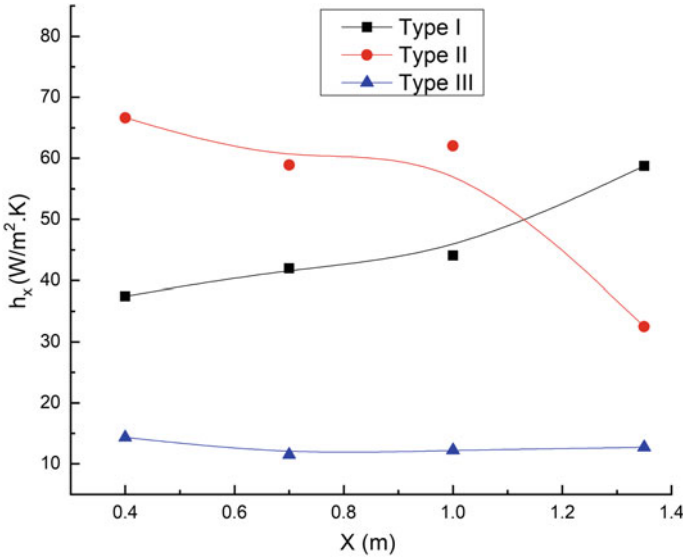
Fig. 8 Variation of the local convective heat transfer coefficient versus the SAH length for three configurations ($\dot{m} = 0.03$ kg/s)

$= 0.04$ kg/s. The local convective coefficient obtained from Eq. (10) describes the quality of heat transfer. It is shown that the SAH (Type II) presents the higher local convective coefficient over all the SAH duct where it varies from 77 to 30 (W/m² K), followed by Type I, while the less of local convective heat transfer coefficient in smooth duct (Type III) due to the lack of baffles.

Figure 9 shows the thermal efficiencies of different SAHs configurations versus $\dot{m}$. The thermal efficiency increases with increasing air mass flow rate. The maximum efficiencies for all the configurations were obtained for air mass flow rate from 0.03 (kg/s) to 0.035 (kg/s). The thermal efficiency of Type II is higher than Type I and the latter was higher than that of Type III (no turbulence) in the higher values of air volume flow rate. As seen from Table 1, the efficiency values were obtained for Types I, II, and III need to be compared, the optimal values of efficiency (or the best turbulence) were in Type II for all operating conditions. We presented the verification of thermal efficiency of the current study for Type II with some studies from the literature in Table 2.
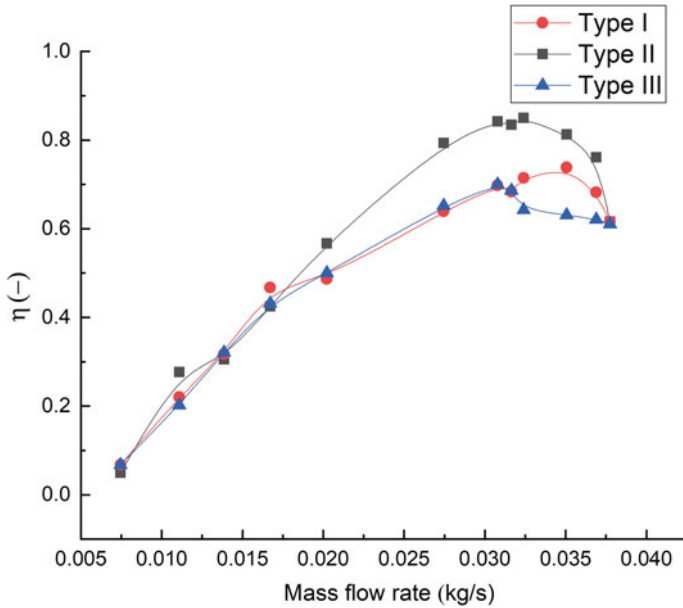
Fig. 9 Thermal efficiency versus air volume flow rate for different configurations

Table 1 Thermal efficiency of the tested configurations of the solar air heaters

Solar air heaters	$\dot{m}$ (kg/s)	η (%)
Type I	0.017	43
	0.025	58.5
	0.035	77
Type II	0.017	45.3
	0.025	63
	0.035	78
Type III	0.017	35
	0.025	51
	0.035	72

Table 2 Verification of thermal efficiency values of the present work with literature

	$\dot{m}$ (kg/s)	η (%)
Karim and Hawlader [22]	0.02	40.21
	0.03	48.73
Esen [23]	0.025	65
Current study (Type II)	0.025	63
	0.035	78

4   Conclusions

In the current study, three configurations of solar air heaters SAHs were tested and their thermal performances were compared to valorize thermal conversion systems of solar energy. It was shown that the efficiency depended on solar radiation, the air mass flow rate, and the position of roughness in the air duct. The heat transfer and the thermal efficiency were higher when the baffles were fixed over all the tested channel of the SAH. The solar radiation, the type and location of baffles, and air mass flow rate were principal parameters which affected the performance of SAH. The configurations presented here can be utilized for the SAH's enhancement.

References

1. Labed A, Moummi N, Aoues K, Benchabane A (2016) Solar drying of henna (*Lawsonia inermis*) using different models of solar flat plate collectors: an experimental investigation in the region of Biskra (Algeria). J Clean Prod 112:2545–2552
2. Sreekumar A (2010) Techno-economic analysis of a roof-integrated solar air heating system for drying fruit and vegetables. Energy Convers Manage 51:2230–2238
3. Arkar C, Šuklje T, Vidrih B, Medved S (2016) Performance analysis of a solar air heating system with latent heat storage in a lightweight building. Appl Therm Eng 95:281–287
4. Prasad B, Saini J (1988) Effect of artificial roughness on heat transfer and friction factor in a solar air heater. Sol Energy 41:555–560
5. Habib MA, Mobarak AM, Sallak MA, Hadi EAA, Affify RI (1994) Experimental investigation of heat transfer and flow over baffles of different heights. J Heat Transfer 116:363–368. https://doi.org/10.1115/1.2911408
6. Ahmed-Zaïd A, Moulla A, Hantala MS, Y Desmons J (2001) Amélioration des Performances des Capteurs Solaires Plans à Air: Application au Séchage de l'Oignon Jaune et du Hareng
7. Ay H, Jang J, Yeh J-N (2002) Local heat transfer measurements of plate finned-tube heat exchangers by infrared thermography. Int J Heat Mass Transfer 45:4069–4078
8. Moummi N, Youcef-Ali S, Moummi A, Desmons JY (2004) Energy analysis of a solar air collector with rows of fins. Renew Energy 29:2053–2064. https://doi.org/10.1016/j.renene.2003.11.006
9. Ho CD, Yeh HM, Wang RC (2005) Heat-transfer enhancement in double-pass flat-plate solar air heaters with recycle. Energy 30:2796–2817
10. Hans VS, Saini RP, Saini JS (2009) Performance of artificially roughened solar air heaters—a review. Renew Sustain Energy Rev 13:1854–1869. https://doi.org/10.1016/j.rser.2009.01.030
11. Labed A, Noureddine M, Aoues K, Zellouf M, Moummi A (2009) Etude théorique et expérimentale des performances d'un capteur solaire plan à air muni d'une nouvelle forme de rugosité artificielle
12. Gupta MK, Kaushik SC (2009) Performance evaluation of solar air heater for various artificial roughness geometries based on energy, effective and exergy efficiencies. Renew Energy 34:465–476. https://doi.org/10.1016/j.renene.2008.06.001
13. Akpinar EK, Koçyiğit F (2010) Experimental investigation of thermal performance of solar air heater having different obstacles on absorber plates. Int Commun Heat Mass Transfer 37:416–421
14. El-Khawajah MF, Aldabbagh LBY, Egelioglu F (2011) The effect of using transverse fins on a double pass flow solar air heater using wire mesh as an absorber. Sol Energy 85:1479–1487. https://doi.org/10.1016/j.solener.2011.04.004

15. Chabane F, Hatraf N, Moummi N (2014) Experimental study of heat transfer coefficient with rectangular baffle fin of solar air heater. Front Energy 8:160–172. https://doi.org/10.1007/s11708-014-0321-y
16. Aissaoui F, Benmachiche AH, Brima A, Bahloul D, Belloufi Y (2016) Experimental and theoretical analysis on thermal performance of the flat plate solar air collector. Int J Heat Technol 34:213–220
17. Bensaci C-E, Labed A, Zellouf M, Moummi A (2017) Numerical study of natural convection in an inclined enclosure: application to flat plate solar collectors. Math Model Eng Probl 4:1–6
18. Menasria F, Zedairia M, Moummi A (2017) Numerical study of thermohydraulic performance of solar air heater duct equipped with novel continuous rectangular baffles with high aspect ratio. Energy 133:593–608. https://doi.org/10.1016/j.energy.2017.05.002
19. Ghritlahre HK, Prasad RK (2018) Prediction of heat transfer of two different types of roughened solar air heater using artificial neural network technique. Therm Sci Eng Prog 8:145–153. https://doi.org/10.1016/j.tsep.2018.08.014
20. Baissi MT, Brima A, Aoues K, Khanniche R, Moummi N (2019) Thermal behavior in a solar air heater channel roughened with delta-shaped vortex generators. Appl Therm Eng
21. Duffie JA, Beckman WA (2013) Solar engineering of thermal processes, 4th edn. Wiley, New York
22. Karim MA, Hawlader MNA (2006) Performance investigation of flat plate, v-corrugated and finned air collectors. Energy 31:452–470
23. Esen H (2008) Experimental energy and exergy analysis of a double-flow solar air heater having different obstacles on absorber plates. Build Environ 43:1046–1054. https://doi.org/10.1016/j.buildenv.2007.02.016

Impact of Carbonization on the Combustion and Gasification Reactivities of Olive Wastes

Hakan Cay, Gozde Duman, Gizem Balmuk, Ismail Cem Kantarli and Jale Yanik

Abstract As an alternative to biomass, biochar is known as a promising candidate to replace or co-process with coal as solid fuel. In this study, biochars were obtained from pyrolysis of olive tree pruning (OP) at different temperatures and duration in order to investigate their possible use in combustion and gasification processes alone or with lignite. Steam gasification experiments of raw biomass, biochars and their blends with lignite were conducted in two-stage reactor at 850 °C to produce hydrogen-rich gas. The combustion behavior of fuels was investigated using thermogravimetric analyzer. The temperature was more effective than duration on the yield and properties of biochar. Biochars obtained above 350 °C had more aromatic structure with higher fixed carbon content. Gasification of biochar was more efficient than that of biomass, due to its high carbon content, homogeneous properties, and minimized tar formation. Hydrogen yield increased with the increase in the potassium and fixed carbon contents of biochars. Slagging and fouling indices of biochars indicated the tendency of slagging and fouling during their combustion alone. For the blends containing OP and biochars produced at low temperatures, antisynergistic effect was observed, lowering the combustion reactivity. In contrast, no interaction was found for the blend containing high-temperature biochar.

Keywords Pyrolysis · Steam co-gasification · Co-combustion · Biochar · Olive tree pruning

H. Cay · G. Duman (✉) · G. Balmuk · J. Yanik
Chemistry Department, Faculty of Science, Ege University, Izmir, Turkey
e-mail: gozdeduman@gmail.com

H. Cay
e-mail: hakn.cay@gmail.com

G. Balmuk
e-mail: gizem_balmuk@hotmail.com

J. Yanik
e-mail: jale.yanik@ege.edu.tr

I. C. Kantarli
Ataturk Medical Technology Vocational School, Ege University, Izmir, Turkey
e-mail: ismail.cem.kantarli@ege.edu.tr

1 Introduction

Overpopulation and industrialization of the world led to increase of worldwide fossil fuel consumption for energy production and hence to the increase in amount of CO_2 released from the combustion of fossil fuels, which are responsible for 65% of total greenhouse gas (GHG) emissions. Therefore, reduction of the use of fossil fuel in energy systems is a fundamental requirement to reduce GHG emissions. This can be achieved by renewable energy sources, namely wind, solar, geothermal and biomass. Among renewable energy sources, biomass represents the only renewable resource of liquid, solid, and gaseous fuels that contain carbon. Biomass mainly refers to materials of plant origin such as wood, wood processing waste, plant cultivated as energy crops, agricultural residues, and organic waste.

Biomass has advantages such as reducing pollutant greenhouse gas emissions, extremely lower sulphur and nitrogen content compared to coal, local availability and sustainability [1, 2]. Biomass is also considered as carbon neutral. Despite these advantages, the direct usage of biomass in existing combustion systems is limited by its physicochemical properties such as heterogeneity, low bulk, and energy density, high ash content, and high moisture content. These undesirable properties of biomass bring technical and economical concerns related to storage, transportation, and operation [3]. Moreover, co-combustion of biomass with coal has been also attempted for electricity generation in existing coal-firing power stations [4, 5]. Tillman pointed out that low percentage of biomass species is available for co-firing [6]. Besides, limitations due to the physical and chemical differences between coal and biomass make difficulties and challenges to operate blends in firing systems, particularly in case of blends with the biomass ratio higher than 5% [7]. From the point of biomass processing in the current coal gasification systems, high tar formation is the main problem, which may lead to blockages in the equipment and poor gasification efficiency [8, 9]. Therefore, co-gasification was also suggested and some studies focusing on co-gasification of biomass and coal have been attempted [8, 10]. The main concern of these studies was on tar reduction, which can be mostly achieved by low ratio of biomass/coal blends. Howaniec and Smolinski reported a correlation between synergic effect and alkali and alkaline earth metals (AAEM) content [8]. Improvement on the reactivity of blends of coal and biomass was observed due to the catalytic properties of biomass ash. Even though formation of potassium silicates during co-gasification may inhibit gasification reactions, higher K/Al ratio in blends by increase of biomass ash may overcome this problem [11].

Taking the advantages of better fuel characteristics, the use of biochar reduces the deficiencies of biomass and enables the implementation of blends in current coal combustion and gasification systems by less investment and adjustment. Therefore, it is of great importance that biomass is converted into biochar to utilize as solid fuel [12]. Different thermochemical processes can be applied to convert biomass to a stable and energy-intensive biochar. The most common of these thermochemical methods is pyrolysis. Pyrolysis is a thermochemical method that subjects biomass to thermal decomposition at moderate temperatures (between 200 and 600 °C) in

an inert atmosphere [12, 13]. Slow pyrolysis is usually applied as a pre-treatment of biomass in order to eliminate technology barriers during its utilization as solid fuel [3]. By pyrolysis at lower temperatures, a high percent of the biomass energy (up to 95%) and mass (up to 90%) are conserved in produced biochars. Many studies exist in literature about biochar production by pyrolysis of different types biomass including mainly agricultural residues such as pine sawdust [14], vineyard pruning [15], palm kernel shell [16], eucalyptus wood [17, 18] rice straw [19], corn stover [20] and agro-industrial residues such as orange pomace [15] and grape pomace [21].

Lately, most of the research studies regarding biochar combustion have focused on utilization of different types of biochars blending with coal [22–26]. Ro et al. studied combustion behavior of biochars obtained from chicken manure by two different thermochemical methods, namely pyrolysis and hydrothermal carbonization [27]. They also tested the blends of biochars and coal with different ratios and suggested that the usage of blends is more preferable than the replacement of coal with biochar due to the significant difference in combustion characteristics of biochars and coal. In a study reported by Gil et al. [28], biochars obtained from pyrolysis of three types of biomass (pine, black poplar, and chestnut woodchips) at 240 and 300 °C were combusted in an entrained flow reactor at 1300 °C. By pyrolysis, the grindability of raw biomasses was improved, while chestnut biochar at 280 °C was the easiest one to pulverize. Compared to coal combustion, lower NO and SO_2 emissions were detected in case of blends of the biochar and coal. The burnout of coal and blends were close due to the high reactivity of coal at higher oxygen concentration and temperature. At low oxygen concentration, burnout improved for the blend prepared with a ratio of 10:90 biochar and coal.

In our previous study, combustion of biochars derived from lignocellulosic biomass and animal wastes and their blends with lignite were performed by using thermogravimetric analyzer under air atmosphere [26]. Lower ignition and burnout temperature were obtained by mixing coal with lignite at a ratio of 1:1 resulting from high reactivity of biochars. It is worth noting that an interaction between blends was apparent only at char combustion step. Liu et al. investigated combustion behavior of bamboo, torrefied bamboo, coal, and their blends by using thermogravimetric analyzer (TGA) [24]. Compared to raw bamboo, the reactivity of pyrolyzed bamboo was lower with higher ignition and burnout temperatures. They also reported that char combustion step of coal and pyrolyzed bamboo was similar revealing that co-combustion of their blends is more feasible.

Compared to biomass gasification, biochar gasification is reported to show great superiority due to low tar content and high gasification performance of biochars [7]. It was reported that AAEM in biomass remains in biochar, which is a potential catalyst for gasification reactions [28]. Therefore, co-gasification of biochar and coal, instead of biomass and coal, can be an effective way to obtain tar free gas products. Nevertheless, only our recent study exists in the literature about co-gasification of biochar with coal [29]. In our study, blends of coal with raw sunflower seed and its biochar obtained at 300 and 500 °C were gasified under a steam atmosphere in a vertical fixed bed reactor. The results revealed that blends of lignite/biochar at 300 °C showed stronger synergic effect than blends of lignite/biomass and lignite/biochar at

500 °C. We concluded that besides AAEM, volatile matter (VM) content of biochar had also an important role in synergic reactions between biochar and lignite.

Olea europaea, the olive tree, has been traditionally cultivated for centuries mainly in the Mediterranean countries and is being increasingly cultivated in the rest of the world for the production of oil and table olives due to their benefits to human health and very tasty characteristics [30–32]. The FAO statistics reveals that the amount of areas used for olive tree cultivation increased from 10,131,418 to 10,804,517 ha worldwide between 2014 and 2017 [33]. Olive tree pruning is implemented every 2 years during cultivation in order to rejuvenate trees and increase olive production and produces a large amount of lignocellulosic biomass, known as olive tree pruning waste (OP) including mainly old branches [34]. It is stated by Hodaifa et al. that, on average, 3000 kg/ha of OP is produced annually [35] and 30 Mt/year of OP is predicted to occur from the olive trees cultivated over 10 million ha of land all over the world [34]. OP finds a limited industrial application. Larger branches of OP are used as firewood in small industries, while the rest of OP is directly burnt or used as a vegetal additive to soil in the olive cultivation fields, as stated by Ruiz et al. [32]. Environmental problems such as fire risk and uncontrolled CO_2 emissions would occur in case of combustion of OP in the field. Papadakis et al. reported that burning OP increases average fine PM levels by more than a factor of 2 [36].

The main novelty of this study is the investigation of both combustion and gasification properties of the biochars obtained at different carbonization temperatures. Specific objectives of this study were to evaluate (1) the effect of pyrolysis conditions (duration and temperature) on the yield and characteristics of biochar (2) the impact of biochar properties on combustion behavior and gasification performance of biochar alone and mixing with lignite.

This case study provides important insights on utilization of olive tree pruning as potential substitute fuels for co-combustion and co-gasification with coal, for the first time.

2   Materials and Methods

2.1   Material

OP was collected from agricultural fields in Manisa, Turkey. After OP was dried at 105 °C overnight, it was ground and sieved less than 1.00 mm in order to provide homogeneity of the biomass for the experiments, and then they were stored in sealed containers until use. Component analysis was done by an ANKOM 200 Fiber Analyzer according to Van Soest et al. [37]. OP contains, 10.8% hemicellulose (+soluble inorganics), 16.7% cellulose, 17.8% lignin (+silica), 19.0% extractives and 35.6% carbohydrates (sugars, starch, pectin) and protein.

2.2 Pyrolysis Experiments

A stainless steel 1 L vertical reactor was used for pyrolysis experiments. The experiments were carried out at different temperatures between 250 and 500 °C under nitrogen (30 mL min^{-1}) as inert and sweeping gas. In a typical experiment, first, 100 g of OP was placed into the reactor. Then, the system was heated to the desired temperature at a rate of 7 °C min^{-1} and held at this temperature for 1 or 2 h. The volatile products passing through collection flasks cooled with a water-ice mixture were condensed as the liquid products. In some experiments, liquid phase involved two phases: bio-oil and aqueous phase. Aqueous phase was separated by separatory funnel from bio-oil in two-phase liquid products. The non-condensable volatiles were collected in Tedlar Bag as the gaseous products. At the end of the experiment, reactor was cooled down under nitrogen gas stream. The amount of biochar produced was determined by weighing. Biochars were ground to <500 mm and stored in sealed containers for further analysis.

Each pyrolysis process was repeated three times. The product yields were calculated as follows:

$$\text{Yield}\% = \frac{m_x}{m_b} * 100 \tag{1}$$

where m_b stands for the mass of raw olive waste and m_x is the mass of product (biochar or liquid product).

2.3 Steam Gasification Experiments

A vertical stainless steel reactor was used for steam gasification experiments. The reactor has top and bottom beds which are separately heated. The fuel (~3 g) was loaded in a basket at the top section of the reactor. A detailed description of the reactor set up and the gasification procedure is given in our previous study [29]. After loading the fuel, first, bottom section was heated to 850 °C under a nitrogen flow of 50 mL min^{-1}. When the temperature reached to 850 °C, heating of top section to 850 °C was started at a heating rate of 8 °C min^{-1}. Once the temperature of top section reached 850 °C, steam with a flow rate of 0.6 mL H_2O min^{-1} was introduced from this section with nitrogen flow (50 mL min^{-1}) at constant temperature for 1 h. During gasification of fuel, the volatiles formed at the top section of reactor passed through the bottom section of reactor (at 850 °C), at where volatiles underwent the secondary reactions (Eqs. 7–10). The tar and unreacted water were collected in the condenser and traps during the passage of the volatiles from reactor. Finally, the resulting gaseous products were collected in a Tedlar bag for further analysis.

2.4 Combustion Experiments

Combustion behavior of biochars and their blends with lignite was investigated by using a thermogravimetric analyzer (Perkin Elmer Diamond TG/DTA). 5–10 mg of sample was heated from room temperature up to 850 °C with a heating rate of 10 °C min^{-1} under airflow (200 mL min^{-1}). Ignition temperature (IT), burnout temperature (BT) and reactivity were calculated from TG/DTG curve as given in the literature [26]. Overall reactivity (R_m) was calculated by average of individual reactivity of first and second peaks.

2.5 Analysis

The elemental composition of biomass and biochars was determined by a LECO CHNS 932 elemental analyzer according to ASTM 5291-96. The ash and volatile matter contents were determined according to EN 14775 and ASTM D1762 – 84, respectively. The inorganic contents of biomass, biochar, and lignite were determined by using XRF analyzer (Spectro X-LabPro). The higher heating values (HHV) of biomass and biochar were calculated according to the formula given by Channiwala and Parikh [38]. Product gas composition was examined by RGA (Agilent Technologies 7890A GC system). HHV of product gas was calculated by equation given in literature [39].

3 Results and Discussion

3.1 Product Distribution of Pyrolysis

As well-known, the pyrolysis product yields depend on the process parameters including temperature, heating rate, duration and particle size besides feedstock type. In this study, the influences of temperature and duration on product yields from slow pyrolysis of OP were investigated.

The product yields from pyrolysis of OP at different temperatures for duration of 1 and 2 h are shown in Fig. 1. It is clear that the carbonization temperature is the main factor affecting product yields. The biochar yield decreased remarkably (from 78 to 40%) with the increase of temperature from 200 to 350 °C, and then slightly decreased above 350 °C. This was possibly due to the higher degradation rates of extractives and hemicellulose within the OP at lower temperatures. In contrast to char yield, the total liquid product yield considerably increased from 11 to 43% as the pyrolysis temperature increased to 400 °C, and then it remained almost constant with further increase in temperature. Similar result was observed in slow pyrolysis of pistachio shell [40]. The liquid products obtained from pyrolysis at 300 °C and below were
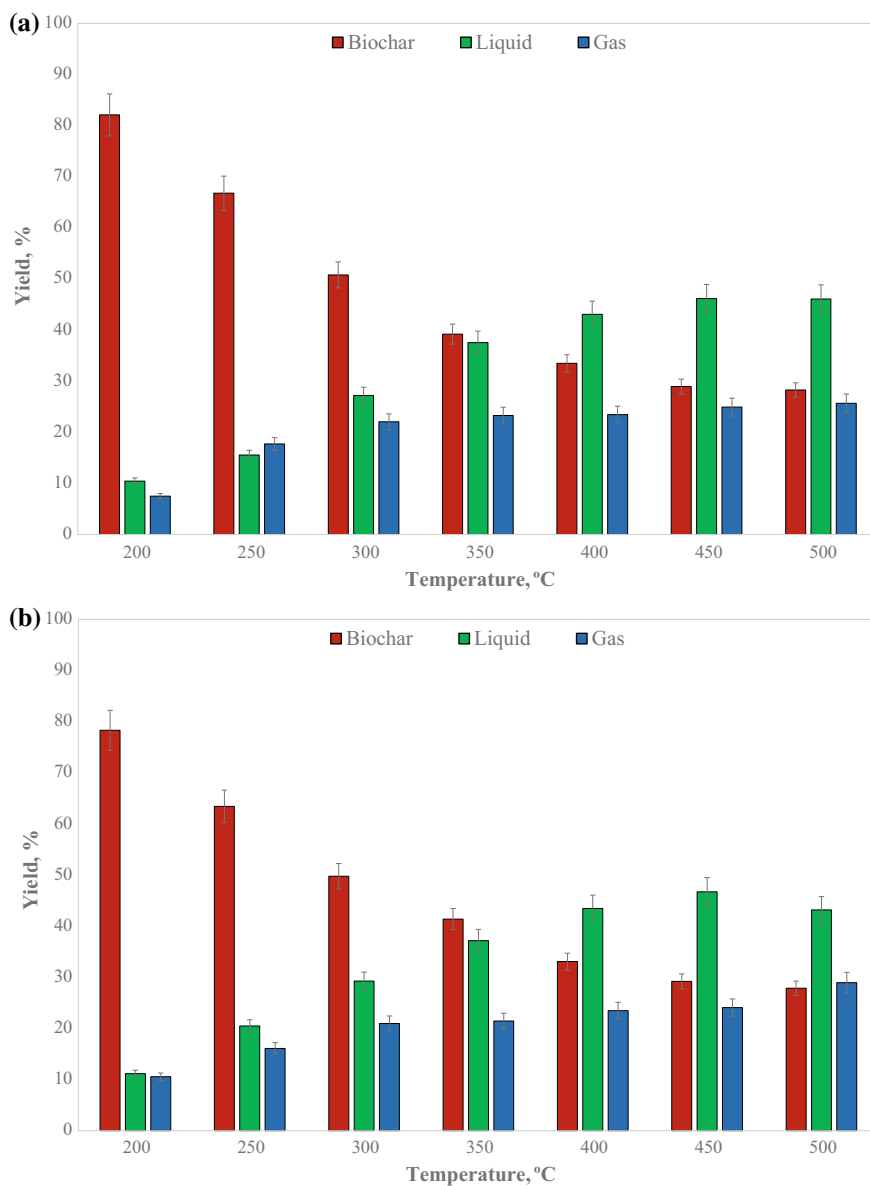
Fig. 1 Product yields of pyrolysis at different temperatures at the duration of **a** 1 h **b** 2 h

observed as one phase with reddish-brown color. But, the liquid products obtained above 300 °C were observed as two phases; bio-oil and aqueous phase. It is well-known that the liquid composition is largely dependent on the intensity of the process, such as temperature and residence of the tar vapors [41]. The liquid product from low-temperature pyrolysis mainly consists of the water-soluble products from degradation of hemicellulose and partly cellulose, besides a significant amount of water originated from dehydration reactions and physically bonded water in the biomass. However, at higher temperatures, tarry compounds (hydrocarbons, aromatic ethers, carbonyl compounds, and long-chain alcohols, aromatic oxygenates, etc.) occur due to the several molecular rearrangements from degradation of lignin and cellulose [42]. The gas yield gradually increased from 7.5 to 22.0 wt% as pyrolysis temperature rose from 200 to 300 °C, and then slightly increased to 28.9% as the temperature rose to 500 °C. Normally, it is expected that higher temperatures led to more production of gases due to the secondary cracking of the oil product. From these results, it can be argued that there is a competition between the formation of pyrolysis products due to the secondary reactions (cracking and recombination), with liquid becoming successively more favored. On the other hand, duration did not affect the product yields significantly. Generally, the effect of duration depends on the temperature and heating rate. For example, Park et al. [43] observed an increase in the char yield with the increase of residence time during the fast pyrolysis of pine sawdust. On the contrary, no considerable change in the biochar yield was noted during the slow pyrolysis of empty fruit bunch [44] and walnut shell [45] with the increase of residence time. Overall, the results indicated that temperature had a significant impact on the yield of products from olive pyrolysis, especially on the liquid and char yields.

3.2 Composition of Gas Products from Pyrolysis

Table 1 summarizes the composition of gases obtained at different pyrolysis temperatures for a duration time of 1 h. Although gas yields did not significantly change

Table 1 Composition of gas products obtained at different temperatures for a duration time of 1 h, % mole

Pyrolysis temperature (°C)	200	300	350	400	450	500
CH_4	–	2.2	10.9	22.1	36.0	42.1
C_2–C_5	–	2.1	9.7	25.2	20.6	9.6
CO_2	81.6	74.4	63.9	36.4	19.9	11.3
CO	18.4	21.0	14.8	12.2	10.7	7.0
H_2	–	0.2	0.7	4.1	12.7	30.0
HHV[a] (MJ/N m^3)	2.3	4.9	12.4	26.8	30.4	27.5

[a]Calculated as N_2 free

above 300 °C, the contents of both methane and hydrogen increased continuously up to 500 °C. In fact, the main difference in gas content was observed when the pyrolysis temperature increased from 350 to 400 °C. At low temperatures, the main gases were CO_x, mainly due to the degradation of hemicellulose and some part of cellulose. At higher temperatures, due to the lignin degradation and secondary cracking of volatiles, more hydrocarbon gases and hydrogen were released. At the pyrolysis temperature above 400 °C, an increase in demethanation and dehydrogenation reactions led to the more production of methane and hydrogen. This result is in good agreement with results of pyrolysis studies carried out with variety of biomasses, such as cherry seed [46] and wheat straw [47].

The heating value of gas product was calculated based on the concentration of each individual gas and its corresponding heating value. The gas products obtained at high pyrolysis temperature have quite high heating value due to the existence of a lot of combustible gases and could provide energy requirements of some part of the pyrolysis plant.

3.3 Chemical Properties of Biochars

The composition of biochar is an important indicator of its availability as fuel. The proximate and ultimate analysis results of biochars obtained at different temperatures for duration of 1 h were given in Table 2. The biochars were coded according to the pyrolysis temperature, e.g. B300 stands for biochar obtained from pyrolysis at 300 °C.

An increase in pyrolysis temperature had a pronounced impact on the biochar properties. The increase in temperature led to an increase in carbon content while

Table 2 Some properties of biochars and raw biomass

	OP	B200	B250	B300	B350	B400	B450	B500
Ultimate analysis (wt%, dry basis)								
C	49.98	55.43	60.29	63.69	64.4	65.48	67.17	67.64
H	6.45	6.15	5.87	5.01	5.02	3.52	2.83	2.31
N	1.88	1.99	2.39	2.69	2.70	2.71	2.79	2.93
S	0.15	0.06	0.08	0.07	0.06	0.07	0.05	0.06
O[a]	36.22	29.78	23.41	18.58	15.88	13.43	10.34	9.60
Proximate analysis (wt%, dry basis)								
Ash	5.3	6.6	8.0	10.0	11.9	14.8	16.9	17.5
Fixed carbon (FC)	26.9	32.0	38.6	56.7	64.7	72.3	71.6	73.8
Volatile matter (VM)	68.0	61.4	53.4	33.3	23.4	12.9	7.5	4.8
HHV (MJ/kg)	21.18	23.35	25.35	25.97	26.47	25.27	25.32	24.94

[a]Calculated from difference

resulting in a lower content of hydrogen and oxygen due to the removal of oxygen and hydrogen-containing functional groups via dehydration, decarboxylation, aromatization, etc. The most significant changes in carbon content occurred in the temperature range of 200–300 °C. On the other hand, nitrogen content of biochars slightly increased with increasing temperature, showing that most of nitrogen compounds in OP retained in biochar.

Change of H/C and O/C ratios during the conversion of OP into biochar by pyrolysis at different temperatures can be followed on the van Krevelen diagram shown in Fig. 2. The biochars became more carbonaceous with the increase of pyrolysis temperature. The decrease in the H/C and O/C ratios was almost linear up to pyrolysis temperature of 350 °C. Low H/C ratio of biochars obtained at temperatures higher than 350 °C indicates the aromatization of structure. Hammes et al. stated that a H/C ratio of around 0.3 indicates substances with highly condensed aromatic ring system, while a H/C ratio of more than 0.7 indicates substances with non-condensed aromatic structures such as lignin [48]. As a result, the biochars obtained at 250 °C and above were comparable to lignite and coal.

The proximate analysis of raw biomass and biochars indicates that the increase of pyrolysis temperature led to a decrease in the VM content and an increase in the FC content of biochar. On the other hand, a significant increase in ash content was observed due to the inorganics retaining in solid product of pyrolysis. Similar results were reported in the previous studies by Xin et al. [49] for cattle manure, by Tag et al. [15] for vine pruning, poultry litter and orange pomace and by Ahmad et al. [50] for soybean stover and peanut shell.
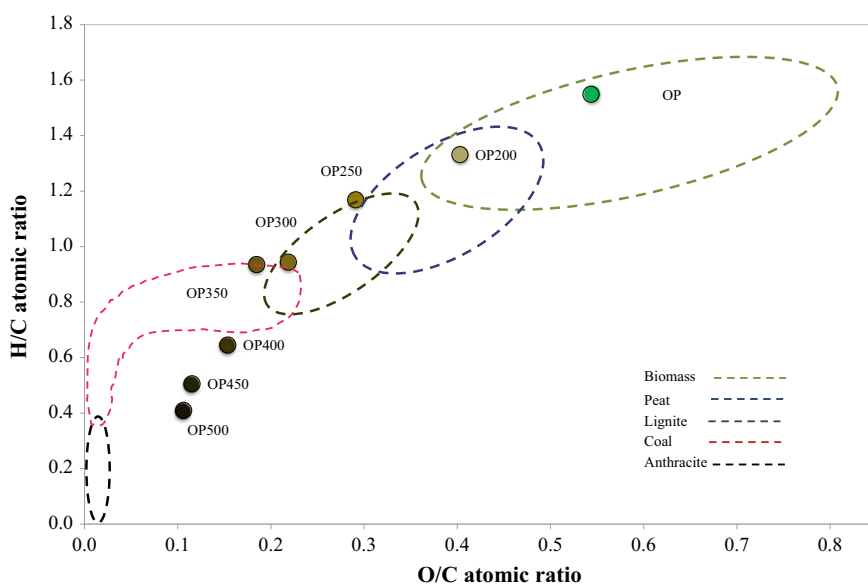
Fig. 2 Van Krevelen diagram

Table 3 Mineral contents (%), fouling and slagging indices of biochars

	OP	B250	B300	B500	Lignite
MgO	0.325	0.459	1.005	1.120	0.369
Al_2O_3	0.061	0.066	0.154	0.157	3.635
SiO_2	0.166	0.169	0.393	0.430	8.340
P_2O_5	0.128	0.232	0.505	0.642	
K_2O	1.550	2.360	4.740	5.260	0.230
CaO	3.485	5.180	10.250	11.850	4.335
TiO_2	0.006	0.008	0.015	0.016	0.230
Fe_2O_3	0.028	0.146	0.199	0.071	1.170
SI	3.5	2.7	2.1	1.8	0.7
FI	36.0	79.4	136.7	159.9	0.115

As well-known, the main technical difficulties in combustion of biomass/biochar in boilers or power plants include slagging and fouling due to their high alkaline content (Ca, K, Mg, and Na). Table 3 lists the mineral composition of biochars as determined by X-ray fluorescence spectroscopy (XRF). To predict the probability of slagging and fouling during combustion, slagging index (SI) and fouling index (FI) were calculated based on the mineral composition of the biochars (Eqs. 2 and 3) [51].

$$SI = \frac{\%(Fe_2O_3 + CaO + Na_2O + K_2O + MgO)}{\%(SiO_2 + Al_2O_3 + TiO_2)} * \%(S)(dry) \qquad (2)$$

$$FI = \frac{\%(Fe_2O_3 + CaO + Na_2O + K_2O + MgO)}{\%(SiO_2 + Al_2O_3 + TiO_2)} * \%(Na_2O + K_2O) \qquad (3)$$

The SI values greater than 2.0 indicate high slagging potential, while the FI values greater than 40.0 indicate high fouling potential. Although the low S content and reasonable calorific value make the biochars attractive for use as a solid fuel in combustion, it can be predicted that they lead to low combustion performance in boilers.

3.4 Steam Gasification of Biochars

Steam gasification is one of the most promising thermochemical processes to produce hydrogen from biomasses. But, the formation of tar that causes plugging in system is the main disadvantage of steam gasification. Tar formation can be reduced in different ways, such as varying the operating conditions and using catalyst [52]. Ex-situ tar steam reforming is known as one of the efficient ways to reduce tar formation by

converting the tar into gas products. In this study, steam gasification experiments were carried out in two-stage gasifier by following reaction pathways.

On top section of reactor:

At temperatures between 200 and 500 °C

$$\text{Pyrolysis of carboneous materials} \rightarrow \text{Char} + \text{Tar} + H_2O$$
$$+ \text{Gases}(CO_2 + CO + H_2 + CH_4 + C_2^+) \quad (4)$$
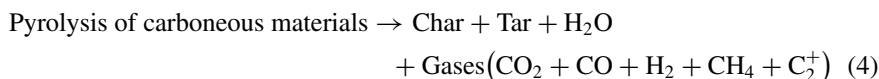
At temperatures between 500 and 850 °C

$$\text{Steam gasification of char} \quad C + H_2O \rightarrow CO + H_2 \quad (5)$$

$$C + 2H_2O \rightarrow CO_2 + 2H_2 \quad (6)$$

On bottom section of reactor:

$$\text{Steam reforming of tar} \quad \text{Tar} + yH_2O \rightarrow wCO + zH_2 \quad (7)$$

$$\text{Water-gas shift reaction} \quad CO + H_2O \rightarrow CO_2 + H_2 \quad (8)$$

$$\text{Methanation} \quad CO_2 + 4H_2 \rightarrow CH_4 + 2H_2 \quad (9)$$

$$\text{Steam-methane reforming} \quad CH_4 + H_2O \rightarrow CO + 3H_2 \quad (10)$$
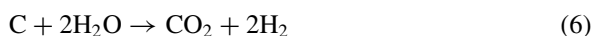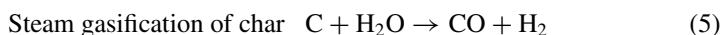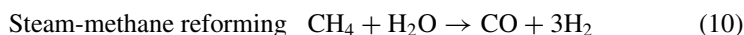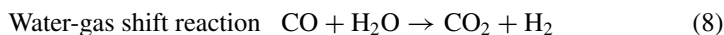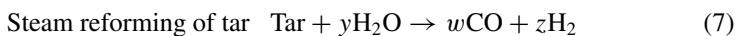
In gasification experiments, besides biochars and their blends with lignite (L), raw biomass (OP) was also gasified for comparison purpose. In our previous study [29], we found that gasification time of 1 h at 850 °C was adequate to gasify biomass and its derived biochars completely. For all types of fuel, the hydrogen-rich gas, consisting of mainly H_2 (58–66%, v/v %) and CO_2 (28–32%, v/v %) was obtained by steam gasification similarly to our previous study about steam gasification of sunflower seed cake and its derived biochars. Figure 3 shows the individual gas amounts (mL g^{-1} fuel) evolved from gasification of OP, biochars and their blends.

As seen from Fig. 3, highest hydrogen yield was obtained from B500 and hydrogen yield sequence followed B500 > B300 > B250 > OP. This result is reasonable, since the contents of AAEMs, particularly K, and FC increase by following the same sequence. B300 and B500 produced 2.3 and 2.6 times more H_2 than OP, respectively. Similarly, previous studies also reported that gasification of biochar was more applicable than that of biomass, due to its higher carbon content and homogeneity and minimized tar formation [28, 53].
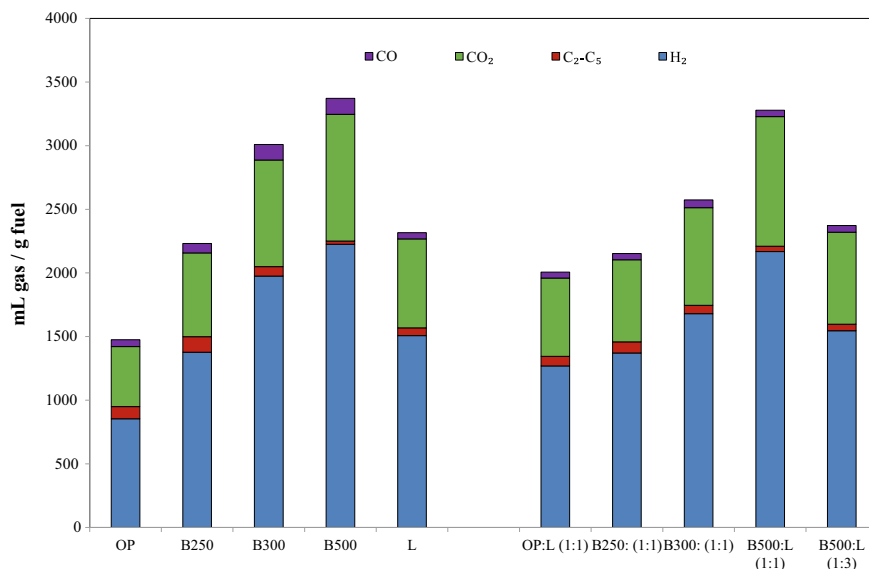
Fig. 3 The gas yields from gasification of the individual fuels and their blends with lignite

On the other hand, the co-gasification of coal and biomass has gained importance as a very effective way to reduce GHG emissions besides fossil fuel dependency. But, in co-gasification of biomass with coal in existing plants, the rate of biomass in blend was limited by the technical challenges including heterogeneity, poor grindability, and low carbon content. Using biochar instead of biomass provides a technical option for high substitution ratios of biomass in the co-gasification systems. In this study, the blends of biochars with lignite (ash: 8.9%, volatiles: 49.0%; C: 71.0%, O: 13.0%) were co-gasified. For comparison purpose, the blend containing parent biomass with lignite was also co-gasified. The mass fractions of lignite in these blends were 50 and 75 wt%, referred to as 1:1 and 1:3, respectively, in Fig. 3. In case of gasification of lignite alone under identical conditions with biochars, the lignite was not completely gasified and 25% of lignite remained as residue after gasification, which equals to 16.1% of the initial mass of lignite on ash-free basis. But, the residues from blend gasification consisted of only inorganics and no char was observed.

From the obtained results, we concluded that there is synergy between biochar and lignite during steam gasification due to the catalytic effect AAEMs in biochars. Thus, the AAEMs in biomass/biochars catalyzed the gasification of lignite char (Eqs. 5 and 6). Here, it should be noted that calcium in lignite could be attributed to calcium aluminosilicate ($CaAl_2Si_2O_8$) [11], not in the salt form as in biochar. The catalytic effect of AAEMs has also been reported in previous gasification studies, such as gasification of corncob char [54], of sewage sludge [53], of tobacco stalk [55], of wheat straw [56].

3.5   Combustion Behavior of Biochars and Their Blends

Although co-combustion of biomass with lignite has been considered as cost-effective technology to convert biomass into energy in existing co-firing plants, co-processing can be difficult due to the several technical challenges arisen from the difference between physicochemical properties of biomass and lignite. Taking the advantages of improved fuel characteristics, biochar is expected as a promising solid fuel, which can be easily operated with lignite. For this purpose, combustion behavior of individual biochar and their blends containing 50% (1:1) and 25% (1:3) was investigated in thermogravimetric analyzer. For comparison, OP and blends containing OP were also combusted under identical conditions.

The DTG curves obtained from combustion of biomass, biochars and their blends with lignite at different ratios are shown in Fig. 4. DTA curve of OP showed the typical combustion behavior of lignocellulosic biomass. DTA curve involves two clear peaks between 190–360 °C and 450–510 °C; first peak is evolution of volatiles and latter is associated with oxidation of char. The first peak is mostly related to the decomposition of cellulose and hemicellulose. Hemicellulose degradation is highlighted by a left shoulder in the first peak. Vamvuka et al. [57] also observed similar combustion profile of olive tree pruning. A small peak around 600 °C, which is related to the decomposition of carbonates of inorganics, was observed in biomass and all biochars.

B250 had similar peaks with OP, while first peak become narrower with disappearance of left shoulder. It can be clearly seen that the intensity of the first peak got dramatically smaller with the increase of the pyrolysis temperature to 300 °C. B500 had only one peak which corresponded to the temperature range of char oxidation. The reason is that hemicellulose and cellulose, from which most of volatiles originated, were decomposed during pyrolysis at higher temperatures. This result is also agreement with the VM content of biomass and biochars (Table 2). Similar observation was also made in a combustion study of rice husk and wood pellets reported by Park and Jang [58]. They observed one broad peak for biochars obtained from pyrolysis ≥400 °C due to their low VM content, whereas biochar produced at 300 °C had two DTG peaks. On the other hand, DTG curves of lignite also give one broad peak at higher temperatures attributed to the simultaneous reactions of volatile evolution and char oxidation [26].

In case of blends of OP and B250 with lignite, the first peak existed in the DTG curves of blends, which is linked to the concentration of OP or B250 in blends. The first peak was smaller at lower blending ratios. In contrast, for blends containing B300 and B500, only one broad peak was observed in DTG curves.

Combustion parameters of individual fuels and their blends are listed in Table 4. Due to their low volatile content, ignition temperature of biochars was higher than that of raw biomass. Ignition temperature of blends (except B500 blends) was found to be higher than that of biomass/biochar alone. This shows that in the initial phase of combustion there was an interaction between the blend components. In contrast, ignition temperatures of B500 blends were very close to that of B500 alone, indicating no interaction in the initial phase of combustion between the blend components.
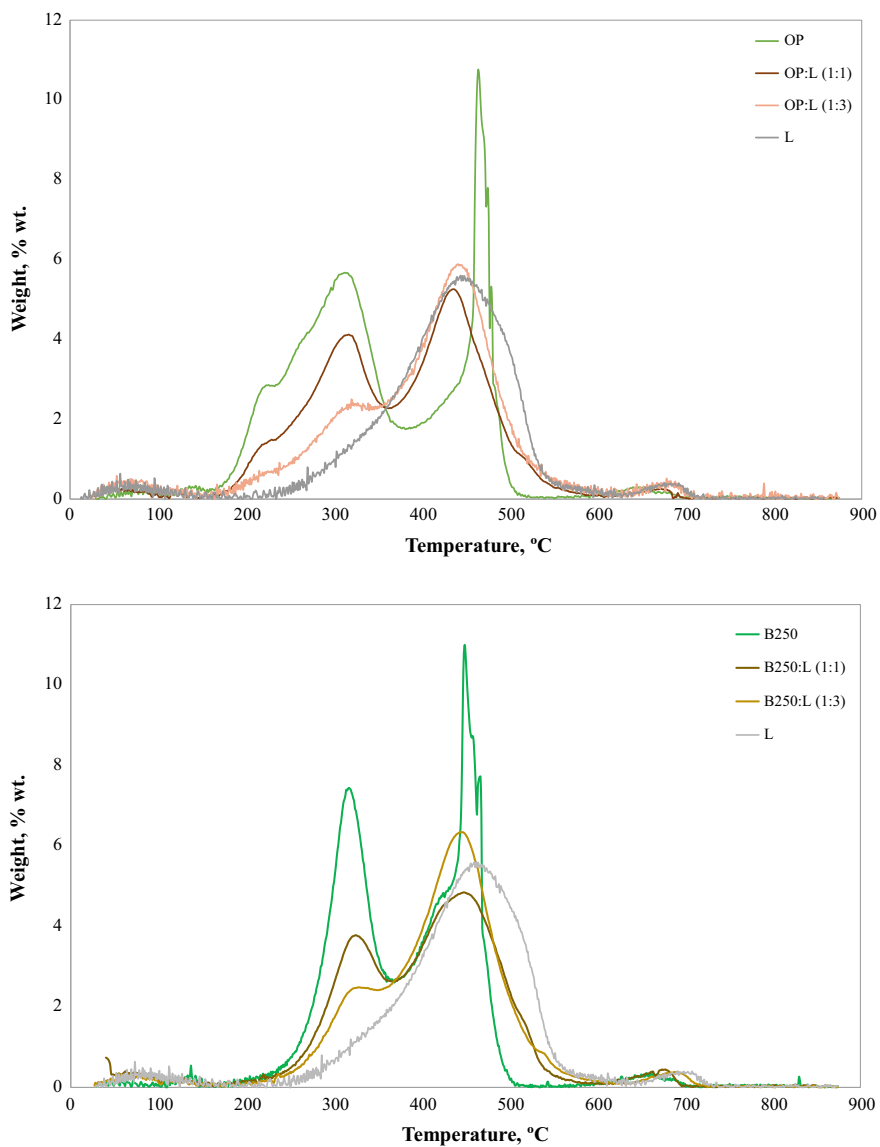
Fig. 4 DTG curves of OP, L, biochars, and their blends
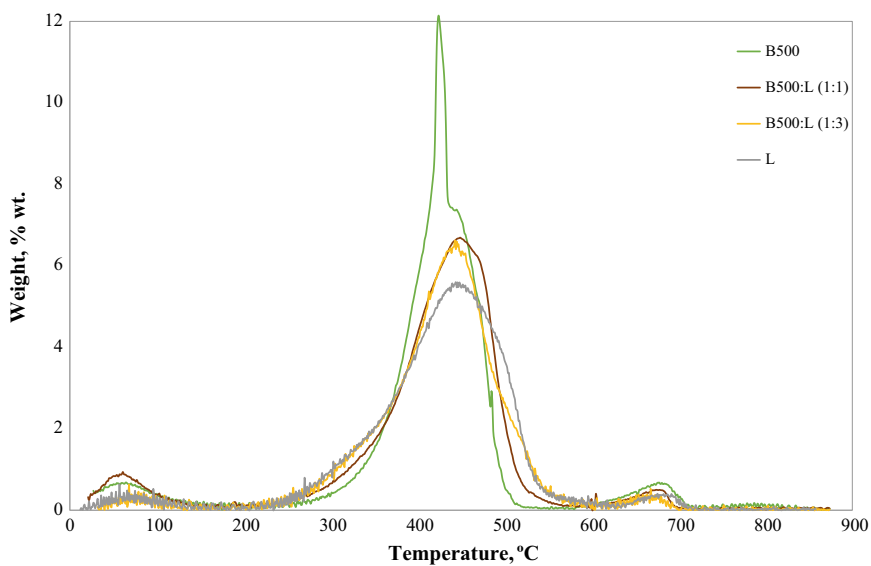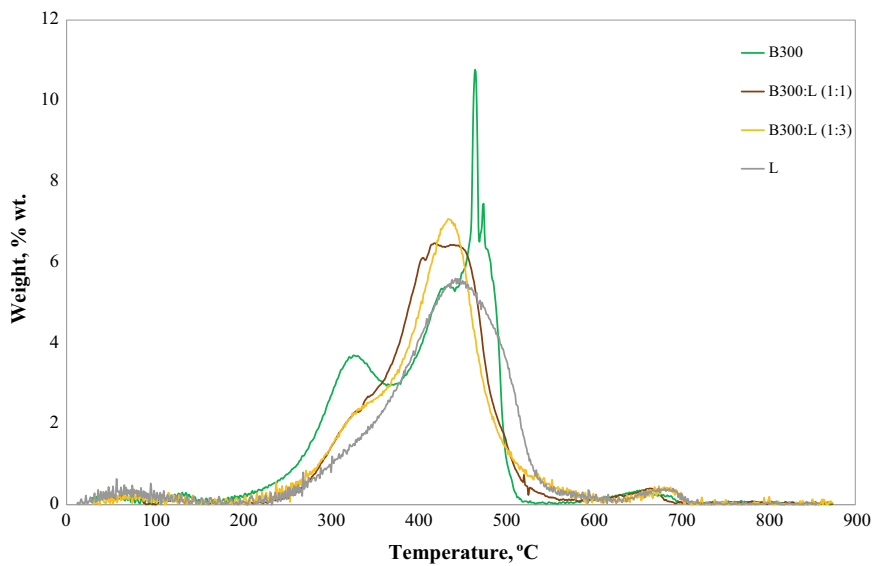
Fig. 4 (continued)

Table 4 Combustion parameters of OP, biochars, and lignite

	IT (°C)	BT (°C)	T_{max} (°C)		Max. combustion rate (% min⁻¹)		Reactivity (% min⁻¹ K⁻¹)		R_m
			1st	2nd	1st	2nd	1st	2nd	
OP	235	494	313	464	5.7	10.8	0.97	1.46	1.21
OP:L (1:1)	244	517	313	437	4.2	5.3	0.71	0.75	0.73
OP:L (1:3)	261	520	328	444	2.4	5.9	0.40	0.82	0.61
B250	281	488	316	449	7.4	11.0	1.26	1.52	1.39
B250:L (1:1)	293	528	342	447	2.5	6.4	0.41	0.89	0.65
B250:L (1:3)	302	528	319	449	3.8	4.9	0.64	0.68	0.66
B300	282	505	324	452	3.7	10.6	0.61	1.46	1.04
B300:L (1:1)	332	510		442		6.4		0.90	0.90
B300:L (1:3)	344	519		436		7.1		1.00	1.00
B500	366	496		424		12.1		1.74	1.74
B500:L (1:1)	370	514		451		6.7		0.93	0.93
B500:L (1:3)	368	533		445		6.7		0.93	0.93
L	382	546		462		5.6		0.76	0.76

The reason might be the negligible amount of volatiles in B500. Ro et al. [27] indicated that low ignition temperatures may cause potential risk of self-ignition of biomass since hot air (around 310–340 °C) is used in coal mill during drying and transporting to burner. On the other hand, lignite can hardly start burning because of its high ignition temperature. Therefore, the utilization of blends with biochars instead of lignite can improve combustion efficiency by lowering ignition temperature of lignite. But, modification of combustor system is needed to avoid self-ignition (except for blends containing biochar obtained at high temperatures).

Pyrolysis temperature had no clear effect on burnout temperature of biochars, which are between 488 and 505 °C. However, the addition of biomass/biochars into lignite lowered burnout temperature of lignite.

The addition of biochar to lignite led to increasing the combustion reactivity except for OP250:L (1:3). In most cases, pyrolysis improved the overall combustion reactivity. The highest reactivity was observed in B500, probably due to its inorganic content. It should be also noted that since overall combustion reactions take place in either one or two-step, it is difficult to compare the average reactivity of fuels. Difference in R_m of biomass and its biochars can be explained by two main reasons, one of them is volatile content that is related to the reactivity of first peak and the other is inorganic content, which affects char oxidation. In addition, porous and disordered structure of biochars may increase the combustion reactivity [59].

The theoretical DTG curves of blends were calculated from experimental data of individual solid fuels (was not presented here) to speculate possible interactions between biomass/biochars and lignite. The curve of B500 coal was almost the same with the experimental curves, indicating that there was no significant interaction between biomass/biochars with lignite. Other blends except B250:L (1:4) lowered the reactivity of char combustion. An antisynergistic effect of these blends might result from the low K/Al ratio in blends containing OP, B250, and B300 possibly due to the deactivation of K by the formation of potassium aluminosilicate components [11].

4   Conclusion

In this chapter, biochar was produced from pyrolysis of olive tree pruning at different temperatures to improve the performance of biomass in the gasification and combustion systems. Blends with different ratios (1:1 and 1:3) were also investigated for their potential usage with lignite in existing coal plants.

The following remarks can be concluded:

– Pyrolysis temperature was much more effective on the yield and properties of biochar than duration. Biochars, even obtained at 250 °C, had nearly same calorific value with lignite. Due to the demethanization and dehydrogenation reactions, pyrolysis conducted at and above 350 °C resulted in biochar with lower H/C ratios, revealing more aromatic nature.

– In case of steam gasification experiments, hydrogen yield was in the order of B500 > B300 > B250 > OP, which is correlated with AAEM and FC content. The addition of biomass/biochars into lignite enhanced the gasification of lignite due to the catalytic behavior of AAEMs in biomass/biochars.

– By increasing of pyrolysis temperatures, the combustion reactivity of produced biochars was improved. Although the low S content and reasonable calorific value make the biochars attractive for utilization as a fuel in combustion, the use of biochar alone may cause a risk of slagging and fouling due to their high SI and FI values.

– In case of co-combustion, no synergetic effect was observed between lignite and biochars. The use of blends instead of biochars alone can be suggested in order to lower the tendency of slagging and fouling during combustion.

References

1. Zhang S, Dong Q, Chen T, Xiong Y (2016) Combination of light bio-oil washing and torrefaction pretreatment of rice husk: its effects on physicochemical characteristics and fast pyrolysis behavior. Energy Fuels 30:3030–3037
2. Missaoui A, Bostyn S, Belandria V, Cagnon B, Sarh B (2017) Carbonization of dried olive pomace: energy potential and process performances. J Anal Appl Pyrol 128:281–290
3. Martín-Lara MA, Ronda A, Zamora MC, Calero M (2017) Torrefaction of olive tree pruning: effect of operating conditions on solid product properties. Fuel 202:109–117
4. Hu MC, Lin CH, Chou CA, Hsu SY, Wen TH (2011) Analysis of biomass co-firing systems in Taiwan power markets using linear complementarity models. Energy Policy 39:4594–4600
5. https://www.power-technology.com/projects/drax. Accessed 21 Apr 2019
6. Tillman DA (2000) Biomass cofiring: the technology, the experience, the combustion consequences. Biomass Bioenergy 19(6):365–384
7. Li YH, Lin HT, Xiao KL, Lasek J (2018) Combustion behavior of coal pellets blended with Miscanthus biochar. Energy 163:180–190
8. Howaniec N, Smoliński A (2014) Effect of fuel blend composition on the efficiency of hydrogen-rich gas production in co-gasification of coal and biomass. Fuel 128:4423–4450
9. Basu P (2013) Biomass gasification, pyrolysis and torrefaction. Practical design and theory, 2nd edn. Elsevier Inc., London
10. Hu J, Shao J, Yang H, Lin G, Chen Y, Wang X, Zhang W, Chen H (2017) Co-gasification of coal and biomass: synergy, characterization and reactivity of the residual char. Bioresour Technol 244:1–7
11. Habibi R, Kopyscinski J, Masnadi MS, Lam J, Grace JR, Mims CA, Hill JM (2013) Co-gasification of biomass and non-biomass feedstocks: synergistic and inhibition effects of switchgrass mixed with sub-bituminous coal and fluid coke during CO_2 gasification. Energy Fuels 27(1):494–500
12. Liu WJ, Jiang H, Yu HQ (2015) Development of biochar-based functional materials: toward a sustainable platform carbon material. Chem Rev 115(22):12251–12285
13. Lehmann J, Joseph S (2009) Biochar systems. In: Lehmann J, Joseph S (eds) Biochar for environmental management: science and technology, 1st edn. Earthscan, London, pp 147–168

14. Gong C, Huang J, Feng C, Wang G, Tabil L, Wang D (2016) Effects and mechanism of ball milling on torrefaction of pine sawdust. Bioresour Technol 214:242–247
15. Tag AT, Duman G, Ucar S, Yanik J (2016) Effects of feedstock type and pyrolysis temperature on potential applications of biochar. J Anal Appl Pyrol 120:200–206
16. Poudel J, Ohm TI, Gu JH, Shin MC, Oh SC (2017) Comparative study of torrefaction of empty fruit bunches and palm kernel shell. J Mater Cycles Waste Manage 19:917
17. Arias B, Pevida C, Fermoso J, Plaza MG, Rubiera F, Pis JJ (2008) Influence of torrefaction on the grindability and reactivity of woody biomass. Fuel Process Technol 89:169–175
18. Almeida G, Brito JO, Perre P (2010) Alterations in energy properties of eucalyptus wood and bark subjected to torrefaction: the potential of mass loss as a synthetic indicator. Bioresour Technol 101:9778–9784
19. Nam H, Capareda S (2015) Experimental investigation of torrefaction of two agricultural wastes of different composition using RSM (response surface methodology). Energy 91:507–516
20. Medic D, Darr M, Shah A, Potter B, Zimmerman J (2012) Effects of torrefaction process parameters on biomass feedstock upgrading. Fuel 91:147–154
21. Pala M, Kantarli İC, Büyükişik HB, Yanik J (2014) Hydrothermal carbonization and torrefaction of grape pomace: a comparative evaluation. Bioresour Technol 161:255–262
22. Haykiri-Acma H, Yaman S (2018) Synergistic investigation for co-combustion of biochars and lignite—thermogravimetric analysis approach. J Therm Sci Eng Appl 11:011006
23. Tong W, Liu Q, Ran G, Liu L, Ren S, Chen L, Jiang L (2019) Experiment and expectation: co-combustion behavior of anthracite and biomass char. Bioresour Technol 280:412–420
24. Liu Z, Hu W, Jiang Z, Mi B, Fei B (2016) Investigating combustion behaviors of bamboo, torrefied bamboo, coal and their respective blends by thermogravimetric analysis. Renew Energy 87:346–352
25. Gil MV, García R, Pevida C, Rubiera F (2015) Grindability and combustion behavior of coal and torrefied biomass blends. Bioresour Technol 191:205–212
26. Toptas A, Yildirim Y, Duman G, Yanik J (2015) Combustion behavior of different kinds of torrefied biomass and their blends with lignite. Bioresour Technol 177:328–336
27. Ro KS, Libra JA, Bae S, Berge ND, Flora JRV, Pecenka R (2019) Combustion behavior of animal-manure-based hydrochar and pyrochar. ACS Sustain Chem Eng 7:470–478
28. Gai C, Chen M, Liu T, Peng N, Liu Z (2016) Gasification characteristics of hydrochar and pyrochar derived from sewage sludge. Energy 113:957–965
29. Cabuk B, Duman G, Yanik J, Olgun H (2019) Effect of fuel blend composition on hydrogen yield in co-gasification of coal and non-woody biomass. Int J Hydrogen Energy. Available online 15 Mar 2019 (in press)
30. Torrecilla JS, Aragón JM, Palancar MC (2006) Improvement of fluidized bed dryers for drying olive oil mill solid waste (olive pomace). Eur J Lipid Sci Technol 108:913–924
31. Christoforou E, Fokaides PA (2015) A review of olive mill solid wastes to energy utilization techniques. Waste Manage 49:346–363
32. Ruiz E, Romero-García JM, Romero I, Manzanares P, Negro MJ, Castro E (2017) Olive-derived biomass as a source of energy and chemicals. Biofuel Bioprod Biorefin 11:1077–1094
33. FAO (2019) http://www.fao.org/faostat/en. Accessed on 10 May 2019
34. Romero-García JM, Niño L, Martínez-Patiño C, Álvarez C, Castr E, Negro MJ (2014) Biorefinery based on olive biomass. State of the art and future trends. Bioresour Technol 159:421–432
35. Hodaifa G, García CA, Rodriguez-Perez S (2018) Revalorization of agro-food residues as bioadsorbents for wastewater treatment (Chapter 9). In: Singh JK, Verma N (eds) Aqueous phase adsorption. Theory, simulation, and experiments. CRC Press Taylor & Francis Group, New York
36. Papadakis GZ, Megaritis AG, Pandis SN (2015) Effects of olive tree branches burning emissions on PM2.5 concentrations. Atmos Environ 112:148–158
37. Van Soest PJ, Robertson JB, Lewis BA (1991) Methods for dietary fiber, neutral detergent fiber and non-starch polysaccharides in relation to animal nutrition. J Dairy Sci 74:3583–3597
38. Channiwala SA, Parikh PP (2002) A unified correlation for estimating HHV of solid, liquid and gaseous fuels. Fuel 81(8):1051–1063

39. Xie Q, Kong S, Liu Y, Zeng H (2012) Syngas production by two-stage method of biomass catalytic pyrolysis and gasification. Bioresour Technol 110:603–609
40. Okutucu C, Duman G, Ucar S, Yasa I, Yanik J (2011) Production of fungicidal oil and activated carbon from pistachio shell. J Anal Appl Pyrol 91(1):140–146
41. Di Blasi C (2008) Modeling chemical and physical processes of wood and biomass pyrolysis. Prog Energy Combust Sci 34(1):47–90
42. Balagurumurthy B, Srivastava V, Kumar J, Biswas B, Singh R, Gupta P, Kumar KLNS, Singh R, Bhaskar T (2015) Value addition to rice straw through pyrolysis in hydrogen and nitrogen environments. Bioresour Technol 188:273–279
43. Park HJ, Park YK, Kim JS (2008) Influence of reaction conditions and the char separation system on the production of bio-oil from radiata pine sawdust by fast pyrolysis. Fuel Process Technol 89(8):797–802
44. Mohamed AR, Hamzah Z, Daud MZM, Zakaria Z (2013) The effects of holding time and the sweeping nitrogen gas flowrates on the pyrolysis of EFB using a fixed bed reactor. Procedia Eng 53:185–191
45. Açıkalın K, Karaca F (2017) Fixed-bed pyrolysis of walnut shell: parameter effects on yields and characterization of products. J Anal Appl Pyrol 125:234–242
46. Duman G, Okutucu C, Ucar S, Stahl R, Yanik J (2011) The slow and fast pyrolysis of cherry seed. Bioresour Technol 102(2):1869–1878
47. Di Blasi C, Signorelli G, Di Russo C, Rea G (1999) Product distribution from pyrolysis of wood and agricultural residues. Ind Eng Chem Res 38(6):2216–2224
48. Hammes K, Smernik RJ, Skjemstad JO, Herzog A, Vogt UF, Schmidt MWI (2006) Synthesis and characterisation of laboratory-charred grass straw (*Oryza sativa*) and chestnut wood (*Castanea sativa*) as reference materials for black carbon quantification. Org Geochem 37(11):1629–1633
49. Xin Y, Cao H, Yuan Q, Wang D (2017) Two-step gasification of cattle manure for hydrogen-rich gas production: effect of biochar preparation temperature and gasification temperature. Waste Manage 68:618–625
50. Ahmad M, Lee SS, Dou X, Mohan D, Sung JK, Yang JE, Ok YS (2012) Effects of pyrolysis temperature on soybean stover- and peanut shell-derived biochar properties and TCE adsorption in water. Bioresour Technol 118:536–544
51. Smith AM, Singh S, Ross AB (2016) Fate of inorganic material during hydrothermal carbonisation of biomass: influence of feedstock on combustion behaviour of hydrochar. Fuel 169:135–145
52. Rios MLV, González AM, Eduardo E, Lora S, Agustin O (2018) Biomass and bioenergy reduction of tar generated during biomass gasification: a review. Biomass Bioenergy 108:345–370
53. Gai C, Guo Y, Liu T, Peng N, Liu Z (2016) Hydrogen-rich gas production by steam gasification of hydrochar derived from sewage sludge. Int J Hydrogen Energy 41(5):3363–3372
54. Ning S, Jia S, Ying H, Sun Y, Xu W, Yin H (2018) Hydrogen-rich syngas produced by catalytic steam gasification of corncob char. Biomass Bioenergy 117:131–136
55. Zhang Y, Gong X, Zhang B, Liu W, Xu M (2014) Potassium catalytic hydrogen production in sorption enhanced gasification of biomass with steam. Int J Hydrogen Energy 39(9):4234–4243
56. Yang H, Wang D, Li B, Zeng Z, Qu L, Zhang W, Chen H (2018) Effects of potassium salts loading on calcium oxide on the hydrogen production from pyrolysis-gasification of biomass. Bioresour Technol 249:744–750
57. Vamvuka D, Tsamourgeli V, Galetakis M (2014) Study on catalytic combustion of biomass mixtures with poor coals. Combust Sci Technol 186:68–82
58. Park SW, Jang CH (2012) Effects of pyrolysis temperature on changes in fuel characteristics of biomass char. Energy 39:187–195
59. Sahu SG, Sarkar P, Chakraborty N, Adak AK (2010) Thermogravimetric assessment of combustion characteristics of blends of a coal with different biomass chars. Fuel Process Technol 91:369–378

Removal of Polyphenolic Compounds from Olive Mill Wastewater with Sunlight Irradiation Using Nano-Zno–Sio₂ Composite

Çağlar Ulusoy and Delia Teresa Sponza

Abstract Olive mill wastewater (OMW) includes high concentrations of polyphenolic organics. Phenolic compounds in OMW cannot be removed with conventional removal processes. In this study, the polyphenols were removed with nano-ZnO–SiO$_2$ under sunlight. The effects of nano-composite levels, irradiation times, and pH on the phenol removals were investigated. The aim of this study is to photodegrade the total phenol and three polyphenols (gallic acid, para-coumaric acid, t-paracoumaric acid) in the OMW using nano-ZnO–SiO$_2$. The behaviors of elevated nano-ZnO–SiO$_2$ doses (0.5, 1, 3, 5 and 10 g/L), the photodegradation intervals (8, 16, 24 and 36 h) and elevated pHs (4, 7 and 10) during sunlight were researched on the removals of polyphenols in the OMW. The best phenol yield was 73% using 3 g/L nano-ZnO–SiO$_2$ under 24 h sunlight at pH 4. The maximum yields for gallic acid, para-coumaric acid, and t-para-coumaric acid were 90%, 5%, and 5%, respectively.

Keywords ZnO–SiO$_2$ · Photocatalytic degradation · Olive mill wastewater · Polyphenols · Phenolic compounds

1 Introduction

The discharge of OMW is dangerous for aquatic and terrestial ecosystems [1], due to their acidic and toxic properties. The OMW toxicity is 200–500 times higher than the other industrial wastes [2] since the elevated doses of polyphenols. The polyphenols can decrease the growth of greens because they are toxic to the microbial activities in plants [3]. OMW proses produce both solid and liquid wastes via olives extracting processes between September and May. Recently, different treatment processes were studied to minimize the pollutants in the OMW [4], i.e., advanced membrane processes, extraction, solid phase, sonication and microwave processes [1]. However,

Ç. Ulusoy (✉) · D. T. Sponza
Environmental Engineering Department, Engineering Faculty, Dokuz Eylul University, Izmir, Turkey
e-mail: ulusoycaglar@gmail.com

D. T. Sponza
e-mail: delya.sponza@deu.edu.tr

these treatment applications were not cost-benefits and were complicated. Therefore, more simple, not expensive and environmentally friendly treatment processes should be used. Adsorption is one of the most effective processes utilized to treat the organics from the wastewaters [5]. Naturally produced sorbents are extensively used in the sorption of some unwanted chemicals [6]. However, elevated doses of total polyphenols in the OMW limit the effective utilization of natural adsorbents [3].

High adsorption efficiencies for gallic acid (63 and 69%) were obtained. Annab et al. [7] used granulated and powdered carbons at pH = 4.5 after 24-h retention time. Mostafa et al. [8] used a high-power sonicator and an electro-Fenton stage to remove the biological oxygen demand (BOD) and chemical oxygen demand (COD) from the OMW at 40 kHz frequency and at 1500 W power. 79% COD and 73% BOD yields were detected. Under these conditions, 86% polyphenol removals were measured. Photocatalysis of nano-metal oxides cause to the "zero waste discharge" in the olive mill, dye, and textile industries due to a low-cost, green treatment technology [9–11].

Zinc oxide (ZnO) is suitable for use in the photocatalysis and has a big direct band gap of about 3.3 eV. Its surface-to-volume ratio is high and exhibits good chemical and thermal stability in the photocatalytic removals of pollutants in wastewaters. It has high activity, has low cost, and is environmental friendly [12]. Therefore, photooxidation with zinc oxide (ZnO) was an effective wastewater purification method by decomposing and mineralizing the organics degraded with difficulty. Zinc oxide is an active semiconducting material oxide and is capable to activate itself by electron transferring process under sunlight and UV. Under these conditions, nano-ZnO must be adsorbed O_2 at optimum amount and reductive organic pollutants. Silicium dioxide (SiO_2) has an elevated activity, a good chemical resistance and high surface areas, therefore, can be available commercially due to aforementioned properties. High surface area provides high adsorption layers and results with the removals of pollutants, greatly. By the synthesis of core and shell-shaped materials, a new nano-composite material was obtained with electron transferring between core and shell substances. SiO_2 is a commonly studied nano-metal oxide since its easy preparation, has good stability and can be combined with other half conductive metal oxides. Therefore, a core/shell-structured nano-composite can be fabricated with ZnO and SiO_2. In the novel produced nano-composite (nano-ZnO–SiO_2) causes a strong interaction between ZnO and SiO_2. SiO_2 can be produced under laboratory conditions easily since it is unexpansive. It has a big surface area (1200 m^2/g) and can be absorbed into the organic pollutants of the wastes. Nowadays, the production of core/shell-shaped nanomaterials is extensively increased [13]. The shell can change the charge and the functionality of nano-composites, and the activity of the surfaces. This elevated the stability and dispersity of the core structure of the nano-composite. Additionally, by doping of photocatalytic and photomagnetic properties of the nano-composites to the core material, the shell structure can be more activated. By the synthesis of core and shell-structured material, new nano-composite materials developed having high photocatalytic activity and additional behaviors [14]. Nano-ZnO–SiO_2 composite was used in the removal of methylene blue via photocatalysis [15, 16] and Rhodamine B [14]. Areerob et al. [17] found 65 and 67% photooxidation yields for methyl orange and rhodamine B dyes with 1 g/L ZnO–SiO_2. Nezamzadeh-Ejhieh and Bahrami [18]

detected 56% photocatalytic treatment yield with 5 g/L ZnO–TiO$_2$. Shah et al. [19]; 67% solvent and 56% red dye and 69% toluene photo-oxidation yields. Rabahi et al. [20] found 67% toluene removal from a petrochemical industry wastewater using 4 g/L ZnO–SiO$_2$.

In this work, SiO$_2$ was doped to ZnO to treat some pollutants present in the OMW. It is assumed that SiO$_2$ will elevate the activity of the superficial domain and will increase the resistance and the dissolubility of the ZnO [12]. More pollutant amount can be removed by using nano-ZnO–SiO$_2$ composite. The goal of this study is the treatment of total phenol and polyphenols (gallic acid, *p*-coumaric acid, and *trans-p*-coumaric acid) from the OMW by nano-ZnO–SiO$_2$ composite under sunlight irradiation.

1.1 Theoretical Backgrounds for Polyphenols

Polyphenols are a diverse group which is naturally occurred organics containing different phenolic compounds with carbonaceous, benzoic, and –OH groups [21]. The natural polyphenols have numerous biological activities. One of them is the antioxidant properties of the polyphenols. The authorities mentioned that some polyphenols improve the human health [22]. Gallic acid (GA) is a natural polyphenolic antioxidant [23] and is widely used in pharmaceuticals and in dermatologic face creams. By releasing hydrogen groups from the carbonaceous ring of GA and by conjugation of GA to chitosan, the carcinogenic activity of chitosan can be increased. Phenolic mixtures of olives have been used extensively due to their anti-carcinogenic and anti-bacterial properties. The olive and olive oils were examined for their phenolic properties since it was used in the Mediterranean diet and has positive effects on the health [24, 25]. The importance of olive oil is related to its highly elevated long-chain non-saturated fatty acids like oleic acid, some aliphatic and tri-terpenic acids, volatile compounds, and several anti-carcinogenic compounds at minor levels. The main anti-carcinogenic volatile polyphenol organics contained carotenes and polyphenolic chemicals. These substances exhibited lipophilic and hydrophilic structures and were used extensively. Tocophenols are not dissolved in water; they can be dissolved in oil. On the other hand, some phenolic alcohols and acids, like hydroxy-isochromans, flavonoids, secoiridoids, and lignins can be dissolved in water. Some polyphenol structures containing benzoic acid with C7–C2 carbon bounds and cinnamic acid with C7–C4 carbon bounds are found extensively in olive fruits. Some polyphenols such as caffeic, vanillic, syringic, *p*-coumaric, *o*-coumaric, protocatechuic, sinapic, and *p*-hydroxybenzoic acid are found in the olive mills. Hydroxytyrosol (3,4-dihydroxyphenyl-ethanol) and tyrosol (*p*-hydroxyphenyl-ethanol) are the main polyphenol alcohols measured in the olives. The secoiridoids (oleuropein aglycon, demethyloleuropein, ligstroside aglycon) and the lignans (1-acetoxypinoresinol, pinoresinol) were extracted and identified in the olive mills. Luteolin and apigenin are the favorite polyphenols present in olive oils [26].

Polyphenolic organics are present in some nutritional compounds and have sensory properties. The polyphenols produced from the degradation of oleuropein increase the brightness of the olive oil. Polyphenols, namely hydroxytyrosol, tyrosol, caffeic acid, coumaric acids, and *p*-hydroxybenzoic acid affect significantly the anticarcinogenetic properties of olive oils [27]. Some polyphenolic organics are very important to human health due to their anti-inflammatory, antiallergic, anti-microbial, and anti-carcinogenic properties [28]. These polyphenols decrease the lipid oxidative process and decrease the density of lipid protein via some antioxidant processes [29]. The levels and the abundance of polyphenolic organics in olive mill severely affected with some agronomical properties like growth of olives [30], point of growth [31], climatic index, level of growth [32], crop months [33], irrigation [34] and growth properties [35].

P-coumaric acid can be exhibited *trans-cis* isomerization via photochemical variation by absorption of the light. The molecular properties of *p*-coumaric acid are to have a ligand in inner structure. The other side of *p*-coumaric acid exhibited crystallographic properties since 2PYP PyMOL binding to the ligand site based on polyphenol [36]. This could be due to the *trans-cis* isomerization of the vinyl double bonds in the *p*-coumaric acid [37–39]. The crystal structure of *p*-coumaric acid bounds to the hydroxyl radicals bond to the C4 carbon of the phenyl ring during the deprotonation process of a phonolite organic group [38, 40]. This could be due to short hydrogen bonding to the proteomic crystal structure of polyphenol. Figure 1 exhibited the properties of *p*-coumaric acid, gallic acid, and *trans-p*-coumaric acid while Table 1 showed the chemical structures of these phenolic compounds.

Gallic acid (3,4,5-trihydroxybenzoic acid) has a benzoic ring with trihydroxyl bonds, and it is found in tea leaves, oak bark, and in olives. It can be found free and it can be combined to the hydrolyzable tannins. The gallic acids are bonded to ellagic acid and formed dimers. The tannins which can be hydrolyzed via hydrolysis produce gallic acid and ellagic acid. These organics are known as gallotannins and ellagitannins, respectively. Gallic acid produces intermolecular esters (depsides) such as digallic and trigallic acids, (depsidones). Gallic acid is extensively used in hospitals to determine the phenolic ingredients of various organics by the Folin-Ciocalteau method, and the data was reported as gallic acid.

The *trans-p*-coumaric acid is a severe organic which kill the bacteria in the treatments containing the microorganisms in some industrial wastewaters. *P*-coumaric acid is a hydroxycinnamic acid, producing from the hydroxylation of cinnamic acid. The isomers were *o*-coumaric acid, m-coumaric acid, and *p*-coumaric acid. The
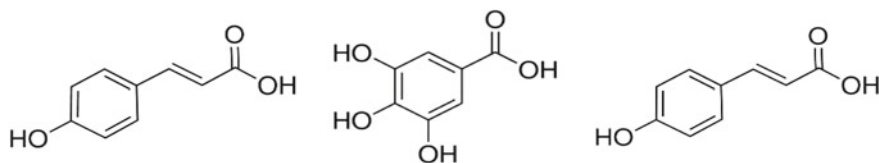
Fig. 1 Structures of *p*-coumaric acid, gallic acid, and *trans-p*-coumaric acid, respectively

Table 1 Chemical properties of polyphenols

Properties	Chemical formula	Molecular weight	Other name	Compound type
Gallic acid	$C_7H_6O_5$	170.12 g/mol	3,4,5-trihydroxybenzoic Acid	Organic
p-coumaric acid	$C_9H_8O_3$	164.16 g/mol	*p*-coumaric acid 4-hydroxycinnamic acid *p*-hydroxycinnamic acid 501-98-4 4-coumaric acid	Organic
Trans-p-coumaric acid	$C_9H_8O_3$	164.16 g/mol	ortho-coumaric acid 2-hydroxycinnamic acid	Organic

structures of these varied by the bonding of the phenyl moieties to the hydroxyl group. *P*-coumaric acid is the most measured polyphenol in the aquatic environment and in the pedosphere. *P*-coumaric acid derivatives were *trans-p*-coumaric acid and *cis-p*-coumaric acid.

OMWs were extremely toxic to gram-negative and gram-positive bacteria, namely *Pseudomonas syringae* and *Corynebacterium michiganense* via phytopathogenic properties of the polyphenolic compounds. These phenolic organics exhibited bactericidal properties to the aforementioned bacteria and to the other heterotrophic bacteria present in the biological treatment processes treating the OMW [41]. Among these, methyl catechol is severely toxic to *Pseudomonas savastanoi* and has bactericidal activity, while was slightly toxic to Coryne. *Michiganense*. Polyphenols namely catechol and hydroxytyrosol also were slightly toxic to *P. savastanoi*, however, is o toxic o Coryne. *Michiganense*. Tyrosol and its derivatives, namely 1,2- and 1,3-tyrosol were not toxic to the aforementioned bacteria. Acetylcatechol and guaiacol were partially toxic for *P. Savastanoi*. Another polyphenol amely *o*-quinone was extremely bactericidal to all bacteria. The carboxylic polyphenols also were not toxic to the bacteria. Catechol and 4-methylcatechol and some carboxylic polyphenols were found to be toxic to some cells in humans. As a result, it was found that the polyphenolic compounds have extremely killing effect on the biological treatment processes to the OMW. On the other hand, some polyphenols were extensively used in pharmaceutical, cosmetic and in hospitals [42]. Besides toxic properties of polyphenols their anti-inflammatory, antimicrobic, and antioxidant activities cause to their extensive utilization in the words.

2 Materials and Methods

2.1 Wastewater Origin

The OMW used in this study is raw, and it was getting from an olive mill industry in Aydin, and it was used without any pre-treatment, in November 2013.

2.2 Synthesis of Nano-ZnO–SiO$_2$ Composite

Nano-ZnO and nano-SiO$_2$ were bought from Ege Nanotek chemical industry. The nano-ZnO–SiO$_2$ composites were produced under laboratory conditions. 1.6 mg of ZnO and 2.8 mg SiO$_2$ were mixed at 120 °C in an thermoreactor during for 2 h. The precursor of the reaction was 0.01 μ four silica particles containing 0.7 mg ZnO, 100 ml ZnO colloid. These components were stirred with 1.2 mg of tetraethoxysilane (TEOS, Sinerji, Turkey). An ultrasonic spray nebulizer with a 1.45 MHz resonator (MERCK) was used, and the nano-composite was performed under nitrogen gas in a tubing reactor. The initial temperatures were 180, 340, and 405 °C. The prepared droplets were collected in a precipitator at 150 °C to decrease the condensation of liquid sample. The ratio of nano-ZnO to nano-SiO$_2$ was 1:1.

2.3 Photocatalytic Experiments

Photocatalytic removal experiences were performed under sunlight in 1 L quartz glass reactors. The studies were performed at increasing times, and the reactors were put to a high wall (5 m of height) with an angle of 90 degrees to the sunlight. The tests were performed with increasing nano-ZnO–SiO$_2$ composite levels (0.5, 1, 3, 5, and 10 g/L).

2.4 Phenol Measurements

The total phenol was measured by MERCK Spectroquant N 1.14551.0001 kits (Merck Germany) in a NOVA-60 spectrophotometer.

2.5 Polyphenol Measurements

The phenolic organic concentrations were investigated by HPLC (Aglent 110). The HPLC consists of a Degasser, a HPLC Pump, a HPLC Auto-Sampler, a HPLC Column Oven and a HPLC Diode-Array-Detector (DAD). External standards were utilized for the calibration curves and graphs. The peak areas obtained from the HPLC chromatograms, were fitted versus to the certain increasing standard doses. About 20 mg phenolic standard was weighed and stirred into a 40 mL flask in a ratio of 1.3:1.3 with MeOH/water to obtain different dilutions. For linear plot, the main solution was mixing with water (4) and MeOH (1) to obtain the level sequences. From the linear drawings and from the equations obtained from the linear regression; the polyphenol equivalents were calculated for 50, 20, 10, 5, and 1 mg/L samples.

2.5.1 Gallic Acid, *P*-coumaric Acid, and *Trans*-*P*-coumaric Acid

Gallic acid was taken from Dr. Ehrenstorfer GmbH (Augsburg, Germany). *P*-coumaric acid and *trans-p*-coumaric acid were taken from Fluka (Buchs, Switzerland). Trifluoroacetic acid (TFA) was bought from Merck (Hohenbrunn, Germany). All chemicals were at a purity of 99.9%. Methanol was taken from Fisher (Fairlawn, NJ). Deionized water with a salinity of 10^{-18} Ω was taken by using an deionized water apparatus (Agilent, Turkey).

The flow rate of the mobile phase was kept at 0,8 mL/min. Mobile phase x was contained 0.06% TFA, and phase y contained methanol with a TFA ratio of 0.06%. The gradient conditions were: 0–6 min, 29% B; 7–13 min, 30–36% B; 14–19 min, 37–56% B; 20–29 min, 57% B; 30–38 min, 58–66% B; 39–41 min, 80% B; 42–44 min, 81–94% B. The column temperature was adjusted to 28 °C. The injection volume was 12 μL. The optimized wavelengths of DAD were set to a wavelength of 258 nm. Calibration graphs of gallic acid, *p*-coumaric acid, and *trans-p*-coumaric acid were summarized in Figs. 2, 3, and 4, respectively.

3 Results and Discussion

3.1 Properties of Raw OMW

The mean total phenol level of the raw olive mill was measured around 659 mg/L, while the mean pH value varied between 3.7 and 4.8. The samples were kept in a refrigerator and mixed before the analysis. Gallic acid, *p*-coumaric acid, and *trans-p*-coumaric acid concentrations were detected as 65.51821, 43.85360, and 43.85381 mg/L, respectively, in the raw OMW (Table 2).

The concentrations of polyphenols present in the OMW in this research are at low level than the mentioned by Casa et al. [43]. This can be attributed to the centrifuging

Calibration graph of gallic acid (R=0,997431)

Fig. 2 Calibration graph of gallic acid
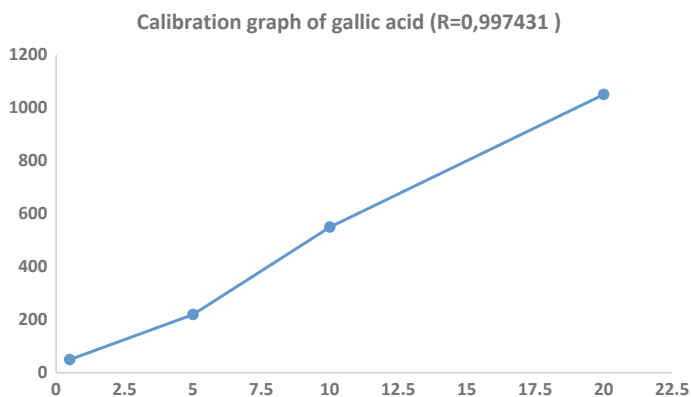
Calibration graph of p-coumaric acid (R=0,994153)
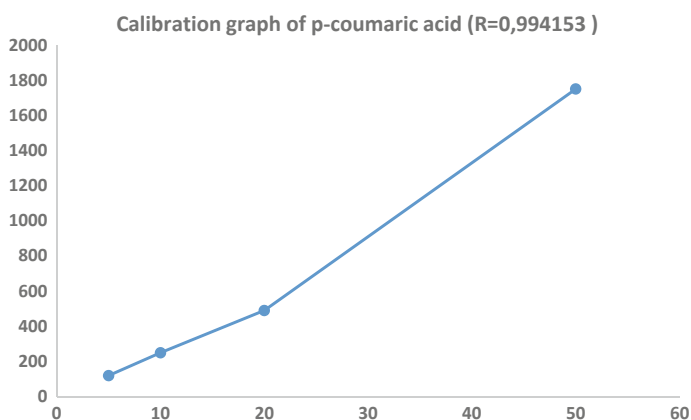
Fig. 3 Calibration graph of *p*-coumaric acid

and filtration of the samples before analytical analysis. In this study, polyphenols were in the acidified OMW and they were not treated before analysis.

3.2 Effects of Increasing Nano-ZnO–SiO$_2$ Composite on the Removal of Total Phenol via Sunlight

The total phenol removals were obtained as 50, 66, 73, 72, and 70% at 0.5, 1, 3, 5, and 10 g/L nano-ZnO–SiO$_2$ composite, respectively, after 24 h irradiation time at a sunlight intensity of 80 W at 34 °C ± 3 °C and at original pH of OMW (Fig. 5). The

Calibration graph of trans p-coumaric acid (R=0,993878)
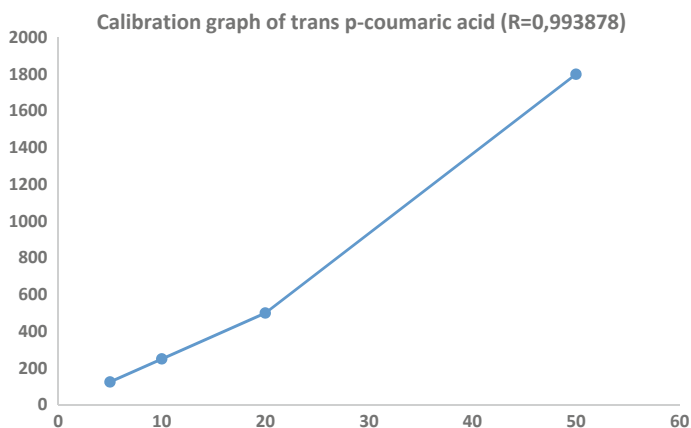
Fig. 4 Calibration graph of *trans-p*-coumaric acid

Table 2 Initial values of polyphenols in OMW

Polyphenol name	Amount (mg/L)
Gallic acid	65.51821
p-coumaric acid	43.85360
Trans-p-coumaric acid	43.85381
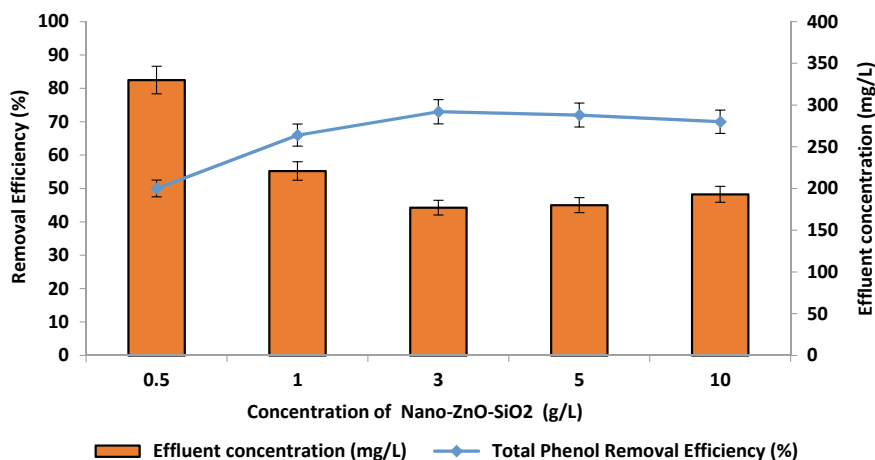
Fig. 5 Effect of concentration of nano-ZnO–SiO$_2$ composite on the total phenol yield (outdoor temperature: 35 °C ± 5 °C, original pH of OMW (4.01), sunlight irradiation time: 24 h, sunlight power: 80 W, influent total phenol concentration: 660 mg/L)

maximum total phenol yield was obtained as 73% at 3 g/L nano-ZnO–SiO$_2$ composite. At high nano-ZnO–SiO$_2$ composite concentrations, the turbidity increased and the light penetration decreased. Turbidity caused to loss of contacting surface area for light-harvesting and as a result, the catalytic activity decreased slightly.

The photocatalytic removal of polyphenol in the OMW using nano-ZnO–SiO$_2$ under sunlight can be summarized with Eqs. (1), (2), (3), (4), and (5) given below;

$$ZnO/SiO_2 + hv \rightarrow e^-_{cb} + h^+_{vb} \tag{1}$$

$$O_2 + e^-_{cb} \rightarrow O_2^{\bullet-} \tag{2}$$

$$O_2^{\bullet-} + H_2O \rightarrow O^\bullet + OH^- + O_2 + HO_2^- \tag{3}$$

$$H_2O + h^+_{vb} \rightarrow HO^\bullet + H^+ \tag{4}$$
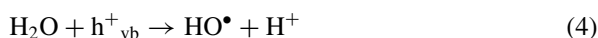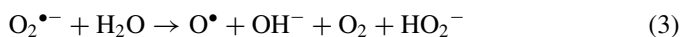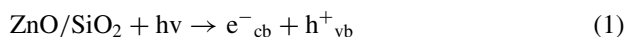
The elevated $HO^\bullet$ and $O_2^{\bullet-}$ concentrations absorbed in the surface of nano-ZnO–SiO$_2$ composite. The polyphenols are broken down through oxidative photodegradation as indicated in (5):

$$Polyphenol + O_2^{\bullet-} + HO^\bullet \rightarrow CO_2 + H_2O + sub\ composite \tag{5}$$
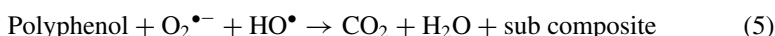
3.3 Effects of Irradiation Time on the Treatment of Total Phenol OMW Under Sunlight

The effects of 8, 16, 24, and 36 h sunlight irradiation times were investigated to obtain the maximum removal efficiency of total phenol with 3 g/L nano-ZnO–SiO$_2$ composite at original pH of OMW (4.01) at outdoor temperature (34 °C $\pm$ 3 °C) and at 80 W sunlight irradiation. 50, 62, 73, and 68% total phenol removal efficiencies were obtained as the sunlight intensity duration was elevated from 8 h to 16, 24, and 36 h, respectively (Fig. 6). The maximum phenol yield was obtained after 24 h sunlight irradiation. Lowering the removal efficiencies with increasing the irradiation time can be associated with metabolite phenolic molecules such as para-coumaric acid and gallic acid formed during photooxidation under long irradiation times. These polyphenolic compounds were shown in further section.
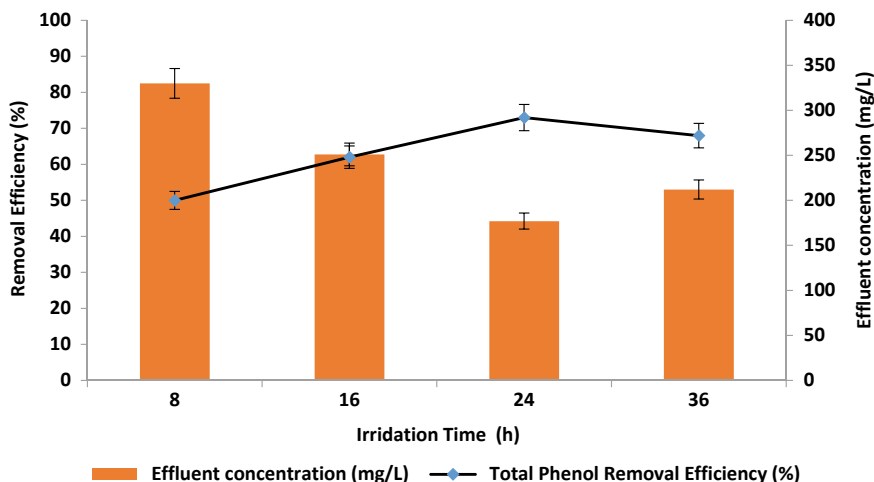
Fig. 6 Effect of irradiation time under sunlight on the total phenol yield (outdoor temperature: 35 °C ± 5 °C, original pH of OMW (4.01), concentration of nano-ZnO–SiO$_2$ composite: 3 g/L, sunlight energy power: 80 W, influent total phenol concentration: 660 mg/L)

3.4   Effect of pH on the Treatment of OMW Under Sunlight

The studies were performed in original pH of OMW (4.01) in pH 7 and in pH 10 to determine the optimum pH for maximum removal of total phenol from OMW. All experiments were performed with 3 g/L nano-ZnO–SiO$_2$ composite, under 80 W power and 24 h irradiation time at 34.9 °C ± 2 °C outdoor temperature. The obtained phenol removal efficiencies were 75, 73, and 70% for original pH of OMW, for pH 7 and for pH 10, respectively, as shown in Fig. 7. The maximum phenol yield (75%) was obtained at original pH of OMW among the pH values studied. At higher pH, the phenol exhibited negatively charged phenolate species [44]. Low photodegradation removals at higher pH are attributed to the inhibition of penetration of UV to the nano-ZnO–SiO$_2$ composite due to low concentration of OH$^-$ radicals in the OMW [45].

3.5   Measurement of the Concentration of Polyphenolic Compounds by HPLC in Raw and Treated OMW with Nano-ZnO–SiO$_2$ Composite Under Sunlight Irradiation

The raw OMW was treated with 1 g/L nano-ZnO–SiO$_2$ composite under 24 h sunlight with an intensity of 80 W at a original pH of OMW (pH 4.01) and at a
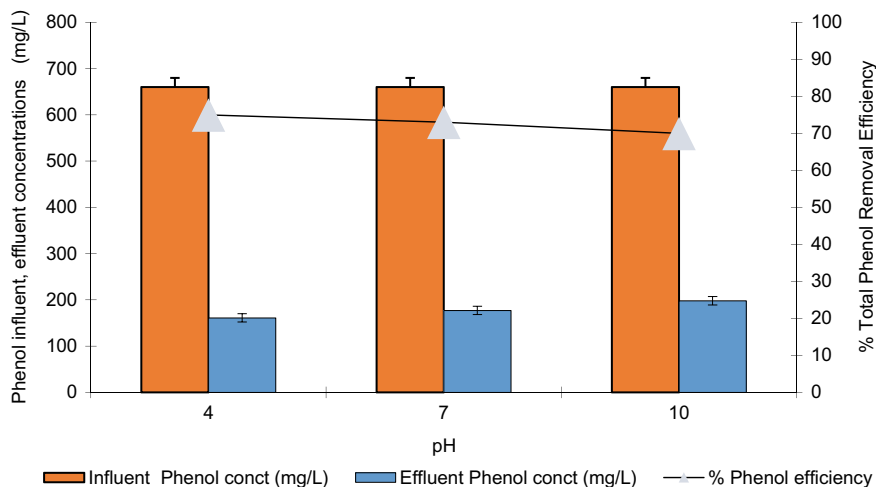
Fig. 7 Effect of pH of OMW on total phenol yields under sunlight (T: room temperature, irradiation time: 15 min, concentration of nano-ZnO–SiO$_2$ composite: 1 g/L, sunlight energy power: 80 W, influent total phenol concentration: 660 mg/L)

room temperature. During this period, the gallic acid, *p*-coumaric acid, and *trans-p*-coumaric acid polyphenol concentrations were measured with HPLC. These polyphenols can be seen from Fig. 8 for raw OMW. The gallic acid amount was measured as 65.51821 mg/L in the raw OMW, however, after treatment with sunlight, the whole of the gallic acid was treated in the OMW. The yield of this polyphenol was recorded as %100 after photo-oxidation. *P*-coumaric acid and *trans-p*-coumaric acid levels were calculated as 43.85360 and 43.85381 mg/L, respectively, in the raw OMW. After treatment under sunlight via photocatalysis, *p*-coumaric acid and *trans-p*-coumaric acid levels were detected as 39.16515 and 39.16585 mg/L, respectively. The removal efficiencies of *p*-coumaric acid and *trans-p*-coumaric acid were % 10 and % 10, respectively. The concentrations of three polyphenol can be seen in Fig. 9 after photocatalytic treatment under sunlight.

Gallic acid was removed completely; on the other hand, coumaric acid and *p*-coumaric acid were removed with low yields under sunlight irradiation. The low yields for the last two polyphenols can be attributed to the ineffective treatment of these polyphenols due to low OH radical formation via nano-ZnO–SiO$_2$ composite photocatalysis (data not shown). This nano-composite was not breakdown to the phenol bounds between benzene and –OH and =O. Sunlight photocatalysis is a cheap treatment method to obtain higher removal yields for phenolic and polyphenolic compounds. The warm regions of the world can be used in this cheap treatment method for the treatment of strict wastewater types. Treatment with sunlight will decrease the cost of treatment methods. Additionally, it supplies high removal yields for pollutants. A summary of initial and effluent concentrations of polyphenols is summarized in Table 3.
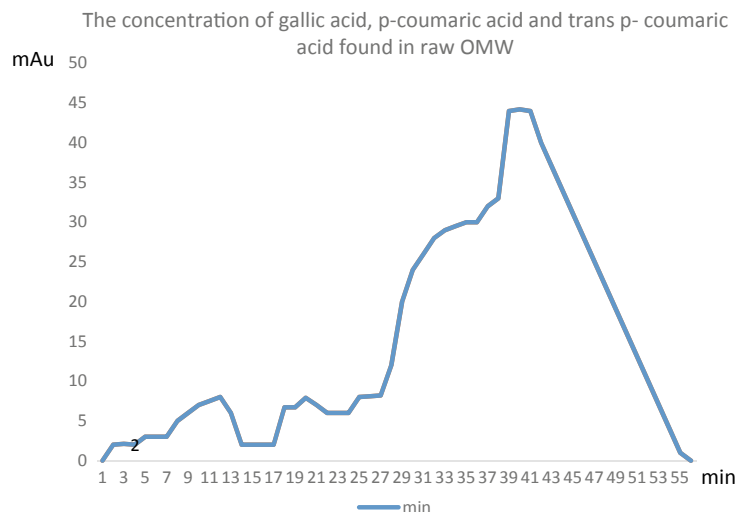
```
RetTime   Type       Area      Amt/Area       Amount    Grp      Name
[min]                [mAU*s]                  [nq/ul]
-------|------|----------|----------|----------|--|------------------
  9.295 BV      207.19920 3.16209e-1   65.51821         qallic
 31.097 VV     2943.03613 1.49008e-2   43.85360         PARA
 31.0995VV     2943.03619 1.49009e-2   43.85381         PARA T


Totals :                                153.22562
```

Fig. 8 Concentration of gallic acid, *p*-coumaric acid, and *trans*-*p*-coumaric acid found in raw OMW

4 Conclusions

Phenol and polyphenol treatments in OMW were carried out under sunlight intensity via nano-ZnO–SiO$_2$ composite in this study. The photocatalytic removal of phenol and polyphenols in the OMW was studied under optimum operational conditions to obtain the maximum treatment conditions. The effects of concentration of nano-ZnO–SiO$_2$ composite, irradiation time and pH of OMW were investigated on the removal efficiencies of pollutant parameters under constant sunlight irradiation. The OMW was photo-oxidized with 3 g/L nano-ZnO–SiO$_2$ composite in which maximum yields of total phenol (73%) were detected after 24-h sunlight irradiation. For aforementioned maximum yields, the pH of original OMW should be 4.01. For maximum removal efficiencies of phenols, long irradiation time (24 h) is required for photooxidation with sunlight. Gallic acid was removed with a yield of 100% while the other two polyphenols were removed with 10% removal efficiencies.
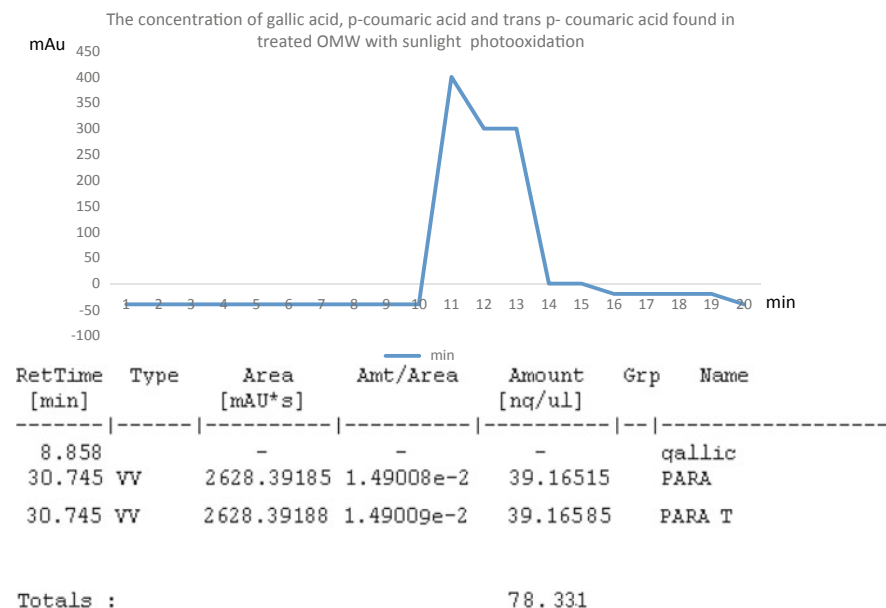
Fig. 9 Concentration of gallic acid, *p*-coumaric acid and *trans-p*-coumaric acid measured in the treated OMW with sunlight photooxidation (nano-ZnO–SiO$_2$ composite concentration: 3 g/L, T: 35 °C ± 5 °C, pH: 4.01, sunlight irradiation time: 24 h, sunlight energy power: 80 W)

Table 3 Removal efficiencies of polyphenols (gallic acid, *p*-coumaric acid, and *trans-p*-coumaric acid) in OMW	Polyphenols	Raw OMW (mg/L)	Treated OMW	Removal efficiency (%)
	Gallic acid	65.51821	0	100
	p-coumaric acid	43.85360	39.16515	10
	Trans-p-coumaric	43.85381	39.16585	10

References

1. Stasinakis AS, Elia I, Petalas AV, Halvadakis CP (2008) Removal of total phenols from olive-mill wastewater using an agricultural by-product, olive pomace. J Hazard Mater 160:408–413
2. Jahangiri M, Rahimpour A, Nemati S, Alimohammady M (2014) Recovery of poly-phenols from olive mill wastewater by nanofiltration. Cell Chem Technol 50(9–10):961–966
3. Rosello-Soto E, Koubaa M, Moubarik AP, Lopes R, Saraiva A, Boussetta J, Grimi N, Barba JF (2015) Emerging opportunities for the effective valorization of wastes and by-products generated during olive oil production process: nonconventional methods for the recovery of high-added value compounds. Trends Food Sci Technol 45:296–310

4. Bertin L, Ferri F, Scoma A, Marchetti L, Fava F (2011) Recovery of high added value natural polyphenols from actual olive mill wastewater through solid phase extraction. Chem Eng J 171:1287–1293

5. Basta AH, Fierro V, El-Saied H, Celzard A (2009) 2-Steps KOH activation of rice straw: an efficient method for preparing high-performance activated carbons. Bioresour Technol 100:3941–3947

6. Pagnanelly F, Sara M, Luigi T (2008) New biosorbent materials for heavy metal removal: development guided by active site characterization. Water Res 42:2953–2962

7. Annab H, Fiol N, Villaescusa I, Essamri A (2019) A proposal for the sustainable treatment and valorisation of olive mill wastes. J Environ Chem Eng 7:102–803

8. Mostafaa H, Iqdiam BM, Abuagela M, Marshall MR, Pullammanappallil P, Goodrich-Schneiderb R (2018) Treatment of olive mill wastewater using high power ultrasound (HPU) and electro-fenton (EF) method. Chem Eng Process Process Intensif 131:131–136

9. Deeb AA, Fayyad MK, Alawi MA (2012) Separation of polyphenols from Jordanian olive oil mill wastewater. Hindawi Publishing Corporation Chromatography Research International Volume, Article ID 812127, 8 p

10. Mulinnacci N, Romani A, Galardi C, Pinelli P, Giaccherini C, Vincieri FF (2001) Polyphenolic content in olive oil wastewaters and related olive samples. J Agric Food Chem 49:3509–3514

11. Leouıfoudı I, Zyad A, Mouse HA, Amechrouq A, Mbarkı M, Oukerrou MA (2013) Identification and characterisation of phenolic compounds extracted from Moroccan olive mill wastewater. Food Sci Technol Camp 34(2):249–257

12. Sangeeta M, Renuka L, Karthik KV, Ravishankar R, Anantharaju KS (2017) Synthesis of ZnO, MgO and ZnO/MgO by solution combustion method: characterization and photocatalytic studies. Mater Today: Proc 4(11):11791–11798

13. Lee HB, Yoo YM, Han YH (2006) Characteristic optical properties and synthesis of gold–silica core–shell colloids. Scripta Mater 55:1127–1129

14. Zhai J, Tao X, Pu Y, Zeng X, Chen J (2010) Core/shell structured ZnO/SiO$_2$ nanoparticles: preparation, characterization and photocatalytic property. Appl Surf Sci 257:393–397

15. Mohamed RM, Baeissa ES, Mkhalid IA, Al-Rayyani MA (2013) Optimization of preparation conditions of ZnO–SiO$_2$ xerogel by sol–gel technique for photodegradation of methylene blue dye. Appl Nanosci 3:57–63

16. Ali MA, İsmail AA, Najmy R, Al-Hajry A (2014) Preparation and characterization of ZnO–SiO$_2$ thin films as highly efficient photocatalyst. J Photochem Photobiol A 275:37–46

17. Areerob Y, Cho JY, Jang WK, Oh WC (2018) Enhanced sonocatalytic degradation of organic dyes from aqueous solutions by novel synthesis of mesoporous Fe$_3$O$_4$-graphene/ZnO@SiO$_2$ nanocomposites. Ultrason Sonochem 41:267–278

18. Nezamzadeh-Ejhieh A, Bahrami M (2014) Investigation of the photocatalytic activity of supported ZnO–TiO$_2$ on clinoptilolite nano-particles towards photodegradation of wastewater-contained phenol. Desalination Water Treat 55(4):1096–1104

19. Shah N, Claessyns F, Rimmer S, Arain MB, Rehan T, Wazwaz A, Ahmad MW, Ul-Islam M (2016) Effective role of magnetic core-shell nanocomposites in removing organic and inorganic wastes from water. Recent Pat Nanotechnol 10(3):202–212

20. Rabahi A, Assadi AA, Nasrallah N, Bouzaza A, Maachi R, Wolbert D (2018) Photocatalytic treatment of petroleum industry wastewater using recirculating annular reactor: comparison of experimental and modeling toluene removal. Environ Sci Pollut Res 1–12

21. Tuchmantel W, Kozikowski AP, Romanczyk LJ Jr (1999) Studies inpolyphenolchemistryandbioactivity. 1. Preparation of building blocks from (+) catechin. Procyanidin formation. Synthesis of the cancer cell growth inhibitor, 3-O-galloyl-(2R,3R)-epicatechin-4β,8-[3-O-galloyl-(2R,3R) epicatechin]. J Am Chem Soc 121:12073–12081

22. Flight I, Clifton P (2006) Cereal grains and legumes in the prevention of coronary heart disease and stroke: a review of the literature. Eur J Clin Nutr 60(10):1145–1159

23. Lu Z, Nie G, Belton PS, Tang H, Zhao B (2006) Structure-activity relationship analysis of antioxidant ability and neuroprotective effect of gallic acid derivatives. Neurochem Int 48(4):263–274

24. Tuck KL, Hayball PJ, Stupans I (2002) Structural characterisation of the metabolites of hydroxytyrosol, the principal phenolic component in olive oil, in rats. J Agric Food Chem 50:2404–2409
25. Visioli F, Poli A, Galli C (2002) Antioxidant and other biological activities of phenols from olives and olive oil. Med Res Rev 22(1):65–75
26. Bendini A, Cerretani L, Carrasco-Pancorbo A, Gomez-Caravaca AM, Segura Carretero A, Fernandez-Gutierrez A (2007) Phenolic molecules in virgin olive oils: a survey of their sensory properties, health effects, antioxidant activity and analytical methods. An overview of the last decade. Molecules 12:1679–1719
27. Kiritsakis AK (1998) Flavor components of olive oil—a review. J Am Oil Chem Soc 75:673–681
28. Medina E, Brenes M, Romero C, García A, De Castro A (2007) Mainantimicrobials compounds in table olives. J Agric Food Chem 55:9817–9823
29. Servili M, Selvaggini R, Esposto S, Taticchi A, Montedoro G, Morozzi M (2004) Health and sensory properties of virgin olive oil hydrophylic phenols: agronomic and technological aspects of production that affect their occurrence in the oil. J Chromatogr A 1054:113–127
30. Tura D, Gigliotti C, Pedo S, Failla O, Bassi D, Serraiocco A (2007) Influence of cultivar and site of cultivation on levels of lipophilic and hydrophilic antioxidants in virgin olive oils (*Olea europaea* L.) and correlations with oxidative stability. Sci Hortic 112:108–119
31. Vinha A, Ferreres F, Silva B, Valentão P, Gonçalves A, Pereira J, Oliveira M, Sebra R, Andrade P (2005) Phenolic profiles of Portuguese olive fruits (*Olea europaea* L.): Influences of cultivar and geographical origin. Food Chem 89:561–568
32. Kalua CM, Allen MS, Bedgood DR, Bishop AG, Prenzler PD (2005) Discrimination of olive oils and fruits into cultivars and maturity stages based on phenolic and volatile compounds. J Agric Food Chem 53:8054–8062
33. Gomez-Alonso S, Salvador MD, Fregapane G (2002) Phenolic compounds profile of Cornicabra virgin olive oil. J Agric Food Chem 50:6812–6817
34. Tovar MJ, Motilva MJ, Romero MP (2001) Changes in the phenolic composition of virgin olive oil from young trees (*Olea europaea* L. cv. Arbequina) grown under linear irrigation strategies. J Agric Food Chem 49:5502–5508
35. Ranalli A, Contento S, Schiavone C, Simone N (2001) Malaxing temperature affects volatile and phenol composition as well as other analytical features of virgin olive oil. Eur J Lipid Sci Technol 103:228–238
36. Genick UK, Borgstahl GE, Ng K, Ren Z, Pradervand C, Burke PM, Srajer V, Teng TY, Schild-kamp W, McRee DE, Moffat K, Getzoff ED (1997) Structure of a protein photocycle intermediate by millisecond time-resolved crystallography. Science 275(5305):1471–1475
37. Hoff WD, Düx P, Hård K, Devreese B, Nugteren-Roodzant IM, Crielaard W, Boelens R, Kaptein R, Van Beeumen J, Hellingwerf KJ (1994) Thiol ester-linked *p*-coumaric acid as a new photoactive prosthetic group in a protein with rhodopsin-like photochemistry. Biochemistry 33(47):13959–13962
38. Premvardhan LL, Buda F, Van Der Horst MA, Lührs DC, Hellingwerf KJ, Van Grondelle R (2004) Impact of photon absorption on the electronic properties of *p*-coumaric acid derivatives of the photoactive yellow protein chromophore. J Phys Chem B 108(16):5138–5148
39. Hellingwerf KJ (2000) Key issues in the photochemistry and signalling-state formation of photosensor proteins. J Photochem Photobiol B Biol 54(2–3):94–102
40. Yamaguchi S, Kamikubo H, Kurihara K, Kuroki R, Niimura N, Shimizu N, Yamazaki Y, Kataoka M (2009) Low-barrier hydrogen bond in photoactive yellow protein. Proc Natl Acad Sci USA 106(2):440–444
41. Capasso R, Evidente A, Schivo L, Orru G, Marcialis MA, Cristinzio G (1995) Antibacterial polyphenols from olive oil mill waste waters. J Appl Bacteriol 79(4):393–398
42. Garcia-Castello E, Cassano A, Criscuoli A, Conidi C, Drioli E (2010) Recovery and concentration of polyphenols from olive mill wastewaters by integrated membrane system. Watr Res 44(13):3883–3892

43. Casa R, D'Annibale A, Pierucetti F (2003) Reduction of the phenolic components in olive-mill wastewater by enzymatic treatment and its impact on durum wheat (*Titricum durum* Desf.) germinability. Chemosphere 50:959–966
44. Kashıf N, Ouyang F (2009) Parameters effect on heterogeneous photocatalyse degradation of phenol in aqueous dispersion of TiO_2. J Environ Sci 21:527–533
45. Qamar M, Muneer M, Bahneman D (2006) Heterogeneous photocatalysed degradation of two selected pesticide derivatives, triclopyr and daminozid in aqueous suspensions of titanium dioxide. J Environ Manag 80:99–106

Catalytic Treatment of Opium Alkaloid Wastewater via Hydrothermal Gasification

Nihal Ü. Cengiz, Mehmet Sağlam, Mithat Yüksel and Levent Ballice

Abstract The wastewater from an opium processing plant should meet the standards as specified in the 'Water Pollution Control Regulation (WPCR), 2004' before being discharged safely into the receiving medium. Treatment of opium alkaloid wastewater is not sufficient using the existing combined methods of aerobic/anaerobic and chemical treatment. Hydrothermal gasification (HTG) is proposed as an alternative treatment in this study. The other aim of this study is to show the ability to manufacture CH_4 and H_2 as renewable energy sources and to determine to what extent the removal of chemical oxygen demand (COD) is. Studies were carried out in batch autoclave reactor systems without catalyst, with original red mud (RM), activated RM, and nickel-impregnated (10, 20, and 30%) forms. Reduction with $NaBH_4$ was done to the nickel-impregnated forms of RM to increase the catalytic activity. Yields of CH_4 and H_2 increased from 16.8 to 28.6 mol CH_4/kg C in wastewater and from 20.3 to 33.3 mol H_2/kg C in wastewater with 20% impregnated nickel and reduced red mud as the highest at 500 °C. The COD of the wastewater was lowered by 81–85% approximately while the TOC content decreased by 85–90%.

Keywords Biomass · Wastewater · Supercritical · Gasification · Hydrogen

Nomenclature

C_i Concentration of component 'i' in the gas product (vol%)

N. Ü. Cengiz (✉) · M. Sağlam · M. Yüksel · L. Ballice
Department of Chemical Engineering, Ege University, Izmir, Turkey
e-mail: nihal.cengiz@ege.edu.tr

M. Sağlam
e-mail: mehmet.saglam@ege.edu.tr

M. Yüksel
e-mail: mithat.yuksel@ege.edu.tr

L. Ballice
e-mail: levent.ballice@ege.edu.tr

HTG	Hydrothermal gasification
n_i	Number of carbon atoms of component 'i' in the gas product
m	Weight of biomass in feed (g)
M	Molar mass of carbon (g mol^{-1})
P	Pressure (Pa)
R	Universal gas constant 8.3143 J mol^{-1} K^{-1}
T	Temperature (K)
V_{gas}	Volume of gas product under ambient conditions (L)
TOC_{aq}	Total organic carbon content of the aqueous product (g L^{-1})
TOC_{ww}	Total organic carbon content of raw alkaloid wastewater (g L^{-1})
COD_{ww}	Chemical oxygen demand raw alkaloid wastewater (g L^{-1})
TOC_{aq}	Chemical oxygen demand of the aqueous product (g L^{-1})

1 Introduction

The alkaloids factory in Turkey manufactures crude morphine and derivatives such as codeine phosphate, codeine hydrochloride, codeine sulfate, and dionine, which meet the pharmacological standards when processing the traditional poppy product. There are only a few countries that are licensed in opium poppy cultivation worldwide, and Turkey has one of the biggest capacity plants in this field and is located in Afyonkarahisar (Turkey). The factory generates a very complex wastewater and has a high *COD* (chemical oxygen demand) content [1]. Afyon alkaloid wastewater has an initial total organic carbon (*TOC*) of 11,500 mg/L and an initial *COD* of 32,050 mg/L. It is resistant to treatment using conventional methods [2], and advanced or pre-treatment techniques are required to reach discharge limits. The *COD* parameter must be less than 1,500 ppm for safe discharge [3] according to the WPCR and the existing treatment system in the plant does not meet the standards and discharging around Lake Eber would increase the environmental pollution when combined with the other plants' wastes in this region.

The utilization of biomass using various conversion techniques for the purpose of energy, fuel, heat, etc., is researched with interest. Combustion, pyrolysis, tor-refaction, conventional gasification, fermentation, hydrolysis, and HTG are the main technologies that have been studied for years [4–9]. The SCWG studies were started by Amin and Modell's investigations at the Massachusetts Institute in the 1970s. Amin realized that organics degraded to hydrogen and methane in a water medium forming a significant amount of char and tar. Modell performed gasification experiments in supercritical water and observed that the char and tar almost disappeared [10]. In the last four decades, HTG has been applied to various biomass types and model compounds to produce hydrogen and methane as renewable energy sources [4]. Industrial wastewaters have been evaluated as feedstock in recent years in HTG (or SCWG) studies to convert organic carbon content into valuable calorific gases and chemicals, and this method is proposed as a treatment alternative [11–15].

Water above the critical point displays extraordinary properties, increasing diffusivity, and decreasing viscosity which provides a homogeneous reaction medium [16]. The density of water decreases with increasing temperature and pressure from ambient to critical conditions: $d = 1$ g/cm^3 at 25 °C and 0.1 MPa to $d = 0.17$ g/cm^3 at 400 °C and 25 MPa substantially. The ambient water hydrogen bond lattice weakens resulting in lower densities at near-critical temperature. Water at normal conditions has a higher dielectric constant ($\varepsilon = 80$) than the SCW ($\varepsilon = 5$) at critical point [17] due to diminishing intermolecular interactions based on hydrogen bonding and decreasing dipoles of molecules [18]. The higher dielectric constant of ambient water makes it a good solvent for polar substances. SCW with its lower dielectric constant like common non-polar solvents $\varepsilon_{\text{ethanol}} = 28$ and $\varepsilon_{\text{benzene}} = 2.3$ at 25 °C [19] gains the ability to solve non-polar organics.

The discharge region of Eber Lake is contaminated with wastewaters from alkaloid plant and other plants around the region. Researchers are focused on solving the treatment problem of this wastewater by applying conventional and novel methods as pre-treatment or advanced treatment alternatives such as anaerobic/aerobic treatment [1, 2, 20, 21], wet air oxidation [22], Fenton oxidation [23], and membrane technology [24]. The *COD* value in the raw wastewater was lowered by 88%, the highest in the reported studies, and took six days to reach this ratio using a biological treatment but could not meet the discharge standards.

This study provides *COD* removals higher than 90% and with 1 h of operation time only using the HTG technique and did not require any pre-treatment. The opium alkaloid wastewater was evaluated to produce valuable gases such as H_2 and CH_4 as a spontaneous result of treatment using this method for the first time. Red mud was used as catalyst since it is a by-product from alumina production and has no cost and is widely used in liquefaction of coal and biomasses [25].

2 Materials and Methods

2.1 *Feedstock and Catalyst*

Feedstock was supplied from an alkaloid manufacturing factory in Turkey with a *COD* of 32,050 mg/L and a *TOC* of 11,500 mg/L. The wastewater characteristics were determined in our laboratories. The 0.5 g of catalyst/20 ml of wastewater was fed into the autoclave reactors after shaking for homogeneity. The experiments were performed at least four times for reproducible results. The catalysts were prepared using the following procedure: The red mud (includes Fe_2O_3, Al_2O_3, and SiO_2 as major components) was supplied by the alumina plant in Turkey. Original red mud was used for comparison with the activated forms of it and referred to as ORM. The precipitation using the K_2CO_3 solution (25%) at a high temperature was the first step then it was filtered, washed, and calcined. Then $Ni(NO_3)_2 \cdot 6H_2O$ was impregnated into the precipitated red mud to obtain various nickel impregnation ratios (10, 20, and

Table 1 Nomenclature of the activated red mud catalysts and the preparation steps of them

	Catalyst CODe	Precipitation agent	Calcination	Nickel impregnation (%)	Reduction by NaBH$_4$
A Group	ARM	K$_2$CO$_3$	+	–	
	ARM-1	K$_2$CO$_3$	+	10	–
	ARM-2	K$_2$CO$_3$	+	20	–
	ARM-3	K$_2$CO$_3$	+	30	–
	ARM-1R	K$_2$CO$_3$	+	10	+
	ARM-2R	K$_2$CO$_3$	+	20	+
	ARM-3R	K$_2$CO$_3$	+	30	+
B Group	BRM	NH$_3$	+	–	–
	BRM-1	NH$_3$	+	10	–
	BRM-2	NH$_3$	+	20	–
	BRM-3	NH$_3$	+	30	–
	BRM-1R	NH$_3$	+	10	+
	BRM-2R	NH$_3$	+	20	+
	BRM-3R	NH$_3$	+	30	+

30%) and ARM-1, ARM-2, and ARM-3 catalysts were obtained as the first group. The Ni-containing red mud catalysts were reduced using NaBH$_4$ to increase the effectiveness and the ARM-1R, ARM-2R, and ARM-3R catalysts were synthesized. As an alternative, an activation procedure was started by precipitation using NH$_3$ (25%, $d = 0.91$ g/cm^3) at a high temperature, then filtered, washed, and calcined. Three other catalysts were prepared at different nickel impregnation ratios (10, 20, and 30%) similarly and referred to as BRM-1, BRM-2, and BRM-3 as the second group. Reduced catalysts were prepared via reduction using NaBH$_4$ and referred to as BRM-1, BRM-2, and BRM-3. Table 1 shows the preparation procedure details of the catalyst types.

2.2 Experimental Procedure

Stainless steel batch autoclave reactors with an inner volume of 100 cm^3 are heated to the reaction temperature of 500 °C. The wastewater and catalyst are loaded into the reactor at a ratio of 20 mL/0.5 g. Then the autoclaves are closed tightly and the air in the reactor is purged with nitrogen gas.

2.3 The Analysis of the Products

The gaseous product distribution is determined with gas chromatography (Agilent Technologies HP 7890A, USA) with a standard deviation of $\pm 2\%$. H_2, CO_2, and CH_4 are the main products and CO, and C_2–C_4 hydrocarbons (C_2H_6, C_2H_4, C_3H_8, and C_4H_{10}) are the minor products. The total gas volume is measured using a gasometer with $\pm 10\%$ accuracy. The *TOC* values of the raw wastewater and aqueous products are measured with a *TOC* analyzer (Shimadzu *TOC*-VCPH, Japan). The *COD* of the raw wastewater and aqueous products were determined using a thermo-reactor (MERCK, Spectroquant TR320) and a spectrophotometer (MERCK, Spectroquant Nova 60), and *COD* kits.

3 Results and Discussion

The opium alkaloid wastewater was gasified in supercritical water conditions at, 500 °C and a pressure range of 40.5–44.0 MPa in the presence of the original and activated red mud catalysts. The experiments were also carried out without a catalyst and with the original red mud (ORM) to understand the effect of activation. In the absence of a catalyst, the pressure reached 36.5 MPa and with ORM, 40.5 MPa was recorded as the reaction pressure. The effect of A and B group catalysts on the carbon gasification efficiencies, gaseous product distribution, and yields of hydrogen, methane, carbon dioxide, C_2–C_4 hydrocarbons, and carbon monoxide are given in Tables 2, 3 and 4 and Figs. 1, 2, 3 and 4. For accuracy, each run was repeated five
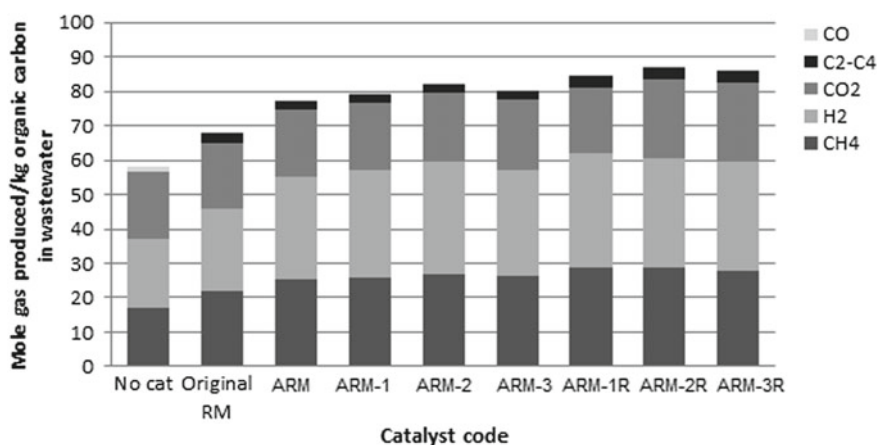
Fig. 1 Effect of catalyst type on gaseous product yields in hydrothermal gasification of alkaloid wastewater in the presence of original red mud and activated red mud derivatives in A group
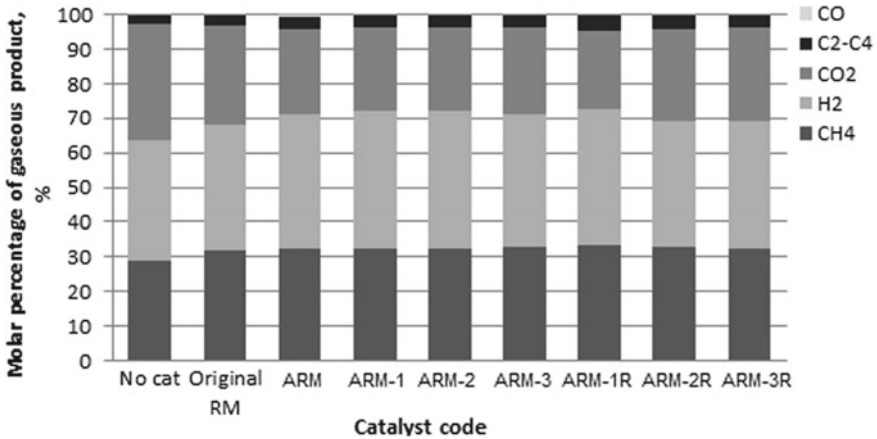
Fig. 2 Effect of catalyst type on gaseous product distribution in hydrothermal gasification of alkaloid wastewater in the presence of A group catalysts
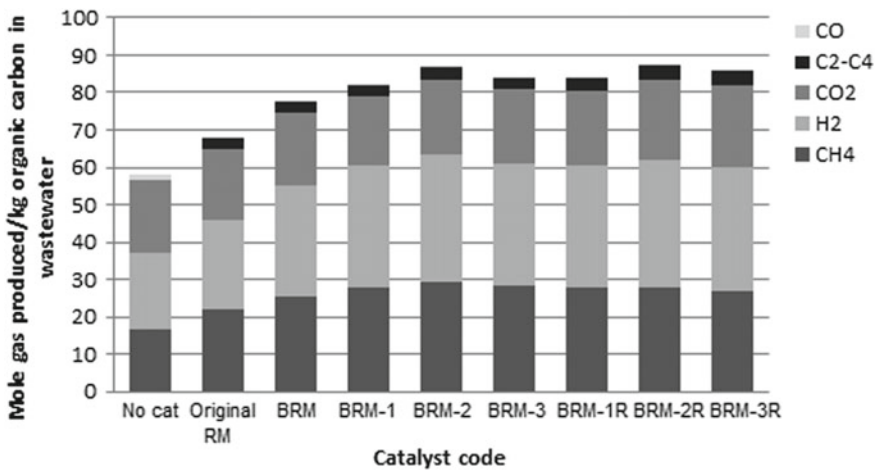
Fig. 3 Effect of catalyst type in B group on gaseous product yields in hydrothermal gasification of alkaloid wastewater

times. The effect of red mud derivatives on the product efficiencies, gaseous product yields, and *COD* and *TOC* removal efficiencies were examined.

The carbon gasification efficiency $(CGE, \%) = \frac{\sum_i n_i C_i \frac{PV_{gas}}{RT} M}{V_{feed} TOC_{ww}} \times 100$

The chemical oxygen demand removal efficiency $(COD_{RE}, \%) = \frac{COD_{ww} - COD_{aq}}{COD_{ww}} \times 100$

Total organic carbon removal efficiency $(TOC_{RE}, \%) = \frac{TOC_{ww} - TOC_{aq}}{TOC_{ww}} \times 100$
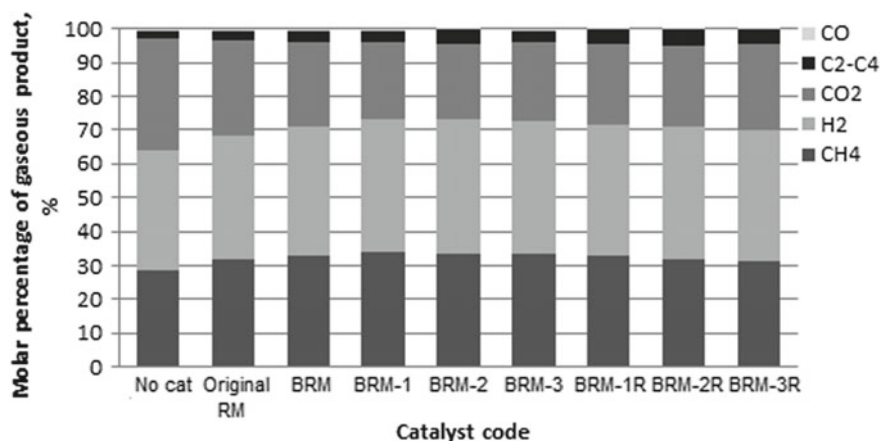
Fig. 4 Effect of catalyst type in B group on the gaseous product distribution in hydrothermal gasification of alkaloid wastewater

3.1 Experimental Results of (A) Group Catalysts

3.1.1 CGE (%) of Wastewater and Total Amount of Produced Gas Per Unit Volume

Carbon gasification efficiencies and the amount of total gas product in the unit of mmol gas/L wastewater are shown in Table 2. A group catalyst promoted the carbon gasification efficiencies by changing ratios of 7–17% with the effect of reduction

Table 2 Reaction conditions, *CGE*, produced gas amount, and the *TOC* values of the hydrothermal gasification of alkaloid wastewater with the effect of A group catalyst

	Reaction temperature (°C)	Reaction pressure (bar)	*CGE* (%)	*TOC* (mg/L)	Produced gas amount (mmol/L wastewater)
No catalyst	500	365	55.5	2843	766
ORM	500	405	57.6	2125	773
ARM	500	430	62.3	1675	896
ARM-1	500	425	62.9	1325	948
ARM-2	500	435	64.2	1200	1000
ARM-3	500	430	64.5	1504	970
ARM-1R	500	420	68.6	1675	979
ARM-2R	500	440	72.6	1500	1010
ARM-3R	500	425	70.8	1760	990

using $NaBH_4$. The original red mud did not have a considerable effect on the gasification but did reduce the *TOC* value of the aqueous product by 25%. The highest gasification ratios were obtained with the reduced form of activated red mud in this group. The reduction process resulted in a better catalytic activity with the red mud as seen from the results: *CGE* with ARM-1, ARM-2, and ARM-3 catalysts were 62.9, 64.2, and 64.5% while with the reduced forms of them (ARM-1R, ARM-2R, and ARM-3R) the *CGE* values increased to 68.6, 72.6, and 70.8%, respectively.

Nickel impregnation slightly increased gasification, while the amount of impregnated nickel did not have a significant effect. The produced gas amounts increased with the addition of the catalysts in A group. The highest gaseous product amounts were reached with 20% nickel containing ARM-2 and ARM-2R (1000 and 1010 mmol/L wastewater) while the others give similar catalytic activity in terms of produced gas quantities. Gaseous product amounts were enhanced by varying ratios of 17–32% within this group.

3.1.2 The Composition and Yields of the Gaseous Product

The main gaseous compounds in the product gas mixture are CH_4, H_2, and CO_2 as expected, and a little amount of CO and C_2–C_4 compounds were also produced. The molar percentage of methane and hydrogen increased while the carbon dioxide decreased. The carbon monoxide and C_2–C_4 hydrocarbons molar ratios were not changed much. The molar percentage of CH_4 increased from 28.8 to 33.6% with ARM-1R as the maximum, while with the other, the catalyst yield of CH_4 is similar. The molar percentage of H_2 increased from 34.9 to 39.7% with ARM-2 as the highest while with the other catalyst, the molar ratio of H_2 changed between 36.5 and 39.4%. The molar percentage of CO_2 decreased from 33% to the levels of 22.6–28.8%. The effect of the catalyst type can be seen in the CO_2 ratios more than the H_2, while hardly seen in the CH_4. The yields of CH_4, H_2, and C_2–C_4 compounds were improved with the addition of a catalyst while the CO_2 did not change remarkably except for ARM-2R and ARM-3R and the yields of CO decreased. A group catalyst enhanced the methane and hydrogen formation greatly, from 16.8 to 28.6 mol CH_4/kg C in wastewater and from 20.3 to 33.3 mol H_2/kg C in wastewater with ARM-1R as the best in the studied range. The yields of CH_4 with a reduced form of red mud are a bit higher than the others but for hydrogen, a generalization cannot be made. In terms of total gaseous product yields, it can be concluded that ARM-1R, ARM-2R, and ARM-3R have slightly higher than non-reduced states of them. The amount of nickel did not make a significant effect.

3.1.3 *COD* and *TOC* Content of the Aqueous Product and Removal Efficiencies

The *COD* and *TOC* contents of the aqueous product at the end of the HTG experiments in this group are given in Table 3. The chemical oxygen demand and total organic

Table 3 *COD* and *TOC* results, removal efficiencies of the SCWG of Alkaloid wastewater in the absence of a catalyst (NC) and in the presence of the A group catalyst

Experiment COD	*COD* of the reactor effluent (ppm)	*COD* removal efficiency (%)	*TOC* of the reactor effluent (ppm)	*TOC* removal efficiency (%)
Raw wastewater	32,050	–	11,500	–
NC	8470	73.6	2843	75.3
ORM	7610	76.3	2125	81.5
ARM-1	4940	84.6	1325	88.5
ARM-2	5860	81.7	1200	89.6
ARM-3	6240	80.5	1500	86.9
ARM-1R	5950	81.4	1675	85.4
ARM-2R	6050	81.1	1500	87.0
ARM-3R	5230	83.7	1760	84.7

carbon in the raw wastewater were reduced using a catalyst in this experiment. The *COD* of the wastewater, 32,050 ppm, was lowered to 4940–6240 ppm levels with a removal range of 81–85% approximately. This is a good result for only 1 h of treatment and applied without a need for pre-treatment or even filtration. The discharge limit in terms of *COD* is 1500 ppm for this special industrial wastewater, to maintain this value, the temperature should be increased. The *TOC* content of the raw wastewater, 11,500 ppm, decreased around to 1200–1760 ppm with removal efficiencies of 85–90%. The effect of the catalyst type within the activated state of red mud in A group cannot be seen clearly since the effectiveness is alike.

3.2 Experimental Results of B Group Catalysts

The investigation of the effect of red mud in HTG studies is very rare. Yanık et al. used red mud in the gasification of various types of waste (sunflower stalk, corncob, and vegetable-tanned leather waste) as a catalyst. They found that red mud increases gasification of corncob significantly and was proposed as a promising natural catalyst [26]. The corncob was gasified in supercritical water at 500 °C and 357 bars in the presence of red mud in this study, and it was seen that the gas amount increased from 340.0 to 426 g gas/kg biomass. Since red mud is a by-product from aluminum production, utilizing it as a catalyst is both valuable and economical.

The produced gas amount was promoted by activation of red mud since all the activated forms increased the gas amount at varying ratios of 17–48%. Nickel impregnation enhanced gasification while the effect of reduction by $NaBH_4$ was not so effective and that can be seen from the results of BRM-2 and BRM-2R, BRM3, and

Table 4 Reaction conditions, *CGE*, produced gas amount, and the *TOC* values of hydrothermal gasification of alkaloid wastewater with the effect of a catalyst type

	Reaction temperature (°C)	Reaction pressure (bar)	*CGE* (%)	*TOC* (mg/L)	Produced gas amount (mmol/L wastewater)
No catalyst	500	365	55.5	2843	766
ORM	500	405	57.6	2125	773
BRM	500	410	62.7	2000	896
BRM-1	500	420	65.3	1250	948
BRM-2	500	410	69.4	1065	1000
BRM-3	500	405	67.1	1201	970
BRM-1R	500	425	68.3	1595	1135
BRM-2R	500	440	71.3	1685	1010
BRM-3R	500	420	70.5	1975	990

BRM-3R which includes 20 and 30% nickel, respectively. At a lower nickel impregnation ratio (10%), reduction has a positive effect on the total produced gas amount as seen from the difference between BRM-1 and BRM-1R.

3.2.1 *CGE* (%) of Wastewater and Total Amount of Produced Gas Per Unit Volume

Carbon gasification efficiencies and the amount of total gas product in the unit of mmol gas/L wastewater are shown in Table 4 for the studied conditions. The addition of a catalyst increases *CGE* and produced significant gas amounts except for the original red mud. Kıpçak et al. used Ni/Al_2O_3 and Ru/Al_2O_3 as catalysts in the gasification of olive mill wastewater within a range of 400–600 °C of reaction temperatures. They also concluded that the catalyst enhanced the gasification and the yields of methane and hydrogen [13]. GCE is promoted from 55.5% in the absence of catalyst up to 70.5 and 71.3% with the catalyst BRM-2R and BRM-3R as maximum. The most effective forms of red mud in terms of carbon gasification into valuable gaseous products are found as 20 and 30% of nickel-impregnated ones.

3.2.2 The Composition and Yields of the Gaseous Product

The molar percentage and the yields of the gaseous product without a catalyst and with red mud catalysts are given in Figs. 1 and 2. The decomposition characteristics of this specific wastewater in HTG have not been studied before in literature. The content of it was investigated in few researches [1, 20, 22]. The alkaloid industry is a biomass-based plant and the wastewater contains 10,000 mg/L of carbohydrate and

5000–6000 mg/L of protein as expected. Additionally, it has acetic acid and sulfuric acid from extraction and has pH adjustment steps during production. The reactions for glucose and acetic acid are given below representing the biomass degradation:

$$C_6H_{12}O_6 + 6H_2O \leftrightarrow 6CO_2 + 12H_2 \tag{1}$$

$$CO + 3H_2 \leftrightarrow CH_4 + H_2O \tag{2}$$

$$CO_2 + 4H_2 \leftrightarrow CH_4 + 2H_2O \tag{3}$$

$$CO + H_2O \leftrightarrow CO_2 + H_2 \tag{4}$$

$$CH_3COOH \rightarrow CH_4 + CO_2 \tag{5}$$
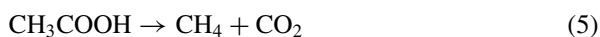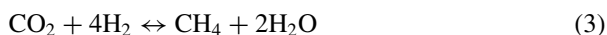
The organic content arising from the carbohydrate and organic acid content in the alkaloid wastewater was decomposed to produce gaseous products, such as CH_4, H_2, CO_2, and CO as stated via reactions [1–5]. Additionally, low amounts of C_2–C_4 hydrocarbons were generated at the end of HTG process. In non-catalytic and catalytic cases at 500 °C, the main gases in the product gas mixture are H_2, CO_2, and CH_4 in hydrothermal gasification of this wastewater in the percentage of H_2 increased from 34.9% to 38.1–39.4% and percentage of CH_4 also increased from 28.8% to 31.5–33.8% at varying ratios with the B group catalyst. Conversely, the molar percentage of CO_2 decreased from 33.0% to between 22.7 and 25.8% with the addition of the B group catalysts of red mud. The nickel impregnation effect in the gaseous product distribution is not clear since the yield of gases should be evaluated to determine this.

The yields of each gas are given in Fig. 3, and the total of the gaseous product yields for each run is given in Table 4. Comparing the yields in the non-catalytic run to the catalytic runs, it is seen that the yields of H_2 and CH_4 dramatically increased. In a study of De Blasio et al., they gasified black liquor in stainless steel and Inconel 625 at supercritical conditions to estimate the catalytic effect of the INCONEL 625 alloy which contains nickel as the main element. They found that the nickel content promotes hydrogen production as in this study while significant influence on carbon gasification efficiency was not observed [27].

The original red mud increased the CH_4 amount (mmol/L wastewater) by 32% while enhancing the H_2 formation by 17%. The catalytic effect of the original red mud originated from the iron and aluminum containing structure of it. Activated red mud catalysts also show good catalytic activity in hydrogen production and the yields of hydrogen reached 34.1 and 34.3 as the highest with the BRM-4 and BRM-4R catalyst while the yield of H_2 was found as 20.3 mol/kg C in wastewater without a catalyst. The other activated red mud derivative results are very similar to the hydrogen yields. The methane yields are extremely enhanced by changing ratios of 52–74% with activated red mud in group B. The yields of CO_2 were slightly

increased with the BRM-2R and BRM-3R catalyst while almost unchanged with others in the B group and original red mud. The yields of C_2–C_4 in a gaseous product increased from 0.2 to 3.9 mol/kg C in wastewater with both the original and activated red mud derivatives in this group. The very low CO level, 1.5, also declines further in the product gas to around 0.2–0.3 mol/kg C in wastewater. These results show us that the original red mud is effective in terms of hydrogen and methane formation in hydrothermal gasification of opium processing wastewater, and the activation and nickel impregnation increased the catalytic effect of it due to higher CH_4 and H_2 yields in the activated forms of it. The changing impregnation ratio of nickel did not make a significant effect. In the case of the promotion of the H_2 and CH_4 production, the order of effectiveness in the catalytic performance of the catalysts may be given as: Original RM < activated red mud without nickel (BRM) < BRM-1, BRM-1R, BRM-3, BRM-3R < BRM-2, BRM-2R.

In the study of Yanık et al., red mud is defined as iron-based catalysts and mentioned that is has a catalytic activity in hydrogen production with the studied feedstock in the operated conditions. Together with the supercritical water acting as a catalyst, iron oxide active sites enhanced the water gas shift reaction toward CO_2 and H_2 from CO as stated similarly in the study of Uddin et al. 2008. The yields of CO decreased with the usage of a catalyst from 17.25 to 3–4 mmol/L levels. Nickel is widely used in biomass gasification as a catalyst [28–30] and it is reported that nickel promotes the hydrogen process for red mud and also promotes the effectiveness of it in the case of hydrogen and methane yields because of it selectivity of H_2.

3.2.3 *COD* and *TOC* Content of the Aqueous Product and Removal Efficiencies

The original alkaloid wastewater, used in this study, had a *COD* of 32,050 ppm and a *TOC* of 11,500 ppm. The *COD* and *TOC* contents of the aqueous product at the end of the HTG experiments are given in Table 5. The results show that the *COD* was lowered to the levels of 5100–6550 ppm using the supercritical water gasification technique in a 1-h operation with the B group of activated red mud. This is a successful result hence it provides a *COD* removal of approximately 84% while the *TOC* removal was achieved at 91% as a maximum in the presence of A3 in this experiment. The catalyst used improved the *COD* and *TOC* removal by 10 and 15%, respectively, at 500 °C. Kazemi et al. investigated the hydrothermal treatment of distillery wastewater in a batch tubular reactor at temperatures of 250–400 °C, with a reaction time of 30–120 min, and an initial *COD* concentration of 9600–26,200 mg l^{-1} at a constant pressure of 25.0 MPa in the presence and absence of various homogeneous and heterogeneous catalysts [12].

They concluded that *COD* removal is mainly dominated by temperature increase while homogeneous and heterogeneous catalysts substantially affected the *COD* and color removal efficiencies. The optimum conditions were obtained at 400 °C, for 30 min with CuO and MnO_2 (~75%) and 400 °C, at 120 min with 5 wt% of CuO (80.9%). The amount of nickel impregnated did not make a sensible change in the

Table 5 *COD* and *TOC* results, removal efficiencies of the SCWG of Alkaloid wastewater in the absence of a catalyst (NC) and in the presence of a B group catalyst

Experiment *COD*e	*COD* of the reactor effluent (ppm)	*COD* removal efficiency (%)	*TOC* of the reactor effluent (ppm)	*TOC* removal efficiency (%)
Raw wastewater	32,050	–	11,500	–
No catalyst	8470	73.6	2843	75.3
ORM	7610	76.3	2125	81.5
BRM	5630	82.4	2000	82.6
BRM-1	5325	83.4	1250	89.1
BRM-2	5025	84.3	1065	90.7
BRM-3	5100	84.1	1201	89.6
BRM-1R	6550	79.6	1595	86.1
BRM-2R	6475	79.8	1685	85.3
BRM-3R	5625	82.4	1975	82.8

COD and *TOC* removal efficiencies while the reduction with $NaBH_4$ had a slightly negative effect. When higher *COD* removals are needed in the case of discharge limits, the reaction temperature or impregnated nickel ratio may be increased.

3.3 Addition of K_2CO_3 to the HTG Runs with B Group Catalysts

B group catalysts were combined with 0.5 g of K_2CO_3 to strengthen the effect on the gasification and *COD* removal efficiency. A 20 mL sample of wastewater and 1.0 g of catalyst were used in the hydrothermal gasification of alkaloid manufacturing wastewater. The reaction pressure was 500 °C and a pressure range of 40.5–44.0 MPa was obtained. The results of the non-catalytic, with original red mud (ORM) catalyst, and the combined catalysts are given for comparison in Tables 5 and 6 and Figs. 5 and 6.

3.3.1 CGE (%) of Wastewater and Total Amount of Produced Gas Per Unit Volume

The addition of K_2CO_3 to the B group catalysts promoted carbon gasification efficiencies from 55.5% up to around 77% as the highest which is significantly higher than the obtained *CGE* values with K_2CO_3 (66%) alone and with the B group catalysts (68%) alone. The effect of the catalyst combinations is clearly seen on the total produced gas amount and gaseous product yields. The amount of the gaseous

Table 6 *COD* and *TOC* results and removal efficiencies of the SCWG of alkaloid wastewater in the absence of a catalyst (NC) and in the presence of a B group catalyst with K_2CO_3

Experiment COD	*COD* of the reactor effluent (ppm)	*COD* removal efficiency (%)	*TOC* of the reactor effluent (ppm)	*TOC* removal efficiency (%)
Raw wastewater	32,050	–	11,500	–
No catalyst	8470	73.6	2843	75.3
ORM	7610	76.3	2125	81.5
BRM + K_2CO_3	6150	80.8	950	91.7
BRM-1 + K_2CO_3	6390	80.1	1515	86.8
BRM-2 + K_2CO_3	7210	77.5	1550	86.5
BRM-3 + K_2CO_3	6325	80.3	1540	86.6
BRM-1R + K_2CO_3	6800	78.8	1610	86.0
BRM-2R + K_2CO_3	5400	83.2	1660	85.6
BRM-3R + K_2CO_3	6875	78.5	1815	84.2
K_2CO_3	5125	84	1200	89.6
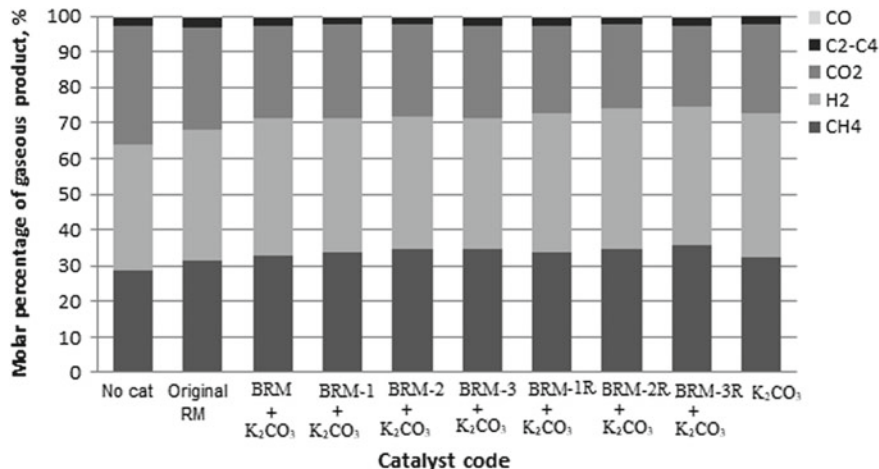
Fig. 5 Effect of catalyst type in B group catalyst with K_2CO_3 on gaseous product yields in hydrothermal gasification of alkaloid wastewater
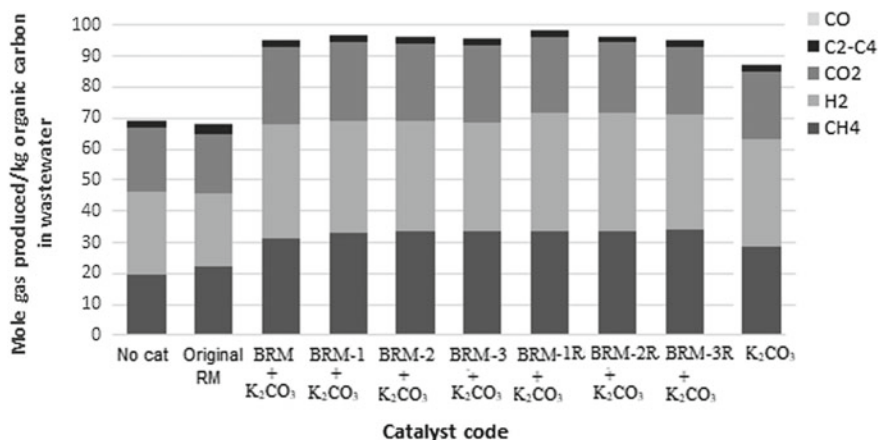
Fig. 6 Effect of catalyst type in B group catalyst with K_2CO_3 on gaseous product distribution in hydrothermal gasification of alkaloid wastewater

Table 7 Reaction conditions, *CGE*, produced gas amount, and the *TOC* values of the hydrothermal gasification of alkaloid wastewater with the effect of the B group catalyst with K_2CO_3

Experiment COD	Reaction temperature (°C)	Reaction pressure (bar)	CGE (%)	TOC (mg/L)	Produced gas amount (mmol/L wastewater)
No Catalyst	500	365	55.5	2843	766
ORM	500	405	57.6	2125	773
BRM + K_2CO_3	500	435	74.0	950	1095
BRM-1 + K_2CO_3	500	425	76.2	1514	1114
BRM-2 + K_2CO_3	500	405	76.4	1550	1108
BRM-3 + K_2CO_3	500	440	76.8	1540	1104
BRM-1R + K_2CO_3	500	422	76.9	1610	1135
BRM-2R + K_2CO_3	500	415	73.6	1660	1112
BRM-3R + K_2CO_3	500	410	74.1	1815	1100
K_2CO_3	500	365	66.2	1200	1003

product was promoted by a ratio varying from 43 to 48%. The amount of product gas did not change with the catalyst type remarkably within this group.

3.3.2 The Composition and Yields of the Gaseous Product

The gaseous product distribution and yields obtained in hydrothermal gasification of alkaloid wastewater with combined catalysts was given in Figs. 5 and 6. The molar percentage of CH_4 and H_2 in the product gas is higher while the composition of CO_2 is lower in the presence of B group and the K_2CO_3 catalyst together. CO and C_2–C_4 hydrocarbons have almost the same molar percentage in the non-catalytic and catalytic cases. The molar percentage of CH_4 increased to 35.5% as the maximum with a combination of alkali (K_2CO_3) and 30% nickel containing the activated and reduced red mud catalyst (BRM-3R) while it was 28.8% in the absence of a catalyst. The effectiveness in methane formation is very similar in this group while the ratio of nickel impregnation has slightly promoted the methane amounts. The molar percentage of H_2 has also enhanced from 34.9 to 39.6% using a catalyst, and BRM-2R with K_2CO_3 was found as the most effective catalyst while the other shows almost indistinguishable catalytic activities. The reduced state of the catalysts slightly increased the H_2 percentages. The molar ratio of CO_2 decreased from 33% to the percentages of 23–26%. The effect of reduction can be seen since slightly lower CO_2 ratios were obtained in the runs of BRM-1 with K_2CO_3, BRM-2 with K_2CO_3, and BRM-3 with K_2CO_3.

The amount of produced gas, in the unit of mol/kg C in wastewater, was increased with the addition of a combined catalyst. The increment in yields of CH_4, and H_2 is virtually high while in yields of CO_2 is less and the rise in the yields of C_2–C_4 compounds and CO are very low. The combined catalysts promoted hydrogen production greatly above 38.0, from 20.3 mol H_2/kg C in wastewater for non-catalytic case. The H_2 yield with A or B group alone was nearly 33–34 mol H_2/kg C in wastewater. This result shows that the addition of K_2CO_3 gives higher yields in case of H_2. CH_4 yields were 16.8 in the non-catalytic case and 28–29 mol CH_4/kg C in wastewater with the A or B group catalyst. The combined catalysts accelerated the formation of methane and the amount produced nearly doubled, to the levels of 34–35 mol CH_4/kg C in wastewater. In terms of methane production, the combined catalyst is the best group in all the activated red mud catalysts. The CO_2 yields generally increased while the reduced catalysts give slightly lower CO_2 yields than the others. The other gases did not considerably vary with the effect of catalyst use and type. The total gaseous product yields reached 97–98 mol/kg C which is 70% higher than the non-catalytic run.

Table 8 Multipoint BET results

Sample CODe	Area (m²/g)	Slope	Y-Intercept	Correlation coefficient	C
BRM-1	48.8	70.8	0.64	0.999917	112
BRM-1R	24.5	140.4	1.82	0.999946	78.3
ARM-1	44.8	77.3	0.49	0.999901	157.1
ARM-1R	24.0	142.6	2.43	0.999919	59.7

3.3.3 *COD* and *TOC* Content of the Aqueous Product and Removal Efficiencies

The *COD* and *TOC* in the raw wastewater were lowered with the combined catalyst in this experimental part and the results are given in Tables 6 and 7. The *COD* of the wastewater, that was 32,050 ppm, was lowered to 8470 ppm without a catalyst using the HTG process at 500 °C and to 7610 ppm with the original red mud. The best *COD* removal was achieved as 5400 ppm impregnated with 20% Nickel and reduced form (BRM-2R) while the others varied from 6150 to 7210 ppm. The addition of K_2CO_3 enhanced the gasification while it did not have a remarkable positive effect on the *COD* removal. The COD_{RE} values were obtained as changing ratios between 78 and 83% while they were 80–84% with A and 81–85% with B. As it is seen, the *COD* removals were not affected much by the type of the activation process and the K_2CO_3 addition to the red mud. The *TOC* content of the raw wastewater decreased with the HGT process by 75% without a catalyst, 81.5% with original red mud, and 90% in the presence of K_2CO_3. BRM with K_2CO_3 is the most effective catalyst in *TOC* removal with 92% and the others have removal efficiencies within the range of 84–87%.

3.4 Characterization of an Activated Red Mud Catalyst

Activated red mud catalysts contain silica, aluminum, iron, calcium, sodium, and titanium, in forms of Fe_2O_3, Al_2O_3, SiO_2, Na_2O, CaO, and TiO_2 and as minor potassium, etc. Also, these catalysts include varying ratios of nickel since they are prepared by impregnation of $Ni(NO_3)_2 \cdot 6H_2O$ and calcinations. Characterization results of one of the activated red mud catalyst are given in Figs. 7 and 8 to represent all others since they have similar structures. The SEM photograph of elemental mapping shows that the nickel is distributed homogenously on the catalyst surface seen in the elemental mapping of the SEM photographs. Some parts have some elements together and may be determined as structures of goethite $(Fe(1-x)AlxOOH)$, calcium aluminum hydrate $(x \cdot CaO \cdot y\ Al_2O_3 \cdot zH_2O)$, kaolinite $(Al_2O_3 \cdot 2SiO_2 \cdot 2H_2O)$, $CaTiO_3$, etc. According to the XRD phase analysis that was shown in Fig. 9, the BRM-1R catalyst has structures of hematite, nickel-titanium oxide and nickel oxide, SiO_2, iron titanium oxide, and cancrinite $Na_6Ca_2[(CO_3)_2|Al_6Si_6O_{24}] \cdot 2H_2O$. In the work
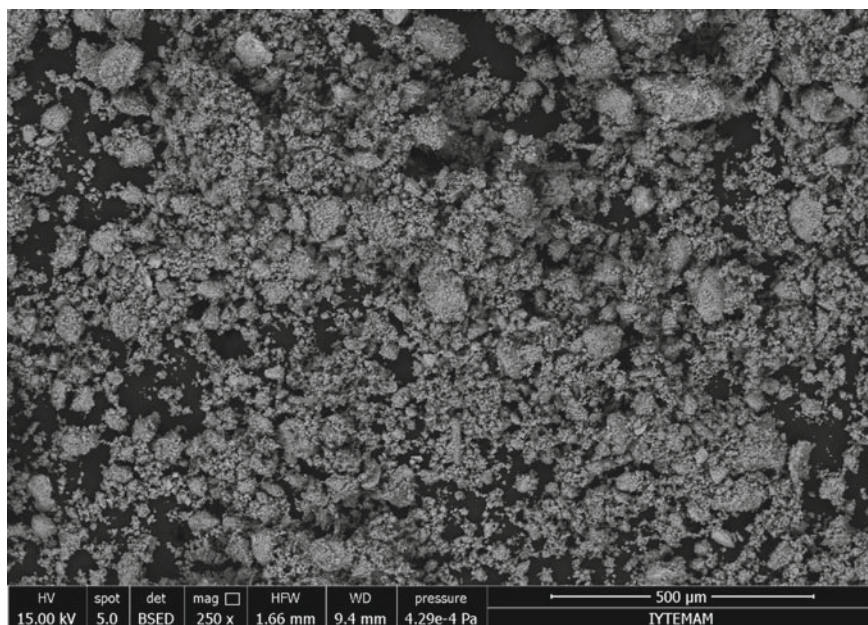
Fig. 7 General electron image of BRM-1R catalysts

of Nath et al., the original red mud characterization was investigated [31] and they found the main phases as hematite (Fe_2O_3), gibbsite ($Al(OH)_3$), rutile (TiO_2), calcite ($CaCO_3$), sodium aluminum silicate ($Na(AlSiO_4)$), dicalcium silicate (Ca_2SiO_4), and quartz (SiO_2). Some differences maybe caused by the activation process of red mud in this study compared to literature findings (Fig. 10).

The mean size of the crystallites from the XRD pattern data by means of Origin software was done and given in Fig. 10. By applying the Scherrer equation on the XRD pattern, the particle size can be calculated as 29.2 nm. The multipoint BET results of the selected catalysts are given in Table 8. The BET results show that the reduction decreased the BET area and the precipitation with NH_3 slightly increased the BET area.

4 Conclusions

In this study, wastewater from opium processing industry was gasified with original and activated red mud as catalyst in supercritical water at 500 °C. The most appropriate catalyst type for maximum H_2 and CH_4 yield and highest COD removal was determined. Effect of nickel impregnation and reducing of the catalyst with $NaBH_4$ were investigated, and some key findings were listed below:
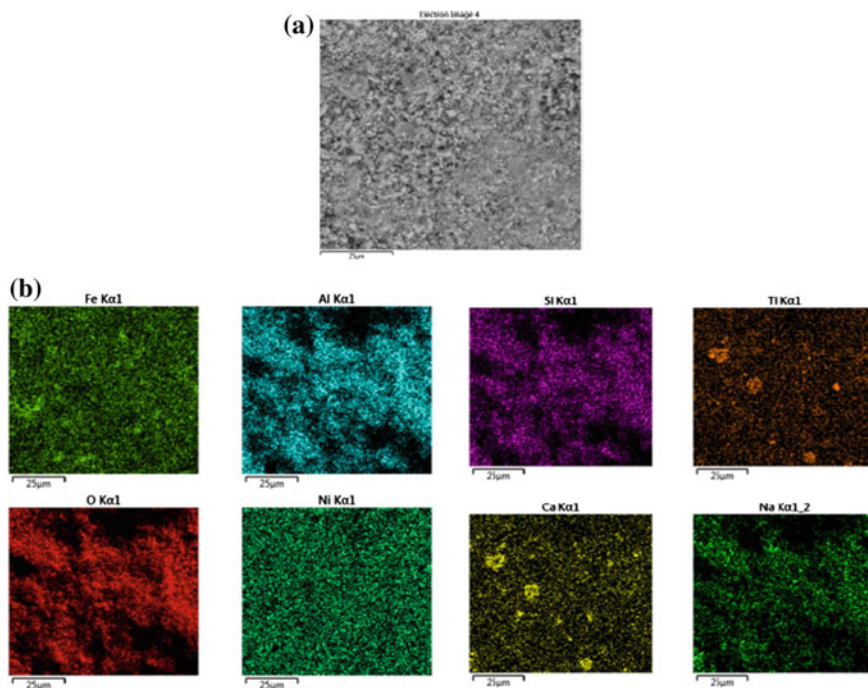
Fig. 8 Electron image (**a**) and elemental mapping (**b**) of BRM-1R catalyst
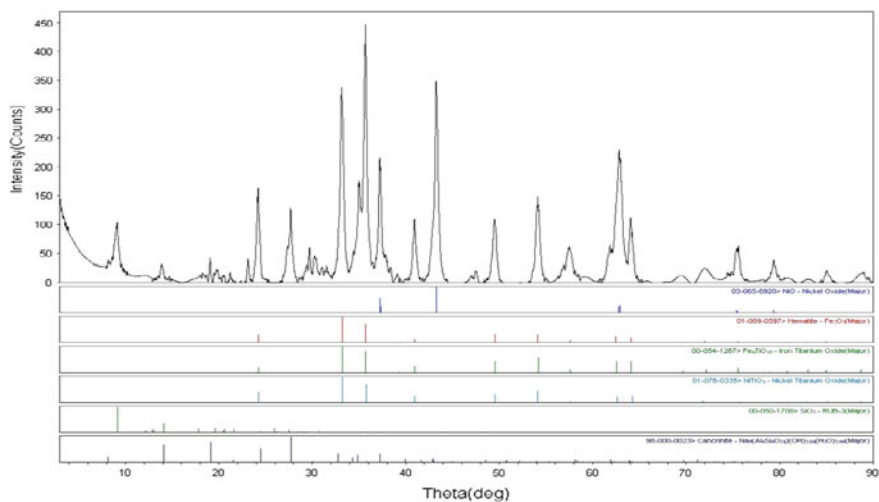
Fig. 9 Plot of intensity versus degree (2θ) within NiO peak in XRD pattern of BRM-1R catalyst

Fig. 10 XRD and phase analysis results of BRM-1R catalyst
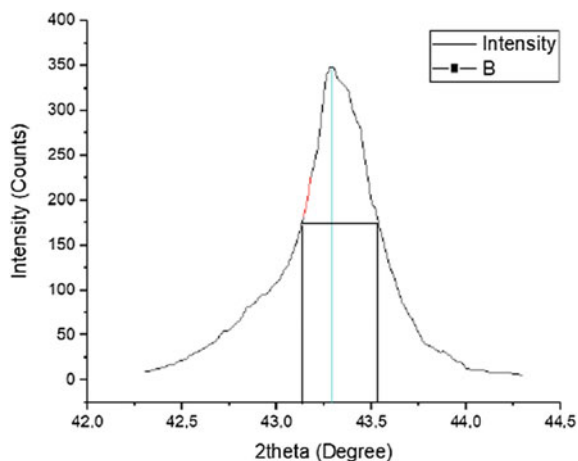
- The original red mud increased the CH_4 amount (mol/L wastewater) by 32% while enhancing the H_2 formation by 17%. It did not make a considerable effect on the gasification but reduced the *TOC* value of the aqueous product by 25%.
- The highest gaseous product amounts were reached with ARM-2 and ARM-2R (1000 and 1010 mol/L wastewater) while the others give similar catalytic activity in terms of produced gas quantities.
- A group catalysts promoted *CGE* and produced gas amounts of the highest gasification ratios were obtained as 68.6, 72.6, and 70.8% with reduced forms of them: with ARM-1R, ARM-2R, and ARM-3R, respectively. Nickel impregnation slightly increased gasification, while the amount of impregnated nickel did not have a significant effect.
- The *COD* of the wastewater was lowered to 4940–6240 ppm levels with a removal range of 81–85% approximately while the *TOC* content decreased to around 1200–1760 ppm with removal efficiencies of 85–90% with group A.
- The effect of catalyst type within the activated state of red mud in A group cannot be seen clearly since the effectiveness is alike.
- B group activated red mud catalysts show good catalytic activity in hydrogen production, and the yields of H_2 reached 34.1 and 34.3 as the highest with BRM-2 and BRM-2R catalyst while the yield of H_2 was only 20.3 mol/kg C in non-catalytic run.
- CH_4 yields are significantly enhanced with the changing ratios of 52–74% with activated red mud in group B.
- The catalyst use (B group) improved COD_{RE} and TOC_{RE} by 10 and 15%, respectively, at 500 °C. The amount of nickel impregnated did not make a sensible change in the COD_{RE} and TOC_{RE} while the reduction with $NaBH_4$ had a slightly negative effect in group B.

- The produced gas amount was promoted with the activation of red mud in group A since all the activated forms increased gas amounts. Nickel impregnation enhanced gasification while the effect of reduction by $NaBH_4$ was not so effective.
- The addition of K_2CO_3 to the B group catalyst gives higher yields in the case of hydrogen, and the combined catalysts accelerated methane formation up to the levels of 34–35 mol CH_4/kg C. In terms of methane production, this group is also the best group in activated red mud catalysts.
- The CO_2 yields were generally increased while the reduced catalysts give slightly lower CO_2 yields than others.

References

1. Aydin AF, Ersahin ME, Dereli RK, Sarikaya HZ, Ozturk I (2010) Long-term anaerobic treatability studies on opium alkaloids industry effluents. J Environ Sci Health Part A, Toxic/Hazard Subst Environ Eng 45(2):192–200. Available from http://www.ncbi.nlm.nih.gov/pubmed/20390859
2. Aytimur G, Atalay S (2004) Treatment of an alkaloid industry wastewater by biological oxidation and/or chemical oxidation. Energy Sources 26(7):661–670
3. Ministry of Environment and Forestry (2004) Water Pollution Control Regulation. Official Newspaper
4. Guo X, Wang S, Wang K, Liu Q, Luo Z (2010) Influence of extractives on mechanism of biomass pyrolysis. J Fuel Chem Technol 38(1):42–46. Available from http://www.sciencedirect.com/science/article/pii/S1872581310600199
5. Kruse A, Ebert KH (1996) Chemical reactions in supercritical water 1. Pyrolysis 83(I):80–83
6. Fritsch C, Staebler A, Happel A, Márquez MAC, Aguiló-Aguayo I, Abadias M et al (2017) Processing, valorization and application of bio-waste derived compounds from potato, tomato, olive and cereals: a review. Sustainability (Switzerland) 9(8):1–46
7. Kruse A (2009) Hydrothermal biomass gasification. J Supercrit Fluids 47:391–399
8. Jeong H, Park SY, Ryu GH, Choi JH, Kim JH, Choi WS et al (2018) Catalytic conversion of hemicellulosic sugars derived from biomass to levulinic acid. Catal Commun 117:19–25
9. Bergman PCA, Kiel JHA (2005) Torrefaction for biomass upgrading. In: 14th European biomass conference & exhibition, Paris, France, p 9. Available from http://scholar.google.com/scholar?hl=en&btnG=Search&q=intitle:Torrefaction+for+biomass+upgrading#0
10. Modell M, Reid RC (1978) SIA. Gasification process, US Patent 4:113,446
11. Breinl J (2015) Hydrothermal gasification of HTL wastewater. By Supervised by 2015
12. Kazemi N, Tavakoli O, Seif S, Nahangi M (2015) High-strength distillery wastewater treatment using catalytic sub- and supercritical water. J Supercrit Fluids 97:74–80. Available from http://www.sciencedirect.com/science/article/pii/S0896844614003611
13. Kıpçak E, Akgün M (2017) Biofuel production from olive mill wastewater through its Ni/Al_2O_3 and Ru/Al_2O_3 catalyzed supercritical water gasification. Renew Energy 1–10. Available from http://linkinghub.elsevier.com/retrieve/pii/S0960148117305797
14. Lee I (2010) Hydrogen production by supercritical water gasification of wastewater from food waste treatment processes. In: 18th world hydrogen energy conference, vol 78, pp 425–429

15. Sö OÖ, Akgün M (2011) Hydrothermal gasification of olive mill wastewater as a biomass source in supercritical water. J Supercrit Fluids 57:50–57
16. Dinjus E, Kruse A (2004) Hot compressed water—a suitable and sustainable solvent and reaction medium? J Phys Condens Matter Vol. 16:S1161–S1169
17. He C, Chen C-L, Giannis A, Yang Y, Wang J-Y (2014) Hydrothermal gasification of sewage sludge and model compounds for renewable hydrogen production: a review. Renew Sustain Energy Rev 39:1127–1142. Available from http://www.sciencedirect.com/science/article/pii/S1364032114005930
18. García Jarana MB, Sánchez-Oneto J, Portela JR, Nebot Sanz E, Martínez de la Ossa EJ 2008 Supercritical water gasification of industrial organic wastes. J Supercrit Fluids 46:329–334
19. Iwamura H, Sato T, Okada M, Sue K, Hiaki T (2016) Organic reactions in sub- and supercritical water in the absence of any added catalyst 1–9
20. Bural CB (2008) Aerobic biological treatment of opium alkaloid wastewater—effect of gamma radiation and Fenton's oxidation as pretreatment
21. Kunukcu YK, Wiesmann U (2004) Activated sludge treatment and anaerobic digestion of opium alkaloid factory. World Water Congress 2004
22. Kaçar Y, Alpay E, Ceylan VK (2003) Pretreatment of Afyon alcaloide factory's wastewater by wet air oxidation (WAO). Water Res 37(5):1170–1176
23. Aydın AF Sarikaya HZ (2002) Biyolojik Proseslerle Arıtılmış Afyon Alkaloidleri Endüstrisi Atıksularının Fenton Oksidasyonu ile İleri Arıtımı. İTÜ Dergisi/d Mühendislik 1(1)
24. Koyuncu I (2003) An advanced treatment of high-strength opium alkaloid processing industry wastewaters with membrane technology: pretreatment, fouling and retention characteristics of membranes. Desalination 155(3):265–275
25. Garg D, Glvens EN (1985) Coal liquefaction catalysis by industrial metallic wastes. Ind Eng Chem Process Des Dev 24(1):66–72
26. Yanık J, Ebale S, Kruse A, Saglam M, Yu M (2008) Biomass gasification in supercritical water: II. Effect of catalyst. Int J Hydrog Energy 33:4520–4526
27. De Blasio C, Lucca G, Özdenkci K, Mulas M, Lundqvist K, Koskinen J et al (2016) A study on supercritical water gasification of black liquor conducted in stainless steel and nickel-chromium-molybdenum reactors. J Chem Technol Biotechnol 91(10):2664–2678
28. Azadi P, Khan S, Strobel F, Azadi F, Farnood R (2012) Applied catalysis B: environmental hydrogen production from cellulose, lignin, bark and model carbohydrates in supercritical water using nickel and ruthenium catalysts. Appl Catal B, Environ 117–118:330–338. Available from http://dx.doi.org/10.1016/j.apcatb.2012.01.035
29. Buffoni IN, Pompeo F, Santori GF, Nichio NN (2009) Nickel catalysts applied in steam reforming of glycerol for hydrogen production. Catal Commun 10(13):1656–1660
30. Minowa T, Zhen F, Ogi T (1998) Cellulose decomposition in hot-compressed water with alkali or nickel catalyst. J Supercrit Fluids 13:253–259
31. Nath H, Sahoo A (2014) A study on the characterization of red mud. Int J Appl Bio-eng 8(1):1–4. Available from http://www.journals-sathyabama.com/archives/iabe_abstract.php?id=115

System Analysis, Modeling and Simulation

Exergetic and Environmental Analyses of Turbojet Engine

Burak Yuksel, Ozgur Balli, Huseyin Gunerhan, Arif Hepbasli and Halil Atalay

Abstract This study deals with exergetic and environmental analyses of turbojet engine used on the military training aircrafts. In the analysis, the engine data measured in the Engine Test Cell at First Air Maintenance and Factory Directorate of Turkish Air Forces in Eskisehir, Turkey are utilized. The exergy balance equations are derived for each component of the engine along with the overall the engine. Several thermodynamic parameters (the fuel exergy depletion ratio, the productivity lack ratio, the relative exergy consumption ratio, exergetic improvement potential, exergetic improvement potential ratio, relative exergetic improvement potential, exergetic fuel-product ratio, and sustainability index) are used to evaluate the performance of the engine and its main components (the air compressor, the combustion chamber, the gas turbine, the exhaust forward duct, the aft exhaust duct, and the mechanical shaft). Exergy losses and destructions are investigated to determine thermodynamic inefficiencies. The exergetic efficiency of the engine is determined to be 18.77%. The highest exergy destruction rate of 2921.01 kW in the engine occurs within the combustion chamber. The mechanical shaft of the engine has the maximum sustainability index of 100.65. An environmental analysis of the engine is also performed.

Keywords Turbojet engine · Exergy analysis · Exergy efficiency · Sustainability index · Environmental analysis

B. Yuksel (✉) · O. Balli · H. Gunerhan · A. Hepbasli · H. Atalay
Mechanical Engineering Department, Faculty of Engineering, Ege University, Ankara, Turkey
e-mail: burakyuksell@gmail.com

O. Balli
e-mail: balli07balli@yahoo.com

H. Gunerhan
e-mail: huseyin.gunerhan@ege.edu.tr

A. Hepbasli
e-mail: arif.hepbasli@yasar.edu.tr

H. Atalay
e-mail: halilatalay16@gmail.com

Nomenclature

c_P	Specific heat capacity (kJ kg^{-1} K^{-1})
$\dot{Ex}$	Exergy rate (kW)
$\dot{Ex}IP$	Exergetic improvement potential (kW)
$\dot{Ex}IPR$	Exergetic improvement potential rate ratio (%)
LHV	Lower heating value of fuel (kJ kg^{-1})
$\dot{m}$	Mass flow rate (kg s^{-1})
p	Pressure (kPa)
$R\dot{Ex}IP$	Relative improvement potential rate (%)
SI	Sustainability index (–)
T	Temperature (K)
$\dot{W}$	Work rate or power (kW)

Greek Letters

α	Fuel exergy depletion ratio (%)
β	Productivity lack ratio in exergetic term (%)
χ	Relative exergy consumption ratio (%)
γ	Fuel exergy grade function
ψ	Exergy (second law) efficiency (%)

Subscripts

a	Air
AC	Air compressor
C	Consumption
CC	Combustion chamber
cg	Combustion gases
D	Destroyed, destruction
EAD	Exhaust aft duct
EFD	Exhaust forward duct
GT	Gas turbine
GTMS	Gas turbine mechanical shaft
in	Input
out	Output
P	Pressure
Pr	Product
ref	Reference

T   Temperature
TJE   Turbojet engine

Abbreviations

AC   Air compressor
EAD   Exhaust aft duct
EFD   Exhaust forward duct
CC   Combustion chamber
GT   Gas turbine
GTMS   Gas turbine mechanical shaft
TJE   Aircraft jet engine

1 Introduction

Using the energy of fuel to produce flights is the job of both the military and civil aviation propulsion system. The military aircraft is used to maximize aerodynamic performance, in which case it complies with some operational constraints and uses fuel less efficiently than an efficient aircraft. High-performance start-up, maximum performance climbing and retrofitting are significantly less fuel-efficient than driving performance [1]. For cost-effective and environmental-friendly aviation, system efficiency should be kept maximum, while minimizing cost and environmental impacts of aircraft engines. In order to achieve these objectives, the engine must be operated in optimum operating mode, the best quality fuel should be selected, the fuel consumption rate and the exergetic consumption (losses and destruction) rate should be reduced and the cost of capital should be diminished. In this context, thermodynamic exergy, exergoeconomic, sustainability, and environmental (exergoeconomic, environmental damage cost) analysis methods are used to evaluate the performance of aircraft engines [2]. The main objective of this study can be summarized as follows:

- Exergetic analyses of J69 turbojet engine used on the military training aircrafts.
- Environmental analyses of J69 turbojet engine used on the military training aircrafts.

The exergy balance equations derived for each component of the engine along with the overall the engine and exergoenvironomic balance equations are given below section.
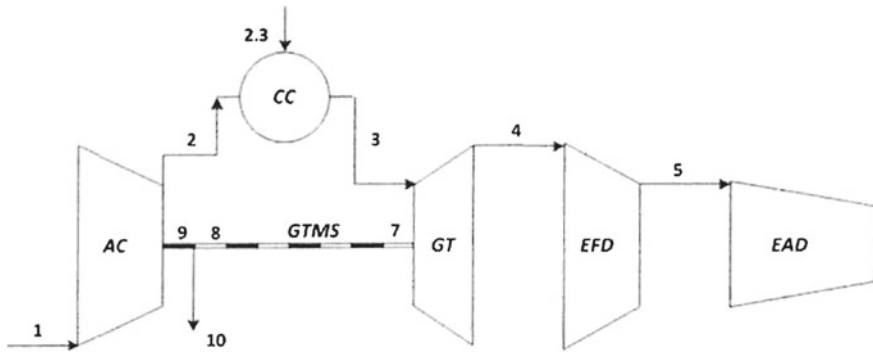
Fig. 1 Schematic of the investigated turbojet engine

2 Methodology

2.1 General Description of TJE with Afterburner

A schematic of the investigated TJE is given in (Fig. 1). This system consists of an air compressor (AC), a combustion chamber (CC), a gas turbine (GT), an exhaust forward duct (EFD), an exhaust aft duct (EAD), and a gas turbine mechanical shaft (GTMS).

2.2 Assumptions

In this study, the assumptions made are listed below:

- The TJE operates in a steady-state.
- The ideal gas principles are applied to air and combustion gas.
- The combustion reaction is complete.
- The changes in the kinetic exergy and potential exergy are assumed negligible.
- The temperature and pressure of dead state are 288.15 K and 99.85 kPa, respectively.
- The exergetic analyses are made on the lower heating value (LHV) basis of liquid JP-8 fuel.
- The chemical formula of jet fuel is assumed as $C_{12}H_{23}$.
- While the engine operates in military operation, air/fuel mass ratio is equal to 65.

2.3 The Exergy Equilibrium Equations

General exergy equilibrium equation is defined in Eq. (1) as under mentioned:

$$\sum \left(1 - \frac{T_o}{T_k}\right)\dot{Q}_k - \dot{W} + \sum_{in} \dot{E}x_{in} - \sum_{out} \dot{E}x_{out} - \dot{E}x_D = 0 \tag{1}$$

where $\dot{Q}_k$ represents the heat transfer rate through the boundary at temperature T_k at the location k, $\dot{W}$ is the work rate, $\dot{E}x$ is the exergy rate of stream, and $\dot{E}x_D$ is the exergy destruction rate.

The total exergy for a system can be given in Eq. (2) as under mentioned:

$$\dot{E}x = \dot{E}x_{kn} + \dot{E}x_{pt} + \dot{E}x_{ph} + \dot{E}x_{ch} \tag{2}$$

where the terms $\dot{E}x_{kn}, \dot{E}x_{pt}, \dot{E}x_{ph}$, and $\dot{E}x_{ch}$ denote the kinetic exergy, potential exergy, physical exergy, and chemical exergy, respectively. In the present study, the changes in the kinetic exergy and potential exergy within the system are assumed negligible.

The physical exergy for air and combustion gaseous with constant specific heat is obtained in Eq. (3) as under mentioned [3]:

$$\dot{E}x_{ph} = \dot{m}c_{P(T)}\left[T - T_o - T_o \ln\left(\frac{T}{T_o}\right)\right] + RT_o\left(\frac{P}{P_o}\right) \tag{3}$$

The chemical exergy of liquid fuels as C_aH_b on a unit mass basis can be determined in Eq. (4) as under mentioned:

$$\frac{\dot{E}x_{ch,f}}{\dot{m}_f LHV_f} = \gamma_f \cong 1.04224 + 0.011925\frac{b}{a} - \frac{0.042}{a} \tag{4}$$

where γ_f denotes the liquid fuel exergy grade function. The chemical formula of jet fuel is assumed as $C_{12}H_{23}$. γ_f is calculated as 1.0596 for this fuel. The sum of fuel chemical exergy and the fuel physical exergy gives fuel energy in Eq. (5) as follows:

$$\dot{E}x_f = \left(\dot{E}x_{ch} + \dot{E}x_{ph}\right)_f \tag{5}$$

2.4 The Exergy Efficiency and Thermodynamic Performance Parameters

The exergy efficiency of the system or subsystems can be defined as the ratio of the exergy in outputs products to the exergy in inputs. The exergy efficiency of air compressor is obtained as under mentioned:

$$\psi = \frac{\dot{E}x_{out} - \dot{E}x_{in}}{\dot{W}} \tag{6}$$

The exergy efficiencies of the n'th component of a system are calculated in Eq. (7) as under mentioned:

$$\psi = \frac{\dot{E}x_{out}}{\dot{E}x_{in}} \tag{7}$$

The exergy efficiency of whole system is obtained as under mentioned:

$$\psi_{SYS} = \frac{\dot{E}x_P}{\dot{E}x_F} \tag{8}$$

The thermodynamic parameters such as the fuel depletion rate, relative irreversibility, and productivity lack, are used in evaluating the exergetic performance of the system [4]. These are given in Eqs. (9)–(16) as follows:

The fuel exergy depletion ratio is written as the ratio of the exergy consumption of n'th component to the fuel exergy rate input the TJE such as:

$$\alpha_j = \frac{\dot{E}x_{C,j}}{\dot{E}x_f} \tag{9}$$

The productivity lack ratio is written as the ratio of the exergy consumption of n'th component to the exergy of products as:

$$\beta_j = \frac{\dot{E}x_{C,j}}{\dot{E}x_{P,TJE}} \tag{10}$$

The relative exergy consumption ratio is defined as the ratio of the exergy consumption of n'th component to the exergy consumption of the TJE system as:

$$\chi_j = \frac{\dot{E}x_{C,j}}{\dot{E}x_{C,TJE}} \tag{11}$$

Van Gool also stated that maximum improvement in the exergy efficiency for a process or system could be achieved when the exergy consumption is minimized. Consequently, he suggested that it is useful to employ the concept of an exergetic improvement potential when analyzing different processes, as applied by some investigators [5]. The exergetic improvement potential can be written as follows [2]:

$$\dot{E}x\dot{I}P_j = (1 - \psi)\dot{E}x_{C,j} \tag{12}$$

The exergetic improvement potential ratio:

$$\dot{\mathrm{ExIPR}}_j = \frac{\dot{\mathrm{ExIP}}_j}{\dot{\mathrm{Ex}}_{\mathrm{D},j}} \tag{13}$$

The relative exergetic improvement potential:

$$\dot{\mathrm{RExIP}}_j = \frac{\dot{\mathrm{ExIP}}_j}{\dot{\mathrm{ExIP}}_{\mathrm{tot}}} \tag{14}$$

Exergetic fuel-product ratio:

$$\mathrm{FPR}_{\mathrm{ex},j} = \frac{\dot{\mathrm{Ex}}_{\mathrm{in},j}}{\dot{\mathrm{Ex}}_{\mathrm{out},j}} \tag{15}$$

Sustainability index:

$$\mathrm{SI}_j = \frac{1}{(1 - \psi)} \tag{16}$$

2.5 The Specific Heat Capacity of Air and Combustion Gases

Combustion equilibrium equation for the engine is given as under mentioned:

$$C_{12}H_{23} + 379.61(0.7748N_2 + 0.2059O_2 + 0.0003CO_2 + 0.019H_2O)$$
$$\rightarrow 12.11CO_2 + 18.71H_2O + 60.41O_2 + 294.12N_2 \tag{17}$$
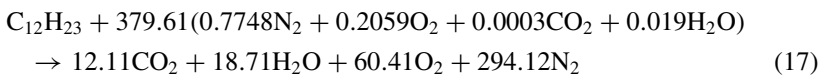
The specific heat capacity of the combustion gases:

$$c_{\mathrm{P,cg}}(T) = 0.91582 + \frac{0.01102}{10^2}T + \frac{0.01556}{10^5}T^2 - \frac{0.06724}{10^9}T^3 \tag{18}$$

The specific heat capacity of air is a function of temperature [6]:

$$c_{\mathrm{P,a}}(T) = 1.04841 - 0.000383719T + \frac{9.45378T^2}{10^7} - \frac{5.49031T^3}{10^{10}} + \frac{7.92981T^4}{10^{14}} \tag{19}$$

2.6 The Exergy Equilibrium Equations of the TJE and Its Components

The exergy equilibrium equations for the TJE and its primary segments are shown in Eqs. (20)–(29):

For air compressor:

$$\dot{E}x_1 + \dot{E}x_{11} - \dot{E}x_2 = \dot{E}x_{D,AC} \tag{20}$$

For combustion chamber:

$$\dot{E}x_2 + \dot{E}x_{2.3} - \dot{E}x_3 = \dot{E}x_{D,CC} \tag{21}$$

For gas turbine:

$$\left(\dot{E}x_3 - \dot{E}x_4\right) - \dot{E}x_7 = \dot{E}x_{D,GT} \tag{22}$$

For exhaust forward duct:

$$\dot{E}x_4 - \dot{E}x_5 = \dot{E}x_{D,EFD} \tag{23}$$

For aft exhaust duct:

$$\dot{E}x_5 - \dot{E}x_6 = \dot{E}x_{D,EAD} \tag{24}$$

For mechanical shaft:

$$\dot{E}x_7 - \dot{E}x_8 = \dot{E}x_{D,GTMS} \tag{25}$$

Work rate distribution:

$$\dot{E}x_{11} = \left(\dot{E}x_8 - \dot{E}x_9\right) \tag{26}$$

For the whole engine:

$$\left(\dot{E}x_1 + \dot{E}x_{2.3}\right) - \dot{E}x_6 = \dot{E}x_{D,ENG} \tag{27}$$

$$\dot{E}x_6 - \dot{E}x_{P,ENG} = \dot{E}x_{L,ENG} \tag{28}$$

$$\dot{E}x_{C,ENG} = \dot{E}x_{L,ENG} + \dot{E}x_{D,ENG} \tag{29}$$

2.7 Exergoeconomic Analysis

The economic analysis, conducted as part of the exergoeconomic analysis, provides the appropriate monetary values associated with the investment, operation, maintenance, and fuel costs of the system being analyzed [7, 8]. These values are used in the cost balances [9].

2.8 Exergoenvironomic Analysis

To minimize the environmental impacts, a primary target is to increase the efficiency of energy conversion processes and, thus, decreases the amount of fuel and the related overall environmental impacts, especially the release of carbon dioxide, which is one of the main components of greenhouse gas [10]. In this study, three steps were applied to carry out the exergoenvironomic analysis of gas turbine system. The first step is the determination of pollutant emission (CO and NO_x) in grams per kilogram of fuel, the estimation of the total cost rate of product and environmental impact and CO_2 emission calculation.

2.9 Determination of Pollutant Emission

In order to determine the pollutant emission in grams per kilogram of the fuel, the adiabatic flame temperature in the combustion chamber has to be computed first. The adiabatic flame temperature in the primary zone;

$$T_{PZ} = A\sigma^\alpha \exp\big(\beta(\sigma + \lambda)^2\big)\pi^x \theta^y \psi^z \tag{30}$$

where π is a dimensionless pressure P_2/P_{ref} (P_2 being the combustion pressure and $P_{ref} = 101{,}300$ Pa); θ is a dimensionless temperature T_2/T_{ref} (T_2 being the inlet temperature and $T_{ref} = 298.15$ K); ψ is the H/C atomic ratio ($\psi = 4$); $\sigma = \emptyset$ for $\phi \leq 1$ (ϕ is the fuel to air equivalent ratio), and $\sigma = \phi - 0.7$ for $\phi \geq 1$. Moreover, x, y, and z are quadratic functions of σ based on the following equations [11]:

$$x = a_1 + b_1\sigma + c_1\sigma^2 \tag{31}$$

$$y = a_2 + b_2\sigma + c_2\sigma^2 \tag{32}$$

$$z = a_3 + b_3\sigma + c_3\sigma^2 \tag{33}$$

Table 1 Constant for Eqs. (31)–(33)

Constants	0.3 < φ < 1		1 < φ < 1.6	
	0.92 < θ < 2	2 < θ < 3.2	0.92 < θ < 2	2 < θ < 3.2
A	2361.7644	2315.752	916.8261	1246.1778
α	0.1157	−0.0493	0.2885	0.3819
β	−0.9489	−1.1141	0.1456	0.3479
λ	−1.0976	−1.1807	−3.2771	−2.0365
a_1	0.0143	0.0106	0.0311	0.0361
b_1	−0.0553	−0.045	−0.078	−0.085
c_1	0.0526	0.0482	0.0497	0.0517
a_2	0.3955	0.5688	0.0254	0.0097
b_2	−0.4417	−0.55	0.2602	0.502
c_2	0.141	0.1319	−0.1318	−0.2471
a_3	0.0052	0.0108	0.0042	0.017
b_3	−0.1289	−0.1291	−0.1781	−0.1894
c_3	0.0827	0.0848	0.098	0.1037

where parameters A, α, β, λ, a_i, b_i, and c_i are constant parameters. These parameters are given in Table 1 regarding Eqs. (31)–(33) [12]. The calculated exergy rate and other thermodynamic parameters of the components of the TJE are given in Table 2.

The amount of CO and NO_x produced in the combustion chamber and combustion reaction depends on the adiabatic flame temperature [11]. Accordingly, to determine the pollutant emission in grams per kilogram of the fuel were used in this study.

$$\overset{\bullet}{m}_{NO_x} = \frac{0.15E16\tau^{0.5}\exp(-71,100/T_{PZ})}{P_2^{0.05}(\Delta P_2/P_2)} \quad \overset{\bullet}{m}_{CO} = \frac{0.719E9\exp(7800/T_{PZ})}{P_2^2\tau(\Delta P_2/P_2)} \quad (34)$$

where τ is the residence time in the combustion zone (τ is assumed constant and is equal to 0.002 s); T_{pz} is the primary zone combustion temperature; P_2 is the combustor inlet pressure; $\Delta P_2/P_2$ is the non-dimensional pressure drop in the combustion chamber.

2.10 Cost of Environmental Impact

The cost of environmental impact expresses the environmental impact as the total pollution damage ($/h) due to CO and NO_x emission by multiplying their respective flow rates by their corresponding unit damage cost (C_{CO}, and C_{NO_x} are equal to 0.02086 $/kgCO and 6.853 $/kgNO$_x$) [8]. In the present work, the cost of pollution damage is considered to be added directly to the expenditures that must be paid.

Table 2 Exergy rate and other thermodynamic parameters of the components of the TJE

Component	Ex_{in} kW	Ex_{out} kW	Ex_c kW	ψ %	α %	β %	χ %	ExIP kW	ExIPR %	RExIP %	FPR –	SI –
AC	2349.56	1664.23	685.33	70.83	10.79	57.51	13.29	199.9	29.17	4.77	1.41	3.43
CC	8013.21	5092.20	2921.01	63.55	46.01	245.11	56.64	1064.78	36.45	25.42	1.57	2.74
GT	2401.66	2349.56	52.10	97.83	0.82	4.37	1.01	1.13	2.17	0.03	1.02	46.10
EFD	2690.53	2643.97	46.56	98.27	0.73	3.91	0.90	0.81	1.73	0.02	1.02	57.79
EAD	2643.97	2597.54	46.44	98.24	0.73	3.90	0.90	0.82	1.76	0.02	1.02	56.94
GTMS	2349.56	2326.22	23.34	99.01	0.37	1.96	0.45	0.23	0.99	0.01	1.01	100.65
Total destruction				3786.78	317.76	73.43		59.64	1270.41	33.55	30.33	
Total loss				1370.47	115	26.57		21.59	459.77	33.55	10.98	
Engine basic	6348.97	1191.72	5157.2	18.77	81.23	432.76	100	4189.22	81.23	100	5.33	1.23
Engine improved	6348.97	2921.91	3427.07	46.02	53.98	117.29	100	1849.87	53.98	44.16	2.17	1.85

Where, Z_k, C_f, C_D, and C_{env} are the purchase cost of each component, fuel cost, cost of exergy destruction, and cost of environmental impact, respectively.

2.11 CO₂ Emissions Calculation

Using the combustion equations, the normalized CO_2 emission is expressed as below [13]:

$$\varepsilon = \frac{m_{CO_2}}{W_{net}} \tag{35}$$

The effect of CO_2 emissions is of considerable significance, such that reduction of its harmful release is twofold. The first is obviously related to communal and environmental health. The second, as suggested in many references, is improvement in reduction of harmful emissions in the combustion chamber can lead to improvements of gas turbine cycle efficiency. Reduction of the harmful emissions in the combustion chamber to the environment has proven its benefits in increasing system efficiency, which in turn increases sustainability by lengthening the lives of the fuel resources. A depletion number Dp could characterize the efficient fuel consumption.

The relationship between the depletion number and the exergy efficiency and SI are described by:

$$\eta_{ex} = 1 - Dp \quad SI = \frac{1}{Dp} \tag{36}$$

3   Results and Discussion

The exergoeconomic parameters considered in this study include average costs per unit of fuel exergy C_F and product exergy C_P, rate of exergy destruction $\dot{E}_D$, cost rate of exergy destruction $\dot{C}_D$, investment and O&M costs rate $\dot{Z}$, and exergoeconomic factor f. In analytical terms, the components with the highest value of $\dot{Z}_k + \dot{C}_{Dk}$ are considered the most significant components in terms of an exergoeconomic perspective. This provides a means of determining the level of priority a component should be given with respect to the improving of the system. For all the engines considered, the combustion chamber and air compressor have the highest value of the sum $\dot{Z}_k + \dot{C}_{Dk}$. Therefore, they are the most important components from the exergoeconomic viewpoint. The low value of exergoeconomic factor, f, associated with the combustion chamber suggests that the cost rate of exergy destruction is the dominate factor influencing the component. Hence, it is implied that the component efficiency is improved by increasing the capital investment. This can be achieved by increasing

gas turbine inlet temperature (GTIT). Table 3 shows the results of exergoenvironmental analysis of this work. The computed exergoenvironmental parameters are CO_2 emission, depletion number, sustainability index, cost flow rate of environmental impacts ($\dot{C}_{env}$) in \$/h, and total cost rates of products ($\dot{C}_{Tot}$) in \$/h. The study shows that increasing exergetic efficiency results in CO_2 emission reduction. The increase of exergetic efficiency is related to reduction of ambient inlet air temperature into the

Table 3 Exergy rate and other properties at various system locations for TJE

State	Fluid type	m (kg s^{-1})	p (kPa)	T (K)	c_p (KJ kg^{-1} K^{-1})	Ex (kW)	
0	Air	9.10	99.85	288.15	1.0037	0.00	
1	Air	9.10	99.85	288.15	1.0037	0.00	
2	Air	9.10	389.42	525.65	1.0342	1664.23	
2.3	Fuel (JP-8)	0.14	220.64	298.15		6348.97	
3	Combustion gases	9.24	369.94	1111.67	1.1261	5092.20	
4	Combustion gases	9.24	115.61	942.30	1.0832	2690.53	
5	Combustion gases	9.24	113.30	899.16	1.0822	2646.29	
6	Combustion gases	9.24	111.03	894.70	1.0812	2597.54	
7	Mechanical work					2349.56	
8	Mechanical work					2326.22	
9	Mechanical work					2314.22	
11	CO_2 emissions (kgCO$_2$/MWh)						112.75
12	Depletion number (Dp)						0.69
13	Sustainability index (SI)						1.23
14	Cost flow rate of env. $\dot{C}_{env}$ (\$/h) impact						796.54
15	Total cost rates of pr. $\dot{C}_{Tot}$ (\$/h)						3256.83

compressor. The efficiency of the system is directly linked to the entire system. However, it is apparent that the overall exergy destruction of the cycle decreases, while the sustainability index increases with decreasing compressor inlet temperature.

4 Conclusion

Exergy analysis provides useful information about the performance of the turbojet engine.

- The exergetic efficiency of the engine is accounted for 18.77% with 1191.72 kW as exhaust gases product for thrust.
- The highest exergy destruction between the components of the engine occurs within the combustion chamber with 2921.01 kW, as expected; hence, the combustion reaction is an irreversible process.
- The constructional and thermodynamic improvements on the engine can be made to decrease the exergy destruction and losses rate. After this improvements, the exergetic efficiency increases from 18.77 to 46.02%.
- The results from the exergoeconomic analysis, in common with those from the exergy analysis, show that the combustion chamber has the greatest cost of exergy destruction compared to other components. In addition, the results show that by increasing the turbine inlet temperature (TIT) the gas turbine cost of exergy destruction can be decreased.
- The finding solidifies the concept that the exergy loss in the combustion chamber is associated with the large temperature difference between the flame and the working fluid. Reducing this temperature difference reduces the exergy loss. Furthermore, cooling compressor inlet air allows the compression of more air per cycle, effectively increasing the gas turbine capacity.
- The cost rate of environmental impact is 796.54 $/h.
- The study further shows that increasing exergetic efficiency of gas turbine engine results in CO_2 emissions reduction. The increase of exergetic efficiency is related to reduction of ambient inlet air temperature into the compressor. This implies that improvement of a system's efficiency is twofold. By improving the most inefficient components of the system and utilizing the minimum adequate fuel flow rate ensuring maximum burn. The reduction in wasted unburned fuel and the reduction in overall system inefficiencies results in net CO_2 emissions reduction.

References

1. Lucia DJ (2011) Cruising in afterburner: air force fuel use and emerging energy policy. Energy Policy 39:5356–5365
2. Balli O, Hepbasli A (2014) Exergoeconomic, sustainability and environmental damage cost analyses of T56 turboprop engine. Energy 64:582–600

3. Kotas TJ (1995) The exergy method of thermal plant analyses, Reprint edn. Kieger, Malagar
4. Xiang JY et al (2004) Calculation for physical and chemical exergy of flows in system elaborating mixed-phase flows and a case study in an IRSOFC plant. Int J Energy Res 28:101–115
5. Van Gool W (1997) Energy policy: fairly tales and factualities. In: Innovation and technology-strategies and policies, pp 93–105. https://doi.org/10.1007/978-0-585-29606-7_6
6. Moran MJ, Shapiro HN (1995) Fundamentals of engineering thermodynamics. Wiley, New York
7. Siahaya Y (2009) Thermoeconomic analysis and optimization of gas turbine power plant. In: Proceedings of the international conference on fluid and thermal energy conversion
8. Ahmadi P, Dincer I (2011) Thermodynamic and exergoenvironmental analyses, and multi-objective optimization of a gas turbine power engine. Appl Therm Eng 31:14–15
9. Bejan A, Tsatsaronis G et al (1996) Thermal design and optimization. Wiley, New York
10. Ahmadi P, Rosen MA et al (2011) Greenhouse gas emission and exergo-environmental analyses of a trigeneration energy system. Int J Greenh Gas Control 5:1540–1549
11. Ahmadi P, Dincer I (2010) Exergo-environmental analysis and optimization of a cogeneration engine system using multimodal genetic algorithm (MGA). Energy 35:5161–5172
12. Gulder O (1986) Flame temperature estimation of conventional and future jet fuels. J Eng Gas Turbine Power 108:376–380
13. Altayib K (2011) Energy, exergy and exergoeconomic analyses of gas turbine based systems. M.Sc. thesis, University of Ontario Institute of Technology

Effect of Hydrogen Enrichment on Pollutant and Greenhouse Gases Formation and Exergy Efficiency of Methane MILD Combustion

Amin Khanlari, Ali Salavati-Zadeh, Mobin Mohammadi, Seyyed Bahram Nourani Najafi and Vahid Esfahanian

Abstract The present study aims to investigate the effect of hydrogen enrichment of the methane jet fuel on the formation of pollutants and greenhouse gases and exergy efficiency of a burner working on flameless MILD combustion mode for different amounts of oxygen present in the hot air co-flow stream using computational fluid dynamics coupled with detailed chemistry. OpenFOAM v. 3.0 is employed for the simulations. The results indicate considerable the pivotal role of the amount of hydrogen present in the fuel stream. It is also evident that hydrogen enrichment could be considered as a promising strategy for further increasing the exergy efficiency of burners working in MILD combustion mode.

Keywords MILD regime · Hydrogen enrichment · Exergy efficiency · Nitrogen oxide · Carbon monoxide · Greenhouse gases

Nomenclature

c_p Specific heat capacity

A. Khanlari · V. Esfahanian
Vehicle, Fuel and Environment Research Institute, University of Tehran, Tehran, Iran
e-mail: khanlari.amin@ut.ac.ir

V. Esfahanian
e-mail: evahid@ut.ac.ir

A. Salavati-Zadeh (✉)
Niroo Research Institute (NRI), Tehran, Iran
e-mail: asalavatizadeh@nri.ac.ir

M. Mohammadi
Faculty of Engineering, School of Mechanical Engineering, University of Tehran, Tehran, Iran
e-mail: mobin_mohammadi@ut.ac.ir

S. B. N. Najafi
Energy and Sustainability Research Institute Groningen (ESRIG), University of Groningen, Groningen, The Netherlands
e-mail: s.b.nourani.najafi@rug.nl

ex   Intensive molar exergy
Ex   Extensive molar exergy
R Universal gas constant
V Velocity
x Mole fraction

Greek Letters

η Thermodynamics efficiency
μ Dynamic (absolute) viscosity
ρ Density

Subscripts and Superscripts

2nd   Pertinent to second law
ch   Pertinent to chemical
D   Pertinent to destructed exergy
dry   Pertinent to dry
in   Pertinent to inlet
liq   Pertinent to liquid water
out   Pertinent to outlet
ph   Pertinent to physical
Q Pertinent to heat
ref   Pertinent to reference
sat   Pertinent to saturated
sp   Pertinent to species
vap   Pertinent to water vapor
W Pertinent to work

1   Introduction

One of the bases of industrial development is combustion of fossil fuels, which play a role in many processes, e.g., casting of metals, petroleum refining. Today, about 80% of the energy demand all over the world, which may grow speedily in the coming years, is provided through burning of fossil fuels [1]. On the other hand, despite the fact that enhancement of the energy efficiency of combustion process in industrial applications has been the serious duty for long time, other issues including

pollution emissions have also attracted the researchers and experts attention considering the strict regulatory agenda. In this framework, besides efficiency, air pollution, and global warming, which is believed to be mainly due to the increased emission of greenhouse gases, e.g., carbon dioxide, water vapor, and nitrous oxide are the main matters that should be taken into account in the forthcoming innovations and technologies related to industrial combustion.

Moderate or intense low-oxygen dilution (MILD hereafter) combustion [2] is a novel technology known to be a subset of high-temperature air combustion (HiTAC) [3], or more generally the high-temperature combustion technology (HiCOT). The cradle of these technologies is the idea of "large excess enthalpy combustion" presented in the beginning of 70s decade [4, 5]. This idea engages preheating the reactants by utilizing the hot flue gases. In MILD combustion regime the temperature distribution is uniform, and it comes with higher efficiency compared with conventional combustion regimes. Bearing all these into mind, MILD burners are becoming interesting choices to be employed in many industries, e.g., steel, cement, and glass-making factories [6, 7], industrial boilers [8] and also gas turbines [9–14]. More recently, MILD combustion is also playing role in a more innovative combustion technology referred to as MILD-oxyfuel combustion [15–17].

Using hydrogen as a clean fuel has attracted attention of many researchers. In spite of this, its usage comes with severe difficulties considering its high diffusivity, wide flammability limits, high flame speed, along with its tendency to form nitrogen oxides, especially in presence of air as oxidizer [18]. Nevertheless, many investigations address using hydrogen blended with natural gas in conventional combustion applications, e.g., internal combustion engines [19], along with mild combustors (e.g. [20–22]). The latter comes with several advantages considering the potential of MILD combustion for forming low amount on nitrogen oxides [23]. In this framework, the possibility of approaching a zero-emission MILD furnace for pure hydrogen fuel without air preheating was indicated by Ayoub et al. [24].

The dissimilarities between MILD and conventional combustion regimes have made many researchers investigate the characteristics of MILD burners. Some researches indicated the crucial role of the model considered for simulating the interaction between the combustion chemistry and turbulence phenomena within the flow field [7, 25–27]. The latter showed shortcomings associated with the well-known EDC model [28–30], in simulating the MILD flame structure especially in the presence of very low oxygen. Later, many researches employed Partially Stirred Reactor (PaSR) [31], as an improved form of the EDC model (e.g. [32, 33]). On the other hand, importance of boundary condition treatment was also proved, especially in case of blend of CH_4/H_2 MILD combustion [34, 35]. Also, the importance of considering molecular diffusion in simulating MILD burners was proved by Parente et al. [25], Mardani et al. [36], and Salavati-Zadeh et al. [1]. The indispensable importance of employing actual temperature profile instead of nominal in DNS simulation of MILD combustion on prediction of ignition delay is shown [37]. More recently, Chitgarha and Mardani [38] analyzed the flamelet approach for simulation of MILD burners.

They recommended employment of higher values for scalar dissipation rates when increasing the amount of oxygen in the hot air co-flow stream.

The potential of MILD combustion regime for the production of very low amounts of nitrogen oxides could be considered as one of its most interesting features. According to literature, this important characteristic could be contemplated to be due to three main reasons [23]. First, the homogenous combustion zones which cause reduction in maximum temperature and accordingly in the amount of NO_x formed [39], second, local reduction in availability of the main reactants leading to nitrogen oxides, i.e., oxygen, and finally affecting the NNH, N_2O, prompt along with NO_x re-burning paths causes change in the chemistry of NO_x formation. Nicolle and Dagaut [40], used PaSR model to study the mechanisms of formation and destruction of NO_x under MILD combustion regime. This research proved that in contrast to normal burning regimes, the NNH and N_2O routes are significantly important when being in MILD combustion regime. It also addressed the role of NO_x re-burning regime, whose significance was previously highlighted [41]. The conclusion of Nicolle and Dagaut [40] regarding the importance of NNH and N_2O routes was later approved by Galletti et al. [7], especially when hydrogen was present in the fuel stream. Sepman et al. [42] studied the effects of adding hydrogen to laminar MILD flame of methane and proved the formation of NO from fuel burning to be insignificant, comparing to mixing of the nitrogen oxide produced in the co-flow with the MILD combustion products. Later, Li et al. [43] indicated the influence of equivalence ratio on significance of different paths of forming NO in MILD combustion regime under lean conditions. The N_2O route was proved to be dominant for equivalence ratios less than 0.8. It was also shown that this conclusion does not depend on the amounts of hydrogen and oxygen present in the fuel and hot oxidizer co-flow streams. Nevertheless, for higher equivalence ratios, they proved that the amount of hydrogen present in the fuel stream begins to become important increasing the role of NNH intermediate route and decreasing the influence of prompt path. For lower equivalence ratios, they also pointed out that the NO re-burning reaction has a crucial role in reduction of the amount of nitrogen oxide produced. In spite of this, Galletti et al. [44] proved the significant role of NNH route in some locations which contributes to more than 50% of the total NO produced in higher equivalence ratios, using reduced NO mechanisms for CFD results post-process.

On the other hand, formation of CO and CO_2 has also been the subject of many investigations. Yu et al. [45] stated that increasing the amount of hydrogen used for enrichment of the fuel stream will decrease formation of CO in MILD regime. The research of Mardani et al. [46] could be considered as one of the most comprehensive examples in this regard. Using CFD modeling and well-stirred reactor zero-dimensional analysis, formation of carbon oxides from pure CH_4 oxidation under MILD conditions were investigated. Along with illustrating an unpredicted behavior of carbon oxides formation when reducing the amount of oxygen in oxidizer stream, which was previously concluded also by Christo and Dally [47], Mardani et al. [46] also stated that higher levels of O_2, the activation of methane low oxidation

pathways is responsible for enhancement of CO formation under MILD conditions. While Mardani et al. [46] mostly addressed contribution of CH_3 conversion path to ethane, the importance of acetylene in formation of CO was found to be comparable to the mentioned path under MILD conditions by Zou et al. [48], who opted opposed flame configuration to conduct their research. The impact of other parameters, e.g., equivalence and entrainment ratios on reduction of carbon monoxide formation was also pointed out by Zou et al. [48].

It is also found crucial to recognize the factors causing failure to make good use of energy in combustion systems. Besides, analyzing the energy from the aspect of its quality and usefulness is also crucial. Hence, several works have addressed exergy analysis based on the second law of thermodynamics in different systems, e.g., power plants, internal combustion engines, gas turbines, fuel cells, etc. [49–56]. Some researchers have also addressed the exergy analysis for MILD burners. Chen et al. [57] studied the impact of air inlet temperature and the equivalence ratio on entropy generation in counter-flow diffusion flames of hydrogen/air mixtures for different combustion regimes and concluded that in contrast to MILD combustion of methane in the same configuration, in which dilution decreases the entropy generation strength, this intensity for the MILD H_2-air counterflow diffusion flame shows variable trend, i.e., it may increase for higher dilutions. Later, Hosseini and Wahid [58] performed second law analysis of methane combustion in both conventional and flameless modes. They reported 13% higher exergy efficiency for flameless combustion mode with respect to conventional combustion at stoichiometric conditions, at which the maximum exergy efficiency was yielded. More recently, Liu et al. [59] performed exergy efficiency analysis on MILD Oxyfuel combustion of methane and identified the major parameters contributing to destruction of exergy.

At the present state, it seems pivotal to focus on the influence of hydrogen addition to methane on exergy efficiency of MILD combustion in co-flow configuration for different amounts of oxygen present in hot co-flow stream, which is the main aim of the current investigation. Besides, the flame structure along with formation of NO, CO, and CO_2 are also studied. To accomplish this, CFD is coupled with detailed chemistry to simulate the burner previously studied experimentally by Dally et al. [60].

2 Flow Field Simulation Strategy

The methodology of the simulations follows the path reported by Salavati-Zadeh et al. [1], for the similar burner configuration (Adelaide fuel-jet-in-hot-co-flow burner [60]) using the same computational grid. Nevertheless, to achieve more accurate results on distribution of species, especially when very low amount of oxygen molecule is present in the hot air co-flow stream, the KEE-58 reduced scheme utilized in the above-mentioned research for simulating the combustion chemistry is substituted by

the GRI-Mech 3.0 detailed mechanism. The simulations are carried out for 3 different amounts of oxygen in hot diluted co-flow stream, i.e., 3, 6, and 9%, and 5 different amounts of hydrogen in the fuel stream, 3, 5, 7, 9, and 11%. All the amounts are expressed on mass basis. The simulations are carried out using OpenFOAM v. 3.0 software package.

2.1 Exergy Efficiency Analysis

In order to recognize the sources of entropy generation in this combustion system, i.e., mixing, reaction, mass diffusion, etc., an exergy analysis for steady, reactive flow is performed over the control volume surrounding the reaction zone. Exergy content of both input and output streams is considered to be summation of two parts, i.e., physical and chemical. Taking the ideal gas assumption into account, Eq. (1) is utilized for calculation of the mixture's physical exergy [61]:

$$
\begin{aligned}
\mathrm{ex_{ph}} &= (h - h_{ref}) - (s - s_{ref}) + \frac{1}{2}\left(V^2 - V_{ref}^2\right) \\
&= c_p T_{ref}\left[\left(\frac{T}{T_{ref}}\right) - 1 - \ln\left(\frac{T}{T_{ref}}\right)\right] + R T_{ref}\ln\left(\frac{P}{P_{ref}}\right) + \frac{1}{2}V^2
\end{aligned}
\tag{1}
$$

The standard environmental conditions are considered to be the dead state as $p_{ref} = 101.325$ kPa and $T_{ref} = 298.15$ K. NASA polynomials are employed for computation of the specific heat capacity. It is worth noting that during combustion process, the pressure is constant and is equal to p_{ref}. On the other hand, chemical exergy is obtained from Eq. (2) [58]:

$$
\mathrm{ex_{ch}} = \sum_{i=1}^{n_{sp}} x_i \mathrm{ex_{ch}^i} + R T_{ref} \sum_{i=1}^{n_{sp}} x_i \ln_{x_i}
\tag{2}
$$

where x_i and $\mathrm{ex_{ch}^i}$ are mole fraction and molar standard chemical exergy of ith species, respectively, and n_{sp} stands for number of species which are taken into account in the calculations. It should be considered that GRI-3.0 contains 53 species. Nevertheless, 32 species are collected as in Table 1. The contents of this table are obtained by indirect method using the concept of Gibbs formation free energy of each species and its related primary reactions, as in [62]. The eliminated species have small amounts in reaction zone. Due to the non-uniform distribution of temperature field in output stream, it would be possible that a fraction of water vapor be condensed. Therefore, it is essential to correct the chemical exergy of the output stream to take the amount of liquid water formed into account. Partial pressure of water vapor in mixture is obtained by Eq. (3) [63]:

$$
P_{vap} = x_{vap} P_{ref}
\tag{3}
$$

Table 1 Standard molar chemical exergy

Species	$\text{Ex}_{ch}\left(\frac{KJ}{mole}\right)$	Species	$\text{Ex}_{ch}\left(\frac{KJ}{mole}\right)$
C	1485.5	O	233.7
CH	1225.5	O_2	3.97
CH_2	1030.5	H	331.3
CH_3	900.5	H_2	236.09
CH_4	831.2	H_2O	9.5
C_2H	1217.35	H_2O_2	134.58
C_2H_2	1265.0	N	455.94
C_2H_3	1312.65	N_2	0.72
C_2H_4	1360.3	N_2O	106.9
C_2H_5	1427.65	NO	88.9
C_2H_6	1495.0	NO_2	55.6
C_3H_8	2152.8	NH	489.66
CH_2O	538.4	NH_2	672.74
CH_3OH	721.61	NH_3	337.9
CO	274.71	CN	845.0
CO_2	19.48	HCN	682.72

where x_{vap} is mole fraction of water vapor, p_{vap}, having a corresponding T_{vap} in equilibrium conditions, is calculated in each computational cell within the output region. The relation between this pressure and temperature is expressed as a function using interpolating Lagrangian polynomials over experimental data. If T_{vap} is less than T_{ref}, the amount of water which converts from vapor to liquid state, is found using Eq. (4) [63]:

$$P_{sat} = \frac{x_{vap}}{x_{vap} + x_{dry}} P_{ref} \tag{4}$$

where $p_{sat} = 0.0316$ is partial pressure of water vapor in T_{ref} [58] and x_{dry} is the mole fraction of all non-water species. To calculate the revised value of the chemical exergy, Eq. (5) is employed:

$$ex_{ch,rev} = x_{dry} \times ex_{ch,dry} + x_{liq} \times ex_{ch,liq} \tag{5}$$

where, x_{liq} and $ex_{ch,liq}$ are mole fraction and chemical exergy of the liquid water formed, respectively. As aforementioned, the summation of contributions of both physical exergy (ex_{ph}) and revised chemical exergy ($ex_{ch,rev}$) at each section, i.e., inlet and exhaust, yields the total exergy.

Finally, the rate of exergy destruction in the control volume over the flame should be calculated. To accomplish this, one should bear in the mind that employment of zero gradient assumption for temperature in boundaries has eliminated the heat

transfer phenomenon from the walls and the exergy flow associated with it. Meanwhile, the exergy flow due to mechanical work is also zero considering the fact that no mechanical work exists within the burner. So, the destructed exergy, $\dot{Ex}_D$, could simply be computed by subtracting the output exergy from the input exergy, i.e., Equation (6);

$$\dot{Ex}_D = \sum \dot{m}_{in} ex_{in} - \sum \dot{m}_{out} ex_{out} \qquad (6)$$

Eventually, the second law efficiency could be achieved with Eq. (7):

$$\eta^{2nd} = \frac{\dot{Ex}_{out}}{\dot{Ex}_{in}} \times 100 \qquad (7)$$

3 Results and Discussion

The contours of temperature within the burner are brought in Figs. 1, 2 and 3 for oxygen mass concentrations of 3, 6, and 9% in diluted hot co-flow, respectively. Meanwhile, in each figure, the results corresponding to different amounts of hydrogen in the fuel stream is also depicted. It could be indicated from the figures that with increase in the amount of hydrogen, the hot region begins to grow and approaches the fuel nozzle, which is especially obvious for the case of hot co-flow with 3% of oxygen, i.e., Fig. 1. Also, it could be observed that the maximum temperature is sensitive to the amount of oxygen in the hot co-flow stream. With increase in the amount of oxygen, the peak temperature increases. The oxygen amount in the hot co-flow stream also makes the hot region grow. This could be observed by comparing Figs. 1, 2 and 3. With increase in the amount of oxygen, the temperature of the hot zone, i.e., the peak temperature, increases, and this zone becomes thicker.

These observations could also be interpreted under the light of an assessment on the influences of the oxygen in the hot air co-flow stream and hydrogen in the fuel stream on the distribution on hydroxyl and formaldehyde radicals in the field which is brought in Figs. 4, 5, 6, 7, 8 and 9.

Declaration on the roles of hydroxyl, formyl, and formaldehyde in indication of flame existence and heat release quality has previously been addressed in some researches [32, 33, 47, 64]. Presence of OH is considered to be an important sign of stronger flame front with thicker hot zone, whereas formation of formaldehyde (CH_2O) along with formyl (HCO) radicals ends in a weaker flame by increasing the dissipation of heat and reducing the reaction rates. This point is discussed here for sake of more clarity: The inevitable dissipation of heat from the flame area coupled with high residence time of methane molecule in this area, end in passing of some portion of those molecules through the flame front and formation of some premixed regions which burn when facing the hot co-flow stream of air having a temperature
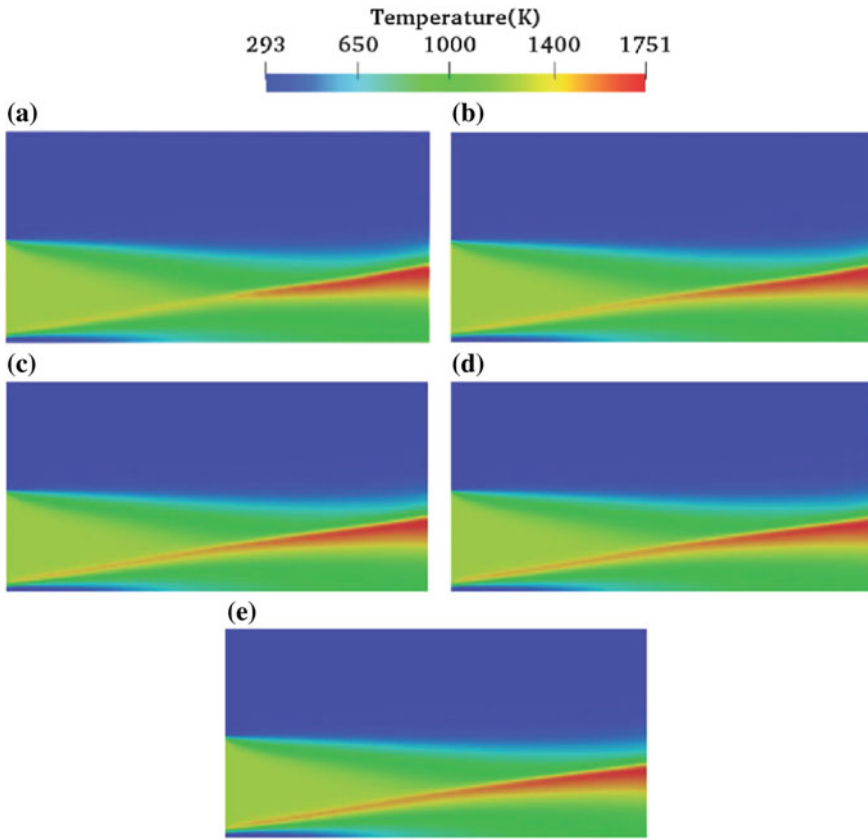
Fig. 1 Temperature field for case: **a** O_3H_3, **b** O_3H_5, **c** O_3H_7, **d** O_3H_9 and **e** O_3H_{11}

higher than the self-ignition temperature. Formation of formaldehyde radical is a criteria for fuel diffusion to hot oxidizer stream and existence of such bubble-shaped premixed regions, which in turn enhances the dissipation of heat and depletion of the reaction rates. Increasing the amount of H_2 and O_2 in the flame improves the reaction rates and the mixture capability to ignite and strengthen the flame (Figs. 4, 5 and 6). On the other hand, this rise in the amounts of oxygen and hydrogen molecules causes disappearance of the mentioned premixed zones (Figs. 7, 8 and 9).
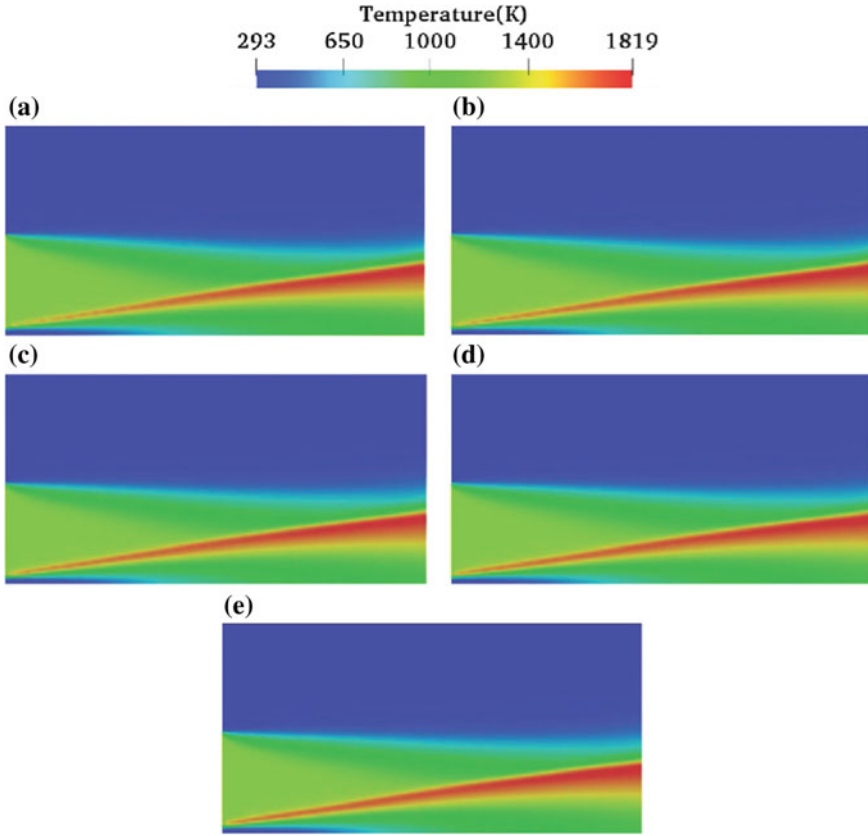
Fig. 2 Temperature field for case: **a** O_6H_3, **b** O_6H_5, **c** O_6H_7, **d** O_6H_9 and **e** O_6H_{11}

The temperature profiles for the different flames studied are brought in Fig. 10. The data are illustrated for two different positions from the nozzle. The temperature profile for 30 mm from the nozzle is depicted in the figures on the left side, whereas the same data for axial distance of 120 mm from the nozzle are brought in the plots on the right side of the figure. It could be indicated from the figures that when being close to nozzle, addition of hydrogen to fuel stream will cause an increase in the peak temperature. Same result can be deduced for increasing the amount of oxygen in the hot air co-flow stream. However, for higher amounts of oxygen, the effect of hydrogen on the peak temperature in the small axial distances from the nozzle becomes little as could be observed from Fig. 10a, c, e. Also, as we go far from the nozzle and at the axial distance of 120 mm, increasing the amount of hydrogen in the fuel stream has negligible effect on the peak temperature, which could be due to entrainment of oxygen from the surrounding air. In spite of this, the average temperature slightly increases when having more hydrogen within the fuel stream (Fig. 10b, d, f).
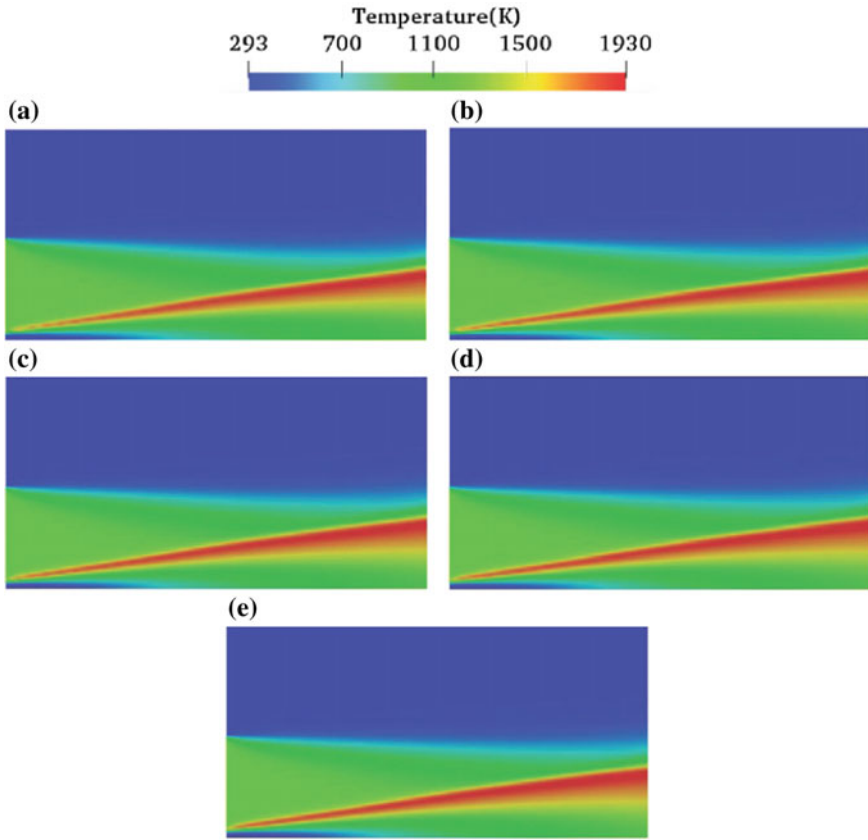
Fig. 3 Temperature field for case: **a** O_9H_3, **b** O_9H_5, **c** O_9H_7, **d** O_9H_9 and **e** O_9H_{11}

Same results could be indicated from the profile of NO in two different axial positions from the nozzle, 30 mm illustrated in Fig. 11a, c, e, and 120 mm illustrated in Fig. 11b, d, f. At the axial distance of 30 mm, any rise in the amount of hydrogen present in the fuel stream, will increase production of NO. This increase could be interpreted through dominancy of zel'dovich mechanism, i.e., thermal NO (Eq. 8a–8c). Increase in the amount of hydrogen, as seen before, ends in higher temperature and higher amount of hydroxyl radical, which taking the zel'dovich mechanism into account, enhances the production of NO (Eq. 8c):

$$N_2 + O \rightleftharpoons NO + N \tag{8a}$$

$$N + O_2 \rightleftharpoons NO + O \tag{8b}$$

$$N + OH \rightleftharpoons NO + H \tag{8c}$$
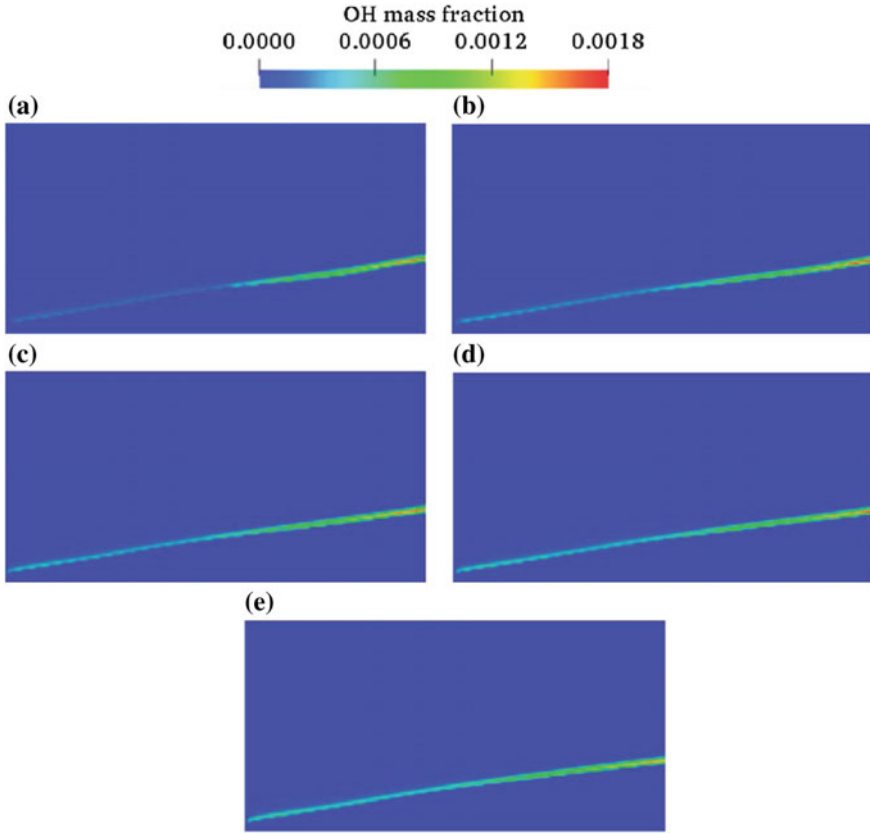
Fig. 4 OH distribution for case: **a** O_3H_3, **b** O_3H_5, **c** O_3H_7, **d** O_3H_9 and **e** O_3H_{11}

The same phenomenon could be observed when increasing the amount of oxygen molecule in the hot co-flow stream. Again, increase in temperature and availability of reactants could be considered to justify the observations. Meanwhile, as the distance from the nozzle increases, i.e., Fig. 11b, d, f, the sensitivity of NO formed to the amount of hydrogen present in the fuel stream begins to decay. This influence is less in higher amounts of oxygen present in the hot air co-flow stream. The profile of show similar behavior with respect to amount of hydrogen and oxygen (Fig. 12a–f). Additionally, it has a minimum in the same radial position where NO has a peak, proving the importance of re-burning path in formation of NO_2.
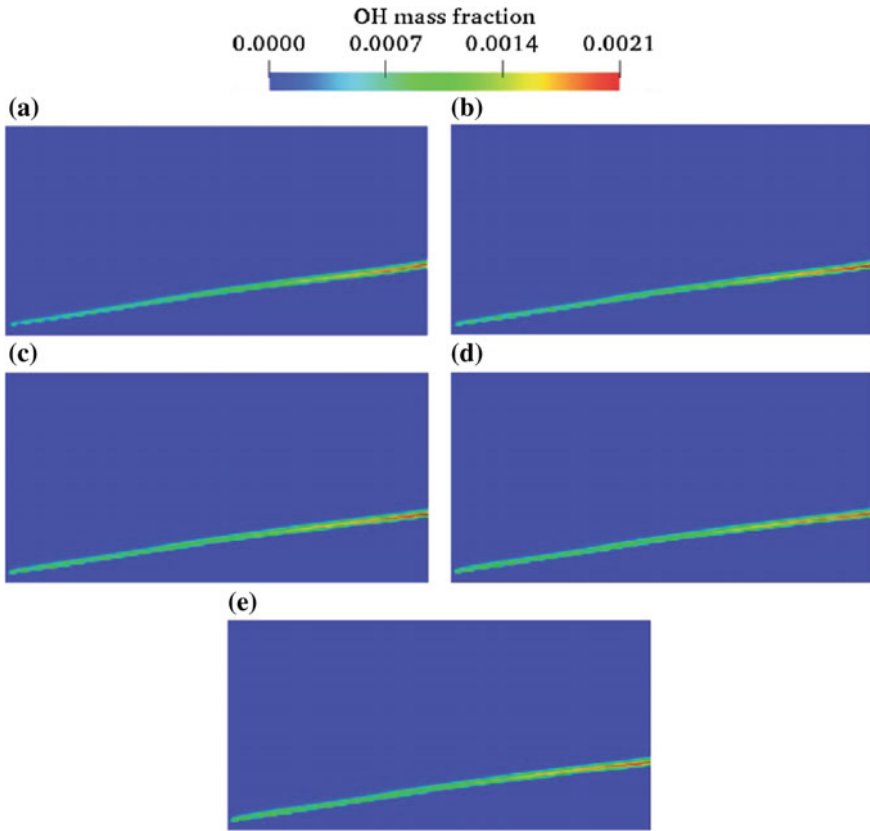
Fig. 5 OH distribution for case: **a** O_6H_3, **b** O_6H_5, **c** O_6H_7, **d** O_6H_9 and **e** O_6H_{11}

Assessment on the results depicted in Figs. 13 and 14 justify the increase in the amount of carbon oxide species with increase in the amount of oxygen, considering increase in the availability of the reactants. On the other hand, increase in the amount of hydrogen present in the fuel stream also enhances the formation of CO. This influence decays as we go far from the nozzle. It could be indicated from Fig. 13a–f that the peak amount of carbon monoxide does not depend on the amount of hydrogen present in the fuel stream. The effects of oxygen and hydrogen present in hot air co-flow and fuel streams on the second law efficiency of the burner are illustrated in Fig. 15. In all the cases, high second law efficiency of MILD combustion is evident, which seems to be due to more uniform distributions within a MILD burner, causing depletion of exergy destruction. As depicted, increase in the amount of hydrogen will enhance this efficiency monotonically, whereas the slope of increase in second law efficiency with increase in the amount of oxygen decays. Therefore, it seems that there would be a maximum, after which the efficiency begins to become lower as we proceed to conventional combustion regime.
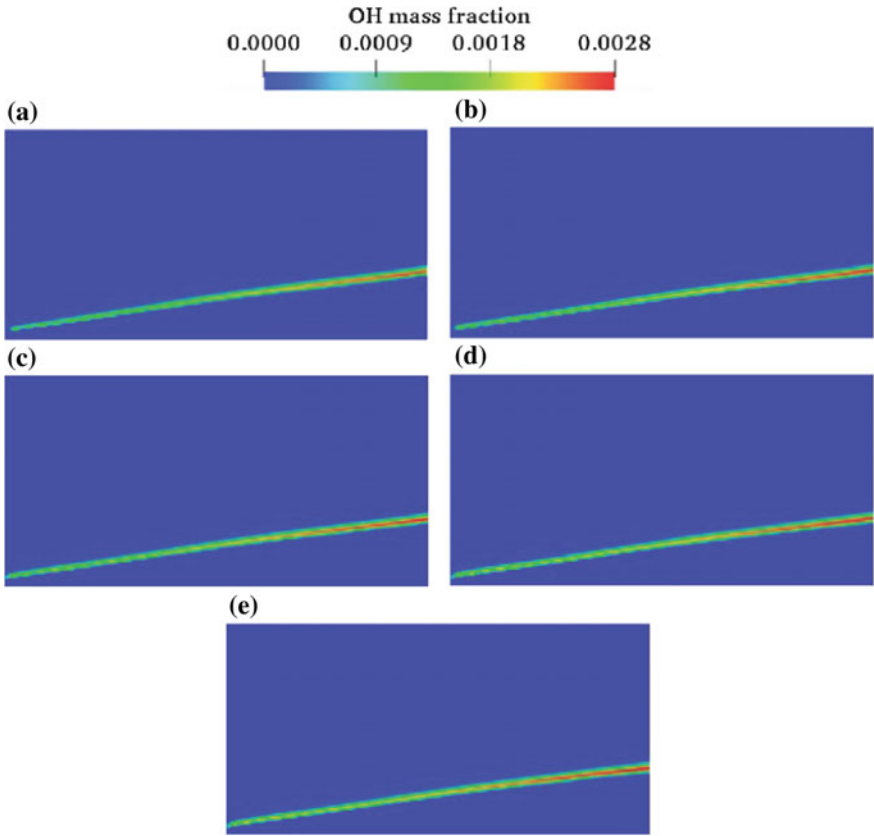
Fig. 6 OH distribution for case: **a** O_9H_3, **b** O_9H_5, **c** O_9H_7, **d** O_9H_9 and **e** O_9H_{11}
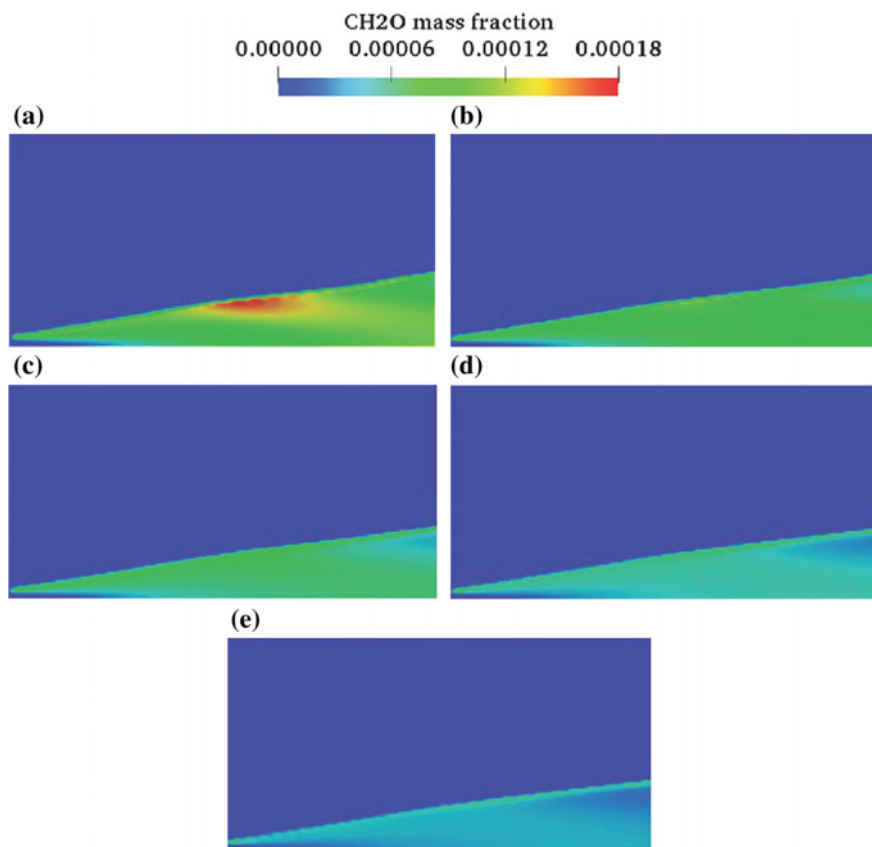
Fig. 7 CH$_2$O distribution for case: **a** O$_3$H$_3$, **b** O$_3$H$_5$, **c** O$_3$H$_7$, **d** O$_3$H$_9$ and **e** O$_3$H$_{11}$
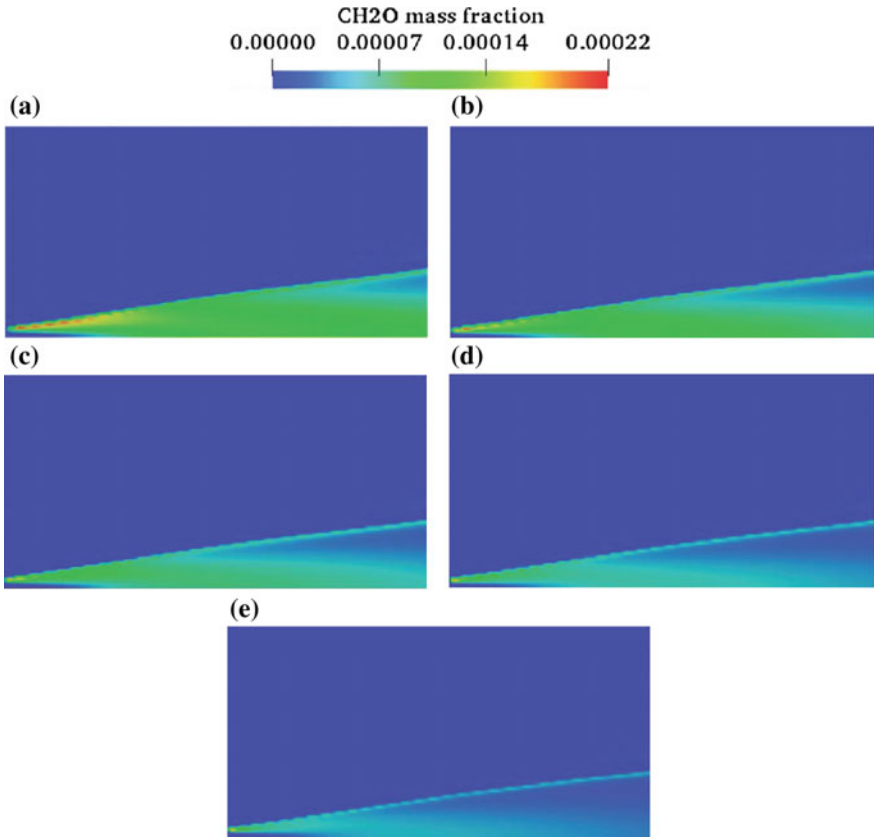
Fig. 8 CH_2O distribution for case: **a** O_6H_3, **b** O_6H_5, **c** O_6H_7, **d** O_6H_9 and **e** O_6H_{11}
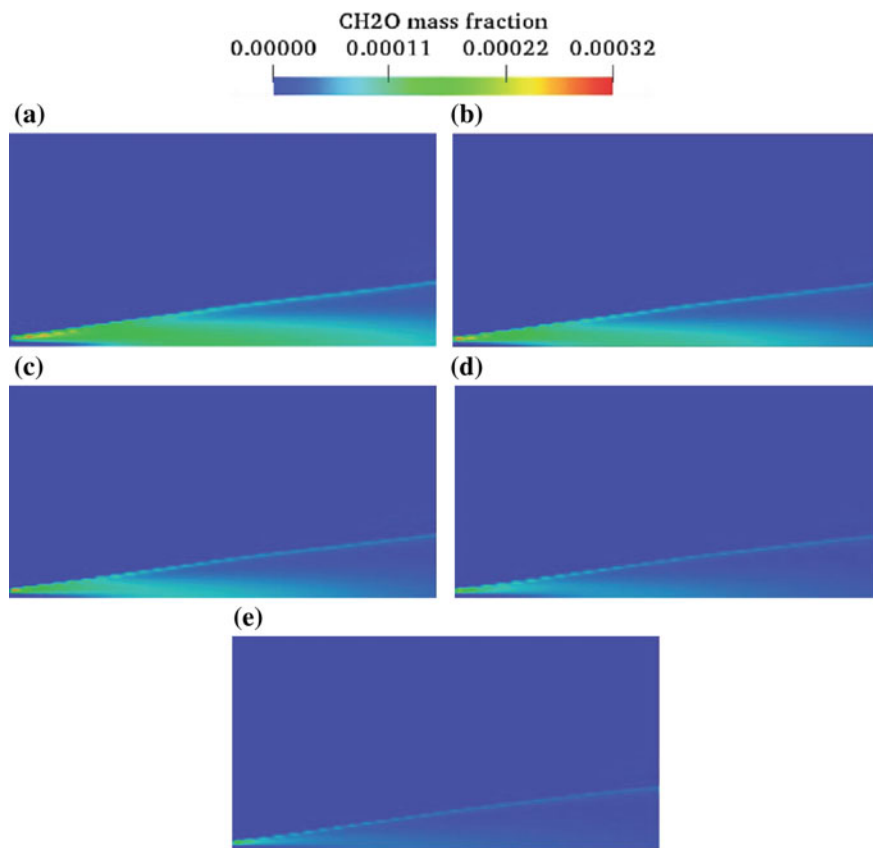
Fig. 9 CH_2O distribution for case: **a** O_9H_3, **b** O_9H_5, **c** O_9H_7, **d** O_9H_9 and **e** O_9H_{11}
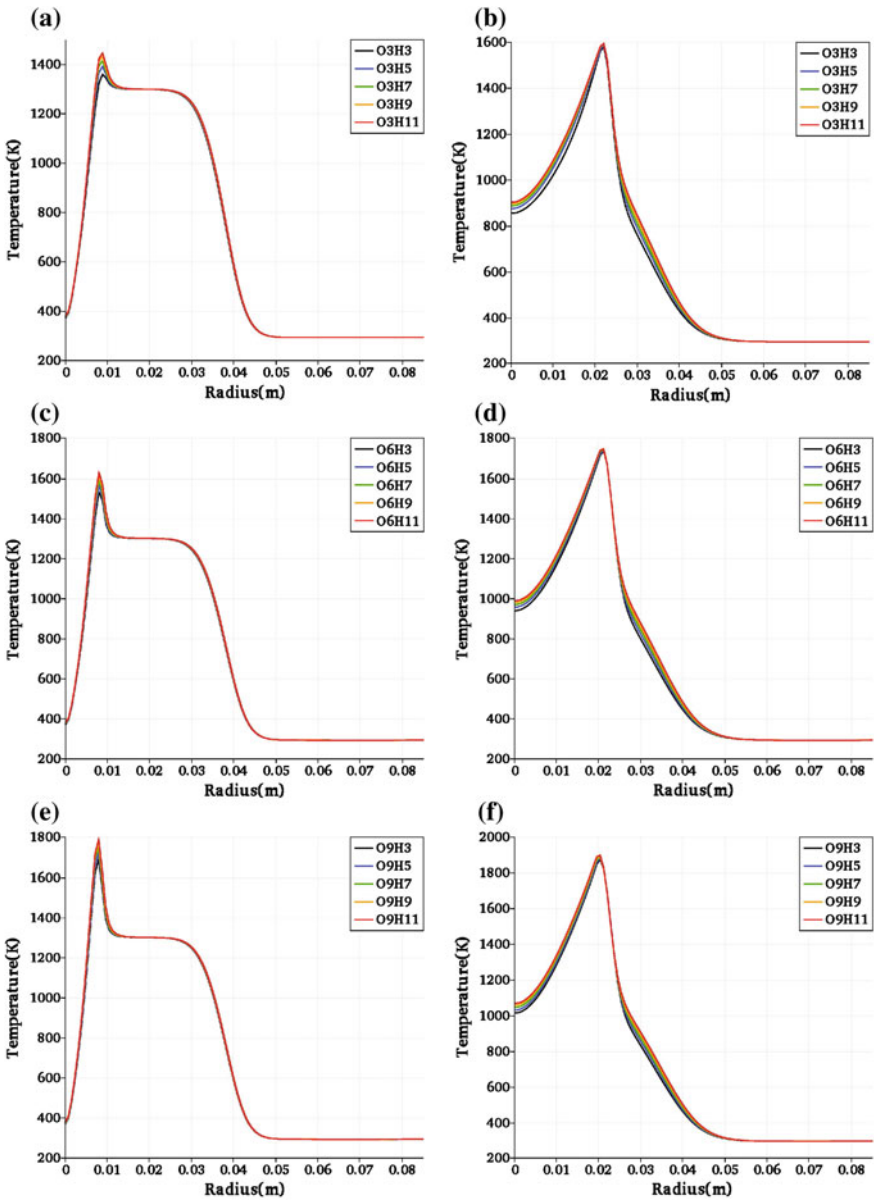
Fig. 10 Diagram of radial temperature for: **a** O_3 at $Z = 3$ cm, **b** O_3 at $Z = 12$ cm, **c** O_6 at $Z = 3$ cm, **d** O_6 at $Z = 12$ cm, **e** O_9 at $Z = 3$ cm, **f** O_9 at $Z = 12$ cm
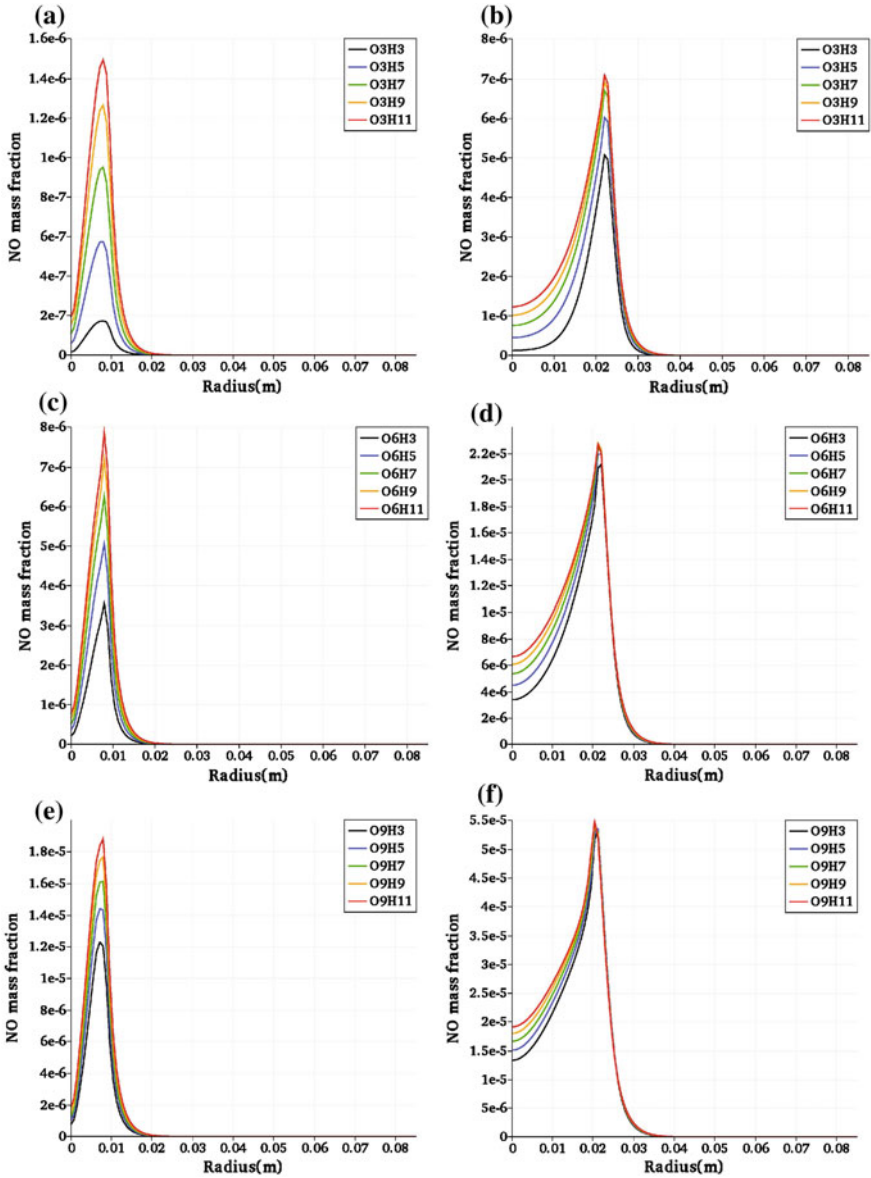
Fig. 11 Diagram of radial NO mass fraction for: **a** O_3 at $Z = 3$ cm, **b** O_3 at $Z = 12$ cm, **c** O_6 at $Z = 3$ cm, **d** O_6 at $Z = 12$ cm, **e** O_9 at $Z = 3$ cm, **f** O_9 at $Z = 12$ cm
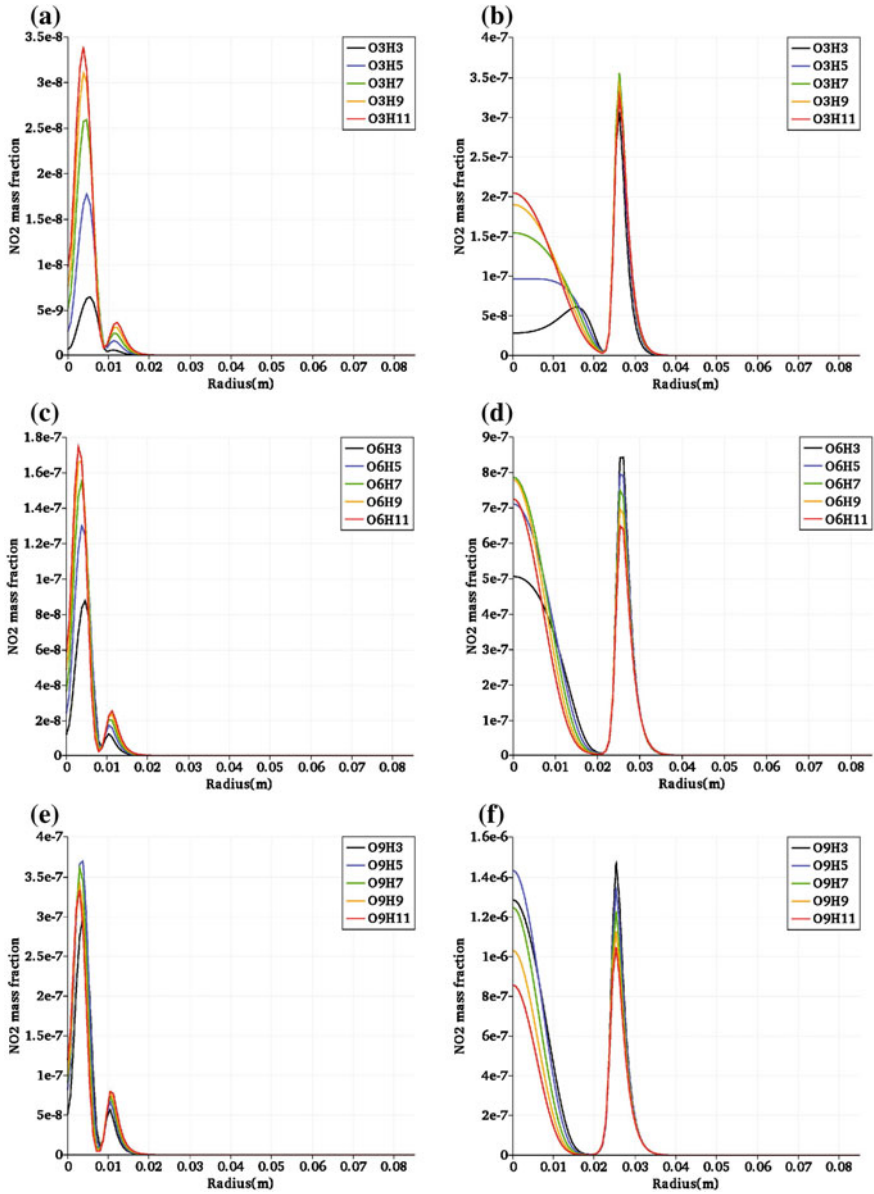
Fig. 12 Diagram of radial NO$_2$ mass fraction for: **a** O$_3$ at $Z = 3$ cm, **b** O$_3$ at $Z = 12$ cm, **c** O$_6$ at $Z = 3$ cm, **d** O$_6$ at $Z = 12$ cm, **e** O$_9$ at $Z = 3$ cm, **f** O$_9$ at $Z = 12$ cm
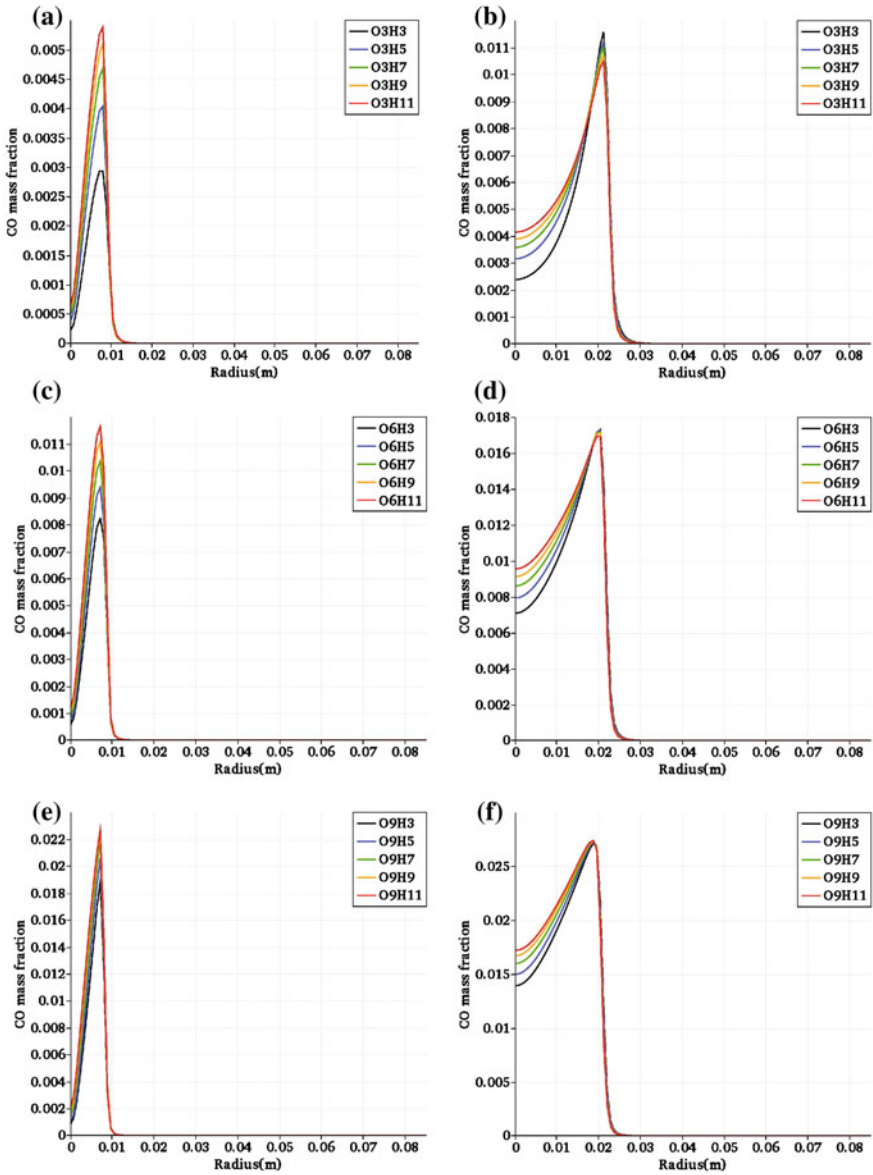
Fig. 13 Diagram of radial CO mass fraction for: **a** O_3 at $Z = 3$ cm, **b** O_3 at $Z = 12$ cm, **c** O_6 at $Z = 3$ cm, **d** O_6 at $Z = 12$ cm, **e** O_9 at $Z = 3$ cm, **f** O_9 at $Z = 12$ cm
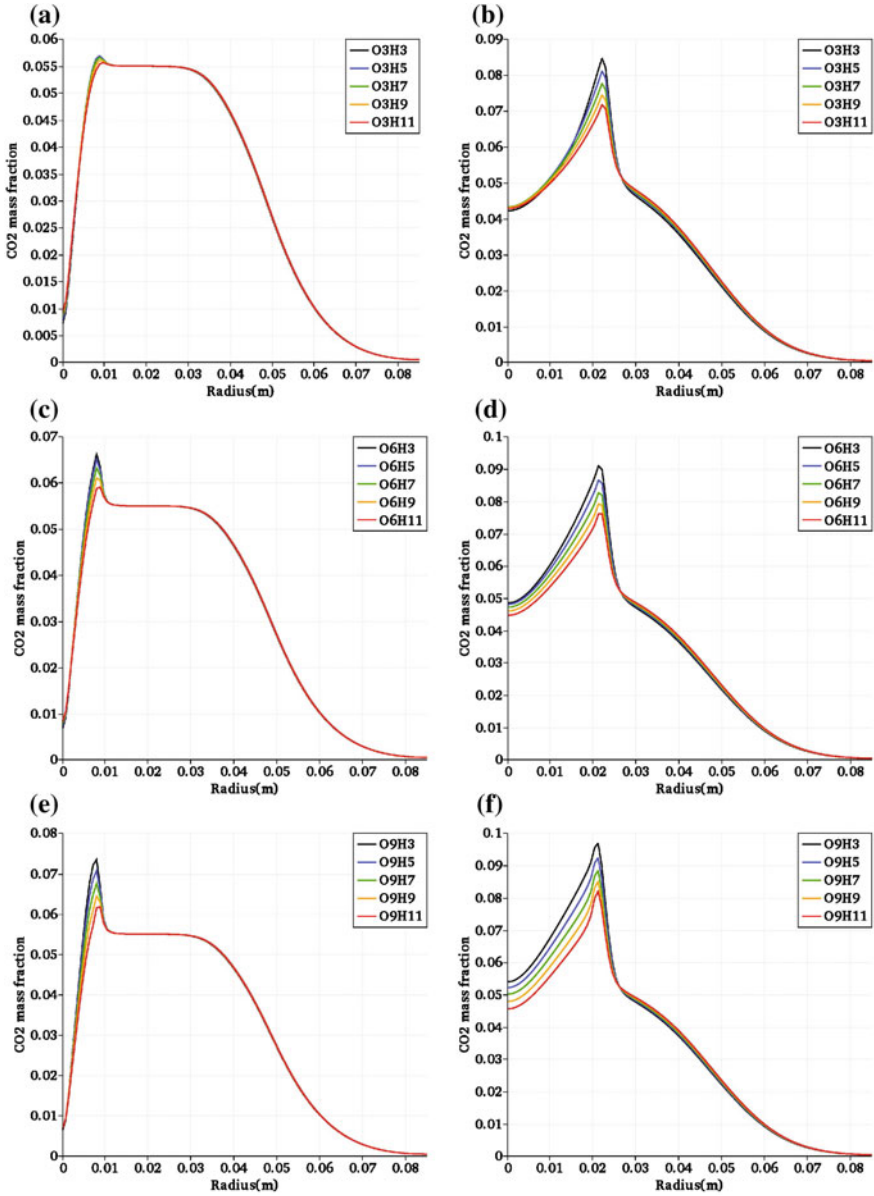
Fig. 14 Diagram of radial CO_2 mass fraction for: **a** O_3 at $Z = 3$ cm, **b** O_3 at $Z = 12$ cm, **c** O_6 at $Z = 3$ cm, **d** O_6 at $Z = 12$ cm, **e** O_9 at $Z = 3$ cm, **f** O_9 at $Z = 12$ cm
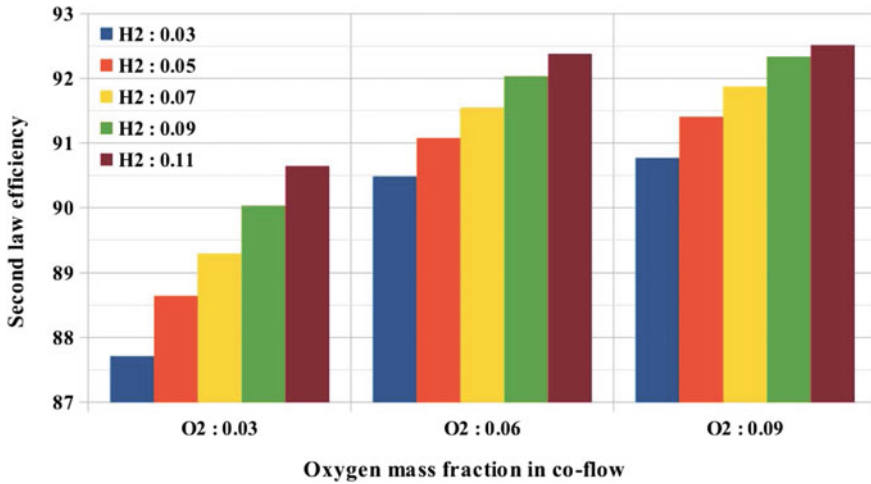
Fig. 15 Exergy analysis

4　Conclusion

For a MILD burner working with blended CH_4/H_2 fuel [60], the effect of hydrogen in fuel stream and oxygen in the hot air co-flow stream on formation of pollutants and CO_2 is studied. The simulations are carried out using OpenFOAM v. 3.0 solver package. The RNG $k - \epsilon$ model is employed for simulation of turbulence flow field, chemistry-turbulence interaction is simulated using Partially Stirred Reactor (PaSR) model. The GRI-Mech 3.0 detailed chemical scheme is utilized to model the combustion chemistry. The following results were obtained:

1. Increase in the amount of hydrogen and oxygen cause growth of hot zone and increase in the peak temperature.
2. With increase in the amount of hydrogen present in the fuel stream, the peak temperature rises. Nevertheless, for higher amounts of oxygen in hot air co-flow stream, the effect of hydrogen on the peak temperature in the small axial distances from the nozzle becomes little.
3. As we go far from the nozzle, increasing the amount of hydrogen in the fuel stream has negligible effect on the peak temperature.
4. Increase in the amount of oxygen and hydrogen will cause production of more NO in axial positions close to fuel nozzle. For axial positions far from the nozzle, especially at higher amounts of oxygen, the influence of hydrogen on the maximum value of NO vanishes.
5. An increase in the amount of hydrogen present in the fuel stream also enhances the formation of CO. This influence decays as we go far from the nozzle.
6. An increase in the amount of hydrogen will enhance the second law efficiency monotonically, whereas the slope of increase in second law efficiency with increase in the amount of oxygen decays.

References

1. Salavati-Zadeh A, Esfahanian V, Nourani Najafi SB, Saeed H, Mohammadi M (2018) Kinetic simulation of flameless burners with methane/hydrogen blended fuel: effects of molecular diffusion and Schmidt number. Int J Hydrog Energy 43(11):5972–5983. https://doi.org/10.1016/j.ijhydene.2017.11.149
2. Cavaliere A, de Joannon M (2004) Mild combustion. Prog Energy Combust Sci 30(4):329–366. https://doi.org/10.1016/j.pecs.2004.02.003
3. Katsuki M, Hasegawa T (1998) The science and technology of combustion in highly preheated air. Symp (Int) Combust 27(2):3135–3146. https://doi.org/10.1016/s0082-0784(98)80176-8
4. Weinberg FJ (1971) Combustion temperatures: the future? Nature 233(5317):239–241. https://doi.org/10.1038/233239a0
5. Hardesty DR, Weinberg FJ (1973) Burners producing large excess enthalpies. Combust Sci Technol 8(5–6):201–214. https://doi.org/10.1080/00102207308946644
6. Choi GM, Katsuki M (2001) Advanced low NO_x combustion using highly preheated air. Energy Convers Manag 42(5):639–652. https://doi.org/10.1016/S0196-8904(00)00074-1
7. Galletti C, Parente A, Derudi M, Rota R, Tognotti L (2009) Numerical and experimental analysis of NO emissions from a lab-scale burner fed with hydrogen-enriched fuels and operating in MILD combustion. Int J Hydrog Energy 34(19):8339–8351. https://doi.org/10.1016/j.ijhydene.2009.07.095
8. Kawai K, Yoshikawa K, Kobayashi H, Tsai JS, Matsuo M, Katsushima H (2002) High temperature air combustion boiler for low BTU gas. Energy Convers Manag 43(9–12):1563–1570. https://doi.org/10.1016/S0196-8904(02)00036-5
9. Luckerath R, Meier W, Aigner M (2008) FLOX combustion at high pressure with different fuel compositions. J Eng Gas Turbines Power 130(1):011505–011505-7. https://doi.org/10.1115/1.2749280
10. Lammel O, Schutz H, Schmitz G, Luckerath R, Stohr M, Noll B, Aigner M, Hase M, Krebs W (2010) FLOX combustion at high power density and high flame temperatures. J Eng Gas Turbines Power 132(12):121503–121503-10. https://doi.org/10.1115/1.4001825
11. Arghode VK, Gupta AK (2011) Development of high intensity CDC combustor for gas turbine engines. Appl Energy 88(3):963–973. https://doi.org/10.1016/j.apenergy.2010.07.038
12. Zornek T, Monz T, Aigner M (2015) Performance analysis of the micro gas turbine Turbec T100 with a new FLOX-combustion system for low calorific fuels. Appl Energy 159:276–284. https://doi.org/10.1016/j.apenergy.2015.08.075
13. Kruse S, Kerschgens B, Berger L, Varea E, Pitsch H (2015) Experimental and numerical study of MILD combustion for gas turbine applications. Appl Energy 148:456–465. https://doi.org/10.1016/j.apenergy.2015.03.054
14. Xing F, Kumar A, Huang Y, Chan S, Ruan C, Gu S, Fan X (2017) Flameless combustion with liquid fuel: a review focusing on fundamentals and gas turbine application. Appl Energy 193:28–51. https://doi.org/10.1016/j.apenergy.2017.02.010
15. Liu Y, Chen S, Yang B, Liu K, Zheng C (2015) First and second thermodynamic-law comparison of biogas MILD oxy-fuel combustion moderated by CO_2 or H_2O. Energy Convers Manag 106:625–634. https://doi.org/10.1016/j.enconman.2015.09.076
16. Mardani A, Fazlollahi Ghomshi A (2016) Numerical study of oxy-fuel MILD (moderate or intense low-oxygen dilution combustion) combustion for CH_4-H_2 fuel. Energy 99:136–151. https://doi.org/10.1016/j.energy.2016.01.016

17. Chen S, Liu H, Zheng C (2017) Methane combustion in MILD oxyfuel regime: influences of dilution atmosphere in co-flow configuration. Energy 121:159–175. https://doi.org/10.1016/j.energy.2017.01.011

18. Skottene M, Rian E (2007) A study of NO_x formation in hydrogen flames. Int J Hydrog Energy 32(15): 3572–3585. https://doi.org/10.1016/j.ijhydene.2007.02.038

19. Salavati-Zadeh A, Javaheri A, Ghavami SV, Esfahanian V, Tehrani MM, Akbari H (2016) A detailed kinetic investigation on the effects of hydrogen enrichment on the performance of gas-fueled SI engine. Int J Green Energy 13(10):1042–1049. https://doi.org/10.1080/15435075.2016.1206007

20. Mardani A, Tabejamaat S (2010) Effect of hydrogen on hydrogen methane turbulent non-premixed flame under MILD condition. Int J Hydrog Energy 35(20):11324–11331. https://doi.org/10.1016/j.ijhydene.2010.06.064

21. Wang F, Mi J, Li P, Zheng C (2011) Diffusion flame of a CH_4/H_2 jet in hot low-oxygen coflow. Int J Hydrog Energy 36(15):9267–9277. https://doi.org/10.1016/j.ijhydene.2011.04.180

22. Chen S, Zheng C (2011) Counterflow diffusion flame of hydrogen-enriched biogas under mild oxy-fuel condition. Int J Hydrog Energy 36(23):15403–15413. https://doi.org/10.1016/j.ijhydene.2011.09.002

23. Perpignan AA, Gangoli Rao A, Roekaerts DJ (2018) Flameless combustion and its potential towards gas turbines. Prog Energy Combust Sci 69(2018):28–62. https://doi.org/10.1016/j.pecs.2018.06.002

24. Ayoub M, Rottier C, Carpentier S, Villermaux C, Boukhalfa A, Honor D (2012) An experimental study of mild flameless combustion of methane/hydrogen mixtures. Int J Hydrog Energy 37(8):6912–6921. https://doi.org/10.1016/j.ijhydene.2012.01.018

25. Parente A, Galletti C, Tognotti L (2008) Effect of the combustion model and kinetic mechanism on the MILD combustion in an industrial burner fed with hydrogen enriched fuels. Int J Hydrog Energy 33(24):7553–7564. https://doi.org/10.1016/j.ijhydene.2008.09.058

26. Mardani A, Tabejamaat S, Mohammadi MB (2011) Numerical study of the effect of turbulence on rate of reactions in the MILD combustion regime. Combust Theory Model 15(6):753–772. https://doi.org/10.1080/13647830.2011.561368

27. Aminian J, Galletti C, Shahhosseini S, Tognotti L (2012) Numerical investigation of a MILD combustion burner: analysis of mixing field, chemical kinetics and turbulence-chemistry interaction. Flow Turbul Combust 88(4):597–623. https://doi.org/10.1007/s10494-012-9386-z

28. Magnussen B, Hjertager B (1977) On mathematical modeling of turbulent combustion with special emphasis on soot formation and combustion. Symp (Int) Combust 16(1):719–729. https://doi.org/10.1016/S0082-0784(77)80366-4

29. Magnussen B, Hjertager B, Olsen J, Bhaduri D (1979) Effects of turbulent structure and local concentrations on soot formation and combustion in C_2H_2 diffusion flames. Symp (Int) Combust 17(1):1383–1393. https://doi.org/10.1016/S0082-0784(79)80130-7

30. Ertesvåg IS, Magnussen BF (2000) The eddy dissipation turbulence energy cascade model. Combust Sci Technol 159(1):213–235. https://doi.org/10.1080/00102200008935784

31. Chomiak J, Karlsson A (1996) Flame liftoff in diesel sprays. Symp (Int) Combust 26(2):2557–2564. https://doi.org/10.1016/S0082-0784(96)80088-9

32. Afarin Y, Tabejamaat S (2013) Effect of hydrogen on H_2/CH_4 flame structure of MILD combustion using the LES method. Int J Hydrog Energy 38(8):3447–3458. https://doi.org/10.1016/j.ijhydene.2012.12.065

33. Afarin Y, Tabejamaat S (2013) The effect of fuel inlet turbulence intensity on H2/CH4 flame structure of MILD combustion using the LES method. Combust Theory Model 17(3):383–410. https://doi.org/10.1080/13647830.2012.742570

34. Frassoldati A, Sharma P, Cuoci A, Faravelli T, Ranzi E (2010) Kinetic and fluid dynamics modeling of methane/hydrogen jet flames in diluted coflow. Appl Therm Eng 30(4):376–383. https://doi.org/10.1016/j.applthermaleng.2009.10.001

35. Aminian J, Galletti C, Shahhosseini S, Tognotti L (2011) Key modeling issues in prediction of minor species in diluted-preheated combustion conditions. Appl Therm Eng 31(16):3287–3300. https://doi.org/10.1016/j.applthermaleng.2011.06.007

36. Mardani A, Tabejamaat S, Ghamari M (2010) Numerical study of influence of molecular diffusion in the Mild combustion regime. Combust Theory Model 14(5):747–774. https://doi.org/10.1080/13647830.2010.512959
37. Göktolga MU, van Oijen JA, de Goey LPH (2015) 3D DNS of MILD combustion: a detailed analysis of heat loss effects, preferential diffusion, and flame formation mechanisms. Fuel 159(1):784–795. https://doi.org/10.1016/j.fuel.2015.07.049
38. Chitgarha F, Mardani A (2018) Assessment of steady and unsteady flamelet models for MILD combustion modeling. Int J Hydrog Energ 43(32):15551–15563. https://doi.org/10.1016/j.ijhydene.2018.06.071
39. Biagioli F, Güthe F (2007) Effect of pressure and fuel-air unmixedness on NO_x emissions from industrial gas turbine burners. Combust Flame 151(1):274–288. https://doi.org/10.1016/j.combustflame.2007.04.007
40. Nicolle A, Dagaut P (2006) Occurrence of NO-reburning in MILD combustion evidenced via chemical kinetic modeling. Fuel 85(17):2469–2478. https://doi.org/10.1016/j.fuel.2006.05.021
41. Wünning J (1997) Flameless oxidation to reduce thermal no-formation. Prog Energy Combust Sci 23(1):81–94. https://doi.org/10.1016/S0360-1285(97)00006-3
42. Sepman A, Abtahizadeh E, Mokhov A, van Oijen J, Levinsky H, de Goey LPH (2013) Experimental and numerical studies of the effects of hydrogen addition on the structure of a laminar methane nitrogen jet in hot coflow under MILD conditions. Int J Hydrog Energy 38(31):13802–13811. https://doi.org/10.1016/j.ijhydene.2013.08.015
43. Li P, Wang F, Mi J, Dally B, Mei Z, Zhang J, Parente A (2014) Mechanisms of no formation in MILD combustion of CH_4/H_2 fuel blends. Int J Hydrog Energy 39(33):19187–19203. https://doi.org/10.1016/j.ijhydene.2014.09.050
44. Galletti C, Ferrarotti M, Parente A, Tognotti L (2015) Reduced NO formation models for CFD simulations of MILD combustion. Int J Hydrog Energy 40(14):4884–4897. https://doi.org/10.1016/j.ijhydene.2015.01.172
45. Yu Y, Gaofeng W, Qizhao L, Chengbiao M, Xianjun M (2010) Flameless combustion for hydrogen containing fuels. Int J Hydrog Energy 35(7):2694–2697. https://doi.org/10.1016/j.ijhydene.2009.04.036
46. Mardani A, Tabejamaat S, Hassanpour S (2013) Numerical study of CO and CO_2 formation in CH_4/H_2 blended flame under mild condition. Combust Flame 160(9):1636–1649. https://doi.org/10.1016/j.combustflame.2013.04.003
47. Christo F, Dally B (2005) Modeling turbulent reacting jets issuing into a hot and diluted coflow. Combust Flame 142(1):117–129. https://doi.org/10.1016/j.combustflame.2005.03.002
48. Zou C, Cao S, Song Y, He Y, Guo F, Zheng C (2014) Characteristics and mechanistic analysis of CO formation in mild regime with simultaneously diluted and preheated oxidant and fuel. Fuel 130:10–18. https://doi.org/10.1016/j.fuel.2014.04.004
49. Javaheri A, Esfahanian V, Salavati-Zadeh A, Darzi M (2014) Energetic and exergetic analyses of a variable compression ratio spark ignition gas engine. Energy Convers Manag 88:739–748. https://doi.org/10.1016/j.enconman.2014.09.009
50. Fallah M, Siyahi H, Ghiasi RA, Mahmoudi S, Yari M, Rosen M (2016) Comparison of different gas turbine cycles and advanced exergy analysis of the most effective. Energy 116:701–715. https://doi.org/10.1016/j.energy.2016.10.009
51. Szablowski L, Krawczyk P, Badyda K, Karellas S, Kakaras E, Bujalski W (2017) Energy and exergy analysis of adiabatic compressed air energy storage system. Energy 138:12–18. https://doi.org/10.1016/j.energy.2017.07.055
52. Fallah M, Mahmoudi S, Yari M (2017) Advanced exergy analysis for an anode gas recirculation solid oxide fuel cell. Energy 141:1097–1112. https://doi.org/10.1016/j.energy.2017.10.003
53. Koroglu T, Sogut O (2018) Conventional and advanced exergy analyses of a marine steam power plant. Energy 163:392–403. https://doi.org/10.1016/j.energy.2018.08.119
54. Rashidi H, Khorshidi J (2018) Exergy analysis and multiobjective optimization of a biomass gasification based multigeneration system. Int J Hydrog Energy 43:2631–2644. https://doi.org/10.1016/j.ijhydene.2017.12.073

55. Cruz P, Navas-Anguita Z, Iribarren D, Dufour J (2018) Exergy analysis of hydrogen production via biogas dry reforming. Int J Hydrog Energy 43(26):11688–11695. https://doi.org/10.1016/j.ijhydene.2018.02.025
56. Özgür T, Yakarylmaz A (2017) A review: exergy analysis of PEM and PEM fuel cell based CHP systems. Int J Hydrog Energy 43(38):17993–18000. https://doi.org/10.1016/j.ijhydene.2018.01.106
57. Chen S, Liu J, Zheng C (2012) First and second thermodynamic-law analyses of hydrogen-air counter-flow diffusion combustion in various combustion modes. Int J Hydrog Energy 37(6):5234–5245. https://doi.org/10.1016/j.ijhydene.2011.12.039
58. Hosseini S, Wahid M (2014) Enhancement of exergy efficiency in combustion systems using flameless mode. Energy Convers Manag 86:1154–1163. https://doi.org/10.1016/j.enconman.2014.06.065
59. Liu Y, Chen S, Liu S, Feng Y, Xu K, Zheng C (2016) Methane combustion in various regimes: first and second thermodynamic-law comparison between air-firing and oxyfuel condition. Energy 115:26–37. https://doi.org/10.1016/j.energy.2016.09.009
60. Dally B, Karpetis A, Barlow R (2002) Structure of turbulent non-premixed jet flames in a diluted hot coflow. Proc Combust Inst 29(1):1147–1154. https://doi.org/10.1016/S1540-7489(02)80145-6
61. Bejan A (2006) Advanced engineering thermodynamics, 3rd edn. Wiley, Hoboken
62. Querol E, Gonzalez-Regueral B, Perez-Benedito J (2013) Practical approach to exergy and thermoeconomic analyses of industrial processes, 1st edn. Springer, Heidelberg
63. Dincer I, Rosen M (2007) Exergy: energy, environment and sustainable development, 1st edn. Elsevier, Oxford
64. Bilger R, Stårner S, Kee R (1990) On reduced mechanisms for methane-air combustion in nonpremixed flames. Combust Flame 80(2):135–149. https://doi.org/10.1016/0010-2180(90)90122-8

Energetic, Exergetic, and Environmental Assessments of a Biomass Gasifier-Based Hydrogen Production and Liquefaction System

Yunus Emre Yuksel and Murat Ozturk

Abstract In this chapter, a novel hydrogen generation and liquefaction process is presented. The source for this plant straw is chosen as biomass source. Biomass-based hydrogen generation and liquefaction plant consist of biomass gasifier, air separation unit, catalyst bed component with helium expander and liquid hydrogen storage tank sub-component. To examine the performance of plant, energy, and exergy analyses have performed. Also, the environmental analyses for various system design based on generation options have been conducted to reveal the CO_2 emission of system. The energetic and exergetic efficiencies of plant for the base design parameters have been found as 68.26% and 64.72%, respectively. Parametric analysis results also indicate the effects of some variables on system performance and environmental effect of the system.

Keywords Biomass gasification · Hydrogen · Liquefaction · Energy · Exergy · Environmental analysis

1 Introduction

As energy demand increases with decreasing fossil fuel sources, finding of novel, clean and cheap alternatives for present energy framework has been must. There are ongoing researches either to improve present energy systems or develop novel energy systems. One of the alternative for current energy infrastructure is to change energy carrier to hydrogen. Hydrogen is the most abundant element in the universe however it is not free but bonded to other elements in compounds. So, there needs energy to dissociate hydrogen from those compounds. If this dissociation energy is

Y. E. Yuksel
Education Faculty, Math and Science Education, Afyon Kocatepe
University, ANS Campus, 03200 Afyonkarahisar, Turkey
e-mail: yeyuksel@aku.edu.tr

M. Ozturk (✉)
Department of Mechatronics Engineering, Faculty of Technology, Applied Science
University of Isparta, Cunur West Campus, 32200 Isparta, Turkey
e-mail: muratozturk@isparta.edu.tr

met by clean, cheap and renewable sources, hydrogen will be also clean and cheap solution.

Some advantages of hydrogen have been listed by Dincer and Acar [1] as high efficiency for energy conversion, no emission when produced from water, abundance, various storage options, long-distance transportation, ease of conversion to other energy types and high HHV and LHV.

There are many hydrogen production methods currently used and found in literature. Unfortunately, hydrogen is mostly produced from fossil sources of which 48% from natural gas, 30% from heavy oils and 18% of coal [2, 3].

Hydrogen generation from biomass is a good method for the regions having sufficient biomass sources. Recently, biomass gasification processes have been developed to produce syngas, hydrogen, methane and other chemicals by using wastes as biomass source [4]. In biomass gasification process, liquid or solid phase source is converted to gas/vapor phase usually called syngas having high heating power [5]. There are several gasification technologies compared in terms of their working conditions, efficiency and conversion percentage [6]. Shayan et al. [7] have compared biomass gasification agents (air, oxygen, oxygen-enriched air, and steam) in order to reveal the impacts of those agent on plant efficiency after biomass gasification processes being popular. Results of the study concluded that the best energy efficiency result occurs when air gasification is used, and the highest exergy performance value is reached with steam gasification system.

In this study, a novel hydrogen generation and liquefaction method are presented with energy and exergy efficiency analyses. Moreover, environmental analyses have been performed for this plant by presenting CO_2 emission amounts. Analysis results have been supported by parametric analysis in order to see the impacts of different variables.

2   Plant Description

The schematic flow diagram of biomass-based hydrogen generation and liquefaction plant is given in Fig. 1. Firstly, air is supplied to air compressor then compressed air is sent to air separation unit (ASU) to dissociate oxygen and nitrogen. Then air with the flow 3 enters gasifier. In this gasification process, straw, air coming from ASU and steam coming from water–gas shift reactor are gasified. Produced syngas with the stream numbered 12 goes through heat exchangers (HEX) 1 and 2, respectively. To separate tar, syngas enters to gas conditioning, and then flows through water–gas shift reactor. Steam produced here is sent to gasifier. Syngas is sent to sulfur removal and CO_2 capture rooms, respectively. After this point produced hydrogen is sent to pressure swing adsorption unit with the flow 21. Purge gas is exhausted from this unit, hydrogen goes to hydrogen compressor to be compressed. Then compressed hydrogen enters the hydrogen liquefaction sub-system using four helium turboexpanders. In each stage, hydrogen will be cooled down by passing through eight heat exchangers and three catalyst beds. In this hydrogen liquefaction
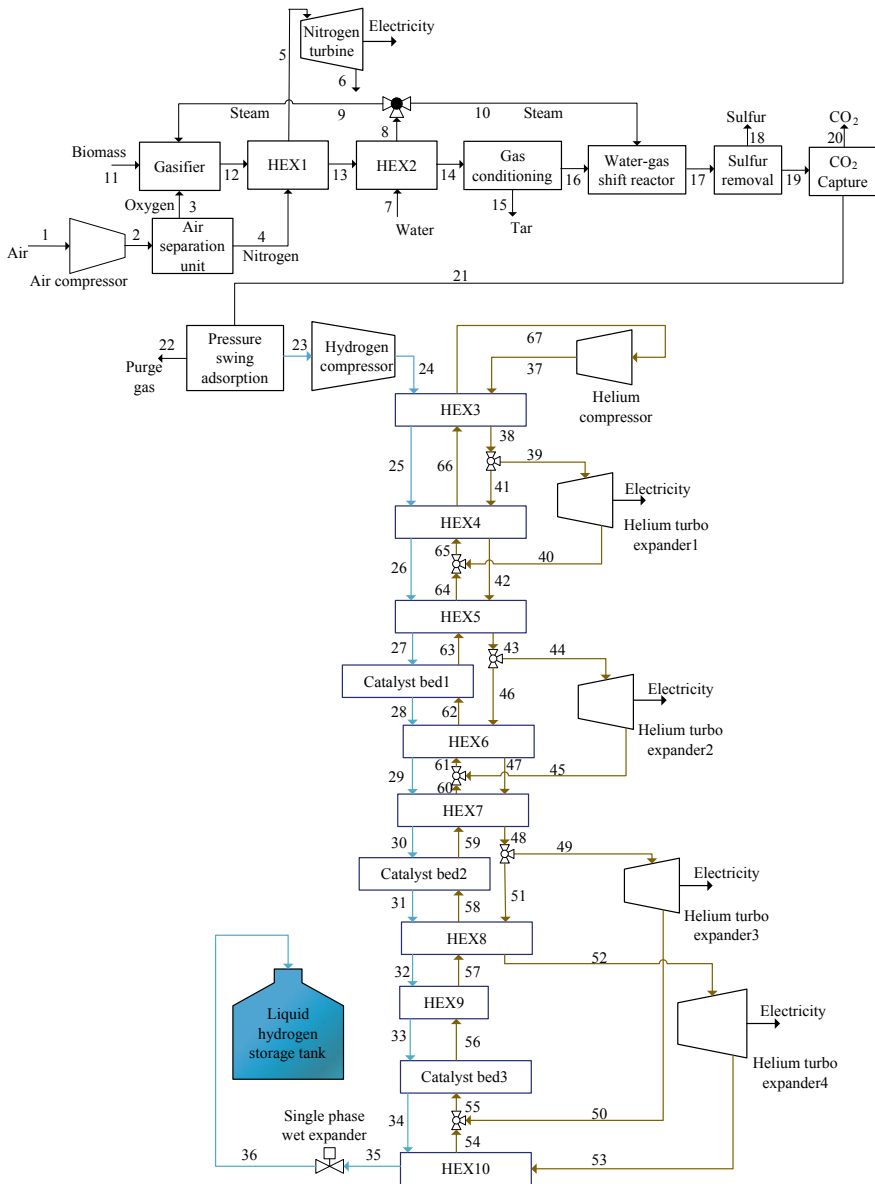
Fig. 1 Biomass gasification-based hydrogen generation and liquefaction plant

Table 1 Design indicators of integrated plant

Parameter	Value
Dead state temperature, T_o (°C)	25
Dead state pressure, P_o (kPa)	101.3
Compressor pressure ratio, r_{AC}	6
Mass flow rate of biomass, $\dot{m}_{11}$ (kg/s)	6.72
Biomass gasifier temperature, T_{BG} (°C)	780
Nitrogen turbine inlet temperature, T_5 (°C)	420
Nitrogen turbine inlet pressure, P_5 (kPa)	1500
Isentropic efficiency of nitrogen turbine, η_{NT} (%)	85
Hydrogen compressor exit pressure, P_{24} (kPa)	2125
Helium compressor exit pressure, P_{37} (kPa)	1522
Helium turbo expander1 exit temperature, T_{40} (°C)	−133.5
Helium turbo expander2 exit temperature, T_{45} (°C)	−199
Helium turbo expander3 exit temperature, T_{50} (°C)	−226.5
Helium turbo expander4 exit temperature, T_{53} (°C)	−253.8
Single phase wet expander input pressure, P_{35} (kPa)	2125
Single phase wet expander exit pressure, P_{36} (kPa)	202.5

unit, helium helps to cool down hydrogen and phase change. Also, helium turbo expanders produce electricity. Finally produced liquid hydrogen is sent to liquid hydrogen storage tank with the flow 36 (Table 1).

3 Thermodynamic Analysis

For thermodynamic analyzing of a control volume, four topics should be analyzed, such as mass, energetic, entropy, and exergetic balance. By defining, these equalities for each component of integrated system, thermodynamically equalities should be analyzed rightly. According to the conservation of mass principle, mass going into the control volume equals to mass leaving from this volume as given below;

$$\sum_{in} \dot{m} = \sum_{out} \dot{m} \tag{1}$$

Here, $\dot{m}$ is the mass flow rate. Based on the First Law of Thermodynamics, energy conservation equality can be given as

$$\sum_{in} \dot{m}h + \sum_{in} \dot{Q} + \sum_{in} \dot{W} = \sum_{out} \dot{m}h + \sum_{out} \dot{Q} + \sum_{out} \dot{W} \tag{2}$$

Here, $\dot{Q}$ and $\dot{W}$ show heat transfer rate and power, h denotes specific enthalpy. An entropy balance equality applied to a control volume should be defined as;

$$\sum_{\text{in}} \dot{m}s + \sum_{\text{in}} \frac{\dot{Q}}{T} + \dot{S}_{\text{gen}} = \sum_{\text{out}} \dot{m}s + \sum_{\text{out}} \frac{\dot{Q}}{T} \tag{3}$$

where s and $\dot{S}_{\text{gen}}$ are specific entropy and entropy generation rate. Based on the second law of thermodynamics, the exergy balance equality is

$$\sum_{\text{in}} \dot{m}ex + \sum_{\text{in}} \dot{E}x^Q + \sum_{\text{in}} \dot{E}x^W = \sum_{\text{out}} \dot{m}ex + \sum_{\text{out}} \dot{E}x^Q + \sum_{\text{out}} \dot{E}x^W + \dot{E}x_D \tag{4}$$

Here, $\dot{E}x_D$ is the exergy destruction rate, and should be given as

$$\dot{E}x_D = T_0 \dot{S}_{\text{gen}} \tag{5}$$

An exergy rate of heat energy transfer should be given as

$$\dot{E}x_Q = \left(1 - \frac{T_o}{T}\right)\dot{Q} \tag{6}$$

An exergy rate associated with shaft work is

$$\dot{E}x_W = \dot{W} \tag{7}$$

A specific exergy can be given as

$$ex = ex_{\text{ph}} + ex_{\text{ch}} \tag{8}$$

where ex_{ph} and ex_{ch} show physical and chemical exergy content, and can be written as

$$ex_{\text{ph}} = (h - h_o) - T_o(s - s_o) \tag{9}$$

$$ex_{\text{ch}} = \sum n_i \left(u_i^0 - u_i^{00}\right) \tag{10}$$

where u_i^0 and u_i^{00} show chemical potential of ith section in the thermomechanical equilibrium and chemical equilibrium [8]. The balance equalities for sub-systems are written in Table 2.

Table 2 Balance equations of biomass gasification-based integrated system

Components	Mass balance	Energy balance	Entropy balance	Exergy balance
Biomass gasifier	$\dot{m}_3 + \dot{m}_9 + \dot{m}_{11} = \dot{m}_{12}$	$\dot{m}_3 h_3 + \dot{m}_9 h_9 + \dot{m}_{11} h_{11} = \dot{m}_{12} h_{12} + \dot{Q}_{L,BG}$	$\dot{m}_3 s_3 + \dot{m}_9 s_9 + \dot{m}_{11} s_{11} + \dot{S}_{g,BG} = \dot{m}_{12} s_{12} + \dot{Q}_{L,BG}/T_{BG}$	$\dot{m}_3 ex_3 + \dot{m}_9 ex_9 + \dot{m}_{11} ex_{11} = \dot{m}_{12} ex_{12} + \dot{Ex}^Q_{L,BG} + \dot{Ex}_{D,BG}$
Air compressor	$\dot{m}_1 = \dot{m}_2$	$\dot{m}_1 h_1 + \dot{W}_{AC} = \dot{m}_2 h_2$	$\dot{m}_1 s_1 + \dot{S}_{g,AC} = \dot{m}_2 s_2$	$\dot{m}_1 ex_1 + \dot{W}_{AC} = \dot{m}_2 ex_2 + \dot{Ex}_{D,AC}$
Air separation unit	$\dot{m}_2 = \dot{m}_3 + \dot{m}_4$	$\dot{m}_2 h_2 = \dot{m}_3 h_3 + \dot{m}_4 h_4$	$\dot{m}_2 s_2 + \dot{S}_{g,ASU} = \dot{m}_3 s_3 + \dot{m}_4 s_4$	$\dot{m}_2 ex_2 = \dot{m}_3 ex_3 + \dot{m}_4 ex_4 + \dot{Ex}_{D,ASU}$
HEX1	$\dot{m}_4 = \dot{m}_5$ $\dot{m}_{12} = \dot{m}_{13}$	$\dot{m}_4 h_4 + \dot{m}_{12} h_{12} = \dot{m}_5 h_5 + \dot{m}_{13} h_{13}$	$\dot{m}_4 s_4 + \dot{m}_{12} s_{12} + \dot{S}_{g,HEX1} = \dot{m}_5 s_5 + \dot{m}_{13} s_{13}$	$\dot{m}_4 ex_4 + \dot{m}_{12} ex_{12} = \dot{m}_5 ex_5 + \dot{m}_{13} ex_{13} + \dot{Ex}_{D,HEX1}$
Nitrogen turbine	$\dot{m}_5 = \dot{m}_6$	$\dot{m}_5 h_5 = \dot{m}_6 h_6 + \dot{W}_{NT}$	$\dot{m}_5 s_5 + \dot{S}_{g,NT} = \dot{m}_6 s_6$	$\dot{m}_5 ex_5 = \dot{m}_6 ex_6 + \dot{W}_{NT} + \dot{Ex}_{D,NT}$
HEX2	$\dot{m}_7 = \dot{m}_8$ $\dot{m}_{13} = \dot{m}_{14}$	$\dot{m}_7 h_7 + \dot{m}_{13} h_{13} = \dot{m}_8 h_8 + \dot{m}_{14} h_{14}$	$\dot{m}_7 s_7 + \dot{m}_{13} s_{13} + \dot{S}_{g,HEX2} = \dot{m}_8 s_8 + \dot{m}_{14} s_{14}$	$\dot{m}_7 ex_7 + \dot{m}_{13} ex_{13} = \dot{m}_8 ex_8 + \dot{m}_{14} ex_{14} + \dot{Ex}_{D,HEX2}$
Gas conditioning	$\dot{m}_{14} = \dot{m}_{15} + \dot{m}_{16}$	$\dot{m}_{14} h_{14} = \dot{m}_{15} h_{15} + \dot{m}_{16} h_{16}$	$\dot{m}_{14} s_{14} + \dot{S}_{g,GC} = \dot{m}_{15} s_{15} + \dot{m}_{16} s_{16}$	$\dot{m}_{14} ex_{14} = \dot{m}_{15} ex_{15} + \dot{m}_{16} ex_{16} + \dot{Ex}_{D,GC}$
Water–gas shift reactor	$\dot{m}_{10} + \dot{m}_{16} = \dot{m}_{17}$	$\dot{m}_{10} h_{10} + \dot{m}_{16} h_{16} = \dot{m}_{17} h_{17} + \dot{Q}_{L,WGSR}$	$\dot{m}_{10} s_{10} + \dot{m}_{16} s_{16} + \dot{S}_{g,WGSR} = \dot{m}_{17} s_{17} + \dot{Q}_{L,WGSR}/T_{WGSR}$	$\dot{m}_{10} ex_{10} + \dot{m}_{16} ex_{16} = \dot{m}_{17} ex_{17} + \dot{Ex}^Q_{L,WGSR} + \dot{Ex}_{D,WGSR}$
Sulfur removal	$\dot{m}_{17} = \dot{m}_{18} + \dot{m}_{19}$	$\dot{m}_{17} h_{17} = \dot{m}_{18} h_{18} + \dot{m}_{19} h_{19}$	$\dot{m}_{17} s_{17} + \dot{S}_{g,SR} = \dot{m}_{18} s_{18} + \dot{m}_{19} s_{19}$	$\dot{m}_{17} ex_{17} = \dot{m}_{18} ex_{18} + \dot{m}_{19} ex_{19} + \dot{Ex}_{D,SR}$

(continued)

Table 2 (continued)

Components	Mass balance	Energy balance	Entropy balance	Exergy balance
CO$_2$ capture	$\dot{m}_{19} = \dot{m}_{20} + \dot{m}_{21}$	$\dot{m}_{19}h_{19} = \dot{m}_{20}h_{20} + \dot{m}_{21}h_{21}$	$\dot{m}_{19}s_{19} + \dot{S}_{g,CC} = \dot{m}_{20}s_{20} + \dot{m}_{21}s_{21}$	$\dot{m}_{19}ex_{19} = \dot{m}_{20}ex_{20}$ $+ \dot{m}_{21}ex_{21} + \dot{Ex}_{D,CC}$
Pressure swing adsorption	$\dot{m}_{21} = \dot{m}_{22} + \dot{m}_{23}$	$\dot{m}_{21}h_{21} = \dot{m}_{22}h_{22} + \dot{m}_{23}h_{23}$	$\dot{m}_{21}s_{21} + \dot{S}_{g,PSA}$ $= \dot{m}_{22}s_{22} + \dot{m}_{23}s_{23}$	$\dot{m}_{21}ex_{21} = \dot{m}_{22}ex_{22}$ $+ \dot{m}_{23}ex_{23} + \dot{Ex}_{D,PSA}$
Hydrogen compressor	$\dot{m}_{23} = \dot{m}_{24}$	$\dot{m}_{23}h_{23} + \dot{W}_{HyC} = \dot{m}_{24}h_{24}$	$\dot{m}_{23}s_{23} + \dot{S}_{g,HyC} = \dot{m}_{24}s_{24}$	$\dot{m}_{23}ex_{23} + \dot{W}_{HyC}$ $= \dot{m}_{24}ex_{24} + \dot{Ex}_{D,HC}$
HEX3	$\dot{m}_{24} = \dot{m}_{25}$ $\dot{m}_{37} = \dot{m}_{38}$ $\dot{m}_{66} = \dot{m}_{67}$	$\dot{m}_{24}h_{24} + \dot{m}_{37}h_{37}$ $+ \dot{m}_{66}h_{66} = \dot{m}_{25}h_{25}$ $+ \dot{m}_{38}h_{38} + \dot{m}_{67}h_{67}$	$\dot{m}_{24}s_{24} + \dot{m}_{37}s_{37}$ $+ \dot{m}_{66}s_{66} + \dot{S}_{g,HEX3}$ $= \dot{m}_{25}s_{25} + \dot{m}_{38}s_{38} + \dot{m}_{67}s_{67}$	$\dot{m}_{24}ex_{24} + \dot{m}_{37}ex_{37}$ $+ \dot{m}_{66}ex_{66} = \dot{m}_{25}ex_{25}$ $+ \dot{m}_{38}ex_{38} + \dot{m}_{67}ex_{67} + \dot{Ex}_{D,HEX3}$
Helium compressor	$\dot{m}_{67} = \dot{m}_{37}$	$\dot{m}_{67}h_{67} + \dot{W}_{HeC} = \dot{m}_{37}h_{37}$	$\dot{m}_{67}s_{37} + \dot{S}_{g,HeC} = \dot{m}_{37}s_{37}$	$\dot{m}_{67}ex_{67} + \dot{W}_{HeC} =$ $\dot{m}_{37}ex_{37} + \dot{Ex}_{D,HeC}$
Helium turbo expander1	$\dot{m}_{39} = \dot{m}_{40}$	$\dot{m}_{39}h_{39} = \dot{m}_{40}h_{40} + \dot{W}_{HTE1}$	$\dot{m}_{39}s_{39} + \dot{S}_{g,HTE1} = \dot{m}_{40}s_{40}$	$\dot{m}_{39}ex_{39} = \dot{m}_{40}ex_{40}$ $+ \dot{W}_{HTE1} + \dot{Ex}_{D,HTE1}$
HEX4	$\dot{m}_{25} = \dot{m}_{26}$ $\dot{m}_{41} = \dot{m}_{42}$ $\dot{m}_{65} = \dot{m}_{66}$	$\dot{m}_{25}h_{25} + \dot{m}_{41}h_{41} + \dot{m}_{65}h_{65}$ $= \dot{m}_{26}h_{26} + \dot{m}_{42}h_{42} + \dot{m}_{66}h_{66}$	$\dot{m}_{25}s_{25} + \dot{m}_{41}s_{41}$ $+ \dot{m}_{65}s_{65} + \dot{S}_{g,HEX4}$ $= \dot{m}_{26}s_{26} + \dot{m}_{42}s_{42} + \dot{m}_{66}s_{66}$	$\dot{m}_{25}ex_{25} + \dot{m}_{41}ex_{41}$ $+ \dot{m}_{65}ex_{65} = \dot{m}_{26}ex_{26}$ $+ \dot{m}_{42}ex_{42} + \dot{m}_{66}ex_{66} + \dot{Ex}_{D,HEX4}$
HEX5	$\dot{m}_{26} = \dot{m}_{27}$ $\dot{m}_{42} = \dot{m}_{43}$ $\dot{m}_{63} = \dot{m}_{64}$	$\dot{m}_{26}h_{26} + \dot{m}_{42}h_{42}$ $+ \dot{m}_{63}h_{63} = \dot{m}_{27}h_{27}$ $+ \dot{m}_{43}h_{43} + \dot{m}_{64}h_{64}$	$\dot{m}_{26}s_{26} + \dot{m}_{42}s_{42}$ $+ \dot{m}_{63}s_{63} + \dot{S}_{g,HEX5}$ $= \dot{m}_{27}s_{27} + \dot{m}_{43}s_{43} + \dot{m}_{64}s_{64}$	$\dot{m}_{26}ex_{26} + \dot{m}_{42}ex_{42}$ $+ \dot{m}_{63}ex_{63} = \dot{m}_{27}ex_{27}$ $+ \dot{m}_{43}ex_{43} + \dot{m}_{64}ex_{64} + \dot{Ex}_{D,HEX5}$

(continued)

Table 2 (continued)

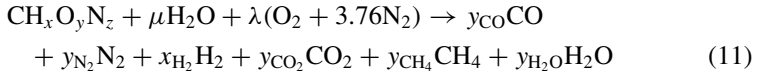| Components	Mass balance	Energy balance	Entropy balance	Exergy balance
Catalyst bed1	$\dot{m}_{27} = \dot{m}_{28}$ $\dot{m}_{62} = \dot{m}_{63}$	$\dot{m}_{27}h_{27} + \dot{m}_{62}h_{62}$ $= \dot{m}_{28}h_{28} + \dot{m}_{63}h_{63}$	$\dot{m}_{27}s_{27} + \dot{m}_{62}s_{62} + \dot{S}_{g,CB1}$ $= \dot{m}_{28}s_{28} + \dot{m}_{63}s_{63}$	$\dot{m}_{27}ex_{27} + \dot{m}_{62}ex_{62}$ $= \dot{m}_{28}ex_{28} + \dot{m}_{63}ex_{63} + \dot{Ex}_{D,CB1}$
Helium turbo expander2	$\dot{m}_{44} = \dot{m}_{45}$	$\dot{m}_{44}h_{44} = \dot{m}_{45}h_{45} + \dot{W}_{HTE2}$	$\dot{m}_{44}s_{44} + \dot{S}_{g,HTE2} = \dot{m}_{45}s_{45}$	$\dot{m}_{44}ex_{44} = \dot{m}_{45}ex_{45}$ $+ \dot{W}_{HTE2} + \dot{Ex}_{D,HTE2}$
HEX6	$\dot{m}_{28} = \dot{m}_{29}$ $\dot{m}_{46} = \dot{m}_{47}$ $\dot{m}_{61} = \dot{m}_{62}$	$\dot{m}_{28}h_{28} + \dot{m}_{46}h_{46}$ $+ \dot{m}_{61}h_{61} = \dot{m}_{29}h_{29}$ $+ \dot{m}_{47}h_{47} + \dot{m}_{62}h_{62}$	$\dot{m}_{28}s_{28} + \dot{m}_{46}s_{46}$ $+ \dot{m}_{61}s_{61} + \dot{S}_{g,HEX6}$ $= \dot{m}_{29}s_{29} + \dot{m}_{47}s_{47} + \dot{m}_{62}s_{62}$	$\dot{m}_{28}ex_{28} + \dot{m}_{46}ex_{46}$ $+ \dot{m}_{61}ex_{61} = \dot{m}_{29}ex_{29}$ $+ \dot{m}_{47}ex_{47} + \dot{m}_{62}ex_{62} + \dot{Ex}_{D,HEX6}$
HEX7	$\dot{m}_{29} = \dot{m}_{30}$ $\dot{m}_{47} = \dot{m}_{48}$ $\dot{m}_{59} = \dot{m}_{60}$	$\dot{m}_{29}h_{29} + \dot{m}_{47}h_{47}$ $+ \dot{m}_{59}h_{59} = \dot{m}_{30}h_{30}$ $+ \dot{m}_{48}h_{48} + \dot{m}_{60}h_{60}$	$\dot{m}_{29}s_{29} + \dot{m}_{47}s_{47}$ $+ \dot{m}_{59}s_{59} + \dot{S}_{g,HEX7}$ $= \dot{m}_{30}s_{30} + \dot{m}_{48}s_{48} + \dot{m}_{60}s_{60}$	$\dot{m}_{29}ex_{29} + \dot{m}_{47}ex_{47}$ $+ \dot{m}_{59}ex_{59} = \dot{m}_{30}ex_{30}$ $+ \dot{m}_{48}ex_{48} + \dot{m}_{60}ex_{60} + \dot{Ex}_{D,HEX7}$
Catalyst bed2	$\dot{m}_{30} = \dot{m}_{31}$ $\dot{m}_{58} = \dot{m}_{59}$	$\dot{m}_{30}h_{30} + \dot{m}_{58}h_{58}$ $= \dot{m}_{31}h_{31} + \dot{m}_{59}h_{59}$	$\dot{m}_{30}s_{30} + \dot{m}_{58}s_{58} + \dot{S}_{g,CB2}$ $= \dot{m}_{31}s_{31} + \dot{m}_{59}s_{59}$	$\dot{m}_{30}ex_{30} + \dot{m}_{58}ex_{58}$ $= \dot{m}_{31}ex_{31} + \dot{m}_{59}ex_{59}$ $+ \dot{Ex}_{D,CB2}$
Helium turbo expander3	$\dot{m}_{49} = \dot{m}_{50}$	$\dot{m}_{49}h_{49} = \dot{m}_{50}h_{50} + \dot{W}_{HTE3}$	$\dot{m}_{49}s_{49} + \dot{S}_{g,HTE3} = \dot{m}_{50}s_{50}$	$\dot{m}_{49}ex_{49} = \dot{m}_{50}ex_{50}$ $+ \dot{W}_{HTE3} + \dot{Ex}_{D,HTE3}$

(continued)

Table 2 (continued)

Components	Mass balance	Energy balance	Entropy balance	Exergy balance
HEX8	$\dot{m}_{31} = \dot{m}_{32}$ $\dot{m}_{51} = \dot{m}_{52}$ $\dot{m}_{57} = \dot{m}_{58}$	$\dot{m}_{31}h_{31} + \dot{m}_{51}h_{51}$ $+ \dot{m}_{57}h_{57} = \dot{m}_{32}h_{32}$ $+ \dot{m}_{52}h_{52} + \dot{m}_{58}h_{58}$	$\dot{m}_{31}s_{31} + \dot{m}_{51}s_{51}$ $+ \dot{m}_{57}s_{57} + \dot{S}_{g,HEX8}$ $= \dot{m}_{32}s_{32} + \dot{m}_{52}s_{52} + \dot{m}_{58}s_{58}$	$\dot{m}_{31}ex_{31} + \dot{m}_{51}ex_{51}$ $+ \dot{m}_{57}ex_{57} = \dot{m}_{32}ex_{32}$ $+ \dot{m}_{52}ex_{52} + \dot{m}_{58}ex_{58}$ $+ \dot{Ex}_{D,HEX8}$
Helium turbo expander4	$\dot{m}_{52} = \dot{m}_{53}$	$\dot{m}_{52}h_{52} = \dot{m}_{53}h_{53} + \dot{W}_{HTE4}$	$\dot{m}_{52}s_{52} + \dot{S}_{g,HTE4} = \dot{m}_{53}s_{53}$	$\dot{m}_{52}ex_{52} = \dot{m}_{53}ex_{53}$ $+ \dot{W}_{HTE4} + \dot{Ex}_{D,HTE4}$
HEX9	$\dot{m}_{32} = \dot{m}_{33}$ $\dot{m}_{56} = \dot{m}_{57}$	$\dot{m}_{32}h_{32} + \dot{m}_{56}h_{56}$ $= \dot{m}_{33}h_{33} + \dot{m}_{57}h_{57}$	$\dot{m}_{32}s_{32} + \dot{m}_{56}s_{56} + \dot{S}_{g,HEX9}$ $= \dot{m}_{33}s_{33} + \dot{m}_{57}s_{57}$	$\dot{m}_{32}ex_{32} + \dot{m}_{56}ex_{56}$ $= \dot{m}_{33}ex_{33} + \dot{m}_{57}ex_{57}$ $+ \dot{Ex}_{D,HEX9}$
Catalyst bed3	$\dot{m}_{33} = \dot{m}_{34}$ $\dot{m}_{55} = \dot{m}_{56}$	$\dot{m}_{33}h_{33} + \dot{m}_{55}h_{55}$ $= \dot{m}_{34}h_{34} + \dot{m}_{56}h_{56}$	$\dot{m}_{33}s_{33} + \dot{m}_{55}s_{55} + \dot{S}_{g,CB3}$ $= \dot{m}_{34}s_{34} + \dot{m}_{56}s_{56}$	$\dot{m}_{33}ex_{33} + \dot{m}_{55}ex_{55}$ $= \dot{m}_{34}ex_{34} + \dot{m}_{56}ex_{56}$ $+ \dot{Ex}_{D,CB3}$
HEX10	$\dot{m}_{34} = \dot{m}_{35}$ $\dot{m}_{53} = \dot{m}_{54}$	$\dot{m}_{34}h_{34} + \dot{m}_{53}h_{53}$ $= \dot{m}_{35}h_{35} + \dot{m}_{54}h_{54}$	$\dot{m}_{34}s_{34} + \dot{m}_{53}s_{53} + \dot{S}_{g,HEX10}$ $= \dot{m}_{35}s_{35} + \dot{m}_{54}s_{54}$	$\dot{m}_{34}ex_{34} + \dot{m}_{53}ex_{53}$ $= \dot{m}_{35}ex_{35} + \dot{m}_{54}ex_{54}$ $+ \dot{Ex}_{D,HEX10}$
Single phase wet expander	$\dot{m}_{35} = \dot{m}_{36}$	$\dot{m}_{35}h_{35} = \dot{m}_{36}h_{36}$	$\dot{m}_{35}s_{35} + \dot{S}_{g,SPWE} = \dot{m}_{36}s_{36}$	$\dot{m}_{35}ex_{35} = \dot{m}_{36}ex_{36}$ $+ \dot{Ex}_{D,SPWE}$

3.1 Gasifier Sub-component

For this book chapter, the straw is chosen as biomass sources, and its composition assessment based on the dry basis and dry ash-free basis is defined in Table 3.

The equality of biomass gasification reaction is given as

$$CH_xO_yN_z + \mu H_2O + \lambda(O_2 + 3.76N_2) \rightarrow y_{CO}CO$$
$$+ y_{N_2}N_2 + x_{H_2}H_2 + y_{CO_2}CO_2 + y_{CH_4}CH_4 + y_{H_2O}H_2O \qquad (11)$$

Biomass resource chemical exergy content is calculated as given below equation;

$$Ex_{bm}^{ch} = \beta_{bm}LHV_{bm} \qquad (12)$$

Here β_{bm} shows the chemical exergy ratio [9], and also is calculated from

$$\beta_{bm} = \frac{1.044 + 0.016\frac{H}{C} - 0.34493\frac{O}{C}\left(1 + 0.0531\frac{H}{C}\right)}{1 - 0.4124\frac{O}{C}} \qquad (13)$$

LHV_{bm} gives the biomass lower heating value, and should be computed as given below [10];

$$LHV_{bm} = (1 - \epsilon_{MC})HHV_{bm} - E_w\left(\xi_{HC}HCm_{H_2O}\right) - E_{we}\epsilon_{MC} \qquad (14)$$

where ϵ_{MC} shows the biomass moisture content, and can be given as

$$\epsilon_{MC} = \frac{18w}{25.93 + 18w} \times 100\% \qquad (15)$$

ξ_{HC} shows the biomass hydrogen content, E_{we} is the energy required for water evaporation (~2.26 MJ/kg), and HHV_{bm} is the biomass higher heating value, and can should be given as [11];

Table 3 Ultimate assessment for biomass source

Compound	Straw	
	Dry basis	Dry ash free basis
C	44.86	47.66
H	3.82	4.06
N	0.73	0.78
S	0.11	0.12
O	44.59	47.37

Table 4 LHV_{bm} and HHV_{bm} of biomass source

Heating value	Straw	
	Original basis (kJ/kg)	Dry basis (kJ/kg)
LHV_{bm}	16,525	18,020
HHV_{bm}	17,785	19,225

Table 5 Chemical composition of produced synthesis gaseous

Component	% mol
Hydrogen	21.28
Carbon monoxide	43.16
Carbon dioxide	13.45
Methane	15.83
Acetylene	0.36
Ethylene	4.62
Ethane	0.62
Tars	0.40
Hydrogen sulfur	0.08
Azote	0.37

$$HHV_{bm} = 0.3491z_C + 1.1783z_H - 0.1034z_O$$
$$- 0.0151z_N + 0.1005z_S - 0.0211z_A \tag{16}$$

where z_C, z_H, z_O, z_N, z_S and z_A shows the percentage mass for C, H, O, N, S and ash in biomass samples. Finally, the LHV_{bm} and HHV_{bm} of biomass sample, and chemical composition of produced synthesis gaseous are given in Tables 4 and 5, respectively.

3.2 Air Compressor Sub-component

Air at dead state temperature and pressure enters the air compressor sub-component for using in the air separation unit. The exit temperature of compressed air can be calculated as given below;

$$T_2 = T_1\left[1 + \frac{1}{\eta_{AC}}\left(r_{AC}^{\frac{\gamma_{ac}-1}{\gamma_{ac}}} - 1\right)\right] \tag{17}$$

Here η_{AC} shows isentropic efficiency of air compressor sub-component, r_{AC} is compressor pressure ratio, and γ_{ac} is specific heat ratio. The consumption work for

compressor sub-system should be calculated as

$$\dot{W}_{\mathrm{ac}} = \dot{m}_9 C_{\mathrm{p,ac}}(T_{10} - T_9) \tag{18}$$

Here $C_{\mathrm{p,ac}}$ shows air specific heat, and should be defined as [12]

$$C_{\mathrm{p,ac}} = 1.048 - \left(\frac{3.83T}{10^4}\right) + \left(\frac{9.45T^2}{10^7}\right) - \left(\frac{5.49T^3}{10^{10}}\right) + \left(\frac{7.92T^4}{10^{14}}\right) \tag{19}$$

3.3 Catalyst Bed Sub-component

According to the molecular temperature function, the ortho-hydrogen (o-H_2) and para-hydrogen (p-H_2) nuclear spin combinations are present for hydrogen molecule. At dead state temperature status, the percent of nuclear spin combination for hydrogen molecule are given as 74.93% o-H_2 and %25.07 p-H_2. In addition to that, the percent of p-H_2 reaches nearly 100% at -253 °C. The o-H_2 to p-H_2 transformation cycle in catalyst beds give the important amount of waste heat energy (almost 0.146 kWh/kg) because p-H_2 compositions have the lower energy quantity than o-H_2 compositions [13]. When required transformations happen, the particle bonds of o-H_2 are broken, and furthermore the e$^-$ spins rearranged to produce p-H_2. A transformation of chemical reactions in the catalyst beds can be defined as

$$2C + (\text{o-}H_2) \leftrightarrow 2CH_2 \leftrightarrow 2C + \left(\text{p-}H_2\right) \tag{20}$$
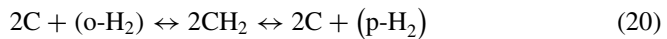
Here, C shows the hydrogen production and liquefaction cycle catalyzer. The o-H_2 and p-H_2 have different several thermodynamic property diversities. Enthalpy and entropy properties equations for o-H_2 and p-H_2 mixture can be calculated as follows [14]

$$h_{\mathrm{mx}} = x_{\mathrm{p}} h_{\mathrm{p}} + x_{\mathrm{o}} h_{\mathrm{o}} \tag{21}$$

$$s_{\mathrm{mx}} = x_{\mathrm{p}} s_{\mathrm{p}} + x_{\mathrm{o}} s_{\mathrm{o}} - R_{\mathrm{H_2}}\left(x_{\mathrm{p}} \ln x_{\mathrm{p}} + x_{\mathrm{o}} \ln x_{\mathrm{o}}\right) \tag{22}$$

Here, x, p and o are mass fraction, p-H_2 and o-H_2. Also, $R_{\mathrm{H_2}}$ shows gas constant of hydrogen. The mass transfer equality of catalyst can be defined as given below

$$\frac{y_{\mathrm{out}} - y_{\mathrm{eq}}}{y_{\mathrm{in}} - y_{\mathrm{eq}}} = \mathrm{e}^{-\gamma \lambda_{\mathrm{p}} L_{\mathrm{cb}} / \dot{m}_{\mathrm{H_2}}} \tag{23}$$

Here, y shows p-H_2 mass fraction and eq is equilibrium case, γ gives total mass transfer conductivity, and L_{cb} is length of catalyst bed. Also, λ_{p} shows transfer

perimeter, and can be calculated as

$$\lambda_p = \frac{6(1-\varepsilon)}{d_p} A_c \tag{24}$$

Here, d_p, ε and A_c are particle sphere diameter, volume void fraction, and cross-sectional area. By using Eqs. (23) and (24), y is

$$-\ln\left(\frac{y_{out} - y_{eq}}{y_{in} - y_{eq}}\right) = \gamma \frac{6(1-\varepsilon)A_c L_{cb}}{d_p \dot{m}_{H_2}} \tag{25}$$

3.4 Liquid Hydrogen Storage Tank Sub-component

The flow exergy rate of generated hydrogen plus the primary exergy content of liquid hydrogen storage tank (LHST) equivalents to the whole total of exergy rate for liquid hydrogen in LHST plus the exergy destruction during the cycle. By utilizing the model, the exergy balance equality for LHST should be calculated as

$$\left(\dot{m}_{36} t_{pt}\right) ex_{35} + m_{H_{2,f}} ex_{ie,f} = m_{H_{2,l}} ex_{ie,l} + Ex_{D,chst} \tag{26}$$

where t_{pt} is process time, $m_{H_{2,f}}$ and $m_{H_{2,l}}$ show hydrogen mass in the LHST at first time interval and each time interval, $ex_{ie,f}$ and $ex_{ie,l}$ give the initial exergy content of LHST tank at first time interval and each time interval, and $Ex_{D,chst}$ is the exergy destruction of LHST. Also, $ex_{ie,f}$ and $ex_{ie,l}$ are

$$ex_{ie,f} = \left(u_{ie,f} - u_o\right) - T_o\left(s_{ie,f} - s_o\right) + P_o\left(v_{ie,f} - v_o\right) \tag{27}$$

$$ex_{ie,l} = \left(u_{ie,l} - u_o\right) - T_o\left(s_{ie,l} - s_o\right) + P_o\left(v_{ie,l} - v_o\right) \tag{28}$$

where $u_{ie,f}$ and $u_{ie,l}$ show the internal energy of liquid hydrogen in the LHST sub-component at first time interval and each time interval. Also, $v_{ie,f}$ and $v_{ie,l}$ give the specific volume of hydrogen in LHST at first time interval and each time interval.

3.5 Energetic and Exergetic Efficiencies

According to the energetic and exergetic viewpoints, a parameter of how efficiently the input is converted to the useful output is the ratio of output to input. Therefore, the energetic efficiency can be defined as

$$\eta = \frac{\text{Energy output in product}}{\text{Energy input}} = 1 - \frac{\text{Energy loss}}{\text{Energy input}} \tag{29}$$

If we consider the useful part of energy, the exergetic efficiency can be given as follows;

$$\psi = \frac{\text{Exergy output in product}}{\text{Exergy input}} = 1$$
$$- \frac{\text{Exergy waste emission} + \text{Exergy destruction}}{\text{Exergy input}} \tag{30}$$

The energetic and exergetic performance equations for gasifier sub-plant is

$$\eta_{\text{BG}} = \frac{\dot{m}_{12}\text{LHV}_{\text{Syngas}}}{\dot{m}_{11}\text{LHV}_{\text{BM}} + \dot{m}_3 h_3 + \dot{m}_9 h_9} \tag{31}$$

$$\psi_{\text{BG}} = \frac{\dot{m}_{12}\text{ex}_{\text{Syngas}}}{\dot{m}_{11}\text{ex}_{\text{BM}} + \dot{m}_3 \text{ex}_3 + \dot{m}_9 \text{ex}_9} \tag{32}$$

The energetic and exergetic performance equalities for ASU sub-plant can be written as

$$\eta_{\text{ASU}} = \frac{\dot{m}_3 h_3 + \dot{W}_{\text{NT}}}{\dot{m}_1 h_1 + \dot{W}_{\text{AC}}} \tag{33}$$

$$\psi_{\text{ASU}} = \frac{\dot{m}_3 \text{ex}_3 + \dot{W}_{\text{NT}}}{\dot{m}_1 \text{ex}_1 + \dot{W}_{\text{AC}}} \tag{34}$$

The energetic and exergetic performance equations for hydrogen generation sub-component can be written as

$$\eta_{\text{HP}} = \frac{\dot{m}_{21} h_{21}}{\dot{m}_{10} h_{10} + \dot{m}_{16} h_{16}} \tag{35}$$

$$\psi_{\text{HP}} = \frac{\dot{m}_{21} \text{ex}_{21}}{\dot{m}_{10} \text{ex}_{10} + \dot{m}_{16} \text{ex}_{16}} \tag{36}$$

The energetic and exergetic performance equalities for hydrogen liquefaction sub-system is defined as

$$\eta_{\text{HL}} = \frac{\dot{E}_{\text{H}_2,l} + \sum \dot{W}_{\text{Exp}}}{\dot{E}_{\text{H}_2,g} + \dot{W}_{\text{HyC}} + \dot{W}_{\text{Hl/C}}} \tag{37}$$

$$\psi_{\text{HL}} = \frac{\dot{\text{Ex}}_{\text{H}_2,l} + \sum \dot{W}_{\text{Exp}}}{\dot{\text{Ex}}_{\text{H}_2,g} + \dot{W}_{\text{HyC}} + \dot{W}_{\text{Hl/C}}} \tag{38}$$

The energetic and exergetic efficiency equalities for whole system can be written as;

$$\eta_{WS} = \frac{\dot{W}_{NT} + \dot{E}_{H_2,l} + \sum \dot{W}_{Exp}}{\dot{m}_{11} LHV_{BM} + \dot{W}_{AC} + \dot{W}_{HyC} + \dot{W}_{HlC}} \tag{39}$$

$$\psi_{WS} = \frac{\dot{W}_{NT} + \dot{Ex}_{H_2,l} + \sum \dot{W}_{Exp}}{\dot{m}_{11} ex_{BM} + \dot{W}_{AC} + \dot{W}_{HyC} + \dot{W}_{HlC}} \tag{40}$$

4 Environmental Analysis

The air-polluting emissions, such as NO_x, CO_2, SO_2, CH_4 and Hg compositions associated with producing power and liquid hydrogen from biomass resources should be considered for environmentally benign system design. But, SO_2 and NO_x emissions from biomass gasification process are very low compared to CO_2, they are not considered in the calculations. The CO_2 emission rate for biomass gasification-based hydrogen generation and liquefaction plant can be calculated as follows:

$$\varepsilon_{WS} = \frac{\dot{m}_{CO_2}}{\dot{W}_{net} + \dot{E}_{H_2,l}} \tag{41}$$

5 Results and Discussion

The energetic, exergetic and environmental assessments of hydrogen production and liquefaction plant integrated with biomass gasifier have been presented. Table 1 indicates the design parameter of this integrated system. Ultimate analysis and LHV and HHV values of biomass source which is straw chosen for this study are given in Tables 3 and 4, respectively.

5.1 Effects of Dead State Temperature

Dead state temperature is an important parameter for integrated energy systems affecting energy and exergy performance consequently products' rate of plant. Energy efficiencies of biomass gasifier, air separation unit, hydrogen generation, and liquefaction sub-systems are directly proportional to the dead state temperature. Increasing dead state temperature by fixing other variables as in Table 1 makes LHV of biomass source increase. Therefore, higher efficiency of the main source of the

system which is biomass causes higher energetic efficiencies in other sub-systems too. When considered especially whole system energetic efficiency, it is seen that given the range of 0–40 °C, energetic performance of whole plant rises from 67 to 69%.

Similar to Figs. 2 and 3 demonstrate the positive effect of dead state temperature increase on exergetic performances of sub-plants and whole plant. Increasing dead state temperature causes to decrease the difference between system working temperature and dead state temperature. Consequently, exergy destruction rates decrease.
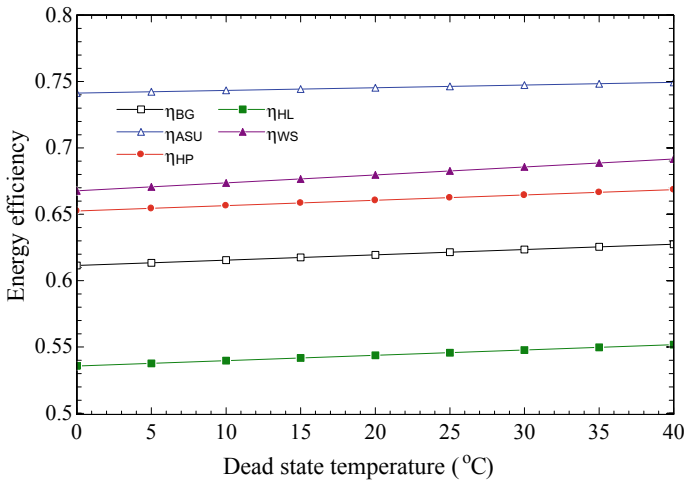
Fig. 2 Effects of dead state temperature on energetic performance
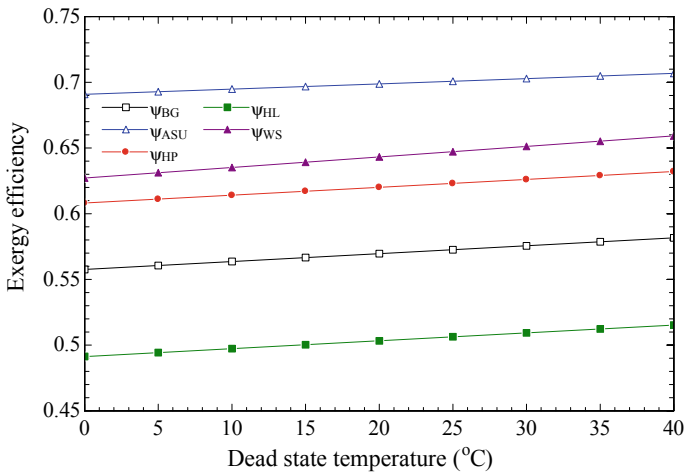
Fig. 3 Effects of dead state temperature on exergetic efficiencies
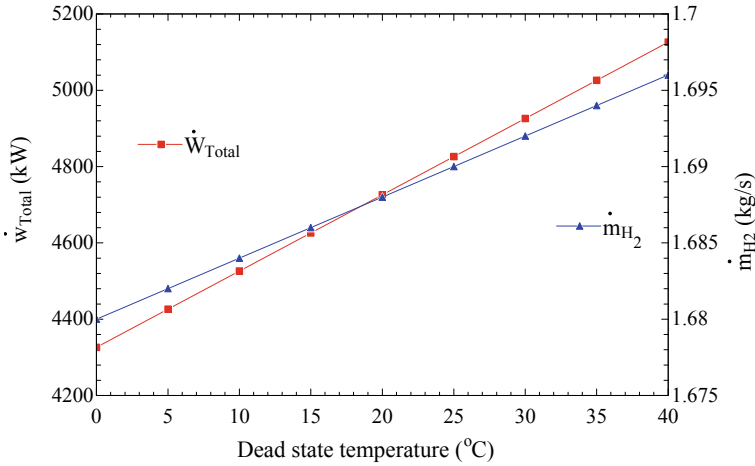
Fig. 4 Effect of dead state temperature on total power and hydrogen generation

Higher energetic and exergetic efficiencies of sub-systems and whole system mean higher products obtained from that system. Figure 4 reveals the increase in generated electricity and hydrogen rates as dead state temperature rises from 0 to 40 °C. Generated power rises from 4320 to 5120 kW and hydrogen generation rates from 1.680 to 1.696 kg/s for given range of dead state temperature (Fig. 5).

As expected from previous results, exergy destruction rate and emitted CO_2 decrease with increasing dead state temperature. For calculated temperature range,
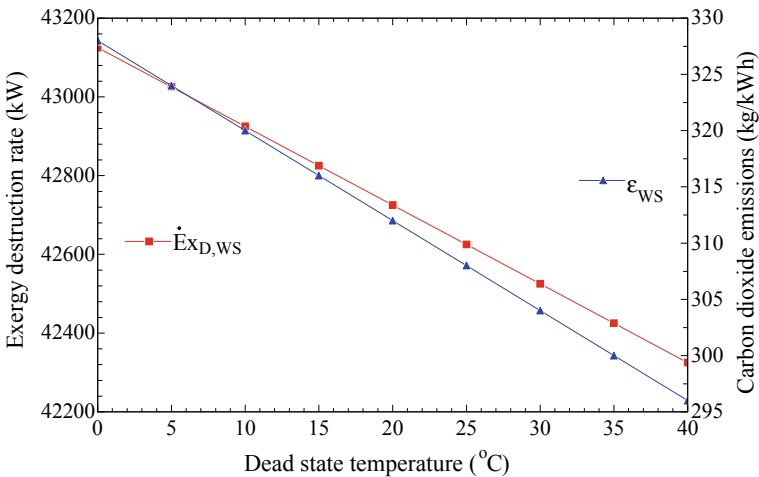
Fig. 5 Effects of dead state temperature on exergy destruction and CO_2 emission

irreversibility rate of whole plant decreases from 43,120 to 42,330 kW and amount of emitted CO_2 decreases from 328 to 296 kg/kWh.

5.2 Effects of Biomass Gasifier Temperature

Another significant parameter affecting the plant performance is biomass gasifier. Following four figures show the effects of biomass gasifier temperature on energetic efficiency, exergetic efficiency, production rates, and exergy destruction rate and amount of emission, respectively.

As biomass gasifier temperature varies between 680 and 840 °C, energy performances of all sub-plants and whole plant slightly increase as seen from Fig. 6. For given range of biomass gasifier temperature, energy performance of whole plant rises from 66 to 69% (Fig. 7).

Exergetic performances of all sub-plants and whole plant are affected positively with rising biomass gasifier temperature. For varying biomass gasifier temperature from 680 to 840 °C, exergy performance of whole plant changes from 62% to nearly 67%. Direct proportional between total power and biomass gasifier temperature is seen in Fig. 8. Moreover, hydrogen production rate is directly proportional to biomass gasifier temperature. For calculated range of biomass gasifier temperature, total power production rises from 4320 to 5140 kW and consequently hydrogen generation rate increases 1.650–1.716 kg/s.

As reflected in Fig. 9, exergy destruction of whole plant decreases from 48,400 to 38,970 kW. Also, the CO_2 emissions decrease sharply from 345 to 287 kg/kWh. As biomass gasifier temperature analyses show, it has a positive effect on system
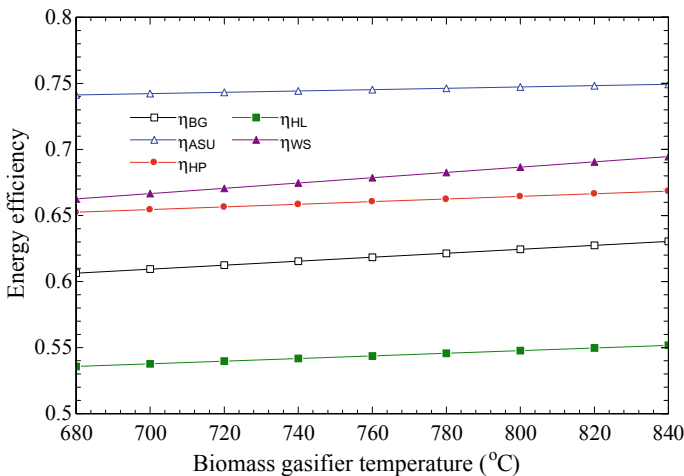
Fig. 6 Impact of biomass gasifier temperature on energy efficiencies
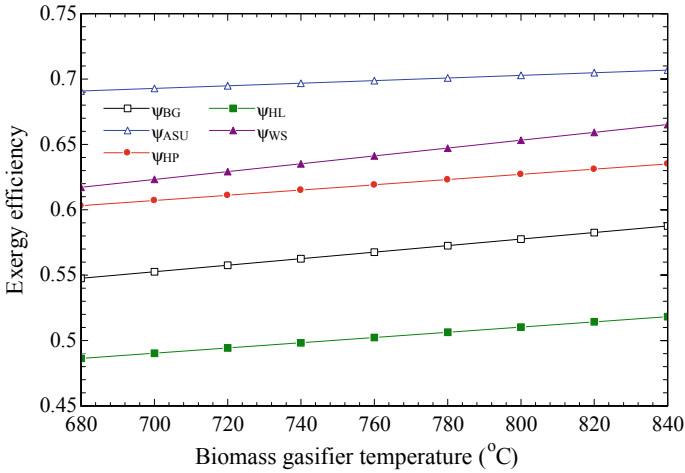
Fig. 7 Impacts of biomass gasifier temperature on exergy efficiencies
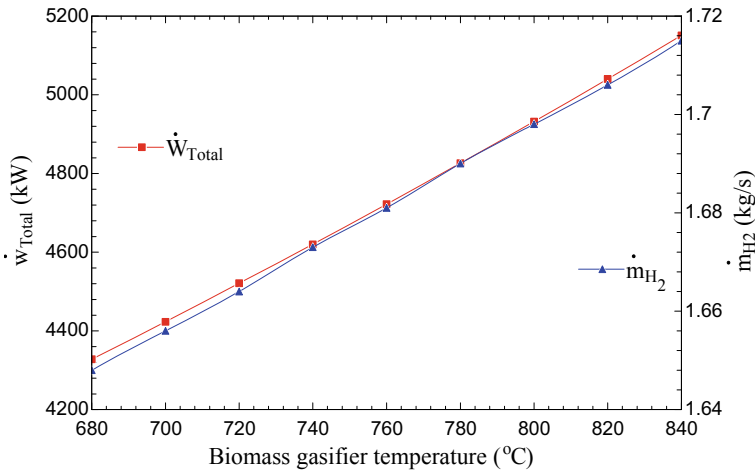
Fig. 8 Impacts of biomass gasifier temperature on total power and hydrogen generation

performance for given range of temperature. Increasing gasifier temperature makes endothermic gasification reaction shifts toward the right side. This leads to higher heating rates during the gasification process. Hence, an increment in biomass gasifier temperature causes system works more efficiently and emissions decrease [15].
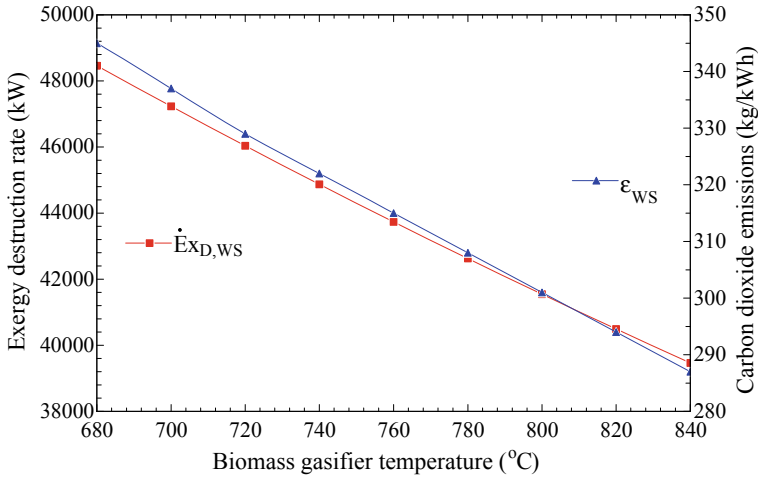
Fig. 9 Impacts of biomass gasifier temperature on exergy destruction and CO_2 emission

5.3 Effects of HEX2 Pinch Point Temperature

Because pinch point temperature is a crucial design indicator for HEXs, the third parameter analyzed in this study is HEX2 pinch point temperature which ranges from 10 to 40 °C. In general, raising pinch point temperature causes system performance goes down. The reason lying behind this situation is that rising pinch point temperature leads to reduce the energy recovered by heat exchangers. Figures 10 and 11 shows decreasing energetic and exergetic efficiencies of all sub-plants and whole
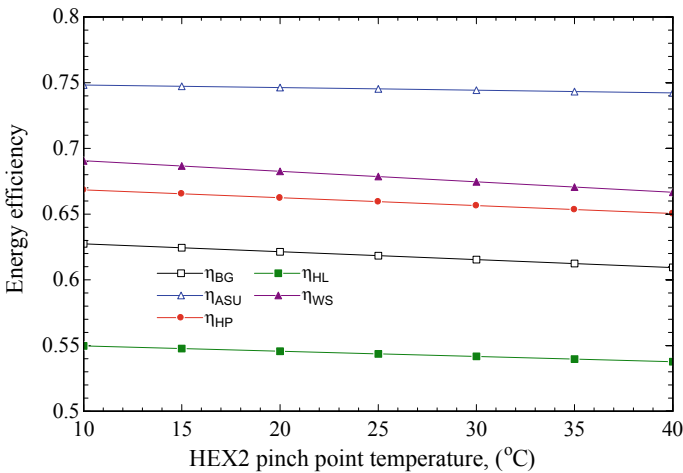
Fig. 10 Effects of HEX2 pinch point temperature on energy efficiencies
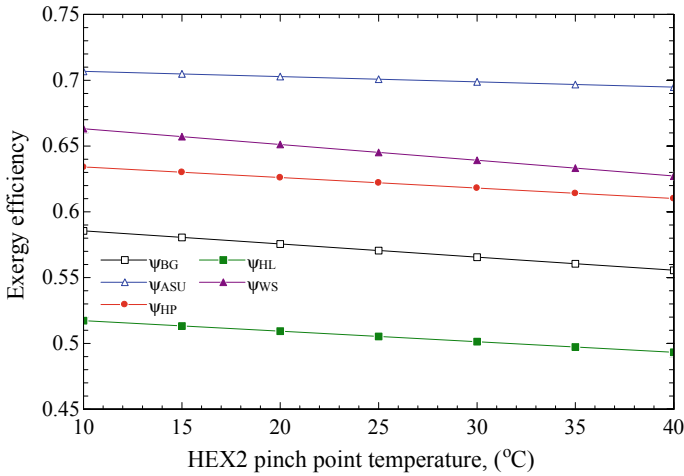
Fig. 11 Effects of HEX2 pinch point temperature on exergetic efficiencies

plant with raising HEX2 pinch point temperature.

Figure 10 illustrates the effect of HEX2 pinch point temperature on energy efficiencies of sub-systems and whole plant. As HEX2 pinch point temperature increases from 10 to 40 °C, energy efficiencies of all sub-systems and whole plant decrease. When considered the energetic efficiency of whole plant, it decreases from 69 to 66.6%. Energy efficiencies of other sub-components decrease also 2–3 points while HEX′ pinch point temperature increases.

Similar to energy analysis, exergy analysis show decrease in exergy performances of sub-plants and whole plant with increasing HEX2 pinch point temperature. As seen from Fig. 11 for given range, higher pinch point temperature has negative impact on plant performance. As expected after energy and exergy analyses, increasing HEX2 pinch point temperature causes decrease in both total electricity and hydrogen generation. As HEX2 pinch point temperature varies between 10 and 40 °C, total electricity generation decreases from 5060 to 4400 kW and hydrogen generation declines from 1.71 to 1.64 kg/s, as given in Fig. 12.

As demonstrated in Fig. 13, increasing HEX2 pinch point temperature makes exergy destruction rate and CO_2 emission decrease. For given range, exergy destruction rate drops from 45,000 to 38,000 kW and CO_2 emissions change from 324 to 279 kg/kWh.

5.4 Effects of Compressor Pressure Ratio

The last parameter investigated in this study compressor pressure ratio. There is a peak value of compressor pressure ratio affecting system performance [16]. The
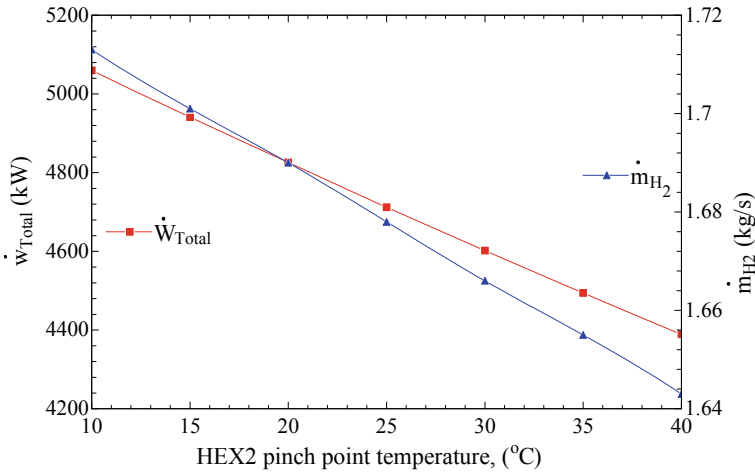
Fig. 12 Effects of HEX2 pinch point temperature on total power and hydrogen generation
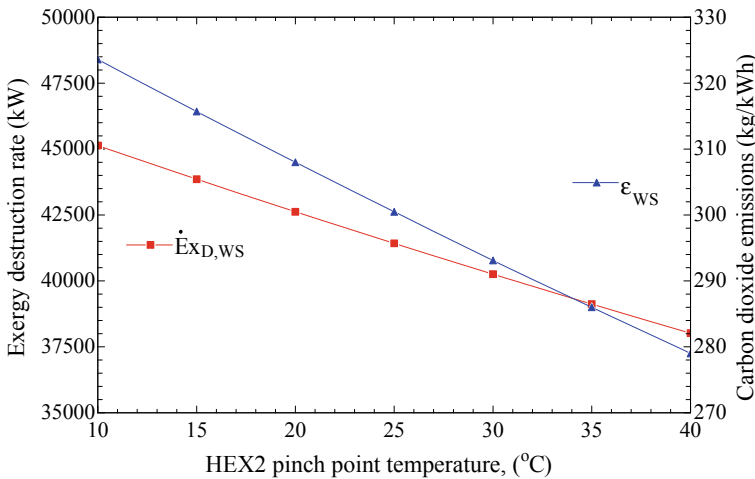
Fig. 13 Effect of HEX2 pinch point temperature on exergy destruction rate and CO_2 emission

highest energy efficiency value of whole system occurs at compressor pressure ratio 6 which is 67.3%.

As seen from Fig. 14, the best energy performance values of other sub-systems occur at compression pressure ratio 6, too. When compressor pressure ratio is 6, minimum biomass fuel will be sufficient for gasification process.

As seen in Fig. 15, compressor pressure ratio 6 is again is the best value for exergy performances of whole plant and other sub-systems. The largest exergy efficiency of whole plant which is 65% appears at compressor pressure ratio 6.
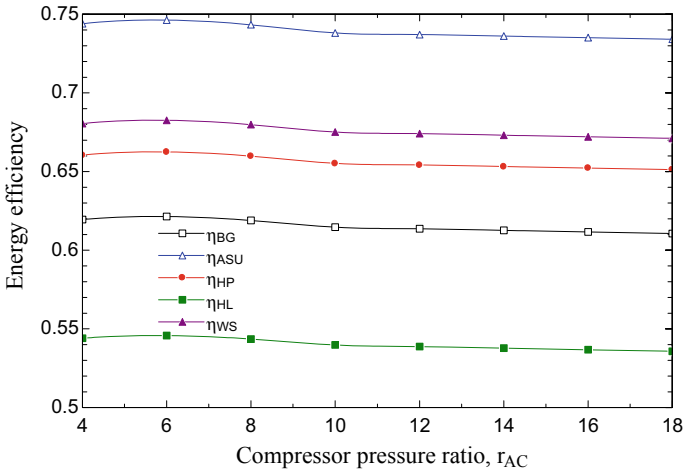
Fig. 14 Impacts of compressor pressure ratio on energy efficiencies
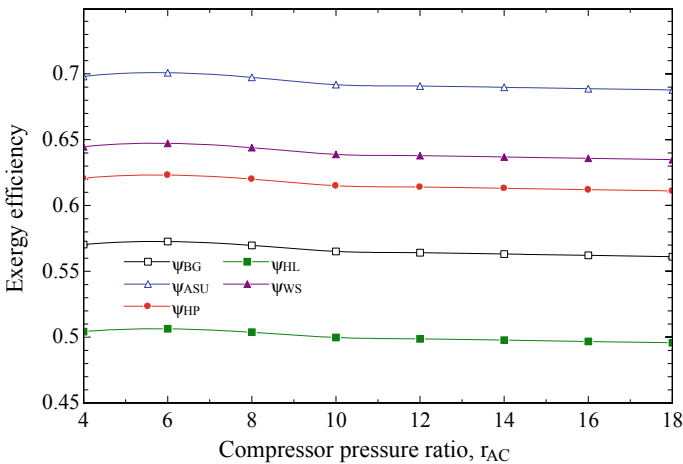
Fig. 15 Impact of compressor pressure ratio on exergy efficiency

As seen from Fig. 16, when compressor pressure ratio is fixed at 6, total power production and hydrogen generation rate reach the peak value of them which are 4960 kW and 1.67 kg/s, respectively. As expected, highest efficiency and highest production rates result in compressor pressure ratio 6, Fig. 17 indicates CO_2 emissions drop the minimum value which is 306 kg/kWh. Also, exergy destruction rate falls off the minimum value which is 42,450 kW.
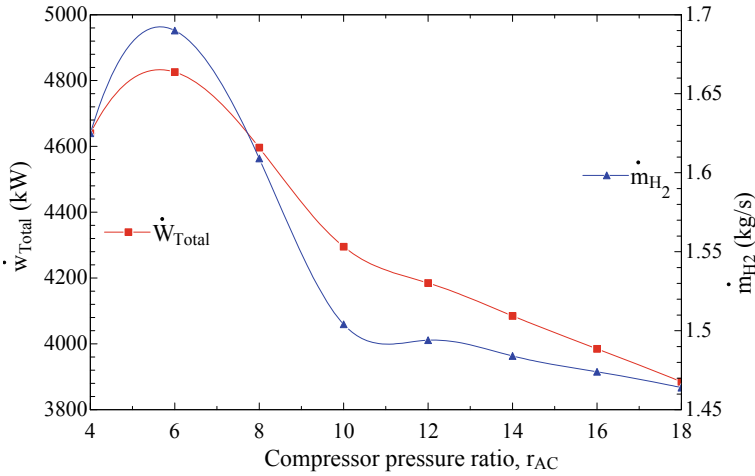
Fig. 16 Impact of compressor pressure ratio on total power and hydrogen generation
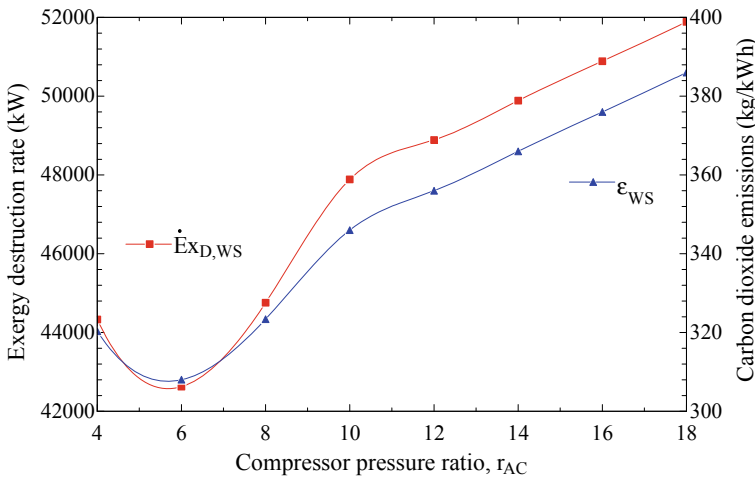
Fig. 17 Impact of compressor pressure ratio on exergy destruction rate and CO_2 emission

6 Conclusions

The aim of this book chapter is to determine the energetic, exergetic and environmental effects of biomass-based hydrogen generation and liquefaction plant. Hydrogen, as future energy carrier, is chosen for the main product with power generation. Therefore, some indicators affecting energy and exergy efficiency, CO_2 emissions, electricity, and hydrogen production rates are investigated. Some concluding outputs of this book chapter are given as

- When other parameters keep fixed as design parameters, increasing dead state temperature with the range of 0–40 °C has a positive effect on energetic efficiency, exergetic efficiency, power, and hydrogen production rate.
- Maximum hydrogen production rate occurs when biomass gasification temperature is 840 °C, by fixing other variables.
- While HEX2 pinch point temperature rises from 10 to 40 °C, exergy performance of whole plant drops from 66 to 63% and hydrogen generation rate declines from 1.71 to 1.64 kg/s.
- Being another parameter affecting system performance, the best value of compressor pressure ratio is 6 for energetic and exergetic efficiency and power and hydrogen production.

References

1. Dincer I, Acar C (2015) Review and evaluation of hydrogen production methods for better sustainability. Int J Hydrog Energy 40(34):11094–11111
2. Kothari R, Buddhi D, Sawhney RL (2008) Comparison of environmental and economic aspects of various hydrogen production methods. Renew Sustain Energy Rev 12(2):553–563
3. Balat H, Kirtay E (2010) Hydrogen from biomass—present scenario and future prospects. Int J Hydrog Energy 35(14):7416–7426
4. Sikarwar VS, Zhao M, Clough P et al (2016) An overview of advances in biomass gasification. Energy Environ Sci 9(10):2939–2977
5. Molino A, Chianese S, Musmarra D (2016) Biomass gasification technology: the state of the art overview. J Energy Chem 25(1):10–25
6. Heidenreich S, Foscolo PU (2015) New concepts in biomass gasification. Prog Energy Combust Sci 46:72–95
7. Shayan E, Zare V, Mirzaee I (2018) Hydrogen production from biomass gasification; a theoretical comparison of using different gasification agents. Energy Convers Manag 159:30–41
8. Dincer I, Rosen MA (2012) Exergy: energy, environment and sustainable development. Elsevier, Oxford
9. Szargut J, Styrylska T (1964) Approximate evaluation of the exergy of fuels. Brennst Wärme Kraft 16(12):589–596
10. van den Broek R, Faaij A, Wijk AV (1996) Biomass combustion for power generation. Biomass Bioenergy 11(4):271–281
11. Channiwala SA, Parikh PP (2002) A unified correlation for estimating HHV of solid, liquid and gaseous fuels. Fuel 81:1051–1063
12. Ahmadi P, Dincer I, Rosen MA (2012) Exergo-environmental analysis of an integrated organic Rankine cycle for trigeneration. Energy Convers Manag 64:447–453
13. Scott RB, Brickwedde FG, Urey HC, Wahl MH (1934) The vapor pressures and derived thermal properties of hydrogen and deuterium. J Chem Phys 2:454–464
14. Sullivan NS, Zhou D, Edwards CM (1990) Precise and efficient in situ ortho-para-hydrogen converter. Cryogenics 30:734–735
15. Lapuerta M, Hernández JJ, Pazo A, López J (2008) Gasification and co-gasification of biomass wastes: effect of the biomass origin and the gasifier operating conditions. Fuel Process Technol 89(9):828–837
16. Mohtaram S, Chen W, Zargar T, Lin J (2017) Energy-exergy analysis of compressor pressure ratio effects on thermodynamic performance of ammonia water combined cycle. Energy Convers Manag 134:77–87

Energy, Exergy and Environmental Analyses of Biomass Gasifier Combined Integrated Plant

Fatih Yilmaz and Murat Ozturk

Abstract The fundamental purpose of this chapter is to examine a novel renewable energy supported combined plant. The suggested chapter occurs with biomass gasifier unit, gas turbine system, Rankine cycle, single-effect absorption cycle, hydrogen generation unit, dryer cycle, and hot-water production unit. This chapter is designed and developed for useful outputs, such as heating, cooling, electricity, hydrogen, drying and hot water with a single biomass energy input. In this context, detailed energy and exergy efficiency, and also environmental effect analyses are carried out with Engineering Equation Solver software. The effects of environment and gasification temperatures and biomass mass flow rate changes on the plant performance and on carbon emissions are investigated and presented as graphs. Results display that the energetic and exergetic efficiency of integrated plant are found as 63.84 and 59.26%. Also, the overall hydrogen generation and exergy destruction rate are 0.068 kg/s and 52,529 kW, respectively.

Keywords Biomass · Energy · Exergy · Environment · Integrated system

Nomenclature

E	Energy (kJ)
$\dot{E}$	Energy rate (kW)
$\dot{E}x$	Exergy rate (kW)
ex	Exergy
h	Specific enthalpy (kJ/kg)

F. Yilmaz
Department of Electrical and Energy, Vocational School of Technical Sciences,
Aksaray University, 68100 Aksaray, Turkey
e-mail: fatiyilmaz7@gmail.com

M. Ozturk (✉)
Department of Mechatronic Engineering, Faculty of Technology, Isparta University
of Applied Sciences, 32100 Isparta, Turkey
e-mail: muratozturk@isparta.edu.tr

P	Pressure (kPa)
s	Specific entropy (kJ/kg-K)
T	Temperature (°C-K)
$\dot{m}$	Mass flow rate (kW)
$\dot{Q}$	Heat transfer rate (kW)
$\dot{W}$	Work rate (kW)

Greek letters

η	Energy efficiency
ψ	Exergy efficiency
ε	Emission rate

Subscripts

BGS	Biomass gasification system
cogen	Cogeneration
DC	Dryer cycle
e	Exit
en	Energy
ex	Exergy
GTS	Gas turbine system
HP	Hydrogen production
HPT	High pressure turbine
HWP	Hot-water production
i	Input
LPT	Low pressure turbine
RC	Rankine cycle
sngen	Single generation
trigen	Trigeneration
WS	Whole system

Abbreviations

COP	Performance coefficient
HEX	Heat exchanger
HHV	Higher heating value
LHV	Lower heating value

1 Introduction

The demand for energy throughout globe is continuously rising every passing day, especially in the last 50 years [1]. To meet this rise in the power demand in globe, the use of fossil-based sources continues to increase in parallel. According to the 2015 report of World Bank Data, the fossil energy consumption in the world is about 80% [2]. In this case, the environmental problems triggered by fossil-based fuels, for example, acid rain, ozone layer depletion, global warming and climate change are increasing [3]. In order to prevent environmental problems, it is very significant to efficiently use energy sources as well as the renewable sources supported plants. The clean energy sources are mainly solar, wind, hydro, geothermal, and biomass. Also, it can be stated that these energy sources have no harm to the environment, and there is abundant on the earth.

On the other hand, renewable energy-assisted integrated plants play a key role in the effective use of energy and manage to sustainable energy production as well. A combined multigeneration system can be defined as a system that can produce a variety of useful products [4]. In these cycles, various renewable power resources, such as solar, wind, geothermal, and biomass should be utilized as an energy source. In addition, multigeneration energy production has many advantages, such as high plant process, diminished energetic and exergetic losses, reduced material waste, reduced maintenance prices, and reduced GHG impacts [4, 5]. There are several studies related to different renewable energy sources supported multigeneration plants in the literature and also the interest in this subject has been increasing in the last few decades.

Safari and Dincer [6] have examined a new biomass-supported combined plant for multiproduction. They performed thermodynamic performance evaluation of combined plant, and also the energetic and exergetic efficiency of investigated cycle is computed as 63.6 and 40%. Sung et al. [7] have presented a thermo-economic evaluation of biogas-fueled gas turbine with organic Rankine cycle (ORC). According to the results of their study, the economy of plant is very sensitive to the variations in biogas methane ratio and electricity prices.

Sevinchan et al. [8] have reported an energetic and exergetic analyses of biogas-based combined cycle. Their work outcomes display that the highest exergetic efficiency of combined plant is found as 30.44% and also the maximum irreversibility rate is seen in the combustor sub-system. Wu et al. [9] have analyzed an energetic, environmental, and economic evaluation of three utilization pathways for biogas-assisted plant; heating with cooling, biomethane, and fuel cell. According to the results, the biogas upgrade path has the maximum energy efficiency with 46.5%, and the shortest repayment period is 8.9 years.

Giarola et al. [10] have demonstrated an energy, exergy, and economic examination of biogas fed SOFC combined plant for heat and power production. Their study results show that the SOFC technology means that today's capital costs are not exactly competing with traditional alternatives. Taheri et al. [11] have analyzed the thermodynamical and economical analyses of new biomass-based combined plant

with hydrogen generation and LNG regasification process. Increment in the fuel mass flow rate gives rise to a reduction of the overall energy efficiency about 8.5%, according to their analysis results.

Karellas and Braimakis [12] have conducted a thermodynamic and economic examination of biomass and solar-power-assisted cogeneration and trigeneration cycle. For the studied operating temperatures, the ORC energetic performance is defined to be maximized at 5.5% with evaporator temperature 90 °C and R245fa fluid. Sulaiman et al. [13] have comprised a performance assessment of three trigeneration cycles using ORCs. Their proposed cycles are including the SOFC, biomass and solar-supported trigeneration. According to their results, the CO_2 emission per MWh electrical energy for biomass and SOFC supported trigeneration cycles is high.

Sulaiman et al. [14] have illustrated an exergetic and GHG emission examinations of biomass-based combined ORC cycle for heating, cooling, and power productions. Their results demonstrate that once the trigeneration case is used, the exergetic performance rises to about 27%. At the same time, in the literature, some studies related to the province of different renewable energies (solar, geothermal, and ocean) based on multigeneration plants are presented [15–20].

The main intention of this book chapter is to examine the biomass-based combined multigeneration plant for cooling, heating, power, hydrogen, hot water and drying purposes. In this context, the energetic and exergetic efficiency, irreversibility and environmental impact assessments of suggested plants and its sub-parts are investigated by using the thermodynamic laws. In general, this proposed study has four main objectives, which can be definite as follows;

* To design and investigate a novel biomass-based combined plant,
* To study the energetic and exergetic performance and environmental evaluation of proposed cycle,
* To define the irreversibility rate and locations for suggested combined plant,
* To analyze the hydrogen, power, cooling, heating, drying and hot-water productions from biomass energy.

2 System Definition

The schematic illustration of proposed biomass gasifier combined plant for various useful products is presented in Fig. 1. The overall combined plant can be divided into seven main sub-systems; (a) biomass gasifier unit, (b) gas turbine cycle, (c) Rankine cycle, (d) single-effect absorption cooling (SEAC) cycle, (e) hydrogen production unit, (f) dryer cycle and (g) hot-water storage system. In the suggested chapter, the straw enters at point 1 and is used as fuel for combined plant. Firstly, the air entering from point 12 is pressurized at compressor 1 and compressor 2 and then enters the combustion chamber at point 16. Then, it transfers the biogas temperature coming from point 11 to the air and the power generation occurs in the gas turbine.
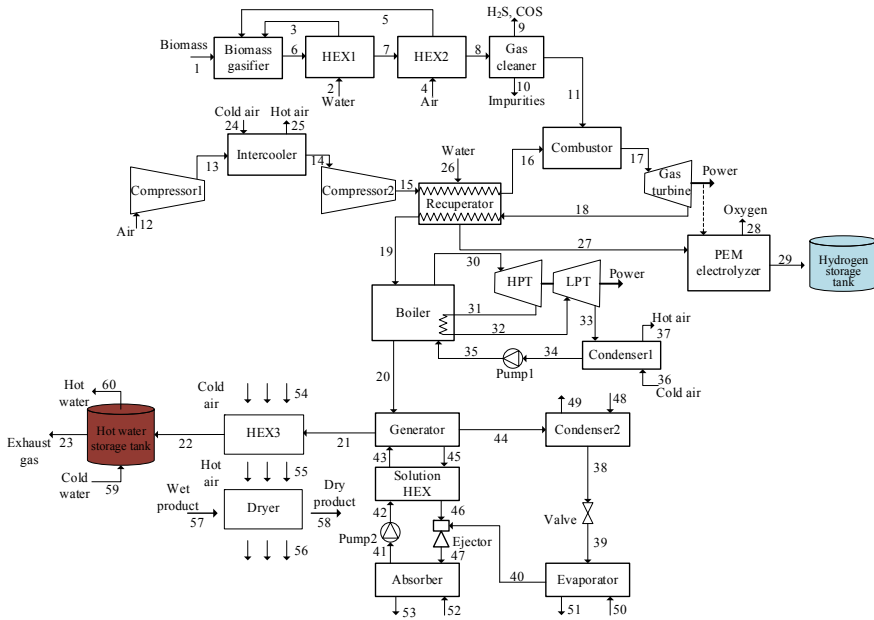
Fig. 1 Schematic diagram of biomass gasifier combined plant

After that, the exhaust gas from point 18 enters boiler and generator, respectively, and then it transfers the heat energy to the Rankine cycle and SEAC sub-systems. On the hand, in the pure water recuperator entering the reference conditions at point 26, it is heated to about 80 °C and then enters the PEM electrolyzer. Then, some of the produced electricity by using the gas turbine enters the PEM, and then hydrogen generation occurs.

Finally, the proposed plant is designed to perform the useful outputs, for example, hydrogen, power, heating, cooling, hot water, and drying, with assisted by biomass energy. The design parameters of biomass gasifier supported integrated cycle are tabulated in Table 1. On the other hand, the ultimate assessment, and also lower heating and higher heating values (LHV and HHV) of biomass source are given in Tables 2 and 3.

3 Thermodynamic Assessment

In this section, a comprehensive thermodynamic and environmental evaluation of biomass gasifier combined plant is conducted for useful commodities. In this context, the thermodynamic performance and irreversibility rate of whole system and its sub-parts are investigated according to various parameters. The general mass,

Table 1 Design parameters of biomass gasifier combined integrated plant

Parameters	Values
Ambient temperature, T_o (°C)	25
Ambient pressure, P_o (kPa)	101.3
Pressure ratio of compressors, r_{AC}	8
Isentropic efficiency of compressors, η_{AC} (%)	85
Mass flow rate of biomass fuel, $\dot{m}_1$ (kg/s)	6.14
Biomass gasifier temperature, T_{BG} (°C)	780
Syngas combustor temperature, T_{SC} (°C)	875
Input pressure of gas turbine, P_{17} (kPa)	506.6
Input temperature of gas turbine, T_{17} (°C)	870
Input pressure of high-pressure turbine, P_{30} (kPa)	6370
Input temperature of high-pressure turbine, T_{30} (°C)	785
Input pressure of low-pressure turbine, P_{32} (kPa)	2305
Input temperature of low-pressure turbine, T_{32} (°C)	324
Isentropic efficiencies of gas turbine, $\eta_{is,GT}$ (%)	80
Isentropic efficiencies of pumps, $\eta_{is,P}$ (%)	80
Isentropic efficiencies of high and low-pressure turbine, $\eta_{is,T}$ (%)	80
PEM temperature, T_{PEM} (°C)	81
PEM electrolyzer thickness, D_{PEM} (µm)	100
COP_{en} of SEAC	0.7863
COP_{ex} of SEAC	0.2561

Table 2 Ultimate assessment of biomass source utilized in biomass gasifier unit

Compound	Straw	
	Dry basis (wt%)	Dry-ash-free basis (wt%)
C	45.02	48.13
H	3.91	4.23
N	0.72	0.76
S	0.10	0.11
O	43.86	46.24

Table 3 LHV and HHV of biomass source in the biomass gasifier unit

Heating value	Straw	
	Original basis (kJ/kg)	Dry basis (kJ/kg)
LHV	17,342	18,910
HHV	18,664	20,175

energy, entropy, and exergy equilibrium equalities of plant and sub-systems are written with EES program [21]. Some important assumptions made in thermodynamic calculations can be explained as follows;

- All systems and elements are running in the steady-state conditions.
- The kinetic and potential energies are disregarded.
- The pressure drops in pipelines have been neglected.
- The heat loss between the plant and environment has been neglected.

The general mass, energy, entropy, and exergy balance equation should be given as below [22–24];

$$\sum \dot{m}_i = \sum \dot{m}_e \tag{1}$$

where $\dot{m}$, i, and e represent the mass flow rate, inlet, and outlet conditions. The energy equilibrium equation can be inscribed as;

$$\sum \dot{m}_i h_i + \sum \dot{Q}_i + \sum \dot{W}_i = \sum \dot{m}_e h_e + \sum \dot{Q}_e + \sum \dot{W}_e \tag{2}$$

where $\dot{Q}$ is heat transfer rate, h is specific enthalpy and $\dot{W}$ is work rate. The general entropy and exergetic balance equalities can be depicted as below;

$$\sum \dot{m}_i s_i + \sum \left(\frac{\dot{Q}}{T}\right)_i + \dot{S}_{\text{gen}} = \sum \dot{m}_e s_e + \sum \left(\frac{\dot{Q}}{T}\right)_e \tag{3}$$

$$\sum \dot{m}_i \text{ex}_i + \sum \dot{E}x_i^Q + \sum \dot{E}x_i^W = \sum \dot{m}_e \text{ex}_e + \sum \dot{E}x_e^Q + \sum \dot{E}x_e^W + \dot{E}x_D \tag{4}$$

The exergy destruction rate is symbolized by $\dot{E}x_D$ and also the heat and work rate of exergy can be described as follow;

$$\dot{E}x_D = T_0 \dot{S}_{\text{gen}} \tag{5}$$

$$\dot{E}x_Q = \left(1 - \frac{T_o}{T}\right)\dot{Q} \tag{6}$$

$$\dot{E}x_W = \dot{W} \tag{7}$$

$$\text{ex} = \text{ex}_{\text{ph}} + \text{ex}_{\text{ch}} \tag{8}$$

The physical exergy can be inscribed as;

$$\text{ex}_{\text{ph}} = h - h_o - T_o(s - s_o) \tag{9}$$

Balance equations of biomass gasification supported combined plant are illustrated in Table 4. The energetic and exergetic performance equalities for biomass gasifier combined multigeneration system and its sub-system can be defined as given below;

For biomass gasification sub-system;

$$\eta_{BGS} = \frac{\dot{m}_{11}h_{11}}{\dot{m}_1 h_1 + \dot{m}_3 h_3 + \dot{m}_5 h_5} \tag{10}$$

$$\psi_{BGS} = \frac{\dot{m}_{11}ex_{11}}{\dot{m}_1 ex_1 + \dot{m}_3 ex_3 + \dot{m}_5 ex_5} \tag{11}$$

For gas turbine cycle sub-system;

$$\eta_{GTS} = \frac{\dot{W}_{GT} - \left(\dot{W}_{AC1} + \dot{W}_{AC2}\right)}{\dot{m}_{17}h_{17}} \tag{12}$$

$$\psi_{GTS} = \frac{\dot{W}_{GT} - \left(\dot{W}_{AC1} + \dot{W}_{AC2}\right)}{\dot{m}_{17}ex_{17}} \tag{13}$$

For Rankine sub-system with two turbines;

$$\eta_{RC} = \frac{\dot{W}_{HPT} + \dot{W}_{LPT}}{\dot{W}_{P1} + (\dot{m}_{19}h_{19} - \dot{m}_{20}h_{20})}. \tag{14}$$

$$\psi_{RC} = \frac{\dot{W}_{HPT} + \dot{W}_{LPT}}{\dot{W}_{P1} + (\dot{m}_{19}ex_{19} - \dot{m}_{20}ex_{20})} \tag{15}$$

For single-effect absorption cooling sub-system;

$$\eta_{SEAC} = \frac{\dot{Q}_{Cooling}}{(\dot{m}_{20}h_{20} - \dot{m}_{21}h_{21}) + \dot{W}_{P2}} \tag{16}$$

$$\psi_{SEAC} = \frac{\dot{Ex}^Q_{Cooling}}{(\dot{m}_{20}ex_{20} - \dot{m}_{21}ex_{21}) + \dot{W}_{P2}} \tag{17}$$

For hydrogen production sub-system;

$$\eta_{HP} = \frac{\dot{m}_{29}LHV_{H_2}}{\dot{m}_{27}h_{27} + \dot{W}_{PEM}} \tag{18}$$

$$\psi_{HP} = \frac{\dot{m}_{29}ex_{H_2}}{\dot{m}_{27}ex_{27} + \dot{W}_{PEM}} \tag{19}$$

Table 4 Balance equations of biomass gasification-based integrated system

Components	Mass balance	Energy balance	Entropy balance	Exergy balance
Biomass gasifier	$\dot m_1 + \dot m_3 + \dot m_5 = \dot m_6$	$\dot m_1 h_1 + \dot m_3 h_3 + \dot m_5 h_5 = \dot m_6 h_6$	$\dot m_1 s_1 + \dot m_3 s_3 + \dot m_5 s_5 + \dot S_{g,\mathrm{BG}} = \dot m_6 s_6$	$\dot m_1 ex_1 + \dot m_3 ex_3 + \dot m_5 ex_5 = \dot m_6 ex_6 + \dot{Ex}_{D,\mathrm{BG}}$
HEX1	$\dot m_2 = \dot m_3$ $\dot m_6 = \dot m_7$	$\dot m_2 h_2 + \dot m_6 h_6 = \dot m_3 h_3 + \dot m_7 h_7$	$\dot m_2 s_2 + \dot m_6 s_6 + \dot S_{g,\mathrm{HEX1}} = \dot m_3 s_3 + \dot m_7 s_7$	$\dot m_2 ex_2 + \dot m_6 ex_6 = \dot m_3 ex_3 + \dot m_7 ex_7 + \dot{Ex}_{D,\mathrm{HEX1}}$
Gas cleaner	$\dot m_8 = \dot m_9 + \dot m_{10} + \dot m_{11}$	$\dot m_8 h_8 = \dot m_9 h_9 + \dot m_{10} h_{10} + \dot m_{11} h_{11}$	$\dot m_8 s_8 = \dot m_9 s_9 + \dot m_{10} s_{10} + \dot m_{11} s_{11} + \dot S_{g,\mathrm{GC}}$	$\dot m_8 ex_8 = \dot m_9 ex_9 + \dot m_{10} ex_{10} + \dot m_{11} ex_{11} + \dot{Ex}_{D,\mathrm{GC}}$
Compressor1	$\dot m_{12} = \dot m_{13}$	$\dot m_{12} h_{12} + \dot W_{\mathrm{Compl}} = \dot m_{13} h_{13}$	$\dot m_{12} s_{12} + \dot S_{g,\mathrm{Compl}} = \dot m_{13} s_{13}$	$\dot m_{12} ex_{12} + \dot W_{\mathrm{Compl}} = \dot m_{13} ex_{13} + \dot{Ex}_{D,\mathrm{Compl}}$
Intercooler	$\dot m_{13} = \dot m_{14}$	$\dot m_{13} h_{13} + \dot m_{24} h_{24} = \dot m_{14} h_{14} + \dot m_{25} h_{25}$	$\dot m_{13} s_{13} + \dot m_{24} s_{24} + \dot S_{g,\mathrm{IntC}} = \dot m_{14} s_{14} + \dot m_{25} s_{25}$	$\dot m_{13} ex_{13} + \dot m_{24} ex_{24} = \dot m_{14} ex_{14} + \dot m_{25} ex_{25} + \dot{Ex}_{D,\mathrm{IntC}}$
Recuperator	$\dot m_{15} = \dot m_{16}$ $\dot m_{18} = \dot m_{19}$ $\dot m_{26} = \dot m_{27}$	$\dot m_{15} h_{15} + \dot m_{18} h_{18} + \dot m_{26} h_{26} = \dot m_{16} h_{16} + \dot m_{19} h_{19} + \dot m_{27} h_{27}$	$\dot m_{15} s_{15} + \dot m_{18} s_{18} + \dot m_{26} s_{26} + \dot S_{g,\mathrm{Rec}} = \dot m_{16} s_{16} + \dot m_{19} s_{19} + \dot m_{27} s_{27}$	$\dot m_{15} ex_{15} + \dot m_{18} ex_{18} + \dot m_{26} ex_{26} = \dot m_{16} ex_{16} + \dot m_{19} ex_{19} + \dot m_{27} ex_{27} + \dot{Ex}_{D,\mathrm{Rec}}$
Combustor	$\dot m_{11} + \dot m_{16} = \dot m_{17}$	$\dot m_{11} h_{11} + \dot m_{16} h_{16} = \dot m_{17} h_{17}$	$\dot m_{11} s_{11} + \dot m_{16} s_{16} + \dot S_{g,\mathrm{Cb}} = \dot m_{17} s_{17}$	$\dot m_{11} ex_{11} + \dot m_{16} ex_{16} = \dot m_{17} ex_{17} + \dot{Ex}_{D,\mathrm{Cb}}$
Gas turbine	$\dot m_{17} = \dot m_{18}$	$\dot m_{17} h_{17} = \dot m_{18} h_{18} + \dot W_{\mathrm{GT}}$	$\dot m_{17} s_{17} + \dot S_{g,\mathrm{GT}} = \dot m_{18} s_{18}$	$\dot m_{17} ex_{17} = \dot m_{18} ex_{18} + \dot W_{\mathrm{GT}} + \dot{Ex}_{D,\mathrm{GT}}$
PEM electrolyzer	$\dot m_{27} = \dot m_{28} + \dot m_{29}$	$\dot m_{27} h_{27} + \dot W_{\mathrm{PEM}} = \dot m_{28} h_{28} + \dot m_{29} h_{29}$	$\dot m_{27} s_{27} + \dot S_{g,\mathrm{PEM}} = \dot m_{28} s_{28} + \dot m_{29} s_{29}$	$\dot m_{27} ex_{27} + \dot W_{\mathrm{PEM}} = \dot m_{28} ex_{28} + \dot m_{29} ex_{29} + \dot{Ex}_{D,\mathrm{PEM}}$

(continued)

Table 4 (continued)

Components	Mass balance	Energy balance	Entropy balance	Exergy balance
Boiler	$\dot{m}_{19} = \dot{m}_{20}$ $\dot{m}_{30} = \dot{m}_{31} = \dot{m}_{32} = \dot{m}_{35}$	$\dot{m}_{19}h_{19} + \dot{m}_{31}h_{31} + \dot{m}_{35}h_{35} = \dot{m}_{20}h_{20} + \dot{m}_{30}h_{30} + \dot{m}_{32}h_{32}$	$\dot{m}_{19}s_{19} + \dot{m}_{31}s_{31} + \dot{m}_{35}s_{35} + \dot{S}_{g,BI} = \dot{m}_{20}s_{20} + \dot{m}_{30}s_{30} + \dot{m}_{32}s_{32}$	$\dot{m}_{19}ex_{19} + \dot{m}_{31}ex_{31} + \dot{m}_{35}ex_{35} = \dot{m}_{20}ex_{20} + \dot{m}_{30}ex_{30} + \dot{m}_{32}ex_{32} + \dot{Ex}_{D,BI}$
HP Turbine	$\dot{m}_{30} = \dot{m}_{31}$	$\dot{m}_{30}h_{30} = \dot{m}_{31}h_{31} + \dot{W}_{HPT}$	$\dot{m}_{30}s_{30} + \dot{S}_{g,HPT} = \dot{m}_{31}s_{31}$	$\dot{m}_{30}ex_{30} = \dot{m}_{31}ex_{31} + \dot{W}_{HPT} + \dot{Ex}_{D,HPT}$
LP Turbine	$\dot{m}_{32} = \dot{m}_{33}$	$\dot{m}_{32}h_{32} = \dot{m}_{33}h_{33} + \dot{W}_{LPT}$	$\dot{m}_{32}s_{32} + \dot{S}_{g,LPT} = \dot{m}_{33}s_{33}$	$\dot{m}_{32}ex_{32} = \dot{m}_{33}ex_{33} + \dot{W}_{LPT} + \dot{Ex}_{D,LPT}$
Condenser1	$\dot{m}_{33} = \dot{m}_{34}$ $\dot{m}_{36} = \dot{m}_{37}$	$\dot{m}_{33}h_{33} + \dot{m}_{36}h_{36} = \dot{m}_{34}h_{34} + \dot{m}_{37}h_{37}$	$\dot{m}_{33}s_{33} + \dot{m}_{36}s_{36} + \dot{S}_{g,Con1} = \dot{m}_{34}s_{34} + \dot{m}_{37}s_{37}$	$\dot{m}_{33}ex_{33} + \dot{m}_{36}ex_{36} = \dot{m}_{34}ex_{34} + \dot{m}_{37}ex_{37} + \dot{Ex}_{D,Con1}$
Pump1	$\dot{m}_{34} = \dot{m}_{35}$	$\dot{m}_{34}h_{34} + \dot{W}_{P1} = \dot{m}_{35}h_{35}$	$\dot{m}_{34}s_{34} + \dot{S}_{g,P1} = \dot{m}_{35}s_{35}$	$\dot{m}_{34}ex_{34} + \dot{W}_{P1} = \dot{m}_{35}ex_{35} + \dot{Ex}_{D,P1}$
Generator	$\dot{m}_{20} = \dot{m}_{21}$ $\dot{m}_{43} = \dot{m}_{44} + \dot{m}_{45}$	$\dot{m}_{20}h_{20} + \dot{m}_{43}h_{43} = \dot{m}_{21}h_{21} + \dot{m}_{44}h_{44} + \dot{m}_{45}h_{45}$	$\dot{m}_{20}s_{20} + \dot{m}_{43}s_{43} + \dot{S}_{g,Gn} = \dot{m}_{21}s_{21} + \dot{m}_{44}s_{44} + \dot{m}_{45}s_{45}$	$\dot{m}_{20}ex_{20} + \dot{m}_{43}ex_{43} = \dot{m}_{21}h_{21} + \dot{m}_{44}ex_{44} + \dot{m}_{45}ex_{45} + \dot{Ex}_{D,Gn}$
Condenser1	$\dot{m}_{44} = \dot{m}_{38}$ $\dot{m}_{48} = \dot{m}_{49}$	$\dot{m}_{44}h_{44} + \dot{m}_{48}h_{48} = \dot{m}_{38}h_{38} + \dot{m}_{49}h_{49}$	$\dot{m}_{44}s_{44} + \dot{m}_{48}s_{48} + \dot{S}_{g,Con1} = \dot{m}_{38}s_{38} + \dot{m}_{49}s_{49}$	$\dot{m}_{44}ex_{44} + \dot{m}_{48}ex_{48} = \dot{m}_{38}ex_{38} + \dot{m}_{49}ex_{49} + \dot{Ex}_{D,Con1}$
Valve	$\dot{m}_{38} = \dot{m}_{39}$	$\dot{m}_{38}h_{38} = \dot{m}_{39}h_{39}$	$\dot{m}_{38}s_{38} + \dot{S}_{g,V1} = \dot{m}_{39}s_{39}$	$\dot{m}_{38}ex_{38} = \dot{m}_{39}ex_{39} + \dot{Ex}_{D,V1}$
Evaporator	$\dot{m}_{39} = \dot{m}_{40}$ $\dot{m}_{50} = \dot{m}_{51}$	$\dot{m}_{39}h_{39} + \dot{m}_{50}h_{50} = \dot{m}_{40}h_{40} + \dot{m}_{51}h_{51}$	$\dot{m}_{39}s_{39} + \dot{m}_{50}s_{50} + \dot{S}_{g,Eva} = \dot{m}_{40}s_{40} + \dot{m}_{51}s_{51}$	$\dot{m}_{39}ex_{39} + \dot{m}_{50}ex_{50} = \dot{m}_{40}ex_{40} + \dot{m}_{51}ex_{51} + \dot{Ex}_{D,Eva}$

(continued)

Table 4 (continued)

Components	Mass balance	Energy balance	Entropy balance	Exergy balance
Absorber	$\dot{m}_{47} = \dot{m}_{41}$ $\dot{m}_{52} = \dot{m}_{53}$	$\dot{m}_{47}h_{47} + \dot{m}_{52}h_{52} =$ $\dot{m}_{41}h_{41} + \dot{m}_{53}h_{53}$	$\dot{m}_{47}s_{47} + \dot{m}_{52}s_{52} + \dot{S}_{g,Ab} =$ $\dot{m}_{41}s_{41} + \dot{m}_{53}s_{53}$	$\dot{m}_{47}ex_{47} + \dot{m}_{52}ex_{52} =$ $\dot{m}_{41}ex_{41} + \dot{m}_{53}ex_{53} + \dot{Ex}_{D,\text{Abs}}$
Ejector	$\dot{m}_{40} + \dot{m}_{46} = \dot{m}_{47}$	$\dot{m}_{40}h_{40} + \dot{m}_{46}h_{46} = \dot{m}_{47}h_{47}$	$\dot{m}_{40}s_{40} + \dot{m}_{46}s_{46} + \dot{S}_{g,Ej} =$ $\dot{m}_{47}s_{47}$	$\dot{m}_{40}ex_{40} + \dot{m}_{46}ex_{46} =$ $\dot{m}_{47}ex_{47} + \dot{Ex}_{D,Ej}$
Solution HEX	$\dot{m}_{42} = \dot{m}_{43}$ $\dot{m}_{45} = \dot{m}_{46}$	$\dot{m}_{42}h_{42} + \dot{m}_{45}h_{45} =$ $\dot{m}_{43}h_{43} + \dot{m}_{46}h_{46}$	$\dot{m}_{42}s_{42} + \dot{m}_{45}s_{45} + \dot{S}_{g,\text{SHEX}} =$ $\dot{m}_{43}s_{43} + \dot{m}_{46}s_{46}$	$\dot{m}_{42}ex_{42} + \dot{m}_{45}ex_{45} =$ $\dot{m}_{43}ex_{43} + \dot{m}_{46}ex_{46} +$ $\dot{Ex}_{D,\text{SHEX}}$
Dryer	$\dot{m}_{55} = \dot{m}_{56}$ $\dot{m}_{57} = \dot{m}_{58}$	$\dot{m}_{55}h_{55} + \dot{m}_{57}h_{57} =$ $\dot{m}_{56}h_{56} + \dot{m}_{58}h_{58}$	$\dot{m}_{55}s_{55} + \dot{m}_{57}s_{57} + \dot{S}_{\text{Dry}} =$ $\dot{m}_{56}s_{56} + \dot{m}_{58}s_{58}$	$\dot{m}_{55}ex_{55} + \dot{m}_{57}ex_{57} =$ $\dot{m}_{56}ex_{56} + \dot{m}_{58}ex_{58} + \dot{Ex}_{D,\text{Dry}}$
Hot-water storage tank	$\dot{m}_{22} = \dot{m}_{23}$ $\dot{m}_{59} = \dot{m}_{60}$	$\dot{m}_{22}h_{22} + \dot{m}_{59}h_{59} =$ $\dot{m}_{23}h_{23} + \dot{m}_{60}h_{60}$	$\dot{m}_{22}s_{22} + \dot{m}_{59}s_{59} + \dot{S}_{g,\text{HWST}} =$ $\dot{m}_{23}s_{23} + \dot{m}_{60}s_{60}$	$\dot{m}_{22}ex_{22} + \dot{m}_{59}ex_{59} =$ $\dot{m}_{23}ex_{23} + \dot{m}_{60}ex_{60} +$ $\dot{Ex}_{D,\text{HWST}}$

For dryer cycle sub-system;

$$\eta_{DC} = \frac{\dot{Q}_{Dryer}}{\dot{m}_{56}(h_{56} - h_{55})} \tag{20}$$

$$\psi_{DC} = \frac{\dot{Ex}^Q_{Dryer}}{\dot{m}_{56}(ex_{56} - ex_{55})} \tag{21}$$

For hot-water production sub-system;

$$\eta_{HWP} = \frac{(\dot{m}_{60}h_{60} - \dot{m}_{59}h_{59})}{(\dot{m}_{22}h_{22} - \dot{m}_{23}h_{23})} \tag{22}$$

$$\psi_{HWP} = \frac{(\dot{m}_{60}ex_{60} - \dot{m}_{59}ex_{59})}{(\dot{m}_{22}ex_{22} - \dot{m}_{23}ex_{23})} \tag{23}$$

For whole system;

$$\eta_{WS} = \frac{\dot{W}_{GT} + \dot{W}_{HPT} + \dot{W}_{LPT} + \dot{m}_{29}LHV_{H_2} + \dot{Q}_{Heating} + \dot{Q}_{Cooling} + \dot{Q}_{Dryer} + \dot{Q}_{Hot\_water}}{\dot{m}_1 LHV_{biomass} + \sum \dot{W}_P + \sum \dot{W}_{AC}} \tag{24}$$

$$\psi_{WS} = \frac{\dot{W}_{GT} + \dot{W}_{HPT} + \dot{W}_{LPT} + \dot{m}_{29}ex_{H_2} + \dot{Ex}^Q_{Heating} + \dot{Ex}^Q_{Cooling} + \dot{Ex}^Q_{Dryer} + \dot{Ex}^Q_{Hot\_water}}{\dot{m}_1 ex_{biomass} + \sum \dot{W}_P + \sum \dot{W}_{AC}} \tag{25}$$

The energetic and exergetic COP for cooling plant can be defined as given below, respectively;

$$COP_{en} = \frac{\dot{Q}_{Eva1}}{\dot{Q}_{Gn} + \dot{W}_{P2}} \tag{26}$$

$$COP_{ex} = \frac{\dot{Ex}^Q_{Eva1}}{\dot{Ex}^Q_{Gn} + \dot{W}_{P2}} \tag{27}$$

To investigate the energetic, exergetic performance and also environment analyses of some different generation options, the energetic and exergetic equalities for single-, co-, tri- and multigeneration are given below;

For single generation (power generation);

$$\eta_{sngen} = \frac{\dot{W}_{GT} + \dot{W}_{HPT} + \dot{W}_{LPT}}{\dot{m}_1 LHV_{biomass} + \sum \dot{W}_{AC} + \dot{W}_{P1}} \tag{28}$$

$$\psi_{sngen} = \frac{\dot{W}_{GT} + \dot{W}_{HPT}}{\dot{m}_1 ex_{biomass} + \sum \dot{W}_{AC} + \dot{W}_{P1}} \tag{29}$$

For cogeneration I (power and cooling generation);

$$\eta_{\text{cogen},I} = \frac{\dot{W}_{\text{GT}} + \dot{W}_{\text{HPT}} + \dot{W}_{\text{LPT}} + \dot{Q}_{\text{Cooling}}}{\dot{m}_1\text{LHV}_{\text{biomass}} + \sum \dot{W}_{\text{AC}} + \dot{W}_{P1} + \dot{W}_{P2}} \tag{30}$$

$$\psi_{\text{cogen},I} = \frac{\dot{W}_{\text{GT}} + \dot{W}_{\text{HPT}} + \dot{W}_{\text{LPT}} + \dot{E}x_{\text{cooling}}^{Q}}{\dot{m}_1\text{ex}_{\text{biomass}} + \sum \dot{W}_{\text{AC}} + \dot{W}_{P1} + \dot{W}_{P2}} \tag{31}$$

For cogeneration II (power and heating generation);

$$\eta_{\text{cogen},II} = \frac{\dot{W}_{\text{GT}} + \dot{W}_{\text{HPT}} + \dot{W}_{\text{LPT}} + \dot{Q}_{\text{Heating}}}{\dot{m}_1 LHV_{\text{biomass}} + \sum \dot{W}_{\text{AC}} + \dot{W}_{P1}} \tag{32}$$

$$\psi_{\text{cogen},II} = \frac{\dot{W}_{\text{GT}} + \dot{W}_{\text{HPT}} + \dot{W}_{\text{LPT}} + \dot{E}x_{\text{Heating}}^{Q}}{\dot{m}_1\text{ex}_{\text{biomass}} + \sum \dot{W}_{\text{AC}} + \dot{W}_{P1}} \tag{33}$$

For cogeneration III (power and hydrogen generation);

$$\eta_{cogen,III} = \frac{\dot{W}_{GT} + \dot{W}_{HPT} + \dot{W}_{LPT} + \dot{m}_{29} LHV_{H_2}}{\dot{m}_1 LHV_{biomass} + \sum \dot{W}_{AC} + \dot{W}_{P1}} \tag{34}$$

$$\psi_{\text{cogen},III} = \frac{\dot{W}_{\text{GT}} + \dot{W}_{\text{HPT}} + \dot{W}_{\text{LPT}} + \dot{m}_{29}\text{ex}_{H_2}}{\dot{m}_1\text{ex}_{\text{biomass}} + \sum \dot{W}_{\text{AC}} + \dot{W}_{P1}} \tag{35}$$

For trigeneration I (power, cooling, and hot-water generation);

$$\eta_{\text{trigen},I} = \frac{\dot{W}_{\text{GT}} + \dot{W}_{\text{HPT}} + \dot{W}_{\text{LPT}} + \dot{Q}_{\text{Cooling}} + \dot{Q}_{\text{Hot\_water}}}{\dot{m}_1\text{LHV}_{\text{biomass}} + \sum \dot{W}_{\text{AC}} + \dot{W}_{P1} + \dot{W}_{P2}} \tag{36}$$

$$\psi_{\text{trigen},I} = \frac{\dot{W}_{\text{GT}} + \dot{W}_{\text{HPT}} + \dot{W}_{\text{LPT}} + \dot{E}x_{\text{cooling}}^{Q} + \dot{E}x_{\text{Hot\_water}}^{Q}}{\dot{m}_1\text{ex}_{\text{biomass}} + \sum \dot{W}_{\text{AC}} + \dot{W}_{P1} + \dot{W}_{P2}} \tag{37}$$

For trigeneration II (power, cooling, and heating generation);

$$\eta_{\text{trigen},II} = \frac{\dot{W}_{\text{GT}} + \dot{W}_{\text{HPT}} + \dot{W}_{\text{LPT}} + \dot{Q}_{\text{Cooling}} + \dot{Q}_{\text{Heating}}}{\dot{m}_1\text{LHV}_{\text{biomass}} + \sum \dot{W}_{\text{AC}} + \dot{W}_{P1} + \dot{W}_{P2}} \tag{38}$$

$$\psi_{trigen,II} = \frac{\dot{W}_{GT} + \dot{W}_{HPT} + \dot{W}_{LPT} + \dot{E}x_{cooling}^{Q} + \dot{E}x_{Heating}^{Q}}{\dot{m}_1 ex_{biomass} + \sum \dot{W}_{AC} + \dot{W}_{P1} + \dot{W}_{P2}} \tag{39}$$

For trigeneration III (power, cooling, and hydrogen generation);

$$\eta_{\text{trigen},II} = \frac{\dot{W}_{\text{GT}} + \dot{W}_{\text{HPT}} + \dot{W}_{\text{LPT}} + \dot{Q}_{\text{Cooling}} + \dot{m}_{29}\text{LHV}_{H_2}}{\dot{m}_1\text{LHV}_{\text{biomass}} + \sum \dot{W}_{\text{AC}} + \dot{W}_{P1} + \dot{W}_{P2}} \tag{40}$$

$$\psi_{\text{trigen},III} = \frac{\dot{W}_{\text{GT}} + \dot{W}_{\text{HPT}} + \dot{W}_{\text{LPT}} + \dot{E}x_{\text{cooling}}^{Q} + \dot{m}_{29}\text{ex}_{H_2}}{\dot{m}_1\text{ex}_{\text{biomass}} + \sum \dot{W}_{\text{AC}} + \dot{W}_{P1} + \dot{W}_{P2}} \tag{41}$$

Finally, the energy and exergy performance terms for biomass-based multigeneration plant and its components are defined in Table 5. To present environment analysis for generation options of biomass gasification combined system, the carbon dioxide emission equations for generation options are given as follows;

$$\varepsilon_{\text{SG}} = \frac{\dot{m}_{\text{CO}_2}}{\text{Single} - \text{generation}} \tag{42}$$

$$\varepsilon_{\text{CG}} = \frac{\dot{m}_{\text{CO}_2}}{\text{Co} - \text{generation}} \tag{43}$$

$$\varepsilon_{TG} = \frac{\dot{m}_{CO_2}}{Tri - generation} \tag{44}$$

$$\varepsilon_{\text{MG}} = \frac{\dot{m}_{\text{CO}_2}}{\text{Multi} - \text{generation}} \tag{45}$$

4 Results and Discussion

In this chapter, the energetic, exergetic, and environmental assessments of a new biomass gasifier combined plant for useful commodities are performed. The calculated values based on thermodynamic analyses for suggested plants and its sub-plants are tabulated in Table 6. The overall exergy performance of proposed plant is to be 59.26%, and the whole irreversibility rate is to be 52,529 kW. The biomass-based combined plant useful outputs are calculated and presented in Table 7. As shown in Table 7, the produced electricity from gas turbine is 18,425 kW, produced electricity from Rankine cycle is 8348 kW, cooling load is 5104 kW, heating load is 4356 kW, and produced hot water is 7826 kW. In addition, the hydrogen generation rate is 0.068 kg/s.

In the design of thermal power generation systems, the varying environment temperature is one of the most significant characteristic properties. Therefore, Figs. 2, 3, and 4 illustrate the impact of reference conditions temperature on the investigated system and sub-part performance (energy and exergy efficiency) and useful outputs as well.

Figure 2 expresses the effect of reference temperature on the energy performance of whole system and its sub-system. When the rise in reference temperature from 0 to 40 °C, the energy performance of whole cycle and sub-systems increases. It can be concluded from this figure that rising reference temperature has an optimistic impact on the whole plant efficiency. Likewise, the impact of dead-state conditions temperature on the exergetic performance of whole cycle and its sub-parts are depicted in Fig. 3. Similar to Fig. 2, the rise in the environment temperature results in a rise in the exergy performance of whole cycle and its sub-cycles. The cause for this rise is

Table 5 Energetic and exergetic efficiency equalities of integrated plant components

Components	Energy efficiency equations	Exergy efficiency equations
Biomass gasifier	$\eta_{BG} = \dot{m}_{11}h_{11}/(\dot{m}_1h_1 + \dot{m}_3h_3 + \dot{m}_5h_5)$	$\psi_{BG} = \dot{m}_{11}ex_{11}/(\dot{m}_1ex_1 + \dot{m}_3ex_3 + \dot{m}_5ex_5)$
HEX1	$\eta_{HEX1} = \dfrac{(\dot{m}_3h_3 - \dot{m}_2h_2)}{(\dot{m}_6h_6 - \dot{m}_7h_7)}$	$\psi_{HEX1} = \dfrac{(\dot{m}_3ex_3 - \dot{m}_2ex_2)}{(\dot{m}_6ex_6 - \dot{m}_7ex_7)}$
Gas cleaner	$\eta_{GC} = \dfrac{\dot{m}_{11}h_{11}}{\dot{m}_8h_8}$	$\psi_{HEX1} = \dfrac{\dot{m}_{11}ex_{11}}{\dot{m}_8ex_8}$
Compressor1	$\eta_{Comp1} = (\dot{m}_{13}h_{13} - \dot{m}_{12}h_{12})/\dot{W}_{Comp1}$	$\psi_{Comp1} = (\dot{m}_{13}ex_{13} - \dot{m}_{12}ex_{12})/\dot{W}_{Comp1}$
Intercooler	$\eta_{IntC} = \dfrac{(\dot{m}_{25}h_{25} - \dot{m}_{24}h_{24})}{(\dot{m}_{13}h_{13} - \dot{m}_{14}h_{14})}$	$\psi_{IntC} = \dfrac{(\dot{m}_{25}ex_{25} - \dot{m}_{24}ex_{24})}{(\dot{m}_{13}ex_{13} - \dot{m}_{14}ex_{14})}$
Recuperator	$\eta_{Rec} = \dfrac{(\dot{m}_{19}h_{19} - \dot{m}_{18}h_{18}) + (\dot{m}_{27}h_{27} - \dot{m}_{26}h_{26})}{(\dot{m}_{15}h_{15} - \dot{m}_{16}h_{16})}$	$\psi_{Rec} = \dfrac{(\dot{m}_{19}ex_{19} - \dot{m}_{18}ex_{18}) + (\dot{m}_{27}ex_{27} - \dot{m}_{26}ex_{26})}{(\dot{m}_{15}ex_{15} - \dot{m}_{16}ex_{16})}$
Combustor	$\eta_{Cb} = \dfrac{\dot{m}_{17}h_{17}}{(\dot{m}_{11}h_{11} + \dot{m}_{16}h_{16})}$	$\psi_{Cb} = \dfrac{\dot{m}_{17}ex_{17}}{(\dot{m}_{11}ex_{11} + \dot{m}_{16}ex_{16})}$
Gas turbine	$\eta_{GT} = \dot{W}_{GT}/(\dot{m}_{17}h_{17} - \dot{m}_{18}h_{18})$	$\psi_{GT} = \dot{W}_{GT}/(\dot{m}_{17}ex_{17} - \dot{m}_{18}ex_{18})$
PEM electrolyzer	$\eta_{PEM} = \dfrac{(\dot{m}_{28}h_{28} + \dot{m}_{29}h_{29})}{\dot{m}_{27}h_{27} + \dot{W}_{PEM}}$	$\psi_{PEM} = \dfrac{(\dot{m}_{28}ex_{28} + \dot{m}_{29}ex_{29})}{\dot{m}_{27}ex_{27} + \dot{W}_{PEM}}$
Boiler	$\eta_{Bl} = \dfrac{(\dot{m}_{30}h_{30} - \dot{m}_{35}h_{35}) + (\dot{m}_{32}h_{32} - \dot{m}_{31}h_{31})}{(\dot{m}_{19}h_{19} - \dot{m}_{20}h_{20})}$	$\psi_{Bl} = \dfrac{(\dot{m}_{30}ex_{30} - \dot{m}_{35}ex_{35}) + (\dot{m}_{32}ex_{32} - \dot{m}_{31}ex_{31})}{(\dot{m}_{19}h_{19} - \dot{m}_{20}h_{20})}$
HP Turbine	$\eta_{HPT} = \dot{W}_{HPT}/(\dot{m}_{30}h_{30} - \dot{m}_{31}h_{31})$	$\psi_{HPT} = \dot{W}_{HPT}/(\dot{m}_{30}ex_{30} - \dot{m}_{31}ex_{31})$
LP Turbine	$\eta_{LPT} = \dot{W}_{LPT}/(\dot{m}_{32}h_{32} - \dot{m}_{33}h_{33})$	$\psi_{LPT} = \dot{W}_{LPT}/(\dot{m}_{32}ex_{32} - \dot{m}_{33}ex_{33})$

(continued)

Table 5 (continued)

Components	Energy efficiency equations	Exergy efficiency equations
Condenser1	$\eta_{\text{Con}1} = \dfrac{(\dot{m}_{37}h_{37} - \dot{m}_{36}h_{36})}{(\dot{m}_{33}h_{33} - \dot{m}_{34}h_{34})}$	$\psi_{\text{Con}1} = \dfrac{(\dot{m}_{37}\text{ex}_{37} - \dot{m}_{36}\text{ex}_{36})}{(\dot{m}_{33}\text{ex}_{33} - \dot{m}_{34}\text{ex}_{34})}$
Pump1	$\eta_{P1} = (\dot{m}_{35}h_{35} - \dot{m}_{34}h_{34})/\dot{W}_{P1}$	$\psi_{P1} = (\dot{m}_{35}\text{ex}_{35} - \dot{m}_{34}\text{ex}_{34})/\dot{W}_{P1}$
Generator	$\eta_{\text{Gen}} = \dfrac{(\dot{m}_{44}h_{44} + \dot{m}_{45}h_{45} - \dot{m}_{43}h_{43})}{(\dot{m}_{20}h_{20} - \dot{m}_{21}h_{21})}$	$\psi_{\text{Gen}} = \dfrac{(\dot{m}_{44}\text{ex}_{44} + \dot{m}_{45}\text{ex}_{45} - \dot{m}_{43}\text{ex}_{43})}{(\dot{m}_{20}\text{ex}_{20} - \dot{m}_{21}\text{ex}_{21})}$
Condenser2	$\eta_{\text{Con}2} = \dfrac{(\dot{m}_{37}h_{37} - \dot{m}_{36}h_{36})}{(\dot{m}_{44}h_{44} - \dot{m}_{38}h_{38})}$	$\psi_{\text{Con}2} = \dfrac{(\dot{m}_{37}\text{ex}_{37} - \dot{m}_{36}\text{ex}_{36})}{(\dot{m}_{44}\text{ex}_{44} - \dot{m}_{38}\text{ex}_{38})}$
Valve	$\eta_{V1} = \dot{m}_{39}h_{39}/\dot{m}_{38}h_{38}$	$\psi_{V1} = \dot{m}_{39}\text{ex}_{39}/\dot{m}_{38}\text{ex}_{38}$
Evaporator	$\eta_{\text{Eva}} = \dfrac{(\dot{m}_{51}h_{51} - \dot{m}_{50}h_{50})}{(\dot{m}_{39}h_{39} - \dot{m}_{40}h_{40})}$	$\psi_{\text{Eva}} = \dfrac{(\dot{m}_{51}\text{ex}_{51} - \dot{m}_{50}\text{ex}_{50})}{(\dot{m}_{39}\text{ex}_{39} - \dot{m}_{40}\text{ex}_{40})}$
Absorber	$\eta_{\text{Abs}} = \dfrac{(\dot{m}_{53}h_{53} - \dot{m}_{52}h_{52})}{(\dot{m}_{47}h_{47} - \dot{m}_{41}h_{41})}$	$\psi_{\text{Abs}} = \dfrac{(\dot{m}_{53}\text{ex}_{53} - \dot{m}_{52}\text{ex}_{52})}{(\dot{m}_{47}\text{ex}_{47} - \dot{m}_{41}\text{ex}_{41})}$
Ejector	$\eta_{\text{Ejec}} = \dot{m}_{47}h_{47}/(\dot{m}_{40}h_{40} + \dot{m}_{46}h_{46})$	$\psi_{\text{Ejec}} = \dot{m}_{47}\text{ex}_{47}/(\dot{m}_{40}\text{ex}_{40} + \dot{m}_{46}\text{ex}_{46})$
Solution HEX	$\eta_{S\_\text{HEX}} = \dfrac{(\dot{m}_{46}h_{46} - \dot{m}_{45}h_{45})}{(\dot{m}_{42}h_{42} - \dot{m}_{43}h_{43})}$	$\psi_{S\_\text{HEX}} = \dfrac{(\dot{m}_{46}\text{ex}_{46} - \dot{m}_{45}\text{ex}_{45})}{(\dot{m}_{42}\text{ex}_{42} - \dot{m}_{43}\text{ex}_{43})}$
Dryer	$\eta_{\text{Dry}} = \dfrac{(\dot{m}_{58}h_{58} - \dot{m}_{57}h_{57})}{(\dot{m}_{55}h_{55} - \dot{m}_{56}h_{56})}$	$\psi_{\text{Dry}} = \dfrac{(\dot{m}_{58}\text{ex}_{58} - \dot{m}_{57}\text{ex}_{57})}{(\dot{m}_{55}\text{ex}_{55} - \dot{m}_{56}\text{ex}_{56})}$
Hot-water storage tank	$\eta_{\text{HWST}} = \dfrac{(\dot{m}_{60}h_{60} - \dot{m}_{59}h_{59})}{(\dot{m}_{22}h_{22} - \dot{m}_{23}h_{23})}$	$\psi_{\text{HWST}} = \dfrac{(\dot{m}_{60}\text{ex}_{60} - \dot{m}_{59}\text{ex}_{59})}{(\dot{m}_{22}\text{ex}_{22} - \dot{m}_{23}\text{ex}_{23})}$

Table 6 Calculated values for biomass energy based combined plant and its sub-parts

Sub-parts	Energetic efficiency (%)	Exergetic efficiency (%)	Exergy destruction rate (kW)	Exergy destruction ratio (%)
Biomass gasifier system	55.64	51.83	16,525	31.46
Gas turbine system	48.37	44.14	14,452	27.51
Rankine cycle	41.73	38.26	6401	12.19
SEAC	16.92	15.08	3356	6.39
Hydrogen production	53.42	50.13	5837	11.11
Dryer cycle	68.41	64.15	3132	5.96
Hot-water storage system	65.32	61.27	2826	5.38
Whole system	63.84	59.26	52,529	100

Table 7 Integrated biomass gasification-based power plant outputs

Plant outputs	Values
Produced electricity from gas turbine, $\dot{W}_{GT}$	18,425 kW
Produced electricity from Rankine cycle, $\dot{W}_{RC}$	8348 kW
Produced cooling, $\dot{Q}_{Cooling}$	5104 kW
Produced heating, $\dot{Q}_{Heating}$	4356 kW
Produced hot water, $\dot{Q}_{Hot\_water}$	7826 kW
Produced drying, $\dot{Q}_{Drying}$	6874 kW
Mass flow rate of produced hydrogen, $\dot{m}_{Hydrogen}$	0.068 kg/s
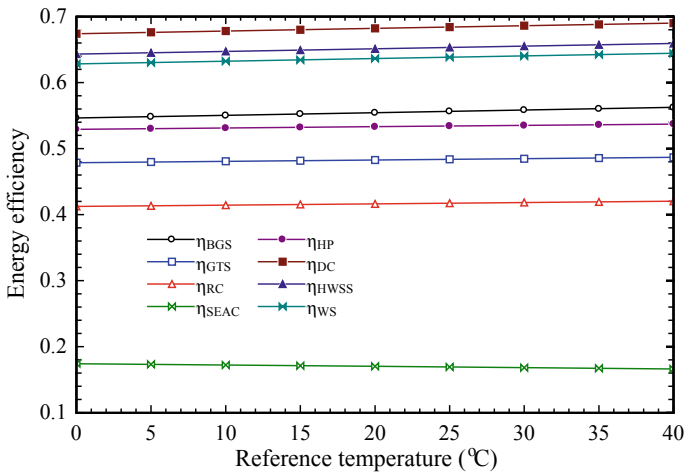
Fig. 2 Effects of reference temperature on energetic efficiencies
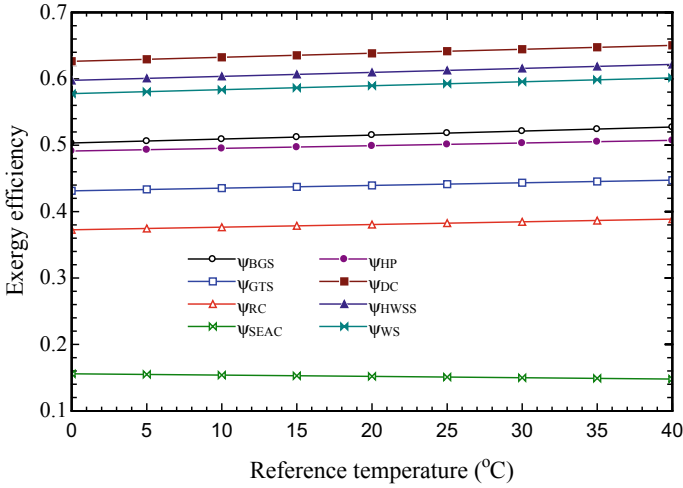
Fig. 3 Effects of reference temperature on exergetic efficiencies
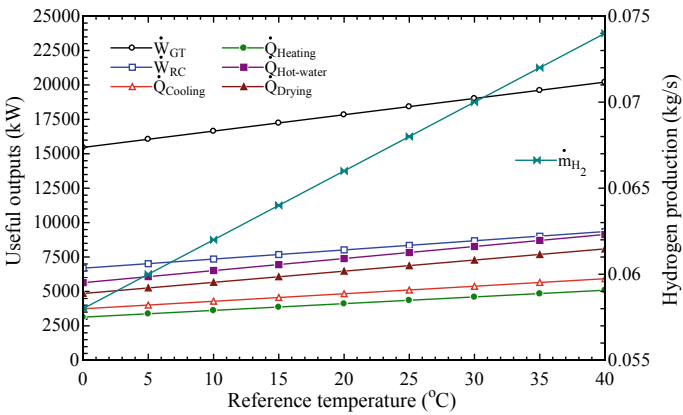
Fig. 4 Effects of dead-state temperature on the useful outputs and hydrogen generation

the increase in the useful generations obtained from the sub-plants as a result of an increase in the ambient temperature.

Figure 4 demonstrates that the impact of dead-state conditions temperature on the useful generations from integrated plant. As shown in Fig. 4, the useful outputs from integrated plant increase linearly with the rise in the reference temperature. Increase in the reference temperature about 40 °C leads to rising in the hydrogen production from about 0.055 to 0.075 kg/s. The rise in the hydrogen production rate is the same direction for both system performance and useful outputs. The cause for this situation is the reduction of the irreversibility rate of plant and sub-systems as a result of the environment temperature approaching the plant operating temperature.

In the proposed chapter, another significant parameter in the system design is the mass flow rate of biomass. Figure 5 demonstrates the impact of mass flow rate of biomass on the energetic performance of integrated system and its sub-cycles. The energetic efficiency of combined plant and sub-systems rise as the mass flow rate of biomass raised from 3.64 to 8.14 kg/s. Similarly, the exergy efficiency increased as straight line as the mass flow rate of biomass increased as illustrated in Fig. 6. It can be said that the rise in the mass flow rate of biomass has an optimistic effect on the thermodynamic efficiency of suggested cycle and its sub-parts. The reason for
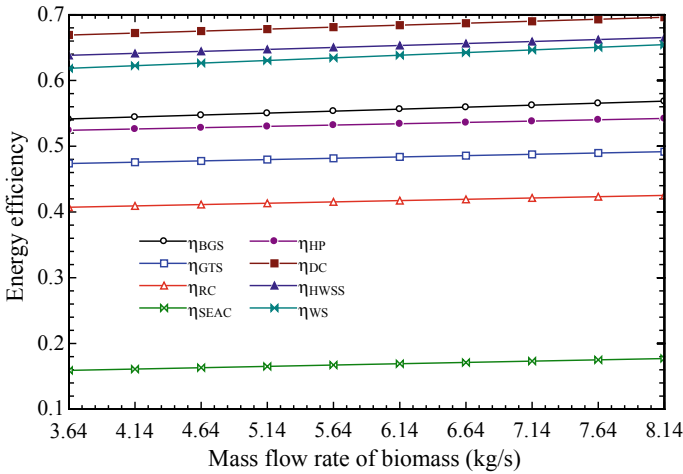
Fig. 5 Impacts of mass flow rate of biomass on energetic efficiencies
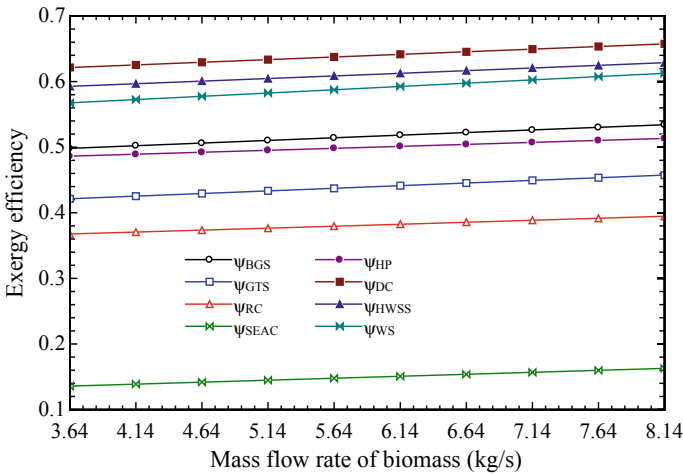
Fig. 6 Impacts of mass flow rate of biomass on exergy efficiencies

this situation is that the useful outputs and hydrogen generation from investigated process and its sub-parts increase with the mass flow rate of biomass.

Furthermore, the useful products from whole cycle and its sub-parts increased as the mass flow rate of biomass increases as shown in Fig. 7. As can be illustrated in Fig. 7, the hydrogen generation rate increases in a straight line from 0.04 to 0.09 kg/s with rise in the mass flow rate of biomass. As can be revealed in Fig. 7, the hydrogen generation rate increases in a straight line from 0.04 to 0.09 kg/s, as increased in the mass flow rate of biomass. It is clearly seen that the rise in the generation of electricity from the gas turbine is directly proportional to a rise in hydrogen generation.

In Figs. 8, 9, and 10, the impact of biomass gasifier temperature on the performance
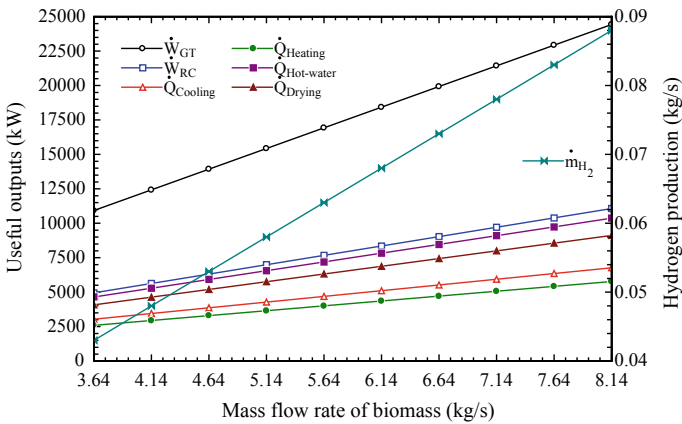
Fig. 7 Impacts of mass flow rate of biomass on useful outputs and hydrogen generation
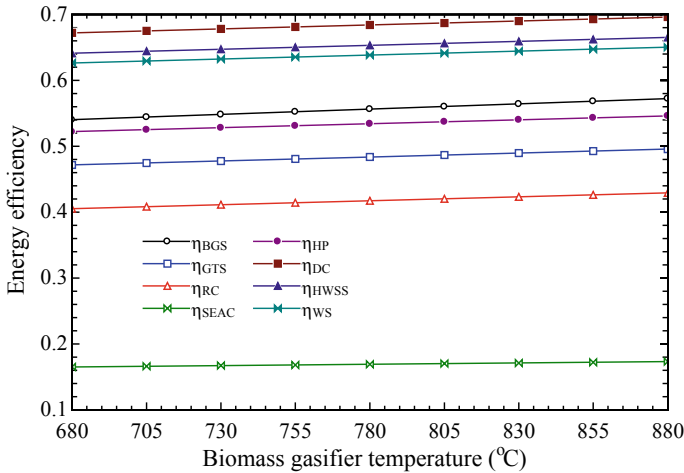
Fig. 8 Impacts of biomass gasifier temperature on energy efficiencies
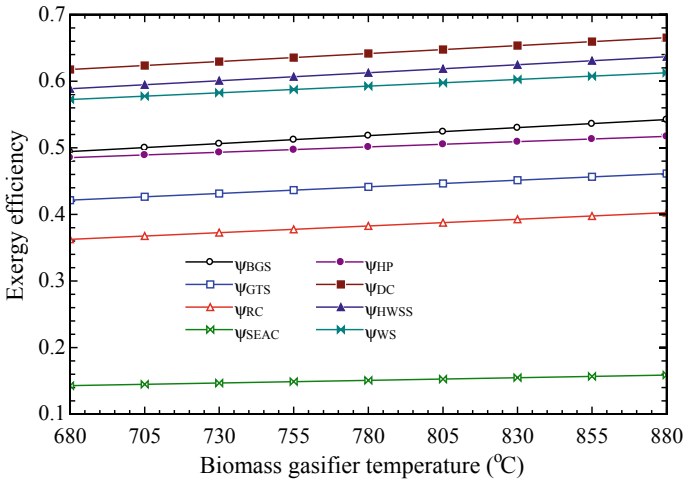
Fig. 9 Effects of biomass gasifier temperature on exergy efficiencies
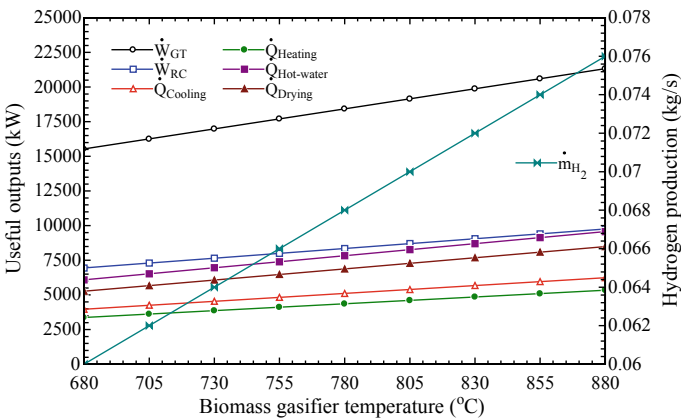
Fig. 10 Effects of biomass gasifier temperature on the useful outputs and hydrogen generation

and useful outputs of combined cycle and sub-parts are analyzed. Figure 8 shows the effect of biomass gasification temperature on the energetic performance of combined plant and its sub-parts. When the biomass gasifier temperature rises from 680 to 880 °C, the energy efficiency of integrated system and its sub-parts increases, as shown in this graph. However, it has no significant effect on this increase. Likewise, the impact of biomass gasifier temperature on the exergy performance of whole cycle and its sub-parts is proved in Fig. 9. It is obvious that unlike energy performance in Fig. 8, the increase in exergy efficiency here is more evident. The cause for this rise is that rise in the biomass gasifier temperature leads to the higher temperatures air enters into the gas turbine and then obtained higher power generation rate.

Moreover, the useful products from whole system and its sub-parts increased as the biomass gasifier temperature increases from 680 to 880 °C as indicated in Fig. 10. As given in Fig. 10, the hydrogen production rate increases in a straight line from 0.06 to 0.076 kg/s with rise in biomass gasifier temperature. Also, the hydrogen generation rate increases in a straight line as increased in the biomass gasifier temperature. It is obviously shown that the rise in the electricity generation from gas turbine is directly proportional to a rise in the hydrogen generation.

Moreover, in this chapter, the assessments of environmental impact are carried out to investigate the CO_2 and CO emissions. Figure 11 displays the comparison of energetic and exergetic efficiency, and also the carbon dioxide and carbon monoxide emissions of biomass gasifier combined plants. It can be seen from Fig. 11 that the energetic and exergetic efficiency of integrated plant is higher than the other generation options. In addition, the lowest CO_2 and CO emissions are observed in the multigeneration plant. Also, it is clearly understood from this graph that multigeneration plants are more advantageous in terms of thermodynamic and environmental evaluations.

The effect of biomass gasification temperature on the carbon dioxide emission of proposed various plants is displayed in Fig. 12. The increase in biomass gasification temperature of 680 to 880 °C causes the reduction of carbon dioxide emissions of suggested whole plants. The reason for this situation is the increase in the useful outputs from whole system and sub-systems with the rise in the gasification temperature. Also, this graph is consistent with the above-mentioned Fig. 10.

Finally, Fig. 13 illustrates that the effect of biomass gasifier temperature on the carbon monoxide emission suggested various outputs from proposed plant. As shown in Fig. 13, while the biomass gasifier temperature increases from 680 to 880 °C, the decrease in the carbon monoxide emissions from the different generation options for

Fig. 11 Comparison of energy efficiency, exergy efficiency, carbon dioxide, and carbon monoxide emissions of biomass gasifier combined generation plants
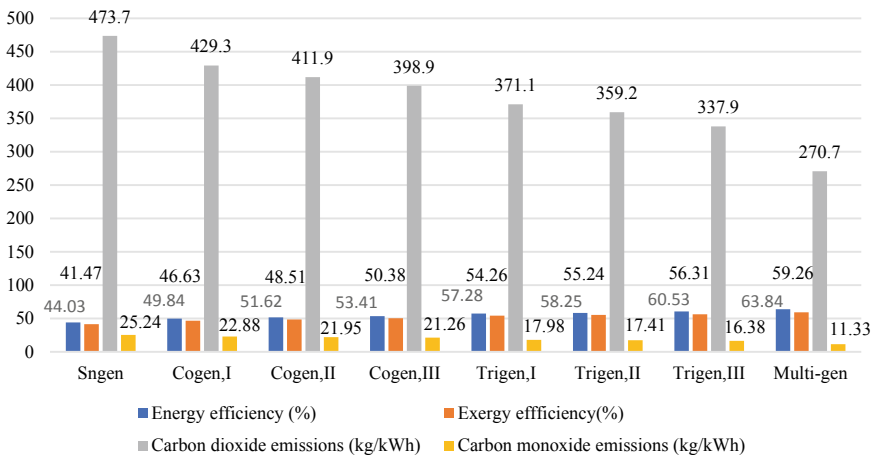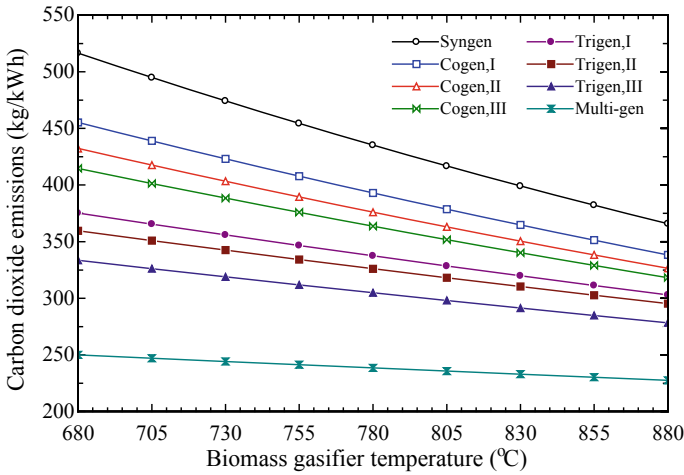
Fig. 12 Comparison of energy efficiency, exergy efficiency, carbon dioxide, and carbon monoxide emissions of biomass gasifier combined generation plants
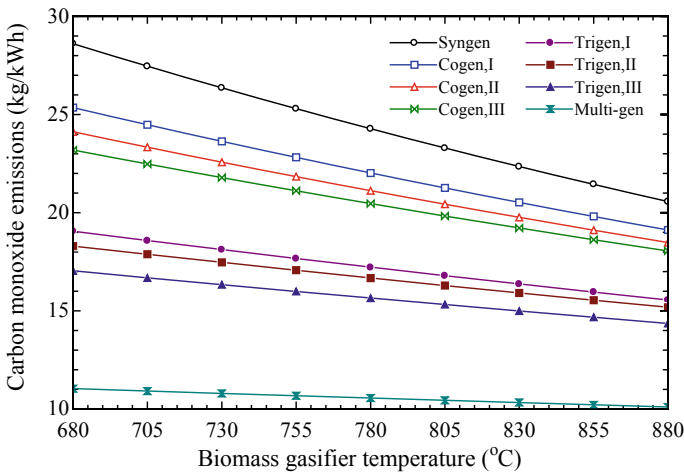
Fig. 13 Impacts of biomass gasifier temperature on carbon monoxide emissions

proposed different plants. Again, the lowest carbon monoxide emissions are observed in the multiproduction plant.

5   Conclusion

In the suggested chapter, the detail thermodynamic and environmental effect assessments of a new biomass-supported multigeneration system are performed for various useful products. The changing in the thermodynamic efficiency and irreversibility of integrated plant and sub-parts are investigated with respect to several factors, such as environment and gasifier temperatures as well as the mass flow rate of biomass. Also, the carbon dioxide and carbon monoxide emissions are analyzed and also compared for various generation options of proposed plant. Some important outcomes of the thermodynamic and environmental impact examine are listed below;

- The maximum exergy performance in the sub-plants is calculated in the dryer cycle with 64.15%. In contrast, the minimum exergetic performance is observed in SEAC sub-system with 15.08%.
- The energetic and exergetic performance of gas turbine system is computed as 48.37 and 44.14%, also the energetic and exergetic efficiency of Rankine sub-system are computed as 41.73 and 38.26%.
- The energetic and exergetic efficiency of investigated system is 63.84 and 59.26%.
- The hydrogen production rate of proposed biomass-based integrated plant is 0.0368 kg/s.
- The increase in biomass gasifier temperature has a positive effect on the plant efficiency and useful products.
- The carbon dioxide and carbon monoxide emission of multigeneration plant is found as 270.7 and 11.33 kg/ kWh, respectively.
- The lowest carbon dioxide and carbon mono-oxide emissions are shown in the multigeneration plant, while the highest is shown in the single generation plant.

References

1. Khalid F, Dincer I, Rosen MA (2016) Techno-economic assessment of a renewable energy based integrated multigeneration system for green buildings. Applied Thermal Engineering 99:1286–1294. https://doi.org/10.1016/j.applthermaleng.2016.01.055
2. Data WB Fossil fuel energy consumption. https://data.worldbank.org/indicator/eg.use.comm.fo.zs. Accessed 28 April 2019
3. Dincer I (2000) Renewable energy and sustainable development: a crucial review. Renew Sustain Energy Rev 4:157–175. https://doi.org/10.1016/S1364-0321(99)00011-8
4. Ozturk M, Dincer I (2013) Thermodynamic analysis of a solar-based multi-generation system with hydrogen production. Appl Therm Eng 51:1235–1244. https://doi.org/10.1016/j.applthermaleng.2012.11.042
5. Dincer I, Zamfirescu C (2012) Renewable-energy-based multigeneration systems. Int J Energy Res 36:1403–1415. https://doi.org/10.1002/er.2882
6. Safari F, Dincer I (2019) Development and analysis of a novel biomass-based integrated system for multigeneration with hydrogen production. Int J Hydrogen Energy 44:3511–3526. https://doi.org/10.1016/j.ijhydene.2018.12.101

7. Sung T, Kim S, Kim KC (2017) Thermoeconomic analysis of a biogas-fueled micro-gas turbine with a bottoming organic Rankine cycle for a sewage sludge and food waste treatment plant in the Republic of Korea. Appl Therm Eng 127:963–974. https://doi.org/10.1016/j.applthermaleng.2017.08.106

8. Sevinchan E, Dincer I, Lang H (2019) Energy and exergy analyses of a biogas driven multigenerational system. Energy 166:715–723. https://doi.org/10.1016/j.energy.2018.10.085

9. Wu B, Zhang X, Shang D, Bao D, Zhang S, Zheng T (2016) Energetic-environmental-economic assessment of the biogas system with three utilization pathways: combined heat and power, biomethane and fuel cell. Bioresour Technol 214:722–728. https://doi.org/10.1016/j.biortech.2016.05.026

10. Giarola S, Forte O, Lanzini A, Gandiglio M, Santarelli M, Hawkes A (2018) Techno-economic assessment of biogas-fed solid oxide fuel cell combined heat and power system at industrial scale. Appl Energy 211:689–704. https://doi.org/10.1016/j.apenergy.2017.11.029

11. Taheri MH, Mosaffa AH, Farshi LG (2017) Energy, exergy and economic assessments of a novel integrated biomass based multigeneration energy system with hydrogen production and LNG regasification cycle. Energy 125:162–177. https://doi.org/10.1016/j.energy.2017.02.124

12. Karellas S, Braimakis K (2016) Energy-exergy analysis and economic investigation of a cogeneration and trigeneration ORC-VCC hybrid system utilizing biomass fuel and solar power. Energy Convers Manag . https://doi.org/10.1016/j.enconman.2015.06.080

13. Al-Sulaiman FA, Hamdullahpur F, Dincer I (2011) Performance comparison of three trigeneration systems using organic rankine cycles. Energy 36:5741–5754. https://doi.org/10.1016/j.energy.2011.06.003

14. Al-Sulaiman FA, Hamdullahpur F, Dincer I (2011) Greenhouse gas emission and exergy assessments of an integrated organic Rankine cycle with a biomass combustor for combined cooling, heating and power production. Appl Therm Eng 31:439–446. https://doi.org/10.1016/j.applthermaleng.2010.09.019

15. Yilmaz F, Ozturk M, Selbas R (2018) Thermodynamic performance assessment of ocean thermal energy conversion based hydrogen production and liquefaction process. Int J Hydrogen Energy 43:10626–10636. https://doi.org/10.1016/J.IJHYDENE.2018.02.021

16. Bicer Y, Dincer I (2016) Analysis and performance evaluation of a renewable energy based multigeneration system. Energy 94:623–632. https://doi.org/10.1016/j.energy.2015.10.142

17. Safari F, Dincer I (2018) Assessment and optimization of an integrated wind power system for hydrogen and methane production. Energy Convers Manag 177:693–703. https://doi.org/10.1016/J.ENCONMAN.2018.09.071

18. El-Emam RS, Dincer I (2018) Investigation and assessment of a novel solar-driven integrated energy system. Energy Convers Manag 158:246–255. https://doi.org/10.1016/j.enconman.2017.12.062

19. Yuksel YE, Ozturk M (2017) Thermodynamic and thermoeconomic analyses of a geothermal energy based integrated system for hydrogen production. Int J Hydrogen Energy 42:2530–2546. https://doi.org/10.1016/j.ijhydene.2016.04.172

20. Ahmadi P, Dincer I, Rosen MA (2014) Multi-objective optimization of a novel solar-based multigeneration energy system. Sol Energy 108:576–591. https://doi.org/10.1016/J.SOLENER.2014.07.022

21. EES: Engineering Equation Solver| F-Chart Software : Engineering Software/Academic Version n.d. http://www.fchart.com/ees/. Accessed 19 Feb 2019

22. Çengel YA, Boles MA (2015) Thermodynamics : an engineering approach, 8th edn. Mc. McGraw-Hi. n.d

23. Kotas TJ (1985) The exergy method of thermal plant analysis, 1st edn. Butterworths

24. Dincer I, Rosen M (2012) Exergy: energy. Environment and sustainable development. Elsevier Science, Amsterdam

Optimum Insulation Thickness for Cooling Applications Using Combined Environmental and Economic Method

Emin Açıkkalp, Süheyla Yerel Kandemir, Önder Altuntaş and T. Hikmet Karakoc

Abstract Buildings cause to meanly one-third of carbon dioxide release and energy consumption. That is why, decreasing fuel consumption in building is the considerable aim for scientists and engineers. The easiest way of this is to insulate building walls. Insulation thickness optimization is conducted via a new method named as combined environmental and economic method (CEEM). Through this method, environmental costs are integrated in the fuel and insulation material costs. Environmental pollution cost of carbon dioxide, insulation materials and fuels are added to their cost, and total annual cost for the system is calculated and results are investigated according to insulation thickness. In this paper, insulation thickness optimization is researched for cooling applications. Results for the life cycle-integrated economic analysis and economic approach in terms of insulation thickness are presented.

Nomenclature

A	The area of the heat transfer area (m^2)

E. Açıkkalp
Department of Mechanical Engineering, Bilecik S.E. University, Bilecik, Turkey

S. Y. Kandemir
Department of Industrial Engineering, Bilecik S.E. University, Bilecik, Turkey
e-mail: syerel@gmail.com

Ö. Altuntaş · T. H. Karakoc
Faculty of Aeronautics and Astronautics, Anadolu University, Eskisehir, Turkey
e-mail: onderaltuntas@gmail.com

T. H. Karakoc
e-mail: hikmetkarakoc@gmail.com

E. Açıkkalp (✉) · S. Y. Kandemir
Bilecik S.E. University, Energy Technologies Application and Research Center, Bilecik, Turkey
e-mail: eacikkalp@gmail.com

C_s	Net money save for the economic approach ($/m^2)
C_T	Total cost for the economic approach ($/m^2)
CEEM	Combined economic and environmental methods
COP	Coefficient of performance
c_{el}	Specific cost of the electricity ($/kWh)
c_{ins}	Specific cost of the insulation material ($/m^3)
D_{CO_2}	Cost of CO_2 for CEEM ($/m^2)
D_e	Environmental cost of the electricity for CEEM ($/m^2)
D_{ins}	Cost of insulation combined with environmental cost ($/m^2)
D_s	Net saving for the CEEM ($/m^2)
D_T	Total cost for the CEEM ($/m^2)
d_{el}	Environmental effect of electricity (kg/kWh)
d_{CO_2}	Environmental cost of CO_2 ($/kg)
dt	Annual operation hours (h)
GWP_{ins}	The global warming potential of the insulation material
g	Incorporated with inflation rate
i	Interest rate
$i*$	Interest rate adjusted for the inflation rate
k	Thermal conductivity of the insulation material (W/mK)
N	Lifetime of the insulation material (year)
PWF	The present worth factor
$\dot{Q}$	Heat transfer rate (W)
PP_C	Payback period for economic approach (year)
PP_D	Payback period for CEEM approach (year)
$R_{T,nins}$	Total thermal resistance for non-insulation conditions (m^{2}K/W)
$R_{T,ins}$	Total thermal resistance for insulation conditions (m^{2}K/W)
T_a	Ambient temperatures (K)
T_s	Design temperatures (K)
U_{nins}	Heat transfer coefficient for the insulation conditions (W/m^{2}K)
U_{ins}	Heat transfer coefficient for the non-insulated conditions
x	Insulation thickness (m)
ρ_{ins}	Density of the insulation material (kg/m^3)

1 Introduction

The population at the augmentation and technological developments lead to excessive energy consumption. Rate of total energy consumption in buildings is about 34% in Turkey [1]. This means that second energy consumer of Turkey is buildings and residences [2]. Considering Turkey import their energy about 75% [3], it can be seen that any energy saving in this sector has big importance and potential. Insulation is the easiest way to save energy for the heating and cooling processes in buildings. Hence, insulation thickness optimization is significant to energy saving, to reduce

Fig. 1 Composite wall
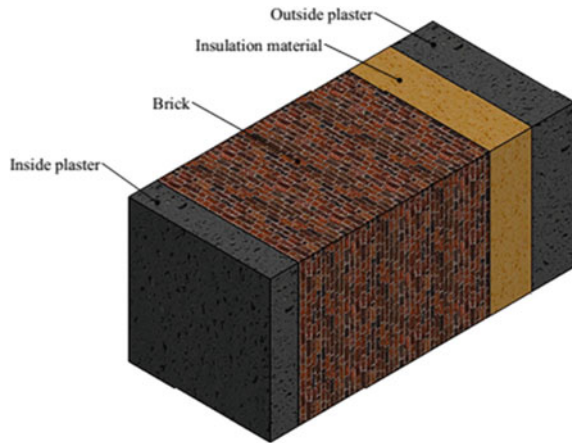
environmental impact and costs. Especially, in summer times, cooling load is really high and it would be very advantageous to reduce it.

In the open literature, some examples of the insulation thickness optimization for refrigeration systems can be found. Ozel [4] conducted the insulation thickness optimization for refrigeration conditions at Antalya. Soylemez and Unsal [5] researched insulation thickness optimization for cooling conditions at different regions. Kurekci [3] searched optimum insulation thicknesses in Turkey's provincial centers using cooling degree days values. Bolatturk [6] investigated insulation thicknesses optimization with heating and cooling degree days methods. In addition, exergetic approach for determining insulation is taken into account by several authors. Aslan and Kose [7] found optimum insulation thickness for buildings by means of thermoeconomic method considering condensed vapor. Arslan et al. [8] used exergetic approach for insulation thickness optimization including natural gas and lignite.

Kanbur et al. suggested a novel way of integrated economic and environmental impact costs. By means of method, costs of environmental impact of fuel and greenhouses gasses and materials get involved in the economic cost. Because, at the present day, economical analysis is not enough as only decision-making criterion and environmental assessments should be considered simultaneously. In this paper, a technique suggested by Kanbur et al. [9] is adjusted for insulation optimization. Authors are named as combined environmental and economic method (CEEM). In this research, CEEM is employed and compared to economic method.

2 Materials and Methods

A city, which is in Turkey, called Bilecik is selected for research, and investigations are carried out for summer time. In Fig. 1, one can see the composite wall studied is taken into account. Rockwool and glass wool are selected as materials. Coefficient

of performance (COP) of the system is 2.5 and heat transfer rate (W) is [4]:

$$\dot{Q} = UA(T_a - T_s) \tag{1}$$

where the heat transfer coefficient is U (W/m^2 K),the heat transfer area is A (m^2), in this study, calculations are made for unit area. T_a and T_s (K) are ambient and design temperatures; respectively, they are equal to 313.15 and 253.15 K. Electric energy given to refrigerator (kWh/m^2) is calculated as [4]:

$$E = \frac{\dot{Q}dt}{\text{COP}} \tag{2}$$

where dt is the annual operation hours and it is assumed as 8760 (h). Heat transfer coefficients are expressed in Eqs. (3) and (4), respectively:

$$U_{\text{nins}} = \frac{1}{R_{T,\text{nins}}} \tag{3}$$

$$U_{\text{ins}} = \frac{1}{R_{T,\text{ins}}} \tag{4}$$

2.1 Economic Evaluation

Life cycle cost technique is utilized, costs are equal to whole of electricity cost, material cost, operation and maintenance costs are considered. The electricity cost per unit area ($/m^2) can be described as:

$$C_{el} = (Ec_{el})\text{PWF} \tag{5}$$

where the specific cost of electricity is c_{el} ($/kWh) and total cost:

$$C_T = (Ec_{el})\text{PWF} + c_{\text{ins}}x \tag{6}$$

where the cost per volume of the material is c_{ins} ($/m^3) and the thickness of the material is x (m). The present worth factor (PWF) should be figured out to describe the cost over the service time. PWF involved with inflation rate, g and interest rate, i. Interest rate $i*$ adapted for inflation could be described follows:

$$i^* = \begin{cases} \frac{i-g}{1+g}; & i > g \\ \frac{g-i}{1+i}; & i < g \end{cases} \tag{7}$$

PWF is described as:

$$\text{PWF} = \begin{cases} \frac{1-(1+i^*)^{-N}}{i^*}; & i \neq g \\ (1+i)^{-1}; & i = g \end{cases} \tag{8}$$

where the service time is N and the interest rate i^*, which is adjusted for the inflation rate. The optimum insulation is achieved by taking the C_T derivative according to x and then it is solved equalizing to zero. C_T is minimum at optimum point. It is expressed as:

$$x_{\text{opt},C} = \frac{-\text{COP}^2 c_{\text{ins}} k R + \sqrt{\text{COP}dt c_{\text{el}} c_{\text{ins}} k \text{PWF} T (T_a - T_s)}}{\text{COP}^2 c_{\text{ins}}} \tag{9}$$

Payback period for CEEM can be calculated as follows:

$$PP_C = \frac{c_{\text{ins}} x}{S_C} \tag{10}$$

2.2 Assessment with CEEM

Environmental costs given in ref. [9] are taken into account. Costs involving environmental impact and economical values are united, in this way, environmental and economical values are taken into account. Application of CEEM, firstly, cost of the electricity, materials including economic and environmental values, is described and then insulation optimization and cost saving could be identified.

$$D_{el} = (E c_{el})\text{PWF} + D_{\text{CO}_2} \tag{11}$$

where D_{el} is the environmental impact expense of the electricity ($/m^2$). Cost of environmental impact of the CO_2 based on electricity is written as:

$$D_{\text{CO}_2} = \left(E d_{\text{el}} d_{\text{CO}_2}\right) \tag{12}$$

where specific environmental cost of CO_2 is d_{CO_2} ($/kg). Cost of the insulation is

$$D_{\text{ins}} = \left(c_{\text{ins}} + \text{GWP}_{\text{ins}} d_{\text{CO}_2} \rho_{\text{ins}}\right) x \tag{13}$$

where insulation material global warming potential is GWP_{ins} and insulation material density is ρ_{ins} (kg/m^3). Cost balance for the CEEM is written as:

$$D_T = (E c_{el})\text{PWF} + \left(E d_{\text{el}} d_{\text{CO}_2}\right) + \left(c_{\text{ins}} + \text{GWP}_{\text{ins}} d_{\text{CO}_2} \rho_{\text{ins}}\right) x \tag{14}$$

The optimum point is achieved by taking the D_T derivative according to x and then it is solved equalizing to zero. D_T is minimum at the optimum point. It is expressed as:

$$x_{\text{opt},D} = \frac{\text{COP}kR\left(c_{\text{ins}}+d_{\text{CO}_2}\text{GWP}_{\text{ins}}\,\rho_{\text{in}}\right)+\sqrt{\text{COP}dt\left(c_{\text{el}}+d_{\text{el}}\,d_{\text{CO}_2}\right)k\text{PWF}\left(c_{\text{ins}}+d_{\text{CO}_2}\text{GWP}_{\text{ins}}\rho_{\text{ins}}\right)(T_a-T_s)}}{\text{COP}\left(c_{\text{ins}}+d_{\text{CO}_2}\text{GWP}_{\text{ins}}\rho_{\text{ins}}\right)}$$

(15)

Payback period for CEEM can be calculated as follows:

$$\text{PP}_D = \frac{D_{\text{CO}_2}}{S_D}$$

(16)

3 Results and Discussion

In this section, results for the CEEM and economic approach are presented and discussed. Parameters used in calculations are shown in Table 1. Bilecik is analyzed for rock wool and glass wool materials; results are offered and compared for economic approach and CEEM.

Change of the total costs is shown in Fig. 2. As it can be seen that they decrease with insulation thickness and have optimum minimum cost values. After this point, they begin to rise again. Optimum points for the CEEM and the economical approach are obtained at $x = 0.24$ m and $x = 0.23$ m, respectively, for the glass wool. Corresponding values are 53.39 ($/m^2$) and 48.37 ($/m^2$). Similarly, for the rock wool, optimum insulation thicknesses are acquired at the $x = 0.23$ m for both methods, and corresponding values are 67.04 ($/m^2$) and 60.61 ($/m^2$). According to these, cost values are bigger for the rock wool, and cost of the CEEM is bigger than the economical approach. When we compare the costs at the optimum thickness with non-insulated conditions, one can see that costs decrease about 84–85% for rock wool and about 80–81% for the glass wool.

Table 1 Parameters used in calculations [9–11]

Parameter	Unit	Value
c_{el}	$/kWh	0.101
c_{ins} (rock wool)	$/m^3	132
c_{ins} (glass wool)	$/m^3	103
d_{CO_2}	$/kg	0.0327
d_{el}	kg/kWh	0.54
GWP (glass wool)		2.2
GWP (rock wool)		1.45
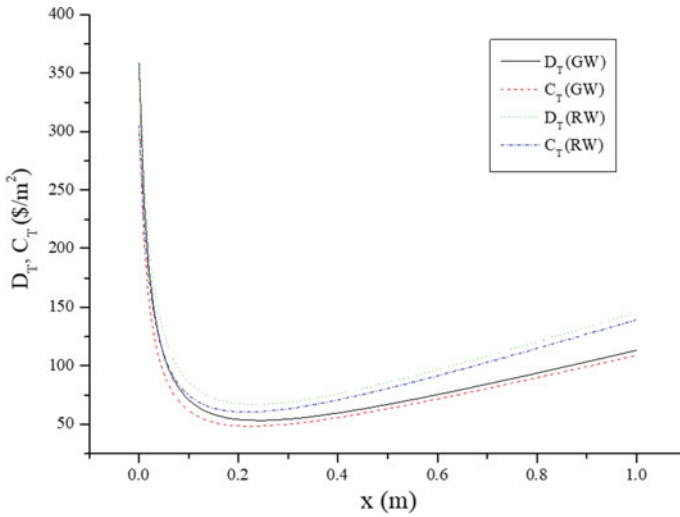
Fig. 2 Variations of the cost with insulation thickness
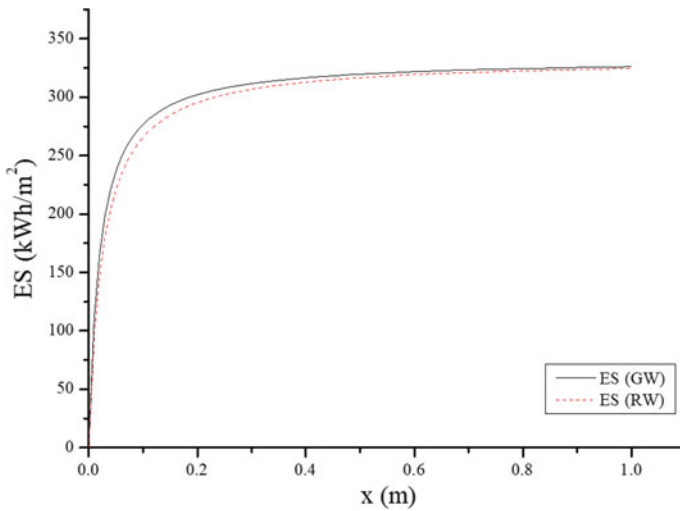
Fig. 3 Variations of the energy saving with insulation thickness

In Fig. 3, one can see energy savings. If results are investigated, it can be seen that rising at the energy saving is very dramatic until the optimum points and then it is nearly linear and increasing rate is very slow. For the glass wool, energy saving reaches to 326.06 kWh/m² and similarly, energy saving for the rock wool reachs to 324.46 kWh/m². As can be seen, energy saving for the glass wool is bigger than the rock wool.
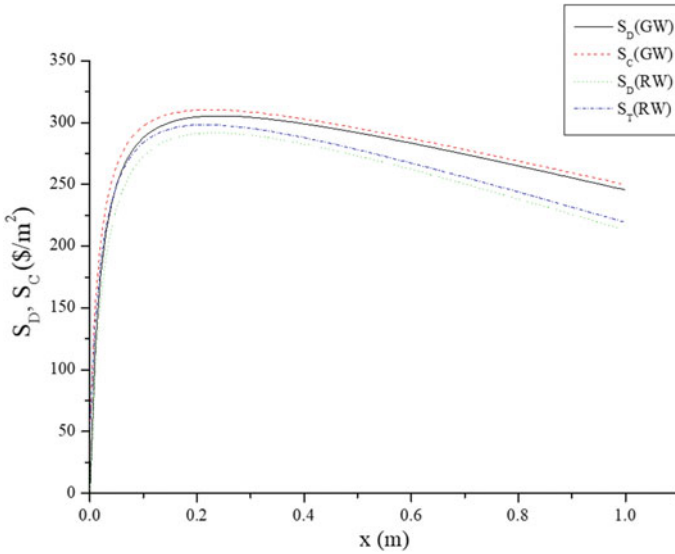
Fig. 4 Variations of the cost savings with insulation thickness

In Fig. 4, cost saving is depicted. Tendencies for the saving costs are the direct opposite of the cost variation and, naturally, maximum saving is obtained at the optimum insulation thickness. For the glass wool, maximum saving for the CEEM is equal to 305.46 ($/m^2) and maximum saving for the economic approach is 310.47 ($/m^2). According to results for the rock wool, maximum savings are 291.80 ($/m^2) and 298.23 ($/m^2) for the CEEM and economical approach, respectively. As it can be seen, saving for the economic approach is bigger than CEEM and savings are bigger for the glass wool.

Variation of the payback period variation is shown in Fig. 5. Payback-Periods increase nearly linear. Payback-Period of the glass wool is shorter than the rock wool, because thermal conductivity of the glass wool is smaller and price of the glass wool is lower too. Comparing economic and CEEM approaches, one can see that payback period of the CEEM is longer than the economic approaches because of the integration of the environmental costs. Payback periods increase with insulation thickness naturally; however, as it can be seen, payback periods are relatively low. This is resulted from the high electricity prices in Turkey and energy savings have higher rates, especially considering electricity consumption and price, it is reasonable. For the glass wool, PP_C and PP_D values reach to 0.41 (year) and 0.43 (year). Similarly, for the rock wool, PP_C and PP_D values reach to 0.60 (year) and 0.64 (year). Although these values are obtained at the one-meter insulation thickness, it can be said that payback period, which is nearly eight months, is very advantageous.

If results are interpreted, one can say that costs and cost saving for the economical approach are lower than CEEM. Similarly, glass wool is more advantageous insulation material from the rock wool.
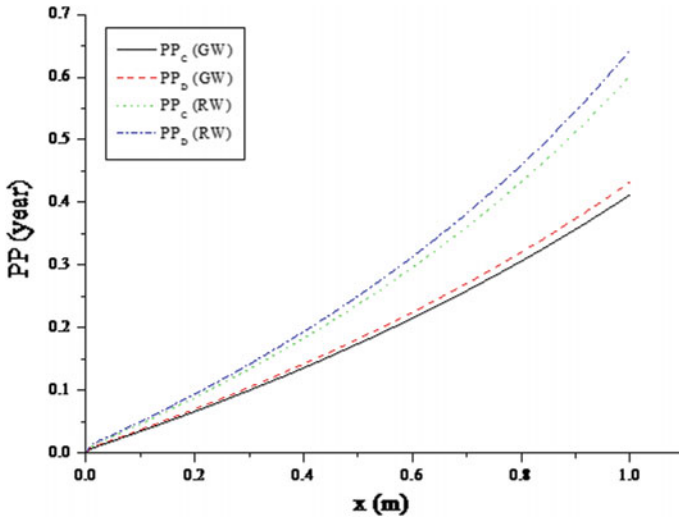
Fig. 5 Payback period variation

4 Conclusions

In this paper, a novel method to determine the optimum insulation thickness is presented called CEEM.

Results of CEEM are compared with economic approach. Investigations are performed for cooling applications. Rock wool and glass wool are chosen as insulation materials. According to results:

- Optimum insulation thickness for the rock wool is 0.23 and 0.24 m for the glass wool in terms of CEEM.
- Optimum insulation thickness for the rock wool is 0.23 and 0.22 m for the glass wool in terms of economical approach.
- Energy saving for the rock wool reaches to 324.46 and 326.06 kWh/m^2 for the glass wool at the optimum points.
- Cost savings are 305.46 \$/m^2 for the glass wool and 291.80 \$/m^2 for the rock wool at the optimum points in terms of CEEM.
- Cost savings are 310.46 \$/m^2 for the glass wool and 298.23 \$/m^2 for the rock wool at the optimum points in terms of CEEM.
- Maximum payback period is around 5–8 months.

This method is combined environmental and economical aspects, and it is suggested to use it for the optimum insulation thickness. In future studies, this method can be adopted for the exergy approaches. According to these results, one can see that optimum insulation thickness values obtained by CEEM are bigger than the economical approaches because environmental costs are added to CEEM methods as well as insulation material and fuel cost. Finally, it can be said that CEEM method is very

useful because of considering environmental impacts and other costs together. Exergetic values are important because decrease in these values causes efficient usage of the energy source. It is recommended that this method should be used for the optimum insulation thickness applications, and exergetic evaluation should be assessed.

References

1. National Energy Conservation Center (2006) The Principles of Energy Management in Industry, Ankara
2. Dombaycı OA (2009) Degree-days maps of Turkey for various base temperatures. Energy 34:1807–1812
3. Kurekci NA (2016) Determination of optimum insulation thickness for building walls by using heating and cooling degree-day values of all Turkey's provincial centers. Energy Build 118:197–213
4. Ozel M (2013) Determination of optimum insulation thickness based on cooling transmission load for building walls in a hot climate. Energy Convers Manage 66:106–114
5. Soylemez MS, Unsal M (1999) Optimum insulation thickness for refrigeration applications. Energy Convers Manage 40:13–21
6. Bolattürk A (2008) Optimum insulation thicknesses for building walls with respect to cooling and heating degree-hours in the warmest zone of Turkey. Build Environ 43:1055–1064
7. Arslan O, Kose R (2006) Thermoeconomic optimization of insulation thickness considering condensed vapor in buildings. Energy Build 38:1400–1408
8. Arslan O, Ozgur MA, Yildizay HD, Kose R (2009) Fuel effects on optimum insulation thickness: an exergitic approach. Energy Sources Part A Recovery Utilization Environ Effects 32:128–147
9. Kanbur BB, Xiang L, DubeyS, Choo FH, Duan F (2017) 'Life cycle integrated thermoeconomic assessment method for energy conversion systems', Energy Convers Manage 148:1409–25
10. Ardente F, Beccali M, Cellura M, Mistretta M (2008) Building energy performance:a LCA case study of kenaf-fibres insulation board. Energy Build 40:1–10
11. LOCOG Guidelines on carbon emissions of products and services—version 1, http://learninglegacy.independent.gov.uk/publications/locog-guidelines-on-carbon-emissions-of-products-and-ser.php. Access date: February 2018

Energy Efficiency Estimation of Induction Motors with Artificial Neural Networks

Mine Sertsöz, Mehmet Fidan and Mehmet Kurban

Abstract Induction motors make up 90% of today's motors in the industry. For this reason, the contribution of energy efficiency analyses to induction motors is very important. There are many techniques for measuring the efficiency of electric motors. These are the generally experimental ones as specified in certain standards. Experimental methods can also be divided into direct (IEEE 112-B, CSA-390) or indirect (IEC 34-2, JEC 37) methods. The use of experimental methods is not common due to the cost of installing and operating test laboratories worldwide. Therefore, energy efficiency estimation methods are used in worldwide. In this study, efficiency estimations are made with artificial neural network (ANN), which is an optimization-based estimation method with using data of 307 induction motors' (from small to large) from three different companies (AEG-TECO-GAMAK). The results are very close to the efficiency values given in catalog values. However, another noteworthy issue is that the estimation errors of the efficiency change from company to company. The errors of one company are higher than the others.

Keywords Induction motors · Efficiency estimation · Energy efficiency · Efficiency estimation methods

M. Sertsöz (✉) · M. Fidan
Eskişehir Technical University Vocational School of Transportation, Eskisehir, Turkey
e-mail: msertsoz@eskisehir.edu.tr

M. Fidan
e-mail: mfidan@eskisehir.edu.tr

M. Kurban
Department of Electrical and Electronics Engineering, Bilecik Şeyh Edebali University, Bilecik, Turkey
e-mail: mehmet.kurban@bilecik.edu.tr

Nomenclature

ANN   Artificial Neural Networks
ME   Mean Error
RMSE Root Mean Square Error

1 Introduction

The total electricity consumption for electric motors is estimated at 7.200 TWh per year, representing 46% of global electricity consumption in 2006. 38.3% of electric consumption by motors is used by pumps, fans, and compressors in heating, ventilation, and air-conditioning (HVAC) systems in the commercial sector; motors in the industrial sector account for 68.9% of electricity use, mostly in manufacturing and production areas [1].

Alternating current's three-phase induction motors are efficiency and low cost, so they are widely used in commercial buildings and industrial applications such as fans, pumps, and compressors, where they need to continuously operate [2].

$$\text{Efficiency \%} = \frac{\text{Mechanical Output Power}}{\text{Electrical Input Power}} \times 100 \tag{1}$$

or

$$\text{Efficiency \%} = \frac{\text{Electrical Output Power} - \text{Losses}}{\text{Electrical Input Power}} \times 100 \tag{2}$$

All the motor losses must be known according to Eq. (2). Sometimes, it is difficult to know all the losses; so, mechanical output power gives more accurate results (in Eq. 1); IEEE 112-B and CSA-390 are direct methods and Eq. (1) is used for calculation efficiency.

It is important to note that these tests are a long procedure and have their standards. IEEE 112-B and CSA-390 have different tests generally according to motor sizes. It is possible to find a brief of these tests below:

IEEE 112-B includes eleven different efficiency tests, namely Method A, B, $B1$, C, E, $E1$, F, $F1$, C/F, E/F, $E1/F1$. To briefly mention these:

Method A: By using input–output.
Method B: By using input–output and the indirect measurements of the stray loss and by separating losses.
  Method $B1$: By using input–output and the indirect measurements of the stray loss and a default temperature by separating losses.
Method C: By using input–output and the indirect measurements of the stray loss by separating losses of the equivalent machines.

Method *E*: By separating the losses and using the electric power measurement under the charge and direct measurement of the stray loss.

    Method *E*1: By separating the losses and using the electric power measurement under the charge and supposedly measurement of the stray loss.

Method *F*: By using the direct measurement of the stray loss and using the equivalent circuit.

    Method *F*1: By using the supposed measurement of the stray loss and using the equivalent circuit.

Method *C/F*: By using the equivalent circuit that is calibrated to the *C* charge point each method and using the indirect measurement of the stray loss.

Method *E/F*: By using the equivalent circuit that is calibrated to the *E* charge point each method and using the direct measurement of the stray loss.

Method *E*1/*F*1: By using the equivalent circuit that is calibrated to the *E* charge point each method and using the assumption of the stray loss.

CSA-390 includes three different efficiency tests, namely Method (1), Method (2), and Method (3). To briefly mention these:

Method (1): Input–output Method with Indirect Measurement of the Stray-load Loss and Direct Measurement of the Stator Winding, Rotor Winding, Core and Windage-friction Losses

Method (2): Input Measurement Method with Direct Measurement of All Losses

Method (3): Equivalent Circuit Calculations with Direct Measurement of Core Loss, Windage-friction Loss, and Stray-load Loss

It is necessary to measure both the mechanical output power and the electrical input power according to Eq. (1). Electrical input power is measured accurately using a simple installation of medium-priced equipment. The mechanical output power is defined as multiplication torque by angular velocity. While it is possible to get accurate efficiency results with a relatively simple product (± 1 RPM), and this producer requires inexpensive hardware for speed measurement. However, it requires a more detailed setup and this setup causes more expensive types of equipment to get accurate results.

IEC 34-2 and JEC 37 are indirect methods. But they are "experimental methods" too. To avoid the torque measurements' complexity and cost, the motor's efficiency is indirectly determined by the following equation:

$$\text{Efficiency \%} = \frac{\text{Electrical Input Power} - \text{Losses}}{\text{Electrical Input Power}} \times 100 \qquad (3)$$

IEC 34-2 includes eight different efficiency tests for induction motors, namely Method 2-1-1A, 2-1-1B, 2-1-1C, 2-1-1D, 2-1-1E, 2-1-1F, 2-1-1G, 2-1-1H. To briefly mention these:

Preferred testing methods

Method 2-1-1A: Direct measurement of input and output

Method 2-1-1B: Summation of losses, additional load losses according to the method of residual loss

Method 2-1-1C: Summation of losses with additional load losses from assigned allowance

Testing methods for field or routine-testing

Method 2-1-1D: Dual supply back-to-back-test

Method 2-1-1E: Single supply back-to-back-test

Method 2-1-1F: Summation of losses with additional load losses determined by the test with the rotor removed and reverse rotation test

Method 2-1-1G: Summation of losses with additional load losses determined by Eh-star method

Method 2-1-1H: Determination of efficiency by use of the equivalent circuit parameters.

This calculation requires the measurement of motor losses as it can be seen from Eq. (3). A lot of motor losses (mechanical, copper, iron) can be measured accurately. But the other losses, as leakage losses, are not measurable. JEC 37 neglects the leakage losses.

Numerous methods are proposed in the literature for the efficiency determining of induction motors. These methods are as follows:

(1) Current Method;
(2) Slip Method;
(3) Simplified Equivalent Circuit Method [3];
(4) Simplified Loss Segregation Method [4];
(5) Nonintrusive Air-gap Torque (AGT) (NAGT) Method [5];
(6) Optimization-based Methods [6–16].

Determining the energy efficiency of induction motors is a very important detection of using energy. Nowadays, developing efficiency estimation methods are very important because of the difficulty and cost of field testing. It is not an efficient way to test the motors by interrupting the operation of them.

An optimization-based search algorithm (genetic algorithm, bacterial feed algorithm, artificial neural networks, and multi-objective optimization) is generally used for the estimation of motor efficiency in real industrial conditions.

Researchers provide (in balanced resource conditions) optimization-based techniques for estimating efficiency based on a literature review. In some studies, the genetic algorithm (GA) is combined with the equivalent circuit method deal with the problem of estimating the efficiency, especially in unbalanced feeding conditions. These studies are given below:

A new approach to nonintrusive in situ efficiency determination of an induction motor is presented in this paper. An equivalent circuit-based optimization process—using the genetic algorithm—is calculated the motor efficiency by monitoring the input currents, the input voltages, the input power, and the motor speed. The convergence and precision have been improved by taking into account several load points in the objective function and temperature dependency of the stator and rotor resistances.

The method which depends on parameter changes is presented [6]. In this study, a nonintrusive method is used for estimating field efficiency of induction motor at different frequencies and loads using with data from field measurement. Torque and efficiency which are some performance values of motors can be estimated by using measurement data coupled with the use of a genetic algorithm based on the modified motor equivalent circuit concept [7]. This study proposes an economical method to replace inefficient motors with efficiency ones. Field efficiency of motors is studied without interrupting the work of the motors and any requirement of measuring the output power. Genetic algorithms are coupled with a few sets of measured data from the field tests and this novelty method that is used for evaluating motor equivalent circuit parameter, no requirements no load and blocked-rotor tests. The result of efficiency estimation is very close to calculated obtained from the standard evaluations. So, it is suitable for conducting on-site energy audits of motors to project cost savings and payback and to support a confidence decision regarding the investment in higher efficiency motors [8]. In this article just like previous studies, a new evolutionary-based in situ efficiency estimation technique is proposed without the requirement of the no-load test but an extra this method can be used for balanced or unbalanced power supply conditions. Experimental results are compared with the estimation results [9]. This study suggests a hybrid method based on the air-gap torque method and genetic algorithms because there is a requirement non-intrusive methods for testing in-service motors' efficiency [10]. This paper focused on the estimation of the parameters of three-phase induction motors using a few sets of data from the field tests of motors. This technique, which coupled with the genetic algorithm for evaluating the equivalent circuit parameters, does not need no-load and blocked-rotor tests [11]. Anew, a genetic algorithm is used for in situ induction motor efficiency determination in this study. Estimation results are compared with torque-gauge results [12]. This study has some differences from previous studies. This study which is an optimization based is the realization of efficiency estimations of induction motors at 17 different power types with artificial neural networks and linear estimation by looking at the speed values, current and moment, listed in the manufacture's catalog in full load. Before obtaining the estimations, the statistical analysis of the correlations between efficiency and moment, efficiency and speed, efficiency and current of the motor was applied [13]. This new technique, which are genetic algorithms, based on the method of symmetrical components of voltage and considering parameters variations (especially in the rotor) related to the effect of negative sequence voltage system is used for estimating parameters as shaft power and efficiency losses, of three-phase induction motors in field conditions under unbalanced voltages or deviated voltage and frequency without caring out special tests, removing the motors, or measuring the output power or torque. As a result, with these parameters (voltage, current, power and speed or slip, measured in the motor in situ) are known, it is possible to estimate the efficiency [14]. This paper introduces a method based on multi-objective evolutionary algorithms for the determination of in-service induction motor efficiency. But this method has a disadvantage of multi-objective evolutionary algorithms. Determination efficiency values will not be readily visible in the multi-objective evolutionary optimization algorithms; the Non-dominated Sorting Genetic

Algorithm-II (NSGA-II) and Strength Pareto Evolutionary Algorithm-2 (SPEA2), are successfully applied to the efficiency determination problem in induction motor [15]. In this method, using the stator current, stator voltage, stator resistance, input power, and rotor speed of the in-service motor, motor efficiency estimation can be made. The bacterial foraging (BF) algorithm is used for evaluating the equivalent circuit parameters of the motor instead of using the no-load and locked-rotor tests. The efficiency is estimated using a modified motor model [16].

This study is different from the other because it is simulation-based. This paper investigates the effects of different voltage magnitude unbalances with the same voltage unbalance factor (VUF) on the stator, rotor copper and total copper losses of three-phase induction motor from three different companies. The copper losses of three different three-phase induction motor for full load conditions have been analyzed through simulation under six different voltage magnitudes unbalance conditions [17].

A summary will be made below about efficiency determinations of the motors:

- The motor current and the slip methods are easy, but the stability is relatively fewer than the other methods.
- Air-gap torque methods, loss separation methods, and lastly torque measurement methods give more accurate results, but not easy to apply in the field.
- The circuit equation methods are used, especially when removing the running when motors are not possible. The performance of any overhead induction motor is determined by the six circuit parameters consisting of core loss resistances, stator and rotor windings, magnetic reactance and stator, rotor leakage in the circuit equations [18].

Each method has its advantages and disadvantages. But optimization-based methods can be declared as the most useful method in motor efficiency estimation nowadays. In this study, any circuit parameters are required from the companies. Only the efficiency, speed, power, power factor and torque data that present in the companies' catalogs are used for this study. But, it is assumed that all the voltage and current values are under balanced source conditions.

This study has five parts. In Sect. 2, general information is given about induction motors, and information is given about the company named Gamak, AEG, and TECO motor companies whose motors are used in the study. The 307 induction motors' values which are used in this study are taken from these three companies (Fig. 1).

In Sect. 3, information is given about the method ANN. The structure of ANN is introduced. Toolbox of MATLAB which solves the problem with an artificial neural network is used for network training and testing. Efficiency estimation is performed with ANN for 307 induction motors. Firstly, the ANN model is introduced, and the specifications for this are given in Table 1. Section 4 is Results and Discussion. The transfer function is chosen as a hyperbolic tangent sigmoid transfer function, the learning function is trainlm and network type is backpropagation. Training of networks for three companies is given. Then, the network structures are given in

Fig. 1 Simplest form of an induction motor
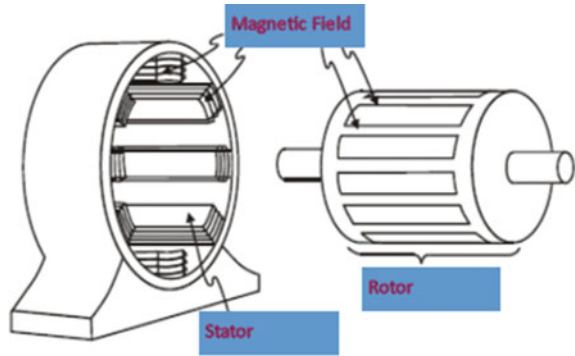
Table 1 Training parameters of neural networks

Epochs	1000
Error Goal	0
max_fail	6
Momentum update	0.001

Figs. 2, 3, and 4. Errors of efficiency estimation results for three companies are declared. Section 5 is Conclusion. According to Sect. 4's outcomes, the results and future studies are discussed.

2 Induction Motors

In industrial plants, motors are used to convert electrical energy into motion energy. The alternating current is given to the motor windings than a magnetic field, which
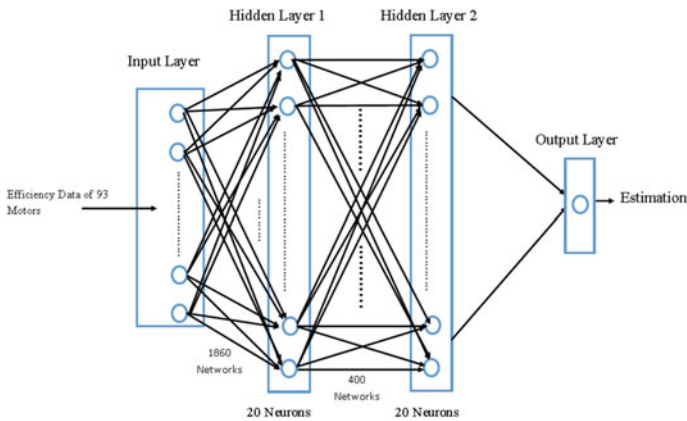
Fig. 2 Networks of efficiency estimation for AEG
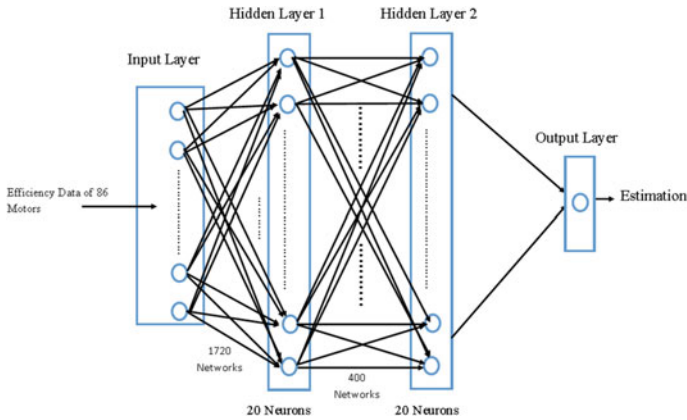
Fig. 3 Networks of efficiency estimation for GAMAK
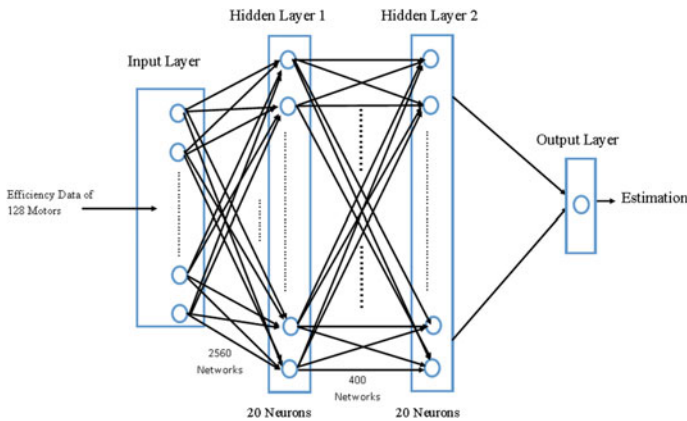
Fig. 4 Networks of efficiency estimation for TECO

has a rotational speed, is get. Te rotational speed of the rotor is different from each other. These motors are called as "induction motors" and also they work according to the principle of induction.

Induction motors are cheap and require low maintenance; they do not cause arcs during their operations; they can be manufactured from small powers up to thousand kW. They are the most widely used motors in the industry due to the high moments and changing of speed limits aim of the developing technology. There are dozens of electric motors in practice. However, the rate of use of induction motors is very high. Induction motors are generally composed of the following parts:

- Stator: Windings are located. Windings are used for generating rotating magnetic fields in motors, which work with alternating voltage.

- Rotor: Rotor is rotating part inside the magnetic field which stator generates and aims of this part, and mechanical energy is received.
- Body and Covers: These parts are made of aluminum, iron or another iron type which alloy against external influences.

  The central position of the rotor in the stator is to cover the task.

- Beds and Bearings: Mechanical parts that make the rotor to rotate easily.
- Cooling Fan: It is air cooled in motors with 0–20 kW power. It is connected to the rotating shaft of the motor. A plastic or metal propeller allows the body to easily dispose of the temperature.

Induction motors can be classified according to the number of phases, the structure, type of work, working conditions, and structure of the rotor.

According to the number of phases:

- Three-phase induction motors
- One-phase induction motors.

  According to structure:

- Induction motors with short-circuit rotor (squirrel cage)
- Induction motors with the winding rotor.

  According to the types of construction:

- Open-type induction motors
- Closed-type induction motors
- Flanged induction motors.

  According to rotor construction:

- High-resistance induction motors (rotor ohmic resistance is large)
- Low-resistance induction motors (rotor ohmic resistance is small)
- High-reactance induction motors (rotor inductive resistance large)
- Double squirrel cage motors with rotor.

2.1 Working Principle

Operation of induction motors is based on the following three principles:

- In stator windings where alternating current is applied should be a rotating magnetic field.
- If a current is passed through a conductor that is inside the magnetic field, the conductor is pushed out of the magnetic field.
- The same poles push each other; the opposite poles pull each other.

They work according to the principle of induction. The magnetic field formed in the stator allows the electric current to be induced (occurred) in the rotor. Any more rotor has a magnetic field because of the electric current. As a result, these two magnetic fields (rotating magnetic field formed in the stator and rotor's magnetic field) cause to rotate the rotor by pushing and pulling.

2.2 Motor Companies Using in the Study

AEG Industrial Engineering is a company for electrical plants of the industry, the energy industry, and transportation. They are located at the traditional location of AEG industrial facilities, the Hohenzollerndamm in Berlin. They are in close contact with current and former AEG factories. The main focus of their works is drive and automation systems, switchgear, transformers, generators/turbines, and diesel generator sets. They also deal with general industry electronics and high- and low-voltage compensation systems. Together with their representatives and their local subsidiaries, they serve their international clients [19].

The company Gamak was founded in 1961, and it is the domestic product of "Electric Motor" which is one of the most important products that the Turkish industry needs for production. In a short period, Gamak started production of the first electric motor to be produced in Turkey.

Gamak is one of the most important producers of electric motors in the world, not just in Turkey. With electric motors produced in the power range of 0.06–1000 kW, it can meet almost all the engine needs of the industry. Gamak can almost provide all the parts required for electric motor production at its facility and collect the entire production under one roof. The company has one of the most distinguished laboratories in Europe.

TECO is a local motor manufacturer in Taiwan. It was established before about 70 years. TECO gives attention to Quality First concept beginning of its history. Teco's motors are from 1/4 Hp to 60,000 Hp, a maximum of 14,200 V and a broad selection of engineered products, especially high efficiency motors, inverter duty motors and explosion-proof motors to meet a variety of customer needs TECO has earned a world-renowned reputation and become a leading manufacturer in the world [20].

3 Materials and Methods

The power, speed, power factor, moment, and efficiency values of 307 induction motors' (AEG (93), TECO (128) and GAMAK (86)) [21] used in this study are taken from three different motor companies, (AEG [22], TECO [23] and GAMAK [24]). These values are getting from companies' motor catalog which all data can get easily and motors arranged from small to large.

Total 1535 (307 × 5) data is used for the construction of the estimation method. The estimation method is artificial neural network which is an optimization-based method. Specifications are given below about the artificial neural network.

3.1 Structure of Artificial Neural Network (ANN)

Artificial neural network (ANN) is a part of artificial intelligence science and includes studies to learn computers. Computers were previously only used to perform complex calculations, but today, they can summarize large amounts of data and have a position to comment on the current situations. Sometimes to formulate as mathematically of some problems is impossible, at such times ANN intuitively performs the solution of the problems. ANN's skill is very benefit when problems can not be solved. It is the artificial intelligence in the computer that always is used. The most prominent feature of this example is that it can make inferences of the problems that it has never seen before by understanding the weave of the event by using previous samples.

Layer and neurons can be changed as desired in artificial neural networks. The increase of a number of layers has a direct proportional with nonlinearity. Deciding about a number of neurons is often made by testing and several tests are needed to achieve the best possible number of neurons. Because the internal structure of artificial neural networks is not known and this is a disadvantage of ANN. When selecting the network structure, it is found in the same way as the neuron numbers. Experiences show that to choose the learning coefficient in the 0.2–0.4 band and to choose the momentum between 0.6 and 0.8 is a good choice. However, this value is the optimum value and varies with the type of the problem. The basic principle is that artificial neural networks can achieve the optimum solution, but this does not mean that this is the best solution. However, it responds better in many applications which are nonlinear, complex, high probability of error, etc., in general evaluation. Therefore, when selecting the problems which fit this frame will cause better results.

In this study, the network type is selected as backpropagation. In the backpropagation networks, the outputs are generated by the network according to inputs then these outputs compared with the expected outputs. This difference is called an error and the goal is to reduce this error. The sigmoid transfer function is also selected in the transfer function because it is one of the best responsive transfer functions in the backpropagation. The formulas are given below:

The Sigmoid Transfer Function:

$$o = \frac{2}{1 + e^{-2i}} - 1 \qquad (4)$$

o outputs
i inputs

Here, (*i*) the input is obtained as a linear weighted combination of the outputs from the neurons of the previous layer.

Backpropagation Networks:

$$\text{Un} = -[JT \times J + \propto I]^{-1} \times J^{\text{T}} + e \tag{5}$$

J   the Jacobian matrix containing the first derivatives of the network errors according to weight and deviation

e   errors

μ a parameter which should be decreased after each successful step but sometimes only after a temporary step the error term (or when the performance function increased) should be increased. Therefore, the performance function is decremented or constrained at each iteration [25].

This study is performed using the ANN toolbox of the MATLAB. The performance measurement of the network is calculated by MSE. The training parameters are as follows in Table 1:

Training performance is calculated and best validation performances are 0.0016348 at epoch 10 for AEG, 0.0063555 at epoch 10 for GAMAK, 0.0018569 at epoch 10 for TECO.

In this study, the test values and the simulation values are the same (all in one test method). Normalization process is applied to all input values for all tests. The formula of the normalization is given below:

$$\text{Normalize } X = \frac{\text{Variable } - \text{ Minumum Variable of the Series}}{\text{Maximum } \text{ Variable of the Series } - \text{ Minumum } \text{ Variable of the Series}} \tag{6}$$

This study aims to determine the efficiency of the motors according to the inputs, which are taken from three different motor companies.

4   Results and Discussion

Tests are done with ANN. The test and result details are given below. Experiments are performed using 2 layers and 20 neurons (because this is the best combination of our tests). Transfer function is hyperbolic tangent sigmoid transfer function, network type is backpropagation, and learning function is trainlm. Details are given in Sect. 3.1 about these choices.

Network types are given below as Figs. 2,3, and 4:

The input value is the only efficiency of the motors for Figs. 2, 3, and 4. There are power, speed, power factor, and moment as inputs too. Efficiency estimation is made using all these inputs. But the only efficiency input is shown.

The proposed efficiency estimation method works well according to Figs. 5, 6, and 7. Catalog efficiency data are same as the estimation except for small deviations. These deviations are generally in small motors, especially in AEG. The large motors
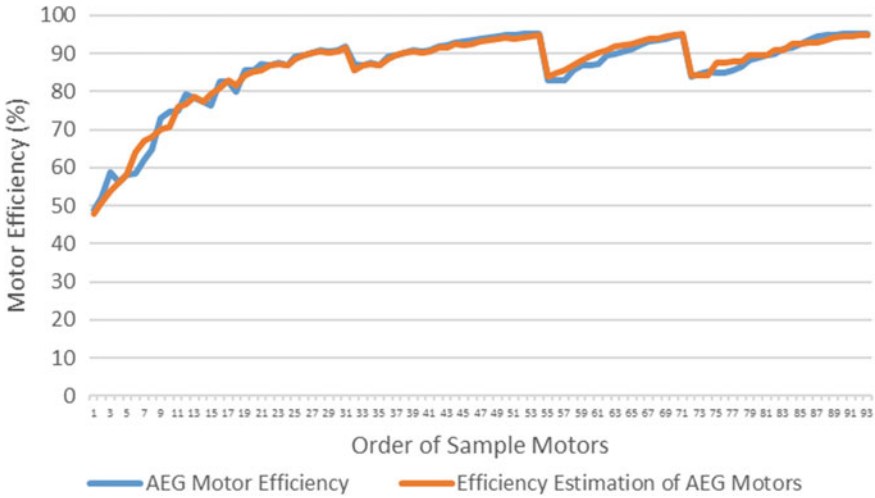
Fig. 5 Estimation results for AEG
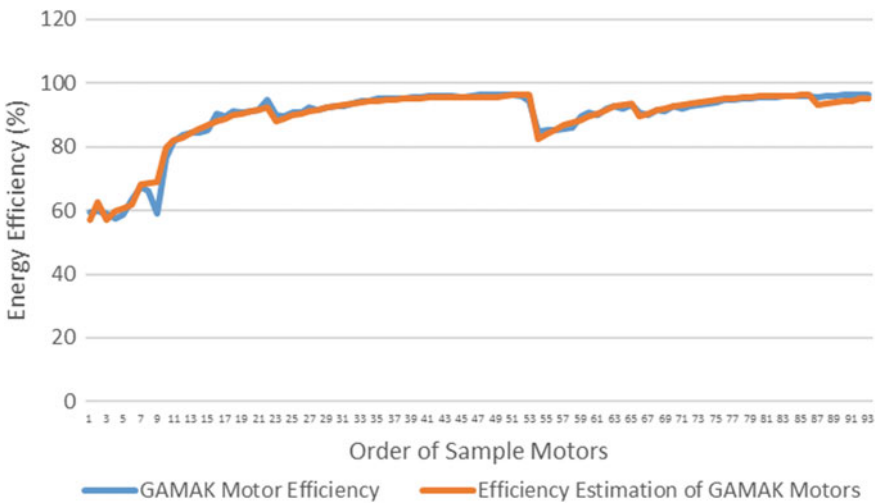
Fig. 6 Estimation results for GAMAK

have few deviations. As a result, the estimation techniques can get more accurate results in the large motors.

Error rates are calculated according to Eqs. 7, 8, 9, and 10 given below:

$$ME = Mean\,(Efficiency - Estimation) \tag{7}$$
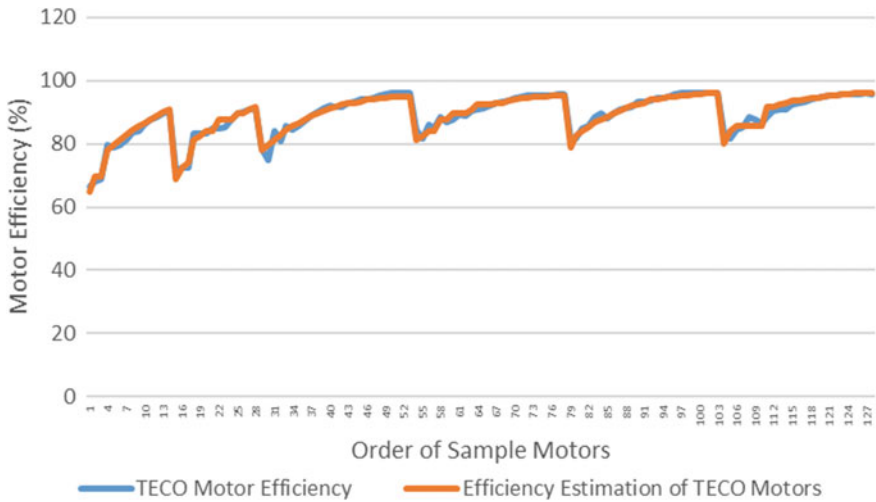
Fig. 7 Estimation results for TECO

Table 2 Errors of efficiency estimation results for three companies

	AEG	GAMAK	TECO
ME	0.1338	−0.0312	−0.0251
ME_percentage	0.1552	0.0349	0.0282
RMSE	1.5551	1.5601	1.2172
RMSE_percentage	1.7911	1.7345	1.3614

$$\text{ME}_{\text{percantage}} = \% \big[(100 \times \text{Mean (Efficiency} - \text{Estimation)} / \text{Mean (Efficiency)} \big] \tag{8}$$

$$\text{RMSE} = \sqrt{\text{Mean} \left[(\text{Efficiency} - \text{Estimation})^2 \right]} \tag{9}$$

$$\text{RMSE} = \% \left[\left(100 \times \sqrt{\text{Mean} \left[(\text{Efficiency} - \text{Estimation})^2 \right]} \right) \Big/ \sqrt{\text{Mean} \left(\text{Efficiency}^2 \right)} \right] \tag{10}$$

It is possible to say that error rates are very low by making an estimation with ANN for Table 2. However, if the companies are compared with each other, TECO has the best results according to error rates. The worst results belong to AEG, in most kinds of errors.

5 Conclusions

It is clear that ANN is a good estimation method that can be used to estimate the efficiency of induction motors. However, some companies respond with a lower error

rate, while others have a higher error rate. It would not be correct to relate the reason with the number of training used. Because, when the number of training increases, accuracy will increase according to the principle. The order should be in the form of TECO (128), AEG (93) and GAMAK (86) according to this principle. However, in the experiments performed, the order was in the form of TECO, GAMAK, and AEG. This means that the number of training alone is not effective in the accuracy; it is also relevant to the tests that the companies used in determining the efficiency of the motors in the catalog.

There is one more result, especially in small motors, companies' error rates are much more than large motors except TECO. AEG is the company with the highest error rate compared to the others. But when all tests are evaluated, the total error is 0.15% for ME; RMSE did not exceed 1.79% in three companies.

These error rates are quite satisfactory for the efficiency estimation of induction motors.

In future studies, two different studies can be developed taking this study as an example. Firstly, more motor values can be used by different companies. According to their error rates, a classification problem can be described. Secondly, a hybrid method using other estimation method can be created to reduce the error rates of estimations.

References

1. Waide P, Brunner CU (2011) Energy efficiency policy opportunities for electric motor-driven systems. International Energy Agency, Paris
2. DOE (2008) Improving motor and drive system performance: a sourcebook for industry. U.S. Department of Energy, Office of Energy Efficiency and Renewable Energy, Washington, DC
3. Kueck JD, Olszewski M, Casada DA, Hsu J, Otaduy PJ, Tolbert LM (1996) Assessment of methods for estimating motor efficiency, load under field conditions. Oak Ridge Nat. Lab., Oak Ridge, TN, Rep. ORNL/ TM-13165
4. In-plant electric motor loading and efficiency techniques. Ontario Hydro, Toronto, ON, Canada, Rep. TSDD-90-043, 1990
5. Lu B, Habetler TG, Harley RG (2008) A nonintrusive and in-service motor-efficiency estimation method using air-gap torque with considerations of condition monitoring. IEEE Trans Ind Appl 44(6):1666–1674
6. Charette A, Xu J, Ba-Razzouk A, Pillay P, Rajagopalan V (2000) The use of the genetic algorithm for in situ efficiency measurement of an induction motor. In: Proceedings of IEEE power engineering society winter meeting, pp 392–397
7. Phumiphak P, Chat-uthai C (2008) Nonintrusive method for estimating field efficiency of inverter-fed induction motor using measured values. In: Proceedings IEEE international conference on sustainable energy technology, pp 580–583
8. Aspalli MS, Shetagar SB, Kodad SF (2008) Estimation of induction motor field efficiency for energy audit and management using genetic algorithm. In: Proceedings of international conference on sensor technologies, pp 440–445
9. Siraki A, Pillay P (2012) An in situ efficiency estimation technique for induction machines working with unbalanced supplies. IEEE Trans Energy Convers 27(1):85–95
10. Lu B, Wenping C, French I, Bradley KJ, Habetler TG (2007) Nonintrusive efficiency determination of in-service induction motors using genetic algorithm and air-gap torque methods. In: Conference on record IEEE 42nd IAS annual meeting, pp 1186–1192

11. Phumiphak T, Chat-uthai C (2002) Estimation of induction motor parameters based on field test coupled with genetic algorithm. In: Proceedings of international conference on power system technology, pp 1199–1120

12. Pillay P, Levin V, Otaduy P, Kueck J (1998) In-situ induction motor efficiency determination using the genetic algorithm. IEEE Trans Energy Convers 13(4):326–333

13. Sertsöz M, Fidan M, Kurban M (2018) Efficiency estimation of induction motors at different sizes with artificial neural networks and linear estimation using catalog values. Anadolu University J Sci Technol A Appl Sci Eng 19(2):293–302

14. Gomez JR, Quispe EC, de Armas MA, Viego PR (2008) Estimation of induction motor efficiency in-situ under unbalanced voltages using genetic algorithms. In: Proceedings of international conference electrical machines, pp 1–4

15. Cunkas M, Sag T (2010) Efficiency determination of induction motors using multi-objective evolutionary algorithms. Adv Eng Softw 41(2):255–261

16. Sakthivel VP, Bhuvaneswari R, Subramanian S (2010) Non-intrusive efficiency estimation method for energy auditing and management of inservice induction motor using bacterial foraging algorithm. IET Elect Power Appl 4(8):579–590

17. Siddique A, Yadava GS, Singh B (2004) Effects of voltage unbalance on induction motors. In: Conference on record of IEEE international symposium on electrical insulation, pp 26–29

18. Hughes A (2006) Electric motors and drives fundamentals, types and applications, 3rd edn. Elsevier Ltd., Burlington

19. http://www.aeg-ie.com/. Accesed on 19th May 2019

20. Sertsöz M, Fidan M, Kurban M (2019) Three autoregressive-neural network hybrid models for energy eciency estimation of induction motors. In: COMPEL—the international journal for computation and mathematics in electrical and electronic engineering, 2019

21. http://www.teco.com.tw/fa/about.htm. Accesed on 19th May 2019

22. http://www.grittielettrotecnica.it/cataloghi/AEG_motori_trifase_uk.pdf. Accesed on 20th March 2018

23. http://www.teco-group.eu/Resources/Electric-Motors/Catalog2018.Manuals/TECO_Motor_Katalog_UK_web-2014. Accesed on 20th March

24. http://www.gamak.com/uploads/files/catalogue/Gamak-2016-Urun-katalogu-tr.pdf. Accesed on 20th March 2018

25. Hagan MT, Menhaj MB (1994) Training feed forward techniques with the Marquardt algorithm. IEEE Trans Neural Netw 5:989–993

A CFD Study on Photovoltaic Performance Investigation of a Solar Racing Car

Check for updates

Talha Batuhan Korkut, Aytaç Goren and Mehmet Akif Ezan

Abstract The increasing trend of the energy consumption of humanity has brought forward the efficient use of current energy resources and seeking for the adaptation of renewable energy resources. Integration of renewable energy into transportation, on the other hand, has crucial importance as it reduces the emissions in the urban regions and increases the life quality by reducing the noise in solar-powered electric vehicles. Solar-powered vehicles, automobiles or planes, with photovoltaic panels (PVPs) are widely in use for decades. However, there are several aspects, such as electrical conversion and storage efficiencies, that should be improved. It is known that increasing the temperature of the PVPs adversely affects both the panel lifetime and electrical conversion efficiency. In this study, a 3D CFD model of a solar-powered racing car is developed in ANSYS-FLUENT to investigate the power outputs of the PVPs that are placed on different positions of the vehicle under various velocities, i.e., 30–120 km/h, and solar irradiations, i.e., 300–900 W/m^2.

Keywords Solar car · Photovoltaic efficiency · PV modeling · CFD · Aerodynamics

Nomenclature

Parameters for Cell Current Calculation

I_{ph}	Light-generated current (A)
I_S	Cell saturation of dark current (A)
T_C	Cell temperature (K)
q	Electron charge (1.6×10^{-19} (V))
I_{S1}	First diode saturation current (A)
N_1	Quality factor of D_1

T. B. Korkut (✉) · A. Goren · M. A. Ezan
Department of Mechanical Engineering, Dokuz Eylul University, İzmir, Turkey
e-mail: tbatuhankorkut@outlook.com

V_t Thermal voltage (V)
R_p Internal parallel resistance (Ω)
V Voltage (V)
k Boltzmann cons. (1.38×10^{-23} (J/K))
T_{STC} Cell temperature (K) @STC (@25 °C)
A Ideal factor
I Current (A)
I_{S2} Second diode saturation current (A)
N_2 The quality factor of D_2
R_s Internal series resistance (Ω)

Parameters are Given by Manufacturers

V_{OC} Open-circuit voltage @25 °C (V)
V_m Voltage @MPP@25 °C (V)
P_m Maximum power @25 °C (W)
I_{SC} Short-circuit current @25 °C (A)
I_m Current @MPP@25 °C (A)
t_{PV} The thickness of the laminated PV module

The Energy Need for a Solar-Powered Vehicle

W_T Total resistive forces (N)
W_{R1} Rolling resistance force (1) (N)
W_{R2} Rolling resistance force (2) (N)
W_B Acceleration resistance force (N)
W_{ST} Gradient resistance force (N)
m The total mass of the vehicle (kg)
η Motor, controller and drive train efficiency
η_b Watt-battery eff.
x Distance (m)
W Weight of the vehicle (N)
C_{rr1} Rolling resistance const. (1)
C_{rr2} Rolling resistance const. (2) (Ns/m)
N Number of wheels
h Total height vehicle climbs (m)
N_a Number of times the vehicle will accelerate in a race day
g Accelaration due to gravity constant (m/s^2)

Data Reduction

F_D Drag force (N)
P_D Power consumption (Wh)
F_L Lift force (N)
ρ Density of air (kg/m^3)

Abbreviation and Acronyms

PV   Photovoltaic
SC   Solar car
CAD   Computer-aided Design
CV   Conventional vehicle

1 Introduction

The first solar car (SC), which was invented in 1955, consisted of 12 Selenium PV cells and a small electric motor rotating the rear wheel shaft (Sunmobile, W. G. Cobb, 31.08.1955). Although the first competition on the solar racing car was in 1985 (Tour Del Sol), the competition became popular with the Australian World Solar Challenge (WSC) in 1987. The concept of WSC was devised by Hans Tholstrup, who is a Danish-born adventurer and traveled from Perth to Sydney (4130 km) in 20 days with a solar car called *Quiet Achiever*. Different concept solar car races are being organized in different continents nowadays (Fig. 1).

As the first organizer of WSC and former chair of the International Solar Car Federation (ISF), Mr. Tholstrup describes World Solar Challenge as not a competition but a brain sport for solar people. Currently, the total range of the challenge is 3021 km

Fig. 1 World's first long-distance solar car which is produced by Hans Tholstrup, Quiet Achiever

and includes several control-stops in which the cars are inspected during the race. In this event, the primary purpose of the racing teams is to arrive in Adelaide in the first place. Each team has to organize their strategy due to the energy they can generate from sun and store in their batteries even during the race depending on the performance of the vehicle, weather conditions and the positions of other teams.

1.1 Energy Requirements of a Solar-powered Vehicle

When the top speed and acceleration of vehicles were examined, the increasing of these values compared to the past was observed. When Eq. (1) and Fig. 2 are examined, it is obtained that the power consumption generated by the aerodynamic resistive forces acting on a vehicle increases with the cube of the speed. For this reason, today's rising average speed values have brought along the problem of power consumption. Aerodynamic structures of solar vehicles are designed in such a way that their power consumption is low. Eq. (1) indicates that factors affecting the power expenditure on a solar car are rolling, acceleration, gradient, and aerodynamic resistances [1]. However, influences of rolling and acceleration resistive are assumed to be low on a solar-powered vehicle as conditions and routes of solar challenges and strategy of energy consumption reduce influences of acceleration and rolling resistive forces.

$$W_T = W_L + W_{R1} + W_{R2} + W_B + W_{ST} \tag{1}$$

Total resistive force which is acting on a solar racing car consists of five components (see Eq. 1). W_L is the aerodynamic resistive force, W_{R1} and W_{R2} are rolling resistance forces, W_B is the acceleration resistance force, and W_{ST} is the gradient resistance force. Solar racing cars have a lightweight structure. In addition , solar racing cars use tires with a low rolling coefficient. For this reason, rolling, acceleration, and gradient resistance forces have less importance to the aerodynamic resistance force.

Osawa et al. [2] were examined power consumption components of a solar racing car ('96 Dream). As shown in Fig. 3, when vehicle speed increases, the aerodynamic resistive force increases as the cubic power of the velocity [3]. Thus, the development of the aerodynamic structure of the solar racing car is a critical part of reducing

Fig. 2 Energy requirements for a solar-powered vehicle
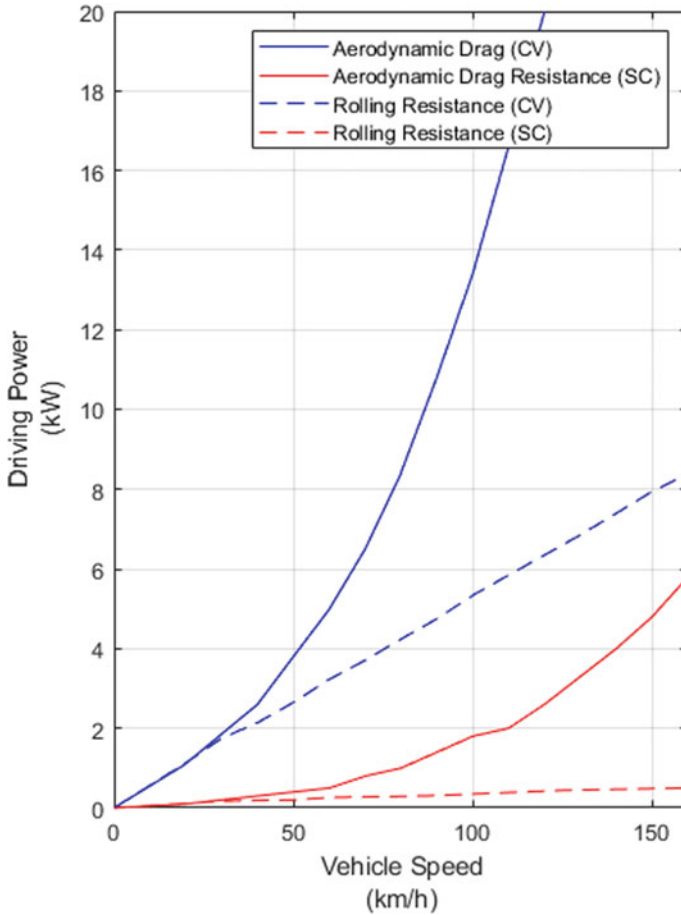
Fig. 3 Comparison of power consumption of the '96 Dream (Solar Car) and conventional vehicle [2]

the power consumption. In addition to power consumption, power generation systems (PV) should be designed in accordance with the aerodynamic structure.

1.2 Aerodynamic Structure of Solar-powered Vehicles

Aerodynamics is a branch of fluid dynamics which deals with the characteristics of airflow moving on solid bodies. The evolution of the automobile technology, from the 1900s to 2019, shows that the aerodynamic structure of ground vehicles is evolving to reduce the energy consumption that arises from the aerodynamic drag. Generally, the aerodynamic drag can be divided into (i) the pressure drag and (ii) the friction drag.

The pressure drag is considered to be induced by eddying motions along the passage of the body and to be related to the formation of a wake. The friction drag arises from the viscosity of air and is related to the Reynolds number and the development of the boundary layer. For streamlined bodies such as fishes, birds, and airfoils with a small or zero angle of attack, the friction drag is dominant. Besides, for the bluff bodies such as balls, bricks, and airfoils with a large angle of attack, the pressure drag is dominant [4].

The aerodynamic drag is linked with five facts as (i) *flow separation*, (ii) *skin friction*, (iii) *boundary layer pressure loss*, (iv) *induced drag*, and (v) *interference drag*. (i) *Flow Separation*: for un-aerodynamically shaped bodies, the flow can separate from sharp corners of the body. This situation creates vortices of turbulence. Flow separation creates a high drag force on the body. For this reason, bodies of solar cars have streamlined bodies in preventing flow separation. (ii) *Skin Friction*: this type of drag occurs between SC body and air, which causes drag force on the body. Skin friction drag proportional to the surface area of SC. Therefore, if the surface area of SC reduces, skin friction drag also reduces. (iii) *Boundary Layer Pressure Loss*: a boundary layer is formed when the air flows over the body. To be able to comprehend this effect, it can be thought that the air consist of very thin layers and many overlapping layers. There is a certain friction force between these layers that are stacked in a row. Due to the frictional force, the speed difference occurs between the layers and this causes turbulence in the flow. *Induced Drag*; all designs made according to the current line are in a structure which can create a lift force when the angle of attack is different from the flow direction. Increasing the lifting or downforce on the body will also increase the aerodynamic drag force. Therefore, the design of the vehicle should be made in such a way as to create a zero-lifting force. The angle of attack edge can be angled to form a zero-lifting force. *Interference Drag*; interference drag occurs on the body due to disturbances on the bolt connection, fairings, canopy, mirrors, or photovoltaic outputs [3, 5, 6].

As the car moves on the road, air flows over the surface of the car. This relative motion is changed by the distribution of pressure on the surface of the car. The external flow also applies a retarding tangential friction force over the car's surface. Total of the external and internal retarding forces is what we call drag force. Drag force is the resistance force caused by the motion of a body through a fluid like water or air. Drag force calculated as:

$$F_D = \frac{1}{2}\rho A V^2 C_D \tag{2}$$

The power required to overcome the aerodynamic drag is given by:

$$P_D = \frac{1}{2}\rho A V^3 C_D \tag{3}$$

When a car with a drag coefficient of 0.32 is traveling at a speed of 100 km/h, according to Eq. (3), 10.371 kW of power is spent to defeat the aerodynamic forces [3].

1.3 Photovoltaic Panels and Thermal Considerations

The silicon photovoltaic structure was discovered during photo-diode experiments in the 1950s [7]. This was a discovery of another property of combination of *p*- and *n*-type semiconductor layers. It was discovered that the structure not only changes its behavior from being an isolator to a conductor but also generates electrical energy when it is exposed to the light. After this invention, researchers considered generating realistic mathematical models of the photovoltaic cell, its behavior under different working and design conditions and the comparison of models. In one of these researches, Ibrahim compared five models and expressed how to find the appropriate model for silicon type different modules [8]. If the V-I graphs of a photovoltaic cell in Fig. 4 are considered, it can be seen that it is important to determine the short-circuit current, the open-circuit voltage, and the photocurrent values of a cell which might be calculated using the equations below.

$$I_{\text{SC}}(G, T) = \left(\frac{G}{G_{\text{STC}}}\right)^a \left[I_{\text{ST,STC}} + \mu_{I_{\text{sc}}}(T_C - T_{\text{STC}})\right]; \alpha = \frac{\ln \frac{I_{\text{SC,STC}}}{I_{\text{SC}}}}{\ln \frac{G_{\text{STC}}}{G}} \tag{4}$$

$$V_{\text{OC}}(G, T) = \frac{V_{\text{OC,STC}}}{1 + \beta \ln\left(\frac{G_{\text{STC}}}{G}\right)} \left(\frac{T_{\text{STC}}}{T_C}\right)^\gamma; \beta = \frac{\left(\frac{V_{\text{OC,STC}}}{V_{\text{OC,G}}}\right)^{-1}}{\ln\left(\frac{G_{\text{STC}}}{G}\right)}; \gamma = \frac{\left(\frac{V_{\text{OC,STC}}}{V_{\text{OC,G}}}\right)}{\ln\left(\frac{T_C}{T_{\text{STC}}}\right)} \tag{5}$$

$$I_{\text{ph,STC}} = \left(1 + \frac{R_s}{R_p}\right) I_{\text{sc,STC}} \left[\exp\left(\frac{V_{\text{oc,STC}}}{n N_s V_{\text{th}}}\right) - 1\right] + \frac{V_{\text{oc,STC}}}{R_p} \left[1 - \exp\left(\frac{I_{\text{sc,STC}} R_s}{n N_s V_{\text{th}}}\right)\right]$$
$$\Bigg/ \left[\exp\left(\frac{V_{\text{oc,STC}}}{n N_s V_{\text{th}}}\right) - \exp\left(\frac{I_{\text{sc,STC}} R_s}{n N_s V_{\text{th}}}\right)\right] \tag{6}$$

Typical silicon base PV cells convert incident light into electricity with an efficiency of 10–20%. The rest of the light is reflected or converted into heat which increases the temperature of the cell. Temperatures over 298.15 K (25 °C) reduce the energy conversion efficiency between 0.4 and 0.5%/K. Efficiency losses which are related to the high PV temperatures are approximately 7.6% of the total annual conversion losses. For a typical silicon-based photovoltaic cell, an electrical model can be developed with using a current source which is connected to a diode in parallel, as defined in the following expression [9, 10].

$$I = I_{\text{ph}} - I_s \left[\exp\left(\frac{q V}{k T_c A}\right) - 1\right] \tag{7}$$

This model corresponds to an ideal PV cell. Figure 5, on the other hand, illustrates the one-diode model in which a parallel resistor is connected to a diode and a serial resistor connected to the system. The relevant equation for this model is defined elsewhere [9, 10],

$$I = I_{\text{ph}} - I_0 \left[\exp\left(\frac{V + \text{IR}_s}{N_1 V_t} \right) - 1 \right] - \frac{(V + \text{IR}_s)}{R_p} \tag{8}$$

Even though there are alternative approaches which involve two-diode models, the one-diode model is one of the most commonly preferred one. The PV cell electrical characteristics are evaluated in laboratories under standard test conditions. The experiments are conducted at 25 °C with a solar irradiance of 1000 W/m^2 [1, 8, 9]. The open circuit voltage output of a silicon type PV cell varies between 0.5–0.6 (V) [11]. However, the voltage output of the cell significantly varies as a load is connected to the PV cell when it is compared with the open voltage. Figure 4 a shows
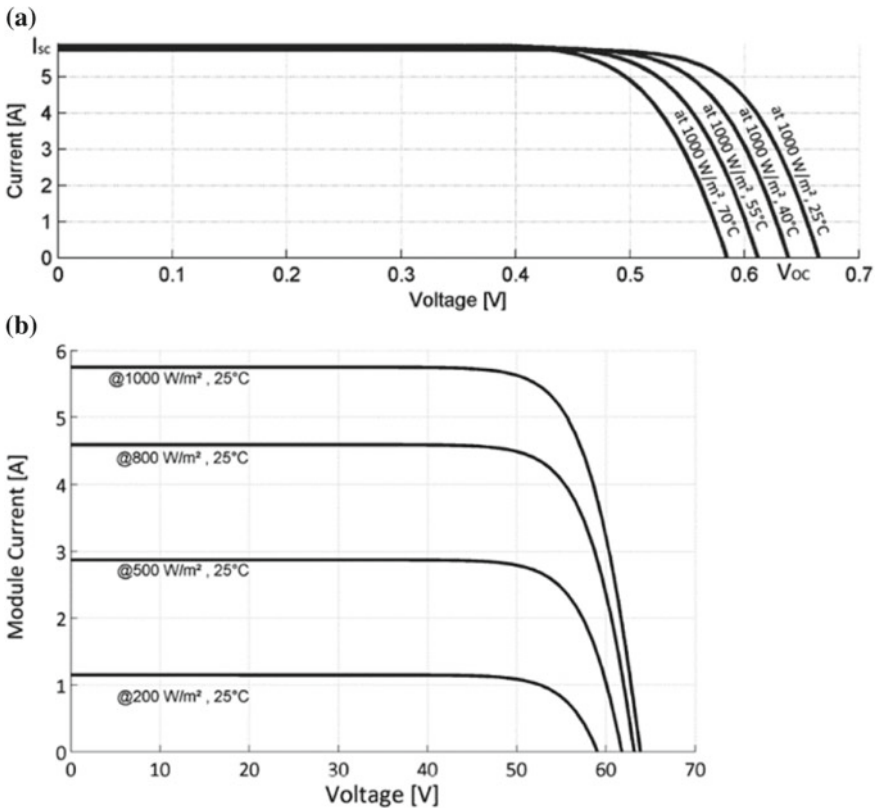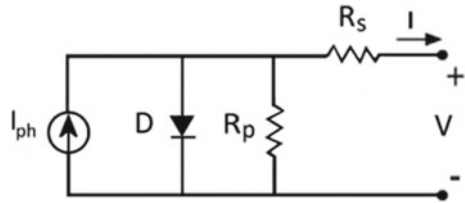

Fig. 4   Voltage–current relation of a PV cell under different cell temperatures and solar irradiances [1]

Fig. 5 One-diode PV cell model [1]

the influences of solar radiation and the PV cell temperature on the voltage output at various currents. Increasing the PV cell temperature reduces the voltage after a constant current region. The influence of the intensity of the incoming solar radiation on the current output of a PV cell is provided in Fig. 4 b.

Most of the panels in the market are devoted using either on buildings or on ground applications, that is, they are laminated to be more robust. They have a long-term stability and maintain the performance of at least 25 years. It is a widespread approach to use glass, ethylene-vinyl acetate (EVA) and Tedlar polyester Tedlar (TPT) for lamination materials and aluminum as the frame. On the other hand, the PV module that is integrated on a solar car must be more light, flexible and has higher efficiency to provide better performance in limited duration. That is, solar panels that are used in solar cars are laminated without using glass. Transparent plastic materials or glass-fiber-reinforced polymer composites are mostly used instead of the glass [12, 13]. PV cells are very fragile, so the lamination procedure and its structure are like the backbone of the PV module. Especially the upper layer of the lamination has the highest importance for a PV panel that is mounted on a solar racing car. The upper layer of the solar panel should possess some unique features such as being flexible, durable, transparent and having higher thermal conductivity. The enhanced flexibility of the solar panel allows mounting the PV panel on the solar racing car, which has a streamlined design. The improved durability prevents the panel against the impacts. The higher transparency and thermal conductivity, on the other hand, allows collecting higher solar irradiation and improves the PV efficiency and reduces the PV temperature during the travel of the solar car by increasing the heat transfer between cells and the surroundings. Semi-flex PV panels which are used on solar vehicles are flexible along one-direction. This advantage makes it possible to cover the surface of the solar vehicle, so it becomes possible to modify the aerodynamic design and achieve a reduced drag on the skin of the solar vehicle.

2 Material and Method

2.1 Definition of the Problem and Boundary Conditions

In the current study, a three-dimensional model is developed to simulate the fluid flow and heat transfer characteristics around a solar-powered racing car. The solar

vehicle containing 384 solar cells is subjected to solar irradiation (see Fig. 6). A part of the incoming solar irradiation is converted into electrical power. Convective and radiative heat transfer takes place between the PV surface and the ambient and the sky, respectively.

In Fig. 7, the dimensions of the solar car, i.e., Solaris 8, are provided. The car is 1.05 m in height, 1.8 m in width, and 4.5 m in length. The car is placed in an extended computational domain to simulate the external flow over the car. The dimensions of the computational domain and the position of the solar car inside the domain are illustrated in Fig. 7. No-slip boundary condition is defined on the surface of the solar car and the ground. Standard wall function is defined on the no-slip boundaries [14].
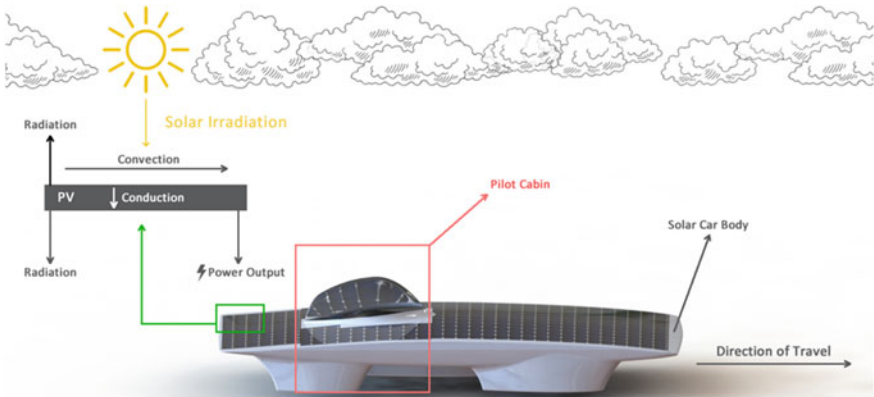
Fig. 6 Definition of the problem
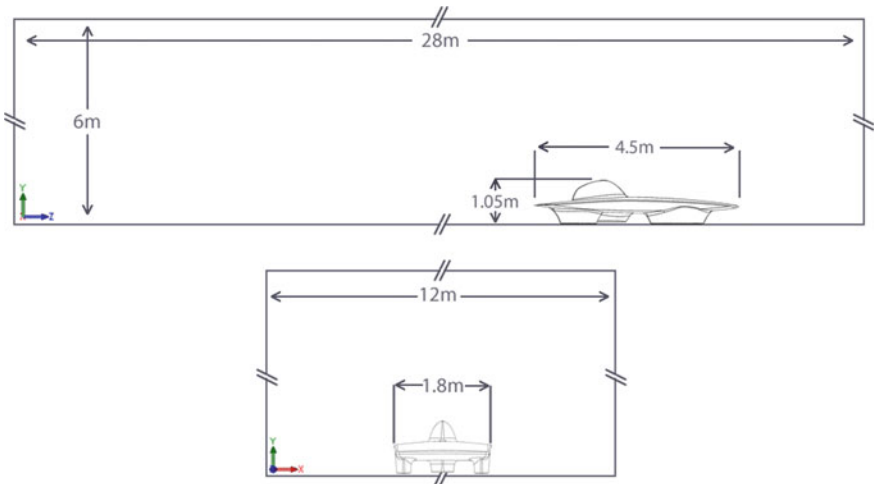
Fig. 7 Dimensions of the solar racing car and the computational domain

Table 1 Boundary conditions in parametric analyses

CASE	Velocity (km/h)	I_{solar} (W/m^2)
A1	70	300
A2	70	500
A3	70	700
A4	70	900
B1	30	700
B2	50	700
B3	70	700
B4	90	700
B5	120	700

At the inlet, the uniform velocity field is defined, and at the outlet section, the pressure outlet boundary condition is defined. A commercial computational fluid dynamics solver ANSYS-FLUENT is used to resolve the flow field and energy equations iteratively. The implementation of the thermal boundary conditions, i.e., solar irradiation, radiative and convective heat transfer, on the PV domain could be found elsewhere [15].

In the current work, the solar irradiation is varied from 300 to 900 W/m^2 to obtain the variation of the PV efficiency and the local temperature nonuniformities on the PV panel as a function of the irradiation. Analyses conducted for different velocities of the air that are defined as 30, 50, 70, 90 and 120 km/h. A total of nine parametric runs are conducted, and the boundary conditions of each case are defined in Table 1.

2.2 Solution Method

Governing equations are expressed in the following forms to resolve 3D and steady-state heat transfer problem over a solar racing car,

for mass:

$$\frac{\partial}{\partial x_i}(u_i) = 0 \tag{9}$$

for momentum:

$$\frac{\partial}{\partial x_i}(\rho u_i u_j) = -\frac{\partial p}{\partial x_i} + \frac{\partial}{\partial x_j}\left[\mu\left(\frac{\partial u_i}{\partial x_j} + \frac{\partial u_j}{\partial x_j} - \frac{2}{3}\delta_{ij}\frac{\partial u_l}{\partial x_l}\right)\right] + \frac{\partial}{\partial x_j}\left(-\rho\overline{u_i' u_j'}\right) \tag{10}$$

for energy:

$$\frac{\partial}{\partial t}(\rho u_i) + \frac{\partial}{\partial x_i}(u_i \rho c_p T) = \frac{\partial}{\partial x_i}\left(\lambda \frac{\partial T}{x_j}\right) + S \tag{11}$$

The Reynolds stresses in Eqs. (10) and (11) are evaluated by using the realizable k-epsilon (k-ε) turbulence model. It has more strong features which accurately predict boundary layers under strong adverse pressure gradients, separation, and recirculation from the other turbulence models. The first transported variable is turbulent kinetic energy (k), and the other transported variable is turbulent dissipation (ε). Transport equations for the realizable k–ε model are as follows

$$\frac{\partial}{\partial x_j}(\rho k u_j) = \frac{\partial}{\partial x_j}\left[\left(\mu + \frac{\mu_t}{\sigma_k}\right)\frac{\partial k}{\partial x_j}\right] + G_k + G_b - \rho \varepsilon \tag{12}$$

$$\frac{\partial}{\partial x_j}(\rho \varepsilon u_j) = \frac{\partial}{\partial x_j}\left[\left(\mu + \frac{\mu_t}{\sigma_\varepsilon}\right)\frac{\partial \varepsilon}{\partial x_j}\right] + \rho C_1 S_\varepsilon - \rho C_2 \frac{\varepsilon^2}{k + \sqrt{\nu\varepsilon}} + C_{1\varepsilon}\frac{\varepsilon}{k}C_{3\varepsilon}G_b \tag{13}$$

For the PV domain, on the other hand, the energy equation is defined as

$$0 = \frac{\partial}{\partial x_i}\left(\lambda \frac{\partial T}{\partial x_j}\right) + S''' \tag{14}$$

where S''' is the volumetric source term and includes the volumetric heat generation (q''') and volumetric power generation (P'''_{out}) within the PV volume,

$$S''' = P'''_{out} + q''' \tag{15}$$

The volumetric heat generation, q''', and the volumetric power generation, P'''_{out}, terms are defined regarding the incoming solar radiation, I_{solar}, and the optical properties of the PV panel as

$$P'''_{out} t_{PV} = -I_{solar}\eta_{PV}\alpha_{PV} \tag{16}$$

$$q''' t_{PV} = I_{solar}(1 - \eta_{PV})\alpha_{PV}\tau_{PV} \tag{17}$$

where α_{PV} and τ_{PV} are the absorptivity and the transmissivity of the PV panel, respectively. The panel efficiency is determined from the well-known Eq. (11) as

$$\eta_{PV} = \eta_{max}(1 - \beta_{ref}(T_{PV} - T_{ref})) \tag{18}$$

where $\eta_{\max}$ is the maximum panel efficiency at the reference temperature, T_{ref}. β_{ref} is the temperature coefficient and T_{PV} is the panel temperature. Parameters of equations are taken from the producer firm and Hendricks et al. [16] (see Table 2).

The mathematical model is developed in ANSYS-FLUENT software and resolved iteratively with using the SIMPLE algorithm. Second-order upwind scheme is implemented to predict the convective terms. Before going through the parametric analyses, a preliminary survey is conducted to ensure that the mesh-independent results are achieved. A nonuniform mesh distribution is generated by increasing the intensity of the mesh near the no-slip surfaces to capture the high gradients. The number of mesh not only affects the accuracy of the predicted results but also strongly determines the required time to achieve the converged solution. In Fig. 8, the influences of the total number mesh on both the drag coefficient and the solution time are given. It is clear that increasing the total number of mesh from 282,832 to 2.6 million significantly affects the drag coefficient. Beyond 2.6 million meshes, however, increasing the number of mesh does not cause any significant change in the predicted results. More intensive mesh structures are also tested but considering the computational cost

Table 2 Standard parameters used in analysis

Parameter	Symbol	Value	Parameter	Symbol	Value
Panel area (m^2)	A	6	Absorptivity constant	α	0.95
Efficiency	η	0.224	Emissivity sky	ε_s	0.95
Emissivity module	ε_{PV}	0.90	Specific heat PV panel	C_{PV}	500
Laminated cell thickness (mm)	t_{PV}	1.1			
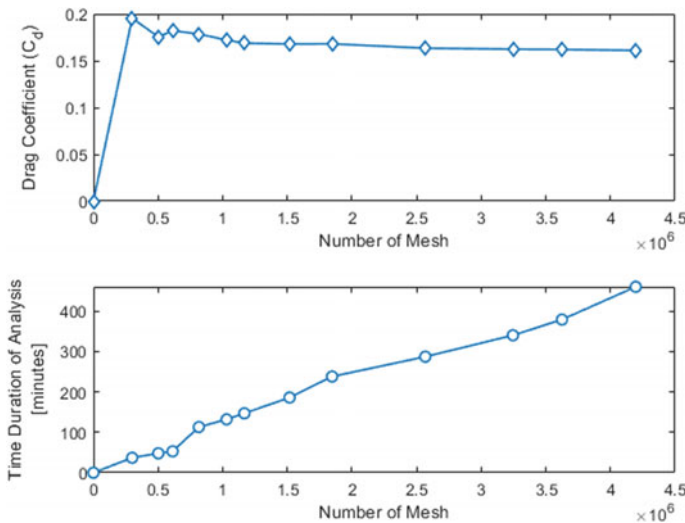
Fig. 8 Influences of the number of mesh on the drag coefficient and required time for a solution

Table 3 Drag coefficient values depending on variable velocity values

	SV (km/h)	C_D	Force (N)	Power (kWh)
Solaris 8 solar car	30	0.191	7.55	0.063
	50	0.183	20.11	0.279
	70	0.178	38.33	0.745
	90	0.175	62.31	1.558
	120	0.145	91.77	3.059

and longer solution durations, see Fig. 8b, the optimum mesh number is determined to be 2.653,423 [17].

3   Results and Discussion

In this section, the results of the numerical analyses are represented by considering the aerodynamic and the thermal outputs. A total of nine steady-state analyses are conducted by varying the velocity of the solar racing car and the incident solar radiation acting on the PV panels.

3.1   Power Consumption of the Solar Racing Car

Table 3 reveals the variation of the drag coefficient of the solar car at five different velocities ranging from 30 to 120 km/h. The C_D reduces from 0.191 to 0.145 as the velocity of the solar racing car increases from 30 to 120 km/h. Here, the aerodynamic forces acting on the car and the power consumptions that are related to the aerody-namic structure of the car are also given. Notice that, increasing the velocity of the car by four times increases the force by 12 times. Besides, the power consumption of the car increases more than 40 times as the velocity of the car increases from 30 km/h to 120 km/h.

3.2   Power Generation of the Solar Racing Car

It is a well-known fact that the electrical output of a PV panel depends not only the intensity of the incident solar radiation but also is affected by the panel temperature. Current work aims to observe the variation of the temperature field on the solar car to predict the distribution of the PV efficiencies. The solar racing car includes four separated PV panels are placed on the top surface as (a) back, (b) side-1, (c) side-2, and (d) front. The positions of the PV panels are illustrated in Fig. 9. In the current work,

Fig. 9 PV group settlements on the solar racing car
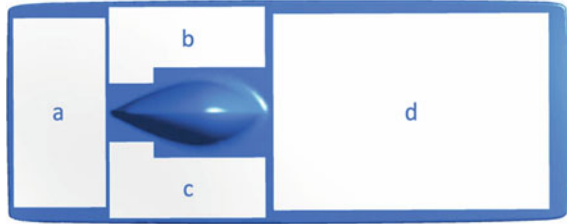
to represent an in-depth understanding of the electrical power generation efficiencies of each PV panel, the local variations are also evaluated along the centerlines.

The influence of incoming solar radiation on the average PV panel temperatures, efficiencies, and the power outputs are given in Table 4. Cases $A1$, $A2$, $A3$, and $A4$ are corresponding to 300, 500, 700 and 900 W/m^2 of solar radiation, respectively. For the current set of analyses, the velocity of the solar racing car is 70 km/h. Referring to Fig. 3, a, b, c, and d indicate the rear, side-1, side-2, and front panels of the solar racing car. Regardless the intensity of the incoming solar radiation, the lowest and highest temperatures are obtained at the front and rear panels, respectively. The temperature difference between the front and rear panel, on the other hand, increases as the solar radiation increases. As an instance, while the temperature difference is 1.76 °C for 300 W/m^2 of solar radiation, the temperature difference becomes almost 6 °C at 900 W/m^2 of solar radiation. The average PV temperature exceeds 60 °C at 900 W/m^2 of solar radiation. At high-incoming solar radiations, the efficiency of the PV panel drops below 20%. Even though the temperature of the rear PV panel is 6 °C higher than the front one, considering the electrical efficiency of the PV panel, the difference is nearly 2%. The side panels, i.e., side-1 and side-2, give almost the same outputs for each case, due to the bilateral symmetry of the domain. Regarding the power outputs of the panels, the highest energy output is obtained for the front panel as the surface area of the front panel is the biggest. One should also notice that increasing the solar intensity by three times, from 300 to 900 W/m^2, the electrical outputs of the panels increase an average of 2.78 times.

Figures 10 and 11 show the temperature contours on the PV surfaces at four different solar radiation values. Increasing solar radiation increases the PV panel temperatures. One should notice that the boundary layer development on the PV panel reduces the convective heat transfer coefficient, and the panel temperature increases along the flow direction from the leading edge to the canopy. It is also interesting to note that the disturbance in the flow field due to the canopy causes an enhanced heat transfer along the centerline of the rear PV and the lower temperatures are observed at the downstream of the canopy.

In Table 5 and Fig. 12, the influence of the velocity of the solar racing car on the average panel temperatures, panel efficiencies, and the power outputs is given. Analyses are conducted for five different velocities with the incoming solar radiation of 700 W/m^2. Cases $B1$, $B2$, $B3$, $B4$, and $B5$ are corresponding to 30, 50, 70, 90, and 120 km/h, respectively. The highest and lowest panel surface temperatures

Table 4 Influence of incoming solar radiation on the power generation

CASE	Average panel temperature (°C)				Panel efficiency (%)				Power output (Wh)			
	a	b	c	d	a	b	c	d	a	b	c	d
A1	38.3	37.5	37.5	36.6	21.5	21.5	21.5	21.6	64.9	38.9	38.9	211.9
A2	46.2	44.8	44.8	43.2	20.9	20.9	20.9	21.1	105.3	63.3	63.2	64.2
A3	54.5	52.4	52.4	50.0	20.3	20.4	20.4	20.6	143.3	86.2	86.2	472.4
A4	63.1	60.4	60.3	57.1	19.7	19.9	19.9	20.1	178.6	107.7	107.7	592.1
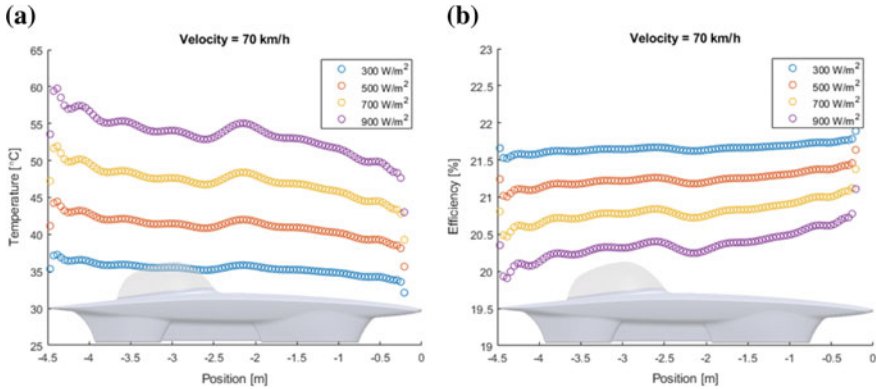
Fig. 10 Temperature and efficiency distribution on PV module groups (Cases A)
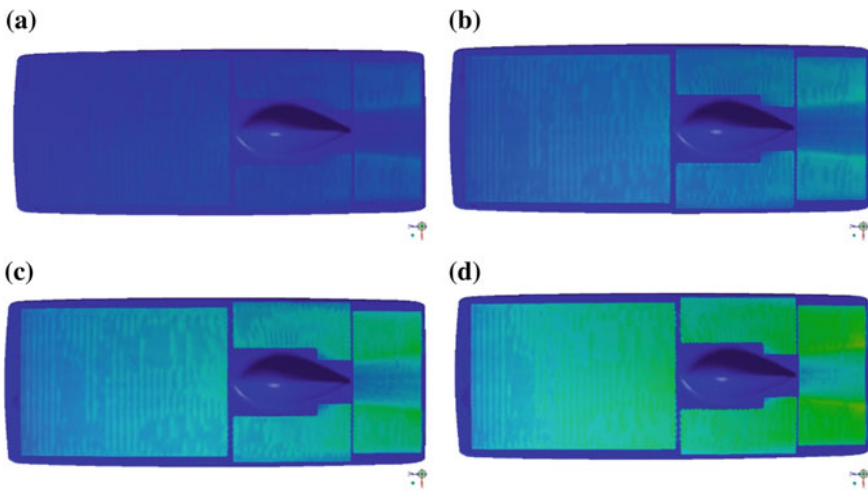
Fig. 11 Temperature distributions on PV module groups (Cases A) (a) 300 W/m^2, (b) 500 W/m^2, (c) 700 W/m^2, (d) 900 W/m^2

are obtained at the front and rear panels, respectively. The temperature difference between the front and rear panels increases as the velocity of the car decreases. For instance, the temperature difference is more than 10 °C at 30 km/h, and the difference drops less than 3 °C at 120 km/h. The panel efficiencies increase as the velocity of the car increases due to the enhanced heat transfer between the panel surface and the ambient. However, even though the variation in velocity has a sharp change in the efficiency at low velocities, the influence of the velocity on the panel efficiency becomes slight at high-velocity values.

In Fig. 13, temperature fields are given on the top surface of the solar racing car. The velocity field strongly determines the temperature distributions on the panels.

Table 5 Influence of incoming solar radiation on the power generation

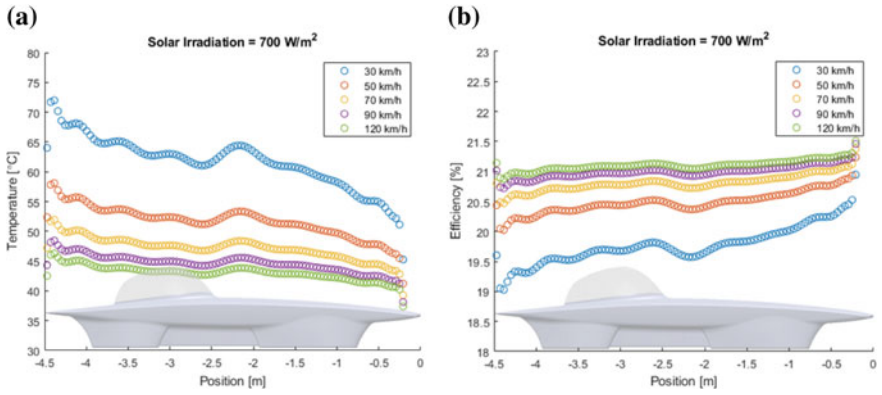| CASE	Average panel temperature (°C)				Panel efficiency (%)				Power output (Wh)			
	a	b	c	d	a	b	c	d	a	b	c	d
B1	73.4	68.9	68.9	63	18.9	19.3	19.3	19.7	133.7	81.1	81.1	450.7
B2	60.3	57.5	57.5	54.1	19.9	20.1	20.1	20.3	140.3	84.6	84.6	465.6
B3	54.5	52.4	52.4	50.0	20.3	20.4	20.4	20.6	143.3	86.1	86.1	472.4
B4	51.2	49.6	49.9	47.7	20.5	20.6	20.6	20.8	144.9	87.0	87.0	476.3
B5	49.1	47.7	47.7	46.2	20.7	20.8	20.8	20.9	146.0	87.6	87.6	478.6

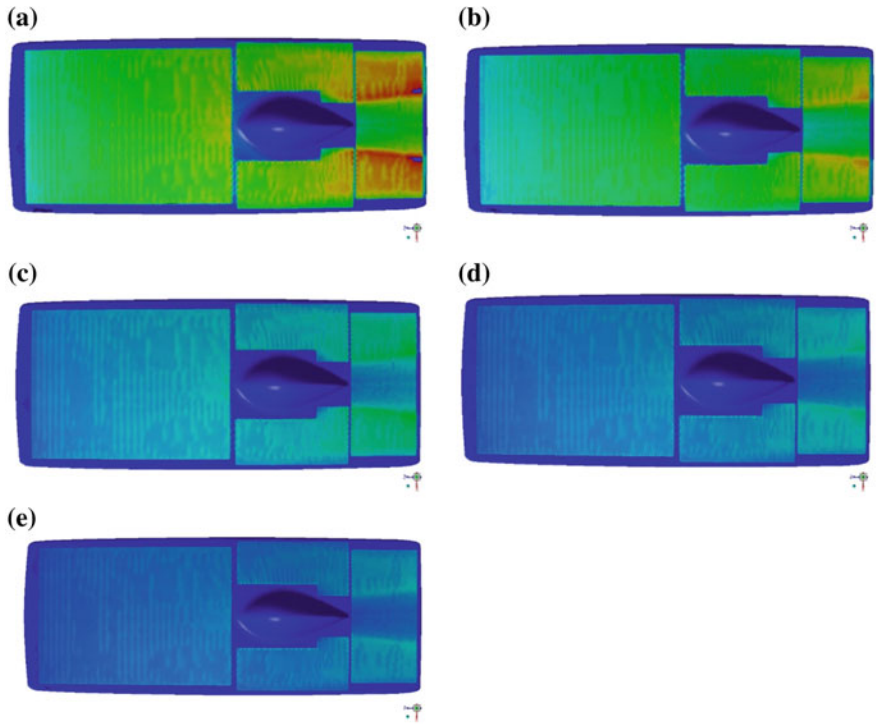**Fig. 12** Temperature and efficiency distribution of PV module groups (Cases B)

Fig. 13 Temperature distributions on PV module groups (Cases B) (a) 30 km/h, (b) 50 km/h, (c) 70 km/h, (d) 90 km/h, (e) 120 km/h

At lower velocities, the nonuniformity in the temperature field is more obvious. Increasing the velocity of the solar racing car, on the other hand, enhances the heat transfer coefficient and helps to keep the panel temperatures within a narrow range.

4   Conclusions

In this work, a mathematical model is developed to predict the power generation of a solar racing car under various working conditions. The model includes both the aerodynamics and thermal aspects and helps to provide an in-depth understanding of the power generation of PV panels.

References

1. Gören A (2017) Solar energy harvesting in electro mobility. In: Lecture notes in energy. https://doi.org/10.1007/978-3-319-49875-1_11
2. Ozawa H, Nishikawa S, Higashida D (1998) Development of aerodynamics for a solar race car. JSAE Rev 19:343–349
3. Jones B (1942) Elements of practical aerodynamics, 3rd edn. Wiley
4. Wang Y, Wu C, Tan G, Deng Y (2017) Reduction in the aerodynamic drag around a generic vehicle by using a non-smooth surface. J. Autom Eng, https://doi.org/10.1177/0954407016636970
5. Douglas RC (2003) The winning solar car: a design guide for solar race car teams. SAE Int ISBN-13: 978-0768011319
6. Thacher EF (2003) A solar car primer. Springer International Publishing AG Switzerland, https://doi.org/10.1007/978-3-319-17494-5
7. Riordan M, Hoddeson L (1998) Crystal fire: the invention of the transistor and the birth of the information age. ISBN 9780393318517
8. Ibrahim H, Anani N (2017) Variations of PV module parameters with irradiance and temperature. In: 9th international conference on sustainability in energy and buildings, https://doi.org/10.1016/j.egypro.2017.09.617
9. Singh J, Agrahari A (2018) The progression of silicon technology acting as substratum for the betterment of future photovoltaics. Int J Energy Res. https://doi.org/10.1002/er.4402
10. Tamrakar V, Gupta SC, Sawle Y (2015) Single-diode PV cell modeling and study of characteristics of single and two-diode equivalent circuit. ELELIJ 4(3) https://doi.org/10.14810/elelij.2015.4302
11. Qazi S (2017) Mobile photovoltaics systems for disaster relief and remote areas. In: Standalone Photovoltaic (PV) systems for disaster relief and remote areas, https://doi.org/10.1016/b978-0-12-803022-6.00003-4
12. Gorter T, Reinders AJME (2012) A comparison of 15 polymers for application in photovoltaic modules in PV-powered boats. Appl Energy 92:286–297. ISSN 0306-2619
13. Krug DJ, Asuncion MZ, Popova V, Laine Rm (2013) Transparent fiber glass reinforced composites. Compos Sci Technol 77:95–100

14. Taherkhani AR, Gilkeson CA, Gaskell PH, Hewson RW, Toropov VV, Rezaienia A, Thompson HM Aerodynamic CFD based optimization of police car using bezier curves. Int J Mater Manuf https://doi.org/10.4271/2017-01-9450
15. Kalkan C, Ezan MA, Duquette J, Yilmaz Balaman Ş, Yilanci A Numerical study on photovoltaic/thermal systems with extended surfaces. Int J Energy Res https://doi.org/10.1002/er.4477
16. Hendricks JHC, van Sark WGJHM (2011) Annual performance enhancement of building integrated photovoltaic modules by applying phase change materials. Progress Photovoltaics Res Appl https://doi.org/10.1002/pip.1240
17. Korkut TB, Gören A, Ezan MA, Photovoltaic panel efficiency for solar powered vehicle, 7th Global Conference on Global Warming (GCGW-2018), https://doi.org/10.13140/RG.2.2.23812.37767

Thermodynamic and Environmental Assessments of Coal Gasification-Based Multigeneration Plant

Murat Koc, Nejat Tukenmez and Murat Ozturk

Abstract Nowadays, the design of multigeneration integrated energy systems to produce hydrogen, power, hot water, cold water, and fresh water plays important role for developed and under developing countries. In this book chapter, the multi-generation energy plant is designed and integrated with the coal gasification, water gas shift reactor, Fisher-Tropsch reactor, single effect absorption chiller, gas turbine cycle, hydrogen production and compression cycle, Kalina cycle, hot water production cycle, drying cycle for power, heating–cooling, hot water, and compressed hydrogen cycle. These subsystems are integrated into each other in order to obtain useful outputs from the integrated energy system. The Engineering Equation Solver software program has been utilized for thermodynamic and environmental analyses of multigeneration integrated energy system. At the same time, the environmental impact analysis is carried out for single production, cogeneration, trigeneration, and multigeneration types. The whole integrated energy system's energetic and exergetic efficiencies are calculated as 59.16 and 56.43%. In addition, the performance analysis of each subsystem is carried out and discussed.

Keywords Multigeneration · Compressed hydrogen · Integrated energy system · Environmental impact analysis

M. Koc (✉)
Vocational School of Technical Science, Isparta University of Applied Science, Cunur West Campus, Isparta 32200, Turkey
e-mail: muratkoc@isparta.edu.tr

N. Tukenmez · M. Ozturk
Faculty of Technology, Department of Mechatronics Engineering, Isparta University of Applied Science, Cunur West Campus, Isparta 32200, Turkey
e-mail: nejattukenmez@isparta.edu.tr

M. Ozturk
e-mail: muratozturk@isparta.edu.tr

1 Introduction

Multigeneration systems play an important role in demanding the energy needs of developed and under developing countries. The increase in the human population and necessities has led to the development of industrialization. Therefore, the energy demand for sustainability development is increasing day by day. But, most of the energy needs are obtained from carbon-based fuels. As it is known, the effects of these energy generation systems on the environment should be considered due to the harmful emission gases emitted by the fossil fuel systems. Therefore, the multigeneration systems play a key role in using fossil fuels more efficiently.

It is a heterogeneous, flammable fossil stone composed of organic and inorganic materials. Its organic structure consists mainly of carbon, hydrogen, and oxygen and a small amount of sulfur and nitrogen. Thousands of years under the appropriate conditions of plants under the fossilization of soil is formed by the content of coal according to the content of plant also shows change. Coal is the most common fossil source in the world.

Rosen and Dincer [1] have demonstrated the relationship between the environmental problems and exergy. In their paper, the energy and environmental relations are mentioned, and energy efficiency decreases the environmental impacts by decreasing energy loss. It was also stated that increasing exergy efficiency in practical applications by using exergy methods is the great importance for environment. In the study, the waste exergy emissions, resource utilization, and environmental relations are revealed.

Wall and Gong [2] have discussed the relationship between sustainable development and exergy analysis. In the first part of this study consisting of two parts, terms and concepts, and in the second part, indicators and methods are discussed. Exergy analysis was found to be a useful way in determining the conversion of cycle from emissions and pollution. The concept of sustainability is explained in relation to the exergy flow across the world.

Rosen and Dincer [3] have examined the power systems in terms of energy, exergy, and cost analyses, and applied the analysis results on a modern coal-fired electric power system. The study is handled in terms of general power plant as well as turbine, generator, steam boilers, heaters, and condensers. One of the most important points here is the relation of thermodynamic losses with cost. The results show that the systematic relationship between the energy losses and unit costs cannot be established, and can be established with exergy loss. The obtained results are useful in terms of the acquiring knowledge about thermodynamic losses and unit costs in the design of systems.

Bisio [4] has discusses what can be done to increase the efficiency of systems that produce low levels of energy. Author emphasized how to increase the efficiency of low enthalpy systems such as geothermal and solar energy. He stated that the absorption of heat or heat exchangers and their combinations in these systems are some of the points that can be improved in low-level energy systems.

Koroneos et al. [5] have stated that despite the existing technology, renewable energy sources are lower than fossil fuel use, but they have shown that oil crises direct people to new energy sources. They considered the solar, wind, and geothermal power as the most important sources of renewable energy, and investigated the system performance based on the exergy analysis.

Rosen and Dincer [6] have examined the results obtained by different selection of dead-state characteristics in the energy and exergy assessments of coal-fired power cycle. The system has been examined both in general and for turbine, boiler, condenser, and heaters separately. The study was placed on two different surfaces. The first one is the energy and exergy values obtained by selecting different dead-state properties, the second is the effects of different dead states on the energy and exergy results of whole system.

Energy, which has an important place in human life, has a significant role in the development of countries and competition between other countries. Energy needs are increasing day by day due to the increase in world population and the development of technology. After the Iindustrial Revolution, energy has been used in every field of life together with the developing industry. Lack of energy in the world, falling standards of living for developed countries means poverty for developing countries [7].

When the world coal reserves are analyzed, it is stated that coal has a life span of approximately 114 years depending on consumption estimates. The countries with the highest reserves worldwide are America, Russia, and China. Considering that the harmful effects of fossil fuels and their duration of extinction are limited, it is very important to use these resources efficiently [8]. The use of fossil resources in world energy production is quite common. More than half of the world's energy production is produced from fossil sources [9]. One of these fossil sources is coal [10].

In addition to generating electricity by burning coal in thermal power plants, it is possible to produce hydrogen energy which is considered as the energy of the twenty-first century by applying different operations. Hydrogen energy is not pure in nature. Because hydrogen is lighter than air, it is present in the earth as components. Therefore, hydrogen is not an energy source but an energy carrier [11].

Mohhimi et al. [12] have examined a novel model of an integrated cooling, heating, and power (CCHP) cycle including 4E (Energy, Exergy, Economic, and Environmental) using a cooling cycle, Rankine cycle, Brayton cycle, and tap water heater in this study. They have performed the performance evaluation of system with energetic and exergetic analyzes. In addition, they have conducted an environmental impact analysis to compare the new multigeneration cycle with simple Brayton cycle.

Ahmadi et al. [13] have realized the efficiency analysis and optimization of multinational combined energy system for heating, cooling, electricity, and hot water production from a common energy source. This multi-energy system consists of four parts: Rankine cycle, ejector refrigeration cycle, gas turbine cycle, and domestic water heater. They have performed an optimization study for system to determine the optimum values of selected design parameters affecting the plant efficiency.

Ghorbani et al. [14] have designed and analyzed an integrated system for cogeneration cycle for residential buildings in one of the Persian Gulf towns in southern Iran.

In order to provide the necessary thermal energy, the collectors on the house roof, Kalina system for integrated power production and seawater desalination systems for fresh water production are used for domestic applications. The system is simulated via TRNSYS, HYSYS, and MATLAB programs.

Dincer et al. [15] have explained the basic principles of energy, entropy, and exergy. They have studied many modeling techniques and optimization methods which are important in energy system optimization. At the same time, they have worked for mathematical modeling of an optimization problem. They have shown that optimization is an important method in engineering to determine the best and optimal value for a decision variable of systems. They have benefited from the different optimization methods for desired equations which are expressed as the objective function. While implementing these optimization methods, they have taken care to keep the parameters that are beneficial for all productivity studies and product quality, and similar system to be considered as a loss to the system and also to minimize the environmental effects, such as global warming. They have benefited from various engineering software programs for mathematical modeling and optimization algorithms. This study provides important information about mathematical modeling and optimization methods for studies in the field of energy systems design and optimization.

Akrami et al. [16] have developed a geothermal-assisted multigeneration plant that includes organic Rankine cycle, domestic water heating, absorption refrigeration system, and PEM electrolyzer to produce electricity, heating, cooling, and hydrogen. In addition, the effects of some important variables on the plant have investigated. The energy and exergy efficiencies of multi-production plant have computed for changing conditions.

Yilmaz et al. [17] have examined a coal gasifier-supported multigeneration plant for hydrogen generation and liquefaction. Their paper results show that the energy and exergy performance of combined system are 58.47% and 55.72%.

The main purpose of this book chapter is to examine the thermodynamic performance and environmental impact evaluation for a new integrated energy system with coal gasification. On this topic, the energetic and exergetic performances and environmental impact evaluations are investigated in detailed for the proposed study. Also, to conduct a parametric work, to define the impacts of different factors on the whole energy and exergy efficiency of combined plant and its subsystems. The private purposes of this suggested book chapter are listed as follows;

- To design a novel coal gasification-supported combined plant for purpose of the multiple production.
- To analyze in detail thermodynamic and environmental impact assessments of proposed plant.
- To investigate energy and exergy loses of the proposed combined plant and its sub-plants.

2 Integrated Plant Design

A schematic presentation of multigeneration integrated energy system, which is carried out for thermodynamic, performance and environmental impact analyses is given in Fig. 1. Also, the design indicators for coal gasification-supported multigeneration system are written in Table 1. The most important component of coal gasification-based system is the coal gasification reactor. The coal, to be fed to the preferred type of gasifier, is sent to the coal gasifier with flow number 1. The air required for gasification takes 2 air flows into the air fan. Then, it sent to the gasifier by flowing through number 3 stream by means of air fan. The produced synthesis gas emerges from the gasifier by stream 4, and enters the cyclone in order to remove the ash. H_2S and CO_2 are then removed from the synthesis gas which is sent to the acid removal unit with flow number 6, and the synthesis gas is sent to HEX 1 by flow 8. After passing the synthesis gas from HEX1, a portion of synthesis gas is sent to the high-temperature- and low-temperature water gas shift (WGS) reactors for hydrogen enrichment in order to generate hydrogen in the system with flow 12. The operating temperature of high-temperature WGS reactor ranges from 350 to 600 °C, and also the temperature of low-temperature WGS reactor ranges from 150 to 300 °C [18]. In addition, the WGS reactors generally operate with an average pressure of 20 bar. The

Fig. 1 Coal gasification-based integrated plant for multigeneration

Table 1 Main input indicators for combined plant

Parameters	Values
Dead-state temperature, T_o (°C)	25
Dead-state pressure, P_o (kPa)	101.3
Air compressor pressure ratio, r_{AC}	8
Isentropic efficiency of air compressor, η_{AC} (%)	83
Coal mass flow rate, $\dot{m}_1$ (kg/s)	2.48
Coal moisture content, (wt%)	4.98
Coal ash content for dry basis, (wt%)	15.92
Lover heating value of coal for dry basis, LHV_{coal} (kJ/kg)	27,128
High heating value of coal for dry basis, HHV_{coal} (kJ/kg)	28,342
Temperature of coal gasifier, T_{CG} (°C)	725
Temperature of combustor, T_{CC} (°C)	850
Gas turbine inlet pressure, P_{23} (kPa)	16,587
Gas turbine inlet temperature, T_{23} (°C)	847
Kaline turbine inlet pressure, P_{46} (kPa)	7746
Kaline turbine inlet temperature, T_{46} (°C)	372
Isentropic efficiencies of gas turbine, $\eta_{is,GT}$ (%)	80
Isentropic efficiencies of pumps, $\eta_{is,P}$ (%)	80
Isentropic efficiencies of Kaline turbine, $\eta_{is,KT}$ (%)	75
PEM temperature, T_{PEM} (°C)	80
PEM electrolyzer thickness, D_{PEM} (µm)	100
COP_{en} of SEAC	0.7654
COP_{ex} of SEAC	0.2453

synthesis gas sent to the compressor by flow 13, and the compressed gas is sent to the WGS reactor by flow 14. It is a process of obtaining gas and liquid hydrocarbon mixtures from synthetic gases containing hydrogen and carbon monoxide gases.

The most important advantage of this technology is that it has a wide product potential. This synthesis, where it is possible to produce products from fuel to other valuable chemicals, does not contains sulfur, nitrogen, or heavy metal contaminants and contains a low number of aromatic hydrocarbons. The synthesis gas, which is rich in hydrogen and carbon monoxide, is sent to the Fischer-Tropsch Reactor (FTR) with flow 15. Synthetic fuel is extracted from the reactor with flow 16. To ensure the cooling requirement, the exhaust gas enters the generator of single-acting absorption cooling cycle with flow 17. The weak fluid solution at number 33 is pumped through the pump 2 to reach the generator of the absorption refrigeration cycle through the passage 34 through the solution-HEX. In stream 37, water is removed from the fluid solution, and the strong fluid solution is sent to solution-HEX. It then passes through expansion valve 2 with flow 38 and returns to the absorber of cooling system with

stream 39. On the other hand, the water vapor exits the generator 1 with flow number 36, and enters the condenser. When the fluid passes through the condenser, heat energy is transferred to the cooling water. The working fluid flows into the expansion valve with flow 30, and the pressure drops at desired levels. Then, the fluid vapor enters the evaporator with stream 31. The saturated steam from evaporator turns into the absorber with flow 32, and also completes the cycle. The water leaving generator 1 then enters the pump with stream 18 before being recycled in the FT reactor and then enters the FT reactor with flow no 19. The synthesis gas is sent to the combustion chamber with flow 10.

At the same time, the air flowing from air compressor is sent to the combustion component with flow 21. To ensure the electricity generation from integrated cycle, the exhaust gas leaving from combustion component enters the gas turbine with flow 22. Because of the high enthalpy of exhaust gaseous from gas turbine with flow 16, it can be used to drive its subsystems. After that, the exhaust gaseous from gas turbine is sent to superheater with flow 23 for Kalina cycle. Then, the exhaust gas enters the evaporator with stream 24. The saturated steam from evaporator, to save energy and reduce emissions is sent to the economizer with flow 25. The exhaust gas from economizer enters the PEM water heater with flow 26. The exhaust gas entering the HEX4 with flow 27 is sent to the hot water storage tank (HWST) with flow 28 to heat the cold water in the HWST. Exhaust gas is released into the environment with flow 29.

The water flowing into the HWST with flow 77 is out of the storage tank as hot water with flow 78. The cold air coming into the system with flow 71 is heated in HEX4, and then the hot air is sent to the dryer with flow 72. In this way, the wet products coming into the dryer with flow 75 come out of the dryer as a dry product by flow 76. With flow 54, the fluid from the economizer enters the evaporator 1 again. The saturated fluid is then sent to the separator with flow 55. The fluid, which is cleaned in the separator, is sent to superheater with flow 56. The clean fluid heated in the superheater is sent to the turbine with flow 46 for electricity generation. The fluid exiting the turbine is sent to the 3-way valve with flow 47. The non-purified fluid in the separator is sent to HEX3 by flow 57. The fluid from HEX3 enters the evaporator 3 with flow 58, and is sent to the 3-way valve with flow 59. The fluid exiting from the 3-way valve enters the HEX4 with flow 48, then sent to condenser 1 for condensation with flow 49, and the condensing fluid sent to pump 3 to be sent back to HEX4 with flow 50. The fluid is then pumped through flow 51 into HEX4. The fluid is sent to HEX3 via flow 52 after leaving HEX4. The fluid coming out of HEX3 is again sent to the economizer with flow 53. The fluid exiting the economizer is sent to evaporator 1 by flow 54. The saturated fluid from the evaporator 1 is sent back to the separator with flow 55. Thus, the Kalina cycle for electricity generation is completed. PEM electrolyzer unit is used to generate hydrogen in the multigeneration energy production cycle. The pure water required for PEM electrolyser is sent to PEM water heater with flow 62. The pure water required for electrolyser is heated up to the electrolysis operating temperature in the PEM water heater, and then enters the electrolyser with flow 63. Oxygen and hydrogen are produced in the PEM electrolyzer. The produced hydrogen is passed

through a 3-stage compression cooling process to the hydrogen storage tank. The stored hydrogen and oxygen are used in subsequent applications.

3 Thermodynamic Assessment of Integrated System

In this subsection, the comprehensive energetic and exergetic modeling examinations are given. The mass, energetic, entropy, and exergetic balance equations are very essential in the first step of energy and exergy analyses for defining the input/output of heat and electricity, entropy generation, and exergy destruction rate, and also energy and exergy efficiencies of analyzed integrated system [19]. The mass, energy, entropy, and exergy balance equalities can be written as

$$\sum \dot{m}_{\text{in}} = \sum \dot{m}_{\text{et}} \tag{1}$$

$$\sum \dot{m}_{\text{in}} h_{\text{in}} + \sum \dot{Q}_{\text{in}} + \sum \dot{W}_{\text{in}} = \sum \dot{m}_{\text{et}} h_{\text{et}} + \sum \dot{Q}_{\text{et}} + \sum \dot{W}_{\text{et}} \tag{2}$$

$$\sum \dot{m}_{\text{in}} s_{\text{in}} + \sum \left(\frac{\dot{Q}}{T} \right)_{\text{in}} + \dot{S}_{\text{gen}} = \sum \dot{m}_{\text{et}} s_{\text{et}} + \sum \left(\frac{\dot{Q}}{T} \right)_{\text{et}} \tag{3}$$

$$\sum \dot{m}_{\text{in}} \text{ex}_{\text{in}} + \sum \dot{E}x_{\text{in}}^Q + \sum \dot{E}x_{\text{in}}^W = \sum \dot{m}_{\text{et}} \text{ex}_{\text{et}} + \sum \dot{E}x_{\text{et}}^Q + \sum \dot{E}x_{\text{et}}^W + \dot{E}x_D \tag{4}$$

In Eq. (1), $\dot{m}$, subscripts in and et show the mass flow rate, inlet, and exit status. In Eq. (2), $\dot{Q}$, $\dot{W}$ and h represent the heat and work transfer rate, and specific enthalpy. In Eq. (3), s and $\dot{S}_{\text{gen}}$ refer the specific entropy and entropy generation rate. In Eq. (4), the exergy destruction rate, exergy rate of heat and work transfer, and specific exergy are

$$\dot{E}x_D = T_0 \dot{S}_{\text{gen}} \tag{5}$$

$$\dot{E}x_Q = \left(1 - \frac{T_o}{T} \right) \dot{Q} \tag{6}$$

$$\dot{E}x_W = \dot{W} \tag{7}$$

$$\text{ex} = \text{ex}_{\text{ph}} + \text{ex}_{\text{ch}} \tag{8}$$

The flow or physical exergy is

$$\text{ex}_{\text{ph}} = h - h_o - T_o(s - s_o) \tag{9}$$

The chemical exergy equation for gas mixture can be defined as

$$\text{ex}^{\text{ch}}_{\text{mix}} = \sum y_i \text{ex}^{\text{ch}}_i + RT_o \sum y_i \ln y_i \tag{10}$$

where y_i shows the mole fraction of component i in gas mixture. The chemical exergetic equation of fuel sources is

$$\text{ex}^{\text{ch}}_{\text{fuel}} = \left(\text{LHV}_{\text{fuel}} + w_m h_{\text{fg}}\right)\beta_{\text{dy}} + 9417\,s \tag{11}$$

where LHV_{fuel} and w_m show the lower heating value and moisture content, h_{fg} illustrates the water latent heat at reference conditions, and also s is the sulfur mass fraction. Finally, β_{dy} can be given depending on the dry decomposition of solid fuels.

$$\beta_{\text{dry}} = 0.1882\frac{H}{C} + 0.061\frac{O}{C} + 0.0404\frac{N}{C} + 1.0437 \tag{12}$$

Equation (12) is valid only when the O/C ratio is less than 0.667. The ultimate analysis results of coal are written in Table 2. In addition to that, the balance equations for integrated system components are given in Table 3.

Energetic efficiency term is an evaluation of beneficial energy form from any plant to the input power for this plant. Also, an exergy efficiency equation should be defined based on an exergetic content of plant inputs and outputs, which presents a better insight of plant performance. The energy and exergy efficiency equations are written for integrated plant and its sub-plants under steady-state status.

For coal gasification sub-plant

$$\eta_{\text{CGP}} = \frac{\dot{m}_9 h_9 + (\dot{m}_{12}h_{12} - \dot{m}_{11}h_{11})}{\dot{m}_1 h_1 + \dot{m}_3 h_3 + \dot{W}_{\text{AB}}} \tag{13}$$

$$\psi_{\text{CGP}} = \frac{\dot{m}_9 \text{ex}_9 + (\dot{m}_{12}\text{ex}_{12} - \dot{m}_{11}\text{ex}_{11})}{\dot{m}_1 \text{ex}_1 + \dot{m}_3 \text{ex}_3 + \dot{W}_{\text{AB}}} \tag{14}$$

For gas turbine cycle sub-plant

Table 2 Ultimate assessment of coal utilized in this study	Compound	Dry basis	Dry ash free basis (wt%)
	C	0.7279	0.8688
	H	0.367	0.441
	N	0.262	0.328
	S	0.138	0.167
	O	0.192	0.234

Table 3 Balance equations of biomass gasification-based integrated system

Components	Mass balance	Energy balance	Entropy balance	Exergy balance
Coal gasifier	$\dot{m}_1 + \dot{m}_3 = \dot{m}_4$	$\dot{m}_1 h_1 + \dot{m}_3 h_3 = \dot{m}_4 h_4 + \dot{Q}_{L,CG}$	$\dot{m}_1 s_1 + \dot{m}_3 s_3 + \dot{S}_{g,CG} = \dot{m}_4 s_4 + \dot{Q}_{L,CG}/T_{CG}$	$\dot{m}_1 ex_1 + \dot{m}_3 ex_3 = \dot{m}_4 ex_4 + \dot{Ex}_{L,CG} + \dot{Ex}_{D,CG}$
Cyclone	$\dot{m}_4 = \dot{m}_5 + \dot{m}_6$	$\dot{m}_4 h_4 = \dot{m}_5 h_5 + \dot{m}_6 h_6$	$\dot{m}_4 s_4 + \dot{S}_{g,Cy} = \dot{m}_5 s_5 + \dot{m}_6 s_6$	$\dot{m}_4 ex_4 = \dot{m}_5 ex_5 + \dot{m}_6 ex_6 + \dot{Ex}_{D,Cy}$
Acid gas removal	$\dot{m}_6 = \dot{m}_7 + \dot{m}_8$	$\dot{m}_6 h_6 = \dot{m}_7 h_7 + \dot{m}_8 h_8$	$\dot{m}_6 s_6 + \dot{S}_{g,AGR} = \dot{m}_7 s_7 + \dot{m}_8 s_8$	$\dot{m}_6 ex_6 = \dot{m}_7 ex_7 + \dot{m}_8 ex_8 + \dot{Ex}_{D,AGR}$
HEX1	$\dot{m}_8 = \dot{m}_9$ $\dot{m}_{11} = \dot{m}_{12}$	$\dot{m}_8 h_8 + \dot{m}_{11} h_{11} = \dot{m}_9 h_9 + \dot{m}_{12} h_{12}$	$\dot{m}_8 s_8 + \dot{m}_{11} s_{11} + \dot{S}_{g,HEX1} = \dot{m}_9 s_9 + \dot{m}_{12} s_{12}$	$\dot{m}_8 ex_8 + \dot{m}_{11} ex_{11} = \dot{m}_9 ex_9 + \dot{m}_{12} ex_{12} + \dot{Ex}_{D,HEX1}$
Compressor	$\dot{m}_{13} = \dot{m}_{14}$	$\dot{m}_{13} h_{13} + \dot{W}_{Comp} = \dot{m}_{14} h_{14}$	$\dot{m}_{13} s_{13} + \dot{S}_{g,Comp} = \dot{m}_{14} s_{14}$	$\dot{m}_{13} ex_{13} + \dot{W}_{Comp} = \dot{m}_{14} ex_{14} + \dot{Ex}_{D,Comp}$
Water gas shift reactor	$\dot{m}_{12} + \dot{m}_{14} = \dot{m}_{15}$	$\dot{m}_{12} h_{12} + \dot{m}_{14} h_{14} = \dot{m}_{15} h_{15} + \dot{Q}_{L,WGSR}$	$\dot{m}_{12} s_{12} + \dot{m}_{14} s_{14} + \dot{S}_{g,WGSR} = \dot{m}_{15} s_{15} + \dot{Q}_{L,WGSR}/T_{WGSR}$	$\dot{m}_{12} ex_{12} + \dot{m}_{14} ex_{14} = \dot{m}_{15} ex_{15} + \dot{Ex}_{L,WGSR} + \dot{Ex}_{D,WGSR}$
Fischer-Tropsch reactor	$\dot{m}_{15} + \dot{m}_{19} = \dot{m}_{16} + \dot{m}_{17}$	$\dot{m}_{15} h_{15} + \dot{m}_{19} h_{19} = \dot{m}_{16} h_{16} + \dot{m}_{17} h_{17} + \dot{Q}_{L,FTR}$	$\dot{m}_{15} s_{15} + \dot{m}_{19} s_{19} + \dot{S}_{g,FTR} = \dot{m}_{16} s_{16} + \dot{m}_{17} s_{17} + \dot{Q}_{L,FTR}/T_{FTR}$	$\dot{m}_{15} ex_{15} + \dot{m}_{19} ex_{19} = \dot{m}_{16} ex_{16} + \dot{m}_{17} ex_{17} + \dot{Ex}_{L,FTR} + \dot{Ex}_{D,FTR}$
Pump1	$\dot{m}_{18} = \dot{m}_{19}$	$\dot{m}_{18} h_{18} + \dot{W}_{P1} = \dot{m}_{19} h_{19}$	$\dot{m}_{18} s_{18} + \dot{S}_{g,P1} = \dot{m}_{19} s_{19}$	$\dot{m}_{18} ex_{18} + \dot{W}_{P1} = \dot{m}_{19} ex_{19} + \dot{Ex}_{D,P1}$
Generator	$\dot{m}_{17} = \dot{m}_{18}$ $\dot{m}_{35} = \dot{m}_{36} + \dot{m}_{37}$	$\dot{m}_{17} h_{17} + \dot{m}_{35} h_{35} = \dot{m}_{18} h_{18} + \dot{m}_{36} h_{36} + \dot{m}_{37} h_{37}$	$\dot{m}_{17} s_{17} + \dot{m}_{35} s_{35} + \dot{S}_{g,Gn} = \dot{m}_{18} s_{18} + \dot{m}_{36} s_{36} + \dot{m}_{37} s_{37}$	$\dot{m}_{17} ex_{17} + \dot{m}_{35} ex_{35} = \dot{m}_{18} h_{18} + \dot{m}_{36} ex_{36} + \dot{m}_{37} ex_{37} + \dot{Ex}_{D,Gn}$

(continued)

Table 3 (continued)

Components	Mass balance	Energy balance	Entropy balance	Exergy balance
Condenser1	$\dot{m}_{36} = \dot{m}_{30}$ $\dot{m}_{40} = \dot{m}_{41}$	$\dot{m}_{36}h_{36} + \dot{m}_{40}h_{40} =$ $\dot{m}_{30}h_{30} + \dot{m}_{41}h_{41}$	$\dot{m}_{36}s_{36} + \dot{m}_{40}s_{40} + \dot{S}_{g,Con1} =$ $\dot{m}_{30}s_{30} + \dot{m}_{41}s_{41}$	$\dot{m}_{36}ex_{36} + \dot{m}_{40}ex_{40} =$ $\dot{m}_{30}ex_{30} + \dot{m}_{41}ex_{41} +$ $\dot{Ex}_{D,Con1}$
Evaporator1	$\dot{m}_{31} = \dot{m}_{32}$ $\dot{m}_{42} = \dot{m}_{43}$	$\dot{m}_{31}h_{31} + \dot{m}_{42}h_{42} =$ $\dot{m}_{32}h_{32} + \dot{m}_{43}h_{43}$	$\dot{m}_{31}s_{31} + \dot{m}_{42}s_{42} + \dot{S}_{g,Eva1} =$ $\dot{m}_{32}s_{32} + \dot{m}_{43}s_{43}$	$\dot{m}_{31}ex_{31} + \dot{m}_{42}ex_{42} =$ $\dot{m}_{32}ex_{32} + \dot{m}_{43}ex_{43} + \dot{Ex}_{D,Eva1}$
Absorber	$\dot{m}_{44} = \dot{m}_{45}$ $\dot{m}_{32} + \dot{m}_{39} = \dot{m}_{33}$	$\dot{m}_{32}h_{32} + \dot{m}_{39}h_{39} + \dot{m}_{44}h_{44} =$ $\dot{m}_{33}h_{33} + \dot{m}_{45}h_{45}$	$\dot{m}_{32}s_{32} + \dot{m}_{39}s_{39} + \dot{m}_{44}s_{44} +$ $\dot{S}_{g,Ab} = \dot{m}_{33}s_{33} + \dot{m}_{45}s_{45}$	$\dot{m}_{32}ex_{32} + \dot{m}_{39}ex_{39} +$ $\dot{m}_{44}ex_{44} =$ $\dot{m}_{33}ex_{33} + \dot{m}_{45}ex_{45} + \dot{Ex}_{D,Abs}$
Combustor	$\dot{m}_{10} + \dot{m}_{21} = \dot{m}_{22}$	$\dot{m}_{10}h_{10} + \dot{m}_{21}h_{21} =$ $\dot{m}_{22}h_{22} + \dot{Q}_{L,cb}$	$\dot{m}_{10}s_{10} + \dot{m}_{21}s_{21} + \dot{S}_{g,Cb} =$ $\dot{m}_{22}s_{22} + \dot{Q}_{L,Cb}/T_{Cb}$	$\dot{m}_{10}ex_{10} + \dot{m}_{21}ex_{21} =$ $\dot{m}_{22}ex_{22} + \dot{Ex}^{\dot{Q}}_{L,cb} + \dot{Ex}_{D,Cb}$
Gas turbine	$\dot{m}_{22} = \dot{m}_{23}$	$\dot{m}_{22}h_{22} = \dot{m}_{23}h_{23} + \dot{W}_{GT}$	$\dot{m}_{22}s_{22} + \dot{S}_{g,GT} = \dot{m}_{23}s_{23}$	$\dot{m}_{22}ex_{22} =$ $\dot{m}_{23}ex_{23} + \dot{W}_{GT} + \dot{Ex}_{D,GT}$
Super heater	$\dot{m}_{23} = \dot{m}_{24}$ $\dot{m}_{56} = \dot{m}_{56}$	$\dot{m}_{23}h_{23} + \dot{m}_{56}h_{56} =$ $\dot{m}_{24}h_{24} + \dot{m}_{46}h_{46}$	$\dot{m}_{23}s_{23} + \dot{m}_{56}s_{56} + \dot{S}_{g,SH} =$ $\dot{m}_{24}s_{24} + \dot{m}_{46}s_{46}$	$\dot{m}_{23}ex_{23} + \dot{m}_{56}ex_{56} =$ $\dot{m}_{24}ex_{24} + \dot{m}_{46}ex_{46} + \dot{Ex}_{D,SH}$
Economizer	$\dot{m}_{25} = \dot{m}_{26}$ $\dot{m}_{53} = \dot{m}_{54}$	$\dot{m}_{25}h_{25} + \dot{m}_{53}h_{53} =$ $\dot{m}_{26}h_{26} + \dot{m}_{54}h_{54}$	$\dot{m}_{25}s_{25} + \dot{m}_{53}s_{53} + \dot{S}_{g,Eco} =$ $\dot{m}_{26}s_{26} + \dot{m}_{54}s_{54}$	$\dot{m}_{25}ex_{25} + \dot{m}_{53}ex_{53} =$ $\dot{m}_{26}ex_{26} + \dot{m}_{54}ex_{54} + \dot{Ex}_{D,Eco}$
Turbine	$\dot{m}_{46} = \dot{m}_{47}$	$\dot{m}_{46}h_{46} = \dot{m}_{47}h_{47} + \dot{W}_{Tur}$	$\dot{m}_{46}s_{46} + \dot{S}_{g,Tur} = \dot{m}_{47}s_{47}$	$\dot{m}_{46}ex_{46} =$ $\dot{m}_{47}ex_{47} + \dot{W}_{Tur} + \dot{Ex}_{D,Tur}$
PEM electrolyzer	$\dot{m}_{63} = \dot{m}_{64} + \dot{m}_{65}$	$\dot{m}_{63}h_{63} + \dot{W}_{PEM} =$ $\dot{m}_{64}h_{64} + \dot{m}_{65}h_{65}$	$\dot{m}_{63}s_{63} + \dot{S}_{g,PEM} =$ $\dot{m}_{64}s_{64} + \dot{m}_{65}s_{65}$	$\dot{m}_{63}ex_{63} + \dot{W}_{PEM} =$ $\dot{m}_{64}ex_{64} + \dot{m}_{65}ex_{65} + \dot{Ex}_{D,PEM}$
Hydrogen compressor1	$\dot{m}_{65} = \dot{m}_{66}$	$\dot{m}_{65}h_{65} + \dot{W}_{HC1} = \dot{m}_{66}h_{66}$	$\dot{m}_{65}s_{65} + \dot{S}_{g,HC1} = \dot{m}_{66}s_{66}$	$\dot{m}_{65}ex_{65} + \dot{W}_{HC1} =$ $\dot{m}_{66}ex_{66} + \dot{Ex}_{D,HC1}$

$$\eta_{GTC} = \frac{\dot{W}_{GT} - \dot{W}_{AC}}{\dot{m}_{22}h_{22}} \tag{15}$$

$$\psi_{GTC} = \frac{\dot{W}_{GT} - \dot{W}_{AC}}{\dot{m}_{22}ex_{22}} \tag{16}$$

For WGSR sub-plant

$$\eta_{WGSR} = \frac{\dot{m}_{15}h_{15}}{\dot{m}_{12}h_{12} + \dot{m}_{14}h_{14}} \tag{17}$$

$$\psi_{WGSR} = \frac{\dot{m}_{15}ex_{15}}{\dot{m}_{12}ex_{12} + \dot{m}_{14}ex_{14}} \tag{18}$$

For FTR sub-plant

$$\eta_{FTR} = \frac{\dot{m}_{16}h_{16} + \dot{m}_{17}h_{17}}{\dot{m}_{15}h_{15} + \dot{m}_{19}h_{19}} \tag{18}$$

$$\psi_{FTR} = \frac{\dot{m}_{16}ex_{16} + \dot{m}_{17}ex_{17}}{\dot{m}_{15}ex_{15} + \dot{m}_{19}ex_{19}} \tag{19}$$

For SEAC sub-plant

$$\eta_{SEAC} = \frac{\dot{Q}_{Cooling}}{(\dot{m}_{17}h_{17} - \dot{m}_{18}h_{18}) + \dot{W}_{P2}} \tag{20}$$

$$\psi_{SEAC} = \frac{\dot{Ex}^{Q}_{Cooling}}{(\dot{m}_{17}ex_{17} - \dot{m}_{18}ex_{18}) + \dot{W}_{P2}} \tag{21}$$

For Kalina cycle sub-plant

$$\eta_{KC} = \frac{\dot{W}_{KC} + (\dot{m}_{61}h_{61} - \dot{m}_{60}h_{60})}{\dot{W}_{P3} + (\dot{m}_{46}h_{46} - \dot{m}_{56}h_{56}) + (\dot{m}_{55}h_{55} - \dot{m}_{54}h_{54}) + (\dot{m}_{54}h_{54} - \dot{m}_{53}h_{53})} \tag{22}$$

$$\psi_{KC} = \frac{\dot{W}_{KC} + (\dot{m}_{61}ex_{61} - \dot{m}_{60}ex_{60})}{\dot{W}_{P3} + (\dot{m}_{46}ex_{46} - \dot{m}_{56}ex_{56}) + (\dot{m}_{55}ex_{55} - \dot{m}_{54}ex_{54}) + (\dot{m}_{54}ex_{54} - \dot{m}_{53}ex_{53})} \tag{23}$$

For hydrogen production sub-plant

$$\eta_{HP} = \frac{\dot{m}_{65}LHV_{H_2}}{\dot{m}_{63}h_{63} + \dot{W}_{PEM}} \tag{24}$$

$$\psi_{HP} = \frac{\dot{m}_{65}ex_{H_2}}{\dot{m}_{63}ex_{63} + \dot{W}_{PEM}} \tag{25}$$

For hydrogen compression sub-plant

$$\eta_{HC} = \frac{\dot{m}_{71} h_{71}}{\dot{m}_{65} h_{65} + \sum \dot{W}_{HC}} \tag{26}$$

$$\psi_{HC} = \frac{\dot{m}_{71} ex_{71}}{\dot{m}_{65} ex_{65} + \sum \dot{W}_{HC}} \tag{27}$$

For dryer cycle sub-plant

$$\eta_{DC} = \frac{\dot{Q}_{Dryer}}{\dot{m}_{73}(h_{73} - h_{74})} \tag{28}$$

$$\psi_{DC} = \frac{\dot{Ex}_{Dryer}^{Q}}{\dot{m}_{73}(ex_{73} - ex_{74})} \tag{29}$$

For hot water production sub-plant

$$\eta_{HWP} = \frac{(\dot{m}_{78} h_{78} - \dot{m}_{77} h_{77})}{(\dot{m}_{28} h_{28} - \dot{m}_{29} h_{29})} \tag{30}$$

$$\psi_{HWP} = \frac{(\dot{m}_{78} ex_{78} - \dot{m}_{77} ex_{77})}{(\dot{m}_{28} ex_{28} - \dot{m}_{29} ex_{29})} \tag{31}$$

For whole system

$$\eta_{WS} = \frac{\dot{W}_{GT} + \dot{W}_{KC} + \dot{m}_{71} LHV_{H_2} + \dot{Q}_{Heating} + \dot{Q}_{Cooling} + \dot{Q}_{Dryer} + \dot{Q}_{Hot\_water}}{\dot{m}_1 LHV_{coal} + \sum \dot{W}_p + \sum \dot{W}_{HC} + \dot{W}_{AC}} \tag{32}$$

$$\psi_{WS} = \frac{\dot{W}_{GT} + \dot{W}_{KC} + \dot{m}_{71} ex_{H_2} + \dot{Ex}_{Heating}^{Q} + \dot{Ex}_{Cooling}^{Q} + \dot{Ex}_{Dryer}^{Q} + \dot{Ex}_{Hot\_water}^{Q}}{\dot{m}_1 ex_{coal} + \sum \dot{W}_p + \sum \dot{W}_{HC} + \dot{W}_{AC}} \tag{33}$$

The energetic and exergetic COP for SEAC sub-plant are

$$COP_{en} = \frac{\dot{Q}_{Eva1}}{\dot{Q}_{Gn} + \dot{W}_{P2}} \tag{34}$$

$$COP_{ex} = \frac{\dot{Ex}_{Eva1}^{Q}}{\dot{Ex}_{Gn}^{Q} + \dot{W}_{P2}} \tag{35}$$

The energetic and exergetic performance equalities for combined plant single generation alternative can be defined as

$$\eta_{\text{sngen}} = \frac{\dot{W}_{\text{RC}} + \dot{W}_{\text{KC}}}{\dot{m}_1 \text{LHV}_{\text{coal}} + \dot{W}_{\text{AB}} + \dot{W}_{\text{AC}} + \dot{W}_{P3}} \tag{36}$$

$$\psi_{\text{sngen}} = \frac{\dot{W}_{\text{RC}} + \dot{W}_{\text{KC}}}{\dot{m}_1 \text{ex}_{\text{coal}} + \dot{W}_{\text{AB}} + \dot{W}_{\text{AC}} + \dot{W}_{P3}} \tag{37}$$

Different energetic and exergetic performance equalities for combined plant cogeneration alternative are given as

$$\eta_{\text{cogen,I}} = \frac{\dot{W}_{\text{GT}} + \dot{W}_{\text{KC}} + \dot{Q}_{\text{Cooling}}}{\dot{m}_1 \text{LHV}_{\text{coal}} + \dot{W}_{\text{AB}} + \dot{W}_{\text{AC}} + \dot{W}_{P2} + \dot{W}_{P3}} \tag{38}$$

$$\eta_{\text{cogen,II}} = \frac{\dot{W}_{\text{GT}} + \dot{W}_{\text{KC}} + \dot{m}_{16} \text{LHV}_{\text{Fuel}}}{\dot{m}_1 \text{LHV}_{\text{coal}} + \dot{W}_{\text{AB}} + \dot{W}_{\text{AC}} + \dot{W}_{P1} + \dot{W}_{P3}} \tag{39}$$

$$\eta_{\text{cogen,III}} = \frac{\dot{W}_{\text{GT}} + \dot{W}_{\text{KC}} + \dot{m}_{71} \text{LHV}_{H_2}}{\dot{m}_1 \text{LHV}_{\text{coal}} + \dot{W}_{\text{AB}} + \dot{W}_{\text{AC}} + \sum \dot{W}_{\text{HC}} + \dot{W}_{P3}} \tag{40}$$

$$\psi_{\text{cogen,I}} = \frac{\dot{W}_{\text{GT}} + \dot{W}_{\text{KC}} + \dot{Ex}^Q_{\text{cooling}}}{\dot{m}_1 \text{ex}_{\text{coal}} + \dot{W}_{\text{AB}} + \dot{W}_{\text{AC}} + \dot{W}_{P2} + \dot{W}_{P3}} \tag{41}$$

$$\psi_{\text{cogen,II}} = \frac{\dot{W}_{\text{GT}} + \dot{W}_{\text{KC}} + \dot{m}_{16} \text{ex}_{\text{Fuel}}}{\dot{m}_1 \text{ex}_{\text{coal}} + \dot{W}_{\text{AB}} + \dot{W}_{\text{AC}} + \dot{W}_{P1} + \dot{W}_{P3}} \tag{42}$$

$$\psi_{\text{cogen,III}} = \frac{\dot{W}_{\text{GT}} + \dot{W}_{\text{KC}} + \dot{m}_{71} \text{ex}_{H_2}}{\dot{m}_1 \text{ex}_{\text{coal}} + \dot{W}_{\text{AB}} + \dot{W}_{\text{AC}} + \sum \dot{W}_{\text{HC}} + \dot{W}_{P3}} \tag{43}$$

Different energetic and exergetic performance equations for combined plant trigeneration alternative can be written as follows:

$$\eta_{\text{trigen,I}} = \frac{\dot{W}_{\text{GT}} + \dot{W}_{\text{KC}} + \dot{Q}_{\text{Cooling}} + \dot{m}_{16} \text{LHV}_{\text{Fuel}}}{\dot{m}_1 \text{LHV}_{\text{coal}} + \dot{W}_{\text{AB}} + \dot{W}_{\text{AC}} + \dot{W}_{P1} + \dot{W}_{P2} + \dot{W}_{P3}} \tag{44}$$

$$\eta_{\text{trigen,II}} = \frac{\dot{W}_{\text{GT}} + \dot{W}_{\text{KC}} + \dot{Q}_{\text{Cooling}} + \dot{m}_{71} \text{LHV}_{H_2}}{\dot{m}_1 \text{LHV}_{\text{coal}} + \dot{W}_{\text{AB}} + \dot{W}_{\text{AC}} + \dot{W}_{P2} + \dot{W}_{P3} + \sum \dot{W}_{\text{HC}}} \tag{45}$$

$$\eta_{\text{trigen,III}} = \frac{\dot{W}_{\text{GT}} + \dot{W}_{\text{KC}} + \dot{m}_{16} \text{LHV}_{\text{Fuel}} + \dot{m}_{71} \text{LHV}_{H_2}}{\dot{m}_1 \text{LHV}_{\text{coal}} + \dot{W}_{\text{AB}} + \dot{W}_{\text{AC}} + \dot{W}_{P1} + \dot{W}_{P3} + \sum \dot{W}_{\text{HC}}} \tag{46}$$

$$\psi_{\text{trigen,I}} = \frac{\dot{W}_{\text{GT}} + \dot{W}_{\text{KC}} + \dot{Ex}^Q_{\text{cooling}} + \dot{m}_{16} \text{ex}_{\text{Fuel}}}{\dot{m}_1 \text{ex}_{\text{coal}} + \dot{W}_{\text{AB}} + \dot{W}_{\text{AC}} + \dot{W}_{P1} + \dot{W}_{P2} + \dot{W}_{P3}} \tag{47}$$

$$\psi_{\text{trigen,II}} = \frac{\dot{W}_{\text{GT}} + \dot{W}_{\text{KC}} + \dot{Ex}^Q_{\text{cooling}} + \dot{m}_{71} \text{ex}_{H_2}}{\dot{m}_1 \text{ex}_{\text{coal}} + \dot{W}_{\text{AB}} + \dot{W}_{\text{AC}} + \dot{W}_{P2} + \dot{W}_{P3} + \sum \dot{W}_{\text{HC}}} \tag{48}$$

$$\psi_{\text{trigen,III}} = \frac{\dot{W}_{\text{GT}} + \dot{W}_{\text{KC}} + \dot{m}_{16} \text{ex}_{\text{Fuel}} + \dot{m}_{71} \text{ex}_{H_2}}{\dot{m}_1 \text{ex}_{\text{coal}} + \dot{W}_{\text{AB}} + \dot{W}_{\text{AC}} + \dot{W}_{P1} + \dot{W}_{P3} + \sum \dot{W}_{\text{HC}}} \tag{49}$$

The energetic and exergetic performance equations for multigeneration option are given in Eq. (32) and (33), respectively. Also, the energetic and exergetic performance equations for integrated plant components are written in Table 4.

3.1 Environmental Impact Assessment of Integrated Plant

The environmental impact assessment study is an investigation of negatively or positively feasible impacts on the natural ambient conditions including ecological process, accounting for technical, financial, and social indexes. The environmental impact analysis includes the identification, evaluation, and assessment of environmental impacts and mitigation options. In this book sub-chapter, the normalized CO_2 emission and sustainability evaluation considerations are utilized for ecological effect analysis for coal gasification-based multigeneration cycle. To investigate the CO_2 emission rates for coal gasification-based plant, four status based on the single generation (SG), cogeneration (CG), trigeneration (TG), and multigeneration (MG) options given in Eqs. (36–49) and Eqs. (32–33) are examined. In addition to that, the CO_2 emission rates are described for each status. In the first status, the electricity generation is investigated based on the CO_2 emission rates. In the second status, different useful cogeneration options are analyzed. In the third status, different useful trigeneration options are investigated based on the CO_2 emission rates. In the last option, the whole multigeneration cycle for power, hydrogen, heating, cooling, hot water, diesel fuel, wax, and LPG generation is investigated. The CO_2 emission rate in each status can be written as given below

$$\varepsilon_{\text{SG}} = \frac{\dot{m}_{\text{CO}_2}}{\dot{W}_{\text{net}}} \tag{50}$$

$$\varepsilon_{\text{CG}} = \frac{\dot{m}_{\text{CO}_2}}{\text{Co} - \text{generation}} \tag{51}$$

$$\varepsilon_{\text{TG}} = \frac{\dot{m}_{\text{CO}_2}}{\text{Tri} - \text{generation}} \tag{52}$$

$$\varepsilon_{\text{MG}} = \frac{\dot{m}_{\text{CO}_2}}{\text{Multi} - \text{generation}} \tag{53}$$

4 Results and Discussion

Table 5 illustrates the energy efficiency for subsystems of integrated energy production system and overall system. As seen from Table 5, the energy and exergy efficiency for Fischer-Tropsch reactor has higher values than the other subsystems.

Table 4 Energetic and exergetic efficiency equalities of integrated plant components

Components	Energy efficiency equations	Exergy efficiency equations
Coal gasifier	$\eta_{CG} = \dot{m}_4 h_4 / (\dot{m}_1 h_1 + \dot{m}_3 h_3)$	$\psi_{CG} = \dot{m}_4 ex_4 / (\dot{m}_1 ex_1 + \dot{m}_3 ex_3)$
Cyclone	$\eta_{Cy} = \dot{m}_6 h_6 / \dot{m}_4 h_4$	$\psi_{Cy} = \dot{m}_6 ex_6 / \dot{m}_4 ex_4$
AGR	$\eta_{AGR} = \dot{m}_8 h_8 / \dot{m}_6 h_6$	$\psi_{AGR} = \dot{m}_8 ex_8 / \dot{m}_6 ex_6$
HEX 1	$\eta_{HEX1} = \dfrac{(\dot{m}_{12} h_{12} - \dot{m}_{11} h_{11})}{(\dot{m}_8 h_8 - \dot{m}_9 h_9)}$	$\psi_{HEX1} = \dfrac{(\dot{m}_{12} ex_{12} - \dot{m}_{11} ex_{11})}{(\dot{m}_8 ex_8 - \dot{m}_9 ex_9)}$
Compressor	$\eta_{Comp} = (\dot{m}_{14} h_{14} - \dot{m}_{13} h_{13}) / \dot{W}_{Comp}$	$\psi_{Comp} = (\dot{m}_{14} ex_{14} - \dot{m}_{13} ex_{13}) / \dot{W}_{Comp}$
Water gas shift reactor	$\eta_{WGSR} = \dfrac{\dot{m}_{15} h_{15}}{(\dot{m}_{12} h_{12} + \dot{m}_{14} h_{14})}$	$\psi_{WGSR} = \dfrac{\dot{m}_{15} ex_{15}}{(\dot{m}_{12} ex_{12} + \dot{m}_{14} ex_{14})}$
Fischer-Tropsch reactor	$\eta_{FTR} = \dfrac{(\dot{m}_{16} h_{16} + \dot{m}_{17} h_{17})}{(\dot{m}_{15} h_{15} + \dot{m}_{19} h_{19})}$	$\psi_{FTR} = \dfrac{(\dot{m}_{16} ex_{16} + \dot{m}_{17} ex_{17})}{(\dot{m}_{15} ex_{15} + \dot{m}_{19} ex_{19})}$
Pump 1	$\eta_{P1} = (\dot{m}_{19} h_{19} - \dot{m}_{18} h_{18}) / \dot{W}_{P1}$	$\psi_{P1} = (\dot{m}_{19} ex_{19} - \dot{m}_{18} ex_{18}) / \dot{W}_{P1}$
Generator	$\eta_{Gen} = \dfrac{(\dot{m}_{36} h_{36} + \dot{m}_{37} h_{37} - \dot{m}_{35} h_{35})}{(\dot{m}_{17} h_{17} - \dot{m}_{18} h_{18})}$	$\psi_{Gen} = \dfrac{(\dot{m}_{36} ex_{36} + \dot{m}_{37} ex_{37} - \dot{m}_{35} ex_{35})}{(\dot{m}_{17} ex_{17} - \dot{m}_{18} ex_{18})}$
Condenser 1	$\eta_{Con1} = \dfrac{(\dot{m}_{41} h_{41} - \dot{m}_{40} h_{40})}{(\dot{m}_{36} h_{36} - \dot{m}_{30} h_{30})}$	$\psi_{Con1} = \dfrac{(\dot{m}_{41} ex_{41} - \dot{m}_{40} ex_{40})}{(\dot{m}_{36} ex_{36} - \dot{m}_{30} ex_{30})}$
Evaporator 1	$\eta_{Eva1} = \dfrac{(\dot{m}_{43} h_{43} - \dot{m}_{42} h_{42})}{(\dot{m}_{31} h_{31} - \dot{m}_{32} h_{32})}$	$\psi_{Eva1} = \dfrac{(\dot{m}_{43} ex_{43} - \dot{m}_{42} ex_{42})}{(\dot{m}_{31} ex_{31} - \dot{m}_{32} ex_{32})}$
Absorber	$\eta_{Abs} = \dfrac{(\dot{m}_{45} h_{45} - \dot{m}_{44} h_{44})}{(\dot{m}_{32} h_{32} + \dot{m}_{39} h_{39} - \dot{m}_{33} h_{33})}$	$\psi_{Abs} = \dfrac{(\dot{m}_{45} ex_{45} - \dot{m}_{44} ex_{44})}{(\dot{m}_{32} ex_{32} + \dot{m}_{39} ex_{39} - \dot{m}_{33} ex_{33})}$
Combustor	$\eta_{Cb} = \dfrac{\dot{m}_{22} h_{22}}{(\dot{m}_{10} h_{10} + \dot{m}_{21} h_{21})}$	$\psi_{Cb} = \dfrac{\dot{m}_{22} ex_{22}}{(\dot{m}_{10} ex_{10} + \dot{m}_{21} ex_{21})}$
Gas turbine	$\eta_{GT} = \dot{W}_{GT} / (\dot{m}_{22} h_{22} - \dot{m}_{23} h_{23})$	$\psi_{GT} = \dot{W}_{GT} / (\dot{m}_{22} ex_{22} - \dot{m}_{23} ex_{23})$
Super heater	$\eta_{SH} = \dfrac{(\dot{m}_{46} h_{46} - \dot{m}_{56} h_{56})}{(\dot{m}_{23} h_{23} - \dot{m}_{24} h_{24})}$	$\psi_{SH} = \dfrac{(\dot{m}_{46} ex_{46} - \dot{m}_{56} ex_{56})}{(\dot{m}_{23} ex_{23} - \dot{m}_{24} ex_{24})}$
Economizer	$\eta_{Eco} = \dfrac{(\dot{m}_{54} h_{54} - \dot{m}_{53} h_{53})}{(\dot{m}_{25} h_{25} - \dot{m}_{26} h_{26})}$	$\psi_{Eco} = \dfrac{(\dot{m}_{54} ex_{54} - \dot{m}_{53} ex_{53})}{(\dot{m}_{25} ex_{25} - \dot{m}_{26} ex_{26})}$
Turbine	$\eta_{Tur} = \dot{W}_{Tur} / (\dot{m}_{46} h_{46} - \dot{m}_{47} h_{47})$	$\psi_{Tur} = \dot{W}_{Tur} / (\dot{m}_{46} ex_{46} - \dot{m}_{47} ex_{47})$
PEM electrolyzer	$\eta_{PEM} = \dfrac{(\dot{m}_{64} h_{64} + \dot{m}_{65} h_{65})}{\dot{m}_{63} h_{63} + \dot{W}_{PEM}}$	$\psi_{PEM} = \dfrac{(\dot{m}_{64} ex_{64} + \dot{m}_{65} ex_{65})}{\dot{m}_{63} ex_{63} + \dot{W}_{PEM}}$
Hydrogen compressor 1	$\eta_{HC1} = (\dot{m}_{66} h_{66} - \dot{m}_{65} h_{65}) / \dot{W}_{HC1}$	$\psi_{HC1} = (\dot{m}_{66} ex_{66} - \dot{m}_{65} ex_{65}) / \dot{W}_{HC1}$

Table 5 Thermodynamic analysis outputs for coal gasification-based combined plant

Sub-parts	Energetic efficiency (%)	Exergetic efficiency %	Exergy destruction rate (kW)	Exergy destruction ratio (%)
Coal gasifier	52.36	48.14	18,245	25.97
Gas turbine cycle	46.17	42.28	13,867	19.74
Water gas shift reactor	48.15	43.58	4102	5.84
Fischer-Tropsch reactor	64.56	61.22	6547	9.32
Hydrogen production	55.72	53.22	6806	9.69
Hydrogen compression	19.21	16.24	3765	5.36
Kalina cycle	22.53	19.67	8246	11.74
SEAC	17.14	15.26	3365	4.79
Dryer cycle	69.34	65.47	2962	4.22
Hot water cycle	76.52	72.43	2338	3.33
Whole system	59.16	56.43	70,243	100

The results of proposed combined plant for multigeneration are given in Table 6. The highest output of the integrated energy system with 7406 kW in gas turbine is shown in Table 6.

The graphs obtained from the results of parametric studies performed by changing the different working parameters of system are given in this section. Parametrical studies are conducted with the help of EES software program to investigate the effects of absorption chiller evaporator temperature, dead-state temperature, coal mass flow rate, and coal gasifier temperature on the system performance and useful outputs.

Table 6 Integrated coal gasification-based power plant outputs

| Plant outputs	Values
Produced electricity from gas turbine, $\dot{W}_{GT}$	16,525 kW
Produced electricity from Kalina turbine, $\dot{W}_{KT}$	6288 kW
Produced cooling, $\dot{Q}_{Cooling}$	4822 kW
Produced heating, $\dot{Q}_{Heating}$	4057 kW
Produced hot water, $\dot{Q}_{Hot\_water}$	7406 kW
Produced drying, $\dot{Q}_{Drying}$	6285 kW
Mass flow rate of diesel fuel, wax, and LPG, $\dot{m}_{Fuel}$	2.437 kg/s
Mass flow rate of produced hydrogen, $\dot{m}_{Hydrogen}$	0.074 kg/s
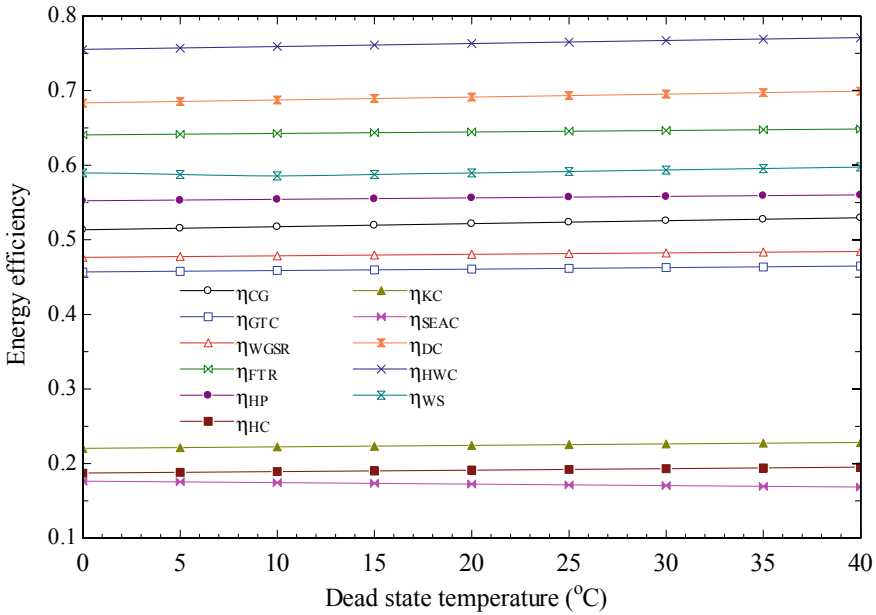
Fig. 2 Impacts of dead-state temperature on energy efficiencies

Analyzing the results of these parametric studies with graphs is very important to see the changes in various sub-components.

The impacts of changing dead-state temperature on the energy and exergy efficiencies, system outputs from subsystems, and the whole system are analyzed. The effects of increased dead-state temperature on the energetic efficiency, exergetic efficiency, and beneficial system outputs of integrated system and its subsystems are illustrated in Figs. 2, 3 and 4, respectively.

The effects of the changing coal mass flow rate on the energy efficiency, exergy efficiency, and system outputs of subsystems and the whole system are investigated. The impacts of increased coal mass flow rate on the energetic efficiency, exergetic efficiency, and beneficial system outputs of the integrated cycle and its sub-cycles are shown in Figs. 5, 6 and 7, respectively. The impact of the changing coal gasifier temperature on the energy efficiency, exergy efficiency, and system outputs of subsystems and the whole system are investigated. The effects of increased coal gasifier temperature on the energetic performance, exergy efficiency, and beneficial system outputs of the integrated system and its sub-parts are presented in Figs. 8, 9 10, respectively.
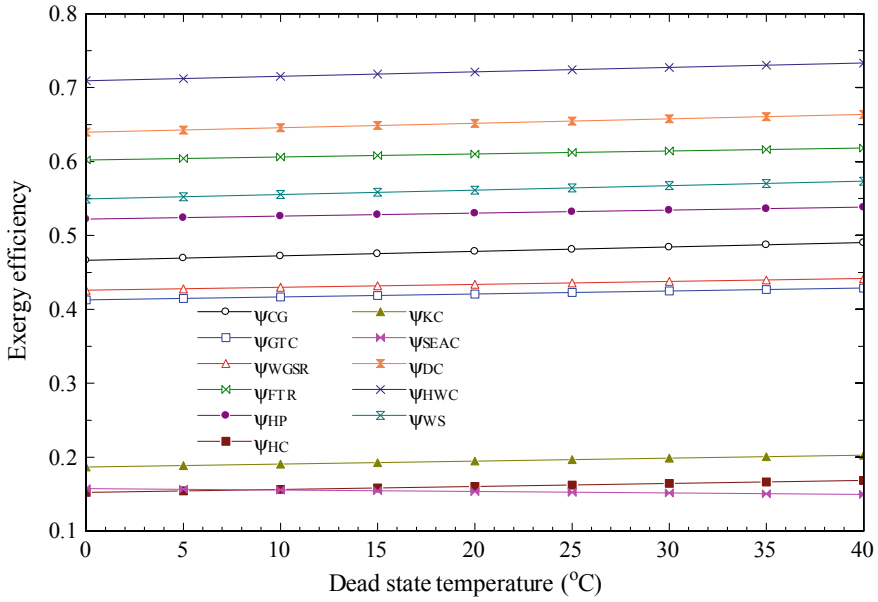
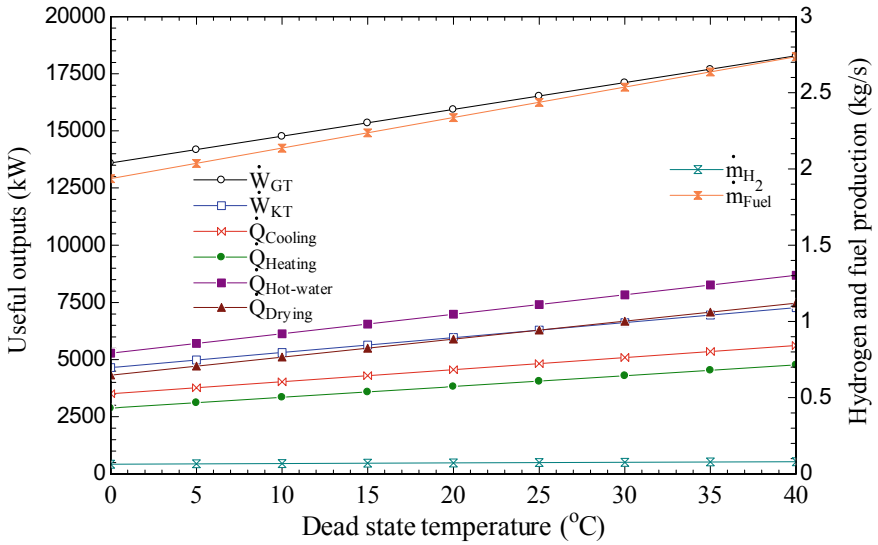**Fig. 3** Impacts of dead-state temperature on exergy efficiencies

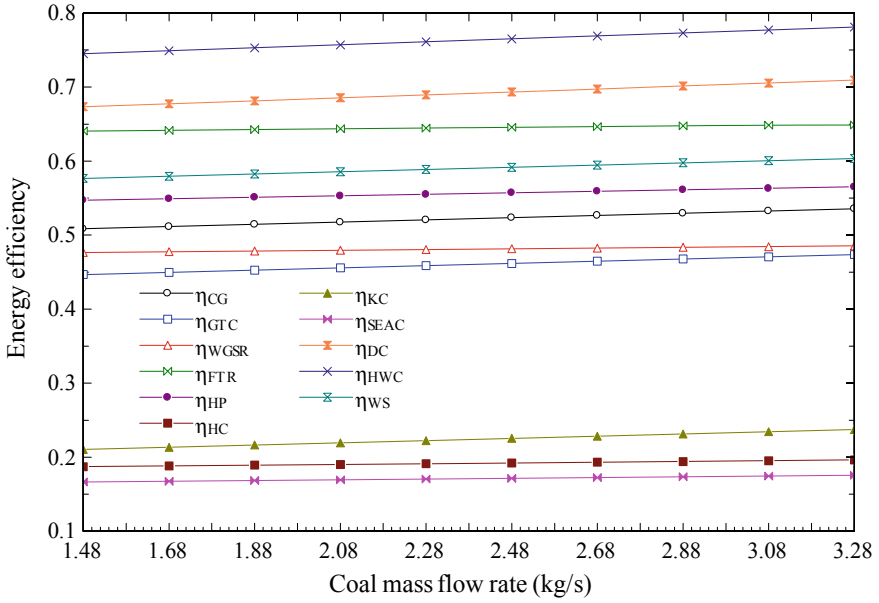**Fig. 4** Effects of dead-state temperature on useful outputs, hydrogen, and fuel production rate

Fig. 5 Effects of coal mass flow rate on energy efficiencies
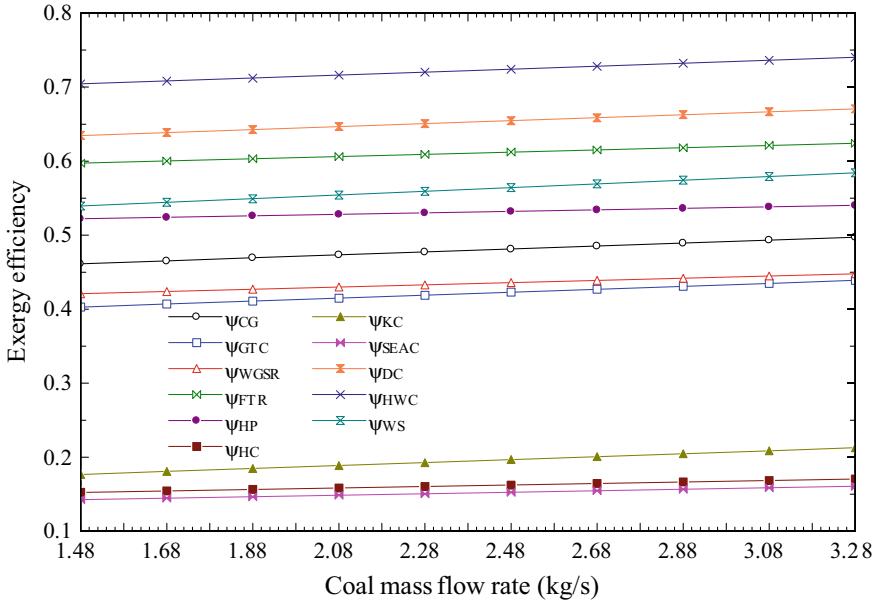

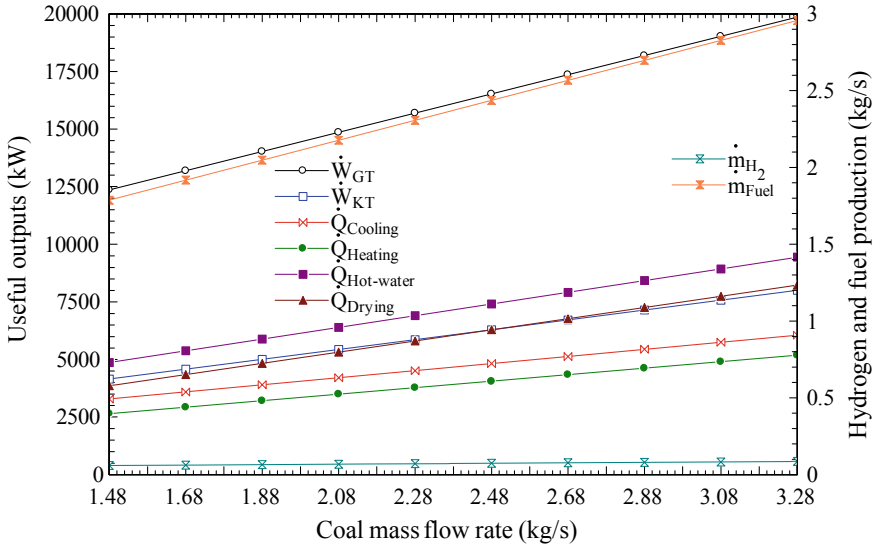**Fig. 6** Effects of coal mass flow rate on exergy efficiencies

Fig. 7 Effects of dead-state temperature on useful outputs, hydrogen, and fuel production rate

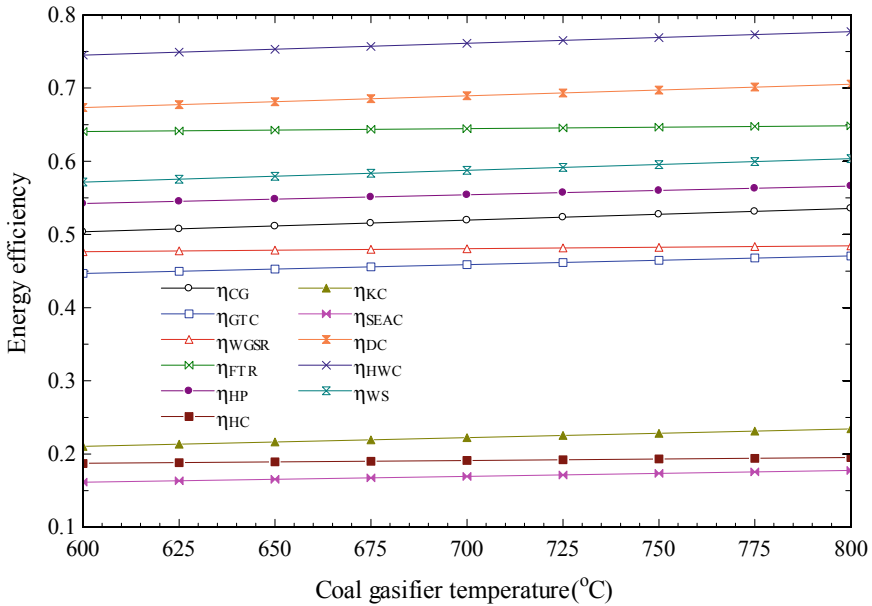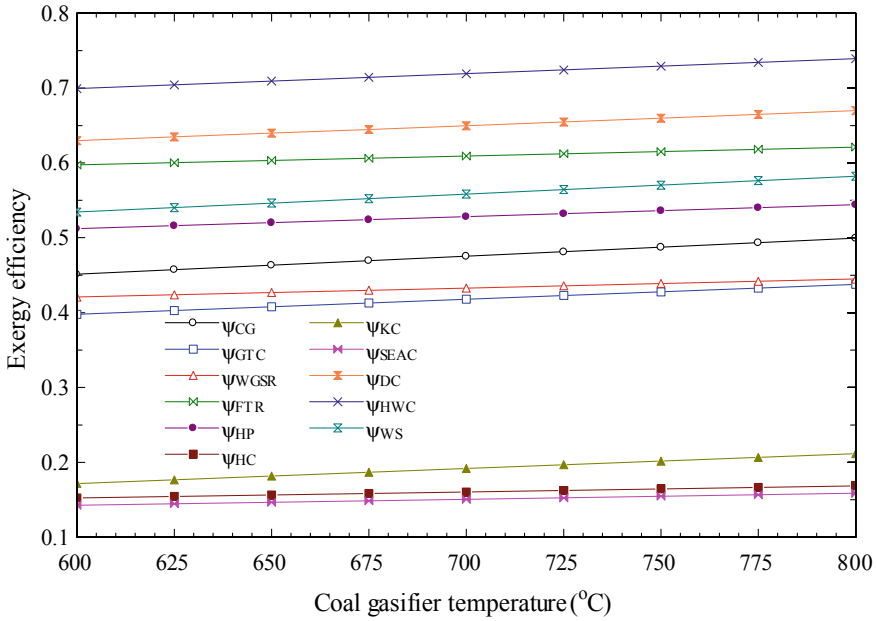**Fig. 8** Effects of coal gasifier temperature on energy efficiencies

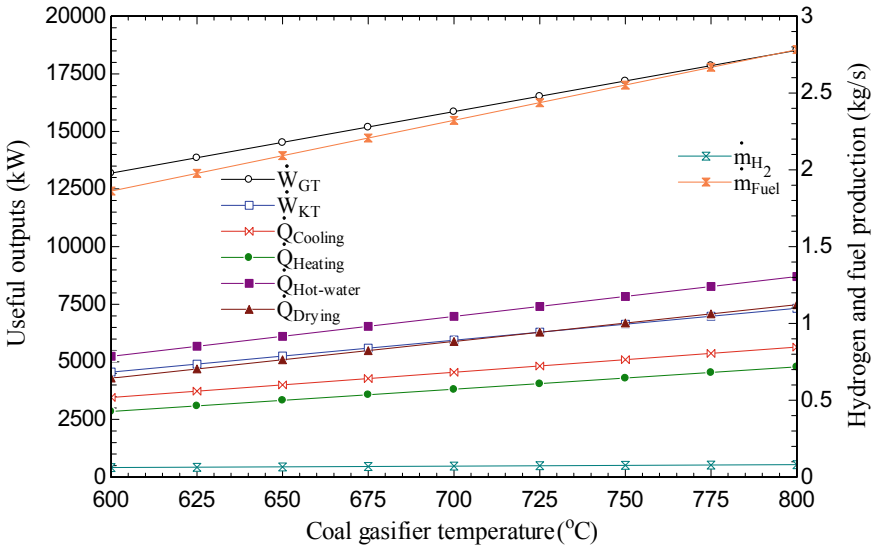**Fig. 9** Effects of coal gasifier temperature on exergy efficiencies

Fig. 10 Effects of coal gasifier temperature on useful outputs, hydrogen, and fuel generation rate
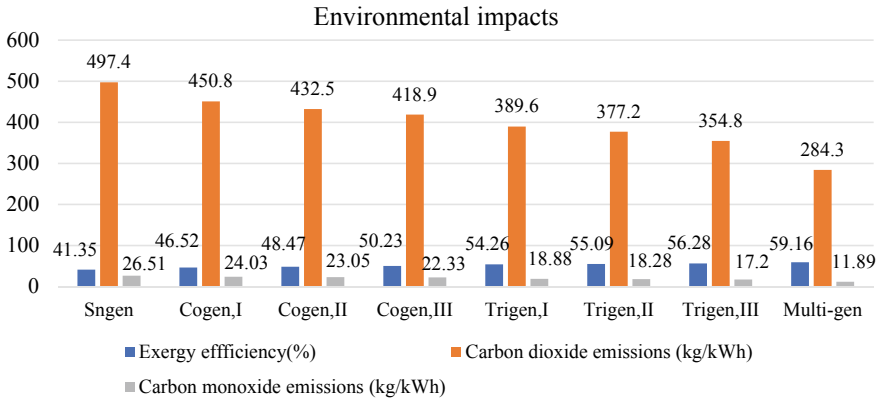
Fig. 11 Comparison of exergy efficiency, carbon dioxide, and carbon monoxide emissions of production system for coal gasification-based integrated system

4.1 Environmental Impact Results

Figure 11 presents a comparison of the exergy efficiency, and also the CO_2 and CO emissions of four production models for (i) power, (ii) power and heating, (iii) power, heating and cooling, and (iv) multigeneration cycles. It is seen that the multigeneration plant has less carbon dioxide emissions than other processes examined, and in addition to that provides an important motivation for the use of multigeneration cycles. It is also seen that the multigeneration process has higher energy and exergy efficiencies than other production processes. Another significant point is that the multigeneration plant has less CO emissions than other production plants, and this provides an important motivation for increasing the use of multigeneration plant. The amount of CO emission is significantly less than the carbon dioxide emission amount of the gasification cycle for multigeneration integrated system.

The effects of changing coal gasifier temperature on the CO_2 and CO emissions for the four production models are investigated. The effects of increased coal gasification temperature on the carbon dioxide and carbon monoxide emissions for the four production models are shown in Figs. 12 and 13, respectively. As seen in these figures, the carbon dioxide and carbon monoxide emissions decrease with the increasing coal gasification temperature from 600 to 800 °C.
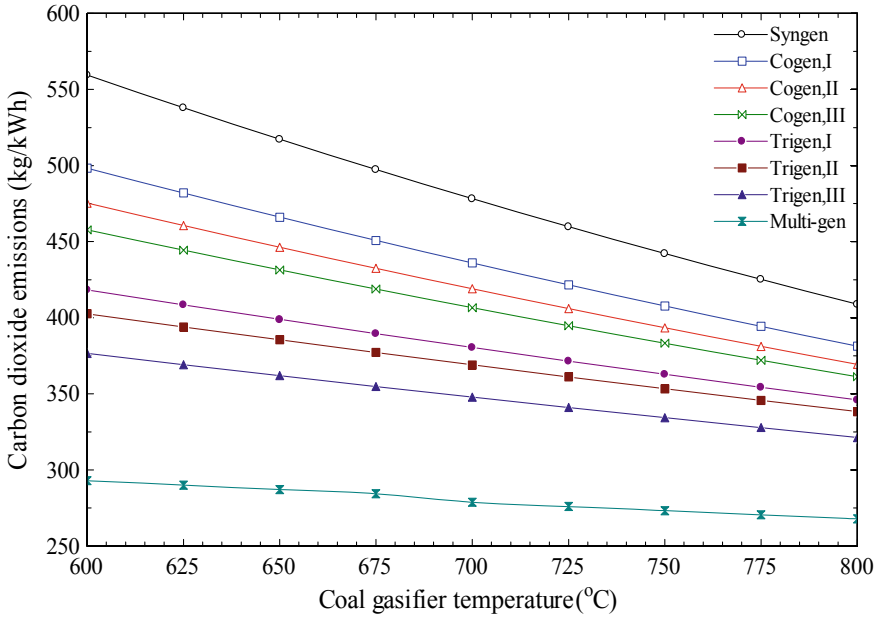
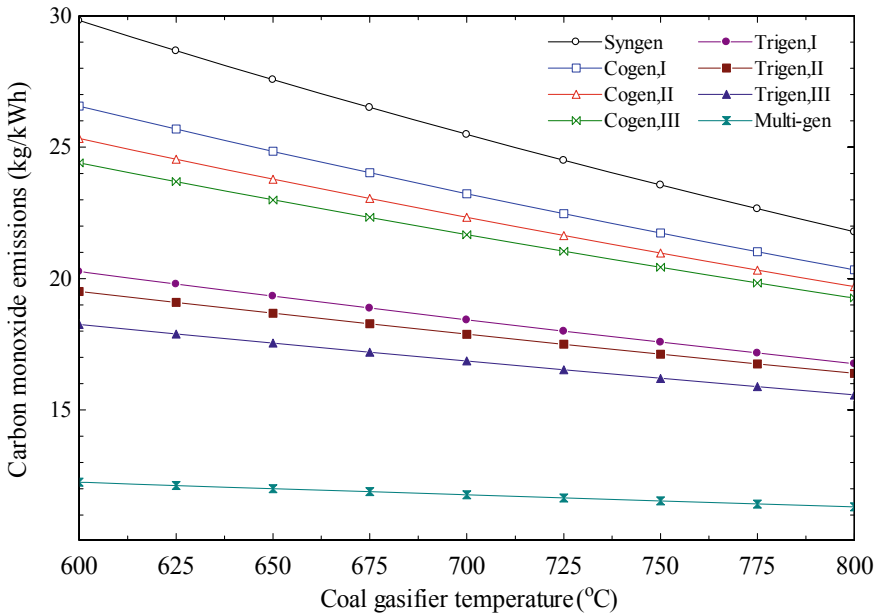**Fig. 12** Effects of coal gasifier temperature on carbon dioxide emissions

Fig. 13 Effects of coal gasifier temperature on carbon monoxide emissions

5 Conclusion

In this book chapter, comprehensive thermodynamic and environmental impact assessments are performed for multigeneration energy plant integrated with coal gasification. In this regard, energetic and exegertic performance, and also the environmental impact analyses are carried out for single production, cogeneration, trigeneration, and multigeneration. The effects of varying environmental and coal gasifier temperatures, as well as the coal mass flow rate on the performance and irreversibility rates of whole system and subsystems are investigated. Finally, the CO_2 and CO emissions of single generation, cogeneration, trigeneration, and multigeneration systems are examined and compared. Some prominent outcomes can be summarized as below:

- The whole combined energy system energetic and exergetic efficiencies are 59.16 and 56.43%, respectively
- The whole irreversibility rate of suggested plant is 70,243 kW. Also, the maximum exergy destruction ratio is shown in the coal gasifier with 25.97%, while the minimum exergy destruction rate is seen in the hot water production cycle with 3.33%.
- The produced electricity from the gas turbine and Kalina cycle are computed as 16,525 and 6288 kW, respectively.
- The cooling and heating loads are calculated as 4822 and 4057 kW, respectively.
- The hydrogen generation rate of the modeled plant is 0.074 kg/s.
- It can be concluded that multigenerational systems are better than other production systems (single, cogeneration, and trigeneration) in terms of their carbon dioxide and carbon monoxide emissions.

Finally, multigeneration energy systems are more advantageous in terms of both thermodynamic and environmental impact assessments. Also, in these systems, it is possible to achieve higher performance with various design variations.

References

1. Rosen MA, Dincer I (1997) On exergy and environmental impact. Int J Energy Res 21:643–654
2. Wall G, Gong M (2001) On exergy and sustainable development—Part 1: conditions and concepts. Exergy Int J 1(3):128–145p
3. Rosen MA, Dincer I (2003) Exergoeconomic analysis of power plants operating on various fuels. Appl Therm Eng 23:643–658
4. Bisio G (1998) Thermodynamic analysis of the main devices for thermal energy upgrading. Energy Conversion Manage 39(3/4):229–242
5. Koroneos C, Spachos T, Moussiopoulos N (2003) Exergy analysis of renewable energy sources. Renew Energy 28:295–310
6. Rosen MA, Dincer I (2004) Effect of varying dead-state properties on energy and exergy analyses of thermal systems. Int J Therm Sci 43:121–133
7. Yuksel YE, Ozturk M (2016) Energy and exergy analyses of an integrated solar and biomass-assisted multi-generation system with hydrogen production. Int J Exergy 20(2):203–235

8. Ozturk M, Dincer I (2013) Thermodynamic analysis of a solar-based multi-generation system with hydrogen production. Appl Therm Eng 51(1–2):1235–1244
9. Self SJ, Reddy BV, Rosen MA (2012) Review of underground coal gasification technologies and carbon capture. Int J Energy Environ Eng 3:16
10. Miller, B.G., 2005. Coal Energy Systems. Academic Press, 1st Edition
11. Gandia LM, Arzamendi G, Dieguez PM (2013) Renewable hydrogen technologies production, purification, storage, application and safety. Elsevier
12. Moghimi M, Emadi M, Ahmadi P, Moghadasi H (2018) 4E analysis and multi-objective optimization of a CCHP cycle based on gas turbine and ejector refrigeration. Appl Therm Eng 141:516–530
13. Ahmadi P, Rosen MA, Dincer I (2012) Multi-objective exergy-based optimization of a poly-generation energy system using an evolutionary algorithm. Energy 46(1):21–31
14. Ghorbani B, Mehrpooya M, Sadeghzadeh M (2018) Developing a tri-generation system of power, heating, and freshwater (for an industrial town) by using solar flat plate collectors, multi-stage desalination unit, and Kalina power generation cycle. Energy Convers Manag 165:113–126
15. Dincer I, Rosen MA, Ahmadi P (2017) Optimization of energy systems. Wiley
16. Akrami E, Chitsaz A, Nami H, Mahmoudi SMS (2017) Energetic and exergoeconomic assessment of a multi-generation energy system based on indirect use of geothermal energy. Energy 124:625–639
17. Yilmaz F, Ozturk M, Selbas R (2019) Design and thermodynamic analysis of coal-gasification assisted multigeneration system with hydrogen production and liquefaction. Energy Convers Manag 186:229–240
18. Callaghan CA (2006) Kinetics and catalysis of the water-gas-shift reaction: a microkinetic and graph theoretic approach. Worcester Polytechnic Institute
19. Dincer I, Rosen MA (2012) Exergy: energy, environment and sustainable development. Elsevier

A Novel Multigeneration Energy System for a Sustainable Community

Reza Alizade Evrin and Ibrahim Dincer

Abstract In this study, we propose and discuss an integrated system that consists of a novel configuration of six subsystems. The proposed system is developed and analysed thermodynamically through energy and exergy approaches. The presented multigeneration energy system is developed for a sustainable community that allows a wide range of conservation and production approaches. The system includes a thermal energy storage system, an absorption cooling refrigeration system, a geothermal steam power plant, a solar photovoltaic/thermal (PV/T) system, wind turbines, a heat pump and a hydrogen storage system. The renewable energy sources considered in this integrated system are geothermal, solar and wind. The proposed multigenerational system can provide five commodities, namely hot water, hydrogen, electricity, heating and cooling. To achieve the zero-energy community (ZEC) concept, the average goal should be in step-by-step fashion. While phase setting is very important in terms of energy, it provides the flexibility to develop an approach to the zero-energy base community, which suggests that energy solutions need to be balanced with budgets. The phase difference extends to the annual cycle. As an example, zero energy approach allows the community to generate additional PV production. This novel multigeneration system has overall energy and exergy efficiencies of 62.5% and 47.3%, respectively.

Keywords Sustainable community · Solar energy · Hydrogen · Energy · Exergy · Efficiency

Nomenclature

$\dot{Ex}$ Exergy rate (kW)

R. A. Evrin (✉) · I. Dincer
Faculty of Engineering and Applied Science, University of Ontario Institute of Technology, 2000 Simcoe Street North, Oshawa, ON L1H 7K4, Canada
e-mail: Reza.Mohammadalizadeh@uoit.net

I. Dincer
e-mail: Ibrahim.Dincer@uoit.ca

ex   Specific exergy (kJ/kg)
$\dot{Ex}_d$ Exergy destruction rate (kW)
h   Enthalpy (kJ/kg)
$\dot{m}$ Mass flow rate (kg/s)
P   Pressure (P)
$\dot{Q}$ Heat rate (kW)
s   Specific entropy (kJ/kg K)
T   Temperature (K)
V   Velocity (m/s)
$\dot{W}$ Work rate (kW)

Greek Letters

η_{en} Energy efficiency
η_{ex} Exergy efficiency
$\boldsymbol{\rho}$ Density (kg/m^3)

Acronyms and Abbreviations

act   Actual
G   Generator
P   Pump
RC   Rankine cycle
LH$_2$ Liquid hydrogen
SOFC   Solid oxide fuel cell
GFE   Gibbs free energy
N   Number of cells in series
LHV   Low heat value
HHV   High heat value
PV/T   Photovoltaic thermal
COP   Coefficient of performance
C   Compressor
EES   Engineering equation solver
TES   Thermal energy storage
FC   Fuel cell
PA   Pump A
PB   Pump B
PEME   Polymer electrolyte membrane electrolysis
GDP   Gross domestic product
GHG   Greenhouse gas
HEXA   Heat exchanger A

HEXD   Heat exchanger D
HS   Heat storage
OWV   One-way valve
EV   Evaporator A
G   Generator
CA   Condenser A
T   Turbine
EVA   Expansion valve A
EVB   Expansion valve B
WVC   Three-way valve C
WVD   Three-way valve D
CAV   Compressed air vehicle

1 Introduction

The world's population and, consequently, demand for energy are increasing while conventional energy sources are being depleted. Meanwhile, the growing alarm related to global warming and increase in the earth's temperature signifies the necessity of a long-term solution for the sustainable development of energy. As seen in Fig. 1, 81% of the world's primary energy is currently supplied from fossil fuels (World energy outlook 2017). Of this, 32% pertains to oil, which is still the largest primary fuel for transportation. Towards the end of 2017, the Government of Canada set an ambitious reduction target to cut greenhouse gas (GHG) emissions by 40% by 2030 and by 80% by 2050, relative to 2005 levels [1].
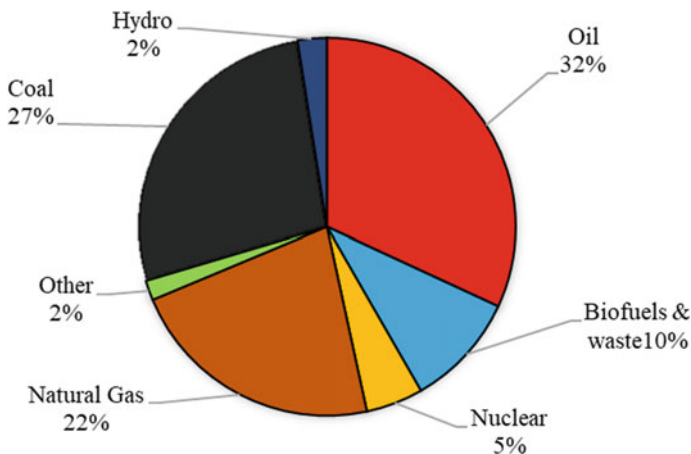

Fig. 1 World's primary energy supply by source IEA 2018

Fossil fuels, which remain the main source of energy for offsetting growing energy consumption, raise several concerns, as mentioned above. Although some technologies are developed for the more sustainable conversion and consumption of fossil fuels, this temporary strategy does not meet the ultimate goals of long-term sustainable development in the context of energy. As a result, as a long-term approach, sustainable energy using renewable sources needs to be developed and well established in the source, system, and service sectors for more efficient and environmentally benign energy systems and reduction of emissions. Alternative fuels play an important role in this approach. Sustainable energy production is based on clean, uncontaminated resources. The main sources of energy for sustainable and clean energy production are solar, hydro, thermal ocean, tidal, wind, biomass and geothermal. These resources can be used to produce clean energy as well as hydrogen. Renewable electricity now constitutes 25% of total power generation worldwide (IEA 2018).

Electricity generation infrastructure in Canada is greatly beneficial to the expansion of sustainable resources. Canada is considered unique in the world of hydropower, sharing 60% of its electricity generation. Nuclear energy, considered a controversial but clean electricity generating technology, constitutes 15% of Canada's electricity production. Other renewable resources (wind, biomass and solar) account for about 2% of the total. It can therefore be concluded that approximately 77% of Canada's electricity comes from a sustainable energy source. Figure 1 depicts Canada's energy production by type of energy source. Hydropower boasts a 95% share in Quebec, but is as important as 28% in Ontario, where nuclear power, with a 45% share, is the most important.

With regard to GHG emissions, two main sectors in Canada are primarily responsible, namely the industrial (with 51%) and the transportation sectors (with 35%), as illustrated in Fig. 2. Thus, it is important to find ways to reduce GHG emissions in these two sectors. Of the two, the transportation sector appears the most challenging to convert to clean energy sources because power generation for vehicle propulsion poses important technical problems regarding the carrying on board of non-polluting energy storage, such as hydrogen or electricity. The transportation sector is Canada

Fig. 2 Electricity generation in Canada per source type, as per cent of total (data from [1])
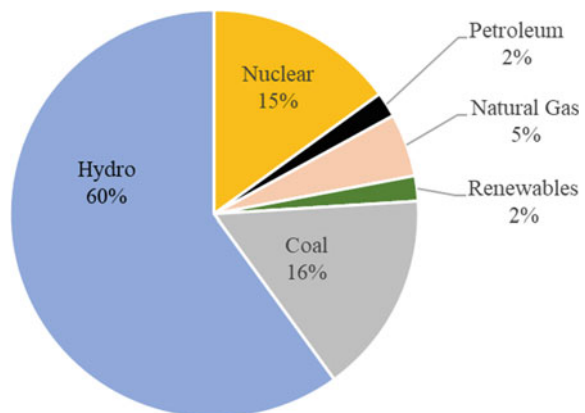
which is mostly based on vehicles using fossil fuel, that is, gasoline and diesel. The rationale behind compressed air vehicle technology development is sustained by two points that result from the above discussion.

Per number of inhabitants, as the number one country in hydropower generation, Canada possesses larger amounts of renewable electricity than any other country. The general aim of the present work is to advance a solution that can lead to important reductions in GHG emissions in Canada's transportation sector, which is the second largest contributor to pollution. In essence, this work proposes using the existing infrastructure for power generation and distribution to produce a zero-emission energy carrier for the transport sector (Fig. 3).

Renewable fuels are basically those fuels made from renewable sources that can be constantly replenished by nature. The main renewable materials for this kind of fuel are biomass and water, which can be found in nature. Biomass is the main source for biofuels such as bioethanol, biodiesel and also hydrogen-rich gas (syngas), while water is the main source for hydrogen production as a carbon-free fuel. Some fuels such as ammonia, which is also a carbon-free fuel, can be produced as a secondary product of renewable sources. In addition, renewable energy sources, such as solar, wind, sunlight, tides and geothermal heat, are constantly reproduced in a human life timescale. Renewable energy can be a promising alternative for fossil fuels in many different areas, such as EVs, ICEs, power plants and thermal applications. Biofuel is a liquid fuel composed of mono-alkyl esters of long-chain fatty acids obtained from bio-based materials such as animal fats or lignocellulosic biomass. The common types of biofuels are bioethanol, bio-methanol, biogas, syngas, biodiesel and biohydrogen. Application of biofuels, which results in lower emissions and fewer carbon footprints in their life cycle, is considered as a safe and clean fuel for the energy and transportation sectors. As seen in Fig. 4, biofuels are basically categorized in four generations based on the feedstock of which they are made.
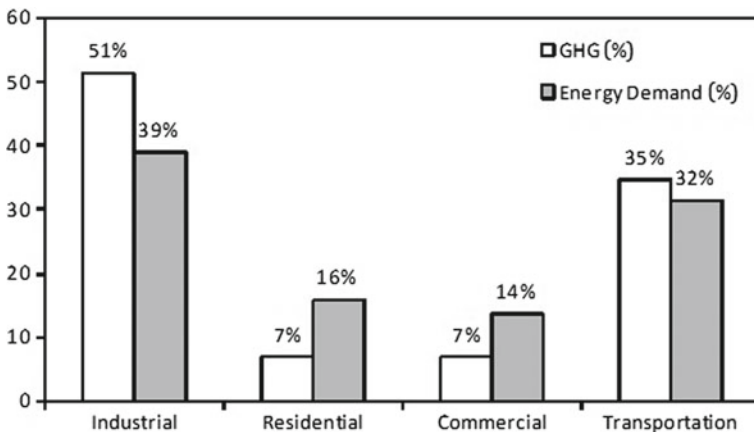

Fig. 3 Energy demand and greenhouse gas emissions in Canada by sectors (data from [1])
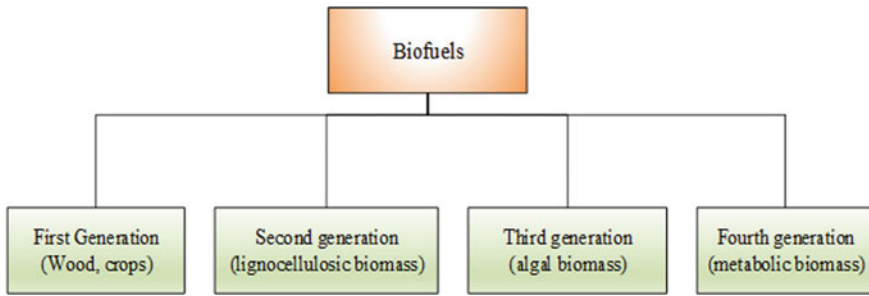
Fig. 4 Main types of biofuels categorized by their feedstock

The first generation of biofuels are made from edible food crops such as canola, corn, wheat and straw. The second generation, which are made of lignocellulosic biomass as agricultural wastes or municipal solid waste, have a lignocellulosic structure. The term lignocellulosic means that they have been constituted via integrating biopolymers of lignin, cellulose and hemicellulose. The main problem associated with second generation, especially agricultural waste, is the conflict of their production with the food chain. However, the second generation of biofuels can be used directly in diesel engines or be added to gasoline as an additive for better combustion and avoiding NO_x. The third generation of biofuels are those fuels that are made of algal biomass, such as microalgae and macroalgae. Algae has the advantage of needing less water for growth and of also not being involved in the food chain. However, the volatile matter of algae, which is less than agricultural waste, usually gains a lower yield of biofuel. While fourth-generation biofuels are defined in different ways in the literature, Lu defined them as a product of metabolic engineering of algae for producing biofuels from oxygenic photosynthetic organisms.

In addition to biomass, solar energy is one of the most important renewable energy sources on the planet. Solar energy generation utilizes solar energy to supply hot water through solar systems or electricity through solar photovoltaics (PV), which are commonly used in home applications. PV cells are devices that convert sunlight or solar energy to galvanic electricity. The main part of the PV system is the PV cell. Solar cells are semiconductor devices that convert solar energy into DC electricity.

Carbon-free fuels are basically fuelling with no carbon in the molecular structure or no carbon emissions in the exhaust gas when burned. Non-carbon fuels are considered to be one of the major solutions to global warming and climate change. These fuels can be used in an efficient and competitive way compared to conventional fuels by making minor modifications to the ICE. Hydrogen, ammonia and nuclear fuel are prime examples of such fuels. Hydrogen is a promising energy carrier and has all the potential to replace fossil fuels. Combustion produces only heat and water without harmful combustion gases. In addition to burning hydrogen, hydrogen can be used in fuel cells that produce electricity by electrochemically reacting with oxygen. More research and development are needed in the field of hydrogen production, use and storage so that hydrogen can be used for future fuels and potentials that can be carried

out environmentally efficiently while meeting sustainability measurements. The high conversion efficiency of the fuel cell can reach up to 60%, while the high efficiency of the electric motor can reach up to 90%, facilitating the combination of a fuel cell and electric motor in a highly efficient combination of ICE efficiency. In addition, gaseous hydrogen can overcome the problem of using liquid fuels in the combustion process of ICE, such as cold quenching, steam lock, poor mixing and improper evaporation. However, several disadvantages can affect the potential of hydrogen as a fuel. As an example, it is not currently possible to apply a global hydrogen economy. There is insufficient hydrogen supply infrastructure to ensure hydrogen use safety due to low volatility and a low flash point when equipped with adequate infrastructure. Hydrogen has a lower volumetric energy density than gasoline. Thus, a large amount of hydrogen is required for its storage. In any case, storing hydrogen in a compressed gas or compressed liquefaction state is not entirely satisfactory and must be further improved and researched.

Ammonia has the potential to replace hydrogen with clean fuel for several reasons. The cost per volume for storing ammonia as an energy source is three times lower than the cost for storing hydrogen. It is possible to supply large volumes of ammonia distribution infrastructure. Ammonia can store hydrogen at 20 °C and 8.7 bar. In addition, since the energy content of ammonia is similar to the energy content of gasoline, it is a convenient alternative to gasoline for vehicles. Using ammonia as a clean energy source is convenient because it can burn environmentally. Due to its high-octane number, it can be efficiently carried out in ICE and is dispersed rapidly into the air due to its light density. Leakage can be detected quickly by the nose, even at concentrations as low as 5 ppm.

The chart illustrated in Fig. 5, which presents the amount of energy consumed in the average Canadian household, is divided into five areas: space heating 63%; water
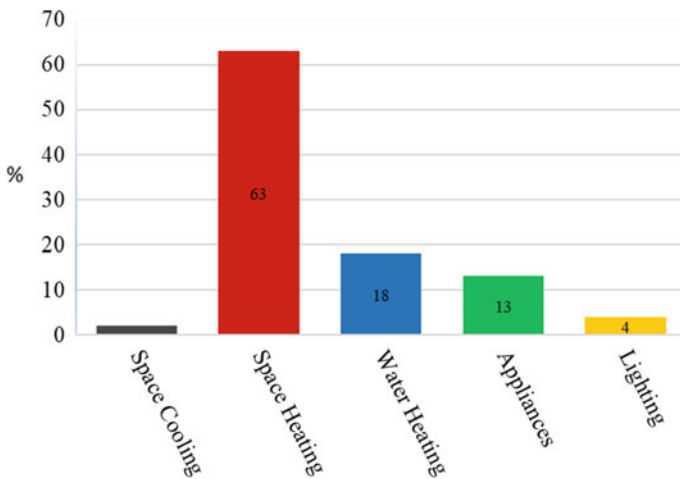

Fig. 5 Energy used by a Canadian household, distribution of residential energy use in Canada (data from [1])

heating 18%; appliances 13%; lighting 4%; and space cooling 2%. Heating habits can affect energy consumption. The effect of cold weather on the heating system is clearly understandable.

Figure 6 shows Canadian household energy use with a breakdown of water heating that is divided into six sections: faucets 34%; showers 25%; baths 17%; laundry 15%; dishwashing 4%; and leaks 5%. In 1999, Canada's per capita water consumption was estimated at 343 l, an increase from 327 l in 1996, but lower than the 1989 amount of 347 L per person in a day (Environment Canada 2014). Most applied studies on energy consumption are related to the heating of water from electric heaters. However, the cost of accessing hot water depends on the type of fuel and hot water system (Table 1).

The main demand for energy, which is increasing significantly throughout the globe, is set to be covered by fossil fuels. However, these fossil fuels carry the drawback of global warming. Thus, most research studies focus on renewable energy sources and integrating these sources with different energy systems for multigeneration purposes [2]. With increasing energy demands and the threat of climate change
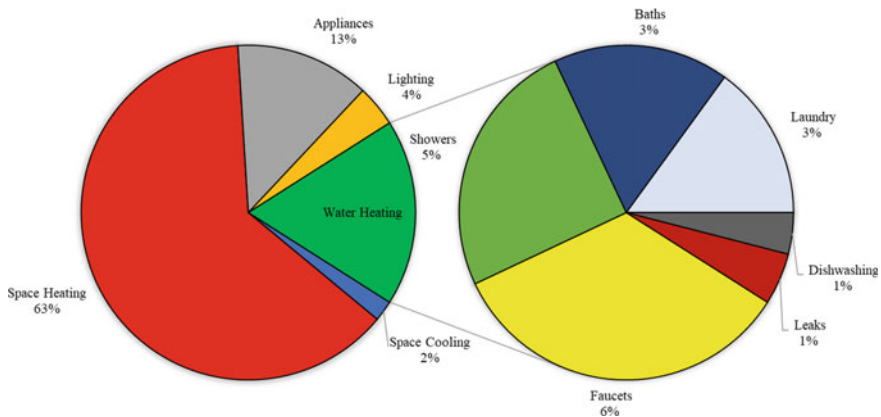
Fig. 6 Canadian household energy use with breakdown of water heating

Table 1 Canadian daily residential per capita water use (data from [1])

Category	Per capita hot water use (litres/day)	Per cent of total hot water use in each category (%)
Faucets	23.6	34
Showers	17.3	25
Baths	11.8	17
Laundry	10.4	15
Dishwashing	2.8	4
Leaks	3.5	5
Indoor Total	69.3	100

resulting from existing fossil fuel-based energy systems, the development of efficient renewable energy systems is a present imperative need. Sustainable communities are expected to include district energy, renewables, wastewater treatment, solid waste management and food production. Ahmadi et al. [3, 4] developed an integrated energy system to enable a village to benefit from various renewable resources with energy storage options in order to meet multiple energy demands, such as home lighting, cooking and community refrigeration. Ozcan and Dincer [5] introduced a system that works with geothermal, solar and wind energy sources. The input energy from renewable sources is converted to heat, cold and electricity for buildings, where each building is connected to an integrated system. Ghosh and Dincer [6] developed an integrated system that employs a solar energy subsystem and produces multiple outputs with high efficiency, low cost and reduced environmental impact. Ratlamwala et al. [7] studied the effects of various parameters of solar PV/T on the heat and power, energy and exergy efficiency of an absorption cooling system, hydrogen production and energy ratio of energy and COP. Yilmaz et al. [8] designed and thermodynamically analysed a new solar energy-assisted generation system. The system is designed to perform heating, cooling, drying, hydrogen and power generation with a single energy input.

Hassoun and Dincer [9] studied a zero-energy house that significantly reduced energy demand by increasing efficiency so that the residual energy demand was met by a renewable energy system that supplies electricity, hot water and seasonal heating and cooling. Zamfirescu and Dincer [10] developed the concept of renewable energy-based multigeneration options based on renewable energy to produce many products such as power, heat, hot water, cooling, hydrogen and freshwater. These multigeneration options obviously improve system performance and reduce environmental impact. The system proposed by Jana et al. [11] incorporated the good concept of integrating multiple utility outputs to achieve a more efficient system. After cogeneration and triple power generation, polygonal formation appears as a sustainable solution with optimal resource utilization, better efficiency and environmental friendliness. Shimizu et al. [12] proposed a method to design a regional energy cooperative network in a way that combines new technologies for heat and power. This method consists of six steps, including the creation of various technology options, energy balance modelling of demand and supply and multiobjective evaluation and optimization. Choi et al. [13] presented a kW-class electrochemical reactor for hydrogen production that was developed by using a bipolar plate. A large-area electrode was fabricated, and a particle electrode manufacturing method was introduced. Hashimoto et al. [14] built a catalyst and industrial scale test plant for an energy-saving cathode for hydrogen production, an anode for O_2 evolution without chlorine production in seawater electrolysis, and methanation of CO_2 by reaction with H_2. McIntyre [15] evaluated Guelph's solar energy potential as an array of grid-coupled, rooftop solar PVs and hot water panels. The concept, method and implementation of a calculator for a lively long-term analysis of residential settlement structures were introduced by Stoeglehner et al. [16]. Meanwhile, Rehkopf et al. [17] investigated the overall social impact of the Residential Energy Efficiency

Project House for sustainable living in Kitchener, Canada. Dampier et al. [18] established that they represent community spending under the coal scenario. The value was then adjusted to indicate community spending under shutdown and biomass scenarios. Examples of onshore wind energy are described and applied by Heinbach et al. [19]. The implementation of the model for the average model autonomy is then explained as a basis for calculating the model results. Three examples were evaluated to confirm the performance of the proposed method by Jafari et al. [20]. In the first case study, the microgrid is isolated from the grid. In the second case study, in grid connection mode, the hybrid method is compared with the wavelet transform uncertainty prediction method. Institutional, financial and technological capacities for long-term sustainability have found that communities can be achieved through community involvement from an early stage, while allowing the freedom to develop governance procedures. At the same time, clarified roles and responsibilities were provided by Katre et al. [21].

The objective of the present study is to conduct a comprehensive thermodynamic analysis of a novel multigenerational energy system for a sustainable community. The specific objectives are as follows:

- To develop a new configuration of a sustainable community for analysis and assessment
- To design thermal storage systems suitable for the various seasons
- To investigate the thermodynamic limits and propose conceptual solutions for heating and cooling during the various seasons
- To conduct energy and exergy analyses on the proposed system and to study energy and exergy efficiencies.

2 System Description

In the proposed energy system, renewable energy sources, such as wind, solar and geothermal, are integrated. The present system (see Fig. 11) includes thermal energy storage, absorption, cooling, refrigeration, a geothermal steam power plant, solar PV/T, wind turbines, a heat pump and a hydrogen storage system. In the boiler, heat is transferred from geothermal steam. The exhaust stream of the turbine is utilized for water heating through a heat exchanger and then stored in thermal energy storage (TES). The heat pump will utilize the TES heat as required. Water enters the turbine at a relatively high temperature and pressure at State point 8 and exits at a comparatively medium temperature and low pressure at State point 7. At Points 1 and 25 in Fig. 11, geothermal and solar hot water enters the proposed system.

The steam is heated by the boiler at Points 3 and 8 and then arrives at the generator where the heat is transmitted to a H_2O–LiBr liquid. The produced vapours then pass over the absorber, an expansion valve and the heat exchanger at State points of 10, 11 and 13, respectively. The heat that is transferred from Point 9–14 increases the H_2O–LiBr solution temperature. These vapours, which reach the condenser at State

point 15, transfer their heat to the cooler and convert to water again. This water leaves as liquid through the condenser via stream 16 and then proceeds through the expansion valve, which results in decreased temperature and pressure. This chilled water then reaches the evaporator through Stream 17 and converts into vapour again by absorbing the cooling load. It is later mixed with a weak solution of $LiBr_2$ and moves towards the generator via the heat exchanger. The compressor compresses the working fluid, and the condenser transfers the required amount of heat to the fluid at State point 29. The expansion valve releases the fluid to the evaporator (Fig. 7).

In this study, the Rankine cycle consists of four stages: compression, boiling, turbine and condensation expansion. The binary steam cycle is defined as a power cycle, which is a combination of two cycles of thermodynamics in the cold and hot zones. Geothermal energy, the power that comes from the heat of the earth, has been used in cooking and heating for thousands of years in many countries. This heat energy is contained in rocks and liquids under the earth's crust. It can be found in shallow ground up to several miles and is far away from the very hot molten rocks known as magma. It is possible to tap the steam and hot water in underground storage facilities to generate electricity or to directly heat or cool buildings. A geothermal heat pump system can utilize 10 feet (3 m) of constant temperature on the Earth's
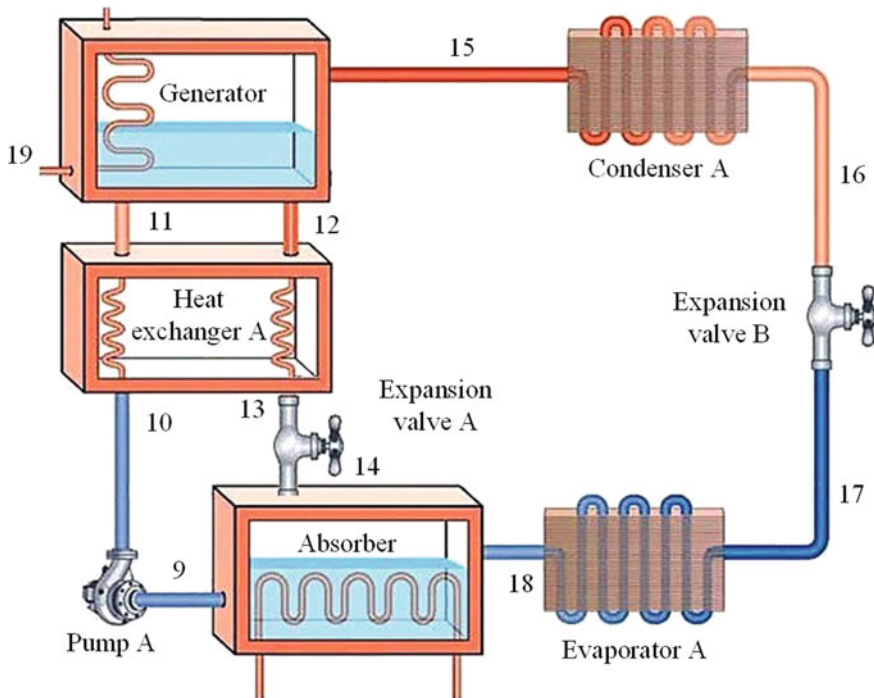

Fig. 7 Simplified diagram of a single-effect H_2O–LiBr absorption cycle

surface to warm a house in winter, or remove heat from the building and return it to a relatively cool floor in summer.

Geothermal water from deeper parts of the earth can be used directly to heat homes and offices or for plants that grow in greenhouses. In some US cities, snow melts into the geothermal hot water beneath the roads and sidewalks. Utilizing steam and hot water to drive a turbine connected to an electric generator, an underground reservoir drilled a well over 1.6 km deep to produce geothermal electricity. The first geothermal electricity was produced in 1904 in Larderello, Italy.

There are three types of geothermal power plants: dry steam, flash and binary. Dry steam, the oldest geothermal technology, is used to extract steam from fractures in the ground and drive turbines directly. Flash plants draw deep, high-pressure hot water into cold low-pressure water. The steam generated in this process is used to drive the turbine. In a binary plant, hot water passes through a secondary fluid with a much lower boiling point than water. This causes the secondary fluid to become steam and the turbine to operate. In the future, most geothermal power plants will be dual plants.

The thermal energy of solar energy can be utilized in two ways. Low-temperature and high-temperature applications are also called concentrated solar energy. Photovoltaic, photovoltaic and bio-photolysis are considered to be low-temperature applications, while solar haemolysis, solar thermochemical cycles, solar gasification, solar modification and solar decomposition are applications of high-temperature condensed solar energy. Intensive solar energy can also be used to produce steam, which can then be used to produce electricity using steam power. The electricity produced can be used to produce hydrogen through electrolysis. In this communication, the above method is only considered in solar applications. The sun only shines during the day and varies depending on regains. Thus, the wind, which blows intermittently and is seasonally variable, does not always blow when energy is needed. Since solar and wind work together with good efficiency in most areas of world, developing a hybrid solar/wind project has the good advantage of the power-generating strengths of each of these two technologies as an effective replacement for fossil fuels.

Solar electric energy generation generates heat by concentrating light from the sun, which generates electricity by turning the generator into electricity by starting the heat engine. The working fluid heated by concentrated sunlight can be liquid or gas. Other working fluids include water, oil, salt, air, nitrogen and helium. In contrast, photovoltaic or PV energy conversion converts solar energy directly into electricity. In other words, solar panels are only effective during the daytime. Heat storage is a much easier and more efficient way to make solar energy a very attractive method of producing large-scale energy (Fig. 8). Heat can be stored during the day and converted to electricity at night. Solar power plants with storage capacity can dramatically improve economic efficiency and solar power generation capability.

Over the last decade, wind energy applications have been developed and expanded for industrial use in some European countries, including Germany, Denmark and Spain. The success of wind power has encouraged other countries to consider wind power as a component of the power generation system. Being both clean and renewable, in some cases the economic features of wind energy are drawing attention from
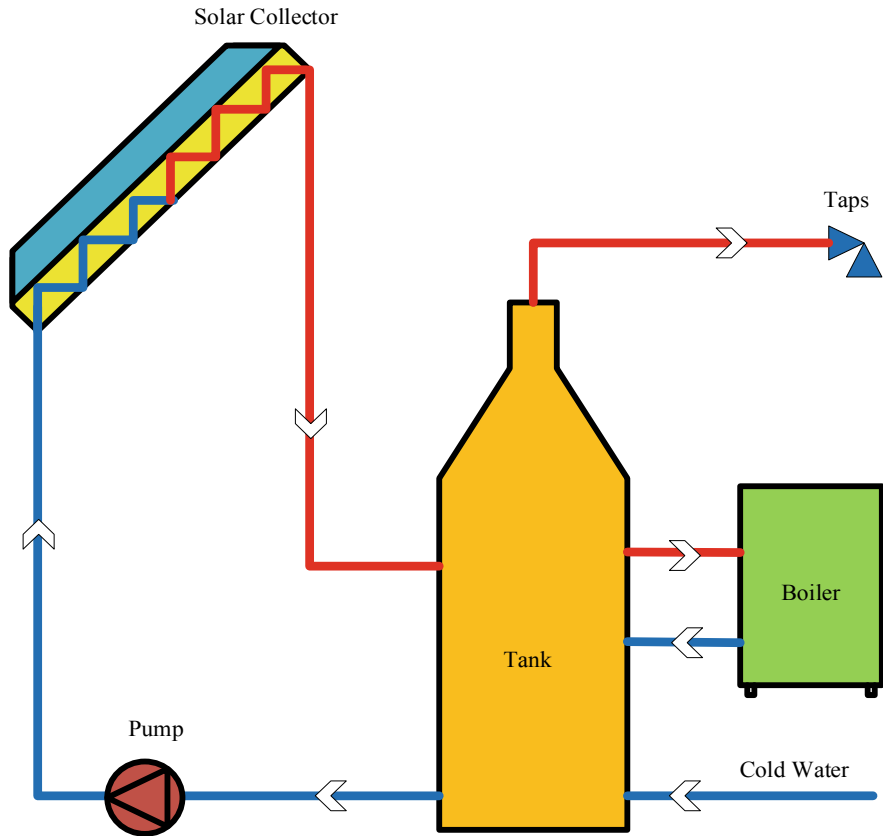
Fig. 8 Solar thermal energy collector

politics, businesses and individuals. Usage has increased due to the development of wind turbine technology. Wind turbine rotor efficiency increased from 35% to 40% in the early 1980s to 48% in the mid-1990s. In addition, the technical availability of these systems has increased to 98%.

Although turbine technology for wind power generation is developing rapidly, it is necessary from a scientific point of view to accurately assess wind behavior. Some of the thermodynamic properties of wind energy have not yet been clearly understood. The power factor of a wind turbine is often described by its efficiency. However, there are difficulties associated with this definition. The efficiency of the wind turbine can be regarded as a ratio of the wind power to the electricity generated in the area swept by the wind turbine. This definition only considers kinetic energy elements of wind. Other components, such as temperature differences, pressure effects and wind characteristics, are ignored. Solar panels produce electricity from sunlight, but

Fig. 9 Polymer electrolyte membrane electrolysis

are also heated under sunlight. However, this wasted heat can be very useful. 'PV-Thermal' or 'PVT' systems produce electricity from sunlight while simultaneously using excessive heat to generate hot water or hot air (Fig. 9).

The advantage of a PVT system is that it produces 20–40% more energy per square metre than a separate PV panel and solar collector depending on size, while the cost of production and installation is lowered by integrating the tw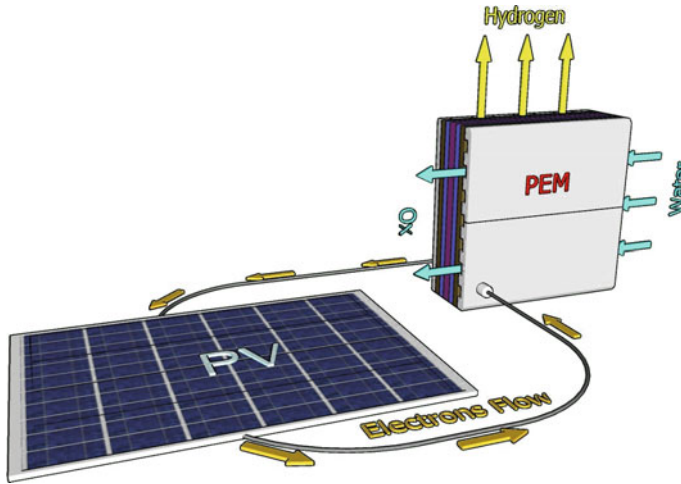o technologies into one. In addition, only one vendor is required, greatly simplifying the deployment preparation and responsibilities of a system once installed. Potential markets are comparable in size to solar collectors. The PVT roadmap describes the latest technology in PVT technology and provides an overview of the commercially available systems and the current and future market for this technology. It also identifies the benefits of technology for the various market players (manufacturers, policy makers, installers, builders and energy consultants) needed to drive successful PVT systems to large-scale market adoption. The point of interest is to create an optimized system through certification, subsidy rules and building regulations, plug and play design, development of design tools and a combination of PVT and other technologies (Fig. 10).

The water is injected into the ground at Stage 19 and then enters the boiler in Step 1. After giving the heat energy to the boiler, the water enters the chiller in Step 2. The remainder of the heat energy is absorbed by the chiller. A concentrated solution of lithium bromide can be used for the absorbent. Since water is very soluble in lithium bromide, a water–lithium bromide solution is formed. This solution is pumped to the generator at Stage 9. Water as a refrigerant is erupted at Stage 17 to a vaporizer with very low pressure and temperature. Since there is a very low pressure inside the evaporator, the water is in both liquid and vapour states. This water refrigerant cools the material and completely evaporates then, in Step 18, enters the absorber. Heat is supplied to the refrigerant water, and the lithium bromide solution in the generator
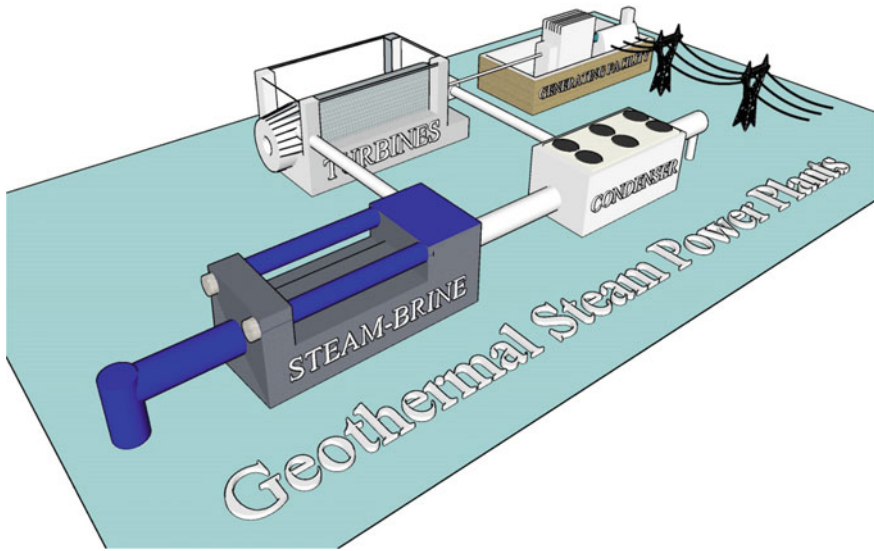
Fig. 10 Geothermal power plant schematic

is absorbed from the steam or hot water. The water is vaporized and transferred to the condenser at Stage 15 to cool. As the moisture refrigerant moves further through the freezing pipe and nozzle, the pressure decreases with temperature. This water refrigerant flows into the evaporator from Stage 16 to generate a cooling effect. Migration repeatedly continues. Meanwhile, lithium bromide leaves the generator at Stage 12 and re-enters the absorber to absorb the water refrigerant.

The heat pump is designed as a heat transport that continuously moves warm air from one place to another as needed. There is heat energy in the air that looks too cold. In cold weather, the heat pump extracts this external heat. Similarly, in hot weather, it moves it inside. The air-source heat pump is a dual-use system that operates as a high-efficient air conditioner in summer and as heating in winter. The refrigeration cycle uses fluids to pass heat through the tubes. This fluid is called refrigerant. During the refrigeration cycle, the refrigerant turns from liquid to gas and back to liquid. When the refrigerant changes from liquid to gas, heat energy is increased (absorbed). This is similar to boiling; when the refrigerant turns from gas to liquid, heat is lost.

In a heat pump's heating cycle, the refrigerant absorbs heat from the ground. The fluid evaporates, and the steam passes through the compressor for increasing pressure. The compressed steam continues to flow into the condenser. Here, the vapour releases the heat absorbed to the medium and turns into a liquid in the process. This high-pressure liquid passes through the expansion valve and reduces the pressure of the liquid. Thus, the refrigerant returns to its original liquid state and the process continues. In the cooling cycle, the refrigerant absorbs heat from the inside of the house and takes it out. The components of the system remain the same and only the

fluid direction changes. Therefore, the same heat pump can be used for cooling as well as for heating.

Hydrogen production system is designed to use solar and wind power as renewable energy sources through generators where a storage system is used to store hydrogen. Proton exchange membrane (PEM) electrolysers are also used for hydrogen production, and hydrogen is produced using three different sources and stored in a hydrogen storage medium (Figs. 11 and 12).

3   Model Development and Analysis

At a glance, research in this area shows a real need to evaluate the benefits of thermodynamics and the practical application of low-exergy systems. When considering previous studies, it is clear that the methods used to prioritize exergy analysis and exergy efficiency of energy conversion technologies must be improved to increase the consistency and universality of the methodology. These assumptions should relate to the principles of thermodynamics and the limitations of certain properties of exergy. Reference environment temperatures should be considered. These methods (computational methods, algorithms) increase the likelihood of using exergy analysis in a real-world study of the system. The consistent analysis of the trend here is based on the preparation of an exergy analysis method for assessing the instantaneous and seasonal efficiency of the system, due to changes in the perimeter base temperature.

In this section, comprehensive energy and exergy analyses are conducted for the proposed community energy system. Such analyses would provide substantial information about the performance, efficiency and emissions of the system. While exergy and energy analyses are performed for the proposed system, detailed thermodynamic analyses are conducted to study mass, exergy, entropy and energy balance equations for the system and its components. The general balance equations can be written as written in Table 2. In contrast, the general mass, exergy, energy and entropy balances can be written as described below.

The mass balance can be written as:

$$\sum_i \dot{m}_i = \sum_e \dot{m}_e$$

The exergy balance can be written as:

$$\dot{\mathrm{Ex}}^Q + \sum_i \dot{m}_i \mathrm{ex}_i = \sum_e \dot{m}_e \mathrm{ex}_e + \dot{\mathrm{Ex}}_W + \dot{\mathrm{Ex}}_d$$

The energy balance can be written as follows:

$$\dot{Q} + \sum_i \dot{m}_i \left(h_i + \frac{V_i^2}{2} + g Z_i \right) = \sum_e \dot{m}_e \left(h_e + \frac{V_e^2}{2} + g Z_e \right) + \dot{W}$$
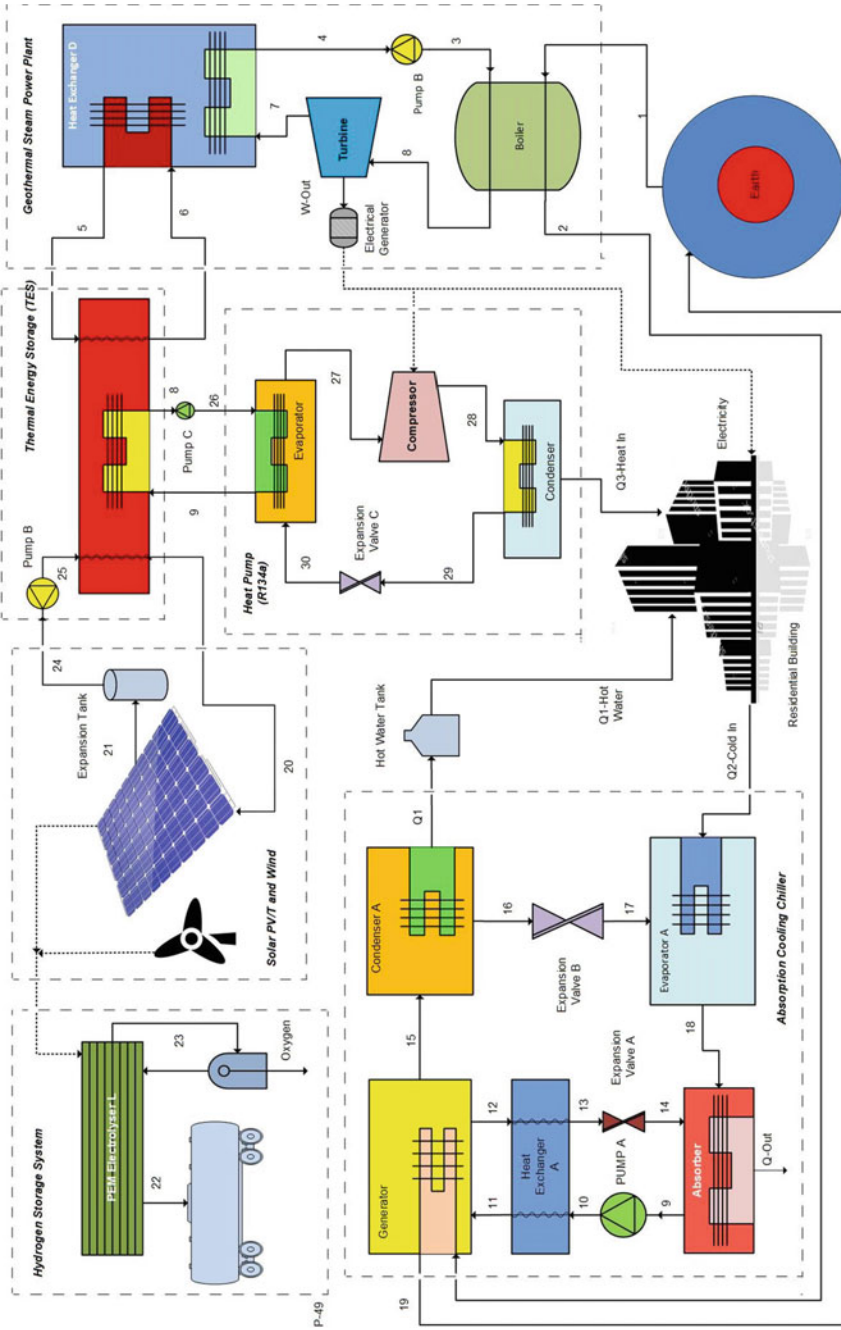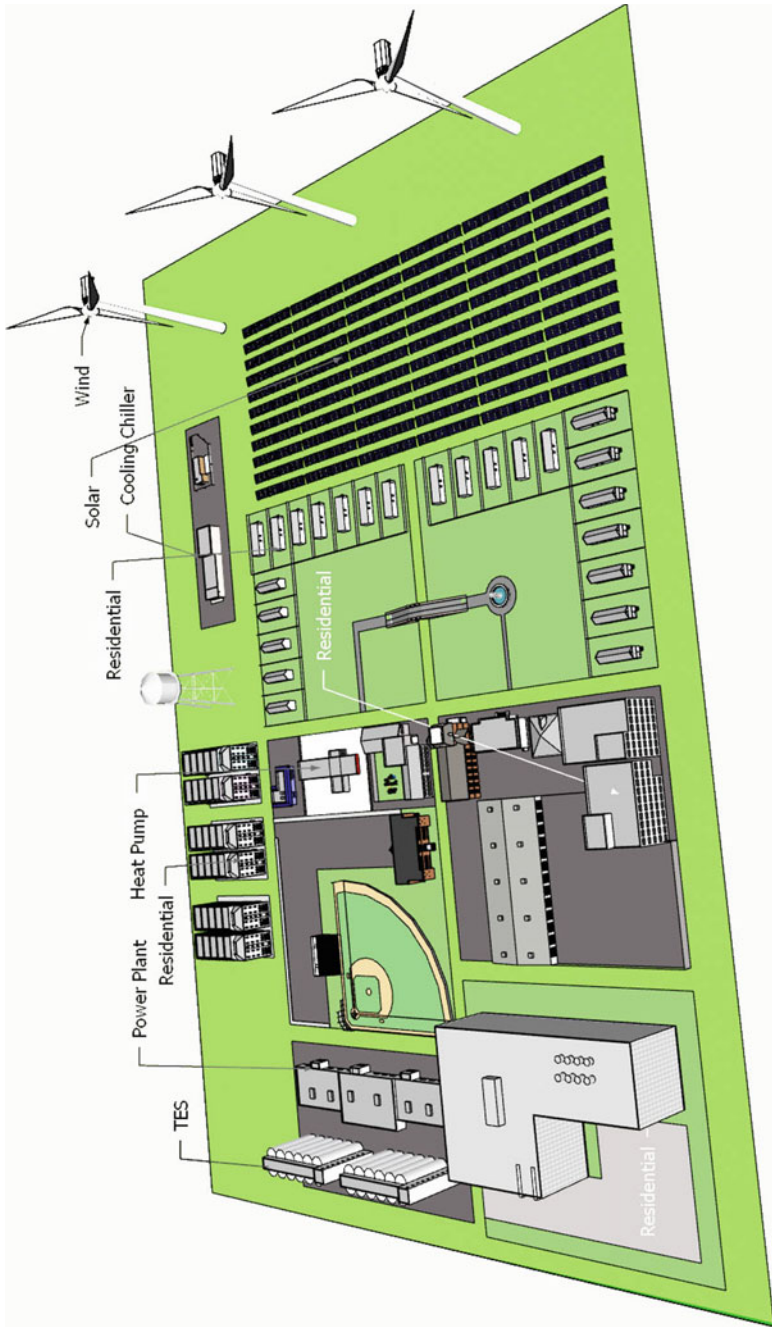
Fig. 11 Proposed system process flow diagram

Fig. 12 Proposed system layout

Table 2 List of mass, entropy, exergy and energy balance equations for the main components

Components	Mass balance	Energy balance	Entropy balance	Exergy balance
Heat exchanger A	$\dot{m}_{11} = \dot{m}_{10}, \dot{m}_{12} = \dot{m}_{13}.$	$\dot{m}_{11}h_{11} + \dot{m}_{13}h_{13} + \dot{Q}_{IN_{Battery}} = \dot{m}_{10}h_{10} + \dot{m}_{12}h_{12} + \dot{Q}_{LOSS_{Heat\ exchanger A}}$	$\dot{m}_{11}s_{11} + \dot{m}_{13}s_{13} + \dfrac{\dot{Q}_{IN_{Battery}}}{T_{Heat\ exchanger A}} + \dot{S}_{gen_{Heat\ exchanger A}} = \dot{m}_{10}s_{10} + \dot{m}_{12}s_{12} + \dfrac{\dot{Q}_{LOSS_{Heat\ exchanger A}}}{T_{Heat\ exchanger A}}$	$\dot{m}_{11}ex_{11} + \dot{m}_{13}ex_{13} + \dot{Q}_{IN_{Battery}}\left(1 - \dfrac{T_0}{T_{Heatexchanger A}}\right) = \dot{m}_{10}ex_{10} + \dot{m}_{12}ex_{12} + \dot{Q}_{LOSS_{Heat\ exchanger A}}\left(1 - \dfrac{T_0}{T_{Heatexchanger A}}\right) + \dot{Ex}_{d_{Heatexchanger A}}$
Boiler	$\dot{m}_9 = \dot{m}_8, \dot{m}_{15} = \dot{m}_{16},$	$\dot{m}_{15}h_{15} + \dot{m}_8h_8 + \dot{Q}_{IN_{Battery}} = \dot{m}_{16}h_{16} + \dot{m}_9h_9 + \dot{Q}_{LOSS_{Boiler}}$	$\dot{m}_{15}s_{15} + \dot{m}_4s_4 + \dfrac{\dot{Q}_{IN_{Battery}}}{T_{Boiler}} + \dot{S}_{gen_{Boiler}} = \dot{m}_{16}s_{16} + \dot{m}_5s_5 + \dfrac{\dot{Q}_{LOSS_{Boiler}}}{T_{Boiler}}$	$\dot{m}_{15}ex_{15} + \dot{m}_4ex_4 + \dot{Q}_{IN_{Battery}}\left(1 - \dfrac{T_0}{T_{Boiler}}\right) = \dot{m}_{16}ex_{16} + \dot{m}_5ex_5 + \dot{Q}_{LOSS_{Boiler}}\left(1 - \dfrac{T_0}{T_{Boiler}}\right) + \dot{Ex}_{d_{Boiler}}$
Heat exchanger D	$\dot{m}_7 = \dot{m}_4, \dot{m}_6 = \dot{m}_5,$	$\dot{m}_7h_7 + \dot{m}_6h_6 + \dot{Q}_{IN_{Battery}} = \dot{m}_4h_4 + \dot{m}_5h_5 + \dot{Q}_{LOSS_{Heat\ exchanger D}}$	$\dot{m}_7s_7 + \dot{m}_6s_6 + \dfrac{\dot{Q}_{IN_{Battery}}}{T_{Heat\ exchanger D}} + \dot{S}_{gen_{Heat\ exchanger D}} = \dot{m}_4s_4 + \dot{m}_5s_5 + \dfrac{\dot{Q}_{LOSS_{Heat\ exchanger D}}}{T_{Heat\ exchanger D}}$	$\dot{m}_7ex_7 + \dot{m}_6ex_6 + \dot{Q}_{IN_{Battery}}\left(1 - \dfrac{T_0}{T_{Heat\ exchanger D}}\right) = \dot{m}_4ex_4 + \dot{m}_5ex_5 + \dot{Q}_{LOSS_{Heat\ exchanger D}}\left(1 - \dfrac{T_0}{T_{Heat\ exchanger D}}\right) + \dot{Ex}_{d_{Heat\ exchanger D}}$

(continued)

Table 2 (continued)

Components	Mass balance	Energy balance	Entropy balance	Exergy balance
Expansion valve A	$\dot{m}_{13} = \dot{m}_{14}$	$\dot{m}_{13}h_{13} = \dot{m}_{14}h_{14}$	$\dot{m}_{13}s_{13} + \dot{S}_{gen_{Expansion\ Valve\ A}} = \dot{m}_{14}s_{14}$	$\dot{m}_{13}ex_{13} = \dot{m}_{14}ex_{14} + \dot{E}x_{d_{Expansion\ ValveA}}$
Compressor	$\dot{m}_{27} = \dot{m}_{28}$	$\dot{m}_{27}h_{27} = \dot{m}_{28}h_{28} + \dot{W}_{in_{comp}}$	$\dot{m}_{27}s_{27} + \dot{S}_{gen_{comp}} = \dot{m}_{28}s_{28}$	$\dot{m}_{27}ex_{27} + \dot{W}_{in_{comp}} = \dot{m}_{28}ex_{28} + \dot{E}x_{d_{comp}}$
Turbine	$\dot{m}_8 = \dot{m}_7$	$\dot{m}_8h_8 = \dot{m}_7h_7 + \dot{W}_{out_{turbine}}$	$\dot{m}_8s_8 + \dot{S}_{gen_{turbine}} = \dot{m}_7s_7$	$\dot{m}_8ex_8 = \dot{m}_7ex_7 + \dot{W}_{out_{turbine}} + \dot{E}x_{d_{turbine}}$
Expansion valve B	$\dot{m}_{16} = \dot{m}_{17}$	$\dot{m}_{16}h_{16} = \dot{m}_{17}h_{17} + \dot{en}_{loss_{One\ way\ valve}}$	$\dot{m}_{16}s_{16} = \dot{m}_{17}s_{17} + \dot{S}_{gen_{One\ way\ valve}}$	$\dot{m}_{16}ex_{16} = \dot{m}_{17}ex_{17} + \dot{E}x_{d_{One\ way\ valve}}$
Evaporator	$\dot{m}_9 = \dot{m}_{30}, \dot{m}_{27} = \dot{m}_{26},$	$\dot{m}_9h_9 + \dot{m}_{27}h_{27} + \dot{Q}_{IN_{Battery}} = \dot{m}_{30}h_{30} + \dot{m}_{26}h_{26} + \dot{Q}_{LOSS_{Heat\ exchangerD}}$	$\dot{m}_9s_9 + \dot{m}_{27}s_{27} + \frac{\dot{Q}_{IN_{Battery}}}{T_{Heat\ exchanger\ D}} + \dot{S}_{gen_{Heat\ exchanger\ D}} = \dot{m}_{30}s_{30} + \dot{m}_{26}s_{26} + \frac{\dot{Q}_{LOSS_{Heat\ exchangerD}}}{T_{Heat\ exchangerD}}$	$\dot{m}_9ex_9 + \dot{m}_{27}ex_{27} + \dot{Q}_{IN_{Battery}}\left(1 - \frac{T_0}{T_{Heatexchanger\ D}}\right) = \dot{m}_{30}ex_{30} + \dot{m}_{26}ex_{26} + \dot{Q}_{LOSS_{Heatexchanger\ D}}\left(1 - \frac{T_0}{T_{Heatexchanger\ D}}\right) + \dot{E}x_{d_{Heatexchanger\ D}}$
Pump	$\dot{m}_9 = \dot{m}_{10}$	$\dot{m}_9h_9 = \dot{m}_{10}h_{10} + \dot{en}_{loss_{Regulator}}$	$\dot{m}_9s_9 + \dot{S}_{gen_{Regulator}} = \dot{m}_{10}s_{10}$	$\dot{m}_9ex_9 + \dot{E}x_{d_{Regulator}} = \dot{m}_{10}ex_{10}$

The entropy balance can be written as follows:

$$\dot{S}_{\text{gen}} + \sum_{i} \dot{m}_i s_i + \sum_{k} \frac{\dot{Q}_k}{T_k} = \sum_{i} \dot{m}_e s_e$$

The total exergy balance can be written as follows:

$$\text{ex} = \text{ex}_{\text{ph}} + \text{ex}_{\text{ch}}$$
$$\text{ex}_{\text{ph}} = h - h_0 - T_0(s - s_0)$$
$$\dot{\text{Ex}}_W = \dot{W}$$
$$\dot{\text{Ex}}^Q = \dot{Q}_i \left(1 - \frac{T_0}{T_i} \right)$$

The entropy generation rate that is generated within the process is called $\dot{S}_{\text{gen}}$. A detailed evaluation by exergy analysis provides valuable results for knowing the details of the overall system (Alizade and Dincer [22]).

Thermal Energy Storage (TES)

The mass balance equation for the heating storage can be written as:

$$\dot{m}_5 = \dot{m}_6, \ \dot{m}_9 = \dot{m}_8, \ \dot{m}_{25} = \dot{m}_{20}$$

The energy balance equation for the heating storage can be written as:
Charging:

$$\dot{m}_5 h_5 + \dot{m}_9 h_9 + \dot{m}_{25} h_{25} + \dot{W}_{\text{in,battery}} + m_{\text{PCM}} \frac{u_{ic}}{\Delta t_c} = m_{\text{PCM}} \frac{u_{fc}}{\Delta t_c} + \frac{Q_{\text{loss,charging}}}{\Delta t_c}$$
$$+ \dot{m}_6 h_6 + \dot{m}_8 h_8 + \dot{m}_{20} h_{20}$$

Storing:

$$m_{\text{PCM}} \frac{u_{id}}{\Delta t_d} = m_{\text{PCM}} \frac{u_{fd}}{\Delta t_d} + \frac{Q_{\text{loss,storage}}}{\Delta t_d}$$

Discharging:

$$\dot{m}_5 h_5 + \dot{m}_9 h_9 + \dot{m}_{25} h_{25} + m_{\text{PCM}} \frac{u_{id}}{\Delta t_d} = m_{\text{PCM}} \frac{u_{fd}}{\Delta t_d} + \frac{Q_{\text{loss,discharging}}}{\Delta t_d}$$
$$+ \dot{m}_8 h_8 + \dot{m}_6 h_6 + \dot{m}_{20} h_{20}$$

The entropy balance equations for the heating storage can be written as:

Charging:

$$\dot{m}_5 s_5 + \dot{m}_9 s_9 + \dot{m}_{25} s_{25} + m_{\mathrm{PCM}} \frac{S_{ic}}{\Delta t_c} + \dot{S}_{\mathrm{gen,charging}} = m_{\mathrm{PCM}} \frac{S_{fc}}{\Delta t_c} + \frac{Q_{\mathrm{loss,charging}}}{\Delta t_c T_0}$$
$$+ \dot{m}_8 s_8 + \dot{m}_6 s_6 + \dot{m}_{20} s_{20}$$

Storing:

$$m_{\mathrm{PCM}} \frac{S_{\mathrm{is}}}{\Delta t_s} = m_{\mathrm{PCM}} \frac{S_{\mathrm{fs}}}{\Delta t_s} + \frac{Q_{\mathrm{loss,storage}}}{\Delta t_c T_0}$$

Discharging:

$$\dot{m}_9 s_9 + \dot{m}_5 s_5 + \dot{m}_{25} s_{25} + m_{\mathrm{PCM}} \frac{S_{id}}{\Delta t_d} = m_{\mathrm{PCM}} \frac{S_{fd}}{\Delta t_d} + \frac{Q_{\mathrm{loss,discharging}}}{\Delta t_d T_0}$$
$$+ \dot{m}_8 s_8 + \dot{m}_6 s_6 + \dot{m}_{20} s_{20}$$

The exergy balance equations for the heating storage can be written as:
Charging:

$$\dot{m}_5 \mathrm{ex}_5 + \dot{m}_9 \mathrm{ex}_9 + \dot{m}_{25} \mathrm{ex}_{25} + \dot{W}_{\mathrm{in,battery}} + m_{\mathrm{PCM}} \frac{\mathrm{ex}_{ic}}{\Delta t_c} = m_{\mathrm{PCM}} \frac{\mathrm{ex}_{fc}}{\Delta t_c}$$
$$+ \frac{Q_{\mathrm{loss,charging}}}{\Delta t_c} \left(1 - \frac{T_0}{T_S} \right) + \frac{\mathrm{Ex}_{\mathrm{des,charging}}}{\Delta t_c} + \dot{m}_8 \mathrm{ex}_8 + \dot{m}_6 \mathrm{ex}_6 + \dot{m}_{20} \mathrm{ex}_{20}$$

Storing:

$$m_{\mathrm{PCM}} \frac{\mathrm{ex}_{\mathrm{is}}}{\Delta t_s} = m_{\mathrm{PCM}} \frac{\mathrm{ex}_{fs}}{\Delta t_s} + \frac{Q_{\mathrm{loss,storage}}}{\Delta t_s} \left(1 - \frac{T_0}{T_S} \right) + \frac{\mathrm{Ex}_{\mathrm{des,charging}}}{\Delta t_s}$$

Discharging:

$$\dot{m}_5 \mathrm{ex}_5 + \dot{m}_9 \mathrm{ex}_9 + \dot{m}_{25} \mathrm{ex}_{25} + m_{\mathrm{PCM}} \frac{\mathrm{ex}_{id}}{\Delta t_d} = m_{\mathrm{PCM}} \frac{\mathrm{ex}_{fd}}{\Delta t_d} + \frac{Q_{\mathrm{loss,discharging}}}{\Delta t_d} \left(1 - \frac{T_0}{T_S} \right)$$
$$+ \dot{m}_{20} \mathrm{ex}_{20} + \dot{m}_8 \mathrm{ex}_8 + \dot{m}_6 \mathrm{ex}_6$$

4   Results and Discussion

There is great significance or value in using several analyses to determine how per-
formance varies according to design parameters. The results of thermodynamic mod-
elling, exergy and optimization are expressed in this section. Exergy analysis, which

can build up strategies and guidelines for more effective and efficient use of energy, is utilized to understand various thermal processes, including power generation and multigeneration. Exergy analysis, which includes recognizing the exergy destruction rate and exergy efficiency of each component in the proposed system, also determines the overall exergy efficiency of the multigenerational system.

Exergy analysis also helps to identify and quantify the source of irreversibility in the proposed systems that are associated with each component. The exergy and energy efficiencies of the major components of the proposed system are calculated and shown in Fig. 13. Maximum efficiencies are observed in the compressor, followed by the turbine, while the third highest efficiency occurs in the evaporator. In order to improve the performance of the overall proposed system, efforts need to be made to increase efficiency in the expansion valves.

The increase in ambient temperature increases the energetic and exergetic output of the system. The proposed system, which offers numerous advantages, will be successful in comparatively similar systems.

The effect of ambient temperature on the overall energy and exergy efficiencies of the proposed system is shown in Fig. 14. As the ambient temperature increases from 5 to 35 °C, the overall energy efficiency of the proposed system changes from 41 to 49% while the overall exergy efficiency increases from 61 to 64%. The increase in ambient temperature increases the energetic and exergetic output of the proposed system. The energy and exergy efficiencies for the major components of the proposed system are calculated and are shown in Table 3.
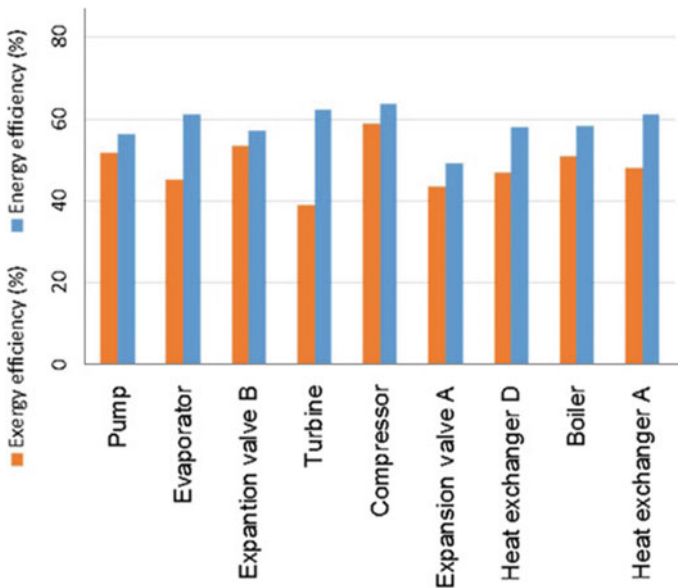
Fig. 13 Energy and exergy efficiencies of the selected units of the proposed system
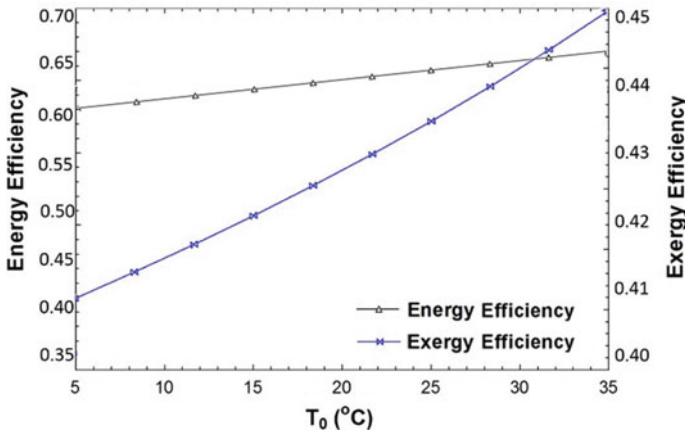
Fig. 14 Effect of ambient temperature on the overall system energy and exergy efficiencies

Table 3 Component energy and exergy efficiencies

Components	Energy efficiency (%)	Exergy efficiency (%)
Heat exchanger *A*	61.2	48.2
Boiler	58.3	50.8
Heat exchanger *D*	58.1	46.9
Expansion valve *A*	49.2	43.4
Compressor	63.7	58.8
Turbine	62.4	38.9
Expansion valve *B*	57.1	53.5
Evaporator	61.3	45.2
Pump	56.2	51.8

The sequel of solar intensity on the overall energy and exergy efficiencies of PV/T is shown in Fig. 15. As the solar intensity increases from 600 to 1000 W/m², the solar energy efficiency changes from 100 to 60% while the overall exergy efficiency decreases from 20 to 16%, meaning that the increase in solar intensity decreases the energetic and exergetic output of the solar.

Increasing the area of the solar collector gradually shifts the system to a permanent regenerative charge, depending on the geothermal flow rate. A faster geothermal hot water pump switches from a lower collector area to a charged state. The exergy efficiency increases because the system charges the high temperature and drains the storage tank. Increasing the limit of the hot water tank is observed in Fig. 16 to show the pattern of exergy efficiency.

As shown in Table 4, the energetic and exergetic renewability ratios of the proposed system are assessed to be 62.5 and 47.3%, respectively.
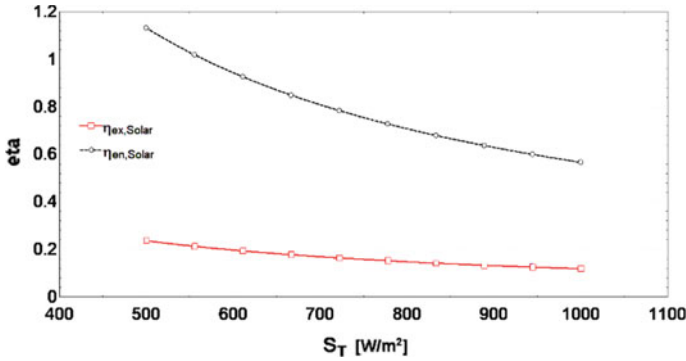
Fig. 15 Effect of solar intensity on the overall energy and exergy efficiencies of PV/T
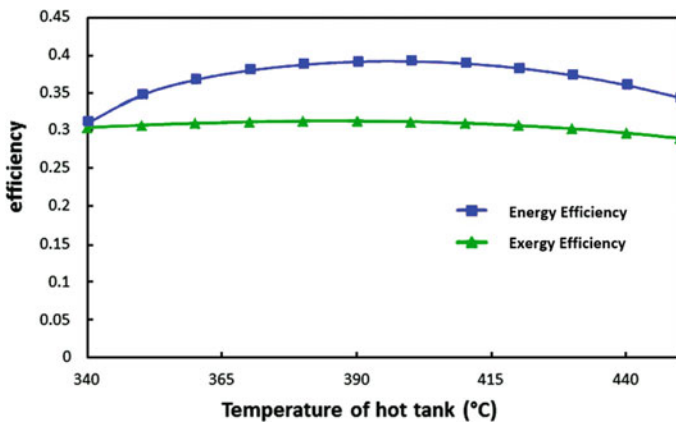
Fig. 16 Effect of temperature of hot storage tank on system energy and exergy efficiencies

Table 4 Overall energy and exergy efficiencies

Parameter	Value (%)
$\eta_{en_{System}}$	62.5
$\eta_{ex_{System}}$	47.3

As the temperature of the hot water tank rises, the temperature of the working fluid in the Rankine cycle also increases. Subsequently, the power that can be generated will rise. However, above a certain temperature that is dependent on the absorbed geothermal energy, the heat loss rate from the receiver tube and the exergy breakdown of components operating at low temperatures exceed the benefit from higher Rankine cycle efficiency.

As shown in Fig. 17, with an increase in the mass rate on the proposed LiBr–H_2O absorption cooling refrigeration system, the overall energy and exergy
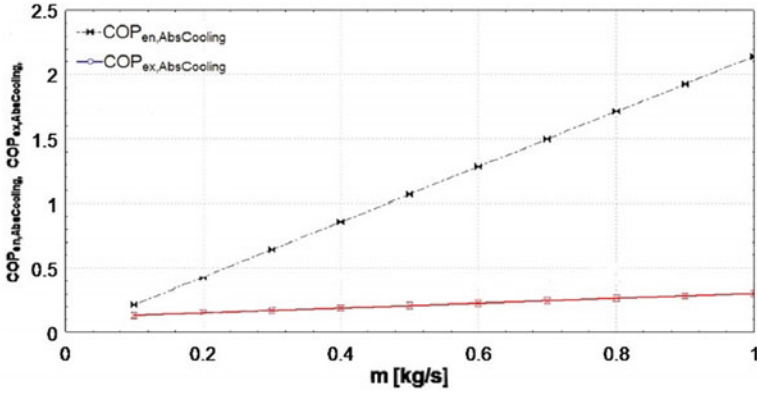
Fig. 17 Effect of mass rate on the overall energy and exergy COP of the proposed LiBr–H$_2$O absorption cooling refrigeration system

COP increases. The exergy destruction rates for the major components of the system are determined, as shown in Fig. 18. The maximum destruction rate occurs in the boiler and the next highest takes place in heat exchanger A while the third highest destruction rate occurs in heat exchanger B.

In order to reduce the exergy destruction rates, it is recommended to decrease the temperature differences, pressure losses and other irreversibilities that are entailed in the energy system.
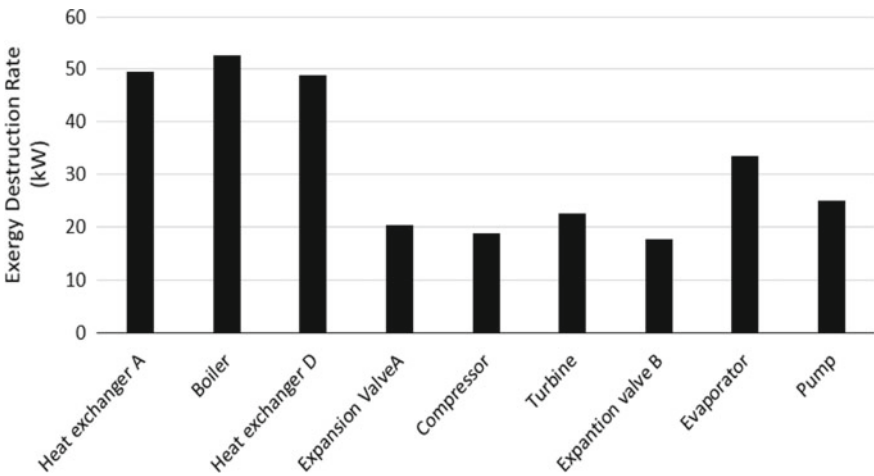
Fig. 18 Exergy destruction rates of selected units of the system

5 Conclusions

The proposed multigeneration energy system is developed for a sustainable community that allows a wide range of energy conservation and production approaches. The designed system includes a thermal energy storage system, an absorption cooling refrigeration system, a geothermal steam power plant, a solar photovoltaic/thermal (PV/T) system, wind turbines, a heat pump and a hydrogen storage system. It has been suggested that net-zero energy buildings can be more convenient if their occupants embody a culture of energy conservation. However, such a claim needs further comprehensive investigation. A zero-energy community that carries out all energy efficiency and safeguarding opportunities and increases energy saving can claim it is able to fully achieve the zero-energy community's performance for reaching milestones. As a result, societies can progress over time and achieve the success of zero aspirations. The zero-energy community is on the pure zero-energy base when it can measure and calculate energy consumption in the community to the extent necessary to reach milestones that seem to be controllable.

One important area for future research is the techno-economic analysis of energy efficiency measures and renewable energy technologies in a sustainable community. Such an analysis will facilitate understanding of how efficient technologies can be adopted in the market and provide a better economic basis for developing net-zero energy sustainable communities. A new community can decide that it cannot reach absolute zero because it does not control all aspects of energy consumption within the community. In this case, it is better to define the energy used in the common areas, then present the amount of energy that represents the area of influence and try to have more control over those parts.

Since the building industry is responsible for 40–50% of total energy consumption, energy efficiency measurements and use of renewable energy should be improved. It is useful to separate the industry into subsets such as residential buildings, commercial buildings, public buildings, transportation within communities and infrastructure. Once the base case is defined and measured, the average goal can be set. Moderate stages can be anything that the community members can visualize, whether large or small. As an example, a community may confirm that it has enough electricity from renewable energy sources that can be equal to zero net per building in elementary school or community. This novel multigeneration system has overall energy and exergy efficiencies of 62.5 and 47.3%, respectively.

References

1. Greening Government Strategy. Government of Canada Treasury Board of Canada Secretariat (2017). https://www.canada.ca/en/treasury-board-secretariat/services/innovation/greening-government/strategy.html. Accessed May Sep 2019
2. Ishaq I, Dincer I, Naterer GF (2018) Performance investigation of an integrated wind energy system for co-generation of power and hydrogen. Int J Hydrogen Energy 43:9153–9164

3. Ahmadi P, Dincer I, Rosen MA (2014) Thermodynamic modeling and multi-objective evolutionary-based optimization of a new multigeneration energy system. Energy Convers Manag 89:147–155
4. Almahdi M, Dincer I, Rosen MA (2016) A new solar based multigeneration system with hot and cold thermal storages and hydrogen production. Renewable Energy 91:302–314
5. Ozcan H, Dincer I (2013) Thermodynamic analysis of an integrated SOFC. Solar ORC and absorption chiller for tri-generation applications. Fuel cells 13(5):781–793
6. Ghosh S, Dincer I (2014) Development and analysis of a new integrated solar-wind-geothermal energy system. Sol Energy 107:728–745
7. Ratlamwala TAH, Gadalla MA, Dincer I (2011) Performance assessment of an integrated PV/T and triple effect cooling system for hydrogen and cooling production. Int J Hydrogen Energy 36:11282–11291
8. Yilmaza F, Ozturk M, Selbas R (2018) Energy and exergy performance assessment of a novel solar-based integrated system with hydrogen production. Yilmaz F et al. Energy and exergy performance assessment of a novel solar-based integrated system with hydrogen production, International J Hydrogen Energy. https://doi.org/10.1016/j.ijhydene.2018.10.118
9. Hassoun A, Dincer I (2016) Analysis and performance assessment of a new multigeneration system for net-zero energy houses. Int J Energy Res 40:36–50
10. Zamfirescu C, Dincer I (2012) Renewable-energy-based multigeneration systems. Int J Energy Res 36:1403–1415
11. Jana K, Ray A, Majoumerd MM, Assadi M, De S (2017) Polygeneration as a future sustainable energy solution—A comprehensive review. Appl Energy 202(2017):88–111
12. Shimizu T, Yasunori Kikuchi Y, Sugiyama H, Hirao M (2014) Design method for a local energy cooperative network using distributed energy technologies. Appl Energy 154(2015):781–793
13. Choi B, Panthi D, Nakoji M, Tsutsumi K, Tsutsumi A (2017) Design and performance evaluation of a novel 1 kW-class hydrogen production/power generation system. Appl Energy 194:296–303
14. Hashimoto K, Kumagai N, Izumiya K, Takano H, Kato Z (2014) The production of renewable energy in the form of methane using electrolytic hydrogen generation. Energy. Hashimoto et al. Energy, Sustain Soc 4:17. http://www.energsustainsoc.com/content/4/1/17
15. McIntyre HJ, (2012) Community-scale assessment of rooftop-mounted solar energy potential with meteorological, atlas, and GIS data: a case study of Guelph, Ontario (Canada). McIntyre Energy Sustain Soc 2:23. http://www.energsustainsoc.com/content/2/1/23
16. Stoeglehner1 G, Baaske W, Mitter H, Niemetz N, Kettl K, Weiss W, Lancaster B, Neugebauer G (2014) Sustainability appraisal of residential energy demand and supply—a life cycle approach including heating, electricity, embodied energy and mobility, Stoeglehner et al. Energy Sustain Soc 4:24. http://www.energsustainsoc.com/content/4/1/24
17. Rehkopf A, Rowlands IH, Tobert D (2019) Assessing the societal impacts of green demonstration homes: a Canadian case study, Rehkopf et al. Energy Sustain Soc 6:19. https://doi.org/10.1186/s13705-016-0084-x
18. Dampier J., E., Shahi, C., Lemelin, H., Luckai, N (2016) Assessment of potential local and regional induced economic impact of an energy policy change in rural Northwestern Ontario, Dampier et al. Energy Sustain Soc 6:14. https://doi.org/10.1186/s13705-016-0079-7
19. Heinbach K, Aretz A, Hirsch B, Prah A, Salecki S (2014) Renewable energies and their impact on local value added and employment, Heinbach et al. Energy Sustain Soc 4:1. http://www.energsustainsoc.com/content/4/1/1
20. Jafari E, Soleymani S, Mozafari B, Amraee T (2018) Scenario-based stochastic optimal operation of wind/PV/FC/CHP/boiler/tidal/ energy storage system considering DR programs and uncertainties, Jafari et al. Energy Sustain Soc 8:2. https://doi.org/10.1186/s13705-017-0142-z
21. Katre A, Tozzi A, Bhattacharyya S (2019) Sustainability of community-owned minigrids: evidence from India, Katre et al. Energy Sustain Soc 9:2. https://doi.org/10.1186/s13705-018-0185-9
22. Alizade R, Dincer I (2015) Analysis and assessment of an integrated hydrogen fuelled energy system for aircrafts. Int J Sustain Aviat 1(4):375–391

Techno-Economic Evaluation of a Residential Roof-Mounted Solar System

Azzam Abu-Rayash and Ibrahim Dincer

Abstract In this chapter, a case study is presented where a residential solar system in Kitchener, Ontario, is analyzed economically as its annual performance is also assessed. The recorded data for this system are investigated further to better assess its technical performance. This system is part of a government-incentive program called microFIT, which allows for generated electricity from renewable sources to feed to the local grid for generous rates ranging between $0.29 and $0.97 per kWh. The system is further examined to show the correlation between climatic parameters such as wind speed and temperature on the overall system performance. Wind speed shows an inverse relationship to the energy output, while the temperature shows a linear relationship. Optimal annual performance is observed when the temperature is at 18 °C and when the wind speed is at 3.8 m/s. Furthermore, using the System Advisor Model (SAM) developed by NERL, a residential solar system has been simulated with the addition of a battery storage in order to understand its impact on the performance and economic aspect of the system. The modeled system without the battery correlates closely with the actual installed system. In fact, the actual ROI for the system is 19.75% while the modeled ROI is 23.5%. The payback time of 5 years is another major highlight of this system. In addition, the actual cost of the system is $18,844 while the projected cost modeled is $15,425. An addition of the battery resulted in insignificant improvements in power generation, higher projected cost $20,466, lower ROI of 17.21% and a longer payback period of 5.8 years. The major losses in the system's production are due to shading and soiling, which add up to 64,899 kWh in the lifetime of the system. Finally, GHG emissions of the current system total up to 38,000 $kgCO_2e/kWh$.

Keywords Solar energy · Photovoltaics · Thermoeconomics · Battery storage · Performance assessment · Cost analysis

A. Abu-Rayash · I. Dincer (✉)
Faculty of Engineering and Applied Science, University of Ontario Institute of Technology, 2000 Simcoe Street North, Oshawa, ON L1H 7K4, Canada
e-mail: Ibrahim.Dincer@uoit.ca

A. Abu-Rayash
e-mail: Azzam.abu-rayash@uoit.ca

Nomenclature

Ac	Area of collector, m^2
Cp	Power coefficient
Cost$_0$	Project initial cost, $
$E_{S,Y}^{SW}$	Incident radiation flux, kW/m^2
h	Heat transfer coefficient, W/m^{2}K
I_b	Beam solar radiation on a horizontal surface, W/m^2
I_d	Diffuse solar radiation on a horizontal surface, W/m^2
Impp	MPP current
Isc	Short-circuit current, A
I_T	Hourly total solar radiation on a horizontal surface, W/m^2
$\dot{N}$	Net negative cash flow, $
Pmax	Maximum power, W
$\dot{P}$	Maximum operational hours in a year, hours/year
$\ddot{P}$	Net positive cash flow, $
$\dddot{P}$	Total project investment, $
PI$_i$	Project's net income in a given year, $
PCF	Periodic cash flow, $/year
Power$_{max}$	Maximum power output, MW
T_{ref}	Reference temperature, °C or K
Vmpp	MPP voltage, V
Voc	Open-circuit voltage, V
YP	Yield production, kWh/kWp

Greek Letters

β_ρ	Temperature coefficient for module efficiency
η_{PV}	PV module efficiency
η_{ref}	PV module efficiency at reference temperature

Abbreviations

GHG	Greenhouse Gas
IESO	Independent Electricity Service Operator
LCA	Lifecycle assessment
microFIT	Micro-feed-in-tariff
NERL	National Exposure Research Laboratory
NPV	Net present value
PV	Photovoltaics

PBT	Payback time
ROI	Return on investment
SAM	System Advisor Model

1 Introduction

During the past decade, solar energy has been increasingly popular and attractive in Canada and the world. In specific, the microFIT program introduced in 2010 by the Ontario government is one of the tools used to increase rates of consumer acceptance of renewable energy sources and at the same time mitigate GHG rates [1]. This program denotes the largest incentive program for solar power in Canada and has successfully attracted solar energy to Ontario, as 98% of Canadian PV capacity is located in Ontario [2]. Tongsopit [3] suggests that feed-in-tariff (FIT) incentive programs are the most common and popular renewable energy support programs worldwide. Indeed, Italy has witnessed a significant expansion in the solar PV market through the continuous and stable support of the FIT programs [4]. For example, FIT programs triggered the growth of solar PV in Italy reaching unprecedented rates such as 382% in 2008 [5]. Similarly, Germany highlights another successful model using FIT programs to enhance solar energy among Germans. FIT programs followed a degradation schedule that responded to the annual solar performance. For example, FIT rates were highest in the beginning in order to attract investors and degraded each year at rate dependent on the solar performance the year before. If targeted capacities were achieved, rates would decline faster; otherwise, rates would decline slower [6]. Moreover, German FIT programs were unlimited and open to everyone as they were supported by binding laws, which were placed in order to meet the national demand to reduce GHG emissions [7]. The Australian model of FIT and solar energy adoption is one of excellence. While Australia is the largest per capita GHG emitter among OECD, it also has one of the highest average solar irradiance levels of any other continent worldwide. In fact, a 1 kW residential PV system is able to generate 1460 kWh in average every year [8]. This significant solar potency in Australia was coupled with very lucrative rebate rates and upfront incentive of $5000 toward the capital cost of solar PV systems making Australia among the countries with the highest rates of solar PV adoption worldwide with approximately 2 million residential rooftop PV systems [9]. In fact, solar PV capacity in Australian skyrocketed between 2007 and 2011 as it increased from 10 MW to approximately 1000 MW [10]. Furthermore, utilizing existing rooftops to harvest solar energy is both a beneficial and profitable idea. In fact, these existing rooftops are considered a significant unutilized asset from an energy perspective. Indeed, novel technologies are introduced to encourage residential solar installations by creating a personalized roof analysis including shading and irradiance as well as 3D modeling of homes. This exciting analysis takes into consideration shadows cast by nearby trees and structures, all possible sun positions over the course of a year, and historical cloud

and temperature patterns that might affect solar energy production. Unfortunately, as the project recently launches, this service is limited to certain American states only.

It is critical to assess the techno-economic of solar systems as their performance may differ. In fact, the novelty of this technology causes the techno-economic assessment to be more valuable. Assessing economic and performance of residential PV systems has been researched by various scientists. Ioannou et al. [11] optimized the design of a residential grid-integrated rooftop PV system. The system considered self-shading effects into the study, and the objective was to provide a design methodology for optimal configuration of the PV rows when installed on rooftop buildings. In this study, rooftops are considered flat and thus PV systems are ground-mounted. Results of this study suggest that in order to maximize the produced energy, the distance between PV rows should be 2.88 m with a spacing factor of 1.8. However, in order to maximize the net present value, the distance is suggested to be 4.14 m with a spacing factor of 2.07. This study used the Perez model to calculate the solar irradiance on the solar system. On the other hand, Axaopoulos and Fylladitakis [12] evaluated the performance and economic assessment of a hybrid PVT system for residential application. The performance of three residential systems located in Athens, Munich and Dundee is examined. Furthermore, the economic assessment is conducted by dwelling into the NPV for each system. Moreover, a techno-economic analysis along with an LCA is conducted on a small-scale rooftop PV system in Greece [13]. Their results suggest that systems that are greater than 5 kW_p are economically viable with their current prices. Environmentally, the module manufacturing process accounts for the majority of the adverse impacts due to the high electricity consumption. They examined five different systems with various capacities in order to determine the optimum size of the PV system. Bicer and Dincer [14] evaluate the performance of a renewable energy-based multigenerational system using energy and exergy efficiencies. The system integrates solar PVT and geothermal. On the other hand, Kalinci et al. [15] performed a techno-economic assessment of a hybrid renewable energy system using hydrogen energy as the energy storage.

In addition, Ning et al. [16] have integrated existing building information model (BIM) modeling techniques to facilitate precise PV system simulation and optimization. Based on the existing BIM model, shading and radiation are analyzed in detail. Based on these design parameters, the model proposes an optimized PV design oriented by the objective of minimal cost-to-power ratio. Their results reveal that this tool has the potential to improve up to 265% in design efficiency, increase 36.1% power output and reduce around 4.5% capital investment per unit power output compared to a human-based design. Akter et al. [17] developed a comprehensive economic evaluation of a residential building with solar PV and battery storage system. They considered NPV, investment and replacement costs, payback period and bill savings for the various scenarios they developed. Solar energy capacity has been steadily increasing in Canada as the cost of solar panels is declining as well. Correspondingly, the installed capacity of the solar thermal power has grown at a rate of 13.8% compound annually since 2004. Interestingly, the period between 2008 and 2014 was marked by significant growth of installed capacity for solar PV systems, reaching up to 1,843 MW of installed capacity in 2014 [18]. Additionally, the

continuous developments in PV technology and reducing the production cost of PV panels make solar energy more affordable and available. For example, the conventional crystalline silicon cells, which are most common and prevalent worldwide, cost \$6.18/W in 2004 and dropped to \$0.85/W in 2014 [19]. In fact, the generation growth from 2005 to 2015 is 2344% with 3007 GWh generated electricity in 2015 [2]. The downside of solar PV in Canada is its cost. The average cost of solar PV in Canada is approximately \$250/MWh, which is significantly higher than other renewable energy options [19]. Therefore, Canada's solar energy remains heavily dependent on incentive and support programs.

The objectives of this contribution are, in this regard, to present a case study of a residential solar PV system and investigate the correlation between climatic conditions and solar systems as well the economic impact of battery storage systems when combined with solar systems. Better understanding of the techno-economic aspects of solar systems in various configurations allows for better design and assessment of energy systems.

2 System Description

As illustrated in Fig. 1, the system analyzed in this study is composed of three main components: Monocrystalline PV panels are roof-mounted to harvest solar energy and convert it to useful electricity. In addition, the mechanical and electrical panel specifications are presented in Table 1. Electricity is then converted from DC to AC through the inverter. Finally, these solar systems are connected to the grid and the harvested electricity is fed into the local distribution companies' main distribution
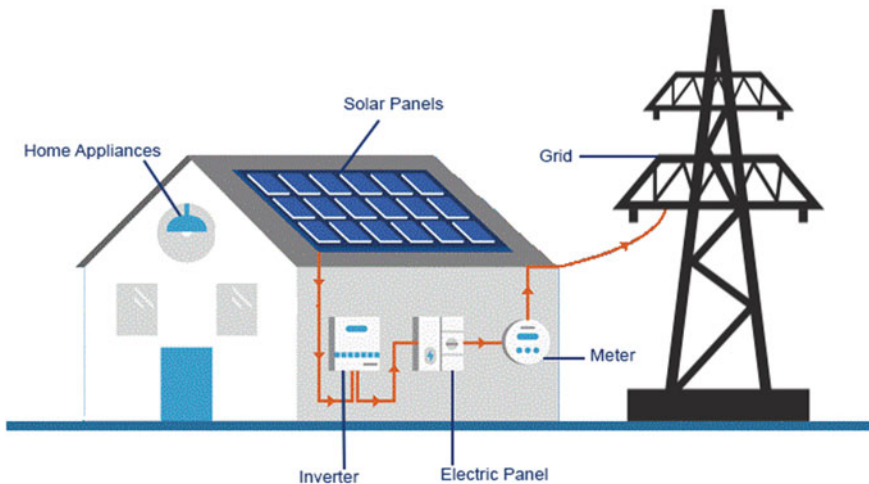

Fig. 1 System design including rooftop panels, inverter and grid integration

Table 1 Mechanical and electrical specifications of the module considered under nominal operating conditions

Item	Specification
Cells	6×10
Cell type	Monocrystalline/P-type
Cell dimensions ($L \times W \times H$)	161.7×161.7 mm/15.25 cm
Front load	6000 Pa
Rear load	5400 Pa
Weight	18.0 kg
Connector type	MC4, JM601A
Maximum power (P_{max})	220 W
MPP voltage (V_{mpp})	29.1 V
MPP current (I_{mpp})	7.56 A
Open-circuit voltage (V_{oc})	36.0 V
Short-circuit current (I_{sc})	8.10 A
Module efficiency	17.5%
Operating temperature	-40 to $+90$

lines. All electricity generated is recorded through the meter for compensation as per the microFIT program. This generated electricity is used for the daily local electric demand in various municipalities and towns across Southern Ontario.

Furthermore, the roofs in this system become useful and help Ontario meet its target toward renewable energy generation and reduction of GHG emissions. In addition, the residential aspect of these projects makes it encouraging for the society to take ownership over renewable energy and solar in specific. Furthermore, the typical size of these systems ranges between 6 and 10 kW. Using 60-cell or 72-cell modules, a residential home can accommodate up to 39 solar PV panels. One of the simulated models using SAM incorporates a battery energy storage in the system design, allowing the system to provide electricity during the nighttime as well. The specifications of the battery type and its properties are presented in Table 2.

Table 2 Technical specifications of the battery energy storage incorporated in the SAM

Item	Specification
Battery type	Lead–acid: VRLA gel
Bank capacity (DC)	10 kWh
Bank power (DC)	5 kWh
Bank voltage (DC)	48 V
Cell nominal voltage (DC)	2 V
Cell capacity	20 Ah
AC–DC conversion efficiency	96%
DC–AC conversion efficiency	96%
Maximum state of charge	95%

Table 3 PV system design parameters and technical specifications

Item	Specification
Collector area	52.1 m^2
Array tilt angle	38°
System size	10 kW
Panel wattage	300 W
Estimated annual revenue	$3721/year
Estimated annual production	9690 kWh/year

All electrical specifications are under nominal operating cell temperature with irradiance of 800 W/m^2, ambient temperature of 20 °C and wind speed of 1 m/s. The modules follow a degradation rate of 0.55% annually. When modeling the battery storage system, the voltage model developed by SAM was used along with other computed properties such as nominal bank voltage. Furthermore, the model assumes battery with specific heat C_p sits in room of fixed temperature. Therefore, heat transfer to room is considered proportional to heat transfer coefficient h.

This contribution extensively investigates a residential rooftop solar system located in Kitchener, Ontario. The actual recorded data are processed and analyzed to further understand the economic aspect as well as the performance of the system with respect to various parameters. This site is a simple 10 kW solar PV system, composed of 37 panels of 300 W. These solar panels are divided into four roofs, with two roofs facing south, one facing east and the last facing west. Table 3 shows the system design parameters.

2.1 Solar Radiation of Tilted Surfaces

The areas of these roof-mounted solar panels are also calculated using the following equation:

$$\eta_{\max} = \frac{P_{\max}}{E_{S,Y}^{SW} \times A_c} \tag{1}$$

where $\eta_{\max}$ is the maximum module efficiency, which is 17.5% according to the panel-type specification, $P_{\max}$ is maximum power output for the target energy demand, $E_{S,Y}^{SW}$ is the incident radiation flux, which is set at 1 kW/m^2 for the purposes of this study, and A_c is the area of collector in square meter.

The estimated annual production for the solar systems is modeled by taking into consideration all the roofs with solar panels, their solar irradiance, azimuth and slope of the roof. Solar modeling is conducted in order to mimic the performance of the solar system throughout the year, while taking into account the shading effect on each roof from the data collected. Other parameters such as the array orientation and tilt are

also taken into consideration. Furthermore, the PV system output is calculated using RETScreen, which approximates this value by firstly calculating the hourly direct irradiance and diffuse irradiance on a horizontal surface for all hours of an average day. The daily global irradiance is set the same as the monthly average. Formulas used are explained further in Duffie and Beckman [20], which were first derived by Erbs, Collares-Pereira and Rabl, and Liu and Jordan. Secondly, the values of global irradiance on a tilted surface are calculated for all hours of the day. This is achieved with a simple isotropic model. Formulae of Braun and Mitchell are used to determine the tracking angles. Finally, the average daily irradiance is obtained by summing the two previous steps. By integrating the hourly total insolation, I_T, between sunrise and sunset, the daily radiation is determined for titled surfaces. Furthermore, the hourly total insolation, I_T, is obtained using the widely used Perez anisotropic model [21]:

$$
I_T = I_b R_b + I_d (1 - F_1) \left(\frac{1 + \cos \beta}{2} \right) + I_d F_1 \frac{a_p}{b_p} + I_d F_2 \sin \beta
$$
$$
+ 1 \cdot \rho_g \left(\frac{1 - \cos \beta}{2} \right) \tag{2}
$$

where I_T is the hourly total solar radiation on a horizontal surface, I_b is the beam solar radiation on a horizontal surface and I_d is the diffuse solar radiation on a horizontal surface. The Perez model is widely used in various academic studies including Ioannou et al. [11], Cronemberger et al. [22] and Compagnon [23]. The actual site uses actual measured irradiance rates.

However, the model simulated on SAM uses a local meteorological library provided by SAM for Windsor, Ontario. Evans model is used to calculate the energy produced by the PV system [24]. In this case, the average efficiency of the PV modules, η_{PV}, is a function of the module operation temperature T_C:

$$
\eta_{PV} = \eta_{\text{ref}} [1 - \beta_\rho (T_C - T_{ref})] \tag{3}
$$

where η_{ref} is the PV module efficiency at reference temperature T_{ref} (= 25 °C) and β_ρ is the temperature coefficient for module efficiency. In this study, the configuration of the solar panels does not account for panels' self-shading, as the roofs are already inclined.

2.2 Cost Assessment

Cost assessment is a critical category when assessing sustainability of energy systems. What does an economically sustainable energy system look like? This critical question must be addressed in any project before embarking on the execution journey. Furthermore, while conventional energy sources are relatively cheaper, renewable energy sources remain quite expensive. However, improved economic planning

and the progress toward cheaper renewable and clean energy are making the competition tougher between energy systems. Moreover, economic factors involved in the operation and design of energy conversion systems have brought the thermal energy storage, for example, to the forefront of its industry [25]. Several thermal energy storage technologies are indeed present in the industry and are used side by side with on-site energy sources to economically buffer variable rates of supply and demand. In addition, an energy system is economically sustainable when they meet the following standards:

- The economic benefit of the energy generation outweighs operational, capital and maintenance cost. Simply, the project is economically viable.
- Energy systems with shorter payback periods are preferred over systems with longer payback periods. This attracts investors.
- Lower levelized cost of energy/electricity. Energy is available for everyone at a relatively lower cost.

In summary, energy systems are economically sustainable if they are profitable, are serviced at lower cost for the consumer and contain the elements of a successful business idea. The score of this category is calculated as such:

$$Y_{\text{ECO}} = (Y_{\text{BCR}} \times W_{\text{BCR}}) + (Y_{\text{PBT}} \times W_{\text{PBT}}) + (Y_{\text{LCOE}} \times W_{\text{LCOE}}) \tag{4}$$

where Y_{BCR}, Y_{PBT} and Y_{LCOE} refer to the scores of benefit–cost ratio, payback time and the levelized cost of energy/electricity, respectively. 'W' terms refer to the weight associated with each indicator. When assessing the economic impact, the proposed model is confined to the following limitations and assumptions:

- The benefit–cost ratio is confined to profitable projects only (i.e., no negative values).
- The payback time for energy projects is assumed to be between 0 and 23 years.
- LCOE target values are limited by values published by the US Energy Department.

The annual revenue for the solar systems is calculated based on the annual production of the system with respect to the rate at which the lease was signed for the microFIT program. For example, similar to the German degradation model, the government of Ontario followed a similar approach, where compensation rates were highest at the launch of the program in order to attract investors and degraded each year, maintaining an attractive rate for investors. Therefore, the annual revenue is calculated using the following equation:

$$\text{Revenue} = \dot{P}\left(\frac{\text{kWh}}{\text{year}}\right) \times r\left(\frac{\$}{\text{kWh}}\right) \tag{5}$$

where $\dot{P}$ is the estimated annual production ($\frac{\text{kWh}}{\text{year}}$) and r is the microFIT rate ($\frac{\$}{kWh}$). In this case, there are two parameters affecting the estimated revenue, including the microFIT rate and the estimated annual production. As for the microFIT rate, it is slightly a fixed variable among all systems in study, as they remain the same

throughout the duration of the lifetime of the solar system. Most solar systems in this study have the same rate at \$0.38/kWh. Again, this is a generous rate as the same could cost less than 1 cent if secured from other energy markets or sources. As for the estimated annual production, a few parameters contribute toward determining its magnitude. This includes irradiance rates. Residential systems vary in production according to their roof tilt, azimuth angle, orientation and the irradiance on that site. Furthermore, some rooftops are better configured than others are as they incline more southerly, yielding higher production rates. Moreover, some roofs might have higher shading effect than others, resulting in lower production rates. The microFIT contract runs for a period of 20 years. Therefore, the projected revenue is calculated based on a lifetime of that period. However, in reality, consumers can still benefit from the solar system financially after the 20-year contract period by enrolling in a net metering program, for instance, in order to reduce their own electricity costs. Therefore, while the total revenue for this system is calculated based on the microFIT timeline, the optimal revenue can be adjusted to match the lifetime of the system.

The payback time of the system refers to the period that the system takes to recover all invested amount. Shorter payback time reflects higher sustainability and favorable investments, while longer payback time suggests the opposite. Payback method does not take into account the time value of money unlike net present value or benefit–cost ratio. The calculation of the payback time is simple. The following equation is used to determine the payback period:

$$\text{PBT} = \frac{\dddot{P}}{\text{PCF}} \tag{6}$$

where $\dddot{P}$ represents the total project investment in (\$) and PCF represents the periodic cash flow in (\$/year). Furthermore, the net present value (NPV) is an important indicator to assess the relationship between the costs of an energy system and the benefits associated with it.

This indicator is informative both quantitatively and qualitatively as it analyzes all the possible benefits and costs. All benefits associated with an energy system are summed, while all costs are subtracted. When conducting a cost–benefit analysis, results that are more accurate are achieved by analyzing the NPV of all future costs and benefits. Simply, if NPV is negative, the project will never pay for itself and thus it is a financially burdening project. However, if NPV is positive, the profits outweigh the costs and the project will pay for itself over time and eventually generate profits. The net present value is calculated using the following equation:

$$\text{NPV} = \sum_{i=1}^{N} \left(\frac{PI_i}{(1+r)^i} \right) - \text{Cost}_0 \tag{7}$$

where PI_i represents the project's net income in a given year. N represents the number of years over which the project income occurs. r is the discount rate and Cost_0 is the project cost, typically assumed in the initial year (0).

Commercial viability and profitability are considered an essential aspect of the growth of any renewable energy source. In fact, if a consumer does not directly benefit financially, the motivation to install a solar system fades away most of the time. Therefore, it is critical to ensure that this investment is profitable and that the return on investment percentage is as high as possible. This is achieved by reducing the costs to an absolute minimum and maximizing the revenue in every way possible. This section will analyze the actual and theoretical financial model of residential solar systems in order to assess the system economically. It is important to mention that the currency used for all financial analysis is the US dollar.

The levelized cost of electricity or energy (used interchangeably) refers to the cost of energy. It accounts for all lifetime costs of the system including operation, maintenance, construction, taxes, insurance and other financial obligations of the project. They are then divided by the expected total energy outcome in the system's lifetime (kWh). Cost and benefit estimates are adjusted to account for inflation and are discounted to reflect the time value of the money. It is indeed a very valuable tool to compare different generation methods. Lower LCOE values resemble low energy cost, which in turn reflects back with high financial profit to the investors and vice versa.

$$\text{LCOE} = \frac{\sum_{i=0}^{N}\left[\frac{I_i + O_i + F_i - \text{TC}_i}{(1+r)^i}\right]}{\sum_{i=0}^{N}\left[\frac{E_i}{(1+r)^i}\right]} \tag{8}$$

where I_i is investment costs in year I, O_i represents the operation and maintenance costs in year i, F_i represents the fuel costs in year i, TC_i represents the total tax credits in year i, E_i represents the energy generated in year i, r is the real discount rate, and N is the economic lifetime of the system.

The value of the LCOE includes the capital cost average, fixed operation and maintenance cost average, variable operation and maintenance average as well as the fuel cost average. The LCOE score is determined by the following equation:

$$Y_{\text{LCOE}} = \frac{X_{\text{LCOE}(T)}}{X_{\text{LCOE}}} \tag{9}$$

where X_{LCOE} represents the actual LCOE of the energy system. $X_{\text{LCOE}(T)}$ represents the target value for the future and long-term LCOE for that system. For the purpose of this study, the values published by the US Energy Department for the LCOE for various energy systems in the year of 2040 will be used in the case studies for the values of $X_{\text{LCOE}(T)}$.

2.3 Sizing Criteria

When designing a solar PV system, the total energy demand needs to be calculated in order to make sure that the energy input from the system meets the target consumption. For this case study, the total electricity demand has been retrieved from the monthly electric bill of the site. The sizing of the battery is also important, and for this case study, deep cycle battery is used. This type of battery is specifically designed to discharge to low energy levels and recharge rapidly when needed. In order to ensure that the size of the battery is large enough to store sufficient energy to operate all the appliances and electric commodities, the following equation is used to determine the battery size:

$$B_{\max} = \frac{110 C_t}{DOD_{\max}} \times D \qquad (10)$$

where $B_{\max}$ is the maximum battery capacity (W h), C_t is the total daily electric consumption (W h/day), D is the number of days of autonomy, and finally $DOD_{\max}$ is the maximum depth of discharge (%), which defines the maximum discharge capacity that a battery can achieve without damages. While Ni–Cd batteries can reach discharge depths of higher than 90%, lead–acid batteries can only discharge up to 70%. Based on the electric demand of the site, the battery size has been calculated as specified in Table 2.

3 Results and Discussion

Due to Canada's harsh winters, solar systems' peak performance is in the summer. Delayed winters allow more solar energy to be harvested during the fall months. However, December, January and February experience the lowest energy production from solar systems. Figure 2 illustrates the collected data for Site 1 over a period of
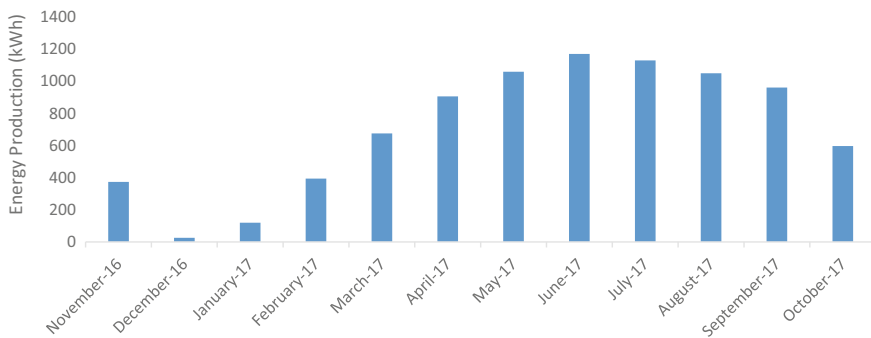

Fig. 2 Annual energy production (kWh) generated from Site 1

one year. The trend of the energy production from this site roughly follows a normal distribution, which is true for all sites as production varies from month to month.

From this collected data, the peak performance for this site is in the month of June, generating close to 1200 kWh, and the lowest is in December with less than 100 kWh generated energy. Furthermore, the fall months of September and October yield in decent rates of energy despite the change of weather during these months. Changes in weather may influence the performance of the solar system depending on the geographical location.

This study analyzes a number of solar sites across Ontario and assesses their energetic performance. The sites vary in their annual estimated revenue as it fluctuates between approximately $3000 and $4500 depending on the annual production. These sites are spread throughout Ontario from Windsor to Peterborough along with a variety of sites across the Greater Toronto Area. Table 4 shows the various production rates along with the estimated revenue for each site annually.

Figure 3 illustrates the systems in study and their geospatial locations throughout Southern Ontario. The systems were selected from various towns and cities in order to have a logical and reasonable representation of Southern Ontario. As mentioned earlier, major cities have also been taken into consideration such as Toronto, Windsor, Hamilton, St. Catharines, Kitchener, Waterloo and Richmond Hill. East of Toronto, we were limited with only two sites at Oshawa and Belleville, while on the west end of the map, Windsor and St. Thomas were selected. In this study, wind speed and atmospheric temperatures are investigated in detail to better understand their

Table 4 Site information for the studied solar systems including location, estimated annual production and estimated annual revenue

| Site number	Location	Estimated annual production (kWh/year)	Estimated annual revenue ($/year)
Site 1	43.40088, −80.52031	9690.00	3721.00
Site 2	44.17745, −77.39015	7378.00	2833.00
Site 3	43.95832, −78.83717	10141.00	3894.00
Site 4	44.33739, −79.7235	10240.00	3932.00
Site 5	43.93968, −79.42635	7313.00	2895.94
Site 6	43.7221, −79.589	10328.00	3966.00
Site 7	43.65317, −79.75156	10053.00	3860.00
Site 8	43.59147, −79.77745	7311.00	2807.00
Site 9	43.49597, −80.55494	11096.00	4261.00
Site 10	43.21367, −79.83092	11475.00	4406.00
Site 11	43.17853, −79.22078	10210.00	3921.00
Site 12	42.97081, −79.2705	10099.00	3878.00
Site 13	43.20989, −80.39676	10807.00	4150.00
Site 14	42.80294, −81.25376	10087.00	3873.00
Site 15	42.3199, −83.00158	10649.00	4217.00
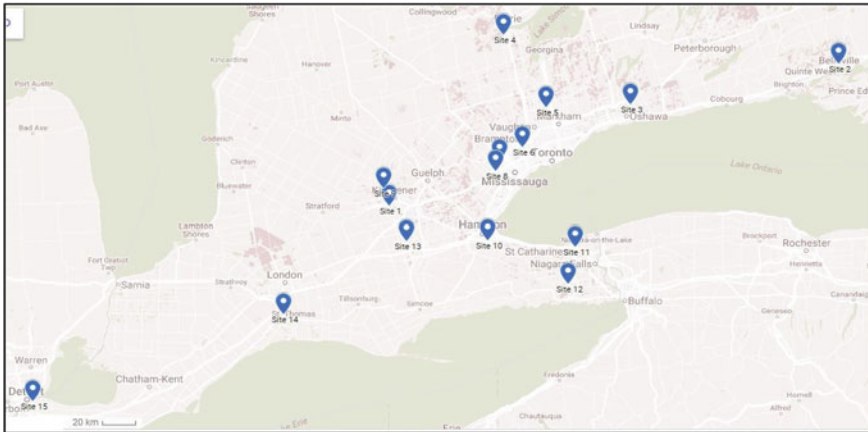
Fig. 3 Map of Southern Ontario and the geospatial location of each site

effect on the performance of solar systems. Figure 3 illustrates the wind speed and temperature data for a period of one year at the site. This figure demonstrates an approximately inverse relationship between wind speed and temperature on their impact on the solar system performance.

For example, when wind speed is high and temperatures are low, the solar system is expected to perform poorly, yielding in lower energy production. On the other hand, as temperatures increase and wind speeds decline, solar performance enhances. This gap between the temperature and the wind speed records is much larger when observing data from other sites. This strengthens the inverse relationship hypothesis. Interestingly for this site, the month of June, which records the highest energy production, locates the intersection of wind speed and temperature in Fig. 4. In this case, the highest energy production is yielded at temperature of 18 °C and wind speed of 3.6 m/s.

The atmospheric temperature influences the energy output of solar systems. In this case, a correlation is observed for the site between the monthly temperature and its corresponding energy output. Figure 5 shows the relationship between the two parameters more illustratively. As the temperature starts to increase in March, the energy output would have preceded this incline 2 months before. However, generally, as the temperature increases toward 20 °C, the energy output increases in a linear fashion almost simultaneously. On the other hand, as the temperature drops the energy output also drops, respectively. This clear correlation between temperature and energy output makes it evident that a relationship between both parameters exists. Moreover, the wind speed resembled an inverse relationship with the temperature throughout the course of the year. This in turn reveals a possible relationship between the wind speed and the energy output.

Figure 6 shows the relationship between wind speed and energy output for the site based on the recorded data over the course of the year. The inverse relationship between the two parameters is quite clear. Whenever the wind is at high speed, the
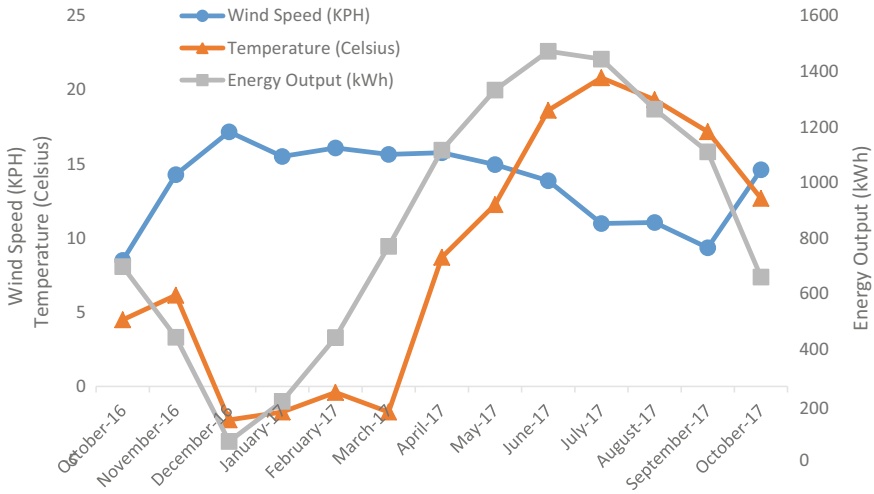
Fig. 4 Recorded annual temperature and wind speed at Site 1 along with energy output
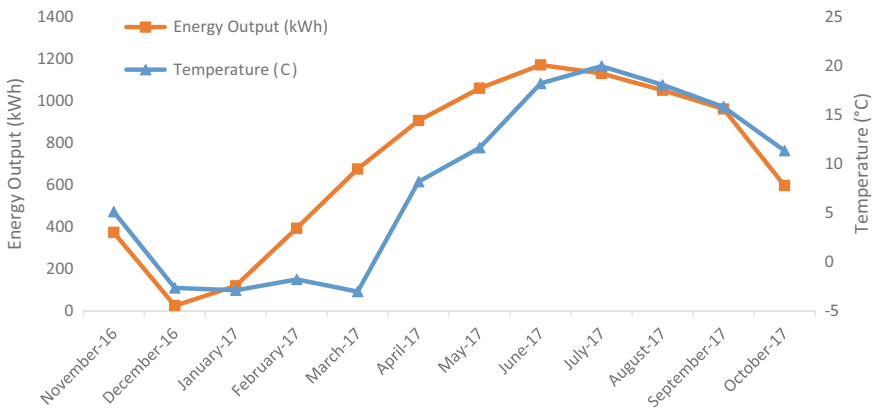
Fig. 5 Annual temperature and respective energy output from site

energy output is low. On the other side, higher energy outputs are achieved during the decline of wind speeds. In fact, the month of June, which yields the highest energy output, experienced a wind speed of 3.8 m/s. However, in December, the lowest energy output is observed with wind speed of 5.1 m/s. Furthermore, while the energy output illustrates a smoother trend, the wind speed fluctuation leads to an irregular trend throughout the year, making the effectiveness of the relationship between the two parameters weaker.

Moreover, there is slight variation between the estimated production forecasted based on RETScreen program and the actual production on site. The actual production only exceeds the estimated production during the fall season, between late August
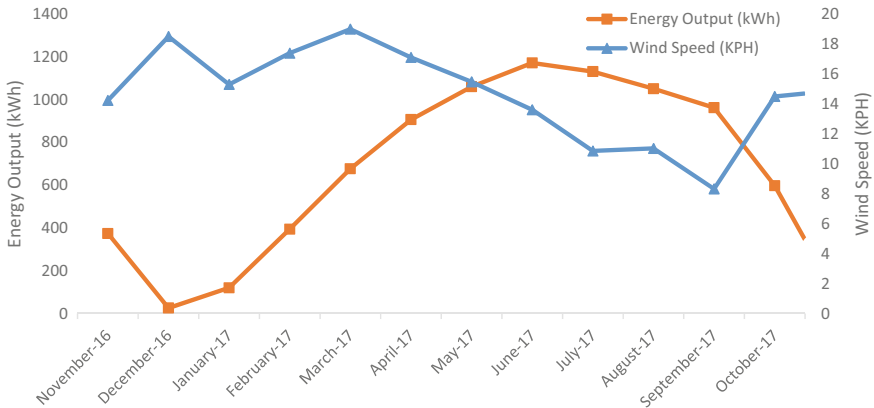
Fig. 6 Recorded annual wind speed and respective energy output from site

and late November. Other than that, the estimated production is slightly more than the actual values. Figure 7 illustrates the relationship between the two variables.

The costs associated with a residential rooftop solar system range from administrative to technical costs as well as equipment purchase. The following cost input highlights the actual cost used in the financial analysis for the site. Administrative costs include parcel register, building permit fees and connection fees. On the other hand, technical fees include the technical feasibility study, engineering costs and system commissioning. Lastly, the purchase of equipment makes up the majority of the costs. Table 5 outlines the different cost categories associated with building a solar system on a residential rooftop.

Indeed, the final cost of the solar system at the site totals up to $2.07/W-DC and an overall cost of $18,844. The solar panels and installation make up more than

Fig. 7 Estimated production compared to actual production of the system

Table 5 Cost category analysis for Site 1

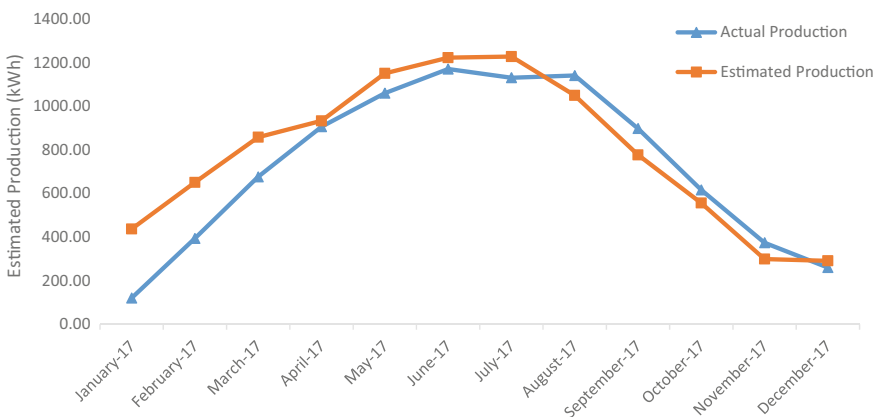| Description	$/W-DC	Total cost ($)
Sales commissions	$0.09	$867
Parcel register	$0.00	$30
Technical feasibility study	$0.03	$290
Engineering	$0.02	$150
Building permits	$0.01	$283
Connection fees (local distribution company)	$0.00	$310
Solar panels	$0.56	$4057.05
Racking	$0.30	$2811
Inverters	$0.13	$1251
Optimizers	$0.15	$1449
Critter guard materials	$0.05	$444
NOL/NOSI	$0.01	$132
Installation (base)	$0.41	$3868
Installation (out of area) add on charge	$0.00	$0
Installation (small system) add on charge	$0.00	$0
Installation (extra) add on charge	$0.00	$0
Monitoring hardware	$0.05	$255
System commissioning	$0.00	$194
S&M overheads	$0.14	$1321
Minimum operating margin	$0.12	$1132
All hard costs	$2.07	$18,844

44% of the total cost. Second highest costs are associated with the inverter, racking, optimizers and O&M overheads.

Figure 7 shows the summary of the cost for this system broken down by main categories of regulatory, solar panels, installation, racking, inverters, optimizers and operation and maintenance. Exactly 50% of the total cost is attributed to the equipment purchase (Fig. 8).

Table 6 shows the bill of materials needed along with their respective cost to build the system on the site. The actual solar panels make up approximately 50% of the equipment cost. The table also shows the racking material costs. In this case, the critter guard length is designed as 290 feet. The site has 37 solar panels, which are 72-cell panels and 360 W. For each solar panel, an optimizer is installed. One inverter is used for the whole system, and the rest of materials are used for installation and mounting of the panels.

In this study, the revenue source is a provincial production-based incentive program. Through the microFIT program, residents of Ontario are able to install any form of renewable energy, in this case rooftop solar systems, and feed it back to the grid at generous rates ranging from $0.288 to $0.97 per kWh depending on the

Fig. 8 Breakdown of total
cost of the solar system
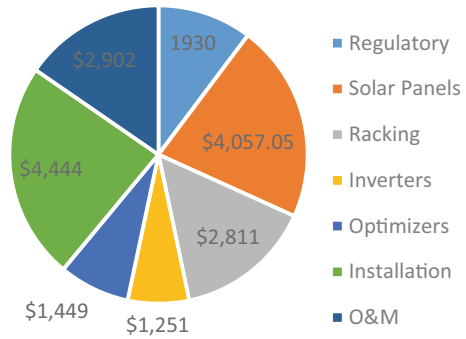including equipment and
installation

Table 6 Cost of material and respective equipment cost for solar system on site

Description	Units	Unit price	Total
360 W-72 cell panels	37	0.43	$4057.05
7.6 kW inverter	1	1251.00	$1251.00
P300 optimizer	37	39.17	$1449.29
KlickTop	90	1.85	$166.50
Solo05-4.2 m	22	27.75	$610.50
EJOT asphalt flashing + JA3-SB	90	9.10	$819.00
Splice Solo05	16	2.90	$46.40
5 k mid-40–50 mm	54	1.95	$105.30
5 k end 40 mm	40	1.95	$78.00
Beaver tooth grounding lugs	10	1.40	$14.00
RPVU 90-black	30	1.20	$36.00
RPVU 90-red	30	1.20	$36.00
MC4-male	8	1.63	$13.00
MC4-female	8	1.63	$13.00
Grand total			$8695.04

contract year. For this site, the microFIT rate is set to be $0.38/kWh. In order to
analyze the revenue, the production of the system must be estimated first. Table 7
shows all the details of the roof of the studied system including the slope, azimuth
and percentage of shading on each roof, and the corresponding estimated production
as well as revenue for each roof. Simply, the total production is sold back to the
Independent Electricity Service Operator (IESO) at the rate specified, yielding in an
estimated annual revenue of $3721.

The solar system has been simulated using System Advisor Model (SAM), which
is a financial and performance model designed to facilitate decision making for those
involved in renewable energy. It is intended specifically for engineers, researchers,
project managers and policy analysts. SAM is developed by the National Renewable

Table 7 Roof details and estimated production per roof for the system in Kitchener

Roof #	No. of panels on roof	Orientation	Roof wattage (kWp)	Slope (degrees)	Azimuth	Shading (%)	Estimated production (kWh)	Estimated revenue
1	17	W	4.34	38	76	8	4450.04	$ 1708.82
2	5	S	1.28	16	14	6	1498.36	$ 575.37
3	3	S	0.77	38	14	2	968.24	$ 371.80
4	12	E	3.06	38	104	8	2773.80	$ 1065.14

Energy Laboratory (NREL) and makes performance predictions as well as cost of energy estimates for power projects that are grid-connected based on their installation, system design parameters and operation costs. Input parameters have been specified to mimic the site in terms of number of solar arrays, their tilts and azimuth, and shading effect. Furthermore, since the site is located in Kitchener, Ontario, the electricity rates were inputted to match that of Kitchener Wilmot Hydro Inc. In fact, they had three different types of rates depending on the time of day.

These three rates were inputted into the model for accurate simulation. SAM's database is American-centric, and thus Kitchener was not part of the location and resource database. Windsor, Ontario, was selected to be the targeted city. Thus, the weather data and annual averages calculated from the weather data are all based on Windsor, Ontario, which is not too far from Kitchener.

The module selected in the simulation is the same as the ones installed, which is specified in Table 1. Weather data used in this study are from NERL's National Solar Radiation Database. Furthermore, the inverter selected also matched that installed on the site. Moreover, the system design mimicked the actual system in terms of shading, azimuth and tilt for each roof along with the observed shading of each roof extracted from site. The degradation rate for the system was set to 0.55% per year, while the total DC power losses were 4.44%. In addition, system cost inputted followed the rates presented in Table 5, which describes the cost per watt for each cost category. Finally, the system incorporated a production-based incentive to simulate the microFIT program. The rate was set to be $0.38/kWh for the term of 20 years, which is the rate and duration that the site is enrolled.

Table 8 presents major financial highlights of both the site and the SAM simulated model. It is evident that values are very close and the simulation seems to be accurate with respect to the actual estimated values. Furthermore, while the SAM produces slightly lower energy production, its system cost is estimated to be cheaper than the actual cost. Thus, the return on investment is simulated to be higher than the actual value. Figure 9 also shows the highlights of the economic variations between the three different systems.

Table 8 Summary of main economic parameters for the solar system

Description	Actual site	SAM (no battery storage)	SAM (battery storage)
Estimated annual production (kWh/year)	9690.00	9542.46	9272.00
Estimated annual revenue ($/year)	$3721.00	$3626.13	$3523.36
Total revenue ($)	$74,422.6	$72,522.7	$70,467.2
System cost ($)	$ 18,844.00	$15,425.00	$20,466.00
ROI (%)	19.75%	23.5%	17.21%
Average monthly revenue ($)	$310.09	$299.06	$293.6
Payback time (years)	5 years	4.25 years	5.8 years
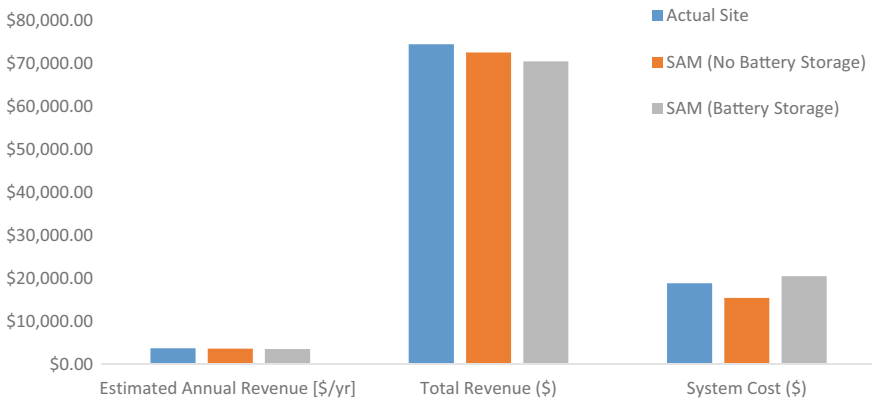
Fig. 9 Highlights of economic variations between the three different systems

It is evident that the battery storage is more costly, yet its return on investment is not significantly high. Thus, it is not an attractive option compared to the grid-integrated PV system. The monthly production of energy of the actual collected data and the simulated SAM data are very similar.

Figure 10 illustrates the monthly energy output for both systems, respectively. SAM overestimates the energy production from December to July. On the other hand, it underestimates the energy production for period between August and November. In general, the approximation of energy output in the simulated model is very accurate when compared to the actual recorded data at the actual site. From this simulation, further assessment is modeled by SAM to illustrate the monthly energy production compared to the monthly electricity load.

Figure 11 illustrates the variation between the monthly energy productions versus the electric load. The bars indicating the cumulative excess generation of energy exceed 3500 kWh in a given year. Moreover, the cumulative generation is the sum
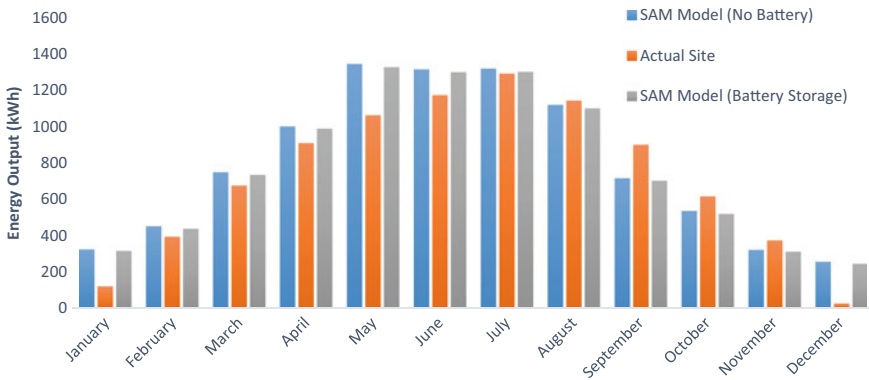
Fig. 10 Monthly energy output for the site and modeled system using SAM
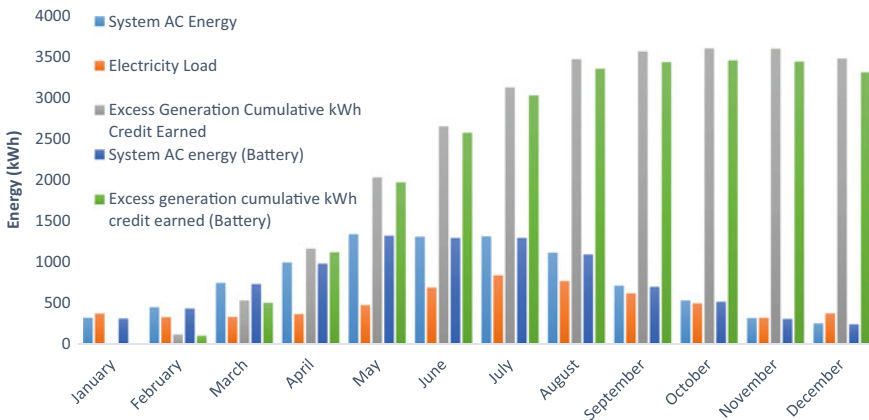
Fig. 11 Monthly energy output for the site and modeled system using SAM

of the production that is left after meeting the monthly electricity demand in this case. The first month, therefore, does not have any cumulative value, while the months that follow carry on any excess energy generated from previous months. Furthermore, it is evident that winter months of December and January experience higher electricity demands than the expected system output. The PV system with battery follows the same trend; however, it always underperforms compared to the system without battery.

Using solar rooftop systems residentially sounds attractive; however, it is critical to understand the financial aspect relative to the local electricity rates. As mentioned earlier, the local electricity rates for Kitchener were inputted into the SAM in order to simulate the influence of the solar system over electricity prices. Indeed, Fig. 12 illustrates this relationship clearly and vividly.
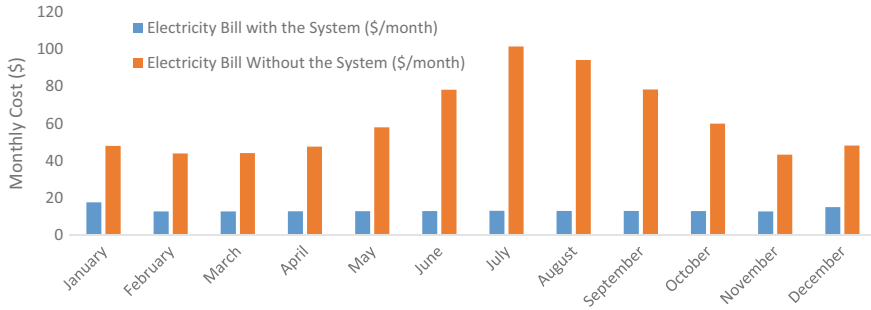
Fig. 12 Monthly electricity cost with and without the modeled solar system (no battery option)

Simulated data show a significant impact of the solar system over the monthly electricity bill at the site. In fact, the solar system normalizes the monthly electricity cost to $12.00 throughout the year, irrespective of seasonal demand variations. Furthermore, without the solar system, electricity costs rise up to $100 in summer months, demonstrating the substantial benefit resulting from the rooftop residential solar system. Evidently, the total PBI income depreciates as the solar panel ages and consequently the production denigrates.

On the other hand, the value of electricity savings increases throughout the year based on the simulated SAM. Moreover, since the microFIT program is a 20-year contract, no income is observed after 20 years. As mentioned earlier, other programs of income such as Net Metering or other programs, which may come to existence later, could be utilized to guarantee the financial gain from this system. The GHG emissions for the current system are the lowest while the simulated systems yielded in higher GHG emissions as illustrated in Fig. 13. This may be due to faults associated

Fig. 13 Total GHG emissions for each model throughout the lifecycle of the system
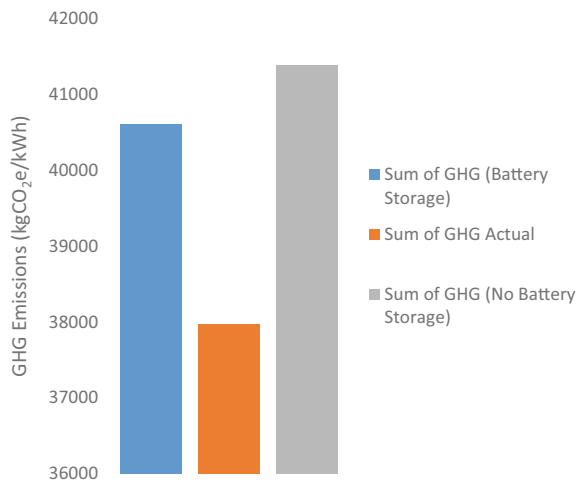
with the simulation, which is clear from the variance between the projected emissions of the actual site versus the projected emissions from the simulated models.

In order to evaluate the effect of the storage on the self-consumption of the PV energy, the household consumption profile must be analyzed. Self-consumption is a nonlinear function with asymptotic relationship between the PV and the battery size. Achieving 100% off-grid system means perfect self-consumption, which is not practical without oversizing the battery size excessively. Furthermore, the battery storage has the potential to maximize self-consumption for solar PV systems under the microFIT program. Moreover, as the battery discharges electricity during the evening hours, self-consumption is maximized.

The actual site emits much less emissions than any of the tested models regardless of battery integration or not. However, the SAM with battery has a total GHG emission slightly less than that system with no storage option. All in all, the total annual emissions for the actual site throughout its annual lifecycle come up to 38,000 $kgCO_2e$/kWh.

The losses associated with this solar system as modeled by SAM vary from one source to another. The major losses are due to the panel of array, specifically the shading and soiling associated with the panels. These losses total close to 65,000 kWh. Furthermore, nominal DC energy losses are ranked second. The losses in this category are due to the module mismatch, module and DC wiring. Thirdly, losses associated with the inverter are also taken into account including the inverter efficiency, inverter power consumption and inverter nighttime consumption. Lastly, losses due to AC wiring are taken into account, resulting in a gross annual production of 9447 kWh. Simulated models with battery energy storage and without both project the same loss patterns in their systems. Figure 14 shows the various loss categories in an illustrative format.

Moreover, the solar irradiance projection at each hour is illustrated for all months of the year for this specific system in Fig. 15. The trend shows higher irradiances after 14:00 h. Summer hours extend as the days are longer. The highest solar irradiance is rated at 22 W/m^2, which is achieved in mid-June.

Nominal POA (kWh)
64,899

Shading
-2.705 %

Soiling
-4.999 %

Nominal DC energy (kWh)
10,855

Snow
-0 %

Module
-5.535 %

Inverter MPPT clipping
-0 %

Module mismatch
-1.973 %

Diodes and connections
-0.493 %

DC wiring
-1.973 %

Tracking error
-0 %

Nameplate
-0 %

DC power optimizer
-0 %

DC availability and curtailment
-0 %

Net DC energy (kWh)
9,798

Inverter power clipping
-0 %

Inverter power consumption
-0.4 %

Inverter nighttime consumption
-0.27 %

Inverter efficiency
-1.954 %

Gross AC energy (kWh)
9,542

AC wiring
-1 %

Transformer loss
-0 %

AC Availability and curtailment
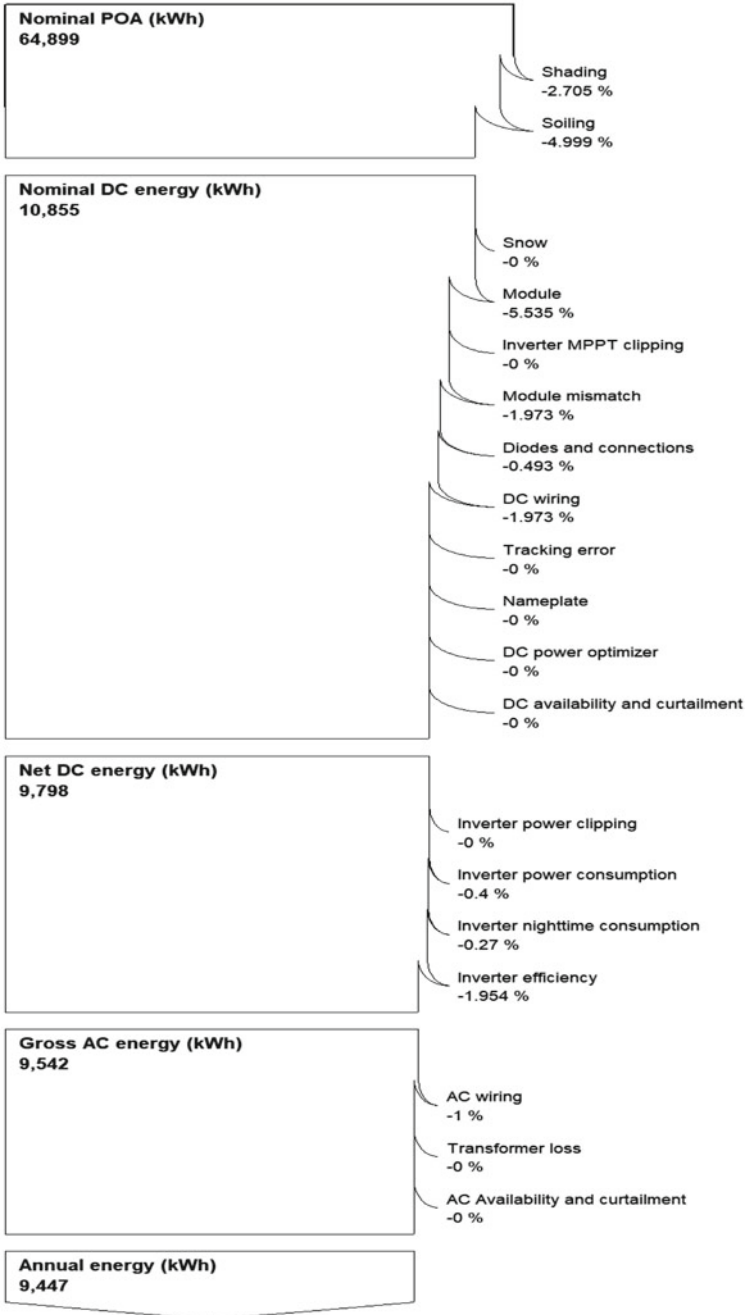-0 %

Annual energy (kWh)
9,447

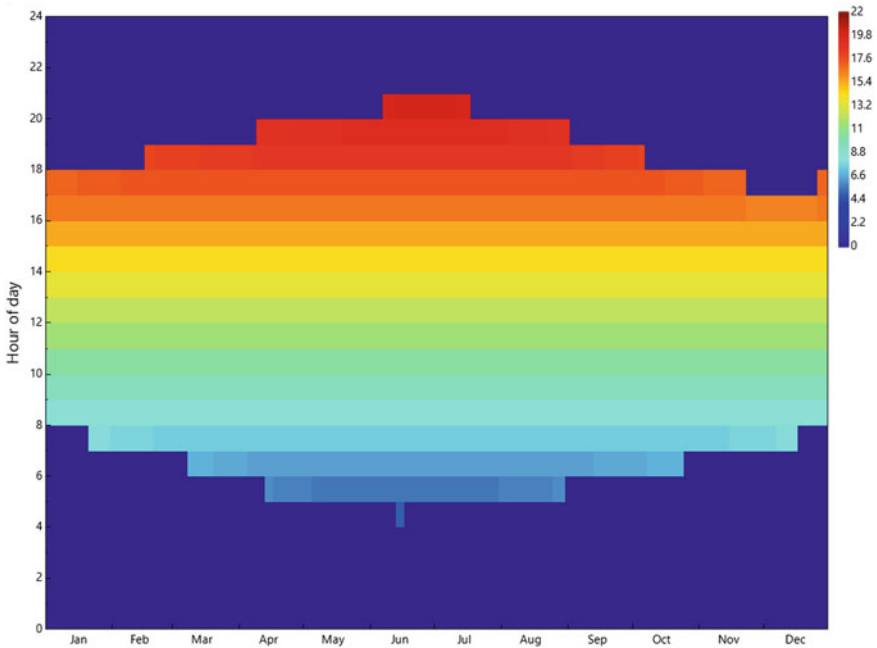**Fig. 14** Projected losses associated with the simulated solar system using SAM

Fig. 15 Projected solar irradiance (W/m^2) based on the hour of day for all months

4 Conclusions

This techno-economic analysis of a residential solar rooftop system highlights critical economic conclusions. While the actual ROI of the solar system is 19.75%, the simulated model using SAM results in higher ROI of 23.5%. The addition of battery to the modeled system reduces this ROI to 17.21%. Furthermore, the annual estimated revenue of the actual system is $3721, while the simulated SAM projected a more conservative yet close estimation of $3626.13. The addition of the battery storage decreases this estimated revenue slightly to $3523.36. Furthermore, the actual total cost of the system is relatively higher than the projected amount by SAM. Logically, the addition of the battery storage increases the total cost as it is estimated to cost $20,466. Moreover, the modeled data of monthly electricity cost after using the solar system indicate that solar energy integrated with the grid is a profitable and sustainable energy source. In specific, the solar system reduces the electricity bill to less than $20 throughout the different months, whereas the minimum bill without the solar system is $42 per month, which is more than double the earlier amount. Shading and soiling make up the main sources for losses in this systems' production, adding up to 64,889 kWh during the system's lifetime.

References

1. Sardianou E, Genoudi P (2013) Which factors affect the willingness of consumers to adopt renewable energies? Renew Energy 57:1–4. ISSN 0960-1481, https://doi.org/10.1016/j.renene.2013.01.031
2. National Energy Board (2016) Canada's energy future 2016 update. Rep. ISSN. 2369-1479. NEB, pp 1–48
3. Tongsopit S (2015) Thailand's feed-in tariff for residential rooftop solar PV systems: progress so far. Energy Sustain Dev 29:127–134. ISSN 0973-0826, https://doi.org/10.1016/j.esd.2015.10.012
4. Antonelli M, Desideri U (2014) The doping effect of Italian feed-in tariffs on the PV market. Energy Policy 67:583–594. ISSN 0301-4215, https://doi.org/10.1016/j.enpol.2013.12.025
5. Spertino F, Ciocia A, Di Leo P, Tommasini R, Berardone I, Corrado M, Infuso A, Paggi M (2015) A power and energy procedure in operating photovoltaic systems to quantify the losses according to the causes. Solar Energy 118:313–326. ISSN 0038-092X, https://doi.org/10.1016/j.solener.2015.05.033
6. Hoppmann J (2014) The role of deployment policies in fostering innovation for clean energy technologies: insights from the solar photovoltaic industry. Bus Soc 54(4):540–558
7. Datta-Barua S, Walter T, Bust GS, Wanner W (2014) Effects of solar cycle 24 activity on WAAS navigation. Space Weather 12(1):46–63. https://doi.org/10.1002/2013sw000982
8. Chapman AJ, McLellan B, Tezuka T (2016) Residential solar PV policy: an analysis of impacts, successes and failures in the Australian case. Renew Energy 86:1265–1279. ISSN 0960-1481, https://doi.org/10.1016/j.renene.2015.09.061
9. Simpson G, Clifton J (2015) The emperor and the cowboys: the role of government policy and industry in the adoption of domestic solar microgeneration systems. Energy Policy 81:141–151. ISSN 0301-4215, https://doi.org/10.1016/j.enpol.2015.02.028
10. Nelson T, Simshauser P, Nelson J (2012) Queensland solar feed-in tariffs and the merit-order effect: economic benefit, or regressive taxation and wealth transfers? Econ Anal Policy 42(3):277–301. https://doi.org/10.1016/s0313-5926(12)50030-5
11. Ioannou AK, Stefanakis NE, Boudouvis AG (2014) Design optimization of residential grid-connected photovoltaics on rooftops. Energy Build 76:588–596. ISSN 0378-7788, https://doi.org/10.1016/j.enbuild.2014.03.019
12. Axaopoulos PJ, Fylladitakis ED (2013) Performance and economic evaluation of a hybrid photovoltaic/thermal solar system for residential applications. Energy Build 65:488–496. ISSN 0378-7788, https://doi.org/10.1016/j.enbuild.2013.06.027
13. Sagani A, Mihelis J, Dedoussis V (2017) Techno-economic analysis and life-cycle environmental impacts of small-scale building-integrated PV systems in Greece. Energy Build 139:277–290. ISSN 0378-7788, https://doi.org/10.1016/j.enbuild.2017.01.022
14. Bicer Y, Dincer I (2016) Analysis and performance evaluation of a renewable energy based multigeneration system. Energy 94:623–632. ISSN 0360-5442, https://doi.org/10.1016/j.energy.2015.10.142
15. Kalinci Y, Hepbasli A, Dincer I (2015) Techno-economic analysis of a stand-alone hybrid renewable energy system with hydrogen production and storage options. Int J Hydrogen Energy 40(24):7652–7664. ISSN 0360-3199, https://doi.org/10.1016/j.ijhydene.2014.10.147
16. Ning G, Junnan L, Yansong D, Zhifeng Q, Qingshan J, Gui W, Geert D (2017) BIM-based PV system optimization and deployment. Energy Build 150:13–22. ISSN 0378-7788, https://doi.org/10.1016/j.enbuild.2017.05.082
17. Akter MN, Mahmud MA, Oo AMT (2016) Comprehensive economic evaluations of a residential building with solar photovoltaic and battery energy storage systems: an Australian case study. Energy Build 138:332–346. ISSN 0378-7788, https://doi.org/10.1016/j.enbuild.2016.12.065
18. Poissant Y, Dignard-Bailey L, Bateman P (2016) Photovoltaic technology status and prospects: Canadian Annual Report 2015. Natural Resources Canada, pp 1–3, Rep.

19. National Energy Board (2017) Canada's adoption of renewable power sources. ISSN. No. 2371-5804. NEB, pp. 1–32
20. Duffie JA, Beckman WA (1991) Solar engineering of thermal processes. Wiley, Hoboken
21. Perez R, Ineichen P, Seals R, Michalsky J, Stewart R (1990) Modeling daylight availability and irradiance components from direct and global irradiance. Solar Energy 44(5):271–289. ISSN 0038-092X, https://doi.org/10.1016/0038-092X(90)90055-H
22. Cronemberger J, Caamaño-Martín E, Sánchez SV (2012) Assessing the solar irradiation potential for solar photovoltaic applications in buildings at low latitudes—making the case for Brazil. Energy Build 55:264–272. ISSN 0378-7788, https://doi.org/10.1016/j.enbuild.2012.08.044
23. Compagnon R (2004) Solar and daylight availability in the urban fabric. Energy Build 36(4):321–328. https://doi.org/10.1016/j.enbuild.2004.01.009
24. Evans DL (1981) Simplified method for predicting photovoltaic array output. Solar Energy 27(6):555–560. ISSN 0038-092X, https://doi.org/10.1016/0038-092X(81)90051-7
25. Dincer I, Rosen MA (2007) Exergy: energy, environment and sustainable development. Elsevier Science Publishers, Amsterdam

Evaluation of an Environmentally-Benign Renewable Energy System for Buildings

Azzam Abu-Rayash and Ibrahim Dincer

Abstract It is very important to have environmentally-friendly solutions based on renewable energy systems for communities. Buildings are large stakeholders in the composition of a community and have substantial energy consumption. In this study, a net zero energy building is considered and modeled using solar PV and geothermal heat pump. The system is assessed for sustainability and energetic and exergetic efficiencies. The solar system considered yields an electricity production capacity of 51.4 kW with exergy efficiency of 15% under atmospheric conditions. The geothermal heat pump has a coefficient of performance of 4.9 and an exergetic coefficient of performance of 2.1. The sustainability index of this system is 0.62 using the hierarchist aggregation method and the weighted geometric mean. Furthermore, the effect of various refrigerants on the thermodynamic performance of the system is investigated.

Nomenclature

Cp	Power coefficient
Cost_0	Project initial cost, $
ex	Specific exergy, kJ/kg
$\dot{\text{Ex}}$	Exergy rate, kW
$\dot{\text{Ex}}_{\text{in}}$	Total exergy input, kW
$E_{S,Y}^{\text{SW}}$	Solar radiation flux, kW/m^2
h	Specific enthalpy, kJ/kg

A. Abu-Rayash (✉) · I. Dincer
Faculty of Engineering and Applied Science, University of Ontario Institute of Technology, 2000 Simcoe Street North, Oshawa, ON L1H 7K4, Canada
e-mail: Azzam.abu-rayash@uoit.ca

I. Dincer
e-mail: Ibrahim.Dincer@uoit.ca

$\dot{N}$	Net negative cash flow, $
$\dot{P}$	Maximum operational hours in a year, hours/year
$\ddot{P}$	Net positive cash flow, $
$\dddot{P}$	Total project investment, $
PI_i	Project's net income in a given year, $
PR	Production rate, tonnes/year
PCF	Periodic cash flow, $/year
Pop	Population
$Power_{max}$	Maximum power output, MW
$\dot{Q}$	Heat rate, kW
R	Recoverable reserves, kg
s	Specific entropy, kJ/kgK
$\dot{S}$	Entropy rate, kW/K
$\dot{S}S$	System size, kW
T	Temperature, K
t	Time, year
v	Specific volume, m^3/kg
W	Weighting factor
$\dot{W}$	Work rate, kW
WAM	Weighted arithmetic mean
WGM	Weighted geometric mean
X	Sustainability indicator
Y	Dimensionless indicator value
YP	Yield production, kWh/kWp

Greek Letters

α	Adjustment factor
η	Energy efficiency
τ	Residence time, hr
ψ	Exergy efficiency

Subscripts

amb	Ambient
Comb	Combustion
Cond	Condense
D	Destruction
ED	Exergy destruction
ER	Energy
EX	Exergy

ENV	Environment
Evap	Evaporator
0	Reference environment
Sust	Sustainability
(T)	Target value

Abbreviations

AP	Acidification potential
AT	Air toxicity
ADP	Abiotic depletion potential
BCR	Benefit–cost ratio
COMM	Commercializability
COP	Coefficient of performance
EI	Educational innovation
EL	Educational level
EP	Eutrophication potential
EES	Engineering Equation Solver
EFI	Environmentally friendliness index
EPA	Environmental protection agency
GHG	Greenhouse gas
GWP	Global warming potential
HH	Human health
HW	Human welfare
IN	Innovation
JC	Job creation
LU	Land use
LCA	Lifecycle assessment
LCOE	Levelized cost of electricity/energy
NPV	Net present value
ODP	Ozone depletion potential
PA	Public awareness
PM	Particulate matter
PV	Photovoltaics
PBT	Payback time
SA	Smog air
SA	Social acceptance
SC	Social cost
TR	Technology readiness
TRAIN	Training
WC	Water consumption
WE	Water ecotoxicity

1 Introduction

Energy management and efficiency enhancements of energy systems have been key strategies in reducing cost and environmental footprint across buildings. Implementing such practices and technologies, energy consumption of buildings can be lowered by up to 35% [1]. Assessment for sustainability of energy systems is significant as it provides a detailed layout of all parameters pertaining energy consumption. A comprehensive sustainability assessment allows for analyzing all system-related parameters, including environmental, economic, social, and technology impacts along with evaluating thermodynamic-based properties. Santoyo-Castelazo and Azapagic [2] included three main indicators to assess the economic category of their sustainability model. They used capital costs, total annualized costs, and levelized costs in order to assess the sustainability of energy systems. They also investigated the social category more comprehensively than other studies by investigating security and diversity of supply of energy, public acceptability, health and safety, and intergenerational issues. Furthermore, the concept of net zero energy houses are widely spreading as their long-term benefits are attractive to national plans of many countries worldwide [1]. For example, the state of California has a policy goal that all new low-rise residences be net zero houses by the year 2020 along with all commercial and high-rise buildings by 2030. Boza-Kiss et al. [3] evaluated policy instruments to foster energy efficiency for the sustainable transformation of buildings. They found that all policy instruments have the potential to generate economic benefit. Furthermore, regulations can be cost-effective in various environments. In addition, public leadership procurement programs have hidden impacts under other instruments. Their data analysis suggests that regulations associated with product energy performance standards have the ability to have the largest lifetime energy-saving impacts. Furthermore, Yi et al. [4] investigated a net zero energy building from an ecological perspective and assessed the sustainability based on emergy theory. Their results show that net zero energy buildings use greater non-renewable emergy to seek a zero-energy budget. Moreover, they claim that sustainable buildings tend to maximize power and not efficiency. Their model included environmental, legal, political, economic, technological, and social factors. Their conclusion indicates that technological and environmental factors were the most influential factors when it comes to sustainability of buildings.

Moreover, Polzin et al. [5] claim that the current financial system is not conducive to an innovation-led energy transition. They indicate that there is a diverse investment demand to make the transition to a more sustainable energy system. They conclude that higher diversity and resilience in financial markets is instrumental to facilitate the transition to clean energy in our current economy. Lastly, Herrero et al. [6] tried to address a critical question whether smart home technologies address key energy challenges in households or not. They claim that real-life evidence of the impact of smart home technologies on everyday life of households is rare. Smart home technologies enable novel ways to use and manage energy in a domestic sphere. In

fact, they argue that smart home technologies may reinforce unsustainable energy consumption patterns in the residential arena and that they are not readily available.

There are technically evident gaps and challenges associated with the concept of a net zero energy building. Although net zero energy buildings require a large capital cost, a quantitative economic assessment remains necessary. Moreover, environmental and social impacts of net zero energy buildings also need to be studied in depth.

The latest technologies and telecommunication techniques in net zero energy building applications have been reviewed by AlFaris et al. [7] who concluded that the renewable energy systems with smart houses are the most cost-effective options. They also claim that the energy performance of such systems is 37% better than ASHRAE standards when integrating renewable energy in smart houses. Furthermore, the energy performances of net zero and near net zero energy buildings were analyzed in New England, and 6 out of 10 houses achieved the net zero standard or better [8]. They also concluded that behavior of occupants, extra equipment, and mechanical problems affected individual energy consumption. Payback time along with other lifecycle analysis of a net zero energy building is presented by Leckner and Zmeureanu [9]. They claim that the energy payback time from solar in this house is between 8.4 and 8.7 years. They also concluded that solar energy conversion also helps in supplying at least 3.5 times more energy than the energy invested for manufacturing and shipping the system. Further financial analysis is presented by Delisle [10] where they evaluated the potential impact of the price fluctuation on net zero energy house construction costs. Their study also compared various combinations of energy efficiency parameters and the annual energy production.

While net zero energy buildings is an attractive idea, which may seem more financially sound and technical feasible, its sustainability or performance is not yet examined in depth. This paper aims to fill this gap by analyzing a net zero energy building, assessing its performance thermodynamically as well as determining the sustainability index associated with this idea. This idea of using the thermodynamic performance along with other major impact of energy systems to assess their sustainability index is novel. Both first and second laws of thermodynamics are considered as the primary criteria of a proposed model to investigate technology development and long-term energy transition [11, 12]. In fact, the authors follow evolutionary forecasting scenarios and use the laws of thermodynamics to simulate the development of energy transformation technologies. The residential energy demand is quiet considerable worldwide, with the majority of the demand belonging to space heating. In Ontario, the residential sector consumes 20% of the total energy consumption in 2017 as illustrated in Fig. 1.
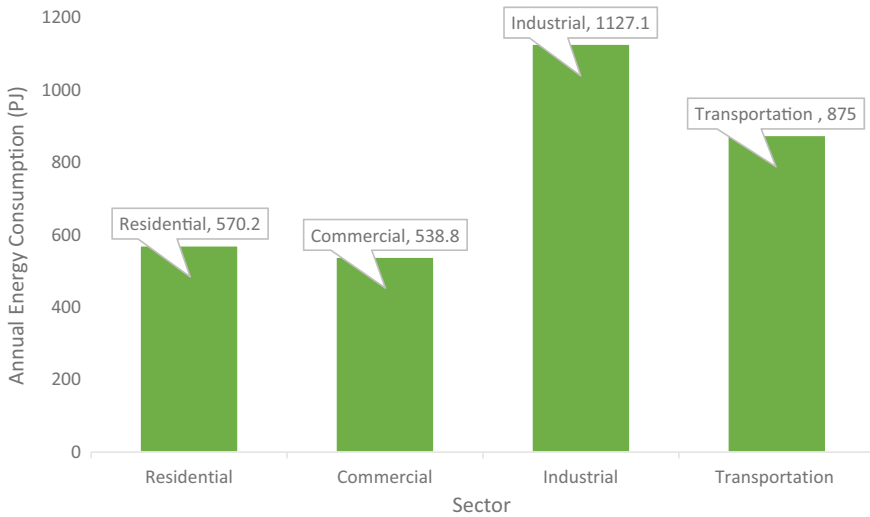
This chapter presents a comprehensive sustainability assessment of a net zero energy building by evaluating the energy system's thermodynamic performance along with other indicators such as economic, social, and environmental impacts. The specific objectives of this study are listed as follows:

- To analyze and assess the performance of a net zero energy house, which uses solar PV and geothermal heat pump.
- To develop a model and assess the sustainability level of the considered system using a comprehensive sustainability assessment model.
- To investigate how changing operating and environment conditions will affect the thermodynamic performance and sustainability of the applied system.

2 System Description

The sustainability assessment is conducted on a residential building in Ontario, Canada. The building is a two-story, 167 m^2 residential complex with an annual natural gas consumption of 35671 kWh and an electric consumption of 5331 kWh annually. The building is located in Bowmanville, specifically at latitude 43.91 and longitude -78.68. The system used to achieve net zero energy is comprised of a grid-integrated, roof-mounted solar PV system, backed up with battery storage. While the solar PV system provides electricity, a ground-source heat pump is employed for heating and cooling applications. Figure 2 illustrates how both systems are connected to the building. Solar PV panels are installed on a south-facing roof, with no shading that surrounds the roof. The panels provide electric power, which is harvested from
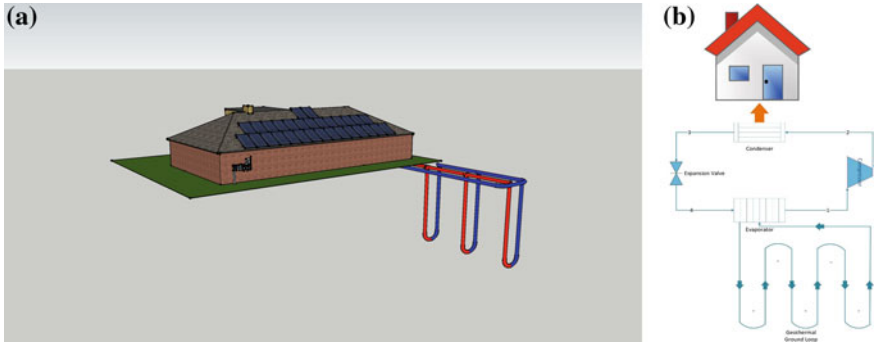
Fig. 2 **a** A 3D illustration of the roof-mounted solar system and the geothermal ground vertical loops and **b** connection between the geothermal ground loop and the heat pump

the sun and converted from direct current to alternating current. Electricity generated through solar is an alternative to current electricity supplied by Ontario energy mix, which is 50% nuclear, 23% hydroelectricity, 10% from natural gas, and the remainder from other renewable sources [14]. The excess electricity is integrated back to the grid under the micro-FIT provincial incentive-based program. Furthermore, heating, cooling, and domestic hot water is supplied by a geothermal vertical loop that is connected with a heat pump system. The design is based on an Ontario residential building of which the electric and gas usage is used for this assessment.

2.1 Solar Photovoltaic System

The electricity generated from the PV systems is used for the overall electric applications of the house as well as to provide the work input for the geothermal heat pump. Additional electricity is fed back to the grid. Due to the intermittent nature of solar energy and seasonal availability, electricity would be required from the grid during nights as well as other periods of low production.

The PV system is composed of 30 panels of 60-cell monocrystalline 300 W modules. The modules have a degradation rate of 0.55% annually and an initial degradation of 2%. It is assumed that all panels fit on the south-facing roof and that the roof is free of any shading surrounding it. Other mechanical and electrical properties of the panels used are presented in Table 1. The solar and geothermal heat pumps are modeled using the Engineering Equation Solver (EES) in order to analyze the system thermodynamically.

Table 1 Mechanical and electrical specifications of the module under nominal operating conditions

Item	Specification
Cells	6 × 10
Cell type	Monocrystalline/P-Type
Cell dimensions ($L \times W \times H$)	161.7 × 161.7 mm/15.25 cm
Front load	6000 Pa
Rear load	5400 Pa
Weight	18.0 kg
Connector type	MC4, JM601A
Maximum power (P_{max})	220 W
MPP voltage (V_{mpp})	29.1 V
MPP current (I_{mpp})	7.56 A
Open-circuit voltage (V_{oc})	36.0 V
Short-circuit current (I_{sc})	8.10 A
Module efficiency	17.5%
Operating temperature	−40 to +90

2.2 Geothermal System

The heat pump is also modeled using the Engineering Equation Solver (EES) in order to analyze the system thermodynamically. The heat pump is designed to meet 90% of the heating demand for the building during the winter season. The demand is evaluated based on monthly utility bills. For this site, natural gas was used for both heating and for hot water. Balance equations for the different states in the system are calculated in order to understand the energetic and exergetic performance of the system. The heat pump uses water glycol solution in the vertical ground loop and ammonia as a refrigerant in the vapor compression cycle for the heat pump, which heats the air for the site. The system is designed to meet the demand of a 7.5 kW load. The vapor compression cycle operates by compressing the working fluid, ammonia, in the compressor to a high pressure and temperature. The compressor for the actual system was assumed to have an isentropic efficiency of 85%. The working fluid (gaseous phase) is then fed into the condenser, which acts as a heat exchanger. Air is heated as the working fluid is condensed. An assumed 50 kPa pressure drop is assumed in the condenser. The working fluid then leaves the condenser as a saturated liquid. From the condenser, the working fluid is throttled in an expansion valve to the evaporator pressure. The throttling process is modeled as an isenthalpic process. The evaporator acts as a heat exchanger transferring heat from the water glycol solution circulating then in the vertical ground loop to the refrigerant. The working fluid enters the compressor as a saturated vapor, repeating the cycle. While Fig. 2a illustrates the connection of the geothermal to the house, Fig. 2b shows the heat pump system. It is assumed that kinetic and potential energy interactions are negligible. In addition, each component is analyzed as a control volume and at a steady state.

The sequence of these equations follows the schematic sketch presented in Fig. 2b. The compressor is labeled as state number 1 followed by the condenser, the expansion valve and finally the evaporator as state number 4.

The heat pump coefficient of performance (COP) is calculated as follows:

$$\text{COP}_{\text{en}} = \frac{\dot{Q}_H}{\dot{W}_C} \tag{1}$$

where $\dot{Q}_H$ is the heat output of the condenser, and $\dot{W}_C$ is work output from the compressor. The energetic performance coefficient COP_{en} is determined by dividing the first term by the second. Furthermore, the exergetic performance coefficient COP_{ex} is calculated using the following equation:

$$\text{COP}_{\text{ex}} = \frac{\dot{\text{Ex}}^{\text{QH}}}{\dot{W}_C} \tag{2}$$

where $\dot{\text{Ex}}^{\text{QH}} = \left(1 - \frac{T_0}{T_H}\right) \times \dot{Q}_H$ is the total exergy of the condenser's heat output.

For the adiabatic compressor, one can write the thermodynamic balance equations as follows:

Mass Balance Equation (MBE):

$$\dot{m}_1 = \dot{m}_2 \tag{3}$$

Energy Balance Equation (EBE):

$$\dot{m}_1 h_1 + \dot{W}_{\text{comp}} = \dot{m}_2 h_2 \tag{4}$$

Entropy Balance Equation (EnBE):

$$\dot{m}_1 s_1 + \dot{S}_{\text{gen}} = \dot{m}_2 s_2 \tag{5}$$

Exergy Balance Equation (ExBE):

$$\dot{m}_1 \text{ex}_1 + \dot{W}_{\text{comp}} = \dot{m}_2 \text{ex}_2 + \dot{\text{Ex}}_{\text{dest}} \tag{6}$$

For the condenser, one can write the thermodynamic balance equations as follows:
Mass Balance Equation (MBE):

$$\dot{m}_2 = \dot{m}_3 \tag{7}$$

Energy Balance Equation (EBE):

$$\dot{m}_2 h_2 = \dot{m}_3 h_3 + \dot{Q}_{\text{out}} \tag{8}$$

Entropy Balance Equation (EnBE):

$$\dot{m}_2 s_2 + \dot{S}_{\text{gen}} = \dot{m}_3 s_3 + \frac{\dot{Q}_{\text{out}}}{T_0} \tag{9}$$

Exergy Balance Equation (ExBE):

$$\dot{m}_2 \text{ex}_2 = \dot{m}_3 \text{ex}_3 + \dot{Q}_{\text{out}} \left(1 - \frac{T_0}{T_0} \right) + \dot{\text{Ex}}_{\text{dest}} \tag{10}$$

For the expansion valve, one can write the thermodynamic balance equations as follows:

Mass Balance Equation (MBE):

$$\dot{m}_3 = \dot{m}_4 \tag{11}$$

Energy Balance Equation (EBE):

$$\dot{m}_3 h_3 = \dot{m}_4 h_4 \tag{12}$$

Entropy Balance Equation (EnBE):

$$\dot{m}_3 s_3 + \dot{S}_{\text{gen}} = \dot{m}_4 s_4 \tag{13}$$

Exergy Balance Equation (ExBE):

$$\dot{m}_3 \text{ex}_3 = \dot{m}_4 \text{ex}_4 + \dot{\text{Ex}}_{\text{dest}} \tag{14}$$

For the evaporator, one can write the thermodynamic balance equations as follows:

Mass Balance Equation (MBE):

$$\dot{m}_4 = \dot{m}_1 \tag{15}$$

Energy Balance Equation (EBE):

$$\dot{m}_4 h_4 + \dot{Q}_{in} = \dot{m}_1 h_1 \tag{16}$$

Entropy Balance Equation (EnBE):

$$\dot{m}_4 s_4 + \frac{\dot{Q}_{\text{in}}}{T_{\text{space}}} + \dot{S}_{\text{gen}} = \dot{m}_1 s_1 \tag{17}$$

Exergy Balance Equation (ExBE):

$$\dot{m}_4 \text{ex}_4 + \dot{Q}_{\text{in}} \left(1 - \frac{T_0}{T_{\text{space}}} \right) = \dot{m}_1 \text{ex}_1 + \dot{\text{Ex}}_{\text{dest}} \tag{18}$$

where the process is isenthalpic and entropy at state 4 can be found using enthalpy and pressure parameters.

2.3 Sustainability Assessment

These two renewable energy systems are assessed from a sustainability perspective in order to gauge the ratio of sustainability they achieve compared to other systems. The sustainability assessment model used is a comprehensive method that integrates various variables together to derive a dimensionless sustainability index. The assessment model takes into consideration environmental, social, and economic impacts along with thermodynamic energy and exergy performances, technology, educational, and sizing indexes. Figure 3 demonstrates the assessment model used for this study, available elsewhere [15]. The energy index accounts for the energy impact on other indexes as the environmentally friendliness impact and the economic impact.

2.3.1 Energy Index

The energy index is assessed using the following formula:

$$Y_{\text{ER}} = \left(\eta \times W_\eta \right) + (Y_{\text{Pr}} \times W_{\text{Pr}}) \tag{19}$$

where Y_{ER} refers to the total score of this index that is calculated by the addition of the scores of the two indicators. η refers to the score of the efficiency of the energy system; W_η refers the weight that is given for this indicator. Y_{Pr} represents the score of the productivity of the energy system, and W_{Pr} represents the weight associated with that indicator. Efficiency refers to the level of performance that describes a process, in which the lowest amount of inputs is used to derive the greatest amount of outputs. It is a measurable concept, which is calculated by determining the ratio between the useful output and the total input. In achieving the desired output, the concept of efficiency minimizes the waste of resource such as energy in any given energy systems. Indeed, efficient energy systems are better able to operate and produce useful energy in a sustainable manner. More efficient energy systems are also more environmentally benign and perform better economically, while less efficient energy systems cause environmental pollution and are less economically favorable. Efficient energy systems have a direct impact on social trends in society such as maintaining a higher standard of living, including living in homes with running water and electricity as well as being mobile. Therefore, energy efficiency is suitable, important, and a reflective indicator to be used in sustainability assessment. Energy efficiency is directly correlated to the first law of thermodynamics. Thus,
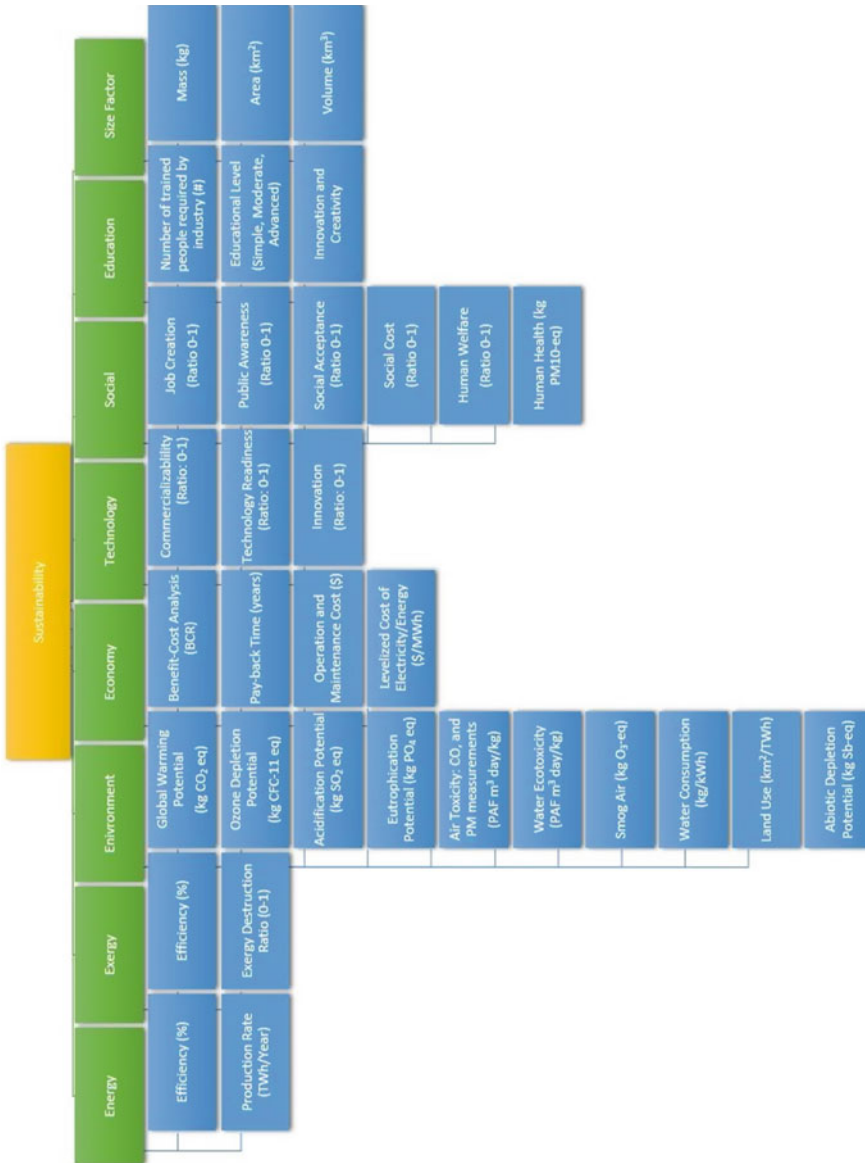
Fig. 3 Integrated sustainability assessment model for energy systems [15]

energy efficiency refers to the ratio of useful energy output in relation to the initial energy input. The actual efficiency of energy systems is always smaller than the upper thermodynamic efficiency limit. This is because the upper limit reflects the reversible reactions, while all energy transformations include irreversibilities that decrease the efficiency below the targeted upper limit. Since the target efficiency is always larger than the actual efficiency, the score for this energy efficiency indicator is evaluated as follows [16]:

$$\eta = \frac{1 - X_{\text{ef}(T)}}{1 - X_{\text{ef}}} \tag{20}$$

where $X_{\text{ef}(T)}$ refers to the target energy efficiency, which is the upper and reversible energy efficiency of the system. X_{ef} refers to the actual energy efficiency achieved by the system, including all the irreversibilities. The term $\left(1 - X_{\text{ef}(T)}\right)$ refers to the minimum amount of unavailable energy, while $(1 - X_{\text{ef}})$ refers to the actual unutilized incoming energy. Production rate compares the design value of the system. Energy systems that produce electricity at higher rates and with larger size are more favorable than the systems that have intermittent or low production rates. The score for this indicator is calculated as follows:

$$Y_{\text{Pr}} = \frac{X_{\text{Pr}}}{X_{\text{Pr}(T)}} \tag{21}$$

where X_{Pr} is the actual production rate of the energy system per hour. $X_{\text{Pr}(T)}$ is the upper target value for production rate in a year. It is calculated using the following equation:

$$X_{\text{Pr}(T)} = \text{PR} \times \dot{P} \tag{22}$$

where PR is the production rate (tonnes/hour) and $\dot{P}$ is the number of maximum operational hours in a year (hour/year). This number varies depending on the type of the system. For example, solar energy is intermittent and dependent on irradiance and sun availability, while nuclear energy is independent of external weather factors. This way, each system is evaluated based on its internal value and function.

2.3.2 Exergy Index

The exergy index is assessed using two main indicators: efficiency and exergy destruction. The score of this index is calculated as such:

$$Y_{\text{EX}} = \left(\psi \times W_{\psi}\right) + (Y_{\text{ED}} \times W_{\text{ED}}) \tag{23}$$

where Y_{EX} represents the total score for the exergy index. The score is a function of these two indicators. ψ represents the exergy efficiency of the system, and W_{ψ}

represents the allocated weight for this indicator. Y_{ED} is the score of the exergy destruction indicator, and W_{ED} is the weight associated with it. Exergy relates to the second law of thermodynamics, which is instrumental in providing meaningful and clearly comprehensible information toward environmental impacts. The most appropriate link between the environmental impact and the second law of thermodynamics has been namely exergy, mainly because exergy is a measurement of the departure of the state of a system from that of the environment. The states of both the system and the environment effect the degree of exergy. In practice, prior to exergy analysis, thermodynamic analysis of the system is conducted by the evaluation of mass and energy balances. Only energy conversion and transfers of the system are taken into consideration in the energy analysis, while exergy analysis focuses on the quality of energy by measuring the degradation of energy or material in the system. Therefore, exergy analysis is associated to the first and second laws of thermodynamics and has the ability to identify the energy quality issues in the system or the work potential. Thus, exergy directly correlates with sustainability, as the assessment should also focus on the loss of energy quality along with the loss of energy itself in the system. Simply, exergy is an effective tool to measure the usefulness of an energy system and the degree of environmental impact an energy system has on the environment. Moreover, in order for energy systems to be considered smart, they need to be exergetically sound [17]. This implies that the system reduces exergy destruction to the minimum while simultaneously increases exergy efficiency to a maximum. When assessing the exergy impact, the proposed model is confined to the following limitations and assumptions:

- This model is confined to energy systems that are in operation.
- The target exergy efficiency is assumed to be greater than the actual exergy efficiency.
- When using linear aggregation, double counting may occur.
- Exergy-based indicators provide solutions for objective and robust measurements.
- The use of exergy in this sustainability assessment is limited to material exchanges, excluding exchanges with society.

Exergy efficiency could be a more important indicator than energy efficiency as it usually gives a finer understanding of performance [18]. Exergy efficiency highlights that losses and internal irreversibilities are to be assessed in order to improve performance. Higher exergy efficiency reflects higher energy quality used in the system, which consequently makes the system more sustainable while lower exergy efficiencies reflect energy losses and internal irreversible reactions; thus, low energy quality and worse sustainable score. Furthermore, exergy analysis enables the identification of energy degradation in an energy system and provides an accurate measure of the useful work that can be utilized from the system. Therefore, the exergy efficiency indicator is a useful tool for maximizing the benefit and efficiently using the resources.

Similar to the energy efficiency, the exergy efficiency's score is calculated as such [16]:

$$\psi = \frac{1 - X_{\psi\text{ef}(T)}}{1 - X_{\psi\text{ef}}} \tag{24}$$

where $X_{\psi\text{ef}(T)}$ represents the reversible exergy efficiency of the system, while $X_{\psi\text{ef}}$ represents the actual exergy efficiency of the system. Exergy destruction is a measure of resource degradation. While exergy efficiency measures the quality of exergy, the system is harnessing, and exergy destruction ratio is assessing the degraded resources and specifies the elements in the system where destruction is occurring. The exergy destruction ratio is calculated as such:

$$\dot{\text{Ex}}_d = (1 - \psi)\dot{\text{Ex}}_{\text{in}} \tag{25}$$

where $\dot{\text{Ex}}_{\text{in}}$ is the total exergy input to the system. For example, solar irradiance is the exergy input to solar energy applications, while chemical and physical exergy of fossil fuels is the exergy input to fuel-based energy applications.

2.3.3 Environmentally Friendliness Index

In addition, the environmentally friendliness index uses numerous indicators such as potential non-air environmental impacts, land use, water consumption, water quality of discharge, solid waste and ground contamination, and biodiversity. The score of this index is calculated as such:

$$
\begin{aligned}
Y_{\text{ENV}} = {}& (Y_{\text{GWP}} \times W_{\text{GWP}}) + (Y_{\text{ODP}} \times W_{\text{ODP}}) + (Y_{\text{AP}} \times W_{\text{AP}}) + (Y_{\text{EP}} \times W_{\text{EP}}) \\
& + (Y_{\text{AT}} \times W_{\text{AT}}) + (Y_{\text{WE}} \times W_{\text{WE}}) + (Y_{\text{SA}} \times W_{\text{SA}}) + (Y_{\text{WC}} \times W_{\text{WC}}) \\
& + (Y_{\text{LU}} \times W_{\text{LU}}) + (Y_{\text{ADP}} \times W_{\text{ADP}})
\end{aligned} \tag{26}
$$

where Y refers to the score for the indicators used, while W refers to the weights assigned for the indicator. GWP refers to the global warming potential, ODP to the stratospheric ozone depletion potential, AP to the acidification potential, EP to the eutrophication potential, AT to air toxicity, WE to water ecotoxicity, SA to smog air, WC to water consumption, LU to the land use, and ADP to the abiotic depletion potential. These ten indicators are carefully selected to account for all of the emissions and environmental impression that energy systems leave throughout manufacturing and operation of these systems. Further explanation follows for each indicator. Humans have been cherishing the concept of sustainability since the early civilization developments. Sustainable development however was environmentally friendly. The key milestone that created the gap between energy and the environment is the use of coal for energy production. The industrial revolution and the use of coal have transformed energy production forever because of the environmental impact it had through the massive emissions of greenhouse gases. The regular pollution caused by the coal revolution and later on followed by the oil revolution has rapidly triggered global warming and climate change. Fossil fuels and conventional energy sources

have revolutionized the human lifestyle and social trends. Coal and oil (also known as black gold) have had a tremendous impact on the modern human civilization. However, the ease of lifestyle and comfort in standard of living came at the cost of environmental vulnerability of the planet. Environmental impacts could be local and specific to certain regions or global and widespread without geopolitical considerations. Furthermore, environmental impacts could also be short or long term. This category has been the most commonly used category in all sustainability assessment models. Energy systems are assessed according to their level of pollution and environmental impact. When assessing the environmental footprint, the proposed model is confined to the following limitations and assumptions:

- The target environmental indicators have lower values than the actual indicators.
- Double counting may occur as environmental indicators are not independent.
- This assessment methodology does not take into account all environmental indicators.

Greenhouse gases contribute to the global climate change and global warming as they warm earth by absorbing the incoming solar energy from the sun and trapping it within the atmosphere. Acting like a blanket insulating earth, they slow the rate at which energy escapes. Most common greenhouse gases that account for this include carbon dioxide (CO_2) and methane (CH_4) and chlorofluorocarbons (CFCs). The element carbon is the common factor among the different greenhouse gases. Global warming potential (GWP) is a measure that was developed to compare the impact of different gases on the atmosphere. Specifically, it is a measure of how much energy is absorbed when 1 ton of a specified gas is released to the atmosphere over a period, relative to the emission of 1 ton of carbon dioxide. In this case, the larger the GWP, the more negative it is for the environment. CO_2 equivalence (CO_2-eq) is used as a measure for GWP. The time usually used for GWP is 100 years. Thus, the GWP indicator in this thesis considers the 100 year warming potential of all greenhouse gases throughout their lifecycle. The following equation illustrates the calculation of the GWP score [16]:

$$Y_{GWP} = \frac{X_{GWP(T)}}{X_{GWP}} \tag{27}$$

where X_{GWP} represents the actual greenhouse gas emissions for the period of 100 years. $X_{GWP(T)}$ represents the target value for this time period, which is the minimum greenhouse gas emissions, achieved by solely relying on renewable energy sources. This means that conventional energy sources such as fossil fuels are not considered in any stage of the energy production of the system. These values can be extracted by SimaPro as part of the lifecycle impact assessment.

While life on earth is impossible without light from the sun, solar radiations contain harmful ultraviolet (UV) rays. The ozone layer, located in the lower level of the earth's stratosphere, fortunately blocks these UV rays from reaching the earth's surface. Although some UV rays are beneficial, prolonged exposure is detrimental. Man-made chlorofluorocarbons (CFCs) have adversely affected the ozone layer.

These CFCs react with the UV rays in the ozone layer and form chlorine (Cl) through a chain reaction. Chlorine then reacts with the ozone (O_3) and breaks its formation into (O_2). The breaking of the ozone layer causes a thinner ozone layer and a more opportunity for UV rays to infiltrate and reach earth's surface. First used as working fluids in refrigerators, CFCs have been banned by the Montreal Protocol. However, CFCs have long residence time (45–1700 years) and old equipment that is still in use keeps emitting these substances, which result in a very slow recovery for the ozone layer. CFC-11 is used to describe all ozone-depleting substance emissions. The following equation illustrates the calculation of the ODP score [16]:

$$Y_{ODP} = \frac{X_{ODP(T)}}{X_{ODP}} \tag{28}$$

where X_{ODP} represents the actual annual CFC-11 emissions per capita. $X_{ODP(T)}$ represents the limit of the CFC-11 emissions per capita. Setting this limit for the CFC-11 emissions per capita is a challenging task. This is because it acts as the target value and had it been set to zero, and then, the solution would not be practical or realistic. To counteract this challenge, Hacatoglu et al. [19] proposed another way to calculate an acceptable amount of ozone depletion over the timescale of considering sustainability. The following is the proposed method of calculation [20]:

$$X_{ODP(T)} = \frac{O_3}{k_{Cl-O_3} \times f_{CFC-11} \times n_{Cl} \times POP_{world} \times t_{Sust}} \times \alpha_{ODP} \tag{29}$$

where k_{Cl-O_3} represents the relationship between the concentration of stratospheric chlorine and ozone depletion. f_{CFC-11} represents the fate factor for CFC-11 when emitted from the earth's surface. n_{Cl} represents the number of chlorine atoms in a single CFC-11 molecule. t_{Sust} is the timescale considered for the sustainability assessment. While the timescale for sustainability assessment can range from five years to infinity, using an infinite value will yield in a zero target value. This reflects that there is no tolerance for stratospheric ozone depletion. The timescale used for this thesis is 100 years. This goes in line with the typical GWP calculation. SimaPro is used to conduct all lifecycle assessments in order to estimate the lifecycle emissions and the impact of pollutants. Input data used to assess the ozone depletion is presented in Table 2.

Acidification potential refers to the compounds that are precursors to acid rain. These include sulfur dioxide (SO_2), nitrogen oxides (NOx), nitrogen monoxide (NO), nitrogen dioxide (N_2O), and other various substances. Acidification potential is usually characterized by SO_2-equivalence. These acid gases are usually released into the atmosphere as a result of fuel combustion. On the other hand, newly constructed coal-fired power plants have a desulfurization technique to limit the SO_2 emissions to the environment. Acidification occurs with substances varying in their acid formation potential. The following equation illustrates the calculation of the AP score [16]:

Table 2 Input parameters used in the lifecycle assessment of the ozone depletion indicator for energy systems [16]

Parameter	Value
Area_{S_ON}	97281 km^2
ΔO_3	2%
$f_{CFC\text{-}11}$	2.8×10^{-9}
GHG	$5.8 \text{ Gt CO}_2\text{-eq year}^{-1}$
K_{Cl-O_3}	0.02
MATAI	$\$69{,}300 \text{ year}^{-1}$
n_{Cl}	3
ODP	0.017
Population_{S_ON}	12.11 million
$\text{Population}_{WORLD}$	7 billion
R_{Sb}	$4.63 \times 1015 \text{ kg}$
t_{Sust}	100

$$Y_{AP} = \frac{X_{AP(T)}}{X_{AP}} \tag{30}$$

where X_{AP} represents the calculated acidification potential (concentration of SO_2) in the local environment. $X_{AP(T)}$ is the latest set standard by EPA for the ambient air quality, which is $190 \ \mu g \ m^{-3}$ [21]. X_{AP} is calculated using the following equation:

$$X_{AP} = SO_2, 0 + \frac{SO_2}{\text{Area}_{Community} \times MH_{SO_2}} \times \frac{\tau_{SO_2}}{8760} \tag{31}$$

where $SO_2, 0, SO_2, \tau_{SO_2}, MH_{SO_2}$ represent the background concentration, annualized lifecycle emissions, residence time, and vertical mixing height of SO_2, respectively [16]. For this thesis, $\text{Area}_{Community}$ represents the total area that a community of 150 households occupy.

Eutrophication is a leading cause of impairment for many coastal marine and freshwater ecosystems. It is characterized by excessive growth of algae and plant due to increased availability of one or more limiting growth factors, which are needed to conduct photosynthesis. Eutrophication is characterized by phosphate equivalence (PO_4-eq) in lifecycle impact assessments. Eutrophication is often detrimental to plants and ecosystems and leads to the vulnerability of economic and social structures. The following equation illustrates the calculation of the EP score [16]:

$$Y_{EP} = \frac{X_{EP(T)}}{X_{EP}} \tag{32}$$

where X_{EP} represents the actual lifecycle emissions of PO_4 per capita per year. $X_{EP(T)}$ represents the target value, which is calculated using the following equation [16]:

$$X_{EP(T)} = EP_{ref} \times \alpha_{EP} \tag{33}$$

where EP_{ref} represents the global annual per capita of PO_4 emissions and α_{EP} represents the adjustment factor.

Air pollution is very common with the rise of industrial projects, innovative transportation means, and residential applications. A polluted air imposes a health and safety risk for inhabitants of this world. A number of substances will be assessed under this indicator. Fine particulate matter ($PM_{2.5}$) inflicts a health concern as they make their way to the lungs. While the composition of particulate matter varies with regions, it generally indicates a mixture of solid particles and liquid droplets in the air. $PM_{2.5}$ refers to the particulate matter that is 2.5 microns in diameter or less. In Ontario, $PM_{2.5}$ is largely composed of nitrate and sulfate particles, elemental and organic carbon. Furthermore, while some $PM_{2.5}$ is carried into Ontario from the USA, it is primarily formed from chemical reactions, mainly from the transportation and residential applications. Another subindicator is the coarse particulate matter (PM_{10}), which is 10 microns or less. Carbon monoxide is also assessed in the toxicity of air. It results from incomplete combustion of fossil fuels. It is also a precursor for ground-level ozone formation and smog air. The following equation illustrates the calculation of the AT score [16]:

$$Y_{AE} = \frac{X_{AE(T)}}{X_{AE}} \tag{34}$$

where X_{AE} is the calculated air toxicity from the annual lifecycle emissions. $X_{AE(T)}$ is the target emission value periodically published by EPA for various regions across the world. For the purpose of this study, the target value of the USA, which is 2.5 $\mu g/m^{-3}$ for $PM_{2.5}$, is used [16].

Similar to eutrophication, water ecotoxicity can cause harm to aquatic ecosystems. Emissions of toxic and lethal substances to water bodies are detrimental to the organisms and the sea life. The common unit to measure water ecotoxicity is measuring 1,4-dichlorobenzene (1,4-DCB). The following equation illustrates the calculation of the WE score [16]:

$$Y_{WE} = \frac{X_{WE(T)}}{X_{WE}} \tag{35}$$

where X_{WE} represents the lifecycle emissions of 1,4-DCB per capita per year. $X_{WE(T)}$ represents the target emissions to freshwater systems per capita per year. The upper target value is calculated as such [16]:

$$X_{WE(T)} = WE_{ref} \times \alpha_{WE} \tag{36}$$

where WE_{ref} represents the global annual per capita of 1,4-1DCB emissions to freshwater systems and α_{WE} is the adjustment factor.

Smog air is mainly composed of ground-level ozone and particulate matter formed near the troposphere. It usually appears as haze in the air due to the mixture of smoke, gases, and particles. Smog air has been linked to a number of adverse health and environmental impacts. Health impacts associated with smog air include thousands of premature deaths and increased hospital visits in several communities. Furthermore, adverse environmental impacts on vegetation, visibility, and structures have been traced to smog air. Warmer temperatures and hotter climate make a perfect ingredient for smog air, and thus, it is more common in the summer season. However, smog air is present in the winter as well. Smog's residence time in the troposphere is quiet short (1 h). The following equation illustrates the calculation of the SA score [16]:

$$Y_{SA} = \frac{X_{SA(T)}}{X_{SA}} \tag{37}$$

where X_{SA} represents the calculated concentration of the ground-level ozone (O_3). $X_{SA(T)}$ represents the upper threshold for ground-level ozone set by the latest environmental protection agency standards, which is 150 $\mu g \ m^{-3}$ [21]. The calculated concentration of the ground-level ozone is calculated using the following equation:

$$X_{SA} = O_3, 0 + \frac{O_3}{Area_{Community} \times MH_{O_3}} \times \frac{\tau_{O_3}}{8760} \tag{38}$$

where $O_3, 0, O_3, \tau_{O_3}$, and MH_{O_3} represent the background concentration, annualized lifecycle emissions, residence time, and vertical mixing height of O_3, respectively [16].

Water consumption is an important factor to consider when assessing sustainability of energy systems, especially in arid climates such as Australia, where water evaporation rates are quiet high. While some LCAs have ignored the water requirements and availability for thermal systems, some have recently introduced them. Water consumption refers to the amount of water lost during the process of energy production. The following equation illustrates the calculation of the WC score:

$$Y_{WC} = \frac{X_{WC(T)}}{X_{WC}} \tag{39}$$

where X_{WC} represents the actual used water in the lifecycle of the energy system, and Table 3 shows different values that will be used for each system based on the works of Inhaber [22]. $X_{WC(T)}$ represents the target values for water consumption based on Spang et al. [23].

Abiotic depletion potential is a factor that is assessed in lifecycle assessments. It refers to the measure of the use of non-renewable sources for energy production. The following equation illustrates the calculation of the ADP score [16]:

$$Y_{ADP} = \frac{X_{ADP(T)}}{X_{ADP}} \tag{40}$$

Table 3 Water consumption of electricity generation from various sources (kg/kWh)

Energy source	X_{WC} (L/kWh)
Photovoltaic	10
Hydro	36
Wind	1
Geothermal	12–300
Gas	78
Coal	78

Source Inhaber [22]

where X_{ADP} represents the lifecycle use of antimony and its equivalents per capita per year. $X_{ADP(T)}$ represents the annual sustainable antimony allocation. The threshold value is calculated using the following equation [16]:

$$X_{ADP(T)} = \frac{R_{Sb}}{POP_{world} \times t_{sust}} \times \alpha_{ADP} \tag{41}$$

where R_{Sb} represents the recoverable reserves of antimony.

2.3.4 Economic Index

Economy is a critical category when assessing sustainability of energy systems. What does an economically sustainable energy system look like? This critical question must be addressed in any project before embarking on the execution journey. Furthermore, while conventional energy sources are relatively cheaper, renewable energy sources remain quiet expensive. However, improved economic planning and the progress toward cheaper renewable and clean energy is making the competition tougher between energy systems. Moreover, economic factors involved in the operation and design of energy conversion systems have brought the thermal energy storage, for example, to the forefront of its industry [24]. Several thermal energy storage technologies are indeed present in the industry and are used side by side with on-site energy sources to economically buffer variable rates of supply and demand. In addition, an energy system is economically sustainable when they meet the following standards:

- The economic benefit of the energy generation outweighs operational, capital, and maintenance cost. Simply, the project is economically viable.
- Energy systems with shorter payback periods are preferred over systems with longer payback periods. This attracts investors.
- Lower levelized cost of energy/electricity. Energy available for everyone at a relatively lower cost.

Moreover, the economic index is also taken into consideration when assessing the sustainability of this energy system. Energy systems are economically sustainable if

they are profitable, serviced at lower cost for the consumer and contain the elements of a successful business idea. The score of this index is calculated as such:

$$Y_{\text{ECO}} = (Y_{\text{BCR}} \times W_{\text{BCR}}) + (Y_{\text{PBT}} \times W_{\text{PBT}}) + (Y_{\text{LCOE}} \times W_{\text{LCOE}}) \tag{42}$$

where Y_{BCR}, Y_{PBT}, and Y_{LCOE} refer to the scores of benefit–cost ratio, payback time, and the levelized cost of energy/electricity, respectively. W terms refer to the weight associated with each indicator.

The benefit–cost ratio (BCR) indicator aims to explore the relationship between the benefit and cost of any proposed energy system. This indicator is informative both quantitatively and qualitatively as it analyzes all the possible benefits and costs. All benefits associated with an energy system are summed, while all costs are subtracted. While this analysis is routinely conducted in any business matter, it is novel to the sustainability assessment of energy systems. When conducting a cost–benefit analysis, the results that are more accurate are achieved by analyzing the net present value (NPV) of all future costs and benefits. Simply, if NPV is negative, the project will never pay for itself and thus it is a financially losing project. However, if NPV is positive, the profits outweigh the costs and the project will pay for itself over time and eventually generate profits. The net present value is calculated using the following equation:

$$\text{NPV} = \sum_{i=1}^{N} \left(\frac{\text{PI}_i}{(1+r)^i} \right) - \text{Cost}_0 \tag{43}$$

where PI_i represents the project's net income in a given year. N represents the number of years over which the project income occurs. r is the discount rate, and Cost_0 is the project cost, typically assumed in the initial year (0). On the other hand, the benefit–cost ratio is another method of analyzing the benefits and costs of a given energy system. The following equations are used to determine the benefit–cost ratio:

$$\text{BCR} = \frac{\ddot{P}}{\dot{N}} \tag{44}$$

where $\ddot{P}$ represents the present value of the net positive cash flow and $\dot{N}$ represents the present value of net negative cash flow.

The payback period is an indicator used to assess the short- and long-term benefits of the proposed energy systems if any. Logically, energy systems with shorter payback periods are more economically favorable than those with longer payback periods. Thus, shorter payback period is associated with higher sustainability. The payback time refers to the time it takes in order for the project to recover all invested amounts and is usually expressed in years. Payback method does not take into account the time value of money unlike the previous indicator (net present value or benefit–cost ratio). The calculation of the payback time is simple. The following equation is used to determine the payback period:

Table 4 Scorecard for payback time

Score	Payback time (PBT)
0.76–1	$0 < \text{PBT} < 5$
0.51–0.75	$6 < \text{PBT} < 11$
0.26–0.5	$12 < \text{PBT} < 17$
0–0.25	$18 < \text{PBT} < 23$

$$\text{PBT} = \frac{\dddot{P}}{\text{PCF}} \tag{45}$$

where $\dddot{P}$ represents the total project investment in (\$) and PCF represents the periodic cash flow in (\$/year). Table 4 shows the judgment criteria set to obtain the PBT score. Shorter payback time is advantageous and more attractive.

The levelized cost of electricity or energy (used interchangeably) refers to the cost of energy. It accounts for all lifetime costs of the system, including operation, maintenance, construction, taxes, insurance, and other financial obligations of the project. They are then divided by the expected total energy outcome in the system's lifetime (kWh). Cost and benefit estimates are adjusted to account for inflation and are discounted to reflect the time value of the money. It is indeed a very valuable tool to compare different generation methods. Lower LCOE values resemble low energy cost, which in turn reflects back with high financial profit to the investors and vice versa.

$$\text{LCOE} = \frac{\sum_{i=0}^{N} \left[\frac{I_i + O_i + F_i - \text{TC}_i}{(1+r)^i} \right]}{\sum_{i=0}^{N} \left[\frac{E_i}{(1+r)^i} \right]} \tag{46}$$

where I_i is investment costs in year I, O_i represents the operation and maintenance costs in year i, F_i represents the fuel costs in year i, TC_i represents the total tax credits in year i, E_i represents the energy generated in year i, r is the real discount rate, and N is the economic lifetime of the system.

The value of the LCOE includes the capital cost average, fixed operation and maintenance cost average, variable operation and maintenance average as well as the fuel cost average. The LCOE score is determined by the following equation:

$$Y_{\text{LCOE}} = \frac{X_{\text{LCOE}(T)}}{X_{\text{LCOE}}} \tag{47}$$

where X_{LCOE} represents the actual LCOE of the energy system presented in Table 5. $X_{\text{LCOE}(T)}$ represents the target value for the future and long-term LCOE for that system. For the purpose of this study, the values published by the US Energy Department for the LCOE for various energy systems in the year of 2040 will be used in the case studies for the values of $X_{\text{LCOE}(T)}$.

Table 5 Actual values for the LCOE of various ways of energy generations [25]

Energy source	LCOE (US $/MWh)
Photovoltaic	80
Hydro	36
Geothermal	116
Gas	73
Coal	110
Nuclear	113

2.3.5 Technological Index

The technology index is also taken into consideration. The score of this index is calculated as such:

$$Y_{\text{TECH}} = (Y_{\text{COMM}} \times W_{\text{COMM}}) + (Y_{\text{TR}} \times W_{\text{TR}}) + (Y_{\text{IN}} \times W_{\text{IN}}) \tag{48}$$

where Y_{COMM}, Y_{TR} and Y_{IN} refer to the scores of commercializability, technology readiness and innovation.

2.3.6 Social Index

Moreover, the social index accounts for the social aspects associated with the energy system. The score of this index is calculated as such:

$$Y_{\text{SOC}} = (Y_{\text{JC}} \times W_{\text{JC}}) + (Y_{\text{PA}} \times W_{\text{PA}}) + (Y_{\text{SA}} \times W_{\text{SA}}) + (Y_{\text{SC}} \times W_{\text{SC}}) \\ + (Y_{\text{HW}} \times W_{\text{HW}}) + (Y_{\text{HH}} \times W_{\text{HH}}) \tag{49}$$

where Y_{JC}, Y_{PA}, Y_{SA}, Y_{SC}, Y_{HW}, and Y_{HH} refer to the scores of job creation, public awareness, social acceptance, social cost, human welfare, and human health, respectively. W refers to the weight associated with each indicator. Social aspects of energy systems are very important for their sustainability. Social indicators help assess the impacts on the social system, which is composed of the beneficiaries of the energy system, whether directly or indirectly. In fact, proper utilization of renewable energy for example can have a direct impact socially and economically with further development of secure and sustainable energy supply [26]. On another important note, social morals and ethics is also a critical component of the social category. When addressing the concept of sustainability, adhering to a common set of principles and values can help govern the dynamics and the limits of energy systems. It is important to correctly identify and quantify the social indicators as they contribute to the acceptance and awareness socially. These elements are interconnected because job creation in a community causes awareness publicly and eventually leads to social acceptance. Furthermore, if a system is accepted socially, public awareness has the environment

Table 6 Judgment criteria for assessing the job creation indicator (*source* IRENA and CEM [27])

Score	Employment factor (jobs/MW)
0–0.25	0 < Employment factor < 9
0.26–0.5	10 < Employment factor < 29
0.51–0.75	30 < Employment factor < 49
0.76–1	50 < Employment factor < 69

to flourish. On the other hand, if a system is rejected socially, the other two elements are adversely affected. When assessing the social impression, the proposed model is confined to the following limitations and assumptions:

- The capacity for job creation is up to 69 jobs per megawatts as per IRENA and CEM [27].
- Survey results are considered a reliable source of information. Therefore, the size and quality of surveys are assumed to be of high quality.
- LCA is used to assess the human health indicator.

Energy systems have ever grown in the past few centuries, and they created many niches around them. When assessing an energy system, it is important to understand the social category behind the project and analyze the number of jobs that can be created to the local community or the larger region. Of course, more job creation is considered advantageous as that city prospers and attracts employees, talents from all over the surrounding regions. This increases the social life and the social activity in that local city, thus yielding in favorable results. It is considered sustainable when energy systems have high employment factor. The IRENA and CEM [27] published a report on employment factors for wind and solar energy technologies. For the purpose of this study, the job creation factor is assessed based on the number of jobs created after each newly installed MW. The employment factor is presented in the units of (jobs/MW). Table 6 presents the judgment criteria for assessing this indicator.

Enhancing public knowledge and understanding about the issues that the energy industry is facing is vital to ensuring growth, energy sustainability and security in our communities. Government programs, incentives, and other means of raising awareness all contribute toward creating an informed society. Indeed, innovative and coordinated awareness campaigns have had an impact on Scotland's perspective on renewable energy for example [28]. In this assessment model, it is considered that bigger positive public awareness is sustainable, while smaller awareness is less sustainable. A value of 1 is assigned to systems that have big public awareness, and a value of 0 is assigned to systems that have little awareness. Surveying is used to determine the public awareness of the project in interest.

The power of the people is immense, and thus, for an energy system to be sustainable and operational, it must be accepted and perceived positively by society. For example, debates are still ongoing in several countries against wind energy, mainly because of its visual impacts on landscapes. Social acceptance therefore is an influential factor that could be a powerful barrier to the achievement of the energy targets of the system. This indicator has been neglected at the start of 1980s when

policy programs were drafted at first. Later on, this factor surfaced to prove that it is essential before establishing an energy system in any locality. Therefore, successful energy systems are the ones that succeeded in integrating in the daily life of societies today [17]. Community acceptance goes hand in hand with social acceptance and is essential for sustainability assessment. For this model, the social acceptance score is determined by surveying the social acceptability of the project in interest. A value between 0 and 1 will be assigned to this indicator.

This indicator brings a number of factors together in one value. The social cost is related to the economic category as well as the environmental, energy, and social categories. Energy systems usually come with a cost socially. This indicator has been assessed by calculating the social cost of carbon. This value helps determine the monetary benefit/cost of regulations in reducing carbon emissions. Cost-free behavior of using fossil fuels has led to an addiction over these depleting resources.

Human welfare is a soft indicator that is used in this model to assess energy systems. Energy systems that take into consideration the welfare of society are more favorable and thus more sustainable. On the other hand, systems that are aversive to human welfare are considered less sustainable. A value of 1 is assigned to systems that have positive impact on human welfare, and a value of 0 is assigned to systems that have negative impacts.

With evolving technologies and innovative research, humans are exposed to various inputs that are constantly changing. The human health criterion is a social indicator used to assess energy systems on the effects of any toxic substances on human health. Being exposed to various substances on a regular basis definitely has an impact. As a result, this indicator is considered important in order to comprehensively assess the sustainability of energy systems. A value of 1 is assigned to systems that have minimal human health impacts, and a value of 0 is assigned to systems that have high human health impacts.

2.3.7 Educational Index

The educational index reflects the level of education, training, best practices, and innovation in educational methods adopted in various systems. Therefore, this index is calculated by assessing three main indicators. The score of this index is calculated as such:

$$Y_{\text{EDU}} = (Y_{\text{TRAIN}} \times W_{\text{TRAIN}}) + (Y_{\text{EL}} \times W_{\text{EL}}) + (Y_{\text{EI}} \times W_{\text{EI}}) \tag{50}$$

where Y_{TRAIN}, Y_{EL}, and Y_{EI} refer to the score for the number of trained people required by the industry, educational level, and educational innovation. W refers to the weights associated with each indicator. Lastly, the sizing index refers to the size of the system with respect to volume, mass, and land use of the energy system. The volume and mass parameters are associated with mobile applications such as vehicles. The land use is associated with stationary applications such as a power plant. The sizing index reflects the magnitude of the energy system and consequently gives an accurate

understanding when assessing its sustainability. The sizing index of the energy system in this sustainability assessment model will look at three main indicators: mass, land use, and volume. The score of this category is calculated as such [16]:

$$Y_{\mathrm{MF}} = (Y_M \times W_M) + (Y_{\mathrm{LU}} \times W_{\mathrm{LU}}) + (Y_V \times W_V) \tag{51}$$

where Y_M, Y_{LU}, and Y_V refer to the score for mass, land use, and volume, respectively. W refers to the weights associated with each indicator.

3 Results and Discussion

Thermodynamic assessment on this system is performed in order to understand its technical parameters as well as its energetic and exergetic performance as part of the sustainability assessment. Table 7 presents the main state points of the geothermal system and the thermodynamic parameters associated with each state point, including the pressure, temperature, enthalpy, entropy, exergy, and position.

Furthermore, the influence of the geothermal fluid temperature over the exergetic COP is evident with a positive linear relationship illustrating that higher temperatures of geothermal fluid yield in higher exergetic COPs. However, the COP of the heat pump remains unchanged with varying geothermal fluid temperatures. Figure 4 demonstrates this relationship clearly.

Moreover, the effectiveness of the design for the geothermal heat pump system was dependent on the selection of a refrigerant with favorable thermodynamic and transport properties. Historically, the use of refrigerants has been connected to disastrous environmental consequences; thus, significant consideration was also given to the global warming potential of the refrigerant. Analysis of a vapor compression refrigeration cycle with R134a, R1234yf and ammonia revealed ammonia to be the most favorable refrigerant in terms of its thermodynamic and transport properties. R134a was eliminated as it is currently being phased out due to its 100 year GWP. R1234yf is the least effective in terms of its thermodynamic and transport properties.

Table 7 All state points and thermodynamic properties of the geothermal system

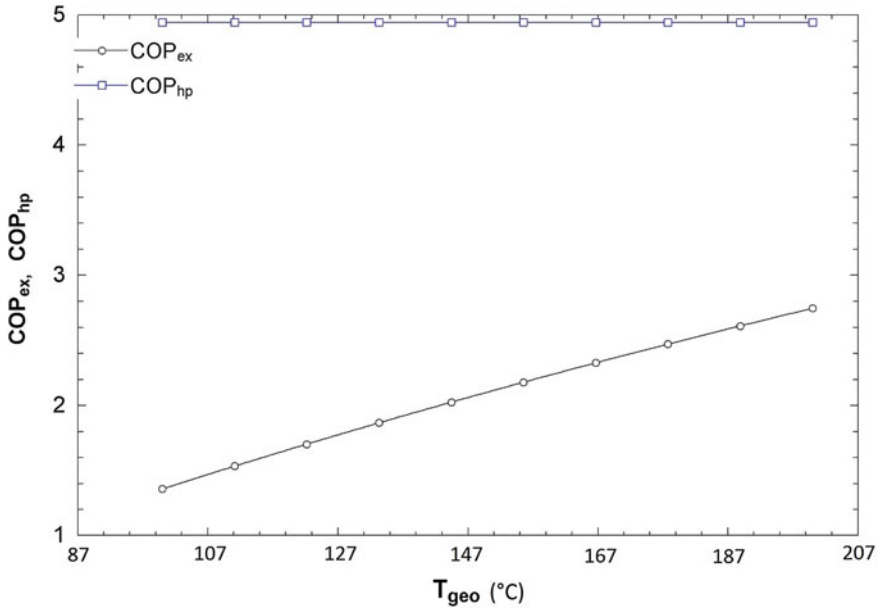| State	Pressure (kPa)	Temperature (K)	Specific enthalpy (kJ/kg)	Specific entropy (kJ/kg K)
0	101.3	298.2	2192	8.122
1	200	−18.85	1439	5.886
2	1200	128.7	1749	6.005
3	1200	30.93	1487	5.253
4	1150	29.5	339.2	1.48
5	200	−18.85	339.2	1.561
6	200	−18.85	1439	5.886

Fig. 4 Impact of the geothermal fluid temperature on the exergetic and energetic COPs

This investigation and comparison of different refrigerants revealed the considerable potential and current need for the continued development of refrigerant, which are both environmentally benign and thermodynamically effective.

Figure 5 shows the exergy destruction of each refrigerant at each stage of the heat pump cycle. The evaporator hosts the most exergy destruction throughout the
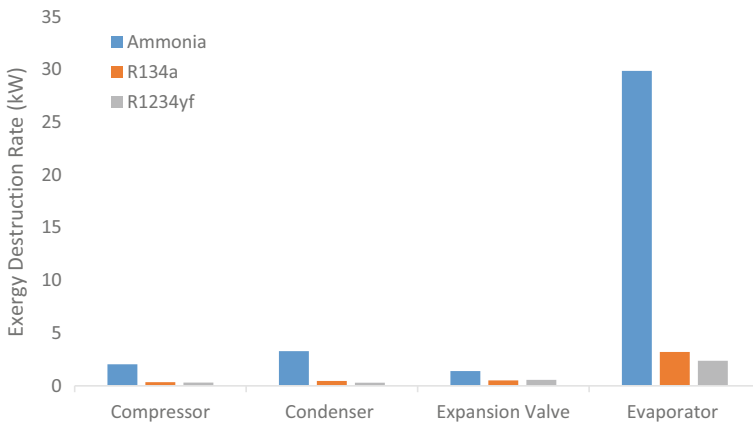

Fig. 5 Exergy destruction rates of the main components of the heat pump system using different refrigerants

different refrigerants with ammonia having a significant exergy destruction at this stage.

On a different note, the impact of the mass flow rate of the geothermal fluid on exergetic and energetic COPs is presented in Fig. 6. The trend shows a negative exponential curve, whereas the mass flow rate increases; both the energetic and exergetic COPs decrease in a similar fashion. Moreover, the exergetic and energetic COPs are assessed for each refrigerant.

Figure 7 shows the outcome, which shows the highest exergetic COP to be that of R1234yf. As for the solar system, the ambient temperature was analyzed for its impact on the exergy destruction of the solar system as well as the exergy efficiency.

It is evident from Fig. 8 that the relationship between these two variables and the ambient temperature is that of a positive linear relationship. As the ambient temperature increases, the exergy efficiency of the system also increases linearly, whereas the exergy destruction also increases in a similar fashion.

On the other hand, the irradiance has a different trend on the exergy destruction and the solar heat output. As shown in Fig. 9, as the solar irradiance increases, the exergy destruction increases in a linear trend. However, the solar heat output also increases in a linear, yet steeper trend than that of the exergy destruction.

The time-space-receptor method was also used in appointing appropriate values for each index. The indexes used in this study vary as some have long-term impact such as exergy and energy indexes while others have short-term impact. Table 8 shows the various indexes and their associated weights as per the schemes used: panel method, individualist, egalitarian, hierarchist, and equal weighting method.
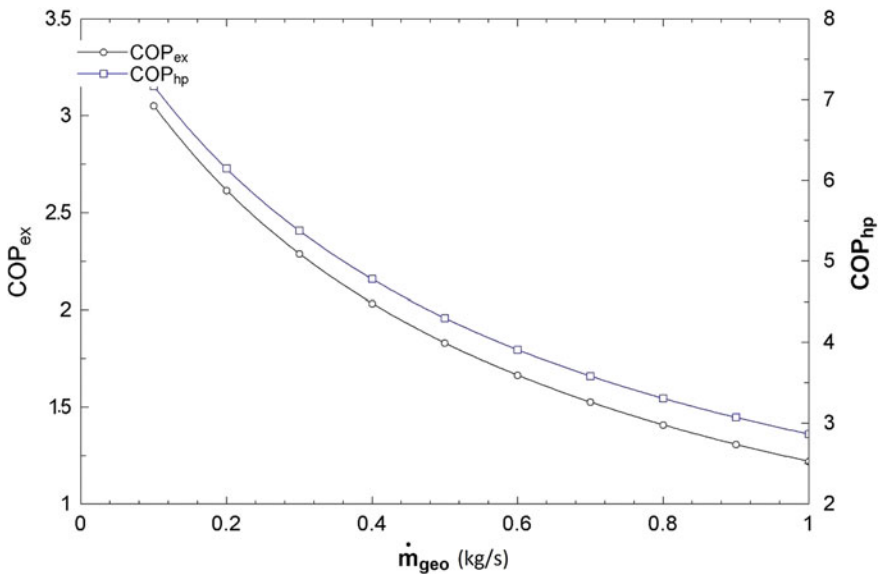

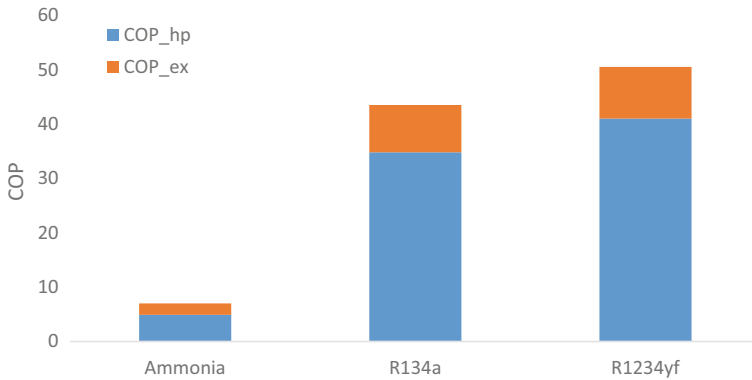**Fig. 6** Impact of the geothermal water mass flow rate on exergetic and energetic COPs

Fig. 7 Exergetic and energetic COPs using different refrigerants
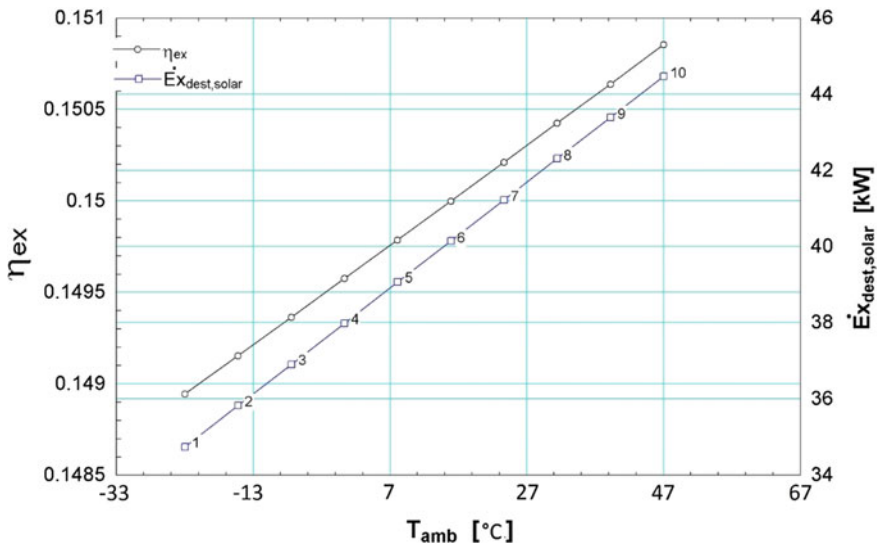

Fig. 8 Impact of ambient temperature on the exergy destruction of the solar system and the exergy efficiency

There are slight variations between the different schemes in prioritizing specific indexes over other indexes as illustrated in Fig. 10. For example, the panel method prioritized the exergy index and neglected the sizing index, while the individualist method prioritized the social index and neglected technology index. Furthermore, the panel gave less priority for education, whereas all the other schemes placed it at a higher priority compared to the panel scheme.

When analyzing the overall system, the sustainability index ranges between 0.57 and 0.66 depending on which aggregation scheme is used. Figure 11 illustrates the
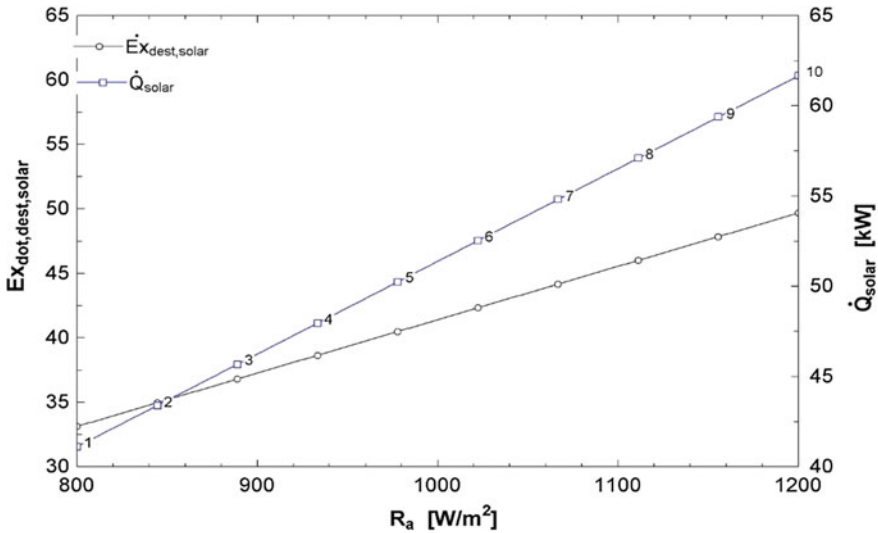
Fig. 9 Impact of solar irradiance on the exergy destruction of the solar system and the solar energy output

Table 8 Priority factors of the eight indexes of the sustainability model with respect to various schemes

Index	Individualist	Egalitarian	Hierarchist	Panel	Equal weighting
Energy	0.13	0.12	0.13	0.10	0.13
Exergy	0.13	0.12	0.13	0.17	0.13
Environmentally friendliness	0.13	0.13	0.15	0.18	0.13
Economic	0.13	0.15	0.13	0.14	0.13
Technology	0.09	0.12	0.12	0.12	0.13
Social	0.17	0.12	0.12	0.15	0.13
Educational	0.13	0.12	0.12	0.09	0.13
Sizing	0.10	0.10	0.12	0.05	0.13

sustainability assessment results of the system with the value 1 being the highest value for sustainability. It is evident that the equal weighting aggregation method yields in higher sustainability values, while the individualist aggregation method yields in lower sustainability values. The purpose behind using different aggregation methods is to reach to an accurate result, which can be considered reliable. It is also used to understand the degree of variance between the results. In this case, the results vary with a maximum of 0.09 points, which if converted into percentage; it is a 9% variance.
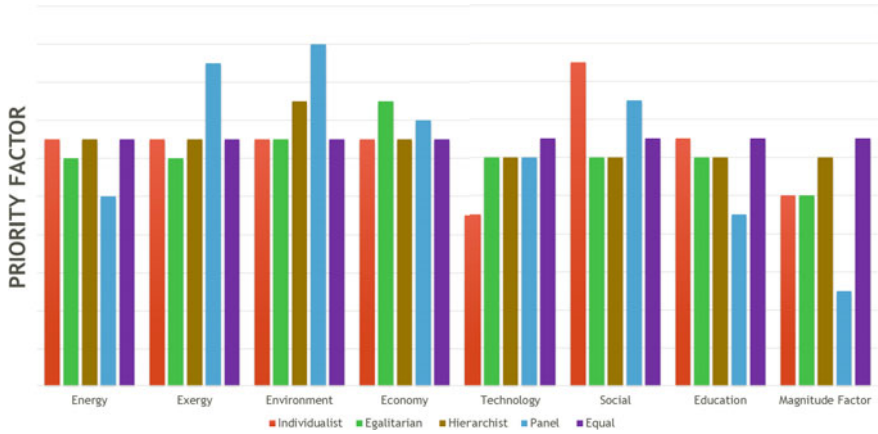
Fig. 10 Distribution of priority factors based on the four schemes for the main indexes used for the sustainability assessment model
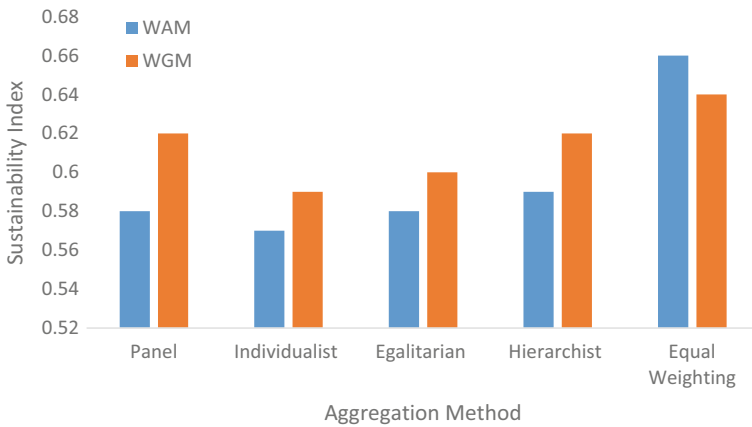

Fig. 11 Distribution of the sustainability index results based on the various aggregation method and characterization scheme

The egalitarian scheme seems to be most moderate and thus to analyze it further; the top three indexes have been investigated in depth. Figure 12 shows the impact of each of these indexes as their value increases from 0.2 to 1 on the overall sustainability index. It is evident that manipulating the economic index yields in the highest change over the sustainability index. However, the sizing index does not influence the overall sustainability index as much.
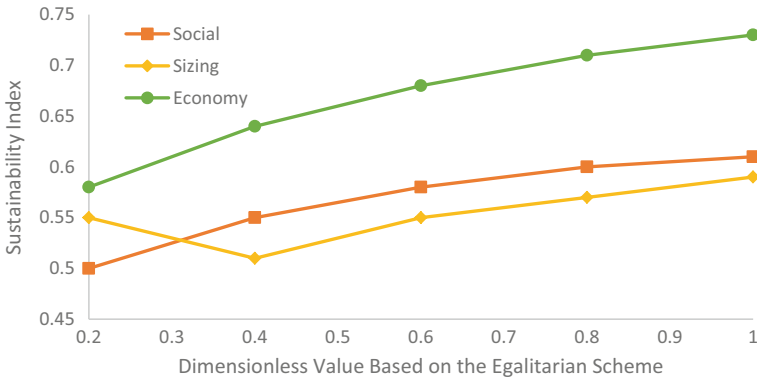
Fig. 12 Comparison of the main indexes using the egalitarian scheme on the overall sustainability index

4 Conclusions

In conclusion, the sustainability assessment of a net zero energy building is conducted. The analysis of the two renewable energy sources included balanced equations for mass, energy, and exergy for both systems and their subcomponents. Energetic and exergetic COPs are calculated. The Engineering Equation Solver (EES) software package is used to perform parametric studies to determine the effects of varying operating and environmental conditions on the system performance. The geothermal heat pump system is designed to satisfy a heating load of 7.5 kW using ammonia as the refrigerant. The COP of the geothermal heat pump is calculated to be 4.9, while the exergetic COP is 2.1. The effect of the condenser pressure on the performance of the heat pump is also analyzed. Increasing the condenser pressure increased the temperature of the refrigerant, leaving the condenser; however, higher pressures required higher compressor work input and decreased the heat output. Overall, increasing the condenser pressure lowered the cycle COP. The performance of the heat pump system using three different refrigerants—R1234yf, R134a, and ammonia—is also investigated. In addition to their thermodynamic properties, the environmental impact of each refrigerant is considered. Ammonia is selected as the most appropriate due to its non-toxicity and low 100-GWP despite inferior COP results. Furthermore, the yielded electricity production from the solar system is 51.4 kW with exergetic efficiency of 15% under atmospheric pressure and temperature. The sustainability index of the system ranges between 57 and 66%. The manipulation of the economic index using the egalitarian aggregation method could yield in a sustainability index of up to 73%.

References

1. Ayoub J (2013) Towards net zero energy solar buildings. CanmetEnergy, Natural Resources Canada, Government of Canada
2. Santoyo-Castelazo E, Azapagic A (2014) Sustainability assessment of energy systems: integrating environmental, economic and social aspects. J Clean Prod 80:119–138
3. Boza-Kiss B, Moles-Grueso S, Urge-Vorsatz D (2013) Evaluating policy instruments to foster energy efficiency for the sustainable transformation of buildings. Curr Opin Environ Sustain 5(2):163–176
4. Yi H, Srinivasan RS, Braham WW, Tilley DR (2017) An ecological understanding of net-zero energy building: evaluation of sustainability based on emergy theory. J Clean Prod 143:654–671
5. Polzin F, Sanders M, Täube F (2017) A diverse and resilient financial system for investments in the energy transition. Current Opinion in Environmental Sustainability 28:24–32
6. Herrero TS, Nicholls L, Strengers Y (2018) Smart home technologies in everyday life: do they address key energy challenges in households? Curr Opin Environ Sustain 31:65–70
7. Alfaris F, Juaidi A, Manzano-Agugliaro F (2017) Intelligent houses' technologies to optimize the energy performance for the net zero energy house. Energy Build 153:262–274
8. Thomas WD, Duffy JJ (2013) Energy performance of net-zero and near net-zero energy houses in New England. Energy Build 67:551–558
9. Leckner M, Zmeureanu R (2011) Life cycle cost and energy analysis of a Net Zero Energy House with solar combisystem. Appl Energy 88(1):232–241
10. Delisle V (2011) Net-zero energy houses: solar photovoltaic electricity scenario analysis based on current and future costs. ASHRAE Trans 112(2):315–322
11. Wang Z, Xu G, Ren J, Li Z, Zhang B, Ren X (2017) Polygeneration system and sustainability: multi-attribute decision-support framework for comprehensive assessment under uncertainties. J Clean Prod 167:1122–1137
12. Wang Z, Wennersten R, Sun Q (2017) Outline of principles for building scenarios—transition toward more sustainable energy systems. Appl Energy 185(Part 2):1890–1898
13. National Energy Board (2017) Canada's adoption of renewable power sources. NEB, pp 1–32. ISSN no. 2371-6804
14. Ontario Ministry of Energy (2017) Ontario's long term energy plan 2017. Ministry of Energy
15. Abu-Rayash A, Dincer I (2019) Sustainability assessment of energy systems: a novel integrated model. J Clean Prod 212:1098–1116. https://doi.org/10.1016/J.JCLEPRO.2018.12.090
16. Hacatoglu K (2014) A systems approach to assessing the sustainability of hybrid community energy systems. Ph.D.'s thesis, University of Ontario Institute of Technology, Oshawa
17. Dincer I, Acar C (2017) Smart energy systems for a sustainable future. Appl Energy 194:225–235
18. Caliskan H, Dincer I, Hepbasli A (2011) Exergoeconomic, enviroeconomic and sustainability analyses of a novel air cooler. Energy Build 55:747–756. https://doi.org/10.1016/j.enbuild.2012.03.024
19. Hacatoglu K, Dincer I, Rosen M (2015) A new model to assess the environmental impact and sustainability of energy systems. J Clean Prod 103:211–218
20. Goedkoop M, Spriensma R (2001) The eco-indicator 99: a damage oriented method for life cycle impact assessment
21. EPA (2011) National ambient air quality standards. Washington D.C. Available online: http://www.epa.gov/air/criteria
22. Inhaber H (2004) Water use in renewable and conventional electricity production. Energy Sources 26(3):309–322. https://doi.org/10.1080/00908310490266698
23. Spang ES, Moomaw WR, Gallagher KS, Kirshen PH, Marks DH (2014) The water consumption of energy production: an international comparison. Environmental Research Letters 9(10):105002. https://doi.org/10.1088/1748-9326/9/10/105002
24. Dincer I, Rosen M (2007) Energetic, exergetic, environmental and sustainability aspects of thermal energy storage systems. NATO Science Series Thermal Energy Storage for Sustainable Energy Consumption, pp 23–46

25. Lazard (2014) Levelized cost of energy analysis, 8th edn. New York City, NY
26. Dincer I, Acar C (2015) A review on clean energy solutions for better sustainability. Int J Energy Res 39(5):585–606
27. IRENA and CEM (2014) The socio-economic benefits of large-scale solar and wind: an econ-Value report
28. McLaughlin J, Smith M (2002) Power of the people: Public awareness and involvement in renewable energy in Scotland. Refocus 3(5):26–29

Numerical Study of Thermal Transport in a Flat-Plate Solar Collector Using Novel Absorber Plate

Hudhaifa Hamzah, Salim Ibrahim Hasan and Serhan Küçüka

Abstract In the light of introducing new techniques to develop the thermal performance of a solar collector, the development of design represents one of the efficient steps in this field. Using numerical analysis to analyze the flow of fluids and heat transfer refers to the most successful methods for comparison with the experimental findings. In this work, analysis of turbulent forced convection flow and heat transfer in a flat-plate solar water collector equipped with a novel absorber plate under constant heat flux boundary condition is numerically studied. Numerical solutions of the flow domain are implemented by resolving the two-dimensional governing equations of continuity, momentum and energy using finite volume method based on the SIMPLE algorithm technique. The influence of some important parameters such as roughness spacing, relative triangular width and Reynolds number on the local and average Nusselt number, velocity vector distribution and temperature contours has been presented and discussed in detail. Special prominence is given to the grid generation near the triangle sectioned. Results indicate that the heat transfer enhancement is achieved by specific selection of absorber geometry. The present results are determined and compared with the previous experimental data, and the results are very close to each other.

Keywords Heat transfer enhancement · Novel absorber plate · Solar collector

H. Hamzah (✉)
Department of Mechanical Engineering, Cukurova University, Adana, Turkey
e-mail: hudhaifahamzah@gmail.com

S. I. Hasan
Department of Mechanical Engineering, Mosul University, Mosul, Iraq
e-mail: mediansalim@gmail.com

S. I. Hasan · S. Küçüka
Department of Mechanical Engineering, Dokuz Eylul University, Izmir, Turkey
e-mail: serhan.kucuka@deu.edu.tr

Nomenclature

C_p	Specific heat, J/Kg K
D_h	Hydraulic diameter, m
H	Channel height, m
h	Triangle height, m
$h_{conv.}$	Convective heat transfer coefficient
K	Fluid thermal conductivity W/m K
k	Turbulent kinetic energy, m/s^2
L	Channel length, m
L_h	Length of absorber plate under solar energy, m
Nu	Nusselt number
p	Pressure, N/m^2
Pr	Prandtl number
Pr_t	Turbulent Prandtl number
q''	Solar heat flux, W/m^2
Re	Reynolds number
s	Roughness spacing, m
T	Temperature, K
u	Axial velocity, m/s
v	Transverse velocity, m/s
w	Relative triangular, m
x	Axial coordinate, m
y	Transverse coordinate, m

Greek Letters

ε	Dissipation rate of turbulent kinetic energy, m^2/s^3
μ	Dynamic viscosity, Pa s
μ_t	Turbulent dynamic viscosity, Pa s
ρ	Density, kg/m^3

Subscripts

o	Inlet conditions
e	Outlet conditions

1 Introduction

In the economy, which is burdened by the costs of increasingly scarce oil and natural gas, as well as the great impact on climate change resulting from fossil fuels, the technological revolution of our time is renewable energy. A solar collector is a special type of heat exchanger that collects the incident sunlight radiation energy and transfers it to an internal transport fluid [1]. For most residential, space heating and small commercial hot water applications, the flat-plate solar collector can make a dramatic financial saving [2]. Most of the previous surveys on environmental and economic analysis of flat-plate solar collectors (FPSCs) demonstrated that there is only an initial cost of these components while its findings in terms of performance, economy, efficiency and environmental protection are very high and sustained.

From our follow-up to previous researches during the last two decades, we found most efforts are focused on improving the flat-plate solar collector efficiency in terms of size reduction and achieving higher fluid temperature at the exit. For this purpose, different efficient techniques have been used to improve the thermal performance of solar collectors, including methods to enhance thermal conductivity of the base fluids [3], heat loss reduction from various sections [4, 5], create recirculation zones [6], increase in heat absorbed from solar radiation [7] and insert enhancement devices [8, 9].

Despite efforts to trip it up, thermal performance of the flat-plate solar collectors continually requires further development for better capture of radiation. Since the absorber is one of the main components of the solar collector and its function is the absorption of different wavelengths of solar radiation, one of the promising technologies in thermal performance improvement schemes is innovative in its plate design. For this requirement, the surface geometries are roughened for the fluid flow passage in the form of repeated wavy or corrugated walls. Several experimental and numerical studies were performed on the flow field and thermal characteristics in various corrugated channels [10–13]. The researchers have found that the using wavy walls can significantly lead to improve heat transfer rate of industrial transport processing. Garcia et al. [14] described the effect of including a convective barrier in the air cavity between the absorber plate and the glass cover experimentally with 35° inclination angle using water as a working fluid, and they found that convection barriers are led to increase the heat loss by 2.9%. A numerical study had been done by Chen and Huang [15] to study the thermal effect of metal-foam blocks equipped with the upper channel plate design, and they concluded that the recirculation produced by the metal-foam block shows a significant increase in the rate of heat transfer on the heated surface. Kiliç et al. [16] introduced experimental investigation about the effects of (TiO_2/water) nanoparticles on the conventional flat-plate solar collector, to obtain in the collector setup, that the highest instantaneous efficiency to be 48.67% for (TiO_2/water) nanofluid; whereas, it was 36.20% for pure water. Hatami and Jing [17] introduced a parametric optimization study to obtain the optimal wavy profile of the bottom plate of absorber solar collector using Al_2O_3-water nanofluid as the working fluid. They confirmed in the analysis that the best case with average wave

numbers and small wave amplitude, and small nanoparticles must be used to achieve a larger Nusselt number.

The numerical modeling is becoming ever more relevant in research around the topics of energy harvesting to apply its findings in different applications of experimental validation, and it became common since the ends of the last century. The objective of this work is to propose a numerical analysis to predict fluid flow and heat transfer in an artificial roughened flat-plate solar water collector with triangle cross-sectional rib on the absorber plate. The effect of roughness spacing and relative triangular width as well as the Reynolds number on the rate of heat transfer near the absorber heated plate is discussed in detail. The results of the present CFD analysis have been compared and validated with the numerical results available in the open literature.

2 Mathematical Analysis

In the present study, a flat-plate solar collector is fitted with rough absorber plate in the form of triangular corrugated section for enhancing heat transfer efficiency as shown in Fig. 1. The computational domain height is H, and the total length is L ($11H$). The heat flux q'' along the finite length of the absorber plate L_h ($5H$) is assumed to be uniform due to the finite distance of solar energy. The remaining upper and lower smooth surfaces are considered as insulated. The values of spacing s and width w of triangular section used in the present study have been tested, while the height h has been fixed. The geometrical parameters for different configurations of the absorber plate are shown in Fig. 2.

The analysis is made for turbulent, steady, incompressible and viscous fluid flow with constant thermophysical properties through a two-dimensional channel. The fluid enters the solar collector channel at ambient temperature and has a fully developed parabolic profile. Besides, the radiation effects are assumed negligible as are those of buoyancy. The length of smooth duct after the absorber plate was selected in order to generate appropriate outflow conditions at the channel exit.
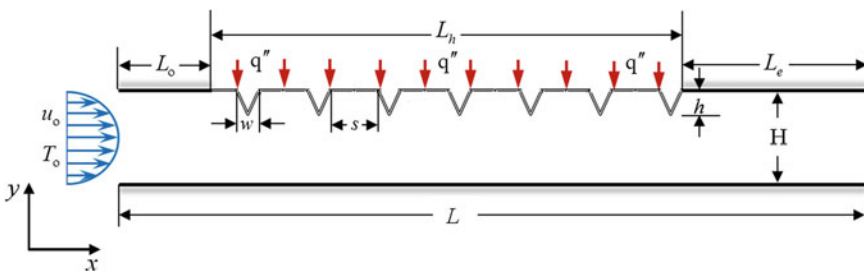

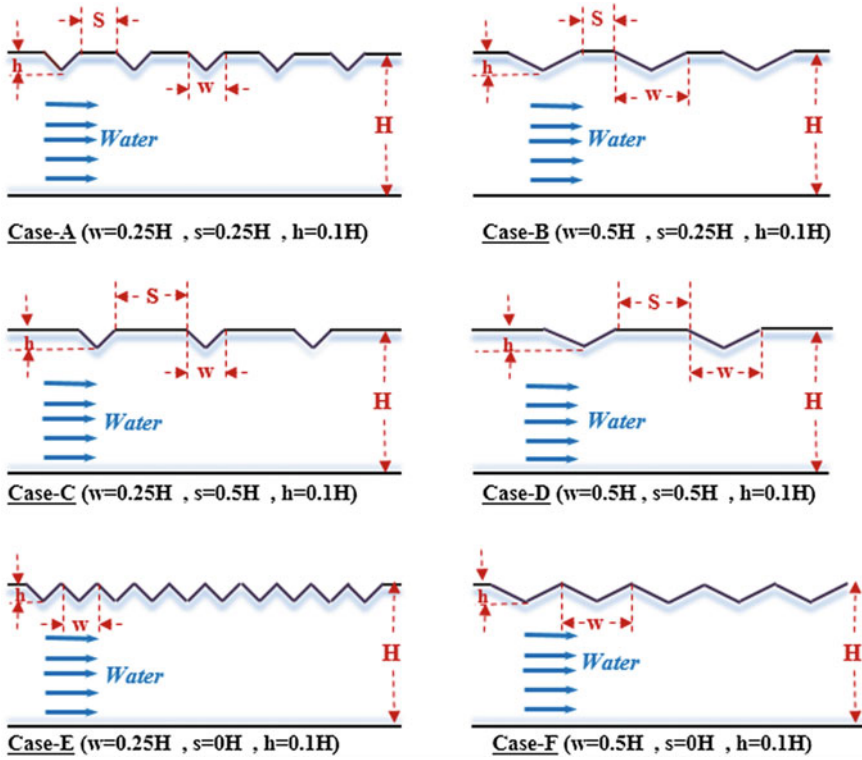**Fig. 1** Schematic of solution domain (not to the scale)

Fig. 2 Geometric parameters for different configurations of absorber plate

The governing fluid flow equations are modeled using standard $k - \varepsilon$ turbulent model in terms of Cartesian coordinates, by considering the above-mentioned assumptions as follows [10]:

Mass conservation:

$$\frac{\partial}{\partial x}(\rho u) + \frac{\partial}{\partial y}(\rho v) = 0 \tag{1}$$

x-momentum conservation:

$$\frac{\partial}{\partial x}(\rho u u) + \frac{\partial}{\partial y}(\rho u v) = -\frac{\partial p}{\partial x} + \frac{\partial}{\partial x}\left[(\mu + \mu_t)\frac{\partial u}{\partial x}\right] + \frac{\partial}{\partial y}\left[(\mu + \mu_t)\frac{\partial u}{\partial y}\right]$$
$$+ \frac{\partial}{\partial x}\left[(\mu + \mu_t)\frac{\partial u}{\partial x} - \frac{2}{3}\rho k\right] + \frac{\partial}{\partial y}\left[(\mu + \mu_t)\frac{\partial v}{\partial x}\right] \tag{2}$$

y-momentum conservation:

$$\frac{\partial}{\partial x}(\rho u u) + \frac{\partial}{\partial y}(\rho u v) = -\frac{\partial p}{\partial x} + \frac{\partial}{\partial x}\left[(\mu + \mu_t)\frac{\partial u}{\partial x}\right] + \frac{\partial}{\partial y}\left[(\mu + \mu_t)\frac{\partial u}{\partial y}\right]$$
$$+ \frac{\partial}{\partial x}\left[(\mu + \mu_t)\frac{\partial u}{\partial x} - \frac{2}{3}\rho k\right] + \frac{\partial}{\partial y}\left[(\mu + \mu_t)\frac{\partial v}{\partial x}\right] \quad (3)$$

Energy conservation:

$$\frac{\partial}{\partial x}(\rho u T) + \frac{\partial}{\partial y}(\rho v T) = \frac{\partial}{\partial x}\left[\left(\frac{K}{C_p} + \frac{\mu_t}{Pr_t}\right)\frac{\partial T}{\partial x}\right] + \frac{\partial}{\partial y}\left[\left(\frac{K}{C_p} + \frac{\mu_t}{Pr_t}\right)\frac{\partial T}{\partial y}\right] \quad (4)$$

The modeled turbulent kinetic energy, k, and its rate of dissipation, ε, with enhanced wall treatment are implemented in this study as shown below:

Turbulent kinetic energy equation [18]:

$$\frac{\partial}{\partial x}(\rho u k) + \frac{\partial}{\partial y}(\rho v k) = \frac{\partial}{\partial x}\left[\Gamma_k \frac{\partial k}{\partial x}\right] + \frac{\partial}{\partial y}\left[\Gamma_k \frac{\partial k}{\partial y}\right] + P_k - \rho(\varepsilon + \varepsilon_w) \quad (5)$$

where (ε_w) is the dissipation rate adjacent to the wall and it is given by

$$\varepsilon_w = 2\frac{\mu}{\rho}\left[\left(\frac{\partial \sqrt{k}}{\partial x}\right)^2 + \left(\frac{\partial \sqrt{k}}{\partial y}\right)^2\right] \quad (6)$$

Turbulent kinetic energy dissipation equation [18]:

$$\frac{\partial}{\partial x}(\rho u \varepsilon) + \frac{\partial}{\partial y}(\rho v \varepsilon) = \frac{\partial}{\partial x}\left[\Gamma_\varepsilon \frac{\partial \varepsilon}{\partial x}\right] + \frac{\partial}{\partial y}\left[\Gamma_\varepsilon \frac{\partial \varepsilon}{\partial y}\right] + (C_1 f_1 P_k - \rho C_2 f_2 \varepsilon)\frac{\varepsilon}{k} + \phi_\varepsilon \quad (7)$$

where

$$\phi_\varepsilon = 2\mu_t \frac{\mu}{\rho}\left[\left(\frac{\partial^2 u}{\partial x^2}\right)^2 + \left(\frac{\partial^2 v}{\partial x^2}\right)^2 + 2\left(\frac{\partial^2 u}{\partial x \partial y}\right)^2 + 2\left(\frac{\partial^2 v}{\partial x \partial y}\right)^2 + \left(\frac{\partial^2 u}{\partial y^2}\right)^2 + \left(\frac{\partial^2 v}{\partial y^2}\right)^2\right] \quad (8)$$

In the above equations, the production rate of the turbulent kinetic energy (P_k) is defined as

$$P_k = \mu_t\left\{2\left[\left(\frac{\partial u}{\partial x}\right)^2 + \left(\frac{\partial v}{\partial y}\right)^2\right] + \left(\frac{\partial u}{\partial y} + \frac{\partial v}{\partial x}\right)^2 - \frac{2}{3}\rho k\left(\frac{\partial u}{\partial x} + \frac{\partial v}{\partial y}\right)\right\} \quad (9)$$

Also, the turbulent eddy viscosity is given by Ref. [18]

$$\mu_t = C_\mu f_\mu \rho \frac{k^2}{\varepsilon} \tag{10}$$

The empirical constants that appear in the above equations are defined as [18]

$$C_\mu = 0.09, C_1 = 1.44, C_2 = 1.92, \sigma_k = 1.0, \sigma_\varepsilon = 1.3, \mathrm{Pr}_t = 0.9 \tag{11}$$

The corresponding boundary conditions needed to complete the formulations on all the boundaries of the computational domain for the current study are presented as follows:

- inlet: $u = 6y(1-y), v = 0, \mathrm{T} = 300$
- lower plate: $u = 0, v = 0, \left.\dfrac{\partial T}{\partial y}\right|_{y=0} = 0$
- upper plate: $u = 0, v = 0, \left.\dfrac{\partial T}{\partial y}\right|_{y=1} = \begin{cases} 0 & \text{insulation walls} \\ -1000/\mathrm{K} & \text{heated wall} \end{cases}$
- exit: $\dfrac{\partial u}{\partial x} = 0, \dfrac{\partial v}{\partial y} = 0, \dfrac{\partial T}{\partial x} = 0$ (12)

The relevant non-dimensional parameters inserted in the present numerical code are the Reynolds number and Nusselt number.

Reynolds number can be expressed as follows:

$$\mathrm{Re} = \frac{\rho u \mathrm{D_h}}{\mu} \tag{13}$$

where D_h is the hydraulic diameter of the inlet flat-plate solar collector which can be defined as

$$D_\mathrm{h} = \frac{4A}{p} \tag{14}$$

The local Nusselt number can be expressed as

$$\mathrm{Nu}_x = \frac{h_{\mathrm{conv.}} D_h}{k} \tag{15}$$

The average Nusselt number can be defined as

$$\overline{\mathrm{Nu}} = \frac{1}{A} \int_0^A \mathrm{Nu}_x \mathrm{d}A$$

3 Solution Method

A finite-volume integration method is employed to discretize the partial differential equations that govern the fluid flow in a flat-plate solar collector with the boundary conditions using the commercial CFD code, ANSYS Fluent 14.0. The SIMPLE algorithm of Versteeg and Malalaserkera [19] is chosen as a scheme to deal with the problem of pressure–velocity coupling. Due to stability considerations, the SECOND-ORDER UPWIND schemes are imposed on all the transport equations. In order to evaluate the accuracy of these computations, the convergence criteria for the residuals of the continuity, momentum and energy equations are assumed to be less than 10^{-5}.

4 Verification Code and Grid Independence

In order to achieve the process of establishing the truth of the numerical algorithm used in the present study, the local Nusselt number of fluid transport along the heated wavy wall for different Reynolds number has been investigated and compared with numerical study accomplished by Wang and Chen [13] as depicted in Fig. 3, and the results achieved a good agreement.

Moreover, in order to check the turbulence model, the average Nusselt number for airflow in smooth duct was compared with the numerical investigation of artificial solar air heater done by Yadav and Bhagoria [20] and Dittus–Boelter empirical correlation, i.e., Equation (16) available for smooth duct. As can be seen from Fig. 4, the current results are very close to the previous ones. This secures the accuracy of the numerical code used for the current study.
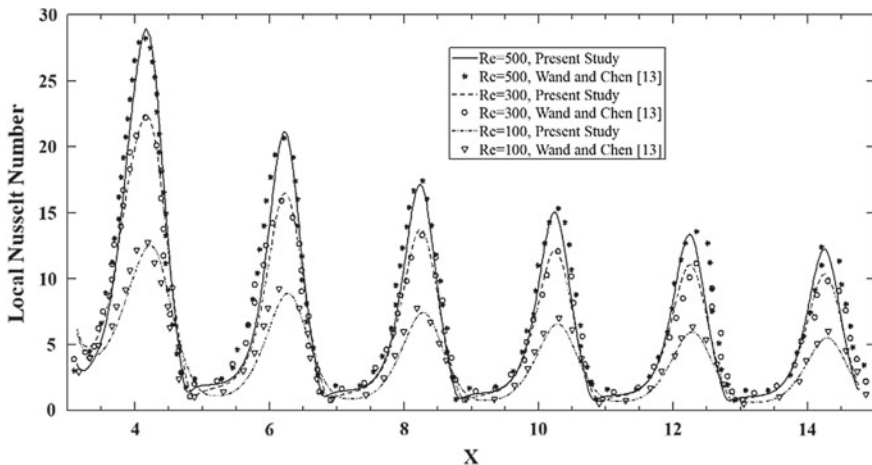

Fig. 3 Comparison with the numerical local Nusselt number accomplished by Wang and Chen [13]
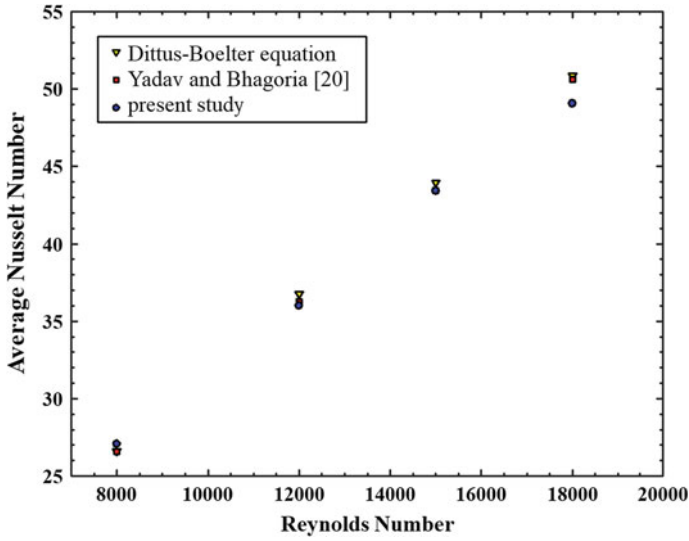
Fig. 4 Comparison between average Nusselt number predictions with numerical results of Yadav and Bhagoria [20] and Dittuse–Boelter empirical correlation for airflow in smooth duct

Dittus–Boelter equation [20]:

$$\overline{Nu} = 0.023Re^{0.8}Pr^{0.4} \qquad (16)$$

Uniform grid distribution in computational domain is generated for flow and thermal calculations using ANSYS ICEM CFD software. Five sets of grid with different sizes (20 * 100, 40 * 200, 60 * 300, 80 * 400 and 100 * 500) as shown in Fig. 5 are utilized for the simulation to ensure that the results are grid independent
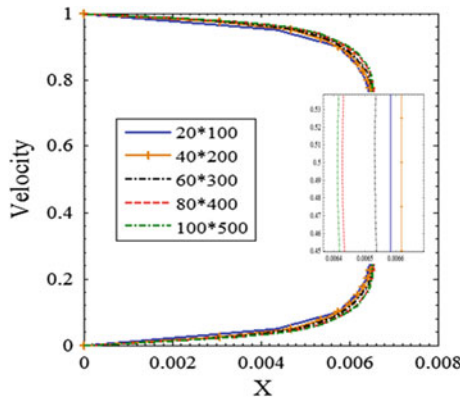

Fig. 5 Grid independence test based on velocity profile

in which the velocity profile is the criterion value. Therefore, the grid size of (80 * 400) is used for all the cases considered in the present study.

5   Results and Discussion

The numerical analysis has been performed for a flat-plate solar water collector with triangle sectioned on the absorber plate. Figure 6 presents the contour map of the velocity vector distribution, isotherm contours and turbulent kinetic energy for Case-F at Re = 18,000. It can clearly be seen from Fig. 6a that the flow reflection (i.e., recirculation flow zones) is formed between triangular rib portions of the absorber plate. This recirculation zones can improve the mixing of the cold fluid in core with the hot fluid near to the channel surfaces. As a result, high level of recirculation zones leads to a high level of heat transfer rate. In general, the peak values of thermal boundary layer are predicted in the vicinity regions of the absorber plate and between the final and pre-final rib as shown in Fig. 6b. The turbulent heat transfer flow behavior in solar water collector with triangular cross-sectional ribs has been demonstrated and elucidated using the turbulent kinetic profile in Fig. 6c. The high intensities of
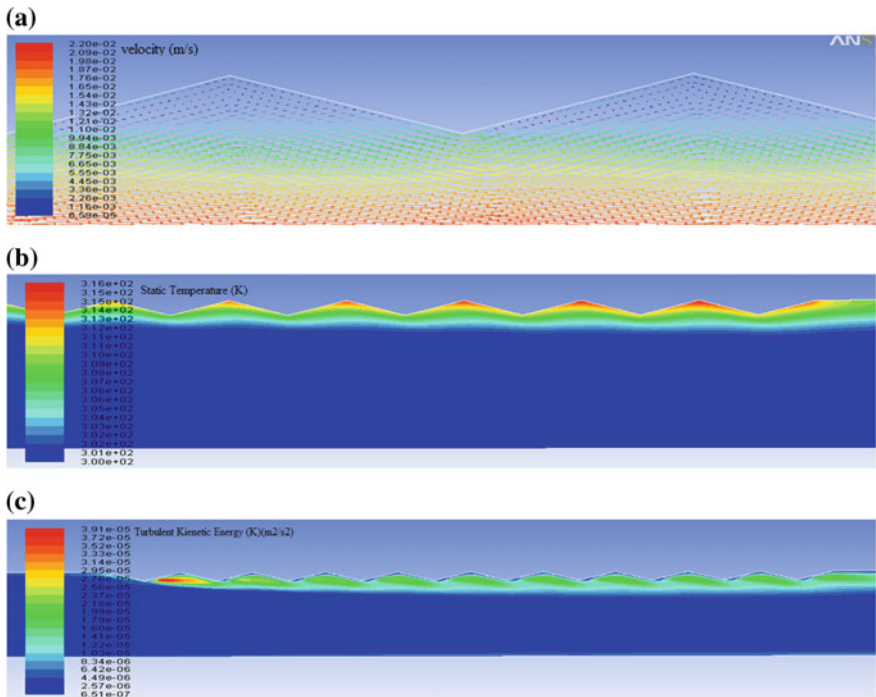

Fig. 6 Contour plot for Case-F at Reynolds number of 18,000 **a** Velocity vector distribution, **b** Isotherm contours, **c** turbulent kinetic energy
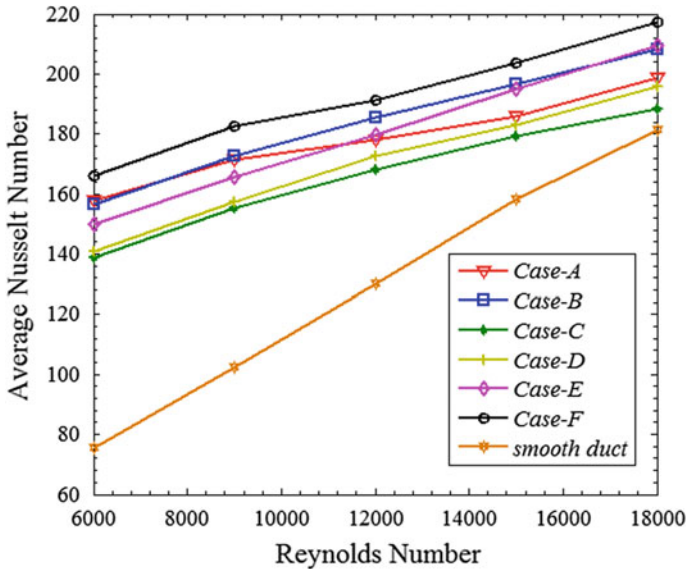
Fig. 7 Average Nusselt number with Reynolds number for all cases

turbulent kinetic energy are estimated at the beginning of absorber plate between the first and the second ribs and then gradually decrease toward the exit; this produces a strong turbulence level to improve the heat transfer rate.

Figure 7 displays the variation of average Nusselt number with Reynolds number for smooth duct and all cases considered in the present work. It is clear that the average Nusselt number has been enhanced by the existence of triangular ribs compared to a smooth duct. As expected, the average Nusselt number for all cases increases with increasing Reynolds number. It should be noted that there is a significant effect of relative triangular width (w) for different roughness spacing (s) on the average Nusselt number. As relative triangular width (w) increases, the flow becomes more disturbed, i.e., improve mixing, causing an increase in the temperature gradient. However, the maximum amount of enhancement was found to be approximately doubled 119.7% between Case-F and smooth duct at Re = 6000.

Figure 8 gives the variation of the local heat transfer coefficient along the absorber plate of solar water collector for smooth duct and Case-F at Re = 18,000. The value of heat transfer coefficient for smooth duct is maximum at the start of absorber heated plate and decreases slightly with axial distance along the collector wall. This is due to the actual behavior of the boundary layer at the entrance of collector which is thinner than the boundary layer at any distance along the duct. For the Case-F, it is found that the peak value of heat transfer coefficient appears at the first triangular cycle and then gradually decreases as the flow crosses the continuous triangular ribs in the direction of flow. This is because of the water flow at inlet of the roughness absorber wall which is cooler than any section along the duct.

Fig. 8 Variations of the
local heat transfer coefficient
along the absorber plate wall
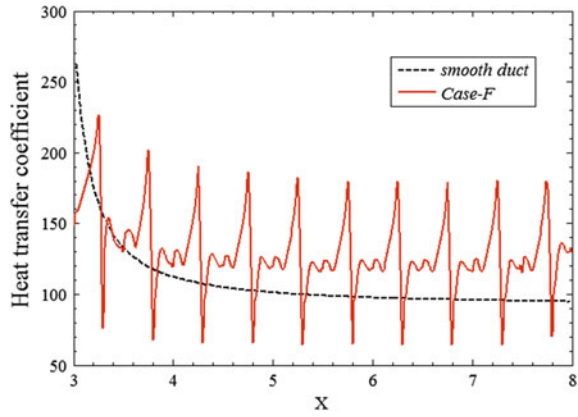for smooth duct and Case-F
at Re = 18,000

Fig. 9 Variations of the
local pressure drop along the
absorber plate wall for **a** $w =$
0.25, **b** $w = 0.5$, with
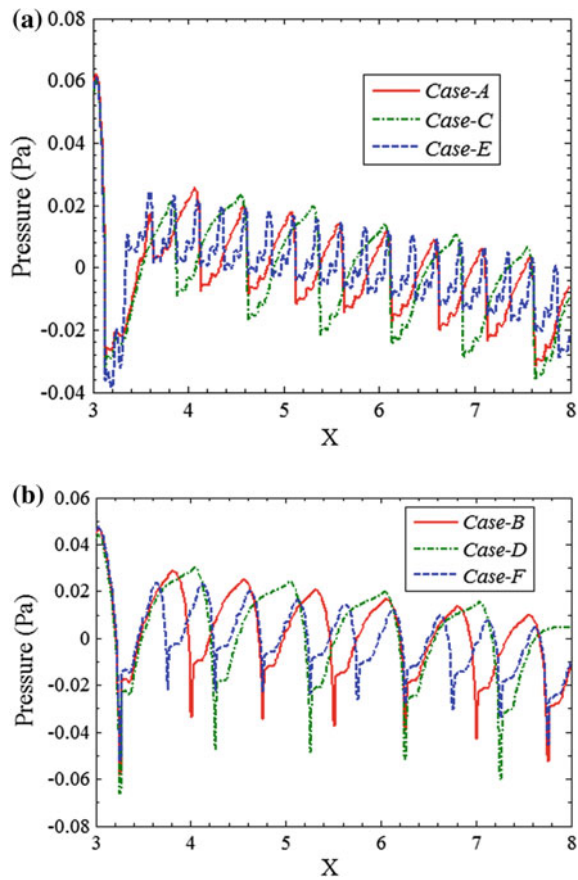different roughness spacing
(*s*) at Re = 12,000

　　Figure 9 shows the variations of the local pressure drop along the absorber plate wall for different cases at Re = 12,000. Generally, the values of local pressure drop decrease gradually toward the exit channel. For all cases when the roughness spacing (*s*) decreases, the fluctuation periods of local pressure drop increase as shown in Fig. 9a and b, respectively, and those periods are directly proportional to the velocity gradient which leads to create flow recirculation in the vicinity region between the triangular ribs as shown in Fig. 6a. Finally, the pressure fluctuation for the cases with higher relative triangular width (*w*) shown in Fig. 9b gives more heat transfer rate compared with the other cases at the same roughness spacing (*s*).

6　Conclusions

In the present work, a two-dimensional fluid flow through solar thermal collector with triangle sectioned on the underside of the absorber plate is studied numerically. The effects of roughness spacing, relative triangular width and Reynolds number on fluid flow process and thermal transport are investigated. The main findings of the study are as follows:

– The use of novel absorber design in the form of triangle sectioned rib in a flat-plate solar collector is an effective technique to improve the rate of thermal transport.
– The maximum enhancement amount of average Nusselt number within the parameters range of the present work has been found to approximately double 119.7% between Case-F and smooth duct at Re = 6000.
– It has been found that the reduction in roughness spacing (*s*) gives a better heat transfer rate at the same relative triangular width (*w*).

References

1. Kalogirou SA (2004) Solar thermal collectors and applications. Prog Energy Combust Sci
2. Pandey KM, Chaurasiya R (2017) A review on analysis and development of solar flat plate collector. Renew Sustain Energy Rev 67:641–650
3. Zamzamian A et al (2014) An experimental study on the effect of Cu-synthesized/EG nanofluid on the efficiency of flat-plate solar collectors. Renew Energy 71:658–664
4. Akhtar N, Mullick S (2012) Effect of absorption of solar radiation in glass-cover(s) on heat transfer coefficients in upward heat flow in single and double glazed flat-plate collectors. Int J Heat Mass Transf 55(1–3):125–132
5. Vestlund J, Rönnelid M, Dalenbäck J-O (2009) Thermal performance of gas-filled flat plate solar collectors. Sol Energy 83(6):896–904
6. Albojamal A et al (2017) Analysis of nanofluid transport through a wavy channel. Numer Heat Transfer, Part A: Appl 72(12):869–890
7. Del Col D et al (2013) Thermal performance of flat plate solar collectors with sheet-and-tube and roll-bond absorbers. Energy 58
8. Hobbi A, Siddiqui K (2009) Experimental study on the effect of heat transfer enhancement devices in flat-plate solar collectors. Int J Heat Mass Transf 52(19–20):4650–4658

9. Sandhu G, Siddiqui K, Garcia A (2014) Experimental study on the combined effects of inclination angle and insert devices on the performance of a flat-plate solar collector. Int J Heat Mass Transf 71:251–263
10. Ahmed MA et al (2015) Numerical and experimental investigations on the heat transfer enhancement in corrugated channels using SiO_2—water nanofluid. Case Stud Therm Eng 6(C):77–92
11. Elshafei EAM et al (2010) Heat transfer and pressure drop in corrugated channels. Energy 35(1):101–110
12. Fabbri G (2000) Heat transfer optimization in corrugated wall channels. Int J Heat Mass Transf 43(23):4299–4310
13. Wang CC, Chen CK (2002) Forced convection in a wavy-wall channel. Int J Heat Mass Transf 45(12):2587–2595
14. Garcia RP, Oliveira SR, Scalon VL (2019) Thermal efficiency experimental evaluation of solar flat plate collectors when introducing convective barriers (report). Sol Energy 182, 278 (2019)
15. Chen C-C, Huang P-C (2012) Numerical study of heat transfer enhancement for a novel flat-plate solar water collector using metal-foam blocks. Int J Heat Mass Transf 55(23–24):6734–6756
16. Kiliç F, Menlik T, Sözen A (2018) Effect of titanium dioxide/water nanofluid use on thermal performance of the flat plate solar collector. Sol Energy 164:101
17. Hatami M, Jing D (2017) Optimization of wavy direct absorber solar collector (WDASC) using Al2O3-water nanofluid and RSM analysis. Appl Therm Eng 121:1040–1050
18. Blazek J (2001) Computational fluid dynamics: principles and applications, 1st edn. Elsevier Science, Oxford [England]
19. Versteeg HK (2007) An introduction to computational fluid dynamics: the finite volume method, 2nd edn. In: Malalasekera W (ed) Pearson Education Ltd., Harlow, New York
20. Yadav AS, Bhagoria JL (2014) A numerical investigation of square sectioned transverse rib roughened solar air heater. Int J Therm Sci 79:111–131

Alternative Materials and Designs

Toward Halogen-Free Flame Retardants for Polystyrene Thermal Insulation Boards

Ebru Erünal

Abstract The limitation of fire class and halogen-containing flame retardants are two significant issues for polystyrene-based insulation materials. In this chapter, the necessity of external thermal insulation composite systems and related concepts are briefly introduced. Then, based on the approaches in the literature to halogen-free flame retardants for polystyrene, melamine-derived and expandable graphite-based substances on polystyrene production and properties are investigated. Flame retardants were added both during and after the polymerization reaction. Chemical and mechanical properties are investigated by means of elemental analysis, high-temperature gel permeation chromatography, thermal gravimetric analysis, tensile and flexural strength together with Young's and elastic moduli. Moreover, the horizontal fire class tests were also performed. According to results, except virgin PS all blended materials passed UL 94 HB test.

1 Introduction

The energy demand for domestic purposes such as heating or cooling of buildings causes significant increase in greenhouse gas emissions. Thus, energy efficiency in buildings is considered as a potential challenge of global warming and climate change [1–3]. In order to overcome this problem, new concepts and standards have been introduced in design and construction of buildings such as low-energy houses, passive houses, or smart housing. Although these concepts or standards have different aspects to achieve the reduction in energy consumption, their common feature is to provide a good insulation [4–11].

In general, insulation of a building is defined as all the processes that maintain the temperature (thermal insulation) and air quality (interior moisture content) in the living spaces. Thus, thermal insulation of a material is specified by thermal transmittance or *U-value* which is the amount of heat loss through unit square meter

E. Erünal (✉)

Chemical Engineering Department, Ceyhan Engineering Faculty, Çukurova University, Adana, Turkey

e-mail: eerunal@cu.edu.tr

of a surface. It is expressed with W/m^2 K in SI units or Btu/h ft^2 °F in USCS units. There is an indirect ratio between the thermal transmittance and the material's resistance to transfer the heat. A better insulation will be provided when the *U-value* is smaller which means the heat resistance will be higher.

In order to estimate the *U-value* of a certain insulation system, which may compose of different components, first the heat resistance (*R-value*) of each component is calculated separately. Heat resistance is simply the ratio of the material thickness (*d, m*) to the material's thermal conductivity (λ, W/K m). Then, all the calculated heat resistances of the components are summed up. Later, by taking the reciprocal of this sum, *U-value* is determined [12]. The relations between *R, U,* and λ can be shown as follows:

$$R = d/\lambda \tag{1}$$

$$U = 1/\Sigma R \tag{2}$$

Accordingly, when the material is thicker, its resistance to thermal conductivity increases, so that its thermal transmittance value decreases. Thermal conductivity (λ) is already a constant value related to directly material and briefly is defined as the ability to conduct the heat of the material. $\sum R$ refers to the sum of all resistances that composed of the insulation system under investigation.

When considering thermal insulation, another crucial concept is the thermal bridges that take place on specific domains of the insulated regions resulting in the decrease in overall heat resistance performance. Those domains are the paths that the rate of heat loss is higher than the rest of the material. They appear due to joints, junction points, cracks, or unbalanced placement of the insulation material. Because they cause the decrease of heat flow resistance, more energy will be required to keep the interior temperature and air quality. Hence, the thermal bridges may cause air flow and condensation; they both decrease the air quality and also insulation material's life span. Sometimes, the low water resistance of insulation material itself might also end up its degradation and cause thermal bridges. Therefore, a careful design by considering the climate, humidity, and compatibility of insulation system with the architecture and static of the building should be done. By this way, the purpose of buildings with decreased energy consumption for long terms can be achieved.

Speaking of insulation in buildings, according to application, it can be grouped into three categories: *(i) internal insulation*, *(ii) sandwich wall,* and *(iii) external insulation*

(i) **Internal insulation** is done only inside the living spaces and on limited areas, but the outside of the building is not considered. Therefore, it is a short-term solution and not preferable since it gives rise to formation of thermal bridges on different areas. Even though, at a first glance, it seems cheaper and more practical than other methods, it may be quite expensive for long term. Another main disadvantage is because the exterior *façade* of the building exposed to different climate conditions, it may get easily wet, and consequently diffusion

of moisture through the walls might take place. After a certain time, this diffused moisture will cause mold, fungus, and similar problems leading to deterioration of the interior paint and internal coating elements. Actually, internal insulation in a building may prevent the humidity on the applied walls if there is no leakage from the exterior wall side; however, it still causes the accumulation of moisture on the non-insulated surfaces like the ceilings, floors, or not carefully isolated corners.

(ii) **Sandwich wall** applications are composed of an insulation material placed between two layers of exterior walls. It is more effective than internal insulation and better for long-term usage. However, they should be applied during the construction of the building and therefore a careful examination of the conditions should be done since once it is applied, it cannot be changed again.

(iii) **External insulation** is the most preferable and effective method among other two methods due to the advantages of possessing a shell-like structure on the exterior *façade* of the building. By this way, building is protected effectively from all external influences such as wind, solar radiation, or humidity.

It should be kept in mind that depending on the conditions that affect and cause the corrosion of building materials, more than one method may be appropriate to apply for insulation of the building. The goal must always be the long-term optimum energy efficiency when insulation design of a building is considered.

1.1 Criteria of Insulation Material Selection for Certain Applications

In theory, same materials for internal and external insulation can be used. However, due to health effects in terms of respiration [13, 14], inorganic-based wool elements are not much preferred for inner spaces if special conditions like sound insulation are not necessary. In case of organic-based insulation boards, 2 or 3 cm thickness is applied for interior walls, while for external insulation this thickness can be much higher up to 5–15 cm which decreases the thermal transmittance value significantly. Therefore, the critical decision of insulation materials must be taken according to following criteria: thermal transmittance value, water absorption ratio, dimensional stability, and fire class of the insulation material.

1.1.1 Thermal Transmittance Value

A brief definition of transmittance value (U) is given in introduction part. The lower the thermal transmittance value is, the better insulation will be provided. There are several standard methods to determine thermal transmittance value of insulation boards such as EN 12667, ISO 8301, BS EN ISO6946, BS EN ISO 13370, BS EN ISO 10077-1, ASTM C518 depending on the legislations of countries or regions [15–20].

1.1.2 Water Absorption Ratio

Water absorption ratio is an important feature for insulation materials. If the material's water absorption capacity is not as low as possible, the weight of the material will increase causing an addition static load on the building. Apart from static stress, the decrease in insulation properties and also deterioration of the material due to high water amount is not wanted at all. Since water is a very good conductor of heat, it will increase *U-Value*. Therefore, materials with lower water absorption ratio such as below 0.5% are preferred. If the material is hydrophobic and has a closed cell structure, its water absorption capacity will be lower. This ratio is determined by volume percent in Turkish Standards TS EN 13164 [16].

Another criterion related to water is water vapor permeability which refers to the amount of water vapor passing through the unit area of the material with a specific thickness per unit of time under certain temperature, humidity. It is denoted by μ. The water vapor permeability is affected by density, thickness, surface structure, and cell structure (open or closed cells) of the material.

1.1.3 Dimensional Stability

The dimensional stability is quite important for the durability of the insulation. If the dimensions (Width x Length x Thickness) of insulation boards vary depending on climate conditions or as a function of time, it will lead to poor insulation conditions. Therefore, the selected material must be flexible and strong enough to withstand the climate and the application conditions.

1.1.4 Fire Class

By legislations in many countries, it is ensured that materials used as insulation purposes must provide a certain fire class depending on the height of the buildings (on the exterior *façade* of buildings). Especially at higher buildings above 18 m, only A1-type fire class materials are allowed to use. However, since A1 class-type materials are basically inorganic-based, the load they cause on the building may affect the static of building. Therefore, there are some suggestions on the usage of combined materials such as applying flammable but light organic-based insulation boards on the walls while A1 class materials only on the sites where flames can spread through such as window frames. Generally, fire classification of materials is done according to their reaction to fire or in other words fire growth. There are many parameters to determine fire class of materials. Flammability, flame spread, (non)-combustibility, development of smoke (toxic gas release), and melt droplets are main parameters to classify insulation materials. The fire classifications according to European Standard for Fire Test to Building Material are EN 13501-1 [15] as "Fire classification of construction products and building elements—Part 1: Classification using test data from reaction to fire tests" are given in Table 1. In Turkish Standards,

Table 1 Material classifications according to their reaction against fire and additional classifications for smoke emission levels and melting droplets [15–19]

EN 13501-1 and TS EN 13501-1	DIN 4102	Definition
A1	A1	Non-flammable—not contribute in any stage of the fire
A2	A2	Non-flammable—not significantly contribute to the fire
B	B1	Not easily flammable—very limited lateral spread of flame
C		Not easily flammable—limited lateral spread of flame
D	B2	Flammable—average contribution to fire
E		Flammable—highly contribution to fire
F	B3	Easily flammable

Smoke emission level		Melting droplets/particles	
Code	Definition	Code	Definition
s1	Very low	d0	No particles/droplets formation at a certain time
s2	Medium	d1	Particles/droplets formation at a certain time
s3	Very high	d2	High content of particles/droplets formation at a certain time

they are classified under TS EN 13501 [16]. Corresponding German Standards are classified under DIN 4102 classes [19]. These classes are determined according to the non-combustibility, ignitability, flame spread, calorific value of the material as well as smoke emissions, the formation and duration of the melting droplet or particles. Actually the generation and spread of fire, smoke formation within the building, and the contribution of the building products to a fully developed fire are considered when these standards are formed.

In that sense, for example, class A1 materials rated as not contributing in any stage of fire at all, while class A2 materials rated as not significantly contributing in fire load and growth. On the other hand, materials that are capable of resisting fire for a short period but flammable without substantial flame spread in case of contact with flame are considered as class E. If material is resistant to fire for longer period and has limited heat release but still flammable as similar in class E, it is classified as D. In case the material has limited lateral spread of flame but does not burn down when flame is not contacting on the material anymore and can resist to fire again longer period, it is then class C. Actually apart from nuances, the classifications can be easily interpreted as non-flammable materials for class A, not easily flammable materials for classes B and C, flammable materials for classes D and E, and easily flammable material as F. For not easily flammable, flammable, and easily flammable materials, there are additional standards due to smoke formation and flaming particles or droplets. They are determined by observing the materials during burning in a certain time [15–19].

Table 2 Classification according to UL94 standards [20]

| Class	Specimen/direction flame applied	Burning observations	Burning termination
HB	Bar- or plaque-type specimen/horizontal	Slow burning Burning rate <76 mm/min for specimen thickness <3 mm	Stops before 100 mm
5VA	Bar- or plaque-type specimen Vertical	No drips without hole development on the specimen	≤60 s
5VB		No drips, specimens may develop a hole	≤60 s
V-0		Drips of not inflamed particles	≤10 s
V-1		Drips of not inflamed particles	≤30 s
V-2		Drips of flaming particles	≤30 s
HF-1	Foam- or film-type specimen, Horizontal	No burning drips Afterglow less than 30 s	≤2 s
HF-2		Burning drips Afterglow less than 30 s	≤3 s

Another type of classification which is issued by Underwriters Laboratories (UL) from USA is known as UL94: Standard for Safety of Flammability of Plastic Materials for Parts in Devices and Appliances testing [20]. The plastic material's tendency to either extinguish or spread the flame once ignited is determined by this standard. Depending on the time that the burning terminates, drip and hole formation from the burning specimens and after glowing, the classifications are done as shown in Table 2.

1.2   External Thermal Insulation Composite Systems (ETICS)

Exterior insulation boards are applied with a series of additional items on the walls of buildings. Therefore, this whole system is generally called as external thermal insulation composite systems (ETICS). Basically, ETICS are composed of minimum six layers including adhesive, base coats, reinforcement which is usually a glass fiber mesh, finishing coat and thermal insulation material which is mechanically fastened with anchors. The layers are shown in Fig. 1 according to the application order [4, 21–26].

Typical thermal insulation boards can be grouped as inorganic-based or polymeric-based materials. Most common polymeric-based insulation materials are polystyrene (PS), polyurethane (PUR), polyisocyanurate (PIR) (and phenolic may also be

Fig. 1 External thermal insulation composite systems (ETICS) on a building wall. Layers as listed: (1) adhesive, (2) thermal insulation material (fixed with additional mechanical fastening), (3) and (5) base coat, (4) reinforcement, (6) finishing coat
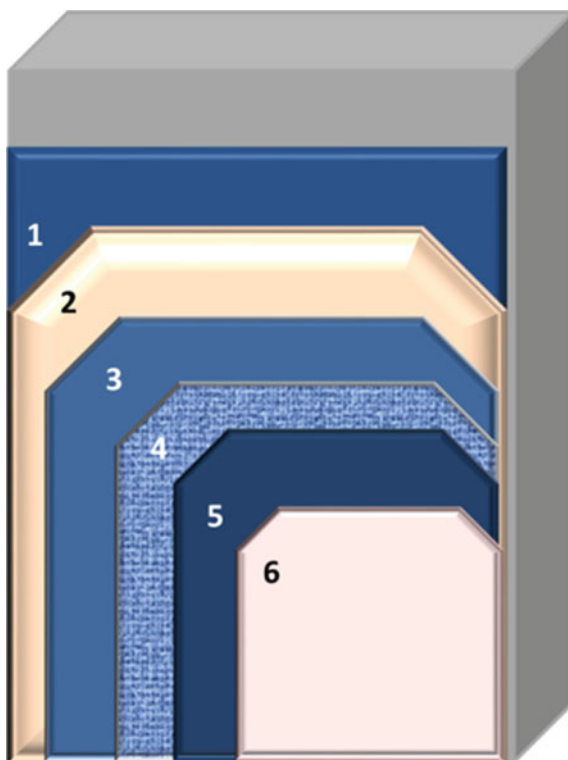
included in this group), while glass wool, stone wool, and wood wool can be considered as inorganic-based materials. Due to their chemical compositions and manufacturing processes, they have different properties which may be advantageous or disadvantageous for the desired insulation applications. Main advantage of inorganic-based materials is their fire resistance. They are classified as non-flammable materials. However, their dense nature and water absorption ratio are considered to be their disadvantages. On the other hand, although these properties are better for organic based materials, their flammable nature is their weak point [4, 21–26].

The first layer of ETICS, adhesive, is generally special for insulation boards; cement, acrylic or polyurethane-based polymer additive depending on the application surface. For inorganic-based insulation boards, phenolic resins are widely used. The insulation board is covered with adhesive via trowel, and then, the board is attached to the wall. The covering can be done on total surface of the board (if the surface is smooth) or through spot/edge bonding style. A less used method is applying the adhesive on the wall with machine and then attaching boards but since it requires a smooth surface, machinery and more amount of adhesive, it is not always economical. If the adhesive is not homogeneously distributed between walls, insulation boards and between the boards, formation of thermal bridges is inevitable. The important point is that adhesive should be able to bind both insulation material and the applied

Insulation board type	Adhesive strength (kPa)
Polymeric-based	≥ 80
Inorganic-based	≥ 6

Table 3 Minimum adhesive strengths on various insulation boards based on TS EN13494 [16]

surface [21]. Some of the minimum adhesive strengths of various insulation boards are given in Table 3 [16].

After fixing the thermal insulation board on the wall via mechanical fastenings, the base coat is applied. The plug- and anchor-type fixings are generally composed of a polypropylene material and a metal pin with a plastic head. Fixing materials should also prevent thermal bridge formation, and their tensile strength should not be lower than 0.20 kN [21]. After the insulation board is coated with either mortar or a suitable base coat, reinforcement is applied in order to prevent the mortar's tensile stress that may lead to the cracking of mortar. By this way, long durability of the ETICS can be maintained. The reinforcement is actually a fiberglass material of mesh strips whose dimensions are 3.5 × 3.5, 4 × 4, or 5 × 5 mm [15]. This material is both resistant to alkali conditions and increase strength for impact loading, hydrothermal shock and water penetration. The reinforcement is found between two base coatings. The finishing coating applied on the last layer of ETICS has both decorative and protecting functions. They are generally composed of synthetic or silicone acrylic resins or cement-based materials with waterproof and poor vapor permeability properties to enable a good resistance to hydro-thermostress. They might be colored or paintable when necessary. For environmental concerns finishing coatings must be solvent-free.

1.3 Comparison of Insulation Boards

Polystyrene is one of the most used polymeric-based insulation materials [4, 21, 22]. There are two different polystyrene boards according to manufacturing technique: Expanded Polystyrene (EPS) and Extruded Polystyrene (XPS).

Expanded Polystyrene is manufactured through the interaction of steam with expandable polystyrene beads which contain pentane droplets inside. When the beads come into contact with steam, they can expand up to 40 times larger than their initial volume. This phase of manufacturing is known as pre-expansion [21, 22, 26]. In fact, expansion of the beads takes place due to the fact that the permeation of steam is faster than the permeation of pentane. When steam diffuses into the closed cells that exist in expandable polystyrene beads already, it increases the total cell pressure decreasing the bulk density of the material. By this way, a quite light and stable material is obtained. After this stage, the expanded beads are molded and cut according to insulation board standards [21, 22]. Actually, the raw material of EPS is produced through either suspension polymerization of styrene monomer [26–32] or melt impregnation process [33, 34]. The latter technique is applied for more "black

EPS" grades which has a lower thermal conductivity value due to carbon black or graphite in it [20–22].

On the other hand, during the manufacturing of XPS insulation boards, general-purpose polystyrene is fed to an extruder following up addition of blowing agents, fire retardants, and other necessary additives. Even though manufactured from the same raw material, and both have closed cells, EPS and XPS boards have different properties. XPS has very low water absorption ratio but not resistant to UV light, so mostly it is preferable in water-dense areas but not exterior parts that exposed directly to sunlight while EPS is used on exterior walls of buildings [26].

Other insulation board materials will not be discussed here in detail since the scope of this chapter is only related to polystyrene-based materials. However, it is already pointed out that applying one type of insulation material is not a correct attitude for different applications. Better way is choosing appropriate material for the needs. Therefore, the purpose of Table 4 is just to show advantages and disadvantages of materials in case certain applications are needed.

Along with thermal transmittance, fire class, dimensional stability, and water absorption ratio, commercially density of thermal insulation boards is also important. Actually, together with density and thickness, thermal transmittance value can be adjusted. But the commercial boards are manufactured according to certain standards in different countries. For example in Europe, minimum thickness of polystyrene-based EPS boards is 150 mm, while in Turkey this is the thickest value that applied on colder regions [4, 15, 20–22]. In addition to these properties, compressive and tensile strengths, corrosion potentials might also be important in certain insulation applications but for simplicity, they are not shown in Table 4 in detail.

As can be seen from the table, EPS and XPS insulation boards have many advantages like being light, having stable thermal resistance, and resistance to water and air changes for long term. Also they are relatively easy to apply and economical. However, their fire class limits their usage. The compositions of the flammable gases and their volumetric ratios during the burning of polystyrene are given in Table 5.

Table 4 Comparison of different insulation boards [4, 15, 20–22, 26]

Insulation board type	Density (kg/m^3)	Thermal conductivity (W/mK)	Water absorption ratio (%)	Water vapor permeability, μ	Fire class
EPS	25–45	0.033–0.037	4–5	20–40	E
XPS	25–45	0.035–0.045	1–3	80–200	E
PUR/PIR	40–60	0.023	3	100	E
Stone wool	150	0.036	9–12	1	A1
Glass wool	10–130	0.031–0.043	46–88	1	A1

Table 5 Volumetric ratio of the flammable gases that emerge during burning of polystyrene [35]

Material	Compositions of the flammable gases	Volumetric ratios (PPM)			
		300 °C	400 °C	500 °C	600 °C
Polystyrene (E1)	CO	10	50	500	1000
	Monostyrene	50	100	100	50
	Benzene/homolog	Minor	20	20	30
	Halogen compounds	10	15	13	11

1.4 Polystyrene and Fire Resistance

In order to increase the fire resistance of polystyrene, flame retardant additives are already being used during polystyrene production and/or its manufacturing. However, two important issues are in discussion with these flame retardants [26, 36]. First, the current additives can increase material's fire resistance only up to class E. Therefore, it cannot be used on higher buildings as external thermal insulation material due to the strict the national and international fire legislations [20, 21]. Second issue is the environmental concerns about the halogenated flame retardant additive known as hexabromocyclododecane (HBCD) which is a persistent, bio-accumulative, and toxic material emanating from bromine within the material [37]. Up to 2013, it was used worldwide but its usage was banned in Europe and developed countries [38, 43–45]. Even though there are alternative high-molecular weight polymers (molecular weights over 1000 g/mole) [46–48], they still host the halogen Br in their molecular structures. Even though the macromolecule might prevent the diffusion of bromine into the environment, these new materials may also be banned in future with the same argument of hosting hazardous bromine due to degradation kinetics [49]. Moreover, the new substitutes have some issues with the compatibility of polystyrene during manufacturing. Therefore, to develop a halogen-free alternative flame retardant to be used in polystyrene products is of crucial importance.

1.4.1 Polystyrene Production

Polystyrene (Fig. 2a), which is produced from styrene monomer with several ways, has been used in daily life for many purposes such as insulation boards, roofing

Fig. 2 Chemical formula of **a** polystyrene (PS) **b** hexabromocyclododecane (HBCD)
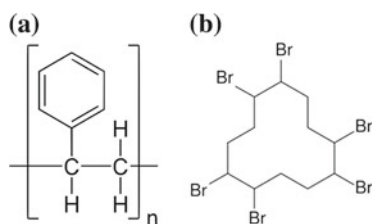
materials, industrial packaging, and parts in white goods. Therefore, it is one of the most widely used thermoplastics. Besides, the low polarity of styrene molecule makes it as one of the few monomers able to be polymerized under free radical, anionic, cationic, and metal-catalyzed conditions [26, 27].

The main commercial polystyrene processes without considering copolymers can be grouped into two: One is known as mass or bulk polymerization, which is a combination of continuously stirred tank and plug flow reactors in series. In general, this process can be conducted only by thermally or in the vicinity of initiators [26, 32, 50]. However, the other additives such as flame retardants, masterbatches, and blowing agents are added by the manufacturers during the processing of polystyrene. The other process is suspension polymerization which is composed of a batch-type reactor [26, 28–30, 33, 34]. Spherical expandable polystyrene (EPS) beads are mainly obtained by suspension polymerization process. The necessary additives like flame retardants and blowing agent are added during the suspension polymerization of polystyrene before sent to the manufacturers. Unlike mass polymerization, suspension polymerization is much harder to control due to the dependence of suspension stability on many factors like the reactor geometry, agitation conditions, temperature control, and the effect of different additives [26–30].

Flame retardants are one of the most important additives for EPS insulation boards in order to provide the national and international fire legislations used in construction industry. So far, hexabromocyclododecane (HBCD, Fig. 2b) was extensively used as the preferred flame retardant due its compatibility with polystyrene molecule. However, the environmental concerns lead to restrict HBCD usage in Europe and developed countries since it is known to be a persistent, bio-accumulative, and toxic material emanating from bromine within the material [36–45]. Current attempts are focused on high-molecular weight polymers (>1000 g/mole) including bromine and compatible with polystyrene polymer [46–49].

1.4.2 Mechanism of Flame Inhibition and Role of Flame Retardant Additives

Various flame retardant additives are used in different industrial materials to improve the fire resistance of materials [26, 36]. Flame retardants (FR) are defined as materials that can prevent the spread of flame and the formation of combustion products. In the case of polymeric-based materials, the combustion behavior is in a continuous cycle.

Accordingly, during combustion, the heat generated by the flame, volatiles, and small particles returns back on the surface of the burning polymer. When these small particles spread to the flame zone and react with oxygen, more heat is released and the cycle continues. In order to decrease flammability and increase fire resistance of a polymeric substance, this cycle should be disrupted [51]. It can be achieved by three ways:

(i)   *Solid-Phase Inhibition*: Formation of new barriers on the surface of the polymer during heat release is provided so that the polymer and these layers prevent further combustion.

(ii) *Gas-Phase Inhibition*: Its purpose is to transform the highly reactive free radicals released during combustion to much less reactive compounds by the help of volatile free radicals. Actually, it ends the radical reaction that occurs during fire.

(iii) *Endothermic Reduction*: It provides the formation of products that help to cool down the surface and remove the energy required for new flame formation from fire environment.

In general, flame retardant materials can be classified as organic- and inorganic-based. Organic phosphorus compounds and organic halogenated compounds are the most popular organic-based flame retardants, while aluminum hydroxide, magnesium hydroxide, and borates are known as the inorganic-based additives. Phosphorus-containing phenol formaldehyde resins act according to solid-phase inhibition mechanism by forming protective layer on the surface with the formation of polyphosphoric acid through a network of carbon and phosphoroxides. The expandable graphene, which can expand up to 300 times at 300 °C, is also among the leading flame retardants in recent years. Metal hydroxides, especially Mg and Al hydroxides, increase the flame resistance by releasing water (endothermic reduction) and also reduction of smoke formation during fire. $Mg(OH)_2$ is active around at 320–340 °C, while $Al(OH)_3$ is around 180–200 °C. Metal borates generally emit water during fire, but they may be used synergist in FR systems [51–54].

Peculiarly for polymers, in order to get effective flame retardancy, the additive should degrade at a closer temperature which polymer decomposes. On the other hand, depending on the structure and the fire behavior of the polymer, sometimes additives might be mixed to get a synergistic effect. Both for EPS and XPS, up to 2013, Br-containing HBCD flame retardant materials were used since it is compatible with polystyrene. This halogen-based organic flame retardant acts according to the principle of gas-phase inhibition to increase the fire resistance. However, after 2013, usage of HBCD started to be banned in many countries because of its negative effects on the environment and human health. Since then, alternatives for HBCD in polystyrene materials have been focused on halogenated long-chain macromolecules which make it difficult them to diffuse in living organisms and harm environment. Unfortunately, it still has some minor problems during the production of expandable polystyrene in suspension polymerization when added at this stage. Another approach used in Far East is applying an inorganic–organic FR coating on EPS beads after pre-expansion phase. However, these coatings increase density of the insulation boards and also decrease their flexibility [55].

### 1.4.3   Melamine Alternatives as a Flame Retardant for Polystyrene Industry

Melamine (Fig. 3) and its derivatives are commonly used as FR additives in different industries. For example, especially in wood industry, they are matter of choice since they act also as plasticizers. Moreover, they are used in polyurethane flexible foams for upholstered furniture in homes, railway, and aircraft seats for flame retarding. Their high sublimation energy around -29 kcal/mole and sublimation temperature up to 350 °C, provides a cooling effect by retarding ignition along with other dissociated products that act as diluents for the combustion. Especially nitrogen inside their structure makes them a strong flame retardant. During burning, the release of inert gases such as ammonia and nitrogen into the gas phase leading to cooling. Melamine vapor is said to be capable of endothermic dissociation to cyanogens [36].

Some of the melamine derivatives used for flame retarding are as follows: Melamine cyanurate (MC) which is one of the most known halogen-free flame retardants generally used in reinforced polyamide 6 and 66, polyurethanes, epoxies, and polyolefins. It is stable up to 320 °C and has gas-phase inhibition mechanism by oxygen dilution due to the vaporization of melamine during fire. On the other hand, melamine polyphosphate (MPP) is used in glass fiber reinforced polyamide 6 and 66. Especially together with metal phosphinates, it shows a synergistic effect. In addition, melamine poly (zinc- or aluminum) phosphates have a synergistic effect with metal phosphinates when used in polyamides and polybutylene terephthalate. Along with aluminum and magnesium hydroxide, they are very effective in cable applications. Actually, melamine phosphate-based salts release water above 200 °C acting as endothermic inhibitors. Plus, above 350 °C melamine-poly-phosphate undergoes decomposition and forms a char around the polymer leading to prevent oxygen interaction during combustion. Melamine-based hindered amine light stabilizer (HALS) is used in polyolefin films. The mode of action is based on the enhanced degradation of the polyolefin by radicals, which may also act in the gas phase [54].

Blends and Copolymers of Polystyrene and Melamine

There have been different studies to improve fire resistance of PS either with addition of melamine derivatives through melt extrusion process or addition of melamine derivatives directly during the polymerization step. It has been known that melamine can be used up to 50% in polystyrene [36].

Fig. 3 Melamine formula
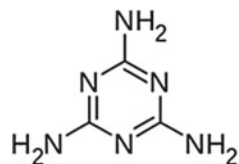
Mainly polystyrene was blended with polyphenylene oxide (PPO) and a combination of ternary flame retardant powder system composed of ammonium polyphosphate, pentaerythritol, and melamine (APP-PER-MEL). In such physical mixtures, the main problem to overcome was reported as the heterogeneity in hydrophilic nature, particle size, and consequently mixing of the powders homogeneously. Different strategies like wet ball milling are applied to make a homogenous and narrow-particle-sized powder. Moreover, improved fire resistance of high-impact polystyrene (HIPS)/polyphenylene ether (PPE) blend was recorded with the addition of melamine cyanurate (MC) and different phosphate resin mixtures [56–58]. Expandable graphite was also used as a synergist for melamine phosphate as flame retardant additive for polystyrene. Despite the enhancement of fire inhibition, a decrease in tensile and flexural strength of the materials was reported [59]. Also nanoclay synergists together with triphenyl phosphate and melamine cyanurate were blended with PS in the literature [60].

On the other hand, the efforts on copolymers produced via emulsion or suspension polymerization of styrene and melamine derivatives focused mainly on the mixtures of expandable graphite (EG) with melamine salts [61–63]. Jankowski and Kedzierski [63] suggested a method for in situ synthesis of melamine salts (cyanurate or phosphate) in the presence of EG. Then, they used these modified EG materials as FR additives during suspension polymerization of styrene. After the optimization of PS/FR additive weight ratio for the best fire resistant class, they reported the samples with a weight ratio of 100/15 (PS/FR additive) showed HF-1 and V-0 class performance during fire resistant tests.

2 Materials and Method

In order to make a comprehensive research for developing a PS compatible FR additive, two different approaches—in terms of nature of FR additives—were applied. Both approaches were based on Jankowski and Kedriezski's study [63].

In the first approach, the compatibility of PS and melamine derivatives was investigated. For that purpose, initially melamine derivatives as melamine cyanurate (MC) and melamine phosphate (MP) were synthesized separately. Then, these materials were added as FR additives during suspension polymerization. Besides, derivation of melamine substances was tried simultaneously during suspension polymerization of styrene instead of adding FR substances after obtaining.

In the second approach, using of expandable graphite (EG) modified with melamine derivatives (MC and MP, separately) as FR additives was tried. After the synthesis of modified EG with MC and modified EG with MP, separately, they were added during the suspension polymerization reaction. Moreover, instead of adding during polymerization phase, mixing of (blending or compounding) these additives to directly polystyrene was performed.

Apart from this work, in order to choose and optimize the most effective suspension polymerization of styrene reactions, two recipes similar to industrial production

Table 6 List of methods used to investigate alternative halogen-free flame retardant for polystyrene

Method No.	Definition
2.1	**Suspension Polymerization of Styrene**
2.1.1	Surface Agents: Nanoclay Bentonite–Gelatin (NB-G)
2.1.2	Surface Agents: Trisodium phosphate and Tricalcium phosphate (TSP-TCP)
2.2	**Investigation on Compatibility of PS and Melamine Derivatives**
2.2.1	Preparation of Melamine-Derived Additives: Melamine Cyanurate and Melamine Phosphate
2.2.2	Addition of Melamine Derivatives During Suspension Polymerization
2.2.2.1	Simultaneous Synthesis of Melamine Salts during Suspension Polymerization
2.2.3	Addition of Melamine Derivatives during Compounding
2.3	**Addition of Modified Expandable Graphite Materials on Polystyrene**
2.3.1	Modification of Expandable Graphite (EG): with Melamine Cyanurate (EGMC) and with Melamine Phosphorate (EGMP)
2.3.2	Addition of Modified EG during Suspension Polymerization
2.3.3	Addition of Modified EG during Compounding

of polystyrene were investigated. In one method, bentonite and gelatin boveskin were used as surface active agents, while in the other one trisodium phosphate and tricalcium phosphate were used as surface active agents.

All the methodology of this research has been submitted in Table 6.

2.1 Suspension Polymerization of Styrene

A 750-ml flat-bottomed reactor with heat jacket and a mechanical stirrer was used to obtain polystyrene through suspension polymerization of styrene. The stirrer was composed of two impellers; each impeller was three curved bladed type. The impeller at the bottom of the stirrer had a bigger diameter than the impeller placed a few cm above it.

All reactions were carried at 90 °C and between 7 and 8 hours. Benzoyl peroxide (Merck, CAS #: 94-36-0) was used as catalyst. Temperature was tracked with a Pt-100 thermo-element. Two different surface agent systems were applied: In one reaction, nanoclay bentonite and gelatin were used, while on the other reaction trisodium phosphate and tricalcium phosphate were added to the reactor.

2.1.1 Surface Agents: Nanoclay Bentonite–Gelatine (NB-G)

Nanoclay bentonite (Sigma Aldrich, CAS #:1302-78-9) and gelatin (Sigma Aldrich, CAS #: 9000-70-8) were used as suspension agents together with polyvinyl alcohol as organic phase. Then this phase was mixed with water phase in which styrene monomer was added previously. The procedure was done similar to reference [63] without the addition of flame retardants.

2.1.2 Surface Agents: Trisodium Phosphate and Tricalcium Phosphate (TSP-TCP)

Trisodium phosphate and tricalcium phosphate were used as suspension agents. Organic and water phases mixed initially, and the addition of the other substances was done sequentially according to the recipe applied in Ref. [30]. Differently, Licocene PE 520 wax was used as nucleation agent. Normally, during production of EPS, PE wax is used as nucleation agent. But because of some instabilities of the reactor system with TSP-TCP surface agents, PE wax was added to create a synergistic effect for surface agents.

Polymerization with NB-G surface agents was more effective than TCP-TSP surface agents. The possible reasons were discussed in part 3.1. All in all, in the next steps, suspension polymerization was done with NB-G surface agents.

2.2 Investigation on Compatibility of PS and Melamine Derivatives

2.2.1 Preparation of Melamine-Derived Additives: Melamine Cyanurate and Melamine Phosphate

Melamine cyanurate (MC) was synthesized from melamine (Sigma Aldrich, CAS #: 108-78-1), DI water, and cyanuric acid (Sigma Aldrich, CAS #: 108-80-5) at 90 °C in 250 ml flasks by stirring vigorously (650–800 rpm) with magnetic stirrer for 5 hours.

Melamine phosphate (MP) was synthesized from melamine (Sigma Aldrich, CAS #: 108-78-1), DI water, and phosphoric acid (Sigma Aldrich, CAS #: 7664-38-2). First, melamine and DI water were mixed in a 250-ml flask by stirring vigorously (650–800 rpm), and the system was heated to 90 °C. At around 80 °C, phosphoric acid was added. The reaction was conducted at 90 °C for 5 hours.

After each reaction, the solid materials were filtered, washed, and dried under vacuum oven at 40 °C.

During the filtration of MP material, after the filtered water gets colder, the formation of white fiber-like precipitates was observed. They are analyzed with elemental

analysis and found that melamine components were on these fiber-like parts as well. The solubilities of the materials in different organic substances were also examined. MP was insoluble in different organic solvents and water, while MC could only be dissolved in highly toxic trifluoroacetic acid (TFA).

2.2.2 Addition of Melamine Derivatives During Suspension Polymerization

The prepared melamine derivatives MC and MP were added during the suspension polymerization. Addition of these materials was tried both in the beginning and after the polymerization reached around 40%.

Observations: Most of the trials end up in emulsion phase. Only MC-added suspension system resulted succesfully in solid particles to be examined. (S + MC)

Simultaneous Synthesis of Melamine Salts During Suspension Polymerization

Because both the polymerization reaction and melamine derived materials synthesized at the same temperature, all materials were (melamine, cyanuric acid and phosphoric acid) added in the beginning of the suspension polymerization.

2.2.3 Addition of Melamine Derivatives During Compounding

5 gr of total mixture of polystyrene (Trinseo), filler (talk powder), and melamine derivatives was used in a laboratory-type HAAKE Mini Jet Pro compounder with two screws. Temperature was kept around 200 °C with a torque of 60 rpm.

2.3 Addition of Modified Expandable Graphite Materials on Polystyrene

2.3.1 Modification of Expandable Graphite (EG): With Melamine Cyanurate (EGMC) and with Melamine Phosphorate (EGMP)

The procedure was done according to Jankowski and Kedriezski's work [63]. 20 g EG was mixed with the appropriate amount of melamine and acids. After 5 h synthesis, the obtained materials were filtered and dried overnight at 40 °C in a high air-circulated oven.

Both EG-modified melamine cyanurate (EGMC) and EG-modified melamine phosphate (EGMP) were obtained without any problems. However, after filtration of

EGMP, when the liquid filtrate was cooled down, the formation of white fiber-like particles was observed in MP synthesis (2.2.1). The analysis showed that melamine was mostly on this liquid phase. Therefore, a sample was obtained via rotary evaporator at 40 °C to avoid loss of material through filtering.

2.3.2   Addition of Modified EG During Suspension Polymerization

The addition of the materials was done similar to 2.2.2.

2.3.3   Addition of Modified EG During Suspension Polymerization

The addition of the materials was done similar to 2.2.2. Polymerization degree was quite low.

2.3.4   Addition of Modified EG During Compounding

The commercial Trinseo PS was used to obtain the blends. The materials were blended with a Plasti Corder, Brabender blender at 200 °C and 40 rpm rotation. A total of 40 g mixture was obtained and placed in a $100 \times 100 \times 2.5$ mm mold. Then, it was hot pressed in a Wickert Hot Press machine at 80 bar and 200 °C. After 10 min, it was transferred to a Hofer cold press machine to cool down. The sample list with corresponding compositions is given in Table 7. All compounds were prepared according to 40 g weight material. First material was pure PS as a reference, and last material was a combination of nanoclay bentonite and melamine without modified EG. The ratio of modified EG materials was kept max. 10. The material obtained via suspension polymerization was also mixed (SEGMC) with addition of pure EG as well. The materials were then cut with a disk saw to 30 mm width for fire behavior and other mechanical tests. The materials are shown in Fig. 4.

3   Results and Discussion

Elemental analyses were taken with a Thermo Fisher Elemental Analyzer for C, H, N, and S elements. The results are given in Table 8.

High-temperature gel permeation chromatography (HT-GPC) dissolved in Trichlorobenzene was conducted on the suspension polymerization products synthesized in 2.2 and on the commercial PS that was used for compounding in 2.3. Since melamine derivative and EG materials could not be dissolved in Trichlorobenzene at high temperatures very well, only polystyrene included materials could be analyzed. The results are given in Table 9.

Table 7 List of blended compounds

Sample No.	Materials	Weight (g)	Observations
1	PS	40	Reference material
2	PS/EGMC	33/7	The viscosity is low with respect to PS. Hardly separated from the mold. The material was soft during cutting
3	PS/EGMC	30/10	Good blending. Separation from mold was easier than sample #3. The material was soft during cutting
4	PS/EGMP	35/5	Similar to sample #3. Separation from mold was even easier than sample #3
5	PS/EGMP	30/10	The surface of the molded sample had small fractures. During hot mold, formation of too much air bubbling was heard
6	PS/SEGMC/EG	25/10/5	Easily separated from the mold. A smooth surface was obtained
7	PS/NB/M	30/5/5	A homogenous blend obtained unlike PS/Melamine trial done at 6.2.2. The material was harder than EG-containing materials during cutting

Abbreviations of the materials as in the order of appearance: *PS* commercial polystyrene, *EG* expandable graphite, *MC* melamine cyanurate, *MP* melamine phosphate, *EGMC* expandable graphite + melamine cyanurate, *EGMP* expandable graphite + melamine phosphate, *SEGMC* polystyrene obtained via suspension polymerization + expandable graphite modified via melamine cyanurate, *NB* nanoclay bentonite, *M* melamine
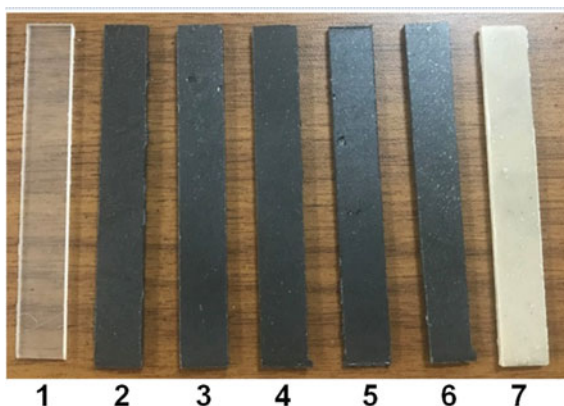
Fig. 4 Blended and prepared test specimens

Table 8 Elemental analysis of synthesized materials

Related part	Sample	Sample amount (mg)	C %	H %	N%	S%
2.2.1	MC	3.297	9.92	4.75	17.43	–
	MP	2.943	15.84	4.26	40.45	–
2.2.2	S + MC	2.795	63.96	6.73	<0.4	–
2.2.2.1	S + M + CA	2.300	90.07	7.50	0.86	–
	S + M + CA + PA	2.297	89.44	7.51	<0.4	–
2.3	EG (Raw Material)	2.57	4.79	0.48	0.081	0.99
2.3.1	EGMC	2.586	8.74	1.26	10.07	1.33
	EGMP(liquid)	3.003	16.23	5.02	36.13	3.27
	EGMP	3.061	4.83	1.14	5.20	2.15

Abbreviations of the samples as in the order of appearance: *MC* melamine cyanurate, *MP* melamine phosphate *S* styrene, *CA* cyanuric acid, *M* melamine, *PA* phosphoric acid, *EG* expandable graphite, *EGMC* expandable graphite + melamine cyanurate, *EGMP* expandable graphite + melamine phosphate

Table 9 High-temperature gel permeation chromatography (GPC) results

Related part	Material	Molecular weight (M_w)	Molecular weight distribution (M_n)	Polydispersity index (M_w/M_n)
2.2.2	S + MC + MP	144,500	49,800	2.90
2.2.2.1	S + M + CA + PA	148,300	54,700	2.71
2.3	Commercial PS	328,200	142,800	2.30

Thermal gravimetric analysis (TGA) was conducted with a PerkinElmer TGA 4000 instrument under nitrogen atmosphere for materials prepared with melamine-derived substances (shown in Fig. 5), while both nitrogen and oxygen were used for the blended compounds separately (shown in Fig. 6a, b). Temperature started from 30.00 to 900.00 °C at a rate of 20.00 °C/min.

In Fig. 5a, the weight losses are given according to the original starting weights of materials instead of weight loss percentage in order to show the differences more drastically. In Fig. 5b, weight loss % graph can also be seen. The degradation temperature of synthesized PS seems around 462.58 °C. MC-added PS material also has similar degradation temperature (460.88 °C) which gives a hint about incorporation of MC into the structure since MC itself has also a closer degradation temperature around 450 °C. Interestingly, MP has two steps of degradation curve; one is at 346.86 °C and the other around 442.77 °C, but the material obtained through addition of MP during PS reaction has a sharp decrease around 462.58 °C. This can be attributed to the dominant nature of PS within the material and not much incorporation of MP into PS. Lastly, the material that was obtained through the addition of
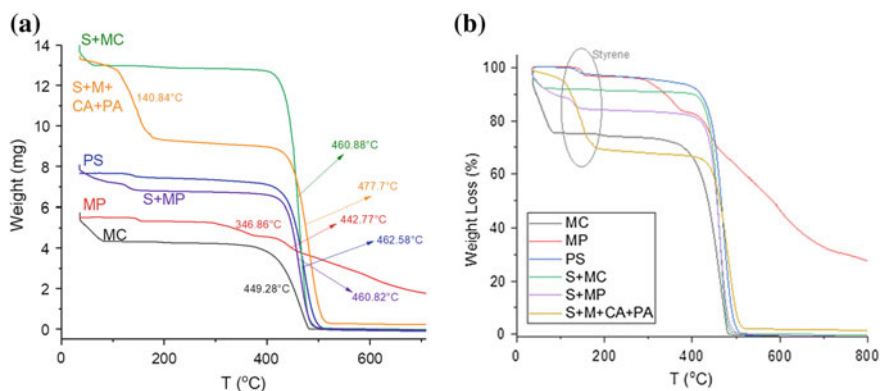
Fig. 5 Thermal gravimetric analysis (TGA) of synthesized polystyrene (PS), melamine-derived materials **a** actual weights **b** weight loss percentage (MC: melamine cyanurate, MP: melamine phosphate) and the end products of their additions to suspension polymerization (S + MC: melamine cyanurate-added suspension polymerization product, S + M + CA + PA: melamine-, cyanuric acid-, and phosphoric acid-added suspension polymerization product)
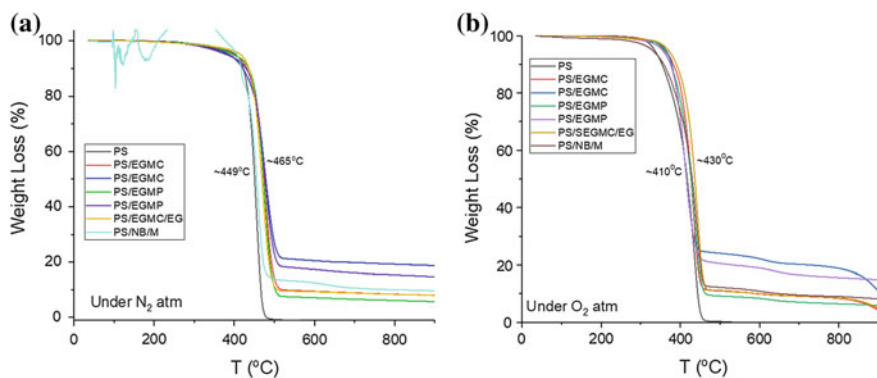

Fig. 6 Thermal gravimetric analysis (TGA) of polystyrene and modified expandable graphite compounds taken **a** under N_2 atmosphere **b** under O_2 atmosphere

all substances (melamine, cyanuric acid and phosphoric acid) during the polymerization reaction gives two sharp loss curves. The first loss is due to the evaporation of styrene in the material because styrene's boiling point is around that temperature. The second loss is around 477.7 °C which possess a higher temperature than other materials. Actually, for PS, S + MP and PS substances, small loss curves around styrene's boiling point like the first loss curve in this material can be tracked too. This is better seen in Fig. 5b.

In Fig. 6a, b, TGA of the blended PS compounds under nitrogen and oxygen atmosphere are given, respectively. All materials showed similar behavior in both atmospheres except bentonite which has fluctuations under N_2 atmosphere. More or

less, for all blended materials, the degradation temperature seems to be dominated by high amount of commercial PS within the compounds. Unlike synthesized PS, no weight loss related to styrene at lower temperature is seen.

3.1 Suspension Polymerization Conditions

Polymerization with NB-G surface agents was more effective than TSP-TCP surface agents. Obviously, TCP-TSP system is more sensitive to stable reactor conditions. Hence, vortex formation was observed when stirrer had only one impeller while too much swinging was observed when the impeller number was doubled. Similar to other agitation including processes, a homogeneous and stable stirring is the key point of suspension polymerization, too. Since the stability could not be achieved during TSP-TCP reaction, this result was obvious. The addition of PE wax might also cause the instability of the system because the addition of different substances changes the viscosity of the system. Moreover, it might be related to the hygroscopic nature of catalyst which lumping was observed during the syntheses. Therefore, catalyst's effective ratio might not be correct due to the recipe used. In order to overcome the problems during addition of flame retardants, NB-G surface agents were used in suspension polymerization reactions.

3.2 Investigation on Compatibility of PS and Melamine Derivatives

3.2.1 Preparation of Melamine-Derived Additives

The elemental analyses of melamine-derived additives can be found in Table 8. The elements' percentages (%) in melamine are 28.56, 4.80, and 66.6 for C, H, and N, respectively. When the analyses are compared, MP material seems to be in consistency with theory but MC was not. The expected elemental percentages (%) of MC are 28.23, 3.56, 49.4, 18.81 for C, H, N, O, while it was found that 9.92, 4.75, and 17.43 for C, H, and N. For MP, theoretical percentages (%) are 16.07, 4.05, 37.50, 28.56, and 13.82 for C, H, N, O, and P, respectively. The obtained elemental percentages (%) are 15.84, 4.26, and 40.45 for C, H, and N.

3.2.2 Addition During Suspension Polymerization

The ratio of the additives was around ~4/100 mg (MC/S or MP/S) used in the suspension polymerization. Since they were in lower amount, the elemental analysis results seem also very low. The best way to track the existence of melamine derivatives is

checking N% in elemental analysis. In Table 8, for MC-containing material, it was detected below 0.4. The HT-GPC result also indicates addition of MC inhibited the polymerization degree.

Simultaneous Synthesis of Melamine Salts During Suspension
Polymerization

The elemental analyses given in Table 8 show that when melamine and cyanuric acid are added separately during the suspension polymerization (S + M + CA), N % seems to increase compared to materials when melamine cyanurate (S + MC) is added. This can be interpreted as increase in nitrogen amount from both melamine and cyanuric acid together may directly incorporate into the polymer structure. However, in that case, N% would be expected even higher when melamine, cyanuric acid, and phosphoric acid are added separately during polymerization (S + M + CA + PA). Hence, it is seen that N % is much lower than 0.4% like S + MC case.

According to HT-GPC results given in Table 9, both materials synthesized via melamine and its derivatives had much lower molecular weight (M_w) and molecular weight distribution (M_n) when compared to commercial polystyrene. Molecular weight was found around 144,500 and 148,000, while molecular weight distribution was around 50,000 and 55,000 for (S + MC + MP) and (S + M + CA + PA), respectively. On the other hand, M_w and M_n of commercial PS found around 328,000 and 143,000, respectively. In both cases, addition of melamine and its derivatives inhibits the polymerization at a certain rate and degree.

3.2.3 Addition of Melamine Derivatives During Compounding

In the literature, it was reported that blending of polystyrene with melamine is hard [26, 36, 51]. In order to imitate industrial conditions, talk powder was also added as filler to the mold. However, a homogeneous blend of PS could not be obtained with or without talk powder. The higher softening temperature of melamine and its derivatives make this blending process harder.

3.3 Addition of Modified Expandable Graphite Materials on Polystyrene

3.3.1 Modification of Expandable Graphite (EG): With Melamine Cyanurate (EGMC) and with Melamine Phosphorate (EGMP)

The elemental analyses showed that EG-modified materials have S which already comes from EG itself with 4.79% C, 0.48% H, 0.081% N, and 0.99%S. The modification seems better for EGMC then EGMP. The ratios for EGMC were found as 8.74% C, 1.26% H, 10.07% N, and 1.33% S. According to the experience from MP synthesis, the white fiber-like precipitates in the cold filtered water was collected and also analyzed. Results showed that most of the elements coming from melamine phosphate are found in this liquid-phase material while modified EG material has only 4.83% C, 1.14% H, 5.20% N, and 2.15% S, but the precipitate ratios are 16.23, 5.02, 36.13, and 3.27%, respectively. Even though with MP modification some of the materials seem lost during filtration, still EG seems modified effectively as both N % and C % can be seen increased due to the raw material itself.

3.3.2 Addition of Modified EG During Suspension Polymerization

Polymerization was not completed, ending up with high styrene amount, glue-like materials. Therefore, further investigations cannot be done at this stage. Since the additive ratios were given between certain ranges by Jankowski and Kedzierski [63], with flame retardant additives, the ratios experienced without FR additives in part 2.1.1 might also need to change. Besides, with the addition of FR materials, maybe the reactor stability was also not stable as in the case of TSP-TCP surface agent added suspension polymerization.

3.3.3 Addition of Modified EG During Compounding

The observations during compounding and cutting of specimens were disclosed in part Sect. 3.3.3.

Mechanical Test Results of Blended Specimens

Both tensile strength and flexural strength of the blended specimens were done with a Zwick/Roell Testing Machine according to ASTM D 638 and ASTM D 790 standards, respectively. The testing apparatus is shown in Fig. 7a, b.

The tensile strength tests were done according to the following conditions: The grip-to-grip separation at the starting position was 30.9 mm with a test speed of
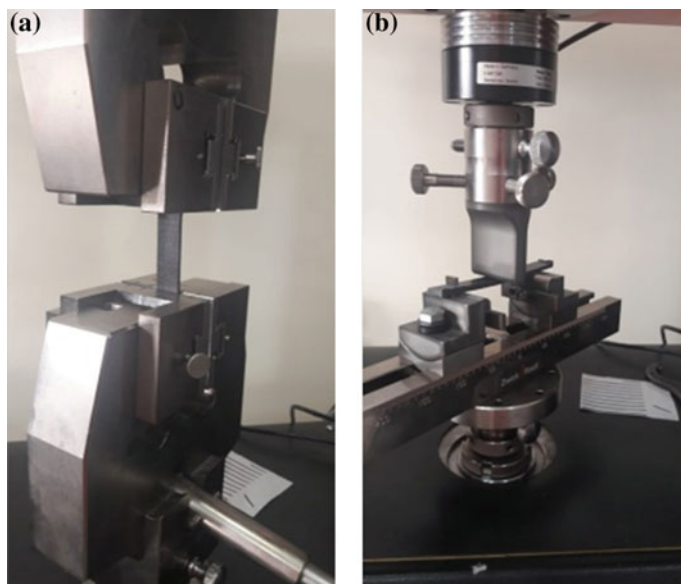
Fig. 7 Zwick/Roell testing apparatus for **a** tensile strength and **b** flexural strength

Table 10 Tensile strength test results of the blended compounds

Sample No.	Compounds	Tensile strength, MPa (σ)	Strain, % (ε)	Young's modulus, MPa (E)
1	PS	22.6	0.066	342.42
2	PS/EGMC	24.2	0.062	390.32
3	PS/EGMC	17.4	0.12	145.00
4	PS/EGMP	23.1	0.063	366.67
5	PS/EGMP	20.8	0.05	416.00
6	PS/SEGMC/EG	23.1	0.059	391.52
7	PS/NB/M	16.5	0.059	279.66

0.2 in/min. The preload was 1 MPa. The test apparatus is shown in Fig. 7a. Tensile strength, % strain (%), and Young's modulus of the specimens are given in Table 10.

The least resistant polystyrene compound to elongation with the lowest Young's modulus was the blending of nanoclay bentonite and melamine. Even during cutting for the preparation of the specimen, it was observed that the material was harder than EG-containing materials during cutting. This shows that bentonite and melamine makes the structure more brittle. Except this one, other materials have higher Young's modulus which means higher resistance to deformation during elongation than polystyrene itself. On the other hand, the highest Young's modulus was obtained with modified expandable graphite with melamine phosphate.

Table 11 Flexural strength test results of the blended compounds

Sample No.	Compounds	Flexural strength, MPa (σ_{fM})	Strain, % (ε_M)	Flexural strength at break, MPa (σ_{fB})	Elastic modulus, MPa (E_H)
1	PS	46.1	0.015	46.1	2850
2	PS/EGMC	42.4	0.013	33.8	4220
3	PS/EGMC	33.4	0.11	24.3	3810
4	PS/EGMP	48.9	0.019	34.3	3290
5	PS/EGMP	39.1	0.016	26.2	3580
6	PS/SEGMC/EG	40.6	0.011	28.4	4310
7	PS/NB/M	39.9	0.013	35.7	3650

The flexural strength tests were done according to the following conditions: Both test speed and flexural modulus speed were kept at 0.05 in/min. The preload was 0.1 MPa with a support span of 64 mm. The test apparatus is shown in Fig. 7b. Flexural strength, flexural strength at break, strain on the outer surface, and elastic modulus of the specimens are given in Table 11.

PS/PSEGMC/EG compound has the highest elastic modulus which means that it is stiffer than other materials. All materials have higher elastic modulus than PS. This shows that addition of melamine derivatives or modified expandable graphite or bentonite–melamine mixture makes PS structure stiffer. However, this might be also due to melamine and its derivatives since all materials have one of them. In terms of flexural strength, PS/EGMP has the highest bending resistance.

3.4 Flammability Tests of Blended Specimens

Two flammability tests were conducted according to horizontal flammability test with UL 94 HB standards on the blended specimens. The results are summarized in Table 12. All materials passed the test except PS which continued to burn after flame

Table 12 Horizantal flammability test results

Sample No.	Compounds	UL 94 HB
1	PS	Not passed
2	PS/EGMC	Passed
3	PS/EGMC	Passed
4	PS/EGMP	Passed
5	PS/EGMP	Passed
6	PS/PSEGMC/EG	Passed
7	PS/NB/M	Passed

was not given on the specimen and a black smoke release with ashes while black droplets was observed.

Physical blending of polystyrene and these additives has promising effects in terms of enhanced fire resistance. In preliminary trials, it was found that addition of only melamine does not have any significant fire resistant due to inhomogeneous blending. Contrarily, when melamine was used together with nanoclay bentonite, a synergistic effect was observed as well but the obtained material was brittle. Especially the addition of modified expandable graphite with melamine derivatives to polystyrene during blending showed promising effects with enhanced fire resistance and softening of the material as also shown with similar approaches in the literature [56–63].

4   Conclusions and Remarks for Future Investigations

The compatibility and effect on material properties of melamine cyanurate, melamine phosphate, and modified expandable graphite materials were investigated throughout this chapter.

It was found that in order to provide the addition of these materials through suspension polymerization, a more controlled reactor should be employed. Especially when TSP-TCP surface agents are added to the reactor, glue-like end materials showed the necessity of a better controlled system. The reaction conditions were easier to control with bentonite system though. More or less in both conditions the polymerization degree is hindered with the addition of melamine salts. Synthesize of MC was easier than MP so that MC additive or modifying EG with MC was better than MP. Thus, there are also good findings with MP materials in the literature [63].

On the other hand, physical blending of polystyrene and these additives has promising effects in terms of enhanced fire resistance. However, during the compounding, addition of sole melamine to PS does not have any significant fire resistant due to inhomogenities during blending. When melamine was used together with nanoclay bentonite, a synergistic effect was able to observe but the specimen became more brittle. Especially, the addition of modified expandable graphite with melamine derivatives to polystyrene during blending showed promising effects with enhanced fire resistance and softening of the material.

In order to develop an environmentally safe, halogen-free, and industrially applicable flame retardant for polystyrene insulation products, a well-designed and controlled pilot reactor should be developed for suspension polymerization of polystyrene to obtain industrially applicable recipes. Moreover, for the blending part, optimization of the additive ratios should be worked more in detail to get best material properties with fewer amounts of additives.

As a conclusion, all these efforts will lead to a better future with less energy consumption, more energy saving by environmentally friendly insulation boards leading to decrease the potential thread of global warming.

References

1. IEA International Energy Agency https://www.iea.org. Accessed 01 June 2019
2. International Energy Agency (IEA) (2008) Worldwide trends in energy use and Efficiency. OECD/IEA, France
3. Pérez-Lombard L, Ortiz J, Pout C (2008) A review on buildings energy consumption information. ENERG BUILDINGS 40(3):394–398
4. European Association of External Thermal Insulation Composite Systems (EA-ETICS) https://www.ea-etics.eu/etics/about-etics. Accessed 01 June 2019
5. United Nations Environment Programme (UNEP) (2008) The Kyoto protocol, the clean development mechanism, and the building and construction sector
6. World Business Council for Sustainable Development (WBCSD) (2007) Energy efficiency in buildings: business realities and opportunities
7. World Green Building Council (2009) Perspectives on green building. Renew Energy Focus (Nov/Dec 2009)
8. UK Green Building Council (2009) http://www.ukgbc.org. Accessed on 03 June 2019
9. Retzlaff R (2009) Green building and building assessment systems: a new area of interest for planners. J Plan Lit 24:3–21
10. Cotterell J, Dadeby A (2012) The passivhaus guide. Green Books, Devon
11. Desideri U, Asdrubali F (eds) (2018) Handbook of energy efficiency in buildings: a life cycle approach. Elsevier, Oxford; Hens H (2007) Building physics—heat, air and moisture. Wiley, Berlin
12. Kudo Y, Aizawa Y (2009) Behavior of rock wool in lungs after exposure by nasal inhalation in rats. Environ Health Prev Med 14(4):226–234
13. Hansen EF, Rasmussen FV, Hardt F, Kamstrup O (1999) Lung function and respiratory health of long-term fiber-exposed stonewool factory workers. Am J Respir Crit Care Med 160:466–472
14. European Standards (EN) https://www.en-standard.eu. Accessed on 03 June 2019
15. Turkish Standards Institute (TSE) https://www.tse.org.tr. Accessed on 03 June 2019
16. International Organization for Standardization (ISO) https://www.iso.org/home.html. Accessed on 03 June 2019
17. American Society for Testing and Materials (ASTM) https://www.astm.org/Standard/standards-and-publications.html. Accessed on 03 June 2019
18. German Institute for Standardization (DIN) https://www.din.de/en. Accessed on 03 June 2019
19. UL Standards https://ulstandards.ul.com/. Accessed on 15 June 2019
20. Association of thermal insulation, waterproofing, sound insulation and fireproofing material producers, suppliers and applicators (IZO-DER) https://www.izoder.org.tr/ Accessed on 15 June 2019
21. Turkish EPS. Industry association of expandable polystyrene (EPS-DER) https://www.epsder.org.tr/eng/ Accessed on 15 June 2019
22. European Manufacturers of Expanded Polystyrene (EUMEPS) https://eumeps.org/. Accessed on 15 June 2019
23. Polyisocyanurate Insulation Manufacturers Association (POLYISO) https://www.polyiso.org/. Accessed on 15 June 2019

24. European Insulation Manufacturers Association (eurima) https://www.eurima.org/. Accessed on 15 June 2019
25. Polyurethane-Europe https://www.pu-europe.eu/ Accessed on 15 June 2019
26. Scheirs J, Priddy D (2003) Modern styrenic polymers: polystyrenes and styrenic copolymers. Wiley, US
27. Matar S, Hatch LF (2000) Polymerization. In: Matar S (ed) Chemistry of petrochemical processes, 2nd edn. Gulf Publishing Company, Houston, pp 315–316
28. Lenzi MK, Silva FM, Lima EL, Pinto JC (2003) Semibatch styrene suspension polymerization. J Appl Pol Sci 89:3021–3038
29. Erbay E, Bilgic T, Karali M, Savasci O (1992) Polystyrene suspension polymerization: the effect of polymerization parameters on particle size and distribution. Polym-Plast Technol 31(7–8):589–605
30. Erünal E (2018) Bead size distribution dependency on reactor geometry and agitation conditions of polystyrene production with suspension polymerization. Ç Ü Müh Mim Fak Dergisi 33(2):125–138
31. Lay PN, Rück S, Schiessl M, Witt M, Zettler HD, Baumgartel M, Dembek G, Hahn K, Holoch J, Husemann W, Kaempfer K (1999) US Patent 5,905,096 18 May 1999
32. Hogt AH, Fischer B (2011) US Patent 2012/0245315 A1, 27 Sep 2012
33. Casalini A, Felisari R (2007) US Patent 8,535,585 B2, 18 May 2007
34. Nising P (2009) US Patent 7,625,953 B2, 1 Dec 2009
35. Neufert E, Hartmann GH (1964) Styropor-Handbuch Bauverlag, Germany
36. Pritchard G (1998) Plastics additives: an A-Z reference. Springer, Bristol
37. United States Environmental Protection Agency (2014) Flame retardant alternatives for hexabromocyclododecane (HBCD) final report: IN: https://www.epa.gov/sites/production/files/2014-06/documents/hbcd_report.pdf
38. Stockholm Convention. Hexabromocyclododecane. In: Chemicals listed in Annex A http://chm.pops.int/Implementation/Alternatives/AlternativestoPOPs/ChemicalslistedinAnnexA/HBCD/tabid/5861/Default.aspx. Accessed on 15 June 2019
39. Covaci A, Harrad S, Abdallah MAE, Ali N, Law RJ, Herzke D, de Wit CA (2011) Novel brominated flame retardants: a review of their analysis, environmental fate and behaviour. Environ Int 37:532–556
40. Birnbaum LS, Staskal DF (2004) Brominated flame retardants: cause for concern? Environ Health Perspect 112(1):9–17
41. Koch C, Schmidt-Kötters T, Rupp R, Sures B (2015) Review of hexabromocyclododecane (HBCD) with a focus on legislation and recent publications concerning toxicokinetics and—dynamics. Environ Pollut 199:26–34
42. Marvin CH, Tomy GT, Armitage JM, Arnot JA, McCarty L, Covaci A, Palace VP (2011) Hexabromocyclododecane: current understanding of chemistry, environmental fate and toxicology and implications for global management. Environ Sci Technol 45(20):8613–8623
43. United States Environmental Protection Agency (2010) Hexabromocyclododecane (HBCD) action plan. In: Assessing and managing chemicals under TSCA. https://www.epa.gov/sites/production/files/2015-09/documents/rin2070-az10_hbcd_action_plan_final_2010-08-09.pdf. Accessed on 15 June 2019
44. T.C. Çevre ve Şehircilik Bakanlığı (2018) Bazı zararlı kimyasalların ihracat ve ithalatına dair yönetmelik. Turkey, 08 Mar 2018
45. European Union Law, Council decision document No. 52013PC0134, https://eur-lex.europa.eu/legal-content/EN/TXT/?uri=celex%3A52013PC0134 Accessed on 15 June 2019
46. Lanxess Datasheet (2016) Emerald innovation™ 3000 brominated polymeric flame retardant for polystyrene foams. http://add.lanxess.com/fileadmin/product-import/Emerald%20Innovation%203000.pdf Accessed on 15 June 2019
47. ICL Industrial Products Datasheet, FR-122 P Polymeric FR: Application datasheet for EPS foam. http://icl-ip.com/wp-content/uploads/2012/03/FR-122EPSICLIP_02_2012.pdf Accessed on 15 June 2019

48. Corp Albemarle (2014) Albemarle and ICL-IP to form polymeric flame retardant manufacturing joint venture. Addit Polym 10(1):5. https://doi.org/10.1016/S0306-3747(14)70146-0
49. Koch C, Nachev M, Klein J, Köster D, Schmitz OJ, Schmidt TC, Sures B (2019) Degradation of the polymeric brominated flame retardant "polymeric fr" by heat and UV exposure. Environ Sci Technol 533:1453–1462
50. Allen JI, Marshall WR, Wightman (1943) GE US Patent 2,496,653, 12 Oct 1943
51. Innes A, Innes J (2011) Flame retardants. In: Kutz M (ed) Applied plastics engineering handbook. Elsevier, Germany
52. Hastie JW (1973) Molecular basis of flame inhibition. J Res NIST-A. Phys and Chem 77 A:733–754
53. Camino G, Costa L, Luda di Cortemiglia MP (1991) Overview of fire retardant mechanisms. Polym Degrad Stab 33(2):131–154
54. Flameretardants-Online. https://www.flameretardants-online.com/ Accessed on 16 June 2019
55. Seop EB (2016) Korean Patent WO2016056717 (A1) 14 Apr 2016
56. Yan H, Dong B, Du X, Ma S, Wei L, Xu B (2014) Flame-retardant performance of polystyrene enhanced by polyphenylene oxide and intumescent flame retardant. Polymer-Plastics Tech and Eng 53:395–402
57. Cui W, Guo F, Chen J (2007) Flame retardancy and toughening of high impact polystyrene. Polym Compos 28(4):551–559
58. Nishihara H, Tanji S, Kanatani R (1998) Interactions between phosphorus- and nitrogen-containing flame retardants. Polymer J 30(3):163–167
59. Wang G, Bai S (2017) Synergistic effect of expandable graphite and melamine phosphate on flame-retardant polystyrene. J Appl Polym Sci. https://doi.org/10.1002/app.45474
60. Kaynak C, Sipahioglu BM (2013) Effects of nanoclays on the flammability of polystyrene with triphenyl phosphate based flame retardants. J Fire Sci 31(4):339–355
61. Xiao M, Sun L, Liu J, Li Y, Gong K (2002) Synthesis and properties of polystyrene/graphite nanocomposites. Polymer 43:2245–2248
62. Uhl FM, Wilkie CA (2004) Preparation of nanocomposites from styrene and modified graphite oxides. Polym Degrad Stab 84:215–226
63. Jankowski P, Kedzierski M (2013) Polystyrene with reduced flammability containing halogen-free flame retardants. Polimery 58(5):342–349

Modeling of TiB$_2$–BN Composites as Cathode Materials for Aluminum Electrolysis Cell

Check for updates

Eda Ergün Songül and İsmail Duman

Abstract Aluminum is the third most common element and the crust's most abundant metal. Nowadays, aluminum is an important metal in industrial production. Due to the lightweight, corrosion resistance, low density, and easy working probability, combine with its compatibility for recycling, support its position as the material of option for many utilization and it begins more favored in automotive, spacecraft components, and architectural construction with its extensive utilization area. In this work, the aim was targeted to evaluate the energy consumption in manufacture of the primary aluminum. The life of aluminum electrolysis cell, carbon cathode wear against arc blow, cryolite and abrasion of aluminum film was studied. It was found that TiB$_2$–BN composite was a better option as cathode due to wear resistance, high electrical conductivity and machinability.

Keywords Aluminum electrolysis · Titanium diboride · Boron nitride · Wear resistance · Electrical conductivity · Modeling

1 Introduction

Aluminum and its alloys are the choice of materials for automotive and aerospace applications due to their high corrosion resistance, machinability, high electrical conductivity, high thermal conductivity and particularly high strength/weight ratio [1–3].

The Hall–Héroult electrolytic method is the well-known method for the manufacture of primary aluminum [4]. Pure alumina is mixed with cryolite which is electrolyzed to produce pure aluminum. Cryolite is basically Na$_3$AlF$_6$ which is added to

E. Ergün Songül (✉)
Department of Metallurgical and Materials Engineering, İstanbul University-Cerrahpasa, 34320 İstanbul, Turkey
e-mail: eda.ergun@istanbul.edu.tr

İ. Duman
Department of Metallurgical and Materials Engineering, İstanbul Technical University, İstanbul, Turkey
e-mail: iduman@itu.edu.tr

decrease the working temperature of the bath. The process is quite energy consuming mainly due to electro–magneto–hydrodynamic forces and the anode effect [5].

During electrolysis, as alumina is consumed, the surface of the anode wetted by the electrolyte increases. Additionally, bubbles rising toward the surface of the bath decrease the contact between the anode and the electrolyte. Thus, the current efficiency decreases. Consequently, resistance and cell voltage increase.

The continuous addition of alumina in the chamber will result in the sedimentation toward the bottom of the furnace. A well-known phenomenon called "sludge" occurs. As a result, oxygen deficiency in the cell takes place. It is important that the liquid aluminum has to be collected from the furnace in order to keep the energy consumption to minimum. Convection is observed due to Eddy–Fuko current if the liquid aluminum stays in the cell. The liquid droplets of aluminum will sink to the bottom in accordance with Stokes' law as long as the critical radius is exceeded. The anode–cathode distance can be reduced to 2.5–4 cm from 5–7 cm [6]. In this case, the arc blow of the cathode carbon will decrease, the aluminum film will have an abrasion effect, and thereby the cathode efficiency will decrease.

1.1   General Structure of the Cathode

The base is made of 10–12 mm steel sheet welded in a box. The base of the case is covered with a layer of chamotte scraps, and it is designed to have a few rows of low-density bricks and a chamotte brick at the top. Figure 1 illustrates the schematic drawing of the general structure of the cathode for the aluminum electrolysis cell (Modified from [7]).
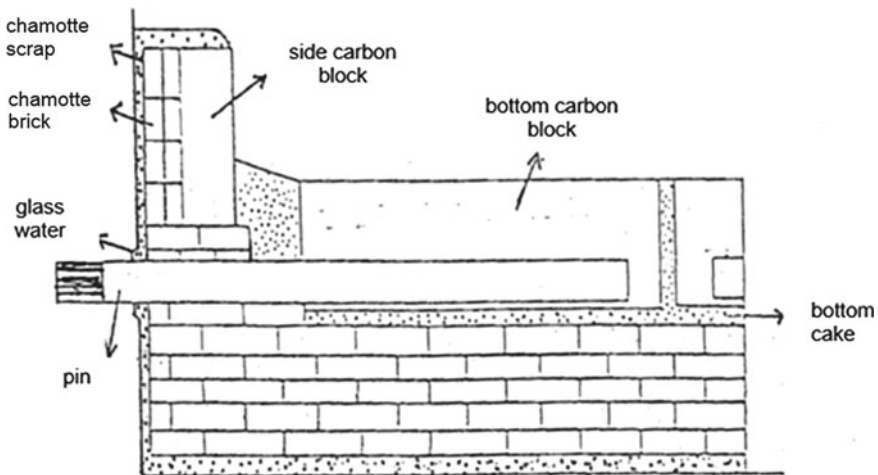

Fig. 1   General structure of the cathode (Modified from [7])

1.2 Design of the Aluminum Electrolysis Cell

Aluminum reduction cells are used today: prebaked anode cell and Söderberg cell. Aluminum has started with prebake cells which are produced under industrial conditions. During the First World War, the "self-baking" anodes were developed by Carl W. Söderberg in Norway. The use of these cells increased in the 1940s and 1950s. Figure 2 illustrates the schematic drawing of the (a) prebake-type cell and (b) Söderberg-type cell (Modified from [7]). Cells are usually 9–12 m long, 3–4 m wide and 1–1.2 m high.

1.3 Energy Efficiency During Aluminum Production

By decreasing the amount of alumina during the electrolysis, the angle of wetting of the anode surface by the electrolyte increases. In this way, the gas bubbles increase on the surface of the anode, which is not well wetted, and the contact between the electrolyte and the anode surface cuts off and prevents the passage of the current.

Due to the production of alumina charged to the cell from 8 to 2% over time due to production, oxygen deficiency occurs in the cell. Carbon electrode reacts with more positive fluorine ions due to lack of oxygen to form CFx gases.

The gases formed cling to the anode surface and began to cover the surface. Combined gas sensors enclose the anode surface by forming a gel-like structure, and the anode cannot be wetted by the electrolyte. As a result, the current density increases, and the polarization curve goes to infinity [7].

It is seen that the loss of aluminum particles due to reoxidation and back dissolution reduces not only the current efficiency of aluminum electrolysis but also the energy efficiency up to 30%. One of the measures to improve energy efficiency is the elimination of the effect of inductive currents. The most practical way to achieve this is to get rid of the liquid aluminum cushion. However, when we get rid of the liquid aluminum cushion, the carbon cathode will not be based on arc blowing, cryolite and the etching effect of the aluminum film in a continuous flow. To eliminate all these negative effects, the coating on carbon cathodes will be a solution.

1.4 Titanium Diboride (TiB_2) and Boron Nitride (BN)

1.4.1 Titanium Diboride (TiB_2)

Titanium diboride is known as high strength and strong ceramic material [8]. The TiB_2 structure consists of Ti–Ti, Ti–B and B–B bonds. There are strong covalent bonds between atoms, which means high melting point and high hardness [9]. Figure 3 shows the (a) hexagonal TiB_2 unit cell (b) hexagonal layered TiB_2 structure [8].
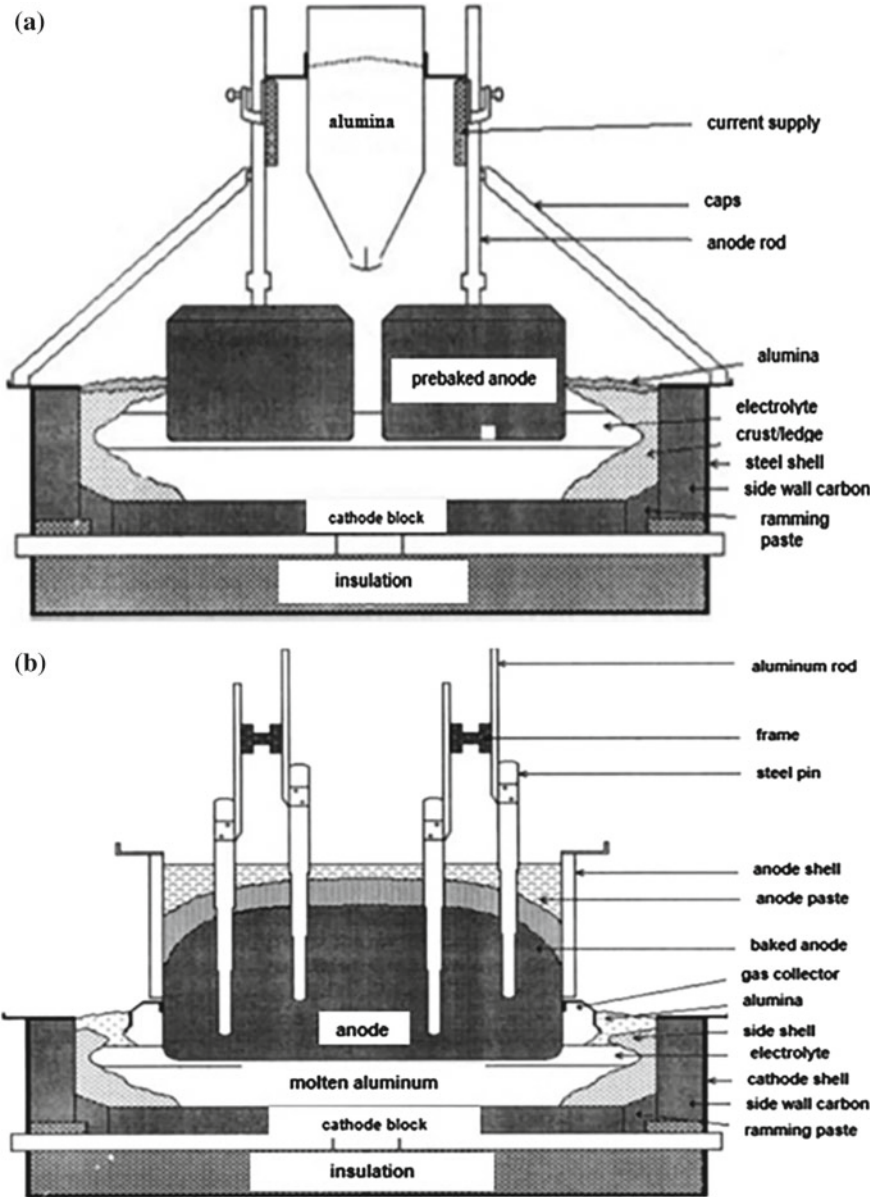
Fig. 2 **a** Prebake-type cell and **b** Söderberg-type cell (Modified from [7])

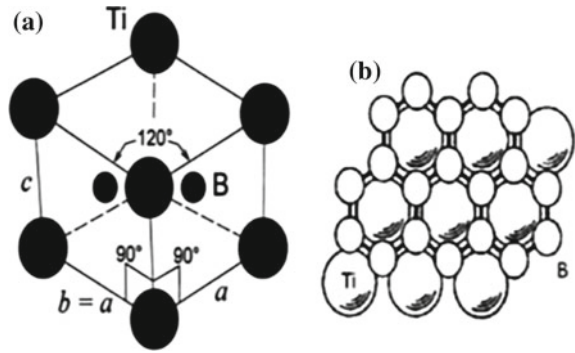**Fig. 3** **a** Hexagonal TiB$_2$ unit cell **b** Hexagonal layered TiB$_2$ structure [8]

Table 1 General properties of the TiB$_2$ [10]

M (g/mol)		69.54
Color		Gray
Density (kg/m^3 10^{-3})		4.52
Melting temperature (°C)		2920
Crystal structure		Hexagonal
Lattice parameters	a (nm)	0.3030
	b (nm)	–
	c (nm)	0.3230
Thermal conduction coefficient	300–1300 K	24.0
	1300–2300 K	26.3
Hardness (1 N) (GPa)		25.5
E (GPa)		541
Poisson's ratio, υ		0.09–0.11
Compression strength (MPa)		1350
Tensile strength (MPa)		127
Conductivity S/cm		10^5

Table 1 shows the general properties of the TiB$_2$ [10]. It is generally characterized by its high melting point, high wear resistance, very high Young's modulus, density ratio strength and high hardness [11, 12]. Figure 4 shows the Ti–B phase diagram [13].

1.4.2 Boron Nitride

Boron nitride, which has the empirical formula BN, contains equal amounts of boron and nitrogen atoms. The boron and nitrogen atoms adjacent to the nitrogen atom in the periodic table are connected to each other by carbon–carbon bonds [14]. Figure 5 illustrates the B–N phase diagram [15].
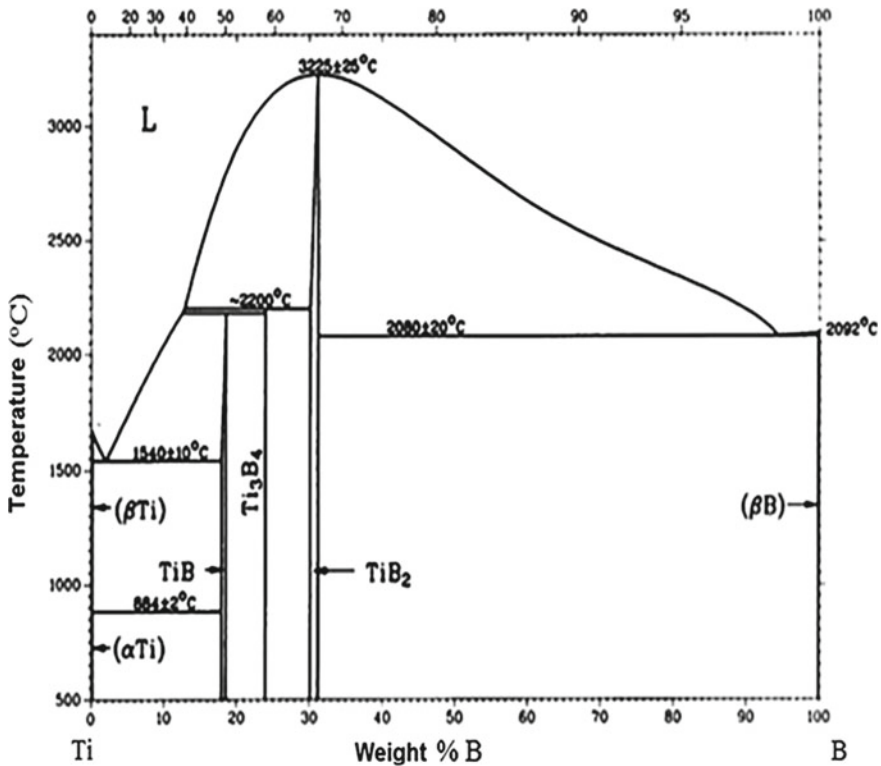
Fig. 4 Ti–B phase diagram [13]

Boron nitride has three basic crystallographic structures. These include the hexagonal form (h-BN), the cubic form (c-BN) and the wurtzite form (w-BN). The three crystal forms also have very different physical properties and are used in many different applications [15].

Hexagonal Boron Nitride (H–BN)

The hexagonal structure consists of strong covalent bonds between BN atoms in hexagons and weak van der Waals bonds between layers. Figure 6 shows the (a) hexagonal BN structure (b) graphite structure [15].

Cubic Boron Nitride (c-BN)

Four nitrogen atoms surround one boron atom, and sp3 hybridization is present [16]. Cubic boron nitride crystal structure and other features are similar to diamonds.
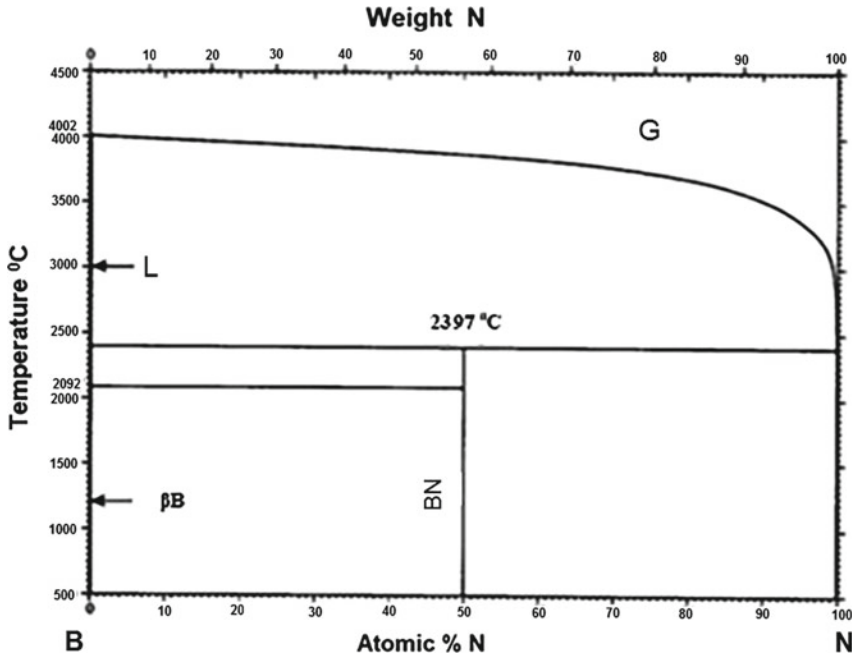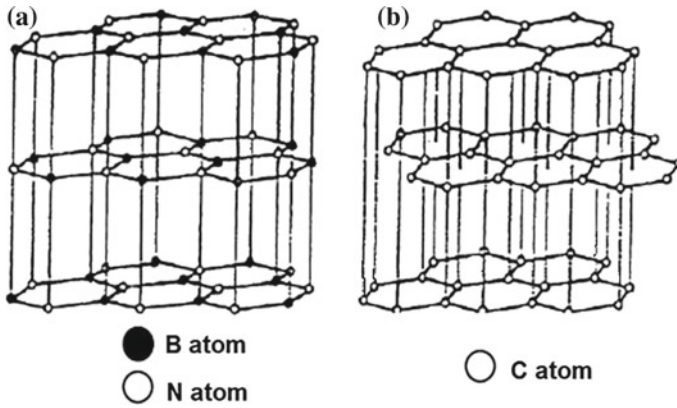
Fig. 5 B–N phase diagram [15]

Fig. 6 **a** Hexagonal BN structure **b** graphite structure [15]

Figure 7 illustrates the cubic boron nitride (c-BN) structure [16]. Table 2 shows the general properties of the h-BN and c-BN [16].

Wurtzite Boron Nitride (W-BN)

The rigid package is not a stable form of boron nitride wurtzite structure in its hexagonal form and can only be achieved under static high pressure (average 13 GPa at room temperature) or by dynamic shock methods [16].

Fig. 7 Cubic boron nitride (c-BN) structure [16]
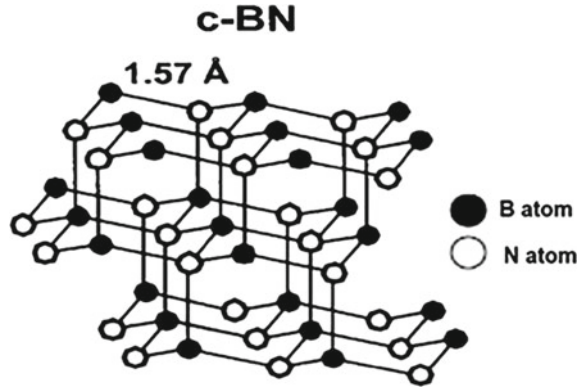
Table 2 General properties of the h-BN and c-BN [16]

(h)BN	(c)BN
2.27 (g/cm^3)	3.48 (g/cm^3)
980 °C (Air oxidation)	1200 °C (Air oxidation)
Soft	Hard
Lubricating	Grinding
Electrical conductivity 10^{-7} S/cm	Electrical conductivity 10^{-7} S/cm
Thermal conductivity 55 W/mK	Thermal conductivity 1300 W/mK
Melting temperature 2700 °C	Melting temperature 2973 °C
Oxidation temperature 980 °C	Oxidation temperature 1200 °C

2 Materials and Design

Titanium diboride is a high resistance and toughness ceramic material. TiB$_2$ also has numerous different properties, like high stiffness, high Young's modulus and high heat resistance. It can be used as cutting tools or wear resistance applications [17]. Such properties make TiB$_2$ an attractive choice of material for use in cathode material in the Hall–Heroult process. However, there are some disadvantages as well. The sintering temperature is higher than 2400 °C due to the strong covalent bonding and high melting temperature, and it is not machinable. Since the diffusion coefficient is low, the sinterability is also limited. An alternative method involves the use of hot pressing. It is important to note that during this process, enhanced grain growth is observed, and internal stress increases which leads to micro cracking [8, 9, 18].

Ceramic materials are not easily machined but boron nitride (BN) is the easiest one among the most ceramics. It has unique features like as low dense, high thermal conductivity, high resistance to chemical attack, excellent electrical and wear resistance. For these reasons, it is usually utilized as a coating for refractory molds used in glass forming and in superplastic forming of titanium. The position of boron in the periodic table is close to carbon, and also boron and nitrogen elements form a compound, BN, which is isoelectronic with carbon. Therefore, BN is isostructural to the polymorphous of carbon [19, 20].

Boron nitride has three main polymorphs: hexagonal, cubic and wurtzite form [21, 22].

- h-BN: It is corresponding to the layered graphite, and the density of h-BN is 2.3 g cm^{-3} [22].
- w-BN: It is formed by compressing hexagonal boron nitride under high pressures at low temperatures close to 1700 °C, and the density of w-BN is 3.49 g cm^{-3} [22].
- c-BN: It is made by compressing hexagonal boron nitride powder under 5 GPa pressures at higher temperatures, and the density of c-BN is 2.2 g cm^{-3} [21].

In this work, h-BN was selected owing to its low degree of compactness of a substance. It is the lowest one among the ceramic materials in terms of density. Boron nitride powder is converted to h-BN in nitrogen flow at temperatures above 1500 °C. The unmatched features of h-BN can be exhibited as stated: low dielectric constant, high thermal conductivity, good chemical inertness against wetting by most molten metals, glasses and salts. h-BN is being used as an electrical insulator because of the combination of low dielectric constant and volume resistivity [23, 24].

Boron nitride can be added to titanium diboride, and the sintering warmth can be decreased. Warmth resistance of TiB$_2$–BN composites is excellent, but the electrical conductivity of TiB$_2$–BN composites is very weak. Also, its wettability is very low which makes it easy to separate the liquid metal and slag.

This project was separated into three major missions:

– Production of the TiB$_2$–BN composite materials,
– Modeling the TiB$_2$–BN composite materials in industrial cells,
– Pilot-scale testing of TiB$_2$–BN composite materials.

A hexagonal geometry was chosen as the substrate for the coating of TiB$_2$–BN. A thread was drilled in the center in order to generate a solid non-sagging plate tiles as seen in Figs. 8, 9.

TiB$_2$–BN screw (as seen in Fig. 9a) was bolted to the holes in Fig. 8. Hexagonal geometry was designed in an aim to supply a rigid structure that could be tiled easily. Optimum geometry was obtained for better coating with maximum area and minimum material use. In this way, the leakage of liquid aluminum was also impeded. The tiles fastened on the cathode floor with screws lock their three neighbor tiles to
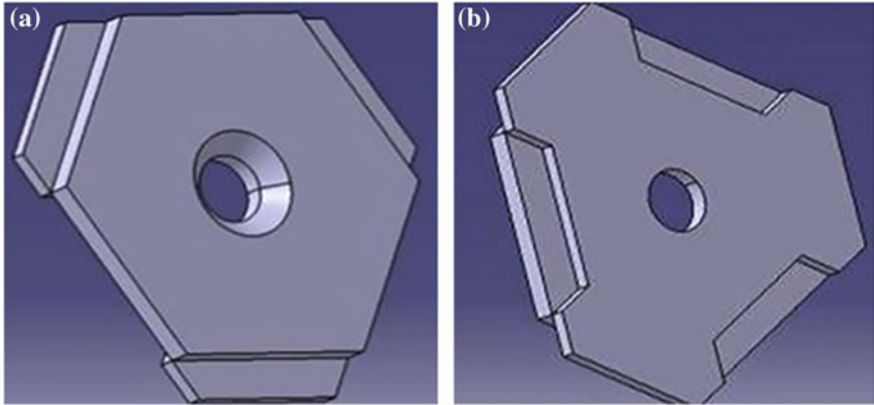
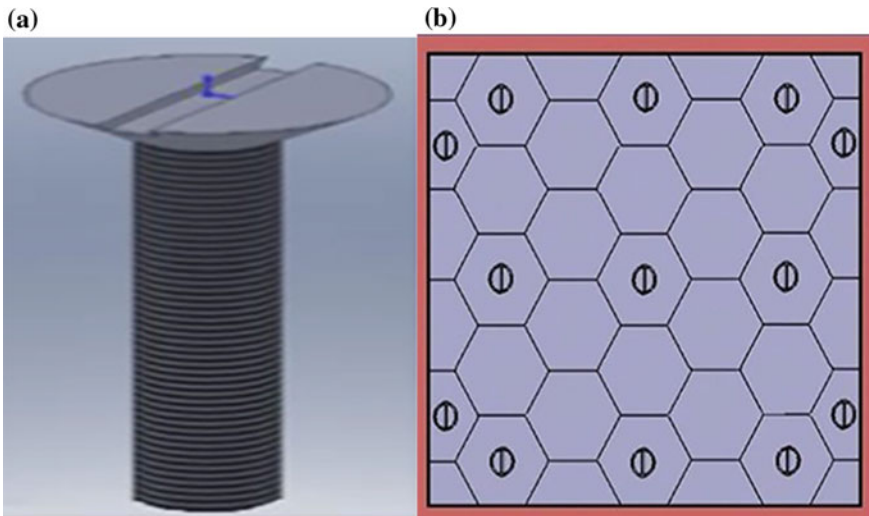**Fig. 8** **a** Front view of TiB$_2$–BN tile, and **b** Back view of TiB$_2$–BN tile

Fig. 9 **a** TiB$_2$–BN screw, and **b** TiB$_2$–BN tiles fastened on the cathode floor with screws

Table 3 Boron nitride powders content

B	Min. 41%
O	Max. 7%
B$_2$O$_3$	5–8%
H$_2$O	Max. 0.7%
C	Max. 0.1%
Crystal structure	Hexagonal

Table 4 Titanium diboride powders content

B	Min. 30%
C	Max. 0.5%
O	Max. 1.1%
N	Max. 0.6%
Fe	Max. 0.1%
Crystal structure	Hexagonal

the bottom. TiB$_2$–BN tiles fastened on the cathode floor with screws are shown in Fig. 9b.

During our experiments, hexagonal boron nitride and titanium diboride powders from German H. C. Starck were used. The information presented by the company for these products is shown in Tables 3 and 4.

Production diagram of titanium diboride doped hexagonal boron nitride-based composites is followed in Fig. 10.

Mass percentages of samples contents are seen in Table 5. Three different composite samples and graphite are prepared for electrical conductivity test.

3 Results and Discussion

The formability of TiB$_2$–BN composite by machining varies according to BN ratio. The sample containing 20% BN, which was prepared for use in the abrasion resistance, was broken during machining. For this reason, 20% BN-containing composites were found to have no machinability. The easiest way of shaping was achieved at 40% BN. Graphite sample is processed without any problem. As a result of the experiments, when the amount of BN in the composite increased, the machinability increased.

Since 20% BN was not machined, the rest of the samples were subjected to wear tests. Wear tests were carried out under 1300 rpm for 72 h in liquid aluminum under argon atmosphere. The weight change was recorded after the tests were completed. The results are given in Table 6.
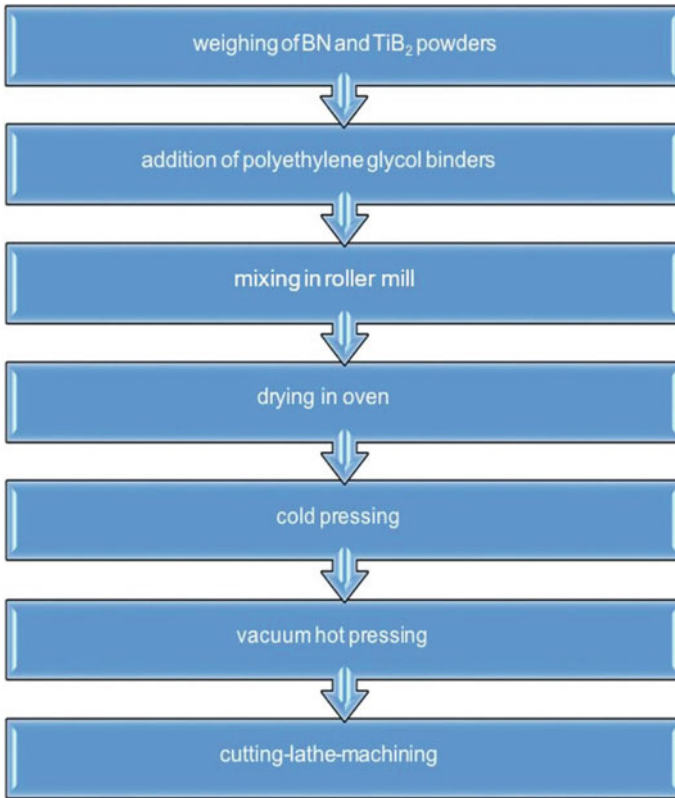
Fig. 10 Production diagram of TiB$_2$–BN composites

Table 5 Sample contents

Sample	BN (% weight)	TiB$_2$ (% weight)
1	20	80
2	30	70
3	40	60

Table 6 Weight measurements of wear test samples

	30% BN (Sample 2)	40% BN (Sample 3)	Graphite
First weight (g)	10.004	9.221	5.57
Final weight (g)	9.988	9.119	5.29
Difference (g)	0.016	0.102	0.28
Difference (%)	0.16	1.106	5

Table 7 Electrical conductivity of graphite and composites

Electrical conductivity (1/Ωm) × 10^3	
Graphite	10.998
Sample 1	2706
Sample 2	1440
Sample 3	856

As the BN ratio of the composite was decreased, the wear rate was decreased. However, it has been determined that wear of composites with 30% BN and 40% BN, which can be applied to wear resistance test, is much less than graphite.

In order to compare the electrical conductivity of composites with graphite, four-point conductivity test is applied. Electrical conductivity values of graphite and composites are included in Table 7.

It was determined that the electrical conductivity values decreased with the increase of BN ratio in the composite. In spite of this, the conductivity values of the samples containing 20% BN, 30% BN and 40% BN were found to be higher than the conductivity value of graphite.

According to the wear test results, it was found that the wear rate was improved 7 million times based on an 800 kg capacity aluminum production. In other words, the wear rate was found to be resistant for 13 years.

The comparison of wear resistance, machinability and electrical conductivity of carbon and TiB$_2$–BN composite was analyzed. The machinability of the composite was found to be depended on the BN content. As BN ratio was increased, machinability was increased. The electrical conductivity was decreased with increased BN content. Similarly, the wear resistance was also decreased with increased BN content. Figure 11 shows the samples for wear resistance test.

4 Conclusions

The importance of reducing the energy consumption of the aluminum cell is known to increase the competitiveness of the aluminum industry. Due to the lightweight, corrosion resistance, low density, and easy working probability, combine with its compatibility for recycling, support its position as the material of option for many utilization and it begins more favored in automotive, spacecraft components, and architectural construction with its extensive utilization area.

In this work, the aim was targeted to evaluate the energy consumption in the manufacture of the primary aluminum. It has been experimentally proven that it is possible to improve the energy performance of aluminum electrolysis cells with a new modeling approach. The life of aluminum electrolysis cell, carbon cathode wear against arc blow, cryolite and abrasion of aluminum film was studied. It was found that TiB$_2$–BN composite was a better option as cathode due to wear resistance, high electrical conductivity and machinability.
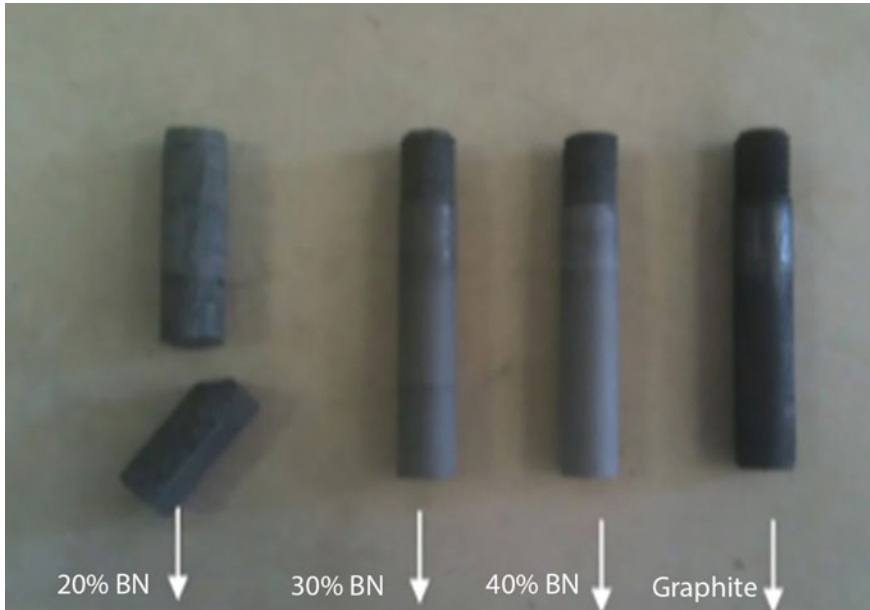
Fig. 11 Samples of wear resistance test

By decreasing the amount of alumina during the electrolysis, the angle of wetting of the anode surface by the electrolyte increases. In this way, gas bubbles increase on the surface of the anode, which is not well wetted, and the contact between the electrolyte and the anode surface cuts off and prevents the passage of the current. Due to the production of alumina charged to the cell from 8 to 2% over time due to production, oxygen deficiency occurs in the cell. Carbon electrode reacts with more positive fluorine ions due to lack of oxygen to form CFx gases. It is seen that the loss of aluminum particles due to reoxidation and back dissolution reduces not only the current efficiency of aluminum electrolysis but also the energy efficiency up to 30%. One of the measures to improve energy efficiency is the elimination of the effect of inductive currents. Almost all of the research and technical improvements to improve aluminum electrolysis in the last 20 years have been aimed at reducing or completely eliminating the anode effect and aiming to avoid the CF_X penalty. By reducing the amount of CF_4 and C_2F_6 generated during the anode effect, the environmental compensation payment of the factories can be eliminated.

References

1. Bardal E (2004) Corrosion and protection. Springer-Verlag, London Limited
2. Kaufman JG (2000) Introduction to aluminium alloys and tempers. ASM International, Ohio
3. Revie RW (2011) Uhlig's corrosion handbook, 3rd edn. Willey, New York

4. Prasad S (2000) Studies on the Hall-Heroult aluminum electrowinning process. J Braz Chem Soc 11:245–251
5. Welch BJ (1981) Advances in aluminium smelter technology. Chem Eng Aust 5:26–32
6. Gusberti V et al (2011) Modelling the aluminium smelting cell mass and energy balance—a tool based on the 1st Law of Thermodynamics. In: 10th Australasian aluminium smelting technology conference
7. Habashi F (1997) Handbook of extractive metallurgy: primary metal, secondary metals, light metals (Cilt 2, 1044). Wiley-VCH Verlag, Weinheim
8. Munro RG (2000) Material properties of titanium diboride. J Res Nat Inst Stand Technol 105:709–720
9. Einarsrud MA, Hagen E, Pettersen G, Grande T (1997) Pressureless sintering of titanium diboride with nickel, nickel boride, and iron additives. J Am Ceram Soc 80:3013–3020
10. Yücel O, Derin CB, Kol Zİ. Ve Alkan M (2008) Magnezyotermik yöntemle TiB$_2$ tozu üretimi, TÜBİTAK MAG Proje 105M339, İstanbul
11. Matkovich VI (1977) Boron and refractory borides. Springer-Verlag, New York
12. Jüngling T, Sigl LS, Oberacker R, Thümmler F ve Schwetz KA (1993) New hardmetals based on TiB$_2$. Int J Refract Metals Hard Mater, 12:71–88
13. Aynibal F (2009) IV grubu metal borürlerin ve lantan hekzaborürün mekanokimyasal reaksiyon ortamında sentezlenmesi, (yüksek lisans tezi). İstanbul Teknik Üniversitesi, Fen Bilimleri Enstitüsü, İstanbul
14. Weimer AW (1997) Carbide, nitride and boride materials synthesis and processing (sf. 90–237). Chapman & Hall, Colorado
15. Vel L, Demazeau G ve EtourneauJ (1991) Cubic boron nitride: synthesis, physicochemical properties and applications. Mater Sci Eng: B 10:149–164
16. Haubner R, Wilhelm M, Weissenbacher R ve Lux B (2002) High performance non-oxide ceramics II: Boron nitrides—properties, synthesis and applications (Cilt 102, sf. 1–45). Springer-Verlag, Berlin
17. Surendranathan AO (2015) An introduction to ceramics and refractories. CRC Press, Taylor & Francis Group
18. Weirauch DA, Krafick WJ, Ackart G ve Ownby PD (2005) The wettability of titanium diboride by molten aluminum drops. J Mater Sci 40:2301–2306
19. Bernard S, Miele P (2014) Polymer-derived boron nitride: a review on the Chemistry, shaping and ceramic conversion of borazine derivatives. Materials 7:7436–7459
20. Bernard S, Miele P (2014) Nanostructured and architectured boron nitride Mater. Today 17:443–450
21. Vel L, Demazeau G ve Etourneau J (1991) Cubic boron nitride: synthesis, physicochemical properties and applications. Mater Sci Eng: B, 10:149–164
22. Jansen M (2002) High performance non-oxide ceramics II: hexagonal boron nitride. Springer-Verlag, Berlin, pp 4–38
23. Lipp A, Schwetz KA ve Hunold K (1989) Hexagonal boron nitride, fabrication properties and applications. J Eur Ceram Soc 5:3–9
24. Lelonis DA (2003) Boron nitride powder a review. GE Advanced Ceramics Publications (2003)

Optimum Operating Temperature Range of Phase Change Materials Used in Cold Storage Applications: A Case Study

Gulenay Alevay Kilic, Enver Yalcin and Ahmet Alper Aydin

Abstract The storage of latent heat, one of the thermal energy storage systems (TESs), is now used in cold storage applications. PCM's use in the refrigeration industry has been integrated into systems without mechanical chiller, as stated in the literature. In this case, PCMs play a promising role in increasing the performance of cooling systems and refrigeration applications. The aim of the present study is to determine energy consumption changes and without PCMs. The temperature of the cold storage and PCM were investigated and the on-off times of the compressor were also analyzed experimentally. Furthermore, the on/off period times of the cold storage were analyzed for the cold store without PCM. The results indicated that off period time increased, while working period time increased, significantly. PCM application provided a total energy efficiency increase of 20–22%. In addition, the phase change materials used as insulation material have a wide range of working temperatures, which has created another positive effect of the study.

Keywords PCM · Optimization · Energy storage · Efficiency

1 Introduction

Scientific developments in cold storage emerged after World War II. The imbalance between production and consumption after the war, in particular, has increased the

G. A. Kilic (✉)
Department of Electric and Energy, Yalova Vocational School, Yalova University, 77100 Yalova, Turkey
e-mail: gulenay.kilic@yalova.edu.tr

E. Yalcin
Department of Mechanical Engineering, Engineering Faculty, Balikesir University, 10145 Balikesir, Turkey
e-mail: eyalcin@balikesir.edu.tr

A. A. Aydin
Department of Chemical Engineering, Faculty of Chemical and Metallurgical Engineering, Istanbul Technical University, Maslak, 34469 Istanbul, Turkey
e-mail: aydinal@itu.edu.tr

importance of storage. At the same time, the delivery of all kinds of cold storage products to the consumer on time has gained a special importance. Hence, these transported products must be presented to the consumer without breaking the cold chain. Therefore, transporting the materials without being affected by the seasonal conditions constitutes the most important stage of the cold chain. This is done by refrigerated vehicles with mechanical cooling systems that maintain the temperature and humidity of the products in a certain range [1].

The latent heat thermal energy storage system, by changing the phase change of a material, is more advantageous than sensible heat storage and is often used today due to the energy-saving and high system efficiency. Phase change materials (PCM) are materials that store high amounts of heat as energy without noticeable temperature rise during the phase change of the material. In order to change its phase, the material absorbs a large amount of heat energy from the medium, or it releases it into the environment. Thus, the amount of energy stored in the unit requires less volume per energy. The most commonly used physical property of PCMs in the storage of heat energy is solid–liquid phase separation [2–6]. Besides, due to the narrow temperature range occurring during phase change heat transfer, it has attracted the attention of many researchers. The studies on the use of PCM in TES systems in the literature are examined below.

1.1 Studies on the Application of PCM Usage in Buildings from TES Systems

Improved methods of thermal storage have remained behind compared to other developments in buildings and this is a subject of energy saving. Hawes revealed this requirement in his work. In the study, concrete construction materials were selected on the latent heat storage in concrete. It has been chosen as an ideal candidate for improving the heat storage capacity of these materials. This process was obtained by adding organic PCM to the concrete. PCMs absorb or release the latent heat of freezing at a selected temperature and thus greatly increase the heat storage capacity of the impregnated concrete over a smaller temperature range. The combination of these additional materials has been investigated to optimize the heat storage performance of buildings and reduce the cost of concrete. Various manufacturing procedures have also been developed. Two types of PCM were found to be satisfactory. In addition to that, the performance of several other promising PCM candidates used to impregnate in different forms within the concrete has also been studied in order for the optimization of future studies and has been modified to improve the compatibility of concrete to PCMs. A total of four types were studied and three of them were found to be suitable for pre-impregnation. In this research, it was mentioned that the energy stored in the concrete and the waste heat has a wide usage area for the storage of the heat from the solar collectors or outside the peak hours or the low-cost heat. It has also been described that these materials can be used by reducing the operating

frequency of this equipment to improve the burner and cooler performance by heat storage. These materials have been shown to be cost-effective in areas with high fuel costs and favorable temperature fluctuation, as well as being used in colder areas [7].

Justin et al. [8] presented a review of cold thermal energy storage technologies. They studied PCMs because it provides high energy density and small temperature change interval during the melting and solidification process. The high latent heat produced by the hydrates of the salts during solidification is particularly interesting due to their high thermal conductivity and low flammability properties, and they facilitate the use in buildings compared to organic PCMs. Experimental studies, theoretical analysis, and system performance studies from actual case studies have revealed some problems with the material. In order to provide cost-effectiveness, future studies in the secret heat storage area with salt hydrates indicated that there should be appropriate methods for incompatible melting and subsequent cooling limitation without compromising storage density. In addition, it has been emphasized that it is improvable in terms of innovative design for latent heat storage system integration, as well as high power and storage capacity in cold applications, and for the dimensioning, control and elimination of PCM encapsulation such as to be optimized for the load.

Kuznik et al. [9] have tested the PCM, which is used as a supporter for the restoration of third-order buildings, for two identical rooms. The sidewalls and ceiling of one of the rooms were equipped with PCM wall cladding, while the other room had no operation. As a result of the test, it was observed that the wall covering with PCM increased the heat comfort and convenience of the occupants in the room due to the radiation effects of the walls and the air temperature.

Sharif et al. [10] assert that the cost-effective and efficient way for preheated domestic water used in buildings is solar (heated with solar energy) domestic hot water. This study examines the melting process of PCM in an evacuated solar collector containing an absorbent RT82, PCM storage system. A three-dimensional mathematical model has been developed using FLUENT 14.0 software program. It is accepted in the literature that there is no heat loss and there is natural heat transfer. Simulation results show that the PCM storage system has a considerable effect on the increased solar density of PCM over the dissolution time.

In their study, Costa et al. [11] used PCM to reduce the electrical energy used for heating of houses system consists of aluminum PCM containers, translucent polycarbonate, fluid passing tubes, and electrical heater. Enthalpy formation and closed finite difference method were used, and the thermal performance of the storage system was analyzed.

In another study, it has been proposed to optimize PCM in the coating of floors. By making a validated numerical model of the system, the effect of the thickness of the slab, the inter-slab clearance, and the mass flow rate was investigated by making a parametric study [12].

In a study performed by Sarı et al. [13], an appropriate amount of paraffin impregnated with expanded graphite was determined to obtain a fixed structure composite as PCM.

A research was carried out by Konuklu and Paksoy [14] on building applications of PCM technology. Phase change models in buildings, wall, roof, floor, and cooling systems have been reviewed.

The design and analysis of PCM-based thermal energy storage systems for active building cooling were studied by Patil et al. where $CaCl_2$ used as PCM. The freezing temperature of H_2O was used for the cooling water during the night, and this cooled water was circulated through the fan heat exchanger unit (FCU). The air passing through the fan heat exchanger unit was cooled by the heat transfer given to the water, and the clean and cooled air was sent inwards of a room. Concealed heat storage materials in the range of 20–35 °C, which are comfortable for the human and the tolerance range of electronic equipment, are very effective [15].

In order to reduce the energy consumption of a building, TES system was investigated by Anisur et al. as an alternative solution for air cooling–heating application. For this application, different types of phase-changing materials have been investigated together with the TES system with different geometries. In this study, a theoretical model was used for air cooling–heating application. The circulation of air in the pipe with PCM was investigated on the outer side of the double-walled circular pipe. In the process, laminar flow was forced together with variable wall temperature and the convection was taken into account. It has been found that the internal radius and thickness of the pipe are an important parameter in the system design. Because the change in air temperature from the system is due to the reduction of the inner radius and the thickness of the pipe, the performance coefficients for cooling (COP) were found to be 8.79 and 7.20 for the PCM container with an internal radius of 15 mm and 25 mm, respectively. It was stated that the system could be optimized by reducing the volume of the PCM container [16].

1.2 Research on the Usage of PCM in TES Systems for Cooling Applications

Cooling systems, cabinet interiors, and/or other equipment changes can improve the energy performance of refrigerators. Such changes include the use of variable speed/capacity compressors, installation of larger heat exchangers, better fan systems with the fixed magnet, optional defroster systems, hollow insulation panels, thicker insulation, better sealing, magnets, door seals, and new types of coolers [17]. The use of PCMs to increase the energy efficiency of refrigerators has attracted attention over the last decade [18–20]. The right PCM and packaging system design provides significant benefits in energy efficiency without the need for serious design changes in refrigerators.

Gholap et al. [21] used PCMs in the devices together with heat exchangers. The applied heat exchanger has primarily reduced energy consumption and increased heat storage capacity. The heat exchanger has influenced the energy efficiency of the

cooler such as evaporator and compressor. In the study, a difference of 5.95% was observed in a daily energy measurement between experimental and simulation.

In the study conducted by Wang et al., they tried to save energy through PCM use in refrigeration systems. By using a variety of eutectic mixtures, approximately 8% of energy savings have been achieved in the cooling system. The performance coefficient (COP) of the system has been calculated to increase by about 6%. In the study, PCM was applied passively in the refrigerator system. PCM was not included in the refrigerator cooling system. Eutectic mixtures were used as PCM [22].

Klimes and et al. [23] stated that PCMs were a good method for stable heat storage and many possible applications. In their study, cold storage effect was investigated experimentally by using solar collector with heat capacity method and differential scanning calorimeter techniques. The results of the study were also compared with the numerical method. It was mentioned that in the two separate techniques used during the use of solar air collectors, uncertainty in the material properties and the common problems in the simulation environment were encountered.

Mehling and Cabeza [24] in their study investigated PCM applications developed in transport boxes, pharmaceutical industry, blood transport, electronic circuits, preservation of cooked foods, biomedical transport and in many other areas related to the protection of temperature. Information was provided about the commercially available PCM products for the transport of products studied in the pharmaceutical industry and other sensitive temperatures.

Mondieig et al. [25] applied molecular transports in the transportation of biomedical products. Mixtures of different substances were prepared so that the molecular alloys had a high heat capacity. The mixtures whose molecular structures of the components are very close to each other are referred to as molecular alloy. Thus, they could obtain PCMs which could operate in very different temperature ranges. They also asserted that by using n-alkanes, a wide range of −50 to 100 °C can be reached. Thus, biomaterial storage was provided for 6 h at a temperature below 10 °C.

Ventola et al. [26] reported that the fact that various PCMs have a melting range more than a constant melting point is particularly desirable in different areas. It was also studied with molecular alloys in order to store thermal energy and keep the temperature constant in a certain range. Especially, n-alkanes entering the organic class have been used in the preparation of molecular alloy and it has been explained that the obtained temperature of 69–85 °C has a wide range of application areas such as food sector.

Tyagi et al. [27] conducted an experimental study of overcooling and pH behaviors of a typical PCM for TES. In this study, overcooling behavior of a typical PCM and the effect of the pH value on this case were investigated. The results obtained by the experimental study were compared with the results obtained by differential scanning calorimetry (DSC) and were found to be in good compliance with each other.

Li et al. [1] separately studied the last developments of cold storage materials for the applications below zero for PCM storage and absorption storage depending on the type of storage media and the shape of storage media used. PCMs consisting of eutectic saline aqueous solutions and non-eutectic saline aqueous solutions were

discussed in terms of thermal and physicochemical properties such as fusion temperature, thermal conductivity, phase separation, overcooling, corrosion, inflammation, and the like. Problems with such PCMs and their solutions have been revealed. Microencapsulated PCMs having excellent loop stability due to restricted phase separation in microscopic distances and presenting excellent heat transfer performance toward the environment due to a large surface area per capsule volume have been introduced. PCMs containing nanoparticle additives were also discussed because they have higher thermal conductivity for better storage.

He [28] asserts that cold–heat storage systems not only have the potential to be one of the primary solutions of the imbalance between electricity production and demand, but also prevent intensive demand charges by pulling the use of cooling energy in the peak periods out of peak demand hours. These systems increase the possibilities of use of renewable energy sources and the use of waste heat for refrigeration production. In addition, cold storage can actually increase the combined heat and power (CHP) production efficiency when the combination of heat-induced cooling and CHP is achieved. Subsequently, cold storage can prevent heat demand peak times for refrigeration production and this means that CHP can often operate under design conditions. The potential for PCM storage to reduce peak consumption in different cooling systems has been demonstrated. A computer model has been developed for fast phase balance calculation. The use of phase balance data in the design of the cold storage system is presented as a general methodology.

The recent developments in the cold storage materials for air conditioning applications have been examined by Kılıçcaslan and Koyun [29]. The commercial aspect of storage materials was also discussed.

Sönmez et al. [30] examined the effect of the semi-circular-shaped flaps placed on a cold storage tank with rectangular geometry and consisted of water as PCM in different numbers and positions on the solidification process. The obtained results showed that the position and number of the flaps on the geometry significantly increased the rate of heat transfer and solidification ratio.

Cheralathan et al. [31] studied the behavior of the cylindrical storage tank filled with PCM in phase changes in the cold storage system. They also evaluated the phase change temperature ranges of the heat transfer fluid at any location during the charging period with a simulation program. When the results were examined, PCM pore structures in the number ranges of Stanton, Stefan, and Peclet were also compared. In their experimental and numerical studies, they concluded that if the Stanton number was in the range of 0.7–1, higher energy storage capacity and faster charging times could be achieved.

In their study, Fertelli et al. [32] examined the effects of placing single and two cylinders in a cold storage tank in different positions in the tank on ice formation. Temperature distributions, liquid ratios, and solidification ratios were obtained. It is seen that the solidification rates obtained in case of single-cylinder placement in different positions ($h = d$ and $h = 2d$) in the lower part of the tank are completely same, while the solidification rates are increased in case of placing the cylinders close to the upper part of the tank ($h = 8d$ and $h = 9d$). When the number of cylinders in the tank is two and they are at the bottom of the tank ($h = d$ and $h = 2d$), the

solidification rates are the same, and when the two cylinders are placed close to the upper part, it is seen that the maximum solidification rates are obtained as in the single cylinder.

Zalba et al. [33] have studied the implementation of PCM in free cooling systems. Statistical analysis showed that the thickness of the encapsulation, the interior temperature, the airflow, and the interaction of thickness and temperature had a great impact on the solidification process.

Ryu et al. [34] studied the heat transfer characteristics of cold thermal storage systems. The heat transfer characteristics of the cold thermal storage units during the filling period were studied by using 2% by mass of sodium sulfate decahydrate in aqueous solution as phase change material. The vertical and horizontal pipe systems were compared in terms of heat transfer rate, performance coefficient, and overcooling status of the phase change material. It was found that PCM crystals were grown into coaxial circles in horizontal tubes while growing in vertical pipes into convex circles. The crystal growth patterns for vertical pipes arise due to the thermocline of the heat transfer fluid surrounding the pipes. As a result of this, the vertical pipe system has a better thermal performance than the horizontal pipe system. For the cold thermal energy storage system, the total amount of energy stored in order to form the basic data for using in the design of the pipe types has been correlated in terms of Fourier, Stefan, and Reynolds numbers.

For air conditioning applications, Hasnain [35] describes the naturally occurring pros and cons of commercially available and widely used TES technology (i.e., cold water and ice storage). Case studies on cold–heat storage not only saved energy and other operating and maintenance costs, but also showed significant savings in initial capital cost. This article also examines the use of cold thermal storage equipment for gas turbine inlet air cooling, which can increase efficiency in a positive way. It has been determined that TES applications predominantly occur in North America. However, in the mid-1990s, applications in Asia, Australia, Europe, and South America began to emerge. Finally, expectations from TES technologies for electrical charge management in Saudi Arabia have also been revealed.

The computable flowing dynamic simulation was used by Gowreesunker and Tassou [36] to assess the effectiveness of the soil wall coatings used as PCM, which reduces the maximum indoor temperature in non-air-conditioned areas in the summer months.

In their study, Gu et al. [37] developed a system that produces low-grade hot water for domestic hot water by recovering the heat produced by the air conditioning system and integrating PCM into the system. Their study reveals that the heat produced by the air conditioning system can also heat the environment.

In the study made by Farrell et al. [38] because PCMs are in direct contact with the metal pipes, plates, or bodies, the parameters affecting the thermal energy storage environment negatively were examined. They measured the corrosion rates for aluminum alloys and copper used in heat exchangers in the air conditioning sector by performing a metallographic examination following corrosion tests. Corrosion prevention methods for copper and aluminum in the use of such PCM are discussed.

Mondal [39] have made an examination on the working principle of PCMs with applications for smart temperature-regulating textiles. Recently, interest in research on the incorporation of PCMs into textiles by coating or encapsulation in order to make thermo-regulating smart textiles has grown. A large number of different phase-shifting materials have been introduced, and the issues related to the placement of PCM into the textile structure were summarized. Thermal comfort, clothing for a cold environment, phase-shifting materials, and the concept of clothing comfort were discussed in this review article. Some new applications related to PCM added textiles have been indicated. Finally, the PCM market in the textile field and some difficulties has been mentioned.

1.3   Basic Thermodynamics of PCM

PCM are materials that can store a high amount of thermal energy during phase separation at constant temperature. Sensible heat storage, which is much weaker than latent heat storage, has been used for the heating of living environments for centuries. However, the fact that high-temperature differences or large volumes are required in order to store the same amount of heat makes it more efficient to store thermal energy in the form of latent heat.

During the storage of heat energy, PCM first increases its temperature as it absorbs heat by acting like an ordinary heat storage material. But unlike other materials, when it reaches the phase change temperature, it absorbs much larger amounts of energy without displaying a significant temperature change. While the temperature around the material decreases, the material acts in the opposite direction, releasing the latent heat to the environment. Such materials can store much more heat per unit mass than other materials such as water, wood, stone [35].

The most important feature sought in phase-changing materials is that they have a high phase transformation temperature [40]. Heat flow temperature graph in Fig. 1 shows the latent heat stored in the phase change temperature range. Along the x-axis, PCM melting/solidification graph is given, depending on the temperature. They are found in solid, 'mush' (solid–mush and mush–liquid), and liquid form and are shown in Fig. 2.

1.4   Application of PCM in Industry

The fact that a material has a high latent heat enthalpy and a phase change temperature suitable for the system to be used is preferably the two most important elements for a PCM. However, the other properties that a material should have, other than these basic properties, are listed in the thermophysical, chemical, and economic subgroups in Table 1.
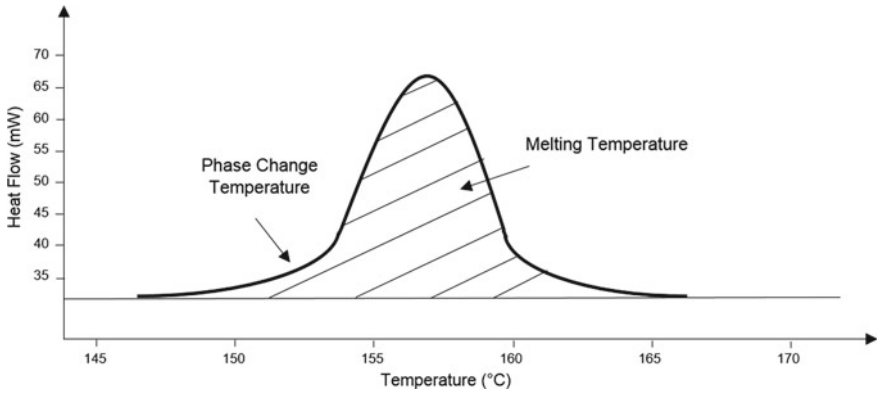
Fig. 1 PCM temperature heat flow distribution

Fig. 2 Geometric array of the macrocapsules **a** fan air outlet temperature, **b** global sensor (humidity, airspeed, temperature), **c** compressor sensor (temperature), **d** PCM internal temperature, **e** PCM surface temperature, and **f** cabin inner wall surface temperature
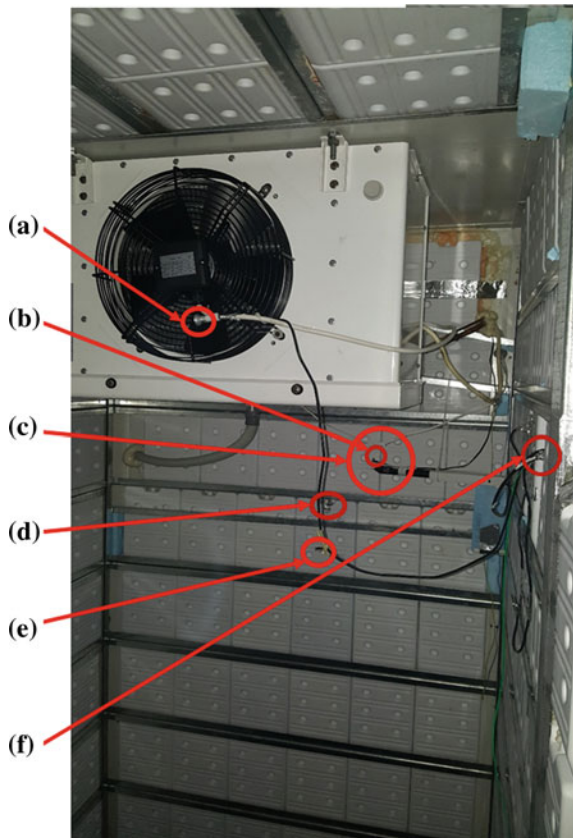
Table 1 Properties of PCMs [40]

Thermophysical properties
Phase change at desired temperature
High latent heat enthalpy per unit volume/mass
High sensible heat coefficient
High thermal conductivity
Low volume changes and vapor pressure during phase change
Regular phase change characteristic
Low melting and freezing temperature difference
Chemical properties
Reversible freezing and melting cycle
No chemical degradation after a high number of phase change cycles
Lack of corrosive effect of material
The material is not toxic, flammable, or explosive due to safety reasons
Economic features
Low price
Reuse of material for environmental and economic reasons
Easy to obtain material

In this study, it was aimed to reduce the working time of the compressor by working in combination with the mechanical cooling group of the latent heat storage system and thus extend the stop period. Thanks to PCM's latent heat storage capacity, (excess) energy consumption caused by mechanical cooling groups will be avoided.

In order to conduct the study experimentally, the cold storage room, in which latent heat energy system is integrated, was established in the Air Conditioning Laboratory of Balıkesir University. In the first stage, the cooling capacity of the room was determined and PCM, which will provide the energy required for the system, was dimensioned. During this dimensioning, it was ensured that the laboratory ambient temperature was stable so that the experiments could be carried out under the same conditions.

2 Experimental Approach: Material and Method Experimental Procedure

This study has been conducted actively working a cold store in which external walls of the room consist of polyurethane panel and extrude polystyrene foam and are 160 mm thick. For PCM integration, 310 macrocapsules have been produced and 70% of the inner surface of the storage room was covered (Fig. 2).

Furthermore, 85% of the total volume in the macrocapsules was filled with PCM due to the expansion of the fluid during solidification. Experiments were carried out in a laboratory with constant ambient temperature of 24/+26 °C. Melting/freezing temperature of PCM is −7.9/−14.7 °C, and it is an eutectic mixture used for commercial purposes. The thermophysical properties of the PCM are given in Table 2.

Table 2 Thermophysical properties of PCM

Properties, unit	Value
Melting/freezing temperature, °C	$-14.7/-7.9$
Dynamic viscosity, kg/m s (25 °C)	5.5×10^{-4}
Density, kg/m^3 (25 °C)	1040
Enthalpy, kJ/kg	274.3
Specific heat (kJ/kgK)	3.408
Heat transfer coefficient (W/mK)	0.547

The determined cabin storage temperature set value is $-16/-13$ °C, and the cooling load is 310 W. The scenario consists of 36-hour monitoring of the on–off periods of the compressor. The ambient temperature, relative humidity, airspeed, PCM temperature, and outdoor temperature have been recorded with 10-second intervals. Performing an uncertainty analysis in such experimental studies significantly affects the reliability of the experiment. One of the subjects that must be taken into consideration in the experiments is distinguishing the constant errors and random errors [41]. Constant errors are the same for each value read during the experiment and can be eliminated with a suitable calibration and correction [42]. Accordingly, all measurement errors were taken into consideration. The goal of this study is to decrease the operation time, thus extending the stop period of the compressor with the help of latent heat storage system.

2.1 Economical Assessment Procedure

Life cycle costing (LCC) method is widely used for economical assessment. Traditionally, it takes into account mainly investment, operation, maintenance, and end-of-life disposal costs. The aim of LCC analysis is to select the most economical approach. In order to determine LCC for a system, existing approaches are the net present value (NPV) and internal rate of return (IRR) or economic rate of return (ERR). In this study, NPV approach is used for the economical comparison of systems mentioned above. The cost of each option is converted into present value (PV) via this approach and the highest NPV is chosen as a preferred option among the alternatives. Equations of NPV value can be given as follows (Eq. 1) [43]:

$$NPV = PV(\text{Benefits}) - PV(\text{Costs}) \tag{1}$$

$$NPV = \sum_{n=k+1}^{t} \frac{B_n}{(1+i)^n} - \sum_{n=0}^{k} \frac{C_n}{(1+i)^n} \tag{2}$$

where B_n and C_n are benefit and cost values corresponding to systems' life span (n in years), respectively. (i) symbol represents the annual interest rate. Because there

is no cash inflow in process, benefit part of Eq. (2) is taken as zero. Thus, the cost term in Eq. (1) is taken into consideration. The main cost parameters are initial cost of the cold storage system including installation and electricity cost for operating. Repair and maintenance cost and the salvage value of both systems are not taken into consideration during the calculations because they were assumed as same costs. The considered systems' life span, (n), is assumed as 10 years. In this study, the annual interest rate is taken as 10%.

3 Case Study: Optimization of Best Temperature Range

On–off periods of the compressor working with and without PCM in reference to the last 6 h are presented in Table 3. As it is seen in Table 3, the storage room without PCM worked 30.09% more compared to the storage room with PCM. Additionally, it has been demonstrated that the stop time of the compressor has been 21.64% less in the room without PCM than the room with PCM. Such situation asserts the positive contribution of PCM. Figure 3 shows that the temperature set point of the cold storage without PCM and PCM in 6 h.

Table 3 Temperature set point of the cold storage without PCM and PCM is −16 °C, while the 36 h and last 6 h compressor on–off times

SET −16 °C	36 h			Last 6 h		
	Without PCM	With PCM	Difference (%)	Without PCM	With PCM	Difference (%)
On times (s)	51,920	44,820	−13.67	8740	6110	**−30.09**
Off times (s)	77,080	84,650	9.82	12,660	15,400	**21.64**

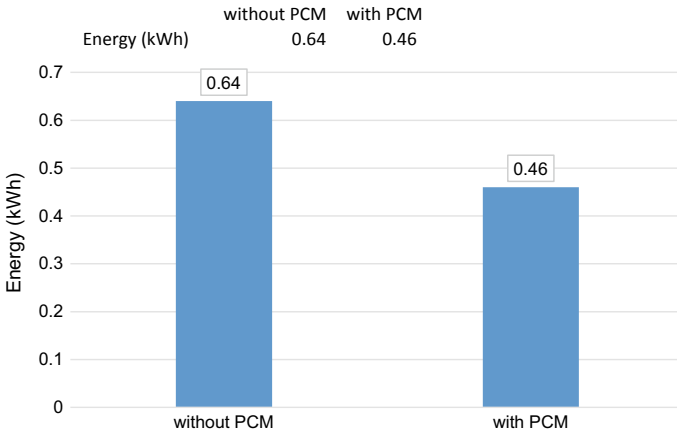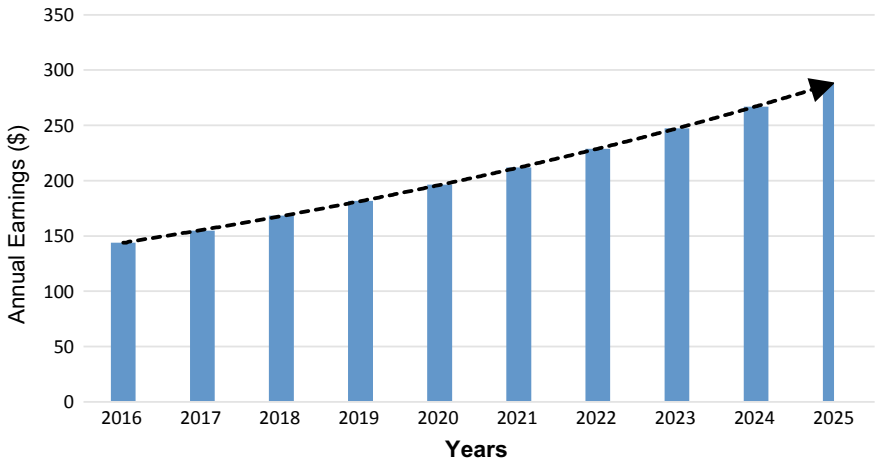**Fig. 3** Temperature set point of the cold storage without PCM and PCM in 6 h

	without PCM	with PCM
Energy (kWh)	0.64	0.46
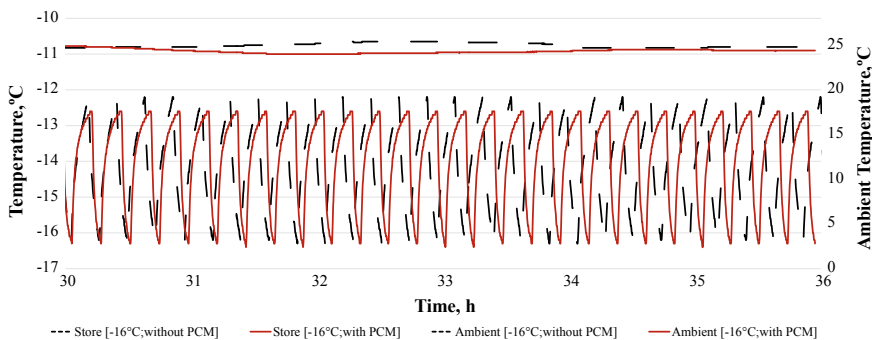
Fig. 4 Hourly consumed energy values

Years	2016	2017	2018	2019	2020	2021	2022	2023	2024	2025
Annual Earnings ($)	143.82	154.89	168.4	181.87	196.42	211.97	228.93	247.25	267.03	288.39

Fig. 5 Distribution of the energy savings by years

In this study, the total error in the temperature measurement has varied between 0.1 and ±0.756 °C in uncertainty error analysis. The calculated error analysis values are within the limits accepted for this study [43].

As of the year 2016, unit price of the PCM macrocapsules is $2.60, and the total cost of 310 pieces is $805.31. Hourly energy consumption values in the storage room with and without PCM in reference to the value of 6 hours are presented in Fig. 4.

It has been observed that the electric energy consumption of the room with PCM was 28.13% less than the condition without PCM at $-16\,^{\circ}\mathrm{C}$ (Fig. 4).

As it is seen in Fig. 5, distrubution of the energy savings within the cabin with PCM by years. It has been determined by using the NPV method that the payback period of the initial investment is 4 years and 9 months.

4 Conclusions

The use of PCMs in the cooling industry has generally been applied without a mechanical cooling group, as indicated in the literature. With this study, it has been presented that a mechanical cooling system and PCM can be used actively in conjunction. It has been seen that when the storage room set temperature value and the differential temperature range are selected correctly, PCM can significantly decrease the electric energy consumption. It has been revealed that PCM must operate at temperatures around the solid phase. In this context, on–off periods of a cold store with and without PCM were experimentally examined. The results indicated that off period time increased 21.64%, whereas working period time decreased 30.09%, significantly. PCM application provided a total energy efficiency increase of 28.13%. Furthermore, the decrease of the initial investment costs will take place upon the increase of PCM demands in business.

References

1. Li G, Hwang Y, Radermacher R (2012) Review of cold storage materials for air conditioning application. Int J Refrig 35(8):2053–2077
2. Abhat A (1983) Low temperature latent heat thermal energy storage: heat storage materials. Solar EnergyJ J 30:313–332
3. Zalba B, Marin JM, Cabeza LF, Mehling H (2003) Review on thermal energy storage with phase change: materials, heat transfer analysis and applications. Appl Therm Eng J 23(2):251–283
4. Farid M, Khudhair AM, Razack SAK, Al-Hallaj S (2004) A review on phase change energy storage: materials and applications. Energy Convers Manage J 45:1597–1615
5. Kilic GA (2018) Endüstriyel soğutma uygulamalarında ötektik soğutucuların etüdü ve parametrelerinin incelenmesi. Ph.D. Thesis, Balikesir University Institute of Science, Mechanical Engineering Department, Turkey, p 9
6. Dutil Y, Rousse DR, Salah NB, Lassue S, Zalewski L (2011) A review on phase-change materials: mathematical modeling and simulations. Renew Sustain Energy Rev J 15(1):112–130
7. Hawes DW (1991) Latent heat storage in concrete. Ph.D. Thesis, Concordia University, Montreal, Quebec, Canada
8. Chiu JNW, Martin V, Setterwall F (2010) A review of thermal energy storage systems with salt hydrate phase change materials for comfort cooling. KTH Department of Energy Technology, Brinellvägen 68, SE-100 44, Sweden
9. Kuznik F, Virgone J, Johannes K (2011) Insitute study of thermal comfort enhancement in a renovated building equipped with phase change material wallboard. Renew Energy 36(5):1458–1462

10. Sharif MKA, Sopian M, Rosli MAM, Sopian K, Sulaiman AMY, Al-abidi A (2014) Numerical study of PCM melting in evacuated solar collector storage system. Comput Appl Environ Sci Renew Energy, ISBN: 978-960-474-370-4

11. Costa M, Buddhi D, Oliva A (1996) Laboratori de Termotecnia I Energetica. Department de Maquines i Motors Termics, *ETSEIT*, E-08222, Terrassa, Barcelona, Spain

12. Amin NAM, Belusko M, Bruno F (2009) Optimisation of a phase change thermal storage system. World Academy of Science, Engineering and Technology

13. Sarı A, Karaipekli A (2007) Thermal conductivity and latent heat thermal energy storage characteristics of paraffin/expanded graphite composite as phase change material. Appl Therm Eng 27(8–9):1271–1277

14. Konuklu Y ve Paksoy HÖ (2011) Faz Değiştiren Maddeler ile Binalarda Enerji Verimliliği. X. Ulusal Tesisat Mühendisliği Kongresi, Nisan 2011, İzmir, 919–929

15. Patil ND, Raisoni GH, Karale SR (2012) Design and analysis of PCMs based thermal energy storage for active building cooling a review. Int J Eng Sci Technol (IJEST), ISSN, 4(6)

16. Anisur MR, Kibria MA, Mahfuz MH, Saidur R, Metselaar IHSC (2013) Analysis of a thermal energy storage system for air cooling–heating application through cylindrical tube. J Energy Convers Manag 76:732–737

17. Gin B, Farid MM, Bansal PK (2010) Effect of door opening and defrost cycle on a freezer with phase change panels. Energy Convers Manage 51:2698e2706. http://dx.doi.org/10.1016/j.enconman.2010.06.005

18. Yılmaz S, Paksoy HO (2012) Subcooling in phase change materials used for cooling. In: Proceeding of Innostock. 13th International Conference on Energy Storage, Lleida, Spain

19. Oro E, De Gracia A, Castell A, Farid MM, Cabeza LF (2012) Review on phase change materials (PCMs) for cold thermal energy storage applications. Appl Energy 99:513–533

20. Yılmaz S, Altunbas SE, Kardas G, Paksoy HO (2013) A new approach for testing corrosion behaviour of various metals in contact with phase change materials. In: Proceedings of 2nd International Conference on Sustainable Energy Storage, Dublin, Ireland

21. Gholap AK, Khan JA (2007) Design and multi-objective optimization of heat exchangers for refrigerators. Appl Energy 1226–1239

22. Wang F, Maidment G, Missenden J, Tozer R (2007) The novel use of phase change materials in refrigeration plant. Part 1: Experimental investigation. Appl Therm Eng 1–9

23. Klimes L, Charvat P, Ostry M (2012) Challenges in the computer modeling of phase change materials. Mater Technol 46(4):335–338, ISSN 1580-2949

24. Mehling H, Cabeza LF (2008) Heat and cold storage with PCM: an up to date introduction into basics and applications. Springer, Berlin, Germany, p 107

25. Mondieig D, Rajabalee F, Laprie A, Onk HAJ, Calvet T, Cuevas Diarte MA (2003) Transfus Apheres Sci 28:143–148

26. Ventola L, Cuevas Diarte MA, Calvet T, Angulo I, Vivanco M, Bernar M (2005) Molecular alloys as phase change materials for energy storage and thermal protection at temperatures from 70 to 85 °C. J Phys Chem Solids 1668–1674

27. Tyagi VV, Kaushik SC, Pandey AK, Tyagi SK (2011) Experimental study of supercooling and pH behaviour of a typical phase change material for thermal energy storage. Indian J Pure Appl Phys 49:117–125

28. He B (2004) High-capacity cool thermal energy storage for peak shaving a solution for energy challenges in the 21st century. Ph.D. Thesis, Department of Chemical Engineering and Technology Energy Processes KTH, Stockholm, Sweden

29. Kılıçaslan L, Koyun T (2013) İklimlendirme uygulamaları için soğuk depolama malzemelerinin araştırılması. 11. Ulusal Tesisat Mühendisliği Kongresi, İzmir, Turkey 763–777

30. Sönmez N, Fertelli A, Buyruk E (2009) Numerical investigation for solidification around various cylinder geometries. J Sc Ind Res 68:122–129

31. Cheralathan M, Velraj R, Renganarayanan S (2006) Heat transfer and parametric studies of an encapsulated phase change material based cool thermal energy storage system. J Zhejiang Univ Sci, A, ISSN, 1886–1895

32. Fertelli A, Buyruk E, Günhan G (2013) Bir soğuk depolama tankı içerisindeki silindir pozisy-onlarının buz oluşumuna etkisinin sayısal olarak incelenmesi. 11. Ulusal Tesisat Mühendisliği Kongresi, 169–176
33. Zalba B, Marin JM, Cabeza LF, Mehling H (2004) Freecooling of building with phase change materials. Int J Refrig 27(2004):839
34. Ryu HW, Hong SA, Shin BC, Kim SD (1991) Heat transfer characteristics of cool-thermal storage systems. Energy 16(4):727–737, Great Britain
35. Hasnain SM (1998) Review on sustainable thermal energy storage technologies, part II: cool thermal storage. Energy Conversations Manage J 39(11):1139–1153
36. Gowreesunker BL, Tassou SA (2013) Effectiveness of CFD simulation for the performance prediction of phase change building boards in the thermal environment control of indoor spaces. Build Environ 59:612–625
37. Gu Z, Liu H, Li Y (2004) Thermal energy recovery heat recovery system calculation and phase change material development. Appl Therm Eng 24:2511–2426
38. Farrell AJ, Norton B, Kennedy DM (2006) Corrosive effects of salt hydrate phase change materials used with aluminium and copper. J Mater Process Technol 175:198–205
39. Mondal S (2008) Phase change materials for smart textiles: an overview. Appl Therm Eng 28:1536–1550
40. Lane GA (1983) Solar energy latent heat material. Technology 2. CRC Pres Inc
41. Holman JP (1971) Experimental methods for engineers. McGraw-Hill, New York
42. Akpınar EK (2005) Deneysel çalışmalardaki hata analizine bir örnek: kurutma deneylerindeki hata analizi, Mühendis ve Makine J 46 (540)
43. Ozyogurtcu G, Mobedi M, Ozerdem B (2011) Economical assessment of different HVAC systems for an operating room: case study for different Turkish climate regions. Energy and Build J 43:1536–1543

Utilization of Alternative Building Materials for Sustainable Construction

Ahmet Vefa Orhon and Müjde Altin

Abstract The world population is growing at unprecedented rates and it is expected to reach 9.8 billion in 2050. Today, non-sustainable exploitation of non-renewable resources of the Earth due to the high demand of conventional building materials is already an important environmental issue, and for sure, this concern will become of vital importance in the future with rapidly growing world population. Utilization of alternative building materials in construction is a good way to effectively address this concern. Alternative building materials (ABMs) are low-cost building materials that aim to reduce or eliminate the environmental impact of the construction, simply by saving energy and resources, minimizing the emissions through the use of rapidly renewable materials, local resources, recycled content, industrial/agricultural byproducts/wastes, etc. This chapter aims to present prevailing ABMs for sustainable construction, such as bamboo, rammed earth, strawbale, supplementary cementitious materials, cork, mycelium, HempCrete, Ferrock, Papercrete, etc. Current strategies for ABMs are discussed with emphasis on sustainability concerns. Benefits of these materials and ten remarkable case studies benefiting from the use of ABMs such as 3D Printed Gaia House, Jill Strawbale House, The Higo, Hy-Fi Tower, The Acre, The EcoARK, etc. are also discussed.

Keywords Alternative building materials · Non-conventional building materials · Sustainable architecture · Recycled material

1 Introduction

The world population is growing at unprecedented rates, as of 2017 approximately 83 million people per year. According to the population projections made by the United Nations, the world population is expected to reach 9.8 billion in 2050 [1]. In today's increasingly crowded world, fast depletion of non-renewable resources

A. V. Orhon (✉) · M. Altin
Department of Architecture, Dokuz Eylul University, Izmir, Turkey
e-mail: vefa.orhon@deu.edu.tr

M. Altin
e-mail: mujde.altin@deu.edu.tr

of the earth due to the high demand of building materials is already an important environmental issue, and for sure, this concern will become of vital importance in the future with this growth of population. Worse than this, although housing is one of the primary human needs, many cities in the world are already falling short in adequate housing supply. Today, an estimated 1.6 billion people live in inadequate housing globally. By 2025, it is likely that another 1.6 billion will require adequate, affordable housing [2]. In the future, the demand for building materials will exponentially rise with the increasing need for construction and improving living standards. And, humankind is already damaging the environment far much faster than it can recover. In short, the utilization of more sustainable and affordable building materials in construction is an inevitable necessity in order to successfully deal with the current and future environmental, economic and social problems engendered by overpopulation. That's the reason why alternative building materials have started to become a focus in the world of construction.

2   Alternative Building Materials (ABMs)

The buildings and the building construction sector combined are responsible for 36% of global energy consumption and nearly 40% of total direct and indirect CO_2 emissions [3]. In this energy consumption and CO_2 emissions, building materials play an important role. The manufacturing processes and transportation of "conventional building materials" (such as bricks, cement, aggregates, steel, aluminium, wood, plastic, etc.) require a considerable amount of energy, contribute greenhouse gases into the atmosphere, deplete natural resources, release noxious pollutants to the land, air, and water, etc. Aforementioned "rapid urbanization coupled with overpopulation" issue also aggravates the environmental problems by forcing non-sustainable exploitation of conventional building materials.

On the other hand, alternative building materials (ABMs) are low-cost building materials that aim to reduce or eliminate the environmental impact of the construction, simply by providing a host of environmental benefits, such as increased energy efficiency, greater durability, utilization of recycled material, etc. In the architectural literature, the terms "non-conventional building materials", "low-impact building materials", "green building materials", "eco-friendly building materials" are also used interchangeably for ABMs depending on the context. ABMs are environmentally responsible materials as they help in reducing environmental impact. ABMs can augment the sustainability of the construction by:

- saving energy and resources (energy-efficient, resource-efficient etc.)
- reducing the embodied energy of the construction
- minimizing greenhouse gases emission into the atmosphere (carbon-neutral, carbon-negative, etc.)
- using rapidly renewable resources with low emission potential
- having recycled content

– using industrial and agricultural byproducts and wastes
– using local resources
– reducing costs of materials (low-cost, no-cost, affordable, etc.)
– having significant operational savings
– enhancing indoor air quality (moister-regulating, breathable, etc.)
– having preferred material properties (durable, biodegradable, etc.)
– etc.

Some of these features need highlighting. For example, a building material having recycled content provides considerable preservation of raw material while reducing the embodied energy of the construction. It also minimizes/eliminates waste disposal. With the implementation of novel recycling strategies, even no-impact upcycling with renewable energy is possible. For example, Trashpresso is the world's first off-grid, industrial-grade mobile recycling plant that produces upcycled architectural tiles from waste plastic with a minimized impact on the environment (Fig. 1). Solar panels provide renewable energy for the plant. The water, used to filter the residue off the plastic, is cycled back into the process to almost eliminate the need for water input. Solid, upcycled hexagonal tiles can be used in various applications, such as interior or exterior decoration finishes. The plant can recycle any thermoplastic that has a melting point lower than its burning point, such as polyethylene terephthalate (PET) and polypropylene (PP). It takes five water bottles or fifty bottle caps to produce one tile [4].

Many ABMs utilize natural raw materials obtained from rapidly renewable resources such as bamboo, hemp, straw, linseed, rye stalk, rice husk, sunflower stalk, cork, etc. U.S. Green Building Council (USGBC) defines "rapidly renewable" as a building material or product made from agricultural products that are typically harvested within a 10-year or shorter cycle. Since these natural raw materials generally require less "extraction", processing and transportation energy, they reduce the embodied energy of the construction. In general, locally produced bio-based building materials carry less embodied energy than fossil fuel and mineral-based building materials [5]. Some of the plant-sourced bio-based raw materials used in ABMs are

Fig. 1 Trashpresso [4], **a** Trashpresso mobile, plastic recycling plant, **b** upcycled architectural tiles from waste plastic using Trashpresso

Fig. 2 Some of the plant-sourced natural raw materials used in ABMs. **a** Banana fiber, **b** hemp fiber, **c** coconut fiber, **d** straw, **e** rice husk, **f** sugarcane bagasse

seen in Fig. 2; all these materials are waste products obtained from the production and processing of agricultural products.

Bio-based ABMs are also derived from animal sources. For example, sheep wool is used as an animal-based renewable bio-insulation material with self-extinguishing capacity. Sheep wool insulation also demonstrates high moisture buffering capacity and low thermal conductivity [6]. As seen in the use of sheep wool as a renewable low-impact insulation material, apart from reducing environmental impacts, ABMs can also enhance the efficiency with their material properties.

ABMs can be loosely classified into two groups as (1) natural or (2) man-made. Materials such as bamboo, straw, cork, rammed earth, etc. are natural ABMs and have been used for centuries. On the other hand, hand-made ABMs such as HempCrete, Mycelium, Ferrock, Ashcrete, Timbercrete, Papercrete, Engineered Bamboo, etc. are fairly new; these materials are usually produced from renewable materials, industrial and agricultural wastes. Some of the prevailing ABMs are outlined as follows.

2.1 Bamboo

As a plant, bamboo is a treelike woody grass widely distributed in tropical, subtropical and mild temperate zones. Bamboos include some of the fastest-growing plants on the Earth with reported growth rates up to 89 cm within 24 h. Since it grows quickly, bamboo can be harvested annually without depletion and deterioration of the soil. Although it is a very light material, bamboo is generally stronger than steel in tension, and more resistant than conventional concrete in compression [7]. In short, bamboo is a renewable and extremely versatile natural resource with multi-purpose usage—used

for construction, crafts, pulp, paper, panels, boards, veneer, flooring, roofing, fabrics, biomass, and even food (bamboo shoot). While the Earth's forests are experiencing increasing pressure due to overpopulation, bamboo is the most important non-wood forest product and wood substitute in the world.

Since bamboo is a natural composite material with a high strength-to-weight ratio, it can be effectively used in construction. Bamboo is one of the oldest traditional building materials used by mankind. It has a long and well-established tradition as a building material throughout the bamboo-growing regions of the world such as India, China, Peru, Colombia, Ghana, etc. In these regions, bamboo houses are still known to be cheaper than wooden houses, light, strong and earthquake resistant, unlike brick or cement construction alternatives. In 2005, it was estimated that over one billion people worldwide were living in traditional bamboo houses [8].

Nowadays, while bamboo is becoming popular as an excellent substitute for wood, it is widely used in construction, either in its natural form or as a reconstituted material (laminated bamboo boards, composite bamboo panels, etc.) in form of engineered bamboo. There is a growing worldwide interest in the development of engineered bamboo products as a sustainable, cost-effective and ecologic alternative construction material. Engineered bamboo may well replace wood, steel, and concrete in many uses. [8]. Variety and creativity of the use of engineered bamboo can be seen in recent building designs. The Terminal of the Veterans Airport of Southern Illinois (Illinois, U.S.A., 2017, Reynolds, Smith & Hills) is a recent example of the use of engineered bamboo for structural systems. The central atrium of the building has a domed roof structure with hybrid steel and glulam bamboo cross bracing (Fig. 3). The structural bamboo beams are visible in the ceiling within the terminal [9].

A well-known example of the use of engineered bamboo for cladding is the Terminal T4 of Madrid Barajas Airport (Madrid, Spain, 2006, Richard Rogers & Estudio Lamela) (Fig. 4). In the passenger areas of the terminal, there are thousands of square meters of ceiling made of laminated Chinese bamboo planks that have a width of 10 cm with the joints of 5 cm that vary with the geometry. The bamboo planks were treated against fire [10].

Fig. 3 Use of engineered bamboo for the structural system in the Terminal of the Veterans Airport of Southern Illinois [9]

Fig. 4 Use of engineered bamboo for cladding in the Terminal T4 of Madrid Barajas Airport [11]

2.2 Rammed Earth

Earth is the most important natural building material since it is available in most regions of the world. Even today, one-third of the world population resides in earthen houses [12]. When earth is compacted within a formwork to be used in the construction of durable walls, it is called rammed earth. Rammed earth, which consists of natural raw materials such as earth, chalk, lime, clay, sand, gravel, or other aggregate (such as seashells) [13], is filled into formwork in layers of up to 10 cm and thoroughly compacted to a thickness of 6–7 cm with a ramming tool. The rammed earth can be considered as man-made sedimentary rock. Rather than being compressed for many years under deep soil, it is formed by mechanically compressing a proper earth mixture into a hard sandstone-like material.

This ancient building technique has been revived and modernized recently as a sustainable building material to demonstrate the value of earth. Modern rammed earth applications usually include cement stabilized rammed earth (CSRE), which is formed by stabilizing earth with cement and ramming at optimum moisture content [14]. Since earth is the most prevalent building material in most regions of the world, especially in developing countries, use of rammed earth in construction is a viable way to meet the requirements for shelter only by using local building materials and relying on do-it-yourself construction techniques.

2.3 Straw Bale

Straw bale construction is a sustainable, bio-based building method that uses bales of straw, which is a byproduct of cereal farming including wheat, rice, barley, oats, and rye. Straw bales are made of dried, hollow stalks of these cereal grains which has been compacted, cut and bound in a baling machine. Even though the use of straw bales in construction dates back to the invention of the baling machine at the end of the nineteenth century, straw has been used in construction for millennia. For example,

the use of straw as a fibrous material in lime/mud/clay mortars and adobe is an old traditional construction practice worldwide to improve the mechanical properties of the base material.

Straw bale offers good thermal insulation properties; the thermal conductivity of 60 kg m^3 dense straw bale is 0.067 W/(m k) [15]. Straw bales may be used in construction as infill insulation for timber frame buildings with either an external render or timber rainscreen finish [16]. Infill (non-load-bearing) straw bale walls, which are mainly used for external infill above the damp-proof course level, can be constructed either on site or as pre-fabricated panels delivered to site already enclosed in a protective outer finish, such as lime render. Straw bales may also be used in low to modest loadbearing wall applications [16]. Straw bale construction needs careful detailing to avoid the water ingress and retention of moisture.

In recent years, contemporary use of straw bales in construction—as a vapour-permeable, insulated wall construction using locally sourced, low-impact material—has increased significantly. Examples of straw bale buildings dating from the last twenty years can be seen around the world, particularly in U.S.A, Canada, Europe, Japan, and China.

2.4 Supplementary Cementitious Materials

Concrete is the most widely manufactured material in the world—with nearly three tonnes produced each year for each of the earth's inhabitants. The key component of concrete is the cement whose production is an energy and carbon-intensive process. Each tonne of Portland cement produced emits about one tonne of CO_2 to the atmosphere and requires 60–130 kg of fuel oil and 110 kWh of electricity [17]. Due to the large ecological footprint of cement, partially replacing cement in concrete with supplementary materials is an effective way to reduce concrete's environmental footprint. These cementing materials used in concrete in addition to cement are called "supplementary cementitious materials" (SCMs). Most of SCMs are byproducts; thus, their inclusion in concrete provides an important contribution to the "green concrete" through reduced energy consumption and avoidance of cement process emissions. Additional benefits include minimization of waste disposal (landfilling these industrial byproducts), lessened pressure on natural resources and improved concrete properties and durability. Considering these benefits, byproduct SCMs accepted to be alternative building materials. These SCMs include:

(1) Fly ash—a byproduct of burning finely ground coal in thermal power stations.
(2) Ground granulated blast-furnace slag—a byproduct of iron smelting from iron ore.
(3) Silica fume (microsilica)—a byproduct from the production of elemental silicon or ferro-silicon alloys.
(4) Rice husk ash—the residue of combustion of rice husk which is an agricultural waste from rice milling.

Fig. 5 LEED-certified green buildings that include the partial replacement of cement with SCM. **a** The Bank of America Tower—45% blast-furnace slag, **b** The Helena—45% blast-furnace slag, **c** San Francisco Federal Building—50% blast-furnace slag

As a green approach to use of concrete, the partial replacement of cement with SCM has been used in some of the certified green buildings (Fig. 5) such as LEED platinum-certified the Bank of America Tower (New York, U.S.A., 2009, Cook+Fox Architects), LEED gold-certified the Helena (New York, U.S.A., 2005, Fox & Fowle Architects) and LEED silver certified the San Francisco Federal Building (California, U.S.A., 2007, Morphosis). The Bank of America Tower and the Helena buildings were both constructed using a concrete manufactured with 55% cement and 45% blast-furnace slag [18]. The concrete structure of the San Francisco Federal Building was constructed by replacing 50% of cement with blast-furnace slag, preventing approximately 5000 tonnes of CO_2 from being released into the atmosphere [19].

2.5 Mycelium

Mycelium is the thread-like roots of fungi. As it consists of thin, strong fibers running without specific direction, dried mycelium forms a strong and lightweight material that is not only mold and moisture resistant, but also fire resistant and both VOC and aldehyde neutral. The strong, resilient web-like structure of mycelium can grow on any given shape. In recent years, several methods have been developed to use mycelium in the art, design and building applications. Mycelium-based products— such as chipboards wherein glue is replaced by mycelium, insulation or packaging mycelium foam, do-it-yourself kits to grow mycelium etc.—are on the market since 2007 [20]. Mycelium, which is an entirely natural, fast renewable resource, can be used as a natural alternative to wood, lightweight concrete, cork, and plastics.

2.6 Cordwood

Cordwood is an old masonry technique which can be used as wall-filling as well as a structural load-bearing element. The masonry units for cordwood are called log-ends. Debarked log-ends, which are cut to the same length as the width of the wall to be built, are piled crosswire to build a wall, using mortar or cob to permanently secure them [21]. Classic cordwood masonry walls have three material components: the log-ends, the mortar matrix and the insulated cavity within the mortar. Cob is considered as a viable alternative for mortar matrix instead of Portland cement. This type of cordwood masonry is usually known as "cobwood". Cobwood's constituent ingredients are clay (about 20% by volume) sand and chopped straw as reinforcing binder [22].

2.7 Papercrete

Papercrete is a lightweight concrete which consists of re-pulped paper (cellulose fiber) with Portland cement or clay. It is perceived as an environmentally friendly material due to recycled content. Papercrete has much lower thermal conductivity than concrete; therefore, its insulation value is much higher. Thermal conductivity of papercrete is about 0.15 W/(m K) [23]. It is also mold-resistant and has utility as a sound-proofing material. Papercrete walls are typically 25–30 cm thick. A patented papercrete block product—in size of 440 mm $\times$ 215 mm $\times$ 100 mm—is on the European market since 2017. This block, which is a zero-carbon product with a reduction of -174 CO_2 per m^2 wall, uses a third of the energy used in a traditional aerated block. The amount of cellulose fiber within the mixture ranges between 55 and 79% [23].

2.8 Cork

As a rapidly renewable material, cork is harvested from the bark of the cork oak tree (Quercus suber) which grows mainly in the Mediterranean region. The bark has a vegetal tissue with a unique honeycomb structure composed of tiny cells, containing cellulose and suberin. When exposed to high temperature, this tissue expands and suberin—which is a natural adhesive—binds the expanding grains. Expanded/agglomerated cork insulation sheets are produced in this way without the addition of any binder. Waste cork scraps and used wine corks can also be recycled into a range of building materials such as cork boards, cork insulation sheets, flooring, etc. [24].

About 89% of cork tissue consists of gaseous matter sealed in tiny, impermeable cell compartments. Due to this reason, cork is (1) lightweight (2) high flexible (3)

Fig. 6 Use of cork for external cladding. Logowines Winery (Evora, Portugal, 2009, PMC Arquitectos) [26]

highly durable (4) resistant to abrasion (5) impermeable to both liquids and gases (6) natural fire retardant (7) non-toxic during combustion (7) hypoallergenic (8) anti-microbial (9) resistant to insects, mites and mold (10) biodegradable. It has a low conductivity of heat, sound, and vibration. This makes cork offer a perfect vibro-isolation, thermal insulation, and acoustic isolation. Cork is the only ABM traveled to another planet; it was used for thermal insulation in the Viking space probes which landed on Mars in 1976.

Due to its high durability, cork is also used for flooring material which can last well over 50 years. There is also a growing interest in cork as an external cladding material for buildings due to its desirable aesthetic qualities, giving buildings natural patterns with mottled earthy tones (Fig. 6) [25].

2.9 Hempcrete

Hempcrete is a bio-composite building material used for construction and insulation. It consists of hemp hurds and lime binder. Therefore, it is also called as Hemp-lime [27]. The hemp stalk is composed of about 50% carbon by dry weight. Hempcrete is a carbon-negative building material because CO_2 absorbed in the growing process of the hemp is more than the CO_2 produced in the manufacture of the binder. A large portion of the CO_2 emitted in the manufacture of lime (calcium hydrate) is also reabsorbed as it cures and reverts to limestone (calcium carbonate). The carbon footprint of the material is estimated to be -100 kg/m^3 [28]. A hempcrete wall of
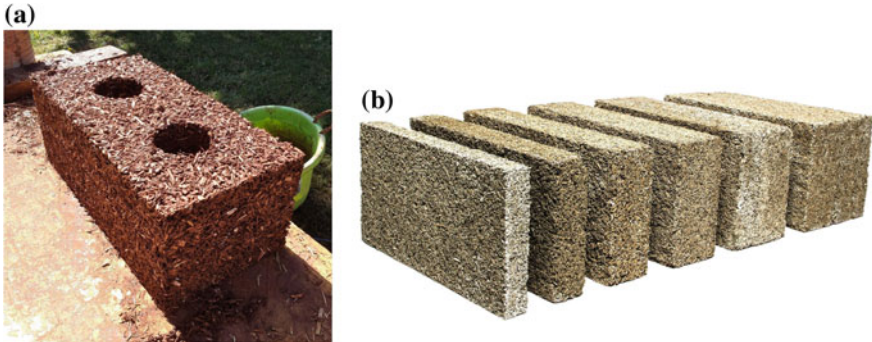
Fig. 7 Hemp blocks, **a** traditionally made hemp-clay block, **b** fabricated hemp-concrete (Hempcrete) blocks [30]

30 cm thickness locks up around 40 kg CO_2 per m^2 wall [29]. Hemp blocks can also be made with clay as seen in Fig. 7.

2.10 Coconut Fiber

Coconut fiber (or Coir) is a natural fiber extracted from the husk of coconut. It is abundantly available as cheap residue from coconut production in tropical regions. Coconut fibers are typically 10–30 cm long with high lignin content. At elevated temperatures and under pressure, lignin acts as a natural glue for the fibers, forming a strong and stable resin-like adhesive. High lignin content helps the raw material to bind into a hardboard without the addition of any binder (filler, resin, glue, etc.). This method is used to produce medium/high-density, binderless, 100% coconut fiber hardboards. These biodegradable boards have natural anti-fungal properties and burn three times slower than wood. They also exhibit excellent properties, which are comparable with or even superior to commercial wood-based panels [31]. Due to their strength, these boards also have the potential to be used for structural elements.

Coconut fiber is also used for acoustic and thermal insulation boards. Insulation made of coconut fibers is permeable and moisture-regulating. Coconut fiber is relatively waterproof and is one of the few natural fibers resistant to damage by saltwater. The material also provides great acoustic damping and has a leveling effect. Coconut fiber has great potential as an ABM to produce environmentally safe and high-performance construction materials.

2.11 Ferrock

Ferrock is an iron-based compound made of 95% recycled materials to be used as an eco-friendly substitute for ordinary Portland cement (OPC) [32]. The main ingredient of ferrock is steel dust, which is a byproduct of steel manufacturing, and silica from recycled glass. Fly ash can also be used instead of silica. During the production process, the iron within the steel dust reacts with CO_2 and rusts to form iron carbonate. That means any carbon produced during production can easily be offset by the amount of airborne carbon used up to produce the final product, making ferrock a carbon-negative alternative to OPC.

3 Architectural Case Studies Benefiting from the Use of ABMs

3.1 3D Printed Gaia House (Massa Lombardo, Italy, 2018)

The Gaia House is a 3D-printed, sustainable building made with ABMs (Fig. 8). Outer walls of this 30-m² house were 3D-printed on-site using a natural mud mixture made from local clay soil, as well as agricultural waste materials such as chopped straw and rice husks. This ABM based, biodegradable printing mixture was layered using

Fig. 8 3D printed the Gaia House [33]

Fig. 9 Construction of the Gaia House [33], **a** 3-D printing of the outer walls with ABM based mixture, **b** vertical cavities of the 3D-printed wall are filled with rice husk for insulation

a crane WASP 3D-printer, creating walls with vertical cavities inside, which are then filled with rice husk for insulation (Fig. 9) [33].

3.2 Bamboo Sports Hall Panyaden International School (Chiang Mai, Thailand, 2017, Markus Roselieb and Tosapon Sittiwong)

Sports Hall of Panyaden International School is a zero-carbon sports building, constructed using only bamboo to maintain the "Green School" mission of Panyaden (Fig. 10). 300-capacity sports and assembly hall, covering an area of 782 m^2, hosts futsal, basketball, volleyball and badminton courts, as well as a liftable stage for

Fig. 10 Bamboo Sports Hall of Panyaden International School [35]

Fig. 11 Bamboo Truss Structure of Sports Hall of Panyaden International School [35]

shows. Balconies on both long sides of the hall provide space for spectators to observe sporting events or shows [34].

The structure of the hall consists of 10 bamboo trusses with a span of over 17 meters without steel reinforcements or connections (Fig. 11). The trusses, which were prebuilt on site, lifted into position with a crane. The finished bamboo structure is left exposed throughout the interior, creating arched openings around the edge of the hall. The sustainable design strategy of the building aims to enable a cool and pleasant climate all year round through open, natural ventilation and roof insulation while exposing the aesthetic value of masterly handcrafted "green" bamboo structure. The building was designed to safely withstand the local high-speed winds, earthquakes and all other natural forces. Since the bamboos used for construction absorbed carbon to a much higher extent than the carbon emitted during treatment, transport, and construction, carbon footprint of the building is zero. No toxic chemicals were involved in the treatment process of the bamboos. The life span of the structure is expected to be at least 50 years [35].

3.3 Nk'Mip Desert Cultural Centre (Osoyoos, Canada, 2006, Dialog Design)

Nk'Mip Desert Cultural Centre is an interpretive center in Osoyoos, British Columbia. It is owned and operated by the Osoyoos Indian Band. It is situated on the edge of the Great American Desert. The climate of the region is extreme. Hot, dry summers and cool, dry winters see average temperatures ranging from −18 to +33 degrees, and often reaching +40 on summer days. The sustainable design of the building includes the largest rammed earth wall in North America [36]. This rammed earth wall, which is 80 m long, 5.5 m high, and 0.6 m thick, was constructed of local soils, concrete, and colour additives (Fig. 12).

Fig. 12 Rammed Earth Walls of Nk'Mip Desert Cultural Centre [36]

3.4 Jill Strawbale House (Strontian, Scotland, 2018)

Jill Strawbale House is an energy-efficient, cruck-frame strawbale house located in the Scottish Highland village of Strontian (Fig. 13). The house has two bedrooms, two bathrooms, a large living area, and kitchen space. The owners built the house using local materials (mainly wood, straw, lime mortar and British clay tiles), doing most of the construction work themselves with the help of their family members and local friends. The project is aimed to be twin houses; the second house named "Jack" is planned to be built later with the same design. The self-build design of the house was largely based on the original concept for this type of cruck-frame strawbale house developed by Brian Waite [37].

Timber framing of the building consists of fourteen large (main structure) and four small (for the porch) crucks. About 500 bales of straw are inserted between the crucks for insulation (Fig. 14). Bales insulate walls and roof in one sweep, rising seamlessly right up to the ridge. The thickness of strawbale insulation is 30 cm. Both, the inside and outside of the finished structure are covered with lime allowing the moisture in the air to move from inside to outside. Roofing material is British clay tiles. In order to keep the bales dry, moisture is absorbed in the inside, passes through the straw and then taken away on the outside. There are two key components of this system to remove the moisture on the outside. The first component is a ventilation gap above the guttering and behind the bottom tile of the roof. This gap is protected from animals and bugs with a stainless-steel mesh. The second component is the ventilated roof ridge. This system simply let the air pass through between the outside of the lime and the underside of the roof [37].
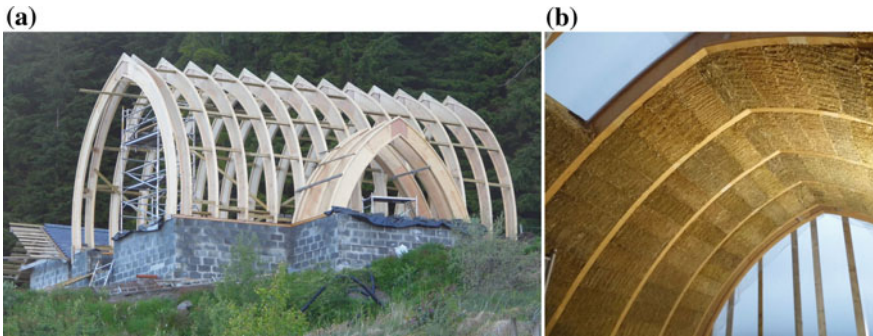
Fig. 13 Jill Strawbale House [38]

Fig. 14 Construction of Jill Strawbale House [38], **a** cruck-frame of the building, **b** strawbale insulation between crucks

3.5 Hy-Fi Tower (New York, U.S.A, 2014, the Living)

Hy-Fi tower was a concept structure displayed in the courtyard of the Museum of Modern Arts (MoMa) in New York in 2014 (Fig. 15). The structure was about 12 m high and consisted of 10,000 organically grown mycelium bricks [39]. The project demonstrated the architectural potential of biological technology with a nearly zero-carbon footprint.

Fig. 15 Hy-Fi Tower made of mycelium bricks [39]

The mycelium bricks are constructed entirely from fungus mycelium which grew from agricultural waste such as sawdust, cardboard, woodchip waste, rice, wheat husks, etc. To make the bricks, molds are filled with organic matter infused with spores. It takes five days for the funguses to transform the organic matter into a brick. Moisture and certain sanitary requirements are needed so that the final product is not infected by bacteria during the process. Finally, mycelium should be dried by hot air to kill the growth process while maintaining cell cohesion. Mycelium brick weighs 43 kg/m^3 with a compressive strength of 0.2 MPa [40]. The bricks can be used both as an insulator and as support for interior walls within the building.

3.6 The HIGO (Sapporo, Japan, 2014, NA Nakayama Architects)

The HIGO is a three-story, steel structure office building in Japan (Fig. 16). The main concept of the project was to use structural materials as thin as a bamboo toothpick, designing with "slim", "thin" and "small" keywords in mind. The steel structure was constructed with 60 mm × 60 mm, 50 mm × 50 mm, and 38 mm × 38 mm

Fig. 16 The HIGO. Use of expanded cork cladding in building skin [41]

steel beams, 60 mm × 128 mm I-beams, 28 mm × 125 mm flat bars, 40 mm × 75 mm channel steel, 4.5 mm steel plates, and 1.2 mm keystone plates [41]. Since the building takes part in a high seismic activity area, lightness of the building skin was essential to be built with steel parts made as slim as possible. With this goal in mind, the feature of the building was the use of 5 cm × 50 cm × 100 cm cork blocks recycled from used wine cork. The 5 cm thick cork blocks, which weigh only 7.5 kg/m^2, were used for external wall and as floor substrate.

3.7   The Acre (Oxford, U.K., 2017, John Pardey Architects)

The Acre at Cumnor Hill (Oxford) is a cluster of five large detached houses (Fig. 17) built with HempCell, a pre-fabricated panel system that uses hemp-lime and natural fiber insulation. Each house in the site has 4–6 bedrooms and a variety of living space provisions in two floors. On the façades, HempCell panel walls of the Acre houses are covered with textured chalky brickwork, larch timber cladding and red-brown pre-patinated zinc cladding [42].

HempCell system used in the Acre is a new panel wall system developed as part of the EU funded Hempsect project (Fig. 18). Hempsect project completed in 2017 was aimed at expanding the market for a bio-based, pre-fabricated, pre-dried, panelized system of hemp-lime construction which significantly reduces both embodied carbon and in-use energy consumption. The core materials of the panel are hemp-lime and natural fiber such as wood fiber or hemp fiber. While hemp-lime exhibits excellent hygric and moderate thermal resistance properties, both hemp and wood fiber exhibit excellent hygric capacity and good thermal resistance property. As a result, HempCell is expected to exhibit much better thermal performance than in situ cast hemp-lime systems [5].

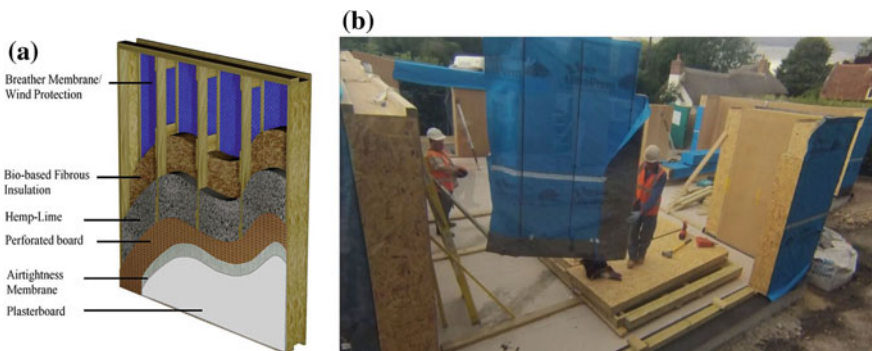**Fig. 17** One of the five house houses in the Acre at Cumnor Hill [42]

Fig. 18 HempCell: a pre-fabricated, pre-dried, panelised system of hemp-lime construction [5]

3.8 Centre for Alternative Technology (Machynlleth, U.K., 2010, Pat Borer & David Lea)

Centre for Alternative Technology (CAT) building of Wales Institute of Sustainable Education (WISE) (Fig. 19) is constructed of materials with low embodied energy such as hempcrete, rammed earth, slate, cellulose, cork, home-grown timber [43].

50 cm thick external walls of the building are of hempcrete, which is cast around the frame to create an insulated, airtight and breathable construction, giving a U-value of 0.14 W/m^2 K. Lime binder of hempcrete used in the building is based on high purity air lime blended with 15% cement. Binder was mixed dry with the hemp fiber. Then, water was added as the material was sprayed into formwork erected round

Fig. 19 Centre for Alternative Technology (CAT) building [43]

the timber frame—similar to the process of casting concrete. The roof was insulated with 45 cm thick Cellulose (recycled paper) achieving a *U*-value of 0.09 W/m² K. 25 cm thick cork was used under timber decking, giving a *U*-value of 0.14 W/m² K [43].

3.9 The EcoARK (Taipei, Taiwan, 2010, Arthur Huang)

The EcoARK in Taipei is a pavilion building built as the principle structure for an international exposition (Fig. 20). The building serves as a public museum now. The main green feature of the building is the building skin fully made of recycled plastic material [44]. The façades and walls of the building are covered with "Polli-Bricks", a hollow, translucent building block made of recycled polyethylene terephthalate (PET). These non-load-bearing bricks were manufactured from PET bottles melted down into PET pellets, moulding into a new bottle shape. The blow-moulded polli-bricks feature interlocking grooves that fit tightly together like building block toys,

(a) (b)
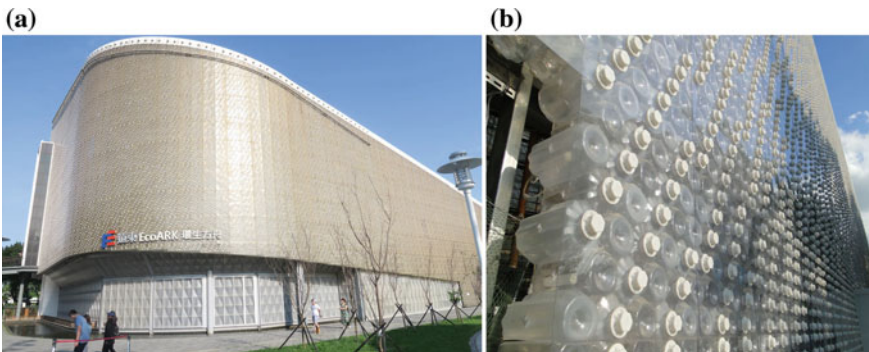
Fig. 20 The EcoARK [44]

Fig. 21 Jackie Chan Stuntman Training Center [45]

being glued with a small amount of silicone sealant between them. Once assembled into flat rectangular panels, polli-bricks are coated with a fire and water-resistant transparent plastic film. The curvy transparent façade of the building is made of these modular panels screwed and mounted onto a structural steel frame.

3.10 Jackie Chan Stuntman Training Center (Tianjin, China, 2017)

Jackie Chan Stuntman Training Center (Fig. 21) is a mega-restoration project based on "recycle and reuse" principal. The half-built, left to decay existing structures—a movie complex, stadium-sized event space, and a shopping mall—have been brought back to life using upcycled materials varying from DVDs for the outer-façade, tires for the flooring, and polyethylene plastic bags for the artificial turf. Intending to limit the use of additional materials and paints, the façade of the building uses no paint. The three-dimensional effect of the façade is achieved by fins made from recycled DVDs that are screwed into a steel backing reclaimed from the original structure. The outdoor structures made from upcycled materials are complemented with interior finishes like lighting fixtures, shelving systems, and furniture also made from trash [45].

4 Conclusions

The main conclusion drawn from all reviewed building materials and discussed case studies is that ABMs are environmentally responsible materials as they help in reducing environmental impact. They reduce or even eliminate the environmental impact

of the construction, simply by saving energy and resources, minimizing the emissions through the use of rapidly renewable materials, local resources, recycled content, industrial/agricultural byproducts/wastes, etc. This makes their environmental impact far less than conventional building materials. In many cases, ABMs also cost less than their conventional alternatives.

Due to the aforementioned environmental, social and economic concerns, there is a growing worldwide interest in the utilization of alternative building materials. The discussed case studies demonstrate that ABMs can effectively replace conventional building materials in many uses as sustainable, cost-effective and ecologic alternatives. As seen in 3D Printed Gaia House, digital technologies such as additive manufacturing may also benefit from the use of ABMs. Use of Mycelium in Hy-Fi Tower proves that there are remarkable biologic alternatives to our current ways of construction such as "growing construction materials". Sports Hall of Panyaden International School, which utilizes bamboo as a structural material, and the HIGO building, which benefits from cork cladding on façades to lighten the building weight without compromising the façade, also demonstrate the functional benefits of rapidly renewable building materials.

Each year, the global production of concrete releases billions of tonnes of CO_2 into the atmosphere contributing to climate change. Hempcrete, cordwood, ferrock, and papercrete are low-impact alternatives to conventional concrete applications. Nk'Mip Desert Cultural Centre, Jill Strawbale House, The Acre, and Centre for Alternative Technology buildings point out the variety and creativity of the contemporary applications of ABMs, such as hempcrete, rammed earth and straw bale in the construction. Finally, the EcoArk and Jackie Chan Stuntman Training Center buildings demonstrate that "Take, Make, Waste" attitude of the industrial age must be replaced with "Reduce, Reuse, Recycle, and Recover" attitude of the sustainability. Developing new ideas on alternative building materials is a good step in this direction.

References

1. UN (2017) 2017 Revision of World Population Prospects. ST/ESA/SER.A/399. Department of Economic and Social Affairs Population Division, United Nations, New York
2. UN HABITAT (2016) World Cities Report 2016: urbanization and development. Emerging futures. UN HABITAT, Nairobi
3. International Energy Agency (2018) Energy Efficiency: Buildings. https://www.iea.org/topics/energyefficiency/buildings/. Accessed 18 Mar 2019
4. Miniwiz. Trashpresso by Miniwiz. https://trashpresso.com/. Accessed 20 Apr 2019
5. Latif E, Lawrence M, Shea A, Walker P (2016) In situ assessment of the fabric and energy performance of five conventional and non-conventional wall systems using comparative coheating tests. Build Environ 109:68–81
6. Zach J, Korjenicb A, Petranek V, Hroudova J, Bednar T (2012) Performance evaluation and research of alternative thermal insulations based on sheep wool. Energy Build 49:246–253
7. Roach M (1996) The bamboo solution: tough as steel, sturdier than concrete, full-size in a year. Discover Magazine 6

8. Lobovikov M, Puadel S, Piazza M, Ren H, Wu J (2007) World bamboo resources: a thematic study prepared in the framework of the Global Forest Resources Assessment 2005. Food and Agriculture Organization of the United Nations, Rome
9. Sullivan CC (2018) Sustainable envelopes with structural engineered bamboo. https://continuingeducation.bnpmedia.com/courses/lamboo-technologies/sustainable-envelopes-with-structural-engineered-bamboo/. Accessed 10 Feb 2019
10. Minke G (2012) Building with bamboo: design and technology of a sustainable architecture. Birkhauser, Basel
11. Rogers, Stirks, Harbour + Partners (2006) T4 Madrid Barajas Airport. https://www.rsh-p.com/projects/t4-madrid-barajas-airport/. Accessed 18 Mar 2019
12. Minke G (2006) Building with earth: design and technology of a sustainable architecture. Birkhauser, Basel
13. Harris CM (1975) Dictionary of architecture and construction. McGraw-Hill, New York
14. Kariyawasam KD, Jayasinghe C (2016) Cement stabilized rammed earth as a sustainable construction material. Constr Build Mater 105:519–527
15. Goodhew S, Griffiths R (2005) Sustainable earth walls to meet the building regulations. Energy Build 37:451–459
16. Sutton A, Black D, Walker P (2011) Straw bale: an introduction to low-impact building materials. Building Research Establishment: Information Paper IP 15/11. IHS BRE Press, UK
17. UNEP (2010) Greening cement production has a big role to play in reducing greenhouse gas emissions. United Nations Environment Programme, Global Environmental Alert Service (GEAS), Alert Report, October 2010
18. Gonchar J (2007) Building even better concrete. Archit Rec 195(2):143–149
19. Orhon AV (2012) Tasarımdan yapıma, sürdürülebilir beton yaklaşımları. In: Proceedings of 2nd project and construction management congress, Izmir Institute of Technology, Izmir, 13–16 Sept, pp 700–706
20. Vallas T, Courard L (2017) Using nature in architecture: building a living house with mycelium and trees. Front Archit Res 6(3):318–328
21. Roy R (2016) Cordwood building: a comprehensive guide to the state of the art. New Society Publishers, Gabriola Island, Canada
22. Rob R (2014) Is cordwood masonry green? http://greenhomebuilding.com/articles/cordwood.htm. Accessed 4 Jan 2019
23. Ekonoblok (2017) Econoblok – product information. Econovate Ltd., Hertfordshire
24. Alter L (2018) Is cork the perfect green building material? https://www.treehugger.com/sustainable-product-design/cork-perfect-green-building-material.html. Accessed 20 Apr 2019
25. Thorns E (2017) Could cork be nature's answer to our environmental and construction needs? https://www.archdaily.com/884983/could-cork-be-natures-answer-to-our-environmental-and-construction-needs. Accessed 20 Apr 2019
26. ArcDaily (2011) Logowines Winery/PMC Arquitectos. https://www.archdaily.com/136301/logowines-winery-pmc-arquitectos. Accessed 22 Apr 2019
27. Sutton A, Black, D, Walker P (2011) Hemp lime: an introduction to low-impact building materials. Building Research Establishment: Information Paper IP 14/11. IHS BRE Press, UK
28. Bevan R, Woolley T (2008) Hemp lime construction: a guide to building with hemp lime. IHS BRE Press, UK
29. Limetechnology (2008) Embodied CO_2. Tradical Hemcrete Information Pack. Limetechnology, Oxfordshire
30. IsoHemp (2019) Hempcrete blocks for naturally efficient masonry. https://www.isohemp.com/en/hempcrete-blocks-naturally-efficient-masonry. Accessed 10 Jan 2019
31. van Dam JEG, van den Oever MJA, Keijsers ERP (2004) Production process for high density high performance binderless boards from whole coconut husk. Ind Crops Prod 20(1):97–101
32. Garcia AL, Achaiah AT, Bello J, Donovan T (2017) Ferrock: a life cycle comparison to ordinary Portland cement. ISE 576 - Industrial Ecology, 24 Apr 2017
33. Jordahn S (2019) 3D-printed Gaia house is made from biodegradable materials. https://www.dezeen.com/2019/02/27/gaia-wasp-3d-printed-house-biodegradable-video/. Accessed 1 Apr 2019

34. Mairs J (2017) Arched bamboo trusses left exposed in Chiang Mai sports hall to create a 'feast to the eye'. Dezeen. https://www.dezeen.com/2017/08/21/chiangmai-life-architects-construction-sports-hall-panyaden-international-school-thailand-arching-bamboo-trusses/. Accessed 18 Mar 2019
35. Chiangmai Life Architects (2017) Bamboo Sports Hall Panyaden International School. https://www.bamboo-earth-architecture-construction.com/portfolio-item/panyaden-international-school-sports-hall. Accessed 18 Mar 2019
36. Arc Daily (2014) Nk'Mip Desert Cultural Centre/DIALOG. https://www.archdaily.com/508294/nk-mip-desert-cultural-centre-dialog. Accessed 18 Feb 2018
37. Sunart Strawbale (2018) Jack and Jill sat on a hill. i-build Mag 46:23–31
38. Sunart Strawbale (2017) Wellcome to Sunart Strawbale. https://www.sunartstrawbale.co.uk/. Accessed 10 Apr 2019
39. Maloney R (2014) Hy-Fi reinvents the brick. Arup News Events Bulletin, 25 June 2014
40. Interesting Engineering (2017) The future of construction: mushroom buildings. https://interestingengineering.com/future-construction-mushroom-buildings. Accessed 20 Feb 2018
41. ArcDaily (2015) HIGO/nA Nakayama Architects. https://www.archdaily.com/778566/higo-na-nakayama-architects. Accessed 20 Apr 2019
42. John Pardey Architects (2017) The Acre at Cumnor Hill. http://www.johnpardeyarchitects.com/modern-architecture/residential-architecture/cumnor-hill/. Accessed 18 Mar 2019
43. CAT (2014) CAT information service: what materials were used to build WISE? http://info.cat.org.uk/questions/wise/what-materials-were-used-build-wise. Accessed 8 Feb 2018
44. Miniwiz (2019) EcoArk. http://www.miniwiz.com/solution_detail.php. Accessed 10 Apr 2019
45. Miniwiz (2019) Jackie Chan Stuntman Training Center. http://www.miniwiz.com/solution_detail.php?id=39. Accessed 20 Apr 2019

Investigation of New Insulation Materials for Environmentally-Benign Food Delivery Bags

Ahmed Hasan and Ibrahim Dincer

Abstract Keeping the quality and freshness of the food delivered to consumers has been a critical problem which is closely related to heat and mass transfer. Among the desired conditions, temperature and moisture levels are considered the most critical ones at delivery. In this chapter, the aim is to model, design, develop and test better food delivery bag designs by considering various thermal insulation materials to improve a popular model delivery bag. A model is developed to simulate the temperatures of the pizzas inside the pizza delivery bag based on, transient thermodynamics and heat transfer. The present model is developed to be used with various thermal insulation materials to simulate the heat retention performance of the delivery bags. Some delivery bags are experimentally tested for their thermal retention capabilities. The vacuum panels, 3M thinsulate, and polyurethane foam are the three reported insulation materials reported in this chapter. The materials were then assessed to determine their thermal retention performance relative to the original bag. All insulation materials perform similarly or better than the original popular pizza delivery bag. The best performances achieved in terms of thermal retention were by the vacuum panels and the polyurethane insulated bags. The theoretical model was validated within 4.01% of the experimental work.

Keywords Heat transfer · Foods · Pizza · Thermal retention · Simulation · Insulation · Delivery bag · Modeling

A. Hasan · I. Dincer (✉)
Clean Energy Research Laboratory, Faculty of Engineering and Applied Science, University of Ontario Institute of Technology, 2000 Simcoe Street North, Oshawa, ON L1H 7K4, Canada
e-mail: ibrahim.dincer@uoit.ca

A. Hasan
e-mail: ahmed.hasan@uoit.ca

Nomenclature

A	Area (m^2)
C_f	Average coefficient of friction
C_p	Specific heat capacity (kJ/kg K)
g	Gravitational acceleration (m/s^2)
h	Average heat transfer coefficient (W/m^2 K)
k	Thermal conductivity (W/m K)
L	Length (m)
L_c	Characteristic length (m)
m	Mass of material (kg)
Nu	Nusselt number
PCM	Phase change material
Q_{Latent}	Latent energy (kJ)
$Q_{Sensible}$	Sensible energy (kJ)
$\dot{Q}$	Heat transfer rate (kW)
Ra	Rayleigh number
RH	Relative humidity (%)
RSD	Relative standard deviation
s	Specific entropy (kJ/kg K)
T	Temperature (K)
T_∞	Fluid temperature (K)
T_S	Surface temperature (K)
T_{Sink}	Ambient temperature (K)
TES	Thermal energy storage
U	Internal energy (kJ)
u_∞	Wind velocity (m/s)
v	Kinematic viscosity (m^2/s)

Greek Letters

α	Thermal diffusivity (m^2/s)
β	Thermal expansion coefficient (1/K)
Δ	Difference
ρ	Density of the fluid (kg/m^3)
τ_s	Average shear stress (Pa)

1   Introduction

The fast-food industry has been growing continuously, because of its convenience for customers. Many fast-food chains offer delivery services to expand their business horizon. It is an effective way of increasing business as there is an increasing number of customers ordering online from delivery companies. Studies show that 10% of people in the U.S order takeout/delivery once a week [1]. That figure adds up to be US$9.7 billion [2] in spending on delivery, making it a sizable business. Furthermore, the same study shows that 72% of those orders are pizzas. Figure 1 displays the breakdown of orders of certain foods from a study [3]. Based on the current statistics there is a growing market for delivery bags. Due to the high consumption of ready-to-eat type pizza, it will be used as the subject of this chapter.

There are many delivery bags currently available in the market. However, the majority of them struggle to keep the food warm and prevent condensation. Although keeping the packages warm is not challenging, moisture/condensation is a challenging problem to control within delivery bags. Moisture could affect the quality of the food during delivery, which would, in turn, affect the customer return rate. The growing market for fast food delivery has to be accommodated for by developing new delivery bags to allow for better delivery services. Better delivery bags are badly needed when the deliveries are being performed in cold weather, as cold temperatures might drastically change the food temperature and induce condensation in short amounts of time.

The main component in improving the thermal retention performance of the delivery bags is the various types of thermal insulation materials. The main property of thermal insulation is its low thermal conductivity to decrease the heat rejection by the bag by the means of conduction of the bag to the surrounding atmosphere. If the conduction levels are low, the surface temperature of the bag will also be limited therefore allowing for lower natural convection rates. Other auxiliary devices that could be used to retain/maintain the thermal energy within the bag are thermal energy storage devices (TES), active electric heaters or a hybrid of both. These considerations are of importance as the temperature of the food by regulation through the Food Safety and Inspection Service for hot food deliveries should not be any lower than 60 °C. Furthermore, there is added merit for having higher internal temperatures within the bag, as it allows for better moisture/condensation control. This is highly due to the relative humidity's relationship with temperature. As the temperature increases the relative humidity decreases.

The initial temperature of pizzas are usually within the following range 79–93 °C. The average delivery time is 20–30 min after the pizzas leave the restaurant. The challenge is to deliver within that time with the pizzas quality in terms of sogginess due to condensation and temperature due to heat loss. In the following sections, different methods will be discussed to enhance the heat retention performance of the bag.
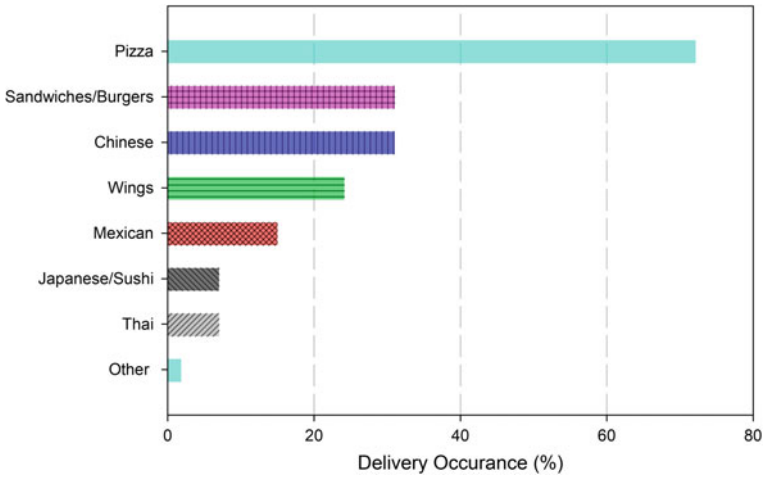
Fig. 1 Statistics of percentage of order deliveries for pizza (Data from [1])

Wang and Sun [4] analyzed the melting characteristics of cheese. In the study, it was found that the influence of the dimensions of cheese slices on the melting property is directly linear. The study concluded that as the cheese slices increased from 25 to 75 mm the meltability increased as well. The meltability was also found to increase when the thickness of the cheese slices increased as well.

Sun and Du [5] investigate the use of computer vision for the inspection of pizza base and tomato sauce spread quality. The study was conducted on 25 samples, using spatial ratio I, spatial ratio II and circularity. A fuzzy logic system was developed to perform the classification process on the pizza spread samples into classes of acceptable and defective. The study concluded that the system in question had a 13% error in base area analysis relative to humans. Furthermore, the study also concluded that the fuzzy logic was 92% accurate using computer vision.

Liberopoulos and Tsarouhas [6] presented statistical failure analysis of an automated pizza production line. The study identified the most important modes of failure and the computation parameters for the theoretical distributions that are fit for the failure data. Furthermore, the existence of any autocorrelations in the failure data. The study was made to allow bakery's and manufacturers to improve the operation of their production lines.

Hasan and Dincer [7] experimentally tested various insulation types that included 3M thinsulate as its main insulator along with Polly batting and mylar (reflective sheet) and two airbag configurations were used. The first airbag setup included a 1-inch-thick polyurethane insulation on the perimeter for each side of the bag. As for the second configuration, three 1″ polyurethane foam ridges spread evenly within the perimeter. The overall performance increase in terms of energy and exergy efficiencies experienced by the airbags were found to be 2–4%. The highest energy and

exergy efficiencies calculated for the "air bags" with no ridges were 88.7 and 83.2% compared to the 86.7 and 81.8% achieved by the control bag.

Yüksel et al. [8] experimentally studied the effective thermal conductivity of multilayer insulation materials. The ETC was tested as a function of temperature within the following domain (0–25 °C). The investigated materials included binary/ternary glass wools or ternary expanded polystyrene foams that were reinforced with aluminum foil. The authors concluded that the ETC decreases as with the reinforcement with aluminum foil at the same temperature. As the temperature increased the aluminum foil reinforced specimens ETC decreased sharply.

The main objective of this chapter is to develop and test novel pizza delivery bags for providing reliable, high performing pizza bags that assure hot and fresh deliveries to the customers. It aims at avoiding heat loss and condensation of the pizza which affects their quality and taste. The delivery bags are also theoretically modeled using heat transfer analysis and then experimentally tested to confirm the performance. A wide range of insulation materials are used in the experiments.

1.1 Heat Retention

Thermal insulation materials are essential for successful heat retention. Thermal insulators contain materials that have low thermal conductivities to retain heat, as it reduces the rate of heat transferred by the means of conduction from the inside of the bag to the outside surface. Reducing conduction heat transfer allows for a lower outer surface temperature for the delivery bag itself, this reduces convection heat transfer as well. Radiation heat transfer is also assessed and could be reduced using reflective sheets. Other methods that could be of use to enhance the performance of delivery bags include Phase Change Materials (PCMs) and active electric heaters. These devices could improve the heat retention performance of the pizza delivery bags. This is important, as the temperature of the pizzas should range from 65 to 70 °C and above when delivered according to the Food Safety and Inspection Service for hot food deliveries [8]. Keeping the temperature higher within the bag also allows for better moisture/condensation control, as the relative humidity decreases when the temperature rises.

Pizzas are usually taken out of the oven at the temperature range of 80–95 °C depending on the oven used. The average delivery time is 20–30 min after the pizzas leave the restaurant. The challenge is to deliver within that time with the quality of the pizza not being jeopardized due to condensation and temperature drop. In the following sections, different methods are discussed to enhance the heat retention performance of the bag.

(a) **Passive Methods**

Passive methods require no electricity and often provide a simpler and cheaper solution. Several insulation materials are considered to enhance the thermal retention performance of the bag, as they require no electric power input. Different insulation

materials are rated based on their thermal conductivity, flexibility, and environmental impact. Furthermore, radiation barriers are another form of passive systems that could work effectively to reduce radiation losses from the bag.

Other forms of passive systems include PCMs that would be used to store the excess heat lost from the pizzas and store it until the pizza temperature is lower than that of the PCMs. When the temperature of the PCM is lower than that of its surroundings, it starts to release the thermal energy stored. PCMs, as mentioned previously, is a form of TES.

(b) **Phase Change Materials**

Some PCMs options are listed in Table 1. The PCMs are chosen based on their melting temperature. The melting temperature of the PCM determines the temperature that the thermal energy is released when discharge occurs. PCMs are reusable and could be sourced from organic resources.

(c) **Active Methods**

Unlike passive systems, active systems require an electric input. Active systems such as silicone electric heaters could be used to maintain the temperature of the pizzas with no challenge, as some models heat up to 100 °C. Most of the silicone electric heaters currently used in delivery bags are powered using car electricity outlets. However, they are relatively expensive and experience mechanical fatigue in short cycles.

Table 1 Summary PCM options based on melting point

Option	Name	Composition	Thermal conductivity (W/m K)	Working temperature (°C)	Latent heat capacity (kJ/kg)	Specific heat capacity (kJ/kg K)
1	PlusICE S70	Hydrated salts	0.570	70	110	2.10
2	PlusICE a70	Organic-based	0.230	70	173	2.2
3	PlusICE X70	–	0.360	70	125	1.57
5	RUBITHERM GR82	35% PCM 65% Clay		82		2
6	RUBITHERM RT70HC	60% PCM		70		2
7	CARBOWAX PEG8000			55–62		0.51
8	CARBOWAX PEG4600			54–60		0.51
9	Sigma-Aldrich 4-Bromophenol 99%	99% 4-Bromophenol		61–65		

(d) **Hybrid Methods**

Hybrid systems between active and passive systems can be developed to enhance the thermal retention performance of the bag. An example of such systems is TES devices such as PCMs being charged with thermal energy before use. When the delivery takes place, the PCM can be inserted in the delivery bag to release heat as the delivery is undergone.

Even though there is an increasing demand for takeout delivery especially for pizzas, the literature is severely lacking any studies about this subject. Furthermore, the literature is also lacking studies about delivery bags.

2 Experimental Apparatus and Procedure
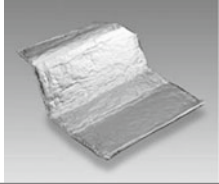
The experimental setup for thermal insulation was designed to record six data points. The thermocouples are placed in the following configuration. Three under each pizza in the pizza box and three outside the delivery bag. This was done to obtain a comprehensive view of what the delivery bag and pizzas experienced during the experimentation period in terms of temperature. The three thermocouples inside the delivery bag were placed under each pizza. The three other thermocouples were used to record the temperature of the top, bottom and left side of the delivery bag. The experimental trials are run for 30 min in the pizza store to mimic the average delivery time; this was based on most deliveries being done within 20–30 min. As soon as the pizzas would leave the oven, they are inserted into pizza boxes followed by the boxes being inserted in the bag at the same time to be tested. The experiments were done using three medium pizzas to have consistent experimental trials. Three medium pizzas are chosen as 90% of pizza deliveries are of that size of order. The same restaurant would be used in all the experiments in an attempt to achieve consistency for the initial temperatures of the pizzas.

The data was recorded during the experiment using an Omega data acquisition module specifically OMB-DAQ-2416. Alongside an expansion module the OMB-AI-EXP32. TracerDAQ was the software used to track the fluctuations in temperature. An empty pizza bag with no insulation was used to test various insulation materials in shorter periods of time, as this reduces the time of manufacturing.

The insulation materials are rated mainly based on their low thermal conductivity and their reaction with humidity and life cycle environmental impact. A summary of some insulation materials is shown in Table 2.

In the theoretical analysis forced convection for a total of 5 min was used to analyze various temperatures. However, given the equipment had to be plugged in at all times to work, the restaurant chosen had a median ambient temperature range of 15–17 °C and only free convection heat transfer is experienced for the most part. The experimental setup can be seen in Fig. 2.

Table 2 Insulation materials properties and description [9–11]

Option	Name	Thermal conductivity (W/m K)	Thickness (mm)	Description
1	Vacuum insulation panel	0.042	12	• Used in refrigerators • High heat insulation properties • Flexible as its made from segments
2	3M thinsulate	~0.042	12	• Commonly used in winter jackets • Has moisture diffusion properties
3	Polyurethane foam	0.026	25	• Provides exceptional insulation • Widely available • Inexpensive

The total uncertainty can be written as follows:

$$U_y = \sqrt{\sum_i \left(\frac{\partial y}{\partial x}\right)^2 U_x^2} \tag{1}$$

where $U = $ Uncertainty of variable.

The experimental uncertainty consists of random and systematic errors as written below.

$$U_i = \sqrt{S_i^2 + R_i^2} \tag{2}$$

where $S_i = $ Systematic errors and $R_i = $ Random errors.

The relative standard deviation is defined as

$$\text{RSD} = \frac{s}{\bar{x}} 100\% \tag{3}$$

where $S = $ Systematic errors and $\bar{x} = $ Mean of results.

Fig. 2 Experimental setup **a** overview, **b** top view, **c** bottom view, and **d** front view

3 Modeling

In this research paper, thermodynamic and heat transfer models are created for simulating the thermal retention performance of different delivery bags with multiple configurations of insulations. The temperature of the pizzas are analyzed for over a span of 30 min. A standard 16″ pizza delivery bag is the basis of the study as it is the most popular size among pizza delivery services. The model includes three different heat transfer conditions. The first one being forced convection and the second is free convection heat transfer. All heat transfer functions are obtained from the EES heat transfer library.

Assumptions

In order to perform the thermodynamic and heat transfer analysis, several assumptions are made. Since the initial conditions of the pizzas are mainly not constant, the initial conditions are required to be assumed. The following assumptions are made for the heat transfer analyses:

- The internal temperature of the car is assumed constant at 20 °C.
- The pizzas are considered isothermal at 90 °C after the oven.

- The heat transfer due to conduction heat transfer occurs in the area of the pizza as it causes the largest temperature gradient difference in the system.
- The surface of the bag is assumed 27 °C in the beginning.
- The surface area of the top and bottom of the bag is calculated at a constant 0.445 m × 0.445 m.
- The surface area of the sides is taken at a constant 0.185 m × 0.445 m.
- The wind speed is assumed 4.25 m/s [12], as it is the average low in Ontario.
- The initial temperature of the PCM is that of the kitchen where the delivery bags are stored which is 25 °C.
- The masses used to define the internal energy of the delivery bag were of a large pizza.
- The following masses are based on a pizza sample that included the following ingredients: 567 g dough, 227 g mozzarella cheese, and 142 g of tomato sauce. The thermal properties of the ingredient were taken from source [3].

The conduction heat transfer occurs when a temperature gradient exists, causing thermal energy to transfer through a medium. To reduce the thermal energy transfer insulation materials are used as they resist thermal conductivities. The insulation and other materials such as PCMs have their thermal conductivities noted by the manufacturer, so they can be used in the analysis. Therefore, using Fourier's law of conduction, the heat flux can be calculated, providing the heat loss from the inside of the bag to the surrounding environment.

In addition, the forced convection heat transfer analysis is also implemented as the pizza bags experience forced convection during transportation from the pizza store to the car and from the car to the customer doorstep. The wind speed chosen for this analysis is based on the average low wind speed in Ontario, which is seven mph (4.25 m/s) [12]. The wind is assumed to pass over five of the sides of the bag, front, top, bottom, left, and right side. The front side experiences flow past a vertical plate. The left, right, top and bottom side all experience flow past a flat plate. The sixth side, which is the backside, is assumed unaffected as the wind is not directly interacting with that side. Using the vertical plate model-free convection, the backside heat transfer can be modeled and simulated.

Free convection heat transfer occurs when a temperature gradient between an object and its environment is present. The analysis is performed to simulate the conditions for a pizza bag in a car with stagnate conditions meaning there are no significant wind speeds. Free convection is assumed to be occurring on all six sides of the bag. To accurately simulate the heat transfer effects on the pizza bag, the top side of the bag experience free convection of a horizontal flat plate, the bottom side experiences free convection of a downward horizontal flat plate, and the other sides experience free convection of a vertical flat plate. Figure 3 displays the dimension of the delivery bag and heat transfer modes that experienced by the delivery bag.

The main goal of using PCMs is to store thermal energy for usage when needed. The excess heat from the pizza will be stored in the PCM as it is a TES device. The utilization of PCMs could extend the duration of sustaining the pizza temperature at 65 °C and above. A conduction heat transfer analysis is used to determine the
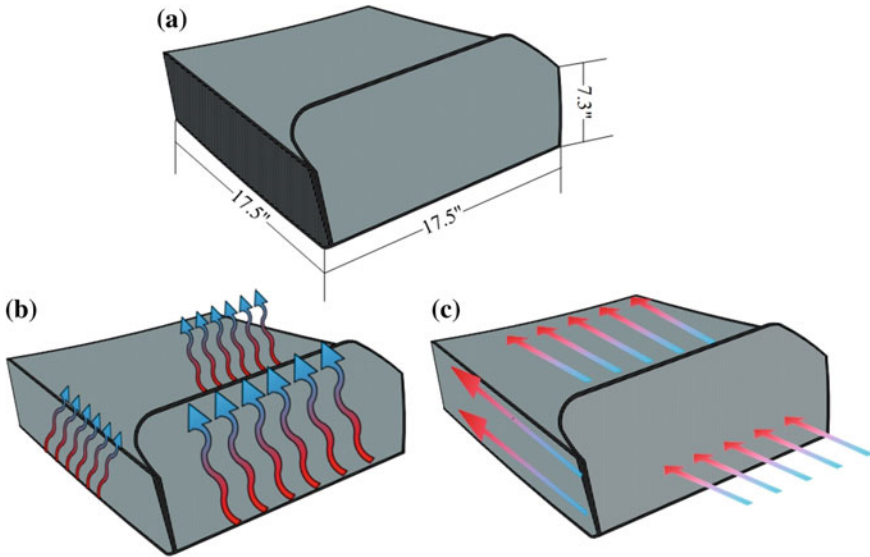
Fig. 3 **a** Dimensions of the delivery bag analyzed **b** free convection experienced by the delivery bag **c** forced convection experienced by the bag

temperature rise of the PCMs. The analysis is identical to the one used to simulate the thermal losses through the insulation layers. However, in this case, the PCM is an additional layer to the bottom side of the bag.

In the following section, the scenario description and development are shown. Furthermore, the assumptions used for the model are also discussed. The delivery scenario is illustrated in Fig. 4. The temperature of the pizzas when placed in the pizza box for delivery are 80–95 °C based on temperatures measured from various restaurants. During this period, heat losses are present due to the heat transfer occurring. In the simulations, it is assumed that the initial temperature of the pizza is 90 °C when it is placed into the delivery bag.
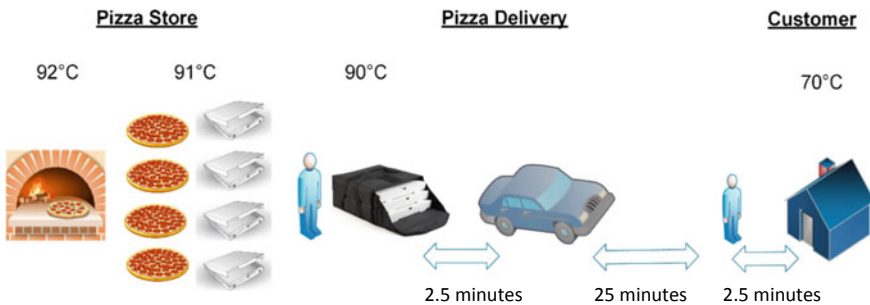
Fig. 4 Delivery scenarios

The analysis includes a 5 m variety number of large pizzas ranging from one to four in one delivery bag. A standard 16″ pizza delivery bag dimensions are used as the basis of the study as it is the most popular size among pizza delivery services. The dimensions of the delivery bag are seen in Fig. 5.

Since the majority of the delivery is done using a vehicle, the ambient temperature is assumed to be 20 °C in the vehicle all year round. The maximum time spent moving the pizza from the restaurant to the delivery car is assumed to be 5 minutes in total is assumed to be spent moving the delivery bag from the car to the customer location. This duration of time allows for a conservative assumption. The analysis includes a variety number of large pizzas ranging from one to four in one delivery bag. A standard 16″ pizza delivery bag dimensions are used as the basis of the study as it is the most popular size among pizza delivery services.

As for the delivery time itself, a time duration of 30 min is assumed as the worst-case scenario. The majority of the delivery process is inside the car, making the delivery bags mostly experience free convection heat transfer.

Heat Transfer Analysis

In the following section, the equations and relations used for both the simulations and calculations for efficiencies for the experimental results are shown.
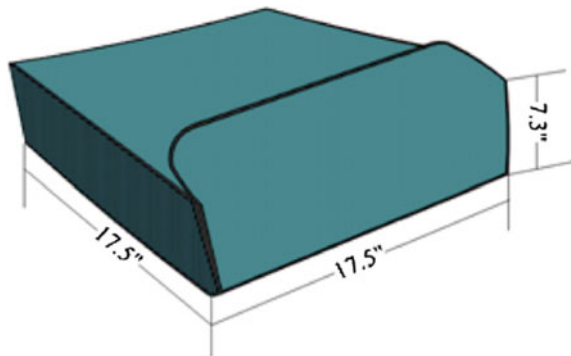
(a) Forced Convection Heat Transfer Analysis

The average coefficient of friction can be written as follows [13]:

$$C_f = \left(\frac{\tau_s}{\frac{\rho u_\infty^2}{2}} \right) \tag{4}$$

where τ_s = avg. shear stress (Pa), ρ = is fluid density (kg/m³), u_∞ = wind velocity (m/s).

Fig. 5 Dimensions of bag used throughout the experiments

The Nusselt number equation can be written as follows:

$$Nu = \left(\frac{hL_c}{k}\right) \qquad (5)$$

where h = average heat transfer coefficient (W/m² K), L_c = Characteristic Length, k = Conductivity (W/m. K).

The average heat transfer coefficient can be written as follows:

$$h = \left(\frac{Nu \cdot k}{L}\right) \qquad (6)$$

where Nu = Nusselt Number, L = Length of heat transfer surface (m), and k = conductivity (W/m K).

(b) **Free Convection Heat Transfer Analysis**

The Rayleigh number used in the analysis is as follows:

$$Ra = \frac{g \times L_c^3 \times \beta(T_s - T_\infty)}{v \times \alpha} \qquad (7)$$

where g = gravitational acceleration (m²/s), L_c = characteristic length (m), T_∞ = ambient temperature (K), and T_s = temperature of surface (K).

The average coefficient of friction over a flat surface can be defined as follows:

$$C_f = \left(\frac{\tau_s}{\frac{\rho u_\infty^2}{2}}\right) \qquad (8)$$

where τ_s = avg. shear stress (Pa), ρ = is fluid density (kg/m³) and u_∞ = wind velocity (m/s).

The Nusselt number equations are written as follows [14]:

$$Nu = 0.54\,Ra^{\frac{1}{4}}$$

where Ra is Rayleigh number Applies when $10^4 < Ra < 10^7$, Pr > 0.7.

$$Nu = 0.15\,Ra^{\frac{1}{3}} \qquad (10)$$

where Ra is Rayleigh number Applies when $10^7 < Ra < 10^{11}$, Pr all of them.

The average heat transfer coefficient can be written as follows:

$$h = \left(\frac{Nu \times k}{L}\right) \qquad (11)$$

where Nu = Nusselt Number, L = Length of heat transfer surface (m) and k = thermal conductivity (W/m K).

(c) **PCM Relations and Calculations**

The sensible energy of the PCM can be written as follows:

$$Q_{sensible} = m \times C_p \times \Delta T \tag{12}$$

where m = Mass of PCM (kg), C_p = Specific heat capacity (kJ/kg K), ΔT = Difference of initial and final temperature.

The latent energy of the PCM can be written as follows:

$$Q_{Latent} = m \times L \tag{13}$$

where m = mass of PCM (kg), L = Specific Latent Heat Capacity (kJ/kg).

4   Results and Discussion

In this research paper, three different insulation materials are tested along with moisture absorption fabrics. The materials are tested to compare their performance in terms of heat retention and moisture control relative to a popular model currently on the market. In the following section, the experimental results for all the insulation. The following section also discusses, the simulation results for the original bag integrated with the vacuum panels.

4.1   Experimental Results for Insulation Materials

The original bag is tested as the benchmark performance for the other bag designs to be compared to. The materials tested included polyurethane foam, 3M thinsulate, and vacuum panels. These materials are chosen based on availability, cost, environmental friendliness and performance. The suggested designs had to retain the pizza temperatures to meet the temperature requirements of a minimum 65–70 °C in the span of 20–30 min of delivery. This parameter assumes that the pizzas will leave the oven at a temperature of 80–95 °C. However, during the experimentation period, it is difficult to have the pizzas start at 90 °C. This is due to the boxes being open to insert the thermocouples and often the pizza would leave the oven at lower temperatures than 90 °C. To assess the performance of the delivery bag designs energy and exergy efficiencies are used. Furthermore, the start temperature of the pizzas has to be accounted for, as the temperature inside the bag increases the rate of heat loss also increases. This is due to the temperature difference gradient is the main factor causing heat transfer. Other factors also include the reaction of the insulation

material to different temperatures, as the rated thermal conductivity are set at room temperature.

Polyurethane non-rigid foam is tested; polyurethane itself has a low thermal conductivity making it a great insulator. What further enhances this specific form of this insulation is that foam acts like a sponge, and it fills its flexible pores with air. This product is widely available and is used to this day in the furniture manufacturing business as the filler for products such as couches and mattresses. The polyurethane foam used is of 1-inch thickness along with bamboo moisture-wicking fabric.

Vacuum panels are the last insulation material to be tested in this study. Vacuum panels are great insulators. However, often their performances might be jeopardized if punctured according to the manufacturers. To test the vacuum panels performance the test was conducted using the original bag. However, two pockets placed on the top and bottom side of the bag where the vacuum panels are placed.

The initial temperature readings of the three pizzas placed on the top side, inside three different bags were recorded as follows: 78.1 °C (original bag), 82.0 °C (polyurethane bag), and 83.3 °C (original bag and vacuum panel). The final temperature readings of the three pizzas placed on the top side, inside three different bags were recorded as follows: 65.3 °C (original bag), 69.2 °C (polyurethane bag), and 69.7 °C (original bag and vacuum panel). The temperature drops experience by the three delivery bags were as follows 12.8 °C (original bag), 12.8 °C (polyurethane bag), and 13.6 °C (original bag and vacuum panel). All three bags performed very similarly in the case with the top pizza. Figure 6 displays the temperature results of the top pizza over a span of thirty minutes for all three bags.

The initial temperature readings of the three pizzas placed in the middle inside the three different bags were recorded as follows: 69.5 °C (original bag), 85.8 °C
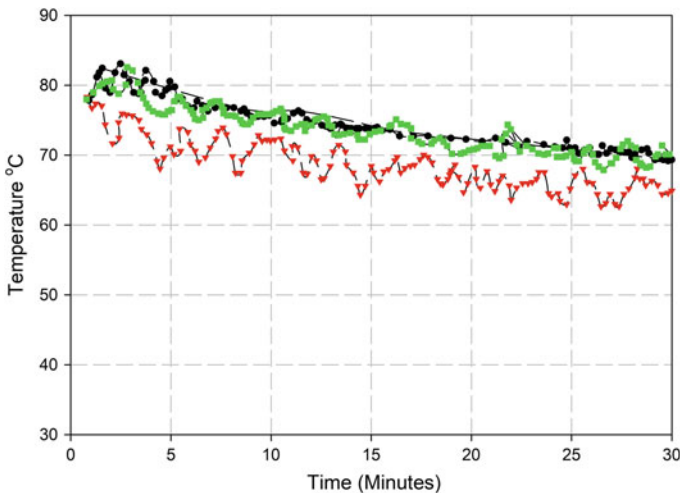

Fig. 6 Top pizza temperature results overtime for the original, polyurethane, and original + vacuum panel bag

(polyurethane bag), and 91.8 °C (original bag and vacuum panel). The final temperature readings of the three pizzas placed in the middle inside the three different bags were recorded as follows: 61.6 °C (original bag), 70.6 °C (polyurethane bag), and 72.5 °C (original bag and vacuum panel). The temperature drops experience by the three delivery bags were as follows 7.9 °C (original bag), 15.2 °C (polyurethane bag), and 19.3 °C (original bag and vacuum panel). The original bag experienced the lowest temperature drop however, it should be noted that the initial temperature of the pizza was significantly lower than the other bags. Figure 7 displays the temperature results of the middle pizza over a span of thirty minutes for all three bags.

The initial temperature readings of the three pizzas placed in the bottom inside the three different bags were recorded as follows: 74.2 °C (original bag), 77.1 °C (Polyurethane bag) and 87.1 °C (Original bag and vacuum panel). The final temperature readings of the three pizzas placed in the bottom inside the three different bags were recorded as follows: 63.8 °C (original bag), 68.3 °C (Polyurethane bag), and 71.8 °C (Original bag and vacuum panel). The temperature drops experience by the three delivery bags were as follows 10.4 °C (original bag), 8.8 °C (Polyurethane bag), and 15.3 °C (Original bag and vacuum panel). In the case with the bottom pizza the polyurethane insulated bag was found to have the lowest temperature deference followed by the original bag. However, it should be noted that both the vacuum panel and polyurethane insulated bag begin with higher temperatures. The higher the temperature the larger the heat transfer gradient. Figure 8 displays the temperature results of the bottom pizza over a span of thirty minutes for all three bags.

The uncertainties for the temperature results for experiments using vacuum panels are seen in Table 3.
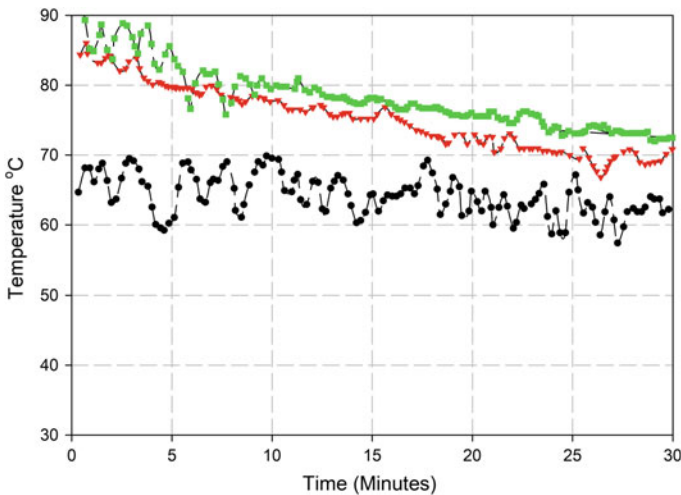

Fig. 7 Middle pizza temperature results overtime for the original, polyurethane, and original + vacuum panel bag
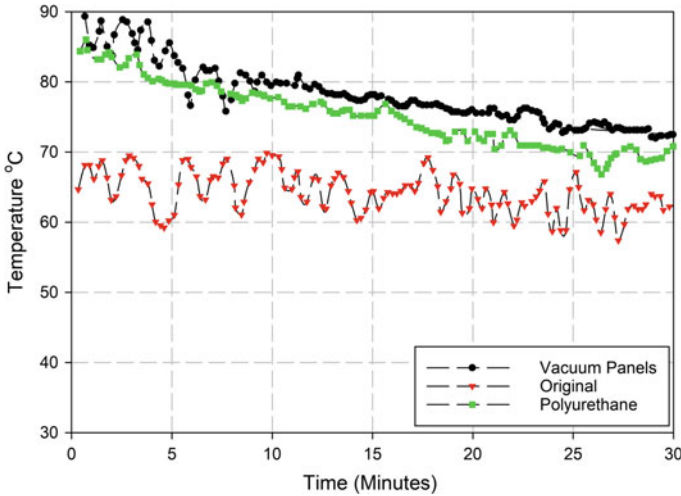
Fig. 8 Bottom pizza temperature results overtime for the original, polyurethane, and original + vacuum panel bag

Table 3 Uncertainties table for results for experiments using vacuum panels

Measurement parameter	Device	Accuracy	Total uncertainties (%)
Temperature	Thermocouple *K*-type	±0.4%	0.78
Temperature	DAQ	±0.5 °C	

4.2 Experimental Results for Moisture Absorption Fabrics

The following section displays the results obtained from testing different types of moisture absorption fabrics. The results obtained are from the humidity sensor that is placed in the bag. The three fabrics tested include Zorb, bamboo and hemp fabric. The moisture absorption fabrics performances are based on the amount of time the humidity starts to decrease relative to the original bag (i.e. without the incorporation of the moisture absorption fabrics). Furthermore, the final relative humidity for each case is considered for each case to assess the fabrics performance.

Zorb, hemp, and bamboo fabrics are used as organic reusable moisture absorption fabrics. The reusability of the fabrics makes them cost-effective as they can be used as long as the delivery bag is in service. The antibacterial properties that these fabrics possess inhibit bacterial growth within the fabric, allowing for a safer food delivery. Furthermore, the organic properties make them biodegradable giving an environmentally benign solution to moisture control problems.

The original bag is replicated by using 3M Thinsulate and polyester batting insulation. For these set of tests no moisture absorption fabric is used to replicate how a standard pizza delivery bag performs in terms of moisture control. The tests are

repeated three times to confirm the results. The ambient temperature during this test is 22 °C. The ambient relative humidity is 33% measured during the test.

4.3 Modeling Results

The configuration of the layers within the bag are shown in Fig. 9. Vacuum Panels are used they are widely available and have great thermal insulation properties. The simulation results for a 16″ delivery bag with the integration of one vacuum panel are seen in Fig. 10. In this simulation, the delivery bag is experiencing forced convection heat transfer with an ambient temperature range of −20 to 20 °C and free convection heat transfer at a constant ambient temperature of 20 °C. Free convection occurs for 25 min and forced convection occurs for a total 5 min. The results display how the pizzas cool down over the assigned total time of 30 min. The analysis shows the results for one large 14″ pizza. Under forced convection with the ambient temperature ranging from −20 to 20 °C the following final temperatures for one pizza are obtained: 48.4, 42.5, 36.5, 30.6, and 24.7 °C.

The simulation results for a 16″ delivery bag with the integration of one vacuum panel are seen in Fig. 11. In this simulation, the delivery bag is experiencing forced convection heat transfer within an ambient temperature range of −20 to 20 °C and free convection heat transfer at a constant ambient temperature of 20 °C. Free convection occurs for 25 min and forced convection occurs for a total 5 min. The results display how the pizzas cool down over the assigned total time of 30 min. The analysis shows the results for two larges 14″ pizzas. Under forced convection with the ambient temperature ranging from −20 to 20 °C the following final temperatures for one pizza are obtained: 64.6, 60.97, 57.3, 53.7, and 50.1 °C.

The simulation results for a 16″ delivery bag with the integration of one vacuum panel are seen in Fig. 12. In this simulation, the delivery bag is experiencing forced
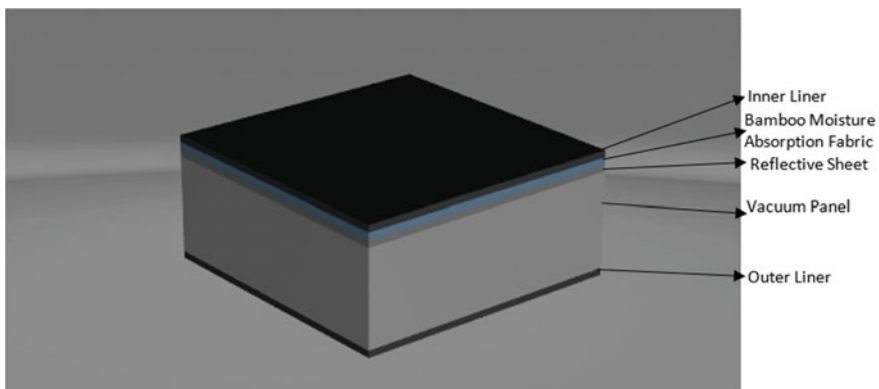
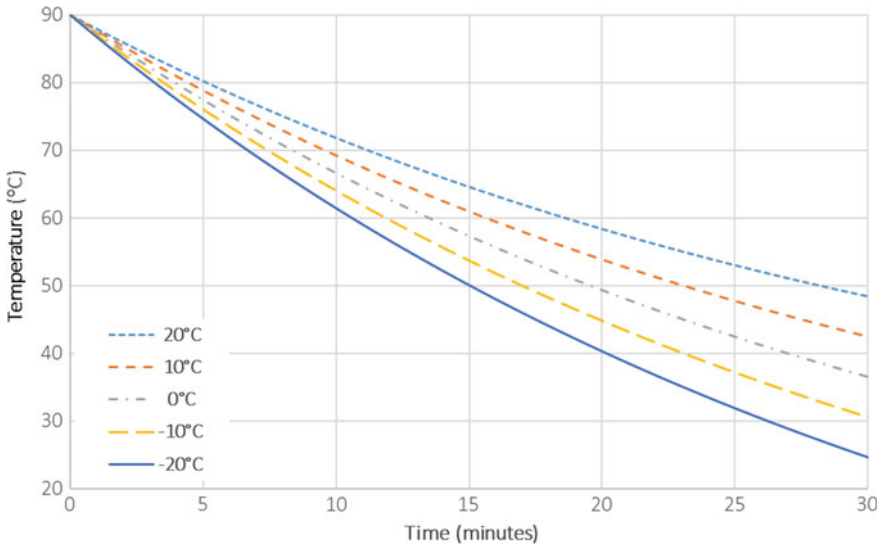**Fig. 9** Insulation configuration using vacuum insulation panel

Fig. 10 Summary of 1 large pizza temperatures in a 16″ delivery bag integrated with vacuum panels in an ambient temperature at −20 to 20 °C in forced convection segment and 20 °C in free convection
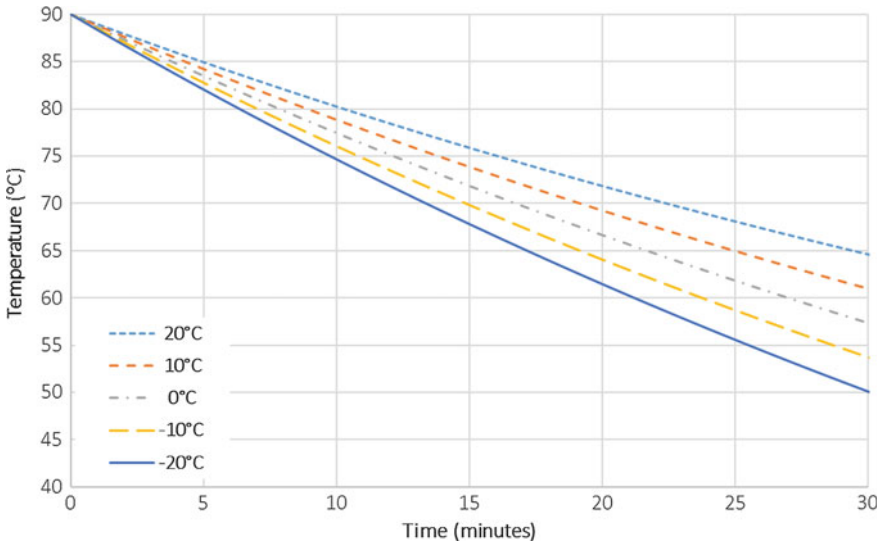

Fig. 11 Summary of 2 large pizzas temperatures in a 16″ delivery bag integrated with vacuum panels in an ambient temperature at −20 to 20 °C in forced convection segment and 20 °C in free convection
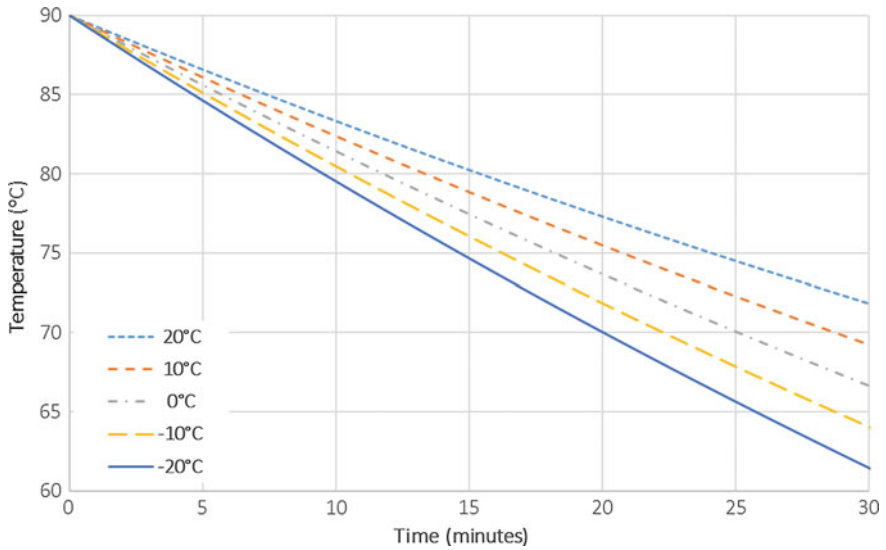
Fig. 12 Summary of 3 large pizzas temperatures in a 16″ delivery bag integrated with vacuum panels in an ambient temperature at −20 to 20 °C in forced convection segment and 20 °C in free convection

convection heat transfer within an ambient temperature range of −20 to 20 °C and free convection heat transfer at a constant ambient temperature of 20 °C. Free convection occurs for 25 min and forced convection occurs for a total 5 min. The results display how the pizzas cool down over the assigned total time of 30 min. The analysis shows the results for three larges 14″ pizzas. Under forced convection with the ambient temperature ranging from −20 to 20 °C the following final temperatures for one pizza are obtained: 71.8, 69.2, 66.6, 64.1, and 61.45 °C.

The simulation results for a 16″ delivery bag with the integration of one vacuum panel are seen in Fig. 13. In this simulation, the delivery bag is experiencing forced convection heat transfer within an ambient temperature range of −20 to 20 °C and free convection heat transfer at a constant ambient temperature of 20 °C. Free convection occurs for 25 min and forced convection occurs for a total of 5 min. The results display how the pizzas cool down over the assigned total time of 30 min. The analysis shows the results for four larges 14″ pizzas. Under forced convection with the ambient temperature ranging from −20 to 20 °C the following final temperatures for one pizza are obtained: 75.9, 73.9, 71.8, 69.8, and 67.8 °C. A summary of the results for ten thermal wrap layer simulation for the final temperature are listed in Table 4.

In order to conclude the simulation section a sample comparison between the simulation and experimental results for the vacuum panel integrated with the original delivery bag are seen in Fig. 14. The initial temperatures of the pizzas and ambient temperatures are set in each case to match that of the experimental temperatures. It could be seen the simulation is accurate as the final temperatures at 30 min are
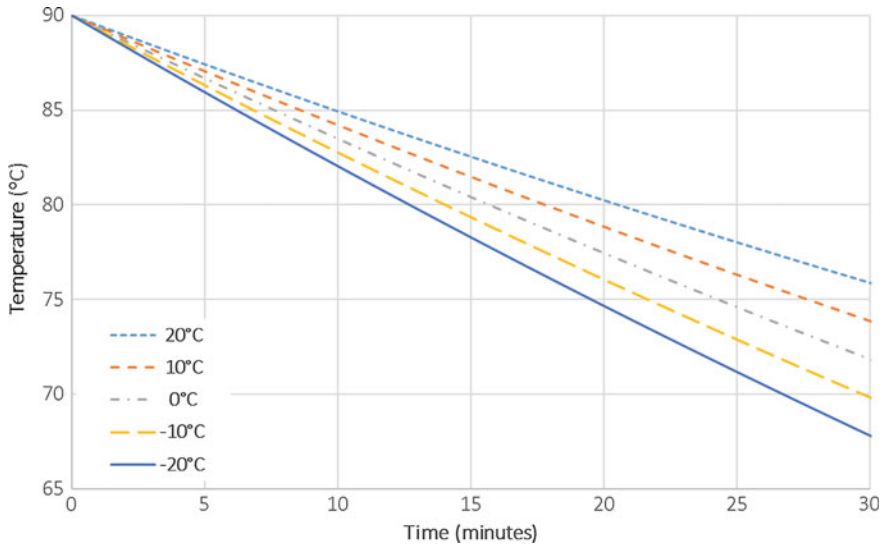
Fig. 13 Summary of 4 large pizzas temperatures in a 16″ delivery bag integrated with vacuum panels in an ambient temperature at −20 to 20 °C in forced convection segment and 20 °C in free convection

as follows: the final simulation temperature is 68.89 °C and the experimental final temperature is 71.8 °C for Fig. 14.

In this section, two PCMs are chosen to be simulated. This section will verify the effects of PCM on the delivery times. In this simulation, the PCMs are used with two sheets of Aerogel sheets as a form of insulation. The phase change temperature of the selected PCMs is critical for the delivery bags.

For the following simulation, the PlusICE A70 PCM is used; it is organic-based making it an environmentally benign choice. The results for the pizza bag integrated with PCM A70 is shown in Fig. 15. The results show that the time for the pizza to cool down to 70 °C has increased from 45.23 to 45.82 min. This is not a significant time increase and is within the margin of error.

The following simulation integrates the PlusICE X70 PCM. The PlusICE X70 is a solid-solid PCM, meaning it does not physically change on a macro level. However, on a micro-level the PCM undergoes lattice structure changes, allowing it to store both sensible and latent heat. The results for the pizza bag integrated with PCM X70 are shown in Fig. 16. The results show that the time for the pizza to cool down to 70 °C has increased from 45.23 to 45.62 min. Again, this is not a significant time increase, as the simulations show, which puts it in the margin of error of the simulation.

The Two PCMs A70 and X70 did not increase the time to cool down to 70 °C significantly. The changes are minor and can be considered within the margin of error of the analysis. The reason behind this insignificant change is highly due to the PCMs not reaching their melting point, which is 70 °C. This is a challenge, as PCMs need to store latent heat energy to release thermal energy when it is needed at the

Table 4 Vacuum panel be livery bag theoretical results summary

Vacuum panel insulation	
Condition	Final temperature (°C)
5 min forced convection 20 °C 25 min free convection 20 °C	–
1 14″ Pizza	48.4
2 14″ Pizza	64.6
3 14″ Pizza	71.8
4 14″ Pizza	75.9
5 min forced convection 10 °C 35 min free convection 20 °C	
1 14″ Pizza	42.5
2 14″ Pizza	60.97
3 14″ Pizza	69.2
4 14″ Pizza	73.9
5 min forced convection 0 °C 35 min free convection 20 °C	
1 14″ Pizza	36.5
2 14″ Pizza	57.3
3 14″ Pizza	66.6
4 14″ Pizza	71.8
5 min forced convection −10 °C 35 min free convection 20 °C	
1 14″ Pizza	30.6
2 14″ Pizza	53.7
3 14″ Pizza	64.1
4 14″ Pizza	69.8
5 min forced convection −20 °C 35 min free convection 20 °C	
1 14″ Pizza	24.7
2 14″ Pizza	50.1
3 14″ Pizza	61.45
4 14″ Pizza	67.8

melting point. The A70 and X70 PCM stopped charging with energy at temperatures of 54.98 and 55.0 °C, which is well below their melting point. A suggestion to fix this issue would be to integrate an electric heater, to ensure that the PCM reaches the melting point. This would surely increase the time for the pizza to cool down to 70 °C.
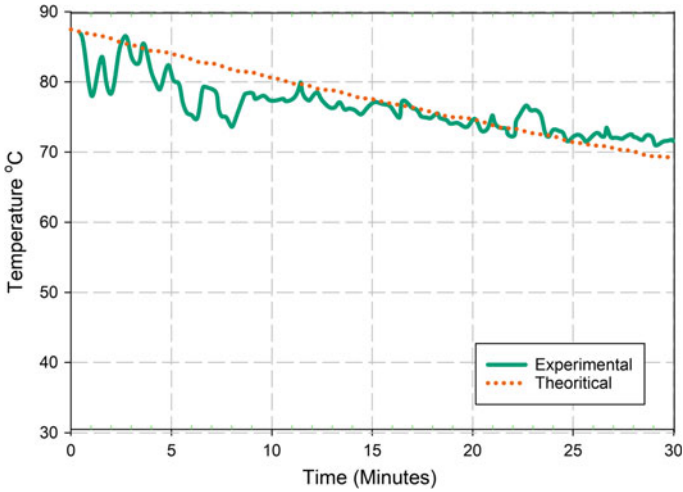
Fig. 14 Comparison between simulation and experimental results for bag with vacuum panel insulation for the bottom pizza
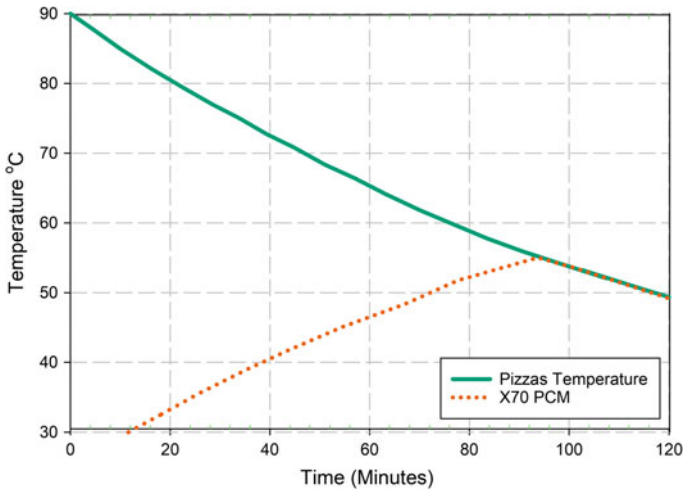

Fig. 15 Forced convection heat transfer analysis with an ambient temperature of 20 °C for a 16″ pizza bag with aerogel insulation integrated with A70 PCM
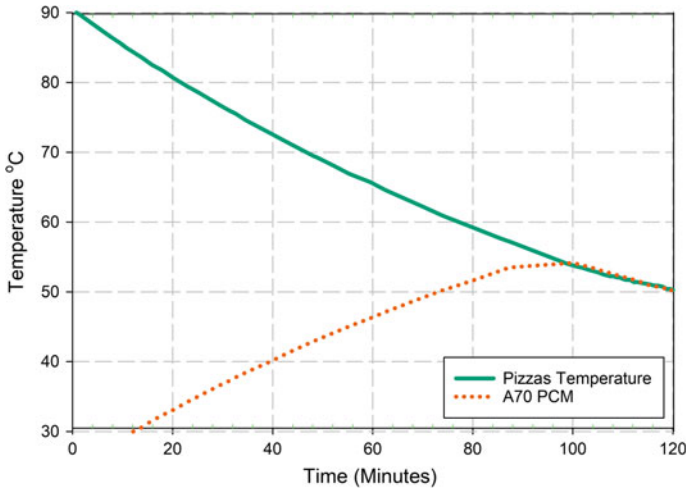
Fig. 16 Forced convection heat transfer analysis with an ambient temperature of 20 °C for a 16″ pizza bag with aerogel insulation integrated with X70 PCM

4.4 Cost Analysis Results for Insulation Materials and PCMs

Cost is a very important factor when it comes to making decisions when improving or introducing a new product. This comes as many insulation materials, active and passive systems would improve the performance of the bag drastically. However, the costs make them often an unfeasible solution. A summary of the prices of the materials used in this study are noted in Table 5. The prices are based in US dollars,

Table 5 Price list per unit ft^2

Material	Price (US$/ft^2)
Cork	2.36
Sheep felt	0.50
Polystyrene	0.032
Corrugated plastic	0.16
Fiberglass	2.18
Foam	0.28
Bamboo	0.10
Hemp	0.16
Zorb	0.05
Vacuum panel	2
Silicon heaters	20–30

Table 6 Material cost of making the bags using insulation materials explored

Cork and sheep (US$)	Polystyrene (US$)	Corrugated plastic (US$)	Fiberglass (US$)	Foam (US$)
19.40	0.20	1.70	12.60	1.7

as it is found that the average delivery bag cost 10–12 US$. The prices listed are based on the wholesale price quotes provided by the suppliers used in this study.

The material cost of making the bags using the insulation materials that were tested are summarized in Table 6.

5 Conclusions

The main concluding remarks obtained through the experimental and theoretical studies are presented. Furthermore, the recommendations based on the attained expertise are listed for future work. This chapter investigated various insulation materials, moisture absorption, and PCMs in the aim to improve and develop delivery bags. The following conclusions can be made from this study:

- The vacuum panel and the polyurethane insulated bag outperformed the original delivery bag.
- The rate of heat rejection was clearly higher in some instances from the vacuum panel and polyurethane insulated bag but that was only due to the pizzas temperatures being higher in the beginning of the experiment.
- The polyurethane foam bag has an advantage over the vacuum panel insulated bag as it is flexible and its structural rigidity is uncompromisable.
- Vacuum panels thermal insulation properties might be jeopardized if they break.
- Polyurethane foam is more widely available and is cheaper than both materials.
- The temperature drops experienced by the top pizzas in the delivery bags were as follows:

  - 12.8 °C (original bag), 12.8 °C (polyurethane bag), and 13.6 °C (original bag and vacuum panel).
  - The temperature drops experienced by the three middle pizzas in the delivery bags were as follows 7.9 °C (original bag), 15.2 °C (polyurethane bag), and 19.3 °C (original bag and vacuum panel).
  - The temperature drops experienced by the bottom pizzas in the three delivery bags were as follows 10.4 °C (original bag), 8.8 °C (polyurethane bag), and 15.3 °C (original bag and vacuum panel).

- PCMs are found to be excessively expensive for current usage in pizza bags.
- PCMs do not provide a significant performance increase.

– If PCMs are to be used inside the bags, it is recommended to heat the PCMs to their melting point before delivery takes place. This would allow the PCM to release latent thermal energy during delivery.

- The final temperature of the pizza was within 4.01% from the experimental result. Therefore, the heat transfer model was validated.
- Silicon heaters are also explored, and they are currently in use in certain bags. The silicon heaters work as they should.
- The cables of the heaters usually experience mechanical fatigue which would require replacing the unit.

In this chapter, various passive and active methods were investigated to improve and develop pizza delivery bags. The analysis and results presented in this chapter provide experts in the field with potential solutions and designs to improve or develop delivery bags. The following recommendations were based on the results of this study:

- The model developed should be used to simulate the use of other insulating materials and PCMs.
- Adsorption materials for higher temperature operations should be investigated, as often they are expensive.
- Further research in using air sealing within delivery bags should be done as it possesses excellent insulation properties and is economically viable.
- Further research should be done in organic materials that could be used for the outer and inner surface lining, to produce a fully biodegradable bag as an environmentally benign choice.
- A model to simulate relative humidity within pizza bags should be developed.

References

1. Statista (2015) Consumer spending on the pizza delivery in the U.S. https://www.statista.com/statistics/259168/pizza-delivery-consumer-spending-in-the-us. Accessed 05 Mar 2017
2. United States Department of Agriculture (2017) Takeout and delivered foods. https://www.fsis.usda.gov/wps/wcm/connect/d16db672-6013-43c9-bce8-40c69a23ade5/Safe_Handling_Take-Out_Foods.pdf?MOD=AJPERES. Accessed 07 Mar 2017
3. Castaigne F, Sablani S, Marcotte M, Baik O (2001) Thermal and physical properties of bakery products. Crit Rev Food Sci Nutr 41(5):321–352
4. Wang H, Sun D (2002) Melting characteristics of cheese: analysis of effect of cheese dimensions using computer vision techniques. J Food Eng 52(3):279–284
5. Du C, Sun D (2005) Pizza sauce spread classification using colour vision and support vector machines. J Food Eng 66(2):137–145
6. Liberopoulos G, Tsarouhas P (2005) Reliability analysis of an automated pizza production line. J Food Eng 69(1):79–96
7. Hasan A, Dincer I (2018) Experimental evaluation of thermal management options for bags. Appl Therm Eng. Available https://doi.org/10.1016/j.applthermaleng.2018.10.082

8. Yüksel N, Avcı A, Kılıç M (2012) The effective thermal conductivity of insulation materials reinforced with aluminium foil at low temperatures. Heat Mass Transfer 48(9):1569–1574. Available: https://doi.org/10.1007/s00231-012-1001-2

9. Schoolphysics (2013) Thermal data. http://www.schoolphysics.co.uk/data/Thermal%20data/index.html. Accessed: 23 Oct 2016

10. 3M™ Thinsulate™ Insulation (2018) 3M. https://www.3m.com/3M/en_US/thinsulate-us/

11. Hitachi - Refrigerator Features (2018) Hitachiconsumer.Com. https://www.hitachiconsumer.com/madeinjapanmicrosite/refrigerator-features-03.html

12. Current Results (2017) Average annual wind speed at Canadian cities. https://www.currentresults.com/Weather/Canada/Cities/wind-annual-average.php. Accessed 17 Apr 2017

13. Incropera F, DeWitt D (1985) Fundamentals of heat and mass transfer, 2nd edn. Wiley, New York, NY, United States

14. Nellis G, Klein S (2008) Heat transfer, 1st edn. Cambridge University Press, Cambridge, United Kingdom

Experimental and Numerical Shortest Route Optimization in Generating a Design Template for a Recreation Area in Kadifekale

Gülden Köktürk, Ayça Tokuç, T. Didem Altun, İrem Kale, F. Feyzal Özkaban, Özge Andiç Çakır and Aylin Şendemir

Abstract As cities grow, their complexity and the complexity of their infrastructure for various applications increase. Especially, transportation design is usually a very cumbersome process in current urban development models, and it is becoming more complex. Traditional approaches are not always sufficient to solve such complex problems, therefore, design disciplines like architecture and urban design need new tools to optimize many parameters related to their design. An alternate way to solve this problem can be via finding shortest routes. In this context, this study aims to evaluate different shortest path algorithms within a methodological approach to urban transportation planning via either experimentation or mathematical modeling. Three methods; namely live slime mold plasmodium, Floyd–Warshall algorithm, and ant

G. Köktürk (✉)
Department of Electrics and Electronics Engineering, Dokuz Eylul University, Izmir, Turkey
e-mail: gulden.kokturk@deu.edu.tr

A. Tokuç · T. D. Altun · İ. Kale · F. F. Özkaban
Department of Architecture, Dokuz Eylul University, Izmir, Turkey
e-mail: ayca.tokuc@deu.edu.tr

T. D. Altun
e-mail: didem.akyol@deu.edu.tr

İ. Kale
e-mail: irem.kale@btu.edu.tr

F. F. Özkaban
e-mail: feyzal.ozkaban@deu.edu.tr

İ. Kale
Department of Architecture, Bursa Technical University, Bursa, Turkey

Ö. Andiç Çakır
Application and Research Center for Testing and Analysis (EGE-MATAL), Ege University, Izmir, Turkey
e-mail: ozge.andic@ege.edu.tr

A. Şendemir
Department of Bioengineering, Ege University, Izmir, Turkey
e-mail: aylin.sendemir@ege.edu.tr

779

colony algorithm are used to design a template for routes within the historical Kadifekale district of Izmir, Turkey. The results from these approaches are compared, contrasted, and discussed in terms of their suitability for use as a guide for route creation. In conclusion, the parameters of an algorithm are significant on suggesting routes, thus the strengths and weaknesses of an algorithm should be carefully considered before application in a design problem.

Keywords Ant colony optimization (ACO) algorithm · Floyd–Warshall (FW) algorithm · Design template · *Physarum polycephalum* (*P. polycephalum*) · Route planning · Slime molds

List of Symbols

D_{ij} The density of pheromone trace between i and j
L_{ij} The length matrix of the edges
A_{ij} The result matrix defining shortest paths
p_{ij}^k The probability between node i and node j
ΔD_{ij}^k The increment of trail level of the edge connecting i and j by ant k
ΔD_{ij} The total increment of pheromone trace on the edge between i and j
η_{ij} Visibility from i to j
α The parameter regulating the effect of D_{ij}
β The parameter regulating the effect of η_{ij}
Q The pheromone amount produced per tour by ant
l_k The tour length of ant k
k Number of ants
λ Evaporation rate
t Number of iterations

1 Introduction

Cities are large constructs that shelter more than half of the human population on Earth. They are complex organisms, and the social and economic well-being of their inhabitants depend largely on the reliability and security of infrastructure systems such as transportation, water and waste flow, emergency services, land use, geographical information, telecommunication, and energy. As the number of inhabitants and the land area increases, the complexity of their networks also increases. Designing urban transportation networks and hubs to serve necessary physical, social, and cultural requirements is a problem in various scales. While non-motorized trips such as walking and biking were often discarded in the planning process, recent demand

made their relevance evident [1]. Parameters in the design of a walkable neighborhood can be classified under the headings of land use (density, diversity, commercial areas, recreational areas, and physical features), traffic safety, security, walking and cycling comfort (sidewalks, comfort elements, and barriers), accessibility (connectivity, non-residential areas, recreational areas, public transportation, and alternative routes), environmental esthetics and upkeep (buildings and natural elements), and others such as social relations within the neighborhood [2]. Aside from these parameters, a well-designed transportation network should decrease both construction and maintenance costs; environmental impacts as well as energy consumed for transportation [3], therefore, route design requires an optimization process that takes many parameters into account.

Solving the shortest path problem is fundamental in navigating complex networks and Dijkstra's algorithm is the most common methodology. This algorithm depends on trying all the possible alternatives and uses combinational optimization; however, in complex problems the computational time increases, especially if the shortest paths between all the node pairs in a network are required [4]. It gives an exact solution; however, combinational optimization in complex problems increase the computational time, therefore, they are inefficient in dealing with large-scale networks [5]. Instead, self-adaptive and iterative algorithms are proposed, such as the use of biologically based algorithms, cellular automata or genetic algorithms. New tools relying on these algorithms can be utilized in design disciplines such as architecture and urban design. A popular biologically based algorithm is ant colony optimization (ACO), which is mostly used for the traveling salesman problem; Haoxiong and Yang [6] utilize ACO to model a congested traffic network. Tero et al. [5] and Adamatzky et al. [7] propose an experimental approach to finding the shortest routes via conducting experimental studies on 2D maps with live biological organisms (slime molds).

Urban parks provide recreational pursuits in a local scale through their accessibility, their provisions to facilitate active pursuits, their capacity to provide opportunities to a wide range of users, and their semi-permanent nature; thus, park design is vitally important for population health [8]. This study aims to investigate the potential utilization of the shortest routes, generated by real slime mold organisms and also two shortest-route algorithms comparatively, to provide a design guide for the planning of routes within an urban recreational area in the historical Kadifekale in Izmir, Turkey. While utilizing shortest route optimization in urban transportation is a widely studied topic, the studies carried out on its use as a design input in urban or other design problems are very few, especially regarding slime mold experimental study, and there is no other similar study conducted in Turkey besides the authors' workgroup within the knowledge of the researchers. In this context, first, experiments with a biological optimization method are carried out (with live slime mold plasmodium) to determine potential pedestrian routes. Yet the experimental work was limited, especially because of the time cost related to the required large number of repetitive experiments for an increasing number of parameters.

One of the most common optimization methods related to transportation network design, the Floyd–Warshall (FW) algorithm, and another common biological-based algorithm, ACO, are also considered. The results from these algorithms are compared and evaluated in terms of their strengths and weaknesses from the point of their usability as a design guide template.

2   Background

Humans follow simple, reproducible mobility patterns, despite inherent anisotropy of their trajectories and travel distance [9]. Studies mostly focus on either betterment of the existing transportation network or designing new transportations systems that offer better options such as shortest routes or times [10]. Intelligent transportation systems and vehicle routing with cellular automata are fairly investigated. Meng and Weng [11] propose an improved cellular automata model to more accurately estimate traffic in work zones. Genetic algorithms rely on selection among a set of candidate routes competing for the optimum solution. Kır et al. [12] have worked on designing a route for a vehicle fleet from one central location to a number of points with the least cost. The central location has a limited capacity. While their string length is usually fixed, Pattnaik et al. [13] propose a variable string length to iteratively change the route set size and the set of solution routes simultaneously. Some common and novel methods include slime mold, FW, and ACO. They are detailed below.

2.1   Slime Mold

The problem of network growth can be found in the food searching mechanism of the plasmodium of *Physarum (P.) polycephalum* species of slime molds, an acellular living organism without either a brain or a nervous system. In order to use the resources in the most efficient way, slime molds combine with cells of their own kind and form a colony, which can be called as a "super organism," and move toward a food source. The food searching mechanism is complex in terms of proximity to food, the type of food, and if it has been to the search site before. It first explores all of the uncharted territory around itself and leaves a chemical sign wherever it has been; it does not go on the same route again until it finds food. It can also create a network connecting multiple food sources. Based on this behavior, Zhang et al. [14] and Adamatzky et al. [7] propose an algorithm of traffic flow between two cities using a gravity model emulating this behavior of slime molds. They explore the cost, efficiency, and robustness of the stable-state network.

Tero et al. [5] created a small map of Tokyo with 17 cm width and placed food on 36 main points of the transportation network. They placed *P. polycephalum* on a central point and observed its growth toward the other points. At the beginning, the plasmodium showed a uniform expansion, yet it created an intricate web as it encountered

food and connected the food sources with thick tubes. They measured and normalized lengths, error tolerances, and minimum lengths between food sources. The authors conclude that the plasmodium made a transportation and distribution network nearly as successful as human engineers.

Adamatzky et al. [7] explored the possibilities of slime mold route modeling on experimental agar models representing the routes of 14 different geographies. After studying the approximation between real roads and plasmodium generated road networks, they have found similarities between manmade roads, yet have not reached a conclusive decision.

Adamatzky [15] and his working group experimentally studied a terrain with elevations in terms of approximation of an actual motorway; the longest route in the USA, Route 20, and the longest national motorway in Europe, Autobahn 7. They built 3D terrain plastic models and placed *P. polycephalum* at an end point of a road and placed food on the other end. In addition, they have done control studies on one flat map and one map without any food. Their results show that the plasmoid found longer routes than the realized one in all cases and path configurations were determined by a level of activity with higher levels of activity leading to shorter paths.

Altun et al. [16] evaluated the road network of Izmir. They experimentally observed the propagation of *P. polycephalum* in Izmir on a two-dimensional map. They later mimicked its behavior using an algorithm developed by utilizing cellular automata and compared its results to the experiments. As a result, their observations have shown that the slime molds optimized the distance between different points, while they were finding the shortest path. They found that the plasmoid steadily performed the task better and in a shorter amount of time.

2.2 Floyd–Warshall Algorithm

FW is a graph search algorithm similar to Dijkstra's. While the Dijkstra algorithm looks at vertices and finds the shortest path between a pair of vertices (nodes), the FW algorithm looks at all pairs of vertices (nodes) to find the shortest path [4]. The FW algorithm is a graph theory-based algorithm that was developed as an alternative to the Dijkstra algorithm. The Dijkstra algorithm is not suitable when the weight function is arbitrary. The FW algorithm is used when the weight function is not positively limited because there is no point in finding the shortest path to any node if there is a negative round starting at i and ending at i.

Pradhan and Mahinthakumar [4] solve the transportation for New York city using both of the algorithms with parallel computing to make the process more efficient and less time-consuming, so that the transportation structure can be monitored and modified in real-time in times of emergency. Since transportation network is dependent on scale, most of the efficient parallel algorithms cannot work with the FW algorithm. Pradhan and Mahinthakumar [4] recommend FW algorithm in large-scale networks because it is scalable and Dijkstra-I is not scalable in terms of memory;

they also recommend the use of functional decomposition in smaller problems and domain decomposition in larger problems. Mączka [17] examined the achievement of the infrastructure goal of the European Commission [18] described as "90% of travelers within Europe are able to complete their journey, door-to-door within 4 h." He proposed a visualized model with daily accessibility as the focus. His FW-based tool does not take time and cost as inputs, yet it provides policy-relevant information about the quality of the transportation network and can be used to evaluate the impact of intervention in quantifiable terms. Sangaiah et al. [19] focused on providing an optimal decision and advisory procedure for various cities in China, especially for the use of tourists. They propose to use FW algorithm in a graph with edge weights.

Matsumoto et al. [3] propose a model to optimize the ideal form of the city and transportation network, taking into account the preferences of citizens and modes of transportation. They firstly express the city in terms of zones (residential, commercial, and working) and calculate the route, which minimizes the actual distance and degree of congestion by FW algorithm. Secondly, they survey the inhabitants on which zone, route, and mobility (walk, bus, bicycle, car, and railway) to move. Then they estimate the parameters, which influence inhabitants' decisions based on their decisions, and evaluate the city form based on these evaluation scores. Consequently, they evaluated Chuo-ku ward and Nadaku ward in Kobe, Japan and proposed several suggestions.

2.3 Ant Colony Optimization Algorithm

Ants are living organisms that can find the shortest path between a food source and their nests, but they also adapt to environmental conditions. Behaviors of ants in biological systems have encouraged a number of methods and techniques. The most successful technique is the general optimization technique known as ACO [20]. The ants benefit from chemical communication that enables them to communicate with each other instead of sight-sensing while finding the shortest path to their nest because their vision is weak. Ants establish a connection with each other through a chemical called 'pheromone'. When an ant moves away from the nest to find food, it leaves pheromone on its way. The possibility of another ant following the same path depends on the amount of pheromone. If the pheromone amounts of all directions are the same, the probability of choosing any of these roads is the same. When the amount of pheromone left by the ants in each direction is considered equal, the shortest paths will have more pheromone per unit time. Thus, the shortest path in relation to time will be selected by ants.

Finding the shortest path to the food of real ant colonies is a process of optimization in nature. The ability to find the shortest path going to the food is performed with ACO in the artificial platform [21, 22]. It is a self-adaptive iterative algorithm, yet it is stochastic and cannot guarantee to find the shortest route [23]. ACO is mostly used for the traveling salesman problem; Haoxiong and Yang [6] utilize this algorithm to model a congested traffic network. ACO algorithm was also proposed for a number of urban network problems. They include limiting urban growth boundaries

[24], efficient control of the physical flow of the supply chain [25], tsunami evacuation zones [26], water resource management [27], and electrical power distribution networks [28].

In addition to the aforementioned studies, some hybrid algorithms were proposed for optimization with ACO including; a hybrid of cellular automata and ACO for spatial land-use allocation [29], a hybrid of ACO with artificial bee colony for distributed energy resources [30], a hybrid of slime mold and ACO for the traveling salesman problem [31], and a hybrid of cellular automata and ACO for zoning of protected natural areas [32].

3   Case of a Recreation Area in Kadifekale

The topic of this study is the generation of a design template with different shortest-route algorithms for the design of walking route in a new recreation area in Izmir. Izmir is the third most-crowded city of the Turkey and is located on the West coast of the country, at Aegean Gulf. The selected site is within the boundaries of old city of Izmir, located in the Kemeraltı District. This site is located between the area, where Alexander the Great reconstructed the city of Symrna in fourth century BC and has been continuously in use until today, and the traditional commercial center of Izmir (Fig. 1). This region contains a number of archeological remains, examples of monumental buildings and civil architecture from Hellenistic, Roman, Byzantine, Ottoman, and Republican periods. The main buildings that contain the inherent cultural values of the region include the agora, theater, stadium, and castle

Fig. 1   Location of the site in Izmir

from the Antiquity; a cistern from the Byzantine period; a large number of inns, baths, mosques, synagogues, churches, and traditional dwellings from the Ottoman period; and commercial buildings and dwellings belonging to the Republican period. The region continued to be a city center from the ancient period till the 1950s; however, it has suffered serious physical and social losses in quality due to both the shift of the city center from the region to the neighboring Alsancak district and intense migration to the area from inside the city. These losses also triggered protection efforts in the region.

In order to preserve the multi-layered cultural structure of the region, the "Traditional Trade and Housing Areas of the Kemeraltı Region" were declared as an urban protection area in 1978. Registration of buildings for conservation started and the development plan of the area for protection purpose was prepared in 1982.

Nowadays, many studies are being carried out in the field within the scope of the Izmir-History Project initiated by the Izmir Metropolitan Municipality, in order to revitalize the region and to make its historical value visible. One of these studies [33] covers the subject area of this chapter. In the early 2000s, massive landslides occurred after heavy rains due to high groundwater levels and steep topographical structure of the region. This caused damages to many residential buildings constructed after 1950s, which were shanty houses. The landslide area was declared as a disaster area by the municipality in 2003, and the residences in this area were expropriated and evacuated. All of the structures at risk were demolished and areas, which are not suitable for construction, are planned to be designed as a recreational area. Within the scope of this reorganization, the site selected for the recreational area is located within the area suggested for the formation of experimental routes (Fig. 2).

After the demolition of the building stock at risk, there remains a big gap in the urban fabric on the slopes between the historical commercial area of the city (Kemeraltı) and Kadifekale. This area, where urban lifestyle is interrupted, must be rapidly integrated into the regional lifestyle, preferably with recreation purpose. The site, designated as the case area of this book chapter is a small part of this large urban vacuum. The main reason for choosing this site is that this land is located at the end of Patlıcanlı Slope, one of the important arteries that connect the Smyrna Agora to Kadifekale. One of the experience routes proposed by the municipality to the historical and cultural values of the region goes through the Patlıcanlı Slope and the selected site. For this reason, the selected site is a priority for the design works in the landslide area.

Fig. 2 Pre-planning studies of experience routes in the context of Izmir-city project [33]

4 Methods

In this study, first of all, living organism experiments were realized on slime mold plasmodium in petri dishes that contain maps of the Kadifekale region. After that, the results of these experiments are comparatively discussed with shortest-route algorithms frequently found in the literature. The reason of this duality is to see whether the algorithms will give a similar result to living organisms—as seen from the slime mold studies in the literature. In addition, experiments need to be repeated many times in order to find out if the experimental results are meaningful, and this requires a long time. The shortest path algorithms are based on graph theory, but the bio-based algorithms are related to the life cycle of living things and their use is increasing with investigations concerning living beings life and technological progress. In this study,
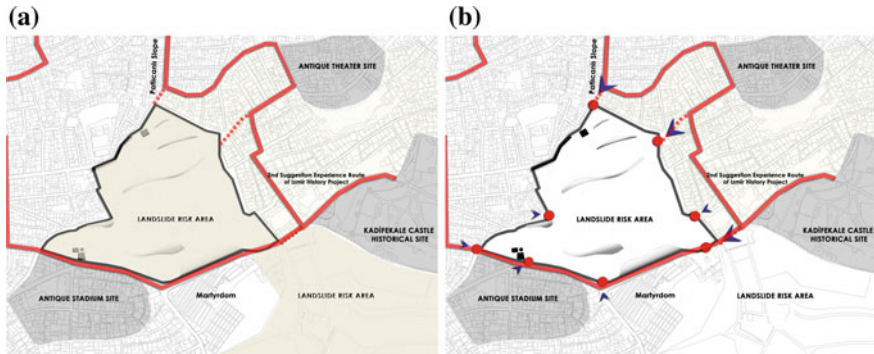
Fig. 3 The problem site; **a** 2D map preparation and **b** entrances and exits

we have investigated both methods which are graph theory-based and biological-based algorithms. These methods used in simulations are FW algorithm and ACO algorithm, respectively. While the former algorithm is the shortest path algorithm based on graph theory, the latter is a biological-based algorithm. There are many bio-based algorithms, but ACO algorithm is selected because of its similarity to the slime mold algorithm [34]. The simulation was implemented using Matlab version 7.10 (R2018b) and executed on an intel core i3 processor at 1.4 GHz with 4 GB RAM running on Windows 10 operating system.

4.1 Map Preparation for Experiment

The study began with the preparation of the map for the site. At this stage, firstly a 2D map was generated. Bevels, sets, chamfers in the topography and historical buildings were marked. Then, important access points were determined to mark entrances and exits (E1–E8 in Fig. 3). The main considerations at this phase were the contextual data, archeological sites, and potential experience routes.

4.2 Slime Mold Experiment

In the live slime mold plasmodium experiments, map of the problem site was represented on the agar surface in 9 cm petri dishes. Sudden topographic shifts were transferred by cutting away the agar since organisms could not thrive there, just like humans do not prefer to climb on a steep slope. Three petri dishes were cultivated using this method; in the first experiment oat flakes (the food source) were placed on all entry and exit points from E1 to E8, and the organism was left on one of them, this petri dish was observed for 4 days. In the second and third experiments, two more
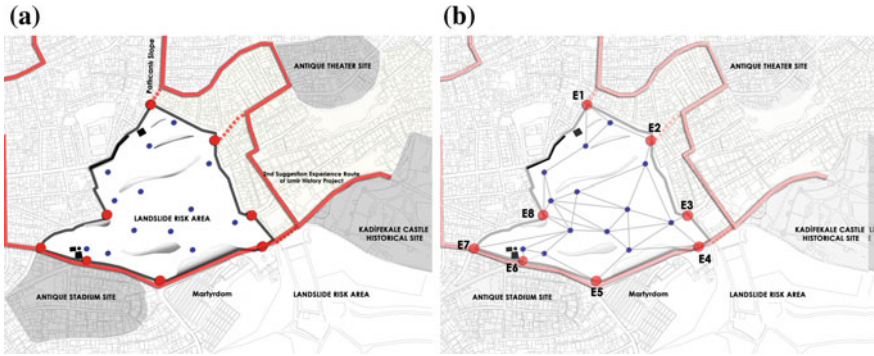
Fig. 4 The problem site; **a** potential interior points for the site and **b** all possible network

oat flakes were randomly placed on two points near the center of the site besides all of the entry-exit points. These two petri dishes were observed for 7 days.

4.3 Map Preperation for Simulation

At the following phase, interior focus points (Fig. 4a) were determined according to the constraints in the site such as historical buildings, topography, and bevels. The reasoning in their placement is to determine as many random points as possible to allow for experiencing the whole site. At last, all of the possible paths were drawn. In the numerical stage of the study, shortest paths were found between points by FW and ACO algorithms (Fig. 4b).

4.4 Floyd–Warshall Algorithm

The most preferred algorithm to find the shortest path is the Dijkstra algorithm. It is mainly chosen because of its short calculation time. However, negatively weighted edges cannot be calculated in Dijkstra algorithm. The FW algorithm is an algorithm that considers the value of the negatively weighted edges. Therefore, in the study, FW algorithm is used instead of the Dijkstra algorithm. Another reason for choosing FW algorithm is the simple coding and the higher productivity in practice. Moreover, FW algorithm in the frequent graphs has high efficiency.

The FW algorithm is an algorithm used to find the shortest path between all node pairs on a graph. The Eq. 4 is used for each i, j node in this algorithm.

$$D_{ij} = \min(D_{ij}, D_{ik} + D_{kj}) \tag{1}$$

In other words, if there is another way to go from i to j, passing through the k-node and this path is shorter, this path between i and j is chosen as the new path.

Let take a directional graph $G(V, E)$ with n-knotted and arbitrary weight function where V is the set of nodes and E is the set of edges. We regard A_{ij} and D_{ij} as $n \times n$ matrices. Shortest path algorithm for this algorithm can be formulated as,

$$\begin{aligned} A_{ij}^k = A_{ij}^{k-1} \text{ and } D_{ij}^k = D_{ij}^{k-1}, & \qquad \text{if } L_{ij}^{k-1} \leq L_{ik}^{k-1} + L_{ij}^{k-1} \\ A_{ij}^k = A_{ij}^{k-1} + A_{kj}^{k-1} \text{ and } D_{ij}^k = D_{ik}^{k-1}, & \text{ otherwise} \end{aligned} \qquad (2)$$

where L_{ij} is a matrix which gives the length of the edges, D_{ij} is weight matrix for the graph, and A_{ij} is a result matrix defining shortest paths. The FW algorithm can also find negative cycles in graph.

4.5 Ant Colony Optimization Algorithm

ACO is a recursive algorithm. In this algorithm, ant behavior is found by a simulation. In the simulation, each edge, which is intuitively located by the ant and gives the distances between the changed nodes, is related to the pheromone amount released by earlier ants. Each ant leaves a trace as it moves from one node to the other. An ant never passes again through a node which it passes once, it moves to the next node in a probabilistic mechanism at every stage of pheromone making [22, 23].

In one tour, each ant leaves the amount of pheromone by Q/l_k where Q is constant and l_k is tour length. Thus, more pheromone accumulates on the edges of shorter lengths and less pheromone occurs on the edges with longer distances. In addition, evaporation rate λ plays an important role in pheromone accumulation. The pheromone values in each iteration step are updated by ants that produce the solution. The trace level of th edge connecting i and j; D_{ij} is updated according to the equation shown below,

$$D_{ij} = (1 - \lambda)D_{ij} + \sum_{k=1}^{m} \Delta D_{ij}^k \qquad (3)$$

where

$$\Delta D_{ij}^k = \begin{cases} Q/l_k & \text{if ant } k \text{ used the edge connecting } i \text{ and } j \text{ in its tour,} \\ 0 & \text{otherwise} \end{cases} \qquad (4)$$

Furthermore, t is number of iterations, $\lambda \in [0, 1]$ is evaporation rate, k is ant number, ΔD_{ij}^k increase of trail level of the edge connecting i and j by ant k, ΔD_{ij}^k is the increment of trail level on the edge connecting i and j by ant k, ΔD_{ij} is the total increment of pheromone trace on the edge between i and j, Q is the pheromone amount produced per tour by ant and is constant, l_k is the tour length of ant k.

In the solution process, ants choose the next destination with a probabilistic mechanism. The higher the probability of the selection of the node to be visited, the higher the level of the track going to this point. This adaptive behavior is based on trace levels and is regulated by the α parameter. The more voracious behavior depends on visibility and is regulated by the β parameter. Ant k when staying in node i, the probability of going to node j,

$$
p_{ij}^k = \begin{cases} \frac{D_{ij}^\alpha \eta_{ij}^\beta}{\sum D_{ij}^\alpha \eta_{ij}^\beta} & \text{if it is taking part in the set of nodes that have not been visited yet} \\ 0 & \text{otherwise} \end{cases}
$$

(5)

where D_{ij} is the density of pheromone trace between i and j, η_{ij} is visibility from i to j, α is the parameter regulating the effect of D_{ij}, β is the parameter regulating the effect of η_{ij}. This selection process continues until all ants have completed a tour. The visited nodes are reduced by one in each recursion t (where t is iteration counter). Through the visit, one node remains and the probability of this node is $p_{ij} = 1$. The length of the tour created for each ant is calculated and updated to the best tour found so far. The next iteration $t + 1$ is started according to the updated pheromone level [33].

In ant systems, each ant leaves pheromones in quantities in accordance with the total length of the route. The existing paths are related to a factor named evaporation rate, λ. The pheromone value is updated by all the ants at each iteration. ACO algorithm highly correlates to the parameters λ, α, and β in the algorithm. In this study, the parameters α and β are fixed to 1 [35]. The optimum value for the parameter λ is experimentally calculated. 0.1 is the optimum value and is used in this solution. Another parameter affecting the algorithm is the number of ants. Although increasing the number of ants improves the solution, increases the time cost of the algorithm. Therefore, the number of ants is selected to be equal to the number of nodes [36]. Either exponential distribution or Poisson distribution can be used to determine the movement of ants. In this study, the exponential distribution was preferred since the operation time in Poisson distribution is higher than the exponential distribution.

The assumptions for the ant model are: (1) each edge between nodes i and j has a resistance proportional to the length of the connected edge D_{ij}, (2) ants travel from edges with a higher resistance to edges with a lower resistance, and (3) the number of ants are fixed in the beginning, they are free to move to the other nodes during the iterations.

The number of ants in each node and the pheromone amount are shown in Fig. 5, when the shortest path is calculated to ACO algorithm from node 'E7' to node 'E1'. The x-axis in Fig. 5 shows the number of iterations. It is 100,000 in this case. As can be seen from Fig. 5, the number of ants in each node reaches a balance as the number of iterations increases. Similarly, the total amount of pheromone reaches an equilibrium value or oscillates between a specific range (from 160 to 180).
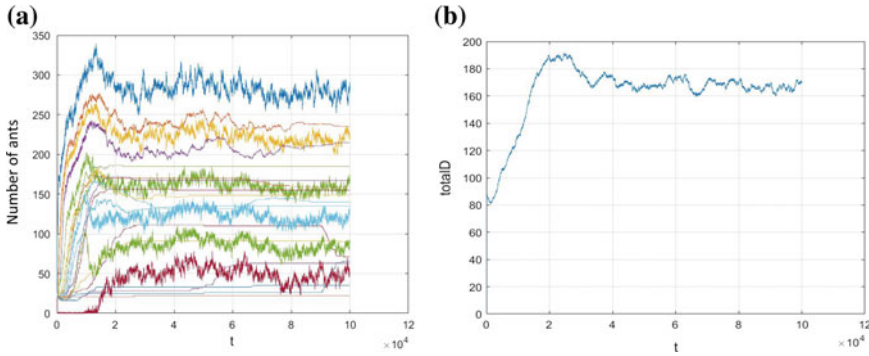
Fig. 5 According to the iteration number from 'E7' to 'E1'; **a** the number of ants in each node and **b** the total pheromone amounts

5 Results and Discussion

Results from the first live slime mold plasmodium experiments are seen in Fig. 6. As can be seen in Fig. 6a, slime mold plasmodium tracks paths only on the edges of the site, in other words between the entrance/exit points in all of the dishes. This is due to absence of food at the center of the area. In the second (Fig. 6b) and third experiments (Fig. 6c), oat flakes are left at the inner regions of the site randomly, and this triggered alternative routes and created a more invasive network. The final diagram of the slime mold network, superposed from the three experiments, is shown in Fig. 7.

Parameters like the evaporation rate, the pheromone amounts, etc., in ACO algorithm are very important for this shortest path problem. When the algorithm is executed, all parameters must be optimized for the application area. Therefore, the calculating shortest paths using ACO algorithm are different than the FW algorithm. Since the FW algorithm is based on graph theory, it takes longer to find the shortest paths than the Dijkstra algorithm in terms of computation time.
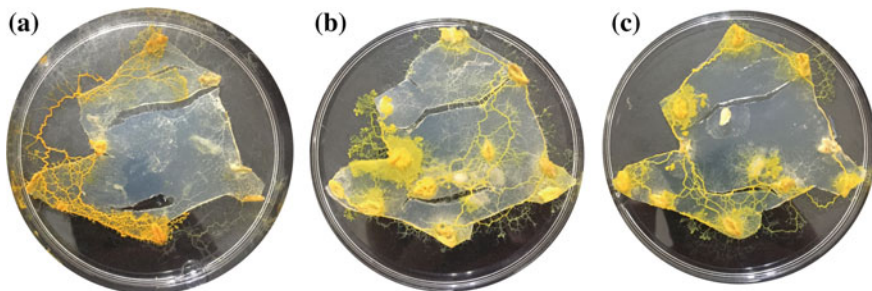

Fig. 6 Experiments with plasmodium in petri dishes

Fig. 7 Superposition of the thickest routes of the shortest paths of live plasmodium

The exponential distributed ACO algorithm and FW algorithm was run for each starting point, from point E1 to point E8. Shortest paths were established in all possible path combinations; the most preferred routes (their thickness is related to their preference frequency) are selected and the results are superposed on the map in Fig. 8 for ACO algorithm and Fig. 9 for FW algorithm. First of all, the main outline of the final graphics is similar, but algorithms could be different in details of the paths. FW algorithm generally points out the shortest links between entrance and exit points in real length measurements and it could be easily perceived. But ACO algorithm runs independent of these lengths. For example, for the shortest path between A and D points (as entrance A, exit D) is measured as 410.85 m in the FW algorithm and 489.86 m in the ACO algorithm; or between F and B points (as entrance F, exit B) is measured as 286.48 m in the FW algorithm and 354.41 m in the ACO algorithm.

It can be said that in FW algorithms shortest paths are reciprocal, for example the paths from entrance A to the exit F are exactly the same as the paths from entrance F to exit A. Meanwhile, the ACO algorithm is obtained by the mathematically modeling the life cycle of ants based on observations. The pheromone amount of ants from source to sink is important in determining the path between these two nodes. Since the ACO algorithm is biologically based, it is preferred in the study because it offers alternative ways in urban planning and is similar to slime mold algorithm, although it cannot find the shortest paths of the FW algorithm.
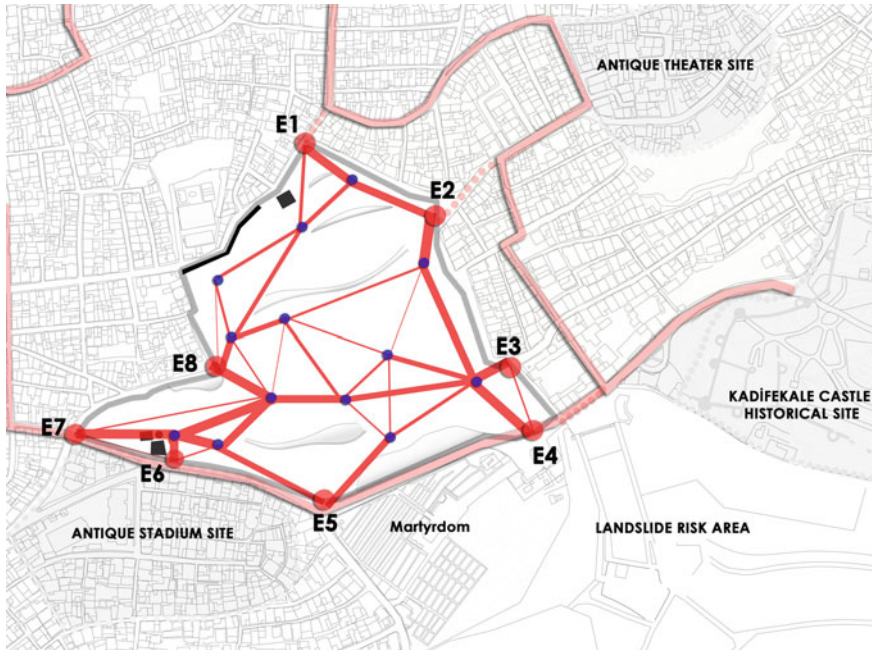
Fig. 8 Superposition of the most preferred routes of the shortest paths from ACO

In this study, the time cost is also investigated for the ACO algorithm and the FW algorithm. The elapsed time for the FW algorithm is 0.4343 and is 229.0451 s for the ACO algorithm. The FW algorithm has a much shorter result, but this is due to the difference in the number of iterations of the algorithms. While the number of iterations in the FW algorithm depends on the matrix size, the time cost is higher because the 100,000 iterations are performed in the ACO algorithm. In addition, the number of iterations in the ACO algorithm are determined by the user. In this algorithm, time cost can be improved by decreasing the number of iterations. The elapsed time in FW algorithm depends on the graph matrix. Therefore, the processing time is shorter.

Accordingly it can be said that bio-based algorithms like ACO algorithm could run as good as graph theory-based algorithms like FW algorithm. Biological-based algorithms are obtained by modeling the life cycles of living things in nature. In nature, there are different species that reach the food source by using the shortest route. Some of these are slime mold and ant. It is exciting that the way of finding the shortest path of living things can be applied to current problems through an algorithm. Therefore, ACO algorithm was used and compared with a graph theory-based algorithm. As a result, it has been shown that biological-based algorithms such as ACO algorithm can be easily applied to urban planning problems.

It is possible to say that the final routes from the petri experiments (Fig. 7) are substantially similar to the final schemes from the ACO and FW algorithms
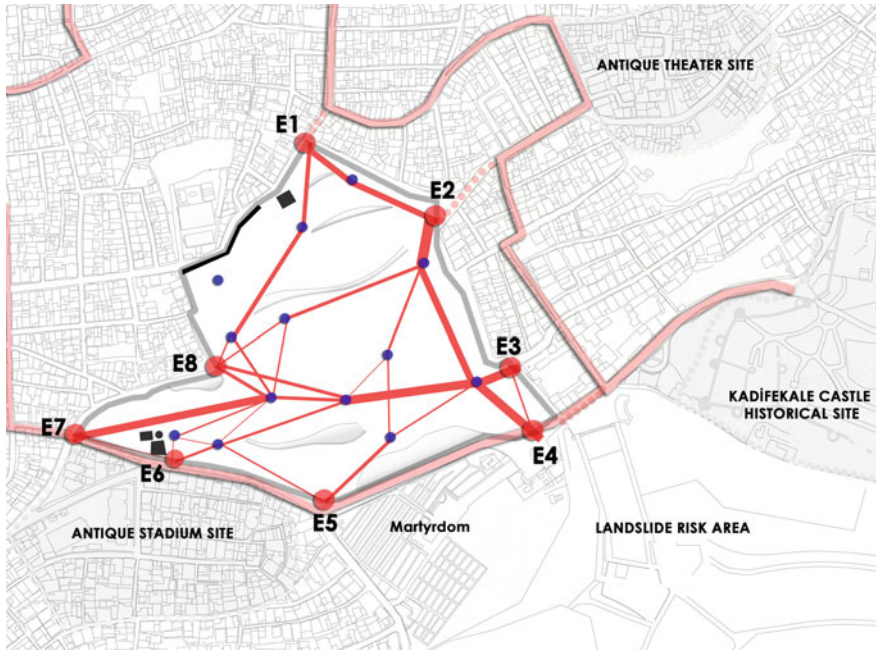
Fig. 9 Superposition of the most preferred routes of the shortest paths from FW

(Figs. 8 and 9). A strong path between E3 and E8 and between E1–E2–E3–E4 could be seen in all methods. Surprisingly, there is a completely flat path on this same line inside the site in reality. However, a concentration is observed at the left side of the site, and the less preferred areas and routes can be perceived from these graphs. The concentrated region is high and flat, dominates the entire site, and has a good landscape in reality.

The final synthesis and proposed design template can be seen in Fig. 10. Some arguments could be proposed in the context of urban design, when considering the results from the petri experiments and the two algorithms. The concentration point at the southwest of the site has the potential to be a focal point, thus, it could be incorporated into the design as an important focus and could dominate the entire site (Fig. 10a). Final routes can be designated as the most active paths for people. People would walk quickly on the main paths; therefore, they could be paved with a rough material (Fig. 10b). Small sales units could also be placed on these paths. Less preferred areas and routes can be evaluated as another design criteria. The points not on the shortest routes display a more passive character in the recreational area. These paths between points can be designed for not so active uses; such as long walks, picnic areas, little amphitheaters, and green areas. They can be paved with a different and more natural cover. Benches and other urban furniture could be placed along these paths.
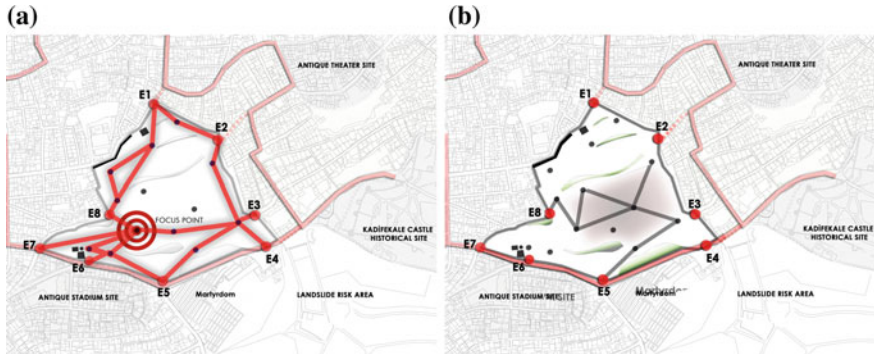
Fig. 10 Final synthesis, **a** concentration point and **b** the proposed design

6 Conclusion

Planning the urban roads or substructure networks is usually a very cumbersome process in urban development models. This interdisciplinary study does not only generate a design base for Kadifekale Recreation Area, it also suggests a new methodology for network generation in urban design, based on shortest path finding. Although there are many studies using the shortest path algorithms for diverse network problems in the urban scale, traditional approaches are not always sufficient to solve these complex problems in terms of human movement and land use. In the specific case of Kadifekale, all of the methods had some similarities. In the first method, real plasmodium experiments, made use of the food searching mechanism of the slime molds on real 2D maps. The routes generated in this method are the most diverse. The second method, FW is a conventional method and displays the shortest routes, yet it is insufficient in modeling parameters besides shortest paths, and leads to the least variety. However, the bio-based ACO can lead to more diverse routes and connections between nodes. While these results can be contributed to the limited number of focal points given as an input to the algorithms, plasmodium experiments benefitted from only two predetermined points. Thus, the wealth of results shows that even though some methods try to mimick natural processes, they are still limited by the strengths and weaknesses of their algorithms.

The three shortest path methods, in this study, can be used to determine the most preferential routes. While these results are for a design problem of small scale and can lead to more or less predictable outcomes, they can be very valuable for bigger areas in the urban scale. The determination of most frequent and shortest routes is a novel design tool that can be incorporated in the first stage of a design problem for empty lots to generate a site-specific design template for an urban route or infrastructure network. Therefore, the inputs and parameters of the methods are significant on suggesting routes since correct design decisions in the early design stage significantly affect the construction costs and lifecycle environmental costs of the application.

In the future studies, more templates will be generated for the Kadifekale Recreation Area with more plasmoid experiments utilizing all of the entrance-exit pairs on both a 2D map and a 3D model. Furthermore, other biologically based algorithms will be simulated to generate design templates. After all the templates are generated, their utilization as a predesign tool will be evaluated to propose rules of thumb for application in design problems. These models would then be analyzed in terms of monetary and lifecycle environmental costs and refined by learning from each other.

References

1. Aziz HA, Park BH, Morton A, Stewart RN, Hilliard M, Maness M (2018) A high resolution agent-based model to support walk-bicycle infrastructure investment decisions: a case study with New York city. Transp Res Part C Emerg Technol 86:280–299
2. Cubukcu E (2013) Walking for sustainable living. Procedia Soc Behav Sci 85:33–42
3. Matsumoto T, Tamaki H, Inamoto T (2010) Autonomous decentralized simulation model of city and urban traffic. In: Proceedings of SICE annual conference 2010, IEEE, pp 1021–1026
4. Pradhan A, Mahinthakumar G (2012) Finding all-pairs shortest path for a large-scale transportation network using parallel FW and parallel Dijkstra algorithms. J Comput Civ Eng 27(3):263–273
5. Tero A, Kobayashi R, Nakagaki T (2006) Physarum solver: a biologically inspired method of road-network navigation. Phys A Stat Mech Appl 363(1):115–119
6. Haoxiong Y, Yang H (2015) Congested traffic based on ant colony algorithm for shortest path algorithm. In: Logistics, informatics and service sciences (LISS), IEEE, pp 1–3
7. Adamatzky A, Akl S, Alonso-Sanz R, Van Dessel W, Ibrahim Z, Ilachinski A, Jones J, Kayem AV, Martínez GJ, De Oliveira P, Prokopenko M (2013) Are motorways rational from slime mould's point of view? Int J Parallel Emergent Distrib Syst 28(3):230–248
8. McCormack GR, Rock M, Toohey AM, Hignell D (2010) Characteristics of urban parks associated with park use and physical activity: a review of qualitative research. Health Place 16(4):712–726
9. Gonzalez MC, Hidalgo CA, Barabasi AL (2008) Understanding individual human mobility patterns. Nature 453:779–782
10. Fatnassi E, Chaouachi J, Klibi W (2015) Planning and operating a shared goods and passengers on-demand rapid transit system for sustainable city-logistics. Transp Res Part B Methodological 81:440–460
11. Meng Q, Weng J (2011) An improved cellular automata model for heterogeneous work zone traffic. Transp Res Part C Emerg Technol 19(6):1263–1275
12. Kır S, Yazgan HR, Tüncel E (2017) A novel heuristic algorithm for capacitated vehicle routing problem. J Ind Eng Int 13(3):323–330
13. Pattnaik SB, Mohan S, Tom VM (1998) Urban bus transit route network design using genetic algorithm. J Transp Eng 124(4):368–375
14. Zhang X, Adamatzky A, Chan FT, Deng Y, Yang H, Yang XS, Mahadevan S (2015) A biologically inspired network design model. Scientific reports, 5
15. Adamatzky A (ed) (2016) Advances in physarum machines: sensing and computing with slime mould. Springer, Berlin
16. Altun A, Köktürk G, Özkaban F, Deniz Can İ, Tokuç A, Kale İ (2019) Physarum Polycephalum Cıvık Mantarları Kullanılarak Yol İzlerinin Bulunması: İzmir Örneği et al. Scientific report
17. Mączka M (2016) Accessibility model for the evaluation of transport infrastructure policy. Trans Inst Aviat 4(245):116–133
18. European Commission (2011) White paper, roadmap to a single European transport area—towards a competitive and resource efficient transport system. Retrieved from http://ec.europa.eu/transport/themes/strategies/2011_white_paper_en.htm. Accessed 1.05.2019

19. Sangaiah AK, Han M, Zhang S (2014) An investigation of Dijkstra and Floyd algorithms in national city traffic advisory procedures. Int J Comput Sci Mob Comput 3(2):124–138
20. Dorigo M, Gambardella LM (1997) Ant colony system: a cooperative learning approach to the traveling salesman problem. IEEE Trans Evol Comput 1(1):53–66
21. Dorigo M, Birattari M, Stutzle T (2006) Ant colony optimization: artificial ants as a computational intelligence technique. IEEE Comput Intell Mag 1556–603X:28–39
22. Wang H, Wang Z, Yu L, Wang X, Liu C (2018) Ant colony optimization with improved potential field heuristic for robot path planning. In: Proceedings of the 37th Chinese control conference, July 25–27, Wuhan, China
23. Liu Z, Yawei K, Bin S (2016) An improved genetic algorithm based on the shortest path problem. In: 2016 IEEE international conference on information and automation (ICIA), pp 328–332
24. Ma S, Li X, Cai Y (2017) Delimiting the urban growth boundaries with a modified ant colony optimization model. Comput Environ Urban Syst 62:146–155
25. Musa R, Arnaout JP, Jung H (2010) Ant colony optimization algorithm to solve for the transportation problem of cross-docking network. Comput Ind Eng 59(1):85–92
26. Forcael E, González V, Orozco F, Vargas S, Pantoja A, Moscoso P (2014) Ant colony optimization model for tsunamis evacuation routes. Comput Aided Civ Infrastruct Eng 29(10):723–737
27. Afshar A, Massoumi F, Afshar A, Mariño MA (2015) State of the art review of ant colony optimization applications in water resource management. Water Resour Manage 29(11):3891–3904
28. Gomez JF, Khodr HM, De Oliveira PM, Ocque L, Yusta JM, Villasana R, Urdaneta AJ (2004) Ant colony system algorithm for the planning of primary distribution circuits. IEEE Trans Power Syst 19(2):996–1004
29. Mi N, Hou J, Mi W, Song N (2015) Optimal spatial land-use allocation for limited development ecological zones based on the geographic information system and a genetic ant colony algorithm. Int J Geogr Inf Sci 29(12):2174–2193
30. Kefayat M, Ara AL, Niaki SN (2015) A hybrid of ant colony optimization and artificial bee colony algorithm for probabilistic optimal placement and sizing of distributed energy resources. Energy Convers Manage 92:149–161
31. Zhang Z, Gao C, Liu Y, Qian T (2014) A universal optimization strategy for ant colony optimization algorithms based on the Physarum-inspired mathematical model. Bioinspiration Biomimetics 9(3):036006
32. Li D (2011) Shortest paths through a reinforced random walk. Uppsala University project report
33. Dokuz Eylul University, Faculty of Architecture (2015) Izmir-history project Anafartalar street 2nd stage and 1st circle pre-planning of housing pattern through operational plan final report, Izmir
34. Jones J (2015) From pattern formation to material computation: multi-agent modelling of physarum polycephalum. Springer Publishing, Berlin, ISBN 978-3-319-16823-4
35. Dorigo M, Stutzle T (2004) Ant colony optimization. MIT Press, Cambridge, MA
36. Söyler H, Keskintürk T (2007) Karinca Kolonisi Algoritmasi ile Gezen Satici Probleminin Çözümü. 8. Türkiye Ekonometri ve İstatistik Kongresi, 24–25 Mayıs 2007, İnönü Üniversitesi, Malatya

Design and Fabrication of Rotimatic Machine

**Tanzila Younas, Muhammad Sarang Memon, Hadi Raza
and Khalil-ur Rehman**

Abstract Roti is very popular in South Asia as it constitutes a major source of dietary protein and calories. Average consumption is about twice to thrice a day. With the rapid growth of population and focus on nutrition, the demand of roti is increasing every day, as it is an essential part of South Asian diet. With increasing demand, traditional roti making cannot keep pace. Roti making has become an established industry providing rotis to many businesses where roti are needed in bulk. As industrialization is moving toward automation, there is a need for automation in roti making. There are many automated and semi-automated roti makers currently in the market each serving a different need. The main aim is to design and fabricate an efficient, compact and user-friendly automatic roti machine to serve the needs of people and improve the quality of life. The machine will alleviate certain problems in cooking of roti. This machine has three main chambers comprises of dough ball formation chamber, pressing tower and cooking chamber. All these chambers are interlinked with one another, which consists of several mechanisms. The input is kneaded flour and final product is healthy and puffed roti.

Keywords Roti · Dough ball · Cooking · Automatic roti machine

T. Younas (✉)
SZABIST University, 100 Clifton, Karachi, Pakistan
e-mail: tanzila@szabist.edu.pk

M. S. Memon
University of Kassel, Mönchebergstraße 19, 34125 Kassel, Germany
e-mail: sarang.hafeez@yahoo.com

H. Raza · K. Rehman
NUST University, Karsaz, Karachi, Pakistan
e-mail: hraza8149@live.com

K. Rehman
e-mail: khalil73362@outlook.com

1   Introduction

The word technology getting expeditious fame by introducing new set of skills, methods, and processes which helps us to accomplish our daily life goals and with the increasing trend it is ruling all over the world. Technology is almost used by every single person and becomes everything for the world. It has significant achievement when it comes to manufacturing applications for automation technology, in some areas such as telecommunications, transportation, service industries, and consumer products. The automation products significantly not only transform current industries and the relationship between end user and manufacturer but it also creates many opportunities for those who know how to run them. Now, the questions arise here what is the impact of automation on natural resources, on energy and on environment? In what ways the machine is going to be beneficial for the industry? This chapter highlights the importance of automation and the impact on environment. It also describes the need and the idea behind to manufacture and fabricate the automatic roti machine. The chapter is divided into three parts.

The first part of the report discussed the importance of the roti in the Middle East. It further described the traditional way of making roti and its ingredients and how beneficial they are for health. Moreover, it also talks about the impact on environment.

The next part discussed the problems faced in the traditional way of making roti and the comparison to the similar product in the market and different techniques that are used for the process of automation of roti.

The last part describes and provides the information about the mechanism techniques that are used in the product by the help of process diagrams and some result carried out in real-time testing.

2   Overview

In India, Pakistan, and Middle East, wheat is one of the daily staples and most common cereal available all over the world. It is in even higher demand in recent years due to its abundant health benefits. It is proven from the research that wheat gives many benefits to human life, and one of the most interesting benefits is it lowers the rate of heart, gallstone, asthma, skin and cancer diseases as it consists of many minerals, nutrition and vitamin E, B, and B6 which also help to improve metabolism [1].

Wheat is the most commonly grown grain on the land; the value of its importance can be predicted by the research of 2010 and the production of wheat all over the world was 651 million tons as it is the most cultivated and consumed than any other crop [2]. The topmost wheat producing countries are China and India [3].

It is consumed in the form of different flat breads such as Chapati, Parotha, Phulka, Puri, and Tandoori Roti. The famous thing made from wheat is roti. It is a Hindi word and comes from Indian subcontinent; roti means flatbread, soft, wholesale, and light.
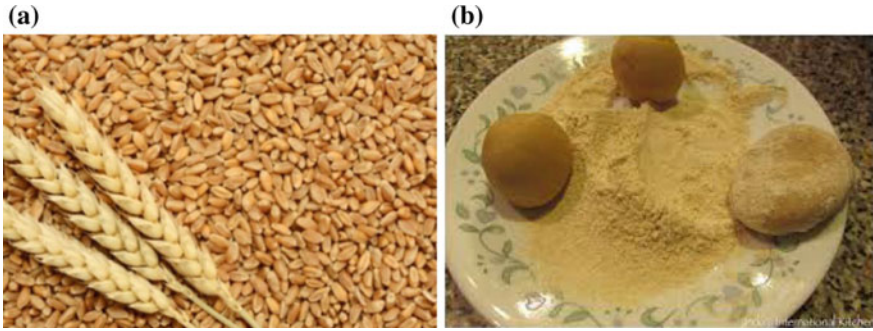
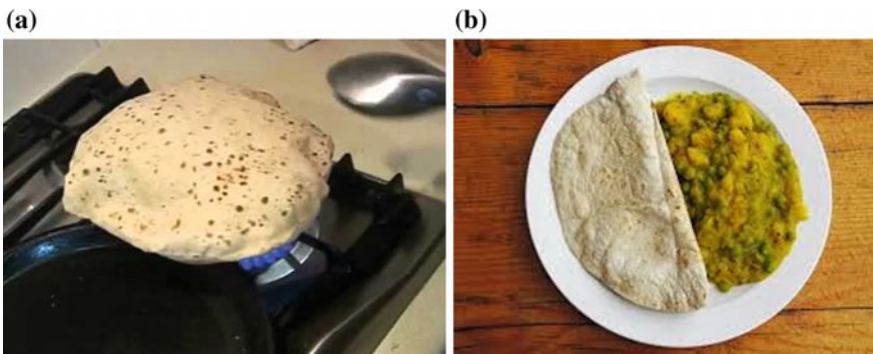**Fig. 1** **a** Original form of wheat and **b** dough ball formation

Fig. 2 **a** Cooking of roti and **b** final form of roti

It is a famous food in the globe, especially in Asia. It is pronounced as "rho-tee" and eaten with many dishes; without it, the dishes are incomplete. It is made of wheat flour, ghee, and water and then cooked on pan called "tawa." The following figures Figs. 1 and 2 show the traditional process of making roti in a house.

Different wheat varieties have been used for the production of flatbreads. In recent years, many researchers have tried to improve ingredient level, baking properties, organoleptic characteristics, nutritional value, and extension of the shelf life of flatbread. They are usually produced from a simple recipe consisting of flour, salt, and water in varying proportions; however, the manufactures also use optional ingredients like yeast fat, skim milk powder, and certain additives like emulsifiers, hydrocolloids, enzymes, and preservatives for quality improvement and shelf life enhancement index.

Table 1 shows the composition of wheat per 100 g edible. Following are the benefits of having wheat in the diet:

- Helps control obesity
- Protects against childhood asthma
- Reduces the risk of type 2 diabetics

Table 1 The composition of wheat per 100 g edible

Wheat	Protein[a]	Fat[a]	Carbohydrate[a]	Starch[a]	Total sugar	Vitamin E[b]	Thainmin[b]	Riboflavin[b]	Niacin[b]	Float[c]
Wheat flour	12.6	2.0	68.5	66.8	1.7	0.6	0.30	0.07	1.7	51

Data taken from Food Standard Agency (2002)
[a]units in g; [b]units are mg; [c]units are μg

- Lowers risk of chronic inflammation
- Improves body metabolism
- Protects against coronary heart disease and heart attack.

3 Scope

3.1 What Is Machine Aim

As we all know about the present trend of factory automation is ruling all over the industries as it is favorable and advantageous in many ways like in productivity exactness perfection validity which results contribution in cost savings.

The main agenda of the project was to design and fabricate an automatic roti machine which has to be established on the foundation of two important qualities; they are it must be environment-friendly means the surrounding in which the person operates the machine and it gives quality product (roti) to the end user (consumer).

3.2 Impact on Environment and Benefits

The current trend in industrial automation is changing toward intelligent manufacturing and automation process. The concept of "smart manufacturing" will lead to a workplace that is more efficient and being more secure for workers and more profitable for employers. One of the major advantages of smart manufacturing is the ability to create a healthy environment [4].

In USA, the one-third of the energy of the globe is processed by the manufacturer of the factory. In 2013, the International Energy Agency reported that manufacturers lost $80 billion in electricity due to outdated manufacturing operations. Updating their manufacturing processes to have a more favorable environmental impact will make companies more popular with consumers, as Nielsen's latest survey indicated. How the machine is beneficial for the environment [4].

- Less fuel consumption
- No emissions
- User-friendly
- Environment-friendly.

3.2.1 Effect of Roti Making Machine on the Environment

The automatic roti making machines use the best quality material which helps to maintain the environment. The cooking chamber uses the iron plates with a coating of retaining which simulates a nonstick effect and uses very low amount of oil. Iron

plates use heat very effectively and save a lot of fuel. A machine which burns less fuel makes the environment healthy. The burners fitted inside the heating chamber are designed in such a way that they pass less fuel while maintaining a certain temperature which is required for cooking. Pressing chamber uses hot nonstick plates which are electrically heated. Nonstick plates are warm in temperature; therefore, they do not produce enough heat. The automatic roti making machine does not produce any harmful gases that affect environment.

4 Problems in Traditional Making

Labor in small-scale industries, such as roti shops, canteen, and food centers, due to direct contact of methane gas used in tandoor creates severe health issue (such as knee, hand, and face burnt for labor), and in addition to this, material wastage and human efficiency are crucial factors which increase the cost per production.

5 Roti Making Machine

To overcome the issue in traditional roti making, an automatic roti maker is proposed for small and large industries, which can benefit them in quality, less material wastage, and high efficiency.

    To resolve the problem of industries, institution, canteens, etc., large quantity of roti are required in less time.

    Many types of roti makers are available in the market but they have some disadvantages which need to be overcome to produce an efficient machine which could fulfill the need of small-scale industry.

5.1 Fully Automatic Roti Making Machine

First automatic machine for industrial use is made by AJ tech. and specifications are mentioned below:

- Stainless steel 202 body on mild steel angle iron frame.
- LPG burners for baking and puffing.
- Stainless steel 304 hopper and food grade conveyor.
- Stainless steel 202 covering baking Oven.
- Fitted with 1/4 HP 3-phase motor.
- Thickness of roti can be adjusted.
- Size of Chapati: 8″.
- LPG consumption 5 kg/h (approx.).

Following are the factors which affect the objectives:

- The system is too huge
- Large consumption of gas and electricity
- Cannot transfer this machine.

5.2 Rotimatic

This machine was invented by Israni couple Pranoti and Rishi Israni which can make one roti a minute. It consists of 300 tiny machine parts out of which 10 are small motors and 15 sensors. This machine is not designed for industrial applications. The production rate of this machine is enough for a home but it cannot fulfill industrial needs.

5.3 Semiautomatic Chapati Making Machine

This automatic machine is made by JAS enterprise. Following are the main features of this machine:

- The machine is fitted with heavy-duty mild steel fabricated structure
- Electric burners to cook the roti
- Fitted with 1/4 HP 3-phase motor
- Easy to clean.

Following are the factors which affect the objectives:

- The system is not portable
- Too much consumption of electricity
- Dependent on operator to feed each and every dough ball.

6 Techniques

Different techniques are adopted to achieve various tasks. One of the main reasons to use different strategies is to increase the rate of production, and for this purpose, the system is being automated. Different techniques are discussed below that can be applied to do the desired task.

6.1 Cooking Techniques

This section will discuss different types of cooking techniques for roti makers.

6.1.1 Conveyor Belt Technique

There are many types of cooking mechanism used in roti machine which are currently available in the market and they are using conveyor belt technique. In this technique, they use endless belt, motor, ribbon burners, and carbon steel slats. The use of conveyor belt technique is not economical because high-power motors are used for the rotation of conveyor which consumes a lot of electricity.

1. Using carbon steel sheet as to make the roti hygienic enhances the cost of the product.
2. It contains large space as roti is baked from both sides; for that, they have used two stages of conveyor belt, which makes its design complex.

The baking source for the ribbon burners is liquefied petroleum gas (LPG) which contains less energy but it is costlier than gasoline. This technique is also not environment-friendly as it produces thermal pollution. The usage of belts makes noise pollution which is injurious to the health of the operator.

6.1.2 Plate Cooking Mechanism

This mechanism involves a single rotating disk with a presser fitted at the center, and burners are installed at the bottom of the plate which keeps the plate warm and cooks the roti. Dough ball is manually placed under the presser which presses the roti and rotates the plate, and as a result, the roti gets enough time and heat to get cooked. Following are the disadvantages of plate cooking mechanism:

1. This is a semiautomatic process and requires at least 3–4 operators to function.
2. Machine requires a human hand to place the dough ball so an accident might occur with the hydraulic presser.
3. This machine requires a lot of space and ventilation.

6.2 Pressing Technique

This section illustrates different techniques for the pressing of roti.
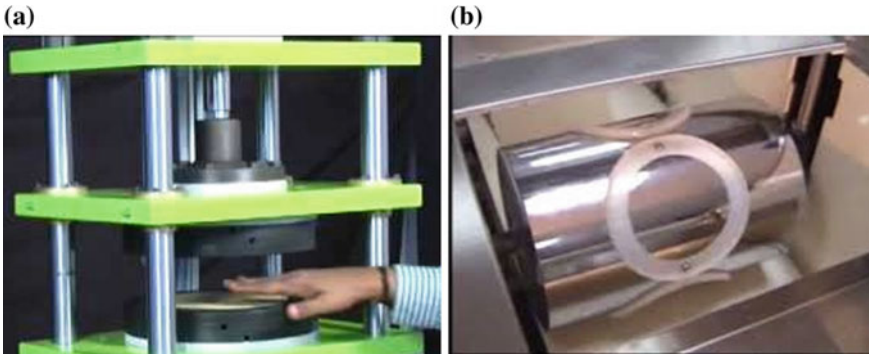
Fig. 3 a Cutter-based mechanism and **b** vertical pressor. Reproduced from https://www.qualimarkmachines.com/pani-puri-making-machine.html

6.2.1 Rolling State Technique

There are many different techniques used for rolling and pressing of the roti in the market. The frequently used technique is big roller technique in which sheets of kneaded wheat are made with huge rollers and the circular shape is embedded at the end, a conveyor collects the kneaded wheat and passes through several rollers making thin sheets of dough, and at the end of each cycle, multiple cutters/molds are fixed which separate circular wheat roti from the sheets as shown in Fig. 3a. But they have a lot of issues such as:

1. Roller techniques is not reliable as so high amount of dough is waste during rolling.
2. Sticking problem occurs.
3. In roller technique thickness of the roti is fixed.
4. Not easy to clean.

6.2.2 Vertical Presser Technique

Vertical presser technique consists of a hydraulic mechanism with two nonstick plates. One plate remains stationary while the hydraulic cylinder is fixed on the pate which moves toward the stationary plate as shown in Fig. 3b.

7   Types of Fuels

7.1   LPG Gas

As discussed earlier that the project is very economical and energy sufficient, we have used LPG as a source of fuel in the project. LPG is composed of two gases that are propane and butane as shown in Fig. 4. LPG is playing vital role in reducing energy poverty that is why nowadays LPG has wide range of supply. It also has the large scale of economies in handling due to its superb portability and convenience.

Following are the things which make us to employee LPG as a fuel.

- It can be very helpful in those areas where natural gas is not available
- It is playing vital role in reducing energy poverty
- LPG is less air polluted gas
- It has less emission which cause lesser global warming.

7.2   Methane Gas

Natural gas is a fossil fuel that is extracted from the ground and used to heat everything from houses to frying pans. The primary ingredient in the gas is methane, a volatile chemical, with other ingredients like carbon dioxide and nitrogen. While natural gas is commonly split into its parts for different applications, the whole mixture can be kept together to become an efficient and high-output fuel source [5].

It is also classified as non-renewable resource, current estimates of remaining natural gas that reserve place is in trillions of cubic feet or we can also say that it will last long [6].
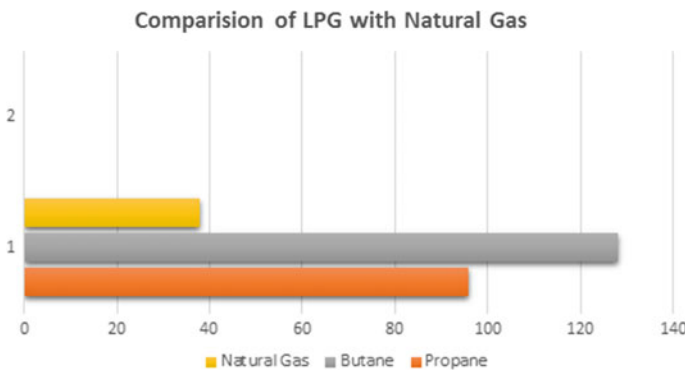

Fig. 4   Comparison of LPG and natural gas [Modified from Woodford (2009/2018)]

Natural gas can be used in the project only if the machine is installed in a single place. Proper gas connected is required as it cannot be transported.

Following are the some facts of natural gas:

- It is cheap
- More affordable because it goes through fewer refinement processes
- Easily available.

7.3 Propane Gas

Propane is a volatile product that is extracted from crude oil and petroleum gas as the materials are refined. The result is a concentrated, high-output fuel that can be used for a whole range of residential and commercial applications, including cooking. Propane is conveniently stored in a cylinder, which is great for short-term use, or a bulk tank, which is better for long-term use [7].

The containers are always painted white to help reflect heat and light and to minimize the possibility that the fuel inside might get expand and explode.

Generally, propane gas will be used in areas outside of major metropolitan areas, typically plumbed to a large tank (cylinder) in the back of the building. This is because propane's portability makes it the ideal and sometimes only choice for more remote areas such as lower Sindh.

Following are some facts of Propane gas:

- Its main advantage over other cooking fuels is its efficiency, that is, it will give you best result over other fuels
- It is readily available, particularly when using small cylinder
- Cooking with propane may actually be safer than natural gas.

8 Block Diagram of the System

This assembly starts with the arrangement of cooking chamber where the final product would be made. The chamber consists of four stoves, two completely flat disks, and two perforated disk. The uncooked roti will flow from the top of the chamber and then it will be collected from the bottom. Obstacles and flaps are inserted at each stage to turn and flip the roti.

First of all, the testing of uncooked roti will be done on the cooking chamber. The pressing tower is built to flatten the dough ball and partially cook it. Two aluminum
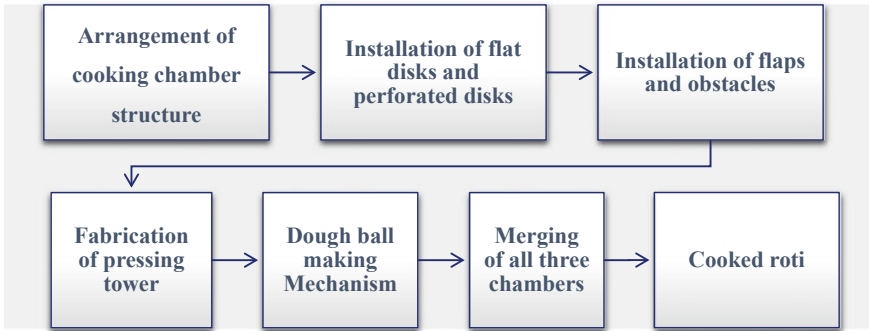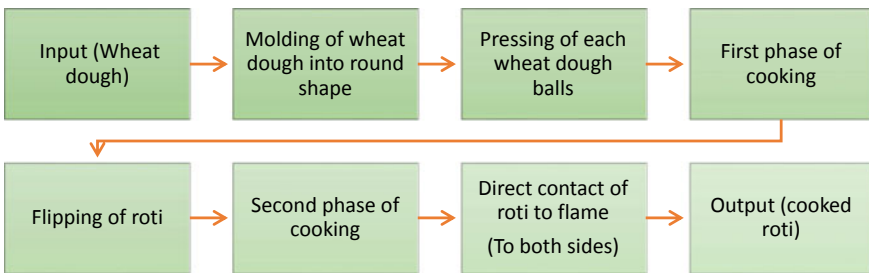
Fig. 5 Block diagram of the rotimatic

Fig. 6 Process diagram of rotimatic

plates coated with nonstick material allows the wheat dough ball to expand and acquire a flat round shape. The dough ball making mechanism is used to produce round dough balls from kneaded wheat.

This is illustrated in block diagram in Fig. 5.

The above block diagram is described in process diagram in Fig. 6.

9 Structure

Problem arises in every project as we have to identify its priorities such as environment, resources, cost, and quality and safety purpose. These are all the terms which have focused in order to make project unique. The structural design and techniques used in this automatic rotimatic are described in this section (Fig. 7).
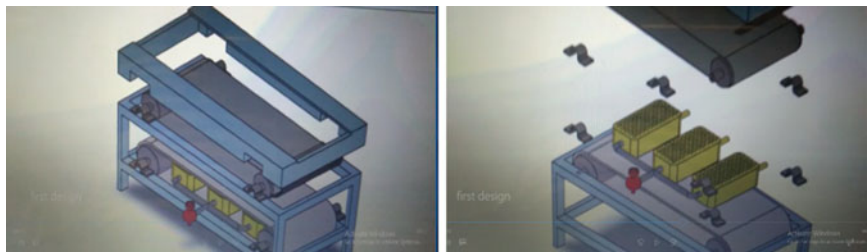
Fig. 7 Conveyor belt roti making machine

9.1 Structure of the Cooking Chamber

The cooking structure case is a four-sided rectangular box which acts as a frame for the system as shown in Fig. 8. The frame is made up of angle iron of size one inch.
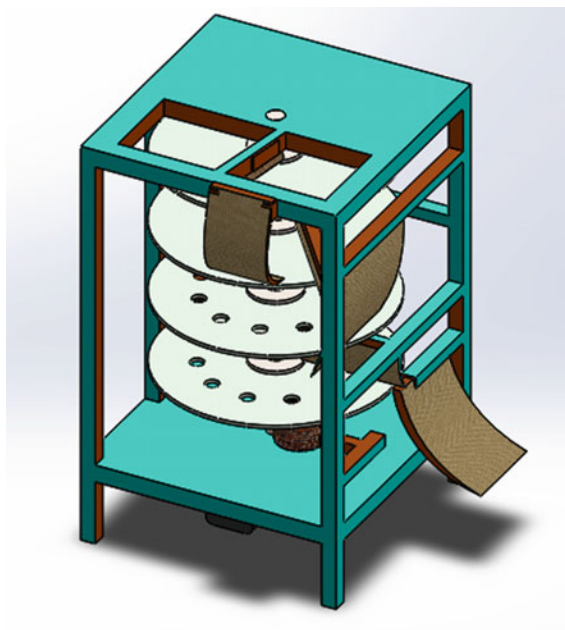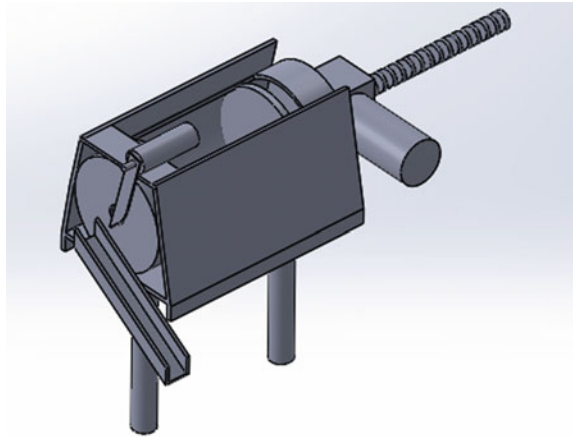

Fig. 8 Structure of cooking chamber

Fig. 9 Dough ball chamber

9.2 Dough Ball Making Chamber (Lead Screw Mechanism)

To make the dough ball, we used round-shaped cylinder embedded in a rectangular box and at the top of the surface, there is a cavity to insert dough as shown in Fig. 9. As the sensor detects the presence of dough, it gives signal to motor which moves the piston that exerts force on dough toward the cutter which is placed at the end of the box.

9.3 Roti Pressing Chamber (Wedge Press Tower)

This machine is used to make a circular-shaped roti from dough as shown in Fig. 10. In this process, two Teflon plates are used for rolling of dough which are coated in order to avoid the sticking of flour and all you have to insert dough between the plates and get circular roti. The pressing of plates can be controlled by motor. Advantages of this technique are:

1. It has 0% waste
2. It can be easily operated
3. It is easier to clean
4. Its easily operated at 120 and 220 V
5. It is safe and compact
6. Smaller in size
7. Thickness can be adjustable.

Fig. 10 Pressing tower
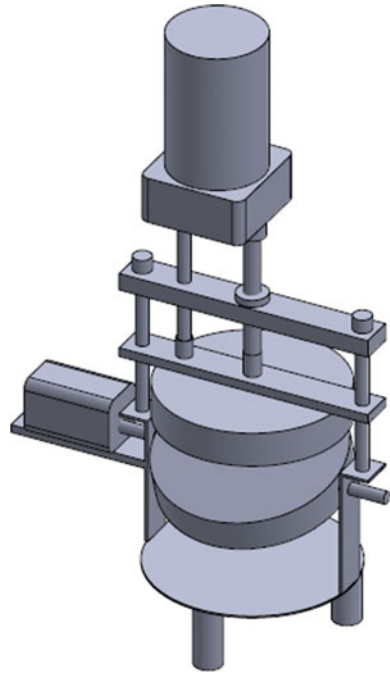
9.4   Cooking Mechanism (Hot Plates Technique)

The technique we used in our machine is hot plates technique. The plates are made up of Teflon material and are covered with steel sheet SS 304 in order to avoid the sticking of roti. SS 304 sheet is a food grade which makes it hygienic and has the property to bear high temperature. The heating system of the machine consists of three burners each of it is attached below to each Teflon plate as shown in Fig. 8. Specifications of the automatic rotimatic are listed in Table 2. Following are the advantages of hot plates technique:

1. It is easy to clean
2. It occupies less space
3. Rustless
4. Economical
5. Hygienic.

Table 2 Specifications of the automatic rotimatic

Specifications	Description
Capacity	350 roti per hour
Mass of machine	90 kg
Material	MS steel, SS 304 grade steel
Motors	Simple dc gear motor of 180 W with voltage regulator for speed controlling purpose
Heating system	Consist of 4 burners
Energy consumption	Motors consumes 2 KW consumption of electricity is 2 unit/h
Size of chapatti	3–4 in. approx
Fuel consumption	4 burners consumes 1.2 kg LPG of gas/hour depends on the rate of production

10 Discussion

In order to reduce emissions in any field, there exist many potential. Emerging technologies are built on these criteria, which provide sustainable energy-efficient systems at no cost of extra energy consumption. This machine offers all the vital benefits of sustainable system such as human, environmental, commercial, and energy efficient. Time to cook one roti at home is 3 min; however, this machine offers 4 rotis in a minute as calculated below.

One Roti Per Round	3.20 min
Roti In A Plate	3 Roti (minimum)
4 Plates Has	12 Rotis
Roti Per Minute	12/3.20 = 3.75 Approx. 4 Rotis
Roti Per Hour	240 Rotis

This vast difference in the production rate makes a remarkable saving in the energy consumption. In addition to this, as the stove is on for a certain time period, environmental temperature will not raise. Human interaction with direct flame is also reduced, and a hygienic roti is produced, which raises the quality of life.

11 Conclusions

In a nutshell, automatic roti maker is the need of era, and it is a kind of device which makes person healthy by giving hygienic roti. From the above discussion, it can be concluded that the other automatic and semiautomatic roti makers which are elegant in shape have low rate of production. They give you a variety of roti but they are not economical and not perfectly designed. However, this machine is compact, user-friendly, and efficient.

References

1. Gfar.net (2019) GCARD2. Breakout session P1.1 national food security—speaker brief—the wheat initiative—an international research initiative for wheat improvement | GFAR. [online]. Available at: https://www.gfar.net/documents/gcard2-breakout-session-p11-national-food-security-speaker-brief-wheat-initiative. Accessed 20 Apr 2019
2. Kumar P, Yadava RK, Gollen B, Kumar S, Verma RK, Yadav S (2011) Nutritional contents and medicinal properties of wheat: a review. Life Sci Med Res LSMR 22:1–10. Available at: http://astonjournals.com/manuscripts/Vol2011/LSMR-22_Vol2011.pdf
3. Finlay PA (1986) Apparatus for rolling circular dough products, EP0191812A1
4. Geospatial World (2018) Factory automation and environmental benefits [online]. Available at: https://www.geospatialworld.net/blogs/factory-automation-and-environmental-benefits/. Accessed 28 Apr 2019
5. Super Healthy Kids (2019) Making your own tortillas is easier than you thought! [online]. Available at: http://www.superhealthykids.com/homemade-whole-wheat-tortillas-with-holiday-breakfast-burrito/. Accessed 20 Apr 2019
6. Anon (2019) [online] Available at: http://totallifestylemanagement.com/eating-well/food-rules/. Accessed 20 Apr 2019
7. Tasty Indian Recipes (2019) How to make Indian chapati—Indian chapati (roti) recipe [online]. Available at: http://www.tasty-indian-recipes.com/indian-breads/indian-chapati-roti-recipe/. Accessed 1 May 2019

Thermoelectric Effects and an Application on a Case Study: Design of Thermoelectric Refrigerator Volume with Computational Fluid Dynamics (CFD)

Manolya Akdemir, Ahmet Yilanci and Engin Cetin

Abstract Current energy needs lead the world countries to take some precautions as to save the possessed energy. Some illustrations of these precautions are said that some insulation materials and photovoltaic usages in the buildings according to regions and also electric cars can be used to decrease the energy consumption and CO_2 emission. When it is examined closely to the whole picture, in the worldwide, the energy consumption of all type pumps is about 40% of the absolute amount of electrical energy consumption. Especially, in a refrigeration cycle, a heat pump is used in large scale, which consumes a high level of energy, alternatively, in a small-scale application; thermoelectric module (TEM) can be used. In this study, the thermoelectricity, thermoelectric materials, and its thermodynamics are described in detail. Refrigeration volumes with TEM design and simulation process are included. The volume is modeled in Solidworks® based on a developed mathematical equation system, including TEM system, TEM (TEC 12706 type), two compact axial fans, and two plate cooler with fins. In the study, computational fluid dynamic (CFD) method is used to analyze the temperature gradient in the refrigerator volume via commercial CFD software, CFX®.

Keywords Thermoelectricity · Design · FEA analysis · Simulation · Refrigeration · TEM

M. Akdemir (✉)
Graduate School of Natural and Applied Sciences, Solar Energy Science Branch, Ege University, Izmir, Turkey
e-mail: mnlykdmr@gmail.com

A. Yilanci
Solar Energy Institute, Ege University, Izmir, Turkey
e-mail: ahmet.yilanci@ege.edu.tr

E. Cetin
Department of Electrical and Electronics Engineering, Pamukkale University, Denizli, Turkey
e-mail: engincetin@pau.edu.tr

817

1 Introduction

The thermoelectric phenomenon involves a conversion process thermal and electrical energy, which is a method to provide heating and cooling of the materials. Thermo-electricity is expected to have an important advantage to meet the energy challenge in the future. Although the use of this phenomenon is quite common in small-scale cooling, it has not been able to replace conventional cooling in large-scale applications. The reason for this is the material competence of the devices using this effect. To increase this competence, essential steps are taken with experimental studies.

In 1821, Thomas J. Seebeck discovered that when a loop consists of two junctions formed by dissimilar conductors when one side of it is heated, an electromagnetic field is created via an electromotor force, which is called as Seebeck effect in thermoelectricity. In 1834, Jean C.A. Peltier discovered a heat gain/dissipation by two dissimilar materials with direct current (DC) application to the material ends (Peltier Effect). This process is the best-known effect in the thermoelectric applications to cool or control the temperature of a system. Another development of the thermoelectricity concept, the thermoelectric refrigeration was found in 1838 is found by Henrich Lenz, who placed a drop of water on the junction of bismuth—antimony; by this way, he obtained an electric current through the junction and the water drop was freeze or vice versa; when the current direction is reversed, the ice was melt. By 1950s, the field of thermoelectric focused on the development of the basic science on the thermoelectric materials. In parallel with this development, heavily doped semiconductors were introduced commercially, and then the commercialization and utilization of thermoelectric modules were significantly increased. The modern theory of thermoelectricity was put forward by Abram Ioffe; and he demonstrated that doped semiconductors had better thermoelectricity properties than other materials (metals) in the 1950s. To usage in this effect, Bi_2Te_3–Sb_2Te_3 alloys were defined as the best materials at room temperature in the 1970s. Nowadays, the scientists study on the semiconductor material to develop the capacity of the thermoelectric effects in the modules [1].

Thermoelectric modules are obtained by combining the thermoelectric phenomenon materials under certain conditions. The thermoelectric module system is obtained by various heat dissipation equipment (heat sink, compact axial fan, etc.), which are added on the thermoelectric module. Generally, these systems are called thermoelectric devices. The thermoelectric device is known as the thermodynamic engine without moving part. Therefore, it is a silent technology to use. Besides, it is an eco-friendly technology since it does not contain a refrigerant-like fluid used by conventional heating or cooling equipment. Although the initial investment and usage cost of the system is quite low, these conditions provide a considerable advantage over conventional systems.

The device can be used to convert heat to electricity (Seebeck effect) and vice versa, by using the electricity, the device can be used as a heat pump between two materials (Peltier and Thomson effects). All thermoelectric devices are comprised of n- and p-type thermoelectric materials within a contact. The thermoelectric module

includes some sections, which include p-type and n-type semiconductor in each contact and each one is connected to the other type semiconductor electrically and thermally. When the heat and current are carried in the module via the electrons and holes, the hot electrons and holes are forced to their locations, and by this way, the heat is transferred between the semiconductors. Aforementioned, vice versa, with applying a reversed electrical current to the module, hot and cold surfaces are changed, and when a temperature gradient is implemented to the thermoelectric module, the electric current is generated in the thermoelectric module [2].

In a typical thermoelectric device, several tens of thermocouples (p- and n-type semiconductor) are connected electrically, in a series way while operating thermally in parallel. To conduct the heat in the system, two conductive metal surfaces (copper, etc.) and the ceramic substrates are located on the top of the module [2–4].

Thermoelectric modules (TEMs) have been widely used in a significant number of applications all around the world as cooler, heater or generator: in the industry, in osmometers, dehumidifiers, laser diodes, etc., in the medication industry; in temperature-controlled therapy pads, DNA amplifies, blood analysers, etc., for the end users (consumers), in picnic boxes, air conditioning in the cars, etc., in the military and aerospace industries; in electronic equipment cooling, military avionics, infrared detectors, etc. While the performance of the TEMs is evaluated and discussed, the coefficient of performance (COP) and figure of merit (ZT) should be defined in the first step. Although their application areas are broad, COP and ZT values of TEMs are still not enough to use in a system instead of the conventional cooler, heater or generator systems. Mainly, COP values of thermoelectric modules depend on the semiconductor materials properties and surface temperatures. Therefore, researchers, especially who study on semiconductor physics, have focused on thermoelectric elements to improve the efficiency of the modules by investigating some materials.

Aforementioned, the thermoelectric construction can be used as the refrigerators, power generators, or temperature controller. This device can be heated up/down since the charge carriers in the material; they can carry heat according to the elastic resistor approach in the semiconductors. Moreover, the charge carriers are named as "*working fluid*" in the thermoelectric module. The thermoelectric modules have significant advantages, with no moving parts, therefore, no liquid refrigerant fluid, etc. But, unfortunately, the devices have a major disadvantage, which brings out low-efficiency level compared to the conventional refrigerators.

The thermoelectric coolers can be powered by a car battery with 12 VDC as to the usage of portable beverage storage, torpedo cooling, or it can be used via a power supply to provide to cool down a computer central processing units or for an infrared detector. Usually, the thermoelectric generators are used as power sources for many of NASA's deep-space probes and also to convert waste heat into electricity in small applications.

To understand the thermoelectricity working principle, semiconductor physics should be scrutinized. The next part of the study focuses on the band theory of materials, including semiconductor material, elastic resistor and thermoelectric materials are explained in detail. In addition to these details, the study includes the CFD and experimental interaction of the module, heat sink and compact axial fan in a thermoelectric system, and various designs based on these studies.

2 Background Information

2.1 Basic Principles

2.1.1 Band Theory of Materials

The energy state (E) is completed by the electron under equilibrium conditions is known as Fermi function determines, whereas Fermi level (E_F) states a carrier distribution in the material At the energy level, which value is lower than the Fermi level, the electrons are filled up this energy level at absolute zero. At higher temperatures than the absolute zero, the Fermi function can reveal above Fermi level of the material. The Fermi level has a significant effect on the band theory of solids. In Solid-state physics, band theory is evaluated as a quantum model and gives the possible energy levels for electrons in solid material, and in this way, the theory explains the electrical conductivity [5].

Most of materials or solids are insulators, to understand the insulator in terms of band theory, where a larger forbidden gap can exist between the energy levels of valance band, the valance band is that the electron exists in orbitals that can transfer and when excited the electron can move into the conduction band. The conduction band is defined as energy level the electron can move through the material freely. In the insulators, in addition to Fermi energy (E_f), there is forbidden energy gap (E_g) between the valance band and conduction band as to separate in a significantly large. Therefore, the electric current cannot flow in the insulators, generally.

The other solid material, which is examined in band theory, is semiconductors. The semiconductors are classified into two groups; intrinsic and doped semiconductors. According to the semiconductor physics, in the structure of intrinsic semiconductors (e.g., silicon and germanium), the Fermi Level can be between the valence and conduction bands.

In a doped semiconductor, impurities define material characteristics and electrical properties known as n-type and p-type semiconductors. Apart from the intrinsic semiconductors, in doped semiconductors, extra some energy levels are added between valance and conduction bands. In the structure, which is doped with a p-type and n-type semiconductor material, the Fermi Level of a material can be shifted by adapting the impurities, by this way, the band gaps of the material are changed. In the semiconductor structure, like the insulators, forbidden energy gap (E_g) is located between
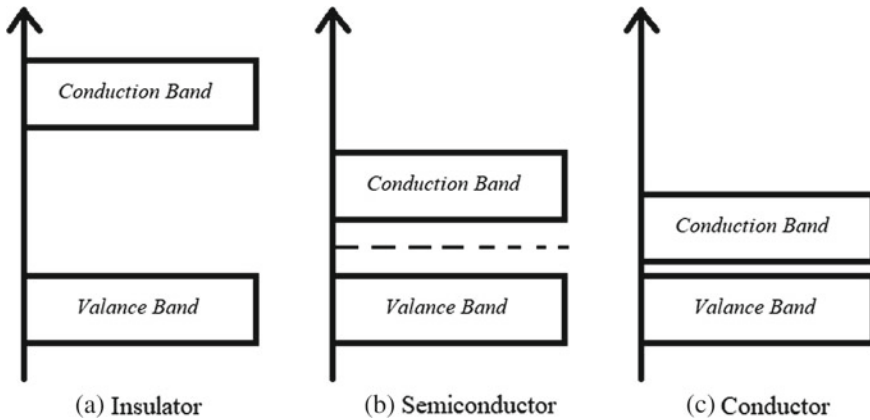
Fig. 1 Band theory diagram of solids

the valance and conduction bands. These two illustrations require to gain energy so that the electron can move to the conduction band [4–6]. According to band theory of solids, the metals have a high capacity to conduct electricity because of the valence electrons can be moved free—between the valance and conduction bands. In the metals structure, the valance and conduction band are close to each other; therefore, the electron may even overlap with *Fermi energy* (E_F). With a different standpoint, in the metals, *Fermi energy level* defines the velocities of the electrons in an electrical conduction process. In the conduction process, the energy with an order of micro-electron volts can be revealed, Fig. 1 illustrates the band theory diagram of solids.

To emphasize the band theory, Fermi level (E_F) and vacuum level (E_{VAC}), work function (W_F), energy gap (E_g), ionization energy (IE), and electron affinity (E_A) are the key points as to define conduction between the valance and conduction bands for any electronic materials. These parameters can show alternations according to the composition, doping level, and morphology properties. To clarify these parameters, in the semiconductor materials, the electron and hole transport values are known as conduction band minimum (CBM) and valance band maximum (VBM), respectively. Energy gap (E_g), also known as transport gap, is the energy level difference between the CBM and VBM bands of material. Vacuum level (E_{VAC}) is the energy level in which an electron can be at rest within a "few nanometers" outside the solid [5].

Work function (W_F) demonstrates the energy value, which requires leaving an electron from E_F level of the material and placing it in free space, to illustrate at E_{VAC}. As can be seen in Eq. 1, in the semiconductor, this circumstance of W_F value is depended on the position of E_{VAC} and E_F, rely on the frequency of the states, temperature, charge carrier density, and doping concentration [7–10].

$$W_F = E_{VAC} - E_F \qquad (1)$$

The all parameters about the semiconductor (e.g. W_F, IE, and EA) can be modified engineers and solid-state physicists by experimental studies [7].

2.1.2 Elastic Resistor

By contacting two type metals or semiconductors, the flow of electrons can be obtained, and this effect is modified with *Fermi functions levels*, $f_1(E)$ and $f_2(E)$ in the materials. The negative contact in the system has extensive $f(E)$; therefore; it leads to having more electron in the channel than the positive contact material. The electrical current is a simple function of $f_1(E)$ and $f_2(E)$, because electrons flow from one energy level to another one when the electric current flows in the opposite direction. Therefore, the electron current directions are always opposite to the electrical current, which can be seen in Fig. 2 [11].

For the ideal elastic resistor, the electrical current in an energy values between E to $E + dE$ is defined as Eq. 2. That allows to get the total electric current (I).

$$dI = \frac{1}{q}dE\, G(E)(f_1(E) - f_2(E)) \tag{2}$$

Using this equation, a statement of the low-bias conductance can be written, where $\left(-\frac{\partial f_0}{\partial(E)}\right)$ visualized as a rectangular pulse of area equal to one, with a width of ~$\pm 2kT$ (Eq. 3):

$$\frac{I}{V} = \int\limits_{-\infty}^{+\infty} dE\left(-\frac{\partial f_0}{\partial(E)}\right)G(E) \tag{3}$$

Fig. 2 Electric current direction versus conventional current in the elastic resistor
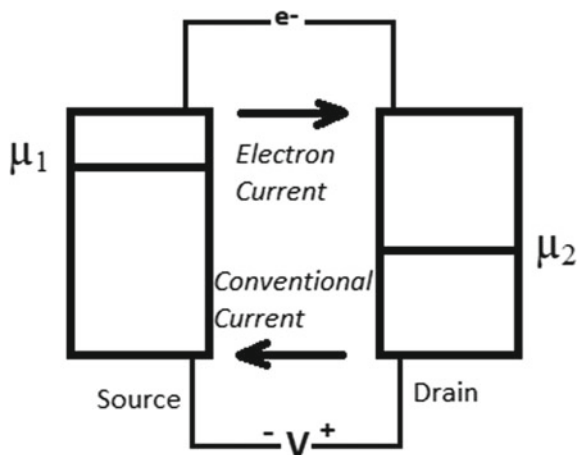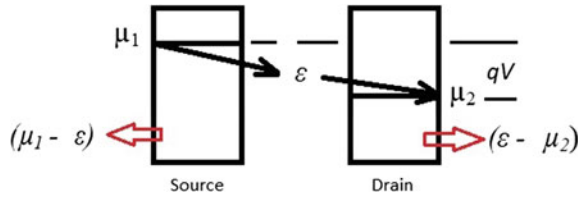
Fig. 3 State changing after electron and heat transfer in the elastic resistor

Nontrivial part of the elastic resistor is that Joule heat dissipation, the electric current flow (I) through the resistor (R) dissipates a Joule heat of I^2R per second [11].

2.1.3 How an Elastic Resistor Dissipates Heat

The elastic resistor is considered with Sharp Energy Level (E), when an electron passes through the channel, which is named as hot electron on the drain energy level with an energy ε above the electrochemical potential μ_2, and can be illustrated in Fig. 3. In the dissipation processes, the electron scatters the excess energy($\varepsilon - \mu_2$), when at the source material end, a hole is left behind an energy level the electrochemical potential μ_1, which is replaced by an electron which dissipates the excess energy ($\mu_1 - \varepsilon$) to the environment. In the effect, in every time an electron and hole replaced between the source and the drain, a total energy value ($\mu_1 - \varepsilon$), another energy value ($\varepsilon - \mu_2$) is dissipated, respectively.

Total dissipated energy is equal to the potential difference by the external battery in Eq. 4:

$$\mu_1 - \mu_2 = qV \tag{4}$$

With the crossed over electrons number of N at time t, and dissipated power can be estimated in Eq. 5.

$$\text{Dissipated Heat} = \frac{qVN}{t} = VI = \frac{qN}{t} \tag{5}$$

where $V \cdot I$ equals to I^2R or V^2G [11].

2.1.4 The Conductance of an Elastic Resistor

Considering the elastic resistor, this has only one energy level in the range of the electrons that transfer between the source and drain. The final and overall electric current can be defined as in Eq. 6 [11].

$$I_{\text{one level}} = \frac{q}{t}(f_1(E) - f_2(E)) \tag{6}$$

where t is the time that electron passes through the source to the drain, and also, the electrical current in energy values between E and $E + dE$ can be described as in Eq. 7.

$$dI = dE \frac{D(E)}{2} \frac{q}{t}(f_1(E) - f_2(E)) \tag{7}$$

Assume that two energy levels between E and $E + dE$ contain $D(E)dE$ states, these energy level can contribute to carry the electrical current from the contacts. To obtain the electrical current through an elastic resistor, Eqs. 8 and 9 should be used.

$$I = \frac{1}{q} \int_{-\infty}^{+\infty} dE\, G(E)(f_1(E) - f_2(E)) \tag{8}$$

$$G(E) = \frac{q^2 D(E)}{2t(E)} \tag{9}$$

If the applied voltage $\mu_1 - \mu_2 = qV$ is much less than kT value of the system, the electric current can be acquired in Eq. 10 [11]:

$$I = V \int_{-\infty}^{+\infty} dE\left(-\frac{\partial f_0}{\partial E}\right)G(E) \tag{10}$$

2.2 Thermoelectricity

As stated previously, the property of thermoelectricity is a phenomenon, which is arisen from two or more metals and semiconductors in coupled in terms of heat and electricity. When two metals are coupled in electrical terms, the electrons and holes cross through the materials. The electron transfer continues until the change in electrostatic potential and the equaled Fermi levels of the two metals/semiconductors (W_1 and W_2) between the two conductors. The system equations can be written in general form, in Eq. 11 [1, 12].

$$\begin{bmatrix} J \\ h \end{bmatrix} = \begin{bmatrix} \sigma & \sigma S \\ \sigma ST & \kappa \end{bmatrix}\begin{bmatrix} -\nabla V \\ -\nabla T \end{bmatrix} \tag{11}$$

where J, h, V, T, σ, κ, and S are electrical current density, thermal flux density, electric potential, temperature, electric conductivity at $\nabla T = 0$, thermal conductivity at $\nabla V = 0$, and thermoelectric power, respectively.

If a closed circuit is established of two different semiconductors, the electromotive force equals to zero in the system since two potentials are opposite of one another, not obtained the electric current. The temperature difference in the system can be raised with respect to other one; the electric current and a total electromotive force are generated in the junction system. Based on identical Fermi levels of the materials, the temperature dependency of material differs from other contact material. Therefore, the thermoelectricity property and aforementioned heat dissipation/gain of the TEM depends on Fermi energy level and temperature reacting of the contact materials [12, 13].

Thermoelectric materials indicates some special effects; Seebeck, Peltier, Thompson, Joule and Fourier effect, which are explained in detail in the next section, in addition, these effects can be examined via the non-destructive evaluation (NDE) technique, which is used to determine the thermoelectricity and its effects in terms of thermodynamics and electrical properties in the thermoelectric devices/material [13].

The thermoelectric module can be used as a cooler and generator according to the effect and application. If the electric current applies to the thermoelectric device, the heat dissipation can be obtained. This device can be used as a cooler or heater in some applications and also vice versa when the heat applies to the device, the electric current can be attained from the system. Therefore, the system with this effect can be defined as generator; the TEM can be seen in Fig. 4 [6, 13].

Edmund Altenkirch invented the maximum efficiencies of the thermoelectric generator and the cooler when the operating conditions were optimized in 1909 and 1911, respectively. This correct relationship is named as figure of merit (ZT), with high Seebeck coefficient, and conductivity of electric to reduce Joule heating, on the other hand, thermal conductivity as to minimize heat loss, which was developed in 1949 by

Fig. 4 Cooler and generator effects in the TEM
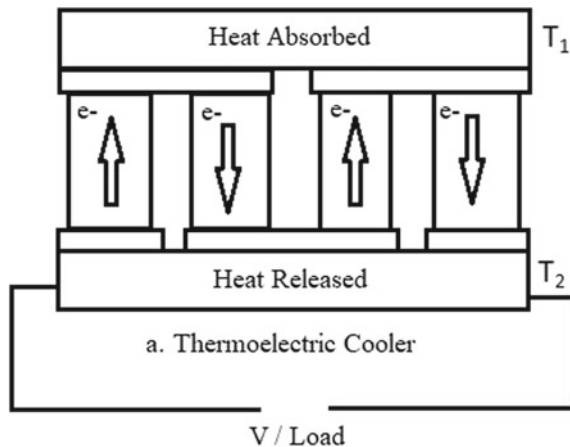
Abram Fedorovich Ioffe. In 1954, H. Julian Goldsmid used thermoelements based on Bi_2Te_3 in a study. He was a pioneer of identifying the impact of superior mobility and active mass and also low lattice thermal conductivity in semiconductors [14].

2.2.1 Seebeck Effect

Seebeck Effect is a phenomenon which is invented by Thomas J. Seebeck in 1821. Seebeck discovered that when a loop consists of two junctions formed by dissimilar conductors or semiconductors and when one side of it is heated, an electromagnetic field is created via an electromotor force. Therefore, the voltage is produced as a proportional to the temperature difference between the hot and cold sides of the material. The magnitude of the *Seebeck coefficient* (α) depends on the material and temperature of room and operation. The coefficient is defined as in Eq. 13 [12]:

$$\alpha = -\frac{\Delta V}{\Delta T} \tag{12}$$

where ΔV and ΔT are the voltage difference, the temperature difference between the hot and cold surfaces in the junction, respectively.

A configuration in the current density J is always zero; therefore, the included J in the matrix (Eq. 11) gives a result like $\nabla V = -S\nabla T$.

The measured Seebeck voltage is defined as Eq. 13;

$$V = \int_{T_1}^{T_2} (S_A - S_B) \mathrm{d}T = \bar{S}_{AB}(T_2 - T_1) \tag{13}$$

where the relative thermoelectric power of the specimen with respect to the reference electrode is $S_{AB} = S_A - S_B$ and the bar indicates averaging between T_1 and T_2 [13].

2.2.2 Peltier Effect

In 1834, Jean C.A. Peltier discovered a heat gain/dissipation in a system, which consists of two dissimilar materials with *direct current* (*DC*) application to the material ends, and since then this effect is named with inventor name, Peltier effect. The process is the best-known effect in the thermoelectric effects and applications because of the wide usage in the systems. The statement of the Peltier effect can be determined as in Eq. 14 [13].

$$\dot{Q}_P = \alpha T I \tag{14}$$

where Q, T, α, and I are absorbed heat by the cold junction, the absolute temperature at the junction, Seebeck coefficient and is the electrical current. This thermoelectric heat pumping is brought about the Peltier effect.

2.2.3 Thomson Effect

According to the Thomson effect, the electrical current streams in the homogeneous conductors, in parallel direction of the thermal control temperature distribution as dT/dx. The effect generates a heating/cooling with the value of qT. Thomson effect is defined a value per unit of conductor length in Eq. 15.

$$qT = \tau I \frac{dT}{dx} \qquad (15)$$

where τ is the Thomson coefficient (V/K), and qT is the heat flow per unit of conductor length (W/m)

2.2.4 Joule Effect

When an electrical current flows along a conductor, a heat (Q_J) is generated, which is called as Joule effect, and this value can be calculated using Eq. 16.

$$\dot{Q}_J = I^2 R \qquad (16)$$

where R means electrical resistance of the material [13].

2.2.5 Fourier Effect

The conductive heat transfer in the thermoelectric devices is known as Fourier effect and it can be expressed in Eq. 17.

$$\dot{Q}_F = -kA \frac{dT}{dx} \qquad (17)$$

where Q_F, k, A, and dT/dx are the heat flow, the thermal conductivity, the intersection area, and the temperature gradient, respectively [13].

2.3 Basic Thermoelectric Science

To define the level of the requirement and optimize the generating /cooling/heating effect, thermoelectric effect and thermoelectric module, semiconductor material should be examined in terms of thermodynamics [14].

William Thompson studied the thermodynamics of the thermoelectric materials in the mid-1900s. He demonstrated a mathematical correlation between the heat and electrical current productions in two connected metals can be demonstrated in Eqs. 18 and 19:

$$J = \sigma(E - S\nabla T) \tag{18}$$

$$Q = (\sigma T S)E - \kappa \nabla T \tag{19}$$

In the equation, J, σ, E, α, T, Q, and κ are the electrical current density, the electrical conductivity, the electric field, the Seebeck coefficient, the temperature, the heat current density, and the thermal conductivity, respectively. α, equals to the average entropy value per charge carrier divided by the electron charge. ΔV, a corresponding voltage can be obtained by electrical conductor even with a small temperature difference in the connected surfaces. If an electrical current does not pass through from the materials, the ratio of $\Delta V/\Delta T$ is the definition of the Seebeck coefficient.

When thermoelectric cooling/heating is a matter of the system, a cooling/heating capacity should be defined according to the specific parameters, the Seebeck coefficient (α, V/K), electric current (I, A), electrical resistivity (R, Ωm), thermal conductance (K_t, W/m^2 K), surface temperatures; the hot and cold surface temperatures (T_h and T_c, °C) and mean temperature of the module (T_m, °C) (Eqs. 20 and 21).

$$Q_{ct} = \alpha I T_c - I^2 R^2 - K_t(T_h - T_c) \tag{20}$$

$$T_m = \frac{T_h + T_c}{2} \tag{21}$$

In addition to the cooling/heating capacity (Q_{ct}), figure of merit (Z) and coefficient of performance (COP) value can be calculated to define the capacitance of the thermoelectric device. As can be seen in Eqs. 22 and 23, the figure of merit calculation consists of the Seebeck coefficient, conductivity properties in terms of the electrical and thermal; to illustrate, the power generation is directly proportionate to the Seebeck coefficient and electrical conductance, whereas on is inversely proportional with the thermal conductance.

$$Z = \frac{\alpha^2}{R K_t} \tag{22}$$

$$M_{\mathrm{C}} = \sqrt{ZT_{\mathrm{m}} + 1} \qquad (23)$$

The semiconductor physical properties can be illustrated with the figure of merit (ZT) is a function which the carrier concentration at the room temperature.

The efficiency of the thermoelectric material relies on the Seebeck coefficient (α), the room temperature (T), and also the electrical resistivity (ρ), the figure of merit (ZT) is defined via Eq. 24;

$$ZT = \frac{T S^2}{\kappa \rho} \qquad (24)$$

Generally, the power generation is divided to work out as to define efficiency value. In the thermoelectric module, the efficiency value is estimated using Eq. 25;

$$\eta = \frac{(T_{\mathrm{h}} - T_{\mathrm{c}})(\gamma - 1)}{T_{\mathrm{c}} + \gamma T_{\mathrm{h}}} \qquad (25)$$

where T_{c} and T_{h} are the temperatures of the cold and hot surfaces, and γ differentiate with the average temperature T. For the refrigeration process, the COP is determined with the work in divided by the heat pumped out and it is given by Eq. 26;

$$\mathrm{COP} = \frac{\gamma T_{\mathrm{c}} - T_{\mathrm{h}}}{(T_{\mathrm{h}} - T_{\mathrm{c}})(1 + \gamma)} \qquad (26)$$

With the Carnot efficiency, the *figure of merit* (ZT) is limited to 1.0 for the refrigeration process. In experimental studies on the thermoelectric refrigeration demonstrates that the figure of merit is ranging from 0.4 to 1.0 at optimum operating conditions [12].

3　Literature Review

Thermoelectric modules have been widely used in great number of applications all around the world, COP, and ZT values are still not enough to use in a system instead of the conventional cooler, heater or generator systems. COP values of the thermoelectric modules depend on the semiconductor materials properties and surface temperatures. Scientists have investigated some doped materials and mobility of the materials. To enhance COP and ZT values and cooling, heating and generator performances, decreasing the thermodynamic interactions between the hot and cold surfaces have the most important roles. To decrease the interaction of the thermoelectric module's surfaces, the heat sink and compact axial fan can be located on the each surface. All the system, including a thermoelectric module with heat sinks and compact axial fans, perform better according to the alone thermoelectric module because of that the hot and cold surface's heat removing via heat transfer, separately.

Therefore, the thermoelectric surfaces, heat sinks, and compact axial fans' heat transfer properties and interactions of fluid (air, water, etc.) should be investigated as to include in the system. To illustrate, the compact axial fan can be optimized to obtain the highest heat transfer from the heat sinks to the free atmosphere. To define the interactions of the system components, the numerical methods can be used. Computational fluid dynamics (CFD) is used to investigate fluid and thermal properties of a system. Like in this study, CFD analyses can be used to study on effects of the thermoelectric module integrated with the heat sinks and compact axial fans. The meshing and the simulation setup is the most important point to find the closed solution results to experimental results.

Pérez–Aparicio et al. [14] focused on the improved finite element, three-dimensional nonlinear formulation, which included Seebeck, Peltier, Thomson, and Joule effects. To optimize the thermoelectric module, the finite element analysis had been used to temperature-dependence of the material properties of electric conductivity. In the Weerasinghe's [15] study, he included a thermoelectric module as Peltier cooler, in the down-hole seismic tooling. In the downhole performance, prediction had been predicted via Star CCM+ as to find the temperature increment and the Peltier integrated decrement in the system. Astrain et al. [16], studied electric and thermal properties of thermoelectric refrigerators with nonlinear equations, including the thermodynamic and thermoelectric equations to define COP value of the refrigerator. And also, experimental studies on the thermoelectric performance under different circumstances. Quental [17] studied the Peltier modules thermal behavior estimation and the thermoelectric assembly. Numerical simulation of the heat sinks had been used to different conditions and turbulence models, simulated on ANSYS ICEPAK. The k–ε, k–w, SST, and ERNG had been used as the turbulence models, and the results were compared to each other. The ERNG was found the most suitable to define the problem. Junior et al. [18] investigated the thermoelectric module with heat exchanger interactions. They designed a prototype on the thermoelectric module and heat exchanger in the cooler. The model was analyzed in CFD with Modelica library TIL (TLK-IfT-Library) modeling and experimental studies of the prototype had been carried out to compare the simulation results. In the "Optimization of a New Thermoelectric Cooling Assembly Using CFD Analysis and Local Modeling of Thermoelectric Effects" paper, Codecasa et al. [19] studied on Fluent 6 used as to analyze the temperature distribution and interactions between the thermoelectric junctions and also the simulation results were evaluated with experimental study's results. Fujisaka et al. [20] conducted thermoelectric module optimization by using the one-dimensional model by using the heat transfer equations with Peltier and Joule effects. Two-dimensional numerical calculations had been carried out in Fluent as to investigate the temperature distributions of the thermoelectric module. The study included the cascade thermoelectric module design and optimization. According to the all studies, one-dimensional analytical results had been compared to two-dimensional numerical results of the conventional and cascade thermoelectric module. Korpyś et al. [21] focused on heat sink performance in the CFD analysis in the experimental and CFD investigation of PC heat sink performance with TEM using water and nanofluids study. They used ANSYS Fluent as to investigate the

heat transfer between the heat sink and CPU. It is assumed that the laminar flow regime was in the fin array area of the heat sink. The nanofluid and water have been used in the study as to obtain better heat transfer model. Högblom [22] studied that the thermoelectric module as a generator in the CFD simulations allowed to investigate thermoelectric performance. The CFD analysis, in the study, was used to define the electrical and thermal performance of the TEM. The dissertation included the CFD analysis validation with experimental studies. In other study, included a CFD and experimental studies were carried out the thermoelectric module as to simulate the thermoelectric performance of the thermoelectric refrigerators in different conditions. Nagy and Buist [23] focused on the thermoelectric module thermal properties and investigated the increase the thermoelectric module integrated to some applications.

Saidur et al. [24] studied a thermoelectric module usage in a refrigerator volume; they carried out some experimental studies as to define maximum cooling effect and temperature distribution and fluctuation of the hot and cold surfaces at ambient temperature versus time. The refrigerator volume included a water bottle in 1 L as to cool down. As a consequence of the thermoelectric devices was carried out in the system, the temperature of the water was cooled up to 8 °C, and wall temperatures of the refrigerator are shown in the study, in detail. In other paper, Mare [25] studied on the milk cooling technology via the thermoelectric modules. The system comprised of some pipe system, photovoltaic panel, cooling tank, battery, charge regulator, and network water supply. A series of some experimental studies were carried out in the study; extremum temperature points of volume, ambient, cold cooling water, and hot cooling water temperatures, DC electric current density, voltage, electric power values were pursued according to the solar irradiation in the system. Esen and Balta [26] performed some studies on a solar-powered thermoelectric cooling system (TEC): an aluminum heat exchanger was placed to the surfaces of TEM in order to transfer heat from the TEM surfaces. Thermoelectric module, heat exchanger and the fan were located on the system volume. This system was operated using air and water-cooled fans. TEC system, using water-cooled fan only power supply mode, when using air cooling fan, power supply, battery, PV, and PV battery operated in four different modes. The COP values of air-cooled and water-cooled systems were calculated.

In the paper, which was prepared by Rajangam and Vekataramanan [27], the design parameters definition and some computational fluid dynamics (CFD) Analysis involved with the thermoelectric cooling system. A prototype of 1.5-L container produced that could be used range from 8 to 35 °C. CFD validation was used to optimize and enhance the design parameters of the system according to the cooling and heating load, weather conditions in the location and application specifications. Some experimental studies had been carried out that the system was cooled to 5 °C.

Another study focused on a designed prototype, including a refrigeration system supply with a solar photovoltaic panel. The experimental prototype comprised of a box with liter capacity, which was cooled via four numbers of TEM. The study demonstrated that the system was cooled down to 11 °C with respect to ambient

temperature (23 °C) and also COP value of refrigeration system was determined as 0.1. [28].

The CFD techniques are a powerful tool to investigate a system in terms of thermodynamics, heat transfer, and fluid properties because of their capabilities. The next part of the study focuses on the optimization of a refrigerator box dimensions based on the interactions of the thermoelectric module surfaces, heat exchangers, and fans via CFX®.

4 Materials and Methods

The thermoelectric module refrigeration system includes thermoelectric module, TEC-12706 with integrated the two heat sinks and the two compact axial fans on the hot and cold surfaces. The heat transfer of the system is released via airflow in two different parts, the first one is from the hot side of the thermoelectric module to the heat sink using the compact axial fan to the free atmosphere, whereas the other one is from the cold side of thermoelectric module to the heat sink using the other compact axial fan and the refrigeration volume. With the Peltier effect, the refrigeration concept volume is getting colder and colder, gradually. To investigate the proposed system in terms of air as fluid and thermal properties, CFD method and also some experimental studies have been carried out in the study. The comparison of concept volume on the CFD analyses with results of the experimental studies, the best convenient mesh, turbulence, and setup structures/models for the system were obtained. CFD analyses have been run via CFX® 18.1 as to examine the thermal behavior of the concept volume. The volume is a kind of rafter blankets with a heat transfer coefficient value as 0.042 W/m K at 25 °C temperature in 190 × 190 × 240 mm dimensions, and it includes the only one TEM system as a cooler.

In the study, Solidworks® is used to design the volume geometry based on the previously made mathematical modeling studies. The mathematical modeling is comprised according to the heat transfer laws, for the system, the insulation and the wall material calculations have been carried out in Matlab®.

To define the optimum design of the box, CFD simulations have been carried out for different electric current values with different box dimensions via thermoelectric module system. On the other hand, by decreasing the thermodynamic interactions between the hot and cold surfaces of the TEM, the cooling, heating, and generator performances are increased. For this reason, the thermoelectric module systems, thermoelectric surfaces, heat sinks, and compact axial fans' heat transfer properties and interactions should be investigated as to interfere in the system. The other part of the study focuses on the experimental studies to investigate the real thermal behavior of the thermoelectric module system. In the grand scheme of things, CFX® and experimental results have been compared to determine the optimum design for the system.

4.1 Experimental

All in all, the experimental studies are carried out as to define the CFD inputs, which are some characteristic curves of TEM and the compact axial fan and temperature distributions of the TEM surfaces. The characteristic curve of TEM is predicated voltage versus temperature and also current versus temperature of the surfaces, whereas the characteristic curve of the fans is predicated volumetric flow rate (m³/h) versus pressure gain (Pa) in the axial direction.

As the first step of the experimental studies is to get accurate results about the temperature distributions in the TEM system according to the surfaces.

The experimental studies include the concept volume with only one thermoelectric refrigeration system. The schematic view and experimental setup of the whole system are demonstrated in Fig. 5. The photovoltaic system is occurred by 12 V, 16.42 A, a charge regulator with specification 24 V, 20 A, and battery 12 V 80 A. The TEM system is occurred by two heat sinks and compact axial fans on the surfaces of TEMs.

As it is mentioned earlier, the experimental setup is comprised to define the temperature distributions of the TEM refrigeration system; the thermocouples have been located into the surfaces of TEM, heat sinks and the fans' outlet. And the system has been worked with different current values; 0.5, 1.0, 1.5, 2.0, 2.5, 3.0, 3.5, 4.0, 4.5, 5.0 A. According to these values, the temperatures distributions of the components of the system have been measured. By this means, the characteristics of the TEM system, TEC 12706, have been identified to integrate these properties into the CFD simulations.

In the experimental studies, a concept volume has been used to compare the temperature distributions with the CFD results. The concept volume dimensions are occurred by a kind of rafter blankets in $190 \times 190 \times 240$ mm dimensions; the rafter blankets have a heat transfer coefficient value as 0.042 W/m K at 25 °C temperature.

Fig. 5 Experimental setup
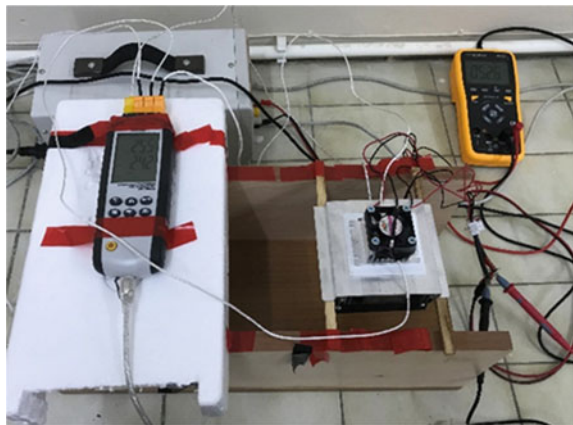
The experimental studies had been carried out by applying different current values to the TEM system, from 0.5 to 5.0 A as to find the temperatures changes of a hot surface, cold surface of the thermoelectric module, compact axial fans, and also volume's average temperature.

4.2   CFD Studies

In the beginning, the concept volume with all properties has been simulated in CFX as to assure the behavior of the compact axial fans and the interactions of the TEM system's components. The simulations bring out 2% margin of error along with the temperature changes and distributions according to the current values with compared to the experimental results, approximately. With these satisfactory results, CFD simulations' mesh and setup structures can be used to define the refrigerator box's dimensions; the box is demonstrated in Fig. 6.

Initially, the refrigerator box dimensions are ranging from $500 \times 500 \times 500$ mm to $250 \times 250 \times 250$ mm, gradually. The design refrigeration system is comprised by four $400 \times 400 \times 25$ mm TEC-12706 thermoelectric module with the $120 \times 100 \times 25$ mm heatsink and the ebmpapst 3412N compact axial fan ($90 \times 90 \times 25$ mm) in the hot side, the $40 \times 40 \times 25$ mm heatsink and the ebmpapst 412F compact axial fan ($40 \times 40 \times 25$ mm) in the cold side. The volumetric flow rates of the compact axial fans are 78, 7.5 m^3/h, respectively. In the light of this information, the CFD simulation geometry preparation, meshing, and setup processes have established, and analyses have been run in CFX®.

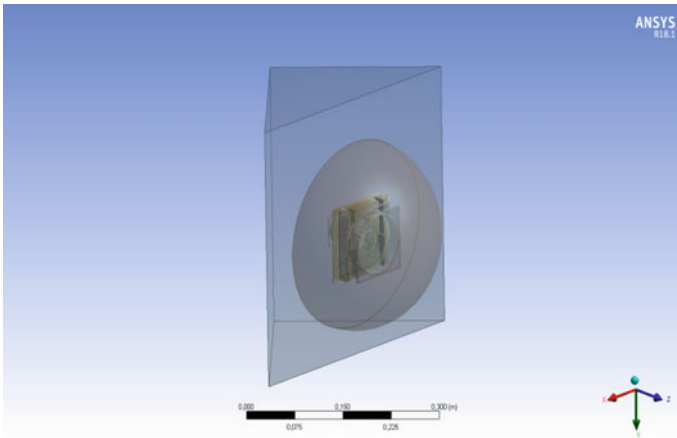**Fig. 6** Proposed refrigeration volume
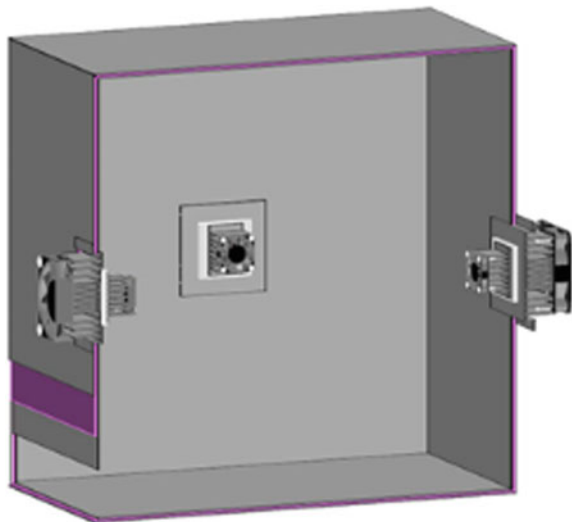
Fig. 7 One-fourth flow domain of the system

In the geometry preparation, the design volume is homogenous; therefore, the volume can be investigated in a periodic form with a ¼ part of it as a subsystem in the CFX®. To integrate the compact axial hot fan behavior to the CFD simulations in CFX®, there has been created a sphere with 200 mm radius in the free atmosphere in the hot side; the all periodic part of the system can be seen in Fig. 7.

In the CFD simulations, to get accurate results for a system from a finite element/volume the meshing and setup process should be setup carefully. Therefore, the mesh and setup structure and also the turbulence models have been conducted to define the best variation in the CFD simulations. The study includes the variation of the mesh, setup, and turbulence models as to define the best convenient combination for the system. The results of the simulations are examined according to the results of the concept volume experimental studies. The results have been conducted according to the turbulence models and the mesh structures, and the results demonstrate the most convenient structure of the whole setup process, in mesh structure as proximity–curvature, conformal as mesh structure, SST as turbulence model, and transient as setup model. This combination is the most convenient one because the transition of the airflow is revealed along with the compact axial fans. The turbulence models are used to define transitions and the temperatures of the subsystems at steady-state conditions, in the simulations. The simulations have been run as to investigate as steady-state, after the decision of the volume dimensions among the aforementioned values, the simulation studies have been carried out as transient analyses [29].

The temperature distributions of the system can be categorized as the heat sink and compact axial fan on the hot surface of the thermoelectric module, the heat sink and compact axial fan on the cold surface of the thermoelectric module.

In the final setup, the all analyses have been carried out and to obtain an average result in the beginning, the thermoelectric module system is worked with 4.0 A in at

1442 s. The simulation has continued up to converge in 4,326,000 s. The time step is set as 1 s equals to 3000 s (in real) on the CFX® setup. Consequently, the temperature of the system can be obtained as required as 10 °C.

5 Results and Discussion

5.1 Experimental

Based on the experimental studies, the results are given in Table 1. Within the scope of the studies carried out, the temperature distribution results of the concept volume obtained according to various current values can be seen in detail. The hot fan outlet temperature, hot surface temperature, cold fan outlet temperature, cold surface temperature, and concept volume temperature were found to be range between 24.07 and 44.44, 27.27 and 48.04, 17.13 and 17.92, 20.71 and 21.48, 18.25 and 16.97 °C, respectively. The working current values were changed between 0.5 and 5 A in an 0.5 A increments, and the best working current value was determined based on the values of temperature distribution on hot and cold surfaces. According to these values, the optimum operating current value of TEM was defined to be 4.0 A.

Table 1 Temperature chances according to the current values in concept refrigerator volume

Direct current value (A)	The hot fan temperature (°C)	The hot surface temperature (°C)	The cold fan temperature (°C)	The cold surface temperature (°C)	The concept refrigerator volume temperature (°C)
0.5	24.07	27.27	17.13	20.71	18.25
1.0	25.57	28.78	16.34	19.92	17.66
1.5	26.68	30.08	18.94	22.52	16.42
2.0	28.99	32.19	18.05	21.63	15.74
2.5	27.08	30.38	15.24	18.82	15.56
3.0	30.65	34.05	16.91	20.49	15.42
3.5	32.95	36.25	18.11	21.69	15.30
4.0	33.92	37.32	16.18	19.76	16.02
4.5	38.01	41.51	17.37	20.95	16.78
5.0	44.44	48.04	17.92	21.48	16.97

Table 2 Temperature values according to the concept refrigerator box

Direct current value (A)	The hot fan temperature (°C)	The hot surface temperature (°C)	The cold fan temperature (°C)	The cold surface temperature (°C)	The concept refrigerator volume temperature (°C)
0.50	22.51	25.64	15.71	19.22	17.22
1.00	23.98	27.12	14.93	18.44	17.34
1.50	25.07	28.40	17.48	20.99	16.13
2.00	27.33	30.47	16.61	20.12	15.24
2.50	25.46	28.69	13.86	17.36	15.34
3.00	28.96	32.29	15.49	19.00	15.00
3.50	31.21	34.45	16.67	20.18	14.87
4.00	32.16	35.49	14.78	18.28	14.33
4.50	36.17	39.60	15.94	19.45	15.47
5.00	42.47	46.00	16.46	19.97	15.13

5.2 CFD Studies

At the beginning of the CFD studies, analysis studies were carried out for this volume to observe whether the concept volume provided the temperature distribution studies; the results obtained in this context are given in Table 2. The hot fan outlet temperature, hot surface temperature, cold fan outlet temperature, cold surface temperature, and concept volume temperature were found to be range between 22.51 and 42.47, 25.64 and 46.00, 15.71 and 16.46, 19.22 and 19.97, 17.22 and 15.13 °C, respectively. The working current values were changed between 0.5 and 5 A in an 0.5 A increments and the best working current value was determined based on the values of temperature distribution on hot and cold surfaces. Table 2 illustrates the temperature distribution according to the direct current in the concept volume in the CFD. However, since the assumption that the semiconductor structure in the TEM is to be disturbed is not included in the studies conducted here, the temperature change is reduced to very good values even for 5.0 A. In real life, since the TEM structure will start to deteriorate at high temperatures, the optimum working current is chosen as 4.0 A for maximum efficiency in CFD studies. In the CFD studies, TEM system has been worked with a good efficiency level with 4.0 A as the electrical current. Therefore, to define dimensions of the box, 4.0 A electrical current has been selected as an optimum one. The CFD simulations have led to find out the temperature values according to the refrigerator box decrements, the temperature distribution of the system is illustrated as in Table 3. The CFX® results show that the most appropriate conditions (inner temperature of the volume as required 10 °C) have occurred in dimensions with 250 × 250 × 250 mm, it can be seen in Fig. 8.

The result is converged to real results. In the CFD analyses, the turbulence models, the size function and the simulation types have been investigated to find the most

Table 3 Temperature distribution values according to the designed refrigerator box volume dimensions

| Dimensions (mm)	Ambient temperature (°C)	The hot fan temperature (°C)	The hot surface temperature (°C)	The cold surface temperature (°C)	The cold fan temperature (°C)	The volume average temperature (°C)
500	25.00	22.87	29.99	17.87	25.88	15.77
450	25.00	23.54	29.65	9.56	25.66	15.02
400	25.00	24.66	31.56	7.68	24.41	14.66
350	25.00	25.96	33.54	3.57	23.33	13.78
300	25.00	26.77	38.78	1.55	22.55	11.45
250	25.00	27.22	42.66	0.69	21.66	9.77
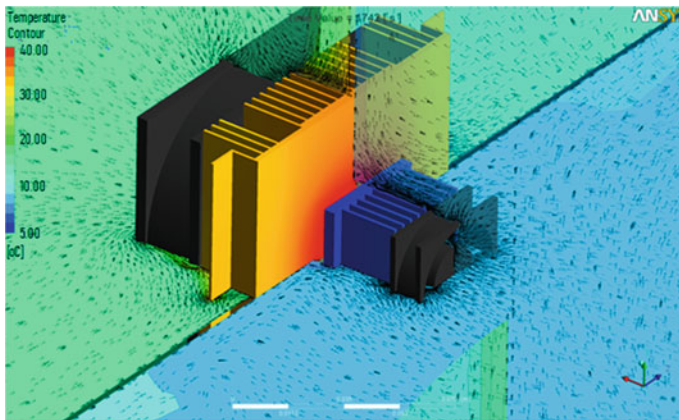
Fig. 8 Temperature distributions of the TEM system in CFX® post

appropriate ones. The CFD studies include a control volume, in the cold side of the thermoelectric module as a quarter of box and in the free atmosphere, there are assumed a sphere with 200 mm radius. According to the simulation results, the required time and the current values have been obtained as to reach the wanted temperature of the average volume. The analyses' results and the experimental results demonstrate the proximity and curvature as function size, shear stress transport (SST) as turbulence model, conformal mesh as mesh structure, and transient as solution type are most appropriate as to find the closed results to experimental data because of the turbulence and interactions of the fans and heat sinks.
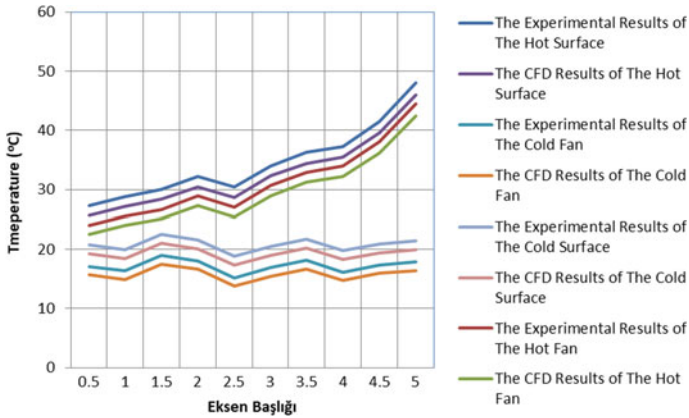
Fig. 9 Comparison of the experimental and CFD results

Considering these studies, it can be said that the difference between CFX® studies and experimental studies is close to 2%; therefore, CFD simulations results of the concept volume can converge to the experimental results, which is demonstrated in Fig. 9.

6 Conclusions

The structure of the study is composed of band theory, semiconductor, thermoelectricity, elastic resistor, and experimental studies and analyzes, in detail. Within the structured mathematical model, the refrigerant volume is designed on Solidworks® considering the cooling capacity of four TEM units. Depending on the design, the entire TEM system is placed in the CFX® for analysis. Based on the study, CFX® analyses were performed; the optimum refrigerant volume dimensions for the system were determined. The most appropriate setup structure to be used in CFX® studies have been used by using previous studies related to this study; it was observed that experimental studies were supported within the scope of CFX® results. Based on the study, studies were carried out to put the theoretical equations into use in both the modeling and the CFX® part, and all analyses were carried out within this systematic. Besides, the optimum operating current range for TEM was determined.

In the study, the initial dimensions were differentiated with CFX® studies; heat transfer and fluid mechanics according to the temperature distributions in the system. To define the dimensions of the refrigerator box volume, the optimum electrical current for the TEC 12706 TEM system has been found as 4.0 A. By this way, the requirements of the system characteristics have been identified. The dimensions of the refrigerator box volume have been defined as $250 \times 250 \times 250$ mm in steady-state

simulation and after that transient. ZT and COP values of the refrigeration system are defined as 0.32 and 0.378, respectively.

References

1. Brief history of thermoelectrics. California Institute of Technology, Caltech Material Science. http://www.thermoelectrics.caltech.edu/thermoelectrics/history.html
2. Rowe DM (2005) Thermoelectrics handbook: macro to nano. Springer, Berlin, 340 p
3. Ioffe AF (1960) Physics of semiconductors. Infosearch, 463 p
4. Sharma A, Gupta S, Kaur K (2014) Thermoelectric effect, its background and scope in dairy: review. Global J Eng Sci Res Manage 15
5. http://hyperphysics.phy-astr.gsu.edu/hbase/Solids/band.html
6. Champier D (2017) Thermoelectric generators: a review of applications. Energy Convers Manage 14
7. http://hyperphysics.phy-astr.gsu.edu/hbase/Solids/Fermi.html#c1
8. Kahn A (2016) Fermi level, work function and vacuum level. Mater Horiz 3:7–10
9. Michaelson HB (1977) The work function of the elements and its periodicity. J Appl Phys 48:4729–4733
10. Lang ND, Kohn W (1971) Theory of metal surfaces: work function. Phys Rev B 3:1215–1223
11. Chinese University of Hong Kong (2017) Elastic resistor. Lessons from nanoelectronics, pp 31–41
12. Sales BC (2001) Thermoelectric devices: refrigeration and power generations with no moving parts. Elsevier Science Ltd., Amsterdam, pp 9179–9186
13. Goldsmid HJ (2010) Introduction to thermoelectricity. Springer series in material science, 250 p
14. Pérez–Aparicio JL, Palma R, Taylor RL (2012) Finite element analysis and material sensitivity of Peltier thermoelectric cells coolers. Int J Heat Mass Transf 12(7)
15. Weerasinghe R, Hughes T (2017) Numerical and experimental investigation of thermoelectric cooling in downhole measuring tools: a case study. Case Stud Therm Eng 10:44–53
16. Astrain D, Vián JG, Albizua J (2005) Computational model for refrigerators based on Peltier effect application. Appl Therm Eng 25(14):3149–3162
17. Quental PRBM (2015) Thermoelectric cooling: designing novel home appliances. Mechanical Engineering, Technico Lisboa, 11, 58 p
18. Junior C, Richter C, Tegethoff W, Lemke N, Köhler J (2008) Modeling and simulation of a thermoelectric heat exchanger using the object-oriented library TIL. The Modelica Association, 6 p
19. Codecasa MP, Colombo E, Inzoli F, Pastorino G, Rizzo C (2003) Optimization of a new thermoelectric cooling assembly using CFD analysis and local modeling of thermoelectric effects. In: 22nd international conference on thermoelectrics, 7 p
20. Fujisaka T, Sui H, Suzuki RO (2013) Design and numerical evaluation of cascade-type thermoelectric modules. J Electron Mater 42(7):1688–1696
21. Korpyś M, Grzegorz Dzido G, WójcikLi J (2012) Experimental and CFD investigation of commercial PC heat sink performance using water and nanofluids. In: 14th European conference on mixing Warszawa, no 6, 13 p
22. Högblom O (2016) Multiscale simulation methods for thermoelectric generators. Ph.D., Department of Chemistry and Chemical Engineering, Chalmers University of Technology, 86, 10 p
23. Nagy MJ, Buist RJ (1994) Effect of heat sink design on thermoelectric cooling performance. In: AIP conference proceedings, pp 147–149
24. Saidur R, Masjuki HH, Hasanuzzaman M, Mahlia TMI, Tan CY, Ooi JK, Yoonve PH (2008) Performance investigation of a solar powered thermoelectric refrigerator. Int J Mech Mater Eng (IJMME) 3(1):7–16

25. Mare R (2012) The behaviour of a solar thermoelectric refrigerator in the case of cooling milk. Math Model Civ Eng (4):125–132
26. Esen DÖ, Balta E (2013) Güneş Enerjisi ile Desteklenen Termoelektrik Soğutma Sistemi Performans Analizi, 11. Ulusal Tesisat Mühendisliği Kongresi – İzmir, 13s
27. Rajangam V, Vekataramanan M (2015) Design and CFD analysis of thermoelectric cooling system. J Chem Pharm Sci (9):399
28. Rawat MK, Sen P, Chattopadhyay H, Neogi S (2013) Developmental and experimental study of solar powered thermoelectric refrigeration system. Int J Eng Res Appl (IJERA) 3(4):2248–9622
29. Akdemir M, Yılancı A, Çetin E (2018) CFD simulation of the heat sink and compact axial fan design on thermoelectric module, IV. In: Anatolian energy symposium with international participation, Trakya University, Turkey, pp 435–444

NEO Energy: The Hybrid Solution

Farhan Mumtaz and Atif Saeed

Abstract In this technological era when the world is endeavoring toward the modern innovations while the energy generation is mainly dependent on the fossil fuels, hydropower, photovoltaic cells, etc. It is for the very first time in Pakistan to integrate two different phenomena for power generation, namely wind and magnetic. The main theme of the project is to operate without fuel and to provide maximum efficiency in comparison to conventional turbines. As the title suggests neo energy (the hybrid solution), it works on the principle of magnetic levitation and wind energy. In order to achieve magnetic levitation, likely pole of magnets in different pairs are mount on circular plates, which is facing each other. These plates mounted on the main shaft of the wind turbine, which produces instability as the turbine moves the output is collected from the DC motor, which is coupled with the main shaft using a pulley. The output can be consumed or stored in DC batteries for later use. This hybrid wind turbine can operate for ten minutes in the absence of wind. Magnet's type and strength can enhance the operating time if the turbine experiences low or no wind power.

Keywords Neo energy · Sustainable · Magnetic levitation

1 Introduction

Recently, population swelling and growing industrialization are becoming tedious issues, especially among the developing nations. Mankind's desire for energy consumption has drastically increased with the passage of time.

Natural resources have always been on priority when it comes to energy generation. Significantly, fossil fuels are consumed for energy generation which are extracted from deep within the Earth's crust. Commercial oil drilling began in the 1850s since then we have consumed approximately 135 billion tons of crude oil.

F. Mumtaz (✉) · A. Saeed
SZABIST University, Karachi, Pakistan
e-mail: farhan.mumtaz@szabist.edu.pk

A. Saeed
e-mail: m.atif@szabist.edu.pk

Fossil fuels are the main source of power plants, automobiles, aerocrafts, and ships; i.e., coal equally contributes among the fossil fuels. Consumption of coal tends to have hazardous environmental effects as it releases CO_2 and SO_2 along with various organic and inorganic compounds [1]. Hazardous emission of coal is one of the major reasons for global warming. Special laws have been developed globally in order to control the effects of global warming. Consumption of fossil fuels has enormous implications, which have led numerous environmental effects globally.

Nowadays, scientists are involved in multiple researches to invent new ways for energy generation using the naturally occurring phenomenon named as renewable energy. The main aim is to generate energy utilizing the sources available that has a negligible effect on the environment globally. Renewable energy is generated using the natural resource, which includes wind energy, solar energy, hydropower energy, and biomass. Particularly, these sources give multiple advantages over conventional fossil fuels, and renewable energy sources are not going to be scarce because all of these are interlinked with the natural phenomenon and they have almost negligible impacts on the environment in comparison to fossil fuels. The field of renewable energy is significantly growing over the period. Similarly, the demand and the dependency towards renewable energy proportionally increasing with the passage of time [2]. However, technological development has also influenced the researches to develop sustainable ways of energy harvesting using renewable sources. It is expected that renewable energy generation will be producing more than 50% of the total energy consumed globally by the end of 2019 [3]. All the renewable energies will be integrated through micro-grids. Micro-grids have the smart system that will utilize the energy with low cost of generation at a particular point of time. Concept of micro-grids will optimize the usage of resources and will decrease the dependency of any single source. Issues related to power conversion, power quality, power storage, and power conversion in micro-grid systems are still under research [4].

1.1 Why Sustainable Energy

Sustainability means to consume one's resources in such an efficient manner that it would not have any harmful effect on owns and other's life. In the current decade, a number of researches are going on to make devices of our current use effective enough so that it would have a minimum environmental impact. The same phenomenon can also be elaborated as to consume earth resources in such effective manner that while fulfilling our current needs we should also have a plan for coming generations so that they could meet their own too. Renewable energy generation methods are known to be a sustainable solution to tackle our current power needs by using resources that are available to its maximum extent throughout the world in masses such as wind, solar energy, and hydro-energy and biofuels. By consuming these sources for our requirements will not only left a better residue for our future generations but is environmental friendly also and will not affect ozone i.e. the matter of critical consideration for most of the environmentalists.

Currently, with the advancement of renewable means of extracting energies, most of the researches direct toward more efficient and smart sustainable ways to extract the same energy, so, that we could utilize maximum of available energy. In this chapter, firstly a short discussion on each of these renewable resources is presented with the mechanics of extracting their mechanical energy and converting it to electrical energy, efficiently [5–8].

1.1.1 Sources of Renewable Energy

Wind Energy

Wind energy is being utilized since decades, and sailors use it to tow or to pull ships through the water. Nowadays, it is also being utilized on land to generate renewable and sustainable energy. Wind energy is comparatively developed technology in comparison with various sources of energy. Wind energy is considered to be ecological and affordable at the same time. Wind energy is widely utilized among the other renewable energy sources. Wind turbines are mainly used for generation and various different shapes and techniques are being used to ensure maximum utilization of power [9].

Horizontal Axis Wind Turbines

Horizontal axis wind turbines are primarily used for high volume of power generation which needs high initial investment. Horizontal axis wind turbines are installed in open spaces because of the massive size of the turbine. Horizontal axis turbines are installed approximately 40–100 m above the ground level to expose the turbines with high wind velocity. To transform the wind energy into the electrical energy, main rotor shaft is pointed toward the direction of wind. Rotor experiences the wind energy and generates a torque on a low-speed shaft. Low-level shaft delivers the energy to a gearbox, high speed shaft and coupled with the generator. Horizontal axis wind turbines generate loud noise while operation and are restricted not be installed near the populated area. Highly trained work force is needed for the commissioning and maintenance of horizontal axis wind turbine as it can generate high volume of power which ultimately reduces the production cost. Horizontal axis turbines are mostly deployed near costal area, offshore, mountain tops, etc. [10].

Vertical Axis Wind Turbines

Vertical axis wind turbines (VAWT) are used for low-volume power generation, and it requires less initial investment. In comparison to horizontal axis turbines, its size is small and it occupies less space for installation. Multiple small turbines (VAWT)
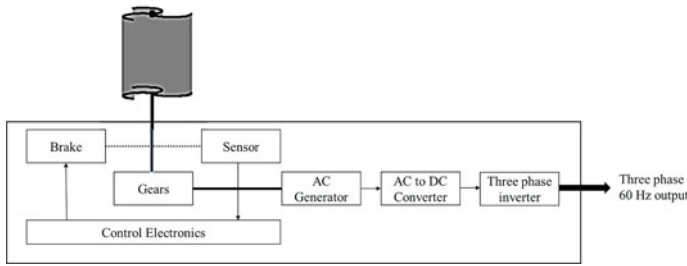
Fig. 1 Mechanical layout of system

can be installed in less space. Vertical axis turbines are used in domestic application as it can be installed on ground level usually rooftops. By being closer to the ground level, they are convenient for maintenance. Vertical axis turbines are less noisy. To transform the wind energy into electrical energy, the rotational axis of vertical axis wind turbine is perpendicular to the direction of wind. The complete schematic is shown in Fig. 1. The rotors shaft is coupled with the gears and generators and in this way, the power generation process is carried out.

Solar

Solar energy has major contributions in renewable energy sources. It is a process of converting radiations of sunlight into electrical energy. However, it is being in used in countries where exposure of sunlight is experienced the most. Accessibility of sunlight makes it an appealing source of power generation, if not utilized on the ground it goes back to the space else absorbed by the oceans, clouds, and landmasses. Solar radiations fall on the photovoltaic cells (PV); these PV cells convert solar radiations into DC electrical power. DC electrical power is fed into the charge controller. The charge controller is primarily responsible to maintain the power quality and to store the DC electrical power in battery banks, which can be utilized in the absence of sunlight. Inverter converts the DC electrical power into AC electrical power if it is directly being consumed as in Fig. 2. Solar power has multiple appealing features which includes no fuel cost, noiseless, pollution free, and being low maintenance system. Its output is entirely dependent on weather conditions which ultimately affect its efficiency. For example, during rainy and cloudy seasons and especially at night time [11].

Hydroelectrical Power

Hydroelectrical power uses water as a resource to generate electrical power. Hydro electrical power is mainly used for higher volume power application. It needs to be
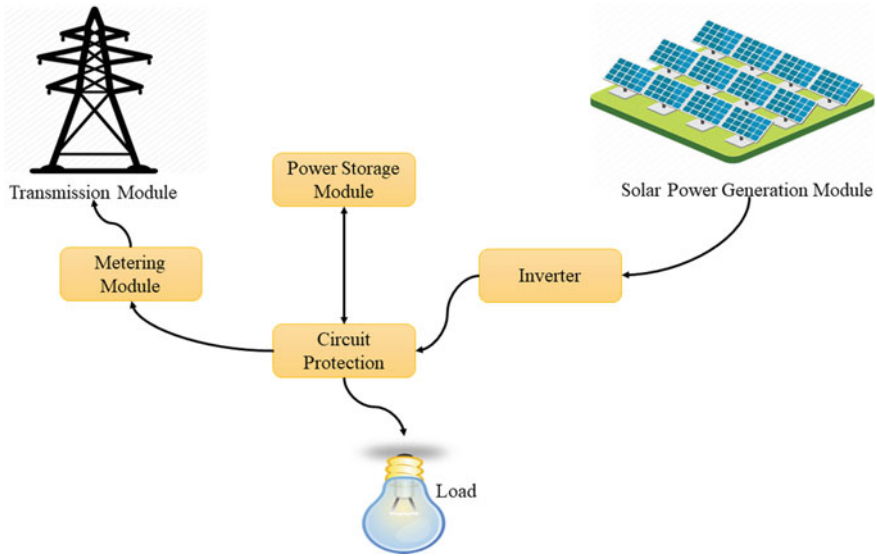
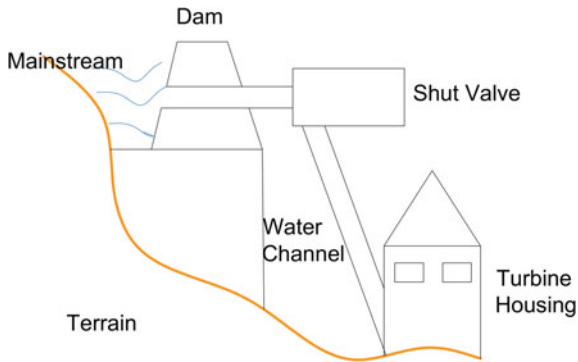**Fig. 2** Solar system layout. Modified from [15]

Fig. 3 Hydroelectric system model. Modified from [16]

planned very precisely as it requires high initial investment. Similarly, it requires technical experts for its operation and maintenance. It follows a simple phenomenon of nature; hydroelectrical power is generated using water currents which flow downward from a height due to gravity. Turbines are installed at the bottom as the waterfalls with high current on the turbines start to move. Turbines are coupled with generators which generate electrical power as in Fig. 3. It is a renewable and sustainable source that does not pollute the environment unlike conventional power plants which operate on fossil fuels. As the water freezes in winters, water current is reduced in winter; this is an issue with hydroelectrical power generation [12, 13].
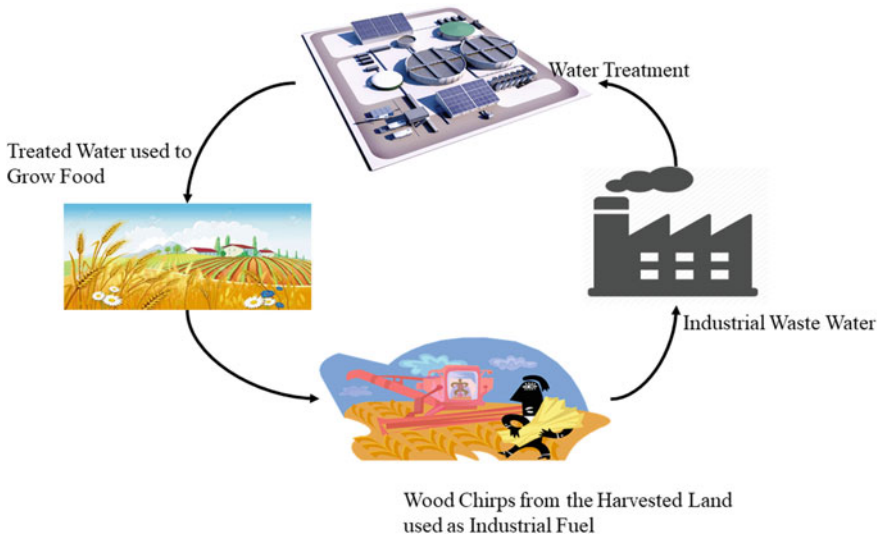
Fig. 4 Biomass system model. Modified from [17]

Biomass

Biomass is a great substitute for fossil fuels and an ongoing research area for renewable and sustainable energy. It is basically an organic material that can be extracted from animals and plants. Biomass contains stored energy from solar radiations. Photosynthesis is a process in which plants absorb solar radiations. Chemical energy and heat are generated by burning of biomass. It can be directly consumed or it can be transformed into liquid biofuels which can be used as fuel in various applications as referred to Fig. 4. Biomass can be extracted from a number of sources which include animal manure, human sewage, leftover food, and plants and fish wastes [14].

It has been observed that many of the power generation projects are rejected by engineers, technocrats, scientists, and social activists as they were harmful toward living beings commonly nuclear generation. When it comes to energy generation using wind turbine it is also discouraged as it has been seen that due to its massive heights it becomes a hurdle for small private jets to fly in that area, it also produces noise pollution, bird accidents more than 200 birds per annum and accidents due to high speed tends to break the propellers of turbine to break and damage the people's property. However, the neo energy is the safest of all in a sense that it surpasses the previous discussed harms to the population. Not only its pollution free but also safer in health perspectives as well the detailed attributes can be seen in Fig. 5.

The main aim of this research is focused to produce the renewable and sustainable energy using a combination of wind energy and magnetic energy. Wind energy is being used to produce energy since decades but producing energy using magnetic levitation principle is also considered to be the potential technique to produce renewable and sustainable energy. Neo energy has an additive advantage of one-time
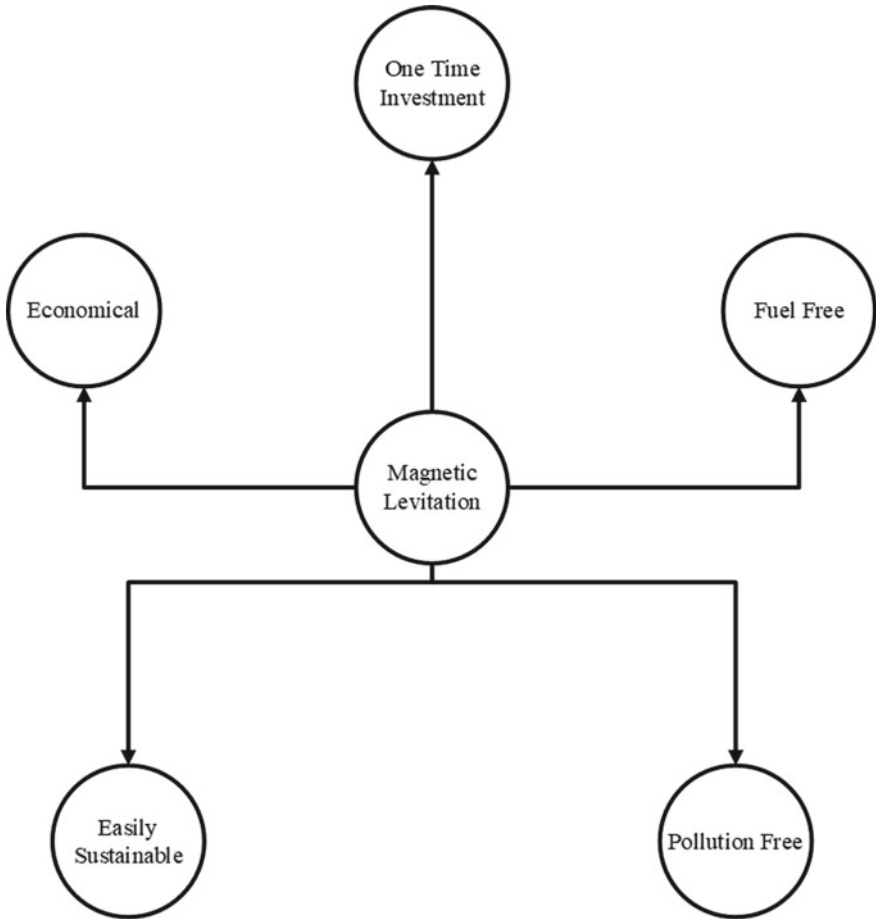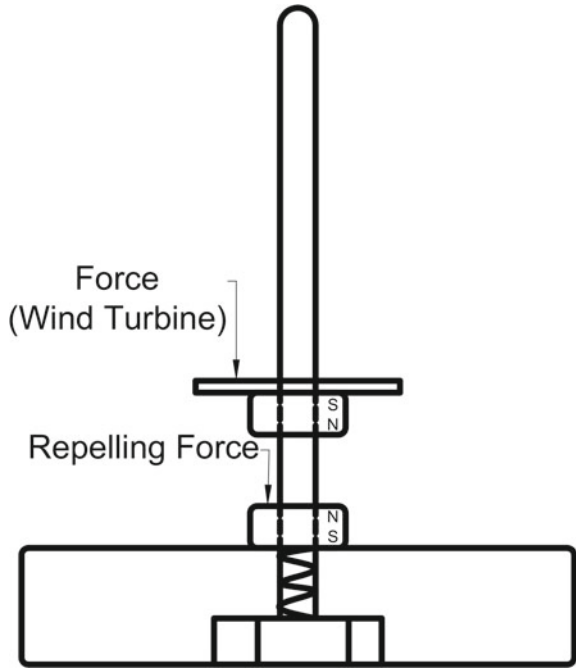
Fig. 5 Magnetic levitated wind turbines attributes

investment. Neo energy reduces the dependency on power provided by private companies. Due to the shortage of electricity, people use back-up power sources that are costly and need a lot of maintenance, whereas neo energy is easy to maintain. This complete project can easily be installed; it does not require any skilled work force as it will affect the overall cost. It is not consumer specific; it can be preferred by any firm or any individual. Its portable design allows the user to be operated in remote locations especially feasible for forces as they are always moving.

2   Method and Materials

This project is primarily focused to design and implement a vertical axis turbine using magnetic levitation that has the ability to generate power in both high and low wind speed conditions. Unlike the conventional designs of vertical axis wind turbines, this design is levitated using the principle of magnetic repulsion vertically on the rotor shaft. This principle of magnetic levitation will contribute as an alternative to ball bearing used in traditional vertical axis wind turbines. The phenomenon of magnetic levitation is achieved by permanent magnets. Magnetic levitation will be applied between the rotating shaft of the circular propellers and complete assembly of the system using pulleys. The process of power generation of a vertical axis wind turbine using repulsion principle is initiated by providing wind power from an ordinary wind blower, and initial excitation is required because the limitation of the size chosen in this experiment is comparatively small enough to be used in open environment with low wind pressure. Once the system becomes stable after getting excitation, propellers rotate tremendously in a very smooth manner. Alignment and precise balance of the propeller base are responsible to keep the complete structure in motion. Misalignment or imbalance in the structure can severely affect the magnetic levitation at the bottom of the propeller structure and tends to have failures. Permanent magnets are mounted on a special material known as Bakelite, and a set of Bakelite plate's structure is used in this project. Bakelite material is a non-conductive material which keeps the isolation between the metallic structure and the permanent magnets responsible to provide magnetic levitation which will ultimately reduce the friction present in the structure and will provide continuous instability as a result our minimum required rpm will never die down. Magnets are arranged in a unique pattern which ultimately increases instability. Main driving shaft of the structure is connected to three important parts. One end of the main driving shaft from the top is coupled with the propeller structure, the center part of the main driving shaft is experiencing the main phenomenon of magnetic levitation, and lastly the bottom of the driving shaft is coupled with a pulley mechanism. Pulley is connected with a DC generator with a suitable ration to achieve the desired rpm for the successful operation of the system. DC generator is primarily responsible for converting all the mechanical motion energy produced using air and magnetic levitation into the DC electrical energy. After the successful process of power generation, the system is flexible to be utilized according to the need. The DC output power can be directly connected to the load after passing it through a circuit which will provide smooth output to the system. In case of AC power applications, the DC power can be converted into the AC power using an inverter circuit, providing an undistorted sine wave with a suitable amplitude is achieved using the inverter circuit. If the system is not being utilized or it is under-utilized, an additive feature of power storage is also present in this system. Capacity of storage ultimately depended on the battery size being used. A charge controller embedded system is connected between the output and the

power storage and it monitors the storage on real-time basis in order to protect the
system from any hazardous accident. Below is the sketched block flow diagram of
the complete system. The basic hardware of magnetic levitated wind turbine is given
in Fig. 6, whereas the flow of project can be seen in Fig. 7.

In this system, we have used multiple pairs of permanent magnets which are
vertically mounted on a Bakelite material housing that are responsible to levitate the
system. As the vertical axis wind turbine is placed on the top of rotating permanent
magnets, it will produce kinetic energy in the system and wind will be an added input
source to increase the efficiency of the system. Initially, the system is initialized using
an external wind source until the system becomes stable, and once the rated RPM
is achieved by the alternator, the external wind source is cut down and the system
operates independently with the help of magnetic levitation. The external source is
provided with the help of a blower.

2.1 Magnetic Levitation

Magnets are used in various applications which may vary according to the principle
how magnets are being used. Magnets have two different behaviors one is attraction
and other is repulsion. If two different poles of magnets, i.e., north and south, are
brought near their magnetic field, they attract each other and this phenomenon is
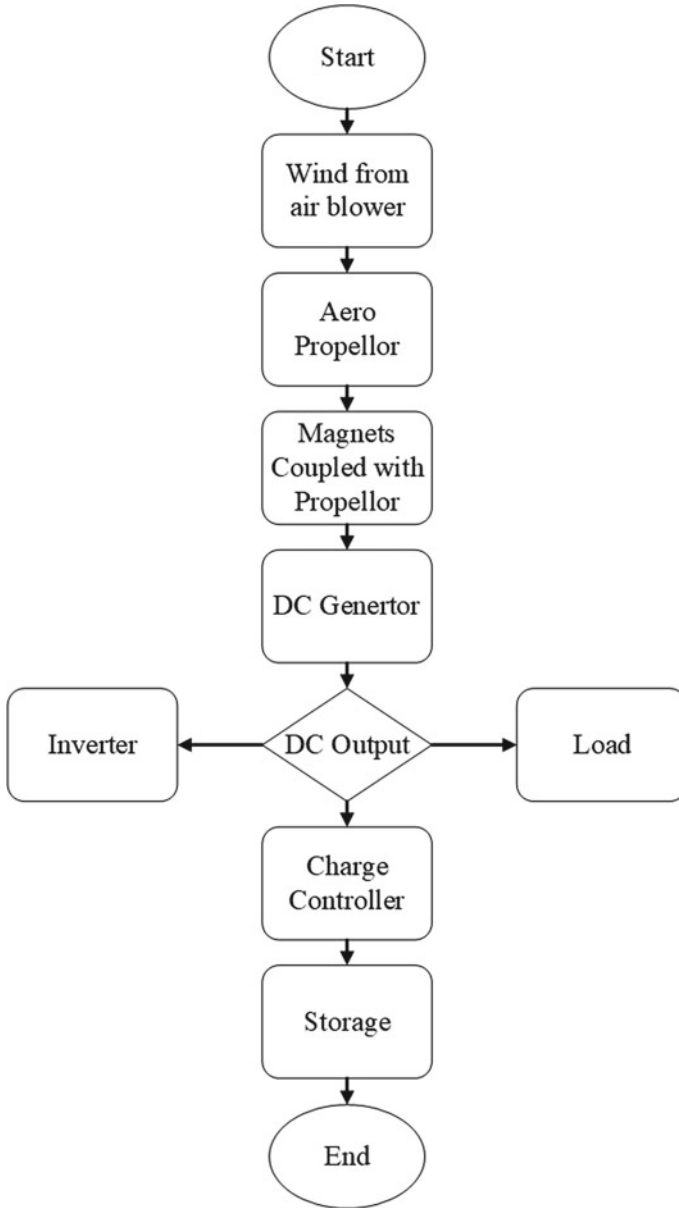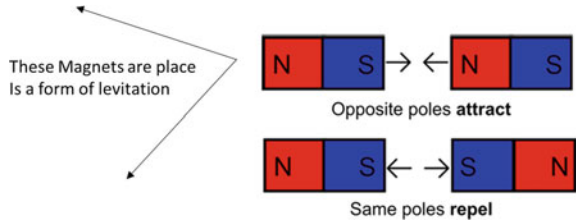
Fig. 7 Overall process flow

These Magnets are place
Is a form of levitation

Opposite poles **attract**

Same poles **repel**

known as attraction. Whereas, when same poles of magnets i.e. south and south are expose to each other within their magnetic field limits they tends to repel each other this phenomenon is known as repulsion. Magnetic levitation uses the repulsion phenomenon for magnetic levitation. Two same poles of magnets are vertically placed on each other, due to its repulsive force the magnet placed on the top will be floating in the air this phenomenon is said to be magnetic levitation as shown in Fig. 8. Magnetic Levitation is a technique used to suspend a desired object by means of magnetic field having no physical contact between the objects which offers negligible friction while the objects are in motion. This technique is used instead of contact bearings and it contains no wear and tear, offers less friction, negligible noise, no need of lubrication and low amount of power loss. In high speed, this technique seems to be beneficial as it eliminates mechanical losses.

However, there is a drastic growth in the usage of materials for designing permanent magnets, magnetic levitation using permanent magnets are also contributing in wind turbines to decrease the cost and increase the overall efficiency of the turbines. There are two main advantages that can be achieved if magnetic levitation principle is used in wind turbines.

1. Less startup speed

As there is no physical link involved in the rotating mechanism, the system requires less startup speed as the system experiences less friction in comparison to conventional designs. It also generates more output with the low speeds.

2. Minimum maintenance

Magnetic levitation eliminates the maintenance cost for the regular lubrication of the wind turbine rotor. Elimination of lubrication also increases the reliability of the system and reduces downtime required for maintenance.

3 Results and Discussion

This project was done in Sir Syed University of Engineering and Technology (SSUET) located in Karachi, Pakistan. It was a final year project, which is basically

mandatory for the completion undergraduate degree in the Department of Electronic Engineering. It was completed over the coarse of one year. Pakistan is experiencing a terrible shortfall of energy and this motivated the students to contribute to the domain of renewable energy, as the country is in the category of lower-middle income countries the solution had to be low cost and robust. After days of research, they concluded to work on wind turbine as they were working in the coastal area they had plenty of wind to work with. But this was not enough as the conventional horizontal wind turbines are being used since decades. They worked on the orientation of the propellers and decided to implement their structure on a vertical axis wind turbine. Vertical axis turbines primarily focus on a small-scale setup. Novelty of this project came later on to integrate the magnetic phenomenon in a wind turbine to reduce the friction losses and keep it in motion for a longer period. Magnetic levitation principle was utilized by the students to make it efficient than a conventional turbine. Pairs of magnets placed on a set of two Bakelite plates were installed underneath the vertical propellers of turbine. The complete system can be distributed into three fundamental components as mentioned below:

(1) Wind + propellers
(2) Magnetic levitation
(3) Power generation

After successful completion of the project, they conducted trials on three different types of load and gathered the result. From this result, the regression model of wind turbine has been generated through best residue fit method. Also, it can be seen from the behavior of graphs, that our system is load dependent, i.e., its working characteristic alters w.r.t change in loading conditions. However, this prototype works best at 50 W as it can be operated for maximum time period, i.e., 623 s as shown in Fig. 9, whereas it works upto 483–485 and 321–325 s for 80 and 100 W, respectively, as shown in Figs. 10 and 11.
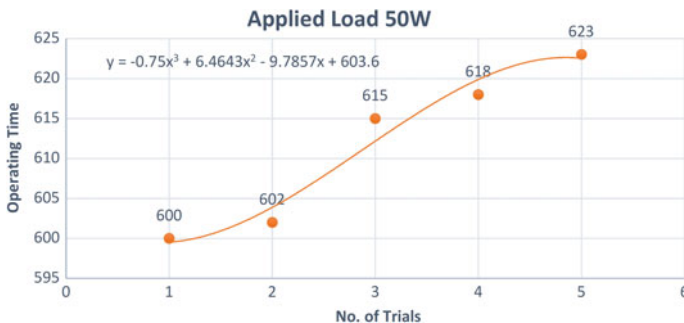
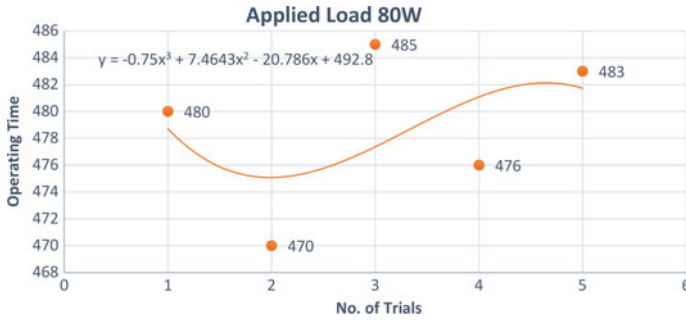

Fig. 9 Load configuration 50 W

Fig. 10 Load configuration 80 W
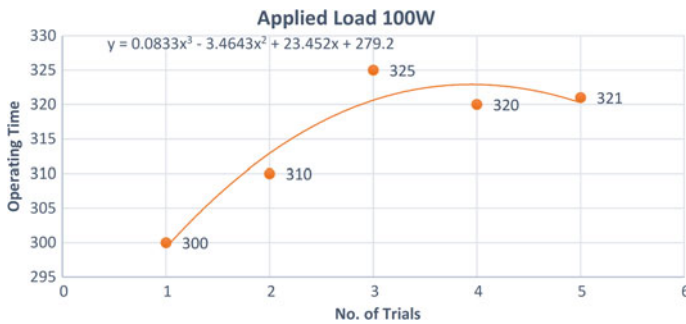
Fig. 11 Load configuration 100 W

4   Conclusion

Renewable energy can be produced using various ways and it depends on the feasible options that are available to a particular area for i.e. solar energy can be installed in hot countries which experience excessive amount of sunlight. This project contributes to the humanity in many aspects which formerly includes a solution to overcome the shortfall of energy crisis and later it ensures to be environmental friendly. According to the research of World Health Organization, air pollution kills an estimated 7 million people worldwide every year. WHO data show that 9 out 10 people breathe air containing high levels of pollutants. WHO is working with countries to monitor air pollution and improve air quality; shortage and high cost of electric energy has become hot issues for today's word, and there is need to find new ways to overcome such problems and neo energy is one of the steps forward toward overcoming the limits of electric energy.

References

1. Junejo F, Saeed A, Hameed S (2018) 5.19 energy management in ocean energy systems. In: Comprehensive energy systems. Elsevier, Amsterdam, pp 778–807
2. Howarth SJ, Callaghan JP (2012) Compressive force magnitude and intervertebral joint flexion/extension angle influence shear failure force magnitude in the porcine cervical spine. J Biomech 45(3):484–490
3. Texley J (2011) Global warming. Sci Child 48(7):66
4. Zeng Z, Zhao R, Yang H, Tang S (2014) Policies and demonstrations of micro-grids in China: a review. Renew Sustain Energy Rev 29:701–718
5. Uqaili MA, Harijan K (2012) Energy, environment and sustainable development. Springer-Verlag, Wien
6. S. Global and E. Outlook (2008) [R]evolution European renewable energy
7. Chu S, Majumdar A (2012) Opportunities and challenges for a sustainable energy future. Nature 488(7411):294–303
8. MacIsaac D (2009) Sustainable energy—without the hot air. Phys Teach 47(8):556
9. European Wind Energy Association (2014) Wind energy—the facts
10. Saeed A et al (2018) Steps toward sustainability: energy through flywheels. In: 2018 7th international conference on renewable energy research and applications (ICRERA), pp 111–116
11. International Energy Agency IEA (2014) Technology roadmap solar photovoltaic energy 2014
12. Paish O (2002) Small hydro power: technology and current status. Renew Sustain Energy Rev 6(6):537–556
13. Saeed A, Ahmed A, Junejo F, Amin I (2017) Design of a small, cheap UUV for underwater exploration. In: 2017 4th IEEE international conference on engineering technologies and applied sciences (ICETAS), pp 1–5
14. Uddin W et al (2016) Biogas potential for electric power generation in Pakistan: a survey. Renew Sustain Energy Rev 54:25–33
15. "Energy Harvesting | Mouser Electronics" [Online]. Available: https://eu.mouser.com/applications/energy_harvesting/. Accessed 27 May 2019
16. Sørensen B (2004) Renewable energy : its physics, engineering, use, environmental impacts, economy, and planning aspects. Elsevier Academic Press, Cambridge
17. "Biomass Energy and Sustainability" [Online]. Available: https://www.bioenergyconsult.com/biomass-energy-sustainability/. Accessed 27 May 2019
18. "Glencoe Physical Science Chapter 8: Magnetism Section 1 Review Flashcards | Quizlet" [Online]. Available: https://quizlet.com/76241314/glencoe-physical-science-chapter-8-magnetism-section-1-review-flash-cards/. Accessed 27 May 2019

Sustainable Transportation System Design

Melis Çolak, İrem Yaprak Utku, Deniz Özmisir, Alican Boz, Tayfun Aydoğdu, Mert Cem Didiş and Emre Nadar

Abstract As reducing the carbon footprint became one of the topmost concerns of the firms, Company X Turkey has a goal of transforming all of its operations in environmentally sustainable manner. Therefore, they specified their main goal as reducing yearly carbon emission levels of the company by five percent calculated in key performance indicator. Although there are several causes of increased levels of carbon emission, since the control capability of the company is limited in other fields, this study focuses specifically on developing a strategy for reducing the carbon emission generated due to Company X's transportation system in Turkey. The aim of this study is to create a well-designed transportation network through the detection of CO_2 emission causes. To lower route-based emission levels, more utilized use of cross-dock locations and alternative fuel usage is recommended, while routing is

M. Çolak (✉)
M.Sc. Industrial Engineering, Baskent University, Ankara, Turkey
e-mail: meliscolak95@gmail.com

İ. Y. Utku
Garanti Bank, Istanbul, Turkey
e-mail: iyaprak.utku@gmail.com

D. Özmisir
M.Sc. Management, Kuhne Logistics University, Hamburg, Germany
e-mail: denizozmisir@gmail.com

A. Boz
Department of Risk Management Levent, Akbank, Istanbul, Turkey
e-mail: alicanboz.26@gmail.com

T. Aydoğdu
Philip Morris International, Ankara, Turkey
e-mail: tayfunaydogdu61@gmail.com

M. C. Didiş
Unilever, Umraniye, Istanbul, Turkey
e-mail: Mert.Didis@unilever.com

E. Nadar
Department of Industrial Engineering, Bilkent University, Ankara, Turkey
e-mail: emre.nadar@bilkent.edu.tr

provided by integer programming. Improvement suggestions including fleet aerodynamics, tire pressure, optimal speed, and acceleration for fleets are constructed in a separate branch to decrease fleet-based carbon emissions in the system.

Keywords Sustainable transportation · LRP · CNG · Fleet improvements

1 Introduction

"Carbon footprint stands for a certain amount of gaseous emissions that are relevant to climate change and associated with human production or consumption activities." As well as other greenhouse gasses (GHGs), it is known that carbon dioxide (CO_2) emissions have a major contribution 81% to climate change in a global manner. Therefore, responsibilities on decreasing the amount of carbon dioxide emissions are shared among all nations around the world, and they try to shift toward a carbon-neutral model in each industry in their nation by trying new methodologies and making changes in their policies.

When analyzing carbon footprint of companies, it is important to differentiate between different sources of direct emissions and indirect emissions. Since people are able to choose their travel destination and their travel method, people's travels cause direct emissions. On the other hand, indirect emissions are generated while transferring products between nodes. Since the customer has no control over the distance between the factory and store, the company is held responsible for reducing emissions. Although there are several factors that contribute to CO_2 emissions in the transportation system, 72% of the carbon dioxide emissions are because of road transportation.

The root causes for CO_2 emissions can be classified into four main headlines as follows: Route-based problems as decisions like which trucks to use in which networks and optimal route selections, physical and mechanical truck-based problems, fuel-based problems, and speed/traffic-based problems. There are various applications of carbon-free transportation in public transportation in metropolises, in logistic departments of several shipment companies, and in the automotive industry. Driving a low-carbon vehicle or the driving style of the driver, inflation of tires, and traffic intensity is some of the factors that may affect the carbon emissions.

The current routing of the company is formed of three round trips. As a first solution, instead of the current trips, if a triangular routing plan is adapted, it is thought that this will mostly cut the emissions and will be beneficial since it annihilates the empty truck movement between nodes of transportation. The second solution approach will only be useful if the company has several locations to visit in a specific area and in the cases where the accessibility of trucks to some areas is harder. This solution includes using one larger truck to transport all products in one site, then parceling out specific deliveries to their local carriers. Another solution can be related to both route-based problems and truck-based problems since it answers the question of which fleet type to use, and it includes a physical change in the current fleet. An

alternative solution can be using a new and modern fleet instead of their current one or changing the type of transportation. In some cities, there are suggestions on using hydrogen power or solar energy vehicles and electric vehicles or dual-energy vehicles instead of the current ones in traffic [1]. However, a significant change in the vehicle types may not be sufficient for a problem where the transportation includes large volumes of fast-moving consumer goods between long distances, since it may require a large budget for the investment.

Decisions including the height, weight or the fullness of each truck, inner temperature of trucks, aerodynamics of trucks, tire inflations, full or incomplete combustion of fuel in the combustion chamber, and efficient usage of the fleet can be listed as the subcategories of the truck-based problems. Since truck-based problems respond to the decisions about the load volumes and weights, using fully loaded trucks or heavier loads in transportation from each node to another will result in a more efficient and sustainable transportation system.

It is also known that the harder the truck moves forward, the more the fuel it uses. This hypothesis is also related to the friction between the road and the tires; therefore, the system can also be utilized by alternative improvement techniques on physical properties of the vehicles in the fleet. Thus, it is important for a vehicle to have a suitable aerodynamic design in a coordinated manner with the physical design of the vehicle, which may include the type of tires or the inflation of tires in some cases, and this can be achieved implementing different strategies for physical and mechanical truck-based problems. By deciding on the correct tire pressure and tire type addition to the design changes in the overall truck, it may be possible to obtain a 5–11% of fuel reduction and 9% carbon dioxide emission reduction in total.

Another main cause of the emission is the speed and traffic-based problems, which include decisions on which hours of the day should the trucks travel at which speed, acceleration of vehicles, and in some cases, this root cause should also cover the road infrastructures under its umbrella. The optimum speed, acceleration of the vehicle, and traffic hours during the whole travel are mentioned as an important controlling factor for emissions. Thus, an implementation on controlling the speed and traffic-based problems will be 5–10% effective in means of its fuel savings, and it will provide a 7% decrease in the carbon footprint.

Finally, fuel-based problems consist of decisions on different types of alternative fuels and the legal requirements that they need to satisfy in each country. On the other hand, the fuel-based problems are not only limited to the scope of transportation of different companies. All around the world, there are ongoing debates about the usage of alternative energy sources instead of fossil fuels, since there is no shortage of them in the near future. However, because of the least cost of fossil fuels, they are commonly preferred among others, but this time, it will lead to an increase in the carbon emissions. Examples for alternative types of fuels are given as biofuels, liquefied natural gas (LNG), compressed natural gas (CNG), gas-to-liquids (GTL), hydrogen fuel cells, and electric vehicles [2].

Since there are many companies from different areas which try to decrease their carbon footprint by various approaches, the efficiency of the outcomes of their solution techniques differs. A summary of the alternative solution techniques for the

Table 1 Estimated reduction in fuel and carbon emissions for alternative solutions

Solution methodology	Estimated fuel reduction	Estimated CO_2 reduction (%)	Source
Improvement in aerodynamics of trucks	3–15%	6	Carbon war room research report
Improvements in tire pressure	5–11%	9	Ramachandran et al. [3]
Speed and acceleration optimization	5–10%	7	Ramachandran et al. [3]
Route optimization	Not mentioned	~60	Tice [4]
Change in fleet (design and fuel)	Not mentioned	20	Tice [4]
Alternative fuel usage (CNG)	Not mentioned	16.2	Beuthe et al. [2]

root causes of the carbon dioxide emissions is given as follows. As the majority of those approaches include route optimization and change in the fleet as an effective solution methodology, it is reasonable to focus on route-based problems and truck-based problems and try to suggest alternative and feasible solutions in that area. In the further steps of this study, the main approach will be concentrating on the two root factors which will likely result in more significant improvements in the carbon dioxide emission levels of the company (Table 1).

1.1 Company X

The company maintains its manufacturing operations in every continent except Antarctica, and its products are sold in 190 countries. Two billion consumers use its products on a daily basis, and seven out of ten households around the world have Company X's products. According to Statista (2016), the company was ranked among the top 10 largest fast-moving consumer goods (FMCG) companies in the world with net sales of about 59.19 billion U.S. dollars based on generated net sales. The company has more than four hundred brands, but it mainly focuses on thirteen brands with more than €1 billion sales a year. Its products can be categorized into four groups: personal care goods, foods, refreshment goods, and homecare goods. The turnover values for those categories are: 20.1, 12.9, 10.1, and 10.2 billion Euro, respectively, according to annual report and accounts 2015 report of the company.

They exist in Turkey market for more than hundred years, and today, one million customers in Turkey use brands of them. Company X not only meets customer demand in Turkey, but also contributes to Turkey's economy by employing Turkish workers, farmers, and suppliers. For manufacturing operations, Company X makes

a lot of investments yearly in eight factories and sales activities in Turkey with more than five thousand employees. Ninety-five percent of the products of Company X are produced in Turkey and being exported to thirty-four countries. Therefore, Turkey is one of the most important centers of logistics, brand-product development, finance, and research and development for the company.

The factories of the company in Turkey are located according to categories of the products. Ice cream factories are located in City A and City B. Margarine factory is in City A, and a tea packing and sauce and soup/bouillon factory is in City C. The factory of detergent, home, and personal care product is in City D. There are three tea factories in City E. In addition, a factory of house cleaning and personal care products which is still under construction is located in City B. The company has six warehouses for its logistic operations which are categorized into three groups according to the storage temperature of warehouses. Frozen warehouses are located in City A and City B. The chilled warehouse is in City A. The ambient warehouses are located in City D, City B, and City E; however, City D warehouse will not continue to operate after March 2017.

1.2 System Description

The company manages a very large volume of production every day and communicates a big portfolio of customers while transporting its goods. Consideration of the transportation volume urges the company to take environmental precautions in order to diminish its impact on the world and be the pioneer in this issue. One of the main goals of the company is to transform its operations into an environmentally sustainable manner. For to that strategy, in 2010, the company launched a plan and shaped its vision through this plan. The plan helps to decrease the environmental footprint of the company and increase positive social impact.

This study focuses specifically on reducing the carbon emission generated due to the company's transportation system in Turkey. The company wants to develop a strategy on transportation rather than other components of the emission because control capability of the company is limited in other fields. To be more specific, raw materials, manufacturing processes, and retailing require bilateral actions, and hence, they include a third-party action in those processes. On the other hand, the transportation system of the company is kept highly private by opening tenders annually and having transport companies only working for Company X. In addition, transportation is a better area to work on rather than disposal steps because disposal requires tracking of goods after the sale, and it is less efficient in the return on investment when compared to transportation. According to the plan, the company aims to decrease the gas emission by reducing it 5% each year and end up with 40% emission reduction by 2020. For this purpose, a key performance measure (KPI_2) is selected by the firm and given in order to be able to compare the findings and recommended solutions for the problem.

$$KPI_2 = \frac{\text{Total kgs of CO}_2}{\text{ton product}} = \left(\frac{\text{Kilograms of CO}_2 \text{ from transportation and warehousing}}{\text{Sales volume (tones)}} \right) \tag{1}$$

According to the data provided by the company, yearly emission levels in terms of KPI_2 fail to meet the global goal set in 2015 and in 2016. In 2016, the company opened its new warehouse in City B, and since the shipments are sent from City B instead of City D, this caused an increase in the total traveled distance. This is the main reason behind the unmet aim of minimizing carbon emissions. Carbon dioxide emission levels are shown in Fig. 1, starting from 2011 to 2016 in terms of kg CO_2 per tones moved. Although emission level has increased in 2012 when compared to 2011, there is a decreasing trend after 2012 till 2016. Emission decrease was 8.6% from 2011 to 2012, 6.4% for 2013 when compared to 2012, and for 2014, 7.9% decrease was obtained. However, 5% reduction could not be achieved in 2015. After the 2.6% decrease in 2015, emission level was increased in 2016 due to pre-specified warehouse location change.

Company X decides which truck type to use in planning step for its shipments. The first category of the trucks that the company uses is market trucks. It is the cheapest way among all others for full truckloads; however, there is a high risk of burglary. The second category of trucks is fleet trucks. For this category, the cost for returning of trucks is paid as well, and thus, it's a more expensive option than the market trucks. In this option, backhaul utilization is also possible for fleet trucks. Therefore, although the prices are higher, fleet trucks can be preferred among the other options. The price is determined for this truck type as a function of distance and duration of shipment. In addition, additional distances cause extra waiting, and drivers are paid for the waiting times as well. Partial trucks (LTL) have a unit-based payment system. Units can be pallets or cases of goods. When the required amount to be shipped is not much in quantity, it is not the optimal decision for the company to send a market or fleet truck for those goods. In such cases, the firm prefers to use partial trucks. The price of partial trucks is higher when compared to per unit pallet cost in other truck options. However, since the amount to be sent is not much, partial trucks compensate the cost.

Fig. 1 Yearly carbon emission values of the company transportation network (kg CO_2/tones sold)
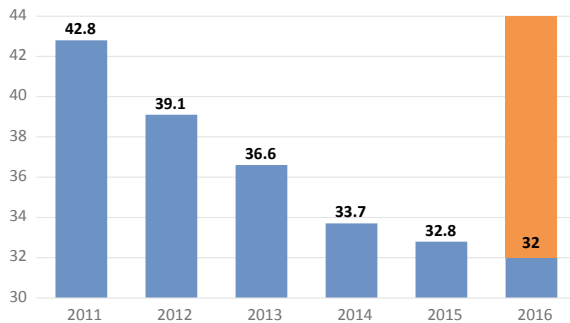
CO$_2$ emission levels for different size of trucks have been investigated to see the effect of truck size, by using a CO$_2$ calculator which is designed to calculate CO$_2$ emission of each particular shipment within company's transportation network. CO$_2$ emission amounts per ton sold for ambient product shipments with different truck sizes and different loadfill values have been calculated and shown in Table 2. Carbon emission level per tones product sold is higher in smaller trucks than bigger trucks. Therefore, total distance traveled by larger trucks should be increased when compared to smaller trucks.

Since the total CO$_2$ kg/tones sold decreases when the loadfill of the trucks increase, the shipments originated from different warehouses of Company X Turkey are investigated to examine the current situation. Findings for pallet loadfill of trucks for more than ten thousand shipments made from January 2016 to November 2016 are shown in Table 3.

Since the amount of order given by one customer in a time period is not always sufficient to constitute the whole loadfill of a truck, the route of a truck may consist of multiple customers in multiple cities in some cases. As the number of cities shipped per truck increases, the distance traveled by a truck increases, and this leads to an increase in CO$_2$ emission. While determining the route of trucks which serve to more than one city, Company X Turkey uses nearest neighborhood method. Thus, an individual truck serves firstly to the closest city to the warehouse which the truck is originated from. Lastly, the truck serves to the farthest city to the warehouse and returns to the warehouse without any loadfill on it. If the pallet loadfill in the final city is below a threshold, it means that the distance traveled by that truck with low pallet loadfill is likely to be high, which is an undesired situation for the firm. The

Table 2 CO$_2$ emission values of ambient product shipments for different truck sizes and different loadfill

Per shipment (kg CO$_2$/tones) moved	Pallet loadfill		
	100%	75%	50%
Tır (24 tones)	3.87	4.84	6.77
Tıryon (14 tones)	5.71	7.21	10.15
Tıryon (12 tones)	6.48	8.19	11.61
Kamyonet (3.5 tones)	15.61	19.44	27.10

Table 3 Pallet loadfill of the trucks originated from different warehouses

Product type	Pallet loadfill		
	<50%	50–75%	>75%
Chilled	0.6%	10.7%	88.7%
Ambient	2.2%	9.7%	88.1%
Frozen	0%	0%	100%

pallet loadfill values, when truck, which serves to more than one city, arrived at the final city are shown in Figs. 2 and 3.

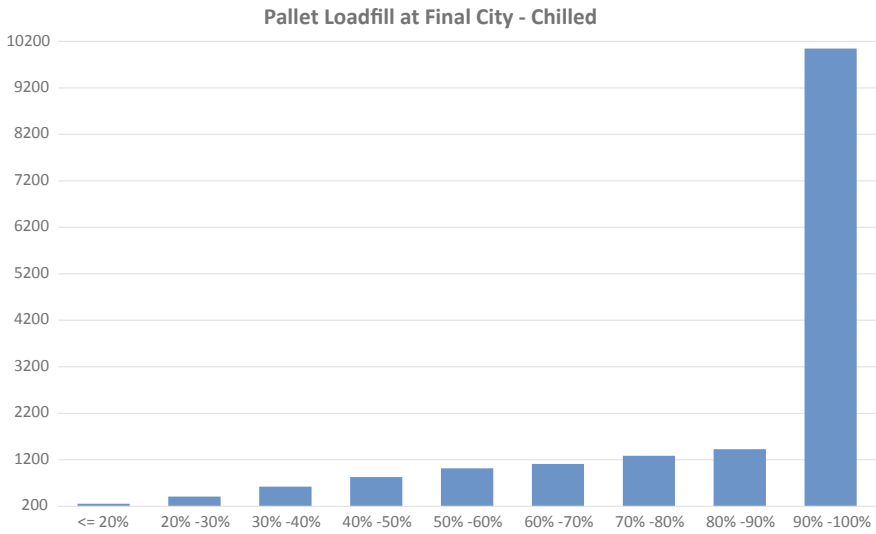**Fig. 2** Pallet loadfill when arrived at final city for trucks which serve to more than one customer and originated from City A chilled warehouse (for shipments made from January 2016 to November 2016)
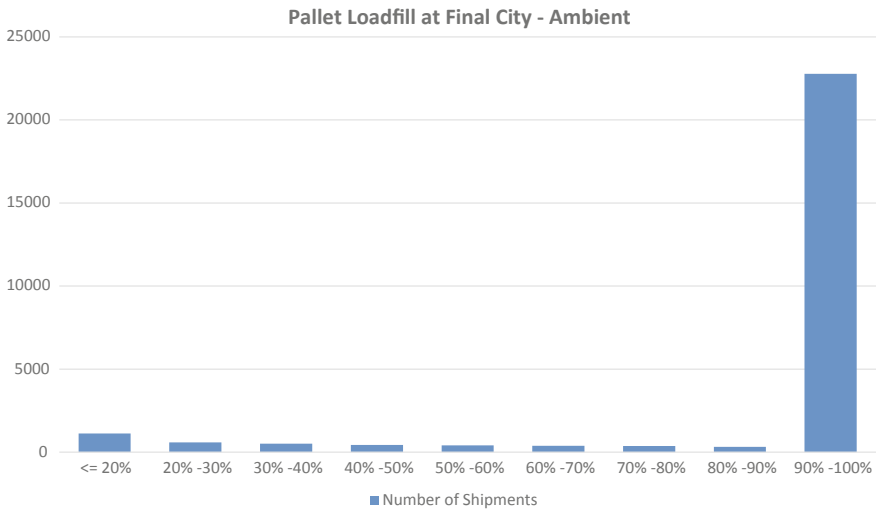

Fig. 3 Pallet loadfill when arrived at final city for trucks which serve to more than one customer and originated from ambient warehouse (for shipments made from January 2016 to November 2016)

Table 4 Findings about network efficiency of different product types

Product type	City/shipment	Customer/shipment	Pallet loadfill at final city (%)
Chilled	1.2–2	3.5–4	92
Ambient	1.2–2	2.4–3	90
Frozen	1.6–2	1.9–2	92

With a better transportation planning strategy, the average pallet loadfill when arrived at the final city can increase. The findings about the relevant performance measure tools are shown in Table 4.

The company uses X-Docks in some locations as small warehouses. Products are first shipped to X-Docks with large trucks, and they are transported with smaller trucks from X-Docks to customers. By this way, unnecessary movements of the goods from a customer to another customer can be avoided. Because of this, most efficient usage of X-Docks is aimed. Efficient use of trucks in terms of vehicle loadfill, improved networks, and effective use of advanced technological tools is expected to help to design a transportation system achieving 5% decrease in carbon dioxide emissions on a yearly basis. Addition to this, it is expected that the outcomes of the study are applicable, cost-effective, and feasible.

2 Materials and Method

As mentioned before, there are several root causes for the carbon emissions in logistics, and for these causes, it is possible to suggest alternative solution strategies. This study includes all branches of the diagram and suggests at least one solution method for all of the main reasons for CO_2 emissions in the fishbone diagram. Therefore, to reduce the number of proposed solutions and to gather them under a general heading, proposed system is divided into two groups as route-based proposed system and fleet-based recommendations portfolio.

2.1 Route-Based Proposed System

Since the carbon emission generated due to big trucks is estimated to be lower than those of smaller trucks when conditions are similar, a model is proposed which aims to maximize total traveled distance with big trucks, while the use of smaller trucks is minimized. New X-Dock locations and a vehicle routing model are proposed in which the predetermined number of trucks is transformed into CNG trucks. The aim is to create the new routing schedule for the transportation system based on the existing CNG station locations and CNG trucks whose number is determined by the firm. By doing so, the model will propose a set of customers who can be served via

CNG trucks and set of customers who will be served via existing diesel trucks. For this model, different runs will be obtained by changing the number of CNG trucks available to show the difference in the customer set that can be covered so that the firm can decide on the number of vehicles to be transformed into CNG. Methodologies are proposed in line with the product types which can be applied.

Chilled X-Dock Model

Strategic, tactical, and operational problems are generally known as distribution network design problems (DNDP). There is an interdependence between the location of facilities, number of facilities, and the routing from those facilities to multiple demand points. Because of this interdependence, a need for the combination of p-hub median problems and vehicle routing problems arose. Location-routing problem (LRP) is a special problem under DNDP. It combines facility location problem and vehicle routing problem. Therefore, in a single problem, it is possible to take strategic location and tactical or operational routing decisions simultaneously. In general, LRP is NP-hard and therefore, common approach in solving LRPs is to develop and use a heuristic approach to reduce the complexity in the model.

There are several inputs required for those models to be clearly identified, and some of those inputs are the same for both models, but some of them differ because of the vehicle-based differences between two types of goods. Since the real-life implementation of this includes cases where some of the customers cannot accept all types of trucks, the vehicle to customer assignments should also consider this constraint within the model. The aim of the proposed model is to minimize carbon emissions without giving up on any customer demand in a timely manner. Therefore, all inputs for the model are determined relatively with this aim in order to determine the outputs of the model, which are: X-Dock locations, the macro-scale transportation of products from warehouses to X-Dock locations, and the micro-scale transportation of products from X-Dock locations to customers with smaller trucks.

In order to offer a X-Dock model for chilled goods, LRP is developed to select the optimum X-Dock locations among 81 possible candidate cities. Then, the model routes vehicles between these X-Dock locations and cities in order to serve the customer portfolio of the company. There are three vehicle types in terms of their sizes. They are classified into two categories as big-sized trucks and smaller-sized trucks. In this case, the model should also consider the emissions from the cooler fuel, in addition to the engine fuel, since those vehicles should be transported in an at most 4 °C environment.

There are six sets within the model as $C = \{1, \ldots, n\}$, $S = \{n + 1, \ldots, n + S\}$, $V = \{1, \ldots, n + S + 1\}$, and $K = \{1, \ldots, b + s\}$ where b is the number of big-sized vehicles and s is the number of small-sized vehicles in the fleet, $BV = \{1, \ldots, b\}$ and $SV = \{1, \ldots, s\}$; which represent customers, X-Docks, all sites, all vehicles, big vehicles, and small vehicles, respectively. $N + S + 1$ shows the depot. $a1_k$ and $a2_k$ are the fuel consumption of empty small and big vehicles, respectively, where $b1_k$ and $b2_k$ represent the fuel consumption of small- and big-sized vehicles per ton

load and km. Additionally, for vehicles that transport frozen goods, $c1_k$ and $c2_k$ are cooler fuel consumption parameters for small and big vehicles. CAP1_k and CAP2_k are load capacities for vehicles, DIST_{ij} is the distance between vertex i and j, and finally, DIST2_s is used to define the distance between depot and a total number r of X-Docks. X_{ijk} is one if vehicle visits j right after visiting i, f_{ijk} shows the flow between i and j with vehicle k, W_s becomes one when a X-Dock is open, Y_{sk} is one if a big vehicle is assigned to one of opened X-Docks, and finally, u_{ik} is the order of visit to i with vehicle k.

$$\text{Min} \sum_{\substack{i,\,j\,\in\,V \\ i\,\neq\,j}} \sum_{k \in SV} \{[(a_k \times X_{ijk} \times \text{DIST}_{ij}) + (b_k \times f_{ijk} \times \text{DIST}_{ij})$$

$$+\left(c_k \times X_{ijk} \times \frac{\text{DIST}_{ij}}{\text{vel}}\right)] + \sum_{j \in S, k \in BV} [(a2_k \times Y_{jk} \times \text{DIST2}_s)$$

$$+(b2_k \times \text{flow}_{jk} \times \text{DIST2}_s) + \left(c2_k \times Y_{jk} \times \frac{\text{DIST2}_s}{\text{vel}}\right)]\} \quad \text{s.to}$$

$$\sum_{j \in S} Y_{jk} \leq 1 \quad \forall k \in BV \tag{2}$$

$$\sum_{i \in S, j \in V} X_{ijk} \leq 1, \quad \forall k \in SV \tag{3}$$

$$X_{ijk} = 0, \quad \forall i, j \in S, k \in SV \tag{4}$$

$$\sum_{i \in V, k \in SV} X_{ijk} = 1, \quad \forall j \in C \tag{5}$$

$$\sum_{j \in S, k \in SV} V_{ijk} = 1, \quad \forall i \in C \tag{6}$$

$$\sum_{\substack{i\,\in\,V \\ i\,\neq\,j}} X_{ijk} = \sum_{\substack{i\,\in\,V \\ i\,\neq\,j}} X_{jik} \quad \forall j \in C, k \in SV \tag{7}$$

$$\sum_{j \in C} X_{ijk} = \sum_{j \in C} X_{jik} \quad \forall i \in S, k \in SV \tag{8}$$

$$f_{ijk} \leq \mathrm{CAP}_k \times X_{ijk}, \quad \forall i, j \in V, k \in SV \tag{9}$$

$$\sum_{j \in V} f_{sjk} - \sum_{i \in C} \mathrm{DEM}_i \times V_{isk} = 0, \quad \forall s \in S, k \in SV \tag{10}$$

$$u_{ik} - u_{jk} + N \times X_{ijk} \leq N - 1, \quad \forall i \in V, j \in C, k \in SV \tag{11}$$

$$u_{ik} \leq N - 1, \quad \forall i \in C, k \in SV \tag{12}$$

$$\sum_{s \in S} W_s = r \tag{13}$$

$$X_{sjk} \leq W_s \quad \forall s \in S, j \in C, k \in SV \tag{14}$$

$$V_{jsk} \leq W_s \quad \forall s \in S, j \in C, k \in SV \tag{15}$$

$$X_{ijk} \in \{0, 1\} \quad \forall i, j \in V, \forall k \in SV \tag{16}$$

$$f_{ijk} \geq 0 \quad \forall i, j \in V, \forall k \in SV \tag{17}$$

$$V_{ijk} \in \{0, 1\} \quad \forall i \in C, j \in S, \forall k \in SV \tag{18}$$

$$u_{ik} \geq 0 \quad \forall i \in V, \forall k \in SV \tag{19}$$

$$W_s \in \{0, 1\} \quad \forall s \in S \tag{20}$$

The objective function for both of the chilled X-Dock model and the ambient X-Dock model minimizes the total carbon emissions due to the transportation of goods. The remaining constraints of the two models are the same. Constraint (2) allows each truck to visit at most one cross dock. Constraint (3) implies that each small vehicle must be assigned to at most one route starting from one of the open cross-dock locations. Constraint (4) prevents small vehicles to travel between cross docks. Constraints (5) and (6) allow each small vehicle to serve only one customer and each customer to be assigned to only one cross-dock location simultaneously. Constraint (7) and Constraint (8) are the flow balance constraint for small vehicles that leave customers and cross docks, respectively. According to the Constraint (9), the model blocks the possibility of transferring goods which excesses the capacity of trucks and determines the upper bound of flow. Constraints (10) makes sure that each truck leaving the cross dock is loaded with the total demand of customers that will be served with that specific truck. Constraints (11) and (12) are the Miller–Tucker–Zemlin

(MTZ) constraints. Constraint (13) is the constraint that determines the number of cross docks to be opened. Constraint (14) and Constraint (15) ensure that vehicles and customers can only be assigned to the same cross dock if that cross dock is opened.

Chilled CNG Model

In this study, the aim is to consider the routing and refueling station locating problems simultaneously. By this, it will result in a true optimal rather than a local optimal solution. At this phase of the study, node-based vehicle routing problem (N-BVRP) is developed for CNG implementation in vehicles used in the transportation of chilled and frozen goods. There is one main warehouse location for chilled goods, and it is located in City A. Warehouse is denoted as node 0 in the model. Within the scope of the model, based on the company's demand, it is assumed that CNG model can only be adapted to a single type of vehicle which is 22T 33P articulated trucks. There are three underlying assumptions as follows: There is exactly one visit to each customer every day, a customer set is defined in the model including only the customers who have demand for that day and the values in this set change according to the daily demands, and finally, each depot is assumed to be a station. It is possible for a vehicle to visit multiple CNG stations in one route if it cannot reach any point without any refuel. In the model, all locations are given based on city locations, and to prevent the model to block any revisit to a specific station, dummy CNG stations are defined and added to the set of stations by duplicating the original stations.

This time, set definitions are changed as $V = \{1, \ldots, n + 2S\}$ is the set for all sites, and $K = \{1, \ldots, M\}$ is the set of all vehicles. The customer set is kept the same, and however this time, a new set of CNG stations $S = \{n + 1, \ldots, n + 2S\}$ is introduced. This time the model and parameters are simplified as follows: fuel consumption of empty vehicle a, fuel consumption of vehicle per ton load and km b, and cooler fuel consumption of vehicle is c. The number of CNG vehicles in the fleet is M, and the capacities of those vehicles in tones are CAP_k where the fuel tank capacity if shown with Q. For the additional decision variables, R_{jk} is the remaining fuel level of vehicle k after delivered to j.

$$\text{Min} \sum_{\substack{i, j \in V, \ k \in K \\ i \neq j}} \left\{ \left[(a_k \times X_{ijk} \times d_{ij}) + (b_k \times f_{ijk} \times d_{ij}) \right. \right.$$
$$\left. \left. + \left(c_k \times X_{ijk} \times \frac{d_{ij}}{\text{vel}} \right) \right] \right\} \quad \text{s.to}$$

$$\sum_{\substack{j \in V \\ j \neq i}} X_{0jk} = \sum_{j \in V} X_{j0k} \quad \forall k \in K \tag{21}$$

$$\sum_{\substack{i \in V \\ i \neq j}} X_{ijk} = \sum_{\substack{i \in V \\ i \neq j}} X_{jik} \quad \forall k \in K, \forall j \in V/\{0\} \tag{22}$$

$$\sum_{i \in V} \sum_{k \in K} X_{ijk} = 1 \quad \forall j \in C \tag{23}$$

$$\sum_{\substack{i \in V \\ j \neq i}} \sum_{j \in S} X_{ijk} \leq 1 \quad \forall k \in K \tag{24}$$

$$\sum_{j \in V/\{0\}} X_{0jk} \leq 1 \quad \forall k \in K \tag{25}$$

$$f_{ijk} \leq \mathrm{CAP}_k \times X_{ijk} \quad \forall k \in K, \forall j \in V, \forall i \in V \tag{26}$$

$$R_{ik} - \left(a \times \mathrm{DIST}_{ij} \times X_{ijk}\right) - \left(b \times \mathrm{DIST}_{ij} \times f_{ijk}\right) - \left(c \times \frac{\mathrm{DIST}_{ij}}{\mathrm{vel}} \times X_{ijk}\right)$$
$$+ Q \times \left(1 - X_{ijk}\right) \geq R_{jk} \quad \forall k \in K, \forall i \in C, \forall j \in V, j \neq i \tag{27}$$

$$Q - \left(a \times \mathrm{DIST}_{ij} \times X_{ijk}\right) - \left(b \times \mathrm{DIST}_{ij} \times f_{ijk}\right) - \left(c \times \frac{\mathrm{DIST}_{ij}}{\mathrm{vel}} \times X_{ijk}\right)$$
$$+ Q \times \left(1 - X_{ijk}\right) \geq R_{jk} \quad \forall k \in K, \forall i \in C, \forall j \in V \tag{28}$$

$$\sum_{i \in V} f_{0ik} - \sum_{\substack{i \in V \\ j \in V, i \neq j}} \sum \mathrm{DEM}_i \times X_{ijk} = 0 \quad \forall k \in K \tag{29}$$

$$u_{ik} - u_{jk} + N \times X_{ijk} \leq N - 1 \quad \forall k \in K, \forall i \in V, \forall j \in V/\{0\}, j \neq i \tag{30}$$

$$u_{ik} \leq N - 1 \quad \forall k \in K, \forall i \in V/\{0\} \tag{31}$$

$$X_{ijk} \in \{0, 1\} \quad \forall i, j \in V, \forall k \in K \tag{32}$$

$$f_{ijk} \geq 0 \quad \forall i, j \in V, \forall k \in K \tag{33}$$

The objective function for both of the chilled CNG model and the frozen CNG model minimizes the total carbon emissions due to the transportation of goods. The remaining constraints of the two models are the same. Constraint (23) makes sure that each customer is served with only one truck. Constraint (24) implies that each station can be visited at most once during a tour. Constraint (25) allows each vehicle to be assigned to at most one route. According to the Constraint (26), the model blocks the

possibility of transferring goods which excesses the capacity of trucks and determines the upper bound of flow. Constraints (27) and (28) are the fuel restriction constraints that limit the movement of vehicles between vertices if there is no sufficient amount of fuel left in each vehicle. Constraint (29) makes sure that each truck leaving the depot is loaded with the total demand of customers that will be served with that specific truck.

Ambient X-Dock Model

For X-Dock offering model in ambient goods, the same strategy with chilled products is applied. For ambient products, the company owns four types of vehicles which are 24T 32P market trucks, 14T 20P fleet trucks, 3T 6P market trucks, and partial trucks. Since the company is not the owner of all goods in partial trucks, those types of vehicles are ignored in the model. Differences between two models are the change in the number of vehicle types and the change in the objective function. The difference in the objective function for the chilled X-Dock model represents the additional carbon dioxide emissions due to the use of cooler fuel in chilled trucks. The remaining constraints of the two models are the same.

Frozen CNG Model

For CNG model in frozen goods, the same strategy is used with chilled goods. Chilled and frozen goods' CNG models differ from each other in means of the number of warehouse locations. While there is one warehouse for chilled goods, there are three warehouses in City F, City A, and City B, where chilled goods are located.

2.2 Fleet-Based Recommendations Portfolio

Improvements in the aerodynamics of trucks can provide a high reduction in CO_2 emission. Additional retrofit technologies include aerodynamic fairings which are attached to different parts of trucks' cabin and trailers. Those fairings can be attached to a truck singly or as a combination. Improvements in the aerodynamics of truck can be achieved in two ways. The first option is replacing the existing fleet with new truck models which have more aerodynamic design and popular in transportation. The second option is improving the aerodynamics of existing fleet through additional retrofit technologies. Since replacing existing trucks with new trucks requires high investment, the second option is considered in this study.

Company Turkey uses different truck types and categories in its transportation network. There is not any standardization about the aerodynamic properties of the truck. Some of the trucks have already aerodynamic fairings attached to their trucks' cabin, while some of them do not have. The procurement department has informed that they are capable of buying the fairings around 720 Turkish Liras for one truck. Due to time restrictions, return of investment analysis was based on to 3% fuel reduction in frozen fleet of The Company Turkey. After some estimations in yearly kilometers and the demand stability for that fleet, the analysis has conducted that

the investment can be compensated in 1.85 month after the implementation of the strategy with yearly 96,000 L fuel saving.

According to the findings, it is seen that speed and acceleration play a significant role in carbon emissions. Speed and acceleration optimization reduces fuel consumption by 5–10% while decreasing the level of CO_2 emissions by 7%. Therefore, optimal speed values will be recommended to achieve lowest fuel consumption and carbon emission levels. Researches indicate that acceleration requires a large input of energy, and therefore for fuel economy and lower carbon emissions, steady speed is crucial since the rate of carbon emission is the lowest at a steady speed [5]. Based on the literature review and speed limitation given by General Directorate of Highways of Turkey, optimal speed ranges are recommended while taking vehicle size and road type into account.

Since tire inflation has a role in CO_2 emissions, it is important to concentrate on it to determine the optimal tire pressure for different types of trucks in different product types. Company Turkey uses market trucks for the shipment of ambient goods, therefore, study on determining tire inflation is performed on only chilled and frozen good. For the shipment of frozen goods, the company uses only one type of truck. However, there are 11 different contractors responsible for the shipment of chilled goods, and since properties of those trucks differ from each other, different tire pressure values are suggested relatively. Tables 5 and 6 show the technical properties of chilled and frozen trucks, respectively.

Maintenance of optimal conditions has a significant role in the sustainability of this application. In addition, regular control of tires and tire pressure at least once in a month will be useful to determine any changes in those values.

Table 5 Technical properties of chilled trucks and suggested tire pressure

Contractor	# of tires	Tire size	# of axle	Empty load on axles (kg)	Load on axles (kg)	Suggested tire pressure (bar)
Kutlu Tır	12	12.5 R 22.5	5	12,500	25,000	5.5
Kutlu Tır (Crone)	12	295/80 R 22.5	5	17,850	40,000	9
Gül Tıryon	10	12.5 R 22.5	3	11,700	13,300	5.5
Gül Tıryon	10	12.5 R 22.5	3	11,800	13,200	5.5
Gül Tıryon	10	12.5 R 22.5	3	12,300	12,700	5.5
Gül Kamyonet	6	215/75 R 17.5	2	3750	4150	4
Karsan 12 (25–20 Ford)	10	12 R 22.5	3	13,200	25,000	5.5
Karsan Tır	12	315 70 22.5	5	17,200	40,000	9

Table 6 Technical properties of frozen trucks and suggested tire pressure

Contractor	# of tires	Tire size	# of axle	Empty load on axles (kg)	Load on axles (kg)	Suggested tire pressure (bar)
Karsan Tır	12	315 70 22.5	5	17,200	40,000	9

2.3 Implementation Plan

Within the scope of proposed route-based recommendations, both CNG and X-Docks models are verified and validated by using Xpress optimization software for small instances of the problem up to eight nodes. However, since NP-hard models are combined to form the CNG model and the X-Dock model, it caused some issues while solving for optimality in bigger scenarios. While implementing the models to the transportation system of The Company Turkey, including all of the nodes in its transportation network, Xpress had difficulties finding the optimal solutions. At this stage, some heuristics are constructed in order to solve both of those models under real-life constraints.

For X-Dock model in both ambient and chilled goods, the optimization software was finding the optimal X-Dock locations based on daily customer locations, their demands, and the routes of each truck used from warehouse to selected X-Dock locations and from selected X-Dock locations to daily customers. As the first heuristic approach, problem is divided into two parts, and two separate Xpress models are created. K-hub median problem is utilized to determine the places of X-Docks in the first Xpress model by not considering the routes. In this Xpress model, the places of X-Dock locations are determined after the user inputs the number of X-Docks to be opened. While doing that, the model considers the demand and place of the customers of that day and sums the total demand of customers if they are in the same city. After obtaining the city-based demand amounts, Xpress is connected to an Excel file, which creates a distance matrix consisting only the cities in which the customer demand exists that day and sends it to the Xpress to use. With those information, Xpress reports the X-Dock locations which offer the least CO_2 emission. Therefore, the output of this first Xpress model is the X-Dock locations and the assignment of each city existing in that day's demand list to one of the X-Dock locations based on leading the least carbon emission level.

The next step after obtaining the determined places of X-Docks is to serve the customers by starting the supply of goods from the main warehouse to selected X-Dock locations with big trucks and rotating the smaller trucks from the X-Dock locations to customers in a proper route. A second Xpress model is created, which is performing the rotations of smaller trucks starting from the X-Dock locations to customers when the user enters the data to that model.

The nearest-neighbor heuristic is one of the first heuristics applied to determine a solution to travelling salesmen problem (TSP). To apply nearest-neighbor heuristic (NNH), the salesman starts from a randomly selected city and then visits the nearest

city after it. Then, it goes to the unvisited city closest to the city that has most recently been visited. A complete tour is obtained by leaving none of the cities unvisited. In both CNG model and X-Dock model, NNH is used as a construction heuristic to come up with an initial tour. The X-Docks locations are selected by inputting the number of X-Dock locations equals to one, three, and five as three different scenarios with the same customer demand input. Following the X-Dock selection, by using the emission calculator that has been created in the beginning of the study, corresponding carbon emissions generated from the routes starting and ending in those X-Dock locations are calculated. After analyzing the outcomes, an intensity map is created showing the optimal location for a X-Dock based on the number of times a city is selected. After determining the number of X-Dock locations and the places that are most effective to submit to the company, the cities in Turkey are assigned to those X-Dock locations so that users from the company will have the opportunity to route the trucks. The intensity maps for three different numbers of X-Dock scenarios are shown in Figs. 4, 5, and 6, respectively.

The CNG routing model could not achieve the routing based on available CNG station locations and the daily demand due to increase in the distance matrix since the stations were being entered to matrix multiple times to allow multiple visits for different trucks. Therefore, a similar logic to code NHH is adapted, but differently, it considers the remaining fuel level. By using the available number of trucks and considering their closeness to both depot and to each other, model creates the most logical set of customers to be shipped with the CNG trucks by using the available stations nearby if their remaining fuel is not adequate. The tours start and end in the main warehouse, and the model informs the user if the available number of trucks cannot serve all customers due to lack of CNG trucks to be utilized. Since the company has not completed the procurement of all CNG transformation in their fleet and CNG stations are not distributed as homogenously as diesel stations in Turkey, in order not to increase the total traveled distance, the final deliverable to the company

Fig. 4 X-Dock intensity map with one possible X-Dock location

Fig. 5 X-Dock intensity map with three possible X-Dock locations

Fig. 6 X-Dock intensity map with five possible X-Dock locations

will be the specific regions and cities to use CNG trucks to supply the daily demands of their customers at the end of the study.

3 Results and Discussion

In order to see the improvement compared to the current system and recommend the possible locations of X-Dock to be opened, thirty-day sales data are analyzed with three different numbers of X-Docks scenarios. As a result, from thirty days with one X-Dock location, the average CO_2 emission is 13,220.4 kg, with three X-Dock locations average is 8896.86 kg, whereas with five X-Dock locations average is 8116.8 kg which indicates the most efficient scenario. When those scenarios are compared to the current system of the company, improvements are obtained as 13.08

and 20.70% for the three and five X-Dock locations, respectively. However, for the one X-Dock location scenario, the average carbon emission value is higher than the current system, and it can be said that it is not reasonable to open one X-Dock location according to the current system of the company. Intensity maps show the possible locations of X-Docks to be opened from most preferred to least. Most preferred cities are shown with the darkest colors, while least ones are shown with lighter colors. Therefore, it can be said that for the three X-Dock locations, frequently offered cities are Bilecik, Sivas, and Kayseri, and for the five X-Dock locations, most preferred cities are Uşak, Sakarya, Sivas, Düzce, and Yozgat to open X-Dock locations.

4   Conclusion and Future Work

It can be seen that CNG fuel implementation has an important effect on reducing emission levels. Therefore, CNG implementation to some fleet, which uses routes that have easy access to CNG stations, decreases the amount of gas emissions since this scenario enables the driver to serve the customers without increasing the total traveled distance. For future work, considering customers' demand intensity, information could be reasonable to come up with possible locations to establish new CNG stations to benefit from both low cost and low-carbon emission opportunities, instead of settling for the existing stations and creating restricted routes because of the necessities.

References

1. Li H (2016) Study on green transportation system of international metropolises. Procedia Eng 137:762–771
2. Beuthe M, Gasca J, Greene D, Lee DS, Muromachi Y, Newton PJ, Plotkin S, Sperling D, Wit R, Zhou PJ (2007) In: Bose R, Kheshgi H (eds) Transport and its infrastructure. Climate change report, pp 323–380
3. Ramachandran K, Kanchustambham S, Wingerden V, Ladipo O, Aggarwal S, Rucke A, Rigel A (2012) In: Lee TM, Cullinen MS (eds) Road transport: unlocking fuel-saving technologies in trucking and fleets. Carbon war room research report, pp 1–28
4. Tice C (2013) How to calculate and reduce your business's carbon footprints? Entrepreneur. Accessed at https://www.entrepreneur.com/article/226467 as of 13 Nov 2016
5. Kay D (2013) The impact of 20 mph limits on carbon emissions and air quality. In: 4th annual 20mph conference
6. Wiedmann T, Minx J (2008) A definition of carbon footprint. In: Ecological economics research trends, Chapter 1. Nova Science Publishers, Hauppauage NY, USA, pp 561–596